Volume 6 Number 1 February 1984

Bulletin of Materials Science

N ACADEMY OF SCIENCES
ion with
NATIONAL SCIENCE ACADEMY

Bulletin of Materials Science

EDITORIAL BOARD

C N R Rao, *Indian Institute of Science, Bangalore (Chairman and Editor of Publi*
D Chakravorty, *Central Glass and Ceramic Research Institute, Calcutta*
K L Chopra, *Indian Institute of Technology, New Delhi*
K P Gupta, *Indian Institute of Technology, Kanpur*
P Rama Rao, *Defence Metallurgical Research Laboratory, Hyderabad*
P Ramachandra Rao, *Banaras Hindu University, Varanasi*
K J Rao, *Indian Institute of Science, Bangalore*
S Ramaseshan, *Indian Institute of Science, Bangalore*
S Ranganathan, *Indian Institute of Science, Bangalore*
N S Satya Murthy, *Bhabha Atomic Research Centre, Bombay*
A K Singh, *National Aeronautical Laboratory, Bangalore*
A P B Sinha, *National Chemical Laboratory, Pune*
C M Srivastava, *Indian Institute of Technology, Bombay*
E C Subbarao, *Tata Research Development and Design Centre, Pune*
G V Subbarao, *Indian Institute of Technology, Madras*
C V Sundaram, *Reactor Research Centre, Kalpakkam*
G Venkataraman, *Reactor Research Centre, Kalpakkam*
R Vijayaraghavan, *Tata Institute of Fundamental Research, Bombay*

Subscriptions

For India, Pakistan, Sri Lanka, Nepal, Bangladesh and Burma, contact
Editorial Office

For other countries, contact:
M/s J C Baltzer A. G.
Scientific Publishing Company
Wettsteinplatz 10
CH-4058 Basel
Switzerland
Telephone: 61-268925 Telex: 63475

Editorial Office:

Indian Academy of Sciences
P.B. No. 8005
Bangalore 560 080
India

The *Bulletin of Materials Science* is published by the *Indian Academy of S*
Bangalore in collaboration with the *Indian National Science Academy, New*
Financial assistance for publication of this Bulletin has been gratefully receive
the *Advanced Centre for Materials Science, Indian Institute of Technology, Kanpu*

Each volume of the Bulletin will consist of at least four numbers issued during th

Bulletin of Materials Science

Volume 6, January–December 1984

CONTENTS

erromagnetic resonance in metallic glasses: study of fracture, stress and hermal stability *R S Parashar, C S Sunandana and Anil K Bhatnagar* 1

nfluence of the presence of Fe^{2+} ion in nickel-zinc ferrite *C M Srivastava, S N Shringi, M J Patni and S M Joglekar* 7

etal-to-ceramic bonding in (Al_2O_3+Fe) cermet studied by Mössbauer pectroscopy *C Bansal* 13

össbauer spectroscopy of titanium-substituted iron garnets *C M Srivastava, S N Shringi, B Uma Maheshwar Rao, D Bahadur and Om Prakash* 17

agnetic properties of metallic glass $Fe_{39}Ni_{39}Mo_4Si_6B_{12}$ *B Bhanu Prasad, Anil K Bhatnagar, S Venkataraman and M N Chandrasekharaiah* 21

agnetic structure of zinc ferrite *C M Srivastava, S N Shringi and M Vijayababu* 27

Mössbauer study of hyperfine interactions in the boroferrite $Fe_{3-x}Ga_xBO_6$ = 0, 0.12) *M Vithal, R Jagannathan and N Ravi* 33

urie temperatures and 0°K magnetic moments of zinc-substituted lithium rrites *Pran Kishan, D R Sagar, S N Chatterjee, L K Nagpaul and K K Laroia* 39

reparation of single crystal films of magnetic bubble materials – Rare earth trium iron gallium garnets by liquid phase epitaxy and their physical roperties *Pragati Mukhopadhyay and B Uma Maheshwar Rao* 47

lectron transport in non-crystalline garnet films *D Bahadur, D Roy, B Singh and D Saran* 53

evelopment of pure and doped gamma ferric oxide *M R Anantharaman, K Seshan, S N Shringi and H V Keer* 59

ependence of microstructure on process variables in manganese zinc ferrites *N Venkataramani, R Aiyar, P S Sekhar and C M Srivastava* 65

igh temperature materials for magnetohydrodynamic channels *V K Rohatgi* 71

ffect of compositional modifications on the piezoelectric properties of spray ied lead zirconate titanate ceramics *Ramji Lal and P Ramakrishnan* 83

se of coal tar pitch for carbon-carbon composites *R L Seth, K K Datta, C L Verma, C Lal and V P Mittal* 91

Amine-cured epoxy/glass fibre composites *D S Varma and R G Raj* 99

Dielectric and pyroelectric studies on triglycine sulphate-polymer composites *K Sreenivas, T Sudersena Rao, Ajay Dhar and Abhai Mansingh* 105

Elevated temperature low cycle fatigue studies on AISI 304 steel *N K Sinha and P Vasudevan* 111

Structure and properties of an investment-cast austenitic stainless steel *P M Jebaraj, Malur N Srinivasan and M R Seshadri* 119

GT No. 1

Sophisticated equipment developed for growth and evaluation of perfection of nearly perfect crystals *Krishan Lal and Ajit Ram Verma* 129

Investigation of hydrogenous materials using neutrons *B A Dasannacharya and P S Goyal* 151

Electrochemical preparation of potassium gold cyanide *Indira Rajagopal and S R Rajagopalan* 165

Hydrothermal growth of $A^{II}B^{VI}$ semiconductors *V A Kuznetsov, I P Kuzmina and I M Sylvestrova* 177

Glass-metal particulate composites *D Chakravorty* 193

Fast ion conducting lithium glasses – Review *A R Kulkarni, H S Maiti and A Paul* 201

Lithium solid electrolytes and their applications *D N Bose and D Majumdar* 223

Electronic conduction in bulk $Se_{1-x}Te_x$ glasses at high pressures and at low temperatures *G Parthasarathy and E S R Gopal* 231

Electrical properties of polycrystalline silicon and zinc oxide semiconductors *S N Singh, S Kumari and B K Das* 243

MnO_2 catalysed carbon electrodes for dioxygen reduction in concentrated alkali *R Manoharan and A K Shukla* 259

Structural and magnetic investigations of some new boron containing rare earth intermetallic compounds *S K Malik, S K Dhar and R Vijayaraghavan* 263

On the mechanism of pairing in the BCS theory *C M Srivastava* 273

Structure and superconductivity in ternary systems of compounds *G V Subba Rao and Geetha Balakrishnan* 283

Pyroelectric materials *M R Srinivasan* 317

Amorphous state ferroelectricity, magnon scattering and phase stability in microparticle materials *M S Multani, P Ayyub, V R Palkar, M R Srinivasan, V Saraswati, R Vijayaraghavan and D O Shah* 327

Radiation effects in nuclear reactor materials – Correlation with structure *P Rodriguez, R Krishnan and C V Sundaram* 339

Structural disorder and solid state transformations in single crystals of $Zn_xCd_{1-x}S$ and $Zn_xMn_{1-x}S$ *M T Sebastian and P Krishna* 369

The pressure-volume relation of ytterbium up to 9 GPa
S Usha Devi and A K Singh 395

Some recent advances in materials technology
S Ramaseshan and N Balasubramanian 405

Yakham Seminar

Foreword 415

High resolution electron microscopy of long range ordered alloys
S Amelinckx, G Van Tendeloo and J Van Landuyt 417

High resolution electron microscopy of superconductors *C S Pande* 453

High resolution electron microscopy as a tool for structural investigations
G Singh and R S Rai 459

Scanning transmission electron microscopy and microdiffraction techniques
J M Cowley 477

Applications of scanning transmission electron microscope microanalysis in the study of materials *Gary R Purdy* 491

X-ray microanalysis in the transmission electron microscope *G W Lorimer* 503

Analytical electron microscopy of aluminium alloys
T R Ramachandran, D C Houghton and J D Embury 513

Electron microscopy of defect clusters produced by radiation damage
S Banerjee 537

Electron microscopy of layered single crystals grown by direct vapour transport method *M K Agarwal, P D Patel, J V Patel and J D Kshatriya* 549

Details of an imaging atom probe
V R Seshadri, K Neelakantan, E Mohandas and V S Raghunathan 569

Field ion microscopic observations of LaB_6 on tungsten
D B Joag, P L Kanitkar, M M Kanitkar and V M Shukla 573

Metallic glasses *C Suryanarayana* 579

High voltage electron microscope irradiation and observations in metallic glasses *R V Nandedkar and A K Tyagi* 595

High resolution electron microscopic studies of $HoAl_3$, $Er_{0.5}Gd_{0.5}Al_3$ and $Y_{0.91}Er_{0.09}Al_3$ in thin film form
Anand Kumar Singh, Ajay Kumar Singh, M S Gupta and O N Srivastava 603

Electron diffraction analysis of antimony films
P D Prabhawalker and Amarjit Singh 611

Formation of lamellar $M_{23}C_6$ on and near twin boundaries in austenitic stainless steels *B Sasmal* 617

ad. Disc. Mtg.

Foreword 625

Observations on the physical basis of mechanical behaviour *S Ramaseshan* 627

Shocks and high velocity deformation *R Chidambaram* 633

Computer simulation of tensile testing *V Sridhar* 643

Instabilities in yielding *G Venkataraman* 645

Serrated plastic flow *P Rodriguez* 653

Repeated yield drop phenomena as a cooperative effect *G Ananthakrishna* 665

Mechanisms and empirical equations for deformation and some principles of alloy design *T Balakrishna Bhat* 677

Superplasticity *K Srinivasa Raghavan* 689

Grain boundary-dislocation interactions *S Ranganathan* 699

Instabilities in first order phase transitions *S Banerjee* 701

Deformation and martensitic transformation *V Seetharaman* 703

Strength and electronic structure *K Govinda Rajan* 717

Ferroelasticity *V K Wadhawan* 733

Effects of mechanical deformation: Exoemission *G Mukhopadhyay* 755

Relevance of liquid state to solid state properties *H R Krishna Murthy and T V Ramakrishnan* 773

Elastic continuum theories of lattice defects: A review *Debendranath Sahoo* 775

Fracture of particulate composites *S Ray* 799

Experimental study of fluctuations in materials *K R Rao* 805

Elementary concepts in chaos and turbulence *Ramakrishna Ramaswamy* 807

Fractals *D Dhar* 81

Summary and outlook *V Balakrishnan* 82

GT No-2 Panel discussion 82

Phase transformations—a physicist's perception *G Venkataraman* 83

Growth of research and development in rare metals extraction in India *~~C V Sundaram~~ and C K Gupta* 90

Plutonium metallurgy in India *P R Roy and C Ganguly* 92

Internal friction in hexagonal metals *M K Asundi and C N Rao* 95

A novel method of RF powder sputtering *K Solomon Harshavardhan and K N Krishna* 97

Preparation and characterisation of β''-Al_2O_3 *H S Kalsi, R P Tandon, Balbir Singh, R C Goel and B K Das* 97

Evidence of screw dislocation on (002) cleavages of lithium carbonate single crystals *K S Raju, M Palaniswamy, P Ramasamy and G S Laddha* 99

Etch pit observations on the habit faces of gel grown nickel molybdate crystals *K V Kurien and M A Ittyachen* 99

Elastic properties of As-Sb-Se glasses *A Giridhar, Sudha Mahadevan and A K Singh* 100

DC electrical conductivity of Na_2O-ZnO-B_2O_3 glass system *R V Anavekar, N Devaraj and J Ramakrishna* 100

Photon, electron and ion beam induced physical and optical densification in chalcogenide films
K L Chopra, L K Malhotra, K Solomon Harshavardhan and S Rajagopalan 1013

Oxidation of thin films of tin at room temperature in hydrogen sulphide atmosphere *C I Muneera and V Unnikrishnan Nayar* 1019

Annealing behaviour of electron-beam deposited tin dioxide films
Arjeesh Gupta, Poonam Gupta and V K Srivastava 1029

Temperature dependence of microhardness in mixed crystals
Sankar P Sanyal and R K Singh 1035

Some aspects of dislocation-precipitate interaction in underaged aluminium-germanium alloy *Kishore* 1041

Evaluation of magnetic hyperfine field distributions from Mössbauer spectra of disordered alloys and metallic glasses *C Bansal* 1047

Spin wave relaxation processes in polycrystalline yttrium iron garnets
S N Bhatia, P B Joshi and C M Srivastava 1053

Spin-wave excitations in amorphous ferromagnets
Anil K Bhatnagar, B Bhanu Prasad, N Ravi and R Jagannathan 1059

Infrared absorption in spinel ferrites
T T Srinivasan, C M Srivastava, N Venkataramani and M J Patni 1063

Influence of spin orbit coupling and lanthanide contraction on the exchange interaction in rare earth garnets *C M Srivastava, C Srinivasan and R Aiyar* 1069

Electrical properties of films at microwave frequencies *D C Dube* 1075

Surface modification of polyvinyl chloride towards blood compatibility
Geetha Kurian and Chandra P Sharma 1087

Bull. Mater. Sci., Vol. 6, No. 1, February 1984, pp. 1–5.
© Printed in India.

Ferromagnetic resonance in metallic glasses: study of fracture, stress and thermal stability

R S PARASHAR, C S SUNANDANA AND ANIL K BHATNAGAR
School of Physics, University of Hyderabad, Hyderabad 500 134, India

Abstract. Effects of fracture, stress and isothermal annealing of Fe–Ni based metallic glasses have been investigated using the ferromagnetic resonance technique. FMR linewidth is quite sensitive to changes in the magnetic and structural order in metallic glasses, and FMR lineshape seems to provide useful qualitative information on the mechanical state of these systems. Our observations are compared with recent work of Baianu and co-workers.

Keywords. Ferromagnetic resonance; metallic glasses; fracture; stress; thermal stability.

1. Introduction

Mechanical and thermal stability are two important aspects in the studies of metallic glasses from theoretical as well as practical points of view. These alloys are distinguished by their exceptional strength and distinctive deformation mechanism (Davis 1976). Magnetic properties of ferromagnetic metallic glasses and the influence of annealing on these properties have received much attention in recent years in view of their potential technological applications (Lubrosky *et al* 1978). Among many other techniques to study the effects of thermal and mechanical treatments on the magnetic and mechanical properties of metallic glasses, ferromagnetic resonance (FMR) is a convenient and very sensitive technique (Baianu *et al* 1979a, b) since FMR linewidths and lineshapes are very sensitive to the magnetic and mechanical states of the system. In this paper our preliminary results of such studies on $Fe_{40}Ni_{40}P_{14}B_6$ (Metglas 2826), $Fe_{29}Ni_{49}P_{14}B_6Si_2$ (Metglas 2826B) and $Fe_{40}Ni_{40}B_{20}$ (vitrovac 0040) are reported.

2. Experimental

Commercially available ferromagnetic metallic glasses $Fe_{40}Ni_{40}P_{14}B_6$ and $Fe_{29}Ni_{49}P_{14}B_6Si_2$ were received from Allied Chemical Corp. (USA) and $Fe_{40}Ni_{40}B_{20}$ was received from Vacuumschmelze (West Germany) in thin ribbon forms. Fractured specimens were prepared by cutting/fracturing by (1) bending on a sharp surgical knife edge by 180° (method A), (2) use of a sharp pair of scissors (method B), and (3) a rotating diamond wheel (method C). All the specimens were cut perpendicular to the long ribbon axis. For annealing studies, samples were first polished by 600 grade emery paper and then isothermally annealed at different temperatures and for different times.

First derivative FMR spectra were recorded on a X-band (9·3 GHz) JEOL ESR spectrometer (model FE-3X) using approximately 1 mW incident radiation power. Specimens were mounted such that the plane of each specimen and its long ribbon axis were always parallel and perpendicular to the applied magnetic field, respectively. For isothermally treated specimens only a small (approximately 1 mm diameter) central portion of the ribbon was exposed to the incident microwaves to minimize demagnetization effects. The observed peak-to-peak FMR linewidth (ΔH_{pp}) of the polished ribbon was approximately 235 Oe.

3. Results and discussion

3.1 *Fracture study*

Amorphous metallic ribbons, when deformed at temperatures much less than the glass transition temperature, develop highly inhomogeneous shear bands. The failure occurs instantaneously at the yield stress by shear rupture through an intense shear band. Propagation of the shear band on an excess volume front gives rise to distinct surface features depending upon the deformation method used, since the distribution of forces exerted by different fracturing methods would be different. So far, fracture studies in these alloys seem to have been limited only to the optical and electron microscopic investigations. In FMR, the magnetization variation at the boundaries as well as surface pits, grain boundaries, and disordered scattering all make contributions to the intrinsic lineshape and linewidth. Hence, FMR studies along with those of scanning electron microscope (SEM) on these alloys could give more detailed information on the magnetic state of the fractured boundaries. SEM observations have shown that fracturing of a metallic glass ribbon by methods A and B give rise to highly inhomogeneous surface boundaries while method C gives rise to the least deformation (Parashar *et al* 1982). The width of the shear lines are observed to vary in the range 0·8–2 μm. FMR results on a Metglas 2826B alloy specimen cut using method A show distorted lineshape, additional satellites and a few extra resonance peaks as shown in figure 1a. We have observed that such effects are considerably reduced in the scissors-cut specimens, as shown in figure 1b, indicating it to be a comparatively better of way of cutting of a metallic glass which gives rise to less mechanical damage at the surface boundary, and less fluctuations in the height of shear markings. Removal of such deformation would result in a smoother surface which would in turn reduce the linewidth. This was done by electropolishing of the specimen. FMR result on a typical electropolished sample is shown in figure 1c. A comparison of FMR spectra in figure 1 shows that the electropolished specimens give smooth and narrow resonance curves. The present results are in qualitative agreement with those reported earlier by Baianu *et al* (1979a). In the case of the diamond wheel cut specimen it was observed that the linewidth changes before and after electropolishing the specimen were minimal indicating that this cutting method, method C, induces least deformation in the specimen.

3.2 *Effect of stress annealing*

It is well-known that the application of a tensile stress tends to align magnetic domains in ferromagnetic amorphous alloys along the direction of the applied stress. The resistivity has been observed to show a linear variation with the applied stress and the slope of the curve depends upon the sign of the magnetostriction coefficient of the amorphous alloy. This behaviour of magnetic metallic glasses is similar to that observed for ferromagnetic crystalline metals. It has been observed that $Fe_{49}Ni_{29}P_{14}B_6Si_2$, when annealed for 20 hr at 450 K, still shows amorphous structure when examined by x-ray diffraction measurements. However, we have observed that

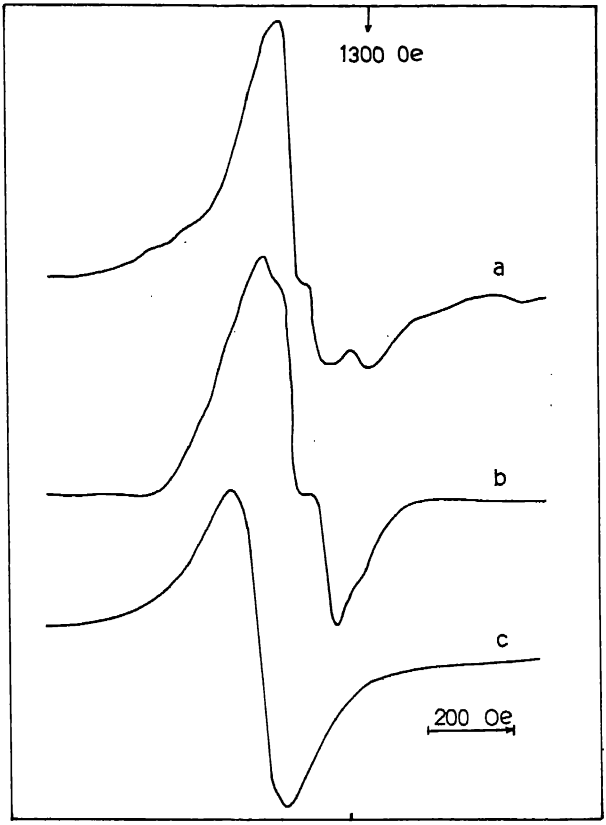

Figure 1. FMR spectra of $Ni_{40}Fe_{40}B_{14}P_6$ amorphous alloy ribbons fractured by (**a**) bending, (**b**) using scissors, and (**c**) scissors, and electropolished subsequently.

samples stress-annealed (temperature varied at the rate of 3 K/min upto 440 K and a load of 9.8 kg/mm^2) showed some precipitated crystalline phase (Parashar and Bhatnagar 1983). Stress-annealed samples have also found to exhibit broad FMR peaks whose linewidths are larger when compared with stress free annealed samples under similar experimental conditions (Parashar and Bhatnagar 1983).

3.3 *Isothermal annealing study*

In view of their metastable equilibrium configuration resulting from rapid quenching, metallic glasses are thermodynamically unstable with respect to both crystalline and fully-relaxed amorphous states. Thus structural relaxations can be induced in these alloys by annealing them at temperatures considerably below their crystallization temperatures. Although amorphous alloys possess neither long-range order nor vacancies, it is nevertheless likely that the structural changes occurring during relaxation involve both the amount and distribution of free volume and the nature of local atomic arrangement. However, they do possess extensive short-range order (quite akin to their crystalline counterparts) which is strongly temperature-dependent. Annealing decreases the fictive temperature (the temperature at which the structure would be in equilibrium with the undercooled liquid) and further increases the short-range order until metastable equilibrium is attained at the annealing temperature. This relaxation, involving collective motion of atoms and exchange of atoms of different chemical species, results in changes of variety of physical properties *e.g.* Curie temperature, thermal expansion coefficient and magnetic amisotropy etc. We have used FMR linewidth as a probe to study the effect of isothermal annealing in $Fe_{40}Ni_{40}B_{20}$ ribbons.

Figure 2 gives the typical variation of ΔH_{pp} with annealing time, for sample annealed at 100°C which is substantially lower than the crystallization temperature (~ 400°C) for $Fe_{40}Ni_{40}B_{20}$ glassy alloy. Two maxima, one around 1 min and the other 10 min, are clearly seen. These peaks, which seem to characterize the short-term and long-term annealing behaviour of this alloy, need to be accounted for in terms of structural and magnetic ordering influenced by annealing.

Baianu *et al* (1979b) in their FMR study on $Fe_{40}Ni_{40}P_{14}B_6$ ribbons have observed a rather different time-dependence for samples annealed at 350°C. The linewidth decreases rapidly at first and slowly later upto annealing periods of 60 minutes and increases thereafter. They have attributed this linewidth narrowing due to magnetic ordering of magnetic dipoles in a matrix involving phosphorous rich regions and with the stress relief within the sample. However, in the present amorphous alloy, annealing at lower temperature (100°C) which causes an increase in linewidth, may be associated with changes in the magnetic atom neighbourhood, by way of local structural regrouping and enhancement of atomic structural inhomogeneity through cluster formation. Mössbauer effect studies indeed show the clustering of Fe–Ni atoms in annealed $Fe_{40}Ni_{40}B_{20}$ samples (Vincze and Babic 1978). Decrease in electrical resistivity may also be a possible cause of an increase in the linewidth (Baianu *et al* 1979a). However, resistivity changes observed by Stubicar *et al* (1977) in $Fe_{40}Ni_{40}B_{20}$ are too small to be correlated with the linewidth changes observed here; therefore, the reason for an increase in linewidth of FMR of $Fe_{40}Ni_{40}B_{20}$ may be due to other reasons like clustering etc.

Recent studies of time-dependence of Young's modulus during isothermal annealing, employing ultrasonic techniques, on $Ni_{40}Fe_{40}B_{20}$ ribbons (Scott and Kursumovic

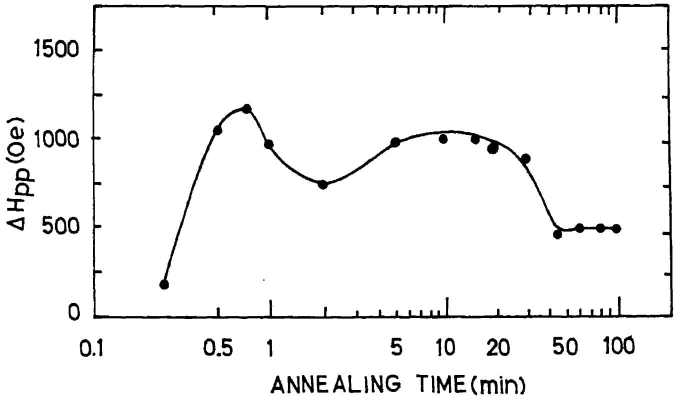

Figure 2. Dependence of FMR linewidth on annealing time for $Ni_{40}Fe_{40}B_{20}$ amorphous alloy ribbons isothermally annealed at 100°C.

1982) and dilatometric studies on the same sample (Kursumovic *et al* 1980) give additional insight into the local atomic rearrangement involving quenched-in defects when they are subjected to isothermal annealing. These defects are nothing but local structural deviations from ideal glass by way of distinctly different metalloid polyhedra around magnetic alloy and annealing causes these defects to relax and their number and mobility decrease as a consequence.

The study by Scott and Kursumovic (1982), Kursumovic *et al* (1980) and Greer and Leake (1979) are 'crossover experiments' in which plots of ultrasonic velocity, dilatation and T_c against annealing time exhibit a minimum for annealing times of the order of a minute. This 'crossover' has been described as a relaxation process involving at least two relaxation times. On the other hand the plot of thermal expansion of Metglas 2826 and Metglas 2826B ribbons against annealing time shows a maximum in annealing time (~ 5 min) when annealed at 250°C, which has been attributed to 'initial rapid stress relaxation' (Steinberg *et al* 1980). Potocky *et al* (1982) have recently investigated the dependence of coercive force on the annealing time on amorphous $Fe_{60}Ni_{20}B_{20}$ ribbons isothermally annealed at temperature well below crystallization temperature. They find that the relaxation of 'quenched-in' stress upon annealing takes place in two stages, the first involving the stress centres and the other involving topological changes. In the light of these observations, the twin maxima in the FMR linewidth vs annealing time plot observed in the present study could be reasonably attributed to relaxation processes involving two magnetically and chemically distinct species. However, a quantitative characterization of relaxation times and the species involved needs theoretical models to be developed which must take into account the nature, number and distribution of metalloid neighbourhoods as well as the magnetic interaction among them. Further more extensive work is continuing to understand this behaviour.

Acknowledgement

The work has been supported by the Science and Engineering Research Council (DST, India).

References

Baianu I C, Patterson J and Rubinson K A 1979a *Mater. Sci. Engg.* **40** 273

Baianu I C, Rubinson K A and Patterson J 1979b *J. Phys. Chem. Solids* **40** 941

Davis L A 1976 in *Rapidly quenched metals,* (eds) N J Grant and B C Giessen (MIT: Cambridge, USA) vol. 1, p. 369

Greer A L and Leake J A 1970 *J. Noncrystalline Solids* **33** 291

Kursumovic A, Scott M G and Cahn R W 1980 *Scr. Metall.* **14** 1245

Luborsky F E, Frischmann P G and Johnson L A 1978 *J. Magn. Magnetic Mater.* **8** 318

Parashar R S, Sunandana C S and Bhatnagar A K 1982 Preprint

Parashar R S and Bhatnagar A K 1983 *J. Magn. Magnetic Mater.* **36** 56

Potocky L, Zentko A, Novak L and Svidron V 1982 *J. Magn. Magnetic Mater.* **26** 115

Scott M G and Kursumovic A 1982 *Acta Metall.* **30** 853

Steinberg J, Tyagi S and Lord Jr A E 1980 *J. Noncrystalline Solids* **41** 279

Stubicar M, Babic E, Subasic D, Pavuna D and Marohnic Z 1977 *Phys. Status. Solidi* **A44** 339

Vincze I and Babic E 1978 *Solid State Commun.* **27** 1425

Bull. Mater. Sci., Vol. 6, No. 1, February 1984, pp. 7–12.
© Printed in India.

Influence of the presence of Fe^{2+} ion in nickel-zinc ferrite

C M SRIVASTAVA, S N SHRINGI, M J PATNI* and
S M JOGLEKAR

Department of Physics, *School of Materials Science, Indian Institute of Technology, Powai, Bombay 400 076, India

Abstract. The presence of small amounts of Fe^{2+} ion in nickel zinc ferrite significantly influences some of its magnetic properties. The lattice parameter increases slightly and the increase Δa is independent of x. The variation of magnetization with zinc concentration is explained on the basis of the Yafet–Kittel model. Increase in the Néel temperature on Fe^{2+} substitution in $Zn_xNi_{1-x}Fe_2O_4$ is remarkable. This has been explained on the basis of a four sublattice model. Our analysis shows that J_{AB} (d^5-d^5) interaction is most affected. The influence of Fe^{2+} ions on the relaxation processes in the Mössbauer line shapes of Ni–Zn ferrite is also investigated and is compared with Cu^{2+} doped Ni–Zn ferrite.

Keywords. Electron exchange; exchange constants; Jahn–Teller ion spinels; sublattices; nickel–zinc ferrite.

1. Introduction

Introduction of small amounts (~10%) of Jahn–Teller ion like Cu^{2+} in Ni–Zn and Fe–Zn ferrites produces local distortion which significantly affects their various magnetic properties (Srivastava *et al* 1981a) and influences their Mössbauer spectra (Srivastava *et al* 1981b). To further investigate the effect of such a crystal distortion on the properties of exchange coupled magnetic ions in magnetically ordered systems we have introduced small quantity of Fe^{2+} ions in Ni–Zn ferrites. In the present investigation we have studied the compositions $Ni_{1-x-y}Zn_xFe^{2+}_y$ ($0 < x < 0.7$; $y = 0$ and 0.1) $Fe^{3+}_2O_4$. The results obtained from Néel temperature, magnetization and Mössbauer measurements are discussed here.

2. Experimental

Samples with compositions $Ni_{1-x-y}Zn_xFe_yFe_2O_4$ ($0 < x < 0.7$; $y = 0$ and 0.1) were prepared using the ceramic technique. In order to maintain the ferrous content, the samples were sintered in purified nitrogen atmosphere. The presintered samples were sintered between 1250 and 1350°C. Nitrogen atmosphere was also maintained during the cooling cycle.

The x-ray analysis carried on the above samples identified them as single phase spinels. The lattice parameter a is plotted in figure 1. The lattice constant increases slightly for all values of x and this increase, Δa, is independent of x. The ferrous content of the samples was determined using the standard chemical analysis (Srivastava *et al* 1976).

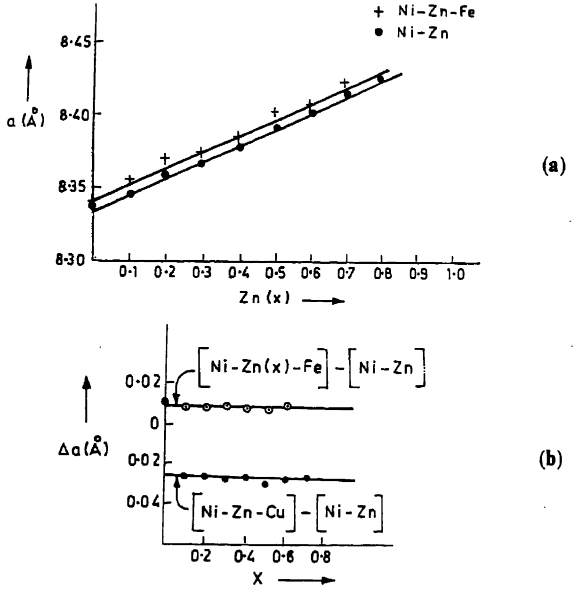

Figure 1. a. Variation of lattice parameter with Zn concentration in Ni–Zn and Ni–Zn– systems. **b.** Change in lattice parameter as a function of Zn concentration for Ni–Zn–Cu a Ni–Zn–Fe systems.

3. Results and discussion

3.1 *The Néel temperature measurements*

The Néel temperature (T_N) for $Ni_{0.9-x}Zn_xFe^{2+}_{0.1}Fe_2O_4$ series is found by the initi susceptibility (χ_i) method. A typical χ_i *vs* T curve is shown in figure 2. The sharp fall the χ_i curve as seen in figure 2 is characteristic of a single phase spinel ferrite. Variatic of T_N with Zn concentration is given in figure 3. The T_N is found to increase c Fe^{2+} ($\sim 10\%$) substitution in Ni–Zn ferrites. The change in T_N for 10% Fe^2 substitution in $Zn_xNi_{1-x}Fe_2O_4$ is about 100°C for values of x from 0 to 0·7. So far suc a large increase in T_N has not been reported. The observed variation of T_N can t explained on the basis of the four sublattice model. The tetrahedral (A) site in tl spinnel ferrite is occupied by Fe^{3+} ions while the octahedral (B) site is split into thr sublattices, corresponding to Fe^{3+}, Fe^{2+} and Ni^{2+} ions. On fitting the experiment data on the above model one observes that the exchange constants show a very min dependence on Zn concentration. The $J_{AB}(d^5 - d^5)$ interaction is most affected, an seems to have largest influence on T_N. In Ni–Zn ferrite this is 30°K while in tl Ni–ZnFe^{2+} ferrite it is 35°K. The increase in $J_{AB}(Fe^{3+}$–$Fe^{3+})$ interaction on Fe^2 introduction may be attributed to the propagating local distortion resulting fro electron hopping $Fe^{3+} \rightleftharpoons Fe^{2+}$ on the B-sublattice. The experimental and theoreticall obtained T_N is plotted in figure 3.

3.2 *Magnetization measurements*

The observed variation of the magnetization at room temperature for Ni–Zn an Ni–Zn–Fe^{2+} systems is shown in figure 4. It is observed that the magnetizatic

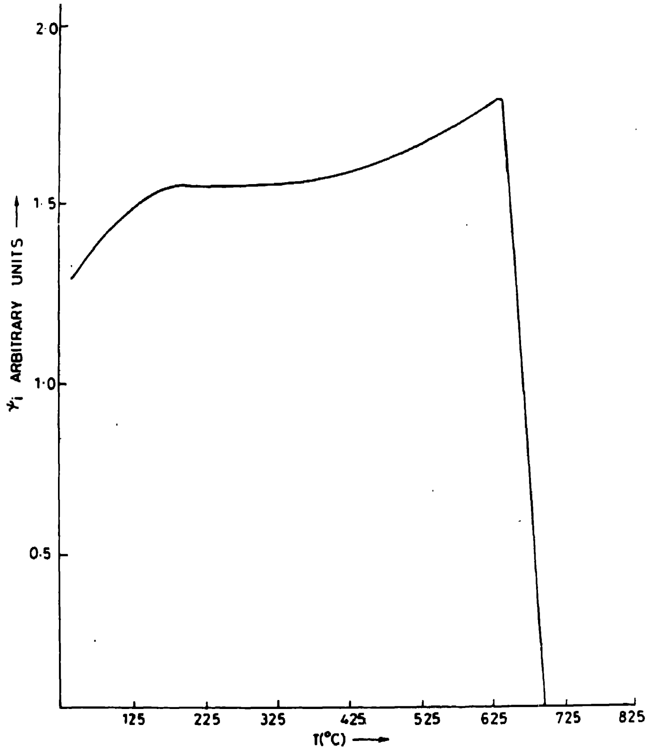

Figure 2. Initial susceptibility *vs* temperature.

increases with Zn-concentration upto $x = 0{\cdot}3$ and then falls off with further increase in Zn-concentration. This variation of magnetization with Zn concentration can be explained on the basis of the Yafet–Kittel model of spin-canting on the B-sublattice (Satya Murthy *et al* 1969).

3.3 *Mössbauer effect measurements*

Introduction of 10% of Cu^{2+} in Ni–Zn ferrite creates local distortion inhibiting the localised domain wall oscillations responsible for the occurrence of central doublet superimposed on the magnetic spectra (Srivastava *et al* 1981b). However, when Fe^{2+} ion which is also a Jahn–Teller ion is introduced in Ni–Zn system, it is observed that the central doublet continues to be present in the system and does not disappear as in the case of Cu substitution.

A possible explanation for this observation is as follows.

From previous studies (Srivastava *et al* 1976) it was shown that the atoms which lie within the range of domain wall displacements, give rise to the doublet. A local distortion produced due to Cu^{2+} seems to inhibit the localised domain wall oscillations. However, if the distortion propagates at the rate higher than the rate of the domain wall oscillations then it is possible to see again the effect of localised domain wall oscillation in the Mössbauer spectrum. Introduction of Fe^{2+} leads to a propagating local distortion due to electron hopping $Fe^{2+} \rightleftharpoons Fe^{3+}$ on the B-sublattice.

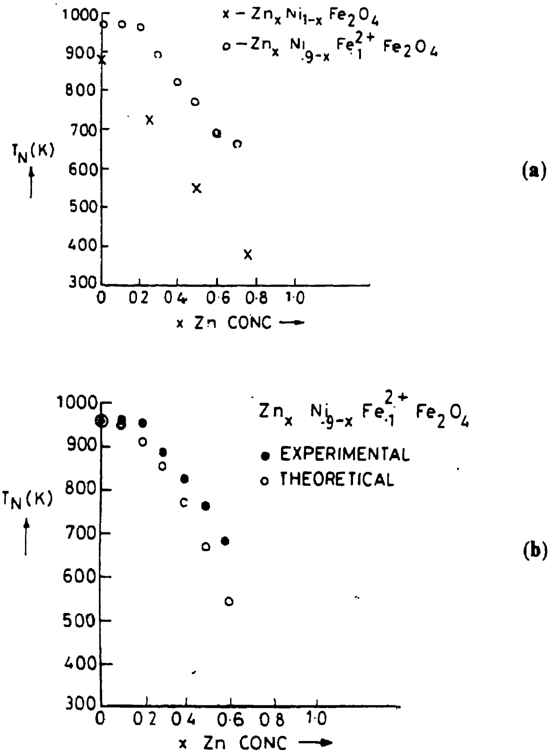

Figure 3. a. Dependence of the Néel temperature T_N on Zn concentration b. Dependence of the Néel temperature T_N on Zn concentration.

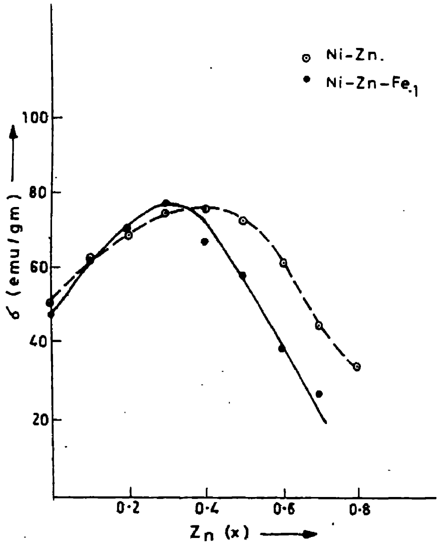

Figure 4. Variation of magnetization with Zn concentration (x), in Ni-Zn and Ni-Zn-Fe systems at 300 K.

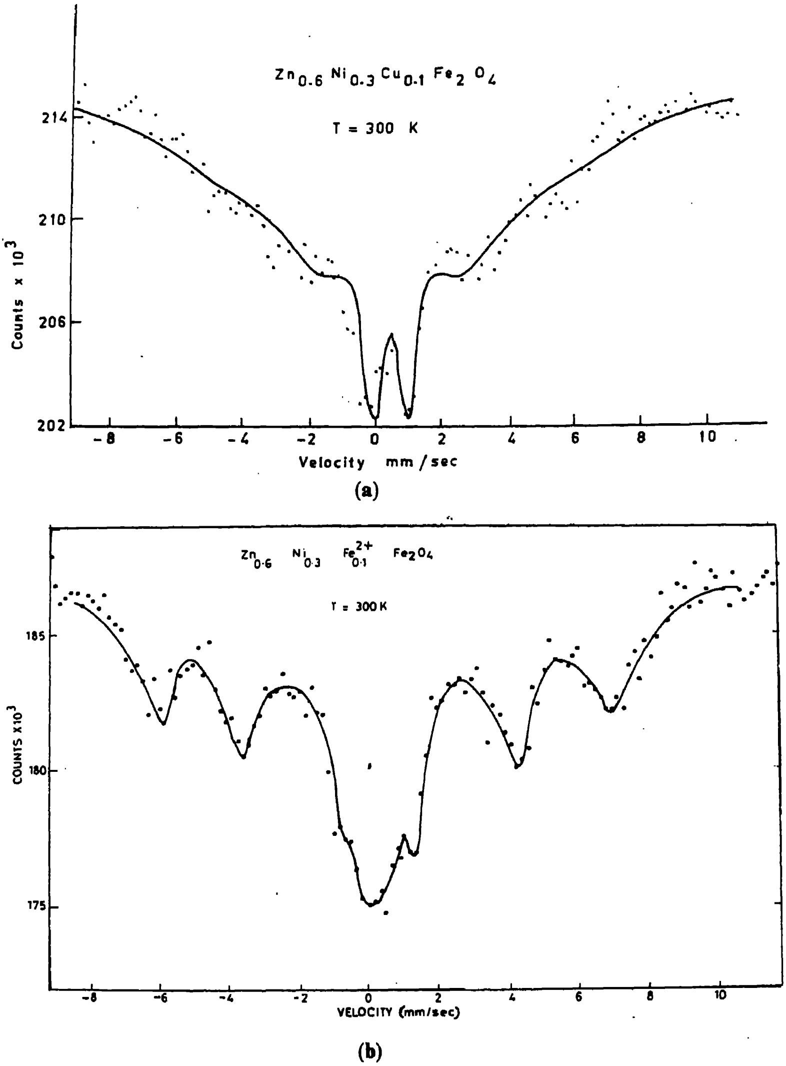

Figure 5. Mössbauer spectra of **a.** $Zn_{0\cdot6}Ni_{0\cdot3}Cu_{0\cdot1}Fe_2O_4$ and **b.** $Zn_{0\cdot6}Ni_{0\cdot3}Fe_{0\cdot1}Fe_2O_4$ at 300 K.

This electron exchange frequency is higher than the frequency of domain wall oscillations. As a result the Mössbauer spectrum remains unaffected after Fe^{2+} substitution. For comparison we give 300 K Mössbauer spectra of Ni–Zn–$Cu^{2+}_{0\cdot1}$ and Ni–Zn–$Fe^{2+}_{0\cdot1}$ for $x = 0\cdot6$ in figure 5.

4. Conclusions

The effect of crystal distortion due to Jahn–Teller effect on thermally-excited localised domain wall oscillations in Ni–Zn spinel ferrites has been studied by substituting small amounts of ferrous ions in these ferrites. The changes in lattice constant, magnetization, Néel temperature and Mössbauer line shapes is different from the changes observ when Cu^{2+} is substituted in Ni–Zn ferrites. The observed effects are explained on t basis of propagating local distortion resulting from the electron exchan $Fe^{2+} \rightleftharpoons Fe^{3+}$ on the *B*-sublattice.

References

Satya Murthy N S, Natera M G, Youssef S I, Begam R J and Srivastava C M 1969 *Phys. Rev.* **181** 9

Srivastava C M, Shringi S N, Srivastava R G and Nandikar N G 1976 *Phys. Rev.* **B14** 2032

Srivastava C M, Patni M J, Srinivasan G and Srinivasan T T 1981a *Bull. Mater. Sci.* **3** 225

Srivastava C M, Shringi S N and Joglekar S M 1981 *Proceedings International Conference on the Applicati of Mössbauer Effect (ICAME), Jaipur, Published by INSA, New Delhi* p. 813

Bull. Mater. Sci., Vol. 6, No. 1, February 1984, pp. 13–16.
© Printed in India.

Metal-to-ceramic bonding in $(Al_2O_3 + Fe)$ cermet studied by Mössbauer spectroscopy

C BANSAL

School of Physics, University of Hyderabad, Hyderabad 500 134, India

Abstract. Although a strong thermo-compression bond is formed between some metals and ceramics, the bonding mechanism is not clearly understood. In the present work ^{57}Fe Mössbauer spectroscopic study of $(Al_2O_3 + Fe)$ cermet is carried out to investigate the reason of adherence at the metal-ceramic interface. The isomer shift, quadrupole splitting and linewidths of Mössbauer spectra indicate that a compound of the spinel type $FeO \cdot Al_2O_3$ is formed but the site symmetry around Fe may be locally distorted by a small amount as compared to that for stoichiometric $FeAl_2O_4$.

Keywords. Cermet; thermo-compression bonds; Mössbauer spectroscopy; spinel.

1. Introduction

A strong bonding between metals and ceramics is produced by thermal compression. It is of interest to find out why adherence is produced between a non-reactive metal (such as Fe) and a refractory oxide (Al_2O_3) although from a thermodynamic point of view the free energy decrease for metal oxide formation (−58 kcal for FeO) is less than the energy required to reduce the refractory oxide (−125 kcal per oxygen atom for Al_2O_3). The methods used to produce these composites and the earlier investigations have been discussed by Klomp (1970). It was earlier hypothesised that there is first an evaporation of Fe on alumina surface and subsequently a contact between the metal-metal interface which results in bonding. However, Klomp and Lindenhovius (1978) prepared sintered compacts of alumina and iron powders to increase surface area and found no evidence for such a mechanism. The resistivity measured for the composite was same as that for pure alumina indicating no increase in metal-metal contacts. Mössbauer spectroscopy is ideally suited to study the bonding mechanism and an investigation of $(Al_2O_3 + Fe)$ system is presented in this work.

2. Experimental procedure

The samples were prepared by sandwiching an alpha iron foil of 10 μm thickness between two sintered alumina discs (1 cm diameter × 0·2 cm thickness). These were then placed under a tightened screw-cap under a pressure of about 0·2 kg/cm^2 and heated in argon atmosphere at 1250 C for 30 minutes (figure 1). This temperature corresponds to 0·9 T_m (where T_m is the melting point of Fe) as recommended by Klomps (1970). Mössbauer spectra were recorded for the sample in transmission geometry with a ^{57}Co in rhodium source.

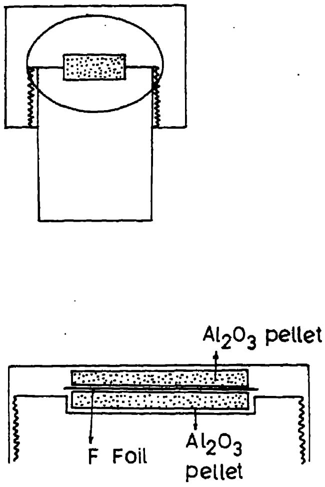

Figure 1. Fe foil sandwiched between two ceramic pellets and pressed in a tightened scr cap. The encircled part is shown in detail in bottom diagram.

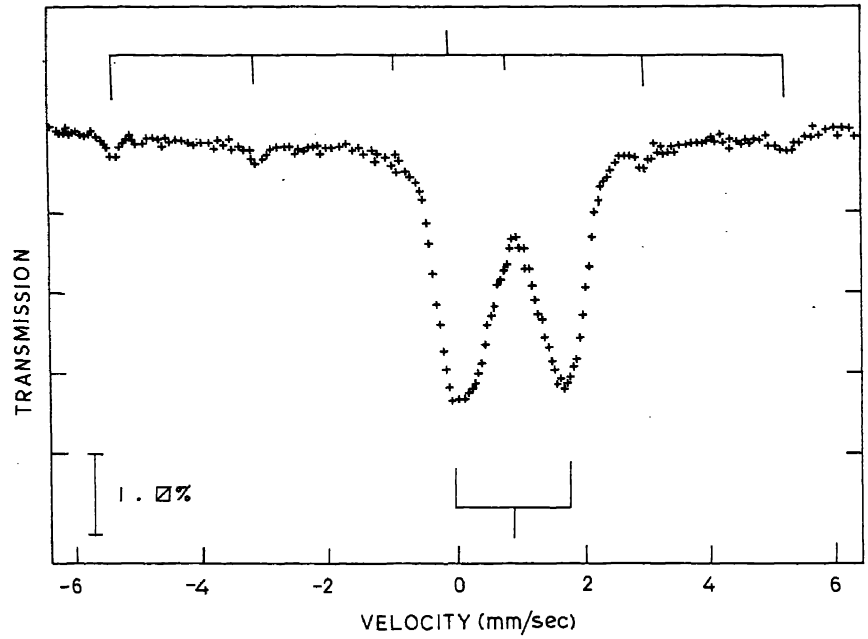

Figure 2. Mössbauer spectrum for the cermet ($Fe+Al_2O_3$) sample. The weak six li spectrum corresponds to alpha Fe and the absorption in central region is due to a broaden quadrupole split doublet. The position of lines obtained by χ^2 fit is indicated.

3. Results

The Mössbauer spectrum at room temperature, shown in figure 2, consists of broadened doublet near the centre together with a small absorption in the high velocity regions. The absorption in the higher velocity regions was identified as that d

Table 1. Comparison of results for (Al_2O_3+Fe) cermet with data of similar systems

Sample	Isomer shift (mm/sec)	Quadrupole splitting (mm/sec)
(Al_2O_3+Fe) cermet	0·94	1·78
Tetrahedrally coordinated ferrous halides	0·8 – 1	—
Fe(II) covalent compounds	0·8 – 1.5	—
$Fe_{1-x}O_x$ (wusite)	Site A: 0·91	0·46
$0·9 \leqslant x \leqslant 0·93$	Site B: 0·86	0·78
αFe_2O_3	0·4 (SS)	0·12
$FeOAl_2O_3$ spinel	1·08	1·6

to a small amount of unreacted iron by comparison with a standard Fe spectrum. The inner lines were fitted to a doublet and the parameters for the fit are shown in table 1. The linewidths of the component lines of the doublet are large (1 mm/sec). However when an attempt was made to fit to two doublets there was a slight increase in χ^2.

In table 1 the isomer shifts and quadrupole splittings are compared for various Fe compounds (Greenwood and Gibb 1971). The observed isomer shift for the cermet lies in the range of isomer shift values for Fe^{2+} covalent compounds. Further, both isomer shift and quadrupole splitting values for the cermet lie very close to the ones for the spinel $FeO \cdot Al_2O_3$. It therefore seems likely that bonding takes place by formation of a spinel-type compound at the surface. The compound formed may not be stoichiometric as is suggested by the large line broadening. A small range of quadrupole splitting values would lead to such a broadening of the lines. The coordination symmetry around Fe is therefore not exactly the same as in the spinel structure but slightly distorted, the amount of distortion varying from site to site. There are other evidences for such a compound formation of contacting materials when Nb, Ti, Ta and Zr metals are involved in bonding with ceramics (Buyers 1963).

4. Conclusion

The ^{57}Fe Mössbauer spectroscopy study of metal and ceramic interface in (Al_2O_3+Fe) cermet shows that (i) there is very little unreacted iron (< 0·1 %). This also confirms with the study of Klomp and Lindenhovius (1978) who ruled out bonding by an increase of metal-metal contacts by resistivity measurements. (ii) Bonding takes place by the formation of a compound of the type of $FeAl_2O_4$ spinel at the interface but with slight deviations from coordination symmetry around the Fe atom as compared to that in $FeAl_2O_4$.

Acknowledgement

The author is grateful to Drs R Jagannathan and N Ravi for useful discussion.

References

Buyers A G 1963 *J. Am. Ceram. Soc.* **46** 245
Greenwood N N and Gibb T C 1971 *Mössbauer spectroscopy*, (London: Chapman and Hall)
Klomp J T 1970 in *Science of ceramics* (eds) C Brosset and E Knopp (Gothenburg; Swedish Institut Silicate Research) Vol. 5, p. 501
Klomp J T and Lindenhovius 1978 *Ceramurgia Int.* 4 59

Bull. Mater. Sci., Vol. 6, No. 1, February 1984, pp. 17–20.
© Printed in India.

Mössbauer spectroscopy of titanium-substituted iron garnets

C M SRIVASTAVA, S N SHRINGI, B UMA MAHESHWAR RAO, D BAHADUR* and OM PARAKASH**

Department of Physics, Indian Institute of Technology, Powai, Bombay 400 076, India
*Advanced Centre for Materials Science, Indian Institute of Technology, Kanpur 208 016, India
**School of Materials Science and Technology, Banaras Hindu University, Varanasi 221 005, India

Abstract. The Mössbauer spectroscopy of polycrystalline $Y_{3-x}Ca_xFe_{5-x}Ti_xO_{12}$ ($x = 0{\cdot}2$, $0{\cdot}5$, $0{\cdot}7$) garnets has been studied at room temperature. The hyperfine fields both at the octahedral and tetrahedral sites decrease with increasing titanium content. The hyperfine fields both at *a* and *d*-sites are linearly proportional to magnetization. The quadrupole splitting for *a*-site shows no dependence on Ti content while the quadrupole splitting for *d*-site increases slightly with *x*. The results are explained on the basis of lattice distortion due to Ti substitution on *a*-site.

Keywords. Garnet; hyperfine field; quadrupole splitting; iron garnet; Mössbauer spectra.

1. Introduction

The Mössbauer spectroscopy of polycrystalline $Y_{3-x}Ca_xFe_{5-x}Ti_xO_{12}$ ($x = 0{\cdot}2$, $0{\cdot}5$, $0{\cdot}7$) garnets has been studied at room temperature. Yttrium iron garnet (YIG) and substituted yttrium iron garnets have been extensively studied because of their technical importance. Garnet structure allows a wide range of diamagnetic ion (Al^{3+}, Ga^{3+}, Si^{4+}, Sn^{4+}, Ti^{4+}) substitution on both octahedral (*a*) and tetrahedral (*d*) sublattices for the control of magnetization. For trivalent substitutions like Al^{3+}, Ga^{3+} the diamagnetic ions distribute themselves between both *a* and *d*-sites. In tetravalent substitutions like Si^{4+}, Sn^{4+}, Ge^{4+}, Ti^{4+} it becomes necessary to substitute a divalent ion like Ca^{2+} for the charge compensation. These ions occupy the dodecahedral site replacing rare earth or yttrium ions. In Ge^{4+} and Si^{4+} substitution the diamagnetic ions have a strong preference for *d*-site, whereas for substitutions like Sn^{4+} and Ti^{4+} the diamagnetic ions occupy an *a*-site alone.

We have studied the effect of substitution of Ti^{4+} on magnetic properties and Mössbauer spectra of YIG. The compositions investigated are $Y_{3-x}Ca_xFe_{3-x}Ti_xO_{12}$ ($0 < x < 1$). As mentioned earlier Ti is expected to occupy the *a*-site. Measurements of Curie temperature (T_c) on these samples indicate that T_c falls rapidly with *x* (Om Parakash and Bahadur 1982). The hyperfine fields (H_{hf}) at Fe^{3+} nuclei also show a similar fall. These results as well as the variation of quadrupole splitting (QS) with Ti substitution are discussed in this paper.

2. Experimental

The samples $Y_{3-x}Ca_xFe_{5-x}Ti_xO_{12}$ ($0{\cdot}2 < x < 1$) were prepared using standard ceramic techniques from high purity Y_2O_3, Fe_2O_3, Ti_2O_3. The preparation of the samples and other magnetic measurements were reported recently (Om Parakash an Bahadur 1982). The x-ray diffraction data of the samples show the presence of singl phase.

For the Mössbauer investigation the Mössbauer absorbers were made from fin powders. The data were collected by transducer drive in conjunction with 102 multichannel analyser in constant acceleration mode.

3. Results and discussion

The Mössbauer spectra of $Y_{3-x}Ca_xFe_{5-x}Ti_xO_{12}$ ($x = 0{\cdot}2, 0{\cdot}5, 0{\cdot}7$) obtained at 300 K are shown in figure 1. From the analysis of the spectra H_{hf} at Fe^{3+} nuclei on *a* an *d*-sites and the corresponding QS are obtained. These data are shown in figures 2 and From figure 2 it can be observed that H_{hf} at *a* and *d*-sites decreases with increase i titanium concentration (*x*). The fall in H_{hf} is linearly proportional to the fall i magnetization. Figure 2 also gives the plots of variation of magnetization with *x*. Th variation of QS is shown in figure 3, and indicates that QS at *a*-site remains constan whereas QS at *d*-site shows a slight increase with increase in *x*. The substitution of Ti o

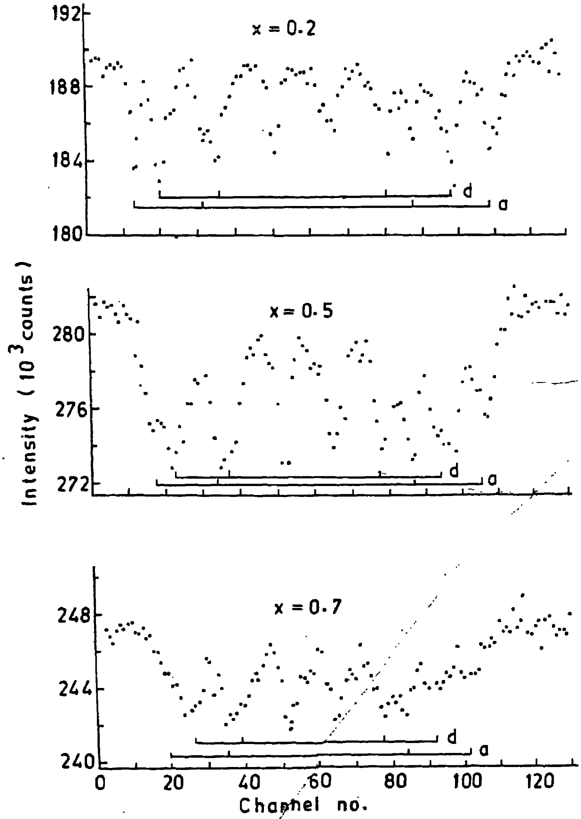

Figure 1. Mössbauer spectra of $Y_{3-x}Ca_xFe_{5-x}Ti_xO_{12}$ at 300 K. (O velocity is at 58 channel; 1 channel = 0·1591 mm/sec).

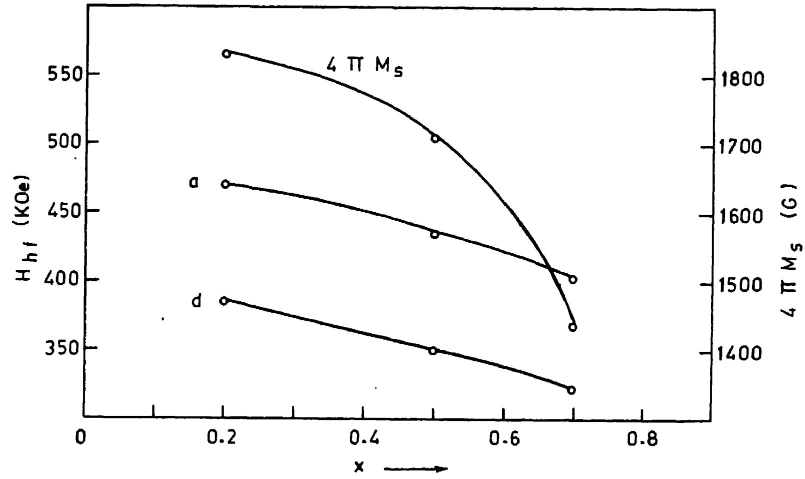

Figure 2. Variation of hyperfine field H_{hf} for *a* and *d* sites and $4\pi M_s$ in $Y_{3-x}Ca_xFe_{5-x}Ti_xO_{12}$ as a function of *x*.

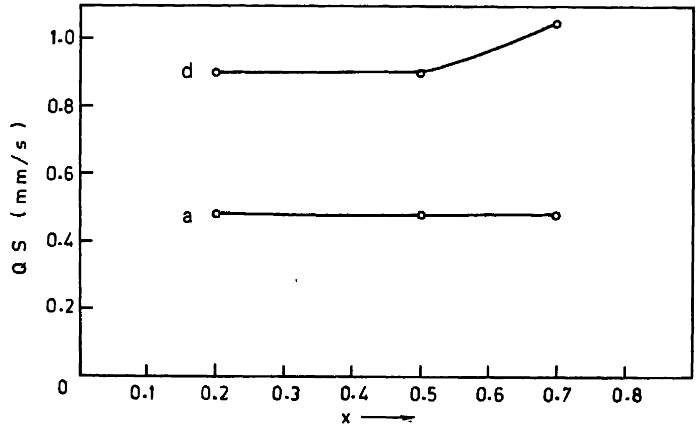

Figure 3. Quadrupole splitting for *a* and *d* sites in $Y_{3-x}Ca_xFe_{5-x}Ti_xO_{12}$ as a function of *x*.

the *a*-site creates an asymmetric displacement of the oxygen ions surrounding the *d*-site. This distortion of the oxygen tetrahedra on the *d*-site due to Ti^{4+} substitution on the *a*-site gives rise to the observed increase in QS of the *d*-site. This observation is consistant with similar observations of QS in $Y_{3-x}Ca_xFe_{5-x}Si_xO_{12}$ (Lyubutin *et al* 1970) and $Y_{3-x}Ca_xFe_{5-x}Sn_xO_{12}$ (Lyubutin *et al* 1967) systems.

4. Conclusion

The study of $Y_{3-x}Ca_xFe_{5-x}Ti_xO_{12}$ system has shown that in the range of $0 < x < 0{\cdot}7$ the H_{hf} falls with increase in *x* in agreement with the observed magnetization data. The QS on the *d*-site is higher than the QS on the *a*-site and the former shows a slight increase with increase in Ti^{4+} substitution. This observation shows that tetragonal sublattice deviates more from the cubic symmetry than the octahedral sublattice and that increase in Ti^{4+} substitution increases the distortion of oxygen tetrahedra on the *d*-site.

References

Lyubutin I S, Markarov E F and Povitsk V A 1967 *Sov. Phys. JETP* **26** 44

Lyubutin I S, Belyaev L M, Vishnyakov Yu S, Dmitrieva T V, Dodokin A P, Dubossarskya V Ya and Shyakhina L P 1970 *Sov. Phys. JETP* **31** 647

Om Parakash and Bahadur D 1982 Magnetic and electrical properties of Ti-substituted yttrium iron garnet. Presented at Third Joint Intermag-Magnetism and Magnetic Materials

Bull. Mater. Sci., Vol. 6, No. 1, February 1984, pp. 21–25.
© Printed in India.

Magnetic properties of metallic glass $Fe_{39}Ni_{39}Mo_4Si_6B_{12}$

B BHANU PRASAD, ANIL K BHATNAGAR,
S VENKATARAMAN and M N CHANDRASEKHARAIAH*

School of Physics, University of Hyderabad, Hyderabad 500 134, India
*Bharat Heavy Electricals Limited (R & D), Hyderabad 500 539, India

Abstract. Magnetic metallic glass $Fe_{39}Ni_{39}Mo_4Si_6B_{12}$ has been studied by the ^{57}Fe Mössbauer spectroscopy. Mössbauer spectra consist of broad and overlapping six-line pattern below the Curie temperature. The Curie and crystallization temperatures of this metallic glass have been determined to be 575 ± 3 K and 725 ± 3 K, respectively. The hyperfine magnetic field at room temperature is approximately 225 kOe. The reduced hyperfine fields of this sample decrease much faster than that observed for other iron-rich metallic glasses like $Fe_{40}Ni_{40}B_{20}$, $Fe_{80}B_{20}$ etc. This behaviour is attributed to the presence of molybdenum atoms in the sample.

Keywords. Metallic glasses; Mössbauer spectroscopy; magnetic properties.

1. Introduction

Magnetic metallic glasses, produced by the rapid quenching of a melt of an iron-rich alloy, have become technological important materials. These materials have high saturation induction and other excellent soft magnetic properties which are now presently being exploited for various applications in electromagnetic industry (Luborsky *et al* 1978). The magnetic properties of these glasses not only depend upon the alloy composition but also on the details of the preparation method, *i.e.* quenching rate etc. Therefore, the investigation of the magnetic properties of commercially available metallic glasses is of importance. In this paper we report the results of the Mössbauer investigations of "as-received" metallic glass $Fe_{39}Ni_{39}Mo_4Si_6B_{12}$ and is a part of our extensive investigations of magnetic and electrical properties of magnetic metallic glasses (Bhanu Prasad *et al* 1980, 1981a,b,c; 1983; Bhatnagar *et al* 1982; Bhatnagar and Ravi 1983).

2. Experimental

Metallic glass $Fe_{39}Ni_{39}Mo_4Si_6B_{12}$ was obtained from Vacuumschmelze (West Germany) in a thin ribbon form having a width of approximately 1 cm and a thickness of approximately 60 μm. The Mössbauer absorber was prepared using two widths of the ribbon clamped between two thin annular rings of oxygen free copper. Mössbauer spectra were recorded on an Elscint spectrometer coupled with 256 channel MCA. The standard transmission geometry was used and the spectrometer in the constant acceleration mode was used. The source was 25 mCi Co in rhodium matrix. The constant Doppler velocity thermal-scan method was used to determine Curie and crystallization temperatures accurately (Chien and Hasegawa 1977).

3. Results and discussion

Mössbauer spectra of "as-received" sample were recorded in the temperature range 77–900 K. Figure 1 shows the spectra recorded at 297, 600 and 750 K. The room temperature (297 K) spectrum consists of broad and overlapping but well-resolved six absorption lines which are characteristic of the ferromagnetic state of the sample. The average linewidth of the outer lines is approximately 1·44 mm/sec, about six times larger than the natural line width of iron. Similar spectra have been observed at other temperatures but below 575 K. These broad and overlapping lines in the spectra are due to the amorphous nature of the sample. Random atomic arrangement in an amorphous solid gives rise to a large number of inequivalent iron-sites. This results in a number of overlapping spectra characteristic of each inequivalent iron-site, and hence the broadening of absorption lines in the spectra. The spectra at and above 575 K but below 725 K consist of quadrupole-split doublet in each spectrum. Figure 1b shows the quadrupole-split spectra at 600 K. The splitting between the doublet is approximately 0·47 mm/sec at this temperature. A slight asymmetry in the doublet should also be noticed which probably arises due to a distribution of isomer-shifts in the amorphous sample. A complex spectrum was observed at 725 K indicating the onset of crystallization at this temperature. Mössbauer spectra taken at 750 K is shown in figure 1c in which extra absorption lines besides the quadrupole-split doublet clearly show the precipitation of α–Fe. From these observations it is concluded that the Curie and crystallization temperatures of "as-received" $Fe_{39}Ni_{39}Mo_4Si_6B_{12}$ sample are approximately 575 and 725 K, respectively. An independent check of these characteristic temperatures of the amorphous sample was done by the constant Doppler velocity

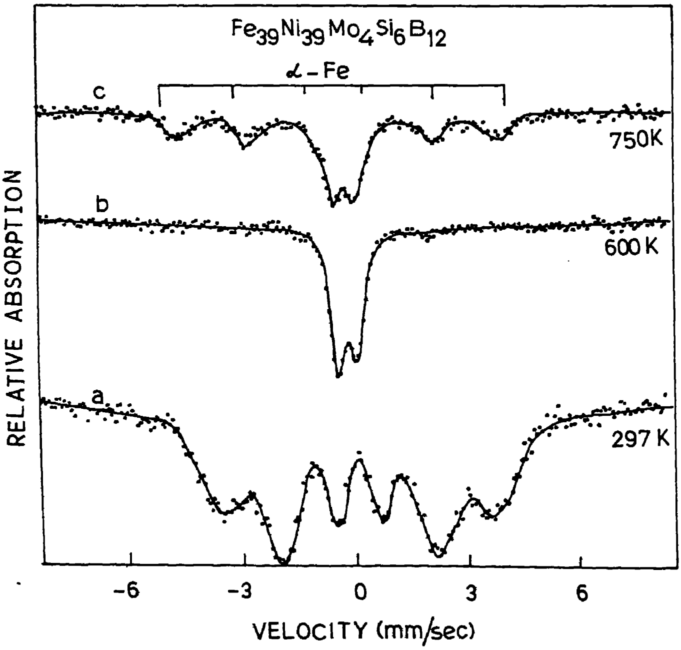

Figure 1. Mössbauer spectra of $Fe_{39}Ni_{39}Mo_4Si_6B_{12}$.

thermal-scan method which also established the Curie and crystallization temperatures to be 575 ± 3 K and 725 ± 3 K, respectively, in agreement with previous results.

The temperature dependence of the hyperfine or internal magnetic field $H_{\text{eff}}(T)$, as determined from the splitting of the outer-most absorption lines in the spectrum, is shown in figure 2. The extrapolation of the $H_{\text{eff}}(T)$ *vs* T curve to $T \rightarrow 0$ and $H_{\text{eff}}(T) \rightarrow 0$ gives $H_{\text{eff}}(0) = 278 \pm 3$ kOe and the Curie temperature $T_c = 575 \pm 5$ K, respectively. The value of T_c, deduced by this method, is also in agreement with the thermal-scan method.

The reduced hyperfine magnetic fields, $H_{\text{eff}}(T)/H_{\text{eff}}(0)$ *vs* the reduced temperature, T/T_c, are plotted in figure 3 along with the Brillouin curve for spin 1 which represents the approximate behaviour of elemental ferromagnets like Fe. It is noticed that the experimental points for $Fe_{39}Ni_{39}Mo_4Si_6B_{12}$ lie much below the Brillouin curve indicating that $H_{\text{eff}}(T)$ decreases much faster with increasing temperature when compared with elemental ferromagnets. This behaviour has been observed in other metallic glasses (Chien and Hasegawa 1977; Bhanu Prasad *et al* 1980; Bhatnagar *et al*

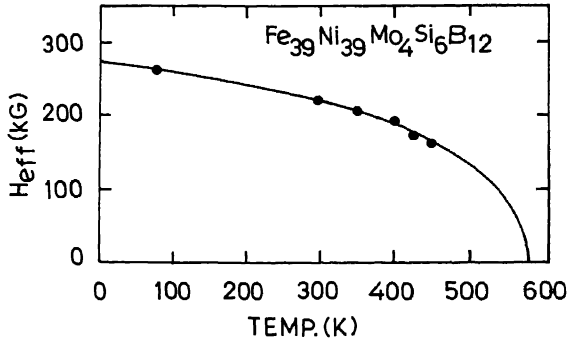

Figure 2. Temperature dependence of hyperfine magnetic field $H_{\text{eff}}(T)$ of $Fe_{39}Ni_{39}Mo_4Si_6B_{12}$ in the glassy state.

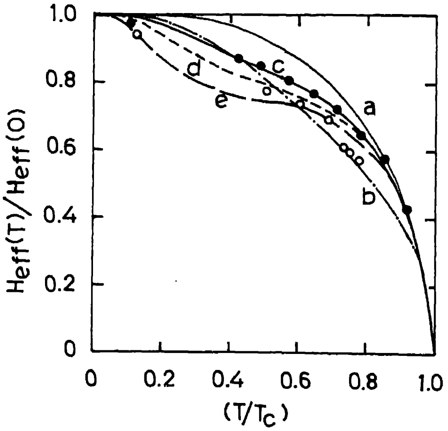

Figure 3. Reduced hyperfine magnetic field *vs* reduced temperature. Circles represent experimental points for $Fe_{39}Ni_{39}Mo_4Si_6B_{12}$ and solid spheres represent experimental points for $Fe_{40}Ni_{40}B_{20}$. Curves a, b, c, d, and e are obtained from equation (1) for $\delta = 0$, $\delta = 0{\cdot}5$, $\delta = 0{\cdot}6(1 - t^2)$, $\delta = 0{\cdot}7(1 - t^2)$ and $\delta = 0{\cdot}8(1 - t^2)$, respectively, where $t = T/T_c$.

1982; Saegusa and Morrish 1982). This behaviour of amorphous ferromagnets i usually explained, at least qualitatively, on the basis of Handrich's model (Handric 1969) in which fluctuations in the exchange interactions due to the random atomi arrangement in an amorphous solid account for this behaviour of $H_{\text{eff}}(T)$. In this mode the reduced hyperfine magnetic field can be expressed as

$$h = H_{\text{eff}}(T)/H_{\text{eff}}(0) = \tfrac{1}{2}B_s[(1+\delta)x] + \tfrac{1}{2}B_s[(1-\delta)x] \qquad (1$$

where $x = [3S/(S+1)]\,(h/t)$ with $t = T/T_c$, B_s is the Brillouin function for spin S, an $\delta\,(0 < \delta < 1)$ is a measure of fluctuations in the exchange interactions. For $\delta = 0$, (1 reduces to the form $h = B_s(x)$ applicable to crystalline elemental ferromagnets. I figure 3 we have also drawn a curve using (1) in which $\delta = 0{\cdot}5$ and $S = 1$ have been used It is observed that the agreement between experimental points and this curve is goo close to T_c, but not good at low temperatures. It has been previously shown by us tha the agreement between experimental points and (1) can be improved vastly if δ i assumed to be a temperature-dependent parameter, *i.e.* $\delta = \delta_0(1-t^2)$ in which δ_0 i used as a fitting parameter. It is found that for a good fit the value of δ_0 lies between 0· and 0·7 (Bhanu Prasad *et al* 1980; Bhatnagar *et al* 1982). For example, we have show that data for $Fe_{40}Ni_{40}B_{20}$ show a good agreement with (1) if $\delta = 0{\cdot}6\,(1-t^2)$ and $S =$ are used in the equation. However, we find that a similar agreement is not found fo $Fe_{39}Ni_{39}Mo_4Si_6B_{12}$ and the experimental points lie much below the curve fo $\delta = 0{\cdot}7\,(1-t^2)$ although some points fall on the curve for $\delta = 0{\cdot}8\,(1-t^2)$ as shown i the figure. We believe that this deviation may be due to the presence of molybdenu atoms in this sample. Further detailed investigation is in progress and will be reporte at a later date.

4. Conclusions

Mössbauer spectroscopy has been used to study metallic glass $Fe_{39}Ni_{39}Mo_4Si_6B_{12}$ i the temperature range 77–900 K. The observed Mössbauer spectra are typical of thos of other iron-rich metallic glasses exhibiting broad and overlapping but well resolve six-line spectra below Curie temperature. The Curie and crystallization temperatures o this sample have been found to be 575 ± 3 K and 725 ± 3 K, respectively. The hyperfin or internal magnetic field, $H_{\text{eff}}(T)$, decreases much faster with rise in temperature tha predicted by the Brillouin curve for spin one, as well as in comparison with othe metallic glasses which contain only ferromagnetic transition metals and metalloids, i.e. Fe–Ni–B, Fe–B–Si etc.

Acknowledgements

AKB thanks the Science and Engineering Research Council (DST, India) and th Department of Atomic Energy, India for the support of this work. SV thanks CSIR, Indi for the fellowship.

References

Bhanu Prasad B, Bhatnagar A K and Jagannathan R 1980 *Solid State Commun.* **36** 661
Bhanu Prasad B and Bhatnagar A K 1981a *Bull. Mater. Sci.* **3** 19

Bhanu Prasad B, Bhatnagar A K and Jagannathan R 1981b *Proc. of Silver Jubilee Physics Symposium*, Department of Atomic Energy, Bombay, India **C24** 97

Bhanu Prasad B, Bhatnagar A K and Jagannathan R 1981c *Proceedings of International Conference on Applications of the Mössbauer Effect*, Jaipur, India (To be published)

Bhanu Prasad B, Bhatnagar A K and Jagannathan R 1983 *J. Appl. Phys.* **54** 2019

Bhatnagar A K, Bhanu Prasad B, Ravi N, Jagannathan R and Anantharaman T R 1982 *Solid State Commun.* **44** 905

Bhatnagar A K and Ravi N 1983 *Phys. Rev.* **B28** 359

Chien C L and Hasegawa R 1977 *Phys. Rev.* **B16** 3024

Handrich K 1969 *Phys. Status. Solidi.* **32** K55

Luborsky F E, Becker J J, Frischmann P G and Johnson L A 1978 *J. Appl. Phys.* **49** 1769

Saegusa N and Morrish A H 1982 *Phys. Rev.* **B26** 10

Bull. Mater. Sci., Vol. 6, No. 1, February 1984, pp. 27–31.
© Printed in India.

Magnetic structure of zinc ferrite

C M SRIVASTAVA, S N SHRINGI AND M VIJAYBABU
Department of Physics, Indian Institute of Technology, Powai, Bombay 400 076, India

Abstract. A detailed analysis of the available experimental data has been made for the ordered phase of $ZnFe_2O_4$. The abnormally low T_N and the observed spin arrangement have been explained on the basis of the hybridization of orbitals on the oxygen ions which gives rise to an anisotropic exchange interaction. The variation of hyperfine field and susceptibility with temperature along with the zero point reduction of the magnetic moment indicate that the $ZnFe_2O_4$ is a two-dimensional antiferromagnet.

Keywords. Critical exponents; hyperfine fields; magnetic structure; overlap integrals; zinc ferrite.

1. Introduction

Zinc ferrite is a normal spinel with a cell constant of 8·44 Å. It is an antiferromagnetic material below 10 K. All the Zn ions occupy only tetrahedral (A) site and all the Fe ions occupy octahedral (B) site and the only exchange interaction present in $ZnFe_2O_4$ is the B–B interaction. However, its properties like sub-lattice magnetization and susceptibility do not show a general three-dimensional (3D) antiferromagnetic behaviour. Its Néel temperature T_N is abnormally low.

Neutron diffraction studies of $ZnFe_2O_4$ at 4·2 K by König *et al* (1970) and Boucher *et al* (1970) have indicated that the magnetic unit cell gets doubled and becomes tetragonal with $a = b = 8{\cdot}43$ Å and $c = 16{\cdot}86$ Å. The conclusions reached through these two studies are not similar. In one case (König *et al* 1970) there are two models which fit the intensities of lines, one collinear and the other non-collinear. In the collinear model the spins make an angle of 45° with the *c*-axis. In the model of Boucher *et al* (1970) the collinear structure has spins pointing along [100] and [010] directions. The magnetic moments on the Fe^{3+} ions in both cases which are close to 4·2 μ_B are much smaller than the expected value of 5 μ_B for Fe^{3+} ions.

Magnetic susceptibility of $ZnFe_2O_4$ has been measured by Lotgering (1966) and also by Arrot and Goldman (1955). At high temperatures ($T > 300$ K) the reciprocal susceptibility is linear (Lotgering 1966). But below 30 K the inverse susceptibility is almost constant with a broad minima at 15 K.

König *et al* (1970) analysed the Mössbauer spectra of $ZnFe_2O_4$ from 4·5 to 12 K. These studies have given the value of T_N as 10 K. The value of the hyperfine field (H_{hf}) extrapolated to 0 K is 515 kOe. They have shown that the H_{hf} variation is markedly different from the Brillouin function $B_{5/2}$.

Heat capacity of $ZnFe_2O_4$ has been measured by Edger *et al* (1957, 1958). There is a peak in the molar heat capacity versus temperature curve around 10 K indicating that T_N is 10 K.

In figure 1, we have plotted the observed values of T_N for several ferrites listed in table 1 as a function of the inverse of the overlap integral (S^{-1}) which for qualitative

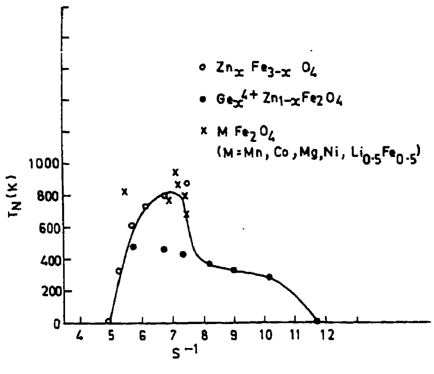

Figure 1. Variation of T_N with the inverse of the overlap integral S^{-1}.

Table 1. The Néel temperature (T_N) lattice constant (a) and the inverse of the ove integral (S^{-1}) for several compositions of spinel ferrites

Composition	T_N (K)	a (Å)	S^{-1}	Composition	T_N (K)	a (Å)	S
$MnFe_2O_4$	823	8·52	5·44	$Zn_{0.6}Fe_{2.4}O_4$	624	8·421	5
$CoFe_2O_4$	790	8·38	7·35	$Zn_{0.8}Fe_{2.2}O_4$	335	8·429	5
$NiFe_2O_4$	858	8·34	7·14	$ZnFe_2O_4$	10	8·440	4
$CuFe_2O_4$	759	8·28	6·83	$Ge_{0.25}Zn_{0.75}Fe_2O_4$	475	8·425	5
$Li_{0.5}Fe_{2.5}O_4$	943	8·33	7·08	$Ge_{0.5}Zn_{0.5}Fe_2O_4$	472	8·419	6
$MgFe_2O_4$	680	8·38	7·35	$Ge_{0.6}Zn_{0.4}Fe_2O_4$	430	8·415	7
Fe_3O_4	875	8·390	7·41	$Ge_{0.8}Zn_{0.2}Fe_2O_4$	325	8·410	8
$Zn_{0.2}Fe_{2.8}O_4$	788	8·399	6·69	$Ge_{0.9}Zn_{0.1}Fe_2O_4$	278	8·413	10
$Zn_{0.4}Fe_{2.6}O_4$	732	8·410	6·13	$GeFe_2O_4$	10	8·414	11

estimate can be defined as

$$S = [(r_a + r_0^{2-}) - \text{interatomic distance}]/[r_a + r_0^{2-}]$$

where r_a and r_0^{2-} are the radii of the cation on the A-site and O^{2-} respectively and interatomic distance is obtained from the observed cell constant a and is equa $a\sqrt{3}/8$. Like the Slater-Bethe curve (Slater 1930; Bethe 1933) for direct overlaj metals we find that in superexchange also the large overlap leads to smaller value exchange and as the overlap decreases the strength of exchange interaction increases goes to a maximum and then decreases. The significant reduction in T $ZnFe_2O_4$ compared with T_N of other spinel ferrites appears to be a consequenc enhanced overlap.

We have attempted to explain these experimental observations assuming that hybridized orbitals located on the oxygen ions introduce left-right asymmetry in exchange interaction. This has been explained using Anderson's model for superexchange.

2. Discussion

In the collinear model (König *et al* 1970) the alignment of spins along a few directions as shown in figure 2 is as follows:

$[110]$ and $[1\bar{1}0]$ - - - ↑ ↑ ↓ ↓ ↑ ↑ - - - - -
$[101]$, $[\bar{1}01]$, $[011]$ and $[01\bar{1}]$ - - ↑ ↓ ↓ ↓ ↓ ↑ ↑ ↑ ↑ ↓ ↓ - - -

This is a complicated structure and requires an asymmetric nearest neighbour exchange interaction. We assume that the dominant interaction between Fe^{3+} ions is along $[110]$ and $[1\bar{1}0]$ directions. In this case a pair of spins ferromagnetically coupled are antiferromagnetically arranged pairwise on the linear chain. A possible explanation for the asymmetric exchange interaction on the left and right of the central spin on a linear chain has to be provided in terms of hybridized sp type of orbitals associated with O^{2-} ions.

The 90° d^5–d^5, B–B super exchange has two types of major interactions, one ferromagnetic ($b_{\sigma\sigma'}$) and the other anti-ferromagnetic ($b_{\pi\sigma}$). These are shown in figure 3.

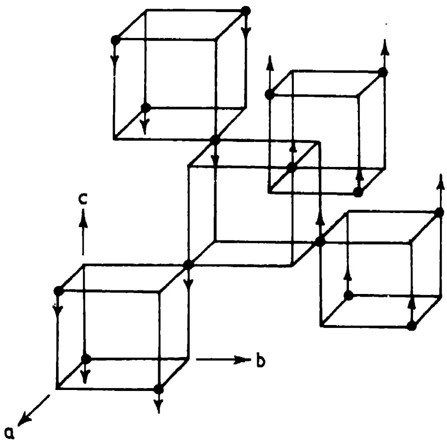

Figure 2. Spin arrangements in the collinear model (König *et al* 1970).

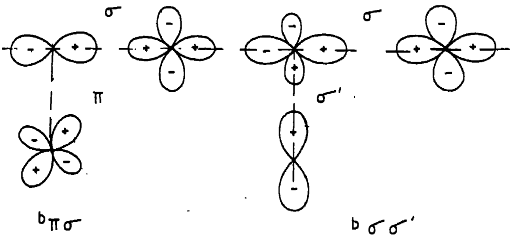

Figure 3. The $b_{\pi\sigma}$ and $b_{\sigma\sigma'}$ transfer integrals before hybridization.

Srivastava *et al* (1979) have shown that

$$J = -(1/25)[(4b_{\pi\sigma}^2/U)-(4b_{\sigma\sigma'}^2/U)],$$

where $U = 10$ eV. If the sp hybridization occurs on the O^{2-} sites the strength of the interaction increases while that of the π interaction is likely to decrease as shown i figure 4. Consequently, the strength of antiferromagnetic interaction $b_{\pi\sigma}^2/U$ goes dow while that of the ferromagnetic interaction $b_{\sigma\sigma'}^2/U$ increases. In the case of pure orbita without hybridization the magnitudes of $b_{\pi\sigma}$ and $b_{\sigma\sigma'}$ are 0·25 and 0·122 eV respectivel (Srivastava *et al* 1979). The steep fall in T_N for $ZnFe_2O_4$ from the case of the ferrit $M_{1-x}^{2+}Zn_xFe_2O_4$ ($x \neq 1$, M = Fe, Ni, Mn, Co) shows that when Zn is completel occupying the A-site the effect of hybridization is most pronounced. A similar effect observed in $Ge_xZn_{1-x}Fe_2O_4$ (Miyahara and Sai 1976; Hartmann-Boutron and Imbe 1968). In this system for $x = 1$, Ge^{4+} ions on the A-site have a very small radius but the have higher ionic charge. The nearest neighbour oxygen ions are therefore attracte towards this ion. Hence, this leads to more reduction in $b_{\pi\sigma}$ compared to $b_{\sigma\sigma'}$ and the 9 Fe^{3+}–Fe^{3+} interaction falls.

From the value of T_N for $ZnFe_2O_4$ which is 10 K assuming the two sublattice mod we obtain in the mean field approximation

$$KT_N = (2/3)(-Z_FJ_F+Z_AJ_A)S(S+1),$$

where Z_F and Z_A are the number of nearest neighbour spins with parallel ar antiparallel arrangements and J_F and J_A are the strength of ferromagnetic ar antiferromagnetic couplings. Taking $Z_F = 4$, $Z_A = 2$, we have

$$J_A - 2J_F = 0{\cdot}86\,^{\circ}\mathrm{K}.$$

This effect of the asymmetric exchange is to reduce significantly the effecti interaction and hence T_N. The spin arrangements discussed above would require th $ZnFe_2O_4$ should behave differently from a 3D antiferromagnetic system. From t observed variation of $H_{\rm hf}$ versus T data we have obtained the value of the critic exponent β as 0·125. This value supports the idea that $ZnFe_2O_4$ is close to a 2 antiferromagnet (Baker 1961). The data on magnetic susceptibility (Lotgering 196 indicating a broad maximum near the transition region and the observed magne moment reduction of 15% at 0 K (König *et al* 1970; Boucher *et al* 1970) are also agreement (Katsumota 1977; Johnson 1981) with a lower dimensionality of t magnetic ordering of $ZnFe_2O_4$.

3. Conclusion

The present available data on $ZnFe_2O_4$ show that the Sp-hybridization of oxygen i orbitals leads to significant changes in the strength and isotropy of the 90° Fe^{3+}–Fe

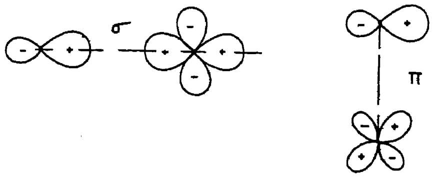

Figure 4. The $b_{\pi\sigma}$ and $b_{\sigma\sigma'}$ transfer integrals after hybridization.

superexchange interaction. The observed magnetic ordering has been attributed to these changes.

Acknowledgement

One of the authors (MV) would like to acknowledge the financial support received from CSIR, New Delhi.

References

Arrot A and Goldman J E 1955 *Phys. Rev.* **98** 1201

Baker G A Jr 1961 *Phys. Rev.* **124** 768

Bethe H 1933 *Handbuch der Physik* **24** Pt2 Ferromagnetism 443

Boucher B, Buhl R and Perrin M 1970 *Phys. Status. Solidi.* **40** 171

Edger F, Westrum J R and Grimes D M 1957 *J. Phys. Chem. Solids.* **3** 44

Edger F, Westrum J R and Grimes D M 1958 *J. Phys. Chem. Sol.* **6** 280

Hartmann-Boutron F and Imbert P 1968 *J. Appl. Phys.* **39** 775

Johnson J E 1981 *Proc. Int. Conf. Mössbauer effect*, Jaipur, India

Katsumota K 1957 *Solid State Commun.* **23** 481

König U, Bertaut E F, Gros Y, Mitrikov M and Chol G 1970 *Solid State Commun.* **8** 759

Lotgering F K 1966 *J. Phys. Chem. Solids* **27** 139

Miyahara Y and Sai F 1976 *J. Phys. Soc. Jpn* **41** 1522

Slater J C 1930 *Phys. Rev.* **36** 57

Srivastava C M, Srinivasan G and Nanadikar N G 1979 *Phys. Rev.* **B19** 499

Bull. Mater. Sci., Vol. 6, No. 1, February 1984, pp. 33–37.
© Printed in India.

A Mössbauer study of hyperfine interactions in the boroferrite $Fe_{3-x}Ga_xBO_6 (x = 0, 0{\cdot}12)$

M VITHAL, R JAGANNATHAN and N RAVI

School of Chemistry, University of Hyderabad, Hyderabad 500 134, India

Abstract. Fe_3BO_6 shows no thermal hysteresis around the phase transition temperature $T_{SR} = 418$ K; $Fe_{2{\cdot}88}Ga_{0{\cdot}12}BO_6$ undergoes spin transition at $T_{SR} = 403$ K resulting in a reduction of the T_{SR}. Both these features are different from the reported observations on α–Fe_2O_3. The two Fe^{3+} sites show difference in their magnetic interactions. Ga^{3+} replaces Fe^{3+} in a random manner.

Keywords. Spin-reorientation; thermal hysteresis; biquadratic exchange interaction; random distribution model; boroferrite; Mössbauer study; hyperfine interactions.

1. Introduction

Boroferrites occur in a variety of structures giving rise to materials like boracite, ludwigite warwickite, etc., which have modifications in structures resulting in interesting electrical and magnetic properties. The present work deals with a detailed study of the simple and substituted boroferrite, Fe_3BO_6. In this system boron has the unusual tetrahedral coordination. It is known to exhibit spin reorientation and the mechanism of spin reorientation is of considerable interest. In addition to a study of the behaviour of metal sites with regard to their magnetic interaction and the spin reorientation behaviour on substitution we also present here an analysis of the Mössbauer spectra of the substituted compounds on the basis of random distribution model (Coey and Sawatzky 1971).

2. Experimental procedure and characterization

The compounds were prepared from the stoichiometric mixture of metal nitrates and 400% excess boric acid as described by Muller *et al* (1978). Mössbauer measurements were made as described earlier (Ravi *et al* 1982). The IR and x-ray analysis confirmed the product formation and their purities.

3. Results and discussion

The Mössbauer spectra of Fe_3BO_6 were recorded in the range 77–520 K. The room temperature Mössbauer spectrum of Fe_3BO_6 yields two well-resolved six-line patterns superimposed on each other with relative intensities of the two sextets in the ratio 2:1. The spin reorientation (T_{SR}) and Curie temperatures (T_c) are 418 and 518 K respectively. The spin reorientation is identified by abrupt and well-characterised changes in the line splittings of the Mössbauer spectra below and above T_{SR} for the two sites (figure 1). The plots of reduced hyperfine fields *vs* reduced temperatures are shown in figure 2. found that one of the sites follows the Brillouin behaviour for $S = 5/2$ whereas the f for the other site deviates significantly. Such a deviation from the Brillouin curve c accounted for by the inclusion of the higher order biquadratic exchange ter discussed later.

The Mössbauer spectra of $Fe_{2.88}Ga_{0.12}BO_6$ were recorded in the range 77–4 This sample is also found to undergo spin reorientation as shown by the line splitt The T_{SR} and T_c are 403 and 494 K respectively. A decrease in spin reorient temperature on substitution is in contrast with that observed in α-Fe_2O_3 by Dezsi

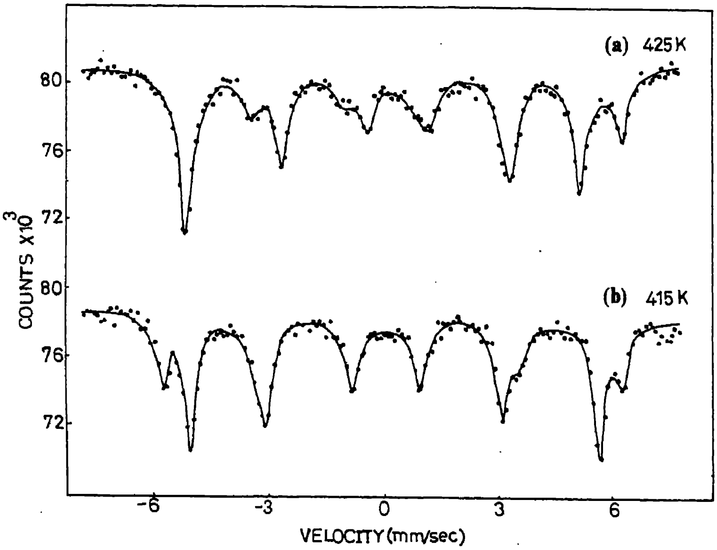

Figure 1. Mössbauer spectra of Fe_3BO_6 (a) below and (b) above T_{SR}.

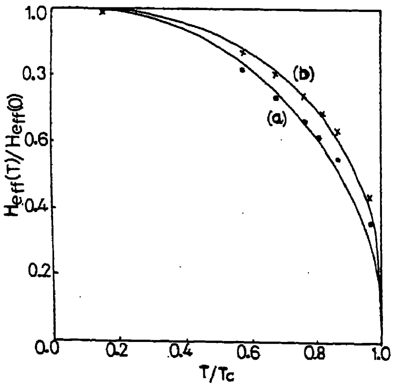

Figure 2. Reduced hyperfine field *vs* reduced temperature in Fe_3BO_6. Solid sphere crosses are experimental points for the 8*d* and 4*c* sites respectively. Solid line (a) theoretical Brillouin curve for $S = 5/2$ and (b) for $S = 5/2$ including biquadratic exc $j/J = 0{\cdot}015$.

(1967) where Rh^{3+} substitution increases the T_{SR}. The Brillouin behaviour of the two sites in this sample is similar to that of the parent material. The room temperature Mössbauer spectrum of $Fe_{2\cdot88}Ga_{0\cdot12}BO_6$ results in significant line broadening and lowering of the internal magnetic field compared to the parent material. The spectrum of the substituted compound may be analysed assuming a random replacement of the magnetic Fe^{3+} ion by the non-magnetic Ga^{3+} ion. Such an analysis enables testing the applicability of the model by comparing the experimental spectrum with theory and obtaining the information on exchange interaction. The computer-simulated spectrum along with the experimental spectrum is given in figure 3.

Spin reorientation can proceed in two ways: (i) the magnetic moment vector may rotate continuously and coherently from the x-axis to z-axis (b) the magnetic moment vector jumps discontinuously from x-axis to z-axis. The former is explained by Landau's theory of second-order phase transition as illustrated in the case of $ErFeO_3$ (Grant and Geller 1969). In α–Fe_2O_3, where a thermal hysteresis behaviour is observed for over a temperature range of 15°, process (b) has been invoked (Nininger and Schroeer 1978). An analysis of the Mössbauer data for the behaviour of isomershift, quadrupole splitting and effective hyperfine field as a function of temperature in the vicinity of T_{SR} shows that these values are reproducible for a given temperature irrespective of whether the measurements are made during heating or cooling in a cyclic manner. Thus in Fe_3BO_6 and $Fe_{2\cdot88}Ga_{0\cdot12}BO_6$ thermal hysteresis is absent. Such a behaviour is in accordance with spin reorientation taking place as a second-order phase transition *viz*., rotation of the magnetic moment vector continuously from x-axis to z-axis. This result also agrees with that of Voigt (1975) who based his conclusion on susceptibility and field-induced phase transition studies.

Fe_3BO_6 is known to have orthorhombic symmetry with space group Pnma, the temperature dependence of the hyperfine field corresponding to the $8d$ site follows

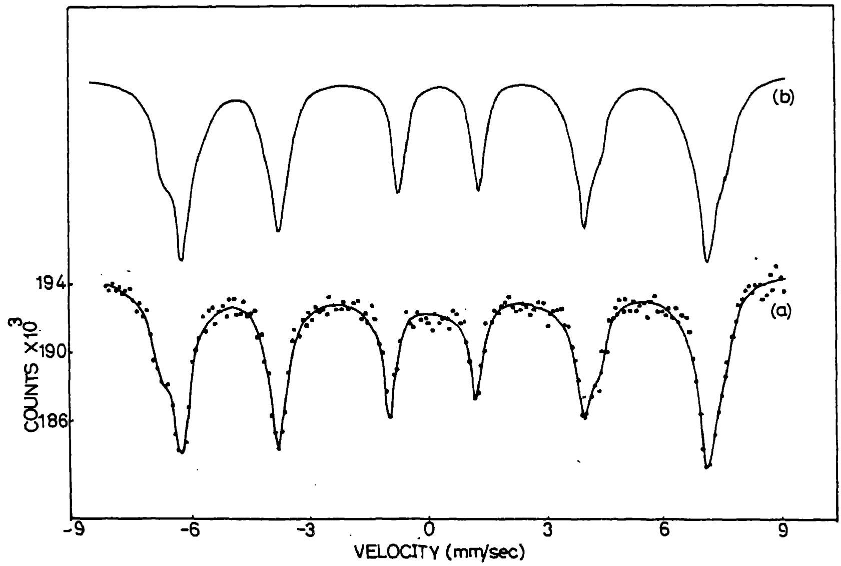

Figure 3. Comparison of (**a**) experimental Mössbauer spectrum at 296 K with (**b**) theoretical spectrum based on the random substitution model.

closely the Brillouin behaviour. On the other hand the 4*c* site gives rise to consistently higher values of $H_{\rm eff}(T)/H_{\rm eff}(O)$ than that predicted by molecular field theory. This type of behaviour has been attributed to the significant contribution due to the biquadratic exchange term of the form

$$J \cdot S_a S_b - j\,(S_a S_b)^2,$$

where $J > 0$ and the magnitude of j can differ depending upon the superexchange interaction (Rodbell *et al* 1967). The theoretical curve with a j/J 0·015 shows close agreement with experimental data for the 4*c* site. Similar values for j/J have been obtained in oxide lattices such as NiO and $LiFeO_2$ (Bhide and Shenoy 1966; Cox *et al* 1963).

For an analysis of the Mössbauer spectra of $Fe_{2\cdot 88}Ga_{0\cdot 12}BO_6$ on the basis of random distribution model (Coey and Sawatzky 1971) the internal magnetic fields were calculated assuming a binomial distribution for different possible near-neighbour environments for a given concentration of nonmagnetic ion. The fields corresponding to each near neighbour environment ($\sigma(Z)$) are given by

$$\sigma(Z) = \beta_s\left(\frac{3S\langle\sigma\rangle_{\rm av}Z}{(S+1)\langle Z\rangle_{\rm av}\tau}\right)$$

where τ is related to the exchange constant J by $\tau = 3kT/2S(S+1)J\langle Z\rangle_{\rm av}$. It is found that the spectrum simulated for $\tau = 0.7$ agreed quite well with experimental spectrum (figure 3) provided the quadrupole interaction is taken into account in computing the line positions. The agreement between the simulated and experimental spectrum shows that Ga^{3+} has no site preference between 4*c* and 8*d*. The exchange constant J is $\sim 10\ {\rm cm}^{-1}$.

4. Conclusions

Fe_3BO_6 undergoes spin reorientation at 418 K. The non-observance of a break in the plots of hyperfine fields, isomer shift and quadrupole splitting *vs* temperature in the vicinity of $T_{\rm SR}$ suggests the absence of thermal hysteresis behaviour. Thus it is concluded that spin reorientation follows a second-order phase transformation. The temperature dependence of hyperfine field for the 8*d* site follows closely the Brillouin function for $S = 5/2$. The deviation of the 4*c* site from the Brillouin curve has been explained by including the biquadratic exchange interaction giving rise to $j/J = 0{\cdot}015$. Substitution of Fe^{3+} by Ga^{3+} brings down $T_{\rm SR}$ from 418 to 403 K. It is found that Ga^{3+} has no site preference. An exchange constant $J \sim 10\ {\rm cm}^{-1}$ has been obtained.

Acknowledgements

Financial assistance from UGC, New Delhi to MV and DST, New Delhi to NR is gratefully acknowledged.

References

Bhide V G and Shenoy G K 1966 *Phys. Rev.* **143** 309
Coey J M D and Sawatzky G A 1971 *Phys. Status. Solidi.* **B44** 673

Cox D E, Shirane G, Flinn P A, Ruby S L and Takei W J 1963 *Phys. Rev.* **132** 1547
Dezsi I, Erlaki G and Keszthelyi L 1967 *Phys. Status. Solidi.* **21** K121
Grant R W and Geller S 1969 *Solid State Commun.* **7** 1291
Muller O, O'Horo M P and O'Neill J F 1978 *J. Solid State Chem.* **23** 115
Nininger R C Jr and Schroeer D 1978 *J. Phys. Chem. Solids.* **39** 137
Rodbell D S, Jacobs I S, Owens J and Hanis E A 1967 *Phys. Rev. Lett.* **11** 245
Ravi N, Jagannathan R, Rama Rao B and Raza Hussain M 1982 *Inorg. Chem.* **21** 1019
Voigt C 1975 *Phys. Lett.* **A53** 223

Bull. Mater. Sci., Vol. 6, No. 1, February 1984, pp. 39–45.
© Printed in India.

Curie temperatures and 0°K magnetic moments of zinc-substituted lithium ferrites

PRAN KISHAN, D R SAGAR, S N CHATTERJEE, L K NAGPAUL and K K LAROIA

Solid State Physics Laboratory, Delhi 110 007, India

Abstract. Because of their several attractive features including relatively high Curie temperatures, substituted lithium ferrites have become important for applications at microwave frequencies. Néel collinear arrangement of spins on *A* and *B* sublattices is unable to satisfactorily explain the 0°K saturation moments and the observed Curie temperatures of the zinc-substituted lithium ferrites, especially at concentrations of zinc $z > 0{\cdot}3$ in the formula $\mathrm{Li}_{0\cdot5-z/2}\mathrm{Zn}_z\mathrm{Fe}_{2\cdot5-z/2}\mathrm{O}_4$. Rosencwaig's localized canting model has been extended and used to compute 0°K magnetic moments and Curie temperatures of these ferrites with substitution levels up to $z = 0{\cdot}7$. Reasonably good agreement between the calculated and experimental values, both for the 0°K magnetic moments and the Curie temperatures, has been obtained using exchange parameters ratios based on the values $J_{aa} = -20°\mathrm{K}$, $J_{bb} = -8°\mathrm{K}$ and $J_{ab} = J_{ba} = -29°\mathrm{K}$.

Keywords. Ferrites; Curie temperature; magnetisation; localised spin canting; exchange parameter.

1. Introduction

Though the two sublattice collinear model (Néel 1948) was the first step in understanding the magnetic behaviour of ferrimagnets, it proved inadequate (Gorter 1954; Geller *et al* 1964) to account for the properties of diamagnetically-diluted systems with spinel and garnet structures. This was particularly so for the 0°K magnetization in spinel ferrites in which magnetically active cations were replaced with diamagnetic zinc ions preferentially occupying tetrahedral *A* sites. Based on collinear model and assuming the cation distribution (Nogues *et al* 1979) of the formula $(\mathrm{Zn}^{2+}_z\mathrm{Fe}^{3+}_{1-z})_A\{\mathrm{Li}^{1+}_{0\cdot5-z/2}\mathrm{Fe}^{3+}_{1\cdot5+z/2}\}_B\mathrm{O}^{2-}_4$ the zinc substitutions in lithium ferrite are expected to monotonically increase the net magnetization with increase in the diamagnetic content through the enhancement of the Fe^{3+} ion concentration of the dominant octahedral *B* sublattice relative to that of *A* sublattice. This progressive increase in magnetization is expected to continue with increasing zinc until a point is reached where the negative intersublattice *A–B* superexchange interaction becomes weaker than one of the two intrasublattice interactions *A–A* or *B–B*, both of which are themselves negative. The two sublattices then transform into two antiferromagnetic states. Experimentally, however, it is observed that zinc substitutions only at low levels cause enhancement in the magnetization followed by a decrease for amounts larger than $z = 0{\cdot}4$. This discrepancy can be explained by assuming a departure from collinearity leading to some sort of a canted spin arrangement resulting from the zinc induced reduction in the normally dominant antiferromagnetic intersublattice exchange interaction. There now exists considerable experimental evidence (Zhilyakov *et al* 1977; White *et al* 1978; Dorman *et al* 1981; Patton *et al* 1982) that supports the presence of spin canting of octahedral Fe^{3+} ions in this material. Several canting models have been proposed (Yafet and Kittel 1952; Nowik 1969; Rosencwaig 1970) and in what follows the Rosencwaig localized canting model (LCM) has been adapted to the case of zinc-substituted lithium ferrites.

2. Extended LCM equations

LCM is a mathematical representation of the proposal of Geller *et al* (1964) and takes into account the role of intrasublattice exchange interactions and also the existence of chemical disorder that is present in the ferrimagnets due to random ionic substitutions. According to this model if substitution of diamagnetic ions takes place in the A sublattice, a localised canting with different angles of cant occurs only at the B sublattice and vice versa. The spins of a particular B site Fe^{3+} ion in the former case see an effective exchange field consisting of the A site intersublattice field which depends on the number of nearest neighbour A site magnetic ions that surround it and a B site intrasublattice contribution which is canted at an average canting angle $\overline{\theta}_b$. Rosencwaig's original equations were derived for diamagnetic substitutions in garnets. These equations when adapted for spinels and further extended for zinc substitutions in lithium ferrite, with one significant difference discussed in § 3, can be written as follows:

The local canting angle $\phi_b(m, q)$ of a B site Fe^{3+} ion which is surrounded by m and q nearest neighbour diamagnetic ions in the A and B sublattices respectively is given by

$$\cos\phi_b(m, q) = \frac{(1 - C\cos\overline{\theta}_b)}{(1 + C^2 - 2C\cos\overline{\theta}_b)^{1/2}}, \tag{1}$$

with

$$C = \frac{S_b}{S_a}\cdot\frac{J_{bb}}{J_{ab}} = \frac{(n_{bb} - q)}{(n_{ba} - m)}\cdot\delta,$$

where S_a and S_b are the vector sums of all the spins of the magnetically active nearest neighbours located on A and B sublattices respectively. $S_a = (n_{ba} - m)S$; $S_b = (n_{bb} - q)S$ where for a Fe^{3+} ion $S = 2{\cdot}5$; n_{ij} is the number of nearest neighbour bonds that an ion on sublattice i makes with ions on the j sublattice with $n_{ab} = 12$, n_{ba} and $n_{bb} = 6$, $n_{aa} = 4$; δ is the ratio between intrasublattice B–B exchange parameter J_{bb} and that of intersublattice exchange parameter $J_{ab}(= J_{ba})$ and the ratio J_{aa}/J_{ab} is represented by γ. The average canting angle $\overline{\theta}_b$ of the B sublattice is given by

$$\cos\overline{\theta}_b = \sum_{m=0}^{n_{ba}} p_{ba}(m)\frac{(n_{ba} - m)}{2\delta\sum_{q=0}^{n_{bb}} p_{bb}(q)(n_{bb} - q)}. \tag{2}$$

The summation factor

$$\sum_{q=0}^{n_{bb}} p_{bb}(q)(n_{bb} - q)$$

in the denominator works out to be equal to $k_b n_{bb}$; $p_{ij}(r)$ is the probability of an Fe^{3+} ion on sublattice i having r of its n_{ij} neighbours on sublattice j as diamagnetic ions while a fraction k_j of the latter is magnetic. For the case under consideration $k_a = (1 - z)$, $k_b = (1{\cdot}5 + z/2)/2$ and from binomial distribution function $p_{ij}(r) = \binom{n_{ij}}{r} k_j^{(n_{ij} - r)}(1 - k_j)^r$. As postulated by Rosencwaig (1970) the individual $\cos\theta_b$ values in (2) before multiplication with the probability $p_{ba}(m)$ are always limited according to

$$\frac{(n_{bb}-m)}{2\delta k_b n_{bb}} = \cos\overline{\theta_b} \leqslant 1.$$

The 0°K magnetic moment $\mu(z, T=0)$ in Böhr magneton is given by

$$\mu(z, T=0) = 10\,k_b \textstyle\sum_{m=0}^{n_{ba}} p_{ba}(m)\cos\phi_b(m, z) - 5k_a \tag{3}$$

where $\cos\phi_b(m, z)$ is obtained from (1) for each m at zinc substitution level z by taking summation over all possible values of q from 0 to n_{bb} and multiplying these with their respective probabilities of occurrence.

The Curie temperatures $T_c(z)$ in °K is given by the expression

$$\frac{T_c(z)}{T_c(z=0)} = \frac{[(\bar{S}+1)/\bar{S}]_z}{[(\bar{S}+1)/\bar{S}]_{z=0}} \cdot \frac{[-V(z)]}{[-V(z=0)]}, \tag{4}$$

where the net spin $\bar{S}$ per ion per formula unit is given by $\bar{S} = (k_a + 2k_b)S/7$ and the total potential energy $V(z)$ per formula unit is represented by

$$V(z) = 2S^2 J_{ab}\left[2k_b \sum_{m=0}^{n_{ba}} p_{ba}(m) \cdot \{(n_{ba}-m)\cos\phi_b(m, z) - k_b n_{bb}\delta\cos 2\phi_b(m, z) - \tfrac{1}{2}k_a^2 n_{aa}\gamma\}\right]. \tag{5}$$

The Curie temperature $T_c(z=0)$ (Pran Kishan *et al* 1981) of the unsubstituted lithium ferrite in these equations has been taken as 913°K.

3. Results and discussion

In lithium ferrite though the zinc ions on substitution occupy tetrahedral A sites, there occurs a simultaneous change in diamagnetic Li^{1+} ion content on B sublattice as well according to the formula given above. The Rosencwaig LC model for doubly-substituted systems (Rosencwaig 1970) should therefore apply. According to the criterion that follows from his arguments the sublattice that has a larger absolute value of the product $l_i k_i n_{ii} J_{ii}$ where l_i is the number of magnetic ions per formula unit in the sublattice i, has its spins subjected to canting. Using the published values of exchange parameters of lithium ferrite as given in table 1 it can be seen that in the ferrite compositions studied here, the canting if occurs does so on the B sublattice only.

Table 1. Exchange parameters of $Li_{0.5}Fe_{2.5}O_4$

J_{aa} (°K)	J_{bb} (°K)	J_{ab} (°K)	$\delta = \left\lvert\frac{J_{bb}}{J_{ab}}\right\rvert$	$\gamma = \left\lvert\frac{J_{aa}}{J_{ab}}\right\rvert$	Reference
−20·0	−8·0	−29·0	0·28	0·69	Srivastva *et al* (1979)
−28·0	−15·0	−34·0	0·44	0·82	Dionne (1976)
−19·5	−10·6	−24·0	0·44	0·81	Rado and Follen (1960)
−8·0	−8·8	−24·0	0·27	0·33	Feldman *et al* (1979)
—	—	—	0·33	0·36	White *et al* (1978)

However, due to random placement of diamagnetic ions in the two sublattices, possible that there might be some regions in the crystal where on localised basis value of $l_b k_b n_{bb} J_{bb}$ becomes smaller than the corresponding value for the A sublattic is, therefore, the latter that should experience canting in that region. To mathematic account for such situations Rosencwaig invoked the concept of localised spin flips t should take place for those A site Fe^{3+} ions that are either weakly or not at magnetically bound to the B sublattice while only the spins of Fe^{3+} ions of the la experience localised canting. This then necessitates the inclusion of an additional fa $\cos\phi_a(t, z)$ in the A sublattice term of equations (3) and (4) with the restriction tha can take only the values 0 or π. Setting $\cos\bar{\theta}_a = 1$ the values of $\cos\phi_a(t, z)$ can calculated from an equation similar to equation (1) but adapted for the case o sublattice.

For an Fe^{3+} ion of A sublattice there are 12 nearest neighbour B site cations. In unsubstituted lithium ferrite on the average 9 of these are bonds to B site Fe^{3+} i while the number t of the bonds to diamagnetic Li^{1+} ions is only 3. But becaus random distribution of ions in the B sublattice the actual values of t for individual A Fe^{3+} ions may vary from 0 to 12 with the probabilities of their occurrence given by binomial distribution function. Calculations for $\cos\phi_a(t, 0)$ show that while ϕ remains zero for all values of t from 0 to 8, the probability of t taking a value larger t 8 is practically zero. At higher z levels the concentration of Fe^{3+} ions on B sublat increases and the probability of t taking higher values reduces still further. That me no spin flips at all on A sublattice while the spins of B site Fe^{3+} ions alone experie canting depending on the zinc substitution level of the ferrite composition. Thus fo present series the factor $\cos\phi_a(t, z)$ always remains equal to one and need no included in (3) and (4) and that the Rosencwaig LC equations for singly-substit systems should apply.

The exchange field seen by a B site Fe^{3+} ion has contributions arising both fro and B sublattice magnetically active ions. While the B sublattice field experienced particular B site Fe^{3+} ion is canted at an average canting angle $\bar{\theta}_b$ which is the same all the Fe^{3+} ions of this sublattice, its magnitude depends on the number of oth sublattice nearest neighbour Fe^{3+} ions that surround it. In singly-substituted gar with diamagnetic ions replacing Fe^{3+} ions on the A sublattice dealt in Rosenc (1970) this number remains unchanged and therefore the corresponding D subla exchange field contribution is the same in magnitude and direction for all the D Fe^{3+} ions. For the present series, however, the number of magnetically activ sublattice ions that surround a B site Fe^{3+} ion changes with z and because of ran distribution of ions on the sublattice it may take any value from 0 to n_{bb} probabilities that can be calculated with the help of the probability equation g earlier. This feature, though unnecessary for the case of a singly substituted ga mentioned above, has to be incorporated in the canting equations for zinc substitut in lithium ferrite. For example in (2) n_{bb}, corresponding to Rosencwaig (1970) has replaced by

$$\sum_{q=0}^{n_{bb}} p_{bb}(q)(n_{bb} - q) = k_b n_{bb}.$$

Similar modifications are needed in other equations as well where n_{bb} and n_{aa} have replaced by $k_b n_{bb}$ and $k_a n_{aa}$ respectively. It may be mentioned here that modificatio the same lines are also necessary in the canting equations proposed in Rosencwaig (1970) for doubly-substituted systems. The k_i factors that already appear in these equations account for changes in the number of magnetic ions only on diamagnetic substitution and not in the number of intrasublattice interaction bonds. Without the suggested extension, one can only expect a qualitative agreement between the theory and the experimental results.

In the extended LCM equations given earlier the exchange constant ratios δ and γ are the most important parameters. Several sets of exchange constants as given in table 1 are available in literature for lithium ferrite. Srivastava *et al* (1979) have shown that a good fit for magnetisation can be obtained with several of these reported sets though that is not so for the susceptibility and that the criterion for the selection of a proper set should be its simultaneous satisfaction of both the data. On this basis these authors determined the exchange parameters for a number of spinels excluding lithium ferrite for which susceptibility data were not available. They, however, chose a set for the latter which was in conformity with the exchange constants of the other similar spinel systems and is thus expected to be the right set for the compound. With this and other sets of exchange constants of table 1, theoretical values of 0°K magnetic moment have been calculated on the basis of LC model for the series of zinc substituted lithium ferrite. These values have been plotted in figure 1 along with experimental results of Gorter (1954). It can be seen that in the substitution range studied here, there is a functional similarity between the experimental data and the calculated values. As expected the agreement is better for the values calculated with exchange parameters reported by Srivastava *et al* (1979). Considering the limitations of the model, one of which is the assumption that the exchange parameters are taken independent of the extent of diamagnetic substitution, the agreement between the theory and experimental data can be regarded as reasonably good.

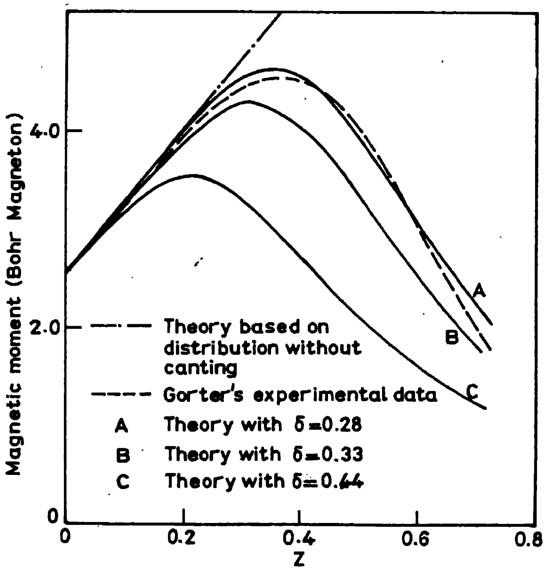

Figure 1. Zero degree K magnetization as a function of Zn concentration z in $Li_{0.5-z/2}Zn_zFe_{2.5-z/2}O_4$.

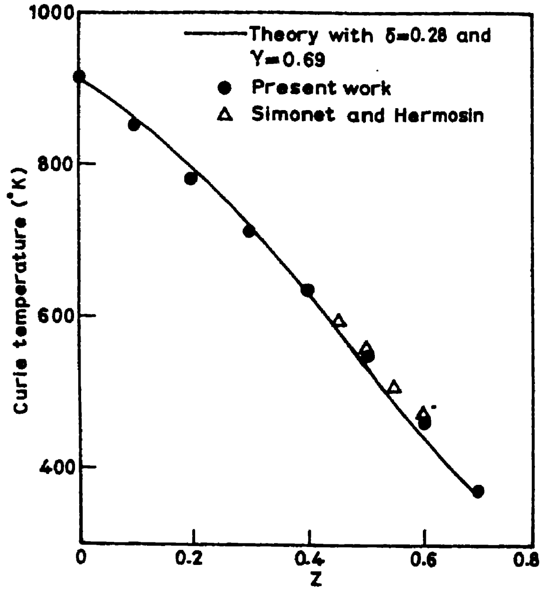

Figure 2. Calculated and experimental Curie temperature for the system with $z = 0$ t $Li_{0.5-z/2}Fe_{2.5-z/2}O_4$.

The same set of exchange parameters *i.e.* $\delta = 0{\cdot}28$ and $\gamma = 0{\cdot}69$ was also used calculation of Curie temperatures of these compositions. As depicted in figure agreement is quite satisfactory with the experimental data of Simonet and Her (1978) and that obtained in the present study. The methods of sample preparatio Curie temperature determination used by us have been reported elsewhere Kishan *et al* 1981).

4. Conclusion

It can be stated that large zinc substitutions in lithium ferrite lead to a noncol spin arrangement adequately described by Rosencwaig localized canting n Furthermore, the set of exchange constants reported by Srivastava *et al* (197 lithium ferrite when used in canting equations predicts reasonably correct values c saturation magnetization and Curie temperatures in zinc-substituted lithium compositions.

References

Dionne G F 1976 *J. Appl. Phys.* 47 4220
Dorman J L, Merceron T and Nogues M 1981 *Applied Mössbauer effect*, Proc. Int. Conf., Jaipur
Feldmann P, Simonet W, Desvignes J M and Le Gall H 1979 Joint Intermag 3M Conf. (New York), A 10 (Unpublished work)
Geller S, Williams H J, Spinola G P and Sherwood R C 1964 *Bell. Sys. Tech. J.* 43 565
Gorter E W 1954 *Phillips. Res. Rep.* 9 295

Néel L 1948 *Ann. Phys. (Paris)* **3** 137
Nogues M, Dorman J L, Perrin M, Simonet W and Gibert P 1979 *IEEE Trans.* **MAG-15** 1729
Nowik I 1968 *J. Appl. Phys.* **40** 5184
Patton C E, Edmondson C A and Liu Y H 1982 *J. Appl. Phys.* **53** 2431
Pran Kishan, Chatterjee S N, Nagpaul L K and Laroia K K 1981 *Indian J. Pure Appl. Phys.* **19** 83
Rado G T and Follen V J 1960 *J. Appl. Phys.* **31** 62
Rosencwaig A 1970 *Can. J. Phys.* **48** 2857, 2868
Simonet W and Hermosin A 1978 *IEEE Trans.* **MAG-14** 903
Srivastava C M, Srinivasan G and Nanadikar N G 1979 *Phys. Rev.* **B19** 499
White G O, Edmondson C A, Goldfarb R B and Patton C E 1978 *J. Appl. Phys.* **50** 2381
Yafet Y and Kittel C 1952 *Phys. Rev.* **87** 290
Zhilyakov S M, Ivolga V V, Mel' tsev V I and Naiden E P 1977 *Sov. Phys. Sol. State* **19** 1817

Bull. Mater. Sci., Vol. 6, No. 1, February 1984, pp. 47–52.
© Printed in India.

Preparation of single crystal films of magnetic bubble materials—Rare earth yttrium iron gallium garnets by liquid phase epitaxy and their physical properties

PRAGATI MUKHOPADHYAY and B UMA MAHESHWAR RAO*

Advanced Centre for Research in Electronics, *Dept. of Physics, Indian Institute of Technology, Powai, Bombay 400 076, India

Abstract. The liquid phase epitaxial growth of rare earth-substituted magnetic garnet films suitable for magnetic bubble domain application by both vertical and horizontal dipping using PbO and B_2O_3 as flux is reported. The dependence of various parameters on lead incorporation in the films present as inhomogeneity has been studied.

Keywords. Liquid phase epitaxy; magnetic bubble materials; saturation temperature; growth temperature.

1. Introduction

To prepare magnetic bubble materials suitable for device application, thin layers of magnetic garnet films showing both high physical perfection and good reproducibility must be prepared. The physical parameters of these thin magnetic garnet layers are determined by their chemical composition which are governed by the growth parameters. In this paper, we report the successful preparation and some physical properties of thin single crystal films of rare earth substituted garnets of the type $Y_{3-x}R_xFe_{5-y}Ga_yO_{12}$ where R is Eu or Sm. The Pb incorporation is always found to be present as an impurity in the films grown at various temperature. These impurities in the film give rise to lattice mismatch and stresses which in turn change parameters like the anisotropy field H_A. The change in the anisotropy field H_A due to Pb impurity has been studied and reported in this paper.

2. Preparation of epitaxial layers

2.1 *Epitaxial growth*

Epitaxial growth of garnet films is achieved using the liquid phase epitaxy (LPE) method (Levenstein *et al* 1971; Giess *et al* 1972; Robertson *et al* 1974) by dipping a non-magnetic GGG (gadolinium gallium garnet) substrate into a supercooled melt containing $PbO–B_2O_3$ flux and garnet components. The ratio of $PbO–B_2O_3$ flux to garnet constituents is chosen such as to give a garnet phase only. Table 1 gives the melt-flux compositions for two different rare earth substituted garnet compositions attempted by us.

2.2 *LPE furnace*

The LPE furnace designed and fabricated is shown in figures 1 and 2. It is a three-zone kanthal wound vertical furnace giving a 8 cm constant temperature zone in the middle

Table 1. Melt-flux compositions (mole %)

Constituents	$Y_{3-x}Eu_xFe_{5-y}Ga_yO_{12}$	$Y_{3-x}Sm_xFe_{5-y}Ga_yO_{12}$
PbO	84·92	85·671
B_2O_3	5·4	5·493
Y_2O_3	0·55	0·25
Eu_2O_3	0·17	—
Sm_2O_3	—	0·047
Fe_2O_3	7·83	7·423
Ga_2O_3	1·13	1·116
T_s (°C)	992 ± 1	890 ± 1
(*)ΔT(°C)	12	15

(*) $\Delta T = T_s - T_g$

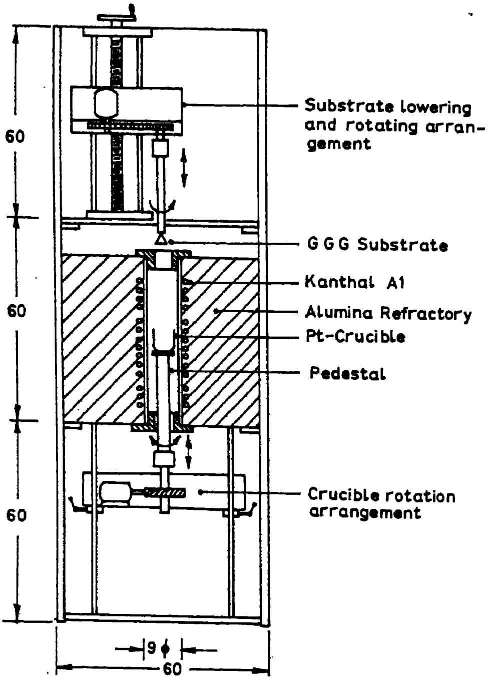

Figure 1. Scheme of liquid phase epitaxy apparatus.

with a temperature stability of ±1°C. The furnace is incorporated with a substrate rotating/lowering unit, a temperature controller and a crucible rotating unit. The whole assembly is placed in a class 100 vertical laminar flow tent as shown in figure 2. This precaution is taken since dust free environment is one of the stringest requirements for growing bubble films.

Figure 2. LPE furnace inside a class 100 laminar flow tent.

2.3 *Substrate cleaning*

Substrate cleaning is an important and crucial factor before growing the films. Film perfection can be achieved mainly on the availability of a dust-free clean substrate. Hence cleaning of the substrate as well as the growth of the epitaxial layer must be done in dust free special clean rooms. Previous studies (Haisma *et al* 1974) have shown that imperfect and dirty GGG substrates can locally dissolve and defects such as small secondary garnet crystals come up. The substrates are cleaned by washing in warm dilute detergent followed by thorough rinsing in deionized water using class 100 chemical benches. Final cleaning before loading the substrate into the furnace is done by treating it ultrasonically in trichloroethylene vapours under dust free condition.

3. Film growth

The garnet oxides and flux powders after mixing thoroughly are placed in the constant temperature zone of the furnace in a platinum crucible with a lid. This mixture is premelted at 1000 °C and this process repeated twice since the volume of the unmelted powders is greater than that of the crucible. For homogenization and complete dissolution of garnet components into the melt, the melt is heated and stirred at 1100 °C for about 8 hours. The substrate is then slowly lowered after decreasing the melt temperature to a fixed growth temperature T_g which is several degrees below the saturation temperature T_s. For horizontal dipping, the substrate is rotated at a constant speed for better uniformity of the layer whereas for the vertical dipping mode no rotation is necessary. In both cases, the substrate is held for a few minutes, prior to dipping, just above the supercooled melt to achieve temperature equilibration and then dipped for a known time. The substrate is removed and cleaned off the residual flux. Figure 3 represents the function and time schedule for our LPE growths. In case of vertical dipping the substrate rotation was zero RPM.

4. Results and discussions

The physical properties of the Eu and Sm substituted gallium garnets were studied by dipping smaller pieces of substrates prior to each run.

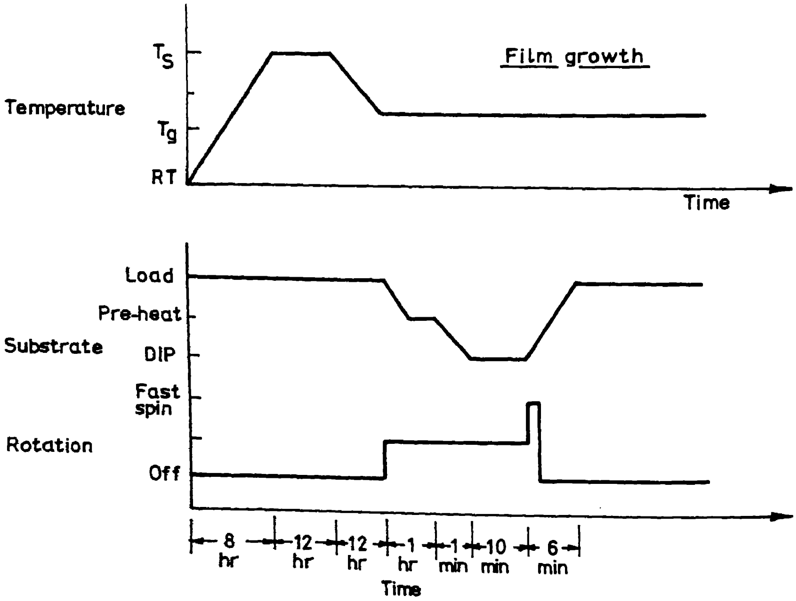

Figure 3. Function and time schedule for LPE film.

The film thickness (h) was measured by interface method by spherical contouring (Rosenbaum 1968), the room temperature saturation magnetisation ($4\pi M_s$) measured by using a vibrating sample magnetometer which was calibrated against YIG standard. The accuracy of the $4\pi M_s$ value is ± 50 Gauss. The film/substrate lattice mismatch Δa ($\Delta a = a_{\text{substrate}} - a_{\text{film}}$) was measured by x-ray diffraction method using CuKα radiation and the symmetric (888) reflection mode from which the film lattice parameter can be calculated (Besser *et al* 1971). The quantitative check on Pb content and the chemical analysis of the LPE films were done by electron microprobe analysis (Zimmer and Tolksdorf 1974) using a scanning electron microscope with an energy dispersive x-ray detector. The anisotropy field H_A was calculated from the ESR spectra.

The study of Pb content in various films showed that: (i) The transparency of the film rapidly diminished and had a brownish colouration for films having larger Pb-content. (ii) Lattice mismatch increases with the Pb-content. (iii) The anisotropy field H_A increased with the increase of Pb-content in the films.

The larger mismatch and higher anisotropy field values due to higher Pb content can be explained by the large stresses present in the film. These stresses are introduced by Pb impurities Pb^{2+} on C-site or Pb^{4+} on a-site.

Some of the stress anisotropy can be removed by annealing the films. The studies on the effect of annealing on anisotropy field are in progress and will be reported elsewhere. Some of the measured parameters and other results are summarized in table 2 and figure 4.

Table 2. Properties of rare earth yttrium iron gallium garnets.

	LPE composition			
Parameter	Eu, Ga: YIG	Sm, Ga: YIG		
h (μm)	$10 \pm 0{\cdot}5$	$6 \pm 0{\cdot}5$	$4{\cdot}5 \pm 0{\cdot}5$	$3 \pm 0{\cdot}5$
a (Å)	$-0{\cdot}015$	$-0{\cdot}02$	—	—
$4\pi M_s$ (G)	200 ± 50	100 ± 50	132 ± 50	150 ± 50
H_A (Oe)	1740	1790	1150	1049
γ(rad Sec^{-1} Oe^{-1})	$1{\cdot}71 \times 10^7$	$1{\cdot}7 \times 10^7$	$1{\cdot}7 \times 10^7$	$1{\cdot}7 \times 10^7$
Pb content (atoms per formula unit)	0·23	0·3	0·13	0·06
ΔT (°C)	12	15	15	15
Rotation rate (RPM)	50	0	0	0
Melt Comp.	$Eu_xY_{3-x}Ga_yFe_{5-y}O_{12}$	$Sm_xY_{3-x}Ga_yFe_{5-y}O_{12}$		
x	0·6	0·38		
y	1·1	1·15		
Film Comp.				
x	0·53	0·2 to 0·25		
y	1·47	1·8 to 2		

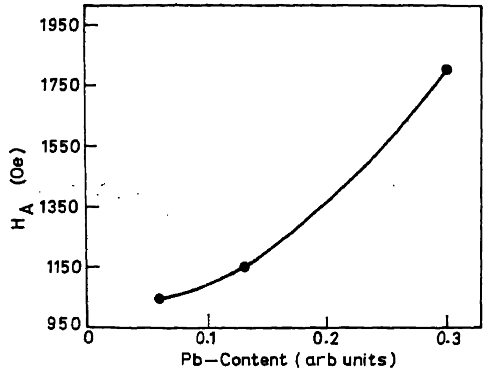

Figure 4. Changes in the anisotropy field with Pb-impurity in the film.

Acknowledgements

Our sincere thanks to Prof. C M Srivastava for his keen interest, continuous hel encouragement throughout this project. We would also like to thank Prc Tolksdorf of Philips GmbH (Germany) for valuable suggestions and for giving standards for electron microprobe analysis. Most of our measurements were using the instruments of RSIC (Regional Sophisticated Instrument Centre) Centre at Bombay.

References

Besser P J 1971 *AIP Conf. Proc.* No. **5** 125
Giess E A, Kuptsis J D and White E A D 1972 *J. Crystal Growth* **16** 36
Haisma J 1974 *Philips Res. Rep.* **29** 493
Levenstein H J, Licht S, Landorf R W and Blank S L 1971 *Appl. Phys. Lett.* **19** 486
Rosenbaum S D 1968 *S.S.E.* **11** 711
Robertson J M, Tolksdorf W and Jonker H D 1974 *J. Crystal growth* **27** 241
Zimmer M and Tolksdorf W 1974 *J. Crystal growth* **23** 331

Bull. Mater. Sci., Vol. 6, No. 1, February 1984, pp. 53–57.
© Printed in India.

Electron transport in non-crystalline garnet films

D BAHADUR, D ROY, B SINGH* and D SARAN*

Advanced Centre for Materials Science, Indian Institute of Technology, Kanpur 208 016, India

*Department of Physics, Indian Institute of Technology, Kanpur 208 016, India

Abstract. Thin films of yttrium iron garnet (YIG) and Gd-substituted YIG of different thickness have been prepared by flash evaporation. The surface DC and AC electrical resistivity and thermopower in these films have been studied. The results are explained on the basis of Mott and Davis model in which narrow tails of localised states exist at the extreme valence and conduction bands and a band of localised levels near the middle of the gap. For the temperature range studied, the main conduction mechanism is on account of excitation of carriers into localised states at the band edges and hopping at energies close to the band tails.

Keywords. Thin films; non-crystalline garnet; electron transport; activation energy.

1. Introduction

The electron transport on polycrystalline and single crystals of yttrium iron garnet and its derivatives has been studied and understood in the last couple of decades (Elwell and Dixon 1968; Larsen and Metselaar 1976; Bahadur *et al* 1981). Some attempts have also been made to prepare non-crystalline garnets and characterise them (Popma and Van Diepen 1974; Cuomo *et al* 1972). We have recently prepared non-crystalline garnet by flash evaporation and investigated the magnetic domains and structural transformations (Bahadur and Rai 1980). To get further insight into the electronic behaviour of these films, a number of films of YIG and Y_2 GdIG have now been prepared and its electron transport behaviour has been studied. The electron transport in bulk samples has been studied recently (Bahadur *et al* 1981). It was therefore considered worthwhile to investigate the effect of disorder and film thickness on the electron transport studies on the films of the same compositions.

2. Experimental

The polycrystalline samples of YIG and Y_2GdIG were prepared by the usual ceramic method of mixing and sintering of constituent oxides at 1350°C. These samples were characterised by x-ray diffraction for a single phase. All the oxides were of high purity. Thin films of these garnets were deposited on a clean glass and quartz substrate by flash evaporation in an ultimate vacuum of 2×10^{-5} torr. Gold electrodes were deposited on the film for electron transport studies. Thickness of these films was measured. The standard error in thickness measurement is ± 20 Å. Before the electron transport measurements, the films were annealed at 450 K for about 72 hr. The surface electrical resistivity (AC and DC) was measured using a Keithley electrometer and 1610 GR impedance bridge with RC oscillator and null detector. I-V characteristics were tested at intermittent temperatures to check its linearity. Thermo-eme was measured using Leeds and Northrup potentiometer.

3. Results and Discussion

All the films are amorphous in nature as evident from x-ray and electron diffr The thickness of different YIG films were 230, 560 and 1330 Å. A typical plot surface electrical resistivity (DC) versus inverse of temperature for YIG film of 2 given in figure 1. Table 1 gives the activation energies of conduction for different for YIG films. Resistivity data was taken while decreasing the temperature a activation energy was seen to be lower. This could be due to the increase in gr after crystallisation reducing the discontinuity in the film which gave an add activation energy for the film. However, no such marked change was obser higher thickness. Resistivity also decreases as the thickness increases and this with the studies on semi-conducting films (Chopra 1969). Activation energy also a similar trend. We have taken thermoelectric power data versus temperature for the YIG films of thicknesses 560 and 1300 Å and the plot for the first is given in fi

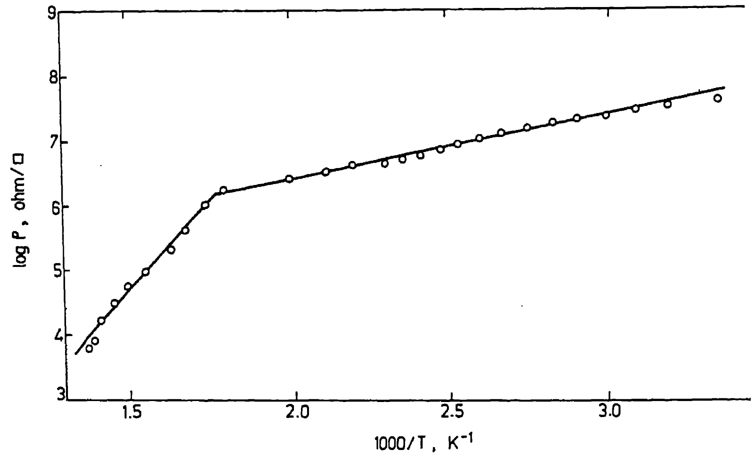

Figure 1. Plot of surface electrical resistivity (DC) versus inverse of temperature for of thickness 230 Å.

Table 1. Activation energies in different ranges for thin films of YIG

Sample's thickness (Å)	Range (K)	Activation energies (eV)
230	300–570	0·20
	570–725	1·06 (0·62)*
560	400–550	0·16
	550–730	0·80
1300	450–540	0·07

*In parenthesis is given the value of activation energy while lowering the temperature

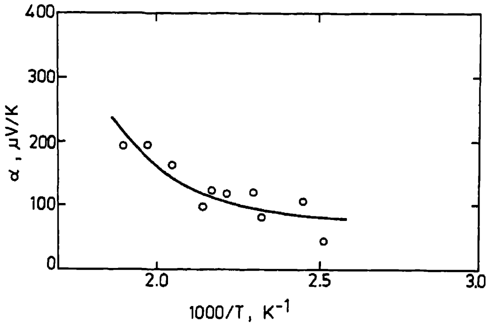

Figure 2. Plot of thermo-electric power versus inverse of temperature for YIG film of 560 Å thickness.

From figure 1 and table 1, we observe two ranges for activation energies of conduction similar to that found in bulk YIG earlier (Bahadur *et al* 1981). However, the values are less than what is observed for bulk YIG. This is to be expected if we assume band model for amorphous systems (Mott and Davis 1979; Nagels 1979) where tails of localised states and band of compensated levels within the gap could, in principle, cause lowering of activation energies.

Thermoelectric power, α, versus inverse of temperature plot shows that α is positive and increases with temperature showing that the holes are the majority charge carriers. However, the values are less than the bulk values which is possibly due to higher density of states at the fermi energy.

A typical plot of surface electrical resistivity (DC) for Y_2GdIG thin film of 420 Å thickness is given in figure 3. For the same film, the log of AC resistivity is plotted against log of frequency in figure 4. The resistivity between 290 and 490 K was measured for three samples of Y_2GdIG. The activation energies of conduction and S values are given in table 2. Only a small change is seen in the activation energies near 390 K for all the three samples. However, no such change was observed in YIG films around this temperature. This change appears to be characteristic of gadolinium substitution; the change is nearly same in all the three samples. In fact, in bulk Y_2GdIG also, an additional range of activation energy has been observed earlier (Bahadur *et al* 1981).

It is interesting that the frequency dependence of resistivity varies approximately as ω^s where $S < 1$ and lies between 0·65 and 0·9. In figure 3(b), it is observed that the S value at room temperature is 0·81 whereas at 475 K, it is 0·78. It has also been observed that $\rho(\omega)$ for this sample exponentially depends upon temperature.

Based on the above observations, we propose that the electronic conduction is on account of excitation of carriers into localised states at the band edges and hopping at energies close to band tails; DC resistivity in such a situation will be given by (Mott and Davis 1979).

$$\rho = \rho_0 \exp[(E_a - E_f + W)/kT],$$

where E_a corresponds to the band edge, W is the activation energy for hopping and ρ_0 is the pre-exponential factor which depends upon the density of states near E_a, hopping distance and the bandwidth of localised states. The essential feature of the Davis and Mott model is the narrow tails of localised states at the extremities of the valence and

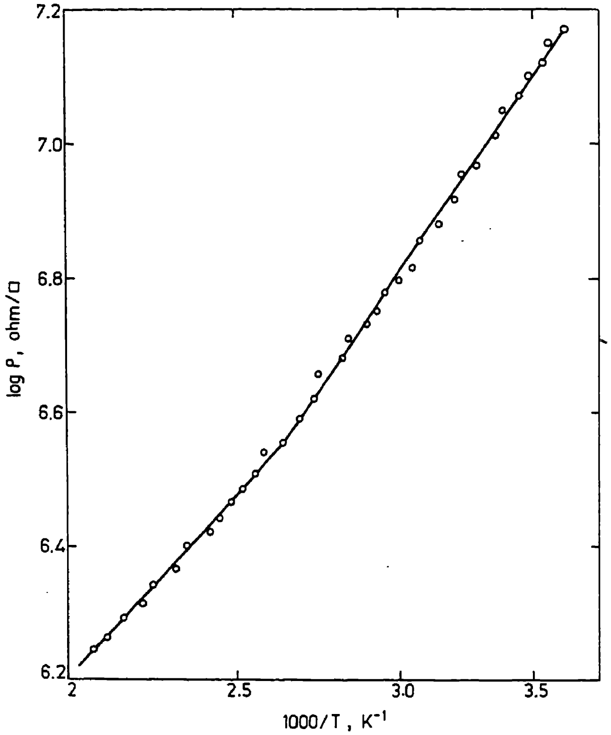

Figure 3. Plot of surface electrical resistivity (DC) versus inverse of tempera Y_2GdIG film of 420 Å thickness.

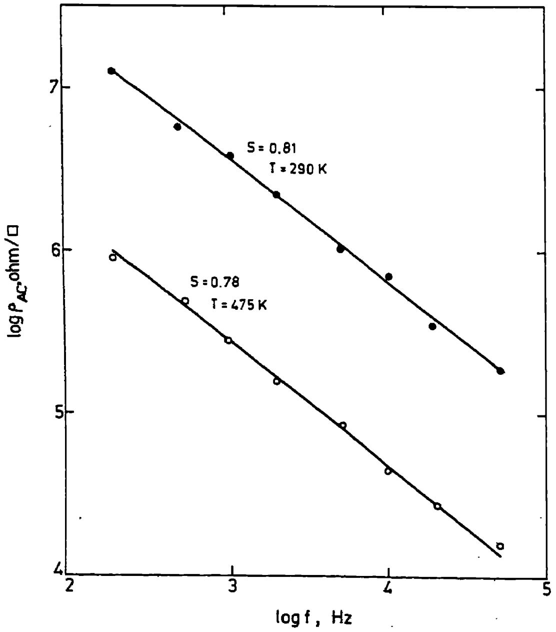

Figure 4. Plot of AC resistivity versus frequency for Y_2GdIG film of 420 Å thic

Table 2. Activation energies in different ranges for thin films of Y_2GdIG

Sample's thickness (Å)	Range (K)	Activation energies (eV)	S value at 290 K
420	290–380	0·14	0·78
	380–475	0·11	
570	330–390	0·20	0·65
	390–485	0·17	
1300	290–380	0·16	0·88
	380–455	0·13	

conduction bands and furthermore of a band of localised levels near the middle of the gap. According to this model, three different conduction mechanisms are possible.

Extended state conduction requires a frequency-independent resistivity and the slope for S and $\log \rho$ *vs* $1/T$ be the same which are not found in the present results. However, at higher temperature, it is not ruled out. Since, most of our results are between 290 and 550 K, our discussion would be limited for this region only. For this range of temperature it appears that the conduction in localised states at the fermi-energy would not be operative. This is indicated by the exponential dependence of $\rho(\omega)$ on temperature which is characteristic of conduction in band tails. Again, it is possible that at low temperature, the conduction is through variable range hopping due to the Anderson localised states at the fermi-energy (Anderson 1958; Rao *et al* 1975). Detailed low temperature studies are in progress to ascertain these facts.

Acknowledgement

Thanks are due to Department of Atomic Energy for the award of research grants.

References

Anderson P W 1958 *Phys. Rev.* **109** 1492
Bahadur D and Rai K N 1980 *Mater. Res. Bull.* **15** 551
Bahadur D, Parkash O and Kumar D 1981 *Bull. Mater. Sci.* **3** 325
Chopra K L 1969 *Thin film phenomena* (New York and London: McGraw-Hill)
Cuomo J J, Sadagopan V, Deluco J, Chaudhary P and Rosenters R 1972 *Appl. Phys. Lett.* **21** 581
Elwell D E and Dixon A 1968 *Solid State Commun.* **6** 585
Larsen P K and Metselaar R 1976 *Phys. Rev.* **B14** 2520
Mott N F and Davis E A 1979 *Electronic processes in non-crystalline materials* (Oxford: Clarendon) p 199
Nagels P 1979 *in Amorphous semi-conductors* (ed.) M H Brodsky (Berlin, Heidelberg and New York: Springer Verlag) p 113
Popma J A Th and Van Diepen A M 1974 *Mater. Res. Bull.* **9** 1119
Rao C N R, Bhide V G and Mott N F 1975 *Philos. Mag.* **32** 1277 (and references therein)

Bull. Mater. Sci., Vol. 6, No. 1, February 1984, pp. 59–64.
© Printed in India.

Development of pure and doped gamma ferric oxide

M R ANANTHARAMAN, K SESHAN, S N SHRINGI* and H V KEER

Department of Chemistry, *Department of Physics, Indian Institute of Technology, Bombay 400076, India.

MS received 7 May 1983; revised 28 December 1983

Abstract. Optimum conditions and experimental details for the formation of γ–Fe_2O_3 from goethite have been worked out. In another method, a cheap complexing medium of starch was employed for precipitating acicular ferrous oxalate, which on decomposition in nitrogen and subsequent oxidation yielded acicular γ–Fe_2O_3. On the basis of thermal decomposition in dry and moist nitrogen, DTA, XRD, GC and thermodynamic arguments, the mechanism of decomposition was elucidated. New materials obtained by doping γ–Fe_2O_3 with 1–16 atomic percent magnesium, cobalt, nickel and copper, were synthesised and characterized.

Keywords. Magnetic recording materials; gamma ferric oxide; thermal decomposition.

1. Introduction

The potential of gamma ferric oxide (γ–Fe_2O_3) as a magnetic tape recording material has provoked a great deal of investigations over the past several years (Smit 1971; Venkatesh Rao *et al* 1974; Seshan *et al* 1981b; Anantharaman *et al* 1981). It can be prepared commercially with the required parameters from synthetic goethite. However the present annual demand of our country (~ 25 MT) is met mainly through import (Patil 1977). Since most of the literature on this method is patented and/or vaguely known, the first step in the indigenization process involves working out the optimum conditions and experimental details of each step of synthesis on a laboratory scale, before it is taken up on a pilot-plant scale. These have been reported in the present communication. Another preparative method involves thermal decomposition of ferrous oxalate dihydrate in an inert atmosphere to magnetite, followed by careful oxidation to γ–Fe_2O_3 (Seshan *et al* 1981a). However, this method involves a costly glycerol medium, which is required to retain acicularity. With a view to economizing the process, a cheap complexing medium of starch has been employed for precipitating acicular ferrous oxalate, almost without loss of quality. Further, the mechanism of thermal decomposition of the oxalate has been reported to involve the existence of FeO and H_2 (Dollimore *et al* 1963; Bevan and Brown 1966; Venkatesh Rao *et al* 1974). Experimental evidences, in conjunction with thermodynamic arguments, are being presented to unequivocally elucidate the mechanism. Finally, since γ–Fe_2O_3, a vacancy-ordered spinel, is thermodynamically unstable with respect to α–Fe_2O_3 at ambient temperatures, efforts were made to stabilize the structure and to develop new materials, by doping with small amounts of magnesium, cobalt, nickel and copper in the atomic percent range 1–16.

2. Experimental

Apart from the conventional solution chemistry precipitation technique, va instrumental methods such as x-ray powder diffraction (XRD), differential the analysis (DTA), thermogravimetry (TG), gas chromatography (GC), magnetic hyst loop tracing (HLT), initial susceptibility (x_i) and transmission electron micros (TEM) were employed to characterize the intermediates at each stage of the rea process. DTA/TG curves were recorded in air and also in oxygen-free moist an nitrogen, using 10 mg of the sample at a heating rate of 5°C/min and a gas flow r 150 ml/min. The XRD of the samples were carried out in a Philips x-ray diffracto (PW1140) using FeK_α radiation. The evolution of hydrogen was detected in an o gas-chromatograph (AIMIL–NCL Dual Column gas chromatograph Mk II) molecular sieve 13 × column in a carrier gas atmosphere of oxygen-free nitrogen magnetic properties were measured on a hysteresis loop tracer and initial suscepti unit (Likhite *et al* 1965; Radhakrishnamurty and Sahasrabudhe 1965). The shap size of the particles were determined from transmission electron micrographs tak a Philips electron microscope (EM301).

2.1 *Synthesis of goethite*

Goethite was synthesized from a solution of $FeSO_4 \cdot 7H_2O$ (Camras 1954) and iron containing a seed solution of α-FeOOH aided by constant aeration (Camras for several hours.

2.2 *Synthesis of ferrous oxalate*

It is well-known that the aqueous medium is unsuitable for the precipitati $FeC_2O_4 \cdot 2H_2O$(FOD), as it yields only spherical particles (Seshan *et al* 1 Literature reports (Berkowitz and Schuele 1968; Seshan 1981b) show employm the costly glycerol as the complexing medium to precipitate acicular FOD. After t several media, it has been found that a saturated solution of starch and water co employed to obtain acicular crystals.

2.3 *Synthesis of mixed oxalates*

The starting materials for the synthesis of doped gamma ferric oxide were oxalates of iron and the dopant (Mg/Co/Ni/Cu), which was co-precipitated f solution of the corresponding sulphates in required proportions, using oxalic aci medium for precipitation was starch and water in order to yield needle-like crys the mixed oxalate. The dopant concentration was varied between 1 and 16 a percent.

3. Results and discussion

3.1 *Formation of maghemite from synthetic goethite*

It is well-known that the preparation of synthetic goethite (α–FeOOH) follo sequence

$$\text{Goethite} \rightarrow \text{Hematite} \rightarrow \text{Magnetite} \rightarrow \text{Maghemite.}$$

nalysis of the XRD pattern showed 3 principal d_{hkl} lines *viz.*, 4·179 Å, 2·440 Å and ·684 Å corresponding to 100, 72 and 45 I/I_0 respectively. These are in good agreement ith the reported ASTM data (1966). DTA of these samples exhibited an endothermic peak t 250°C, with a corresponding mass loss of 10·3 % (from TG) associated with the rmation of Fe_2O_3. Therefore, dehydration of goethite was carried out isothermally at 50°C for a sufficient length of time (30 min) to yield α–Fe_2O_3. The XRD pattern of these mples on analysis indicated the presence of 3 principal d_{hkl} lines, *viz.*, 2·69, 1·69 and ·51 Å corresponding to 76, 38 and 100 I/I_0 respectively. These are in good conformity ith the reported ASTM data (1966).

Further, both α–FeOOH and γ–Fe_2O_3 were found to be acicular (length/breadth 10) from TEM micrographs (cf figure 1). It has been reported (Camras 1954) that duction of α–Fe_2O_3 at about 400°C yields Fe_3O_4. Therefore, α–Fe_2O_3 was othermally reduced at 350°, 370° and 400°C respectively with hydrogen for 45 min. It as found that at 370°C, quantitative reduction to black, acicular Fe_3O_4 takes place. he experimentally observed lattice constant (a = 8·36 Å) agreed favourably with the ported ASTM value of 8·396 Å (1966). Further, the magnetization value of 85 emu/gm as in excellent agreement with the expected one (90 emu/gm).

The oxidation of Fe_3O_4 to γ–Fe_2O_3 is generally carried out in air containing water ipour with $P_{H_2O} \simeq 30$ torr (David and Welch 1956). To find the optimum conditions, TA and TG of Fe_3O_4 were carried out in a current of moist air ($P_{H_2O} \simeq 28$ torr) which

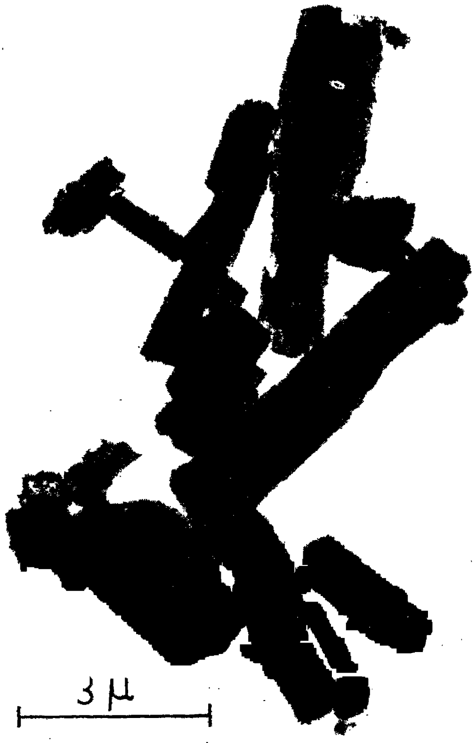

Figure 1. TEM photograph of acicular γ–Fe_2O_3.

indicated an exothermic peak at 250°C, accompanied by a gain in mass of 3·2% corresponding to the formation of Fe_2O_3. Therefore the oxidation process was isothermally carried out in moist air. ($P_{H_2O} \simeq 28$ torr) at 150°, 180°, 210° and 250°C respectively for 30 min each. At a minimum temperature of 180°C, γ–Fe_2O_3 ($a = 8.34$ Å) with required properties (magnetization = 74 emu/gm; coercive field = 290 Oe) was formed.

3.2 *Mechanism of thermal decomposition of ferrous oxalate dihydrate under nitrogen atmosphere*

There have been several reports in the literature about the thermal decomposition o FOD in inert-mainly nitrogen atmosphere (Bevan and Brown 1966; Venkatesh Rao *et a* 1974; Seshan *et al* 1981a). The accepted mechanism of decomposition has been

$$\begin{aligned} FeC_2O_4{:}\ 2H_2O &= FeC_2O_4 + 2H_2O \\ FeC_2O_4 &= FeO + CO + CO_2 \\ 3FeO + H_2O &= Fe_3O_4 + H_2 \end{aligned}$$

This, however, raises a few questions:
(i) Has the existence of intermediate FeO been experimentally established? FeO ha been known to be thermodynamically unstable below 575°C and disproportionate according to

$$4FeO = Fe_3O_4 + Fe$$

(ii) Does the presence or absence of moisture have any effect on the stability of FeO, i at all formed?
(iii) Has the evolution of hydrogen gas been experimentally observed?

In an attempt to prove the existence of FeO at 710 K – the temperature o decomposition inferred from DTA/TG studies – isothermal decomposition of ferrou oxalate dihydrate was carried out in dry as well as in moist oxygen free, ultra high pur nitrogen. The decomposition products were analysed using XRD, GC and magnetizatio measurements. These analyses confirmed the formation of Fe_3O_4 during the decomposition under moist nitrogen atmospheres. The decomposition products obtaine under dry conditions were highly reactive and to inhibit oxidation of the products, the were quickly transferred to molten wax. X-ray analysis of the above products showe

Table 1. Products of decomposition of $FeC_2O_4 \cdot 2H_2O$.

In dry nitrogen				In nitrogen containing water vapour			
d (Å)	I/I_0	*hkl*	Phase	*d* (Å)	I/I_0	*hkl*	Phase
3·742	44	210	Fe_2O_3	4·833	8	111	Fe_3O_4
2·975	3	220	Fe_3O_4	2·960	26	220	Fe_3O_4
2·525	7	311	Fe_3O_4	2·529	100	311	Fe_3O_4
2·489	2	111	FeO	2·410	5	222	Fe_3O_4
2·234	8	321	Fe_2O_3	2·098	23	400	Fe_3O_4
2·141	4	200	FeO	1·710	5	422	Fe_3O_4
1·513	5	220	FeO	1·615	23	511	Fe_3O_4
1·482	22	440	Fe_2O_3				

the presence of FeO lines along with those of Fe_3O_4 and Fe_2O_3. This confirmed the formation of FeO during the course of reaction. The details of the XRD findings are reproduced in table 1 as reported by Anantharaman *et al* (1982). Further, on line GC studies conducted for the isothermal decomposition of ferrous oxalate dihydrate indicated the liberation of hydrogen as required by the suggested mechanism.

Since the standard free energy change for the reaction $Fe + H_2O = FeO + H_2$ is negative ($\sim -2{\cdot}2$ kcal/mol) at 710 K, it is probable that, in the presence of moisture, iron metal resulting from the disproportionation reaction, $4FeO = Fe_3O_4 + Fe$, will get oxidised to FeO. A combination of these two reactions gives

$$3FeO + H_2O = Fe_3O_4 + H_2$$

thus it appears that, in the absence of moisture, 1 mol of Fe_3O_4 is produced from 4 moles of FeO, while in the presence of moisture, only 3 moles are required to yield the same quantity of Fe_3O_4. Therefore, the presence of moisture increases the yield of magnetite – a fact recognized empirically several years ago by David and Welch (1956).

3.3 *Synthesis of doped maghemite*

DTA of all the mixed oxalates in moist nitrogen ($P_{H_2O} \simeq 35$ torr) showed two characteristic endothermic peaks, corresponding to dehydration (~ 495 K) and decomposition (~ 710 K) respectively. Accordingly, the mixed oxalates were decomposed around 710 K for 30 min, followed by oxidation at 475 K in a stream of air. All the compositions were found to be monophasic cubic spinels, with practically no change in lattice parameter from that of pure maghemite. The magnetic properties of the doped compositions have been reported recently by Anantharaman *et al* (1982) and are reproduced in table 2. Indications are that only cobalt-doped γ–Fe_2O_3 has high σ_s and H_C values and, therefore potentially useful in applications.

3.4 *Thermal stability of doped maghemite*

It is well-known that γ–Fe_2O_3 has a defect spinel structure $Fe^{3+}[Fe^{3+}_{5/3}\square 1/3]O_4^{2-}$ where the vacancies are concentrated at the octahedral sites. The structure is unstable and converts irreversibly to rhombohedral α–Fe_2O_3 around 400°C. Thus it may be worthwhile to assess the effect of dopants on the thermal stability of γ–Fe_2O_3 structure.

Table 2. Magnetic properties of doped γ–Fe_2O_3.

	Cobalt		Nickel		Magnesium		Copper	
Dopant (atomic %)	σ_s (emu/g)	H_c (Oe)	σ_s (emu/g)	H_c (Oe)	σ_s (emu/g)	H_c (Oe)	σ_s (emu/g)	H_c (Oe)
1	94	270	83	225	89	320	76	300
2	71	382	86	270	100	270	80	270
4	74	371	78	250	76	230	94	320
6	72	562	75	230	91	270	80	250
8	90	810	73	230	81	210	77	250
10	93	675	81	250	80	200	69*	230
16	81	675	74	250	86	200	55*	250

*Unsaturated

The dopant ions may occupy A or B sites depending on their site preference heat treatment etc.

DTA studies did not provide fruitful results, presumably due to very sm change associated with the $\gamma \rightarrow \alpha$ conversion process. Since the γ-phase is fer and the α-phase antiferromagnetic, initial susceptibility (x_i) measurem employed to serve as a tool for distinguishing between the magnetic (ferrima non-magnetic (antiferromagnetic) state of samples. The onset of $\gamma \rightarrow \alpha$ tran expected to be accompanied by a rapid decrease in x_i value which subsequer reduce to zero.

While pure γ–Fe_2O_3 showed a transition beginning around 275°C, samples consistently showed a higher conversion temperature ($\geqslant 300$°C) greater thermal stability. The stability thus achieved could have been pa increased potential energy determined by the valence states of the dopant a Fe^{3+} ions. To check the microstructural changes thus introduced, p Mössbauer spectra were recorded with a Fe^{57} source at room temperature. fields, isomer shifts and quadrupole splittings were calculated. The values o fields in these samples did not differ from that of pure γ–Fe_2O_3 (505 indicating that the dopant concentrations were too low to introduce variations in the magnetic field. The hyperfine pattern of the Mössbauer s characteristic of a single magnetic field, since the effective magnetic field wa be the same for both A and B sites. The isomer shifts also remained unaff doping suggesting that Fe^{3+} ions do not change their valence state.

Acknowledgement

The authors gratefully acknowledge the financial assistance given by National Science Academy and the CSIR.

References

Anantharaman M R, Seshan K, Chakrabarty D K and Keer H V 1981 *Bull. Mater. Sci.* **3**
Anantharaman M R, Shewale S S, Seshan K and Keer H V 1982 *Indian J. Chem.* **A21** 214
Berkowitz A E and Schuele W J 1968 *J. Appl. Phys.* **39** 1261
Bevan S C and Brown R A 1966 *J. Inorg. Nucl. Chem.* **28** 387
Camras M 1954 US Pat. 2 694 656 (to Armour Research Foundation of Illinois Institute o
David I and Welch A J E 1956 *Trans. Faraday Soc.* **52** 1642
Dollimore D, Griffiths D L and Nicholson D 1963 *J. Chem. Soc.* **4** 2617
Inorganic powder diffraction file 1966 ASTM data card no. 29–7130
Inorganic powder diffraction file 1966 ASTM data card no. 11–614
Inorganic powder diffraction file 1966 ASTM data card no. 24–81
Likhite S D, Radhakrishnamoorthy C and Sahasrabudhe P W 1965 *Rev. Sci. Instrum.* **36** 1
Patil S G 1977 Electronics Information and Planning **4** 979
Seshan K, Anantharaman M R, Venkatesh Rao, Shashimohan A L, Keer H V and Chakraba *Bull. Mater. Sci.* **3** 201
Seshan K, Chakrabarty D K and Biswas A B 1981b *Phys. Status Solidi.* **63A** K123
Smit J 1971 *Magnetic properties of materials* (New York: McGraw Hill Inc)
Venkatesh Rao, Shashimohan A L and Biswas A B 1974 *J. Mater. Sci.* **9** 430
Radhakrishnamurty C and Sahasrabudhe P W 1965 *J. Indian Geophys. Union.* **2** 5

Bull. Mater. Sci., Vol. 6, No. 1, February 1984, pp. 65–70.
© Printed in India.

Dependence of microstructure on process variables in manganese zinc ferrites

N VENKATARAMANI, R AIYAR*, P S SEKHAR** and C M SRIVASTAVA*

Advanced Centre for Research in Electronics, *Department of Physics, **Materials Science Centre, Indian Institute of Technology, Bombay 400 076, India

Abstract. The dependence of microstructure on sintering conditions during hot pressing have been investigated and the densification mechanisms have been used to explain the observed results. The effect of addition of excess ZnO content over stoichiometry on permeability has been studied in the normal sintered Mn–Zn ferrites.

Keywords. Hot pressing; manganese zinc ferrites; densification mechanism; sintering.

1. Introduction

The initial permeability of manganese zinc ferrites is a sensitive function of the microstructure. To achieve high permeability the microstructure has to be controlled. In hot pressed ferrites this can be controlled by the sintering conditions (temperature and pressure) employed in a modified technique developed earlier (Venkataramani *et al* 1982). In normal sintered ferrites the evaporation of Zn during sintering alters the stoichiometry and affects the microstructure and permeability. Thus excess ZnO must be taken to offset this loss due to evaporation. Here we discuss the effect of varying this excess ZnO over stoichiometric content from 0 to 10% on the microstructure.

2. Experimental procedure

2.1 *Hot pressing*

The composition chosen for this study was 53 mol% Fe_2O_3, 27 mol% MnO and 20 mol% ZnO. The powders were processed by the usual ceramic technique. During hot pressing the presintered compact was initially soaked at a lower temperature (1100°C) under pressure ($\sim$ 20 MPa) and subsequently the temperature was increased to the final temperature (1200°C) maintaining the temperature constant, for various sintering times shown in table 1. This was followed by the ejection of the sample at the final temperature and the sintered pellet was cooled in N_2 atmosphere. For comparison we have prepared another pellet by directly heating to 1275°C (without soak) and cooling within the die. To evaluate the mechanism involved during the final stages of sintering, the time of sintering was varied from 0 to 4 hr at the final temperature.

2.2 *Normal sintering*

From the phase diagram for permeability by Roess (1970) the starting composition was chosen as 53 mol% Fe_2O_3, 23 mol% MnO and 24 mol% ZnO. The firing schedule and

Table 1. Densification rates of hot pressed Mn–Zn ferrites

Sintering time (hr)	Observed density (kgm^{-3})	% of theoretical density	Calculated strain rates for Nabarro Herring $10^{-3}\,sec^{-1}$	Coble $10^{3}\,sec^{-1}$	Bird *et al* $10^{4}\,sec^{-1}$	Total densification rate $10^{4}kg\,m^{-3}\,sec^{-1}$	Calculated % density
0·5	4990	97·27	5·68	4·27	2·36	72·0	98·21
1·0	5090	99·22	5·68	4·27	2·36	61·7	98·98
2·0	5093	99·28	3·20	1·80	2·36	11·9	99·46
3·0	5108	99·57	1·80	7·60	2·36	10·3	99·66
4·0	5119	99·79	1·50	3·89	2·36	4·7	99·79

ambient were adjusted to yield good density and single phase. The sintering schedule finally adopted was as follows: 1275°C in $N_2 + 1\,\%\,O_2$ for 3 hr followed by 1350°C in $N_2 + 1\,\%\,O_2$ for 4 hours and cooled in pure N_2 to room temperature. Atomic absorption spectroscopy and wet chemical analysis on several samples showed the final composition to be Zn deficient up to 6 wt% ZnO. Hence different samples were prepared with varying ZnO excess, progressively increasing from 0 to 10 %, keeping the same sintering schedule as above. The results are discussed in § 3.2.

3. Discussion

In this investigation the aim was to study the rate of densification using the hot pressing method by varying the duration of the final sintering. The change in microstructure was also studied. Normal sintering was used to study the effect of zinc loss on microstructure and permeability.

3.1 *Densification mechanism in hot pressing*

There are three significant processes which have been reported to occur during the final stages of hot pressing (Wilkinson and Ashby 1975; Notis *et al* 1975). These are (i) vacancy motion through the bulk lattice along a stress-induced gradient (Nabarro-Herring model) (ii) stress directed diffusional flow along the grain boundaries (Coble model) and (iii) deformation accompanied by climb and glide of dislocations (Bird *et al* model). These mechanisms have been used to compute the strain rate ($\dot{\varepsilon}$) using the equations given in Notis *et al* (1975). These in turn were used to calculate the total densification rate using

$$\dot{\rho} = \dot{\varepsilon}(3/2)^{n+1}\,(g/n)^n \frac{(1-\rho)}{[1-(1-\rho)^{1/n}]^n}, \tag{1}$$

where n is the effective stress exponent obtained from our data, g the stress correction (~ 1) when ρ, the relative density is close to 1. The results of this calculation are given in table 1. In figure 1 we plot the density as a function of sintering time at the final temperature. The observed and calculated values show good agreement.

From table 1 it is clear that the Nabarro-Herring type strain rate is the predominant densification mechanism. This process also leads to higher grain boundary mobilities resulting in enhanced grain growth. It has also been observed that the soak at 1100°C

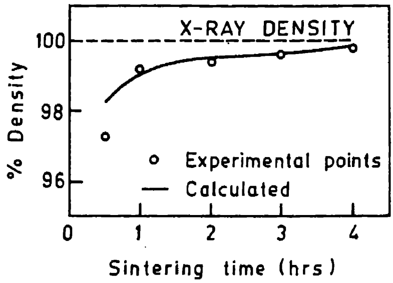

Figure 1. Densification characteristics of hot pressed Mn–Zn ferrites.

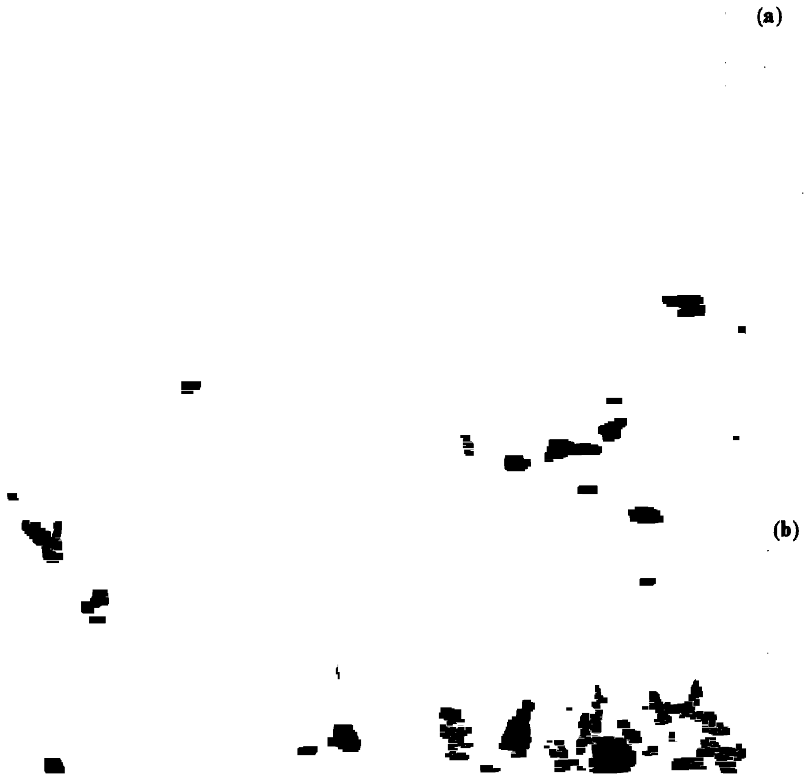

Figure 2. Microstructure photographs of Mn–Zn ferrites (**a**) hot pressed at 1100°C for 2 hr, 1250°C for 3 hr, hot ejected and cooled in N_2 (**b**) hot pressed at 1275°C for 2·5 hr and cooled within the die. (1 cm = 15 μm)

gives higher densities without appreciable grain growth. The energy supplied at 1200°C after the soak period leads to only grain growth since the separation of the densification process and grain growth is seen in this sintering schedule.

Using such an approach we have prepared a large grain Mn–Zn ferrite (~30–40 μm) with useful properties for recording head applications. The permeability is between 4000 and 5000. In contrast a sample sintered at 1275°C without soaking at 1100°C and without hot ejection resulted in a grain size of 10 μm and a density of 5050 kg m^{-3}. These differences are evident from figure 2 which shows the microstructure photographs of these two samples. The second phase precipitation in figure 2(b) is due to cooling within the die.

3.2 *Normal sintered ferrites*

We have observed that as the excess ZnO concentration increases from 0 to 4·5% the initial permeability increases and the microstructure gets refined, becoming more homogeneous. Thereafter the microstructure worsens again leading to discontinuous grain growth which also lowers the permeability. Figure 3 shows the variation of μ_i with excess ZnO concentration and figure 4 shows the microstructures of 2 wt%, 4 wt% and 5 wt% excess, ZnO compositions. From these results we see that the optimum composition is close to 4% excess ZnO. This composition has a density of 4850 kg m^{-3} and an average grain size of 12 μm. On varying the composition in smaller steps in this range the best composition was found to be 4·2 wt% excess ZnO. This composition was prepared and found to have a homogeneous microstructure with minimal pores (figure 5) and an initial permeability ~4000.

4. Conclusions

In hot-pressed manganese zinc ferrites control of grain size with good density can be obtained by soaking at a lower temperature, a suitable choice of the final sintering temperature and hot ejection. To achieve high permeability in normal sintered ferrites

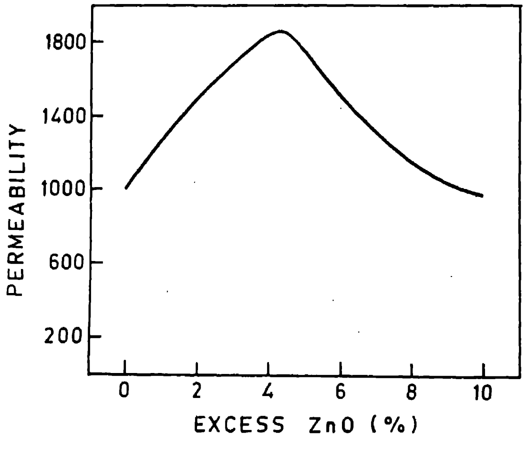

Figure 3. Permeability as a function of excess ZnO in normal sintered Mn–Zn ferrites.

Figure 4. Microstructure photographs of (a) 2 wt% (b) 4 wt% and (c) 5 wt% excess ZnO compositions. (1 cm = 30 μm)

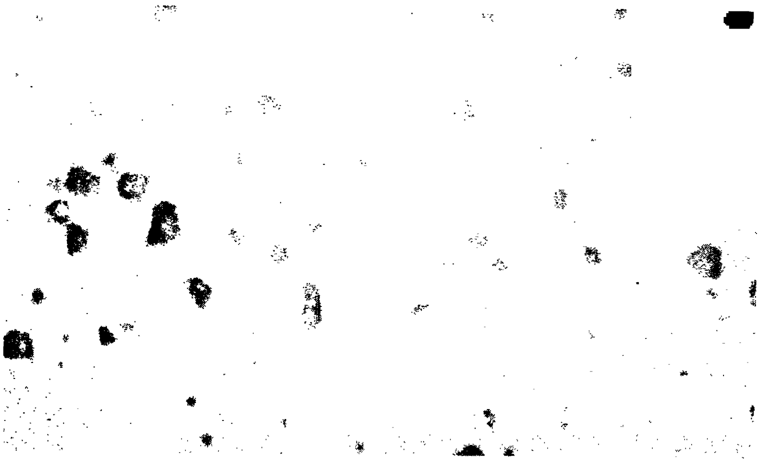

Figure 5. Microstructure photograph of 4·2 wt% excess composition. (1 cm = 15 μm)

using the sintering schedule discussed here an optimum excess of 4·2 wt% ZnO over the stoichiometry is necessary.

Acknowledgement

The authors are grateful to the Department of Science and Technology for financing this study.

References

Notis M R, Smoak R M and Krishnamachari V 1975 *Materials science research* (ed.) G C Kuczynski (New York: Plenum) Vol. 10, p. 493

Roess E 1970 *Ferrites*, Proc. Int. Conf. (eds.) Y Hoshino and S Iida (Tokyo: University of Tokyo Press) p. 203

Venkataramani N, Aiyar R, Sekar P S and Srivastava C M 1982 *Ceramics*, Proc. Int. Symposium (Bangalore: BHEL) p. 6.12

Wilkinson D S and Ashby M F 1975 *Materials science research* (ed.) G C Kuzynski (New York: Plenum) Vol. 10, p. 473

Bull. Mater. Sci., Vol. 6, No. 1, February 1984, pp. 71–82.
© Printed in India.

High temperature materials for magnetohydrodynamic channels

V K ROHATGI

Plasma Physics Division, Bhabha Atomic Research Centre, Trombay, Bombay 400 085, India

Abstract. The development of suitable materials for use in MHD generator is one of the most challenging areas. The very high temperatures (~ 2700 K) coupled with the highly corrosive seed-laden atmosphere limit the choice of materials in contact with the plasma to just a few ceramic oxides. These materials in contact with the high temperature plasmas in MHD generator are simultaneously subjected to stresses of mechanical, thermal, chemical and electromagnetic nature. The development and suitability of the different potential electrode and insulator materials such as lanthanum chromite, zirconia-based materials, alumina, magnesia etc. are reviewed with particular reference to the MHD channel materials programme in the MHD Project at BARC.

The operating experience with alumina-based ceramics and other materials under MHD operating conditions is also detailed. This includes the specifications, processing, bonding of the ceramic materials, the test programme and evaluation. Also presented are some of the novel processing techniques like plasma spraying and their application in the development of MHD materials. The advantages and limitations of each of these materials and their principal mode of degradation while in service are also discussed.

Keywords. Coal-fired MHD generator; high temperature electrode; insulator materials; metal-ceramic joint; slag ceramic interaction

1. Introduction

Magnetohydrodynamic power generation (MHD) is a branch of fluid mechanics dealing with the flow of an electrically-conducting fluid (plasma) in the presence of a magnetic field. The same principles of electromagnetic induction, utilised in conventional rotary generating machine, are applied to conducting fluids flowing through a magnetic field. An MHD generator essentially combines the functions of the steam turbine and electrical generator of a conventional system. In the MHD generator, the thermal energy of the plasma is directly converted into electrical energy—hence the MHD power generation is termed as the direct energy conversion process. As a consequence of high temperature direct conversion operation, the power plants incorporating MHD generators are potentially more efficient than conventional turbine power plants.

The development of MHD generator involves the magnetic system, inverter and channel. The MHD channel which forms the heart of the MHD installation, operates under extreme conditions of temperature, thermal flux, velocity of plasma, magnetic and electric fields. Hence, the design, fabrication and assembly are complex tasks. In principle, a modular structure is preferred. The modular construction, though complex, increases the electrical reliability of channel by prescribing finite potential breaks between various elements.

The materials used in contact with the plasma have to be stable at high temperatures, withstand seed attack and thermal shock, retain their refractoriness, electrical resistivity and mechanical strength during operation and have the capacity of being fabricated to required shapes. These requirements, therefore, impose stringent conditions on the purity of the material, the fabrication techniques and quality control of various processes. As on today, the development of suitable material for channel applications remains an open problem. This problem is being attacked in many ways. Some of the approaches being followed to find suitable answers to the problem are: (i) the development of new technologies and processes; (ii) the development of new materials, and (iii) development of new engineering concepts using standard materials.

2. Materials and techniques

The refractory materials, generally in contact with plasma in the MHD channel serve as electrodes, electrical insulators or as thermal insulators (figure 1). Even though efforts in several countries have been devoted to their development, ideally suitable materials to work in contact with plasma have not been found. Over a period of years significant progress has been made but much more work remains in the field.

The primary constraint of material durability has forced the designers to compromise with less optimum designs of the channel or to think of alternatives like frequent duct changeover. Recent interest in coal-fired MHD plants has introduced additional problems of electrochemical interaction of slag with the channel materials. The slag coating affects both the performance of the generator and the durability of the channel materials. A schematic representation of slag-coated channel wall is shown in figure 2.

The refractory materials in general should have the following desirable properties:

(*a*) *Thermal properties*: The materials must have adequate thermal conductivity to transmit the high heat fluxes from plasmas at temperatures over 2500 K. They should also resist the thermal shock conditions caused by large temperature gradients under operating conditions as well as during start-up and shut down.

(*b*) *Electrical properties*: The electrical resistivity of electrodes should be less than 1 ohm-cm and should withstand current densities of 1–2 A/cm^2. They should also

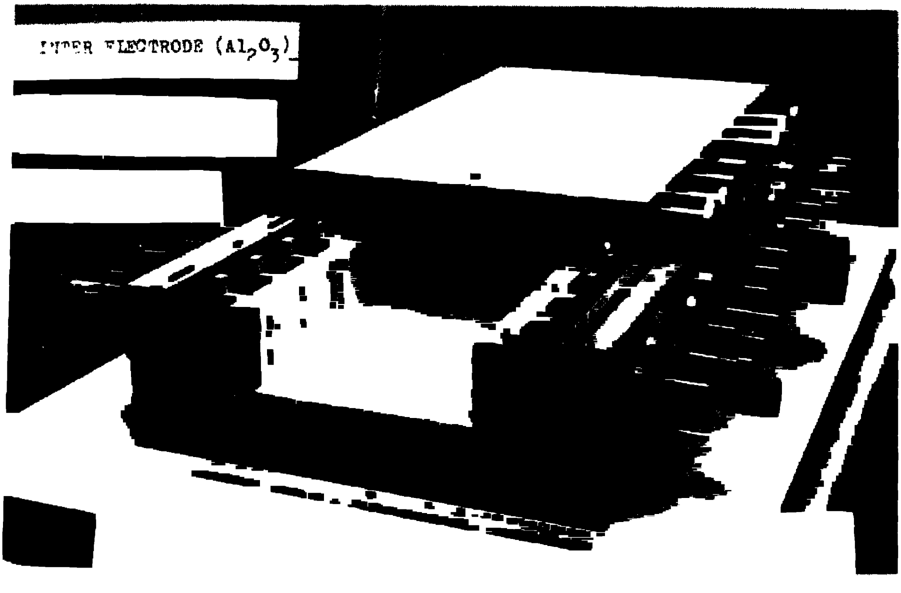

Figure 1. Schematic of Faraday MHD channel.

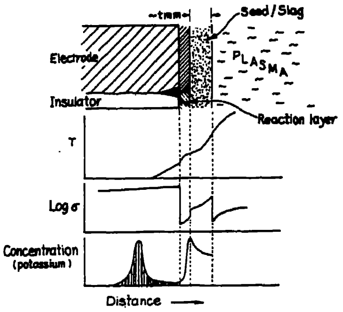

Figure 2. Schematic of slag-coated channel wall showing variation in chemistry and properties through the wall.

possess good electron emission characteristics. The insulators should have resistivities greater than 100 ohm-cm and a dielectric breakdown strength greater than 4 kV/mm at elevated temperatures.

(*c*) *Chemical properties*: The material should withstand seed and coal slag attack and should be stable under oxygen partial pressures of 10^{-2}–10^{-3} atmospheres. In general materials of low vapour pressures and high melting points are required. When different materials are used, they should be chemically compatible with each other.

(*d*) *Mechanical properties*: Sufficient to withstand the effect of high power density fluid without significant creep deformation.

2.1 *Materials for clean fuel* MHD *channel*

Today high purity Al_2O_3 and MgO appear to be popular as insulator materials. These materials exhibit good chemical and structural stability and high electrical resistivities of the order of 10^2–10^5 ohm-cm at 1973 K. Between the two, MgO is preferred because of resistance to seed attack. Sato and Kazukawa (1980) have tested more than 65 kinds of refractories (ceramics, spinel and pure single oxide ceramics) for alkali corrosion using K_2SO_4–K_2CO_3 and K_2SO_4 melts. The results indicate MgO and ZrO_2–CeO_2 have strong corrosion resistance whereas Al_2O_3 showed good results only in K_2SO_4 melts. Combination of MgO and Al_2O_3 are also being evaluated as insulator materials.

In BARC, the alumina modules made from castables, plasma spraying and sintered blocks have been tested extensively by oxy-acetylene flame testing facility. Copper-ceramic module used has been shown in figure 3 and the results tabulated in table 1. The technique of joining metal (copper) to ceramic has also been developed and dealt in § 2.3. The performance of sintered alumina pieces (around 10% porosity) of different shapes in Indian MHD generator test-section (figure 4) has been satisfactorily tested in Soviet U-02 facility in Moscow during May 1980. The total test duration was 64 hours and included electrophysical tests and life tests under applied electrical fields. The results of detailed analysis on the materials used in the channel have shown that improvements should be made on ceramic materials. This will consist of better purity of starting materials, improved processing techniques and more optimal properties like porosity, grain structure and thermal shock resistance (Rohatgi and Shishkov 1981).

For electrodes, apart from metal and their alloys (Hurby *et al* 1980), oxides of zirconia and lanthanum chromite have been investigated extensively. Zirconia

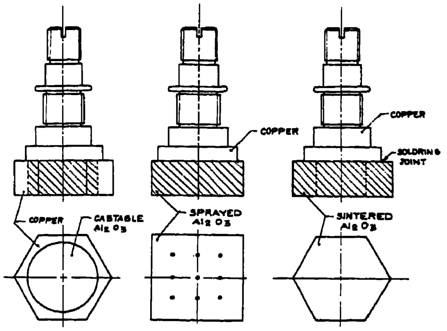

Figure 3. Schematic of copper-ceramic module for flame test.

Table 1. Summary of results of flame testing of materials

Material	Supplier	Total Porosity (%)	Heat flux (MW/m^2)	Maximum surface temperature (K)	Remarks
Alumina castable peg wall	M/s ACC Bombay	45	0·6–0·8	1783	No cracks were observed. Seed penetration was observed throughout the sample.
Sprayed alumina peg wall	BARC	12	0·75–1·1	1873	No cracks were observed. Seed attack was observed.
Sintered hexagonal block soldered to copper	M/s ACC Bombay	10	0·8–1·1	1950	In some samples fine cracks were observed after the test. Seed attack was observed.
Sintered circular block soldered to copper	BHEL R and D Corporate Hyderabad (Trial samples)	3–4	0·7–1·6	1593	Cracks were observed after the test.

stabilized with CeO and Y_2O_3 have yielded encouraging results up to 1700 K. However, the low thermal and electrical conductivity and ionic conduction of zirconia are some of the objectionable features of this material. More than 50 % electronic conduction have been already achieved with CeO doped zirconia. Further, the study indicates that a composition of 80 % CeO_2–18 % ZrO_2–2 % Ta_2O_5 is a better candidate for MHD electrode material (Hosler and Frederikse 1975) as it combines all the good features in one compound mostly, high conductivity, nearly 100 % electronic conduction, single phase structure and chemical stability up to 1900 K. Lanthanum chromite ($LaCrO_3$) has an excellent electrical conductivity but at higher temperature loss of chromium results in degradation of material due to attack by water and seed (Sata and Kasukawa 1980). Nevertheless because of high electronic conduction, this material has a long interest on generator electrode material. Over a period of years many attempts have

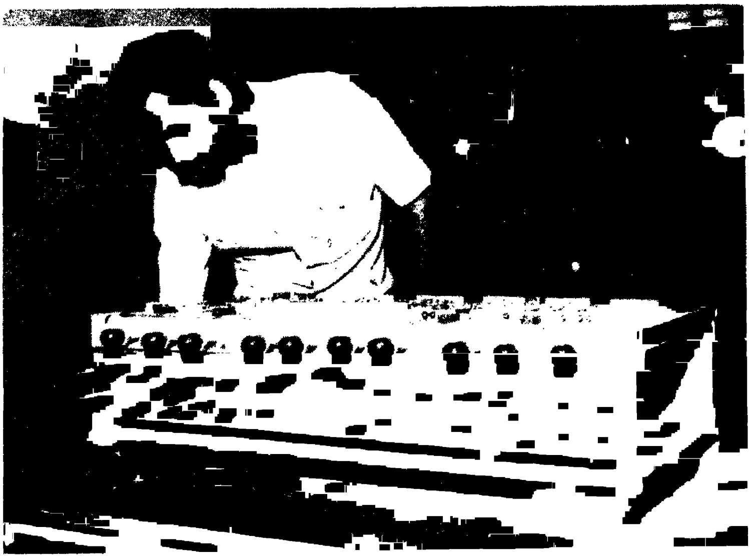

Figure 4. First Indian MHD channel, tested in U-02 facility of Moscow.

been made to improve the properties of this material. Suppression of chromium evaporation in $LaCrO_3$ by substitution with magnesia have been successfully attempted in BARC by George *et al* (1976). The material designated as LC 20 M exhibits good sintering characteristics in single firing at 1650 K with a porosity of less than 10% and grain size of 3–8 μm. The electrical resistivity was around 0·2 ohm-cm with a very low temperature coefficient. The sample withstands current density of the order of 20 Amp/cm^2 for long duration. The thermionic work function $W_p = 2{\cdot}75$ mV and Richardson constant, $A_R = 0{\cdot}11\ \mathrm{A\,cm^{-2}\,K^{-2}}$ were suitable for MHD electrode applications by Pai *et al* (1980). The resistivity of different potential electrode materials (Schneider *et al* 1979) for MHD use is shown in figure 5.

2.2 *Materials for coal fired* MHD *channel*

The properties of slag and slag coated materials have been the subject of investigations in recent years. Effects of slag on MHD generator performance have been studied by Bogdenske *et al* (1975). Very good results have been reported for stainless steel electrodes (operating approximately at 900 K) with moving slag on them. However, difficulties were experienced with suitable insulations between the electrodes and through the side walls in the Faraday generator (figure 6). Use of metal as electrodes (cold wall mode) also exhibits some serious instabilities in the current transfer and to the poor electrical conductivity of solid slag. Migration of oxygen through the slag layer under the influence of the electrical field also causes oxidation of the anodes. To minimise the possible deleterious reactions and degradation of the electrode system, Mason *et al* (1975) have identified $FeAl_2O_4$–Fe_3O_4 spinel (figure 7) as a potential electrode for open cycle coal fired MHD cycles. This spinel-alumina electrode module offers a number of distinct advantages like: (i) completely electronic conductivity; (ii) absence of resistive reaction layer at the electrode face; (iii) diffusion of iron into

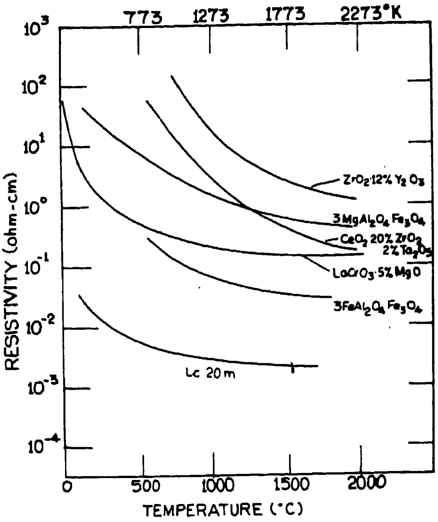

Figure 5. Resistivity of potential electrode materials.

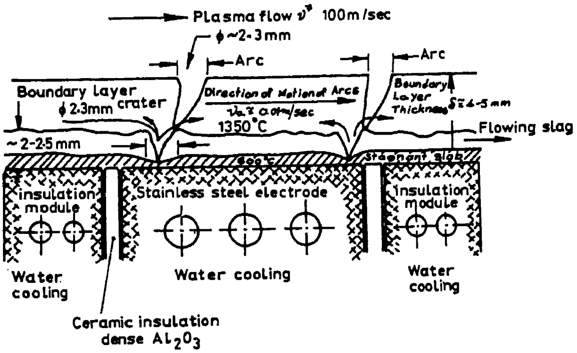

Figure 6. Schematic of arc-slag interaction on cold stainless steel electrode (900 at steel surface).

the alumina; (iv) grading of spinel layer as indicated in figure 7 will minimise the driving force for inter-diffusion with alumina at the hot and of the module adjacent to the slag.

In BARC, the degradation kinetics of ceramics [Al_2O_3 and Calcia stabilised zirconia (CSZ)] by slag reaction has been studied by making ceramic-slag couples and analysing their reaction (Karthikeyan *et al* 1982). The slag powder was prepared by conditioning the fly ash of coal from Bihar fields. The reaction couples were prepared by plasma spray technique. In the study it has been found that the main degradation reaction of alumina is the dissolution of alumina into the slag whereas in CSZ the degradation is mainly due to the depletion of calcia from CSZ resulting in the formation of thermally unstable monoclinic zirconia. The growth of calcia depletion and enrichment zones is shown in figures 8 and 9.

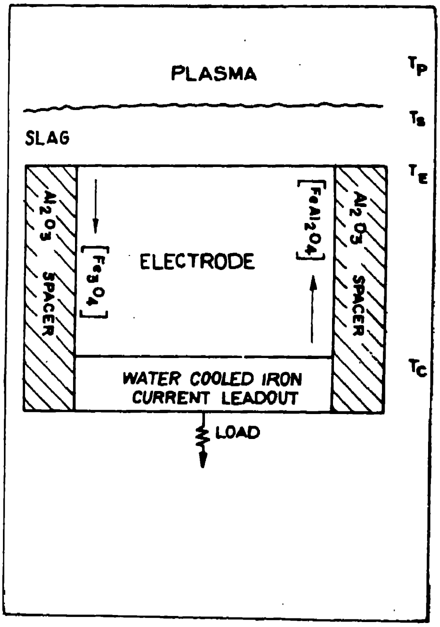

Figure 7. Schematic of spinel ($FeAl_2O_4$–Fe_3O_4) electrode.

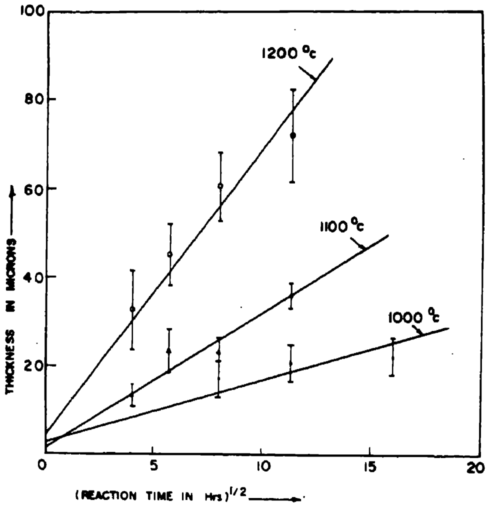

Figure 8. Growth of calcia depletion zone in CSZ.

2.3 *Ceramic-metal joints*

In Faraday MHD generator, joining of ceramic to water-cooled copper plays a vital role. For maintaining the designed heat flux of the channel and surface temperature of ceramic it is essential to join ceramic to metal with good thermal conductance and

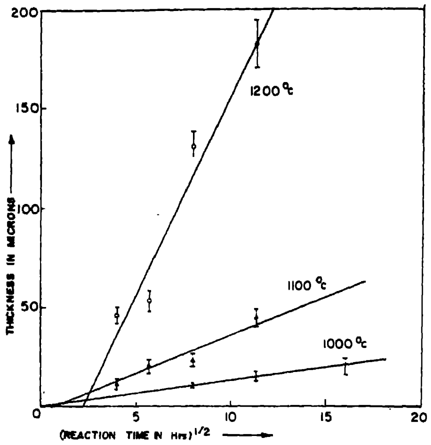

Figure 9. Growth of calcia enrichment zone in slag.

adequate joint strength. The technique of uniform metallic coating to porous alumina ceramic (10% porosity) by electroless method (figure 10) has been successfully developed by Totlani *et al* (1979) in BARC. The technique is essentially a chemical method of deposition constituting bath of metal ion (nickel), suitable complexing agent and a reducing agent. The ceramic surface to be metallised is made catalytic towards reduction of metal ions by rinsing in stannous chloride solution followed by a rinse in a dilute palladium chloride solution. The bonding by such method is purely mechanical interlocking. The metallic coating obtained by this method has better solderability and excellent wear resistance characteristics. The main features of the technique are: (a) No diffusion of metal species in the pores of ceramic, hence does not alter the properties of ceramic. (b) Gives stronger bond. (c) Much cheaper and easy process compared to other techniques.

3. Conclusions

In summary, the development of MHD channel as a power generating device is primarily dependent on the development of suitable ceramic materials that can withstand for long duration in the hostile MHD environment. Some of the new materials have showed excellent promise and have lasted for several hundreds of hours of operation. Table 2 shows the essential current status of this development and the potential candidates for future power channels. The Indian MHD programme is to identify the specialised selective areas for further research in the choice of material and processing techniques.

Acknowledgements

The author is thankful to Shri P B Shrivastava and Dr N Venkatramani for assistance in the compilation of this paper.

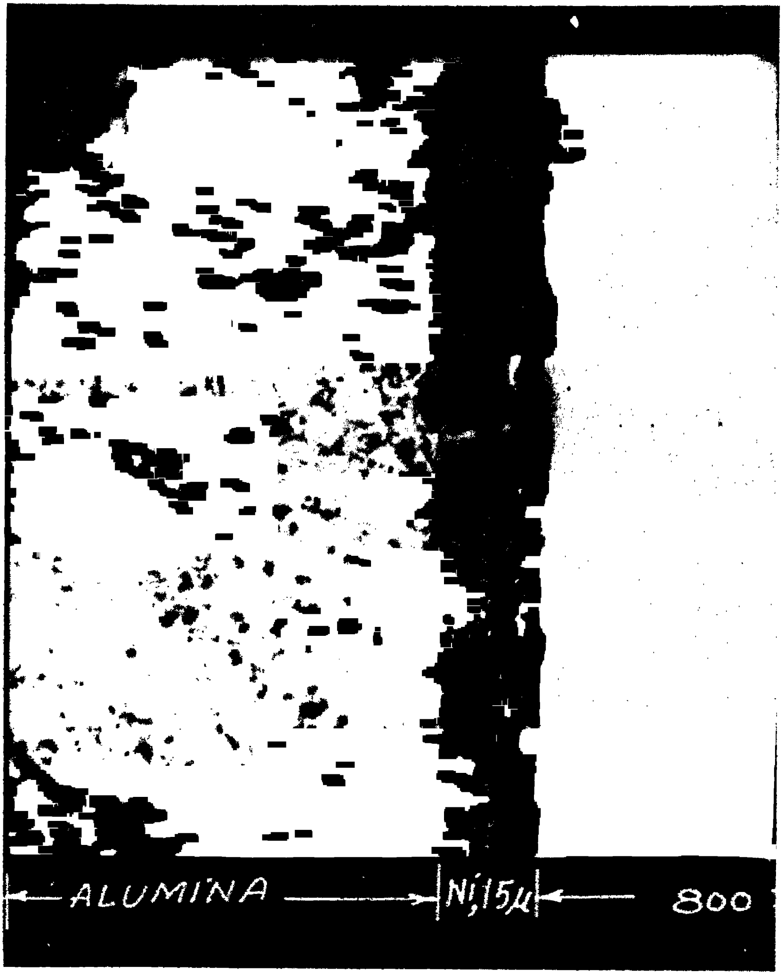

Figure 10. Secondary electron image (SEI) of nickel-alumina junction.

Table 2a. Test result on various MHD electrode materials

Materials	Test facility	Clean or slag	Temperature (°C)	Time (hr)	Maximum current density (A/cm^2)	Observations (by investigator)
1. ZrO_2–11% CeO_2 (hot pressured)	Poznan (4 MW)	Clean	—	—	—	Burned out at 1680°C; current to be limited to 0·8 A/cm^2
2. $88ZrO_2:12Y_2O_3$ $50ZrO_2:50CeO_2$ $25ZrO_2:75CeO_2$ $80CeO_2:18ZrO_2:2Ta_2O_5$	U-02 (US–USSR Joint Test) Phase I	Clean	1720	127	0–1·25	Strong seed penetration CeO_2—loss
3. Hercynite ($FeAl_2O_4Fe_3O_4$)	U-02 (US–USSR Joint Test) (Phase II)	Clean	1650	100	0–0·8	Hercynite melted
4. $3MgAl_2O_3$ $1Fe_3O_4$ (1 mm thick)	AVCO	Slag	1400–1500 (slag surface)	5	—	Most MAFF dissolved. Good continuous slag layer.
5. Cermet ($LaCrO_3$ + 40% Cr + 3% Pd)	U-25	Clean	1500–1700	100	—	Little damage
6. SiC	Westing house	Slag	—	10	—	Oxidation, seed reaction erosion 0·3 mm/hr
7. Copper	AVCO-Mark VI	Clean and slag	200	20	—	Little damage, strong arcing
8. Copper	U-02 (Indo-Soviet Joint Test)	Clean	200	65	—	Little damage, varied from small arcing to strong arcing

Table 2b. Test result on various MHD insulator materials

Materials	Test facility	Clean or slag	Temp. (°C)	Time (hr)	Observations (by investigator)
MgO (98% T.D.)	Westing house	Slag	1600	—	Appreciable damage
MgO (90% T.D.)	U-02 and U-25	Clean	1800	100–300	Good thermal stable, little seed attack
MgO (83% T.D.)	U-02 (US–USSR Test)	Clean	1700	127	Strong seed penetration
MgO-Spinel (90%) (Modular)	U-02 and U-25	Clean	1800	100–300	Better than MgO for Small heat fluxes
Al_2O_3	Poznan	Clean	2000	3	Performed reasonably, partial melting
Al_2O_3 (10% T.D.)	U-02 (Indo-Soviet Joint Test)	Clean	—	65	Alumina peeled off after 9 hrs. of testing, interelectrode alumina performed satisfactorily

References

Bogdancks M, Brzozowski W S, Charuba J, Dabraeski M, Plata M, Zielinski M 1 *generation*, Proc. Sixth conf. (Washington DC: USA) **vol. 2**, p. 9

Bowen H K 1974 Engineering workshop on MHD materials (Sponsored by the Off National Science Foundation) Massachussetts Institute of Technology, Cambr

George A M, Pai J R and Rohatgi V K 1976 *Engineering aspects of MHD*, 15th sympos

Hosler W R and Frederikse H P R 1975 MHD electrical power generation, Sixth Int USA) **vol. 2**, p. 67

Hurby V J, Morenek J, Petty S W and Solben A 1980 *Electrical power generation*, (Washington DC: USA) **vol. 1**, p. 251

Karthikeyan J, Venkatramani N and Rohatgi V K 1982 *Engg. aspects of MHD* Pro USA)

Mason T O, Petuskey W T, Liang W W, Halloran J W, Yen F, Pollak T M, Elliott J F MHD electrical power generation Proc. Sixth Int. Conf. (Washington DC: USA

Pai J R, George A M and Rohatgi V K 1980 *Appl. Phys.* **22** 283

Rohatgi V K and Shishkov E V (eds.) 1981 Scientific report on the joint Indo-Soviet e Indian MHD generator section at the Soviet U-02 experimental facility.

Sato T and Kasukawa K 1980 *Rev. Int. Hautes Temper. Refract. Fr.* **17** 174

Scheider S J, Negas T and Frederikes H P R 1979 *Rev. Int. Hautes Temper Refra*

Totlani M, Athavale S N and Shrivastava P B 1979 *Sintering and sintered products*, Pr BARC) p. 677

Bull. Mater. Sci., Vol. 6, No. 1, February 1984, pp. 83–89.
© Printed in India.

Effect of compositional modifications on the piezoelectric properties of spray dried lead zirconate titanate ceramics

RAMJI LAL and P RAMAKRISHNAN

Department of Metallurgical Engineering, Indian Institute of Technology, Bombay 400 076, India

Abstract. Lead zirconate titanate powders of different compositions varying from 50 to 55 atomic percent zirconium in the solid solution have been prepared by spray-drying technique. The compositions were varied by changing the zirconium-to-titanium ratio in the solid solution and also with the addition of strontium. The amorphous character of the as-prepared powders and the formation of single phase lead zirconate titanate during calcination were also confirmed by x-ray diffraction technique. These powders were then converted to piezoelectric ceramics by compaction and sintering followed by electroding and poling. Effect of the variation of zirconium to titanium ratio and strontium additions on the piezoelectric properties of the finished ceramics have been explained on the basis of improved sintering, uniform grain size, formation of morphotropic phase boundary and subsequent shift to rhombohedral structure.

Keywords. Lead zirconate titanate; piezoelectricity; ceramic materials; spray drying; sintering; amorphous character; morphotropic phase boundary.

1. Introduction

Lead zirconate titanate, Pb(Zr, Ti)O_3, solid solution system exhibits piezoelectric properties when it is converted into the form of ceramics and subjected to high d.c. electric field. Piezoelectric properties of the system are considerably influenced by varying Zr to Ti ratio in the solid solution and acquires maximum value when the ratio corresponds to morphotropic phase boundary composition. However this ratio has been found to have different values from the reported literature of various investigators (Webster *et al* 1965; Ikeda *et al* 1962; Jaffe *et al* 1954, 1955). These variations can be attributed to the difference in the purity, reactivity and homogeneity of the raw materials as well as the nature of calcined lead zirconate titanate (LZT) powders. Majority of these investigators have used the conventional ceramic processing techniques where the process parameters are essentially based on tedious trial-and-error methods. Besides, the starting particle size distribution of powders prepared by conventional processing are non-reproducible and the phase always has a degree of spatial inhomogeneity. The optimum Zr to Ti ratio for the appearance of phase boundary in the solid solution depends upon the method of powder preparation and ceramic processing parameters. Ceramic powders prepared by chemical methods are, therefore, gaining more importance because of their improved homogeneity and reactivity and hence capable of producing decisive morphotropic phase boundary at a particular Zr-to-Ti ratio. Several investigators (Murata and Wakino 1976; Heartling and Land 1972; Mc Namara 1965; de Lau 1970; John Thomson 1974; Ramji Lal and Ramakrishnan 1979, 1980) have reported using chemical processing such as spray-drying, freeze-drying and chemical coprecipitation to prepare electronic ceramics with encouraging results.

The objective of this work is, therefore, to locate the phase boundary composition in LZT ceramics when prepared by spray-dried powders and also to arrive at the best composition in the entire solid solution series. It is also intended to substitute a small quantity of Pb with Sr in solid solution to improve certain important electromechanical properties of the ceramics by optimising strontium concentration.

2. Experimental procedure

Lead zirconate titanate ceramic powders were prepared by spray-drying technique in 6 batches with Zr to Ti ratio varying from 50:50 to 55:45 in the stoichiometric formula Pb $(Zr_xTi_{1-x})O_3$. Lead nitrate, zirconium oxychloride and titanium tetrachloride were used as starting raw materials which were further purified by crystallization and precipitation. These were converted to nitrate solutions and then mixed in the desired proportions for spray drying. A laboratory model spray drier with the following parameters were used for preparing the powders: spray rate of 3 l/hr, speed of centrifugal atomizer 30000 r.p.m., inlet temperature 320–350°C, outlet temperature 90–110°C, solution pH 1·8 and solid content 50 g/litre. The desired characteristics of the powders were confirmed by x-ray diffraction analysis and obtained through the control of calcination parameters. The x-ray diffraction pattern of the powders is shown in figure 1.

Powders of different compositions were calcined at 550°C for 4 hr, 650°C for 2 hr and finally at 750°C for 2 hr which provided the powders of desired characteristics. Chemical analysis of the calcined powders indicated the presence of unreacted PbO varying between 1·5 to 2%. Powders were then compacted into circular discs of

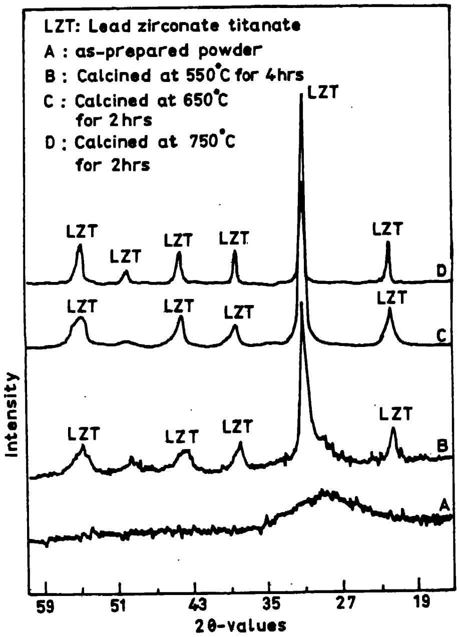

Figure 1. X-ray diffraction pattern of as-prepared powders.

diameter 24 mm and thickness 2 mm by using about 1.5 wt % PVA as binder. These discs were sintered at 1250°C for 2 hr under PbO atmosphere to suppress the lead volatility from the specimens. Sintered discs were lapped to make the surfaces flat and parallel and then electroded by applying silver paste. Electroded ceramics were poled by applying a d.c. electric field of 30 kV/cm at 100°C in silicone oil bath for 15 minutes and piezoelectric properties were measured. Properties of ceramics as a function of composition are shown in figure 2.

Separate batches of composite solutions were also prepared by replacing 3, 6 and 9 at. % of Pb with Sr in the stoichiometric compositions and powders were prepared by following similar technique as described earlier for unmodified compositions and processed into the form of finished ceramics. Piezoelectric properties of the ceramics were measured and reported in table 1. Properties of one batch of ceramics containing 6 at. % Sr have also been plotted as a function of the variation of Zr to Ti ratio and shown in figure 3. In another batch of decomposed powders containing 6 at · % Sr substituted for Pb; 2 wt % of PbO was added in excess and then the powders were calcined and processed by similar processing parameters. Properties of these ceramics are reported in table 2. Compositions with and without Sr were analysed by x-ray diffraction technique using CuK_α radiation to correlate the change in unit cell parameters with the average volume of the substituted ions. X-ray diffraction results of the compositions are shown in table 3. In order to correlate the microstructures, investigations of the sintered ceramics with and without Sr have also been carried out. A few typical photomicrographs of the sintered ceramics are shown in figures 4(a) and 4(b).

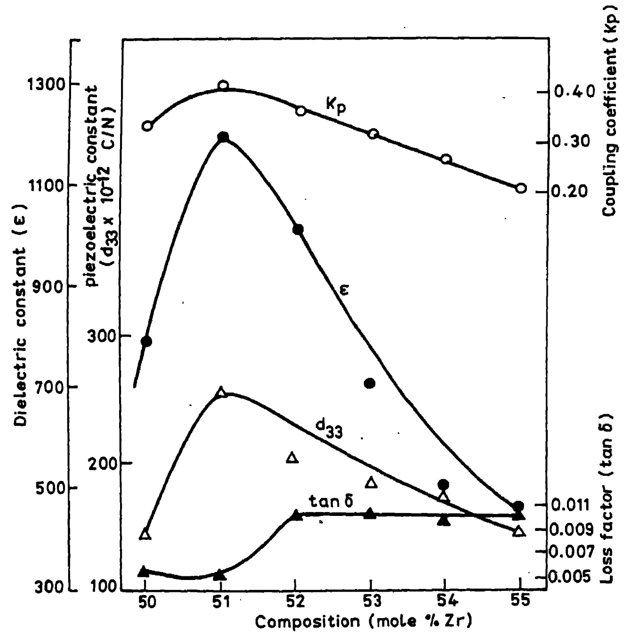

Figure 2. Variation of properties with compositions of unmodified LZT ceramics.

Table 1. Effect of Sr concentration on properties of LZT ceramics

Composition	Properties				
Zr:Ti+Sr. (atomic percent)	ρ	ε	Tan δ	$d_{33}(\times 10^{-12}$C/N)	K_p
51:49+3	7·20	862	0·0075	155	0·32
52:48+3	7·20	911	0·0070	170	0·37
53:47+3	7·20	798	0·0090	153	0·35
54:46+3	7·20	760	0·0096	140	0·32
51:49+6	7·41	886	0·0071	173	0·41
52:48+6	7·44	1050	0·0055	216	0·48
53:47+6	7·49	1532	0·0045	295	0·56
54:46+6	7·48	736	0·0075	150	0·42
51:49+9	7·30	550	0·0120	121	0·32
52:48+9	7·30	560	0·0085	152	0·37
53:47+9	7·30	540	0·0092	141	0·35
54:46+9	7·33	530	0·0120	139	0·31

ρ: density; ε: dielectric constant; tanδ: dielectric loss; d_{33}: piezoelectric constant; K_p: electromechanical coupling coefficient.

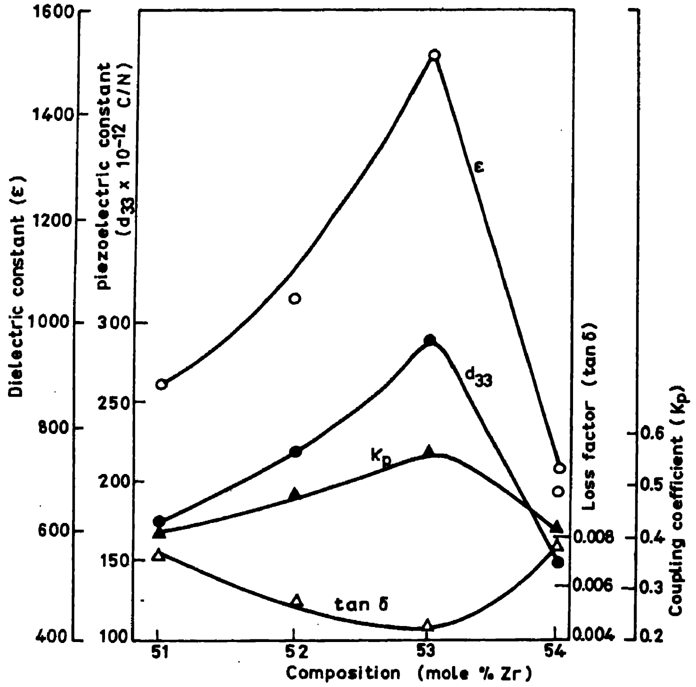

Figure 3. Variation of properties with composition of Sr modified LZT ceramics.

Table 2. Effect of excess PbO on properties of Sr modified LZT ceramics

Composition	Properties				
Pb, Sr, Zr, Ti + PbO (atomic percent) (Excess w%)	ρ	ε	$\tan\delta$	$d_{33}(\times 10^{-12}\mathrm{C/N})$	K_p
94, 6, 51, 49 + 2	7·59	1098	0·0039	223	0·45
94, 6, 52, 48 + 2	7·57	1027	0·0054	214	0·435
94, 6, 53, 47 + 2	7·59	921	0·0180	193	0·39
94, 6, 54, 46 + 2	7·59	890	0·0195	180	0·32

Notation of symbols same as in table 1.

Table 3. X-ray diffraction results of LZT composition

Composition	2θ values							
$Pb_{1\cdot0}(Zr_{0\cdot51}Ti_{0\cdot49})O_3$	21·7	31	38·2	44·2	49·8	55	64·6	73
$Pb_{0\cdot94}Sr_{0\cdot06}(Zr_{0\cdot53}Ti_{0\cdot47})O_3$	21·9	31	38·3	44·8	50·4	55·4	64·8	74

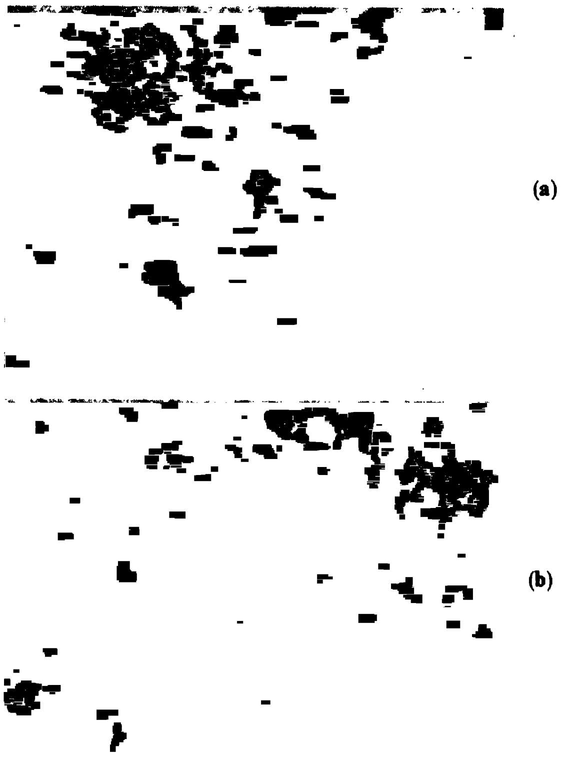

Figure 4. Photomicrographs of sintered LZT ceramics, **a.** unmodified. **b.** Sr-modified.

3. Results and discussion

Spray-dried powders have been found to possess amorphous characteristics according to the x-ray diffraction pattern shown in figure 1. Further the formation of single phase LZT at lower calcining temperatures and the absence of second phase indicate higher reactivity, homogeneity and purity of these powders in relation to conventional processed powders. From the analysis of the piezoelectric properties of LZT compositions shown in figure 2, it appears that dielectric constant (ε), piezoelectric constant (d_{33}) and electromechanical coupling coefficient (k_p) acquire maximum value at a particular Zr-to-Ti ratio whereas dissipation factor ($\tan\delta$) is the minimum at this ratio. Thus it is confirmed that in LZT solid solution system, there exists a phase boundary composition having maximum dielectric, piezoelectric and coupling coefficient and minimum dissipation factor in the entire series. This composition corresponds to approximately 51:49 Zr to Ti ratio. Thus the appearance of phase boundary takes place at a lower ratio of Zr to Ti in composition prepared by spray-dried powders than those prepared from conventional processed powders. This can be attributed to the greater reactivity of spray-dried powders as indicated by the amorphous character from the x-ray diffraction pattern in figure 1. The higher reactivity of spray-dried powders enables more zirconium to react and enter into solid solution and thus achieving the required stoichiometry with starting composition having lower Zr-to-Ti ratio.

A similar trend in properties has also been observed with Sr substituted compositions but the phase boundary has been shifted towards rhombohedral side (*i.e.* from Zr to Ti ratio of 51:49 to 53:47). This shift in the phase boundary composition is in accordance with the phase diagram of $PbZrO_3$-$PbTiO_3$-$SrTiO_3$-$SrZrO_3$ reported by Ikeda (1959). It is also observed that Sr increases the dielectric and piezoelectric constants as well as electromechanical coupling factor and also lowers the dissipation factor when added in A-site in phase boundary composition. This trend increases up to 6 at · % Sr and then decreases when Sr content increases from 6 at · % (table 2). This variation can be explained on the basis of higher sintering rate of Sr due to its greater diffusion characteristics caused by lattice defects (size of Sr being smaller than Pb). Thus Sr acts as a fluxing agent up to a certain concentration. This results in a pore-free grain structure as seen in figures 4(a) and 4(b). Since pore-free grains have fewer mechanisms for dielectric loss, this reduces the value of $\tan\delta$. Better densification and larger grains of ceramics with Sr substitution can be considered as reasons for higher dielectric constant. A comparison of the microstructure of LZT ceramics with and without Sr as shown in figures 4(a) and 4(b) also supports the above argument. Increase of piezoelectric constant in strontium-added ceramics can be explained on the basis of the weakening of dipole–dipole interaction. From the 2θ values of the different compositions obtained from x-ray diffraction and shown in table 3, it can be concluded that Sr addition reduces the unit cell volume of the perovskite structure which is expected due to the smaller size of Sr^{2+} as compared to Pb^{2+}. A comparison of the properties of the compositions containing excess PbO with original compositions (tables 1 and 2) clearly indicates that addition of excess of PbO increases the density of the ceramics and also shifts the morphotropic phase boundary towards lower atomic ratio of Zr to Ti. This shift can be explained from the principle that excess PbO enables more zirconium to enter in the solid solution as $PbZrO_3$ and thus increases the Zr ratio. These data also confirm the shift in the phase boundary reported earlier while discussing the results of Sr substituted compositions. Lower value of $\tan\delta$ can be attributed to the better stoichiometry of the composition. This is also apparant from the gradual increase in tan δ values of the compositions (table 1) when Zr to Ti ratio varies from 53:47 to 51:49 in the solid solution.

4. Conclusions

Lead zirconate titanate powders prepared by spray-drying technique have been found to be amorphous and the formation of single LZT phase is possible at lower calcining temperatures compared to conventionally prepared powders. Piezoelectric properties of the finished ceramics are considerably influenced by the variation of Zr-to-Ti ratio and the values of the properties are optimised at 51 at · % Zr in the stoichiometric formula of Pb $(Zr_xTi_{1-x})O_3$. The relatively lower ratio of Zr to Ti providing optimum properties may be attributed to the higher reactivity, better homogeneity and purity of these powders. Strontium addition to lead zirconate titanate acts as a fluxing agent and thus enhances the sinterability of the powders resulting in improved densification and uniform grain size formation. Sr substitution (6 at · %) for Pb reduces the unit cell volume, shifts the morphotropic phase boundary towards rhombohedral symmetry of the phase diagram and provides optimum piezoelectric properties.

References

de Lau J G M 1970 *Am. Ceram. Soc. Bull.* **49** 572

Heartling G H and Land C E 1972 *IEEE Trans. Sonic Ultrasonic* **SU19** 269

Ikeda T 1959 *J. Phys. Soc. Jpn* **14** 1286

Ikeda T, Okano T and Watnabe M 1962 *Jpn. J. Appl. Phys.* **1** 218

Jaffe B, Roth R S and Marzullo S 1954 *J. Appl. Phys.* **25** 809

Jaffe B, Roth R S and Marzullo S 1955 *J. Res. Nat. Bur. Stds.* **55** 239

John Thomson J R 1974 *Am. Ceram. Soc. Bull.* **53** 421

McNamara 1965 *J. Can. Ceram. Soc.* **34** 103

Murata M and Wakino K 1976 *Mater. Res. Bull.* **11** 323

Ramji Lal and Ramakrishnan P 1979 *Trans. Indian Ceram. Soc.* **38** 166

Ramji Lal and Ramakrishnan P 1980 in *Fine particle processing* (ed). P Somasundaram (New York: Am. Inst. Mining Met. Petrol. Engineers) Vol. 1, p 15.

Webster A H, Mc Donald and Bowman W S 1965 *J. Can. Ceram. Soc.* **34** 97

Bull. Mater. Sci., Vol. 6, No. 1, February 1984, pp. 91–97.
© Printed in India.

Use of coal tar pitch for carbon-carbon composites

R L SETH, K K DATTA, C L VERMA, C LAL and V P MITTAL
Carbon Technology Unit, National Physical Laboratory, New Delhi 110 012, India

Abstract. The paper describes some of the recent applications of carbon-carbon composites with special reference to bio-medical materials. Use of coal tar pitch as a thermoplastic binder and impregnant to produce carbon matrix in the composites has been highlighted. Coal tar processing to make binder and impregnating pitches has been described and some of the results obtained at NPL are reported. Modification of the pitches by thermal and chemical treatment to obtain extra hard pitch and very soft pitch has been described. X-ray diffraction and scanning microscopy techniques have been employed to investigate the structure and optical texture of the modified pitches.

Keywords. Carbon-carbon composites; thermoplastic; carbon matrix.

1. Introduction

Materials science is fast developing so as to provide newer and better materials with improved capabilities. Carbon-carbon composites based on carbon fibres as filler materials and resins as matrix have high mechanical strength and corrosive resistance besides high degree of flexibility. These have been used for special application such as bio-medical engineering. Carbon-carbon composites with thermosetting and thermoplastic resins as matrix precursors have been made by Fitzer and coworkers (Fitzer and Terewisch 1973; Fitzer *et al* 1975, 1980) who have reported the superiority of the precursors with a wide range of temperature of plasticity. In the carbon-carbon composites one of the basic requirement is the high strength and uniformity with minimum flaws. This requires that carbon yield of the matrix must be high and is related to pitch quality, its baking rate, application of pressure during thermal treatment and chemical additions acting as dehydrogenating and crosslinking agents before thermal decomposition of the binder.

The strength of the composites is related to binder bridges and influenced by the structure and morphology of the binder carbon and the adhesion between the filler and the matrix. The selection of the pitch and the control of the pyrolysis process are considered as key points in the fabrication of the carbon-carbon composites. Wetting, binding and coking properties of the pitch play an important role in affecting mechanical properties of the composites. These properties are dependent to a large extent on its resinous components known as α-, β- and γ-resins (Brooke and Taylor 1965; Lowry 1963).

2. Experimental

The coal tar pitches obtained from Shalimar Tar Products and Rourkela Steel Plant were characterised and subjected to chemical and thermal treatment. These pitches were treated with organic solvents such as benzene, toluene, quinoline, xylene, dioxane and trichloroethylene to obtain soluble and insoluble fractions. The fractions we soaked in nitrogen at temperatures 250 to 550°C for 2 hr at any fixed temperature determine their weight losses. The pitches were also oxidized in air and in the presen of elemental sulphur in different weight proportions. Sulphuretted pitches were cok at 850°C and their x-ray profiles were determined using CuK_α radiation at 35 k 12 mA with pulse height analysis in Phillips x-ray generator PW 1300/00 with copp target tube. Some of the sulphuretted pitches were also coked at 2000°C. The optic and scanning microscopy of the pitch fraction was obtained at different magnificati to observe the mesophase spherules.

3. Results and discussion

The comparative properties of the commercial pitches and tar employed are indicat in table 1.

The soluble and insoluble solvent fractions of the pitch were subjected to therm treatment in nitrogen. The results are summarized in table 2. It is clear from this tal that all the insoluble fractions show progressive increase in weight loss as temperature is increased from 250 to 500°C. This clearly indicates that these fractic contain some lower molecular weight components which are lost on heating, wher quinoline insoluble fraction of pitch showed less weight loss, indicating thereby tha contains higher molecular components which are difficult to decompose. The wei

Table 1. Characteristics of commercial coal tar and pitches.

Material	S.P. (°C)	Benzene insoluble (%)	Quinoline insoluble (%)	Coking value (%)	Ash (%)
Coal tar	—	7	3	25	0·07
Shalimar pitch	80	40	9	58	0·25
Rourkela pitch	104	41	14	78	0·2

Table 2. Weight loss (%) of soluble and insoluble pitches on heating for 2 hr in N

Pitch	Temperature (°C)						
	250	300	350	400	450	500	55
Benzene insoluble	3·9	4·7	9·0	11·9	15·7	18·9	19
Toluene insoluble	2·1	3·0	6·1	9·2	14·0	16·7	1
Xylene insoluble	3·0	3·9	6·6	10·5	15·1	16·8	1
Dioxane insoluble	3·3	4·8	8·7	13·8	21·5	19·5	1
Trichloroethylene insoluble	3·3	4·3	6·1	8·9	11·4	13·4	1
Quinoline insoluble	4·3	4·8	4·9	5·3	7·6	7·4	
Benzene soluble	26·8	48·8	61·0	77·8	85·6	87·2	8
Toluene soluble	25·8	40·7	55·9	78·5	85·0	85·2	8
Xylene soluble	24·9	38·7	62·9	78·6	83·6	81·6	8
Dioxane soluble	36·2	53·8	62·7	80·3	82·7	80·8	8
Quinoline soluble	24·1	25·4	39·1	53·9	59·4	61·6	6

losses give a rough picture of the molecular weight distribution of the insoluble portions of the pitch.

Soluble fractions in different solvents (Mantell 1968) of the pitch show higher weight loss values up to 450°C, after which semi-coking starts. The lower molecular weight components in these fractions are decomposed more vigorously even at lower temperatures showing that low molecular weight fraction mostly accounts for the weight loss in the baking process.

Data presented in table 3 show the effect of weight loss of pitch on its benzene insoluble fraction and softening point in air. It was observed that with increase in temperature both the benzene insoluble fraction and the softening point increase, indicating that lower and medium molecular weight components are removed from the pitch during thermal treatment. The increase in softening point shows that more crosslinks are formed. At 300°C almost all the lower molecular weight components are removed and the pitch is left with higher and medium molecular weight components only.

The softening point of the sulphuretted pitches at 250°C increases with increase in sulphur content and benzene insoluble (table 4). This is on account of hardening of the pitch (Kippling *et al* 1963; Otani 1965) and sulphur additions which act as an oxidizing agent (Barr and Lewis 1978). A comparison of the results of thermally treated pitch in the presence of air and sulphur at 250°C shows that sulphur is more effective than air in increasing the softening point (tables 3 and 4). Therefore thermal treatment in the presence of sulphur is an effective method in raising the contents of medium and high

Table 3. Softening point, benzene insoluble and weight loss of pitch on heating at different temperatures for 2 hr in air

Temperature (°C)	Softening point (°C)	Benezene insoluble (%)	Weight loss (%)
25 (Room)	80	40	—
200	99	80·4	3·5
250	114	86	8·7
300	129	94	16·2
350	143	99·9	47·5

Table 4. Benzene insoluble pitch (%) in sulphuretted pitches heated at different temperatures for 2 hr in nitrogen

Sulphur in pitch	Temperature (°C)				
	250	300	350	400	450
0	58·2 107*	60·1	66·4	75·6	87·1
2	61·8 122*	64·0	72·9	88·6	97·8
5	62·5 135*	69·8	81·8	87·8	97·1

* Softening point.

molecular weight fractions represented by benzene and quinoline insolubles respe ively besides increasing the softening point. Thus it was possible to make extra ha pitch even with 5 % S additions.

Soft pitch having softening point around 60°C, quinoline insoluble 3 % and benze insoluble 16 % and Ash 0.16 % can be used as an impregnating pitch for densification composites. This pitch was made from coal tar by thermal treatment. The low softeni point has the advantage of easy flow and penetrates into the porous structure of t composites, thereby making it densified. The work has been done on few gram basis a further work is in progress.

Electrical resistivity of the sulphuretted pitch coke samples containing differe quantities of sulphur on heat treatment up to 2000°C shows that the sulphur additio increase the electrical resistivity values (table 5). The increase in the resistivity is more case where higher concentration of sulphur is added to the pitch coked at 850°C. Up 5 % sulphur additions, the increase is marginal but at 10 % sulphur addition, t resistivity increases about two times. The sulphur additions also facilitates removal peripheral hydrogen, establishes cross-links and increases the number of covale bonds which also increase the electrical resistivity (Kippling *et al* 1966; Socchi *et* 1978).

The effect of sulphur on *d* spacing (table 6) indicates that the *d* value spacing increas when the sulphur content is increased from 0 to 10 % keeping the temperature of coki constant at 850°C. This shows that sulphur affects crystallite parameters of the coke temperatures as low as 850°C. At 1600°C, the value of *d* spacing decreases because t pitch coke containing sulphur has higher value of *d* spacing which clearly indicates th

Table 5. Resistivity of the sulphuretted coke samples after heating at 2000°C and measured at room temperature

Sulphur in pitch coked at 850°C (%)	Wt loss in sulphuretted coke (%)	Electrical resistivity (milli ohm cm)
0	5·2	237
5	2·0	260
10	31·8	534

Table 6. Effect of heat treatment on *d* spacing of sulphuretted cokes

Sulphur in pitch coked at 850°C (%)	Temperature of coking (°C)	*d* spacing (Å)
0	850	3·54
4·5	850	3·57
10	850	3·78
0	1600	3·45
4·5	1600	3·52
10	2000	3·43

the crosslinks introduced as a result of addition of sulphur are sufficiently strong and do not break. At 2000°C, the value of *d* spacing is further reduced to 3·43 Å, showing that the increase of temperature improves the graphitizability of the coke.

Scanning electron micrographs of the toluene extract of the pitch heated to 400°C have been shown in the figures 1, 2 and 3. Two distinct phases are clearly visible. The mesophase spherules are formed but the growth seems to be very little. Only at higher magnification (figures 2 and 3) the spherules are seen predominently. The spherules show also some alignment which could be taken as initiation of the flow structure normally obtained in needle coke. Thus the portion of the pitch soluble in toluene significantly contributes to the structural development in the coke matrix of the composite when the latter is subjected to carbonization.

Work on carbon-carbon composites using coal tar pitch is in progress using carbon fibre as a filler and pitch as a matrix employing techniques of wet winding, carbonization, and repeated impregnation with pitch. The composites have been made with flexural strength as high as 650 MN/m^2 and interlaminar shear strength 17 MN/m^2. The details of the process and testing of the composites have been given in the project report to the Department of Science and Technology relating to the work on the resin project for the period November 1979 to April 1982.

4. Conclusions

The present results indicate that it is possible to make impregnating and extra hard pitches with softening point around 60°C and 136°C by using processes of chemical and

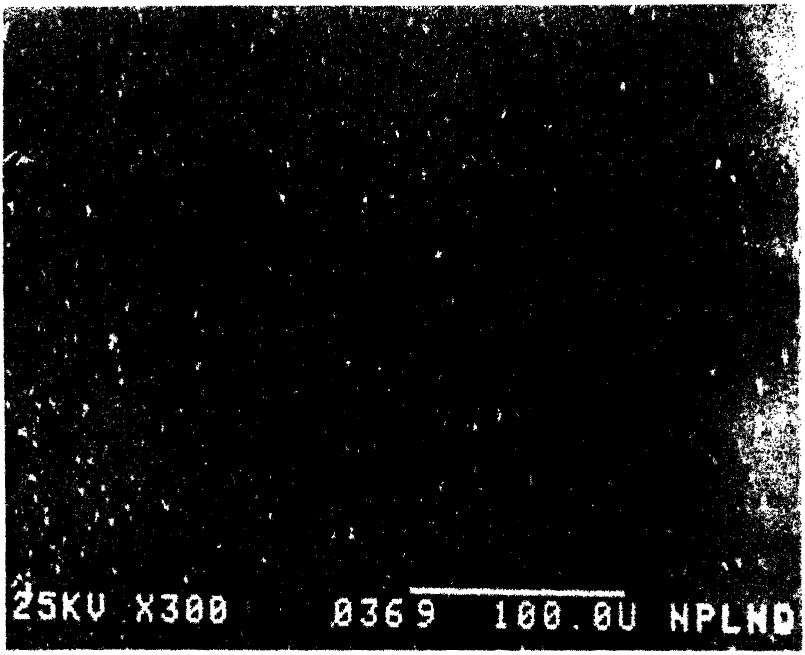

Figure 1. Scanning electron micrograph of toluene extract of the pitch heated to 400°C showing two distinct phases wherein the mesophase spherule growth is severely limited.

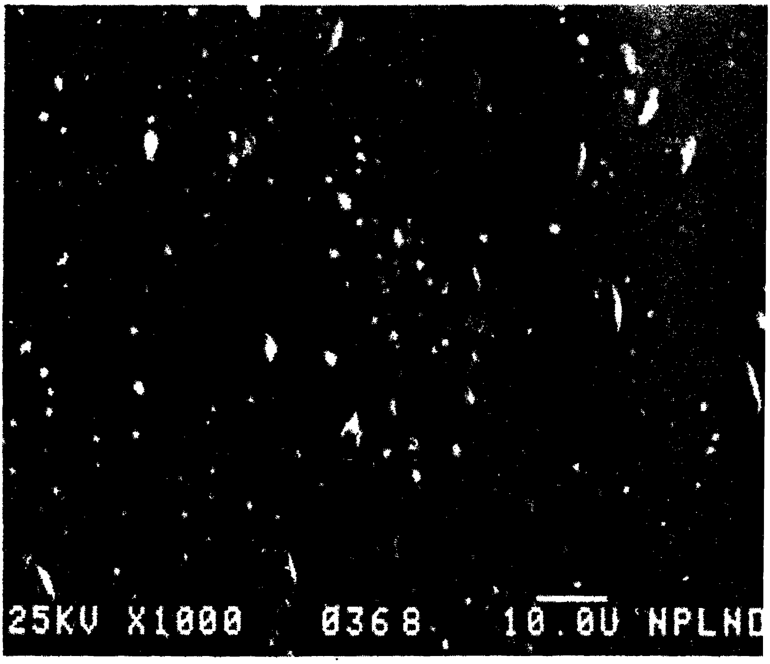

Figure 2. Magnified view of figure 1.

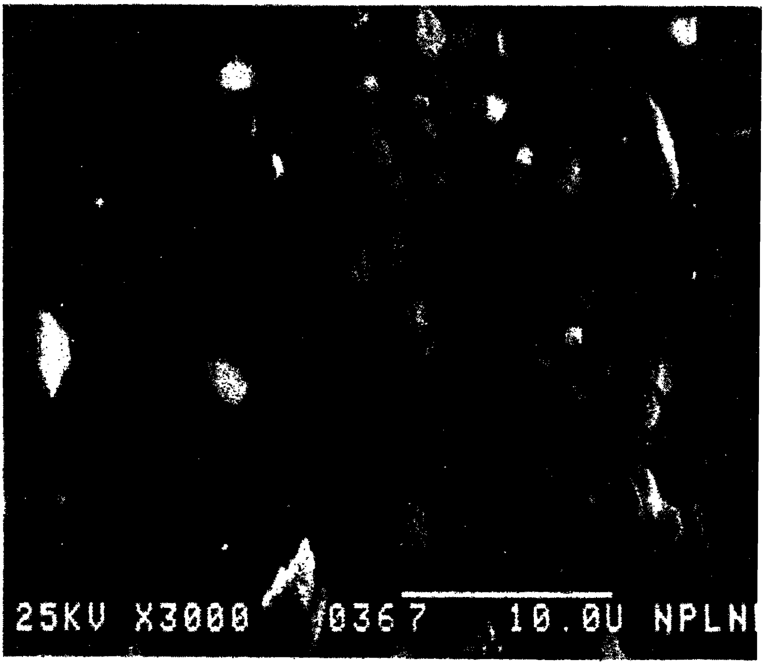

Figure 3. Mesophase spherule on the surface at the higher magnification shown in fig

thermal treatment of the commercial coal tars and pitches. Such pitches have been used to make carbon-carbon composites by several workers.

Acknowledgement

The authors are thankful to the Department of Science and Technology, New Delhi for financial support. Thanks are also due to Dr L M Manocha for assistance in the preparation and testing of carbon–carbon composites.

References

Barr J B and Lewis I C 1978 *Carbon* **16** 444
Brooke J D and Taylor G H 1965 *Carbon* 3 185
Fitzer E and Terewiesch B 1973 *Proc. 11th Conf. on Carbon, Tennessee*
Fitzer E, Burger A, Heym M and Terewiesch B 1975 *Carbon* **13** 149
Fitzer E, Giegel K H and Huttner W 1980a *Carbon* **18** 265
Fitzer E, Huttner W and Manocha L M 1980b *Carbon* **18** 291
Kippling J J, Sherwood J N, Shooter P V and Thomson N R 1963–64 *Carbon* **1** 315
Kippling J J, Shooter P V and Young R N 1966 *Carbon* **4** 341
Lowry H H 1968 *Chemistry of coal utilization* (New York: John Wiley)
Mantall C L 1968 *Carbon and graphite handbook* (New York: Interscience)
Otani S 1965 *Carbon* **3** 31
Socchi O, Onish N, Yamada Y and Honda G 1978 *Carbon* **16** 452

Bull. Mater. Sci., Vol. 6, No. 1, February 1984, pp. 99–104.
© Printed in India.

Amine-cured epoxy/glass fibre composites

D S VARMA and R G RAJ

Department of Textile Technology, Indian Institute of Technology, Hauz Khas, New Delhi 110016, India.

Abstract. Aromatic diamines containing imide groups were prepared for curing epoxy resins. Glass fabric-reinforced epoxy composites were fabricated using these imide-amine hardeners and the mechanical properties were determined. The processing characteristics of these composites were similar to the control based on 4,4′-diaminodiphenyl sulphone and 4,4′-diaminodiphenyl methane. Flexural properties, tensile strength and Izod impact strength (unnotched) of some of these imide-amine and epoxy/glass fabric composites were found to be better than the control.

Keywords. Imide-amine hardness; epoxy resin.

1. Introduction

Epoxy resins constitute one of the most important class of matrix materials in high performance composite systems. This is due to their versatility in processing and curing, high adhesive strength, low shrinkage and excellent mechanical strength and chemical resistance. However, these resins are somewhat brittle due to high cross-link density and can only be used up to a maximum temperature of 180°C. By a modification of epoxy resin or by a proper choice of curing agents it is possible to modify the structure of cured resins and improve thermal and photochemical resistance.

Most of the epoxy resins used for lamination are of low molecular weight and are based on bisphenol-A and epichlorohydrin. However, a wide range of epoxy resins based on halogenated resins, cycloaliphatic diepoxide and novolac have become available for special applications. Epoxy resins are cured through the reaction of epoxy group with amines, acid anhydrides and catalytic curing agents.

A modification in the structure of amines may improve the high temperature capabilities of epoxy resins. Good performance of polyimide resins at elevated temperatures is documented in literature. Imide-amines used as curing agents are expected to improve thermal characteristics of epoxy resins while retaining the processing advantages and better room temperature mechanical properties of epoxy resins. Recently Scola and Pater (1981) have reported novel bisimide-amine and epoxy/graphite fibre composites with better properties than the state-of-the-art epoxy resins.

In the present work aromatic amines containing imide groups were prepared and curing of epoxy resins with such amines was investigated. Glass fabric-reinforced epoxy laminates were fabricated and the mechanical properties were tested.

2. Experimental

2.1 *Synthesis of imide-amine hardeners*

Imide-amines were synthesised by reacting pyromellitic dianhydride (PMDA, Fluka) with 4,4′-diamino diphenyl methane (E. Merck) 4,4′-diamino diphenyl ether (ICN) 4,4′-diamino diphenyl sulphone (Wilson) in dimethyl formamide. The intermedi amic acid was cyclodehydrated by sodium acetate and acetic anhydride.

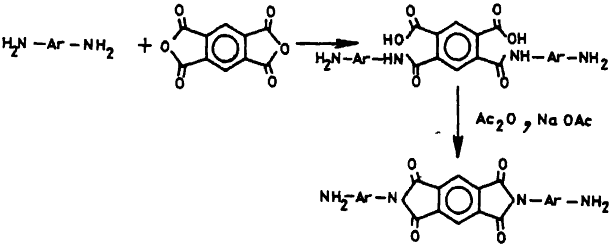

Thus in a typical reaction 0·2 M of diamine was placed in a three-necked flask DMF was added to it. The solution was stirred mechanically and nitrogen was bubb through it. Then 0·1 M of PMDA was added gradually in four portions. After stirrin room temperature for 2 hr, fused sodium acetate and acetic anhydride were added the solution refluxed at 60°C for 2 hr. The amine was recovered by precipitation water. The various hardeners used are given in scheme 2.

S.No.	Structure	symbol
1.	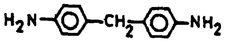	DADPM
2.	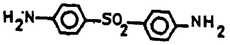	DPS
3.	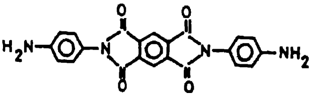	I-P
4.	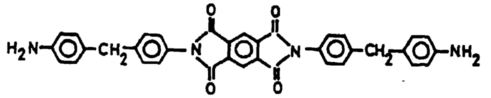	I-D
5.	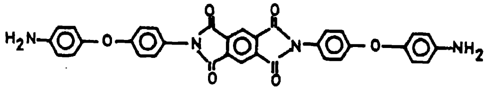	I-E
6.	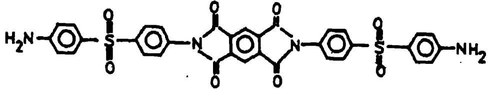	I-S

2.2 *Fabrication of laminates*

Hand lay-up method was used to fabricate laminates by compression molding. E gl fabric, plain weave, epoxy compatable (Pilkington Fiberglass) was used with Aral Ly556 (CIBA–GEIGY), (diglycidyl ether of bisphenol-A resin). Pre-pregs were made coating properly mixed resin and hardener solution (in methyl ethyl ketone or dimet formamide) on the glass-fibre cloth. The pre-pregs were dried at room temperature

15 min, then at 100°C for 10 min. Twelve plies of 20 × 20 cm pre-pregs were stacked in a mold and hot-pressed in a compression moulding machine. The following cure cycle was employed for the laminate fabrication:

Curing temperature	120–180°C
Cure time	4 hr
Heating rate	5°C/min
Pressure	20 kg/cm^2

2.3 *Mechanical properties*

The mechanical properties of the laminates were evaluated by Instron (model 1120). Flexural strength tests were performed using a three-point loading fixture with span-to-depth ratio of 32 : 1. Short-beam shear strength tests were conducted at a constant span-to-depth ratio 5 : 1. All mechanical properties were the averages of 3 test specimens. Fibre content of the laminates was determined by the acid digestion method (ASTM 1978).

3. Results and discussion

The curing and post-curing conditions for the glass-fibre reinforced epoxy resin with different hardeners are given in table 1. Curing time and curing temperatures were higher in imide-amine hardeners than in other systems investigated in the present work. The effect of post-curing time on the tensile and flexural strength of the laminates cured with DADPM, DDS, I–D, I–E and I–S is shown in figures 1 and 2. It can be seen from figure 1 that the tensile strength of the DADPM cured laminates has not increased significantly with post-curing. But the effect of post-curing was much pronounced in I–E and I–S laminates. Further increase in post-curing time failed to increase the tensile strength in the above laminates. From figure 2 it can be seen that the post-curing did not have any effect on the flexural strength of DADPM-cured laminates. I–E and I–S cured laminates have shown improvement in flexural strength after post-curing. The increase in the strength was significant in I–S cured laminates owing to the fact that flexural strength of the laminates depended significantly on the matrix properties of the laminates (Agarwal and Broutman 1980). Figure 3 gives the mechanical properties of the laminates of epoxy cured with DADPM, DDS, I–D, I–E, I–S systems. From the comparison of mechanical properties (tables 2 and 3) it can be seen that the I–S cured laminates showed better

Table 1. Curing conditions of glass fibre-reinforced epoxy resin—different curing systems.

Laminates	Resin-curing agent system	Curing temperature (°C)	Curing time (hr)	Post curing temperature (°C)	Post curing time (hr)
I	Ly556 + DADPM	120	4	150	5
II	Ly556 + DDS	160	4	180	4
III	Ly556 + I–D	160	4	180	4
IV	Ly556 + I–E	170	4	190	4
V	Ly556 + I–S	180	6	200	4

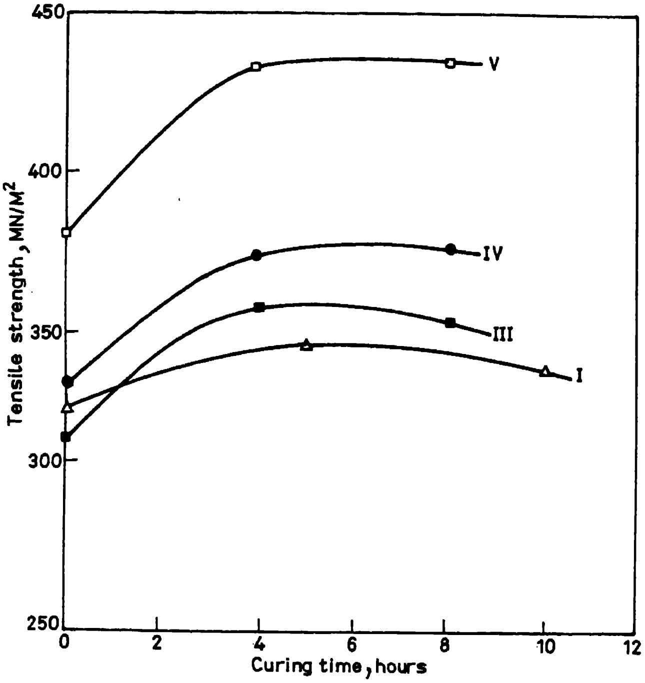

Figure 1. Effect of post-curing time on the tensile strength.

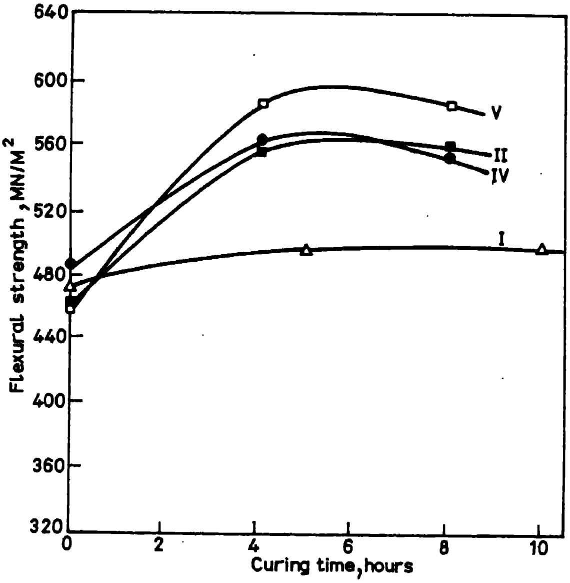

Figure 2. Effect of post-curing time on the flexural strength.

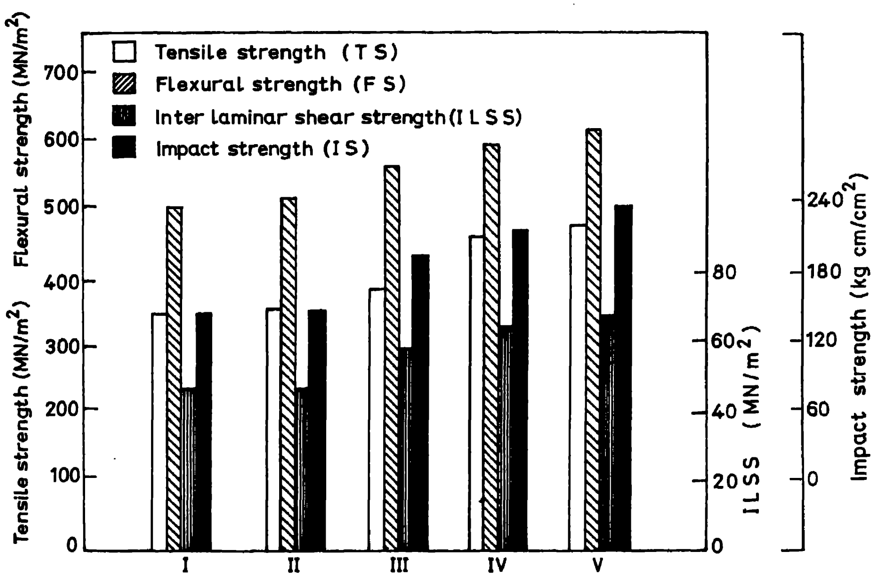

Figure 3. Mechanical properties of glass fibre reinforced epoxy laminates with different curing agent systems.

Table 2. Properties of I-S and DDS cured systems.*

	I–S			DDS	
	Post-curing time			Post-curing time	
Properties	0	4(hr)	8(hr)	0	4(hr)
Tensile strength MN/m²	408·25	474·38	472·10	312·43	350·28
Flexural strength MN/m²	485·75	615·86	616·48	467·59	512·47
Short beam sheer strength MN/m²	54·47	67·43	64·74	40·36	44·89
Izod-impact strength (un-notched) kg.cm/cm²	172·39	218·31	227·43	138·94	142·31

*Effect of post-curing time on the mechanical properties of I–S and DDS cured systems.

mechanical properties of all the systems studied. The increase in short-beam shear strength of I–S cured laminates may be due to the increased toughness of the matrix, which also enhance the impact strength.

4. Conclusion

A new set of aromatic imide-amine hardeners developed for DGEBA epoxy resin showed the following advantages: (a) Good processability of the resin and increased toughness of the cured system with I–E and I–S hardeners. (b) Improved mechanical properties at room temperature as compared to the commercial aromatic diamines, with system I–S having the best properties of all the hardeners studied.

Table 3. Mechanical properties of glass fibre-reinforced epoxy laminates.

	Ly 556 Resin System cured with				
Properties tested	DADPM I	DDS II	I–D III	I–E IV	I–S V
Resin Content	36·7	34·7	37·9	34·1	33·8
Tensile strength (MN/m^2)	346·75	350·28	374·26	430·52	474·3
Tensile modulus (GN/m^2)	23·17	23·44	25·93	28·13	28·4
Flexural strength (MN/m^2)	496·30	512·47	564·84	589·39	615·8
Flexural modulus (GN/m^2)	27·86	28·41	34·68	37·44	37·7
Short-beam shear strength MN/m^2	43·02	44·89	57·16	63·50	67·4
Izod-impact strength (un-notched) $Kg\text{-}cm/cm^2$	123·47	142·31	187·24	201·91	218·3
% Void	0·89	1·03	0·90	0·94	1·0

Curing and post-curing conditions were the same as given in table 1.

References

Agarwal B D and Broutman L J 1980 *Analysis and performance of fibre composites*, (New York: John W
p. 33

ASTM 1978 Fibre content of reinforced resin composites, ASTM D3171–76 annual book of A
Standards, Part 36, page 746

Scola D S and Pater R H 1982 13th National SAMPE Tech. Conf. Oct. 1981, *SAMPE Jl*, p. 16

Bull. Mater. Sci., Vol. 6, No. 1, February 1984, pp. 105–110.
© Printed in India.

Dielectric and pyroelectric studies on triglycine sulphate-polymer composites

K SREENIVAS, T SUDERSENA RAO, AJAY DHAR and ABHAI MANSINGH

Department of Physics and Astrophysics, University of Delhi, Delhi 110007, India

Abstract. Interest in flexible ferroelectric/polymer composite transducers has increased markedly in recent years. The current work describes the fabrication of TGS-polymer composites with varying TGS particle size powders embedded in a polymer matrix. The electrical properties investigated are the dielectric constant and pyroelectric coefficient. Variation in the pyroelectric coefficient and the peak dielectric constant with decreasing particle size of TGS in the composites has been explained on the basis of defective surface layers and lower polarisation values.

Keywords. Dielectric studies; pyroelectric studies; triglycine sulphate polymers.

1. Introduction

In the last few years many composites have been developed, which have both economic as well as performance advantages (Skinner *et al* 1978; Newnham *et al* 1978). Composites are being prepared by mixing two different materials, so as to combine their best individual properties. Most of the work reported till date (Newnham *et al* 1978, 1982; Bhalla *et al* 1982; Safari and Newnham 1982) has been mainly concentrated on piezoelectric composites for transducer applications. It is felt that if good pyroelectric composites could be developed, then the need for large area single crystals and ceramics could be relaxed.

Recent studies on pyroelectric composites (Yamazaki and Kitayama 1981; and Bhalla *et al* 1981) do show potential usefulness of pyroelectric composites. Triglycine sulphate (TGS) has a large pyroelectric coefficient and a high responsivity, but still its use has been mainly restricted by the expense and limitations encountered while growing large area single crystals (Jansson 1974). In the present work we report the pyroelectric and dielectric properties of TGS-polystyrene composites and compare their performance with TGS single crystals and other ferroelectric-polymer composites.

2. Experimental

2.1 *Sample preparation*

The two phases in the present pyroelectric composites are TGS powder and commercially available polystyrene. TGS was prepared by reacting sulphuric acid (H_2SO_4) and hot glycine in proper stoichiometric ratio. Small crystals were grown by slow evaporation of the water solution at 28°C. The crystals were powdered and later separated into different particle sizes (75 to 400 μm) using stainless steel sieves. Toulene was used to dissolve polystyrene.

Fine TGS powder of uniform particle size was then suspended in the polystyre solution. The mixture was mixed thoroughly and then spread uniformly with a spat in the form of a thin layer on a glass plate. The viscosity of the polystyrene solution h to be maintained at a critical level. Thin layers of TGS-polystyrene composite w allowed to dry in air at room temperature for about 24 hours. Thin composite layers area as large as 4 × 4 cm could be peeled off easily, and scissored to get the requi shape. They were thinned to a thickness of 1 mm by grinding and were repolished af thinning. Aluminium electrodes were deposited on both sides for electrical measu ments. In all the samples the TGS content incorporated in the composite was 60 % volume. Samples were prepared in rectangular shapes of 1·3 × 1·8 cm with a unifo thickness of 1 mm. It is possible to prepare reproducible sheets which show lit degradation with time.

2.2 *Measurement method*

The pyroelectric current was measured by the direct method of Byre and Roun (1972). Automated quantitative pyroelectric measurements could be carried out making use of Riken Denshi X–Y_1–Y_2–T recorder. A 610C Keithley electrometer a 150B Keithley micro-voltmeter were used to measure the pyroelectric current a temperature. Dielectric measurements were made on a GR1615A capacitance bridge 100 kHz.

3. Results

3.1 *Pyroelectric measurements*

Figure 1 shows the temperature dependance of pyroelectric current of TGS sin crystals which were grown and later powdered to be employed in the composite un study. The pyroelectric transition observed at 50°C may be due to a slight thermal between the temperature sensor and the sample. The value of pyroelectric coefficien given by,

$$P_i = I/(A \cdot \mathrm{d}\theta/\mathrm{d}t),$$

where I = pyroelectric current, A = the area, $\mathrm{d}\theta/\mathrm{d}t$ = the rate of heating. T calculated value of P_i for TGS crystals is 4.63×10^{-10} C cm^{-2} K^{-1} at 303 K. This l value of P_i may be due to the presence of impurities and crystal defects during crys growth. However, the main purpose of these studies was to compare the results composites, rather than achieving high quality TGS single crystals. Hence, the val obtained for the crystals were considered satisfactory.

Originally, the composite layer was made on a copper foil, so as to have a bott contact for electrical measurements. But, the poor contact and surface inhomogeneit between the copper foil and the composite resulted in a lot of noise during the electri measurements. Hence, they were peeled, thinned and repolished. Figure 2 shows variation of pyroelectric current with temperature of TGS-polystyrene composites w different particle size of TGS. Pyroelectricity was observed even in the composite w the lowest particle size of TGS. The peak values of pyroelectric coefficient at transition temperature decreases with decreasing particle size and the transiti temperature shifts towards the higher temperatures with increasing particle size.

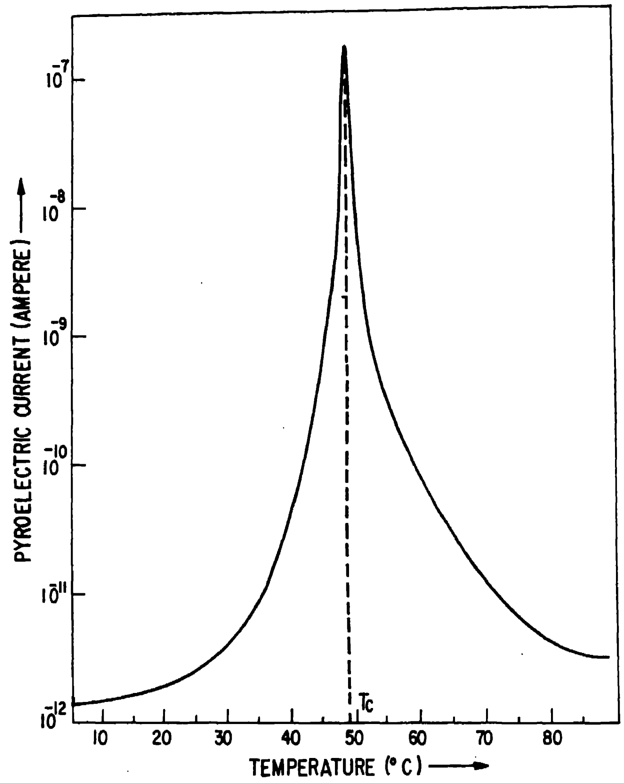

Figure 1. Variation of pyroelectric current with temperature for TGS single crystals.

3.2 *Dielectric measurements*

The temperature dependance of dielectric constant for the four TGS-polystyrene composites is shown in figure 3. The dielectric anomaly was clearly observed down to 75 μm particle-sized composite and the transition temperature shifts towards higher temperatures with decreasing particle size.

4. Discussion

The pyroelectric coefficients calculated for the composites and TGS single crystals at 303 K are given in table 1. The low values of P_t and ε' and the decrease in these values with decreasing particle size of TGS in composites can be qualitatively explained as follows. It has been suggested that for most ferroelectrics the boundary polarisation differs from that of bulk material and there exist non-ferroelectric defective surface layers playing a dominant role (Aizu 1962). Existence of such surface layers has been confirmed by studies on a number of single crystals and compressed ferroelectric powders (Sekido and Mitsui 1967; Goswami 1969; Mansingh and Bawa 1973, 1975; Mansingh *et al* 1975, 1979).

In the present TGS-polystyrene composities it is felt that these surface layers at the boundary of the TGS crystallites are effectively responsible for the low polarisation

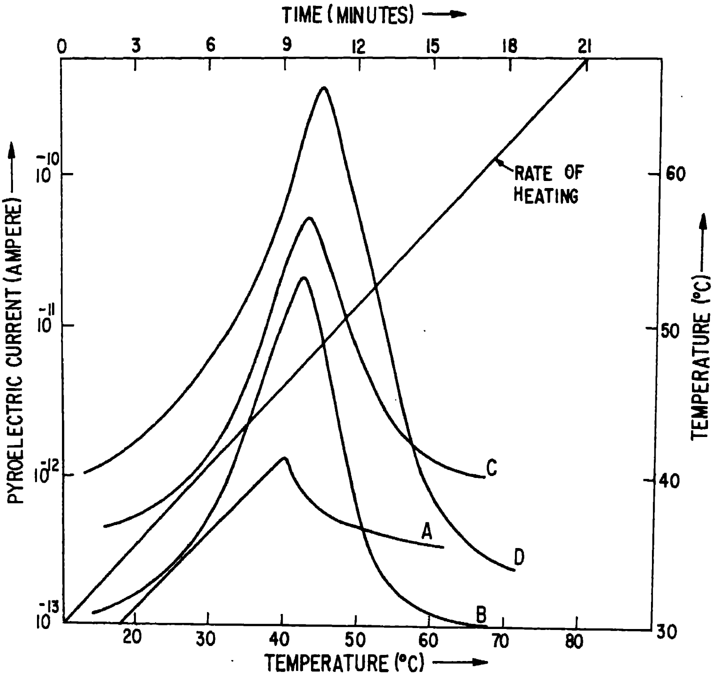

Figure 2. Variation of pyroelectric current for TGS-polystyrene composites with var particle size. A: 75 μm B: 150 μm, C: 250 μm, D: 400 μm.

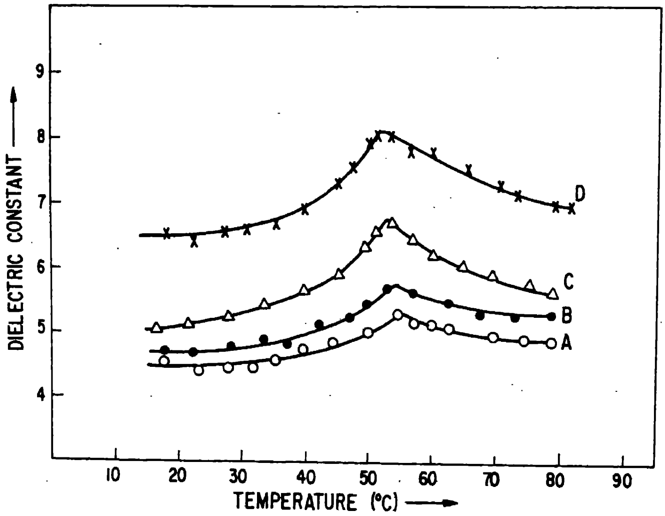

Figure 3. Dielectric constant as a function of temperature for TGS-polystyrene compo A: 75 μm, B: 150 μm, C: 250 μm, D: 400 μm.

Table 1. Room temperature pyroelectric properties and figures of merit for detector operation.

Materials	Pyroelectric coefficient C $\mathrm{cm}^{-2}\,\mathrm{K}^{-1}$	Dielectric constant	Responsivity VW^{-1}	References
TGS-polystyrene composites (μm)				Present studies
1. 400	$1{\cdot}14\times10^{-10}$	6·625	$1{\cdot}15\times10^{-11}$	
2. 250	$2{\cdot}14\times10^{-11}$	5.40	$2{\cdot}65\times10^{-12}$	
3. 150	$1{\cdot}07\times10^{-11}$	4·75	$1{\cdot}50\times10^{-12}$	
4. 75	$8{\cdot}55\times10^{-12}$	4·50	$1{\cdot}27\times10^{-12}$	
PVDF-$\mathrm{PbTiO_3}$ composite	$13{\cdot}00\times10^{-9}$	55·00	$8{\cdot}44\times10^{-11}$	Yamazaki and Kitayami (1981).

values and a decrease in the values of P_i with particle size as evident from the studies on TGS powders (Mansingh *et al* 1975).

The responsivity (R_v) of a pyroelectric detector is given by,

$$R_v = P_i/C\varepsilon' \tag{2}$$

where P_i = the pyroelectric coefficient, ε' = the dielectric constant and C = the volume specific heat. The calculated value of R_v taking $C = 1{\cdot}5\ \mathrm{J\,cm^{-3}\,K^{-1}}$ for composites is reported in table 1 and compared with other ferroelectric polymer composites. The responsivity of TGS-polystyrene composites is about two orders of magnitude lower than that reported for TGS single crystals (Beerman 1969) and lower than the lead titanate-polyvinylidene flouride composite (Yamazaki and Kitayama 1981), in which both the materials were pyroelectric.

5. Conclusions

In summary, we have been successful in developing a cheap, large area flexible pyroelectric composite. The responsivity and sensitivity are lower compared to single crystals. However, considering the problem of growing large area TGS single crystals and hot pressing as well as stretching required for composites based on PVDF (polyvinylidene fluoride) polymers, the TGS-polystyrene composites may still be useful because of the ease in fabrication of large area composites.

References

Aizu K 1962 *Rev. Mod. Phys.* **34** 550
Beerman H P 1969 *IEEE Trans. Elec. Devices* **16** 554
Bhalla A S, Newnham R E, Cross L E, Schulze W A, Dougherty J P and Smith W A 1981 *Ferroelectrics* **33** 139
Bhalla A S, Newnham R E, Shrout T R and Cross L E 1982 *Ferroelectrics* **41** 207
Byre R L and Roundy C B 1972 *Ferroelectrics* **3** 333
Goswami A K 1969 *J. Appl. Phys.* **33** 3125
Jansson P A 1974 *Appl. Opt.* **13** 1293
Mansingh A and Bawa S S 1973 *J. Phys. Soc. Jpn* **35** 1136

Mansingh A and Bawa S S 1975 *J. Phys.* **D8** 1156
Mansingh A, Srivastava K N and Bachchan Singh 1975 *J. Phys.* **D10** 2117
Mansingh A, Srivastava K N and Bachchan Singh 1979 *J. Phys. Chem. Solids* **40** 9
Newnham R E, Skinner D P and Cross L E 1978 *Mater. Res. Bull.* **13** 525
Newnham R E, Rittermeyer K, Shrout T and Schulze W A 1982 *Ferroelectrics* **41** 189
Safari A and Newnham R E 1982 *Ferroelectrics* **41** 197
Sekido T and Mitsui T 1967 *J. Phys. Chem. Solids* **28** 967
Skinner D P, Newnham R E and Cross L E 1978 *Mater. Res. Bull.* **13** 599
Yamazaki H and Kitayama T 1981 *Ferroelectrics* **33** 147

Bull. Mater. Sci., Vol. 6, No. 1, February 1984, pp. 111–118.
© Printed in India.

Elevated temperature low cycle fatigue studies on AISI 304 steel

N K SINHA and P VASUDEVAN

Department of Mechanical Engineering, Indian Institute of Technology, Bombay 400076, India

Abstract. Fully-reversed, total diametral strain-controlled low cycle fatigue tests were conducted in air at 650 and 800°C, and different strain ranges on AISI type 304 stainless steel. Attempts were made to correlate Coffin-Manson relationship for elevated temperatures, Frequency modified law as proposed by Coffin was verified. The results were compared with the relationship proposed by Kanajawa and co-workers.

Keywords. Diametral strain; low cycle fatigue; strain rates; cycle period; frequency-modified life.

1. Introduction

In the accurate fatigue design of high temperature structural components, creep-fatigue interaction has been considered an important subject. Components in nuclear reactors, gas and conventional steam turbines are subjected to quite complex loading cycles of varying duration at elevated temperatures. It requires sufficient documentation of such factors as dwell period, cyclic softening and hardening, stress or strain cycles, thermal cycles, environment, prior history of the fatigue and creep and possible creep-fatigue interaction. All these could influence the subsequent material behaviour.

Many investigators (Coffin 1974; Berling and Conway 1969; Berling and Slot 1969) have shown that low cycle fatigue behaviour of structural materials under high temperature conditions is strongly affected by the frequency of loading. The frequency effect which is considered to be a creep-fatigue interaction is a composite phenomenon, consisting of many factors such as time-dependent and time-independent behaviour of materials. Chemical and physical environments and metallurgical factors under cyclic loading at high temperatures are also important. Manson (1968), Coffin (1973), Campbell (1971) have all studied the above phenomenon and as a result, failure criterion, life prediction and application for design practice have been obtained.

In the present investigation, fully-reversed strain-controlled, low-cycle fatigue tests, for different strain rates and temperatures on AISI type 304 stainless steel available in India, which is mostly used in the construction of nuclear components, have been considered. The frequency modified principle (Coffin 1969) and strain rate effects (Kanajawa and Yoshida 1973; Udoguchi *et al* 1973) have been used to find out the high temperature behaviour of the material. This approach has the attraction that complex fatigue failure could be predicted by simple experiments or from physical data rather than detailed experimentation. Another possible advantage is that, other wave forms of loading could be considered, provided the period remains constant. Frequency modified life concept can be used to predict life even in cases where hold time is introduced in the load program.

2. Effect of frequency on life

Coles and Skinner (1965) proposed frequency time parameters of the term $V^{K} \cdot t =$ where V is the frequency, t is the total time of failure, K and C_1 are constants. M recently Coffin (1969) developed an approach based on the concept of freque modified life. The equation for any specific temperature was developed from experimental results

$$\Delta\varepsilon_p = C_2 N_f^{-\beta} V^{(1-K)\beta},$$

where $\Delta\varepsilon_p$ = plastic strain range and N_f = number of cycles to failure. The total s range found analytically is given by

$$\Delta\varepsilon_t = C_2 (N_f V^{K-1})^{-B} + \frac{A}{E} n' C_2 N_f^{-\beta n'} V^{-\beta n'(K-1)+K_1},$$

where n' is the strain-hardening coefficient and C_2, A, β, K, and K_1 are temperat dependent constants. Equation (2) may be regarded as a generalised fatigue equ applicable to both high and low temperature. At low temperature, the equation ca directly converted into Manson's (1967) method of universal slope.

$$\Delta\varepsilon_t = \frac{3{\cdot}560}{E} \cdot N_f^{-0{\cdot}12} + D^{0{\cdot}6} N_f^{-0{\cdot}6}.$$

Kanajawa and Yoshida (1973) concluded that strain rate rather than freque modified life for hold time was an important factor and the relationship was expr in the form

$$N_f = C\dot{\varepsilon}^{K},$$

where $\dot{\varepsilon}$ = strain rate, K and C are constants. Udoguchi *et al* (1973) who investigate effect of frequency and hold time proposed.

$$N_f = A\tau^{-B},$$

with both A and B independent of τ, the cycle period. The equation for number of c to failure becomes

$$N_f = \alpha\varepsilon_p^{-\beta_1 + \delta \log \tau} \tau^{-\nu},$$

where α, β_1, ν, and δ are temperature-dependent material constants.

The extensive literature survey revealed that the elevated temperature fa behaviour data are obtained from fatigue tests which are costly and time-consu particularly in low frequency and hold time. Moreover, it is difficult to incorpora service conditions into the test set-up. It is desirable that theoretical derivations p long time-elevated temperature behaviour from short-time tests. Also, it is foun various investigators had limited objective in their tests e.g. a particular temper material or environment. It is very important that universal design equations shou developed for any material before using in design applications.

3. Material and specimen details

AISI type 304 stainless steel was obtained in the bar stock form from a single lot mm diameter. The specimens were cut to size, heat-treated and machined t required size.

The chemical composition is Cr 19·3, Ni 9·11, C 0·06 and Mn 1·53. The heat treatment consisted of heating the specimen up to 1150°C and cooling up to 920°C and then air cooling. After heat treatment, tensile and fatigue test specimens were machined to configuration as shown in figure 1(a) and 1(b). The test section of each specimen was polished with fine grade of silicon carbide paper with finishing mark parallel to the longitudinal section of the specimen.

4. Testing machine and experimental procedure

4.1 *Tension test*

The tensile property of the test material was evaluated, using an universal testing machine (USSR, model 50T) at 650 and 800°C. Automatic temperature control (Therelek) resistance type split furnace (capacity: 1200°C) was used in the elevated temperature test. The properties are reported in table 1.

4.2 *Fatigue test*

The elevated temperature fatigue tests were conducted at 650 and 800°C and at three different strain rates *i.e.* $3{\cdot}15 \times 10^{-4}$, $3{\cdot}15 \times 10^{-3}$, $3{\cdot}15 \times 10^{-2}$ sec^{-1} and three total

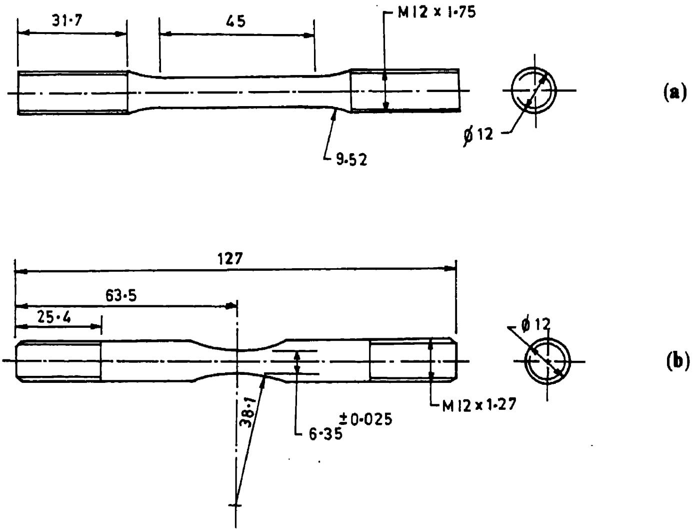

Figure 1. a. Tension test specimen. **b.** Push pull fatigue test specimen.

Table 1. Mechanical properties

Temperature (°C)	Ultimate tensile stress (kg/mm^2)	Reduction in area (%)	Modulus of elasticity (kg/mm^2 × 10^3)
Room temperature	66·5	76	21·2
650	36·8	69·5	16·7
800	73·25	71·5	15·4

strain ranges. A low-cycle push-pull fatigue testing machine, ± 10T capacity (desig and fabricated by the authors) as shown in figure 2 was used. Very low frequency t *i.e.* $3{\cdot}15 \times 10^{-4}$ sec^{-1} which could not be conducted on this machine, were carried on a servohydraulic fatigue testing machine (MTS make, ± 10T).

The push pull fatigue testing machine works on the principle of variable crank rad scotch yoke mechanism on the constant displacement (constant total strain) mode. variable crank radius was obtained by working on a screw-and-nut principle. The cr pin is integral with the nut of the above mechanism and drives the slider of the sco yoke mechanism. The drive system consists of an electric motor, two-stage worm g box and a V belt type variable speed systems. The variable speed drive permitted test different strain rates. The load frame consisted of rigid vertical columns provided w mean loading hand-driven power screw, having strain gauge type load cell, in series w the specimen. This enables various size specimens to be accommodated. The diame strain was measured in the test section by using a calibrated clip gauge t extensometer designed and fabricated by the authors. The diametral strain v converted into equivalent axial strain following the conventional formula (Slot *e* 1969).

The automatic tripping circuit was incorporated for stopping the machine, when specimen fails.

5. Results and discussion

In order to compare the test results with results obtained by others the plastic str range was computed from the total strain range (Raske and Morrow 1969). The gra

Figure 2. Elevated temperature. Low cycle push-pull fatigue test set up.

are plotted showing the fatigue behaviour at different temperatures and strain rates. The various exponents and constants required in the frequency relationship equations (1) and (6) were obtained by regression analysis from the test results. The determined constants and exponents are listed in table 2.

On the basis of the above calculations, theoretically predicted values were obtained and compared (figure 5) with the actual values (table 3). The test results showed a

Table 2. Comparison of life prediction techniques

Constant temperature (°C)	C_2	K	β	Reference	α	β_1	ν	δ	Reference
650	1·108	0·81	0.707	Coffin (1973)	630	1·40	0·275	0·155	Udoguchi *et al* (1973)
650	1·1478	0·6920	0·6919	Present results	$1{\cdot}01 \times 10^{-3}$	1·69	0·193	0·154	Udoguchi *et al* (1977)
650					720	1·1085	0·3468	0·1178	Present results
816	1·72	0·81	0·87	Coffin (1973)					
800	1·3221	0·7580	0·7702	Present results	407	0·9892	0·2858	0·192	Present results

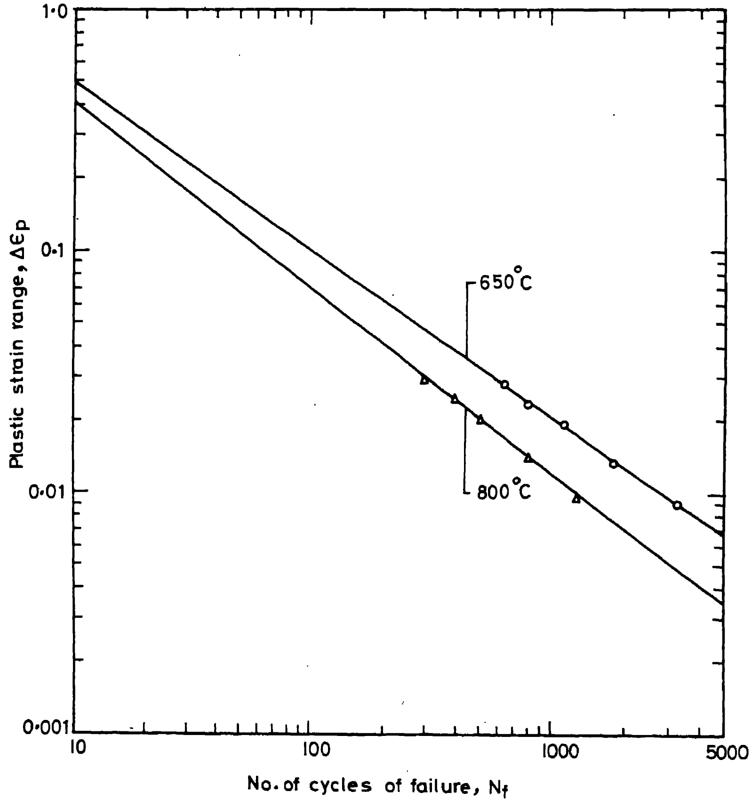

Figure 3. Plastic strain range $\Delta\varepsilon_p$ *vs* number of cycles to failure at 650 and 800°C and strain rate $3{\cdot}15 \times 10^{-2}$ sec^{-1}.

behaviour similar to that of other investigators for the same material such as increasing strain range showed decrease in life (figure 3), (ii) increase in temperatu showed decrease in life (figure 3) and (iii) decrease in strain rate showed a decrease in l (figure 4).

The short-term test results obtained in high frequency were incorporated in t frequency-modified relationship to predict lives at low frequencies and compared w test data.

The coefficients β and K, contrary to the results of other investigators, are n constant with the strain range or temperature. However, it is interesting to see t closeness of the predicted life using these coefficients with the actual test results. Her these can be treated as confirmation of the validity of equation (1).

Using the test results and fitting them into the equation proposed by Udoguchi *et* (1973) the coefficients were calculated. It was found that for the calculated coefficien the test results were close to the observed results. The calculated coefficients wh compared with the results of Berling and Slot (1969) and Udoguchi *et al* (1973) show disagreement. This disproves the universal application of the above equation *i.e.* ea one must fit the test data for a particular material and environment of testing.

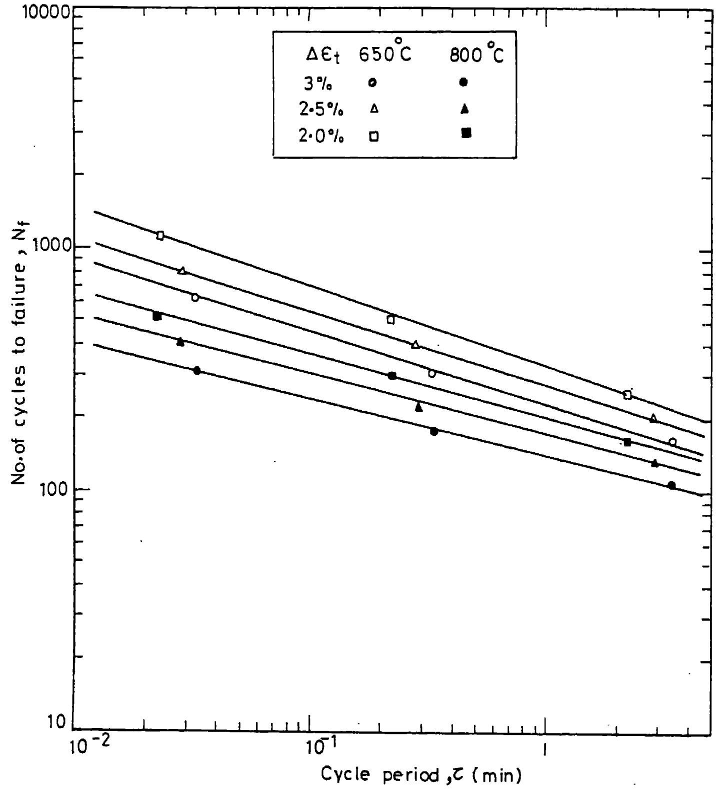

Figure 4. Number of cycles of failure, N_f *vs* cycle period t, at different temperatures T a total strain range $\Delta\varepsilon_t$.

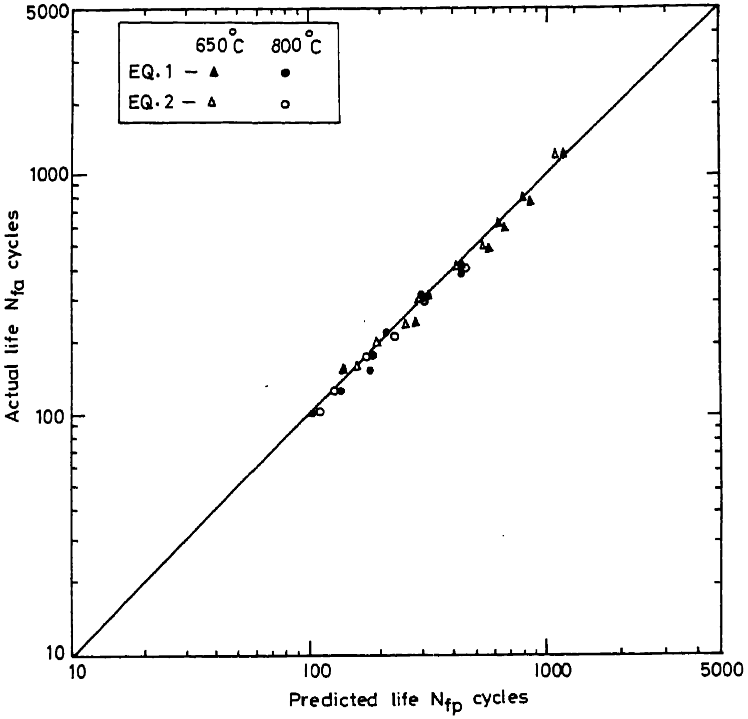

Figure 5. Comparison of actual life (N_{fa}) and predicted life at different temperatures.

Table 3. Results of elevated temperature fatigue studies.

Total Strain range $\Delta\varepsilon_t$ percentage	Strain rate $\dot{\varepsilon}$ (sec^{-1})	650°C			800°C		
		actual fatigue life N_{fa}	predicted fatigue life N_{fp} equation (1)	predicted fatigue life N_{fp} equation (6)	actual fatigue life N_{fa}	predicted fatigue life N_{fp} equation (1)	predicted fatigue life N_{fp} equation (6)
3·0	$3{\cdot}15 \times 10^{-2}$	635	612	626	312	324	311
2·5	$3{\cdot}15 \times 10^{-2}$	806	841	837	415	405	395
2·0	$3{\cdot}15 \times 10^{-2}$	1124	1173	1137	523	575	535
3·0	$3{\cdot}15 \times 10^{-3}$	321	301	318	179	186	182
2·5	$3{\cdot}15 \times 10^{-3}$	413	414	415	227	243	228
2·0	$3{\cdot}15 \times 10^{-3}$	499	576	553	304	329	296
3·0	$3{\cdot}15 \times 10^{-4}$	163	148	162	108	106	107
2·5	$3{\cdot}15 \times 10^{-4}$	201	203	206	133	139	132
2·0	$3{\cdot}15 \times 10^{-4}$	252	285	270	167	188	167

6. Conclusions

(i) Test results agree with that results of other investigators (Coffin 1973). (ii) Using the Coffins frequency-modified relationship the plot of predicted life versus the actual life were linear, thus proving the acceptability of the approach. (iii) The present results agree with results obtained earlier using equations proposed by Udoguchi *et al* (19 (iv) However, the coefficient K at 650 and 800°C varies with temperature. (v) It is that tests should be conducted with various heat treatments for the same materia establish universality of these predictive relations. (vi) The predictive equation, to more useful to the designer, should incorporate coefficients for temperature variati coefficient of strain rate variation and material parameters in the form.

$$\Delta\varepsilon_p = C_2 K_1 N_f^{-B} K_2 V^{K-1}.$$

References

Berling J T and Conway J B 1969 *Pressure vessel technology*, Proc. 1st Int. Conf., Delft, Part II p. 1

Berling J T and Slot T 1969 *ASTM STP* 459, ASTM, Philadelphia, p. 3

Campbell R D 1971 *Trans. ASME* Series p. 887

Coffin L F Jr 1969 *Fracture*, Proc. 2nd Int. Conf., Brighton, p. 643

Coffin L F Jr 1973 ASTM STP 520 ASTM, Philadelphia, p. 5

Coffin L F Jr 1974 *Metall. Trans.* **5** 69

Coles A and Skinner D 1965 *J. R. Aeronaut. Soc.* **69** p. 53

Kanajawa K and Youshida S 1973 *Creep-fatigue in elevated temperature applications*, IME Proc. of C p. 2261

Manson S S 1967 *Thermal and high strain fatigue metals and metallurgy* Proc. Int. Conf., p. 154

Manson S S 1968 *J. Exp. Mech.* 1

Raske D T and Morrow J 1969 ASTM STP 465 ASTM, Philadelphia, p. 1

Slot T, Stenz R H and Berling J T 1969 ASTM STP 465 ASTM, Philadelphia, p. 100

Udoguchi T, Ashaday and Ichino I 1973 *Creep-fatigue in elevated temperature applications*, IME Pro Conf., p 211.1

Udoguchi T, Ashaday, Mitsuhashi and Morimotos A 1977 *Pressure vessel technology*, Proc. Third Int. C

Bull. Mater. Sci., Vol. 6, No. 1, February 1984, pp. 119–128.
© Printed in India.

Structure and properties of an investment—cast austenitic stainless steel

P M JEBARAJ, MALUR N SRINIVASAN and M R SESHADRI
Department of Mechanical Engineering, Indian Institute of Science, Bangalore 560 012, India

Abstract. Test castings of a cast-austenitic stainless steel were made in low and high vacuum in different sizes. The effect of melting and casting environment as well as the cooling rate on delta ferrite features, mechanical properties and corrosion resistance of the castings have been discussed.

Keywords. Microstructure; mechanical properties; corrosion resistance; vacuum casting; investment casting; austenite; delta ferrite; stainless steel.

1. Introduction

Austenitic stainless steels are widely used in applications requiring good corrosion resistance and reasonable mechanical behaviour. Hence the properties are known to be sensitive to variations in microstructure which could be brought about by changes in composition and cooling rate (Pereira and Beech 1980). Investment casting lends itself equally well to melting and casting in air as well as in vacuum. It is a preferable mould than the conventional ones (Luce *et al* 1972).

It is well-known that when melting and casting are performed in vacuum the oxidizing tendency of certain elements is lowered and that the dissolved gas content is reduced as compared to the corresponding air-melted and poured samples (Chandler 1982). In particular, it is to be expected that in stainless steel the tendency of oxidation of chromium and retained nitrogen content would be lower when it is melted and cast in vacuum. Both the elements strongly affect the microstructural constituents in austenitic stainless steel, in particular the delta ferrite content (McTighe and Beech 1977). Further, in a casting the cooling rate is markedly affected by changes in casting size and it has been noted that the delta ferrite content is also affected by the cooling rate (Pereira and Beech 1980; Petrov 1967), the trend in variation being dependent upon the type of solidification (Pereira and Beech 1980).

It is thus clear that the microstructure and hence the properties of austenitic stainless steel could be expected to vary when investment castings of different sizes are made in air and under vacuum. As very little information is available in literature on the effects of casting size as well as melting and casting environment on the structure and properties of investment cast austenitic stainless steel, this investigation was taken up.

2. Experimental

2.1 *Mould*

The investment shell mould, with ethyl silicate as the binder, was used. The cooling rate was varied by altering the bore diameter and the head size, details of which are given in table 1 and figure 1. The investment mould was unbacked and the casting ma vertically.

2.2 *Melting and casting*

Wrought bars of austenitic stainless steel were melted and solidified under thr different environments namely air (at atmospheric pressure), low vacuu (0·25 mm Hg) and high vacuum ($> 10^{-3}$ mm Hg). A medium frequency vacuu induction furnace (GCA Vacuum Industries) and a medium frequency air melti furnance (Brown Boveri) (both having same melting capacity) were used for this purpos Typical compositions of castings made in different environments are listed in table

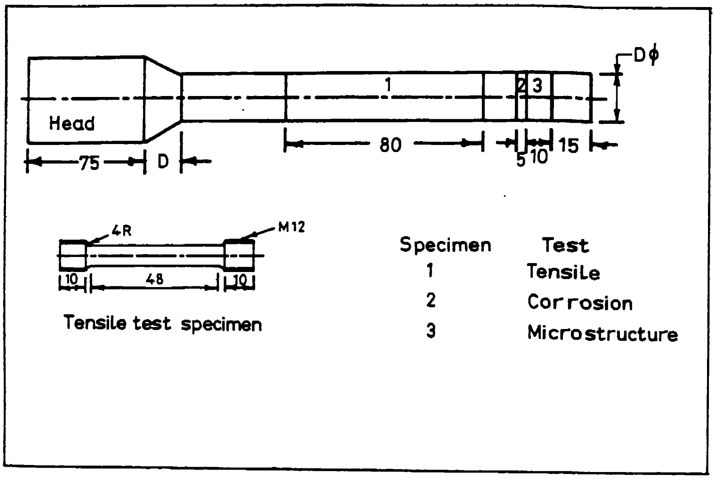

Figure 1. Details of cast test bar.

Table 1. Test casting sizes

Diameter of casting (mm)	Diameter of Head (mm)				
	H1	H2	H3	H4	H5
10	11·84	13·81	15·78	17·75	19·73
15	17·63	20·57	23·51	26·45	29·39
25	30·00	33·83	38·66	43·49	48·32

Table 2. Typical composition of test castings

	Cr	Ni	C	Mn	Si
High vacuum melt	17·3	7·9	0·03	0·6	0·8
Low vacuum melt	17·0	7·9	0·04	0·6	0·8
Air melt	16·0	7·9	0·08	0·6	0·7

2.3 *Metallography*

The test bars were sectioned as indicated in figure 1 and the microstructural features were observed across the cross-section of the test bar at the surface, intermediate and central locations. The etchant used to reveal delta ferrite was 10 normal KOH solution used electrolytically at 2 V for 3 to 5 seconds. Typical microstructures observed by this method are shown in figure 2.

Figure 2. Typical microstructure of delta ferrite.

The amount of delta ferrite was determined at the three locations namely sur intermediate and centre, across the casting section. The normal point count techn (Ratz and Russell 1969; Underwood 1970; Pickering 1976) was used to determin volume fraction of this phase.

2.4 *Mechanical tests*

Tensile test specimens, 40 mm gauge length and 8 mm diameter, were taken from centre of the casting bars (figure 1). Tests were conducted using an MTS universal tes machine.

2.5 *Corrosion tests*

Cylindrical specimens prepared were abraded through 600 grit emery. The dimens were accurately measured and the exposed area to corrosive media was calculated. adhering oil/grease was removed first by a detergent then rinsed in distilled wa degreased electrolytically in 20% sodium hydroxide at 20 mA/cm^2 for 1 hr, rinse distilled water, dipped in hot 10% nitric acid for 30 min to free the surface from oxi thoroughly rinsed in distilled water and dried. This specimen was immersed in the solution (1 normal sulphuric acid) at 25°C for 3 hr along with the stand mercury/mercuric sulphate reference electrode. All the solutions were made fr reagent grade concentrates with suitable dilutions with distilled water. The potential was recorded after 3 hr and the anodic polarization was carried out using electronic potentiostat having a high input impedence. The potential differe between the working electrode (sample under test) and a saturated sulphate electr was increased manually at a constant rate of 350 mV per hour. The procedure precisely followed for each sample to eleminate any variations due to time effect

3. Test results and discussion

3.1 *Delta ferrite*

A study of Table 3 and figure 3 indicates the following:

Table 3. Delta ferrite content at different locations

Casting Dia.	Melt Condition	Volume percentage of delta ferrite at casting		
		Surface	Intermediate	Centre
10	High vacuum	7·29	4·27	2·60
10	Low vacuum	6·39	3·52	1·92
10	Air	Tr	ND	ND
15	High vacuum	6·86	3·90	2·93
15	Low vacuum	6·10	3·20	2·59
15	Air	Tr	ND	ND
25	High vacuum	6·97	4·65	3·25
25	Low vacuum	6·50	4·10	2·85
25	Air	0.50	Tr	Tr

* Tr – Traces, ND – Not detectable

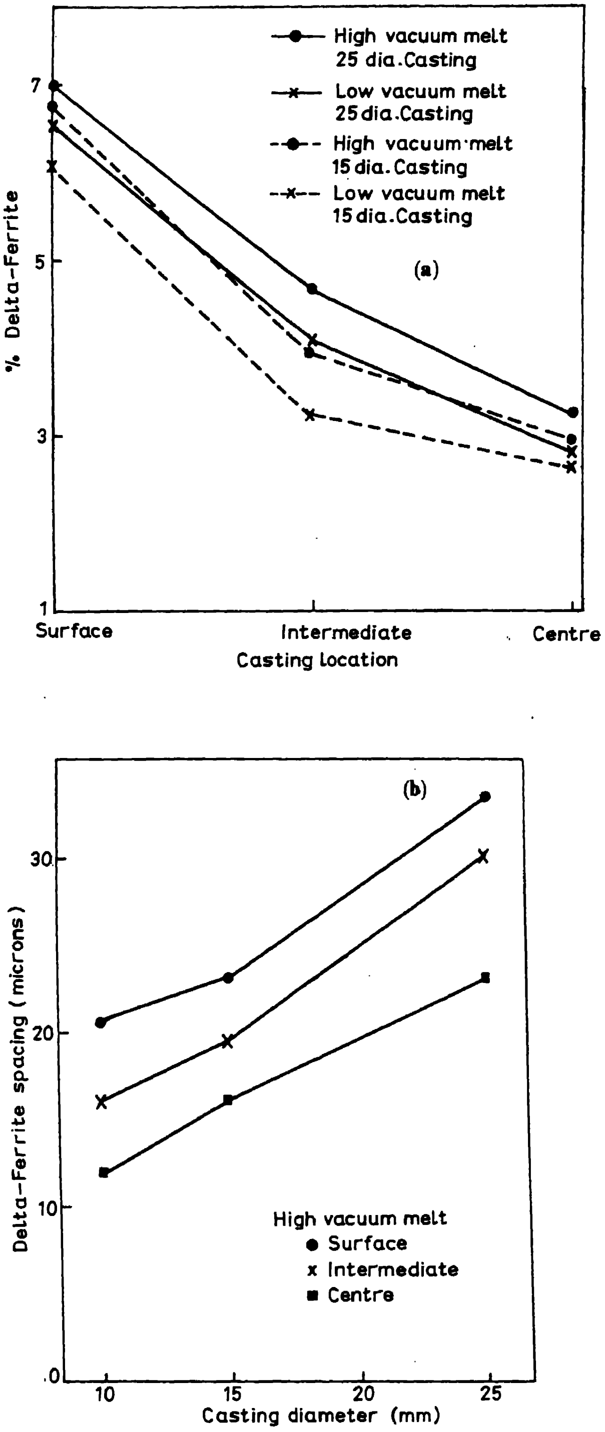

Figure 3. **a.** Delta ferrite content. **b.** Delta ferrite spacing.

In a given casting the delta ferrite content is minimum at the centre and progress increases towards the surface (figure 3a).

At geometrically similar locations (*viz* surface, intermediate or centre) the ferrite content is not appreciably altered when the casting diameter is varied.

The delta ferrite spacing at different locations in each casting is summarised in ta and figure 3b. A study of this table indicates that in a given casting the delta fe spacing is minimum at the centre and progressively increases towards the surfa Thus the larger amounts of delta ferrite observed at the surface may be explaine due to both cooling rate (diffusion time) and delta ferrite spacing being unfavour for attainment of equilibrium. On the other hand, the relatively longer time avail for diffusion and the smaller delta ferrite spacing, especially at the centre of the cast seem to promote equilibrium resulting in lower delta ferrite content.

It is also noted from table 4 that the delta ferrite spacing increases with cas diameter. Thus while the slower cooling rate in larger castings would allow more t for diffusion and subsequent progress of equilibrium the larger delta ferrite spa seems to act in the opposite sense. This appears to be the primary reason for the d ferrite content remaining reasonably constant at geometrically similar location different castings.

The above arguments are largely applicable to vacuum-melted and cast samp Though the air melted and cast samples also indicate similar trend in respect of d ferrite variation in a given casting, the magnitude of this phase is very low in th castings, often approaching not detectable amounts especially in the interior. Furt the delta ferrite content shows a small but discernible increase as the casting diamete increased. The chemical compositions of air-melted and cast specimens (table 2) a indicate that the type of solidification of these castings is likely to be type B. On other hand the vacuum-melted and cast samples seem to solidify according to typ (Pereira and Beech 1980).

A distinctive feature of the delta ferrite in these castings is the reduced spaci towards the interior. Pereira and Beech (1980) also observed that the delta fer spacing in large chilled castings is reduced at the centre. A probable explanation is fragmentation of the growing crystals (Flemings 1974) from the surface as solidificati progresses, owing to thermal convection effects. (All the castings in the present w were top-poured, which would involve some turbulence while filling.)

Table 4. Delta ferrite spacing in microns

Casting diametre (mm)	Melt condition	Delta ferrite spacing (μm.) at casting		
		Surface	Intermediate	Centre
10	Low vacuum	19·06	15·58	10·06
10	High vacuum	20·53	16·10	12·08
15	Low vacuum	22·87	16·82	14·05
15	High vacuum	22·71	19·89	16·10
25	Low vacuum	31·68	27·01	21·96
25	High vacuum	32·07	30·40	23·07

3.2 *Corrosion resistance*

The anodic dissolution parameters of the alloys melted and cast under different environments are in table 5 and figure 4. They indicate the following:

In a given casting (i.e. cooling rate) the passive current density is higher for air and

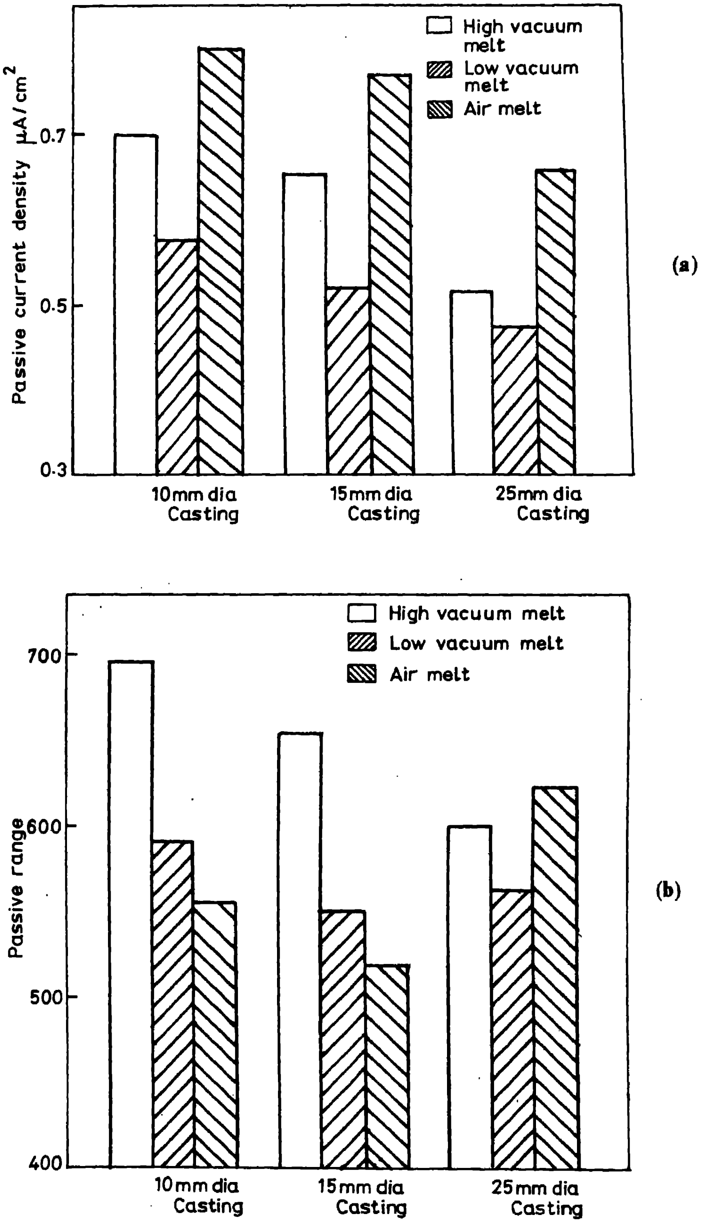

Figure 4. **a.** Passive current density variation. **b.** Passive range variation.

Table 5. Characteristic passivation values of stainless steels tested

Casting diameter. (mm)	Melt condition	Passive range (mV)	Passive current density (μA/cm^2)
10	High vacuum	690	0·697
10	Low vacuum	580	0·575
10	Air	560	0·800
15	High vacuum	660	0·655
15	Low vacuum	550	0·520
15	Air	535	0·766
25	High vacuum	600	0·516
25	Low vacuum	565	0·475
25	Air	625	0·661

Table 6. Mechanical properties

Casting diameter (mm)	Head	Ultimate tensile strength MN/m^2		
		Air melt	Low vac melt	High vac melt
25	H1	376·98	614·51	491·63
	H2	346·09	446·02	505·45
	H3	315·29	386·98	647·85
	H4	325·59	415·92	585·48
	H5	352·37	475·54	580·18
15	H1	–	560·96	531·05
	H2	–	527·03	602·05
	H3	–	499·77	548·80
	H4	–	495·06	519·87
	H5	–	501·33	514·77

high vacuum environments as compared to that of low vacuum environment, highest being for air-melted castings (figure 4a.)

With a decrease in the cooling rate, a decrease in the passive current density res for any given melting and casting environment.

The passive range is influenced by the type of melt and cast environment. At a gi cooling rate the passive range is large for the high vacuum melt and low for the l vacuum melt with air melt falling between the two (figure 4b.)

Further, an increase in the casting size (decreased cooling rate) decreases the pass range.

No simple explanation could be given for the above behaviour. Further experime would aid to clarify this.

3.3 *Mechanical properties*

A study of tables 6 and 7 indicates that the vacuum-melted and cast specimens sh better strength and elongation as compared to their air-melted and cast counterpa

Two factors might contribute to this effect *i.e.* delta ferrite and inclusions (Irvine *e*

Table 7. Mechanical properties

asting iameter (mm)	Head	Percentage elongation		
		Air melt	Low vac melt	High vac melt
	H1	21·33	45·60	25·8
	H2	17·77	26·58	27·17
5	H3	11·39	18·23	27·70
	H4	12·26	38·21	29·30
	H5	14·70	28·22	29·70
	H1	–	49·45	37·69
	H2	–	47·99	44·09
5	H3	–	49·01	28·11
	H4	–	42·68	29·79
	H5	–	43·95	32·57

969; Pickering 1972). Delta ferrite increases the proof stress and tensile strength values y dispersion strengthening effect. In the case of tensile strength the strengthening due o δ ferrite is because of partitioning of carbon and nitrogen to the austenite thereby ncreasing work-hardening rate of austenite. With regard to the inclusions, the amount f non-metallic inclusions like oxides or nitrates are reduced during vacuum melting. It established that the total strain at fracture decreases exponentially with increasing olume fraction of inclusions. This favours higher strength in vacuum melted and cast pecimens. (The delta ferrite does not appreciably affect the total strain at fracture). Considering the variation of mechanical properties due to various heads for a given sting size, it seems that there is no simple relationship between these and the bservable factors. Addition to the delta ferrite content, the segregation pattern, acrostructure etc. might contribute to this behaviour.

Conclusions

n any given casting there is a small, but significant, variation in delta ferrite content om the surface to the interior, the quantity at the surface being maximum. The delta rrite content in a casting is maximum when melted and cast in high vacuum and a ght decrease when the environment is of low vacuum. However, castings made in air ow significantly lower levels of delta ferrite, with the central regions being almost void of this phase. The critical current density increases when the environment is anged from low vacuum to either air or high vacuum. While the passive range creases when the environment is changed from air to vacuum in smaller castings, the nverse appears to be true in larger castings. The ultimate tensile strength and the ongation values are significantly improved when the environment is changed from air vacuum. However, there appears to be no simple relationship between the cooling te and these properties in a given environment.

eferences

andler H E 1982 *Oct. Metal. Progress* **122** 25
mings M C 1974 in *Solidification processing* (New York: McGraw Hill) 227

Irvine K J 1969 *J. Iron Steel Inst.* (London) **207** 1017
Luce W A 1972 in *Corrosion* **28** 115
McTighe J M and Beech J 1977a *J. Res. SCRATA* **37** 43
McTighe J M and Beech J 1977b *Metallography* **10** 363
Pereira O J and Beech J 1980 *Br. Foundryman* **73** 324
Petrov G L 1967 *Welding Production* 1
Pickering F B 1976 in *Quantitative Metallography* (London: ISI)
Pickering F B 1972 in *Towards improved ductility and toughness* (Kyoto: Climax Molybdenu
Ratz G A and Russell B 1969 *Metal Progress* **95** 76
Underwood E 1970 in *Quantitative stereology* (Massachussetts: Addison Wesley)

Bull. Mater. Sci., Vol. 6, No. 2, May 1984, pp. 129–149. © Printed in India.

Sophisticated equipment developed for growth and evaluation of perfection of nearly perfect crystals

KRISHAN LAL and AJIT RAM VERMA

National Physical Laboratory, Hillside Road, New Delhi 110012, India

Abstract. This paper reviews four major equipment developed at the National Physical Laboratory for growth and perfection evaluation of single crystals, namely (i) a crystal puller for growth of nearly perfect crystals by the Czochralski method; (ii) a microfocus x-ray generator; (iii) an x-ray diffraction topography camera; and (iv) a triple crystal x-ray diffractometer. The crystal puller can provide smooth, uniform and variable pulling rates. The maximum length of pull is nearly 60 cm. Efforts have been made to isolate vibrations. Nearly perfect single crystals of KCl, KBr and NaCl with maximum diameter of ~ 60 mm have been grown. The crystals give diffraction curves with half width in the range of 10–30 sec of arc. In the projection topographs, dislocations can be resolved and characterized. The microfocus x-ray generator is a demountable continuously evacuated system with specially designed electron gun and anode assembly. The vacuum is continuously monitored for ease of maintenance. In the point focus mode the spot size is 40 μm on the anode. X-ray topography system is a versatile equipment used for projection and section topography. It can provide 360° rotations to the specimen disc around an axis perpendicular to it. Rotations of a few sec of arc can be given to the specimen around a vertical axis. Typical diffraction curves of a dislocation-free crystal and a crystal with boundaries are shown. Well-resolved images of dislocations are shown in a topograph as an illustration. In the triple crystal x-ray diffractometer a highly collimated and monochromated $K\alpha_1$ exploring x-ray beam is obtained by combining microfocus source, a special collimator and crystal monochromators of Bonse-Hart type. With this beam very narrow diffraction curves with half width of about 5 sec of arc can be recorded. Typical results of measurement of diffuse x-ray scattering (DXS) on nearly perfect silicon single crystals are discussed. It has been observed that the contribution of phonons to the DXS is negligible. The DXS is mainly due to point defect aggregates.

Keywords. Crystal puller; microfocus x-ray generator; x-ray diffraction topography camera; x-ray diffractometer.

1. Introduction

Development of modern science and technology is to a great extent the result of very strong interaction between the experimentalists and the theoreticians. Advances in techniques and equipment have played a vital role in the growth of experimental sciences. Development of better techniques and equipment not only leads to a deep and precise understanding of physical phenomenon but it also leads to discovery of new science and technology.

The role of technique and equipment development in the growth of science and technology in the industrially less-developed countries is all the more important as the infrastructure is weak in these countries. It is, therefore, for the national research institutions to play a leading role in this direction.

The National Physical Laboratory had been set up primarily for the maintenance of standards of units of measurements. Work on some industrially important materials like carbons, piezoelectric ceramics and semiconducting materials was also pursued.

The reproducible preparation of these materials with desired properties requ considerable effort in setting up of infrastructure for preparation and characteriza of materials. Facilities were set up for characterization of materials regarding chen composition, crystalline structure and crystalline perfection. Soon it was realized for the activities in the material science area as well as in the standards measureme the characterization of materials is to play an important role. Without having a fee for the relationship of the properties of a material with its chemical composition real crystalline structure (*i.e.* structure and defects), no real progress can be m Further, the role of crystal growth as an activity occupying central position in mate science as well as solid state physics was identified.

During the last nearly fifteen years, a determined effort was made at the Natic Physical Laboratory to develop a nucleus for design, development and fabricatio sophisticated equipment for growth and characterization of nearly perfect crys regarding perfection. Attempt was made to develop those techniques and equipm which will take the subject to the state of art level. A number of techniques equipment have been successfully developed. Important among the techniques a

(i) a technique for growth of nearly perfect single crystals from the melt by Czochralski method (Krishan Lal *et al* 1982; Verma 1982),
(ii) x-ray diffraction topographic methods for characterization of single crys regarding perfection (Krishan Lal 1981, 1982),
(iii) a high resolution diffuse x-ray scattering techniques for study of point def aggregates in nearly perfect single crystals (Krishan Lal and Singh 1977; Kris Lal 1980; 1982),
(iv) a high resolution x-ray diffraction method for direct observation and characte ation of microstructural changes induced by high electric fields in single crystals insulators and semiconductors (Krishan Lal and Peter Thoma 1981a, b),
(v) a high resolution x-ray Laue method for study of lattice imperfections in whis crystals (Krishan Lal and Peneva 1968, 1969),
(vi) a technique for precise measurement of dielectric constant of solid insulators low frequencies (Krishan Lal and Jhans 1977), and
(vii) a technique for measurement of dielectric loss and electrical conductivity insulating crystals under controlled temperature and environment (Krishan L and Pahwa 1971).

Following are the major equipment that have been developed as a result of this effo

(i) microfocus x-ray generators as sources for high resolution x-ray diffraction wo (Krishan Lal *et al* 1975),
(ii) x-ray diffraction topography cameras similar to Lang camera (Verma *et al* 197
(iii) triple crystal x-ray diffractometers for recording diffraction curves (rocki curves), high resolution topographs and for measurement of diffuse x-r scattering from nearly perfect single crystals at high resolution (Krishan Lal a Singh 1977; Krishan Lal 1980, 1982),
(iv) a triple and a quadruple crystal x-ray diffractometers for study of electric fie induced microstructural changes in semiconductor and insulator single crysta (Krishan Lal and Peter Thoma 1981a, b),
(v) crystal pulling equipment for growth of nearly perfect single crystals from the me by the Czochralski method (Krishan Lal *et al* 1979).

A number of research investigations have been carried out successfully using the techniques and the equipment listed above. These have yielded results of considerable significance (Peneva 1969; Krishan Lal *et al* 1970, 1979; Krishan Lal and Singh 1980; Singh 1980; Krishan Lal and Kumar 1978; Krishan Lal 1980, 1982; Krishan Lal *et al* 1982; Thoma and Krishan Lal 1982; Krishan Lal and Thoma 1982; Kumar 1983).

In the present paper, we shall briefly describe the salient features of the major equipment developed for crystal growth and characterization of single crystals regarding perfection. Some important results obtained with these equipment will also be briefly described.

2. Equipment for growth of nearly perfect crystals from melt

2.1 *Basic principles*

A single crystal by definition is a three-dimensional periodic arrangement of the constituent atoms, ions or molecules in space. In other words, the single crystal has a short and a long range order. However, it is not possible to realize an ideal crystal with a perfect periodic arrangement of constituent units. All real crystals have regions where the periodic arrangement is disturbed by 'lattice imperfections' or 'crystal defects'. The main lattice imperfections are: (i) grain boundaries; (ii) small angle boundaries (iii) dislocations; (iv) impurities and their aggregates; and (v) vacancies and their clusters. A crystal can be considered as nearly perfect when it is free from boundaries and density of its dislocations is less than $10^5/\text{cm}^2$.

For the present-day scientific and technological applications, nearly perfect crystals with controlled chemical composition are required. A number of techniques have been developed for preparation of such crystals. The starting material is a powder or polycrystalline mass. The transformation from one solid (polycrystalline) to the other solid phase (single crystal) is achieved by first converting the starting material into a vapour or a liquid phase (melt). In some extreme situations a solid-to-solid transformation is also used. The intermediate phase is converted into the final solid phase in a controlled manner, so that the product has a nearly perfect ordering of constituents. During this process protection is to be provided against chemical contamination.

The intense research and development work of the last few decades has shown that the techniques employing growth of single crystals from the melt are best suited for economic production of large quantities of nearly perfect single crystals having controlled chemical composition. However, inspite of its extensive applications this method cannot be considered to be a general method. It can be used only if the solid and the liquid phases of the material are in thermodynamical equilibrium with each other near the melting point.

Important methods used for growth of single crystals from the melt are (i) Kyropoulos method, (ii) Bridgman method, (iii) Czochralski method and (iv) Stepanov method or the shaped crystal method.

Among these, the Czochralski method has been most widely used. We shall consider only this method for further discussion.

Figure 1 shows a schematic line diagram depicting the basic features of the Czochralski method. The starting material M is heated in a crucible with the help of a suitable furnace F and the melt is held close to its melting point. A seed crystal S held in

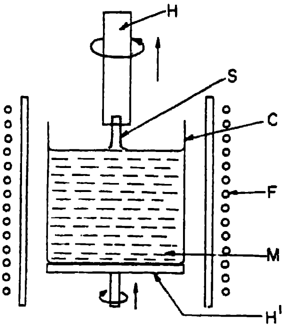

Figure 1. A schematic line diagram showing the ba principle of the techniques used for growth of sin crystals from the melt

a suitable seed-holder *H* is dipped into the melt. The thermal conditions are adjusted such a manner that the seed and the melt are in contact and in thermal equilibrium. Th seed is slowly withdrawn or pulled and the crystal is formed due to freezing of th molten material. The amount of heat supplied to the melt is decreased gradually whi leads to a gradual increase in the lateral dimensions of the crystal. The later dimensions can also be controlled by changing the rate of pulling. A decrease in the ra of pulling produces an increase in the diameter of the crystal. After having achieved predetermined size of the crystal, the power fed to the melt and the rate of pulling a controlled in such a way that the diameter does not change. To avoid strains in th crystal due to small variations in the temperature across its diameter, the seed holder rotated. When crystals with impurity doping are to be grown the uniform distributic of impurity in the melt and the crystal is an additional requirement. The crucible is al rotated but in opposite direction. As the crystal grows, the melt is depleted and its lev falls down. To achieve a very strict temperature control the crucible is lifted at a ra which compensates for the lowering in the level of the melt.

The growth of good quality crystals requires strict control on: (i) quality of the see crystal; (ii) the crucible and the seed-holder materials; (iii) the ambient atmosphere; (i the thermal system; and (v) the mechanical system. The seed crystal should be near perfect and free of undesirable impurities. In the process of attaining the temperatu close to the melting temperature, the crystal should not be subjected to thermal shock The processes like necking are used to eliminate the dislocations originating from th seed into the crystal. Also, by increasing the speed of pulling to rates higher than that the propagation of dislocations, in the initial stage, the dislocations growing from th seed are stopped from being incorporated into the main body of the crystal.

The materials of the seed holder and crucible should not react with the crystal ar should be able to stand the temperature. Also, these should not react with the ambie atmosphere. The control of ambient atmosphere is necessary to avoid chemic contamination of the melt and the crystal and also for controlled heat dissipation. I some case the compounds decompose at melting point, under normal condition Sometimes decomposition can be avoided by heating the starting material und vapours of one of the constituents at high pressures.

The control of thermal system is very vital for growth of high quality crystals. Th furnace is the main source of heat. Heat is transferred by conduction from the melt t the seed, seed-holder etc and ultimately to the surrounding through seed-melt interfac At the interface, latent heat of fusion is generated due to freezing of a part of the melt. I addition, the melt loses heat by radiation and by convection and conduction to th surrounding medium. By suitable choice of the material of the seed holder, a controllable method of cooling it and by controlling the ambient atmosphere, the dissipation of heat is controlled. The axis of the thermal system and the mechanical pulling and rotation system should coincide to avoid thermally-induced strains.

The shape and structure of the interface is sensitive to the perfection and composition of the growing crystal. All efforts are made to eliminate disturbances to these by mechanical vibrations. The pulling and the rotary motions of the seed are performed with the help of the electrical motors. These generate mechanical vibrations. These vibrations are isolated and not allowed to reach the surroundings. Also, there are vibrations in the surroundings which are not allowed to reach the crystal-melt interface.

Due to these considerations an apparatus for growth of crystals by the Czochralski method is required to perform the basic functions: (a) heating the starting material in a suitable crucible to the molten state and controlling the temperature of the melt; (b) providing a seed-holder assembly which can be rotated and lifted at desired rates in a smooth and uniform manner; (c) controlling the environment of the crystal growth system; (d) isolating mechanical vibrations generated in the system and in the surroundings from the crystal-melt interface; and (e) the axis of the crystal pulling and rotation, the axis of the crucible rotation and translation and the axis of the thermal system should coincide.

For details of the crystal growth techniques reference is made to recent publications (Paorici 1982; Pamplin 1975; Bardsley *et al* 1979) and the literature cited therein.

2.2 *The crystal pulling system developed at the National Physical Laboratory*

Figure 2 shows a photograph of the crystal growth system developed at the NPL (Krishan Lal and Singh 1977; Krishan Lal 1981, 1982). The scattering is mainly due to provided by a screw and nut assembly. The seed holder is fixed to the nut and the screw is held at its position and executes only the rotary motion. The nut moves up and down depending upon the sense of rotation of the screw. The screw is a component made to have a uniform pitch along its length of nearly 80 cm.

The nut is also prepared with care and is cut into two equal halves parallel to the axis of threads. The two parts are held together with the help of spring loaded screws. The pulling motion is guided by two steel rods. One of these has a circular cross-section whereas the other has a square cross-section. The surface of the rod with circular cross-section has been lapped after careful machining to ensure uniformity in diameter and straightness. The other rod has been prepared in the same way as surface plates are made. Its surfaces are flat within 5 μm over its entire length of nearly 80 cm. The screw is driven with the help of a variable speed motor and a gear box. The rate of pulling can be varied by a factor of 10 in the range 2 mm/hr to 20 mm/hr. By changing the gear box, it is possible to have another set of pulling rates varying in a range 1:10. The variation in the speed is achieved steplessly with the help of electronic control of the motor. The total length of pulling is about 60 cm.

The seed-holder is fixed to a subassembly fixed to the nut of pulling assembly. On this subassembly a 12 W synchronous motor is mounted which provides the motion to rotate the seed-holder. The speed of rotation can be varied to desired value. The seed holders were made out of stainless steel, silver plated copper or silver plated brass rods. Between the seed-holder and the sub-assembly on the nut a ceramic rod made of

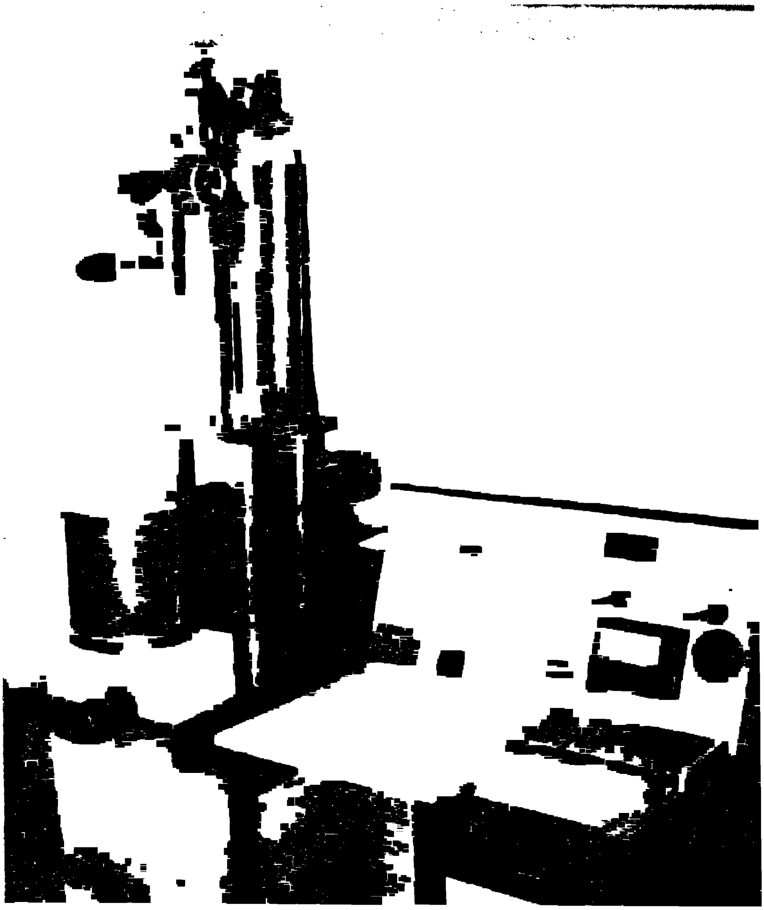

Figure 2. A photograph of the crystal. Pulling system developed at the National Pl Laboratory, New Delhi

alumina provides the thermal insulation. The seed-holder geometry has been optin for controlled heat dissipation during crystal growth experiment.

The screw and the guiding rods are held at place with the help of thick steel pl one each at the two ends. The assembly is fixed on a heavy base plate. To isolat system from the vibrations in the surroundings, the base plate rests on antivibration mountings supplied by M/s Dunlop. The mountings lie on a b prepared out of cement and concrete. The motor and the gear box used to driv screw for pulling motion are mounted on a separate platform. This platform rest small antivibration mountings fixed on the base plate. The couplings between motor and the gear box and the gearbox and the screw are flexible. These arrangem ensure that the vibrations generated by the motor are damped to a low level.

Resistance-heated furnaces have been used for crystal growth experiments. furnace is placed on a platform rigid connected to the base of the crystal puller. The of the furnace, the line of pulling and the axis of rotation of the seed holder coin with each other.

2.3 *Some typical results*

The crystal growth system described above has been used to grow nearly perfect crystals of alkali halides (Krishan Lal *et al* 1982; Verma 1982). Besides optimization of the thermal system and testing of the equipment this experiment had another purpose also. In a recent investigation we had observed that in silicon single crystals, the elastic thermal waves or phonons do not contribute significantly to the diffuse x-ray scattering (Krishan Lal and Singh 1977; Krishan Lal 1981, 1982). The scattering is mainly due to defects. We shall consider this aspect later in this paper in some detail. Since silicon has a high Debye temperature it was considered desirable to perform experiments on crystals with lower Debye temperature. Alkali halides, particularly KCl and KBr not only fulfil this requirement, but have been studied thoroughly in the past (Ramachandran and Wooster 1951; Wooster 1962). However, for diffuse scattering measurements at high resolution nearly perfect crystals are required. Hence, growth of nearly perfect KCl, KBr and NaCl crystals was undertaken. Alkali halide crystals grown by the usual methods are known to possess a low degree of perfection (Krishan Lal 1980; Krishan Lal *et al* 1979).

By controlling (i) the quality of the seed-crystal; (ii) the thermal conditions during crystal growth; and (iii) the rate of pulling during growth, nearly perfect alkali halide crystals have been grown (Krishan Lal *et al* 1982).

The maximum diameter of the crystals was about 60 mm. Figure 3 shows some of the crystals grown on this system.

The alkali halide crystals were thoroughly characterized regarding perfection by using x-ray diffraction topography and multicrystal x-ray diffractometry. These systems are described later in this paper. Figure 4 shows a typical topograph of a KCl crystal. The perfection of these crystals was so high that dislocations could be easily resolved in their topographs. These have been characterized regarding their nature.

Figure 5 shows a typical diffraction curve of a KCl single crystal recorded on the triple crystal x-ray diffractometer. This curve is fairly sharp. The half width of diffraction curves of different alkali halide crystals was found to be in the range 10–30 sec of arc. This is not very large compared to that observed with dislocation free

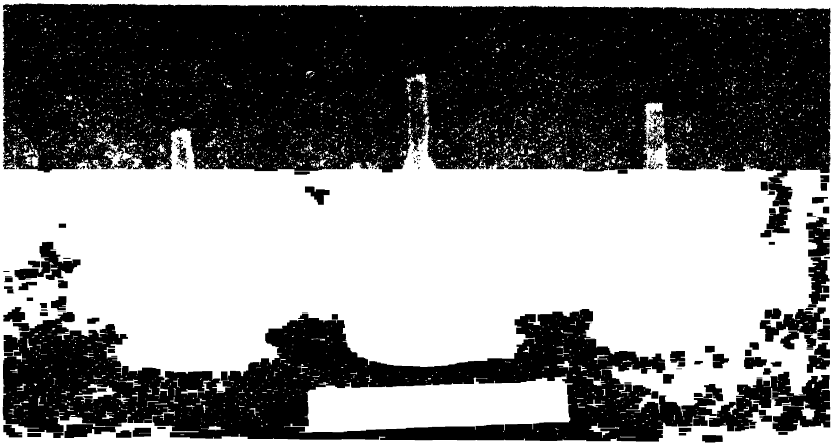

Figure 3. A photograph of a few nearly perfect alkali halide crystals grown on the crystal puller developed at the National Physical Laboratory, New Delhi

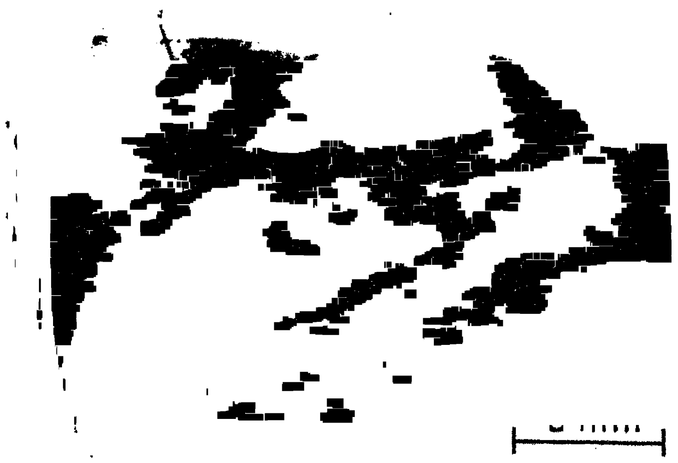

Figure 4. A typical projection topograph of a single crystal of potassium chloride grow the NPL. 020 RELP and MoKα_1 radiation was used.

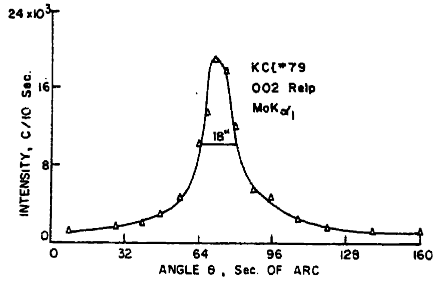

Figure 5. A typical diffraction curve of a nearly perfect single crystal of KCl grown at the NPL, recorded on the triple crystal x-ray diffractometer, in (+, −, +) configuration with MoKα_1 radiation and [002] reciprocal lattice vector

Figure 6. A high resolution ography recorded on the triple c tal x-ray diffractometer, by aligı the specimen KCl single crysta the peak of the diffraction cı shown in figure 5.

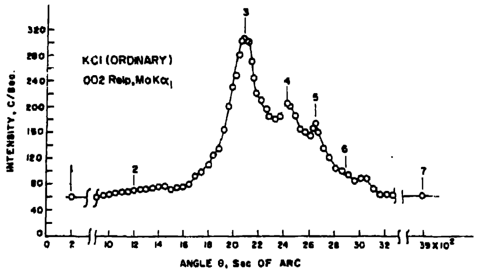

Figure 7. A typical diffraction curve of a potassium chloride single crystal of ordinary perfection recorded on the triple crystal x-ray diffractometer

Si single crystals (5 sec of arc for 111 reflection recorded under similar conditions). High resolution small area topographs can be obtained by recording the diffracted x-ray beam on a film. Figure 6 shows a typical topograph of this type recorded by aligning the crystal at the peak of the diffraction curve shown in figure 5. Uniform distribution of intensity is to be noted.

Crystals having ordinary degree of perfection give diffraction curves spread over large angular range of a degree of arc or so. Figure 7 shows a diffraction curve of one such crystal recorded under the conditions under which the curve in figure 5 was recorded. The high resolution topographs of such crystals are fragmented into small regions.

3. Equipment for characterization of single crystals regarding perfection by using high resolution x-ray diffraction techniques

3.1 *Basic principles*

X-ray diffraction has been extensively used for determination of structure of crystals right from the time of its discovery. The structure obtained in these experiments is based on absolutely ideal periodic arrangement of the constituent units. As mentioned above, the real crystals always contain lattice imperfections or defects. X-ray diffraction methods are also used to study defects. X-ray Laue method could be considered to be the first in a series of methods. The resolution attainable in the Laue method is comparable to that of the other x-ray diffraction methods. It is convenient to define the resolution of the diffraction techniques in terms of: (i) the divergence of exploring x-ray beam in the plane of diffraction which is usually the horizontal plane; (ii) the monochromaticity of exploring x-ray beam; and (iii) the degree of perfection of the specimen crystal.

In most of the standard x-ray diffraction methods the divergence of the exploring beam is of the order of a degree of arc in the horizontal plane. Filtered or crystal monochromated Kα beams are used. Nearly perfect crystals have become available after development of techniques for growth of nearly perfect semiconducting crystals. However, a nearly perfect crystal will diffract over an angular range of a degree of arc when a standard diffraction system is used. As we shall see below this is nearly three orders of magnitude larger than the theoretically expected angular range under ideal experimental conditions. It may be mentioned that such a resolution is good enough for determination of crystal structure. However, when the purpose of the experiment is to observe and characterize defects such a resolution is inadequate.

Let us now consider an ideal experiment in which a perfectly parallel monochromatic beam of x-rays is diffracted from an absolutely perfect cry According to dynamical theory (Batterman and Cole 1964; Tanner 1976) of x diffraction, x-rays will be diffracted over a narrow angular range of a few seconds ol in such an experiment. The half width of the diffraction curve width is given by

$$\theta_{1/2} = \frac{2r_e\lambda C(F_{\bar{g}}F_g)^{1/2}}{\pi V_c|g|\cos\theta_B}$$

where r_e = classical electron radius, λ = wavelength of the exploring x-ray be C = polarization factor, F_g = structure factor for diffraction vector g, g = diffract vector, V_c = volume of the unit cell. Hence, it is seen that the standard x-ray diffract experiments cannot be used for attaining the ideal curves. For this the monochroma ation of the exploring x-ray beam has to be considerably improved. This high resolut is necessary if departures from ideal arrangement of atoms are to be observed characterized. In the following, we shall describe two major equipments, namely: (i) x-ray diffraction topographic system (ii) a triple crystal x-ray diffractometer.

In the first system, the divergence of the x-ray beam is reduced to less than a min arc or so in the horizontal plane. The collimation and the monochromaticity of exploring x-ray beam in the second system is the best achieved so far.

3.2 *Equipment for x-ray diffraction topography: A microfocus x-ray generator an x-ray diffraction topography camera*

3.2*a Basic principle of x-ray diffraction topography*. The basic principle of x- diffraction topography is that the intensity of diffracted x-rays depends upon the deg of perfection of the irradiated volume for a given reflection and x-ray waveleng Hence, a point-to-point variation of diffracted x-ray intensity from a specimen gi information about distribution of defects in the crystal. If we are able to reco diffracted intensity from the entire volume of a specimen in such a manner that ea point in the recorded pattern corresponds to a point in the specimen, the defects will imaged directly in this record. Such a record is known as topograph and is essentiall Laue spot of the entire specimen. The first experiments in this direction were perform by Ramachandran (1944). A number of different approaches have been adopted record the intensity variations in the topographs with sufficiently high resoluti (Krishan Lal 1982; Tanner 1976; Barret 1945; Lang 1970).

For a good correlation between the point-to-point variation of intensity in t topograph and the corresponding variation of perfection in the specimen, t following experimental conditions should be fulfilled (for details see Krishan Lal 198 i.e. (1) The size of the source should be as small as possible; (2) the distance between t source and the specimen should be as large as possible; and (3) the photograph film/plate should be placed very close to the specimen.

Figure 8 shows a schematic line diagram of a typical experimental arrangeme which fulfils the three conditions listed above. It can be seen that the irradiated area the specimen is ribbon shaped, its length being perpendicular to the plane of the figur Since the width is very small (typically 100 μm or less), at a time only a small volume the crystal can be investigated. Lang introduced the technique of moving the specime crystal across the x-ray beam (Lang 1970). The photographic film or plate is rigid coupled with specimen and the two together are traversed across the exploring beam. I

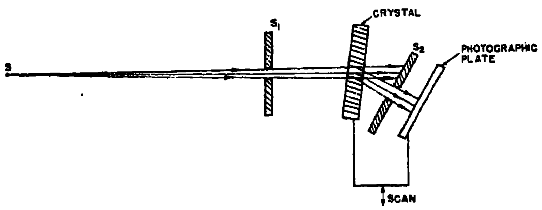

Figure 8. A schematic line diagram of the x-ray diffraction topographic set-up.

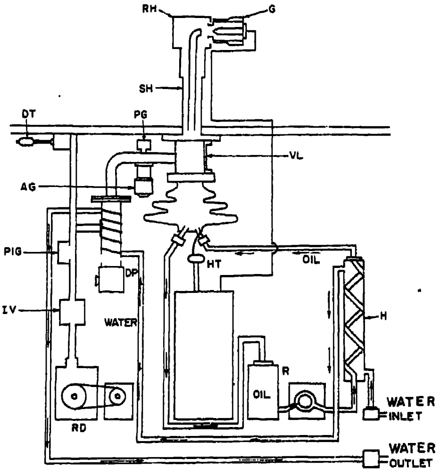

Figure 9. A schematic line diagram of the microfocus x-ray generator developed at the NPL.

this manner crystals with very large volumes (several cm^3) can be investigated. This technique is known as the Lang method.

This method can be used for observation and characterization of grain boundaries, low angle boundaries and dislocations. In the following we shall describe a system developed at the NPL which consists of two major equipment: (i) a microfocus x-ray generator; and (ii) an x-ray diffraction topography camera.

3.2*b* *The microfocus x-ray generator developed at the NPL*: Figure 9 shows a schematic line diagram of the microfocus x-ray generator (Krishan Lal *et al* 1975). Figure 10 is a photograph of this equipment. A hairpin filament fixed in a specially designed electron gun is heated to be a source of electrons. The electrons are accelerated and focussed electrostatically with a bias cup on the surface of the anode. The distance between the surface of the anode and the source of electrons can be varied continuously to optimize the focussing conditions. The path of the electrons is evacuated to be $\sim 10^{-5}$ torr.

Filaments of desired shapes are prepared from thin tungsten wires with the help of special jigs. These are held in supports which are precisely aligned. The filament terminals are connected to insulating feedthroughs which can stand high temperatures and high vacuum. The feedthroughs have been developed in our laboratory.

The bias cup is a precisely made component whose position is fixed accurately with respect to the filament. These components are fixed into the inner part of the electron gun which also has an outer part. Both the parts are made of stainless steel. The filament together with the bias cup can be linearly moved towards or away from the anode when

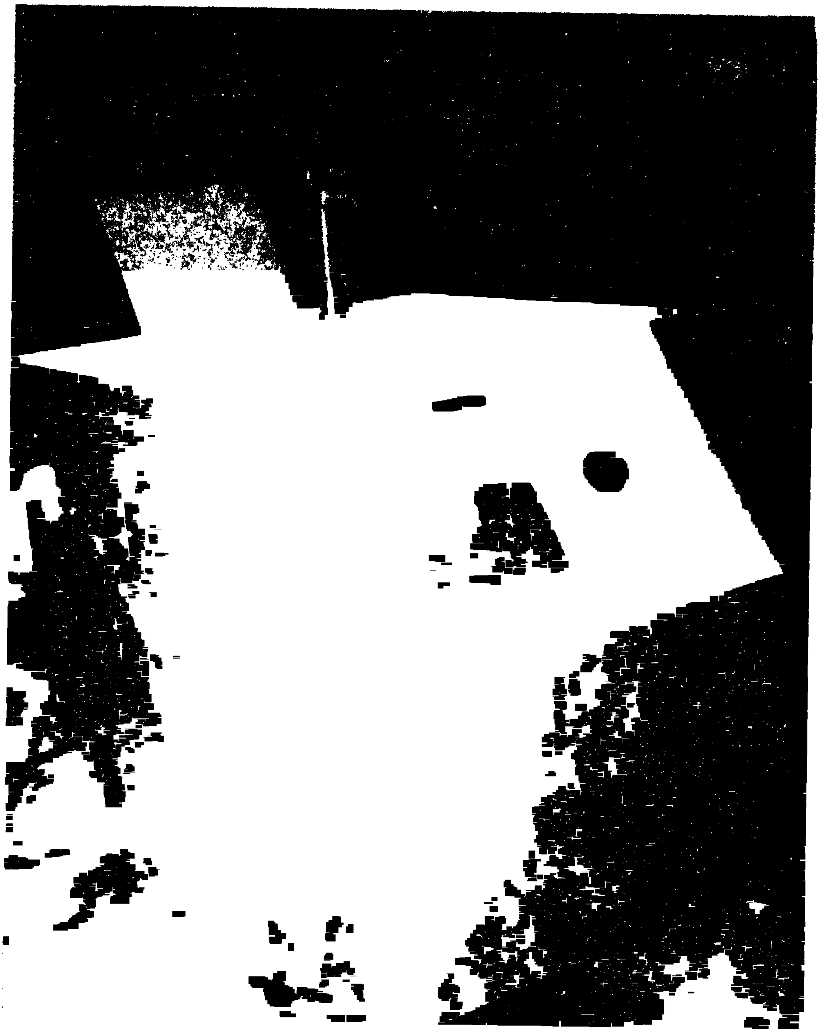

Figure 10. A photograph of the microfocus x-ray generator developed at the NPL.

the generator is in operation. The electron gun after assembly is fixed to the body of the vacuum chamber which also houses the anode.

The anode is a hollow pipe fixed into an insulating epoxy block. Its upper open end is bent by 90° and a thin disc of the target material is welded. (Inside this pipe another small pipe is inserted, which is all along its length and has a small opening in its end just behind the target.) Chilled oil forced through the smaller pipe which hits the back surface of the target and flows to the reservoir through the space between the two pipes. This is the coolant during x-ray generation. In the standard sealed tubes, the targets are cooled by chilled water. However, unlike in this case, in the microfocus generator the anode is at the high positive potential and therefore, water cannot be used as coolant. An oil with good thermal conduction and high insulation strength is used. The high voltage is applied to terminal moulded in the epoxy base.

The electron gun and the anode are fixed to a metal chamber made precisely. It is evacuated to a vacuum of about 10^{-5} torr with the help of an oil diffusion pump backed by a rotary pump. The openings for the electron gun and the anode are made precisely, so that the axis of the electron gun is perpendicular to the surface of the anode. The vacuum in the chamber is continuously monitored. Also the vacuum generated by the backing pump is continuously monitored.

The focal spot on the anode is 40 μm in diameter when the generator is used as a point source. This system can also be used in the line focus mode, with the width of the line as 100 μm and length as ~ 2 mm. The electrical power consumed by the generator is 100 W in line focus mode and only 10 W in the point focus mode. These powers are very small compared to the powers consumed by the sealed tubes (1–2 kW). However, it may be emphasized that in the high resolution experiments, the brilliance of the source is more important. It is defined as the power dissipated per unit area of the source on the anode. The brilliance of the point focus generator is about 8 kW/mm^2 when the power is only 10 W. The standard focal size sealed tubes (1 × 10 mm^2) have a brilliance of 200 W/mm^2 when run at the full power of 2 kW. Recently, fine focus sealed tubes have become available with powers of ~ 2 kW.

3.2*c*. *The X-ray diffraction topography camera developed at the* NPL: Figure 11 is a schematic line diagram of the x-ray diffraction topography camera developed at the NPL. A photograph of this system is shown in figure 12 (Krishan Lal *et al* 1974; Krishan Lal 1982). X-ray beam from a microfocus x-ray source is collimated with the help of a long collimator tube which has a narrow vertical slit at its end away from the source. The tube is 50 cm long, the width of the slit is variable. It is about 100 μm for projection topography. The divergence of the beam can be reduced to less than a min of arc in the horizontal plane (the plane of the figure). A horizontal slit is also generally introduced with the horizontal slit to limit the dimensions of the exploring beam in the vertical direction. The size is governed by the dimensions of the specimen in the vertical direction.

The specimen to be investigated is in the form of a disc which is mounted in a vertical circle goniometer with its larger surfaces in the plane of the goniometer circle. The goniometer provides rotations to the specimen around a horizontal axis which is perpendicular to the surface of the specimen. The goniometer is mounted on a traversing mechanism which in turn is mounted on top of a turntable. The turntable provides rotations to the specimen around a vertical axis passing through its middle. The traversing mechanism provides to- and fro- motion to the specimen across the x-ray beam. A scintillation counter is used as x-ray detector. It is mounted on the turntable with its axis along a radius of the turntable and in the horizontal plane containing the axis of the collimator. The detector can be rotated around the vertical

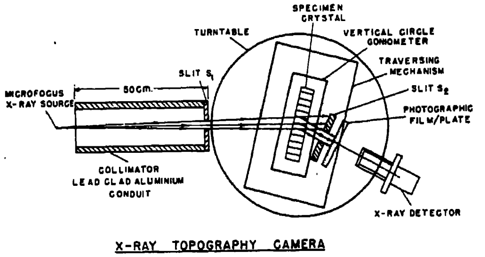

Figure 11. A schematic line diagram of the x-ray diffraction topography camera developed at the NPL.

Figure 12. A photograph of the x-ray diffraction topography camera developed at t

axis of the turntable around which the specimen is also rotated. The angular pos of both can be read on the turntable. The mechanical precision is required to ensur the axis of the collimator is horizontal and intersects the axis of the turntable.

The photographic film or plate is fixed rigidly on top of the traversing mech and very close to the specimen. A vertical slit is introduced between the specime the film/plate. Its position is adjusted to allow only the diffracted beam to pass th and to stop the direct beam. This slit is rigidly coupled to the turntable.

The turntable is required to provide small angular movements of a few sec of the specimen. A long radial arm (50 cm) is attached to the axis of the turntable. Th of this arm is moved with the help of a micrometer screw. The arm can be deco whenever larger angular movements are to be given to the crystal. The an movements of the detector are not required that precisely and therefore this c accomplished without radial arm.

The traversing mechanism is also a component requiring careful design fabrication. It is required to provide very smooth and uniform motion to the spe and the photographic film/plate. It consists of two parts: (i) a base plate and moving platform. The two are coupled to each other with the help of a screw an assembly. The screw is fixed in its position on top of the base plate with its axis alo longer edge of the plate. The nut is rigidly coupled to the bottom of the m platform. When the screw is rotated the upper plate moves linearly due to the m of the nut. This movement is guided with the help of a rod of square cross-section flat plate. These are fixed, one each, along the two longer edges of the base plate. A ball rolls loosely on the flat plate. The upper plate has a flat strip which rests on th when the traversing mechanism is assembled. The other edge of the top plate groove which fits the rod of square cross-section fixed on the base plate. These tw guiding rod and the plate, ensure a smooth and uniform linear movement of the m platform and thus the crystal. The micrometer screw is driven by a synchronous m

(12 W). To reduce the speed of the motor (1500 rpm) a series of gears are introduced between the screw and the motor. The screw rotates at a speed of 5 rpm. The range of scan is adjusted electrically with the help of two microswitches fixed to the base plate and an airbreak contactor. The range of traverse equals the dimensions of the specimen along the line of traverse.

For aligning the specimen for diffraction from a desired set of lattice planes, the detector is rotated from its reference (direct beam receiving) position by an angle 2 θ_B, where θ_B is the Bragg angle. By using the angular movements provided by the vertical circle goniometer and the turntable, it is possible to align the specimen for diffraction from any desired set of lattice planes.

3.2*d Some typical results*: Before recording topographs of the specimen, it is advantageous to first record a diffraction curve or a rocking curve. This curve is obtained by plotting diffracted intensity as a function of the grazing angle covering angular range on both sides of the diffraction peak. The shape of the diffraction curve is very sensitive to the degree of perfection of the specimen crystal. Nearly perfect crystals give well resolved diffraction maxima due to Kα_1 and Kα_2 components of the characteristic radiation. The half width of each peak is dependent on the divergence of the exploring x-ray beam. Figure 13 shows a typical diffraction curve of a dislocation free silicon single crystal.

Specimen crystals containing boundaries give diffraction curves having several peaks separated by large angles. When low angle boundaries are the main defects, the separation between various peaks is of a few min of arc. In the case of grain boundaries the various peaks in the diffraction curve are separated by about a degree of arc. Figure 14 shows a typical diffraction curve of a crystal containing low angle boundaries. It may be remarked that x-ray topography is profitably used to characterize crystals which are free of boundaries. Low angle and grain boundaries can be conveniently studied by x-ray Laue method (Krishan Lal *et al* 1970, 1972).

Figure 15 shows a topograph of a nearly perfect single crystal of α-Al_2O_3 which had been grown by the chemical vapour deposition (Krishan Lal and Kumar 1978). The

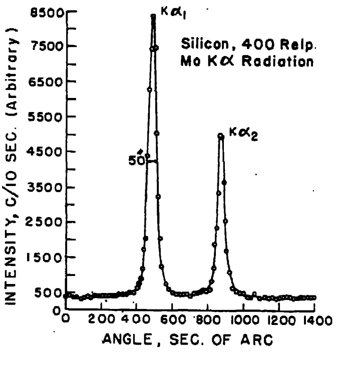

Figure 13. A typical diffraction curve of a nearly perfect crystal recorded on the x-ray diffraction topography camera. Well-resolved peaks due to Kα_1 and Kα_2 components of the characteristic Kα line are observed.

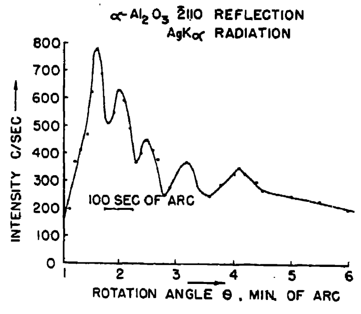

Figure 14. A typical diffraction curve of a crystal containing low angle boundaries. Each peak in this curve corresponds to diffraction from a subgrain of the crystal.

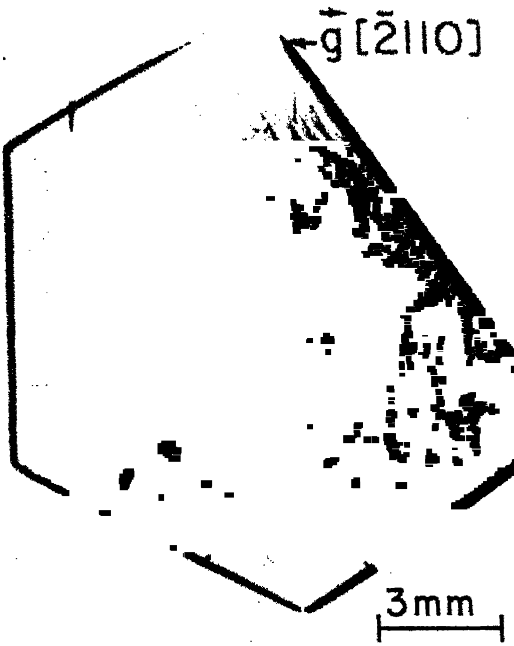

Figure 15. A typical projection topograph of a nearly perfect α-Al_2O_3 single crystal grown by the chemical vapour deposition method. MoKα_1 radiation and [$\bar{2}$ 11 0] diffraction vector was used

lines observed in this topograph are dislocation lines. With this method it is possible not only to observe the dislocations but also to characterize these for their nature (Krishan Lal 1982). This is possible as the strain around dislocations is anisotropic. Maximum strain is produced in lattice planes which are perpendicular to the Burgers vector of the dislocation. The contrast around dislocation images in the topographs depends directly on the strain produced by dislocations in the diffracting planes. Hence by recording topographs with different diffracting planes, the nature of dislocations can be determined from the observed variations in contrast around dislocation images. For details, reference is made to published literature (Krishan Lal 1982; Tanner 1976; Lang 1970).

3.3 *The triple crystal x-ray diffractometer developed at NPL*

3.3*a* *Background.* Chemical composition and the real structure of crystals govern their physical properties. It has been recently realized that the properties of dislocation free crystals having nominally the same chemical composition are different. For example, the electronic properties of dislocation free single crystals vary significantly (Yang *et al* 1978; Yang and Schwuttke 1980). These differences are attributed to point defects and their aggregates. Hence, characterization of dislocation-free crystals regarding perfection, requires information about point defects and their clusters. These defects do not produce sufficient contrast in topographs and it is not possible to use x-ray diffraction topography for this purpose. However, point defect aggregates are known to produce scattering from reciprocal space near a reciprocal lattice point (Krishan Lal 1980, 1982; Krivoglaz 1969; Dederichs 1973; Peisl 1976). This is termed as the diffuse x-ray scattering or DXS. DXS is also produced by phonons as mentioned above (Ramachandran and Wooster 1951; Wooster 1962).

It was of considerable fundamental importance to establish the relative magnitudes of the DXS due to defects and phonons. In the earlier investigations DXS was considered to be due entirely to the phonons (Wooster 1962). Our preliminary experiments even with an x-ray diffraction topographic equipment showed that this is not so (Krishan Lal and Singh 1977; Krishan Lal 1978). In the earlier experiments DXS measurements were made with low resolution experimental set-ups. However, it needs to be stressed that whenever scattering is to be measured near the reciprocal lattice point the resolution of the method becomes all the more important. In view of these considerations, we have designed, developed and fabricated a triple crystal x-ray diffractometer in which the experimental uncertainties have been reduced to a negligible level. Further, the same diffractometer can also be used to record diffraction curves and high resolution small area topographs. This system is described in the following.

3.3*b* *The triple crystal x-ray diffractometer:* Figures 16 and 17, respectively, show a schematic line diagram and a photograph of the diffractometer. A microfocus x-ray generator with a focal spot size of 40 μm size on the anode is used as the source of x-rays. The x-ray beam is collimated, as in the case of the topographic system, to have a divergence of about 1 min of arc in the horizontal plane. This beam is diffracted from a set of two monochromator crystals of the Bonse-Hart type (Bonse and Hart 1965). These are prepared out of a dislocation free Si single crystal block and have their diffracting surfaces parallel to $\{111\}$ in $(+, -)$ configuration. On alignment for diffraction, these monochromators are capable of resolving the $K\alpha_1$ and $K\alpha_2$ components of the $K\alpha$ doublet. A slit is placed in the path of the diffracted beam which allows only the $K\alpha_1$ beam to pass through. The wavelength, direction and spatial spreads of this beam have been experimentally evaluated (Krishan Lal 1979; Krishan Lal and Singh 1979). The divergence could not be detected in the horizontal plane as it was much less than 5 sec of arc, the limit of detection. The wavelength spread in this beam was evaluated by using an analyzer crystal in the dispersive geometry. This was observed to be from 0·7088 to 0·7097Å. The width of the beam in the horizontal plane can be varied from 15 μm to ~ 50 μm. In most of the experiments a width of ~ 50 μm is used.

The specimen is mounted on a specially designed goniometer which in turn is fixed on top of a turntable. The axis of the turntable is vertical and aligned to intersect the

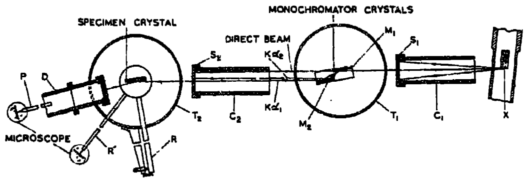

Figure 16. A schematic line diagram of the triple crystal x-ray diffractometer, designed, developed and fabricated at the NPL.

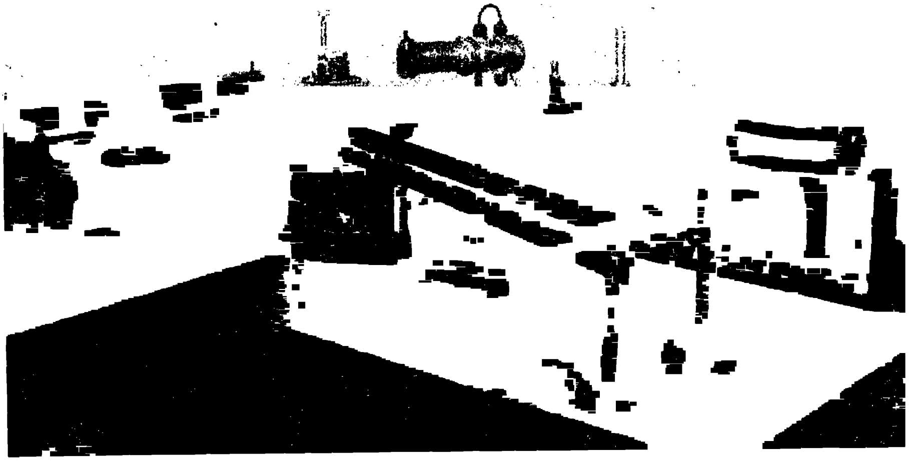

Figure 17. A photograph of the triple crystal x-ray diffractometer

exploring x-ray beam received from the monochromators. The position of goniometer with the crystal, relative to the turntable is fixed in such a way that the a of turntable lies on the surface of the specimen. The surface is parallel to the diffract planes. The goniometer is capable of giving small linear movements to the specimen the horizontal plane along a direction which is parallel to the diffraction vector. It provide rotations around a horizontal axis parallel to the diffraction vector. Minim rotation of ~100 sec of arc can be provided. For high temperature measurement small heater can be attached behind the specimen. Two thermocouples can be attach one on the front surface of the specimen and other on the back surface of the specim

The turntable is required to provide very small angular rotations to the crystal. A long arm is attached to the turntable along a radius. The free end of the arm r against a micrometer under tension of a spring. The fixed micrometer rests agains differential micrometer. In this way very small angular movements of about 0·3 se arc can be provided to the specimen. The angular position of the specimen is measu independently by measuring the displacement of a pointer under a microscope. pointer is attached at the end of a 1 m long arm.

A scintillation counter developed in our laboratory has been used as an x-detector. It is mounted with its axis along one radius of the turntable and intersect on the surface of the specimen at the same point where the axis of the exploring x-beam intersects the specimen. A fine vertical slit is fixed before the detector. Its widt slightly larger than that of the beam diffracted by the specimen. The angular positio the detector is also measured with the help of a microscope.

The diffractometer is generally used in the Bragg geometry in the configuration −, +). For measurement of diffuse x-ray scattering the specimen and the detector rotated with respect to the position of the diffraction maximum by known angles this way reciprocal space in different directions can be explored.

3.3*c* *Some typical results*: Figure 18 shows a typical diffraction curve of a dislocation free silicon single crystal recorded on the triple crystal x-ray diffractometer (Krishan Lal *et al* 1979). This curve is very sharp and has a half width of five sec of arc only. The shape of the diffraction curve is nearly the same as expected theoretically on the basis of the dynamical theory. Hence, we see that the reciprocal lattice point (RELP) can be very accurately located. The uncertainties due to instrumental factors are negligible. It is possible to make DXS measurements very close to RELP and at very small angular intervals of a few sec of arc. This means that the reciprocal space can be explored with a high resolution. High resolution topographs are recorded by aligning the specimen at the peak of the diffraction curve and recording the diffracted beam on a film. We have already shown one such topograph in figure 6.

This system has been used for a detailed and systematic study of diffuse x-ray scattering from nearly perfect single crystals of silicon (Krishan Lal and Singh 1977, 1980; Krishan Lal *et al* 1979; Singh 1980), potassium chloride, potassium bromide (Krishan Lal and Singh 1981a) and copper (Krishan Lal and Singh 1981b). In the first part of these investigations the aim was to evaluate the relative contribution of phonons and defects to the DXS. Fortunately, the DXS distribution due to the two is expected to be different. In the case of thermal diffuse scattering the intensity of DXS (DXS I) is expected to vary as K^{*-2}. **K*** is the wavevector of the elastic thermal waves and in reciprocal space it is obtained by joining the RELP with the elemental volume of the space being explored. The intensity along **K*** and along opposite direction **K*** is expected to be equal. The slopes of the lines in DXS I *vs* $1/K^{*2}$ plots for **K*** perpendicular to the reciprocal lattice vector **R*** are expected to be more than those of the lines with **K*** parallel to **R***. The DXS I is expected to depend only on the temperature of the specimen. In the case of DXS due to defects, the DXS I can vary as K^{*-n} with n having different values. In the DXS I *vs* $1/K^{*2}$ plots the slope of lines with **K*** along **R*** are higher than those expected for the lines with **K*** perpendicular to **R***. The DXS I is not isotropic with respect to the sense of **K***. We shall consider here only one plot to illustrate the main results.

Figure 19 is a DXS I vs $1/K^{*2}$ plot for a nearly perfect silicon single crystal (Krishan

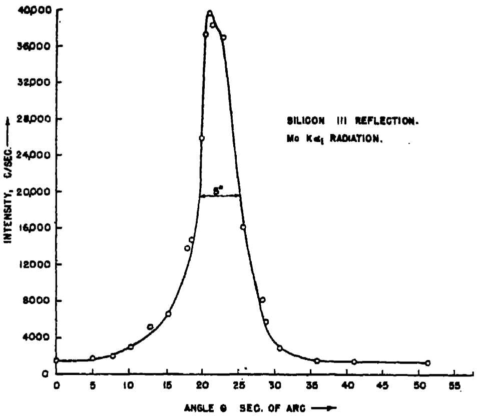

Figure 18. A typical diffraction curve of a dislocation free silicon single crystal recorded on the triple crystal x-ray diffractometer 111 RELP and MoKα_1 radiation was used.

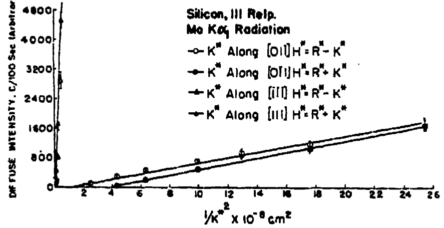

Figure 19. A typical DXS I *vs* $1/K^{*2}$ curve obtained with a dislocation free silicon single crystal. DXS was measured around the 111 RELP with MoKα_1 radiation.

Lal and Singh 1977). It is seen that the lines with **K*** parallel to **R*** have high than the lines with **K*** perpendicular to **R***. If this data is plotted on a log-log sc than one slope is observed. This shows that the observed DXS I is not due t thermal waves.

Experiments have been performed with different specimens of Si, with radiations and using different RELPS and the same results were obtained. Sinc temperature of silicon crystals is very high some experiments were performed temperatures. Only at 300°C some contribution of phonons was observed.

Experiments were performed with materials such as potassium chloride, pc bromide and copper, having low Debye temperatures. These results also sup main conclusions.

However, it was observed that the DXS distribution is very sensitive to the history of the specimen. By analysing the DXS data the size and shape of poi clusters was determined in silicon. In another series of experiments, Si cryst deliberately heated under oxygen and the oxygen aggregates were characterize measurements. This series of investigations has led to the development of a n destructive tool for study of defects in dislocation-free single crystals. The res the contribution of phonons to the DXS is insignificant as compared to that of of considerable importance.

The power of the high resolution x-ray diffraction techniques in reveali changes in atomic arrangement in nearly perfect crystals has been demonstr series of new experiments. In these experiments, microstructural changes ind high electric fields in single crystals of semiconductors and insulators have bee observed and characterized for the first time (Krishan Lal and Peter Thoma 1983; Peter Thoma and Krishan Lal 1982).

References

Bardsley W, Hurle D T J and Mullin J B (eds) 1979 *Crystal growth: A tutorial approach* (Amsterd Holland)

Barret C S 1945 *Trans. AIME* **161** 15

Batterman B W and Cole H 1964 *Rev. Mod. Phys.* **36** 681

Bonse U and Hart M 1965 *Appl. Phys. Lett.* 7 238

Dederichs P H 1973 *J. Phys.* **F3** 471

Krishan Lal 1978 in *Advances in crystallography* (ed.) R Srinivasan (New Delhi: Oxford and IBH Co.) p 136

Krishan Lal 1980 *Proc. Indian Natl. Sci. Acad.* **A47** (Supp) 1 20

Krishan Lal 1981 *Trans. IIM* **34** 398

Krishan Lal 1982 in *Synthesis, crystal growth and characterization* (ed.) Krishan Lal (Amsterd Holland) p 215, 287

Krishan Lal, Anand J R, Kumar H and Rawat J S 1979 Tenth National Conf. Crystallogr. V

Krishan Lal, Anantha Murthy R V, Halder S K, Singh B P and Kumar V 1982 *J. Crystal Gro*

Krishan Lal and Jhans H K 1977 *J. Phys.* **C10** 1315

Krishan Lal and Kumar V 1978 *J. Electrochem. Soc.* **125** 2079

Krishan Lal, Kumar V and Pahwa D R 1975 *National Conf. Cryst.* New Delhi

Krishan Lal and Pahwa D R 1971 *Rev. Sci. Instrum.* **42** 534

Krishan Lal and Peneva S K 1968 *J. Appl. Phys.* **39** 5474

Krishan Lal and Peneva S K 1969 *J. Appl. Phys.* **40** 5045

Krishan Lal, Peneva S K and Verma A R 1970 *Phys. Status. Solidi* **A3** 617

Krishan Lal, Peneva S K and Verma A R 1972 *Proc. Indian Natl. Sci. Acad.* **A38** 173

Krishan Lal and Thoma P 1981a *Solid State Commun.* **40** 637

Krishan Lal and Thoma P 1981b *Acta Crystallogr.* **A37** C262

Krishan Lal and Thoma P 1983 *Phys. Status. Solidi.* **A80**

Krishan Lal and Singh B P 1977 *Solid State Commun.* **22** 71

Krishan Lal and Singh B P 1979 *Indian J. Phys.* **A53** 72

Krishan Lal and Singh B P 1980 *Acta Crystallogr.* **A36** 178

Krishan Lal and Singh B P 1981a *J. Crystal Growth* **54** 493

Krishan Lal and Singh B P 1981b *Acta Crystallogr.* **A37** C-273

Krishan Lal, Singh B P and Verma A R 1979 *Acta Crystallogr.* **A35** 286

Krivoglaz M A 1969 *Theory of x-ray and neutron scattering by real crystals* (New York: Plenum Press)

Kumar V 1983 Ph.D. Thesis Univ. of Delhi

Lang A R 1970 in *Modern diffraction and imaging techniques in material science* (eds) S Amelinckx, R Gevers, G Remant and J Landyut (Amsterdam: North-Holland) p 407

Pamplin B R (ed) 1975 *Crystal Growth* (New York: Pergamon Press)

Paorici C 1982 in *Synthesis, crystal growth and characterization* (ed.) Krishan Lal (Amsterdam: North-Holland) p 133

Peisl H 1976 in *Defects and their structure in non-metallic solids* (eds) B Henderson and A E Hughes (New York and London: Plenum Press) p 381

Peneva S K 1969 Ph.D. Thesis, Univ. of Delhi, Delhi

Ramachandran G N 1944 *Proc. Indian. Acad. Sci.* **A19** 280

Ramachandran G N and Wooster W A 1951 *Acta Crystallogr.* **4** 385, 431

Singh B P 1980 Ph.D. Thesis, Univ. of Delhi, Delhi

Tanner B K 1976 *X-ray diffraction topography* (Oxford: Pergamon Press)

Thoma P and Krishan Lal 1982 in *Syntheses, crystal growth and characterization* (ed.) Krishan Lal (Amsterdam: North-Holland) p. 427

Verma A R 1982 in *Synthesis, crystal growth and characterization* (ed.) Krishan Lal (Amsterdam: North-Holland) p 1

Verma A R, Krishan Lal, Pahwa D R, Kumar V and Aggarwal K 1974 *Indian I. Pure and Appl. Phys.* **12** 350

Wooster W A 1962 *Diffuse x-ray reflections from crystals* (Oxford: Clarendon Press)

Yang K H, Kappert H F and Schwuttke G H 1978 *Phys. Status Solidi* **50** 221

Yang K H and Schwuttke G H 1980 *Phys. Status. Solidi.* **58** 127

Bull. Mater. Sci., Vol. 6, No. 2, May 1984, pp. 151–164. © Printed in India.

Investigation of hydrogenous materials using neutrons

B A DASANNACHARYA and P S GOYAL
Nuclear Physics Division, Bhabha Atomic Research Centre, Bombay 400 085, India

Abstract. Slow neutrons have proved to be a very powerful probe for examining materials in general and hydrogenous materials in particular. In this article we review various neutron scattering techniques which have been utilised to investigate different aspects of a variety of hydrogenous materials. Translationally as well as orientationally disordered materials, ferroelectrics, superconductors, metal-hydrogen systems, polymers and biological molecules have been chosen as illustrative examples.

Keywords. Neutrons; hydrogenous materials; ferroelectrics; disordered materials; superconductors; metal-hydrogen systems; polymers; biological molecules.

1. Introduction

Hydrogen is the most predominant element in nature. It behaves in very different ways in different environments thus giving rise to types of materials which show an extremely wide variety of properties. Not surprisingly, every possible method has been used to examine them. During the last quarter of a century neutron scattering techniques have made a very important contribution in the investigation of these materials. This is because of certain unique properties of slow neutrons which make them particularly suitable for such studies.

Neutron scattering consists of a family of techniques which give a host of complementary information about any substance. Coherent scattering (diffraction) of neutrons is well known for the information it gives on the crystallographic structures of hydrogenous materials; incoherent elastic scattering which is less commonly used can be particularly useful in studying Debye-Waller factor of hydrogen and the 'elastic' form factor which is connected with hydrogen atom distribution over a very large time interval; coherent inelastic scattering experiments determine phonon dispersion curves, whereas incoherent inelastic and quasi-elastic scattering measurements lead to phonon frequency distribution functions and give the nature of random atomic motions (translational and/or rotational) in solids and liquids; small angle scattering of long wave-length neutrons leads to information on large molecules (polymers or biomolecules) or congregation of molecules (precipitates etc). Most of the above mentioned techniques have been used extensively at Trombay during the last two decades. This overview will, with some representative examples, endeavour to bring out the scope of these neutron techniques, particularly as applied in connection with hydrogenous materials.

2. Principles

2.1 *Basic interaction*

Slow neutrons which typically have wavelength in the range of 1 to 10 Å are mainly scattered from the nucleus of atoms*. The scattering, being essentially from a scatterer ($\sim 10^{-13}$ cm), is isotropic. The extent of scattering, which is proportio the square of the bound nuclear scattering amplitude, b, varies for any element fro isotope to another and also depends on the spin of the scattering nucleus. Henc random assembly of atoms a configurational average, $\langle ---- \rangle$, has to be taken. gives rise to a 'coherent' scattering cross-section, $\sigma_{\text{coh}} = 4\pi \langle b \rangle^2$ where the inten proportional to the square of the average scattering amplitude and an incoh scattering which is the difference between the total, $4\pi \langle b^2 \rangle$, and the coh scattering; $\sigma_{\text{inc}} = 4\pi[\langle b^2 \rangle - \langle b \rangle^2]$. Table 1 gives the coherent and incoh scattering cross-sections and scattering amplitudes for some elements.

Several features of this table are worth noting: σ_{inc} for H practically domina scattering, σ_{coh} for H is comparable to that of other elements and the scatt amplitudes of H is negative whereas most other elements have a positive value These along with the other properties of neutrons, that is, their high penetrabil materials and wavelength-energy (λ-ω) relationship similar in order-of-magnitu that of material lattices are utilised in most neutron scattering experiments.

A typical block diagram for a neutron scattering experiment is shown in figur neutron source, usually a nuclear reactor provides a continuous source of chromatic neutrons. A monochromator which may be just a large single crysta more complicated mechanical device, is used to get a mono-energetic beam of neu of energy E_0 having a wavelength λ_0 and wave-vector $\mathbf{k}_0$; $|k_0| = 2\pi/\lambda_0$, $E_0 = \hbar^2 k$ These neutrons are scattered from the material under study. In a diffraction exper

Table 1.

	$\sigma_{\text{coh}}(10^{-24}\,\text{cm}^2)$	$\sigma_{\text{inc}}(10^{-24}\,\text{cm}^2)$	$b\,(10^{-12}\,\text{cm})$
H	1·759	79·7	−0·3741
D	5·597	2·0	0·6674
C	5·554	0·0	0·6648
O	4·235	0·0	0·5805
Fe	11·437	0·21	0·954
Pb	11·106	0·0	0·9401

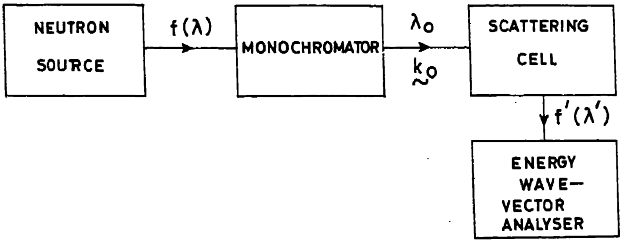

Figure 1. Schematic drawing of a neutron scattering experimental set-up.

---

* Materials having a magnetisation distribution also show a magnetic scattering which comparable to nuclear scatterings; we will not consider such substances here.

one measures the angular distribution of the scattered neutrons. In a more general inelastic or quasi-elastic scattering experiment both the angular (giving wavevector transfer, **Q**) and energy distributions are measured. Thus, in the latter the scattering cross-section for wavevector transfer $\mathbf{Q} = \mathbf{k}_0 - \mathbf{k}'$ and energy transfer, $\varepsilon = \hbar\omega = E_0 - E'$, are determined.

For convenience, we collect the relevant expressions for cross-sections here (Kostorz and Lovesey 1979). The examples of their use will form the subject matter of the rest of this article.

2.2 *Diffraction: Coherent scattering*

The angular distribution of coherently scattered neutrons per unit volume of the sample is given by:

$$(\mathrm{d}\sigma/\mathrm{d}\Omega)_{\mathrm{coh}} = N_0 \frac{(2\pi)^3}{V_0} \sum_{\tau} \delta(\mathbf{Q} - \tau) |F(\tau)|^2, \tag{1}$$

where

$$F(\tau) = \sum_{l} \langle b_l \rangle \exp(i\tau \cdot \mathbf{r}_l) \cdot \exp\{-W_l(\tau)\}.$$

Here $\mathbf{r}_l$ denotes the co-ordinates of lth nucleus in the unit cell, τ the reciprocal lattice vector and $\exp\{-W(\tau)\}$ the Debye-Waller factor for the lth nucleus. V_0 is the volume of the unit cell and N_0 is the number of unit cells per unit volume of the sample. The δ-function in (1) signifies that intensity appears only at angles satisfying the Bragg reflection condition $\mathbf{Q} = \tau$. In a crystallographic experiment, the quantity of interest is the structure factor $|F(\tau)|^2$.

2.3 *Diffraction: Incoherent scattering*

The angular distribution of intensity of incoherently scattered neutrons is given by:

$$(\mathrm{d}\sigma/\mathrm{d}\Omega)_{\mathrm{inc}} = N_0 \sum_{l} \frac{\sigma^l_{\mathrm{inc}}}{4\pi} \exp\{-2W_l(Q)\}. \tag{2}$$

This intensity, in hydrogenous materials, for all practical purposes is due to hydrogen alone (due to its large σ_{inc}) and one measures essentially the Debye-Waller factor of the hydrogen atoms.

2.4 *Inelastic coherent scattering: One phonon process*

The coherent one-phonon scattering cross-section per unit volume for neutron energy loss is given by:

$$(\mathrm{d}^2\sigma/\mathrm{d}\Omega\,\mathrm{d}E')_{\substack{\mathrm{Coh.}\\ \mathrm{inel}}} = \frac{k'}{k_0} \frac{(2\pi)^3}{V_0} \sum_{\tau, j, q} |G_j(\mathbf{q}, \mathbf{Q})|^2 \frac{[n_j(\mathbf{q}) + 1]}{\omega_j(\mathbf{q})} \times \delta[\omega - \omega_j(\mathbf{q})]\, \delta(\mathbf{Q} - \mathbf{q} - \tau), \tag{3}$$

where the structure factor is

$$G_j(\mathbf{q}, \mathbf{Q}) = \frac{1}{(2M_l)^{1/2}} \sum_{l} \langle b_l \rangle \{\mathbf{Q} \cdot \mathbf{e}^l_j(\mathbf{q})\} \exp(i\mathbf{Q} \cdot \mathbf{r}_l) \exp\{-W_l(\mathbf{Q})\}.$$

Here **q** is the wavevector of the phonon being excited and j its polarization index. $\omega_j(\mathbf{q})$

is the angular frequency of the mode and $\mathbf{e}^l_j$ ($\mathbf{q}$) its polarisation vector for lth whose mass is M_l. $(n_j(\mathbf{q})+1)$ is the polulation factor. Here both energy and wave conservation conditions have to be satisfied through the two-δ-functions. This re is utilized for determining phonon dispersion curves.

2.5 *Inelastic incoherent scattering: One phonon process*

For incoherent scattering, scattering cross-section for unit volume of the sam given by:

$$\left(\frac{\mathrm{d}^2\sigma}{\mathrm{d}\Omega\,\mathrm{d}E'}\right)^{\mathrm{inc}}_{\mathrm{inel}}=\frac{k'}{k_0}\sum_{ljq}\left(\frac{\sigma^l_{\mathrm{inc}}}{4\pi}\right)\frac{[n_j(\mathbf{q})+1]}{2M_l\omega_j(\mathbf{q})}\,|\mathbf{Q}\cdot\mathbf{e}^l_j(\mathbf{q})|^2$$
$$\times\exp\{-2W_l(\mathbf{Q})\}\,\delta(\omega-\omega_j(\mathbf{q})).$$

The cross-section now depends on the number of modes satisfying the e conservation condition. This gives a polarisation weighted phonon frequency bution function. Incoherent inelastic scattering is particularly useful in exam phonon spectra of hydrogenous materials.

2.6 *Quasi-elastic incoherent scattering: Diffusive motion*

Random dynamical motions such as molecular reorientations and diffusion give a line broadening of the incident monoenergetic beam. This is referred to as quasie scattering. In the case of a hydrogen atom translationally diffusing in a solid or (Springer 1972)

$$\left(\frac{\mathrm{d}^2\sigma}{\mathrm{d}\Omega\,\mathrm{d}E'}\right)_{\substack{\mathrm{inc}\\ \mathrm{q\cdot el}}}=\frac{N\sigma_{\mathrm{inc}}}{4\pi^2\hbar}\frac{k'}{k_0}\exp\{-2W(Q)\}\sum_p g_p(Q)\frac{f_p(Q)}{\omega^2+f_p^2(Q)},$$

with the normalising condition $\sum_p g_p(Q)=1$. Here N is the number of hydrogen per unit volume. The widths, $f_p(Q)$ of the Lorentzians are decided by the diff coefficient, and $g_p(Q)$ is related to the actual geometry of jump diffusion.

The incoherent scattering from reorienting molecular groups, like NH_4, CH_3 given by

$$\left(\frac{\mathrm{d}^2\sigma}{\mathrm{d}\Omega\,\mathrm{d}E'}\right)^{\mathrm{inc}}_{\mathrm{q\cdot el.}}=\frac{N\sigma_{\mathrm{inc}}}{4\pi^2\hbar}\frac{k'}{k_0}\exp\{-2W(Q)\}$$
$$\times\left[\pi A(Q)\delta(\omega)+\sum_p g'_p(Q)\frac{f_p(Q)}{\omega^2+f_p^2(Q)}\right]$$

with the normalising condition $\sum_p g'_p(Q)+A(Q)=1$. The relative intensities elastic and quasielastic parts (form factor) are dependent on the geometry of mol reorientation. The width of the Lorentzian is related to the reorientation Incoherent elastic scattering experiment (§ 3.2) will usually examine the first te (6). However, the measured intensities can have a small contribution from the se term also depending on the relative values of $f_p(Q)$ and the instrumental resolution in such an elastic scattering experiment.

2.7 *Small angle neutron scattering: Molecular form factor*

Whenever the object of scattering, say, a polymer or a precipitate, is much large the wavelength of the radiation scattered, the scattering is confined to small a

Hence special techniques have been developed for studying large scatterers (size typically $> 50\,\text{Å}$). The technique basically depends on the contrasts in scattering between the object under study and the matrix holding this object. Fortunately for neutrons, since the scattering amplitude for hydrogen and deuterium is very different, it is possible to produce good contrast in scattering. The angular distribution is given by (King 1980).

$$(d\sigma/d\Omega)_{\underset{\text{SAS}}{\text{Coh}}} = N_c n^2 (b_s - b_h)^2 f(Q) \tag{7}$$

Here N_c is the number density of large molecules and n is the number of atoms in the molecule, b_s and b_h are the average scattering amplitudes of the scatterer and the host and $f(Q)$ is a form factor associated with the molecule.

3. Experimental results

3.1 *Structures by coherent scattering*

Neutron diffraction as a crystallographic tool is particularly suitable for the accurate determination of the positions of hydrogen atoms, in contrast to the more commonly used x-ray diffraction, since the scattering amplitude for hydrogen is comparable to that of most other elements. Literature is full of examples of inorganic, organic and biologically interesting structures determined using neutron diffraction (Dachs 1978) and it would be impossible even to give a flavour of the variety of such studies. We content ourselves by giving an example of a simple compound, $(NH_4)_2\,CuCl_4 \cdot 2H_2O$, which shows some subtle structural features in relation to the two ammonium ions in the molecule.

The framework of $(NH_4)_2\,CuCl_4 \cdot 2H_2O$ is made up of columns of NH_4Cl and $CuCl_2 \cdot 2H_2O$ along *c* direction; the columns alternate along *a* and *b* directions. The cube of NH_4Cl is rather similar to that of pure NH_4Cl, with NH_4^+ residing on a tetrahedral site surrounded by eight Cl ions, four of type-I and four of type-II (figure 2). Infra-red absorption experiments (Oxton and Knopp 1977) and Raman scattering experiments (Bansal *et al* 1979) alternatively suggested that NH_4^+ ions are ordered with N–H bond pointing towards Cl(I) and that they are disordered. Neutron diffraction experiments (Bhakay-Tamhane *et al* 1980) not only unequivocally decided that they were disordered but could quantitatively assign the site occupancy ratio as 0·64 : 0·36 in favour of Cl(I) as shown in figure 2, a task not easily achieved by any other method. However, one notes that diffraction experiment itself is not able to answer whether this disorder is static or dynamic. We will address ourselves to this question presently.

3.2 *Hydrogen diffusion, reorientations through incoherent diffraction and incoherent 'elastic' scattering*

In a diffraction experiment the coherent Bragg peaks which are measured to determine the structure, ride over an incoherent uniformly varying intensity which is very large for hydrogenous substances and is almost entirely due to incoherent scattering from hydrogens. The angular variation of this intensity is given by $\exp -Q^2 \langle u^2 \rangle$ where $\langle u^2 \rangle$ is the mean squared amplitude of the hydrogen atoms, assuming harmonic vibrations. When only vibrations are present this gives an accurate measure of $\langle u^2 \rangle$.

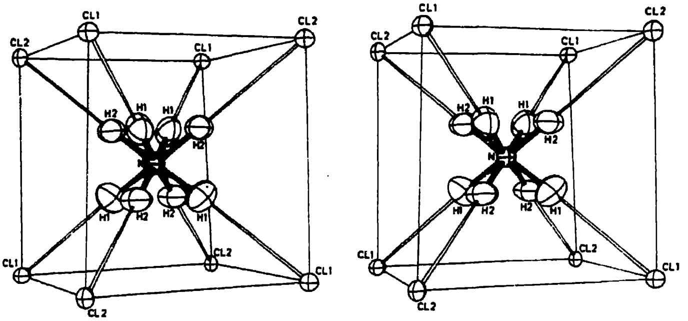

Figure 2. An illustration of surroundings of ammonium ions in $(NH_4)_2$ $CuCl_4 \cdot 2H$ room temperature. 64% NH_4^+ ions have orientation corresponding to H(1) and corresponding to H(2). The thermal ellipsoids shown in this figure have been scaled to in 30% probability (Bhakay-Tamhane *et al* 1980).

As described earlier (§2.6), it is also possible to do incoherent 'elastic' scatte experiment instead of incoherent diffraction. In such an experiment only the 'el component of the scattered neutrons is measured. In an ideal 'elastic' scatte experiment one observes the time average, over infinite time, of the motion of hydrogen atom. In real life experiment this averaging is qualitatively over a $\Delta t = h/\Delta E$ where ΔE is the energy resolution of the 'elastic' scattering experin Thus, whenever in addition to vibrational motion the hydrogen atom also perfo diffusive translational movements (as in metal-hydrogen systems) or large reo tational jumps (as in plastic solids, liquids or molecular crystals) the 'elastic' incohe intensity depends on the characteristics of the diffusion times and distances.

Results of such an experiment on NH_4Br, NH_4I, $(NH_4)_{0.16}$ $K_{0.84}I$ $(NH_4)_{0.16}$ $K_{0.84}$ Br are shown in figure 3 (Bragg peaks are not shown for the sak clarity) (Goyal and Dasannacharya 1979). In the case of NH_4Br one finds that distribution (figure 3a) with an elastic resolution of 12 meV (×) is the same as that a resolution of 1·3 meV (o), showing that the reorientation times of NH_4^+ ions in room temperature phase (CsCl phase) of NH_4Br are much larger than a $h/\Delta E = h/1{\cdot}3$ meV $\sim 3 \times 10^{-12}$ sec. Consequently the angular distribution $\langle u^2 \rangle$ which is 0·04 Å^2. The angular distribution in the other three examples, howe shows a much steeper non-gaussian fall, clearly indicating a rapid reorientatio tetrahedral NH_4^+ ions in their first neighbour octahedral environment. Assumi model for the geometry of reorientation it was found that, τ, the reorientation time the time between two reorientational jumps) is $\sim 5 \times 10^{-12}$ sec and depends only weakly on temperature between 300 and 140°K.

Similar measurements at a fixed angle but as a function of temperature can reveal existence of phase transitions (de Graff 1980) and can also throw light on tempera dependence of diffusion coefficient (Leadbetter *et al* 1976). They are rather simila nature to the line width measurements in NMR. While these measurements can be to make a quick tour through the momentum-transfer to temperature space, they not capable of giving detailed spatial information regarding the nature of the motio hydrogen. For this one resorts to quasi-elastic scattering which is unique in this resp

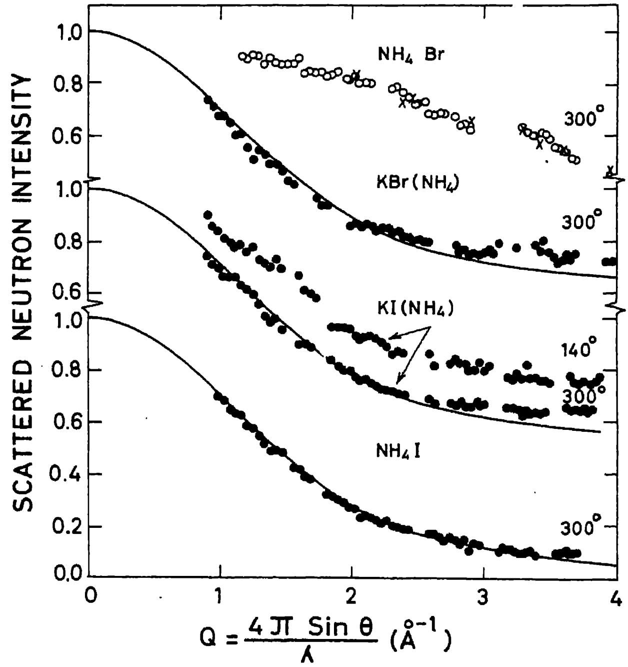

Figure 3. Scattered neutron intensity versus wavevector transfer for various salts as obtained from neutron incoherent "elastic" scattering experiment. (**a**) NH_4Br at 300 K (**b**) $(NH_4)_{0\cdot16}K_{0\cdot84}Br$ at 300 K (**c**) $(NH_4)_{0\cdot16}K_{0\cdot84}I$ at 140 K (upper curves) and 300 K (lower curves) and (**d**) NH_4I at 300 K. The instrumental resolution ΔE = 1·30 meV (FWHM) for all distributions except the one shown by crosses (×) in (**a**). For crosses ΔE = 12·0 meV. Filled circles (●) correspond to the NaCl phase. Open circles (o) and crosses (×) correspond to the CsCl phase of NH_4Br. Full curves are calculated using the octahedral jump model for τ = 5 psec and $\langle u^2 \rangle$ = 0·125 A^2. (Goyal and Dasannacharya 1979).

3.3 *Stochastic motions in metal-hydrogen systems and ferroelectrics through incoherent quasielastic scattering*

As indicated in §2.6, neutrons are quasi-elastically scattered whenever hydrogen performs random motions. If the motion is purely translational as, for example, with hydrogen in metals, the scattered spectrum consists of a broadened line whose total intensity as a function of angle of scattering depends on the detailed geometry of the translational jumps of the proton (equation (5)). Such measurements were first reported for PdH by Skold and Nelin (1967) whose results, that hydrogen diffusion in PdH occurs by the jumps of hydrogen through octahedral interstitial sites in Pd, have been further confirmed on single crystals of $PdH_{0.03}$ by Rowe *et al* (1972). Figure 4 shows results of Rowe *et al* (1972) which also gives the average time between jumps to be 2·8 picosec. Similar experiments have also been performed on V, Nb and Ta which show a more complicated jump pattern through tetrahedral interstitial sites (Lottner *et al* 1979; Springer 1977). More recently measurements have been greatly refined and tunneling states in Nb $O_{0.013}H_{0.016}$ (Wipf *et al* 1981), hydrogen trapping cum diffusion in hydrogen storage material $Ti_{1.2}Mn_{1.8}H_3$ (Hempelmann *et al* 1982) and multiple interstitial occupancy and jumps in La Ni_5H_6 have been observed (Richter *et al* 1982).

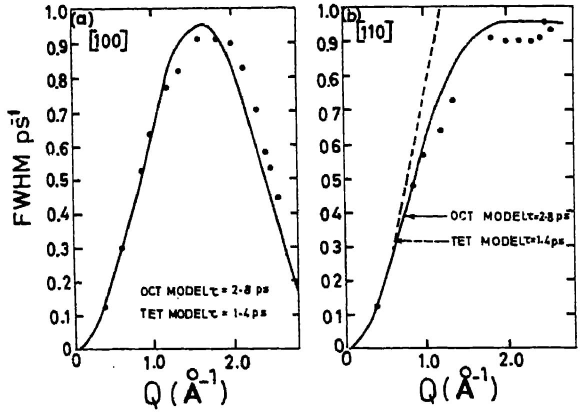

Figure 4. Variation of line-width of quasielastic line as a function of wavevector transfer single crystal of Pd $H_{0\cdot03}$ along (100) and (110) directions. (Rowe *et al* 1972)

Another class of experiments involves investigation of reorientation in solids wi molecular groups containing hydrogen. In such a case the scattered spectrum consi of a sum of a purely elastic part (equation (6)) and a quasi-elastic part. An example this class is ammonium sulphate. With two NH_4^+ ions in the molecule, it shows a pha transition at −50°C from a paraelectric phase to a possibly ferrielectric phase. NI results of O'Reilly and Tsang (1967) suggested that in the paraelectric phase the tv types of NH_4^+ ions have similar reorientation times τ_I and τ_{II}. However, from simil NMR experiments Kydon *et al* (1969) concluded that τ_I is smaller by almost an order magnitude compared to τ_{II} and that NMR is sensitive only to type II ions in t paraelectric phase. The situation was clarified with neutron quasielastic scatteri experiments which demonstrated without doubt that in the paraelectric phase τ_I and are comparable. Using mixed salts like $[(NH_4)_{0.16}K_{0.84}]_2SO_4$ and pure $(NH_4)_2SO$ was shown that at room temperature $\tau_I = 10{\cdot}4 \pm 3$ picosec and $\tau_{II} = 15{\cdot}8 \pm 1{\cdot}1$ picos (Goyal and Dasannacharya 1978). The angular dependence of the elastic scatteri (equation (6)) in the above two salts further showed that the experiments are consiste with reorientation about all four N–H bonds in NH_4^+ (I) being equally probable b that the reorientation probability about the four N–H bonds in NH_4^+ (II) is not t same. In the ferroelectric phase, neutron experiments (Dasannacharya *et al* 1982) a consistent with NMR results of O'Reilly and Tsang (1967). Similar studies have be conducted on several other systems showing interesting phase transitions resulti from/in slowing down of reorientational motions (Springer 1977). We will howev now pass on to examples of inelastic scattering studies.

3.4 *Ferroelectrics, superconductors, metal-hydrogen systems, hydrogenated metalli glasses through incoherent inelastic scattering*

We have noted earlier that incoherent inelastic scattering arising out of one-phon scattering relates to the polarisation weighted phonon frequency distribution functi of hydrogen atoms under the reasonable assumption that scattering from other ato can often be neglected (see table 1). Unlike infrared absorption and Raman scatteri studies which are normally sensitive to phonons of long wavelength ($q \sim 10^5$ Å^{-1}) only, the neutron scattering experiments provide information about phonons over the whole Brillouin zone ($q \sim 10^8$ Å^{-1}). Experiments with single crystals can be utilised further to throw light on the nature of the polarisation vector associated with certain frequency modes (Thaper *et al* 1970). Though in suitable cases, these experiments have been used for obtaining the phonon frequency distribution function (Goyal *et al* 1972) more often these experiments have been performed to gain knowledge about the general features of the frequency distribution function leading to the understanding of phenomena like order-disorder transition, ferroelectricity, superconductivity etc. in hydrogenous systems. Some examples are given below:

We discussed the reorientations of NH_4^+ in ammonium sulphate earlier. $(NH_4)_2SO_4$ is a ferroelectric with T_c of -50°C, but the isomorphic K_2SO_4 does not undergo a transition down to 4·2°K. It is therefore of interest to systematically examine the role of replacing NH_4^+ with K^+. Results of inelastic scattering experiments at 110°K, in the ferroelectric phase of $(NH_4)_2SO_4$ are shown in figure 5 (Chandra *et al* 1976). The two prominent peaks at 390 and 350 cm^{-1} are associated with the librational modes of the two ammonium ions NH_4^+ (I) and NH_4^+ (II) in the unit cell (Schlemper and Hamilton 1966). On the other hand, the spectrum for $[(NH_4)_{0.16}K_{0.84}]_2SO_4$ shows only one group of librational frequencies at 350 cm^{-1}. As the concentration of NH_4^+ increases beyond 50% the frequency at 390 cm^{-1} starts building up and finally grows into full intensity for the pure ammonium salt. These measurements are interpreted to mean that NH_4^+ ion first preferentially goes to one type of site, NH_4^+ (II), till most of that site is occupied. In combination with dielectric measurements (Sawada *et al* 1975) which show that $[(NH_4)_xK_{1-x}]_2SO_4$ shows ferroelectric properties only for $x \gtrsim 0{\cdot}45$, the

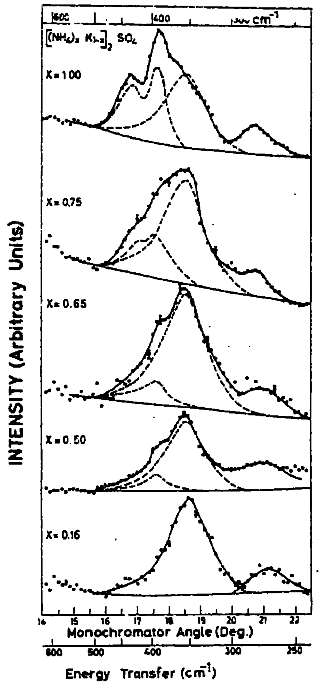

Figure 5. Spectra of incoherent inelastically scattered neutrons for $[(NH_4)_xK_{1-x}]_2SO_4$ for different x values at 110 K (Chandra *et al* 1976).

neutron results can be interpreted to mean that the presence of NH_4^+ (I) is neces the onset of ferroelectricity in this compound. These results also indica librational modes of NH_4^+ (II) are not directly involved in the ferroelectric tra since the NH_4^+ (II) frequency in the ferroelectric sample with $x > 0{\cdot}45$ are ide those in the paraelectric samples with $x < 0{\cdot}45$.

In addition to such measurements (by forming isomorphic mixed salts) stud also been conducted by deuterating or partially deuterating the samples in (identify the role and coupling of a particular hydrogen atom in a compoun studies have been carried out on a number of organic compounds, polymers acids, etc (Reynolds and White 1969; Twisleton and White 1972; Thaper *et a* Some measurements have also been made to study the role of hydrogen adso nickel (Stockmeyer *et al* 1975), platinum black (Howard *et al* 1977) and in (Stockmeyer and Monkenbusch 1980).

Metal hydrogen systems like Zr H_2, YH_2, NbH_x, VH_x, PdH_x, etc. ha extensively studied by inelastic scattering methods (for a review see Dasann 1980). Systematics of the vibrational frequency against metal hydrogen dista hydrogen in octahedral and tetrahedral sites have been evolved (Hunt and Ros Thus, it is now possible to predict the nature of site occupancy by know vibrational frequency. More recently, measurements have also been carried metallic glasses (Rush *et al* 1980, Kajitani *et al* 1982) loaded with hydrogen. Th of Ti Cu H (Rush *et al* 1980) in the crystalline and glassy state are shown in figur large broadening of the vibrational density of states in the glassy state is beli arise because of a large variation in the local environment of hydrogen at compared to that in the crystalline materials where hydrogen occupies the tetr interstitial site.

Finally, this technique has also been used to examine the role of hydrog possibly that of optical phonons in superconductivity of Th_4H_{15} and PdH_x (Di *al* 1977; Rowe *et al* 1974).

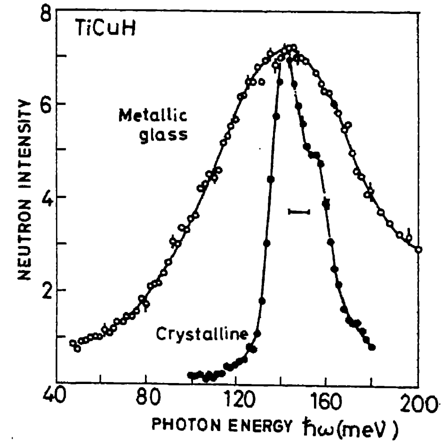

Figure 6. Scattered neutron spectra measured at 78 K for crystalline $TiCuH_{0\cdot}$ amorphous Ti Cu $H_{1\cdot3}$ (o). The energy resolution (FWHM) near the peak is ind horizontal bar (Rush *et al* 1980).

3.5 *Molecular crystals, polymers through coherent inelastic scattering*

Coherent scattering measurements are the only known method for detailed measurement of phonon dispersion curves. In addition to the normal difficulty of getting a single crystal, in the case of hydrogenous substances one may have the additional problem of obtaining deuterated samples. However, having overcome these difficulties one stands the chance of obtaining information which is unique and extremely detailed in nature. Successful experiments have been carried out on inorganic crystals (Smith *et al* 1969; Vagelatos *et al* 1975), molecular crystals (Chaplot 1983), metal-hydrogen systems (Springer 1978) and polymers (King 1974). As an example, we show the dispersion curve for polyethylene measured by Feldkamp *et al* (1968) (figure 7). We, however, also mention in passing that these measurements are difficult and time-consuming and have been successfully attempted only recently.

3.6 *Polymers and bio-molecules through small angle neutron scattering*

Small angle neutron scattering (SANS) technique, which examines the sample with a typical spatial resolution of ~ 100 Å, is an excellent tool for determining the configuration of polymer chains and that of large size molecules of biological interest by measuring their radius of gyration. This is in fact the only technique for examining the chain configurations in solid polymers, polymer melts and concentrated polymer solutions. The other available techniques (small angle x-ray scattering or light scattering) can be used only for dilute polymer solutions (Higgins and Stein 1978).

The importance of SANS technique in the study of hydrogen and hydrogenous materials emerges from the fact that hydrogen and deuterium have quite different neutron coherent scattering amplitudes (see table 1). In a given hydrogenous material, it is thus possible to enhance the contrast between one set of molecules as compared to the other by deuterating them. For example, in a study of biological molecules where sample is often dissolved in water, the contrast between the sample molecules and the solvent molecules can be varied in a continuous way by using mixtures of H_2O and D_2O. The major components of biological materials are proteins, nucleic acids, carbohydrates and lipids. The scattering densities of these components are all different, but are between the scattering densities of H_2O and D_2O. Thus a variation in contrast

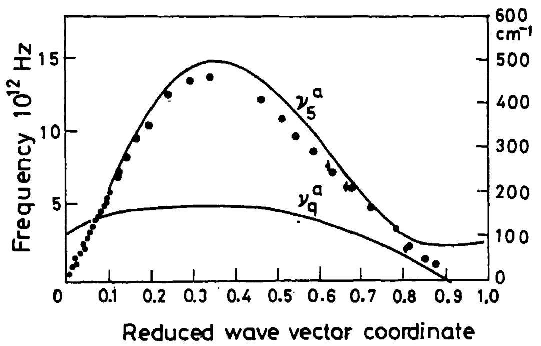

Figure 7. Comparison of experimental and calculated dispersion curves for deuterated polyethylene (Feldkamp *et al* 1968).

greatly helps in determining the spatial arrangements of various components ir biological material. This method has been successfully used to separate out RNA protein part of the structure in spherical viruses and ribosomes (Zaccai 1978). Fig shows the organization of protein and RNA in turnip yellow mosaic virus (TYMV) cucumber mosaic virus (CMV) as obtained using SANS technique (Jacrot *et al* 1977). shaded regions in this figure correspond to RNA, and show that penetration of RNA i protein shell is larger in CMV than that in the case of TYMV.

For solid polymers samples, where all chains are identical, contrast between a g chain and the neighbouring chains can be enhanced by deuterating that chain. Scatt neutron intensity in SANS experiment on such a polymer sample is decided by concentration of the labelled chains and by the contrast factor $|b_s - b_h|^2$, where b_s b_h are the scattering amplitudes of the monomers in the labelled chains and ir matrix chains respectively (equation (7)). Though earlier studies (Cotton *et al* 197 polymer systems were carried out using low ($< 1\%$) concentration of labelled chai is possible to gain in intensity by using higher (upto 50%) concentration of lab chains without spoiling the quality of information obtained (Akcasu *et al* 1980; G *et al* 1983). For example, in their SANS studies on solid polystyrene, Tangari *et al* (1 used 30% tagging and obtained results similar to those obtained by Cotton *et al* (1 using low concentration tagging. This is shown in figure 9, where the measured ra of gyration R_w for polystyrene has been plotted as a function of its molecular weigh

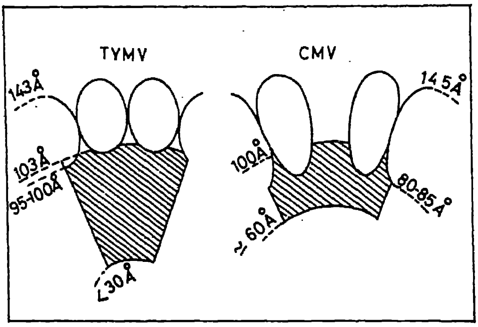

Figure 8. Sketch of the organisation of protein and RNA in turnip yellow mosaic vir cucumber mosaic virus as obtained using neutron scattering data. The shaded corresponds to RNA (Jacrot *et al* 1977).

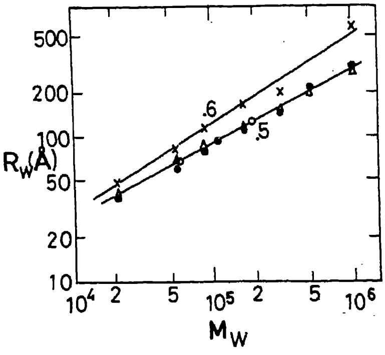

Figure 9. Radius of gyration R_w as a tion of molecular weight M_w for polyst Solid (●) and open (o) circles corresp solid polystyrene. Filled circles were ob using low concentration tagging and circles were obtained using high concent tagging. Crosses (×) correspond to tyrene in CS_2 and (Δ) correspond to styrene in cyclohexane at 36°C (Tangar 1980).

for different experimental conditions. Filled circles (●) and open circles (o) in this figure correspond to solid polystyrene and have been obtained using low (Cotton *et al* 1974) and high (Tangari *et al* 1980) concentration tagging. It is found that for solid polystyrene R_w varies as $M_w^{0.5}$, beautifully confirming, Flory's (1953) prediction based on his random coil model for solid polymers. Figure 9 also shows results of SANS experiments for polystyrene dissolved in a good solvent (CS_2) and a theta solvent (cyclohexane at 36°C) (Cotton *et al* 1974). For good solvents (×), R_w varies as $M_w^{0.6}$ whereas for theta solutions (+), $R_w \sim M_w^{0.5}$. During last decade, a number of polymer systems have been studied using SANS technique (Higgins 1979). Dynamics of these chains have also been investigated through quasielastic scattering (Higgins 1979).

4. Concluding remarks

Neutrons are the single most powerful probe for investigating hydrogenous substances. It is the purpose of this review to illustrate this through examples of different neutron scattering techniques and a wide variety of materials. Though it has not been possible to include all the methods, it is hoped that the main point has been conveyed.

References

Akcasu A Z, Summerfield G C, Jahshan S N, Han C C, Kim C Y and Yu H J 1980 *Polymer Sci.* **18** 1963

Bansal M L, Sahni V C and Roy A P 1979 *J. Phys. Chem. Solids* **40** 109

Bhakay-Tamhane S N, Sequeira A and Chidambaram R 1980 *Acta Crystallogr.* **B36** 2925

Chandra P P, Dasannacharya B A, Goyal P S, Iyengar P K, Rao K R, Thaper C L and Venkatesh A H 1976 *Phys. Lett.* **A57** 463

Chaplot S L 1983 *Nuclear Physics and Solid State Phys. India* **A26** (in press)

Cotton J P, Decker D, Benoit H, Farnoux B, Higgins J, Jannink G, Ober R, Picot C and des Coiseaux J 1974 *J. Macromol.* 7 863

Dachs H 1978 *in Topics in current physics* Vol. 6 (Berlin: Springer-Verlag)

Dasannacharya B A 1980 *Hydrogen in metals* (Bombay: Dept. Atomic Energy) pp 59

Dasannacharya B A, Richter D and Subramanian R 1982 *Nuclear Physics and Solid State Physics* (*India*) **C25** (in press)

de Graff L A, Chr. Steenbergen and Heidemann A 1980 *Physica* **B101** 209

Dietrich M, Reichardt W and Rietschel H 1977 *Solid State Commun.* **21** 603

Feldkamp L A, Venkataraman G and King J S 1968 *Inelastic scattering of neutrons* (Vienna: IAEA) pp 159

Flory P J 1953 *Principles of chemistry,* (Ithaca, New York: Cornell University Press)

Goyal P S, Dasannacharya B A, Thaper C L and Iyengar P K 1972 *Phys. Status. Solidi.* **B50** 701

Goyal P S and Dasannacharya B A 1978 *J. Chem. Phys.* **68** 2430

Goyal P S and Dasannacharya B A 1979 *J. Phys.* **C12** 219

Goyal P S, King J S and Summerfield G C 1983 *Polymer* **24** 131

Hempelmann R, Richter D and Heidemann A 1982 *J. Less Common Metals* **88** 343

Higgins J S 1979 *Treatise on materials science and technology* Vol. 15, (ed.) G Kostorz (New York :Academic Press) pp 381

Higgins J S and Stein R S 1978 *J. Appl. Crystallogr.* **11** 346

Howard J, Waddington T C and Wright C J 1978 *J. Chem. Soc. Faraday II* **73** 1768

Hunt D G and Ross D K 1976 *J. Less Common Metals* **49** 69

Jacrot B, Chauvin C and Witz J 1977 *Nature* (*London*) **266** 417

Kajitani T, Kaneko H and Hirabayashi M 1981 Science Report of the Research Institutes, Tohuku University, Sendai, Japan **A29** 210

King J S 1974 *Spectroscopy in biology and chemistry* (eds) S H Chen and S Yip (New York: Academic Press) pp 235

King J S 1980 *Methods of experimental physics* (New York: Academic Press) Vol. **A16**, pp 480

Kostorz G and Lovesey S W 1979 *Treatise on materials science and technology*, (ed.) G Kostorz (New Academic Press) Vol. 15

Kydon D W, Petch H E and Pintar M 1969 *J. Chem. Phys.* **51** 487

Leadbetter A J, Richardson R M, Dasannacharya B A and Howells W S 1976 *Chem. Phys. Lett.* 3

Lottner V, Buchenau V and Fitzgerald W J 1979 *Z. Phys.* **B35** 35

O'Reilly D E and Tsang T 1967 *J. Chem. Phys.* **46** 1291

Oxton I A and Knopp O 1977 *Chem. Phys. Lett.* **49** 560

Reynolds P A and White J W 1969 *Disc. Faraday Soc.* **48** 131

Richter D, Hempelmann R and Vinhas L A 1982 *J. Less Common Metals* **88** 353

Rowe J M, Rush J J, de Graff L A and Fergusen G A 1972 *Phys. Rev. Lett.* **29** 1250

Rowe J M, Rush J J, Smith H G, Mostoller M and Flotow H E 1974 *Phys. Rev. Lett.* **33** 1297

Rush J J, Rowe J M and Maeland A J 1980 *J. Phys* **F10** L283

Sawada A, Ohya S, Ishibashi Y and Takagi Y 1975 *J. Phys. Soc.* (*Jpn*) **38** 1408

Schlemper E O and Hamilton W C 1966 *J. Chem. Phys.* **44** 4498

Skold K and Nelin G 1967 *J. Phys. Chem. Solids* **28** 2369

Smith H G, Traylor J G and Reichardt W 1969 *Phys. Rev.* **181** 1218

Springer T 1972 *Springer-tracts in modern physics* (Berlin: Springer-Verlag) Vol. 64

Springer T 1977 *inTopics in current physics* (eds) S W Lovesey and T Springer (Berlin: Springer-Verlag) pp 255

Springer T 1978 *in Topics in applied physics* (eds) G Alefeld and J Volkl (Berlin: Springer-Verlag) V pp 75

Stockmeyer R, Conrad H M, Renouprez A J and Fouilloux P 1975 *Surface Sci.* **49** 549

Stockmeyer R and Monkenbusch 1980 Paper presented at the 5th International Conference on Ze Napoli.

Tangari C, Summerfield G C, King J S, Berliner R and Mildner D F R 1980 *Macromolecules* **13** 1

Thaper C L, Dasannacharya B A, Sequeira A and Iyengar P K 1970 *Solid State Commun.* **8** 497

Thaper C L, Sinha S K and Dasannacharya B A 1982 *Neutron scattering* 1981 (ed.) John Faber Jr (New American Institute of Physics) pp 249

Twisleton J F and White J W 1972 *Neutron inelastic scattering* (Vienna: IAEA) pp 301

Twisleton J F and White J W 1972 *Polymer* **13** 40

Vagelatos N, Rowe J M and Rush J J 1975 *Phys Rev.* **B10** 4522

Wipf H, Magerl A, Shapiro S M, Satija S K and Thomlinson W 1981 *Phys. Rev. Lett.* **14** 949

Zaccai G 1978 in *Topics in current physics* (ed.) H Dachs (Berlin: Springer-Verlag) Vol. 6, pp 243

Bull. Mater. Sci., Vol. 6, No. 2, May 1984, pp. 165–175. © Printed in India.

Electrochemical preparation of potassium gold cyanide

INDIRA RAJAGOPAL and S R RAJAGOPALAN

Materials Science Division, National Aeronautical Laboratory, Bangalore 560017, India

Abstract. The essential requirements for the industrial preparation of potassium gold cyanide (PGC) are: (a) high rate of dissolution and (b) smooth and uniform dissolution. Employing galvanostatic and potentiostatic polarisation data and observations on the surface topography of anodes dissolved by both the techniques, it is shown that potentiostatic dissolution of gold in potassium cyanide at +0·345 V satisfies the above requirements.

Keywords. Electrochemical preparation; anodic dissolution; gold plating salt; plating; potassium gold cyanide.

1. Introduction

Electroplated coatings of gold are characterised by high conductivity, excellent resistance to corrosion, low contact resistance, and remarkable ability to form very good thermocompression bonds. Because of these properties electroplated gold coatings are extensively used in electronics and aerospace industries. These properties have their maximum value when the purity of deposited gold is highest, which in turn depends on the purity of the gold salt used in the preparation of the bath. Be it an acid, neutral phosphate, citrate or alkaline cyanide gold plating bath, potassium gold cyanide (PGC) is the starting material. It is therefore important that PGC used for preparing plating baths must be very pure.

There are two methods of preparing PGC namely, chemical and electrochemical. In the chemical method, gold is dissolved in aquaregia and is precipitated as fulminate by neutralising the solution with ammonia (Blum and Hogaboom 1958). There are a number of problems with this method. The fulminate should always be kept wet to prevent it from exploding. The yield of PGC depends critically on the conditions of precipitation. Under the best conditions the yield is 95 % (Blum and Hogaboom 1958).

Even though the loss is only 5 %, it is significant because of the high cost of gold. The purity of the salt prepared chemically will depend on the purity of gold used as a starting material. Besides it will invariably contain certain amount of chloride as an impurity. This is not desirable in the plating bath since it causes the dissolution of stainless steel anodes and thereby contaminates the bath with iron which is a deleterious impurity (Fischer and Weimer 1964; Graham Silver 1969). During the conversion of $AuCl_3$ to PGC by reaction with cyanide only auricyanide ($Au(CN)_4^-$) is formed which gets reduced to aurocyanide ($Au(CN)_2^-$) slowly or rapidly, depending on the conditions of plating (Britton and Dodd 1949; Foulke 1974). Thus a plating bath made from chemically prepared PGC will contain both mono and trivalent gold in solution. Their ratio will keep changing with the age of the bath, thereby making it difficult to judge the time needed to deposit a certain thickness. Thus it is seen that the chemical method is laborious, needs the skill of a trained person and yields a pl solution which contains undesirable chloride and auricyanide.

The electrochemical method depends on the direct anodic dissolution of gc cyanide solution (Blum and Hogaboom 1958; Visco 1974). Excepting fo description of a practical procedure for preparing PGC—by dissolving gold at cor current (Natarajan and Lalitha 1970)—no detailed study of this method appe: have been made.

The electrochemical method, though simple has its own problems. Gold ex passivity in cyanide solution at a relatively low current density (CD). Hence the a dissolution has to be carried out at a very low CD. The consequent disadvantage (a) the process is slow (b) it results in loss of gold due to disintegration of the a resulting from the etching type of dissolution that takes place at very low CD/s. though usable CD for dissolution can be increased by (a) vigorous stirring (b) rotating anode and (c) using forced circulation, the dissolution will still be c etching type. Besides, these methods of enhancing the rate are accompanied by th of loss of expensive gold solution by spillage and spray.

It has been demonstrated that alloying of gold with thallium or addition of tha to the electrolyte can prevent the gold becoming passive during its anodic dissolut cyanide solution (Cathro and Koch 1964). This method would not be acceptable f preparation of plating grade PGC because it would introduce thallium impurity i Thallium is an objectionable impurity in gold plating solution since it causes bonding of electrodeposited gold (Joshi and Stein 1972; Joshi *et al* 1975).

If the electrochemical method is to be useful for the industrial preparation of must satisfy the following requirements: (a) the rate of anodic dissolution m large; (b) the dissolution must be smooth and uniform; (c) it must be simi electropolishing.

Even though the anodic behaviour of gold in cyanide solution has been invest off and on during the last three decades, no systematic study for its use i preparation of PGC has been reported. In recent times, many workers (Kirk *et al* Pan and Van 1979; Kirk and Foulkes 1980; Kirk *et al* 1980; Thurgood *et al* have investigated the mechanism of anodic dissolution of gold in aqueous cy solution. These studies have thrown light on the mechanism of anodic dissol Information on the morphological characteristic of gold dissolved anodically different conditions is not available in the literature. This is essential for arriv conditions suitable for the electrochemical preparation of PGC. Hence we investigated the nature of the surface that results from the anodic dissolution o under different conditions and the results are presented here. From this stud conditions for the electrolytic preparation of PGC have been derived and the sa also presented.

2. Experimental

A H-type cell with a sintered glass-disc fused in the centre of the horizontal limb H-cell to prevent the mixing of the catholyte and anolyte was used. The cathode platinum wire wound as a coil. Gold was rolled as a sheet and used as an an microelectrode was used as anode for measurement with a bridge filled with solution of the same concentration (4%) as that of the anolyte and terminatir luggin capillary was used to measure the potentials. The luggin tip was placed close to the anode to minimise IR drop. The *I-E* curves under galvanostatic and potentiostatic polarisation were measured with standard experimental set-up.

Before each experiment the anode was cathodically cleaned in a 10% NaOH solution at a CD of $0{\cdot}2\ \mathrm{A/cm^2}$ for 1 min, rinsed in distilled water, dried and weighed. The anode was weighed after the experiment to determine the rate of dissolution for measuring current efficiency. The number of coulombs were calculated by integrating current time curves.

Experiments on the preparation of PGC were carried out using the H-type cell described above and employing gold foil of area $4\ \mathrm{cm^2}$ as anode. Ultrasonic agitation was done using vibronics ultrasonics tank (Vibronic model VPL-P1) at an intensity of $0{\cdot}3\ \mathrm{W/cm^2}$. All solutions were prepared from Analar KCN.

3. Results and discussion

Galvanostatic anodic *I-E* curves for gold in 40 g/l KCN solution after dissolving gold for different intervals of time at a CD of $10\ \mathrm{mA/cm^2}$ are given in figure 1. In all the polarisation curves, it is seen that anodic dissolution starts at a very negative potential, the actual value being dependent on the electrolyte composition. At potentials more negative to $-0{\cdot}6$ V, the current efficiency for dissolution is more than 100%. This is because at such potentials the dissolution of gold proceeds by chemical and electrochemical processes. The plateau in the *I–E* curve can be taken to represent approximately the limiting CD for dissolution of gold. It progressively decreases with increasing time of electrolysis because free cyanide concentration decreases and that of PGC increases with increased times of electrolysis. If this interpretation is correct, one would expect an enhancement of CD corresponding to the plateau in stirred solutions. The effect of ultrasonic (US) agitation is shown in figure 2. A two-fold increase in the limiting CD is noticed, which lends support to the view that the plateau is caused by diffusion limitation.

Photomicrographs of gold galvanostatically dissolved in KCN solution at various CD/s are given in figures 3 to 6 and using the data on current efficiency (table 1), *I–E* curves and observation of the surface under microscope, the following inferences can be made. At low CD (the region A–B in figure 1) gold is dissolved by crystallographically-controlled etching. Facets of grains and grain boundaries are clearly seen (figures 3, 4).

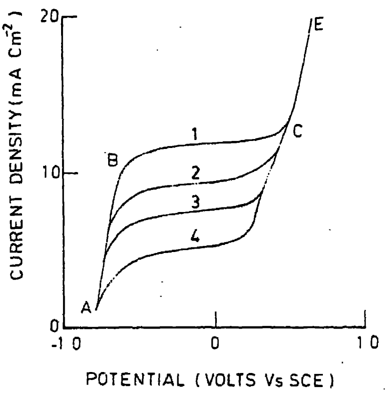

Figure 1. Galvanostatic anodic *I–E* curve for gold in KCN solution into which gold is dissolved for different intervals of time. Concentration of KCN (in gpl) and $\mathrm{KAu(CN)_2}$ respectively **1.** 40·0; **2.** After 1 hr of electrolysis at $10\ \mathrm{mA/cm^2}$. 35·7, 9·60; **3.** After 2 hr of electrolysis at $10\ \mathrm{mA/cm^2}$. 31·4, 19·4; **4.** After 3 hr of electrolysis at $10\ \mathrm{mA/cm^2}$. 27·1, 28·9 gpl.

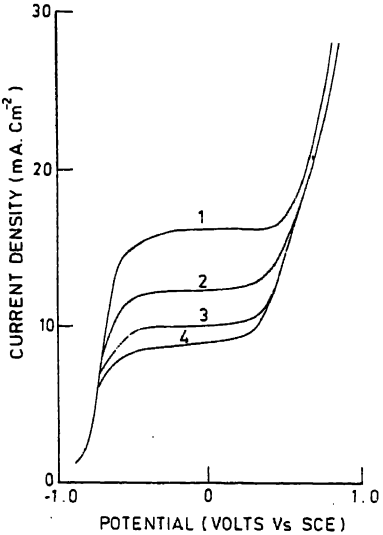

Figure 2. Galvanostatic anodic
for gold in KCN in the presence of
The other conditions are same as fo

The surface of the anode dissolved at BC corresponding to the plateau region, (
does not show grain boundary delineation and is smooth. In this region, the dis
of the metal must be occurring through pores present randomly in the film; whi
soluble in the electrolyte must be getting continually renewed. Hence the disso
similar to electropolishing. In the region, CE, the current rises rapidly be
oxygen evolution. The anode surface, under these conditions, is seen to be cove
a brownish film, which is probably the polymeric HCN film. The current e
progressively decreases with CD in this region because the anode is passive. Un
conditions the anode surface is seen to be pitted (figure 6).

From the point of view of preparation of PGC, the best condition
corresponding to the plateau. In practice, it will not be possible to keep the ano
plateau region for the entire period of the galvanostatic preparation of PG
following reasons: (a) The plateau region is an unstable region. (b) The CD cor
ing to the plateau region progressively decreases with increased times of ele
(curves 2,3,4 in figure 1). Hence if galvanostatic dissolution is employed, to s
the anode can be made to dissolve in the plateau region, but very soon, i

Table 1. Data on current efficiency for the galvanostatic dissolution of gold in 40 g
of KCN at 30°C.

CD (mA/cm^2)	t (min)	CE (%)
1	125	110 ± 3
2·5	50	102 ± 3
5	25	100 ± 2
7·5	14	100 ± 2
10	12.5	100 ± 2
15	8	90
20	6	70

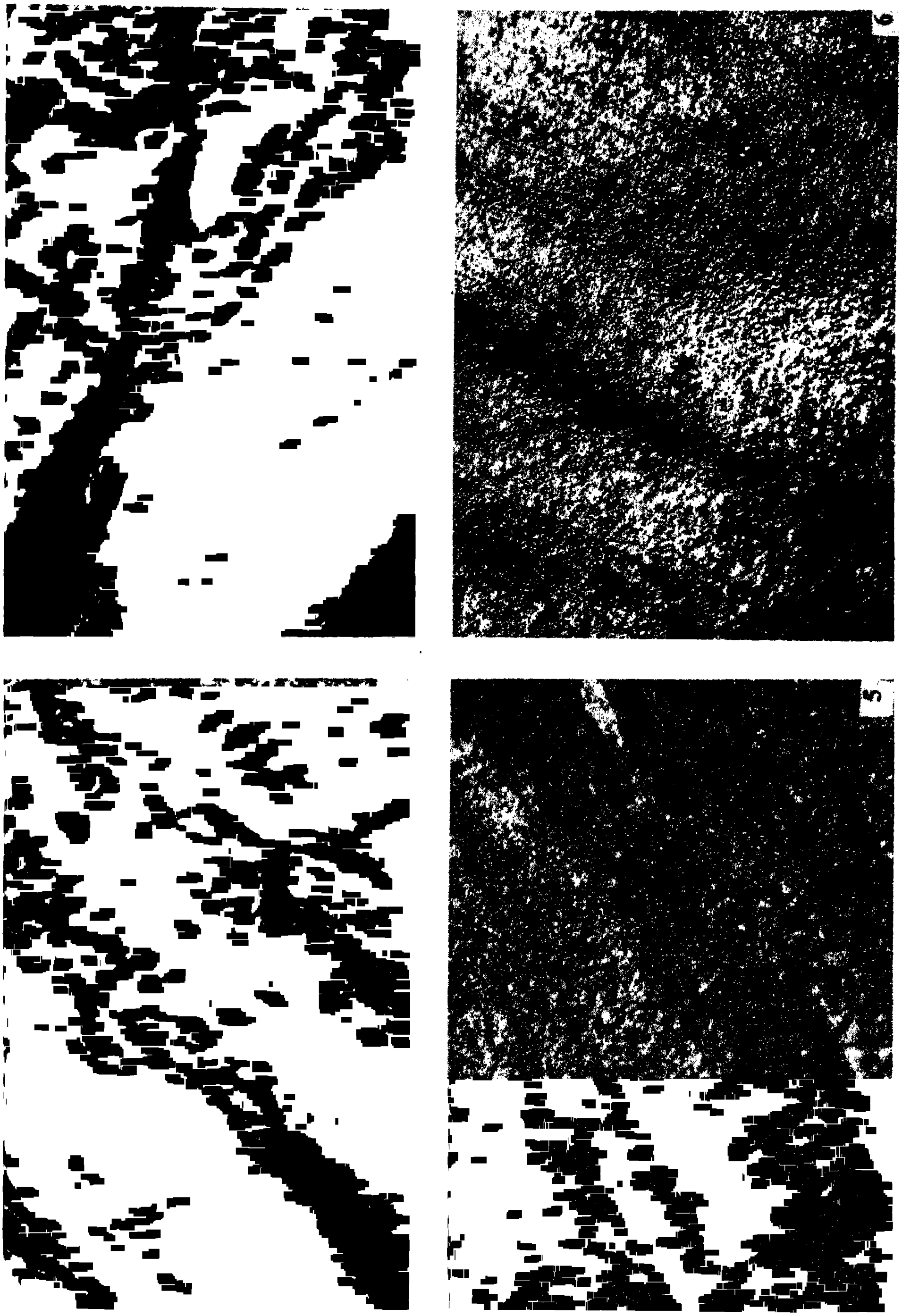

Figures 3–6. Photomicrograph of gold after dissolution for 10 min at 3. 2; 4. 8; 5. 10; 6. 14 mA/cm^2. (×100)

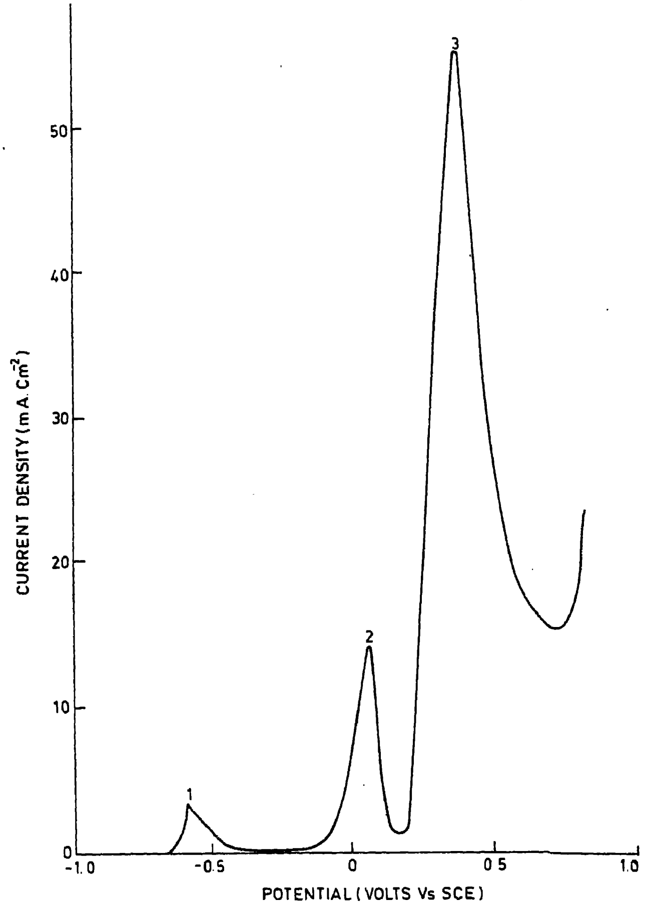

Figure 7. Potentiostatic anodic I–E curve for gold dissolution in 40 gpl KCN soluti

dissolving in the region CE. This is because, the limiting CD gets lowered as concentration of KCN decreases. If the anode is to be dissolved in the plateau re throughout the preparative run, the anode CD must be decreased in a program manner, which is not practical. Hence in practice for galvanostatic preparation o one has to employ only a very low CD falling in the region AB and has to accep concommitant disadvantages of low rate of production and loss of gold d disintegration of the anode towards the end of its dissolution.

A comparison of the galvanostatic and potentiostatic polarisation curve (fig reveals that the potential of the second and the third peak is in the plateau region galvanostatic polarisation curve.

Using the observation of Kirk *et al* (1979) that gold dissolves in potassium cyan the monovalent state at potentials less than + 0·4 V (SCE) and the current efficienc presented here, it is concluded that gold dissolves as aurocyanide at pote corresponding to second and third peak. Greater than 100% current effic observed at − 0·6 V is probably due to the additional chemical dissolution. Si behaviour was found in the galvanostatic dissolution.

Table 2. Data on current efficiency for the potentiostatic dissolution of gold in 40 gpl solution of KCN at 30°C.

Anode potential *vs* SCE (V)	*t* (min)	CE (%)
−0·4	120	110 ± 2
+0·5	60	102 ± 2
+0·35	30	100 ± 2
+0·75	60	90 ± 2
+0·85	30	80 ± 5

At a potential of −0·6 V gold appears to be undergoing etching type of dissolution (figure 8). The surface of the anode dissolved at +0·02 V appears relatively smooth and shows appreciable grain boundary attack (figure 9). Probably the dissolution is partly of the electropolishing type and partly of the crystallographic etching type. Kirk *et al* (1980) have ascribed the peak at +0·02 V to the formation of Au(OH) film which is not easily soluble in the electrolyte—hence the absence of electropolishing type dissolution.

The surface of the anode dissolved at the potential of +0·345 V (corresponding to the third peak) appears very smooth, bright and does not show grain boundary attack figure 10. No disintegration of the metal was noticed till the last trace of it was dissolved. The third peak was ascribed to the passivation by Au_2O_3 (MacArthur 1972; Cathro and Koch 1964) and to $Au(OH)_3$ (Pan and Wan 1979). Both Au_2O_3 and $Au(OH)_3$ can dissolve in cyanide solution and hence can result in electropolishing by the mechanism suggested by Hickling and Higgins (1956) and Hoar and Mowat (1950). Cathro and Koch (1964) found by reflectivity measurements an enhancement of reflectivity in the region of the third peak. These observations published in the literature and our observations on the microstructure of the anode polarised to +0·345 V compel us to conclude that at peak 3, an electropolishing type dissolution occurs. Even though the passive film at peak 3 contains trivalent gold, gold still dissolves only in the monovalent state (See current efficiency data in table 2.). This has been pointed out by Pan and Van (1979) and Kirk *et al* (1979). Our current efficiency data also confirm this.

If the passive layer causing the anodic peak is capable of dissolving in the electrolyte, one would expect the CD corresponding to the peak to increase with stirring. In figure 11 the effect of ultrasonic stirring on the potentiostatic polarisation curve for gold dissolution in a solution containing 28 gpl of $KAu(CN)_2$ and 29 gpl of KCN is shown. It is seen that ultrasonic stirring increases the peak CD thereby proving that the passive layer is soluble in the electrolyte. From the above discussion it is clear that potentiostatic dissolution of gold at +0·345 V (*vs* SCE) can be used for the electrochemical preparation of PGC. In our laboratory this method has been used quite successfully. The PGC prepared by this method is shown to be very pure by emission spectrographic examination. Without using ultrasonic stirring this method is 10 times faster than the galvanostatic dissolution method.

By this method gold foil can be dissolved almost completely without the foil getting necked at the solution air interface (figure 12) and subsequently getting detached at the necked region. Such necking and detachment takes place in galvanostatic dissolution

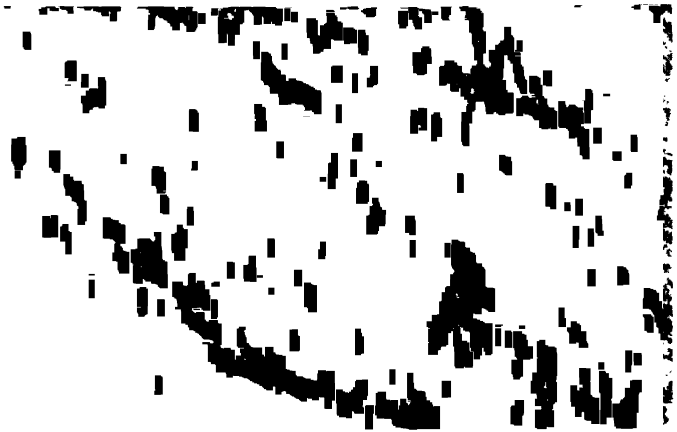

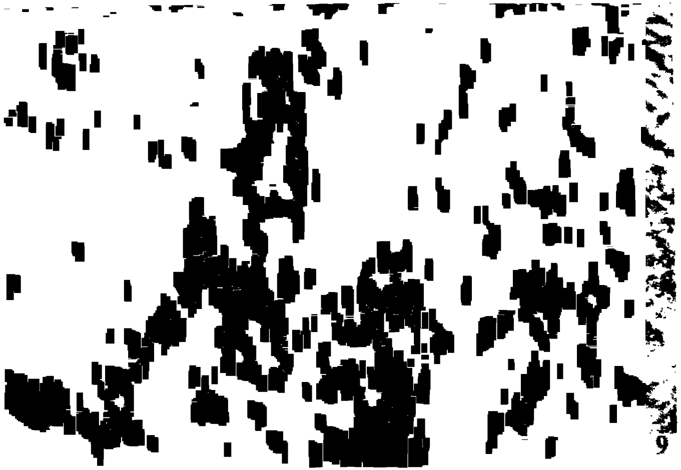

9

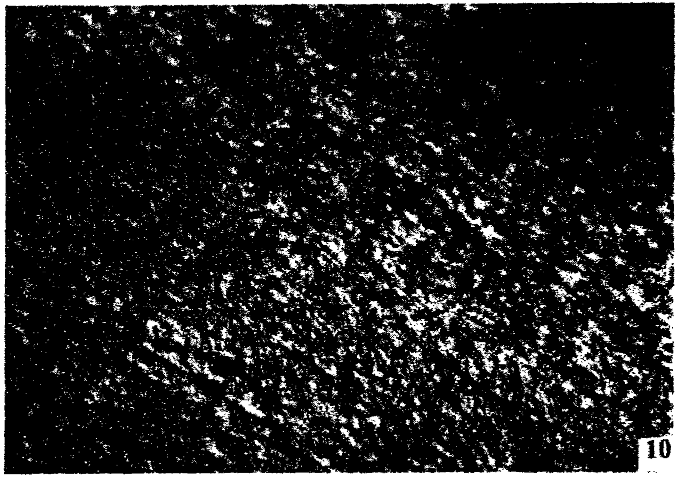

10

Figures 8–10. (× 100) Photomicrograph of gold dissolved under potentiostatic conditions for 10 mins at **8.** −0·6; **9.** 0·02; **10.** 0·345 V (*vs* SCE).

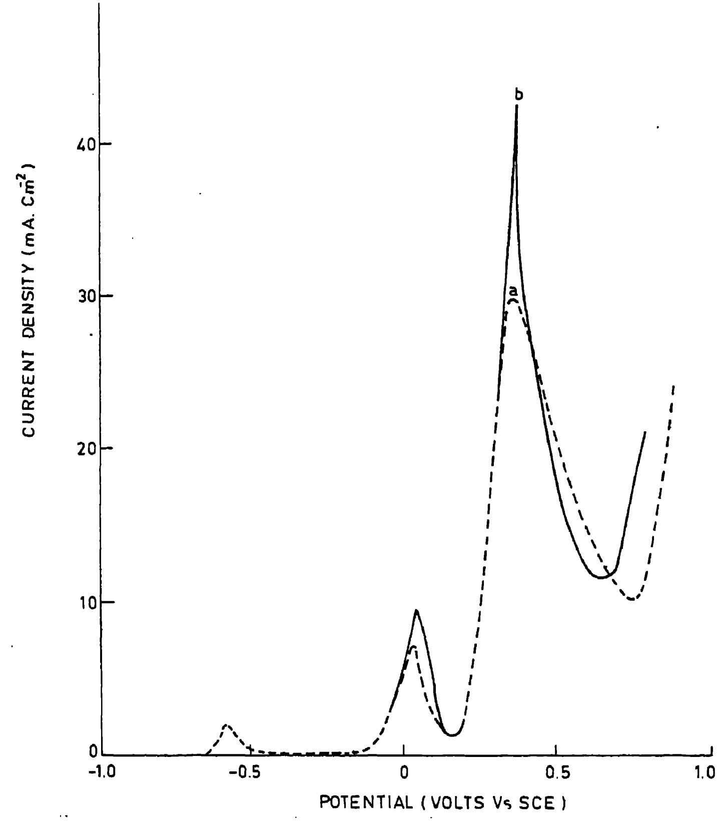

Figure 11. Potentiostatic anodic *I–E* curve for gold in KCN solution after 2 hr of dissolution (a) without US and (b) with US agitation.

(figure 13). Further this process helps to dissolve the gold foil very uniformly without disintegration from the start to finish (figures 14, 15).

In order to give an idea of the time needed for preparation of PGC the following data from our experience is given. 10 g of gold was rolled into a foil 12 cm long and 2 cm wide. This was dissolved in 200 ml of 40 gpl potassium cyanide solution potentiostatically at +0·345 V (*vs* SCE). In 1 hr the foil was completely dissolved.

4. Conclusions

Plating grade PGC can be prepared conveniently by the potentiostatic dissolution of gold in KCN solution at +0·345 V (*vs* SCE). This method is at least 10 times faster than the galvanostatic method. The rate of dissolution by this method can be enhanced by using ultrasonic stirring. The PGC produced by this method is free from chloride and auricyanide. In this method there is no loss of gold due to disintegration of the anode.

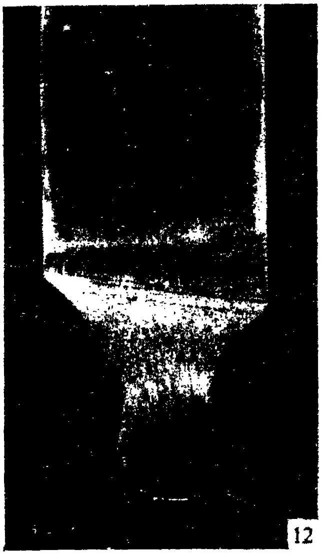

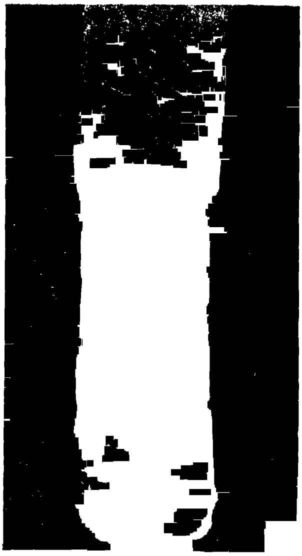

Figure 12. Appearance of gold foil anode after 95% of the foil has been dissolved potentiostatically at +0·345 V (*vs* SCE). The surface is seen to be smooth. No necking at the solution-air interface is observed.

Figure 13. Appearance of gold foil anode after 20% of the foil has been dissolved galvanostatically at 10 mA/cm^2.

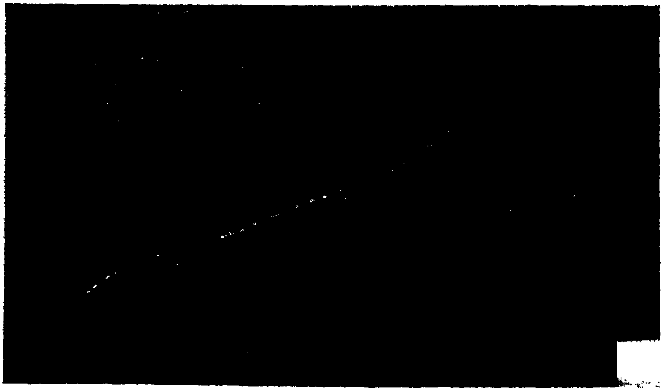

Figure 14. Cross-section of gold foil before dissolution (× 1).

Figure 15. Cross-section of gold foil after 95% of the foil has been dissolved potentiostatically at +0·345 V (*vs* SCE) (× 200).

References

Blum W and Hogaboom G B 1958 *Principles of electroplating and electroforming* (New York: McGraw Hill) p. 304

Britton and Dodd 1949 *J. Chem. Soc.* 1835

Cathro K J and Koch F A 1964 *J. Electrochem. Soc.* **111** 1416

Fischer J and Weimer D E 1964 *Precious metal plating* (Teddington: Robert Draper Ltd) 107

Foulke D G 1974 *Gold plating technology* (eds) F H Reid and W Goldie (Scotland: Electrochemical Publications Ltd) 21

Graham Silver H 1969 *J. Electrochem. Soc.* **116** 741

Hickling A and Higgins J K 1953 *Trans. Inst. Met. Finish* **31** 274

Hoar T P and Mowat J A S 1950 *Nature* (London) **165** 64

Joshi A and Stein D F 1972 *ASTM STP* **499** 104

Joshi A, Davies L E and Palmberg P W 1975 in *Methods of surface analysis* (ed) Czanderna (Amsterdam: Elsevier) 213

Kirk D W and Foulkes F R 1980 *J. Electrochem. Soc.* **127** 1994

Kirk D W, Foulkes F R and Graydon W F 1978 *J. Electrochem. Soc.* **125** 1436

Kirk D W, Foulkes F R and Graydon W F 1979 *J. Electrochem. Soc.* **126** 2287

Kirk D W, Foulkes F R and Graydon W F 1980 *J. Electrochem. Soc.* **127** 1962

Kushner J B 1940 *Prod. Finish* p. 32

MacArthur D M 1972 *J. Electrochem. Soc.* **119** 672

Natarajan S R and Lalitha K S 1970 *Met. Finishing* **68** 2

Pan P and Wan C C 1979 *J. Appl. Electrochem.* **9** 653

Thurgood C P, Kirk D W, Foulkes F R and Graydon W F 1981 *J. Electrochem. Soc.* **128** 1680

Visco R E 1974 in *Modern electroplating* (eds) E F A Lowerhem (New York: John Wiley) p. 225

Bull. Mater. Sci., Vol. 6, No. 2, May 1984, pp. 177–192. © Printed in India.

Hydrothermal growth of $A^{II}B^{VI}$ semiconductors

V A KUZNETSOV, I P KUZMINA and I M SYLVESTROVA

Institute of Crystallography of USSR Academy of Sciences, Leninsky pr. 59, Moscow 117333, USSR

Abstract. Hydrothermal method is used for growing ZnO, ZnS and HgS single crystals. This method is more advantageous compared to the other ones and enables one to obtain large bulky crystals of technically convenient habit with low concentration of defects. Some physical properties of these single crystals were studied and active elements for the new advanced piezoelectric, electro-optic and laser devices are reported.

Keywords. Semiconductors; hydrothermal growth; piezoelectric; electro-optic; laser devices.

1. Introduction

$A^{II}B^{VI}$ semiconductors—zinc oxide and sulphide, mercury sulphide—are widely known as the advanced materials for different fields of technology due to the combination of various physical properties. Interest in these compounds was stimulated in recent years by the development of new methods of growth and possibilities of studying more profound properties. Thus, detailed investigation of zinc oxide elastic and electric characteristics puts this material in the forefront among the possible high-temperature piezoelectrics. Cubic ZnS is a potentially useful material for optical shutters and electro-optical modulators. Cinnabar, or mercury sulphide, can be used where a combination of acousto-optical and piezoelectric properties is required. Piezoelectric modulus of Cinnabar is greater by an order of magnitude, than that of quartz while electromechanical coupling coefficient is two times larger. The acousto-optical interaction coefficient (M_2) for $\lambda = 632$ nm, and longitudinal wave propogating along the optical axis with $2{\cdot}45 \times 10^5$ cm/sec rate, is 690×10^{-18} sec^3/g. This value is comparable with that of TeO_2, used in optoacoustical devices. The large value of rotation of plane of polarization and other interesting properties of Cinnabar are also well-known.

The new prospects of technical application of the above materials demand good crystals and methods for obtaining them. The crystal should possess: high optical homogeneity, perfect structure and thechnically convenient habit. Traditional methods of growing ZnO, ZnS and HgS single crystals (from a melt, vapour phase, flux) do not always meet these requirements.

Thus, the Stockbarger's technique, developed for growing zinc sulphide from the melt at 50–200 atm. of inertial gas pressure (Shternberg *et al* 1962; Kuznetsov 1964; Ananiev 1968; Kozielski 1967; Sysoev 1972; Obuhova *et al* 1977) enables one to obtain large ZnS crystals up to 40 mm in size (Kozielski 1967), (this method is not practically used for ZnO and HgS because of high melting-point and high vapour pressure at melting point), but crystals grown by this method are structurally inhomogeneous—containing a high concentration of packing faults and the combination of the cubic and hexagonal ZnS modifications (the cubic one being larger in proportion). Under crossed polarizers the crystal produces a pattern of alterating dark and light lines, indicative of its optical inhomogeneity, making it impossible for use in electrooptics.

In spite of numerous attempts, the flux method failed to provide large bulky ZnO, ZnS and HgS crystals. For ZnO the slow cooling of zinc oxide solution in lead fluoride melt (Kashyap 1973; Nielson and Dearborn 1960) from 1150 down to 800°C enabled to obtain large, but very thin ZnO plates. The same results were obtained by the other workers (Wolff and Labelle 1965; Chase and Osmer 1967; Timofeeva 1965; Wanklyn 1970). Besides the "inconvenient" habit, the flux grown ZnO crystals are non-stoichiometric, extremely heterogeneous and contain high concentration of impurities and melt inclusions.

The flux method yields only small zinc and mercury sulphide crystals of several mm in size (Harsy 1968; Babansky *et al* 1971; Chernyshev and Babansky 1977; Laudise 1963; Mita 1962; Parker and Pinnel 1968; Linares 1968; Samelson and Brophy 1961; Garner and White 1970; Nistor *et al* 1980). As a rule they are very faulty, contain large amount of melt inclusions and have dendrite morphology. However, ZnS obtained by this method proved to be perfect enough. Practically, ZnS crystals, grown at 575°C (Nistor *et al* 1980), were cubic. This fact shows, that on the contrary to melt methods, ZnS crystallization at low temperatures (much lower, than wurtzite-sphalerite phase transition point (1020°), enables to obtain crystals with high structure homogeneity.

This is clearly revealed when ZnS crystallizes from a vapour phase. At crystallization temperatures higher than 1000°C (Iwanaga *et al* 1979; Scharowsky 1953; Park and Reynolds 1967; Dodson and Savage 1968; Nielson 1968; Hirose 1971) the crystals were characterized by the high packing faults concentration like the melt grown ones. Under polarized light they produce the clear pattern of dark and light lines similar to the melt grown samples. Crystals were small, and only at maximum temperatures (1500–1600°C) samples of length 30–40 mm and diameter 10 mm were obtained.

The lowering of the crystallization temperature below 1000°C (Neviantseva *et al* 1972; Rabadanov *et al* 1970; Piper and Roth 1953; Green *et al* 1958) significantly improves the perfection of the crystals—packing fault concentration falls drastically—and there are even some evidences of pure cubic ZnS formation at 770–900°C (Piper and Roth 1953). However, large bulky crystals more than several mm in size at such low temperatures could not be obtained.

All attempts to obtain cinnabar crystals from vapour phase resulted in growing of either faulty and apparently inhomogeneous crystals up to 7 mm (at 580–750°C), or rather perfect, but small 1–2 mm crystals (at temperatures lower than 344°C) (Brafman *et al* 1964; Brafman and Steinberger 1966; Rumiantsev 1965).

Much progress was achieved in developing methods for growing ZnO from the vapour phase—(Rumiantsev *et al* 1965; Alexander *et al* 1970; Lendway 1971; Sasaki 1975; Shichiri *et al* 1978; Russel and Woods 1979; Pashkovsky *et al* 1961; Carloon 1967; Pottor and Barnes 1978; Faile 1978). These methods are based either on oxidation of zinc chalcogenides by oxygen or water vapour (Pashkovsky *et al* 1961; Carloon 1967), or on oxidation of zinc vapour by oxygen (Lendway 1971) at 1150–1350°C. The latter enabled to obtain some ZnO crystals of 7 × 7 mm^2 in size (Shichiri *et al* 1978; Russel and Woods 1979), but the yield of crystals was small, and the samples were mainly needles with the length not more than 10 mm. Moreover as grown ZnO crystals are highly nonstoichiometric.

Thus, each of the above methods results in specific faults in the crystals. None of them meets the requirements specified above. Crystallization at relatively high temperatures results in noticeable nonstoichiometry (for ZnO) and structural inhomogeneity (for ZnS, HgS).

Lowering of the crystallization temperature significantly improves the crystal quality, but the small dimensions exclude their wide practical application. It is difficult to choose a versatile method which enables growth of crystals for all applications, but in the light of earlier discussion, combining low crystallization temperatures with the possibility of obtaining large crystals seems to be the most advanced one.

The present work discusses growth of ZnO, ZnS and HgS by the hydrothermal method. Relatively low crystallization temperatures—200–400°C (*i.e.* much lower than their melting and phase transition points) enable one to reduce the amount of faults which are characteristic for high temperature samples. Moreover, by varying chemical crystallization conditions, it is possible to control the defect structure and stoichiometry and by continuing of the process it is possible to obtain large crystals. Thus, the hydrothermal method seems to be the most advanced one meeting all the requirements.

2. Methods

The hydrothermal method is based on the crystallization of a substance from overheated aqueous solutions at pressures (usually 100–2000 kg/cm^2) (Michaelski *et al* 1979). The process is carried out in the special steel autoclaves. In the more often used variant of 'direct temperature drop' method the initial charge is placed in the lower part of the vessel, where the temperature is maintained higher, than in the upper part. The latter contains a seed crystal. Temperature drop (ΔT) between the zones of growth and dissolution leads to a convection inside the autoclave: in the lower zone, the solution gets saturated with the charge, heats up and moves to the upper zone. It cools here, becomes supersaturated and the excess substance condenses on the seed. The cooled solution goes down and the process repeats until all the initial charge is transferred to the upper zone. We have used this method in this work. The parameters that are varied: supersaturation (expressed in terms of supercooling ΔT for convenience), composition and concentration of the solution, seed orientation and temperature. The experiments have shown, that pressure was not significant in our cases, except in some special situations.

2.1 *Growth of ZnO crystals*

The growth was performed in KOH and NaOH solutions, where ZnO solubility reaches a significant value at elevated temperatures (Laudise and Caporaso 1964; Anamov *et al* 1972; Kuznetsov and Lobachov 1972; Kuzmina *et al* 1970). The solutions contained the adding of LiOH, which influenced the morphology, growth rates and quality (Laudise and Caporaso 1964). Optimum solution concentrations, crystallization temperatures and temperature gradients were found experimentally. The initial charge contained chemical ZnO agent and polycrystalline ZnO, hydrothermally synthesized beforehand. The first seeds were grown from the flux according to Kashyap (1973) and Nielson and Dearson (1960) and later on replaced by the hydrothermal ones. In some cases ZnO needles and plates, grown by gas transport reactions, were used as seeds. Our preliminary studies have shown, that growth of the crystal is fastest in the (0001) direction. So, the plates oriented parallel to (0001) planes, were used as seeds. The temperature range under study was 200–450°C. Figure 1 presents the concentration dependence of (0001) plane growth rate for ZnO at $T = 270°C$, $\Delta T = 70°C$ (ΔT is measured along the outside autoclave wall). The exponential form of the curve is universal, *i.e.* is not influenced by temperature and temperature gradients.

Figure 2 presents (0001), (000$\bar{1}$), (10$\bar{1}$0) growth rates *vs* temperature for two temperature gradients ($\Delta T_1 = 50°C$, $\Delta T_2 = 75°C$) in 5·15 m KOH + 1·2 m LiOH solution. One can see that the growth rates increase with temperature, but their relationship decreases. The values obtained for critical supersaturation (expressed in terms of ΔT_{cr}), have shown, that ΔT_{cr} is minimum for (0001) plane, which grows noticeably at low supersaturations (Lobachev *et al* 1982).

Since the growth rates in KOH solutions are higher than in NaOH solution under similar conditions, KOH solutions were used. ZnO growth kinetics was not practically influenced by the pressure changes within 100–600 kg/cm^2, however the crystal quality declined significantly at lower pressures (< 100 kg/cm^2). The above experimental data show that the large growth rates of ZnO (> 0·1 mm/day) can be achieved within the wide temperature and solution concentration ranges. For better understanding of the

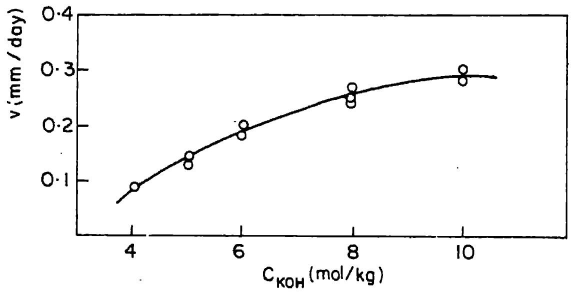

Figure 1. KOH concentration dependence of (0001) plane growth rate for ZnO.

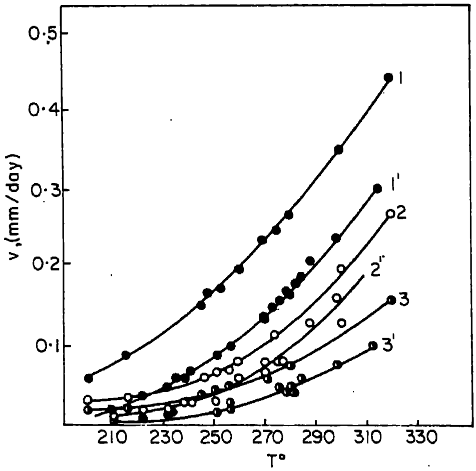

Figure 2. Temperature dependence of (0001) (curves 1, 1'), (000$\bar{1}$) (curves 2, 2') and (10$\bar{1}$0) (curves 3, 3') growth rates for ZnO. ($C_{KOH} = 5{\cdot}15$ m/kg, $C_{LiOH} = 1{\cdot}2$ m/kg, $\Delta T = 75°$ and $T = 50°$ for curves 1–3 and 1'–3' respectively.).

crystallization conditions cathodoluminescence study of variously grown ZnO crystals was performed (Lobachev *et al* 1977). The spectral analysis, mainly of the half-width of narrow resonance cathodoluminescence lines and the possibility of their resolution, shows, that the crystals grown at 250–300°C, with supersaturations corresponding to $\Delta T = 40$–$50°\text{C}$ have better perfection (Laudise and Caporaso 1964; Kuzmina *et al* 1970; Lobachev *et al* 1982). The crystal perfection declines, when the temperature lies outside the above range.

Assuming all the experimental data, we have optimized ZnO growth conditions: crystallization temperature = 260–290°C, $\Delta T = 40$–$50°\text{C}$, pressure ~ 600 kg/cm^2, concentration of KOH = 5–10 m, LiOH = up to 1·5 m. (0001) growth rate was 0·1–0·25 mm/day under these conditions, which enabled one to obtain bulky ZnO crystals of several cm^3 in size in the prolonged experiments. Figure 3 represents one of such crystals.

Despite the low crystallization temperatures, hydrothermal ZnO crystals, as well as other grown ones, are not stoichiometric enough, which might be conditioned among other reasons by the reductional medium inside the autoclave. The excess zinc atoms (their concentration may reach 10^{15}–10^{19} cm^3), located in the interstitials, and oxygen vacancies are fixed in the crystals. These point defects are responsible for the light yellow colouration of the crystals (also caused by Fe impurity) and the elevated

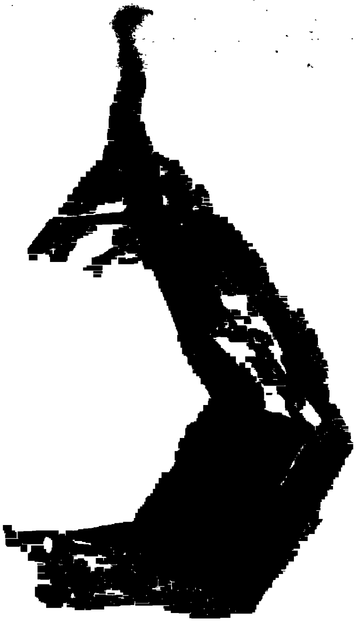

Figure 3. Hydrothermal ZnO crystal (natural size).

conductivity; usual ZnO resistance lies within 10^1–10^4 ohm. cm. The annealin 700°C in the presence of lithium salts (Laudise and Caporaso 1964) leads to a signif rise of resistance. Lithium doping during the annealing increases the resistance u 10^{11} ohm. cm which broadens their practical application.

The hydrothermal growing of large, isometric ZnO crystals, enabled to make evaluations of their elastic, dielectric, piezoelectric and laser properties (Croxall 1974; Heiland *et al* 1959; Tokarev *et al* 1975; Kurbatov *et al* 1980). Table 1 present complete set of elastic, dielectric and piezoelectric constants of ZnO at room tempera

The measurements have revealed the unique feature of ZnO crystallization- slight dependence of the elastic characteristics and the electromechanical cou coefficients on temperature (figure 4). Thus, the average temperature coefficient v of the elastic constants proved to be equal within 300–700°C range. (in gra $T^E_{s_{11}} = 7{\cdot}5 \times 10^{-5}$, $T^E_{s_{12}} = 5{\cdot}4 \times 10^{-5}$, $T^E_{s_{55}} = 7{\cdot}1 \times 10^{-5}$, $T^D_{33} = 12{\cdot}3 \times 10^{-5}$, T $-6{\cdot}9 \times 10^{-5}$.

Coefficients of dielectric constants, measured at room temperature (in grad^{-1}

$$T^T_{11} = 4{\cdot}3 \times 10^{-4}, T^T_{33} = 4{\cdot}4 \times 10^{-4}.$$

Electromechanical coupling coefficients of ZnO are the largest among all the kn nonferroelectrics and are practically constant up to 1000 K. Thus, piezoel properties of ZnO are preserved in a wider temperature range than those of the w used materials (quartz, for instance). It enabled to construct high effective piezoel

Table 1. ZnO elastic, dielectric and piezoelectric constants at room temperature

Characteristics	Numerical value	Characteristics	Numerical value
s^E_{11}	0·791	c^E_{11}	20·70
s^E_{33}	0·72	c^E_{33}	20·95
s^E_{12}	−0·33	c^E_{12}	11·77
s^E_{13}	−0·235	c^E_{13}	10·61
s^E_{55}	2·23	c^E_{55}	4·48
s^E_{66}	2·42	c^E_{66}	54·46
s^D_{11}	0·765	c^D_{11}	20·96
s^D_{33}	0·56	c^D_{33}	22·1
s^D_{12}	−0·36	c^D_{12}	12·04
s^D_{13}	−0·17	c^D_{13}	10·13
s^D_{55}	2·14	c^D_{55}	4·61
d_{31}	−5·12	e_{31}	−0·62
d_{33}	12·3	e_{33}	0·96
d_{15}	−8·3	e_{15}	−0·37
k_{31}	0·181	ε^t_{11}	8·67
k_{33}	0·466	ε^t_{33}	11·26
k_{15}	0·199	ε^s_{11}	8·33
k_t	0·229	ε^s_{33}	8·81

($s - 10^{-11}$m^2/n, $d - 10^{-12}$q/n, $c - 10^{-10}$n/m^2, $e -$ q/m^2)

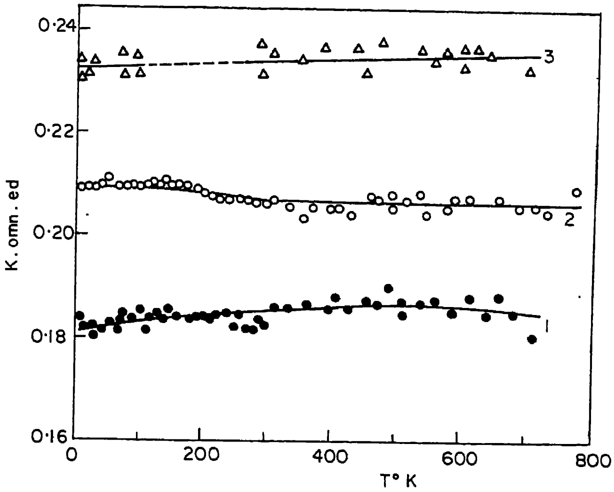

Figure 4. Electromechanical coupling coefficients temperature dependence for ZnO. 1. k_{31}; 2. k_{15}; 3. k_t (Tokarev *et al* 1975).

sound transducers on lithium doped ZnO crystals, worktable up to 1000 K (Tokarev *et al* 1975).

ZnO active elements for semiconductor electron pumped lasers in UV range have also been designed (figure 5) (Kurbatov *et al* 1980). ZnO lasing spectrum presents two lines with 375 and 383 nm maxima and 1·5–2 nm halfwidth (figure 6). The value of the radiation power reaches 3–5 kW in 3–5 nc pulse at 80 K as well as at room temperature (voltage $U = 115$ kV, electron beam density $j = 60$ A/cm^2).

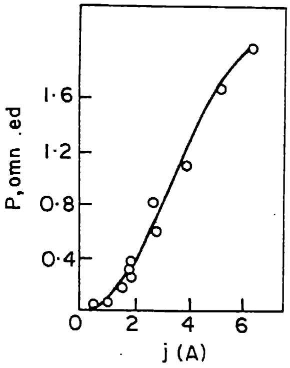

Figure 5. Pumping current I and acceleratng voltage V dependence of radiation pulse power *P* for sealed lasers (Kurbatov *et al* 1980).

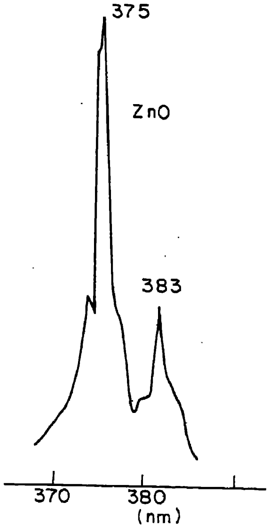

Figure 6. Lasing spectrum of ZnO laser targets at liquid nitrogen cooling. (Kurbatov *et al* 1980).

ZnO laser with an output power about 300 W allowing filtering, has bee constructed. The lasing was observed at liquid nitrogen cooling with threshold electro beam density $j = 60$ A/cm^2 and voltage $U = 34$ kV.

2.2 *Growth of ZnS crystals*

The wide stability zone of ZnS in hydrothermal solutions provides the fundamenta possibility of usage of various media when crystal growing, which enables wid variation of physical-chemical crystallization conditions. Two procedures for Zn growth are the most applied ones: in the extremely acid (H_3PO_4) and alkaline (KOH CsOH) solutions. The comparison of the crystals, grown under such differen conditions, enabled to evaluate the influence of physical-chemical parameters on th faults present.

ZnS crystallization in H_3PO_4 solutions was performed at 380–450°C with H_3PO concentration up to 50 mass %. The seed crystal fast growing plane (111) growth ra reached ~ 0·15 mm/day, which enabled to obtain 2–3 cm^3 ZnS crystals in prolonge experiments. Lowering of H_3PO_4 concentration leads to diminishing of growth rate and its increase provides an extremely reducing condition in the autoclave (due to H_2 intensive releasing, when dissolving of the initial ZnS charge), which results i increasing amount of defects. First of all it caused the intense colouration of th crystals.

ZnS crystallization study in KOH and CsOH solutions was performed withi 350–420°C range, at concentrations up to 10 m. Figure 7 presents KOH concentratic dependence of ZnS (111) plane growth rate. The dependence is the same in CsO solutions. Temperature slightly influences ZnS crystallization rate, which practical does not change at constant temperature and with KOH concentration more th ~ 4 m (figure 7). The crystal growth was performed at 380°C, KOH and CsO concentrations ~ 8 m, $\Delta T = 5$–10°C. Under these conditions (111) growth ra reached 0·1 mm/day in KOH solutions and 0·07 mm/day CsOH solutions. V preferred to use CsOH solutions, because the crystals grown in them were more perfe although the growth rate in CsOH solution was less. One such as-grown ZnS crystal presented in figure 8.

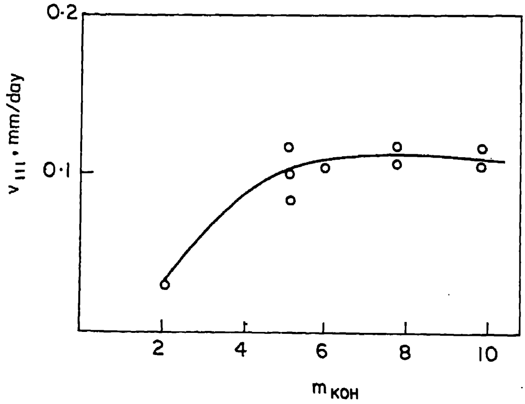

Figure 7. KOH concentrational dependence of (111) plane growth rate for ZnS ($T = 38$ $\Delta T = 8$°C).

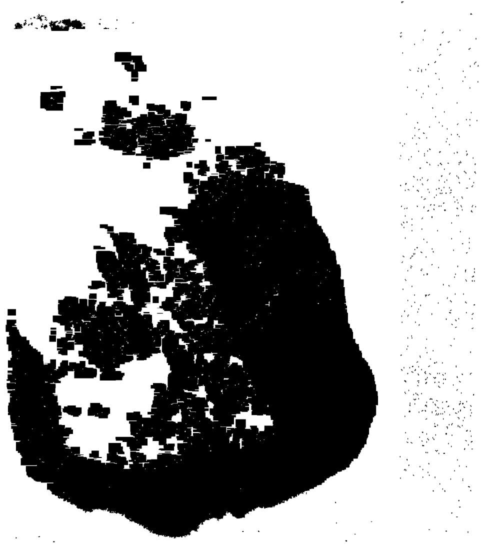

Figure 8. Hydrothermal ZnS crystal (× 4).

Optical and cathodoluminescence studies have shown a substantial difference in the defect structure of variously grown ZnS crystals (Shalimova *et al* 1974a, b; Morozova *et al* 1979; Galstian *et al* 1980). First of all, it is visually revealed in the different optical homogeneity of the materials. H_3PO_4 grown ZnS crystals are more optically homogeneous and as a rule look isotropic under crossed polarizers. Alkaline grown ZnS crystals are usually anisotropic. The reasons for this lie mainly in the different way of oxygen impurity trapping. Indeed, the chemical analysis showed that oxygen impurity containment in KOH grown ZnS crystals reached 0·7 at . %, while in CsOH — ~ 0·3 at . % (the quantity of oxygen impurity is correlated with that of the alkaline metal: K enters ZnS up to 0·3 at . % facilitating oxygen trapping according to the volumetric compensation principle, while Cs^+ concentration does not exceed ~ 0·1 at . %). Oxygen impurity concentration in H_3PO_4 grown ZnS crystals does not exceed 0·4 at . %. Cathodoluminescence spectra provide more detailed information concerning ZnS defect structure. The most characteristic spectral features of various ZnS crystals are as follows:

335 and 415 nm radiation and the intense edge luminescence are characteristic for H_3PO_4 grown crystals. Such a spectrum is indicative of the high concentration of point defects, practically no packing faults, and oxygen impurity, concentrating mainly on the specific defects (radiation at 415 nm).

338 and 368 nm radiation and the weak edge luminescence are characteristic of KOH and CsOH grown crystals. 415 nm radiation is not present. Such a spectrum is indicative of an elevated oxygen impurity concentration (sometimes it precipitates in the form of microscopic Zn(S, O) solid phase inclusions), the very low point faults

concentration, but higher (in comparison with 'acid' samples) packing faults concentration (not exceeding 1 %). The elevated presence of oxygen impurity in 'alkaline' ZnS and its precipitation in the form close to Zn(S, O) solid solution result in the above mentioned optical inhomogeneity of such crystals (Morozova *et al* 1979). Since oxygen is less trapped in CsOH solutions, the crystals obtained are more optically homogeneous.

Besides optical homogeneity, the differences in ZnS defect structure are revealed in some other properties also. Thus, the elevated point defects concentration in acid grown samples is responsible for their higher photoconductivity and lower resistance in comparison with alkali-grown samples (~ 10^{10} Ohm/cm against ~ 10^{12} Ohm/cm). Acid grown samples are mainly greenish-brown, while alkaline grown ones are colourless and transparent within 0·23–12 nm (Shamburov *et al* 1970). All these distinctions are significant for usage of ZnS as electro-optic material.

Figure 9 presents the typical light transmission curves of 'alkaline' (111) ZnS cuts at transverse electro-optic effect under crossed polarisers *vs* voltage V (Shamburov *et al* 1970). One can observe the initial light transmission, characterizing optical homogeneity of the crystals, to be about 1·5–2 %. The measured halfwave voltage is ~ 10·5 kV at 630 nm and falls to ~ 8·5 kV at 500 nm (figure 10). The residual voltage of 'acid' crystals is lower than that of 'alkaline' ones, but the halfwave voltage varies from ~ 8 to ~ 15 kV. The latter might be conditioned by the screen effects due to the electric field application and higher mobility charge carriers in such crystals.

Thus, on account of the homogenous nature of ZnS obtained by hydrothermal method, the crystals can be used in optical shutters and light modulators within 0·4–13 nm. Note, that cubic ZnS, on the contrary to uniaxial crystals, enables to create wide angle modulators, necessary, *e.g.* in convergent beams modulation. So, it is possible to obtain 100 % modulation depth for the beam converging at 12°, when applying the transverse electro-optic effect in (110) cut at $\langle 1\bar{1}0 \rangle$ field orientation; the crystals were 4 and 0·4 mm in light and field directions respectively (Shamburov *et al* 1970).

ZnS transparency in UV region enables their effective usage for overfrequency

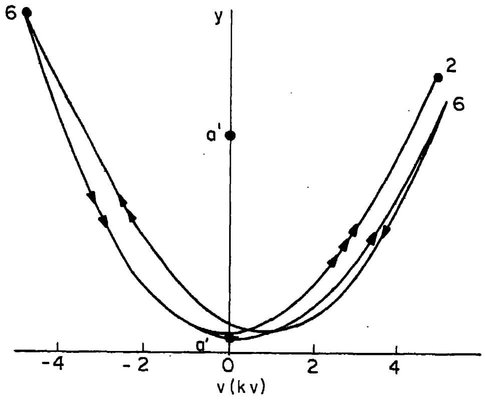

Figure 9. Light transmission curve for transverse electro-optic effect in ZnS crystal (111) cut when crossed polarizers. The curve looks like a "butterfly" hysteresis loop (Shambunov *et ai* 1970).

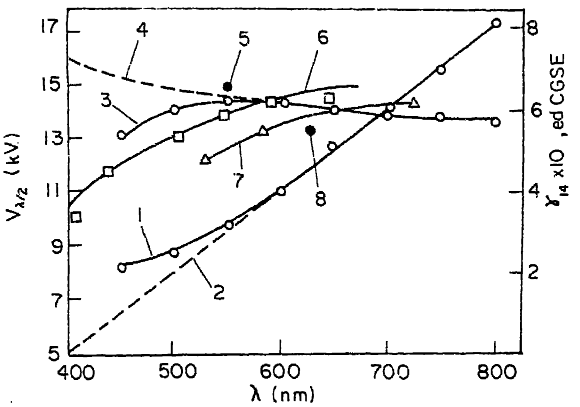

Figure 10. Wave length (λ) dependence of halfwave voltage $V_{\lambda/2}$ and electrooptical coefficient r_{41} (Shamburov *et al* 1970). **1.** $V_{\lambda/2}$ (λ); **2.** the extension of curve 1 linear part; **3.** $r_{41}(\lambda)$; **4.** the curve 3 extension, corresponding to curve 2; **5, 6, 7, 8**—$r_{41}(\lambda)$ for natural ZnS.

Table 2. Optical characteristics of ZnS and ZnSe.

λ nm	$M_\omega \cdot \tau_\lambda$ %	
	ZnS	ZnSe
0·44	16	—
0·53	17	16
0·63	18	21

τ_λ–modulation depth; M_ω–crystal transparency.

modulation of the radiation with < 0·5 nm (Kuznetsov *et al* 1980). Table 2 compares the characteristics of ZnS and ZnSe, widely used for this purpose now. At 0·53 nm ZnS is more effective than ZnSe, and below 0·53 nm ZnSe is not used because of high absorption. So, ZnS enables to perform overfrequency modulation of the radiation with $\lambda < 0{\cdot}5$ nm.

The spectra of electron pumped ZnS lasing have been studied (Kurbatov *et al* 1980). Laser target resonators have been specially made by spalling along the cleavage plane. Minimum ZnS lasing voltage was 40 kV at threshold electron beam density of 11 A/cm^2. A set of lines within 330–337 nm range with the most intensive one at 336 nm (~ 1·5 nm halfwidth (figure 11) was fixed in the lasing spectrum. The radiation power was 500–700 W in 3–5 nc pulse at 80 K. The lasing parameters are indicative of the high laser quality of ZnS, radiating in the most shortwave range in comparison with other known materials.

2.3 *α-HgS crystallization*

Unlike ZnS, the narrow stability zone of cinnabar substantially limits the solvents selection for crystal growth (Kuznetsov *et al* 1973; Tondic *et al* 1972). Rather intensive HgS recrystallization (without decomposition) was found to occur in sodium and potassium hydrosulphide solutions with pH 9–13 (Efremova *et al* 1976). HgS solubility

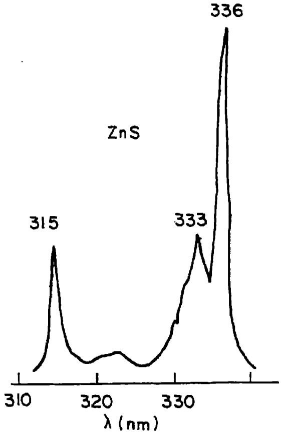

Figure 11. Lasing spectrum of ZnS laser targets at liquid nitrogen cooling (Kurbatov *et al* 1980).

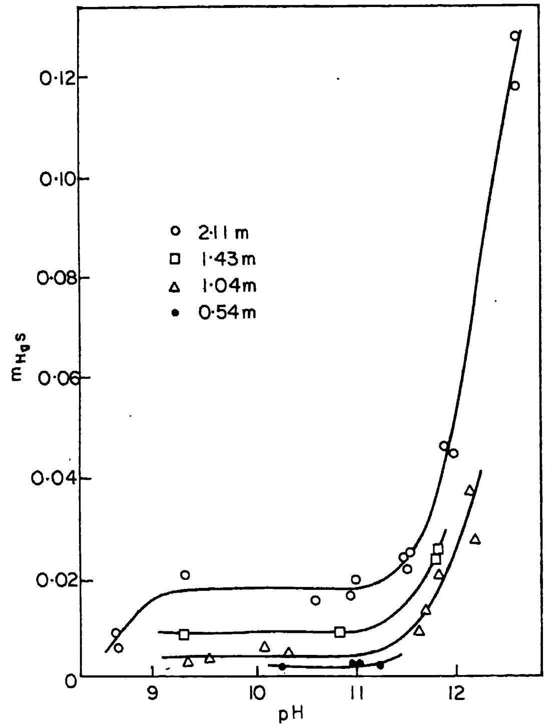

Figure 12. α-HgS solubility within 8·5–12·5 pH range in NaHS solutions of different concentrations (Efremova *et al* 1976).

study in NaHS solutions enabled to choose two pH zones (figure 12): the one, where HgS solubility does not depend on pH (9–11·5), the other, where solubility rises when pH increases (pH > 11·5). Such solubility behaviour is conditioned by various compositions of the Hg complexes formed in solution (Efremova *et al* 1982).

Table 3. Growth rates of HgS on (0001) and (1010).

Solution	pH	V(mm/day)	
		(0001)	$(10\bar{1}0)$
$Na_2S + H_2S$	9–11	0·5	0·3
$Na_2S + H_2S$	12–13	0·1	0·05
$Na_2S + NH_4Cl$	12–13	0·05	0·02
$Na_2S + NaHCO_3$	12–13	0·2	0·07

(Temperature – 280°C; ΔT – 30°C)

Assuming the solubility data, cinnabar crystallization in NaHS solutions was performed within 9–11 and 12–13 pH intervals. The solutions with such pH values were obtained by: the saturation of Na_2S solution (pH > 13) with hydrosulphide, by addition of ammonium chloride or sodium bicarbonate or both to Na_2S solution. The latter was used for preparing only of 12–13 pH solutions. Table 3 presents HgS (0001) and (1010) growth rates in these solutions.

In Na_2S solutions, saturated with hydrosulphide up to pH = 9–11, HgS growth rates did not exceed 0·05 mm/day. At the same time, as-grown crystals were usually defective, with large amount of gas-liquid inclusions and obvious columnar crystallization traces. Moreover partial decomposition of HgS was sometimes found under these conditions, apparantly due to the low redox potential, when considerable hydrosulphide was saturated into the initial Na_2S solution.

Within 12–13 pH interval cinnabar growth rates are noticeably higher in the same ($Na_2S + H_2S$) solutions; the amount of gas-liquid inclusions starts decreasing and columnar crystallization traces start vanishing. However, it was not always possible to avoid partial HgS decomposition. Moreover, saturation of Na_2S with hydrosulphide solution is rather technically complicated. So, in subsequent experiments we added ammonium chloride or sodium bicarbonate to Na_2S solutions to reach a pH of 12–13. In the first case HgS growth rate was lowered (see table 3). HgS decomposition with the formation of metallic mercury was found in none of the experiments. When sodium bicarbonate was added to Na_2S solution, the growth rates, on the contrary, increase, but HgS decomposes, indicating the considerable redox conditions change inside the autoclave in the presence of sodium bicarbonate. The best results were obtained using $Na_2S + NH_4Cl + NaHCO_3$ solutions (pH = 12–13). The growth rates in these solutions reached 0·1–0.15 mm/day without HgS decomposition. As-grown HgS crystals were 1·5 cm in size (see figure 13).

The samples of necessary orientation and shape for piezoelectric, elastic and dielectric constants measurements were made from the grown crystals. The bars and plates cut from the pure crystal did not exceed 4·8 × 2·5 × 1·5 (– 1·8) mm and 6 × 4 × 1·1 mm in respective size. Maximum dimensions of the parallelepipeds were of 6 × 4 × 5 mm^3.

Piezoelectric properties of α-HgS are described by two independent moduli d_{11} and d_{14}. The resonance-antiresonance method was used for their measurements. The compression-tension oscillations of X-cut bar with the length along Y, excited by X-directed electric field and countour shear and thickness shear vibration of Y-cut plates were measured at room temperature.

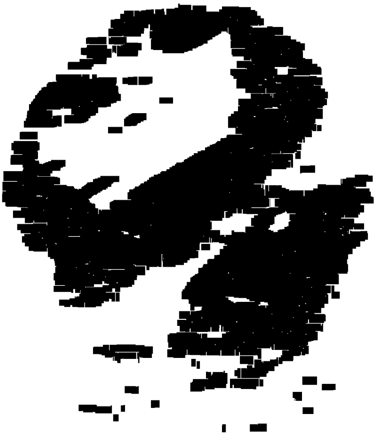

Figure 13. Cinnabar (α-HgS) crystal, grown in the sulphide-chloride carbonate solution (×2).

The independently measured values of the electromechanical coupling coefficients and dielectric constants enabled to calculate the effective values of piezoelectric moduli d_{ik}.

The velocities of ultrasonic wave propagation along various crystallographic directions were measured by the pulse ultrasonic method. It enabled to calculate the effective value of elastic modulus and all its six independent constants, characterizing the elastic constant tensor of a crystal.

Table 4. Dielectric, elastic and piezoelectric constants of cinnabar and quartz crystals

Cinnabar		Quartz	
Piezoelectric modulus, 10^{-12}k/n	Our data	*a*	*b*
	d_{11} = −21·3	−19·0	−2·25
	d_{14} = 15·43	+2·0	+0·86
Elastic compliances, 10^{-12} m²/n	s_{11} = 42·82	41·0	12·79
	s_{12} = −17·8		−1·535
	s_{13} = −4·31		−1·1
	s_{14} = −32·2		−4·46
	s_{33} = 21·11		9·56
	s_{44} = 80·75		19·78
	s_{66} = 121·24		28·65
Dielectric constants	ε^T_{11} = 17·6	18·2	4·58
	ε^T_{33} = 27·8		4·7

[a] Data from Jaffe and Berlincourt (1965); [b] Physical acoustics (1964) data.

Table 4 presents the dielectric, elastic and piezoelectric constants. The analogous data for widely used quartz single crystals of the same modification and some literature data on constants (Physical Acoustic data 1964; Jaffe and Berlincourt 1965) are also given in the table.

α-HgS piezoelectric moduluses are almost an order of magnitude larger, than that of quartz. As for elastic properties, one can see their strong anisotropy. The crystal is soft, its Young's moduli ($E_{11} = s_{11}^{-1}$) and ($E_{33} = s_{33}^{-1}$) are 3·34 and 2·22 times less, than those of quartz. Note, that for HgS E_{33} is nearly two times larger than E_{11}.

Conclusions

For ZnO, ZnS and HgS crystals the hydrothermal growth method is preferable to high temperature methods. The main advantages offered by hydrothermal method are low crystallization temperatures and the possibility to realize prolonged growing cycles when using the oriented seeds. It enables to obtain convenient bulky crystals with low concentration of defects, characteristic for high temperature methods. For ZnS and HgS hydrothermal method seems to be the only convenient route for obtaining low-temperature modifications of these materials with homogeneous crystal structure. Appropriate techniques were developed and large single crystals of ZnO, ZnS and HgS, useful in piezoelectric, electro-optic and laser devices, were grown.

References

Adamov L C, Sarkisov L L and Sysoov L A 1972 *Monocryst. i technica* (ed.) E F Chaykovsky VNII Monocryst. Harcov **6** 91
Alexander E, Kalman Z N, Mardix S and Steinberger I T 1970 *Philos. Mag.* **21** 1237
Ananiev T V, Dubensky K K, Ryskin A I and Hilko G I 1968 *FTT* **10** 1800
Babansky M D, Stroitelev A D and Chernyshev A I 1971 *Materiali Yubileynoi nauchnoi konferentsii, posviashennoi 50-letiyu gelogicheskogo obrazovaniya v TGU*, Tomsk, TGU
Brafman O, Alexander E, Fraenkel B S, Kalman Z and Steinberger I T 1964 *J. Appl. Phys.* **35** 1855
Brafman O and Steinberger I T 1966 *Phys. Rev.* **143** 501
Carlson S H 1967 *J. Cryst. Growth* **1** 271
Chase A B and Osmer J A 1967 *J. Am. Ceram. Soc.* **50** 325
Chernyshev A I and Babansky M D 1977 *Reaktsionnaya sposobnost veschestv*, Tomsk TGU 34
Croxall D E, Ward R C C, Wallace C A and Koll R C 1974 *J. Cryst. Growth* **22** 117
Dodson E M and Savage J A 1968 *J. Mater. Sci.* **3** 19
Efremova E P, Kuznetsov V A and Kotelnikov A R 1976 *Krystallografia* **21** 583
Efremova E P, Kuznetsov V A and Shikina N D 1982 *Geochimia* **1** 56
Faile S P 1978 *J. Cryst. Growth* **43** 129
Galstian V G, Morozova N K, Kuznetsov V A, Shternberg A A and Muratova V I 1980 *Krystallografia* **25** 829
Garner R W and White W B 1970 *J. Cryst. Growth* **7** 343
Greene L C, Reynolds D C, Czyzak S J and Baker W M 1958 *J. Chem. Phys.* **29** 1375
Harsy M 1968 *Mat. Res. Bull.* **3** 483
Heiland G, Mollwo E and Stockman F 1959 *Solid State Phys.* **8** 121
Hirose M 1971 *Jpn. J. Appl. Phys.* **10** 401
Iwanaga H, Yosiil T, Yamaguchi T and Shifeta N 1979 *J. Cryst. Growth* **47** 703
Jaffe H and Berlincourt D A 1965 Piezoelectric transducer materials *Proc. IEEE* **57** 1372
Kashyap Subhash C 1973 *J. Appl. Phys.* **44** 4381
Kozielski M 1967 *J. Cryst. Growth* **1** 293
Kuznetsov V A, Efremova E P and Kolonin G R 1973 *Geochimica* **5** 653

Kuznetsov V A, Efremova E P and Kotelnikov A P 1974 *Geochimia* 7 963
Kuznetsov V A 1964 *Rost Kristallov.* (eds) A V Shubinkov and N N Sheftal (M: Nauka) IV 144
Kurbatov L N, Kozina G S, Kostinskaya T A, Rudnevsky V S, Lobachev A N, Kuznetsov V A, Kuzmina I P, Shaldin Yu V and Shternberg A A 1980 *Kvantovaya Electr.* 7 378
Kuznetsov V A and Lobachov A N 1972 *Kristallografia* **17** 878
Kuzmina I P, Lobachev A N and Triodina N S 1970 *Issledovanie protsessov krystallizatsii v gydrotermalnych usloviyach* (ed.) A N Lobachev (M: Nauka) 29
Kuznetsov V A, Nesterova Z V, Popov Yu V and Shternberg A A 1980 *Optica i Spectrosk.* **48** 1028
Kuzmina I P, Nikitenko V A, Terestchenko A I, Shaldin Yu V and Lazarevskaya O A 1982 *Gidrotermalny syntoz i vyrastchivanio monocrystallov.* (ed.) A N Lobachev (M: Nauka) 40
Laudise R A 1963 *The art and science of growing crystals* (ed.) J J Gilman (New York: Wiley) 252
Laudise R A and Caporaso E D 1964 *J. Am. Ceram Soc.* **47** 9
Lendway E 1971 *J. Cryst. Growth* **10** 77
Linares R C 1968 *Trans. Mat. Soc. AIME* **242** 441
Lobachev A N, Kuzmina I P and Lazarevskaya O A 1982 *Gydrotermalny syntez i virastenivanic monocrystallov.* (ed.) A N Lobachev (M: Nauka) 26
Lobachev A N, Kuzmina I P, Shaldin Yu V, Lazarevskaya O A and Belogurov D A 1977 *Rost Krystallov iz vysokotemperaturnych vodnych rastvorov* (ed.) A N Lobachev (M: Nauka) 158
Mita Y 1962 *J. Phys. Soc. Jpn.* 17 784
Michaelski E, Demianiuk M, Kaczmerek S and Zmija J 1979 *Acta Phys. Pol.* **A56** 333
Morozova N K, Kuznetsov V A, Shternberg A A and Karetnikov I A 1979 *Krystallografia* **24** 1088
Neviantseva P P, Levitskaya T D, Kidiarov B I, Demianov E A and Pasko P G 1972 *Izv. Akad. Nauk SSSR Neorg. Mater.* **8** 488
Nielsen K F 1968 *J. Cryst. Growth* **3–4** 141
Nielsen J W and Dearborn E E 1960 *J. Phys. Chem.* **64** 1762
Nistor L C, Nistor S V and Tasczan M I 1980 *J. Cryst. Growth* **50** 557
Obuhova N F, Atroshenko L V and Kolodiashzky A I 1977 *Izv. Akad. Nauk. SSSR, Neorg. Mater.* **13** 1390
Parker S G and Pinnel J E 1968 *J. Cryst. Growth* **3/4** 490
Park J S and Reynolds D C 1967 *J. Appl. Phys.* **38** 756
Pashkovasky M V, Savitsky I V and Lutsiv R V 1961 *Ukr. Fiz. Zh.* **6** 691
Piper W W and Roth W L 1953 *Phys. Rev.* **92** 503
Pottor R W II and Barnes H L 1978 *Am. Miner.* **63** 1143
Rabadanov R A, Semiletov S A and Magomedov Z A 1970 *FTT* **12** 1431
Rumiantsev Yu M, Kuznetsov F A, Stroitelev S A 1965 *Kristallografia* **10** 263
Russel G J and Woods J 1979 *J. Cryst. Growth* **47** 647 .
Sasaki K 1975 *Sci. Rep. Hirosaki Univ.* **22** 56
Samelson H and Brophy V A 1961 *J. Electrochem. Soc.* **108** 150
Scharowsky A 1953 *Z. Phys. B.* **135** 318
Shamburov V A, Kuznetsov V A, Lobachev A N, Charitonova I V and Soshnikov V G 1970 *Krystallografia* **15** 302
Shalimova K V, Morozova N K, Malov M M, Kuznetsov V A, Shternberg A A and Lobachev A N 1974 *Krystallografia* **19** 147
Shalimova K V, Morozova N K, Kuznetsov V A, Kotelnikov A P and Veselkova M M 1974 *Krystallografia* **19** 634
Shternberg A A 1970 *Issledovanie protsessov krystallizatsii v gydrotermalnych usloviyach* (ed.) A N Lobachev (M: Nauka) 199
Shichiri T, Aikami T and Kakinoki J 1978 *J. Cryst. Growth* **43** 320
Shternberg A A, Kuzmina I P and Kuznetsov V A 1962 *Kristallografia* 7 334
Sysoev L A 1972 *Izv. Akad. Nauk SSSR, Neorg. Mater.* **8** 639
Timofeeva V A 1965 *Rost Kristallov* (ed.) N N Sheftal (M: Nauka) VI 85
Tokarov E F, Kobiakov I B, Kuzmina I P, Lobachev A N and Pado G S 1975 *FTT* 17 980
Toudic Y, Regreny A, Passaret M, Aumont R and Bayon J F 1972 *J. Cryst. Growth* **13/14** 519
Wanklyn B M 1970 *J. Cryst. Growth* 7 107
1964 *Physical Acoustics* (ed.) W P Mason 1 Part A
Wolf G A and LaBelle H E 1965 *J. Am. Ceram. Soc.* **48** 441

Bull. Mater. Sci., Vol. 6, No. 2, May 1984, pp. 193–200. © Printed in India.

Glass-metal particulate composites

D CHAKRAVORTY*

Central Glass and Ceramic Research Institute, Calcutta, 700 032, India

* On leave of absence from Indian Institute of Technology, Kanpur

Abstract. Oxide glasses containing ultrafine metal particles have interesting physical properties and have been widely used in practical systems. The various preparational techniques developed so far for making these materials are discussed. Electrical conduction in these composites is controlled by electron tunnelling between the metal islands. At high electric fields certain glasses containing bismuth granules show a memory switching effect. The latter has been explained by a particle stretching model. Optical absorption characteristics of these composites can be explained on the basis of various effective medium theories developed so far for inhomogeneous materials. Glasses containing ferromagnetic metal grains show a superparamagnetic behaviour with a transition temperature below 300 K. Improvement in the mechanical properties of glasses can be achieved by incorporating metal particles of suitable characteristics within them. In this paper the present state of understanding of all these properties is reviewed.

Keywords. Glass-metal composites; oxide glasses; composites; electrical properties; optical properties; magnetic properties; mechanical properties.

1. Introduction

Glasses containing colloidal metal particles of dimensions of the order of a few hundred angstroms have found extensive uses in the preparation of photosensitive glasses, glass-ceramics (Araujo 1977) coloured glasses (Rawson 1980), photochromic glasses (Araujo 1977), thermally darkenable photochromic glasses (Seward 1975) and polychromatic glasses (Stookey *et al* 1978). These materials are prepared by photo-chemical methods. Ion-exchange followed by reduction treatments have also been found to be suitable for this purpose (Chakravorty *et al* 1975). Recent investigations show the possibility of inducing electronic conductivity to oxide glasses by precipitating metal granules within them (Chakravorty 1981). Some of these micro-composites also exhibit memory switching (Chakravorty 1975). Glasses containing ultra-fine ferromagnetic metal particles exhibit superparamagnetic behaviour (Datta *et al* 1983a). Glass-metal composite systems have also been studied in recent years to obtain improvement in the toughening of oxide glasses (Krstic 1981). A powder metallurgy technique however was used to make the composites for the study of their mechanical behaviour. In this paper we review the recent advances made in the understanding of the preparation and properties of glass-metal particulate composites.

2. Preparation of glass-metal particulate composites

There are broadly two different techniques for making the composites under discussion. The first is essentially a chemical one, whereas the second is based on hot pressing of a powder compact.

Metal particles are precipitated in photosensitive glasses by irradiating them with UV radiation and then heating the glasses at a suitable temperature (Araujo 1977). Some sensitizer *e.g.*, CeO_2, Sb_2O_3 which has a variable valence ion is included in the glass compositions to increase their photosensitivity. Similar method is employed in the preparation of photochromic (Armistead and Stookey, 1965) and polychromatic glasses (Stookey *et al* 1978). A typical reaction involving the precipitation of silver by irradiation from a heat-treated photochromic glass containing a dispersion of silver chloride crystals can be represented by

$$Ag^{+} + Ce^{3+} + h\nu \rightarrow Ag^{\circ} + Ce^{4+}. \qquad (1)$$

Colloidal metal particles of copper, silver, gold, platinum and bismuth can be precipitated in oxide glasses by melting a suitable salt of the metal along with the relevant oxides for the specific glass composition and some reducing agents like SnO or Sb_2O_3 (McMillan 1979; Chakravorty *et al* 1977). The precipitation of a metal phase from a dissolved ion in an oxide glass melt can be considered to be an equilibrium situation. It has been shown specifically in the case of formation of iron, cobalt and nickel metal phase in a borosilicate glass melt that an equilibrium between metal and dissolved ion is established over a range of oxygen fugacities at a particular temperature (Schreiber 1983). These ions are introduced into the glass melt as their respective oxides. Some recent investigation show that metal phase can be precipitated in an oxide glass by melting the latter with an organometallic compound containing the metallic species (Datta and Chakravorty 1983). A borate glass with nickel granules has been made using nickel oxinate as one of the raw materials. This method appears to be suitable for making various glass-metal microcomposites by a melting operation under ordinary atmospheric condition. It is believed that favourable oxygen fugacities are attained locally within the melt because of the breaking up of the organometallic compound releasing carbon, hydrogen and nitrogen atoms.

Metallic particles can also be precipitated within an alkali-containing glass by subjecting the latter to an ion-exchange and reduction treatment (Chakravorty *et al* 1975). The ion-exchange reaction is carried out by immersing the glass in a molten salt bath containing the required ion for a suitable duration. The reduction of the ion-exchanged surface is brought about by passing a mixture of nitrogen and hydrogen gases over it for a specific period. Sodium $\rightleftharpoons$ copper (Chakravorty *et al* 1975) and sodium $\rightleftharpoons$ silver (Sarkar *et al* 1982) exchange in silicate glasses have been investigated in detail. It is observed that the precipitation of metal grains within the glass is controlled by a nucleation and growth process. Accordingly there is an optimum reduction temperature at which the nucleation rate is a maximum. Table 1 summarises the nucleation temperature data etc. for various systems studied so far. It is also found that the phase morphology of the glass after the ion exchange step has a pronounced effect on the subsequent metal precipitation. For instance, the metal dispersoids are observed to be concentrated in the interconnected metal rich phase in sodium $\rightleftharpoons$ copper exchanged float glass (Chakravorty *et al* 1975).

Glass-metal particulate composites have also been prepared by hot-pressing of a mixture of glass powder and metal particles (Krstic *et al* 1981; Stett and Fulrath 1968; Nivas and Fulrath 1970). Silicate glasses have been used with metallic particles of nickel (Krstic *et al* 1981; Stett and Fulrath 1968), tungsten (Nivas and Fulrath 1970) and aluminium (Krstic *et al* 1981) respectively the latter having diameters in the range 40 μm–120 μm. To improve the bonding between the metallic particles and the glass

Table 1. Reduction temperature for maximum nucleation of metal phase in different ion-exchanged glasses

Glass system	Ion-exchange treatment		Reduction temperature for maximum nucleation	Reference
	Species	Temperature/time		
Float glass	$Na^+ \rightleftharpoons Cu^+$	550°C/1 hr	450°C	Chakravorty *et al* 1975)
...	...	660°C/1 hr	...	
...	...	650°C/1 hr	...	
C-glass	$Na^+ \rightleftharpoons Ag^+$	330°C/6 hr	250°C	(Sarkar *et al* 1982)
...	...	...	...	
...	...	...	...	
64 SiO_2, 26 B_2O_3, 10 Na_2O (mole %)	...	...	300°C	(Sarkar *et al* 1982)

matrix the former are oxidised in air prior to mixing with the glass for subsequent hot-pressing operation. The mixtures are then vacuum hot-pressed—typical temperature and pressure being 500–700°C and 0·3 MPa respectively (Krstic *et al* 1981). Glass compositions have been chosen such that their thermal expansion coefficients are of the same order of magnitude as those of the metallic species concerned.

One of the most important aspects in the preparation of glass-metal particulate composites is the glass-to-metal interfacial bonding. A number of studies have been reported on the wetting of metals by molten glasses using sessile drop technique (Pask and Fulrath 1970; Nagesh *et al* 1983) under controlled atmospheres. It is believed that a strong chemical bond at the interface requires the presence of a transition layer consisting of metal atoms exhibiting both metallic and ionic–covalent bonds and oxygen atoms which are also part of the glass structure. In the absence of such a zone at the interface a weaker bond of the van der Waals type exists which causes a poor adherence of the metal phase to the glass.

3. Properties of glass-metal particulate composites

3.1 *Electrical*

Electrical conduction in glass-metal composites with metal grains having sub-micron dimensions has been explained as arising due to the transport of electrons by tunnelling from one metal grain to the next (Chakravorty 1977). The theoretical model which has been used to analyse the experimental results obtained for these materials is identical to that developed for electrical conduction in granular metal films or cermets (Abeles *et al* 1976). According to this model, the generation of a charge carrier *viz* electron involves the creation of a pair of positively and negatively changed grains. The energy E_c^0 to create such a pair is given by

$$E_c^0 = 2e^2/Kd \tag{2}$$

where e is the electronic charge, d the metal grain diameter and

$$K = \varepsilon[1 + (d/2s)] \tag{3}$$

ε being the dielectric constant of the insulating matrix and s the inter-particle separation.

The mobility of the charge carrier in the present system is proportional to the tunnelling probability exp $(-2\chi s)$ where,

$$\chi = [2m\phi/\hbar^2]^{1/2} \qquad (4$$

m being the electronic mass, ϕ the effective barrier height and h the Planck's constant The conductivity σ can therefore be written as (Abeles *et al* 1976)

$$\sigma \propto \int_0^\infty \beta(s) \exp[-2\chi s - (C/2\chi s k T)] \qquad (5$$

where $C \equiv \chi s E_c^0$ (6

and β(s) is the density of percolation paths associated with s. Abeles *et al* (1976) have shown that by making certain approximations, (5) can be simplified to the form,

$$\sigma = \sigma_0 \exp[-2(C/kT)^{\frac{1}{2}}]. \qquad (7$$

The variation of electrical resistivity as predicted by the above equation has been found to be valid in various glass-metal systems. Table 2 summarises the E_c^0 values for different systems as obtained from the experimental data. The table also gives the calculated E_c^0 values using the average diameters of metal islands as estimated from electron microscopic investigations. Table 3 summarises the results obtained on some glass fibres in which silver granules have been precipitated by subjecting the former to a

Table 2. E_c^0 values in various glass-metal particulate systems

Glass composition (mole %)	Metallic species	Average particle diameter (A)	E_c^0 Expt. (eV)	E_c^0 Calc. (eV)	Reference
64 SiO_2 18 B_2O_3 8 Bi_2O_3 10 Na_2O	Bismuth	50	$4{\cdot}0 \times 10^{-2}$	$9{\cdot}0 \times 10^{-2}$	(Chakravorty *et al* 1977)
80 V_2O_5 15 P_2O_5 5 Bi_2O_3	...	50	$1{\cdot}2 \times 10^{-2}$	$1{\cdot}3 \times 10^{-2}$	(Chakravorty *et al* 1979)
70 V_2O_5 15 P_2O_5 15 Bi_2O_3	...	100	$4{\cdot}7 \times 10^{-3}$	$3{\cdot}9 \times 10^{-3}$	...
75 V_2O_5 15 P_2O_5 10 Ag_2O	Silver	200	$1{\cdot}6 \times 10^{-3}$	$1{\cdot}6 \times 10^{-3}$	...
85 B_2O_3 5 Na_2O 10 Bi_2O_3	Bismuth	120	$1{\cdot}4 \times 10^{-2}$	$1{\cdot}5 \times 10^{-2}$	(Chakravorty an Chakrabarti 1980)
75 B_2O_3 20 PbO 5 Bi_2O_3	...	400	$4{\cdot}2 \times 10^{-3}$	$3{\cdot}8 \times 10^{-3}$	...
46 SiO_2 25 B_2O_3 11 K_2O 9 Al_2O_3 4 Sb_2O_3 1 As_2O_3 4 Ag_2O (in fibre form)	Silver	500	$1{\cdot}7 \times 10^{-2}$	$2{\cdot}2 \times 10^{-2}$	(Chakravorty *et al* 1979b)

Table 3. E_c^0 values in glass-metal particulates produced by ion-exchange and reduction treatments

Glass composition (mole %)	Ion-exchanging species	Metallic species	Average particle diameter (A)	E_c^0		Reference
				Experimental (eV)	Calculated (eV)	
64 SiO_2 26 B_2O_3 10 Na_2O	Sodium ⇌ silver	Silver	115	$8{\cdot}7 \times 10^{-3}$	$2{\cdot}3 \times 10^{-2}$	(Arul Mozhi and Chakravorty 1982)
Commercial C-glass	...	...	160	$1{\cdot}5 \times 10^{-2}$	$1{\cdot}9 \times 10^{-2}$	...

sodium ⇌ silver ion exchange followed by reduction (Arul Mozhi and Chakravorty 1982). In all cases, the experimental and calculated values of E_c^0 are found to be in reasonable agreement.

Some oxide glasses containing fine bismuth particles exhibit memory switching with a threshold field of the order of 10^4 V/cm (Chakravorty and Murthy 1975) the samples changing their resistivity by about two to three orders of magnitude. Typical resistivity values in the off and on-states are 10^4 Ω cm and 5 Ω cm respectively for a silicate glass containing bismuth (Chakravorty and Murthy 1975). The corresponding values in a vanadium phosphate glass containing bismuth are 250 Ω cm and 3 Ω cm respectively (Das and Chakravorty 1980, 1982). The switched samples can be brought back to the off-state by either applying a pulse of large amplitude and small width or by heating them above ~ 200°C and then quenching the same (Chakravorty and Murthy 1975). A particle stretching model has been developed to explain the memory switching behaviour of these glass-metal particulate composites (Das and Chakravorty 1980, 1982). According to this theory, the joule losses in the off-state cause the metal grains to get heated. When these attain a molten state they are subjected to two opposing forces, one of which is due to the coulombic attraction between polarized neighbouring grains and the other arising out of the surface tension force in the molten particles. Under equilibrium condition the molten particles are deformed and the critical or switching field is reached when the interparticle separation becomes equal to zero. An implicit approximation in this model is that there are some filamentary regions across the sample extending from one electrode to the other in which the metal grains have small inter-particle separation. At the threshold field therefore grains in these regions coalesce giving rise to filamentary conducting paths in the sample which bring about switching to the highly conducting on-state. The threshold field E_t in this model has been shown (Das and Chakravorty 1980) to be given by,

$$E_t = \left(1 + \frac{d}{s_0}\right)^{-1} \left\{\frac{8\gamma}{\varepsilon d}\left[\left(1 + \frac{s_0}{d}\right) - \left(1 + \frac{s_0}{d}\right)^{1/2}\right]\right\} \tag{8}$$

where, s_0 is the average inter-particle separation, γ is the specific surface energy of metal glass interface, and ε is the dielectric permittivity of glass matrix.

In table 4 the experimental and theoretical switching fields for two glass-metal systems are shown. The agreement between the two sets of values is found to be

Table 4. Switching fields in different glass-metal particulate systems

Glass composition (mole %)	Metallic species	Maximum diameter of metal granules (A)	E_t		Reference
			Experimental (V/cm)	Theoretical (V/cm)	
$64\ SiO_2\ 18\ B_2O_3$ $8\ Bi_2O_3\ 10\ Na_2O$	Bismuth	500	$1{\cdot}2 \times 10^4$	$1{\cdot}1 \times 10^4$ $(s_{o/d} = 0{\cdot}03)$	(Das and Chakravorty 1980)
$80\ V_2O_5\ 15\ P_2O_5$ $5\ Bi_2O_3$	...	800	$4{\cdot}0 \times 10^3$	$5{\cdot}1 \times 10^3$ $(s_{o/d} = 0{\cdot}03)$	(Das and Chakravorty 1980)

reasonable. This model also satisfactorily explains the negative resistance behaviour of these glass-metal systems prior to attaining the on-state (Das and Chakravorty 1982).

3.2 *Optical*

Heterogeneous materials exhibit optical properties which are dependent on the relative dielectric permittivities of the different phases present in the system (Landauer 1978). The glass-metal particulate composites with metal granules having dimensions of the order of a few hundred "angstroms also show characteristic optical absorption". Table 5 summarises the results reported so far on optical properties of various glass-metal systems. The Maxwell Garnett and Bruggeman effective medium theories have been used to calculate the optical absorption spectra of these materials which agree qualitatively with the experimental data (Datta *et al* 1983; Das 1982; Sarker *et al* 1982).

3.3 *Magnetic*

Recently magnetic properties of a borate glass containing up to 0·4 wt% nickel dispersed as metal granules of diameters around 70 Å within the matrix have been reported (Datta *et al* 1983). The ultrafine nickel particles exhibit a superparamagnetic behaviour. Both EPR and magnetization measurements indicate that there exists a broad range of transition temperatures below 300 K. The mean values of the transition temperatures as obtained from EPR and magnetisation data are around 190 K and 90 K respectively. The transition has been explained as arising due to the interaction between the magnetic particles which generates a field analogous to the Lorentz field in Debye's theory of polar molecules (Soffge and von Horsten 1981).

3.4 *Mechanical*

Mechanical properties of glass-metal particulate composites have been extensively investigated with a view to achieving improved toughness in these materials (Krstic *et al* 1981; Stett and Fulrath 1968; Nivas and Fulrath 1970). However, it has not been possible to gain substantial improvement because of the presence of residual stresses and/or poor interfacial bonding between the metal and the glass phases. The residual stresses can be minimised by choosing a glass with a thermal expansion coefficient

Table 5. Optical absorption in different glass-metal particulate composites

Glass systems	Metallic species	Preparation technique	Particle diameter range (Å)	Wavelength for absorption maximum (nm)	Reference
Float glass	Copper	Sodium ⇌ copper + Reduction	50–300	434 and 574	(Chakravorty *et al* 1975)
C-glass	Silver	Sodium ⇌ silver + reduction	50–200	400	(Sarkar *et al* 1982)
64 SiO_2 26 B_2O_3 10 Na_2O (mole %)	...	...	50–200	400	...
80 V_2O_5 15 P_2O_5 5 Bi_2O_3 (mole %)	Bismuth	Reduction	50–170	450	(Das 1982)
64 SiO_2 18 B_2O_3 10 Na_2O 8 Bi_2O_3 (mole %)	...	...	60–130	500	...
50 BaO 50 B_2O_3 (wt %) + 0·2 wt % Nickel	Nickel	Organo-metallic	40–150	250	(Datta and Chkravorty 1983)

Table 6. Mechanical properties of glass-metal particulate composites prepared by hot-pressing techniques

Glass system	Metal species	Diameter of metallic particles μm	Volume fraction of metals	Bending strength (MN/m^2)	Fracture toughness ($MN/m^{3/2}$)	Reference
70 SiO_2 16Na_2O 14 Li_2O (wt %)	Nickel	44–63	0·20	83 (50% increase)	—	(Stett and Fulrath 1968)
65 SiO_2 8·5 Na_2O 26·5 B_2O_3 (wt %)	Tungsten	3–13	0·50	155 (172% increase)	—	(Nivas and Fulrath 1970)
50 SiO_2 37 Na_2O 8 Al_2O_3 5 Li_2O (wt %)	Aluminium	100–120	0·20	—	6·0 60 × increase	(Krstic *et al* 1981)

comparable to that of the metal. The interfacial bonding has been somewhat enhanced by oxidising the metal particles partly before fabricating the composite. In table 6 the best set of data obtained in various glass-metal systems are summarised. In each case the glass composition chosen is such that its thermal expansion coefficient matches that of the corresponding metal. The amounts of increase in the bending strength or the fracture toughness over the base glass are shown within brackets in the appropriate column. The data also show that the strength of the composite is inversely proportional to the square root of the inter-particle spacing. It is to be noted that the composites studied so far contain metal particles having diameters of the order of a few microns and with an inter-particle spacing of similar magnitude. It will be interesting to investigate the behaviour of glass-metal composites having particle diameters of the order of 50–100 Å. It is expected that with the techniques developed recently (Datta and Chakravorty 1983a) to make such composites it will be possible to study their mechanical behaviour.

References

Abeles B, Sheng P, Coutts M O and Arie Y 1976 *Adv. Phys.* **47** 2200

Araujo R J 1977 in *Treatise on materials science and technology* (eds) M Tomozawa and R W Doremus (New York: Academic press) p. 71

Armistead W H and Stookey S D 1965 U.S. Patent 3 108 860

Arul Mozhi T and Chakravorty D 1982 *J. Mater. Sci. Lett.* **1** 426

Chakravorty D, Shuttleworth A and Gaskell P H 1975 *J. Mater. Sci.* **10** 799

Chakravorty D and Murthy C S 1975 *J. Phys.* **D8** L162

Chakravorty D, Bandyopadhyay A K and Nagesh V K 1977 *J. Phys.* **D 10** 2077

Chakravorty D, Haranahalli A R and Kumar D 1979a *Phys. Status Solidi* **51** 275

Chakravorty D, Keshavram B N and Venkateswaran A 1979b *J. Mater. Sci.* **14** 2991

Chakravorty D and Chakrabarti S 1980 *J. Non-Cryst. Solids* **38, 39** 295

Chakravorty D 1981 in *Preparation and characterization of materials* (eds) J M Honig and C N R Rao (New York: Academic Press) p. 515

Das G C and Chakravorty D 1980 *J. Appl. Phys.* **51** 3896

Das G C 1982 *Memory Switching and Optical Properties of Glass-Metal Microcomposites* Ph.D. Thesis, IIT, Kanpur

Das G C and Chakravorty D 1982 *J. Phys.* **D15** 2255

Datta S, Bahadur D and Chakravorty D 1983 *J. Phys.* **D** (in press).

Datta S and Chakravorty D 1983 *J. Mater. Sci. Lett.* **2** 329

Krstic V V, Nicholson P S and Hoagland R G 1981 *J. Am. Ceram. Soc.* **64** 499

Landauer R 1978 *AIP Conf. Proc.* **40** 2

McMillan P W 1979 *Glass Ceramics* (London, New York: Academic Press) p. 61

Nagesh V K, Tomsia A P and Pask J A 1983 *J. Mater. Sci.* **18** 2173

Nivas Y and Fulrath R M 1970 *J. Am. Ceram. Soc.* **53** 188

Pask J A and Fulrath R M 1962 *J. Am. Ceram. Soc.* **45** 592

Rawson H 1980 *Properties and applications of glasses* (*Glass Science and Technology 3*) (Amsterdam: Elsevier Publishing Co.) p. 218

Sarkar P, Kumar J and Chakravorty D 1982 *J. Mater. Sci.* **18** 250

Schreiber H D, Carpenter B E, Minnix L M, Balazs G B and Solberg T N 1983 *Glastech. Ber.* 56 K Band 2, 1017

Seward T P III 1975 *J. Appl. Phys.* **46** 689

Soffge F and von Horsten W 1981 *Z. Phys.* **B42** 47

Stett M A and Fulrath R M 1968 *J. Am. Ceram. Soc.* **51** 599

Stookey S D, Beall G H and Pierson J E 1978 *J. Appl. Phys.* **49** 5114

Bull. Mater. Sci., Vol. 6, No. 2, May 1984, pp. 201–221. © Printed in India.

Fast ion conducting lithium glasses—Review

A R KULKARNI, H S MAITI and A PAUL

Materials Science Centre, Indian Institute of Technology, Kharagpur 721 302, India

Abstract. For the last few years fast ion conducting lithium glasses are being studied due to their potential use in advanced electrochemical devices. A number of glass systems containing oxides, sulphides and other lithium compounds prepared by both conventional cooling and rapid quenching techniques have been reported. In this paper we review the transport properties of lithium ion conducting glasses. The special features of the ionic conduction process have been highlighted and some experimental techniques to study transport properties have been described. Some of the common observations of the properties have been discussed and finally some important problems for future development have been pointed out.

Keywords. Glassy electrolytes; electrical conductivity; transport number; glass structure; solid state batteries.

1. Introduction

Electrochemical cells using lithium ion conducting electrolytes develop high voltages (> 2 V) and high specific energy density (~ 1000 Wh/kg) due to the light weight and highly electropositive character of the lithium metal. Therefore, many research groups have focussed their attention on lithium-based battery systems. Many of these lithium batteries are primary non-rechargeable batteries with liquid electrolytes and suffer from the fact that the organic solvents usually used are highly reactive and toxic. Solid electrolytes which conduct lithium ions, are expected to play an important role as materials for advanced batteries. In addition, these electrolytes have other applications such as in timers, coulometers, solid state display devices, sensors etc. The crystalline Li-conductors, which have been investigated in greater detail are suspected for large scale production, due to stringent structural requirements for the desired properties. Thus non-crystalline solids, which can be easily produced on larger scales, are receiving recent attention. Glassy lithium-solid electrolytes have been studied extensively and are found to have definite advantages over crystalline conductors like isotropic properties, ease of thin film formation, flexibility of size and shape (at satisfactory cost) etc. One of the important features of glass as solid electrolyte is the possibility of continuously changing composition over a wide limit. Although some of the lithium ion conducting glasses find application as positive electrodes, only those which would be useful as electrolytes are discussed here. This review includes a brief discussion about the general theory of ionic conduction as applied to glasses and the results obtained on some of the promising glass systems. Finally some of the problems for the future development of the glassy solid electrolytes and their applications are discussed.

2. General features of ionic conduction in glasses

The mobile ionic species in a solid conductor move rapidly through a framework which is formed by other atoms of the lattice. This ability of a material to allow the movement of ions through it can be estimated by the measurement of a range of transpo properties like conductivity, diffusion, motional narrowing of NMR lines etc. The ion conductivity of a solid, σ, usually follow an equation of the form

$$\sigma = \sigma_0 \exp(-E/kT), \qquad ($$

where σ_0 = pre-exponential factor, E = activation energy of conductio k = Boltzman's constant and T = absolute temperature. Accordingly, the activatio energy can be estimated from the slope of the plot of log σ *vs* reciprocal temperatur

For simple ionic conductors, (1) may be derived phenomenologically from th general definition of conductivity, in terms of density of charge carriers (n) of charge having a mobility μ given as

$$\sigma = nq\mu. \qquad ($$

The Einstein expression for the drift mobility of a diffusing species is

$$\mu = qD/kT, \qquad ($$

where kT is the Boltzman's factor, and the diffusion coefficient (D), is expressed as

$$D = D_0 \exp(-\Delta G_m/kT), \qquad ($$

contains the Gibb's free energy term given by

$$\Delta G_m = \Delta H_m - T\Delta S_m, \qquad ($$

for the ion jump from one atomic site to a neighbouring vacant site. It follows from (to (5) that E in (1) contains the migration enthalpy (ΔH_m) in addition to any energy E that might be required to create mobile point defects

$$E = \Delta H_m + E_d. \qquad ($$

Oxide glasses are by far the most widely studied systems. The ionic character of th conductivity in oxide glasses has been established by Warburg (1884). These glasses ar formed by network forming oxides (SiO_2, B_2O_3, P_2O_5, GeO_2 etc) giving rise to random corner-linked tetrahedron arrangement broken in some places by the networ modifier alkali oxides. The structure has large holes which facilitate ionic migratio These holes are surrounded by non-bridging oxygens (NBO) which act as host for alkal ions. A two-dimensional schematic diagram is shown in figure 1.

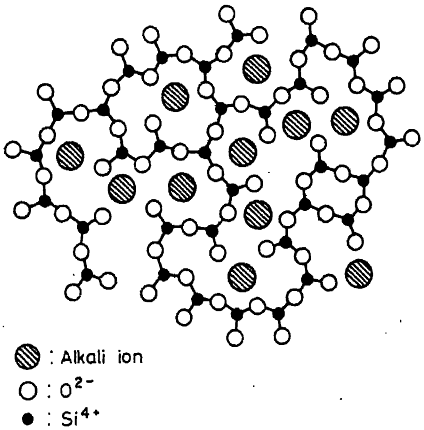

Figure 1. Two dimensional schemati representation of a silica glass with mo difier alkali cations.

The conductivity of a glass shows a behaviour typical of a thermally-activated process as discussed above and the current carriers are predominantly alkali ions. The appropriate model consists of a alkali metal ion in a potential well undergoing thermal vibration and having finite and equal probability of surmounting the barriers and moving to any adjacent potential well. The quantitative treatment of such a model was provided by Stevels (1957) which was later modified by Taylor (1959). The model considers a distribution in the magnitude of the energy barrier and is consistent with the random network of the glasses. Such a model, therefore, gives an average value of activation energy of DC conduction, since the ion encounters potential energy barriers of various heights during the long range motion.

Although a number of different other transport models (Nakajima 1972; Charles 1961; Tomozawa 1977) are available to explain the Arrehenius-like temperature dependence of ionic conductivity in glasses, the models similar to that described above, have been widely accepted (Hughes and Isard 1972).

The ionic conductivity of alkali-containing oxide glasses increases and the activation enthalpy decreases, as the alkali oxide concentration is increased. However, the conductivity is not a linear function of the alkali metal ion concentration. This has led to the concept that some of the alkali metal ions are mobile, while others are "trapped" in the structure and can undergo local, but no long-range motion. The work carried out in recent years has provided more insight into this phenomenon and predicts glass formation in new systems with exceptionally high values of conductivity. One important observation is that the conductivity is proportional to the square root of the alkali oxide activity in the alkali silicates (Ravaine and Souquet 1973, 1977, 1978). This leads to the concept that the alkali metal ions exist in the structure in such a way that one can think in terms of an association-dissociation equilibrium of the alkali oxide in the glass solvent, with the charge carried only by the dissociated cations. This approach is analogous to that used in liquid electrolyte solutions.

The extension of these ideas is to attempt for increasing the oxide activity (concentration) to enhance the conductivity. There are limits as to how far one can go in this direction, before devitrification becomes a problem due to the reduction in the size of the anionic group in the structure. This problem can be overcome and the concentration of undissociated alkali metal ions increased by the addition of alkali halides. In such cases one can assume that neither the alkali metal ion nor the halide ion becomes bound into the macromolecular anionic structure, which consists primarily of shared tetrahedral groups. Quite large concentrations of alkali halides and other simple salts can be incorporated in these glasses and since the cationic and anionic species are highly dissociated, the conductivity can be increased substantially about two orders of magnitude for lithium glasses. As in analogous liquid solutions, the degree of dissociation and thus the contribution to the conductivity is greater, the larger the ion with which the mobile cation is associated. It has also been found that sulphide analogs of the oxide glasses have ionic conductivities about an order of magnitude higher.

3. Techniques for electrical characterization

3.1 *Conductivity measurement*

The most useful parameter of a solid electrolyte is its ionic conductivity as a function of temperature. The parameter determines the mass transport rate through the solid and thus influences the power production of an electrochemical device, of which solid electrolyte forms a part. It can be measured using both AC and DC techniques with ionically blocking or conducting electrodes at two, three or four points of contact. DC measurements present polarisation problems when performed with blocking electrodes whereas use of reversible electrodes may involve appreciable charge transfer resistances due to Faradiac processes at the electrode-electrolyte interface. The single frequency AC measurement provides only an approximate information about the conductivity of a material. The situation in a solid cell, however, is much more complicated since there are various factors which contribute towards ultimate electrical impedance. The contribution due to movement of ions through the bulk of the electrolyte, electrode-electrolyte interface impedance, charge transfer across the interface and the resulting double layer are all summed up in single frequency measurements. All these electrical and electrochemical parameters are functions of applied frequency and their responses are quite different in the different frequency ranges due to their widely different relaxation times. With recent advances in electrochemistry, rigorous analysis of the AC response of an electrolyte or electrochemical cell is possible. Complex impedance (Z^*), admittance (Y^*), permittivity (ε^*) and modulus (M^*) are the four basic functions for analysis of AC data (Hodge *et al* 1976). Baurale (1969) first applied this technique for zirconia solid electrolytes and in subsequent years a large number of materials have been analysed including glasses (Armstrong *et al* 1974; Ravaine and Souquet 1974). The details of the techniques have been comprehensively reviewed (Bottelberghs 1978; McDonald 1976a; Britzs 1980; Johnscher 1978; Shlesing 1980; Grant *et al* 1977; McDonald and Jacobs 1976b). In principle, the various forms of the AC data provide separately the detailed information about various physical processes in an electrochemical cell. This is done by comparing the experimental plots with those that would have been generated by model systems called equivalent circuits which consist of resistances and capacitances combined either in series or parallel.

3.2 *Transport number measurement*

Some of the materials show conductivity due to more than one ion and sometimes also due to electrons. The value of this electronic conductivity largely decides the ultimate device application of the material. For example, an electrolyte for pacemaker application, where low currents and long shelf life is a basic requirement which must not exihibit any electronic leakage current. Hence, the electronic transport number t_{el} (fraction of the total charge carried by electrons) should not exceed 10^{-6}. On the other hand, for load levelling where the system would be cycled daily, it can be as high as few percent if high ionic conductivity is otherwise obtained. Tubandt's (1932) method which is widely used, gives the measure of ionic transport number but does not give an exact idea about the low level electronic conductivity. Wagner's (1956) asymmetric polarisation cell method which employs one electrode reversible to ions and other completely blocking the ion, gives accurate values of electronic conductivity of the electrolytes. The combination of the electronic conductivity, so determined, with total conductivity yields transport number of electrons and ions. Estimation of the electrochemical decomposition potential of the electrolytes is an advantage of this technique. In recent years, pulse technique has also been designed for transport number measurements (Yakoto 1955). The results are generally supplemented by open circuit potential measurements which show near thermodynamic values if the transport number of mobile species is near unity (Wagner 1957).

4. Glass systems

Otto (1966) was the first to report glasses with high Li^+ conductivities at relatively low temperatures. Nearly 100 different compositions in the M_2O-B_2O_2-SiO_2 (M = Li, Na, K) reported by him are still being investigated for possible applications. He observed that high Li^+-conductivities could be obtained in borate glasses if more than 40 m/o lithium compounds could be incorporated in the glass without devitrification. The value of 10^{-1} $(\text{ohm-cm})^{-1}$ at 350°C, reported by him for one of the compositions is still the highest conductivity reported so far, for Li^+-conducting borate glasses. The knowledge about the advanced applications of glasses and their large scale production potential, stimulated the interest of many investigators and the results on a large number of glassy systems have been reported.

4.1 *Alkali borates*

Activation energy of electrical conduction increases linearly with increasing M_2O content (M = alkali metal) in M_2O-SiO_2-B_2O_3 glasses containing less than 25 m/o M_2O (Otto 1966). Replacement up to 50 m/o of B_2O_3 by SiO_2 showed small change in the value of activation energy for a given alkali content. The pre-exponential factor was almost independent of M_2O content. Lithium content of the glasses was further increased by incorporating lithium salts like Li_2SO_4, LiCl or LiF and this helped in obtaining enhanced conductivities than in those containing Li_2O alone. All the conductivity measurements were initially carried out at single frequency (1 kHz). Tuller *et al* (1980) later verified the conductivity values by application of complex impedance analysis.

These results on the borate system promoted interest of many investigators to obtain the crystalline fast ion conducting compositions [$Li_4B_7O_{12}X$ (X = Cl, Br, I)], with boracite structure (Jeitschko 1972a, b; Jeischko *et al* 1977) even in the glassy form. For example the glass system B_2O_3-Li_2O-LiX has shown promising results (Levasseur *et al* 1978, 1979). Ionic conductivity is a strong function of polarizability of the anion or in other words the conductivity is a function of ionic radius of the anion. A glass containing LiI shows a maximum conductivity of $3{\cdot}4 \times 10^{-2}$ $(\text{ohm-cm})^{-1}$ at 350°C with an activation energy of 0·46 eV. As expected the increase in the concentration of Li^+ lead to an increase in the ionic conductivity. Based on this observation various authors have studied multicomponent systems. One such system, Li_2O-LiF-Li_2SO_3-Li_2SO_4-B_2O_3, has been studied (Smedly and Angell 1978) where total Li_2X content is varied between 43 and 84 m/o. A glass with 70 m/o LiX shows a maximum conductivity [$2{\cdot}26 \times 10^{-3}$ $(\text{ohm-cm})^{-1}$] at 200°C. The high conductivity of this glass has been suggested to be due to the salt-like structure of the glass at the higher Li_2X levels. The influence of F/O ratio on conductivity has also been investigated. Glass transition temperature shows dependence on heating and cooling rate (q) during its measurement and also on the F/O ratio. Dependence of heating and cooling rate on T_g leads to the following relationship.

$$\frac{\mathrm{d}\ln|q|}{\mathrm{d}(1/T_g)} = -\frac{\Delta H^*}{R}, \tag{7}$$

where ΔH^* represents the activation energy for structural relaxation. An increase of ΔH^* with increase of LiF content is correlated with increased packing density. Even then, the glass with higher LiF content is reported to exhibit higher conductivity. While attempting to elaborate the conduction mechanism of fluoroborate glasses, an isothermal drift in the conductivity at temperatures below T_g, is observed (Boehm and Angell 1979). Differential scanning calorimetry and conductivity measurement on quenched and annealed glasses, in the temperature range 150–200°C, yield an activation energy which is less by one order of magnitude, than the characteristic activation energy for primary structural relaxation. The discrepancy is explained in terms of secondary structural relaxation, frequently observed in polymeric glasses. The complete AC response of fluoroborate and sulphoborate glasses is studied by combining conductance studies in the frequency range 0·1 Hz to 10^6 Hz with Fourier transform interferrometric spectral measurements, in the range 10^{12}–10^{13} Hz (Angell 1981). The total AC response, is shown in figure 2. It may be noted from the figure that it covers 7 orders of magnitude of frequency-dependent conductivity and the far IR spectrum with the conversion from conductivity to optical absorption coefficient α. These results are interpreted with the help of computer simulation of the observed high fictive temperatures of Li and Na silicate glasses using the principle of motional ion dynamics.

In order to explain the exceptionally high values of conductivities from structural aspects, which would help in predicting new systems, attempts have been made to correlate conductivity results with those obtained from various spectroscopic techniques. Based on some such analysis ionic conductivities in B_2O_3-Li_2O-Li_nX system ($n = 1, X = Cl, Br, I; n = 2, X = SO_4; n = 3, X = PO_4$) have been explained (Levasseur *et al* 1979a,b, 1980, 1981a,b,c; Hagenmuller *et al* 1979; Irion *et al* 1980). The maximum conductivity attained in this system is approximately 10^{-2} (ohm-cm)$^{-1}$ at 300°C and is dependent on Li_2O and Li_nX contents. Raman spectroscopic studies on B_2O_3-xLi_2O and B_2O_3-xLi_2O-yLiCl have been carried out and the results are shown in figure 3a, b. Pure boron oxide glasses are characterised by a strong Raman peak at 806 cm^{-1} (figure 3a). The addition of Li_2O to B_2O_3 brings about a progressive disappearance of

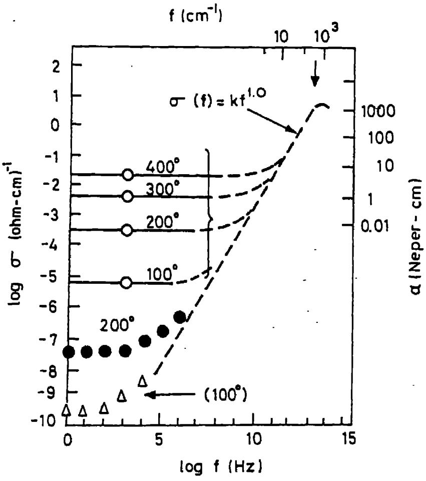

Figure 2. Frequency dependent conductivity of sulphoborate glass. Conductivity at higher frequencies determined from optical absorption coefficient (Angell 1981).

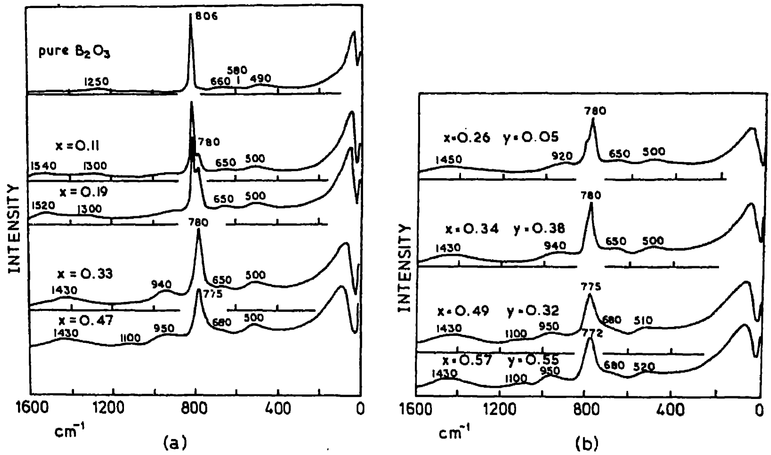

Figure 3. Raman spectra of glasses. **a.** B_2O_3-$x$$Li_2O$ and **b.** B_2O_3-$x$$Li_2O$-$y$LiCl (Levasseur *et al* 1980).

this peak and a quick intensity increase of a new strong peak at 780 cm^{-1}. At $0{\cdot}05 \leqslant x \leqslant 0{\cdot}25$ both the peaks are simultaneously present in the spectra of the B_2O_3-$x$$Li_2O$ glasses, but at $x = 0{\cdot}33$ the 806 cm^{-1} peak has completely vanished. This modification of the spectra is attributed to the progressive substitution of boroxal rings (boron only in III coordination) by triborate and tetraborate groups (boron simultaneously in III and IV coordinations). Comparing the Raman spectra of B_2O_3-$x$$Li_2O$-$y$LiCl glasses, of various compositions, (figure 3b), with that of B_2O_3-$x$$Li_2O$ (figure 3a), it is clear that there are no modifications in the structure. For a given x the spectra for binary and ternary systems are identical and it may be concluded that the addition of LiCl does not induce any modification in the vitreous boron-oxygen lattice and the interpretation of the vibrational spectra of simple borate glasses may be extended to the spectra corresponding to ternary composition. Raman scattering studies of glasses belonging to B_2O_3-$x$$Li_2O$-$y$$Li_2SO_4$ shows no modifications and the spectrum of SO_4^{2-} anions in the glass is analogous to that observed for SO_4^{2-} in aqueous solutions (Walraffen 1965). Therefore it seems that there is no apparent interaction between boron-oxygen lattice and diluted salt solutions. Investigations have also been performed on glasses containing Li_3PO_4 and its behaviour with respect to boron-oxygen network has been studied. The Raman spectra shows that PO_4 units are bound to boron-atoms. The conductivity rise has been attributed to dissociation of lithium salts. Basu *et al* (1983) have reported high values of conductivity nearly 10^{-4} $(\text{ohm-cm})^{-1}$ at 250°C for Li borate glasses containing Li_3PO_4. They have predicted that $(Li_2O + B_2O_3)$ and Li_3PO_4 mix almost ideally without any major structural change. An EPR study of fast Li^+ conducting glasses in B_2O_3-Li_2O-LiCl has been carried out, after x-ray irradiation at room temperature (Levasseur 1979b). Two types of paramagnetic centres have been reported to be present. The first is a Cl_2^- species (V_k centre) present in vitreous domain where low concentration of LiCl prevailed whereas the second is of BOHC (boron oxygen hole centre) type which is reported to be generally present in glasses. Studies on glass-forming ability in Li_2O-LiCl-Al_2O_3-B_2O_3 have been pursued for increasing Li^+ concentration (Takahashi and Yamamoto 1979). A glass with nominal composition of

29 Li_2O-$24Li_2O$-$3Li_2O$-$44B_2O_3$ (in mole %) shows maximum conductivity (7×10^{-3} $(\text{ohm-cm})^{-1}$ at 300°C) with an activation energy of 0·43 eV. Near ideal open circuit voltages of the cells and motional narrowing of ^7Li NMR spectra supports Li^+ motion in these glasses. High Li^+ conductivity has been reported in lithium chloroborate glasses nearly 10^{-2} $(\text{ohm-cm})^{-1}$ at 300°C (Button *et al* 1980). It has been demonstrated that substitutions of Cl for O (not-site-for site) in chloroborate glasses with composition 36·4 m/o Li_2Z ($Z = O, Cl_2$) – 63·6 m/o B_2O_3 results in systematic increase in Li-ion conductivity and decrease in T_g and density. Total B and Li contents have been maintained constant to facilitate changes in O/B ratio. Glasses with same O/B ratio are compared. Most NMR studies predict that the relative numbers of BO_3 and BO_4 units are characteristic of a given O/B ratio and represent overall glass structure (Geissberger *et al* 1982a; Irion *et al* 1980; Bray and O'Keefe 1963). Button *et al* (1982) have, however contradicted this view and visualized a systematically weakened and expanded network to accommodate the excess of LiCl and accordingly the structure must show compositional variation from binary to ternary. The inability of spectroscopic technique leads the authors (Button *et al* 1982) to question the validity of such technique to verify structural hypothesis such as Krogh-Moe model. The tentative model proposed by them is based entirely on the results of T_g and density. They have argued that the large ($r_{Cl^-} = 1{\cdot}8$ Å) negatively charged Cl cannot be accommodated in the structure without significant reorganization.

Figure 4 shows the schematic two-dimensional mode of the structure of a glass at relatively (a) low (b) high alkali contents and (c) a proposed structure for chloroborate glasses. It has been suggested that the Cl^- substitution induces bias for polyborate unit formation with connected BO_4 tetrahedra (*eg* diborate groups) at the expense of units with unconnected tetrahedra (*eg* tetraborate).

The ^{11}B NMR data for the lithium chloroborate and lithium fluoroborate glasses shows that no observable amounts of new covalently bonded boron microstructures (MS) are present in the network of the ternary systems and the types of units present depend on the O/B ratio of the glass (Geissberger *et al* 1982). This implies that the

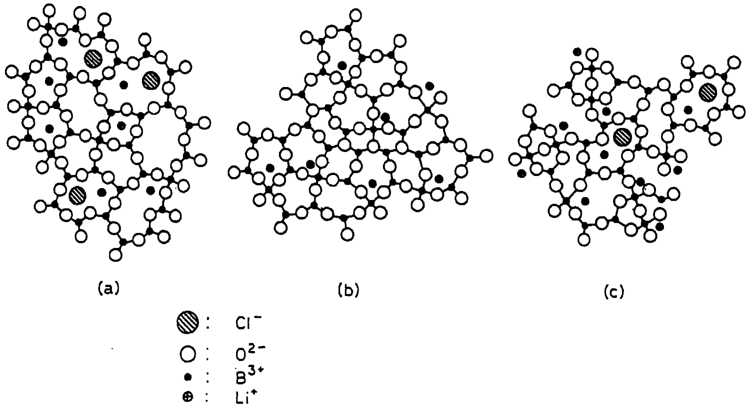

Figure 4. Two dimensional schematic representation of a lithium chloroborate glass. **a.** ternary glass with low lithium content; **b.** binary glass with high alkali content; **c.** proposed weakened and expanded structure for a ternary glass (Button *et al* 1982).

lithium halide enters the borate network interstitially, as dissociated ions and therefore does not contribute to network formation. Motional narrowing studies of the ^{7}Li NMR spectra for one of the glasses indicates that ^{7}Li ion is mobile with a characteristic activation energy of 0·2 eV. Similar studies of the ^{19}F spectra indicate either fluorine ion mobility or a very strong dependence of the ^{19}F spectrum on the lithium ion motion. Bray *et al* (1980), earlier, studied ^{10}B NMR spectra of B_2O_3 and Na_2O-B_2O_3 glasses and extended it to explain the behaviour of Li- borate containing 65 m/o Li_2O. The glasses have been thought to be composed of various structural groupings (tetraborate, metaborate, diaborate etc.) found in crystalline compounds. ^{10}B NMR spectra gives the exact number of each grouping present in the glass and facilitates formulation of specific structural units. Computer simulation techniques, to investigate the second moment and the quadrupolar structure of satellites in borate glasses with low lithia content, have explained the results in terms of BO_3 and BO_4 units (Tabby and Hendrickson 1980).

In the continued efforts to explore the possibility of highly conducting glasses, some of the investigators have studied mixed isotopic conductivity in lithium borate system. The conductivity with various ^{6}Li/^{7}Li ratios has been determined as a function of temperature using impedance analysis (Downing *et al* 1982). The conductivity decreases continuously with slight increase of activation energy as ^{7}Li is substituted for ^{6}Li and the conductivity does not follow the classical diffusion theory. The data are interpreted in terms of an absolute reaction rate theory incorporating quantum partition function. AC and DC conductivities of borate glasses containing a total of 0·2 mole fraction of $^6Li_2O$ and $^7Li_2O$ are measured (Peterson 1982; Abou *et al* 1978) and the observed mixed alkali behaviour is thought to originate from the mass difference of alkali ions.

For application as solid electrolytes, the material with required high ionic conductivity, has also to be compatible with the metal anodes. Conductivities have been optimised for borate glasses but there are no reports about their durability with molten Li or water. Durability of glasses with molten Li and water is the extension of earlier work on borate glasses where durability in molten Li was studied with and without applied field (Barsoum *et al* 1981). The lithium chloroborate glasses, investigated recently, have been studied in the temperature range 180–250°C against Li (Velez *et al* 1982). The formation of reaction layers was observed. The diffusion-controlled chemical attack predicted for corrosion was supported by parabolic increase of layer thickness with time. The rate of corrosion shows dependence on Li_2O content in the Li_2O-B_2O_3 and Li_2X/B_2O_3 (X = Cl, O) ratio in the B_2O_3-Li_2O-$(LiCl)_2$ system. For higher B_2O_3 contents ($>$ 70 m/o) durability decreases with increasing chlorine content. While for lower B_2O_3 concentrations ($<$ 50 m/o), LiCl additions help to increase durability. The activation energy of corrosion varies from 0·5 eV for pure B_2O_3 to 2 eV for high $(LiCl)_2/B_2O_3$ contents. It is suggested that a glass with minimum B_2O_3 content, consistent with glass formability, would show optimum resistance to molten Li attack. Some glasses are also studied for durability in water and buffered solution (pH = 7) at 30 and 40°C. The dissolution takes place by a reaction controlled mechanism. A minimum dissolution rate is obtained for 25–30 m/o Li_2O in the binary Li_2O-B_2O_3 system. This is found to agree well with the maximum structure connectivity for this range. The increased dissolution rate with increased LiCl contents implies a open and weakened structure with LiCl additions proposed earlier (Button *et al* 1982).

4.2 *Alkali silicate glasses*

Glasses in various alkali silicate systems show sharp decrease in resistivity an activation energies with increasing alkali content up to 20–25 m/o M_2O (M = Na, K Li) followed by much smaller changes at larger M_2O contents (Charles 1966; Otto an Milburg 1968; Hakim and Uhlman 1971). Highest conductivities of 7×10^{-6}, $1 \times 10^{-}$ and 1×10^{-6} $(\text{ohm-cm})^{-1}$ at 100°C are observed for glasses with 45 m/o Na_2O, 40 m/ K_2O and 40 m/o Li_2O respectively with activation energies ranging from 0·54–0·60 e Comparison of conductivities of glasses and glass ceramics with compositions relate to that of β-eucryptite, ($LiAlSiO_4$) shows better electrical properties for glasses than th glass ceramics (Johnson *et al* 1975, 1976). Single crystals, however, yield (Biefeld *et* 1978) higher conductivity along *c* axis than the glass but the activation energy is highe (nearly 0·82 eV against 0·62 eV for glass). Attempts have been made to increase th conductivity of the Li_2O-Al_2O_3-$2SiO_2$ glass by substituting Ga for Al, Ge for Si and for Si. However, it does not show any major effect on conductivity. Examination of th effect of replacing Si by S in the system $Li_2Si_2O_5$-Li_2SO_4 shows linear increase i conductivity with Li_2SO_4 content (Kone *et al* 1979). High ionic conductivities ar observed for a glass at the boundary of glass formation region. The activation energ (0·66 eV) does not change with composition and the increase of conductivity i attributed to the increase of σ_0. Electrical conductivity, derived from comple impedance analysis, in Li_2O-SiO_2-Li_2SO_4 system shows slightly higher values [10^{-} $(\text{ohm-cm})^{-1}$ at 100°C] compared to those obtained with single frequency measuremen (Souquet *et al* 1980; Kone *et al* 1982). The Raman spectra indicate the presence o glassy-disilicates and sulphates. From a structural point of view SO_4 tetrahedra seem to be incorporated in the micromolecular skeleton of the silicate groups. This insertio is thought to inhibit recrystallization by destroying the regularity of the SiO_4 chain and allows glass formation with high lithium content (Li/Si = 2·2). The redox stabilit studied by cyclic voltametry, shows extensive stability domain. Prasad *et al* (1980) hav reported glasses in $LiNbO_3$-SiO_2 system with 35 m/o SiO_2 which show conductivity o the order of 10^{-4} $(\text{ohm-cm})^{-1}$ at 200°C. However, a similar glass doped with 0·1 m/ Fe_2O_3 exhibits higher conductivity of nearly 10^{-3} $(\text{ohm-cm})^{-1}$. Higher addition o Fe_2O_3 causes a decrease in conductivity which the authors have associated with th onset of nucleation of crystallites within the glass matrix. A number of observations ar consistent with predominantly ionic conduction; however, no direct verification lik fabrication of concentration cell, has been attempted. Raman spectra of Fe_2O containing SiO_2-Li_2O glasses indicate that a significant fraction of trivalent iro deforms the local glass structure to form a range of structurally distinct sites as i crystalline solids. The trivalent Fe^{3+} exists in its distinct local environment in the glas structure. It has been concluded that the impurities are unable to enhance the electroni conductivity of these glasses.

4.3 *Alkali phosphate glasses*

Exceptionally high values of ionic conductivity in the unusual glass forming syste M_2O-MF-$Al(PO_3)_3$ (M = Li, Na, K, Cs) which does not contain any conventiona glass former, have been reported by Evastrop'eV *et al* (1974). A glass with nomina composition 50 LiF : $30Li_2O$: $20Al(PO_3)_3$ shows the highest conductivity of the orde of 10^{-2} $(\text{ohm-cm})^{-1}$ at 300°C. The corresponding activation energy is 0·52 eV. Th transport number of lithium ion is greater than 0·999 and does not change appreciably with temperature. Fluorine ion does not contribute towards conductivity. Some of these results have been later confirmed by Jagla and Isard (1980) who have prepared a number of glasses with different LiF contents. They have also determined the transport number to be around unity by Tubandt's (1932) method. The conductivity has been determined from a frequency-independent conductance plateau. The mixed alkali effect has been observed in $Al(PO_3)_3$-NaF-LiF system and is supported by electrical measurements, IR spectra, density, refractive index, average dispersion and molecular refraction studies (Pronkin 1978).

A more detailed investigation on the LiF-Li_2O-$Al(PO_3)_3$ has been carried out (Kulkarni *et al* 1981). Glass formation region in this system has been studied in both conventional and rapid quenching technique (Kulkarni 1984). The latter technique gives an extended glass formation region incorporating 40 m/o Li_2O against only 25 m/o in the former technique. DC electrical conductivity of the glasses has been derived from impedance/admittance analysis. Complex impedance has been measured over a wide range of frequency (5 Hz–13 MHz) at various temperatures using silver paste electrodes. A representative impedance plot is shown in figure 5. It may be observed that at each temperature the high frequency data are represented by nearly perfect circular arcs all of which pass through the origin and have their centres on a straightline also passing through origin and making a very small angle of three 3° with the real axis. Therefore, the circular arcs may be considered as nearly perfect semicircles. These semicircular arcs originate from the ionic migration in the bulk of the electrolyte and the intercept on real axis represents true DC value of the resistance excluding electrode polarisation effects which appear at lower frequencies. The observed phenomenon has been accurately modelled by proposed equivalent circuit. A glass with nominal composition 70 LiF-15Li_2O-15$Al(PO_3)_3$ shows the highest value of conductivity [$1{\cdot}3 \times 10^{-3}$ (ohm-cm)$^{-1}$] at 230°C. The electronic conductivity of these glasses has been obtained from Wagner's asymmetric cell and very low values for electronic currents have been recorded ($8{\cdot}57 \times 10^{-7}$ A/cm^2). The transport number of Li^+

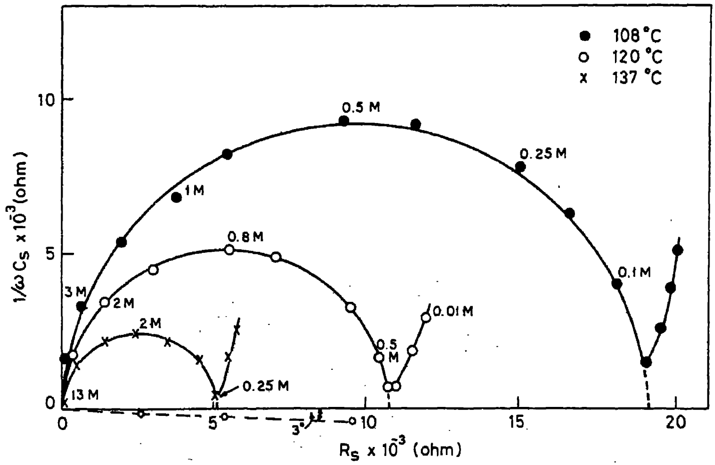

Figure 5. Complex impedance plots of LiF-Li_2O-$Al(PO_3)_3$ glass at various temperatures with silver electrodes (number on top indicate frequency in MHz).

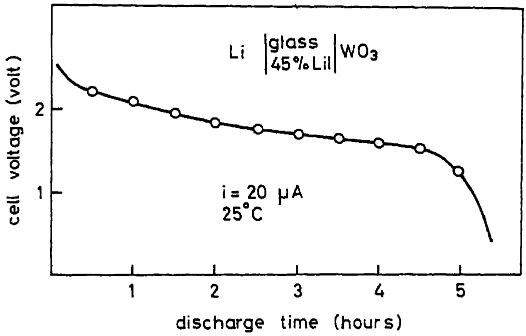

Figure 8. Discharge characteristics of a LiI-Li_2S-P_2S_5 glass in Li/Glass/WO_3 cell (Mercie *et al* 1981).

attributed to the sulphides strongly bonded to the glassy network. The electroactivit range thus determined is about 2·9 V. The discharge characteristics of a cell using Li P_2S_5-Li_2S glass has been studied at room temperature. An output curve obtained fc the cell Li/glass/WO_3 is shown in figure 8. It may be noted that the discharge at 25°C a a current density of 20 μA shows the cell stability for nearly 4 hr.

Souquet *et al* (1980) and Mercier *et al* (1981) have investigated M_2S-GeS_2 syste (M = Li, Na, Ag). GeS_2 formed stable glasses with alkali sulphides in the range 1–0 molar ratio of GeS_2/M_2S. The electrical conductivity of these glasses has bee measured over a range of temperature for different compositions. At 50 m/o Li_2S, tl conductivity is maximum [4×10^{-5} (ohm-cm)$^{-1}$] with an activation energy of 0·51 e The structure investigated by Raman spectroscopy shows that it consists of Ge tetrahedral units. Peaks for Ge-S-Ge and stretching modes of Ge-S bond with no bridging sulphur atoms are detected. At lower frequencies translational and vibration motions of the network fragments and also of Li^+ vibrations are observe Electrochemical stability of these glasses is tested by three-electrode voltametry. Tl stability range of 4 volts observed is slightly greater than that expected fro thermodynamic data corresponding to the formation of pure sulphide (2·3 volts f Li_2S). This is assigned to the lower thermodynamic activity of sulphide in glass and the slow kinetics of electrochemical reaction involving sulphur ions.

4.5 *Quenched glasses*

High Li^+ ion conductivities have also been reported in a number of specially prepar glass systems in which one normally does not expect glass formation. Glasses have be prepared by rapid quenching techniques in Li_2O-Nb_2O_5 (Glass *et al* 1978), Li_2 Ta_2O_5 (Nassau *et al* 1979a, b, 1981a), Li_2O with Al_2O_3, Ga_2O_3 and Bi_2O_3 (Glass a Nassau 1980), WO_3 (Nassau *et al* 1980), MoO_3, Li_2SO_4 with $SrMg(SO_4)_2$ a $La_2(SO_4)_3$ (Nassau and Glass 1981b). The conductivity values are reported to greatly enhanced compared to those normally observed in the corresponding crysta These enhanced conductivities [$\sigma_{250°C} \sim 10^{-3}$ (ohm-cm)$^{-1}$] are almost 10^{20} tim greater at room temperature than in single crystal $LiNbO_3$ and are attributed increased Li^+ ion mobilities. A $LiNbO_3$ glass with octahedrally coordinated niobiu has been visualised. A schematic two-dimensional representation is shown in figure

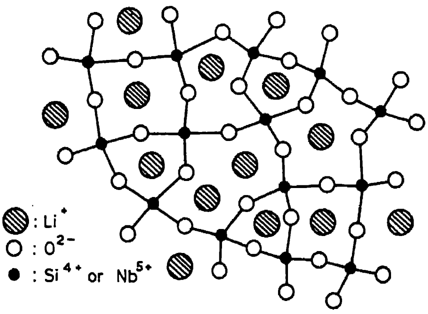

Figure 9. Schematic two dimensional representation of a lithium niobate glass with octahedrally coordinated niobium (Glass *et al* 1979).

This $LiNbO_3$ glass has been compared with silicate glasses containing tetrahedrally coordinated silicon (figure 1). Following are the important differences between these two systems. As mentioned earlier the addition of Li_2O to SiO_2 glass results in non-bridging oxygen ions in the structure which acts as hosts for alkali ions. However, in $LiNbO_3$ the Li^+ is necessary for charge neutrality but not in the structure. The conductivity of all the glasses, when plotted against the lithium atomic fraction, increases and shows a maximum of about 10^{-3} (ohm-cm)$^{-1}$ at 500°K for all the systems. However, the maxima occurred at different values of Li^+ fractions. No single explanation is appropriate for these unusual results. It is thought that the atomic substitutions attempted might have resulted in vacant interstitial sites which depend partly on the degree of short range order and partly on the distance over which the concept of local charge neutrality can be extended. It has been proposed that these glasses be viewed as quenched liquids rather than defected solids. The structure of rapidly quenched Li $(Nb_{0\cdot8}P_{0\cdot2})O_3$ glass is studied by x-ray diffraction and the co-ordination number of Nb is six (Yasui *et al* 1982). By constructing NbO_6 octahedral model the radial distribution function has been calculated. From the density and the radial distribution function a mixed model of ilmenite and pyrochlore is proposed to be most suitable for Li $(Nb_{0\cdot8}P_{0\cdot2})O_3$ glass. Electrical conductivity is around 6×10^{-4} (ohm-cm)$^{-1}$ at 450°K with an activation energy of 0·49 eV.

5. Concluding remarks

Recent studies on conducting glasses reveal some essential features of the research trends of new lithium glasses in connection with the improvement of ionic conductivity.

For some of the systems the results can be compared with the corresponding crystalline form whereas, for others they cannot. In general, the lack of structural knowledge of these glasses has slowed down the process of determining an exact transport mechanism. The distribution and number of charge carriers and their contribution to overall conductivity are not very clearly understood. Nevertheless, large data are available for discussion.

One of the interesting observations is the relative insensitivity of σ_0 to composition. For many orders of change in the magnitude of conductivity, σ_0 changes insignificantly as observed for Li-borate glasses (Angell 1981). In classical ionic conductors $\log \sigma_0$ is expected to vary linearly with composition. The observed fact in highly conducting glasses thus contradicts the classical diffusion theory (Tuller *et al* 1980).

Inorganic glasses containing alkali halides show dependence of conductivity on concentration and are therefore expected to give information regarding structural

Table 1. Ionic conductivities at different temperature and activation energy for number of lithium conducting glasses.

Glass composition	σ(25°C) (ohm-cm)$^{-1}$	σ(T°C) (ohm-cm)$^{-1}$	Activation energy (eV)	Reference
Li_2O-B_2O_3 (42·5–57·5 m/o)	$7{\cdot}1 \times 10^{-8}$	$6{\cdot}1 \times 10^{-3}$ (350)	0·60	Otto (1966)
Li_2O-B_2O_3 (63–37 m/o)	$6{\cdot}3 \times 10^{-11}$	—	0·73	Levasseur *et al* (1979)
Li_2O-Li_2Cl_2-Li_2SO_4-SiO_2-B_2O_3 (35–10–30–12·5–12·5 m/o)	$3{\cdot}3 \times 10^{-6}$	$9{\cdot}7 \times 10^{-2}$ (350)	0·53	Otto (1966)
Li_2O-LiCl-B_2O_3 (31·8–12·3–59·9 m/o)	$3{\cdot}2 \times 10^{-6}$	$1{\cdot}7 \times 10^{-2}$ (300)	0·50	Levasseur *et al* (1979)
Li_2O-LiCl-Al_2O_3-B_2O_3 (29–24–3–44 m/o)	$1{\cdot}3 \times 10^{-6}$	$1{\cdot}5 \times 10^{-2}$ (350)	0·49	Takahashi and Yamamoto (1979)
Li_2O-LiF-Li_2SO_4-Li_2SO_3-B_2O_3 (22·1–12–6–15·8–20·5–28·5 m/o)	$6{\cdot}2 \times 10^{-7}$	$2{\cdot}3 \times 10^{-3}$ (200)	0·57	Smedly and Angell (1978)
Li_2O-Li_3PO_4-B_2O_3 (25–10–65 m/o)	$7{\cdot}44 \times 10^{-9}$	$1{\cdot}0 \times 10^{-3}$ (330)	0·62	Basu *et al* (1983)
Li_2O-LiI-B_2O_3				
Li_2O-LiF-B_2O_3 (20–36–44 m/o)		$3{\cdot}14 \times 10^{-4}$ (200)	0·58	Smedly and Angell (1978)
Li_2O-Li_2SO_4-B_2O_3 (0·71–1·1–1·0 mole ratio)	—	$2{\cdot}10 \times 10^{-2}$ (300)	0·58	Levasseur *et al* (1979)
Li_2O-SiO_2 (40–60 m/o)	$9{\cdot}20 \times 10^{-9}$	1×10^{-6} (100)	0·63	Otto and Milbert (1968)
Li_2O-Al_2O_3-SiO_2 (25–25–50 m/o)	$6{\cdot}20 \times 10^{-10}$	$6{\cdot}1 \times 10^{-4}$ (350)	0·72	
Li_2O-Al_2O_3-SiO_2 (25–25–50 m/o)	$6{\cdot}20 \times 10^{-10}$	$6{\cdot}1 \times 10^{-4}$ (250)	0·72	
Li_2O-B_2O_3-SiO_2 (39–13–48 m/o)	$4{\cdot}30 \times 10^{-9}$	$1{\cdot}5 \times 10^{-3}$ (350)	0·67	Biefeld *et al* (1978)
Li_2O-SiO_2 (33·3–66·7 m/o)	$2{\cdot}8 \times 10^{-9}$	$1{\cdot}9 \times 10^{-3}$ (350)	0·70	
($Li_2Si_2O_5$)				

Li_2O-Li_2SO_4-SiO_2	—	1×10^{-5} (100)	0·56–0·65	Souquet *et al* (1980, 1982)
$LiNbO_3$-SiO_2 (65–35 m/o)	—	1×10^{-4} (200)		Prasad *et al* (1980)
$LiPO_3$-LiF (60–40 m/o)	$6\cdot7 \times 10^{-9}$	—	0·63	Malugani and Robert (1979)
$LiPO_3$-LiCl (70–30 m/o)	$1\cdot0 \times 10^{-7}$	$1\cdot0 \times 10^{-3}$ (220)	0·63	
$LiPO_3$-LiI (67–33 m/o)	$1\cdot0 \times 10^{-6}$	$1\cdot0 \times 10^{-3}$ (194)	0·56	
$LiPO_3$-LiBr (67–33 m/o)	$3\cdot2 \times 10^{-7}$	$1\cdot3 \times 10^{-3}$ (220)	0·57	
$LiPO_3$-Li_2SO_4 (67–33 m/o)	$1\cdot0 \times 10^{-7}$	$3\cdot5 \times 10^{-3}$ (250)	0·66	Malugani *et al* (1978)
Li_2O-LiF-$Al(PO_3)_3$ (30–50–20 m/o)	$5\cdot8 \times 10^{-7}$	$1\cdot0 \times 10^{-2}$ (300)	0·56	Evastrop'eV *et al* (1974), Jagla and Isard (1980)
Li_2O-LiF-Al $(PO_3)_3$ (15–70–15 m/o)		$1\cdot3 \times 10^{-3}$ (220)	0·53	Maiti *et al* (1983)
Li_2S-P_2S_5 (33–66 m/o)	$1\cdot1 \times 10^{-4}$			Ribes *et al* (1979)
Li_2S-LiI-P_2S_5 (37–45–18 m/o)	$1\cdot0 \times 10^{-3}$		0·31	Malugani and Robert (1980), Mercier *et al* (1981)
Li_2S-GeS_2 (50–50 m/o)	$4\cdot0 \times 10^{-5}$		0·51	Souquet *et al* (1981), Ribes *et al* (1980)
Li_2O-Nb_2O_5 (50–50 m/o)	$1\cdot6 \times 10^{-6}$	$5\cdot3 \times 10^{-3}$(350)	0·44	Glass *et al* (1978)
Li_2O-Ta_2O_5 (50–50 m/o)	$5\cdot0 \times 10^{-6}$	$6\cdot4 \times 10^{-3}$(350)	0·39	Nassau *et al* (1979a, b; 1981)

changes. The conductivity tends to increase with a drop in corresponding activati energy. A linear decrease has been observed by Malugani *et al* (1978). Though its orig is not known, it is expected to result from a structural breakdown since the gl transition temperature also repeats this observation. It is assumed that the anion is n inserted into the micromolecular chain and the chain preserves the characteristics of t original glass. This structural hypothesis has been confirmed by Raman spectrosco with borate glasses as well as phosphate glasses. The Raman spectrum does not sh any modification, corresponding to P-O vibrational mode upon addition of lar quantities of halides. Tuller *et al* (1980) have interpreted this model as a form of pha separation which may occur on a scale difficult to identify by most conventional mea Phase separation would, however, be expected to show discontinuous change activation energy as the highly conducting phase changes from isolated pockets to continuous phase throughout the material.

Conductivities of glasses containing alkali salts also show almost linear increase wi radius of halide ion. Two factors have been suggested to explain the observ behaviour. The first concerns the polarizability of anions the larger the anion, t greater is the polarizability, and thus the ease with which its electron cloud may deformed. The second approach considers dilation of structure due to larger radius anions thereby decreasing the packing density which eases the squeezing of the io through the opening. This model also supports the decrease in activation energy, sin the activation energy for motion is inversely proportional to the size of the openin Although these models are reasonable and agree qualitatively with experiment results, the universal acceptance might require data analysis in much greater detail

Quenching techniques show the ability to produce wide variety of new oxide glasse Though the glasses so prepared give thin films or flakes (2 μm thick) the area is too lo (few mm^2) to permit any large scale application. It is therefore necessary to explor techniques which will give films with larger surface area. Structural aspects of thes

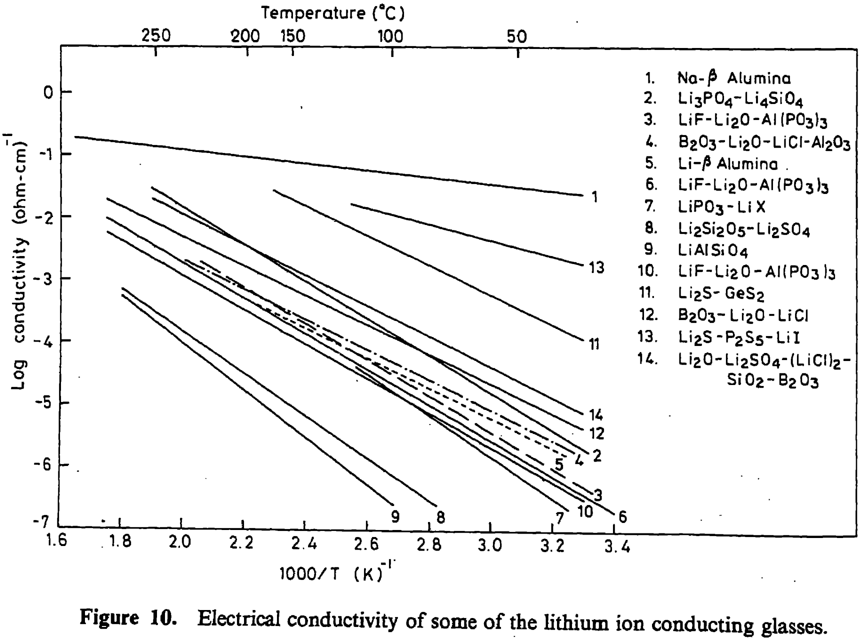

Figure 10. Electrical conductivity of some of the lithium ion conducting glasses.

glasses are not yet very clear as compared to conduction mechanism and it becomes difficult to predict new systems.

To conclude this review on the present knowledge of the electrical properties of glassy electrolytes, we have shown in table 1 a comparison of the performance of different lithium conducting glassy electrolytes. Composition, conductivity and activation energies are included. A plot of log σ *vs* reciprocal of temperature, for different glassy solid electrolytes along with some of the well-known crystalline solid electrolytes like β-alumina, Li_4SiO_4-Li_3PO_4 etc is given in figure 10. It may be noted that the electrical properties of these electrolytes compare quite well with the traditional crystalline electrolytes.

Finally, it may also be noted that most of the conductivity measurements have been inadequately performed without information on possible electronic and anionic transport numbers. Applicability of glasses, characterised for electrochemical applications such as batteries, coulometers, potential memory cells and display devices remain to be tested for many systems. Electrochemical stability range (redox-stability) and charge transfer kinetics are to be optimised to get the most suitable electrolyte. The knowledge about electrochemical performance is, however, not the only essential aspect for future development in this class of materials, but the structural studies will also play an important role to predict new glassy systems, which would be useful for practical applications in future advanced devices.

Acknowledgement

The authors would like to acknowledge financial support from the Electronics Commission, Government of India.

References

Abou El Anour A 1979 Ph.D. Thesis, Besancon

Abour El teil M, Heasley J and Omer M H 1978 *Phys. Chem. Glasses* **19** 37

Angell C A 1981 *Solid State Ionics* **5** 659

Armstrong R D, Dickinson T and Wills P M 1974 *J. Electroanal. Chem.* **53** 389

Barsoum M, Velez M H, Tuller H L and Uhlmann D R 1981 *Surfaces and interfaces in ceramic and ceramic-metal systems* (eds) J Pask and A Evans (New York: Plenum) p. 567

Basu B, Maiti H S and Paul A 1983 *Bull. Mater. Sci.* **5** 21

Bauck F G K 1975 *Mass transport phenomena in ceramics* (eds) A R Cooper and A H Heuer (New York: Plenum) p. 337

Baurale J E 1969 *J. Phys. Chem. Solids* **30** 2657

Biefeld R M, Johnson R T and Banghman R J 1978 *J. Electrochem. Soc.* **125** 179

Boehm L and Angell C A 1979 *Fast ion transport in solids* (eds) P Vashishtha, G K Shenoy and J N Mundy (North-Holland: Elsevier) p. 721

Bottelberghs P H 1978 *Solid electrolytes, general principles, characterization, materials applications* (eds) P Hagenmuller and W vanGool (New York: Academic Press) p. 145

Bray P J and O'Keefe J G 1963 *Phys. Chem. Glasses* **4** 37

Bray P J, Feller S A, Jellinson G E Jr and Yen Y H 1980 *J. Non Cryst. Solids* **38, 39** 93

Britzs D 1980 *Anal. Chem.* **52** 1166

Button D P, Tondon R P and Uhlmann D R 1980 *J. Non Cryst. Solids* **42** 297

Button D P, Tondon R P, King C, Velez M H, Tuller H L and Uhlmann D R 1982 *J. Non Cryst. Solids* **49** 129

Charles R J 1961 *J. Appl. Phys.* **32** 1115

Charles R J 1966 *J. Am. Ceram. Soc.* **49** 55

Doreau M, Anou El Anouar A and Robert G 1980a *Mat. Res. Bull.* **15** 285

Doreau M and Robert G 1980 *Mater. Res. Bull.* **15** 1499

Downing H L, Peterson N L and Jain H 1982 *J. Non Cryst. Solids* **50** 203

Evastrop'eV K K, Veksler G I and Kondrat'eva B S 1974 *Dokl. Akad. Nauk. SSR* **215** 902

Geissberger A E, Bucholty F and Bray P J 1982a *J. Non Cryst. Solids* **49** 117

Glass A M, Nassau K and Negram T J 1978 *J. Appl. Phys.* **49** 4808

Glass A M, Nassau K and Olson D H 1979 *Fast ion transport in solids* (eds) P Vashishtha, G K Shenoy J N Mundy (North Holland: Elsevier) p. 707

Glass A M and Nassau K 1980 *J. Appl. Phys.* **51** 3756

Grant R J, Ingram M D and West A R 1977 *J. Electroanal. Chem.* **80** 239

Hagenmuller P, Levasseur A, Lucat C, Reau J M and Villeneuve G 1979 *Fast ion transport in solids* (P Vashishtha, G K Shenoy and J N Mundy (North-Holland: Elsevier) p. 637

Hakim R M and Uhlmann D R 1971 *Phys. Chem. Glasses* **12** 132

Hodge I M, Ingram M D and West A R 1976 *J. Electroanal. Chem.* **74** 125

Hughes K and Isard J O 1972 *Physics of electrolytes* (ed.) J H Hladik (New York: Academic Press) V p. 351

Irion M, Couzi M, Levasseur A, Reau J M and Brethous J C 1980 *Solid State Chem.* **31** 285

Jagla M and Isard J O 1980 *Mat. Res. Bull.* **15** 1327

Jeitschko W and Bither T A 1972a *Z. Naturforsch.* **B27** 1423

Jeitschko W 1972b *Acta Crystallogr.* **B28** 60

Jeitschko W, Bither T A and Bierstedt 1977 *Acta Crystallogr.* **B33** 2767

Johnscher A K 1978 *J. Mater. Sci.* **13** 553

Johnson R T, Morrison B, Knotek M L and Biefeld R M 1975 *Phys. Lett.* **A54** 403

Johnson R T, Biefeld R M, Knotek M L and Morrison B 1976 *J. Electrochem. Soc.* **123** 680

Kone A, Barrau B, Souquet J L and Ribes M 1979 *Mat. Res. Bull.* **14** 393

Kone A, Ribes M and Souquet J L 1982 *Phys. Chem. Glasses* **23** 18

Kulkarni A R, Maiti H S and Paul A 1981 *Glass formation and electrical conductivity in the system LiF-Li* Al$(PO_3)_3$, paper presented in the 45th Annual Session of Indian Ceramic Society

Kulkarni A R, Maiti H S and Paul A 1984 (to be published)

Kulkarni A R 1984a *Lithium ion conducting glassy solid electrolytes in the* LiF-Li_2O-$Al(PO_3)_3$ *system.* Ph Thesis submitted to IIT Kharagpur

Levasseur A, Cales B, Reau J M and Hagenmuller P 1978 *Mat. Res. Bull.* **13** 205

Levasseur A, Brethous J C, Reau J M and Hagenmuller P 1979 *Mater. Res. Bull.* **14** 921

Levasseur A, Kabla M, Brethous J C, Reau J M, Hagenmuller P and Couzi M 1979a *Solid State Commun.* 839

Levasseur A, Brethous J C, Hagenmuller P, Berge R and Vignand G 1979b *Solid State Commun.* **32** 1

Levasseur A, Brethous J C, Reau J M, Hagenmuller P and Couzi M 1980 *Solid State Ionics* **1** 117

Levasseur A 1981 *Report EUR* 7070 *FR Comm. European Communities Luxemberger* p. 40

Levasseur A, Olazcuaga R, Kabla M, Zahir M, Hagenmuller P and Couzi M 1981 *Solid State Ionics* **2**

Levasseur A, Brethous J C, Kabla M and Hagenmuller P 1981b *Solid State Ionics* **5** 651

MacDonald J R 1976a *Superionic conductors* (eds) G D Mahan and W L Roth (New York: Plenum Pr p. 81

MacDonald J R and Jacobs P W M 1976b *J. Phys. Chem. Solids* **37** 1117

Maiti H S, Kulkarni A R and Paul A 1983 *Lithium conducting glassy solid electrolytes in the LiF-Li* $Al(PO_3)_3$ *system* Paper presented in the 4th International Conference on Solid State Ionics Greno France

Malugani J P, Wasniewski A, Doreau M and Robert G 1978 *C R Acad. Sci. Paris* **287** 455

Malugani J P and Robert G 1979 *Mater. Res. Bull.* **14** 1075

Malugani J P and Robert G 1980 *Solid State Ionics* **1** 519

Mercier R, Malugani J P, Fahys B and Robert G 1981 *Solid State Ionics* **5** 663

Nakajima T 1972 *1971 annual report conference on electrical insulation and dielectric phenomena, Natl. Ac Sci.*

Nassau K, Wang C A and Grasso M 1979a *Am. Ceram. Soc.* **62** 74

Nassau K, Wang C A and Grasso M 1979b *Am. Ceram. Soc.* **62** 503

Nassau K, Glass A M and Olson D H 1980 *J. Electrochem. Soc.* **127** 2743

Nassau K, Cava R J and Glass A M 1981a *Solid State Ionics* **2** 163

Nassau K and Glass A M 1981b *J. Non. Cryst. Solids* **44** 97

Otto K 1966 *Phys. Chem. Glasses* **7** 29

Otto K and Milberg M E 1968 *J. Am. Ceram. Soc.* **51** 326
Peterson N L 1982 *Philos. Mag.* **46** 351
Prasad E, Sayer M and Vyas H M 1980 *J. Non. Cryst. Solids* **40** 119
Pronkin A A 1978 *Sov. J. Phys. Chem.* **4** 388
Ravaine D and Souquet J L 1973 *Proc. 24th Meeting ISE* Eindhoven
Ravaine D and Souquet J L 1974 *J. Chim. Phys.* **71** 693
Ravaine D and Souquet J L 1977 *Phys. Chem. Glasses* **18** 27
Ravaine D and Souquet J L 1978 *Solid electrolytes, general principles, characterization, materials application* (eds) P Hagenmuller and W vanGool (New York: Academic Press) p. 277
Ribes M, Ravaine D, Souquet J L and Maurin M 1979 *Rev. Chim. Miner.* **16** 339
Ribes M, Barrau B and Souquet J L 1980 *J. Non-Cryst. Solids* **38, 39** 271
Smedly S I and Angell C A 1978 *Solid State Commun.* **27** 21
Smedely S I and Angell C A 1980 *Mat. Res. Bull.* **15** 421
Shlesing M 1980 *Bull. Am. Phys. Soc.* **25** 434
Souquet J L, Kone A and Ribes M 1980 *J. Non Cryst. Solids* **38, 39** 307
Stevels J M 1957 *The Electrical properties of glass in Handbook der Physics* (Berlin: Springer-Verlag) Vol. 20 p. 380
Tabby M P and Hendrickson J R 1980 *J. Non Cryst. Solids* **38, 39** 51
Takahashi T and Yamamoto Y 1979 *Chem. Lett.* 135
Taylor H E 1959 *J. Soc. Glass Tech.* **43** 124T
Tomozawa M 1977 *Treatise on materials science and technology* (eds) M Tomozawa and R H Doremus (New York: Academic Press) Vol 12 p. 283
Tubandt C 1932 *Handbuch der Experimental Physik* (eds) W Weiss and F Harms (Leipzig: Akademische Verlagsgesellschaft) Vol 21 p. 383
Tuller H L, Button D P and Uhlmann D R 1980 *J. Non Cryst. Solids* **40** 93
Velez M H, Tuller H L and Uhlmann D R 1982 *J. Non Cryst. Solids* **49** 351
Wagner C 1956 *Z. Electrochem.* **60** 4
Wagner C 1957 *International Committee of Electrochemical Thermodynamics and Kinetics*, Proceeding 7th Meeting Butterworths London
Walraffen G E 1965 *J. Chem. Phys.* **43** 479
Warburg G 1884 *Ann. Phy.* **21** 622
Yakoto I 1955 *J. Phys. Soc. Jpn.* **8** 595
Yasui I, Ohta E, Hasegawa H and Imaoka M 1982 *J. Non Cryst. Solids* **52** 283

Bull. Mater. Sci., Vol. 6, No. 2, May 1984, pp. 223–230. © Printed in India.

Lithium solid electrolytes and their applications

D N BOSE and D MAJUMDAR

Materials Science Centre, Indian Institute of Technology, Kharagpur 721 302, India

Abstract. The preparation, characterisation and applications of two systems of lithium ion conductors, lithium zinc germanate (Lisicon) and lithium germanate vanadate are described. Ionic conductivity studies include ac conductivity, thermopower and NMR which provide complementary information. High pressure studies and fabrication of a solid-state cell are also reported.

Keywords. Lithium ion conductors; NMR; high pressure; ionic conductivity studies; thermopower.

1. Introduction

Solid-state ionics is a developing field in which fundamental interest in the dynamics of ionic motion is matched by a multiplicity of possible technological applications. Among these are electrochromic displays, solid state sensors, thermoelectric devices, fuel cells and finally solid state batteries. As is well known, energy conversion and storage are vital contemporary problems and solid state batteries have the potential of evolving into much-needed storage elements to complement silicon solar cells. However, while new concepts and materials in photovoltaic energy conversion are continuously being generated, energy storage remains in practice tradition-bound to liquid electrochemical systems.

Among solid-electrolyte systems lithium due to its low atomic weight and highly electropositive nature holds a special place. These properties lead to the possibility of high energy storage density and cell voltages up to 3 V. Further, the metal is relatively easy to handle at room temperature and is also less expensive than noble metals such as silver. A number of cathode materials with high lithium diffusion coefficients are also available, some of which utilise the phenomenon of intercalation.

The outstanding problem with most solid electrolytes is their comparatively low conductivity near ambient temperatures. Most lithium solid electrolytes for example have appreciable conductivity only above 250–300°C. Electrode and electrolyte stability over long periods are also remnant problems.

In this paper we review the properties of some lithium ion conducting systems investigated by us. These are lithium germanates (which includes Lisicon) and lithium germanate vanadates. The work involves the preparation of the mixed oxide systems, characterization using x-ray diffraction, DTA and TGA studies, measurements of ionic conductivity, thermopower, NMR line narrowing and also high pressure ionic conductivity studies reported here for the first time. The fabrication of a fully solid-state battery is also described.

2. Structure and preparation

The materials studied belong to two systems:

(i) $Li_{16-2x}D_x(TO_4)_4$ where D is a divalent cation (Zn^{2+} or Mg^{2+}), T is a tetravale cation (Si^{4+} or Ge^{4+}) and $0 < x < 4$.

(ii) $Li_{3+x}Ge_x V_{1-x}O_4$ ($0{\cdot}25 \leqslant x \leqslant 0{\cdot}75$).

A representative of the first system is $Li_{14}Zn(GeO_4)_4$ which was first studied Hong (1978) who named it Lisicon for lithium superionic conductor. At 573 K conductivity was $1{\cdot}3 \times 10^{-1}$ ohm^{-1} cm^{-1}, the highest for any lithium ion conductor this temperature. The crystal structure was orthorhombic and may be visualised comprising a rigid network structure consisting of $[Li_{11}Zn(GeO_4)_4]^{3-}$, the remaini $3Li^+$ ions which give rise to ionic conductivity being distributed among interstitial sit

The second system first investigated by Kuwano and West (1980) is a member of t solid solution $Li_3VO_4 - Li_4GeO_4$. The compounds have tetrahedral structure witl high concentration of interstitial Li^+ ions. Bruce and West (1980) studied the pha diagram of Lisicon and reported that this particular composition was unstable wi respect to annealing at high temperatures resulting in precipitation of Li_4GeO_4. T compound was also very susceptible to atmospheric attack. It was suggested that t composition $Li_{12}Zn_2(GeO_4)_4$ would be more stable as regards both these factors. Th the present investigations examine both compositions in some detail.

There has been some disagreement regarding the magnitude of the ionic conductivi of Lisicon at 300°C since later workers (*e.g.* von Alpen *et al* 1978) obtained values ne $1{\cdot}25 \times 10^{-2}$ ohm^{-1} cm^{-1} using complex plane impedance techniques. The activati energies were also much higher, 0·42–0·56 eV as compared to 0·24 eV found by Ho (1978).

Thus there is considerable interest in examining the ionic conductivity a atmospheric stability of these compounds. The moisture sensitivity has been clea delineated in the present studies by studying the effects of aging on ionic conductivity well as on NMR, the detection of proton resonance signals giving a direct indication the presence of water.

For preparation of Lisicon, mixtures of Li_2CO_3, ZnO and GeO_2 were taken stoichiometric proportions and then fired first in the temperature range 700–750°C f 5–6 hr in order to drive off CO_2. The temperature was then slowly increased in t range 900–950°C and maintained for 2–3 hr cold-pressed specimens being sinter thereafter in air for 2 hr at 1000°C. The densities of the polycrystalline samples th obtained were between 85–90% of the theoretical value.

For the vanadates with the generic formula $Li_{3+x}Ge_xV_{1-x}O_4$, x was varied fro 0·25 to 0·75. Samples were prepared by solid state reaction between appropria proportions of Li_4GeO_4 and Li_3VO_4 and fired at temperatures between 800–1000°

3. Characterization

Samples prepared were characterized using x-ray powder diffraction, the resul obtained being in agreement with those of other workers. Results of DTA and TC studies at heating rates of 10°C/min were carried out on aged samples of compound $Li_{14}Zn(GeO_4)_4$ as well as compound B $Li_{12}Zn_2(GeO_4)_4$. One endothermic pea associated with weight loss was observed for both compounds at 373 K while t second peaks were observed at 943 K and 913 K respectively. These may be associated with loss of water molecules from the intergrain region at lower temperature and from within the grains at higher temperature. The results are discussed in greater detail in conjunction with NMR experiments. For vanadates DTA and TGA results were similar to those obtained with Lisicon indicating three peaks one at ~353 K and the other two between 900 and 1023 K. The effect of moisture absorption was more prominent for samples with lower lithium content.

4. Ionic conductivity and NMR studies

4.1 *Lisicon*

Ionic conductivity measurements were carried out using ac impedance technique at frequencies between 20 Hz–100 kHz. Details of measurement techniques and interpretation of the complex plane plots have been reported elsewhere (Majumdar *et al* 1983). From plots shown in figure 1, the intergrain and intragrain resistances associated with the low and high frequency semi-circles respectively have been obtained at temperatures between 306 and 578 K. The activation energies for compounds A and B thus determined are given in table 1. The intragrain activation energies (0·60 and 0·47 eV respectively) were much larger than the intergrain energies (0·38 and 0·35 eV).

The thermoelectric powers of the compounds determined were found to be negative for both compounds. The activation energies were 0·59 and 0·50 eV respectively for the two compounds, in close agreement with the intragrain activation energies.

NMR line narrowing was observed for both compounds, the onset being at 230 K for A and at 240 K for B. A plot of $1/\tau$ *vs* $1/T$, where τ is the ionic hopping time, is shown in figure 2 from which activation energies for ionic motion were 0·19 and 0·17 eV

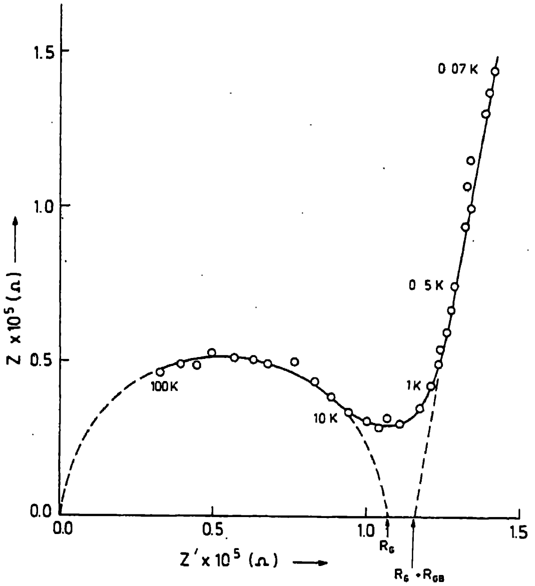

Figure 1. Complex plane impedance plot for compound A. R_G and R_{GB} are grain and grain boundary resistances respectively.

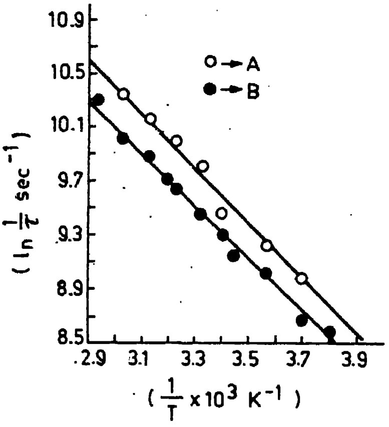

Figure 2. Ln $1/\tau$ *vs* $10^3/T$ for compounds A and B.

Table 1. Intragrain conductivity (σ_G), intragrain and intergrain activation energy in Lisicon compounds.

Compounds	σ_G (ohm^{-1} cm^{-1}) at		Activation energy (eV)	
	306 K	578 K	Intragrain (E_G)	Intergrain E_{GB}
$Li_{14}Zn(GeO_4)_4$	$1{\cdot}3 \times 10^{-6}$	$2{\cdot}47 \times 10^{-2}$	0·60	0·38
$Li_{12}Zn_2(GeO_4)_4$	$3{\cdot}82 \times 10^{-6}$	$9{\cdot}47 \times 10^{-3}$	0·47	0·35

Table 2. Conductivity and activation energy (deduced from conductivity and NMR) in $Li_{3+x}Ge_xV_{1-x}O_4$ $(0{\cdot}25 \leqslant x \leqslant 0{\cdot}75)$.

Compound	σ(ohm^{-1} cm^{-1}) at		E_σ (eV)	E_{NMR} (eV)
	306 K	473 K		
$Li_{3\cdot25}Ge_{0\cdot25}V_{0\cdot75}O_4$	$2{\cdot}26 \times 10^{-6}$	—	—	0·41
$Li_{3\cdot6}Ge_{0\cdot6}V_{0\cdot4}O_4$	$5{\cdot}14 \times 10^{-6}$	$2{\cdot}11 \times 10^{-3}$	0·48	0·44
$Li_{3\cdot67}Ge_{0\cdot67}V_{0\cdot33}O_4$	$1{\cdot}75 \times 10^{-6}$	$7{\cdot}25 \times 10^{-4}$	0·485	0·41
$Li_{3\cdot72}Ge_{0\cdot72}V_{0\cdot28}O_4$	$7{\cdot}35 \times 10^{-7}$	$4{\cdot}27 \times 10^{-4}$	0·49	0·42
$Li_{3\cdot75}Ge_{0\cdot75}V_{0\cdot25}O_4$	5×10^{-7}	$2{\cdot}03 \times 10^{-4}$	0·48	0·43

respectively for compounds A and B. After storage of samples over a few weeks the narrow ^{7}Li NMR line decreased in intensity, while a ^{1}H NMR line appeared indicating the presence of water molecules.

4.2 *Lithium germanate vanadates*

Complex impedance plots for these compounds did not yield complete semicircles due to frequency limitation but the activation energies for intragrain and intergrain conduction could nevertheless be deduced as before. The results are shown in table 2 and indicate an intragrain activation energy of approximately 0·49 eV for all the compositions. In this case fairly good agreement was obtained with the NMR-determined activation energy which was 0·41–0·44 eV.

The effect of aging resulted in a reduction of conductivity by a factor of 3–4 and in an increase in the intragrain activation energy to 0·66 eV. Moisture absorption was directly indicated by the appearance of a strong ^{1}H NMR line.

5. High pressure studies

Ionic conductivity measurements have surprisingly remained limited to pressures below 10–15 kb, in which range small monotonic variations have been noted for compounds such as the mixed silver iodides. Present experiments were conducted at pressures up to 80 kb in a tungsten carbide anvil apparatus employing four-point probes and yielded a wealth of data. At low pressures for all the compounds investigated there was a decrease in conductivity or an increase in resistivity by a factor varying from 1·13 to 1·42. After a resistance maximum at pressures between 20–25 kb for compounds A and B the resistivity decreased sharply and levelled off at the highest pressures. The pressure variation of the vanadates is shown in figure 3, the resistivity being observed to decrease by a factor of 250 at the highest pressure in fresh specimens. On aged specimens the variation of resistivity was much less while the resistivity maxima increased to higher pressures.

Examination of the pressure dependence as a function of temperature enabled the

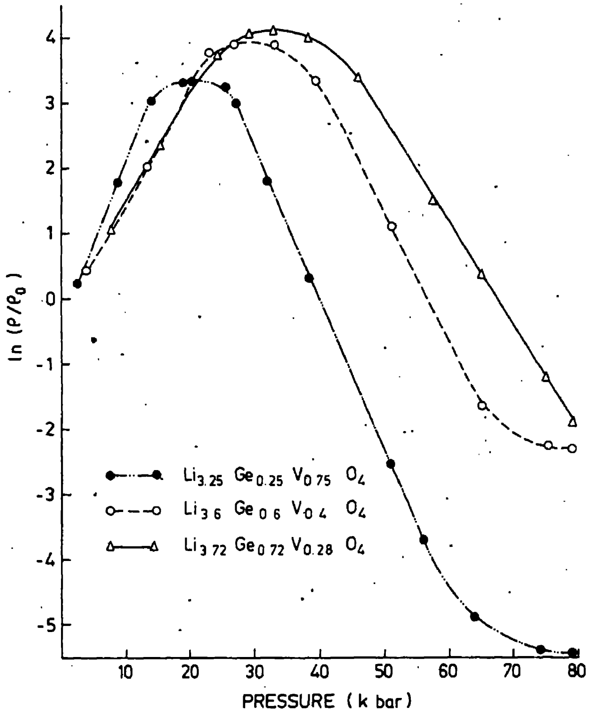

Figure 3. ln (ρ/ρ_0) vs pressure for lithium germanate vanadates.

determination of the variation of activation energy and pre-factor σ_0 with pressur was thus found that both went through maxima at 20–25 kb for Lisicon.

One possible interpretation of the observed behaviour is that the bottlene between which the lithium ions move are reduced in size with the applicatior pressure thus increasing the activation energy. Thereafter a phase transition occur observed in many related lithium compounds (Liebertz and Rooymans 1967) resul in a sharp decrease in activation energy. Alternative interpretations involve the in decrease in entropy with pressure but a discontinuous change in activation volume n be invoked to explain the pronounced resistivity maxima. The aging effect due to inhibition of lithium ion motion by adsorbed water not only reduces the variatio resistivity with pressure, but also shows that such motion of lithium ions is neces for the observed resistivity maximum as would be the case for a displacive pl transition. This may account for the displacement of the resistivity maxima to l pressures in all cases.

6. Solid-state cell

A rechargeable solid-state cell was fabricated to demonstrate the potential of lith solid electrolytes. In this case the structure was:

$$Li_{0.5}VO_2/Li_{3.6}Ge_{0.6}V_{0.4}O_4/TiS_2.$$

Here $Li_{0.5}VO_2$ was used as the lithium source which acted as the anode $Li_{3.6}Ge_{0.6}V_{0.4}O_4$ as the solid electrolyte since it showed the highest conducti among the vanadate systems studied. TiS_2 which is a good electronic conductor used as the cathode which can intercalate lithium ions. The overall cell reaction is gi by

$$Li_{0.5}VO_2 + TiS_2 = Li_{0.5}TiS_2 + VO_2.$$

The cell was prepared by pressing the sandwich structure inside a steel die a pressure of 2 tonnes/inch^2. The cell characteristics were studied at 473 K whe maximum open-circuit voltage of 0·5 V and a current of 5×10^{-6} A/cm^2 was obtai During discharge lithium ions moved into TiS_2 from the electrolyte while during charging cycle externally applied potential drove the lithium ions back into the an Considering the free energy of the above reaction, the theoretical value of open-cir voltage was calculated to be 0·52 eV in good agreement with the experimental va The cell could be discharged and recharged over 20 times although with somev diminishing performance.

7. Discussion

While lithium ionic conductivities up to $2{\cdot}47 \times 10^{-2}$ ohm^{-1} cm^{-1} at 578 K have b found for Lisicon and $2{\cdot}11 \times 10^{-3}$ ohm^{-1} cm^{-1} at 473 K for $Li_{3.6}Ge_{0.6}V_{0.4}O_4$, l conductivity at room temperature is yet to be attained. Shahi and Wagner (1982) reported the use of a dispersed insulating phase to enhance ionic conductivity in si ion conductors. However, such an approach of incorporating alumina or silica w tried with the present systems did not provide encouraging results.

For high conductivity while the lithium ion concentration was important at l temperatures, the concentration of vacant interstitial sites as well as high lithium ion mobility were important factors specially at intermediate temperatures. This was exemplified by the occurrence of highest conductivity for $x = 0{\cdot}6$ in the vanadate system.

The observed conductivities were less than the highest reported in the literature. Although this may be due to differences in sintering procedure and grain size, it is more likely to be due to the high moisture sensitivity of the compounds. The NMR technique was very suitable for detecting presence of water in compounds which inhibited both inter and intragrain conduction. However, while NMR generally sensed short-range motion, ionic conductivity and thermopower were determined by long-range motion with the resultant difference in activation energies.

The high pressure studies provided first observation of pronounced resistivity maxima in solid electrolytes. Further work is obviously required to establish the occurrence of a phase transition which is considered to lead to enhanced conductivity at high pressures. Measurements on single crystals may also throw light on the high pressure behaviour. However, on polycrystalline samples it is apparent that both intergrain and intragrain motions are affected. Chemical methods of structural modification to mimic high pressure behaviour may result in the much-desired high conductivity near room temperature. Alternative approaches may involve the use of r.f. sputtered thin films as recently reported (Ohtsuka and Yamaji 1983). The realisation of high cell voltages necessitates the use of anode material such as LiSi or LiAl with high lithium activity. The study of the stability of electrode-electrolyte systems then becomes of utmost importance for the realisation of practical solid-state batteries.

8. Conclusions

The properties of lithium ion conducting mixed oxides have been examined using a number of techniques. It is shown that complex-plane impedance plots are essential in separating the different components that contribute to conduction and in determining their activation energies. NMR provides a valuable tool in examining microscopic motion as also the effects of moisture. High pressure studies have demonstrated for the first time pronounced conductivity minima followed by enhanced conductivity. Finally a solid state battery using lithium intercalation has been fabricated and tested.

Acknowledgements

The authors thank Prof. M Bose and Dr A Basu for fruitful collaboration in the NMR measurements and Prof. E S R Gopal and G Parthasarathy for the excellent high pressure studies. They are grateful to the Indian National Science Academy for a project which initiated the work.

References

Alpen U V, Bell M F, Wichelhaus W, Cheung K Y and Dudley G J *Electrochim. Acta* 1978 **23** 1395
Bruce P G and West A R 1980 *Mater. Res. Bull.* **15** 379
Hong H Y P 1978 *Mater. Res. Bull.* **13** 117

Kuwano J and West A R 1980 *Mater. Res. Bull.* **15** 1661
Liebertz J and Rooymans 1967 *Solid State Commun.* **5** 405
Majumdar D, Bose D N, Mukherjee M L, Basu A and Bose M 1983 *Mater. Res. Bull.* **18** 79
Ohtsuka H and Yamaji A 1983 *Solid State Ionics* **8** 43
Shahi K and Wagner J B 1982 *J. Solid State Chem.* **42** 107

Bull. Mater. Sci., Vol. 6, No. 2, May 1984, pp. 231–242. © Printed in India.

Electronic conduction in bulk $Se_{1-x}Te_x$ glasses at high pressures and at low temperatures

G PARTHASARATHY and E S R GOPAL

Department of Physics, Indian Institute of Science, Bangalore 560012, India

Abstract. The electrical resistivity of bulk $Se_{1-x}Te_x$ glasses is reported as a function of pressure (up to 8 GPa) and temperature (down to 77 K). The activation energy for electronic conduction has been calculated at different pressures. The samples with $0 \leqslant x \leqslant 0.06$ show a single activation energy throughout the temperature range of investigations. On the other hand samples with $0.08 \leqslant x \leqslant 0.3$ show two activation energies in the different regions of temperature. The observed behaviour has been explained on the basis of band picture of amorphous semiconductors.

Keywords. Chalcogenide glasses; pressure-induced semiconductor-to-metal transitions; amorphous semiconductors.

1. Introduction

In amorphous semiconductors pressure-induced effects, phase transitions and semiconductor-to-metal transitions are the most interesting phenomena (Minomura 1982). Many amorphous chalcogenides become metallic under pressure with a continuous decrease in band gap and resistivity even as they retain their molecular structure (Sakai and Fritzsche 1977; Minomura 1982; Parthasarathy *et al* 1984a). On the other hand tetrahedrally-bonded glasses undergo discontinuous transition with changes in structure to high coordination (Shimomura *et al* 1974). In amorphous selenium the resistivity decreases continuously with pressure by many orders of magnitude and goes to a metallic state with a discontinuous change in the electrical resistivity at high pressures. The value of the transition pressure is about 100–130 kb, which varies from work to work (Witting 1973; Fuhs *et al* 1973; Minomura 1978; Gupta and Ruoff 1978; Bundy and Dunn 1979). The most accepted value of transition pressure is about 13 GPa (= 130 kb).

In our study we find that the nature of the pressure-induced semiconductor-to-metal transition in $Se_{1-x}Te_x$ glasses, changes as a function of tellurium composition (Parthasarathy *et al* 1984 a,b). In this paper we report a systematic study on the pressure and temperature dependence on the electrical resistivity of $Se_{1-x}Te_x$ glasses for $0 \leqslant x \leqslant 0.3$.

2. Experimental details

2.1 *High pressure cell assembly*

The high pressure apparatus to measure the electrical resistance of $Se_{1-x}Te_x$ glasses as a function of pressure and temperature consists of a hydraulic press and a high pressure

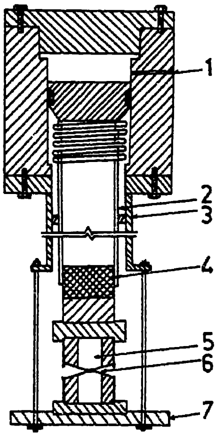

Figure 1. Schematic diagram of the high pressure c assembly. 1. Oil inlet 2. Compression member 3. Tensi member 4. High pressure plug 5. Tungsten carbide anvil Sample 7. Bottom flange.

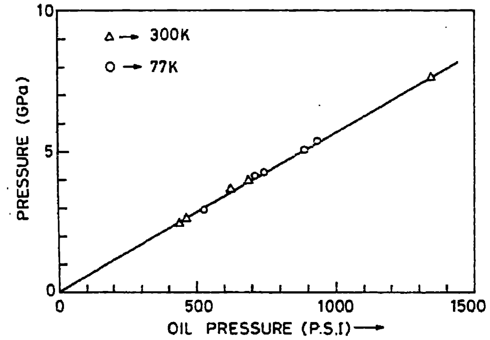

Figure 2. Plot of actual pressure *vs* oil pressure. Triangle for calibration at ro temperature and circle for calibration points at liquid nitrogen temperature.

cell for low temperatures. The hydraulic press for low temperatures is similar to th which was discussed by Fujii and Nagano (1971). The compression member and t tension member are made of stainless steel 304 type. The high pressure cell constructed with opposed tungsten carbide anvils with 6% cobalt binder, with he treated EN-24 steel binding rings. The schematic diagram of the apparatus is shown figure 1.

2.2 *Pressure calibration*

The pressures were calibrated at 300 K using as fixed points the Bi transitions at 2· 2·7 and 7·7 GPa, Yb transition at 4 GPa and Tl transition at 3·75 GPa. The pressu induced transitions in Bi, Yb and Tl at 77 K have been studied. The calibration at lc temperature shows that in this system the pressures at low temperatures were the sa as those calibrated at room temperature.

The fixed points are plotted as a function of oil pressure in figure 2. The detail analysis of the low temperature calibration will be discussed elsewhere (Parthasarat *et al* 1984c).

2.3 *Sample preparations and characterization*

Bulk $Se_{1-x}Te_x$ glasses, with $x = 0, 0{\cdot}02, 0{\cdot}04, 0{\cdot}05, 0{\cdot}06, 0{\cdot}08, 0{\cdot}1, 0{\cdot}2, 0{\cdot}3$, were prepared by melting together appropriate amounts of the elements (5N purity), in sealed, evacuated quartz tubes (10^{-6} torr). The tubes were kept in a rotary furnace for 30 hr at a temperature of 1200 K, and subsequently quenched in an ice water mixture. These samples were confirmed to be amorphous by x-ray diffractometry differential scanning calorimetry and electron microscopic technique.

The room temperature and atmospheric pressure resistivity values are measured by the Van der Pauw (1958) technique. For high pressure and low temperature resistivity values, the change in the dimensions of the samples under pressure is not taken into account; the effect of this on the resistivity is comparatively small compared with the total change in the resistivity. A two-probe method (in sandwitch geometry) is used to measure resistance, where the value of the resistance is more than 500 ohms. For measuring the resistances below 500 ohms a conventional four-probe method is employed. An electrometer (Keithley 616), a constant current source (Keithley 225) and a digital multimeter (Keithley 177) were used as measuring units. A copper-constantan thermocouple was used to measure the temperature. Because of the heavy thermal mass of the system, the temperature is controlled within ± 1 K. The error involved in the measurement of temperature is within ± 0·3 K.

3. Results

The variation of dc conductivity with temperature for $Se_{1-x}Te_x$ glasses at different pressures is shown in figures 3 to 11. For all the samples dc conductivity follows the Arrhenius relation

$$\sigma = \sigma_0 \exp(-\Delta E/kT) \tag{1}$$

where σ_0 ($\Omega^{-1}\,cm^{-1}$) is the pre-exponential factor, ΔE(eV) the activation energy, $T(K)$ the temperature, and k the Boltzmann constant. For $Se_{1-x}Te_x$ glasses with $0 \leqslant x \leqslant 0{\cdot}06$ we realise that the electronic conduction process is thermally activated with a single activation energy for all the pressures, in the temperature range of investigations (figures 3 to 7). On the other hand the glasses with $0{\cdot}08 \leqslant x \leqslant 0{\cdot}30$ show double activation energies in the same temperature range. The conductivity activation energy (ΔE) has been estimated by fitting the conductivity data in (1). The variation of the activation energy (ΔE) as a function of pressure for $Se_{1-x}Te_x$ glasses is shown in figures 12 and 13. The values of the activation energy and the pre-exponential factor σ_0 have been summarised in tables 1 and 2.

4. Discussion

In figure 3 we see that the room temperature and atmospheric pressure resistivity of pure selenium is of the order of 10^{10} ohm cm. Most of the experimental data on pure selenium show that the resistivity is of the order of 10^{10} to 10^{12} ohm cm at normal condition. It has been reported that the room temperature resistivity of pure deoxygenated selenium is of the order of 10^{17} ohm cm, and it drops by seven orders of magnitude through the addition of 20 ppm of oxygen added as SeO_2 to the melt

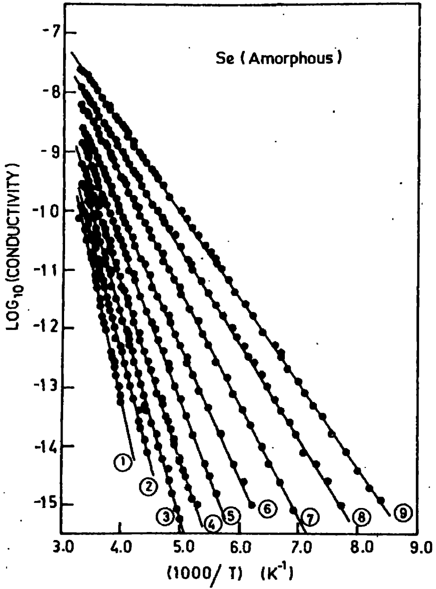

Figure 3. Semilog plot of dc conductivity *vs* (1000/T) for selenium glass at different pressures:

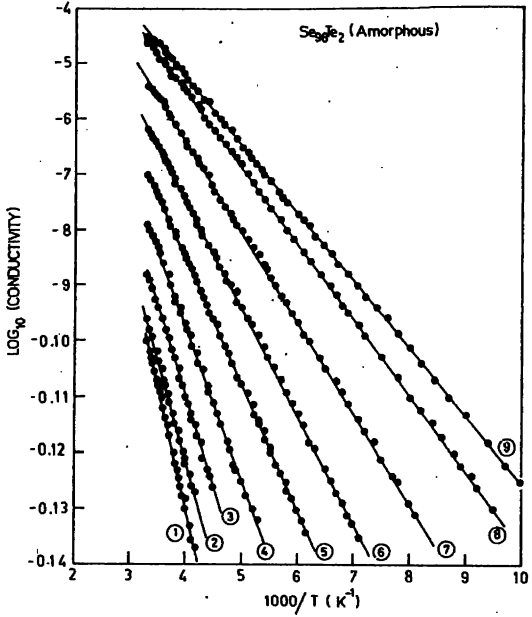

Figure 4. Semilog plot of dc conductivity *vs* (1000/T) for

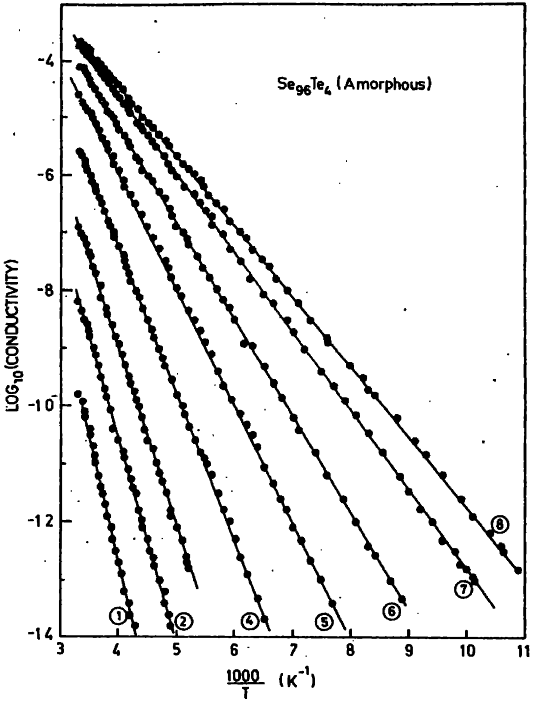

Figure 5. Semilog plot of dc conductivity *vs* (1000/T) for

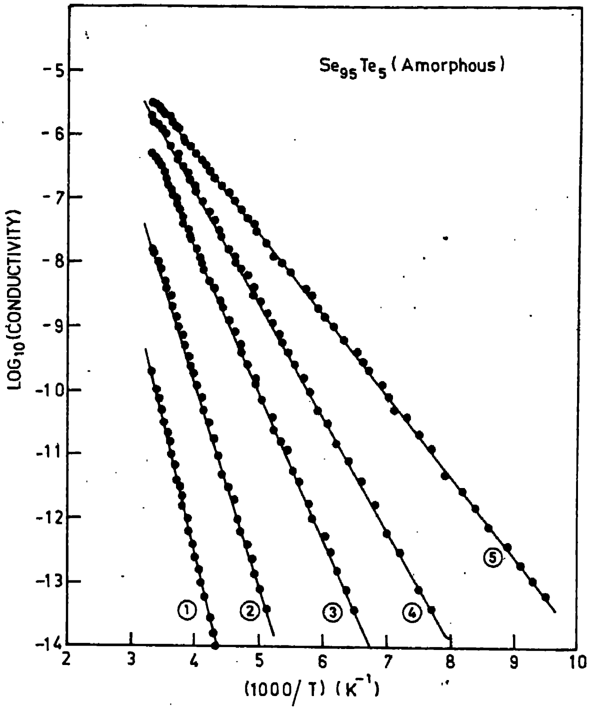

Figure 6. Semilog plot of dc conductivity *vs* (1000/*T*) for $Se_{95}Te_5$ glass at different pressures: Curves (1) 10^5 Pa (2) 1 GPa (3) 2 GPa (4) 3 GPa (5) 4 GPa.

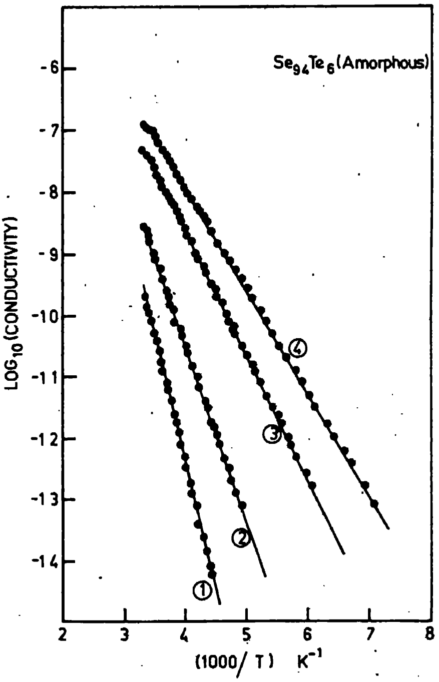

Figure 7. Semilog plot of dc conductivity *vs* (1000/*T*) for $Se_{94}Te_6$ glass at different pressures: Curves (1) 10^5 Pa (2) 1 GPa (3) 2 GPa (4) 3 GPa.

(Lacourse *et al* 1970). Mott (1976) has explained this phenomena in terms of charged dangling bonds (Street and Mott 1975). The conductivity activation ene for pure selenium is given by (Mott 1976)

$$\Delta E = \tfrac{1}{2}B - \varepsilon$$

and for oxygenated selenium it is

$$(\Delta E)_{\mathrm{ox}} = \tfrac{2}{3}(\tfrac{1}{2}B - \varepsilon),$$

where ΔE and $(\Delta E)_{\mathrm{ox}}$ are the activation energies for pure selenium and oxygena selenium respectively. B is the band gap and ε is the difference in energy between middle of the band gap and the Fermi level *i.e.* Fermi level is pinned in pure selenium D^+ and D^- defects at an energy below midgap by an amount ε. The ε value is estima to be roughly 0·13 eV (Mott 1976). The value of the optical band gap B of p amorphous selenium is equal to 2·05 eV (Davis 1970) which is roughly the same va obtained by other workers (Lanyon 1964; Dawar *et al* 1981; Bhatnagar a Subramanyam 1983). If we substitute the B value in (2) and (3), we get $\Delta E = 0{\cdot}895$ and $(\Delta E)_{\mathrm{ox}} = 0{\cdot}60$ eV. Our experimental data on selenium give the value of activati energy (at 10^5 Pa pressure) = 0·896 eV. Recent conductivity experiments by Kotk *et al* (1982) on amorphous and liquid selenium show that the activation energy is equal 0·525 eV for the glassy state and 0·6 eV in the liquid state. Moreover their resistiv value is of the order of 10^8 Ω cm. These results are in good agreement with the value the oxygenated selenium, which is estimated from (3). These effects of the oxyg doping in amorphous selenium require more systematic experiments on transp properties.

Figure 12 shows that the activation energy of electronic conduction for all samples decreases with the increase of pressure. For pure selenium the pressu coefficient of activation energy is found to be −0·08 eV/GPa, which is in excell agreement with the data reported by Fuhs *et al* (1973).

The variation of d.c. conductivity of $Se_{1-x}Te_x$ glasses for $0 \leqslant x \leqslant 0{\cdot}06$ shows that all the samples at all the pressures the conduction is thermally activated with a sin activation energy. If we fit the conductivity data to equation (1), we get the numeri value of activation energy and the pre-exponential factor. These factors are presented table 1. Our experimental value of σ_0 for Se is in good agreement with the va reported by Davis and Mott (1970). In most of the cases the pre-exponential factor σ of the order of 10^4 Ω^{-1} cm^{-1}, which indicates that at atmospheric pressure conduction in all the samples ($0 \leqslant x \leqslant 0{\cdot}06$) is through extended states in temperature range of investigations. With the increase of pressure the σ_0 val decreases continuously by seven orders of magnitude (in the case of selenium, table which indicates that the process of electronic conduction changes from the extend states conduction to the localized state conduction. The decrease of activation ene ΔE with the increase of pressure shows the movement of the Fermi level towards conduction band edge, by the application of the pressure. The variation of ΔE and with pressure for other samples also ($0 \leqslant x \leqslant 0{\cdot}06$) can be explained in the same w

The variation of conductivity with temperature for $Se_{1-x}Te_x$ glasses w $0{\cdot}08 \leqslant x \leqslant 0{\cdot}3$ show a somewhat different behaviour from that for $0 \leqslant x \leqslant 0$ (figures 8–11). For $0{\cdot}08 \leqslant x \leqslant 0{\cdot}3$ the conduction at high temperature region is acr mobility edges and at low temperature region, the conduction process is in the localiz states near the Fermi level by thermally-activated hopping. The first activation ene factor and the activation energy of the Arrhenius formula

	Se		$Se_{98}Te_2$		$Se_{96}Te_4$		$Se_{95}Te_5$		$Se_{96}Te_4$	
Pressure	ΔE	σ_0	ΔE	σ_0	ΔE	σ_0	ΔE	σ_0	ΔE	$\sigma_0 E$
10^5 Pa	0·896	$8·74 \times 10^4$	0·874	$4·90 \times 10^4$	0·85	$3·37 \times 10^4$	0·84	$2·44 \times 10^4$	0·83	$2·06 \times 10^4$
1 GPa	0·76	$3·39 \times 10^3$	0·73	$3·96 \times 10^2$	0·70	$3·61 \times 10^3$	0·63	607·2	0·57	8·32
2 GPa	0·68	74·57	0·62	40·63	0·62	$3·55 \times 10^3$	0·45	19·01	0·40	0·269
3 GPa	0·60	7·49	0·56	34·67	0·50	623·7	0·35	1·53	0·33	$4·47 \times 10^{-2}$
4 GPa	0·52	0·75	0·45	3·64	0·40	130·8	0·25	18·6	—	—
5 GPa	0·44	$5·92 \times 10^{-2}$	0·38	1·50	0·33	30·2	—	—	—	—
6 GPa	0·38	$3·95 \times 10^{-2}$	0·32	1·04	0·27	6·44	—	—	—	—
7 GPa	0·32	$2·84 \times 10^{-3}$	0·27	0·83	—	—	—	—	—	—
8 GPa	0·29	$1·92 \times 10^{-3}$	0·24	0·35	—	—	—	—	—	—

Table 2. Values of the activation energies and the pre-exponential factors at different pressures for $Se_{1-x}Te_x$ glasses ($0·08 \leqslant x \leqslant 0·30$) ($\Delta E$ is in eV and σ_0 is in $\Omega^{-1}\,cm^{-1}$)

	$Se_{92}Te_8$		$Se_{90}Te_{10}$		$Se_{80}Te_{20}$		$Se_{70}Te_{30}$	
Pressure	ΔE	σ_0	ΔE	σ_0	ΔE	σ_0	ΔE	σ_0
10^5 Pa	0·82	$4·81 \times 10^4$	0·797	$4·145 \times 10^4$	0·70	$5·66 \times 10^4$	0·60	$6·02 \times 10^4$
1 GPa	0·72	$1·04 \times 10^4$	0·70	$9·99 \times 10^2$	0·60	$1·39 \times 10^3$	0·45	$5·16 \times 10^4$
	0·19	$2·44 \times 10^{-8}$	0·19	$1·00 \times 10^{-8}$	0·14	$6·64 \times 10^{-8}$	0·10	$5·00 \times 10^{-6}$
2 GPa	0·575	105·6	0·55	3·07	0·46	$5·17 \times 10^3$	0·30	$1·65 \times 10^5$
	0·100	$1·00 \times 10^{-8}$	0·12	$1·46 \times 10^{-10}$	0·10	$2·0 \times 10^{-4}$	0·09	3·607
3 GPa	0·41	112·4	0·38	$1·53 \times 10^{-2}$	0·30	$1·15 \times 10^4$	0·18	$7·19 \times 10^4$
	0·05	$3·34 \times 10^{-8}$	0·06	$5·07 \times 10^{-8}$	0·05	$6·64 \times 10^{-2}$	0·04	30
4 GPa	0·26	$2·09 \times 10^3$	0·22	382	0·14	$3·51 \times 10^3$	0·10	$3·90 \times 10^4$
	0·03	$1·00 \times 10^{-5}$	0·03	$1·0 \times 10^{-4}$	0·03	16·67		
5 GPa	0·15	$1·36 \times 10^5$	0·10	365	0·08	$1·11 \times 10^4$	0·04	$1·10 \times 10^4$
	0·014	$1·25 \times 10^{-2}$	0·018	0·278	0·014	$2·86 \times 10^2$		
6 GPa	0·06	$1·48 \times 10^3$	0·04	$1·926 \times 10^3$	—	—	—	—
7 GPa	—	—	—	—	—	—	—	—

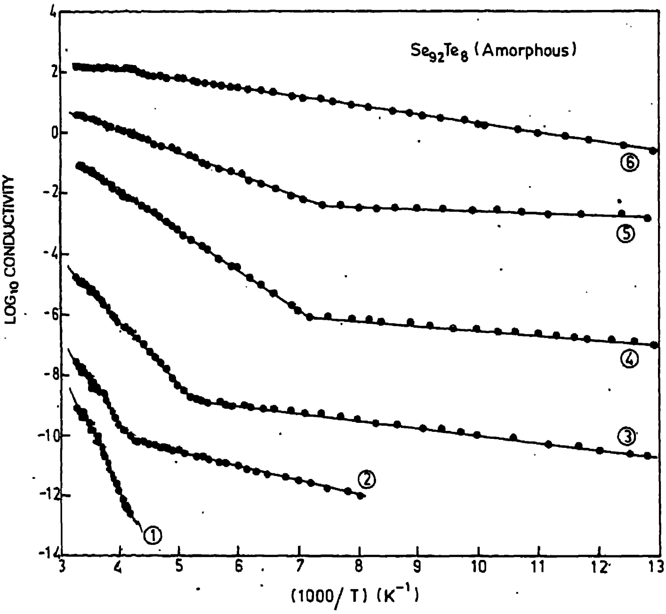

Figure 8. Semilog plot of dc conductivity *vs* (1000/*T*) for $Se_{96}Te_8$ glass at di
pressures: Curves (1) 10^5 Pa (2) 1 GPa (3) 2 GPa (4) 3 GPa (5) 4 GPa (6) 5 GPa (7)

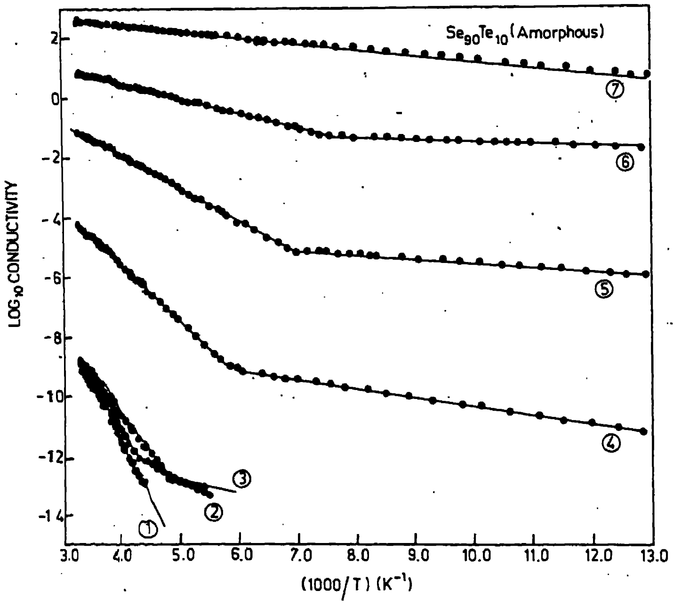

Figure 9. Semilog plot of dc conductivity *vs* (1000/*T*) for $Se_{90}Te_{10}$ glass at diff
pressures: Curves (1) 10^5 Pa (2) 1 GPa (3) 2 GPa (4) 3 GPa (5) 4 GPa (6) 5 GPa (7) 6

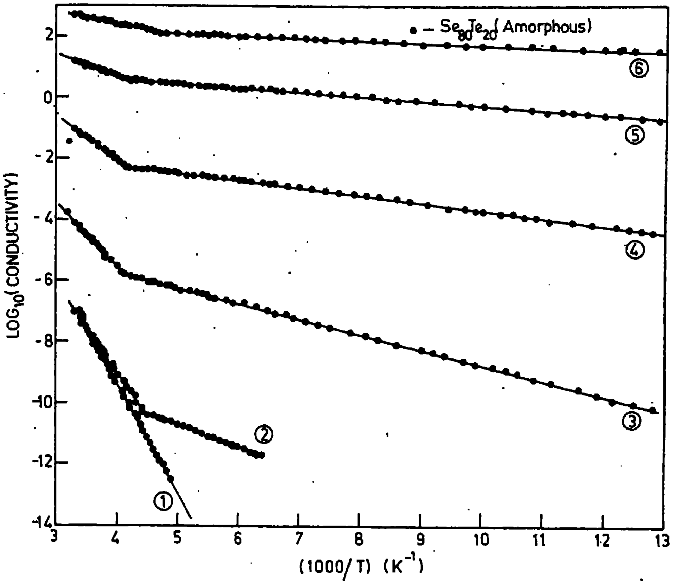

Figure 10. Semilog plot of dc conductivity *vs* (1000/*T*) for $Se_{80}Te_{20}$ glass at different pressures: Curves (1) 10^5 Pa (2) 1 GPa (3) 2 GPa (4) 3 GPa (5) 4 GPa (6) 5 GPa.

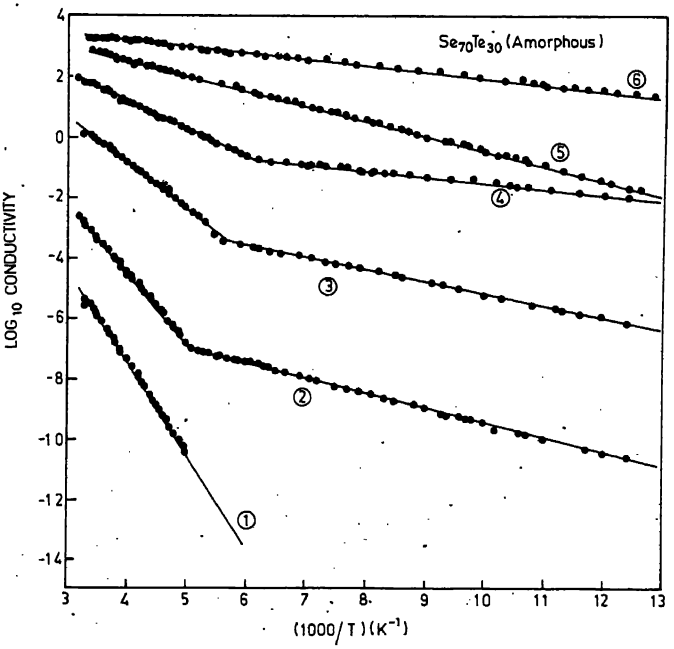

Figure 11. Semilog plot of dc conductivity *vs* (1000/*T*) for $Se_{70}Te_{30}$ glass at different pressures: Curves (1) 10^5 Pa (2) 1 GPa (3) 2 GPa (4) 3 GPa (5) 4 GPa (6) 5 GPa.

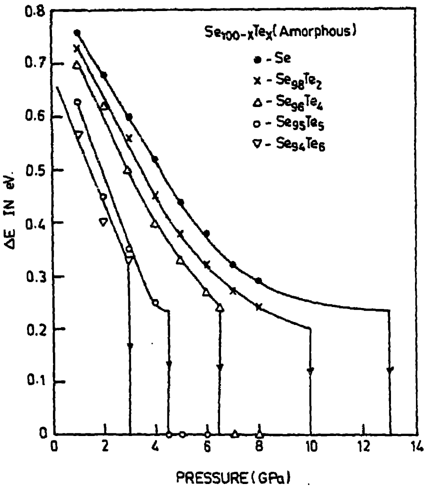

Figure 12. Variation of conductivity activation energy as a function of pressure for $Se_{1-x}Te_x$ glasses ($0 \leqslant x \leqslant 0{\cdot}06$).

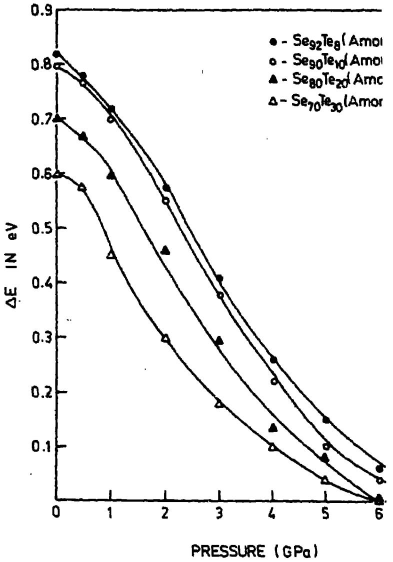

Figure 13. Variation of conductivity activ energy as a function of pressure for $Se_{1-x}Te_x$ g ($0{\cdot}08 \leqslant x \leqslant 0{\cdot}30$).

(in high temperature region) represents the value of $E_c - E_f$ and the second activa energy gives the value of half the width of the localized states near the Fermi level find (table 2) that both the activation energies decrease with increase of pressure, w implies that the fundamental energy gap or in other words the mobility gap decre with increase of pressure. The decrease in the second activation energy indicat decrease in the localization of the gap states. The decrease in both activation ene leads to a metallic phase beyond 7 GPa pressure.

For calling the high pressure phase as metallic we follow the operational definitic metallic conduction put forward by Sakai and Fritzsche (1977) and Mott (1970), w says that the conductivity is metallic if its temperature coefficient is zero or negative if its value is equal or larger than Mott's minimum metallic conductivity. interpretation of the pressure dependence on electrical resistivity is more complic because, the behaviour is determined by the gap, the mobility and also the positio the Fermi level.

From figures 12 and 13 we notice the differences in the variation of the activa energy with pressure. For $0 \leqslant x \leqslant 0{\cdot}06$ the activation energy decreases continuo with the increase of pressure and drops to zero at a certain pressure. On the other h for $0{\cdot}08 \leqslant x \leqslant 0{\cdot}3$, the activation energy decreases continuously to a zero value. M over for $0 \leqslant x \leqslant 0{\cdot}06$, the conductivity activation energy is found to be single ove temperature range of our experiments at all the pressures. On the other hand $0{\cdot}08 \leqslant x \leqslant 0{\cdot}3$ we find two activation energies in different temperature ranges. T observations indicate that there should be some change in the band structur $Se_{1-x}Te_x$ glasses at the value of x between $x = 0{\cdot}06$ and $x = 0{\cdot}08$ (Parthasarathy 1984b).

In the defect model (Mott *et al* 1975; Kastner *et al* 1976; Kastner and Fritzsche 1

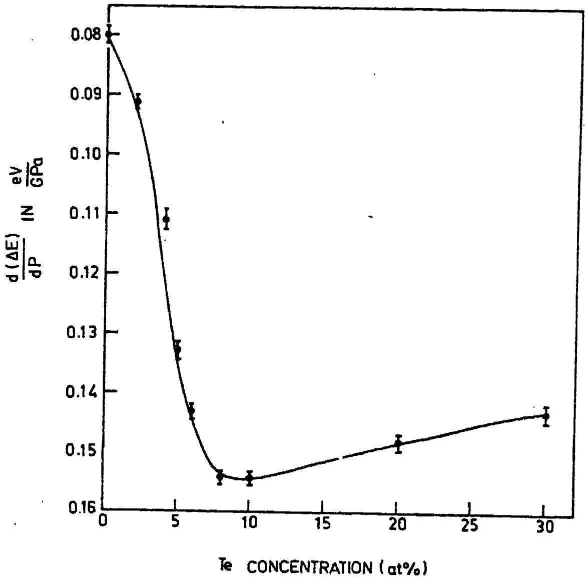

Figure 14. Variation of the pressure coefficient of activation energy as a function of tellurium concentration.

selenium glass is considered to a continuous random network consisting of chains (and few rings) of atoms with two-fold coordination. The defects in glassy selenium may consist of dangling chain ends, which are called as charged dangling bonds denoted by C_3^+, C_1^0 and C_1^- depending on whether 0, 1 or 2 electrons occupy the gap state. We expect that the addition of tellurium (figure 14) in glassy selenium up to 6 atomic percentage does not affect the structure of Se and hence the band picture. But beyond 6 atomic percentage the tellurium atoms create new defect states inside the mid gap which may be over-coordinated (C_3^+) type or under-coordinated (C_1^-) type or both. Hence we observe the single activation energy for $0 \leqslant x \leqslant 0{\cdot}06$ and double activation energies for $0{\cdot}08 \leqslant x \leqslant 0{\cdot}3$ in the same range of temperature. A more detailed discussion on this change in the electronic transport behaviour as a function of tellurium composition will be published elsewhere (Parthasarathy *et al* 1984a).

In conclusion, a systematic study of the electrical conductivity of $Se_{1-x}Te_x$ glasses as a function pressure and temperature is reported. There appears to be some drastic change in the electronic behaviour of these glasses at $x = 0{\cdot}06$ to $0{\cdot}08$. This has to be related to the details of the models for these glasses.

Acknowledgement

The authors wish to thank Dr A K Bandyopadhyay, Dr S T Lakshmikumar and Prof K J Rao for their help and cooperation. Thanks are also due to the DST and CSIR schemes of the Government of India, for financial support.

References

Bhatnagar A K and Subramanyam S V 1983 *Solid State Commun.* **42** 281

Bundy F P and Dunn K J 1979 *J. Chem. Phys.* **71** 1550

Davis E A 1970 *J. Non. Cryst. Solids* **4** 107

Davis E A and Mott N F 1970 *Philos. Mag.* **22** 903

Dawar W, Mell H and Stuke J 1981 *Phys. Status Solidi* **B45** 153

Fuhs W, Schlotter P and Stuke J 1973 *Phys. Status Solidi* **57** 587

Fujii G and Nagano H 1971 *Cryogenics* **11** 142

Gupta M C and Ruoff A L 1978 *J. Appl. Phys.* **49** 5880 and the references therein.

Kastner M, Adler D and Fritzsche H 1976 *Phys. Rev. Lett.* **37** 1504

Kastner M and Fritzsche H 1978 *Philos. Mag.* **B37** 199

Kotkata M F, Kamal G M and El-Mously M K 1832 *Indian J. Technol.* **20** 390

Lacourse W A, Twaddell V A and Mackenzie J D 1970 *J. Non Cryst. Solids* **3** 234

Lanyon H P D 1964 *J. Appl. Phys.* **35** 1516

Minomura S 1978 *High pressure and low temperature physics*, (eds) C W Chu and J A Woolam (New Plenum) p. 483

Minomura S 1982 in *Amorphous semiconductors; technologies and devices* (ed.) Y Hamakawa (Amste North Holland) p. 245

Mott N F 1970 *Philos. Mag.* **22** 7

Mott N F 1976 *Philos. Mag.* **34** 1101

Mott N F, Davis E A and Street R A 1975 *Philos. Mag.* **32** 961

Parthasarathy G, Rao K J and Gopal E S R 1984a (to be published)

Parthasarathy G and Gopal E S R 1984b (to be published)

Parthasarathy G, Bandyopadhyay A K and Gopal E S R 1984c to be published in Proceedings of Indo- Conference on Low Temp. Physics (Jan. 11–14, 1984, India)

Sakai N and Fritzsche H 1977 *Phys. Rev.* **B15** 973

Shimomura O, Minomura S, Sakai N, Asawmi K, Tamura K, Fukushima J and Endo H 1974 *Philos. M* 547

Street R A and Mott N F 1975 *Phys. Rev. Lett.* **35** 1293

Van der Pauw 1958 *Philips Res. Rep.* **13** 1

Witting J 1973 *J. Chem. Phys.* **58** 2220

Bull. Mater. Sci., Vol. 6, No. 2, May 1984, pp. 243–258. © Printed in India.

Electrical properties of polycrystalline silicon and zinc oxide semiconductors

S N SINGH, S KUMARI and B K DAS

National Physical Laboratory, New Delhi 110 012, India.

Abstract. Polycrystalline silicon and zinc oxide ceramic are important electronic materials. The electrical properties which determine the applications of polycrystalline silicon in integrated circuits and solar cells and that of ZnO ceramic in varistors are due primarily to grain boundary effects in them. A large amount of information in this area has already been gathered in literature but the quantitative understanding of grain boundary effects in these materials is not yet complete. In this review the important aspects of grain boundaries and their effects on transport and photoelectric properties of polycrystalline silicon and on the I-V characteristic of ZnO varistors are discussed.

Keywords. Polycrystalline semiconductors; electrical properties; grain boundary effects; polysilion; ZnO varistors.

1. Introduction

The intergranular regions of polycrystalline semiconductors often affect the electrical properties of the solids in such a way that they determine the applications of these solids. There are several ways this can arise. Grain boundaries (GBs) are two-dimensional imperfections containing highly complex structural defects and in most cases are electrically active. Impurity atoms also segregate at the grain boundaries. Any of these conditions can lead to the formation of a space charge layer near the grain boundaries. In case of a metal, this is of such narrow spatial extent that it is best treated in terms of a scattering formalism. In an insulator, the extent of these space charge regions is large and the influence of GB s are better viewed as large perturbations on the bulk Fermi levels. The intermediate case of polycrystalline semiconductors is of considerable technological importance. This is an attempt to review the important properties of grain boundaries and the grain boundary and doping effects on the transport and photovoltaic properties of some semiconductors like silicon and zinc oxide and the methods employed to determine these effects.

2. Polycrystalline silicon

The many emerging applications of polycrystalline silicon (polysilicon) including discrete devices and integrated circuits have prompted several recent studies of carrier transport in polysilicon. The role of these GBs on the photovoltaic properties of inexpensive polycrystalline solar cells has also received considerable attention by various research groups.

2.1 *Grain boundary effects in polycrystalline silicon*

2.1a *Impurity segregation:* The first direct physical evidence of segregation of impurities at GBs in cast and directionally solidified polysilicon was gathered by Kazmerski *et al* (1980). Using scanning Auger microscopy (SAM) and secondary ion mass spectroscopy (SIMS) techniques, they showed that much larger concentrations of Fe, Ti, Co, Ni, Cn, Zn, Sb, C, Al and Mg are present at the grain boundaries as compared to the grain interior. Similar experiments (Kumari *et al* 1983) on grain boundaries of polysilicon of solar grade purity also confirmed the grain boundary enrichment as shown in figure 1. In a different experiment, Pollock *et al* (1982) carried out Cu and P diffusions into cast polysilicon and studied GB enrichment with Cu, H, C and O by the SIM technique. They showed that H, C and O accumulate at GBs (figure 2a). A secondary ion image of Cu obtained using oxygen ion bombardment shown in figure 2b indicates that large clusters of Cu are present along GBs. Segregation of impurities at GBs particularly those giving deep levels can significantly modify the electrical activity of the GBs. This complicates the understanding of the role of GBs in influencing the majority and minority carrier phenomena in polysilicon.

2.1b *Enhanced impurity diffusion:* The diffusion coefficient of impurity is higher in the GBs than in the grains (Matre 1971) and consequently the diffusion of the impurities along the GBs is deeper. This in conjunction with the preferential segregation of impurities at GBs can considerably change the picture of junction formation in polysilicon devices than in single crystalline devices. For example, in polysilicon solar cells, while the enhanced diffusion of dopants along GBs makes the *p-n* junction interface irregular, the enhanced diffusion coupled with the tendency of the impurities to segregate preferentially at GBs reduces the leakage resistance of the junction considerably leading to degradation of the I-V characteristics of polysilicon solar cells (Lindmayer 1978). Figure 3 shows a schematic diagram of an irregular *p-n* junction formed due to the GBs as mentioned above and figure 4 depicts a SEM picture as a direct evidence of deeper diffusion of dopant impurity at GBs (Jain *et al* 1980a). Figure 5 shows how this results in a greater effective junction depth in a small grain polysilicon (Jain *et al* 1981).

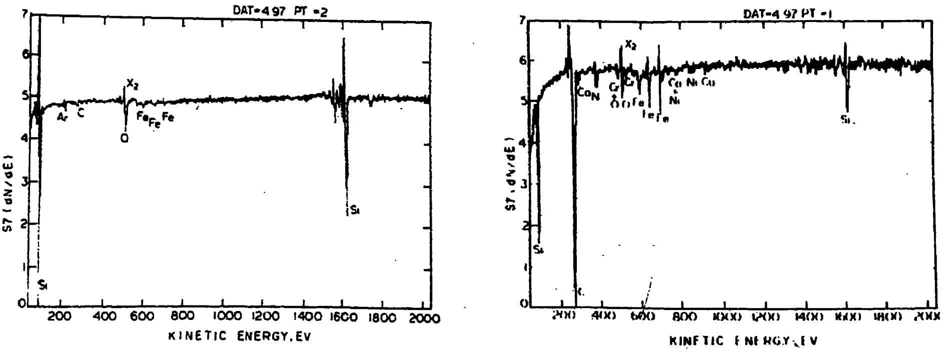

(a) (b)

Figure 1. Auger spectrum taken in **a.** grain region and **b.** GB on a fractured surface of solar grade polysilicon (after Kumari *et al* 1982).

Figure 2. **a.** Secondary ion images of H, C, O and Si obtained using cesium ion bombardment of Cu diffused polycrystalline silicon wafer. **b.** An image of Cu distribution in another area of the above sample (after Pollock *et al* 1982).

2.1c *Majority carrier trapping*: The presence of the defects at grain boundary gives rise to energy states in the forbidden gap (Card and Yang 1977). These states commonly referred to as GB states or the interface states trap majority carriers from the surrounding grains. This decreases the free carrier density in the bulk polysilicon and creates a space charge (or depletion) layer on both sides of a grain boundary (in one-dimensional model). The space charge layer in turn results in the creation of potential barrier at the GB. The nature of the potential barrier is such that it opposes the flow of majority carriers from one grain to the other and favours the flow of minority carriers towards the grain boundary. The band bending at a GB for n-type semiconductor under thermal equilibrium is shown in figure 6. Here the grains have been assumed to be identical. In the figure $d_L = d_R$, at equilibrium, if the grains are identical both structurally and electrically. The difference in the doping level of the grains can result in the asymmetrical band bending. The decrease in the free carrier density in the grains due to their trapping at GB s and the existence of the grain boundary potential barriers, as will be discussed a little later, can have profound effect on the electrical behaviour of poly-silicon.

Equating the depletion layer charge Q_d to the trapped charge Q_T in the GB s, the height of the potential barrier can be easily calculated. For the depletion layer approximation, the solution of Poisson's equation gives (Seager and Castner 1978)

$$Q_d = (8\varepsilon N_D q \phi_B)^{1/2}, \tag{1}$$

Here, ε is the dielectric constant of silicon, q is the electronic charge and N_D is the doping concentration in the grain (in the present case as n-type). For determination of Q_T, however, the knowledge of the nature of the energy level of the interface states (*eg.* whether the states are distributed uniformly throughout the forbidden gap or they have a delta function distribution or some other distribution) is essential. Unfortunately the picture of the energy levels of the GB states is not yet clear. Poon and Hwang (1982) have developed a phenomenological model of grain boundary trapping states in polysilicon

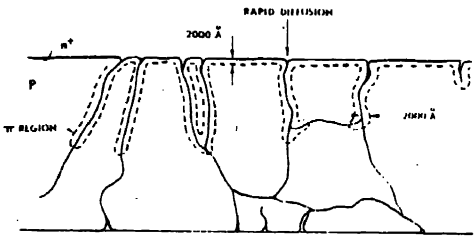

Figure 3. Schematic cross sectional view of diffused semicrystalline structure showing deeper diffusion along the GBs.

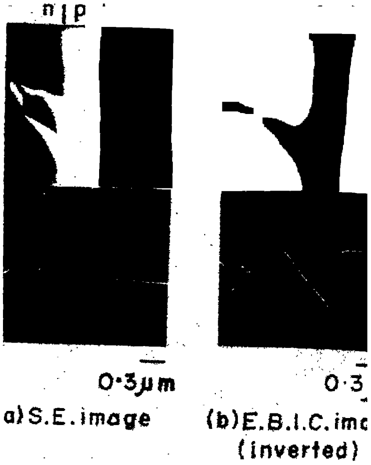

Figure 4. **a.** Secondary emission (SE) a
b. Electron beam induced current (EE
images at the cleaved surface of a pc
crystalline silicon solar cell (after Jain *et*
1981).

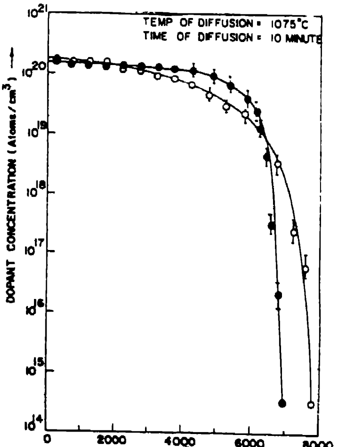

Figure 5. Dopant profile of boron in solar gra
poly (o) and single (●) crystalline silicon (after J
et al 1981).

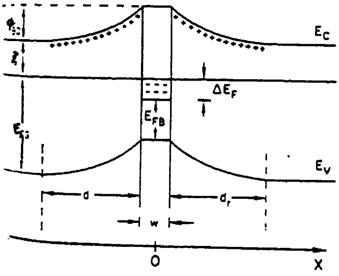

Figure 6. Energy band diagram for two grains ar
their grain boundary region in an *n*-type polysilico
(E_{FG}-Fermi energy level in the bulk of the grain wi
valence band edge as the reference; E_{FD}-the neutr
Fermi level at the GB; ϕ_B height of the grain bounda
potential barrier; d_L and d_R the space charge lay
widths in the left and right grain respectively).

under optical illumination. They find discrete (δ-function) distribution to be inappropriate. However, many experimental data on dark conductivity and Hall mobility agree with δ-function distribution assumption excellently (Kishore *et al* 1983; Baccarani *et al* 1978). For uniform distribution of interface states in the band-gap Q_T can be computed as

$$Q_T = qN_{\text{is}}(E_{FG} - E_{FB} - q\phi_B). \tag{2}$$

For this case ϕ_B can be determined by equating (1) and (2)

$$\phi_B = \delta\left[1 + \frac{\alpha}{2\delta} - \left\{\frac{\alpha}{\delta} + \left(\frac{\alpha}{2\delta}\right)^2\right\}^{1/2}\right], \tag{3}$$

where $\delta = \dfrac{1}{q}(E_{FG} - E_{FB})$,

and $\alpha = \dfrac{8\varepsilon N_D}{q^3 N_{\text{is}}^2}$.

Discrete energy level, on the other hand, is obtained from the solution of equation (Martinez and Piqueras 1980).

$$\left(\frac{8\varepsilon N_D \phi_B}{q^2}\right)^{1/2} = qN_{\text{is}}\left[\frac{1}{1 + \exp[(E_T - E_{FG} - q\phi_B)/kT]} - \frac{1}{1 + \exp[(E_T - E_{FB})/kT]}\right], \tag{4}$$

where E_T is the energy of the trap level and N_{is} is the density of interface states per unit area. In the further discussion (3) and (4) will be used to describe some majority carrier phenomena in polysilicon.

2.1d *Enhanced minority carrier recombination:* The GB states act not only as trap centres for majority carriers but also as efficient recombination centres for minority carriers. The minority carrier recombination at GB is larger if there exists potential barrier at the GB. Following Card and Yang (1977) the minority carrier lifetime in the space charge region of *n*-type polysilicon denoted as τ_{gb} is given by

$$\tau_{gb} = \frac{2d\exp(-q\phi_B/kT)}{3\sigma v N_{\text{is}}(E_{fn} - E_{fp})}, \tag{5}$$

where ϕ_B is the barrier height, d is grain size, σ is the capture cross-section, v is the thermal velocity of carrier, N_{is} is the interface state density and E_{fn} and E_{fp} are the quasi Fermi levels for electrons and holes respectively. The equation is valid for quasi Fermi level for minority carriers remaining flat across the GB. The assumption usually holds for low level conditions unless the recombination velocity of minority carriers (S) at the edge of the depletion layer is infinitely high. However, according to Fossum and Lindholm (1980) τ_{gb} is given by

$$\tau_{gb} = 2Db_0^2, \tag{6}$$

where D is the diffusion coefficient of the minority carriers in the grains and b_0 is related with d, D and S by the following equation

$$b_0 \tan(b_0 d/2) = S/D. \tag{7}$$

If $S \rightarrow \infty$, $b_0 = \pi/d$ and, then,

$$\tau_{gb} = 2\pi^2 D/d^2. \qquad ($$

For this case the effective lifetime τ_{eff} is given by

$$\frac{1}{\tau_{\text{eff}}} = \frac{1}{\tau_n} + \frac{2\pi D^2}{d^2}, \qquad ($$

where τ_n is the lifetime in the grains.

Assuming $D = 25\ \text{cm}^2/\text{sec}$ the effective lifetime of electrons in p-type polysilicon w calculated as a function of d and is depicted in figure 7. For smaller values of d, $\tau_{\text{eff}} <$ but $\tau_{\text{eff}} \rightarrow \tau_n$ for d greater than a certain value d_c, which is smaller for a smaller τ_n. T performance of a solar cell made on polysilicon, in which the grain boundary activiti is high ($S \rightarrow \infty$) is highly limited by its grain size if $d < d_c$.

2.2 *Transport properties of polycrystalline silicon*

Current conduction process in polysilicon is significantly affected due to the presence the grain boundary potential barriers. Thermionic emission (TE) theory has bee applied by many workers [Seto 1975; Baccarani *et al* 1978; Martinez and Piqueras 198 Kumar and Satyam 1981] to describe the current conduction in polysilicon. Accordin to TE theory, the current density J for an applied voltage V across the barrier is given b

$$J = qn_g(kT/2\pi m^*)^{1/2} \exp(-q\phi_B/kT)[\exp(qV/kT) - 1], \qquad (1$$

where n_g is the free majority carrier density in the grain and m^* is the effective mass c the majority carrier. Equation (10) shows that the J-V characteristic of a polysilico

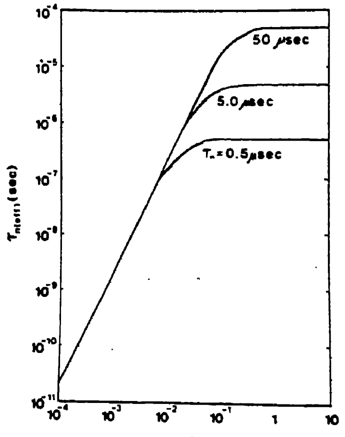

Figure 7. Effective minority carrier life time as a function of grain size for a p-type polysilicon (after Fossum and Lindholm 1980)

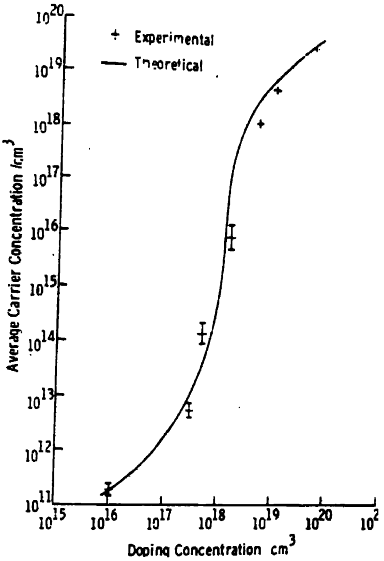

Figure 8. Average carrier concentration *vs* doping concentration for a polysilicon film at room temperature (grain size 200 Å) (after Seto 1975).

specimen is non linear unless the applied voltage drop per GB $V \ll kT/q$. In the ohmic regime ($V \ll kT/q$), the GB potential barrier can have a profound influence on the transport properties of polysilicon. In the following we will discuss GB effect on free carrier density, majority carrier mobility and conductivity of polysilicon.

2.2a *Free carrier density*: The GB states as discussed earlier trap majority carriers from the surrounding grains. The trapping decreases the density of free carriers. The decrease is more, if the interface state density is large, the doping in the grain is small and more significantly if the grain size is small. For very small grain sizes, almost the entire grain regions can be made devoid of the extrinsic carriers. Owing to this reason in small polysilicon, the free carrier density is far too low than the doping concentration (N) unless N becomes larger than a certain value N_c which will be a function of N_{is} and d. Figure 8 shows the average carrier density *vs* doping concentration for a polysilicon film ($d \sim 200$ Å) at room temperature after Seto (1975). The theoretical curve was obtained on the basis of carrier trapping at GB s.

2.2b *Majority carrier mobility*: The GB potential barrier opposes the flow of majority carriers across it and thus effectively the majority carrier mobility is reduced. Many workers have applied TE theory in conjunction with carrier trapping at GB to derive an expression for the effective majority carrier mobility μ_{eff}. For the case of partially depleted grain Seto (1975) obtained

$$\mu_{\text{eff}} = \frac{qd}{(2\pi m^* kT)^{1/2}} \exp(-q\phi_B/kT). \tag{11}$$

This expression ignores the contribution of grain to μ_{eff}. Kumar and Satyam's (1981) expression for μ_{eff} is

$$\mu_{\text{eff}} = \frac{\mu_g}{(1 - n_t t/N_D d) + \dfrac{\mu_g}{sqd}(2\pi m^* kT)^{1/2} \exp(q\phi_B/kT)}. \tag{12}$$

Here n_t is the density of filled states per unit volume, t is the physical thickness of GB, μ_g is the mobility in the grain and s is a fitting constant. There have been a few attempts to explain the mobility (Colinge *et al* 1981; Kim *et al* 1982) data using diffusion theory of current transport also. Recently Kishore *et al* (1983) have derived a rather general expression for μ_{eff}, which is based on the thermionic-emission-diffusion theory of Crowell and Sze (1966). The expression is

$$\mu_{\text{eff}} = \frac{\mu_g}{\left(1 - \dfrac{n_t t}{N_D d}\right) + \dfrac{kT}{q}\dfrac{\mu_g}{d}\left(\dfrac{1}{v_D} + \dfrac{1}{v_R}\right)\exp\left(\dfrac{q\phi_B}{kT}\right)}, \tag{13}$$

where $v_D = \mu_g E_B$.

and $v_R = (kT/2\pi m^*)^{1/2}$.

Here E_B is the field near the potential maximum. For $v_D \gg v_R$ (13) reduces to (12), neglecting the presence of s, and it will reduce to (11) if $v_D \gg v_R$ and the grain size is sufficiently small. All equations (11)–(13) show that μ_{eff} is small if d is small and it increases with d. Equations (12)–(13) show that for very large value of d, $\mu_{\text{eff}} \to \mu_g$. It is also noted that μ_{eff} is less for a higher ϕ_B. Decrease in ϕ_B increases μ_{eff}, which tries to approach μ_g. Under identical conditions, the adverse effect of ϕ_B on μ_{eff} will be pronounced, if d is small.

2.2c *Conductivity*: The effect of GB on the free carrier density and carrier m results in a decrease in the conductivity (σ) of polysilicon. Using (13), σ can be exp as

$$\sigma = \frac{n_g q \mu_g}{\left(1 - \frac{n_t t}{N_D d}\right) + \frac{kT}{2}\frac{\mu g}{d}\left(\frac{1}{v_D} + \frac{1}{v_R}\right)\exp\left(\frac{q\phi_B}{kT}\right)},$$

where n_g is the free carrier density in the grain. Equation (14) represents a genera However, in many cases, in practice, ϕ_B is large and d is small such that the c mobility is given by (11). In such a case the conductivity will be given by

$$\sigma = \frac{q^2 n_g d}{(2\pi m^* kT)^{1/2}}\exp\left(-\frac{q\phi_B}{kT}\right).$$

Substituting the value of n_g from equation

$$n_g = 2\left(\frac{2\pi m^* kT}{h^2}\right)^{3/2}\exp\left(-\xi/kT\right),$$

into (15) we obtain,

$$\sigma = \frac{4\pi m^* kT q^2 d}{h^3}\exp\left(-E_\sigma/kT\right),$$

where $E_\sigma = q\phi_B + \xi$; ξ being the difference in the energies of the conduction band and the Fermi level in the grain.

A comparison of (9) and (15) shows that the activation energy of μ_{eff} and σ a identical. Gaef *et al* (1979) have shown that E_σ is practically independent of T. Thi contrast with ϕ_B which, as seen from (3) or (4), depends on E_{FG} and therefore dec with T owing to the shifting of E_{FG} towards the intrinsic Fermi level at a high

2.3 *Photoelectric properties of polysilicon*

2.3a. *Photovoltaic properties:* Large grain ($d \sim 1$ mm or larger) polysilicon has finding considerable attention due to its potential as low cost material for terre solar cells. The grain boundaries have deleterious effect on the performan polysilicon solar cells. GBS decrease the short circuit current density (J_{sc}), open c voltage (V_{oc}) shunt resistance (R_{sh}) and increase the ideality factor (n) and re saturation current density (J_0) of the solar cell. The effect of J_{sc} is directly related enhanced minority carrier recombination at GBS. In the conventional solar cell d the *p-n* junction is a plane perpendicular to the cell thickness and is situat $\leqslant 0{\cdot}5\ \mu$m below the front surface. In this design the carriers to be collected by t junction travel along the cell thickness. The effect of GBS on J_{sc} is more severe, carriers have to cross GBS before they could be collected. The effect of GBS is mini if the grains are columnar along the cell thickness and therefore in practice polysi cells are generally made on columnar grain polysilicon material. The deeper diffusi the dopant impurity at GB effectively increases the area of the space charge at th junction. This enhances the space charge recombination, which in turn increases

J_0. As a result n and J_0 increase with the decrease in grain size. A combination of effects of GB on J_{sc}, n and J_0 leads to decrease in V_{oc}. Many workers (Fischer and Pschunder 1977; Jain *et al* 1980b) have studied the effect of GBs on the performance of columnar grain silicon solar cells. Representing the J-V_J characteristic by equation.

$$J = J_{sc} - J_{01}\left(\exp\frac{qV_J}{n_1 kT} - 1\right) - J_{02}\left(\exp\frac{qV_J}{n_2 kT} - 1\right) - \frac{V_J}{R_{sh}}, \tag{18}$$

where the second and third terms on the right side represent respectively the contributions of bulk recombination and space charge recombination. Kumari *et al* (1981) have studied the effect of grain size on the photovoltaic properties of P^+N polysilicon solar cells. Effect of grain size on V_{oc}, J_{sc}, curve factor (CF) and efficiency (η) is shown in figure 9 and that on J_{02} and n_2 is shown in figure 10.

Owing to the effect of GBs on the resistivity ρ of polysilicon and minority carrier lifetime, as discussed earlier, the optimal ρ value is relatively higher than for single crystalline cells. A comparison of the efficiencies of single and polysilicon cells as a function of ρ is shown in figure 11 (Kishore 1983).

2.3b *Photoconductive properties*: Figure 12 depicts a light-induced change in the conductance *vs* the position of a He-Ne laser spot on a polysilicon wafer for three different illumination intensities of the laser (Hwang *et al* 1981). In this figure it is noted that the conductance at GB is higher than in the grain and this difference is greater for higher intensity of the laser spot. This is indeed a typical behaviour of all polysilicon wafers with electrically active GBs.

Figure 13 shows the optical picture of a polysilicon solar cell (upper part of the figure) and the response of the cell for $\lambda = 9200$ Å scan (lower part of the figure) (Roy 1980). We see that there is a dip in the response at GB. This is a typical behaviour for all polysilicon cells and shows that the concentration of the photogenerated excess minority carriers present at GB is less than in the grains. This in conjunction with the enhanced photoconductance at GB as noted in figure 12 reveals that unlike the case of single crystal silicon the photoconductivity behaviour in polysilicon is not necessarily a minority carrier or more appropriately the excess carrier phenomenon.

Hwang *et al* (1981) and Kishore (1983) have shown that in polysilicon the low level photoconductivity is mainly due to increase in the majority carrier mobility under illumination and is therefore a majority carrier phenomenon. The increase in mobility is due to the fact that the grain boundary potential decreases under illumination. The decrease of ϕ_B with light intensity was studied for the first time theoretically by Card and Yang (1977). Experimental studies on the effect of illumination on ϕ_B have been made by Seager (1981) and Kishore (1983).

The decrease in ϕ_B under illumination leads to a large decrease in the resistivity (ρ) of polysilicon. The decrease is more, if the grain size is small, the dark value of ϕ_B is high and the temperature of the polysilicon specimen is lower. Figure 14 depicts the effect of illumination on the resistivity *vs* $1/T$ curve for a polysilicon specimen (Kishore 1983). The decrease in ρ is observed to be higher for lower values of T.

2.4 *Evaluation of the electrical activity of grain boundary*

The electrical activity of a GB depends on the density of interface states (N_{is}) and the energy distribution of these states in the band gap. However, its effectiveness also

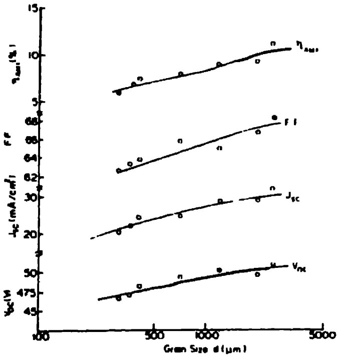

Figure 9. Plots of V_{oc}, J_{sc}, CF and efficiency η as functions of grain size for solar grade polysilicon solar cells (after Kumari *et al* 1981).

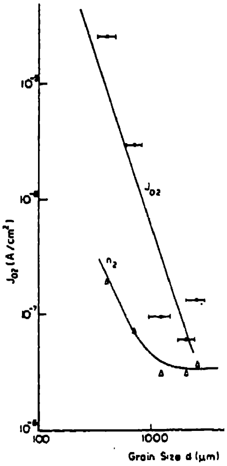

Figure 10. The effect of gr on J_{02} and n_2 for polysilico cells (after Kumari *et al* 1981

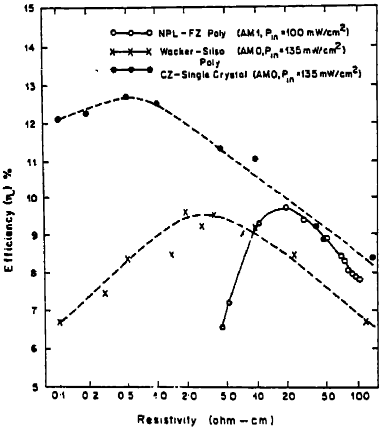

Figure 11. The conversion efficiency η as a function of base resistivity of single and polycrystalline solar cells. (after Kishore 1983).

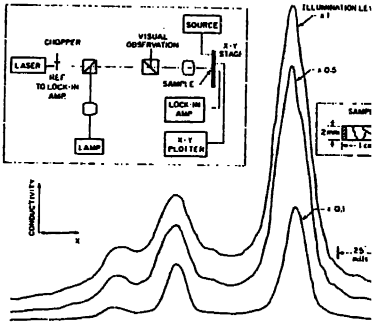

Figure 12. Light induced change in ductance *vs* position of a He-Ne Laser s polysilicon wafer for three different in (after Hwang *et al* 1981).

depends on a number of other parameters *eg*, the doping concentration in the gra grain size, the Fermi level in the GB, the temperature of the specimen and al intensity of the light in case the specimen is under illumination. The GB potentia directly related to the electrical activity of the GB. Therefore, the methods emplo the measurement of the electrical activity of GB essentially measure the qua directly related with ϕ_B. Zero bias high frequency capacitance (ZBHFC) method ha successfully used (Pike and Seager 1981) for the measurement of ϕ_B under da

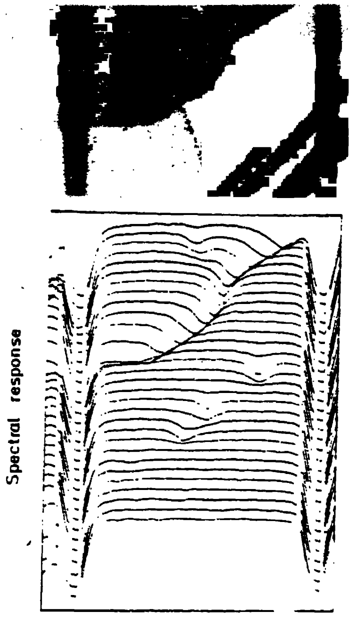

Figure 13. Spectral response of a solar cell at 920 nm in comparison with the optical picture of a solar cell surface. upper part: Optical picture. lower part: Electrical response of the solar cell (after Roy 1980).

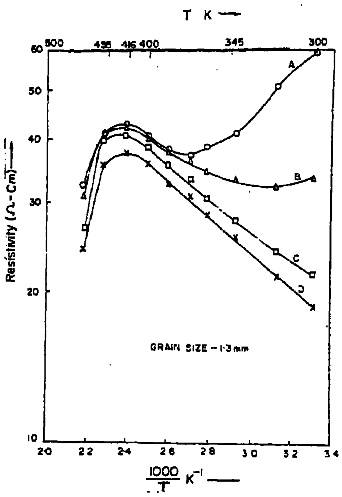

Figure 14. The effect of intensity of illumination on the temperature dependence of resistivity of a polysilicon specimen. **A.** for dark conditions **B-D.** for 30, 50 and 130 mW/cm^2 intensity respectively. (after Kishore 1983).

illumination conditions. ϕ_B is related to the ZBHFC according to the equation

$$\phi_B = q^2 \varepsilon N_D / 8C_{HF} \tag{19}$$

where C_{HF} is the ZBHFC per unit area. As discussed by Lal *et al* (1982) this method requires the GB depletion layer area to be known and is thus suitable only for the specimens (*eg*. bicrystals) where this can be easily determined. Pike and Seager (1981) have used this method for the measurement of ϕ_B as a function of T under dark conditions and Seager (1981) has used it for determining ϕ_B as a function of the light intensity.

The ϕ_B value can also be calculated from the activation energy (E_σ) of zero bias conductance (ZBC) (Pike and Seager 1981) or zero bias resistivity (ZBR) (Seager and Castner 1978) provided that ξ as a function of T is known. The validity of these methods is limited to cases where the grain size is small so that (17) is applicable. ϕ having been determined N_{is} can be calculated using (3) or (4), whichever may be applicable.

Recently some workers [Cheng and Shyu 1981; Shyu and Cheng 1982] have used deep level transient spectroscopy (DLTS) to identify the level location of GB states. Nonseparable nature of the GB levels and the likely presence of impurities in the GBs make the DLTS spectra complex and the identification of GB levels difficult.

In boron-doped bicrystals Shyu and Cheng (1982) found GB level to be at $E_v + 0{\cdot}38$ eV in one sample and at $E_v + 0{\cdot}48$ eV in the other. Application of DLTS may be expected to provide valuable information about the GB level location in n and p type silicon and the effects of heat treatment and hydrogen passivation on the elec activity of GBS.

3. Polycrystalline zinc oxide ceramic

Polycrystalline zinc oxide, when suitably doped with various oxides like Bi_2O_3, Sb CoO, MnO, etc. exhibits voltage-dependent resistance. Since the discovery of varistor action by Matsuka [1971], these materials have attracted the attentio various workers (Morris 1973, 1976; Levinson and Philipp 1975; Clarke 1978; Ki *et al* 1979). The current (I) through a varistor at a voltage (V) is given by

$$I = KV^n = (V/C)^n,$$

where n is the nonlinearity exponent and C is the nonlinear resistance. The nonline coefficient for various types of varistors is shown in figure 15. It can be seen tha performance of the zinc oxide varistor is comparable to that of a zenerdiode.

Zinc oxide varistors are made by sintering highly conducting grains of ZnO i presence of a few mole percent of other metal oxides. The grain size depends upo

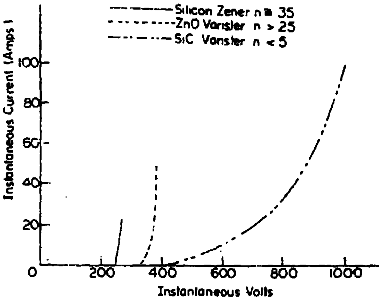

Figure 15. Instantaneous current of silicon zener, zinc oxide varistor and silicon carbide varistor *vs* their instantaneous voltage.

Figure 16. Typical microstructure of a zinc o varistor containing 6% additives.

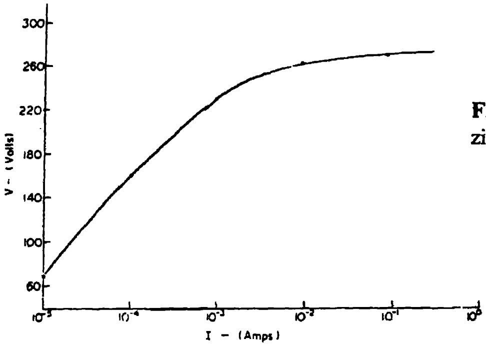

Figure 17. Voltage *vs* current characteristics zinc oxide varistor.

initial particle size and the ceramic processing. The grains are made semiconducting by doping with a suitable metal oxide. They are *n*-type with a donor density of about 10^{17}–10^{19} per cm^3 and show a resistivity of 1 ohm cm. Figure 16 shows the microstructure of a ZnO varistor. Figure 17 shows an I–V characteristic of a ZnO varistor prepared from 94 mol % ZnO and 6 mol % of other additives such as Bi_2O_3, CoO, Sb_2O_3, Cr_2O_3 MnO. The variation of various varistor parameters with preparation conditions is shown in figure 18.

3.1 *Grain boundaries in zinc oxide*

The unusual electrical properties of these zinc oxide varistors are due to the presence of GBs. To understand the mechanism of varistor action, the GBs of these ceramics have been intensively investigated.

Earlier theories were built on a model as given in figure 19. It conceived the material as consisting of two phases—one consisting of an insulating GB phase (probably a glassy phase) coating the GB. This was based on optical and SEM observations. The intergranular layer was believed to be several hundred Angstroms thick.

However detailed examination of the GB region by STEM showed that there is no discrete intergranular phase at the boundary between two grains although an interconnected phase exists at three and four grain corners (Santhanam *et al* 1979). Using high resolution x-ray micro analysis it was shown that the GBs are enriched with bismuth [Clarke 1978; Kingery *et al* 1979]. A model to explain the varistor action should be based on the concentration profile of segregating atoms at the GBs.

3.2 *Origin of varistor action*

Earlier, it was thought that the nonlinear volt-ampere characteristic of the ZnO ceramic was intimately connected with the conduction mechanism in the intergranular

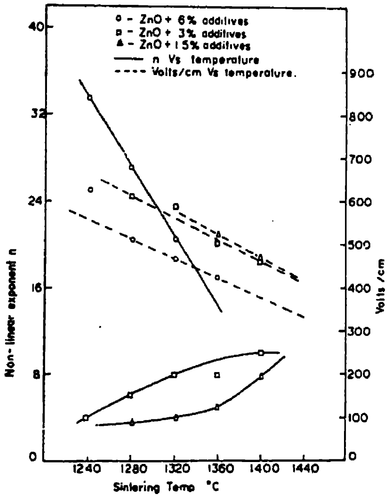

Figure 18. Variation of varistor parameters with sintering temperature (after Kalsi and Das 1983).

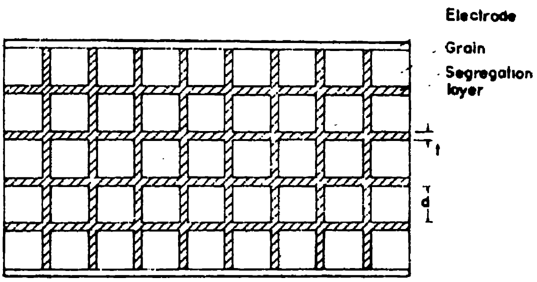

Figure 19. Schematic diagram of microstructure of zinc oxide ceramics.

phase. On the basis of electrical properties measured on ZnO—0·5 mol % $Bi_2($
Morris (1973), the author proposed a combination of electron hopping and tunr
in the thin layers of amorphous Bi_2O_3—ZnO, as the model to explain varistor acti
this material. The author observed the segregation of Bi_2O_3 amorphous phase ε
GBs. He estimated a thickness of ≃ 600 Å for the intergranular phase which is lar
tunneling through it to occur. He then assumed a process consisting of a seri
tunneling and hopping steps (1982).

Later by direct measurements Einzinger emphasized that the presence of he
geneous segregation layers between ZnO grains was no basic requirement fo
varistor effect. According to the author the effect was located in the vicinity c
directly touching ZnO grains and was therefore assumed to be a property of d
ZnO.

Therefore the theories, which depended upon the existence of thick intergra
region are now obsolete. According to the recent theories (Mahan 1982), the impo
intergranular regions, for the nonlinear current properties, are composed of one o
atomic layers. Due to the trapping of excess electrons at the intergranular regi
Schottky barrier is formed, adjacent to the interface, in each ZnO grain. The situ
becomes similar to the one described for polysilicon as discussed under § 2.1c. Th
much experimental evidence for the existence of this double Schottky barrier n
(figure 20). The nonlinear electrical behaviour is caused by electrons trying to get
this barrier. Electron transport through the interface is believed to be a two
process, whereby first the electron goes from ZnO grain to the interface and secc
on to the next ZnO grain.

This simple model is successful in explaining the current to be thermally acti
with an activation energy equal to the barrier height ϕ_B (Mahan 1982). The dc
Schottky barrier in fact behaves as a single barrier at reverse bias as is obvious fro
capacitance measurements.

$$C^{-2} \propto (\phi_B + V).$$

An improvement in this model was proposed to explain the pre-breakdown cu
(Mahan *et al* 1978, 1979). According to them, at higher electric fields, the reverse bi
depletion region becomes very thin and electron tunnelling should be taken
account. The current is then dominated by tunnelling through the depletion re

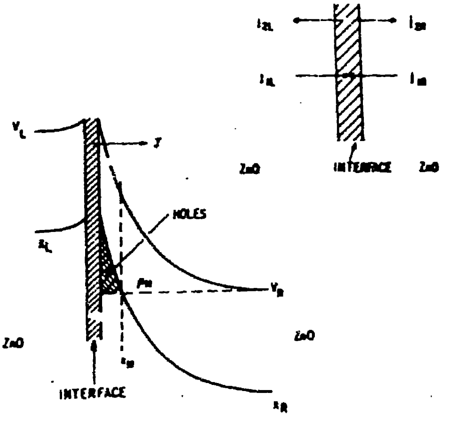

Figure 20. The double Schottk
rier model, showing depletion re
on two sides. The holes only exist
breakdown. The inset shows the
tunneling components in two
transport (after Mahan *et al* 197

rather than thermal excitation over it. The inclusion of this mechanism provides excellent agreement between theory and experiment for the pre-breakdown current.

Various models have been proposed to explain the breakdown in ZnO varistors. Zener tunnelling was suggested as the mechanism (Bernasconi *et al* 1976). Another theory assumes that the breakdown occurs because the barrier heights vanish (Levine 1975; Bernasconi *et al* 1976). Without barriers, the GB no longer offers any resistance. But this theory has not been successful in explaining the sharp rise in capacitance at breakdown.

Mahan *et al* (1978) proposed that breakdown occurred because holes are created in the ZnO valence band, by the excitation of electron hole pairs. These electron hole pairs are excited by the electrons entering the ZnO conduction band. The holes get trapped in the depletion region, providing additional positive charge which makes the depletion region much thinner. The electrons can then easily tunnel through the depletion region. This theory explains the sharp rise in capacitance at the breakdown voltage.

All these theories have used a single GB to describe the nonlinear electrical behaviour. Actual macroscopic devices present the additional problem of a random network of GBS, each with nonlinear behaviour. Little or no progress has yet been made on the macroscopic system of random networks. However, the experiments show that a single GB has the nonlinear electrical properties, and the network is thought to be multistages of the same nonlinear element.

References

Baccarani G, Ricco B and Spadini G 1978 *J Appl. Phys.* **49** 5565
Bernasconi J, Klein H P, Knecht B and Strassler S J 1976 *Electr. Mater.* **5** 473
Card H C and Yang E S 1977 *IEEE Trans. Electron Devices* **ED-24** 397
Cheng L J and Shyu C M 1981 *Semiconductor silicon* (ed.) H R Huff R J Kriegler and Y Takeishi (Pennigton New Jersey: The Electrochemical Society) 390
Clarke D R 1978 *J. Appl. Phys.* **49** 2407
Colinge J P, Demoulin E, Delannay F, Lobet M and Temerson J M 1981 *J. Electrochem. Soc.* **128** 2009
Crowell C R and Sze S M 1966 *Solid State Electron.* **9** 1035
Einzinger R 1982 *Grain boundaries in semiconductors* (eds) H J Leamy G E Pike and C H Seager (New York: North Holland Publn Co.) 343
Fischer H and Pschunder P 1977 *IEEE Trans. Electron Devices* **ED-24** 438
Fossum J G and Lindholm F A 1980 *IEEE Trans. Electron Devices* **ED-27** 692
Gaef M W M, Bloem J, Giling L J, Monkowski J R and Maes J W C 1979 *2nd E C photovoltaic solar energy conf.* Berlin p. 65
Hwang W, Panayotatos P, Poon E and Card H C 1981 *Proc. 15th IEEE Photovoltaic specialists' Conf.* 871
Jain G C, Chakravarty B C and Singh S N 1981 *Appl. Phys. Lett.* **38** 815
Jain G C, Singh S N and Kumari S 1980a *Proc. 3rd E C Photovoltaic solar energy conf.* Cannes, France
Jain G C, Singh S N, Arora N K and Das B K 1980b *Proc. national solar energy convention* Annamalai Nagar, India 317
Kalsi H S and Das B K 1983 *Bull. Mater. Sci.* **5** 33
Kazmerski Ł L, Ireland P J and Ciszek T F 1980 *Appl. Phys. Lett.* **36** 323
Kim D M, Khondker A N, Shah R R and Crosthwait D L 1981 *IEEE Electron Device Lett.* Vol EDL-3 141
Kingery W D, Vander Sande J B and Mitamura T 1979 *J Am. Ceram. Soc.* **62** 221
Kishore R 1983 *Effect of various material parameters on the performance of silicon solar cells* Ph. D Thesis, Agra University, Agra
Kishore R, Singh S N and Singh P K 1983 *Proc. national solar energy convention,* Vadodara, India (to be published)
Kumar K R and Satyam M 1981 *Appl. Phys. Lett.* **39** 898
Kumari S, Arora N K and Jain G C 1981 *Sol. Energy Mater.* **5** 383

Kumari S, Jain S K, Das B K and Jain G C 1983 *Sol. Cells* **9** 209

Lal Mohan, Kishore R, Singh S N and Das B K 1982 *Proc. National Solar Energy Convention*, Delhi 9.040

Levine J D 1975 *CRC Crit. Rev. Solid State Sci.* **5** 597

Levinson L M and Philipp H R 1975 *J. Appl. Phys.* **46** 1332

Lindmayer J 1978 *Proc. 13th IEEE Photovoltaic specialists, conf.* p. 1096

Mahan G D, Levinson L M and Philipp H R 1978 *Appl. Phys. Lett.* **33** 830

Mahan G D, Levinson L M and Philipp H R 1979 *J. Appl. Phys.* **50** 2799

Mahan G D 1982 *Grain boundaries in semiconductors* (ed) H J Leamy, G E Pike and C H Seager (New North Holland Publn Co.) 333

Martinez J and Piqueras J 1980 *Solid State Electron.* **23** 297

Matre H F 1971 *Defect electronics in semiconductors* (New York: Wiley Interscience)

Matsuka M 1971 *Jpn. J. Appl. Phys.* **10** 736

Morris W G 1973 *J. Am. Ceram. Soc.* **56** 360

Morris W G 1976 *J. Vac. Sci. Tech.* **13** 926

Pike G E and Seager C H 1981 *Adv. Ceram.* **1** 83

Pollock G A, Deline V R and Furman B K 1982 *Grain boundaries in semiconductors* (ed) H J Leamy, G and C H Seager (New York: North Holland Publn Co.) 71

Poon E and Hwang W 1982 *Solid State Electron.* **25** 699

Roy K 1980 *Proc. symp. on electrical and optical properties polycrystalline or impure semiconductors an silicon growth methods* (eds) K V Ravi and B O'Mara (Pennigton New Jersey: The Electroch Society) (eds) 1

Santhanam A T, Gupta T K and Carlson W G 1979 *J. Appl. Phys.* **50** 852

Seager C H 1981 *J. Appl. Phys.* **52** 3960

Seager C H and Castner T G 1978 *J. Appl. Phys.* **49** 3879

Seto J Y W 1975 *J. Appl. Phys.* **46** 5247

Shyu C M and Cheng C J 1982 *Grain boundaries in semiconductors* (ed) H J Leamy, G E Pike and C H (New York: North Holland Publn Co.) 131

ull. Mater. Sci., Vol. 6, No. 2, May 1984, pp. 259–261. © Printed in India.

MnO$_2$ catalyzed carbon electrodes for dioxygen reduction in oncentrated alkali

R MANOHARAN and A K SHUKLA*

Solid State and Structural Chemistry Unit, Indian Institute of Science, Bangalore 560 012, India

Abstract. A process to deposit γ-MnO$_2$ catalytic oxide onto coconut-shell charcoal substrate is described. Current-potential curves for electroreduction of dioxygen with electrodes fabricated from this catalyzed substrate are obtained in 6M KOH under ambient conditions. The performance of these electrodes is competitive with platinized carbon electrodes.

. Introduction

fficient reduction of oxygen under ambient conditions is a reaction of great mportance for fuel-air fuel cells and metal-air batteries (Bockris *et al* 1981). The evelopment of a low cost electrocatalyst capable of reducing oxygen reversibly is a hallenge of the present day oxygen electrochemistry.

In recent years, several metal oxides have been explored as electrocatalysts for oxygen reduction in alkaline media (Egdell *et al* 1983; Horowitz *et al* 1983; Trasatti 980). Manganese dioxide which is readily available and is cheap enough athyanarayana and Sridharan 1976) has been claimed to be a promising oxide catalyst r the electroreduction of oxygen (Armstrong 1975). This oxide catalyst exists in veral forms. Of these, the oxygen-deficient γ-MnO$_2$ possesses the maximum catalytic tivity (Brenet 1979; Trasatti 1980). Electrocatalytic activity of γ-MnO$_2$ towards ygen reduction has been explained by Brenet (1979) in light of the redox couples Mn^{4+}/Mn^{3+}) through the following mechanism:

$$\mathrm{Mn}^{4+} \xrightarrow{\bar{e}} \mathrm{Mn}^{3+} \xrightarrow{\mathrm{O_2(ads)}} \mathrm{Mn}^{4+} + \mathrm{O_2^-(ads)}.$$

his material, however, has certain drawbacks such as its low surface area and the poor ectrical conductance. These problems could easily be overcome by depositing it onto a nducting and high surface area carbon substrate. This paper describes an attempt to posit the appropriate amount of γ-MnO$_2$ catalyst onto the coconutshell charcoal bstrate and the electrochemical performance of the electrodes fabricated from such a bstrate for dioxygen reduction in concentrated alkali.

---

ntribution No. 252 from the Solid State and Structural Chemistry Unit.

o whom all correspondence should be addressed.

2. Experimental

2.1 *Deposition of γ-MnO_2 onto the carbon substrate*

The chemical method adopted to prepare γ-MnO_2 catalytic oxide is similar to described by Gattow and Glemser (1961). $KMnO_4$ containing desired weight pe of MnO_2 was dissolved in distilled water and mixed with an appropriate quantity carbon substrate to form a thick slurry. Freshly prepared sulphurous acid obtain saturating water with sulphur dioxide was added to this slurry with constant sti The resultant mass was filtered, washed repeatedly and dried in an air oven at a 80°C. The process resulted in the deposition of γ-MnO_2 onto the carbon subs Formation of γ-MnO_2 catalytic oxide was ascertained by x-ray powder diffracti diffused diffraction pattern characteristic of amorphous γ-MnO_2 was obt (Zwicker *et al* 1962).

2.2 *Preparation of the electrodes*

Electrodes of various carbon specimens were prepared by hot pressing the γ-M deposited carbon substrate at 140°C at an optimized pressure of 0·05 ton/c expanded platinum metal screens with 20% polythylene as binder. The det procedure of fabricating such electrodes is described elsewhere (Manoharan Shukla 1983).

2.3 *Measurements of the electrochemical performance of the electrodes*

The electrochemical cell designed to measure the polarization performance cont the porous carbon working electrode catalyzed with γ-MnO_2, Hg/HgO, OH^- refe electrode equipped with a luggin capillary, a high surface area flat bed counter elec made from sintered nickel and a magnetic stirrer submerged in 6M KOH electr The details of the electrochemical assembly have been described earlier (Manoh and Shukla 1983). The cell assembly had a gas compartment on the rearside o working electrode which was sealed by making the current collecting metal block tightly against the electrode.

Galvanostatic polarization studies were carried out using a regulated dc p supply and a high-power rated rheostat in series with the electrochemical cell.

3. Results and discussions

The room temperature (~30°C) polarization curves for carbon electrodes with va loading levels (2, 4 and 8 wt %) of γ-MnO_2 catalyst at a gas pressure of 130 mm H shown in figure 1. For comparison the polarization curves for the bare (withou catalyst) and 7 wt % Pt catalysed carbon electrodes are also shown in the figure. curves are experimentally obtained and are not IR corrected. The experiments repeated with a minimum of two electrodes each time and were reproducible electrocatalytic activity of γ-MnO_2 deposited carbon electrodes increased with dec in its loading concentration. A 2 wt % of the oxide catalyst deposited onto the ca substrate showed the maximum activity. This signifies that only an appropriate am of oxide catalyst is required to be deposited onto the carbon substrate in or facilitate the catalytic action without increasing the mass transfer and

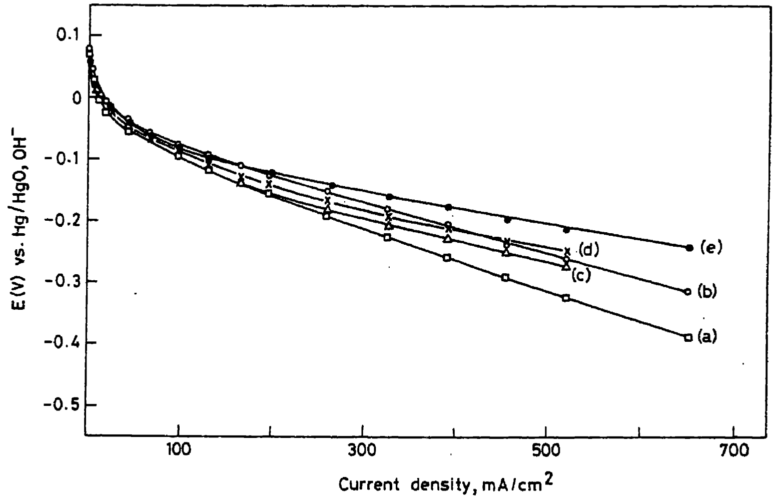

Figure 1. Current-potential curves for the electroreduction of dioxygen on (a) bare carbon electrode, (b) a 7 wt % Pt catalyzed carbon electrode, (c) a 8 wt % (d) a 4 wt % (e) a 2 wt % γ-MnO_2 catalyzed carbon electrode.

polarization components. The activity for dioxygen reduction on the carbon electrodes catalyzed with 2 wt % of γ-MnO_2 is competitive with the 7 wt % platinized carbon electrodes. The 2 wt % γ-MnO_2 catalyzed carbon electrode could be loaded with a current density of 650 mA/cm^2 at the polarization potential of $-0{\cdot}24$ V *vs* Hg/HgO, OH^-. To avoid the cathodic reduction of γ-MnO_2 catalyst (Sathyanarayana and Sridharan 1976) (which takes place at $-0{\cdot}3$ V *vs* Hg/HgO, OH^-) the electrodes were not subjected to polarization beyond this potential.

Acknowledgement

Authors are thankful to Prof C N R Rao for inviting them to contribute this article. Financial support from DST is gratefully acknowledged.

References

Armstrong W A 1975 in *Power sources* (ed) D H Collins (New York: Academic Press) 5 p. 393

Bockris J O, Conway B E, Yeager E and White R E 1981 *Comprehensive treatise of electrochemistry* (New York: Plenum Press) Vol 3

Brenet J P 1979 *J. Power Sources* **4** 183

Egdell R G, Goodenough J B, Hamnett A and Naish C C 1983 *J. Chem. Soc., Faraday Trans.* **1** 79

Gattow V G and Glemzer O 1961 *Z. Anorg. Allgem. Chem.* **309** 20

Horowitz H S, Longo J M and Horwitz H H 1983 *J. Electrochem. Soc.* **130** 1851

Kozawa A and Brodd R J 1975 *Manganese dioxide symposium* (Cleveland: I.C. Sample office, Union Carbide Corporation) Vol 1

Manoharan R and Shukla A K 1983 *J. Power Sources* **10** 333

Sathyanarayana S and Sridharan L N 1976 A Report entitled *Electrochemical energy storage systems for rural applications* submitted to the Department of Science and Technology, Government of India

Trasatti S 1980 *Electrodes of conductive metallic oxides* (Amsterdam: Elsevier Scientific)Parts A and B

Zwicker W K, Groeneveld Meijor W O J and Jaffe H W 1962 *Am. Mineral* **47** 246

Bull. Mater. Sci., Vol. 6, No. 2, May 1984, pp. 263–272. © Printed in India.

Structural and magnetic investigations of some new boron containing rare earth intermetallic compounds

S K MALIK, S K DHAR and R VIJAYARAGHAVAN

Tata Institute of Fundamental Research, Bombay 400005, India

Abstract. By alloying boron with RPd_3 (R = rare earth) compounds, new ternary alloys of the formula RPd_3B_x ($0 \leqslant x \leqslant 1$) have been prepared. The parent RPd_3 compounds crystallise in the cubic $AuCu_3$ type structure. The addition of boron does not change the structure but results in an expansion of the lattice. Therefore, it is likely that the small boron atoms occupy the vacant body centred position in $AuCu_3$ type structure. It is also observed that compounds of the composition RRh_3B can be formed in the cubic structure for all rare earths R though the parent RRh_3 compounds exist only for R = Ce ($AuCu_3$ type) and La, Sm, Nd and Gd (all hexagonal $CeNi_3$ type). This points out the role of boron in stabilising new crystallographic phases. The results of susceptibility measurements on some of the RPd_3B and RRh_3B compounds are presented. In particular, it is noted that while $GdPd_3$ orders antiferromagnetically with $T_N = 6$ K, $GdPd_3B$ does not order magnetically down to 4·2 K.

Keywords. Boron: rare earths; magnetic susceptibility; structural investigations.

1. Introduction

During the last few years a new class of rare earth compounds known as rare earth ternary borides have attracted a great deal of attention. The interest in these compounds is due to their fascinating magnetic and superconducting properties. For example, in the series of ternary borides represented by the formula RRh_4B_4 (R = rare earth), first synthesized by Matthias *et al* (1977a, b), the compounds with Th, Y, Nd, Sm, Er, Tm and Lu are superconducting whereas those with Gd, Tb, Dy and Ho undergo ferromagnetic ordering. Following the RRh_4B_4 series of compounds, many other ternary borides forming at different stoichiometries have been synthesised and investigated for magnetic and possible superconducting behaviour. In this paper we report the formation of new boron containing rare earth compounds represented by the formula RPd_3B_x ($0 \leqslant x \leqslant 1$) and RRh_3B where R = La to Lu. Magnetic studies on some of these alloys are also presented.

An indication that alloys of the formula RRh_3B_x and RPd_3B_x may well exist came first during the course of our investigations on RRh_3B_2 compounds described elsewhere (Malik *et al* 1983). In the initial stages of our work on these, we observed, in the x-ray diffraction pattern of $CeRh_3B_2$, the existence of some extra lines which could not be ascribed to hexagonal $CeRh_3B_2$ compound. A careful analysis showed that these extra lines could be indexed on the basis of a cubic structure. The lattice constant of this cubic phase turned out to be slightly larger than that of $CeRh_3$ which crystallises in the cubic $AuCu_3$ structure type (Harris and Norman 1967). Because of the structural considerations of the $AuCu_3$ type crystal lattice, to be discussed below, the formula of this new cubic phase was presumed to be $CeRh_3B_x$ ($0 < x \leqslant 1$). Subsequently we found that starting with appropriate amounts of Ce, Rh and B, cubic compounds having the formula $CeRh_3B_x$ ($0 < x \leqslant 1$) could indeed be formed. The formation of alloys of the above composition immediately suggested the likely existence of RPd_3B_x compoı The RPd_3 compounds also crystallise in the $AuCu_3$ structure type (Harris and Ra 1965) with lattice constants comparable to that of $CeRh_3$. Later investigations (] *et al* 1981a) verified the formation of RPd_3B_x ($0 < x \leqslant 1$) alloys for all the rare e R. Further extension of the work showed that RPd_3Si_x alloys could also be for though silicon content is much smaller.

2. RPd_3B_x ($0 < x \leqslant 1$; R = Rare earth) alloys

2.1 *Synthesis and structure*

Master RPd_3 alloys were first prepared by melting together stoichiometric amouı the rare earth and the Pd metal in an arc furnace. The alloy ingots were turnec melted several times to ensure homogeneity. Approximately half the amount of RPd_3 alloy was remelted with an appropriate amount of boron in a water cı copper boat in an induction furnace to form RPd_3B alloys. This preliminary mixi boron with RPd_3 achieved by induction heating was necessary as otherwise b chunks were found to shatter and fly away on coming under the arc in the arc fur In order to ensure complete mixing the fused charge of RPd_3 and boron was rem in the arc furnace. Alloy formation at the stoichiometry RPd_3B_x ($0 < x \leqslant 1$) was for few rare earths only, *e.g.* La, Ce, Pr, Eu, Gd and Dy and these were obtainı remelting appropriate proportions of RPd_3 and RPd_3B. In the case of europiun ytterbium compounds, excess amount of the rare earth was taken to compensate fı loss due to evaporation during melting. Powder x-ray diffraction patterns recorded using CuK_α radiation.

The RPd_3 compounds are known to crystallise in the cubic $AuCu_3$ type struı space group *Pm3m* (figure 1a). The rare earth atoms occupy the cube corners ar atoms are on the face centred positions. The various atomic positions in the unit cε given by (Pearson 1967)

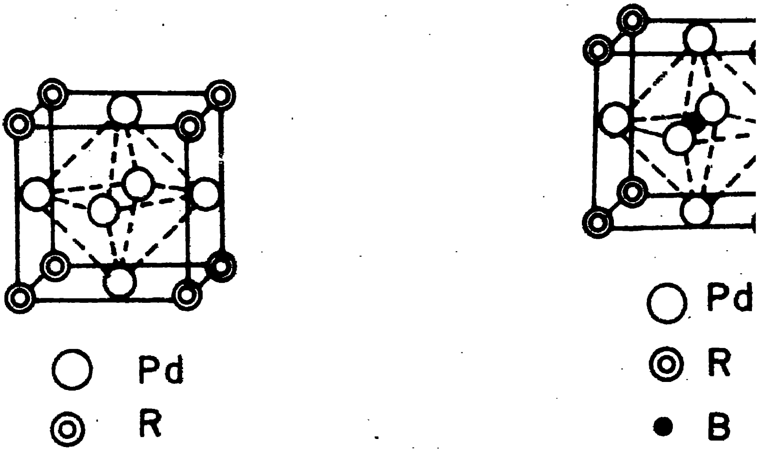

Figure 1a. The unit cell of RPd_3 (R = rare earth) compounds crystallising in AuC structure. **b.** The proposed crystal structure of RPd_3B compounds.

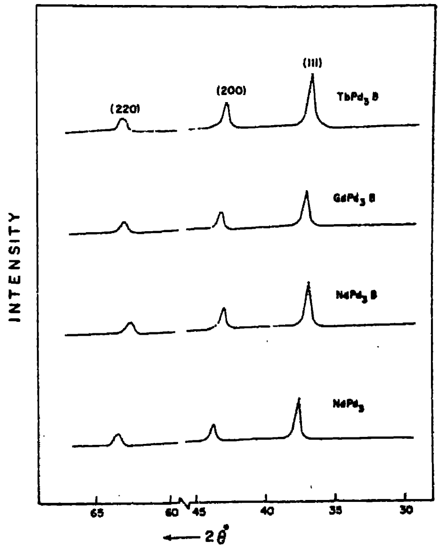

Figure 2. The x-ray diffraction patterns of NdPd$_3$ and some RPd$_3$B (R = Nd, Gd and Tb) compounds.

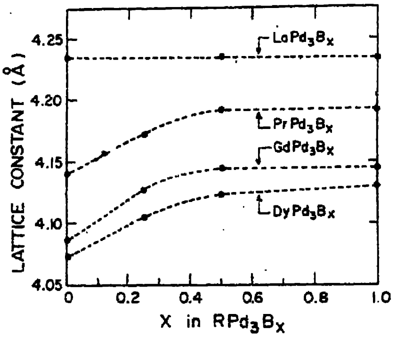

Figure 3. Lattice parameter of RPd$_3$B$_x$ (R = La, Pr, Gd and Dy) alloys as a function of boron concentration x.

R (1*a*) *m*3*m* : 0, 0, 0
Pd (3*c*) 4/*mmm* : 0, 1/2, 1/2; 1/2, 0, 1/2; 1/2, 1/2, 0.

The x-ray diffraction patterns of RPd$_3$B$_x$ (for all x) compounds are identical to that of the RPd$_3$ compounds (figure 2) and hence can be fitted to cubic structure type. However, the lattice parameter of the former is observed to be slightly larger than that of the parent RPd$_3$ compound and depends on the boron concentration x. Figure 3 shows the dependence of lattice parameter on boron concentration in some of these alloys. The relatively small boron atoms presumably occupy the vacant body-centred position in the RPd$_3$ unit cell to give rise to an $E2_1$ anti-perovskite arrangement, space group *Pm*3*m* (figure 1b). Thus RPd$_3$B$_x$ alloys may be considered to result from "addition" of boron to parent RPd$_3$ compound. Many compounds which have the AuCu$_3$ type structure are known to accommodate smaller non-metallic elements like B, C, N, Si etc. at the body-centred position resulting in anti-perovskite compound formation (Gschneidner *et al* 1978). The various atomic positions in the RPd$_3$B unit cell are given by (Pearson 1967)

R (1*a*) *m*3*m* : 0, 0, 0
Pd (3*c*) 4/*mmm* : 0, 1/2, 1/2; 1/2, 0, 1/2; 1/2, 1/2, 0.
B (1*b*) *m*3*m* : 1/2, 1/2, 1/2.

Table 1 lists the lattice constants of RPd$_3$ and RPd$_3$B compounds and the same information is plotted graphically in figure 4. It should be noted that the expansion in the cell volume of Ce and Eu compounds is relatively larger. Because of the highly volatile nature of Yb, efforts to make single phase YbPd$_3$B did not succeed. However, the extra phase in the alloy is estimated to be less than 10%.

Table 1. Lattice constants of RPd_3 and RPd_3B (R = rare earth) compounds

Compound	Lattice constant a (Å)	Compound	Lattice constant *a* (Å)
$LaPd_3$	4·229	$LaPd_3B$	4·229
$CePd_3$	4·124	$CePd_3B$	4·203
$PrPd_3$	4·141	$PrPd_3B$	4·194
$NdPd_3$	4·132	$NdPd_3B$	4·187
$SmPd_3$	4·110	$SmPd_3B$	4·156
$EuPd_3$	4·102	$EuPd_3B$	4·196
$GdPd_3$	4·087	$GdPd_3B$	4·146
$TbPd_3$	4·080	$TbPd_3B$	4·138
$DyPd_3$	4·073	$DyPd_3B$	4·132
$HoPd_3$	4·067	$HoPd_3B$	4·126
$ErPd_3$	4·061	$ErPd_3B$	4·121
$TmPd_3$	4·055	$TmPd_3B$	4·111
$YbPd_3$	4·050	$YbPd_3B$	4·088
$LuPd_3$	4·045	$LuPd_3B$	4·090

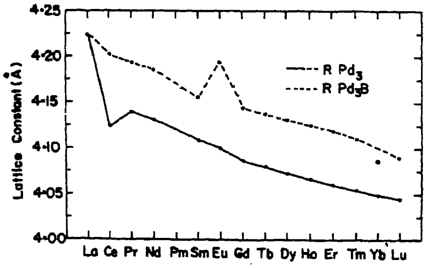

Figure 4. Lattice parameter of and RPd_3B (R = rare earth) comp

2.2 *Magnetic susceptibility measurements*

From figure 4 it is seen that with the exception of $EuPd_3B$, the lattice constant of RPd_3B compounds follows the usual lanthanide contraction for trivalent rare ions. Susceptibility measurements carried out on some of these compounds for R = Pr, Nd, Sm, Gd, Tb, Dy, Er and Tm, in the temperature range 77 to 3 confirm the trivalency of rare earth ions. For $GdPd_3$ and $GdPd_3B$ susceptil behaviour down to 4.2 K was recorded for reasons given below. (The addition of b to $CePd_3$ and $EuPd_3$ results in unusual lattice expansion and changes the mag properties of Ce and Eu ions drastically; results are discussed elsewhere (Dhar 1981b; 1982).

With the exception of $SmPd_3B$ all other RPd_3B compounds, investigated magnetic behaviour, show a linear χ^{-1} *vs* T behaviour (figures 5 and 6). effective paramagnetic moments were determined by using the for $\chi(T) = N\mu_{\mathrm{eff}}^2/[3k_B(T-\theta_p)]$. The values of μ_{eff} thus obtained are seen to be almost e to the free ion value for the trivalent state and are listed in table 2. Small θ_p va suggest that magnetic ordering in RPd_3B compounds may occur only at very temperatures. The nonlinear behaviour of χ^{-1} *vs* T observed in $SmPd_3B$ (figure 6)

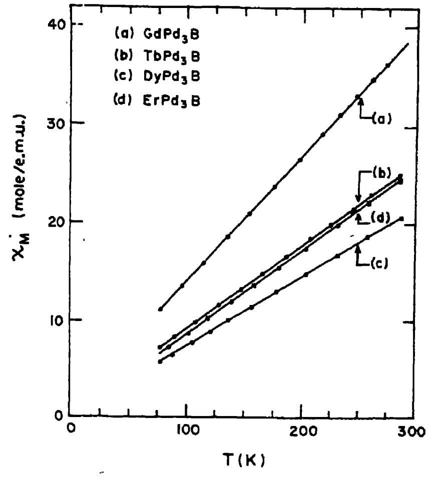

Figure 5. The plot of inverse susceptibility *vs* temperature of RPd_3B (R = Gd, Tb, Dy and Er) compounds.

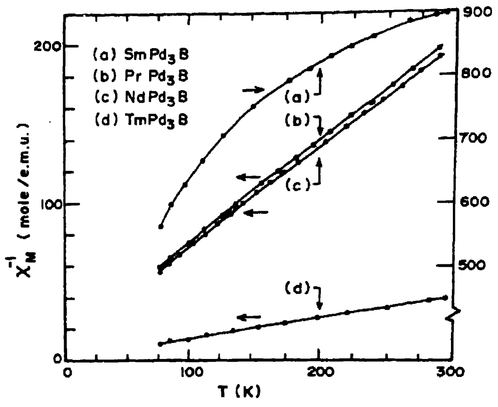

Figure 6. The temperature dependence of inverse susceptibility of RPd_3B (R = Sm, Pr, Nd and Tm) compounds.

Table 2. The effective paramagnetic moment μ_{eff} and paramagnetic Curie temperature θ_p in some RPd_3B and RRh_3B (R = rare earth) compounds.

Compound	$\mu_{eff}(\mu_B)$	$\theta_p(K)$
$NdPd_3B$	3·54	−12·0
$PrPd_3B$	3·54	−13·0
$TbPd_3B$	9·76	−11·0
$DyPd_3B$	10·73	−7·8
$ErPd_3B$	9·74	−5·0
$TmPd_3B$	7·76	−4·0
$NdRh_3B$	3·75	−7·0
$PrRh_3B$	3·80	−18·0
$TbRh_3B$	9·77	5·0
$DyRh_3B$	10·69	4·0
$ErRh_3B$	9·64	5·0

consequence of the temperature independent contribution arising due to narrow multiplet separation of Sm^{3+} ion.

Introduction of non magnetic boron in the RPd_3 compounds, besides expanding the lattice, will also change the electron concentration in the conduction band. Since RKKY interaction responsible for magnetic ordering in rare earth compounds is electron concentration-dependent, any change in the latter would be expected to modify the exchange interaction between the rare earth ions. Examples exist in literature where such effects have been found. For instance while the moment carrying trivalent rare earths RAl_2 order ferromagnetically (except $CeAl_2$), the compound $EuAl_2$ in which Eu is divalent and, therefore, contributes one electron less to the conduction band, is antiferromagnetic (Wallace 1973). In the pseudobinary $Eu_xLa_{1-x}Al_2$ a reversal magnetic coupling from antiferromagnetic to ferromagnetic with increasing x, alters the electron concentration, is observed (Mader and Wallace 1968). Sin while GdAg and GdIn order antiferromagnetically with Neel temperatures of and 28 K respectively, the pseudobinary solutions $GdAg_xIn_{1-x}$ exhibit ferrom ism for $0{\cdot}8 < x < 0{\cdot}3$ with Curie temperature increasing with increasing x (Sek and Yasukochi 1966). The dependence of exchange interaction on the el concentration can be understood from the formula

$$\theta_p = -\frac{3\pi Z^2|J(0)|^2}{k_B E_F} S(S+1)\sum_i F(2k_F r_i),$$

where θ_p is the paramagnetic Curie temperature, Z is the average number of co tion electrons per atom, $2J(0)$ is the exchange interaction constant betwe rare earth spin S and conduction electron spin s, E_F is the Fermi energ $F(x) = (x \cos x - \sin x)/x^4$. In the molecular field approximation θ_p is identica the magnetic ordering temperature. The sign of $F(x)$ determines the kind of ma order that develops: antiferromagnetic if sum is positive and ferromagnetic if the negative. With the increase in electron concentration, *i.e.* an increase in Z and he k_F (assuming crystal structure remains the same) x increases and $F(x)$ sho oscillatory behaviour from positive to negative values.

In order to see if the addition of boron is accompanied with any el concentration effects, magnetic behaviour of $GdPd_3$ and $GdPd_3B$ was studied dc liq.He temperature. The compound $GdPd_3$ was chosen because it is the only com in the RPd_3 series that orders magnetically above 4·2 K (Gardner *et al* 1972). Fi shows the magnetisation as a function of temperature in $GdPd_3$ and $GdPd_3B$. external field of 4 kOe magnetisation of $GdPd_3$ shows a sharp singularity at which corresponds to an antiferromagnetic ordering in this compound. No feature is observed in $GdPd_3B$ which continues to remain paramagnetic down to These observations show that the addition of boron modifies the exchange inter

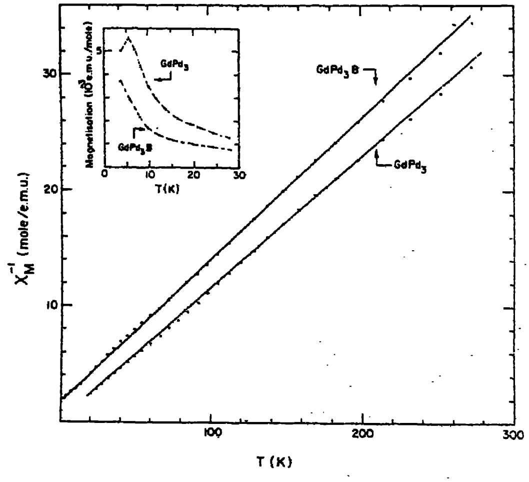

Figure 7. The inverse susceptibility of $GdPd_3$ and $GdPd_3B$ as a function of tem The inset shows the temperature dependence of magnetization (in a field of 4 kOe

between the rare earth ions either due to lattice expansion, or by changing electron concentration or a combination of both. Extension of magnetisation below 4·2 K may, perhaps, show evidence of magnetic ordering in $GdPd_3B$.

3. RRh_3B compounds

3.1 *Synthesis and structure*

In the beginning of this paper we mentioned that alloys of the formula $CeRh_3B_x$ could be formed. This observation together with the fact that alloys of the composition RPd_3B_x exist for all R prompted us to investigate whether single phase RRh_3B_x alloys could be synthesised. It was found that RRh_3B compounds, do indeed, form for all rare earths R. The x-ray diffraction patterns of RRh_3B compounds (figure 8) are similar to those of RPd_3B compounds. Therefore, presumably RRh_3B compounds also crystallise in the anti-perovskite or filled $AuCu_3$ type structure. It may be noted that while the parent RPd_3 compounds exist for all R, such is not the case with RRh_3 compounds. The latter form only for R = Ce ($AuCu_3$ type structure) and La, Sm, Nd and Gd (hexagonal $CeNi_3$ type structure) (Iandelli and Palenzona 1979). The non-metallic element boron, therefore, has the effect of stabilising the cubic RRh_3B phase. In fact, while our experimental investigations were on, we came across instances in the literature where complex metallic phases are stabilised by atoms like C, B, N, Si etc (Stadelmaier 1979). The alloys of composition RRh_3C_x ($x \sim 1$) for all R also exist in the perovskite structure (Holleck 1971), thus strengthening our conclusions, reached independently by us, about the crystal structure of RRh_3B compounds.

In contrast to RPd_3B_x alloys where $0 < x \leqslant 1$, it appears that RRh_3B_x compounds do not form below a certain minimum concentration of boron ($CeRh_3B_x$ being an exception). Thus for $x = 0{\cdot}5$ no perovskite formation was observed for R = La, Nd and Er. Though, this was not tested for other rare earths we believe similar considerations should hold. We have not determined the minimum value of x for which RRh_3B_x alloys can be stabilised.

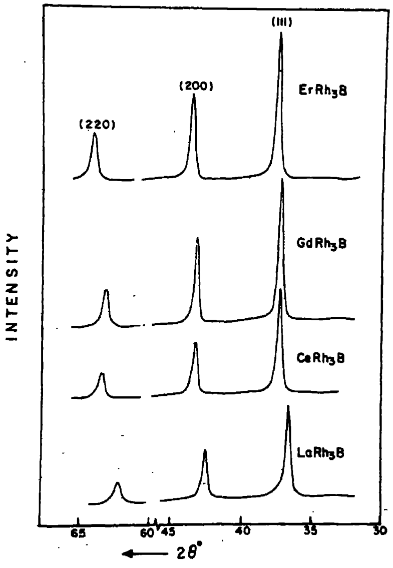

Figure 8. The x-ray diffraction patterns of some RRh_3B (R = La, Ce, Gd and Er) compounds. These patterns can be indexed on the basis of a cubic unit cell.

3.2 *Magnetic susceptibility and ^{151}Eu Mössbauer measurements*

The lattice constants of RRh_3B compounds are plotted in figure 9. With the excep of $CeRh_3B$, the usual lanthanide contraction with no anomaly in the lattice parame observed. This points out the trivalent character of rare earth ions in these compou This has been verified from susceptibility measurements carried out on some of t compounds in the temperature range 300 to 77 K. The χ^{-1} *vs* T plots are show figures 10 and 11. For $SmRh_3B$ χ^{-1} *vs* T is non-linear for reasons similar to those g for $SmPd_3B$. The effective paramagnetic moments (very close to free ion value) paramagnetic Curie temperatures are listed in table 2.

In case of $EuRh_3B$, the trivalency of Eu has been confirmed from ^{151}Eu Mössb spectroscopy. A single Mössbauer absorption with isomer shift of 2·4 ± 0·1 mm characteristic of trivalent Eu in metallic environments, is observed at 300 K (figure There is no change in isomer shift on lowering the temperature to 88 K.

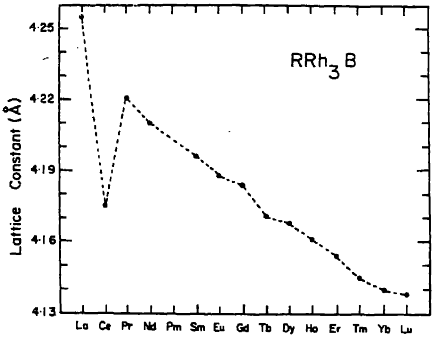

Figure 9. The lattice paramete RRh_3B (R = rare earth) compou

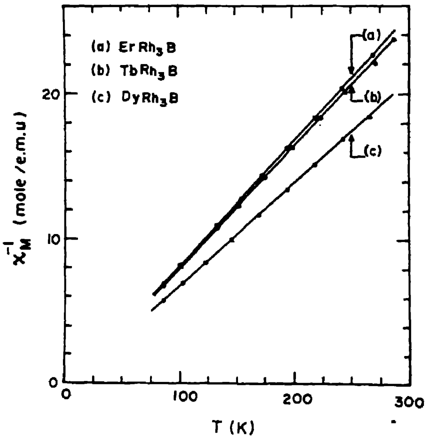

Figure 10. Inverse susceptibility as a function of temperature in RRh_3B (R = Er, Tb and Dy) compounds.

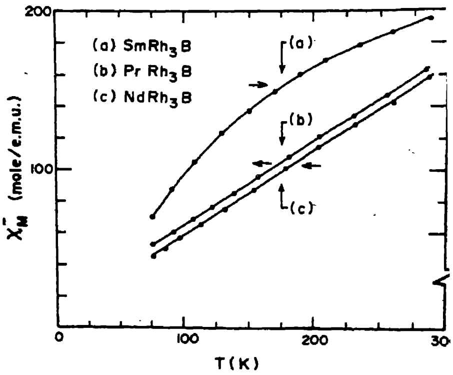

Figure 11. Inverse susceptibility *vs* temperature RRh_3B (R = Sm, Pr and Nd) compounds.

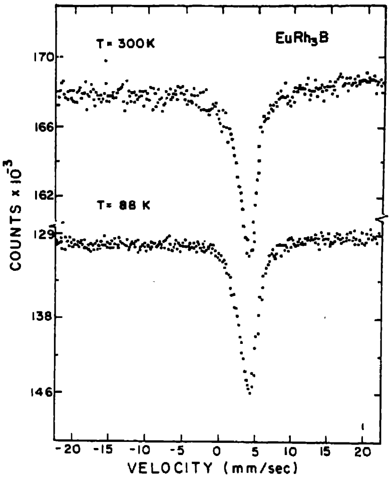

Figure 12. ^{151}Eu Mössbauer spectrum of EuRh$_3$B at 300 and 88 K.

Silicon addition to RPd_3 compounds

rom the structural considerations of the RPd_3 unit cell mentioned above, we oncluded that the small boron atoms in the RPd_3B_x alloys occupy the interstitial acant body-centred position. It was, therefore, natural to investigate whether other on-metallic elements could be introduced in the RPd_3 lattice. In this direction we tried he synthesis of RPd_3Si_x alloys for $R = La$, Ce and Eu only. It was found that like oron, silicon can also be alloyed with RPd_3 compounds. However, the atomic ercentage of silicon that can be dissolved into RPd_3 lattice is far less than that of oron. Only up to $x \sim 0{\cdot}3$, single phase cubic alloys were obtained for RPd_3Si_x omposition. This may be related to the relatively larger atomic volume of silicon ompared to that of boron. From volume filling considerations alone it may not be ossible to accommodate as many number of silicon atoms as boron. The addition of ilicon, like boron, to parent RPd_3 compound leads to lattice expansion. Results of agnetic susceptibility and ^{151}Eu Mössbauer spectroscopy on $CePd_3Si_x$ and uPd_3Si_x, where a valence change of Ce and Eu ions is observed on alloying with Si, are resented elsewhere (Malik *et al* 1982; Dhar *et al* 1983).

Carbon addition to RPd_3 compounds was also tried and it was found that carbon annot be alloyed with RPd_3 compounds.

eferences

har S K, Malik S K and Vijayaraghavan R 1981a *Mater. Res. Bull.* **16** 1557
har S K, Malik S K and Vijayaraghavan R 1981b *Phys. Rev.* **B24** 6182
har S K, Malik S K, Rambabu D and Vijayaraghavan R 1982 *J. Appl. Phys.* **53** 8077
har S K, Nagarajan R, Malik S K, Rambabu D and Vijayaraghavan R 1983 *J. Magn. & Magn. Mater.* **393** 31–34
ardner W E, Penfold J, Smith T F and Harris I R 1972 *J. Phys.* **F2** 133
schneidner Jr K A, MaMasters O D and Ostenson J E 1978 *J. Less-Common Metals* **62** 167
arris I R and Raynor G V 1965 *J. Less Common-Metals* **9** 263
arris I R and Norman M 1967 *J. Less Common-Metals* **13** 629

Holleck H 1971 in *Rare earths and actinides* (ed) E W Lee (London: Creative Offset Ltd.) p. 109

Iandelli A and Palenzona A 1979 in *Handbook on the physics and chemistry of rare earths* (eds Gschneidner Jr and L Erying Ch. 13 (Amsterdam: North Holland)

Mader K H and Wallace W E 1968 *J. Chem. Phys.* **49** 1521

Malik S K, Vijayaraghavan R, Boltich E B, Craig R S, Wallace W E and Dhar S K 1982 *Solid State Co* **43** 243

Malik S K, Vijayaraghavan R, Wallace W E and Dhar S K 1983 *J. Magn. & Magn. Mater.* **37** 30

Matthias B T, Corenzwit E, Vandenberg J M and Barz H E 1977 *Proc. Nat. Acad. Sci. USA* **74** 1

Pearson W B 1967 *Handbook of lattice spacings and structure of metals* (New York: Pergamon) Vol. 2, 57

Sekizawa K and Yasukochi K 1966 *J. Phys. Soc. Jpn* **21** 684

Stadelmaier H H 1969 in *Developments in the structural chemistry of alloy phases* (ed.) B C G (New York: Plenum)

Vandenberg J M and Matthias B T 1977 *Proc. Natl. Acad. Sci. USA* **74** 1336

Bull. Mater. Sci., Vol. 6, No. 2, May 1984, pp. 273–281. © Printed in India.

On the mechanism of pairing in the BCS theory

C M SRIVASTAVA

Department of Physics and Advanced Centre for Research in Electronics, Indian Institute of Technology, Bombay 400 076, India

Abstract. An explanation has been offered for the mechanism of cooper pairing in the BCS theory of superconductivity on the basis of the relativistic Darwin interaction. The theory leads to an expression for critical temperature which depends on a few atomic parameters. Calculated values of T_c for elements and alloys are in good agreement with experiment.

Keywords. Cooper pairing: BCS theory; superconductivity; pairing interaction; critical temperature.

1. Introduction

The BCS (Bardeen *et al* 1957) theory of superconductivity is based on the pairing hypothesis of a simple model of electron gas with attractive interaction. This interaction is assumed to be mediated by phonons. Despite the striking success of the BCS theory in explaining the essential properties of superconductors, attempts to increase the size of the pairing interaction using BCS theory have not met with much success and we have continued basic materials research without much help from theory (Gamota 1981; Matthias 1976; Hein 1981). It has been suggested that the systematics of T_c in transition series elements can be characterized by an atomic-like parameter (Hopfield 1969; Bennemann *et al* 1972; Collver and Hammond 1973). In this paper we propose to show that pairing occurs due to the Darwin term in the relativistic Hamiltonian. The theory accounts for the success of the reduced BCS Hamiltonian and yields an expression for the dependence of T_c on atomic parameters which is in good quantitative agreement with experiment.

2. The pairing interaction

The reduced BCS Hamiltonian

$$H_{\text{red}} = \sum_{k} \varepsilon_k c_k^+ c_{-k} + \sum_{k,k'} V_{kk'} c_{k'}^+ c_{-k'}^+ c_{-k} c_k \tag{1}$$

contains only the two-body correlations and not the higher ones. Any term not included in H_{red} breaks the pair correlation. The reason for this has not been very clear (Cooper 1962; Blatt 1964) since the beginning of the BCS theory. We show below that this correlation originates due to the Darwin interaction.

It is known that mass-velocity and Darwin terms in the relativistic Hamiltonian h drastic effects on the energy band structure of solids (Johnson *et al* 1963). On accoun the $\mathbf{E}\cdot\mathbf{p}$ form of the Darwin term, it is possible that in a two-electron system, contribution from this repulsive term, under certain conditions, may become less du the dynamical correlation in momentum and thereby leads to Cooper pair formati

Consider a pair of electrons above a quiescent Fermi sphere with Darwin interacti We assume that the charged particle interactions within the metal are coulombic so electron–electron interaction is given by $e^2/|\mathbf{r}_i-\mathbf{r}_j|$ and the electron–ion interactio given by $Z_{\text{eff}}e^2/|\mathbf{r}_i-\mathbf{R}_j|$ where Z_{eff} is the effective ion valency seen by the electro

For a two electron system we take the product wave-function for a singlet spin st

$$\phi\,(\mathbf{k}_1;\mathbf{k}_2;\mathbf{x}_1,\mathbf{x}_2)=\frac{1}{\sqrt{2}}\,[\phi_{\mathbf{k}_1}(\mathbf{x}_1)\,\phi_{\mathbf{k}_2}(\mathbf{x}_2)+\phi_{\mathbf{k}_2}(\mathbf{x}_1)\phi_{\mathbf{k}_1}(\mathbf{x}_2)]$$

where $\phi_{k_i}(\mathbf{x}_j)$ $(i,j=1,2)$ are the one electron Bloch function for a perfectly peric lattice

$$\left\{-\frac{\hbar^2}{2m}\nabla^2+U(\mathbf{x})\right\}\phi_{\mathbf{k}}(\mathbf{x})=\varepsilon_{\mathbf{k}}\,\phi_{\mathbf{k}}(\mathbf{x})$$

The Darwin term in the relativistic Hamiltonian is (Bethe and Salpeter 1957)

$$H_D=-\frac{ie\hbar}{(2mc)^2}\,(\mathbf{E}_1\cdot\mathbf{p}_1+\mathbf{E}_2\cdot\mathbf{p}_2)$$

where $\mathbf{E}_1$ and $\mathbf{E}_2$ are the electric field intensity at the electron positions $\mathbf{x}_1$ and respectively.

We now use first-order perturbation theory to obtain the contribution of H_D to total energy. We assume that there is another state $\phi\,(\mathbf{k}'_1,\mathbf{k}'_2)$ which is degenerate v $\phi\,(\mathbf{k}_1,\mathbf{k}_2)$. For the singlet state it is sufficient to work with unsymmetrized prod wavefunction. Using the momentum representation, the Bloch function is,

$$\phi_{\mathbf{k}}(\mathbf{x})=\frac{1}{\sqrt{N\Omega}}\sum_{\mathbf{G}}f_{\mathbf{G}}(\mathbf{k})\exp\,(i(\mathbf{G}+\mathbf{k})\cdot\mathbf{x})$$

where $\mathbf{G}$ is the reciprocal lattice vector, $f_{\mathbf{G}}(\mathbf{k})$ are c-numbers, Ω is the volume of elementary cell and N is the number of cells in the crystal. The diagonal matrix elen of H_D is,

$$\begin{aligned}H_{11}&=\langle\phi\,(\mathbf{k}_1,\mathbf{k}_2)\,|H_D|\,\phi\,(\mathbf{k}_1,\mathbf{k}_2)\rangle\\&=-\frac{1}{2}\frac{ie\hbar}{(2mc)^2}\,\langle\phi\,(\mathbf{k}_1,\mathbf{k}_2)|\,[\sum_{i=1,2}\mathbf{E}\,(\mathbf{x}_i)\cdot\mathbf{p}_i-\mathbf{p}_i\cdot\mathbf{E}\,(\mathbf{x}_i)]\\&\qquad+\mathbf{E}\,(\mathbf{x}_1-\mathbf{x}_2)\cdot(\mathbf{p}_1-\mathbf{p}_2)-(\mathbf{p}_1-\mathbf{p}_2)\cdot\mathbf{E}\,(\mathbf{x}_1-\mathbf{x}_2)|\phi\,(\mathbf{k}_1,\mathbf{k}_2)\rangle.\end{aligned}$$

In (6) use has been made of the relation

$$\langle\mathbf{E}_1\cdot\mathbf{p}_1+\mathbf{E}_2\cdot\mathbf{p}_2\rangle=-\langle\mathbf{p}_1\cdot\mathbf{E}_1+\mathbf{p}_2\cdot\mathbf{E}_2\rangle,$$

which is valid as long as $\mathbf{E}_1$ $(\mathbf{E}_2)$ is the special function–grad$_1$ V ($-$grad$_2$ V) where the sum of all potentials at 1 (2).

Using Bloch function (5) we obtain,

$$\langle\phi\,(\mathbf{k}_1,\mathbf{k}_2)|\sum_{i=1,2}\mathbf{E}\,(\mathbf{x}_i)\cdot\mathbf{p}_i-\mathbf{p}_i\cdot\mathbf{E}\,(\mathbf{x}_i)|\phi\,(\mathbf{k}_1,\mathbf{k}_2)\rangle$$

$$= \frac{Z_{\text{eff}}}{N\Omega} e\hbar \sum_{\mathbf{G}_1,\mathbf{G}_2,\mathbf{G}_3,\mathbf{G}_4} f^*_{\mathbf{G}_1}(\mathbf{k}_1) f^*_{\mathbf{G}_2}(\mathbf{k}_2) f_{\mathbf{G}_3}(\mathbf{k}_1) f_{\mathbf{G}_4}(\mathbf{k}_2)$$

$$\left\{\delta(\mathbf{G}_2, \mathbf{G}_4) \int d^3\mathbf{x}_1 \exp(i(\mathbf{G}_3 - \mathbf{G}_1)\cdot\mathbf{x}_1) \frac{\mathbf{x}_1\cdot(\mathbf{G}_3 - \mathbf{G}_1)}{|\mathbf{x}_1|^3}\right.$$

$$\left. + \delta(\mathbf{G}_1, \mathbf{G}_3) \int d^3\mathbf{x}_2 \exp(i(\mathbf{G}_4 - \mathbf{G}_2)\cdot\mathbf{x}_2) \frac{\mathbf{x}_2\cdot(\mathbf{G}_4 - \mathbf{G}_2)}{|\mathbf{x}_2|^3}\right\}$$

$$= \frac{4\pi i}{N\Omega} Z_{\text{eff}} e\hbar \sum_{\mathbf{G}_1,\mathbf{G}_2,\mathbf{G}_3,\mathbf{G}_4} f^*_{\mathbf{G}_1}(\mathbf{k}_1) f^*_{\mathbf{G}_2}(\mathbf{k}_2) f_{\mathbf{G}_3}(\mathbf{k}_1) f_{\mathbf{G}_4}(\mathbf{k}_2)$$

$$\{\delta(\mathbf{G}_2, \mathbf{G}_4) + \delta(\mathbf{G}_1, \mathbf{G}_3)\}. \tag{7}$$

We obtain the contribution from the Coulomb repulsion term in (6) by changing to entre-of-mass and relative-motion coordinates

$$\phi(\mathbf{k}_1, \mathbf{k}_2) = \frac{1}{N\Omega} \sum_{\mathbf{G}_1,\mathbf{G}_2} f_{\mathbf{G}_1}(\mathbf{k}_1) f_{\mathbf{G}_2}(\mathbf{k}_2) \exp(i\,\mathbf{k}\cdot\mathbf{X}) \exp(i\,\mathbf{k}\cdot\mathbf{x}), \tag{8}$$

here $\mathbf{X} = \frac{1}{2}(\mathbf{x}_1 + \mathbf{x}_2)$; $\mathbf{x} = \mathbf{x}_1 - \mathbf{x}_2$

$$\mathbf{K} = \mathbf{k}_1 + \mathbf{k}_2 + \mathbf{G}_1 + \mathbf{G}_2; \qquad \mathbf{k} = \tfrac{1}{2}(\mathbf{G}_1 + \mathbf{k}_1 - \mathbf{G}_2 - \mathbf{k}_2). \tag{8a}$$

sing (8) we obtain,

$$\langle \phi(\mathbf{k}_1, \mathbf{k}_2) | \mathbf{E}(\mathbf{x})\cdot\mathbf{p} - \mathbf{p}\cdot\mathbf{E}(\mathbf{x}) | \phi(\mathbf{k}_1, \mathbf{k}_2)\rangle$$

$$= -\frac{2e\hbar}{N^2\Omega^2} \sum_{\mathbf{G}_1,\mathbf{G}_2,\mathbf{G}_3,\mathbf{G}_4} f^*_{\mathbf{G}_1}(\mathbf{k}_1) f^*_{\mathbf{G}_2}(\mathbf{k}_2) f_{\mathbf{G}_3}(\mathbf{k}_1) f_{\mathbf{G}_4}(\mathbf{k}_2)$$

$$\int d^3\mathbf{X} \exp(i(\mathbf{K} - \mathbf{K}')\cdot\mathbf{X}) \int d^3\mathbf{x} \exp(i(\mathbf{k} - \mathbf{k}')\cdot\mathbf{x}) \frac{\mathbf{x}\cdot(\mathbf{k} - \mathbf{k}')}{|\mathbf{x}|^3}$$

$$= -\frac{2}{N\Omega}(4\pi i) e\hbar \sum_{\mathbf{G}_1,\mathbf{G}_2,\mathbf{G}_3,\mathbf{G}_4} f^*_{\mathbf{G}_1}(\mathbf{k}_1) f^*_{\mathbf{G}_2}(\mathbf{k}_2) f_{\mathbf{G}_3}(\mathbf{k}_1) f_{\mathbf{G}_4}(\mathbf{k}_2) \delta(\mathbf{K}, \mathbf{K}') \tag{9}$$

here $\mathbf{K} = \mathbf{k}_1 + \mathbf{k}_2 + \mathbf{G}_3 + \mathbf{G}_4$ $\quad \mathbf{K}' = \mathbf{k}_1 + \mathbf{k}_2 + \mathbf{G}_1 + \mathbf{G}_2$.

rom (6), (7) and (8)

$$H_{11} = \frac{\pi}{2N\Omega}\left(\frac{e\hbar}{mc}\right)^2 \left[\sum_{\mathbf{G}_1,\mathbf{G}_2,\mathbf{G}_3,\mathbf{G}_4} f^*_{\mathbf{G}_1}(\mathbf{k}_1) f^*_{\mathbf{G}_2}(\mathbf{k}_2) f_{\mathbf{G}_3}(\mathbf{k}_1) f_{\mathbf{G}_4}(\mathbf{k}_2)\right.$$

$$\{Z_{\text{eff}}\,\delta(\mathbf{G}_2, \mathbf{G}_4) + Z_{\text{eff}}\,\delta(\mathbf{G}_1, \mathbf{G}_3) - 2\delta(\mathbf{G}_1 + \mathbf{G}_2, \mathbf{G}_3 + \mathbf{G}_4)\}. \tag{10}$$

Due to the normalisation of $\phi_{\mathbf{k}_2}(\mathbf{x}_2)$, the summation over $\mathbf{G}_2$, $\mathbf{G}_4$ in the first term ields 1. The other summation over $\mathbf{G}_1$ and $\mathbf{G}_3$ gives the expectation value of the Dirac elta function $\langle\delta^3(\mathbf{x}_1)\rangle$. Similarly, the second term leads to $\langle\delta^3(\mathbf{x}_2)\rangle$ and the electron-lectron term gives $\langle\delta^3(\mathbf{x}_1 - \mathbf{x}_2)\rangle$. So finally we obtain,

$$H_{11} = \pi\left(\frac{e\hbar}{mc}\right)^2 \{Z_{\text{eff}}\langle\delta^3(\mathbf{x}_1)\rangle - \langle\delta^3(\mathbf{x}_1 - \mathbf{x}_2)\rangle\}, \tag{11}$$

here the expectation value of the Dirac delta function is taken to be the same for the ates $\mathbf{k}_1$ and $\mathbf{k}_2$. In that case $H_{11} = H_{22}$.

Table 1. Atomic parameters related to T_c

Effective principal quantum number (Slater orbital)

$n \rightarrow$	1	2	3	4	5	6	7
$n_{\text{eff}} \rightarrow$	1	2	3	3·7	4·0	4·2	4·4

Element	n	Z_0	Z_0^*	r_s	Metallic $Z_{\text{eff}} = a(r_s - b)$	Atomic Z_{eff} (Slater
Class 1						
Al	3	3	3	2·06	1·55	2·30
Zn	4	2	2	2·30	2·15	1·70
Ga	4	3	3	2·18	1·86	2·30
Cd	5	2	2	2·59	2·70	1·70
In	5	3	2·5	2·52	2·56	2·30
Sn	5	4	2·5	2·55	2·62	2·95
La	6	3	3	2·70	2·92	1·70
Hg	6	2	2	2·66	2·85	1·70
Tl	6	3	3	2·48	2·68	2·30
Pb	6	4	2	2·86	3·39	2·95
Ti	4	4	4	1·93	1·34	1·95
Zr	5	4	4	2·11	1·71	1·95
Hf	6	4	4	2·08	1·66	1·90
Th	7	4	4	2·36	2·25	1·95
U	7	3	3	2·23	2·35	1·80
Class 2						
V	4	5	2·5	2·03	2·81	2·10
Nb	5	5	3	2·13	3·09	1·60
Mo	5	6	4	1·85	1·83	1·75
Tc	5	7	3	2·12	3·23	2·40
Ru	5	6	4	1·77	1·43	2·05
Ta	6	5	3·5	2·03	2·81	2·10
W	6	6	6	1·62	0·64	2·25
Re	6	7	3·5	1·89	2·06	2·40
Os	6	6	3·0	1·89	2·06	3·55
Ir	6	6	4·0	1·79	1·65	2·70

n = Principal quantum number, n_{eff} = effective principal quantum number, Z_0 = va the element, Z_0^* = degree of ionization in the metallic state, Z_{eff} = effective nuclear cha by the electrons.

values suggested by others. For example, according to Pauling (1949) the a valency per atom in white tin is 2·5. Similarly Hume-Rothery *et al* (1962) reporte the atoms in In, Pb and Ti are incompletely ionized which supports our conclı

The constants a and b in (20) have been determined from the data on T_c. Aı shows that these constants are different for $Z_0 \leqslant 4$ and $Z_0 \geqslant 5$. Denoting the for Class 1 and the latter as Class 2, we have obtained the values of a and b which are g table 2.

Table 2. Values of a and b in eq. (20) for metals of classes 1 and 2.

Class	a	b
1	2·07	1·28
2	5·29	1·50

Table 3. T_c for elements

Element class 1	T_c (K) Calc.	T_c (K) Obs.	Element class 2	T_c (K) Calc.	T_c (K) Obs.
Al	1·21	1·20	V	5·94	5·30
Zn	1·88	0·88	Nb	9·36	9·50
Ga	1·14	1·10	Mo	0·88	0·92
Cd	4·06	0·53	Tc	8·78	8·82
In	3·26	3·4	Ru	0·32	0·49
Sn	3·58	3·72	Ta	4·06	4·48
La	4·83	4·90	W	0·01	0·01
Hg	4·32	4·15	Re	1·17	1·70
Tl	2·47	2·39	Os	1·17	0·66
Pb	7·42	7·19	Ir	0·37	0·11
Ti	0·31	0·39			
Zr	0·66	0·52			
Hf	0·50	0·09			
Th	1·41	1·37			
U	0·87	0·80			

3.2 T_c *for elements*

In table 1 parameters relating to T_c are given for elements in Class 1 and 2. The values of Z_{eff} obtained from (19) are compared with those obtained using slater rules for free atoms.

The values of T_c for elements are given in table 3. The experimental values are from Roberts (1964). These are in good agreement with theory except for Zn, Cd and Hf. The discrepancy in Zn and Cd may be due to the large departures in axial ratio c/a from the ideal value 1·633 for hcp structures (Zn: 1·86, Cd: 1·89). This makes the six in-plane *n–n* closer to the central atom compared to the six out of plane *n–n*. Thus the values of r_s are not properly assessed. In Hf again Z_{eff} may not be given by the simple relation (20). The theory gives satisfactory values for T_c of class 2 elements.

3.3 T_c *for alloys*

We find that (19) and (20) also hold for many binary systems. The following rules based on the law of averages are generally applicable to these systems.

(i) A binary alloy $A_x B_y$ behaves as class 1 or 2 depending on the weighted mean value of the valence electrons per atom,

$$\bar{Z}_0 = \frac{x Z_0(A) + y Z_0(B)}{x+y}, \tag{21}$$

where $Z_0(A)$ and $Z_0(B)$ denote the valency of atoms A and B respectively. For $\bar{Z}_0 < 4$, the alloy behaves as Class 1, while for $\bar{Z}_0 > 5$ it behaves as Class 2. For $4 \leqslant \bar{Z}_0 \leqslant 5$, the alloy may behave as either type depending on the nature of the constituent atoms.

(ii) The weighted mean $\bar{r}_s$ for a binary alloy is given by

$$\bar{r}_s = \frac{x r_A + y r_B}{x+y}, \tag{22}$$

Table 4. T_c for some binary compounds, A_xB_y

Compound A_xB_y	$\bar{Z}_0$	Class	Z_0^* A	Z_0^* B	n	$\bar{r}_s$	$T_c(K)$ Calc.	$T_c(K)$ Obs
Al MO_3	5·25	2	3	5	3	1·73	0·46	0·5
Al Zr_3	3·75	1	3	4	3	2·12	1·66	0·7
Ga MO_3	5·25	2	3	5	4	1·84	1·05	0·7
Ga Nb_3	4·50	2	3	3	4	2·15	13·27	12·5
In_2 Ag	2·4	1	3	2	5	2·41	2·30	2·30
In Pb	2·5	1	2·5	2	5	2·69	6·78	6·6
In Nb_3	4·5	2	3	3·5	5	2·13	11·07	9·2
Tl Au	3·0	1	3	2	6	2·44	2·12	1·9
Sn Ta_3	4·75	2	4	3·5	5	2·05	5·50	6·0
Pb_2 Pd	4·00	1	2	4	5	2·54	3·48	2·9
Sb V_3	5·00	1	3	3	4	2·10	0·80	0·8
Sb Ti_3	4·25	2	3	4	4	2·08	8·30	5·8
Bi_2 Pd	4·70	1	3	4	5	2·39	2·10	1·7
$Ti_{0\cdot8}V_{0\cdot2}$	4·20	2	4	2·5	4	1·93	0·30	0·3
$Ti_{0\cdot25}V_{0\cdot75}$	4·75	2	3·0	2·5	4	2·05	6·81	7·1
$V_{0\cdot99}Cr_{0\cdot01}$	5·0	2	3·0	3·0	4	1·95	3·06	4·8
$V_{0\cdot9}Cr_{0\cdot1}$	5·1	2	4·0	3·0	4	1·78	0·6	0·4
$Nb_{0\cdot4}Zr_{0\cdot6}$	4·2	2	3·0	4·0	5	2·12	8·83	8·8
$Nb_{0\cdot9}Zr_{0\cdot1}$	4·9	2	3·0	3·0	5	2·15	10·52	10·5

$\bar{Z}_0$ is the average valency obtained using (21) of the text, Z_0^* is the degree of ionization, n is the effective principal quantum number, $\bar{r}_s$ is the average value of r_s obtained using (22).

where r_A and r_B are the r_s values of pure metals A and B.

(iii) The degree of ionization, Z_0^* of the constituent atoms in the alloy may someti not be the same as in the metal and may vary between the formal valencies elements depending on the relative values of the electronegativity of constituents.

(iv) If the elements A and B in the alloy $A_x B_y$ belong to the same period, the effect principal quantum number is the same as for the constituents. When these do belong to the same period, for $x \gg y$ ($y \gg x$), n_{eff} is that for the atom A (B). In intermediate case, it is lower of the two values, $n_{\text{eff}}(A)$ and $n_{\text{eff}}(B)$.

A few examples of the calculated T_c for the alloys of sp-metals and transition me are given in table 4. In most cases the theory gives satisfactory results.

4. Criterion for superconductivity

The regularity in the T_c of the elements of the periodic table was first emphasized Matthias (1957). This is now found to hold also for compounds and alloys. Some of important regularities are

(i) Superconductivity is observed only in metals and is found in elements for wh $2 \leqslant Z_0 \leqslant 8$. The same generally holds for compounds also.

On our model superconductivity arises when the Fermi surface is cut by the Brillo zone boundaries. The electrons in the Cooper pair state ($k\uparrow$, $-k\downarrow$) move continuou through states on the constant energy surface until they reach a Bragg-reflection plane. At this point they get diffracted and the wavenumbers are changed by a reciprocal lattice vector $\mathbf{G}_0$; $\mathbf{k}' = \mathbf{k} + \mathbf{G}_0$, $-\mathbf{k}' = -\mathbf{k} - \mathbf{G}_0$. For the contribution to energy from the Darwin interaction to vanish the Bragg-reflections should occur frequently. This would require that Fermi surface should be cut by as many Brillouin Zone (BZ) boundaries as possible to increase T_c. This is the reason that metals and alloys with $Z \leqslant 2$ do not become superconductors. For $Z = 1$ the Fermi sphere lies well within the first BZ. For $Z = 2$ the sphere barely touches the BZ. These metals therefore do not superconduct.

(ii) The variation of T_c with e/a *i.e.* the number of valence electrons per atom is different for the nontransition and transition-elements. In the former it is a monotonic increase of T_c with e/a. In the latter these are maxima at $e/a = 3, 5$ and 7.

Since the number of electron pairs formed in the superconducting phase will increase with the number of electrons available at the Fermi surface, T_c should increase with increase in the density of state at the Fermi surface, N (0). This qualitatively explains the reason for high T_c for odd values of e/a in transition metals.

(iii) Certain regularities are connected to crystal structure. A-15 and Cheveral phase compounds [Hein 1981] show high T_c. This is due to the complex shape of the Brillouin Zone boundaries in these structures which increases the number of intersections with the Fermi Surface. There are also no superconductors which do not possess a centre of inversion. This follows since the two electrons in the Cooper pair state are needed to be scattered by $\mathbf{G}_0$ and $-\mathbf{G}_0$ reciprocal lattice vectors.

5. Conclusion

We have outlined a new physical situation under which the BCS reduced Hamiltonian is shown to be applicable for the superconducting systems. The critical temperature derived from the model agrees well for metals and alloys.

References

Bardeen J, Cooper L N and Schrieffer J R 1957 *Phys. Rev.* **108** 1175

Bennemann K H and Garland J W 1972 in *Superconductivity in d- and f- band metals* (ed.) D H Douglass (New York: Am. Inst. Phys.) pp. 103

Bethe H A and Salpeter E E 1957 in *Handbuch der Physik* (Berlin: Springer-Verlag) Vol. 35/1, p. 88

Blatt J M 1964 *Theory of superconductivity* (New York: Academic Press) pp. 181

Collver M M and Hammond R H 1973 *Phys. Rev. Lett.* **30** 92

Cooper L N 1962 *Phys. Rev. Lett.* **8** 367

Gamota G 1981 *IEEE Trans. Mag.* **MAG-17** 19

Hein R A 1981 *IEEE Trans. Mag.* **MAG-17** p. 607

Hopfield J 1969 *Phys. Rev.* **186** 443

Hume-Rothery W and Rayner G V 1962 *The structure of metals and alloys* (London: Institution of Metals) p. 55

Johnson L E, Conklin J B and Pratt G W Jr 1963 *Phys. Rev. Lett.* **11** 538

Matthias B T 1976 in *Superconductivity in d- and f- band metals* (ed.) D H Douglass (New York: Plenum) p. 635

Pauling L 1949 *Proc. R. Soc.* (*London*) **A196** 343

Roberts B W 1964 in *Progress in cryogenics* (ed.) K Mendelssohn (London: Heywood) Vol. 4, p. 159.

Bull. Mater. Sci., Vol. 6, No. 2, May 1984, pp. 283–316. © Printed in India.

Structure and superconductivity in ternary systems of compounds

G V SUBBA RAO* and GEETHA BALAKRISHNAN

Materials Science Research Centre, Indian Institute of Technology, Madras 600 036, India

*Present Address: Alexander von Humboldt Fellow (1983–84), Anorg-Chem. Institute, Westfälische Wilhelms University, 4400 Münster, West Germany

Abstract. A survey of the known high T_c ternary systems of compounds is presented. Special emphasis has been placed on the part played by the crystal structure and bonding in the exhibition of high T_c superconductivity. The superconducting and other physical properties of the ternary borides have been discussed in relatively more detail. Finally, the available guidelines from crystal and solid state chemistry points of view, have been reiterated for a search for new high T_c materials.

Keywords. Ternary systems; superconducting compounds; metal excess systems.

1. Introduction

A ternary compound is one which contains three elements each occupying a distinct set or sets of crystallographic lattice sites and preferably one element should be a non-metal. This crystallographic definition clearly distinguishes ternary compounds from binary or pseudo-binary phases in which only two sets of lattice sites are occupied or which contain only two species of elements. Metal excess ternary system of compounds (METS) are those in which only part of the valence electrons are involved in bonding (say, with the non metal) and the excess valence electrons of the metal(s) will partially fill the conduction band formed by the overlap of the requisite metal *s*, *p* and *d* orbitals (Hulliger 1981; Simon 1981; Corbett 1981). Thus, METS compounds invariably exhibit high electronic conductivity and metallic behaviour. Theoretical considerations reveal that superconductivity in a metallic material can occur whenever there is a large density of electronic states at the Fermi level in a partially filled conduction band (preferably a narrow band) and a favourable electron-phonon interaction. Hence METS, in principle, satisfy the requirements for the exhibition of superconductivity.

Superconductivity, the phenomenon of vanishing electrical resistance in a material below a critical temperature ($T_c > 0$ K), is not uncommon and many elements, alloys intermetallics, binary and ternary chemical compounds exhibit the behaviour. However, of the more than 1000 superconductors known, only a very limited number possess $T_c > 10$ K and the latter are called high temperature superconductors. It is now established that certain particular crystal structure of a binary or ternary (intermetallic or chemical) compound is very conducive to give rise to high T_c superconductivity. The beta-tungsten (A_3B or A15) structure adopted by a large number of intermetallics is the well-known example. The phases Nb_3Al and Nb_3Au have a T_c of 18 and 11 K respectively when crystallized in A15 structure but when prepared in a *bcc* form (with the same composition) they exhibit a T_c of 4 and 1 K. The binary metallic carbides

Table 1. Structure and T_c of high temperature ternary superconductors

Compound	Structure type	Lattice parameter (A)	T_c (K)	Reference
$LuRh_4B_4$	$CeCo_4B_4$ (tetra)	$a = 5{\cdot}3$; $c = 7{\cdot}4$	11·7	Vendenberg and Matthias (1977)
$Y(Rh_{0.85}Ru_{0.15})_4B_4$	$LuRh_4B_4$ (tetra)	$a = 7{\cdot}5$; $c = 14{\cdot}9$	9·6	Johnston (1977)
$LuRuB_2$	$LuRuB_2$ (ortho)	$a = 5{\cdot}8$; $b = 5{\cdot}2$; $c = 6{\cdot}3$	10·0	Ku and Shelton (1980)
Mo_3Al_2C	Beta Mn (cubic)	$a = 6{\cdot}9$	10·0	Johnston *et al* (1964)
Mo_2BC	Mo_2BC (ortho)	$a = c = 3{\cdot}1$; $b = 17{\cdot}4$	7·0	Toth (1967)
$Sc_5Rh_4Si_{10}$	$Sc_5Co_4Si_{10}$ (tetra)	$a = 12{\cdot}3$; $c = 4{\cdot}0$	8·5	Braun and Segre (1980)
$Y_5Os_4Ge_{10}$	$Sc_5Co_4Si_{10}$ (tetra)	$a = 13{\cdot}0$; $c = 4{\cdot}3$	8·7	Braun and Segre (1980)
$YbRh_{1.4}Sn_{4.6}$	$Pr_3Rh_4Sn_{13}$	$a = 9{\cdot}7$	8·6	Remeika *et al* (1980)
ZrRuP	Fe_2P (hexa)	$a = 6{\cdot}4$; $c = 3{\cdot}8$	13·0	Barz *et al* (1980); Müller *et al* (1983)
NbPS	NbPS (ortho)	$a = 3{\cdot}4$; $b = 11{\cdot}9$; $c = 4{\cdot}7$	12·5	Donohue and Bierstedt (1969)
$LaRu_4P_{12}$	$LaFe_4P_{12}$ (cubic)	$a = 8{\cdot}1$	7·2	Meisner (1981)
$LiTi_2O_4$	$MgAl_2O_4$ (spinel)	$a = 8{\cdot}4$	13·7	Johnston (1976)
$BaPb_{0.8}Bi_{0.2}O_3$	$CaTiO_3$ (dist. perov.)	$a \sim 5{\cdot}2$	13·2	Sleight *et al* (1975)
$Zr_{0.6}Rh_{0.3}O_{0.1}$	Fe_3W_3C (cubic)	$a = 12{\cdot}4$	11·8	Matthias *et al* (1963)
$Pb_{0.9}Mo_6S_{7.5}$	$PbMo_6S_8$ (rhombo-hexa)	$a = 9{\cdot}2$; $c = 11{\cdot}48$	15·2	Chevrel *et al* (1971); Matthias *et al* (1972)
$Cu_{1.8}Mo_6S_8$	$PbMo_6S_8$ (distorted)	$a = 9{\cdot}58$; $c = 10{\cdot}25$	10·8	Matthias *et al* (1972)
$Mo_6S_6I_2$	Mo_6Se_8	$a = 9{\cdot}64$; $c = 10{\cdot}44$	14·0	Sergent *et al* (1977); Perrin *et al* (1973).

crystallizing in NaCl or Pu_2C_3-structure types are the other examples. For the METS, the Chevrel phases (AMo_6S_8), rhodium borides ($LnRh_4B_4$-type), ordered Fe_2P-type phosphides constitute the relevant examples (table 1).

Since a large number of compounds are known or can be synthesized and also since chemical manipulation is more easily possible in them, the METS compounds do seem to offer a better scope for the realization of high T_c and high critical magnetic field (H_{c2}) materials. As a result of intense research activity during the past decade many ternary METS have been isolated and studied and a wealth of information and interesting physics have come out not only with respect to the superconducting behaviour but also the coexistence of magnetic order and superconductivity, reentrant behaviour, intermediate valence and mixed (electronic and ionic) conduction.

In the following we give a concise but upto date account of the known high T_c ($\gtrsim$ 10 K) compounds. Special emphasis will be placed on the part played by the crystal structure and bonding exhibited by them. We also give an account of some of the other known METS compounds that are yet to be tested for high T_c behaviour.

2. Ternary borides, AM_xB_y

2.1 *Compounds with AM_4B_4 stoichiometry*

METS borides of the formula AM_4B_4, A = rare earth (Ln), Y, Th have been synthesized by Kuz'ma *et al* (1972) with M = Co and by Vandenberg and Matthias (1977) with M = Rh. These compounds possess a primitive tetragonal ($CeCo_4B_4$-type) structure. Later studies have shown that AM_4B_4-type compounds with M = Os, Ir, Ru also exist with either primitive tetragonal ($NdCo_4B_4$-type), body centered tetragonal (*bct*, $LuRu_4B_4$-type) or orthorhombic ($LuRh_4B_4$-type) structure (Johnston 1977; Ku *et al* 1979; Kuz'ma *et al* 1979; Rogl 1979; Rogl 1980; Yvon and Johnston 1982). Compound formation with the composition AM_4B_4 has been reported with M = Fe and Re but the structure has not yet been elucidated (Johnston and Braun 1982). The rhodium and iridium borides with the $CeCo_4B_4$-type structure exhibit superconductivity while the isotypic cobalt borides have no transition above 1·5 K. The rhodium borides, especially those containing non-magnetic rare earth Lu and Y, exhibit high T_c (11·7 and 11·3 K respectively) (Matthias *et al* 1977; Johnston and Braun 1982). On the other hand, tetragonal compounds with the $NdCo_4B_4$-type structure (LnM_4B_4 with M = Co, Ru, Os and Ir are only known but not with M = Rh) do not exhibit T_c above 1 K. The *bct* borides ($LuRu_4B_4$-type) and orthorhombic phases ($LuRh_4B_4$-type) do exhibit superconductivity. However, depending on the rare earth, Y or Sc occupying the lattice site, the T_c varies only from 1·4–7·2 K. Extensive studies have been carried out on the ternary borides with the $CeCo_4B_4$- type structure by way of chemical substitution at the Ln and M sites and these help in establishing the systematics of superconductivity behaviour and structure-property correlations.

2.1a *Structure*: The four structure types exhibited by the AM_4B_4 compounds (*viz*., primitive tetragonal $CeCo_4B_4$ and $NdCo_4B_4$-types; *bct* $LuRu_4B_4$-type and orthorhombic $LuRh_4B_4$-type) can be described by an arrangement of transition metal tetrahedra, isolated A atoms (including the rare earths) and pairs of boron atoms. The $CeCo_4B_4$, $LuRu_4B_4$ and $LuRh_4B_4$ structure-types are inter-related and all of them contain more or less isolated M_4 tetrahedral clusters while in the $NdCo_4B_4$-type, the M_4-clusters are fused together by sharing edges such that infinite chains are formed along the crystallographic *c* direction.

In the ARh_4B_4 compounds with the $CeCo_4B_4$-structure, the A atoms and Rh_4-clusters (slightly elongated with two short and four long Rh-Rh distances along the tetragonal *a* and *c* axes respectively) occupy the positions of a slightly distorted NaCl lattice (figure 1a). Two orientations of Rh_4 tetrahedra occur and the Rh network can be viewed as forming sheets in the *a*-*b* plane (quasi two-dimensional extended clusters)

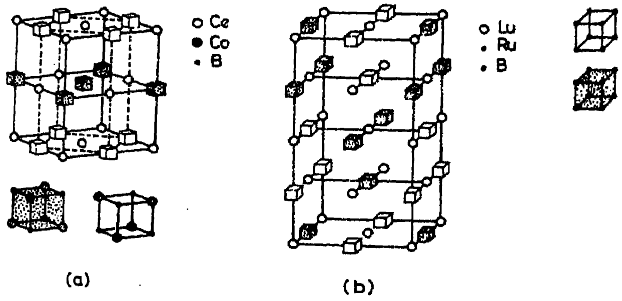

Figure 1. Idealized crystal structures of (**a**) primitive tetragonal $CeCo_4B_4$-type and (**b**) body-centred tetragonal $LuRu_4B_4$-type AM_4B_4 compounds. The dashed lines in (**a**) outline the unit cell. Two orientations of M_4 tetrahedra occur and for clarity, the M_4B_4 cubes are not drawn to scale. The lattice parameters are: $CeCo_4B_4$-type: $a \sim 5{\cdot}3$ Å; $c \sim 7{\cdot}4$ Å; $LuRu_4B_4$-type: $a \sim 7{\cdot}5$ Å; $c \sim 14{\cdot}9$ Å. Actual values will depend on the A and M element.

with an alternate arrangement (stacking) of tetrahedra of different orientations along the *c*-axis. The intra-cluster Rh-Rh distances (2·6–2·8 Å) are approximately the same as in rhodium metal (2·69 Å) but intercluster distances are larger (3·1 Å). The B-B distances are small (1·80–1.83 Å) indicating pair formation whereas the A-A distances are larger ($\gtrsim$ 5 Å) showing negligible interaction between them. However, significant bonding (charge transfer) exists between Rh and B atoms.

The *bct* ($LuRu_4B_4$-type) and orthorhombic ($LuRh_4B_4$-type) phases differ from the $CeCo_4B_4$-type in the relative disposition of the isolated M_4 clusters in the lattice; whereas the M_4 tetrahedra of the same orientation are joined into sheets perpendicular to the *c*-axis in the $CeCo_4B_4$-type, the M_4 tetrahedra of different orientations are distributed equally in each plane in an ordered fashion in the $LuRu_4B_4$- and $LuRh_4B_4$-types (figure 1b) (Johnston 1977; Yvon and Grüttner 1980; Yvon and Johnston 1982). Thus, the *bct* and orthorhombic structures can be viewed as containing two interpenetrating three-dimensional networks or extended clusters of M_4 tetrahedra. These extended clusters are qualitatively different from those in $CeCo_4B_4$-type AM_4B_4 compounds, since in the latter phases they are quasi two-dimensional and do not interpenetrate. However, the unit cell dimensions of the three structures bear simple relationships to each other: $\sqrt{2}\ a \approx c$($CeCo_4B_4$-type) $\approx a \approx (c/2)$ ($LuRu_4B_4$-type) $\approx a \approx (b/3) \approx c$($LuRh_4B_4$-type).

The $NdCo_4B_4$-type structure differs from the $CeCo_4B_4$-type in two ways, *viz*. the M_4 clusters are not isolated from each other but are fused together by sharing edges such that infinite chains are formed along the *c*-axis. Also, the A-A distances are small ($\sim$ 3·8–4 Å $\approx c$ lattice parameter) so that they can be considered to form infinite linear chains along the tetragonal axis (figure 2). On the other hand, the A atoms in the $CeCo_4B_4$ structure are well-separated from each other and form nearly *fcc* array in the primitive tetragonal structure. The differences between the $CeCo_4B_4$ and $NdCo_4B_4$ structure types from a topological view point is also brought out by the fact that the c/a ratio is $\sim$ 1·4 in the former while it is much smaller ($\sim$ 0·53) in the latter. As will be discussed later, these structural differences play a crucial role in the T_c behaviour of the compounds.

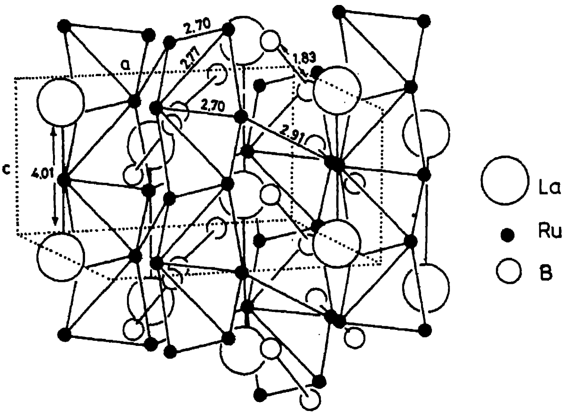

Figure 2. Structure of the tetragonal $LaRu_4B_4$ viewed approximately perpendicular to the tetragonal axis. The numbers indicate the Ru–Ru, La–La and B–B bond lengths. The compound is isostructural to $NdCo_4B_4$. The lattice parameters are a = 7·541 Å, b = 4·012 Å (taken from Grüttner and Yvon 1979).

2.1b *Formation and stability*: The formation and stability of the AM_4B_4 compounds with different types of structures are dependent on the relative ionic sizes of the A and M atoms, valence electron concentration and electronic factors. Thus, the proper phase with the $CeCo_4B_4$-type structure is formed only for the following combinations of elements: M = Co, A(Ln) = Ce, Gd → Tm, Lu; M = Rh, A = Nd, Sm, Gd → Tm, Lu, Y and Th; M = Ir, Ln = Ho, Er and Tm. The *bct* $LuRu_4B_4$-structure easily forms for M = Ru and A = Sc, Y, Th, U and Ln with the only exception when Ln = La. For M = Os, only UOs_4B_4 has been isolated., We note that the proper phase with the $LuRu_4B_4$-structure does not form for M = Co and Rh. However, the structure with M = Rh can be stabilized at the nominal AM_4B_4 stoichiometry by substitution with a few atom percent of Ru. Orthorhombic $LuRh_4B_4$-type compounds are known only for M = Rh and Ln = Ho → Lu. The $NdCo_4B_4$-type structure is adopted for the following combinations: M = Co, Ln = La, Nd, Sm, Eu; M = Ru, Ln = La; M = Os, Ln = La → Eu, Th; M = Ir, Ln = La → Dy, Y and Th. Pseudoternary isostructural solid solutions easily form for isoelectronic M elements (M = Ru and Os or Rh and Ir) but, interestingly enough, solid solutions are also found to form for the combinations $Os_{1-x}Ir_x$ and $Rh_{1-x}Ru_x$ with a given A element.

The L *vs* r^{3+} plots, L being the cube root of the volume associated with one formula unit of AM_4B_4 and r^{3+}, the effective ionic radius of the trivalent rare earth atoms (Grüttner and Yvon 1979) is shown in figure 3. As can be seen the Rh- and Ru-based alloys which crystallize with the $CeCo_4B_4$- and $LuRu_4B_4$-structure types respectively have practically the same atomic volume (L). Since Ru and Rh atoms are very similar in size, this demonstrates the close structural relationship between these two series of compounds. Similar is the case with the Os and Ir alloys which crystallize with the

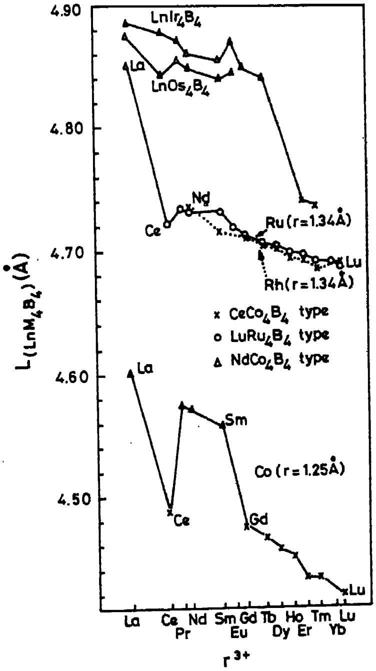

Figure 3. L versus r^{3+} diagram for the LnM_4B_4 compounds containing Co, Rh, Ru, Os and Ir. Full lines and dotted lines join compounds which contain the same transition element.

$NdCo_4B_4$-type structure. The formation of the $NdCo_4B_4$-structure for the Co, Ru, Os and Ir-based alloys, on the other hand, is associated with a rather strong and discontinuous volume expansion and occurs for large ionic radii (lighter) rare earths (figure 3). The switchover from the $NdCo_4B_4$-structure to the $CeCo_4B_4$-structure occurs in the Co- and Ir based alloys for only the smaller ionic radii (heavier) rare earths (Gd → Lu) indicating that geometric factors such as the radius ratio between the Ln and M atoms plays a major role in forming the proper phase. On the other hand, the formation and stability of the $CeCo_4B_4$- and $LuRu_4B_4$-type compounds depends more on the electronic factors, valency of the A atom and valence electron concentration (valence electron/atom ratio). Thus, the Rh-containing phases which normally crystallize with the $CeCo_4B_4$-structure adopt the $LuRu_4B_4$-structure if only 15 % of Rh is substituted by Ru indicating that the arrangement of M atom sublattice in these two structure types is critically dependent on the valence electrons of the M atoms (Rh: 9; Ru: 8 electrons). Perhaps, similar behaviour might be exhibited by the MIr_4B_4 phases ($CeCo_4B_4$–structure) doped with Os.

2.1c *Superconducting properties*: The $LnRh_4B_4$ compounds with the $CeCo_4B_4$-type structure have been studied extensively with respect to superconductivity and related physical properties. As mentioned earlier, the phases containing non-magnetic rare earths Lu and Y exhibit high T_c values (table 2). For Ln = Nd, Sm, Er and Tm which can support a magnetic moment due to the 4*f*-electrons, superconductivity is retained but with a lower T_c (2·7–9·8 K). However, for Ln = Gd, Tb, Dy and Ho, superconductivity is destroyed and the compounds order ferromagnetically with Curie temperatures ranging from 5–12 K (figure 4). The pure compound $ErRh_4B_4$ exhibits a reentrant (metallic) behaviour in the sense, on cooling to 0·9 K (T_c = 8·7 K), the superconductivity is destroyed and the compound becomes a metal; almost simultaneously a ferromagnetic order develops and is retained up to the lowest attainable temperatures.

Solid solutions of the type $(Ln_{1-x}Ln'_x)\,Rh_4B_4$ and $Ln(Rh_{1-x}M_x)_4B_4$ (M = Ir and Ru) have been examined in detail in the literature and provide a wealth of information on the interplay between superconductivity and magnetism in these materials. For the former type, an approximately linear variation of T_c is noticed with x (up to x_c, see figure 5) irrespective of the fact whether Ln and Ln′ carry local magnetic moments or not, provided the end members ($x = 0$ and 1) form the proper phase with the $CeCo_4B_4$-type structure. This behaviour indicates that the rare earth ion-conduction electron exchange interaction is weak in these materials.

Table 2. T_c data on some representative AM_4B_4 compounds[a]

$CeCo_4B_4$-type		bct-$LuRu_4B_4$-type[b]		Ortho $LuRh_4B_4$-type	
Phase	T_c (K)	Phase	T_c (K)	Phase	T_c (K)
$LuRh_4B_4$	11·7	$Lu(Rh_{0.85}Ru_{0.15})_4B_4$	9·0	$LuRh_4B_4$	6·2
YRh_4B_4	11·3	$Y(Rh_{0.85}Ru_{0.15})_4B_4$	9·4	—	—
$ErRh_4B_4$	8·7	$Er(Rh_{0.85}Ru_{0.15})_4B_4$	7·9	$ErRh_4B_4$	4·3
$TmRh_4B_4$	9·8	$Tm(Rh_{0.85}Ru_{0.15})_4B_4$	8·3	$TmRh_4B_4$	5·4

[a] Taken from Johnston and Braun (1982). Phases with the $NdCo_4B_4$-type structure do not exhibit superconductivity above 1 K.

[b] $LuRu_4B_4$ and YRu_4B_4 have a T_c of 2 and 1·4 K respectively.

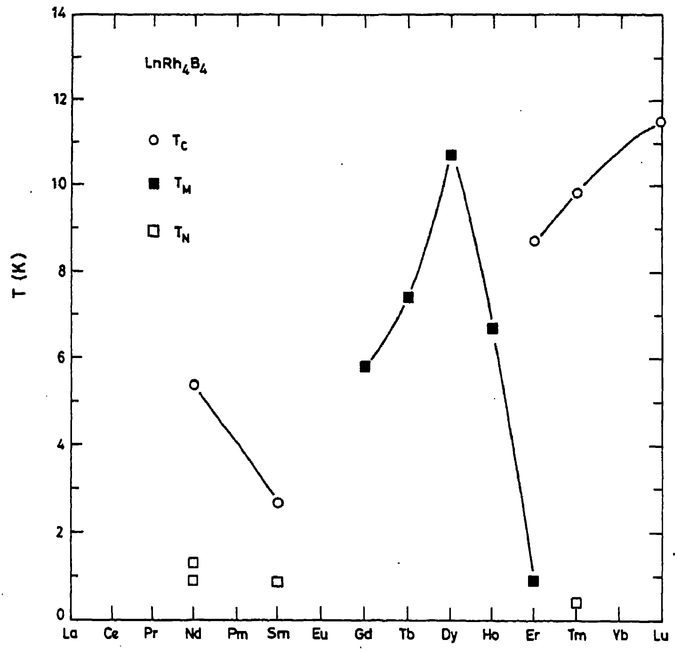

Figure 4. Superconducting (T_c) ferromagnetic (T_M) and antiferromagnetic (T_N) transition temperatures of $LnRh_4B_4$ compounds with the $CeCo_4B_4$-structure. Phases with Ln = Nd, Sm and Tm exhibit antiferromagnetic order coexisting with superconductivity below T_N while $ErRh_4B_4$ orders ferromagnetically below T_M with the destruction of superconductivity (re-entrant behaviour). Phases with Ln = Gd, Tb, Dy and Ho exhibit ferromagnetic order below T_M and do not exhibit superconductivity. Studies on the effect of pressure on T_c and/or T_M indicate positive coefficient of $dT_c(M)/dP$ ($\sim 1-2 \times 10^{-5}$ K/bar) except for Ln = Nd, Sm and Th where it is $\sim -0{\cdot}5 \times 10^{-5}$ K/bar (Maple *et al* 1982; Shelton and Johnston 1978; Shelton *et al* 1980b).

Studies on the $Ln(Rh_{1-x}Ir_x)_4B_4$, Ln = Lu, Dy, Ho and Er solid solutions with the $CeCo_4B_4$-type structure have shown that: (i) superconductivity is induced for $x \geqslant 0{\cdot}2$ for Ln = Tb, Dy and Ho whereas the pure $x = 0$ phases exhibit only ferromagnetism (figure 6), (ii) the superconducting transition temperature drops precipitously with increasing x at $x = 0{\cdot}5$–$0{\cdot}6$ and goes through a minimum for $x = 0{\cdot}8$ for Ln = Dy, Ho, Er and also for non-magnetic Lu (see figure 6). This observation shows that electronic band structure is getting affected and the nature of rare earth ion (both magnetic and non-magnetic) has little effect on the non-linear T_c behaviour. Pseudoternary solid solutions of the non-isoelectronic type, $Ln(Rh_{1-x}Ru_x)_4B_4$-type also exhibit interesting behaviour in the sense that superconductivity is induced for $x \geqslant 0{\cdot}15$ for Ln = Pr, Eu, Dy, Ho, Er and Tm whereas only long range magnetic ordering occurs for the isostructural *bct* $LnRu_4B_4$ with Ln = Nd, Gd, Tb, Dy, Ho and Er. Also, T_c is enhanced for $x = 0{\cdot}15$ with Ln = Lu and Y compared to the $x = 0$ phases (see table 2). Non-linear variation of T_c with x has been found in $Ln(Rh_{1-x}Ru_x)_4B_4$, Ln = Y, Er and Dy at around $x = 0{\cdot}5$–$0{\cdot}6$, a behaviour similar to that encountered in the $Ln(Rh_{1-x}Ir_x)_4B_4$ series of compounds. This indicates that non-magnetic effects like crystallographic order in the M atom array are playing a role in determining the T_c in these pseudoternaries.

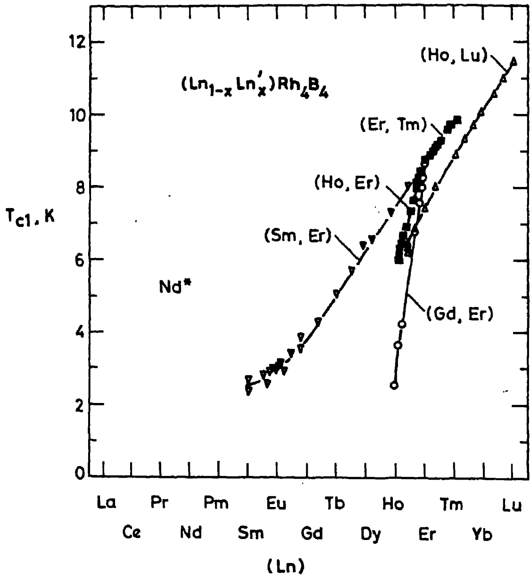

Figure 5. T_c *vs* atomic number (or average atomic number) curves for ternary and pseudoternary $(Ln_{1-x}Ln'_x)Rh_4B_4$ phases with the $CeCo_4B_4$-structure (taken from Johnston and Braun 1982). The approximately linear variation of T_c with composition (for $x < x_c$) irrespective of whether Ln or Ln′ carries a magnetic moment or not indicates that the conduction electron-localised spin interaction is small (x_c refers to the critical concentration at which T_{c1}, T_{c2} and T_M coincide).

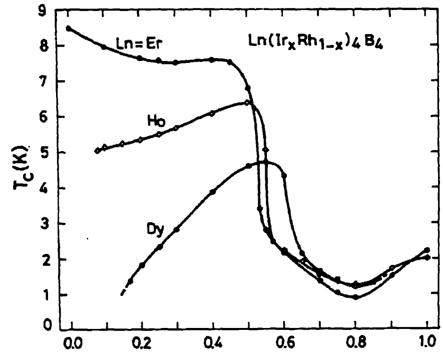

Figure 6. Variation of superconducting transition temperature (T_c) with composition in the $CeCo_4B_4$-type system $Ln(Rh_{1-x}Ir_x)_4B_4$ (after Ku and Acker 1980). As can be seen T_c drops precipitously at $x \sim 0{\cdot}5$–$0{\cdot}6$ and T_c goes through a minimum at around $x = 0{\cdot}8$.

The interesting and unusual properties of the $LnRh_4B_4$ compounds with the $CeCo_4B_4$-type structure can be explained on the basis of the crystal structure: (i) the isolated Rh_4 tetrahedral clusters with strong intra and significant intercluster interactions lead to the formation of partially filled conduction bands with a large density of states at the Fermi level (E_F). Hence the Rh 4*d*-electrons are exclusively responsible for superconductivity and participate in the Cooper pair formation. This has been confirmed by magnetic susceptibility (χ) and other studies (Maple *et al* 1982) and band structure calculations (Freeman and Jarlborg 1982). As shown by the data in figure 5, the Ln ions have only small but non trivial effect on T_c, (ii) the rare earth ions exist in 3+ oxidation state in the lattice and effect a charge transfer (donation of 3 electrons) to the Rh 4*d*-conduction band. This has been confirmed by $\chi - T$ (Maple *et al* 1982) Mössbauer (Shenoy *et al* 1980) and neutron diffraction (Moncton *et al* 1977). Because the Ln–Ln separation is large, there is negligible interaction between them and any magnetic ordering due to Ln-ions (which support a magnetic moment) occurs only at low temperatures ($\leqslant 12$ K) and (iii) the boron atoms which exist as pairs play the role of anion and stabilize the structure.

The fact that a composition-induced redistribution of the electronic density of states at the E_F may induce superconductivity and also bring drastic variation in T_c *vs* x is shown by the solid solutions $Ln(Rh_{1-x}Ir_x)_4B_4$ ($CeCo_4B_4$-type; isoelectronic) and $Ln(Rh_{1-x}Ru_x)_4B_4$; ($LuRu_4B_4$–type; non-isoelectronic) where the integrity of the rare earth sublattice is undisturbed. The nonlinear variation of T_c with composition and the precipitous decrease of it at $x \sim 0{\cdot}5$–$0{\cdot}6$ in both the above solid solution series have been correlated with the crystallographic c/a parameter. For example, in $Ln(Rh_{1-x}Ir_x)_4B_4$' Ln = Er and Dy, Ku *et al* (1979) and Ku and Acker (1980) found that c/a ratio which is constant for $x < 0{\cdot}50$, begins to decrease for $x = 0{\cdot}5$–$0{\cdot}6$. Hence they suggested that for $x \leqslant 0{\cdot}5$, at least one pure Rh_4 cluster per unit cell could exist whereas for $x > 0{\cdot}5$, a random distribution of Rh and Ir atoms in the M_4 cluster may exist to give rise to an abrupt decrease in T_c. Similarly, studies on $Lu(Rh_{1-x}Ru_x)_4B_4$ system have shown that at $x = 0{\cdot}5$–$0{\cdot}6$, a change in the c/a ratio (from < 2 to > 2) and anomalous changes in the interatomic B–B and M–M (intracluster) distances are observed (Yvon and Grüttner 1980; Johnston 1982).

The AM_4B_4 phases with the *bct* $LuRu_4B_4$- or orthorhombic $LuRh_4B_4$-type structure exhibit a lower T_c compared to those possessing the $CeCo_4B_4$-type structure. This is due to the differences in the mode of arrangement of the (M_4B_4) tetrahedra of different orientations in the *a*–*b* plane as well as the stacking of them along the *c*-axis. This can give rise to changes in the density of states at the Fermi level and/or electron-phonon interaction leading to a lower T_c in the *bct* and orthorhombic types. However, since isolated clusters exist in all the three structure types, the phases exhibit superconductivity. On the other hand, the $NdCo_4B_4$-type structure is unfavourable to the occurrence of superconductivity since it does not contain isolated (M_4B_4) clusters and also, perhaps, because of the small A–A separation.

2.1d *Magnetic and non-magnetic contribution to the variation of* T_c: It is important to separate the magnetic from non-magnetic contributions to the variation of T_c in analysing the data for a series of compounds containing rare earth elements. The magnetic contribution is usually analysed in terms of the Abrikosov-Gorkov (AG) theory according to which the exchange interaction between the conduction electrons with spin s and local magnetic moment with spin S ($H = -2IS \cdot s$) results in a reduction of T_c below the value $T_{c(0)}$ it would have had in the absence of exchange scattering, given by $(T_c/T_{c(0)}) = U(\alpha/\alpha_{cr})$ where U is a universal function of (α/α_{cr}) (Maple 1976). The (Cooper) pair breaking parameter α is given by $\alpha = (nN(E_F)I^2/\hbar)$ (dGF) where the deGennes factor (dGF) $= (g-1)^2\,J(J+1)$, g and J being, respectively, the Lande's g factor and total angular momentum of the Ln^{3+} ion Hund's rule ground state. The n represents the concentration of magnetic ions, $N(E_F)$ is the density of states at the Fermi level (E_F) for each spin direction, I is the exchange interaction parameter. α_{cr} is the value of α at which T_c becomes zero. If n, I, $N(E_F)$ and $T_{c(0)}$ are the same for a given isostructural series of phases, then a plot of T_c *vs* (dGF) should scale with the universal

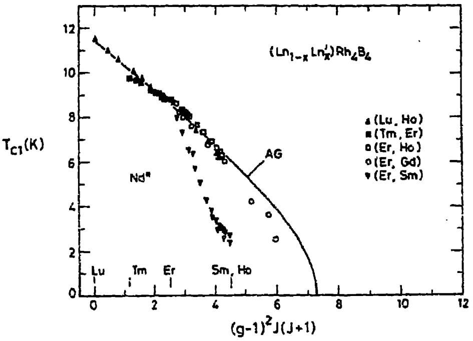

Figure 7. Superconducting transition temperature T_c *vs* deGennes factor for pseudo-ternary solid solutions: $(Ln'_xLn_{1-x})Rh_4B_4$. The solid curve AG is a fit to the data using the Abrikosov–Gorkov theory with the following parameters $T_{c(0)} = 11{\cdot}4$ K; $(dT_c/d(\text{dGF})) = -1{\cdot}09$ K; $nI^2N(E_F) = 2{\cdot}04 \times 10^{-5}$ eV. The large parameters indicate an appreciably larger $N(E_F)$ and/or I^2 for heavy rare earth members of the $CeCo_4B_4$ structure type. Significant negative deviation from AG curve exists for Ln = Pr–Gd (pure or alloys) (see text). (taken from Johnston and Braun 1982).

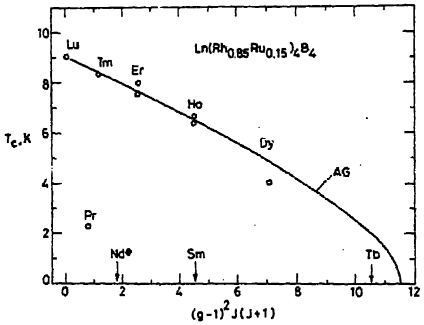

Figure 8. Superconducting transition temperature T_c *vs* deGennes factor for the $LnRu_4B_4$-type compounds: $(Rh_{0.85}Ru_{0.15})_4B_4$. The solid curve AG is a fit to the data using the Abrikosov–Gorkov theory with the following parameters: $T_{c(0)} = 9{\cdot}05$ K; $(dT_c/d(\text{dGF}) = -0{\cdot}54$ K; $nI^2N(E_F) = 0{\cdot}94 \times 10^{-5}$ eV. The parameters are only half of those of figure 7. (Johnston and Braun 1982).

curve. In figures 7 and 8 are shown the available data on $(Ln_{1-x}Ln'_x)Rh_4B_4$ phases with the $CeCo_4B_4$-type structure and $Ln(Rh_{0{\cdot}85}Ru_{0{\cdot}15})_4B_4$ compounds with the *bct*-$LuRu_4B_4$ structure. As can be seen, a good fit of the AG theory to the data is obtained for Ln = Ho → Lu (for dGF < 5) in both the series of compounds and suggests that $T_{c(0)}$ and $I^2N(E_F)$ are independent of Ln for these compounds. However, significant negative deviations occur for the lighter rare earths (dGF $\geqslant$ 5) and the discrepancy (between theoretical and experimental curves) increases as the average size of the Ln increases past that of Ho. The discrepancy could be due to (i) breakdown of AG theory for dGF $\geqslant$ 5; (ii) increase of I^2 and/or $N(E_F)$ with increasing ionic radius and/or the splitting of the Ln-ion energy levels by the crystalline electric field (CEF) which is generally larger for the lighter Ln's; (iii) non-magnetic effects, *i.e.* due to the inherent decrease in the value of $T_{c(0)}$. Experimental and theoretical studies on $SmRh_4B_4$, $(La_xLu_{1-x})Rh_4B_4$ ($x = 0{\cdot}01$–$0{\cdot}6$, $CeCo_4B_4$–type) and $(La_{1-x}Lu_x)$ $(Rh_{0{\cdot}85}Ru_{0{\cdot}15})_4B_4$ ($LuRu_4B_4$-type) indicate that the negative deviations of the data from AG theory in figures 7 and 8 arise largely due to a decrease in $T_{c(0)}$ (Hamaker *et al* 1979; Mackay *et al* 1980; Kumagai *et al* 1981; Johnston 1981). However, factors mentioned in (ii) above may also be responsible to a small extent.

2.1e *Coexistence of antiferromagnetism and superconductivity*: Ternary rhodium borides, $\mathrm{LnRh_4B_4}$, are the ideal systems to study the interplay between magnetic order and superconductivity in materials for the following reasons: (i) The Ln ions are distributed uniformly throughout the crystal lattice (*i.e.*, form part of the network structure) but situated far off from the conduction electron system (Rh-4*d* conduction band) so that there is negligible exchange interaction between the localized electron spins and the electrons responsible for superconductivity. (ii) Rare earth concentration is large ($\sim$ 11 atom %) and in cases where the ions can support a large magnetic moment, magnetic ordering can be expected at low temperatures by interatomic exchange or superexchange interaction. If the rare earth spins are to order antiferromagnetically, there is no macroscopic internally-generated magnetic field to disturb the superconducting state. Hence the coexistence of antiferromagnetic order and superconductivity is expected and indeed observed in $\mathrm{LnRh_4B_4}$ compounds and other related materials. Theoretical treatments have also been successfully developed (Jaric 1979, 1980; Ramakrishnan and Varma 1981; Sakai *et al* 1981; Mahanti *et al* 1981; Suzumura and Nagi 1982).

Detailed studies by way of χ–T, ρ–T, C_p, H_{c2} and neutron diffraction have shown that $\mathrm{LnRh_4B_4}$, Ln = Nd, Sm and Tm exhibit the coexistence behaviour in zero applied magnetic fields with the Néel temperature, $T_N < T_c$ (table 3 and figure 9). Pseudoternary alloys also show this behaviour but a few systems are interesting in that they have $T_N > T_c$. Theoretical models explaining the coexistence behaviour should take cognizance of this fact. The antiferromagnetism (afm) is exclusively due to the Ln-ions but the exact type of ordering has not been established in all the boride phases.

Table 3. Antiferromagnetic superconductors[a]

Compound	Superconductors T_c (K)	Antiferromagnetic Nèel temperature T_N (K)
Rhodium borides		
$\mathrm{NdRh_4B_4}$	5·36	1·3, 0·9[b]
$\mathrm{SmRh_4B_4}$	2·72	0·87
$\mathrm{TmRh_4B_4}$	9·86	0·4
$\mathrm{Ho(Rh_{0\cdot3}Ir_{0\cdot7})_4B_4}$	1·34	2·7
$\mathrm{Dy(Rh_{0\cdot85}Ru_{0\cdot15})_4B_4}$	4·0	1·5[c]
$\mathrm{Dy(Rh_{0\cdot3}Ir_{0\cdot7})_4B_4}$	1·7	4·7[d]
Chevrel phases		
$\mathrm{NdMo_6S_8}$	3·3 (3·6)[e]	0·85 (?)
$\mathrm{GdMo_6S_8}$	1·1 (1·4)	0·85 (0·95)
$\mathrm{TbMo_6S_8}$	1·45 (1·80)	0·90 (1·05)
$\mathrm{DyMo_6S_8}$	2·05 (2·15)	0·40 (0·45)
$\mathrm{ErMo_6S_8}$	1·9 (2·2)	0·15 (0·22)
$\mathrm{YbMo_6S_8}$	9·2 (9·5)	2·6 (2·75) (?)
$\mathrm{GdMo_6Se_8}$	5·6	0·75
$\mathrm{TbMo_6Se_8}$	5·7	1·03 (?)
$\mathrm{ErMo_6Se_8}$	6·0	1·07

[a] Taken from Subba Rao and Shenoy (1981); [b] Two transitions are indicated; [c] Hamaker and Maple (1981); [d] Ku and Acker (1980); [e] Values in paranthesis are the onset temperatures. (?) indicates that the detailed nature of the antiferromagnetic order has not yet been established.

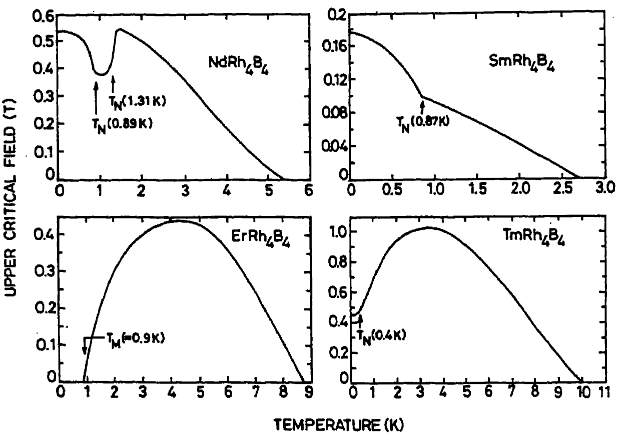

Figure 9. Upper critical magnetic field *vs* temperature for $NdRh_4B_4$, $SmRh_4B_4$, $ErRh_4B_4$ and $TmRh_4B_4$. As can be seen in the compounds with Ln = Nd, Sm, Tm, superconductivity coexists with antiferromagnetism. $ErRh_4B_4$ exhibits a reentrant behaviour (taken from Maple *et al* 1982).

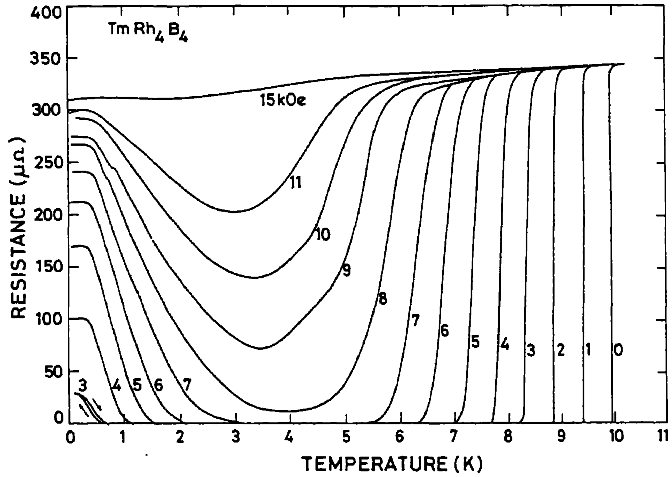

Figure 10. Resistivity *vs* temperature curves at various applied magnetic fields (kOe) for $TmRh_4B_4$. Notice that antiferromagnetic order below T_c gets modified with the applied field (taken from Subba Rao and Shenoy 1981).

Ku *et al* (1980) pointed out that the complex magnetic ordering (as compared to simple afm or fm order) might be a common feature of several $LnRh_4B_4$ compounds where Ln is heavier than Gd. Antiferromagnetic superconducting ternary borides become normal (reentrant behaviour) at T_N and develop some sort of ferromagnetic order by the application of magnetic field ($H \leqslant H_{c2}$) (figure 10).

2.1f *Reentrant and ferromagnetic superconductors*: If the rare earth spins in a $LnRh_4B_4$ systems are to order ferromagnetically the macroscopic dipolar field so created will strongly become competitive with the superconductivity and destroy the latter once the critical magnetic field value for the destruction of superconducting state is reached. Before the full realization of ferromagnetic state (reentrant behaviour), however, the ferromagnetic correlations may lead to an oscillatory magnetic state and the latter can coexist with superconductivity. This has been amply verified in $ErRh_4B_4$ (see below). Theoretical investigations by many workers (Suhl 1978; Ferrel *et al* 1979; Bulaevski *et al* 1979; Matsumoto *et al* 1979; Machida and Matsubara 1979; Greenside *et al* 1981) predict the possibility of several types of the oscillatory magnetic state (spiral, vortex or linearly polarized) but the experimental evidence on $ErRh_4B_4$ and $HoMo_6S_8$ are in favour of transverse linearly polarized state which is coexisting with the superconducting state.

As mentioned earlier, the compound $ErRh_4B_4$ exhibits reentrant superconductivity in zero applied magnetic field with the upper and lower superconducting critical temperatures $T_{c1} = 8{\cdot}7$ K and $T_{c2} \approx 0{\cdot}9$ K respectively, due to the onset of long range ferromagnetic order (alignment of Er^{3+} spins in the basal (*a–b*) plane) at a temperature $T_M \sim T_{c2}$ (see figure 9). Thermal hysteresis at T_{c2} is observed in the measured ρ, χ and C_p (Lander *et al* 1979; Moncton *et al* 1980) and thermal conductivity data (Odoni and Ott 1979) indicating that the transition is first order. Interesting precursor effects by way of the existence of a small angle peak in neutron diffraction have been observed by Moncton *et al* (1980) in $ErRh_4B_4$ in the superconducting state above the magnetic transition temperature. Recent careful neutron diffraction and resistivity studies at low temperatures on single crystals of $ErRh_4B_4$ by Sinha *et al* (1982) have shown that the transition from superconductivity to ferromagnetism proceeds through an intermediate mixed state which displays both superconductivity and long-range magnetic order. This mixed state (or pseudo phase), a mosaic of microscopic superconducting and ferromagnetic regions of size 2000 Å, sets in when the sample is cooled to below 1·2 K and exhibits a ferromagnetic moment *and* modulated moment (transverse linearly polarized, with a period of $91{\cdot}8 \pm 2{\cdot}7$ Å). On further cooling to 0·71 K, the crystal enters into a purely ferromagnetic phase, with the modulated moment *and* superconductivity disappearing simultaneously (figure 11). The latter appears suddenly on warming to 0·775 K. This first order transition is mirrored in the opposite sense by the behaviour of ferromagnetic intensity. An interesting effect of magnetic field on the intermediate mixed state has also been observed by Sinha *et al* (1982). Application of 200 Oe field to the sample at 0·74 K in the superconducting state (reached on cooling) did not produce a change in the satellite periodicity (wavelength of the modulated structure) but its intensity decreased by 45 % while the ferromagnetic intensity increased by 8·8 %. On switching off the external field, the intensity pattern did not restore itself to the previous zero-field value until the sample had been warmed beyond T_m (1·2 K) and recooled.

Reentrant superconductivity is also found in atleast three pseudoternary LnM_4B_4 alloys (table 4) indicating that it is a common phenomena and is not restricted to some special systems. Ku and Shelton (1981) pointed out that a ferromagnetic order may not be necessary to destroy superconductivity in a ternary system. Thus, any type of magnetic order with an internal exchange magnetic field that is large compared to upper critical field H_{c2} when averaged over the superconducting coherence length, will be able to destroy the superconductivity and thus show the reentrant property. When searching for a pseudoternary low temperature phase diagram that may exhibit reentrant superconductivity one must consider, in addition to the ordered states of the pure ternary end members, the rate of depression with composition of both T_c and T_m which

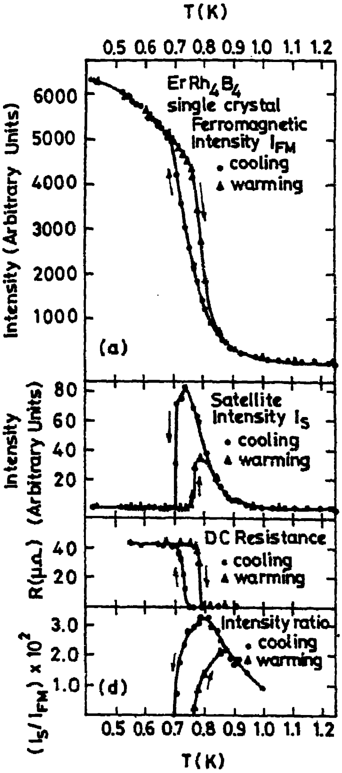

Figure 11. Neutron diffraction and resistivity study of single crystal $ErRh_4B_4$ in the low temperature region. Temperature dependence of (a) ferromagnetic intensity from the (101) Bragg peak (b) satellite intensity due to the modulated magnetic structure (c) bulk dc resistivity and (d) ratio of the satellite to the ferromagnetic intensity for the (101) reciprocal lattice point. Hysteresis is clearly shown in all cases (after Sinha *et al* 1982).

should be sufficiently small to allow these two types of transitions to intersect. Other pseudoternary systems similar to those shown in figure 12 and $Ln(Rh_{1-x}M_x)_4B_4$ (M = Ru, Ir, Os) can thus be profitably be examined.

Coexistence of ferromagnetism and superconductivity has recently been realized in the alloy system $(Ho_xEr_{1-x})Rh_4B_4$ ($0{\cdot}84 \leqslant x \leqslant 0{\cdot}9$) in the temperature range 4·95–5·95 K (for $x = 0{\cdot}84$) and has been conclusively established by χ, ρ and neutron diffraction techniques (table 4; Lynn 1983; Lynn *et al* 1983a,b). No evidence for an oscillatory component due to the magnetization was found and in this respect the alloy system differs from the behaviour of pure $ErRh_4B_4$.

2.2 *Compounds with AMB_2 stoichiometry*

Ku and Shelton (1980) and Shelton *et al* (1980b) discovered that $LnMB_2$ (Ln = rare earth, Y and Sc; M = Ru and Os) crystallize with the orthorhombic structure and $LuRuB_2$ and $YRuB_2$ exhibit high temperature superconductivity with T_c of 10 and 7·8 K respectively. However, the corresponding Os-containing isoelectronic compounds have T_c lowered by a factor of 4. When Ln is a magnetic ion, the phases exhibit magnetic ordering, presumably of a ferromagnetic-type. Ku and Shelton (1981) examined the pseudoternary system $(Lu_{1-x}Tm_x)$ RuB_2 and found reentrant superconducting behaviour for $0{\cdot}52 \leqslant x \leqslant 0{\cdot}68$ (Table 4).

The structure of orthorhombic $LuRuB_2$ is shown in figure 13. It is a cluster compound qualitatively of a different kind from that of the AM_4B_4-type compounds.

Table 4. Reentrant and ferromagnetic superconductors

Compound	Superconductors $T_c(\equiv T_{c1})$ (K)	Reentrant temperature T_{c2} ($\leqslant T_m$, mag. order temperature) (K)	Reference
$ErRh_4B_4$	8·7	0·71 (cooling)[a] 0·775 (warming) ($T_m < 1{\cdot}2$ K)	Sinha *et al* (1982)
$Tm_2Fe_3Si_5$	1·7	1·13	Segre and Braun (1981)
$TmOs_xSn_y$	1·1	0·6	Fisk *et al* (1982)
$ErRh_{1{\cdot}1}Sn_{3{\cdot}6}$	1·36	0·46	Remeika *et al* (1980)
$ErOs_{1{\cdot}1}Sn_{2{\cdot}7}$	1·3	0·5	Fisk *et al* (1982)
$HoMo_6S_8$	1·82	0·612 (cooling) 0·668 (warming)	Lynn *et al* (1981, 1983a)
$Ho(Rh_{1-x}Ir_x)_4B_4$ ($x = 0{\cdot}15$) ($0{\cdot}08 \leqslant x \leqslant 0{\cdot}22$)	5·2	2·0	Ku *et al* (1980)
$(Y_{1-x}Gd_x)Rh_4B_4$ ($x = 0{\cdot}32$)	2·82	1.72	Adrian *et al* (1981)
$Tm_{1-x}Lu_xRuB_2$ ($x = 0{\cdot}6$) ($0{\cdot}52 \leqslant x \leqslant 0{\cdot}68$)	4·3	1·2	Ku and Shelton (1981)
Ferromagnetic[b] superconductors			
$(Ho_{0{\cdot}84}Er_{0{\cdot}16})Rh_4B_4$	5·95	4·95 (resist.) 5·30 (neutron)	Lynn 1983; Lynn *et al* (1983b)
$(Ho_{0{\cdot}5}Eu_{0{\cdot}5})Mo_6S_8$	2·0	0·6	Ishikawa *et al* (1981; 1982)

[a] Below T_m an intermediate mixed state sets in where ferromagnetic domains and superconducting domains coexist (of size ~ 2000 Å), with the superconducting domains further divided into subdomains which contain modulated magnetic moment.

[b] Coexistence of ferromagnetism and superconductivity occurs in the interval $T_{c2} < T < T_{c1}$ for the specific compositions.

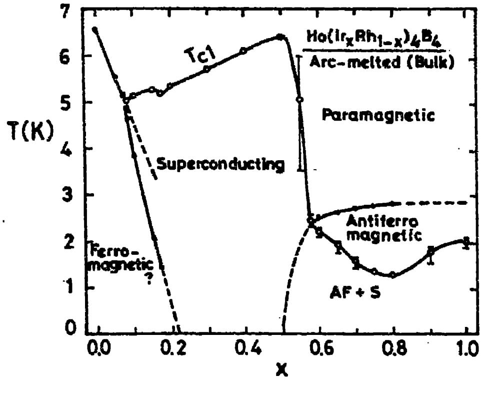

Figure 12. Low temperature phase diagram for the system Ho $(Ir_xRh_{1-x})_4B_4$ determined from ac and static susceptibility measurements on arc melted samples. This system is interesting in that both reentrant behaviour and the coexistence of antiferromagnetism and superconductivity ($T_N > T_c$) are encountered with varying x (taken from Ku *et al* 1980).

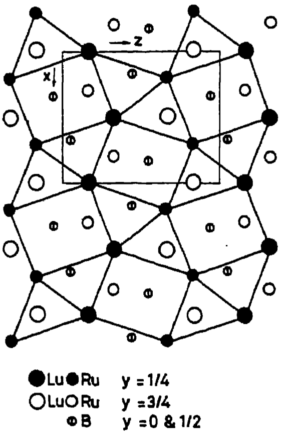

Figure 13. Projection of the orthorhombic $LuRuB_2$-type structure along the (010) direction. Plane net of Lu and Ru atoms are connected by thick lines for $y = 1/4$ plane.

The Lu and Ru atoms form planar nets perpendicular to the *b*-axis. The Lu-Lu distance within the plane is very short (3·1 Å compared to the normal CN12 metallic distance of 3·47 Å) and interlayer distance is only slightly larger (3·34 Å). The intralayer and interlayer Ru-Ru distances are 3·03 and 4·07 Å respectively (compare Ru-Ru distance of 2·71 Å in Ru metal). The Lu atoms form zig-zag chain clusters lying in the *a-c* plane and running in the crystallographic *a*-direction. Strong Lu-Ru bonding exists as is evident by the bond length of 3·05 Å which is very close to that calculated (3·07 Å) from the CN12 metallic radii. The boron atoms are dimerized (d(B-B) = 1·74 Å) and are located between the Lu-Ru planes. The B_2 dimers are weakly coupled to form zig-zag chains running perpendicular to the metal planes (*i.e.*, parallel to the *b*-axis). This is in contrast to the AM_4B_4 compounds where the B_2 pairs are isolated from each other.

It is clear that superconductivity arises in $LnRuB_2$ phases from the Ru 4*d*-electrons but the Ln atoms also play a crucial role because of strong Ln-Ru bonding and Ln-Ln bonding. Superconductivity is not exhibited when Ln ion has a magnetic moment but then the magnetic ordering temperatures are also high (*e.g.*, Ln = Tb, T_m = 45·6; Ln = Dy, T_m = 21·9 K). T_m values are also high in the corresponding osmium phases, $LnOsB_2$ (Ln = Tb, T_m = 39·2 K) but the T_c values are low for non-magnetic Ln (*e.g.*, Ln = Lu, T_c = 2·7; Y, T_c = 2·2 K).

2.3 *Compounds with AM_3B_2 stoichiometry*

Isotypic series of compounds with ACo_3B_2 stoichiometry were first prepared and characterized by Kuz'ma *et al* (1969). Later studies revealed that a large number of compounds with the formula AM_3B_2, A = rare earth, Zr, Hf, Th, Ba; M = Co, Ru, Rh, Os, Ir, Pt do form. The structure types adopted by them are: (i) hexagonal $CeCo_3B_2$-type, (ii) monoclinic $ErIr_3B_2$-type, (iii) hexagonal $Ba_{0.67}Pt_3B_2$-type, and (iv) orthorhombic (?) YOs_3B_2-type. In the $CeCo_3B_2$-type structure the B atoms are isolated from each other and there exists an interpenetrating network of A and M atom clusters. The $ErIr_3B_2$ and $Ba_{0.67}Pt_3B_2$ structures are distorted derivatives of the hexagonal $CeCo_3B_2$ structure. The fact that the latter structure is not conducive to high temperature superconductivity can be seen from the following data: (i) for AM_3B_2, A = rare earth; M = Ru, Os, Rh and Ir, T_c does not exceed 4·6 K (Ku *et al* 1980; Ku and Meisner 1981; Malik *et al* 1982; Dhar *et al* 1983); (ii) LnM_3B_2 (M = Rh, Ir) with the

$ErIr_3B_2$ structure do not have T_c above 1·2 K (Ku and Meisner 1981); (iii) for $A_{0.67}Pt_3B_2$ the T_c are 1·6, 2·8 and 5·6 K for A = Ca, Sr and Ba (Shelton 1978) and (iv) AOs_3B_2, A = Th, T_c = 3 K; A = Y, T_c = 6 K (Ku 1980).

3. Ternary carbides

Of the known ternary carbides, molybdenum borocarbide, Mo_2BC and aluminocarbide, Mo_3Al_2C merit attention since they exhibit superconductivity with T_c of 7·5 and 10 K respectively. Mo_2BC has an orthorhombic symmetry (space group, cmcn) with $a = 3{\cdot}086$, $b = 17{\cdot}35$ and $c = 3{\cdot}047$ Å and the structure can be described as a combination of boride and carbide subcells (figure 14). The carbon atoms are located at the centre of Mo_6 distorted octahedra, which share edges to form layers. The octahedron layers are separated from each other by boron layers, the boron atoms forming zig-zag chains which pass through the trigonal prisms of the Mo-atoms. Recently Lejay *et al* (1981 a,b) synthesized Mo_2BC single crystals and examined their properties. They also found that transition elements Zr, Nb, Rh, Hf, Ta and W can be substituted to a significant extent ($x = 0{\cdot}15$–$1{\cdot}1$ in $Mo_{2-x}M_xBC$) in samples prepared in polycrystalline form by arc melting techniques. While the T_c decreased with increase in x for all the alloys, the Rh-containing alloy exhibited an increase of T_c (up to 9 K) and H_{c2} (27 kOe for $x = 0$) and then a decrease (to 6·7 K) for x ranging from 0–0·3. The authors found a good correlation of T_c with the molar volume and valence electron concentration in all the alloys studied.

Mo_3Al_2C has a cubic β–Mn structure with $a = 6{\cdot}867$ Å. The phase, along with the other M_3Al_2C (M = Ti, V, Cr, Nb and Ta), was first synthesized by Jeitschko *et al* (1963) and later Johnston *et al* (1964) discovered it to be superconducting with a T_c of 10 K. Similar to the Mo_2BC, the C atoms are located in an octahedra of Mo-atoms in Mo_3Al_2C and the Mo–C distance of 2·14 Å indicates strong covalent bonding. The

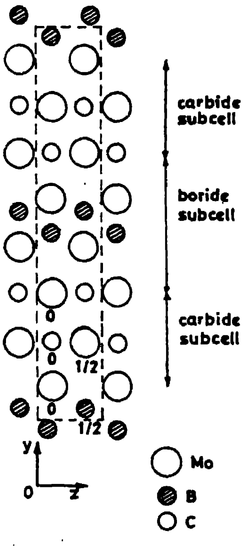

Figure 14. Crystal structure of Mo_2BC. Projection of the ZOY plane is shown.

β–Mn structure is without doubt conducive to high T_c superconductivity since oth phases with M $\neq$ Mo, crystallizing in a hexagonal structure do not have a T_c abo 4·2 K.

4. Ternary silicides

Ternary silicides have attracted wide attention in recent years and a variety of phas with different stoichiometries have been synthesized and studied. The importa systems are: (i) LnMSi, (Ln = rare earth or Y; M = Rh and Ir) with the TiNi structure for Ln = Gd → Er and Y and with the ZrOS (or $SrSi_2$: Cubic) structure f LaRhSi and LnIrSi (Ln = La → Nd) (Chevalier *et al* 1982a,b; Klepp and Parthe 198 (ii) $LnMSi_2$ (Ln = La → Gd; M = Rh and Ir) with the orthorhombic CeNiS structure (Chevalier *et al* 1982c,d; Chevalier *et al* 1983); (iii) $LnRh_2Si_2$ (Ln = La → E Y) with the tetragonal $ThCr_2Si_2$ structure (Ballestraci 1976; Chevalier *et al* 1983; Feln and Nowik 1983); (iv) Ln_2RhSi_3 (Ln = La → Er; Y) with a hexagonal structu (Chevalier *et al* 1982c,d; Chevalier *et al* 1983); (v) $LnRu_3Si_2$ (Ln = La → Yb; Y and with the hexagonal $LaRu_3Si_2$ structure (Barz 1980; Vandenberg and Barz 1980) ar $LnRh_3Si_2$ (Ln = La → Er and Y) with hexagonal $CeCo_3B_2$-type structure (Chevali *et al* 1981); (vi) $Ln_2M_3Si_5$ (Ln = Sm → Lu; Sc and Y; M = Fe, Ru and Os) with tl tetragonal $Sc_2Fe_3Si_5$-structure (Braun 1980, 1981; Braun *et al* 1981) and Ln_2Rh_3S (Ln = La → Er and Y) with the orthorhombic $U_2Co_3Si_5$-type structure (Chevalier *et* 1982e) and (vii) $Sc_5M_4Si_{10}$ (M = Co, Rh, Ir) and $Ln_5Ir_4Si_{10}$ (Ln = Dy → Lu, Y) wi the tetragonal $Sc_5Co_4Si_{10}$-type structure (Braun *et al* 1980; Braun and Segre 198 1981). Of the above, many phases are superconducting for Ln = Sc, Y, La, Lu, but hi T_c superconductivity is realized only in the phases $LaRu_3Si_2$ (T_c = 7·6 K), Lu_2Fe_3S (T_c = 6·1 K) and $Sc_5M_4Si_{10}$ (M = Rh and Ir; T_c = 8·5–8·6 K). It is significant to no that $LaRu_3Si_2$ is a distorted version of the hexagonal $CeCo_3B_2$ structure and contai triangular Ru_3 clusters. On the other hand, the $LnRh_3Si_2$ phases crystallize with tl undistorted $CeCo_3B_2$-structure and the latter, as noted earlier, is not very conducive high T_c superconductivity. Hence it is not surprising that $LnRh_3Si_2$ (Ln = La and are not superconducting above 0·05 K (Chevalier *et al* 1981).

4.1 *Primitive tetragonal $Sc_2Fe_3Si_5$ and $Sc_5Co_4Si_{10}$ structures*

Isostructural primitive tetragonal phases of the formula $Ln_2M_3Si_5$ exist for tl following combinations: M = Fe, Ln = Sm → Lu, Y, Sc; M = Ru and Os, Ln = Lu, and $Y_2Re_3Si_5$. The *a* and *c* values respectively are ~ 10·3 and ~ 5·3 Å. One interesti aspect is that the Fe-containing phases with Ln = Lu, Sc and Y exhibit T_c of 6·1, 4·5 a 2·4 K respectively, relatively high values for an iron (3*d* metal)-based compoun Remarkably enough, reentrant superconductivity has been discovered in Tm_2Fe_3S with T_{c1} = 1·3 K and T_{c2} = 1·1 K (table 4) (Segre and Braun 1981). Mössbauer studi of $Ln_2Fe_3Si_5$ (Cashion *et al* 1980, 1981) have shown that the magnetic moment on atoms (iron occupies two sets of point positions in the structure) is less than 0·03 μ_B a indicate that the iron 3*d*-electrons are non-magnetic and participate in strong bondi with Si atoms. When Fe is replaced by the isoelectronic Ru or Os, superconductivi disappears for Ln = Lu and Y and this fact raises the important question whether t Fe–3*d* electrons participate in superconductivity or not. When Ln is a magnetic ra earth, the Fe-containing phases exhibit antiferromagnetism with T_N ~ 10 K.

Primitive tetragonal $Ln_5M_4Si_{10}$ compounds with $a \sim 12$ Å and $c \sim 3{\cdot}9$ Å form for Ln = Sc and M = Co, Rh and Ir and for Ln = Dy → Lu, Y for M = Ir. In the prototype compound $Sc_5Co_4Si_{10}$, the Co and Si atoms form planar nets of hexagons and pentagons which are connected along (001) axis *via* Co-Si-Co zig-zag chains to form a three-dimensional network. The hexagon-pentagon layers are separated by layers of Sc atoms and the Co atoms are isolated from each other. The Sc-containing phases are superconductors with $T_c = 5$, 8·5 and 8·5 K for M = Co, Rh and Ir. The Ir containing phases with Ln = Lu and Y are also superconducting ($T_c = 3{\cdot}8$ and 3 K) whereas those with Ln = magnetic ions, are magnetic at low temperatures. It is interesting to note that the Co compound has a fairly high T_c and χ–T data reveal that the Co atoms do not carry any localized magnetic moment (Braun and Segre 1981); the quenching of the moment correlates well with the short (covalent) Co-Si and Si-Si interatomic distances in the structure.

5. Ternary germanides

Well-defined rare earth ternary germanides are few in number and have only recently been isolated and studied. They are: (i) $Y_5M_4Ge_{10}$ (M = Ir and Os) with the tetragonal $Sc_5Co_4Si_{10}$-type structure (Braun and Segre 1980, 1981; Braun *et al* 1980). For M = Os, $T_c = 8{\cdot}7$ K whereas for M = Ir, T_c is only 2·6 K. (ii) $Ln_3M_4Ge_{13}$ (Ln = Ce → Lu, Y; M = Ru and Os) with the primitive cubic $Pr_3Rh_4Sn_{13}$-type structure (Segre *et al* 1981). The lattice constants are ~ 9 Å and when Ln = Y and Lu, the phases are superconducting with T_c less than 3·9 K. When the Ln is a magnetic ion, the compounds order magnetically with T_m as high as 16 K. (iii) LnM_2Ge_2 (Ln = La, Yb; M = Pd, Pt) with the tetragonal $ThCr_2Si_2$ structure (Hull *et al* 1981). T_c is around 1 K for Ln = La, Yb and M = Pd whereas $LaPt_2Ge_2$ has a T_c of 0·55 K. (iv) LnMGe (M = Co, Ni; Ln = Gd → Lu, Y; Sc; M = Rh, Pd, Ir, Pt; Ln = La → Tm; Y; Sc). The phases adopt either the orthorhombic TiNiSi- or $CeCu_2$-type or hexagonal ZrNiAl (Fe_2P)-type or tetragonal LaPtSi-type structure (Hovestreydt *et al* 1982).

6. Ternary stannides

A large number of ternary stannides, AM_xSn_y, have been isolated and studied in recent years with the specific aim of examining the interplay between superconductivity and magnetic order. An advantage in these stannides is that most of them are cubic systems and large single crystals can be grown employing metallic tin as flux. The ideal stoichiometry established by single crystal x-ray data is $Ln_3Rh_4Sn_{13}$ (Ln = Pr and Yb) and the phases are isotypic with the germanides, $Ln_3M_4Ge_{13}$ (M = Ry and Os). However, the formula is usually written as $A_{1{\cdot}00}M_xSn_y$ with $x = 1$–$1{\cdot}5$ and $y = 3{\cdot}1$–$4{\cdot}5$. Primitive cubic $Pr_3Rh_4Sn_{13}$-type structure (phase I with $a \sim 9{\cdot}7$ Å) is encountered for A = Ca, Sr with M = Co; A = Ca; Sr, Ln (rare earth) and Th with M = Ru and Ir; A = La with M = Ru and A = Ca with M = Pt (Espinosa 1980; Espinosa *et al* 1980; Remeika *et al* 1980; Vandenberg 1980; Hodeau *et al* 1980; Cooper 1980). Tetragonal (phase II with $a \sim 13{\cdot}7$; $c \sim 9{\cdot}7$ Å) stannides are found for $LnRu_xSn_y$. Ln = Er, Lu; $ErCo_xSn_y$; $LnRh_xSn_y$, Ln = Sc, Y, Ho → Lu and $LnIr_xSn_y$, Ln = Sc, Er → Lu (Remeika *et al* 1980; Espinosa 1980; Cooper 1980; Andres *et al* 1981; Chenavas *et al*

1981). *Fcc* (phase III with $a \sim 13{\cdot}7$ Å) stannides are found for $\mathrm{LnM_xSn_y}$, Ln = and M = Ru and Os; $\mathrm{LnRh_xSn_y}$, Ln = Tb → Tm; $\mathrm{LnIr_xSn_y}$, Ln = Y, Gd (Espinosa *et al* 1980; Remeika *et al* 1980; Espinosa 1980; Cooper 1980; Chenava 1981; Lambert *et al* 1981). The lattice parameters of phases I, II and III are r $\sqrt{2}\,a\,(\mathrm{I}) \approx a\,(\mathrm{III}) \approx a\,(\mathrm{II}) \approx (c(\mathrm{II})/2)$. Hence the structure of phase I, which is k in detail, might be related to the phases II and III.

The $\mathrm{Pr_3Rh_4Sn_{13}}$ structure with 2 formula units per unit cell has a numl interesting features: (i) the tin atoms occupy two different types of positions: 2 atoms per unit cell form a *bcc* sublattice and appear to be cationic in charact remaining 24 tin atoms, Sn(2), are anionic in nature and coordinate the Sn(1), Pr a atoms. The formula can then be written as $\mathrm{Sn(1)Pr_3Rh_4Sn(2)_{12}}$. Mössbauer s have corroborated the existence of two kinds of Sn atoms in the structure (Shenc 1980), (ii) the Pr and Sn(1) atoms together form the beta-W (A15) structure in nonintersecting and mutually perpendicular chains of Pr atoms run across the cel (figure 15). However, the Pr-Pr distances are large. The Rh atoms foı interpenetrating simple cubic array and one $\mathrm{Rh_8}$ cube is situated at the centre o A15 unit cell as shown in figure 15. The $\mathrm{Sn(1)Pr_3Rh_4}$ sublattice resembles the ch type structure of $\mathrm{Na_xPt_3O_4}$. However, the Rh-Rh distances are large (much g than the intermetallic distance in Rh metal) and there is only weak Pr-Rh bo Thus, there are no Sn(1)–Sn(1), Pr-Pr or Rh-Rh clusters. Hodeau *et al* (1980 shown that Yb and Sn(1) atoms in $\mathrm{Sn(1)Yb_3Rh_4\text{–}Sn(2)_{12}}$ show mutual substitu disorder on the Sn(1) and Yb sites of the structure (5·7 and 8·5 atom % respec This disorder may have a significant effect on the superconducting and other pro of the phase I stannides, (iii) the Sn(2) atoms effectively isolate each Pr and Rh from the others but they themselves form pairs with the Sn(2)–Sn(2) distance s less or almost equal to that encountered in tin metal. Hence the phase I stannides therefore, be expected to exhibit physical properties typical of sp-band metals since the A or Ln element occupies a distinct position in the crystal lattice, tho which support a magnetic moment may exhibit magnetic ordering at low temper

Phase I (primitive cubic) stannides exhibit superconductivity for A = Ca, Sr, or Yb (table 5) with a high T_c of 8·7 K for the $\mathrm{CaRh_{1.2}Sn_{4.5}}$. It is significant that t containing compound also exhibits a relatively high T_c (5·9 K). The Ln compounds with the phase II and III structures show superconductivity when t earth is nonmagnetic. $\mathrm{ErRh_{1.1}Sn_{3.6}}$ (Remeika *et al* 1980; Shenoy *et al* 1980; O 1981) and $\mathrm{ErOs_xSn_y}$ (Espinosa *et al* 1980) have been found to exhibit a ree behaviour at zero applied magnetic field and $\mathrm{TmRh_{1.3}Sn_4}$ in applied fields great 1·2 kOe (Lambert *et al* 1981). Recent studies on phase III $\mathrm{LnOs_xSn_y}$ by Fisk *et al*

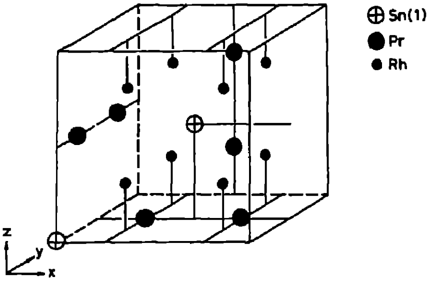

Figure 15. Structure of $\mathrm{Pr_3Rh_4Sn(2)_{12}}$ showing the Sn(1 sublattice. The disposition of t atoms not shown. These exist with interatomic distance simila in Sn metal (after Hodeau *et al* 1 discussion see text.

Table 5. Structure, T_c and T_m data of select AM_xSn_y stannides

A	M	Sn	a_o (Å)	c_0 (Å)	T_c (K)	T_m (K)
Phase I compounds (Prim. cubic; $Pr_3Rh_4Sn_{13}$-type structure)						
Ca	$Rh_{1\cdot2}$	$Sn_{4\cdot5}$	9·702	—	8·7	—
Sr	Rh_x	Sn_y	9·800	—	4·3	—
La	Rh_x	Sn_y	9·745	—	3·2	—
Eu	Rh_x	SS_y	9·749	—	—	11
Yb	Rh_x	Sn_y	9·676	—	8·6	—
Th	Rh_x	Sn_y	9·692	—	1·9	—
Ca	Ir_x	Sn_y	9·718	—	7·1	—
Sr	Ir_x	Sn_y	9·807	—	5·1	—
Ca	Co_x	Sn_y	9·584	—	5·9	—
La	$Ru_{1\cdot5}$	$Sn_{4\cdot5}$	9·772	—	3·9	—
Phase II compounds (tetragonal structure)						
Sc	Rh_x	Sn_y	13·565	9·558[a]	4·5	—
Y	Rh_x	Sn_y	13·772	9·707	3·2	—
Er	$Rh_{1\cdot1}$	$Sn_{3\cdot6}$	13·733	9·139	1·36	0·46[b]
Lu	$Rh_{1\cdot2}$	$Sn_{4\cdot0}$	13·693	9·648	4·0	—
Lu	Ir_x	Sn_y	13·708	9·661	3·2	—
Phase III compounds (fcc structure)						
Tb	$Rh_{1\cdot1}$	$Sn_{3\cdot6}$	13·774	—	—	4·0
Dy	$Rh_{1\cdot1}$	$Sn_{3\cdot6}$	13·75	—	—	2·1
Y	Os_x	Sn_y	13·801	—	2·5	—
Gd	Os_x	Sn_y	13·773	—	—	—
Tb	$Os_{1\cdot5}$	$Sn_{2\cdot6}$	13·812	—	1·4	—
Dy	$Os_{1\cdot5}$	$Sn_{2\cdot5}$	13·792	—	—	—
Ho	$Os_{1\cdot2}$	$Sn_{2\cdot5}$	13·776	—	1·4	—
Er	$Os_{1\cdot1}$	$Sn_{2\cdot7}$	13·760	—	1·3	0·5[b]
Tm	Os_x	Sn_y	13·744	—	1·1	0·6[b]
Y	Ir_x	Sn_y	13·773	—	2·2	—

[a] The c_0 values should be multiplied by $2\sqrt{2}$ to obtain the true tetragonal *c*-axis val (Chenavas *et al* 1981).
[b] Re-entrant superconductor.

have shown that only superconductivity is observed for Ln = Tb and Ho, those of and Tm are reentrant superconductors whereas those of Gd and Dy appear to exhib some type of short-range magnetic order at low temperatures.

In contrast to the behaviour of $ErRh_4B_4$ and $HoMo_6S_8$, the stannide $ErRh_{1\cdot1}Sn$ exhibits no thermal hysteresis at the reentrant transition measured either resistive or inductively. Neutron diffraction data (Remeika *et al* 1980) show that even $T = 0·07$ K, true long-range order does not develop in the compound; presumably, t substitutional disorder at the Er site (by the Sn(1) atoms) may affect the integrity of t rare earth sublattice. This may also explain the sample dependence of the sup conductivity and magnetic behaviour of stannides observed by Ott *et al* (1981). We al note from table 5 and the work of Espinosa *et al* (1982) that detailed studies are yet to carried out on many of the stannide phases.

7. Ternary phosphides and pnictides

7.1 *Niobium sulpho phosphide, NbPS*

Donohue and Bierstedt (1969) discovered that niobium sulphophosphide, Nb superconducting with a T_c of 12·5 K. The compound, along with the other anolo TaPS and NbPSe can be synthesized only under high pressure and high tempera conditions (65 kb, 1200°C). The structure of NbPS is orthorhombic (space g Immm $Z = 4$, $a = 3{\cdot}438$, $b = 11{\cdot}88$, $c = 4{\cdot}725$ Å). The structure shows several inte ing features: The Nb atoms are 8-fold coordinated by 4 P and 4 S atoms at the corne a bicapped trigonal prism. The prisms share faces, in pairs, through the 4 P at resulting in a short Nb-Nb distance of 2·93 Å (compare interatomic distance of 2·8 in Nb metal). This distance suggests the presence of a metal–metal bond. The pai bicapped trigonal prisms share triangular faces in the *a* axis direction, with this Nb distance being that of the *a* axis. The sulphur atoms are coordinated by 4 Nb ator the corners of a distorted tetrahedron. The P atoms are coordinated to 4 Nb atoms one P atom. The P atoms form continuous strings in the *c* axis direction alternating short and long distances (2·22 and 2·15 Å respectively). The short dista are within the normal P–P covalent bond distances found in many other compo This led Donohue and Bierstedt to propose an ionic formula of the $(\mathrm{Nb})_2^{4+}(\mathrm{P}_2)^{4-}\mathrm{S}^{2-})_2$ for the compound NbPS where the Nb is present in a oxidation state (d^1 system). Surprisingly enough NbPSe and TaPS, which structurally analogous to NbPS do not exhibit superconductivity down to 1·25

7.2 *ZrRuP-type compounds*

The fact that a particular structure for a ternary system can favour the hi superconductivity is nicely demonstrated by the recent work of Barz *et al* (1980), M *et al* (1983) and Meisner *et al* (1983) on the equiatomic (1 : 1 : 1) ternary transition phosphides and arsenides of the general formula, *MM′X* (*M* = Ti, Zr, Hf, Nb *M′* = Ru, Rh, Os; *X* = P, As). The compound ZrRuP can crystallize either hexagonal ZrRuSi (ordered Fe_2P or ZrNiAl, Johnson and Jeitschko 1972)-type the orthorhombic TiNiSi-type (ordered Co_2P or anti $PbCl_2$, Shoemaker Shoemaker 1965). Hexagonal ZrRuP and ZrRuAs show a T_c of 13 and 11·7 K (temperatures are 13·5 and 11·9 K) respectively whereas the orthorhombic Z exhibits a low T_c of 3·46 K (onset at 3·82 K). Detailed studies are yet to be made on of the above phases but the available data reveal that the orthorhombic struct adopted by the compounds with M = Nb, Ta and the hexagonal arsenide phas metastable at low temperatures. The T_c data are summarised in table 6.

An important structural feature of the hexagonal ZrRuP (space group, P $Z = 3$) over that of the orthorhombic polymorph (space group, Pnam; $Z = 4$) i layered structure of the Zr and Ru atoms (each layer, parallel to the *x*-*y* plan separated by a distance of $c/2$, is occupied by either Zr and P atoms or Ru and P a only) and the existence of Ru_3-triangular clusters (short Ru-Ru distances, 2·63 Å; f 16). In contrast, the orthorhombic structure has layers which are filled with Zr a atoms and these layers are all equivalent; also, there do not exist the Ru_3-clusters (M *et al* 1983). Recent heat capacity data (Stewart *et al* 1982) on the supercondu hexagonal phosphides show that the density of states at the Fermi level i

Table 6. T_c data on equiatomic MM′X ternary pnictides*

Hexagonal structure (Fe_2P–type)				Orthorhombic structure (Co_2P-type)	
Phase	T_c (K)	Phase	T_c (K)	Phase	T_c (K)
TiRuP	1·3	—	—	ZrRuP‡	3·46
ZrRuP**	13·0	ZrRuAs	11·7	ZrRhP	< 1·1
HfRuP	10·9	HfRuAs	4·9	NbRuP	—
TiOsP	1·2	—	—	NbRhP	4·08
ZrOsP	7·4	ZrOsAs	8·0	TaRuP	—
HfOsP	6·1	HfOsAs	3·2	TaRhP	4·41

* The phases with M′ = Fe, Co, Ni exist and crystallize in the Co_2P-structure (Rundqvist and Nawapong 1966; Rundqvist and Tansuriwongs 1967) but do not exhibit superconductivity.

** $a = 6{\cdot}459(6)$; $c = 3{\cdot}778(4)$ Å

‡ $a = 6{\cdot}4169(6)$; $b = 7{\cdot}3215(8)$; $c = 3{\cdot}8623(4)$ Å

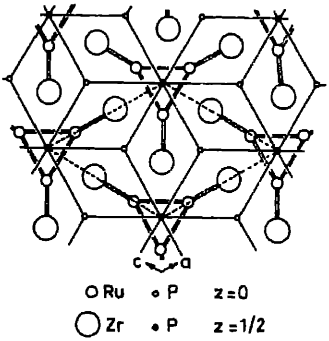

Figure 16. Projection of the ZrRuP structure along the hexagonal c axis. Double lines represent the metallic bonding of the Ru–Zr chains and Ru–Ru triangular clusters and the dashed line indicates the boundary of the hexagonal unit cell.

ılarly large (0·76 ± 0·15 states/eV-atom) for ZrRuP with a T_c of 13 K and ıre, 1·08 for Ru metal with a T_c of 0·5 K) and hence the high T_c must be due to sed electron-phonon interaction in the ternary system.

’nictides of the type LnM_4X_{12}

ry pnictides of the formula, LnM_4X_{12}, where Ln = rare earth or Th; M = Fe, Ru s and X = P, As and Sb, represent a group of isostructural compounds with a *bcc* ıre with *a* varying from 7·8 to 9·1 Å (space group, *Im*3; *Z* = 2; density 5–8 g/cc). A ıf 42 compounds have been synthesized by Jeitschko and coworkers (Jeitschko raun 1977; Braun and Jeitschko 1980a,b,c). Due to the existence of strong X–X ng to give rise to X_4 groups, the phases can be considered to be metal excess y systems and interesting physical properties can be expected. Indeed, Meisner discovered superconductivity in the phosphides, LaM_4P_{12} (M = Fe, T_c = 4·1 K; ʀu, T_c = 7·2 K). Detailed studies have not yet been carried out.

he $LaFe_4P_{12}$ structure, the Fe atom has an octahedral coordination and the La has a 12-fold (nearly icosahedral) coordination. Each P atom is surrounded by two other P and two Fe atoms forming a distorted tetrahedron with an La atom o one face of the tetrahedron. The FeP_6 octahedra share all their corners with ad octahedra and thus the Fe : P ratio is 1 : 3. The octahedra are rotated in such a wa for every 4 octahedra, one large void is formed and this is filled by the La (figure 17). Also, rotation of the octahedra permits a close approach of the P (or Sb) atoms which thereby form rectangular, nearly quadratic, four-membered (P_4 (see figure 17a). The Fe or La atoms do not form clusters and the interatomic dis are large (Fe–Fe ~ 3·9 Å); La–La ~ 6·8 Å). However, significant bonding between the metal atoms and P and, also between the P atoms. Jeitschko and (1977) suggested an ionic formula Ce^{4+} (or Th^{4+}) $(FeP_3)_4^{1-}$ or $Ce^{4+}Fe_4^{2+}(P_4)_3^{4-}$ i Ce-containing phosphide and also proposed a one-electron energy band model i $LaFe_4P_{12}$-type compounds. According to the latter, the conduction band is r composed of Fe-metal 3*d* and/or 4*s*, 4*p* bands and assuming an electronic (transfer from Ln atoms, the band is partially filled for Ln^{3+} whereas, it is com filled for Ln = Ce^{4+} or Th^{4+}. The latter compounds should be semicond whereas the La^{3+} compound should be metallic. This is in accord with the prelin observed data in that $CeFe_4P_{12}$ did not show any magnetic or supercond transition above 0·35 K. Measurements by Meisner (1981) showed that LnM_4P_1 Ln = Pr and Nd and M = Fe and Ru exhibit magnetic transitions at or below

Recent Mössbauer studies on $LaFe_4P_{12}$ by Shenoy *et al* (1982) show that th atoms in the compound carry no magnetic moment ($< 0{\cdot}01\ \mu_B$) and are preser spin-paired 3*d* configuration. The observed centre shift and area under resonanc temperature could be fitted to a curve with $\theta_D = 450 \pm 20$ K. Assuming a va $N(E_F) = 2$ states/(eV-spin), Shenoy *et al* (1982) estimated that the electron-pl coupling is weak ($\lambda = 0{\cdot}4$–$0{\cdot}5$) in this material.

7.4 *Pnictides of the type* $A_2M_{12}X_7$

Isostructural compounds (about 55 known) of the general formula A_2M where A = rare earth (Ln), Y or Zr; M = Fe, Co, Ni and X = P or A known (Jeitschko *et al* 1978). These possess the hexagonal $Zr_2Fe_{12}P$ structure with $a \sim 9$ Å and $c \sim 3{\cdot}8$ Å and have high coordination for all the atoms, as is the case for typical intermetallic compounds. The P atoms a isolated (and thus no P–P bond exists) and have a nine-fold coordination. T

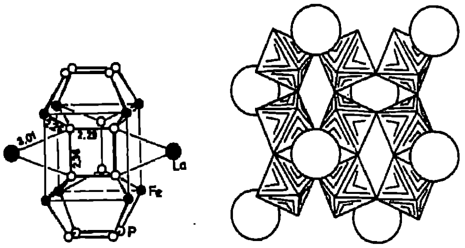

(a) (b)

Figure 17. Crystal structure of $LaFe_4P_{12}$. (**a**) Near neighbours of the P_4 gro $LaFe_4P_{12}$. Interatomic distances are in Å. (**b**) One layer of the corner shared FeP_6 octah shown with the adjacent La atoms (spheres) above and below. The corners of the oct represent the P atoms. The Fe atoms inside the octahedra are not shown.

r atoms have 12- and 18-fold coordination respectively. The Fe–Fe distances are (2·495 Å compared to 2·482 Å in iron metal) indicating strong bonding and antial Fe–P bonding also exists. Jeitschko and coworkers proposed an ionic ulation of the type $(Ln^{3+})_2 (M^{1.25+})_{12} (X_7^{3-})$ and $Zr_2^{4+} (M^{1.08+})_{12} (X^{3-})_7$ for the s where the non-integral oxidation states written for M only means a delocaliz- of the electrons on the metals (Fe, Co and Ni) rather than mixed valence. Unit cell ne and crystal chemical considerations indicate that an intermediate valency may for Ce, Eu and Yb-containing phases.

Pnictides of the type LnM_2X_2

earth ternary pnictides of the $ThCr_2Si_2$-type LnM_2X_2 (Ln = rare earth or Th; Fe, Co, Ni and X = P, As or Sb) have been recently synthesized and characterized hko and Jaberg 1980; Ruhl and Jeitschko 1979; Marchand and Jeitschko 1978). uctural phosphides CaM_2P_2 (M = Ni, Cu), BaM_2P_2 (M = Zn and Mn) and $_2As_2$ are also known. The compounds possess a body-centred tetragonal ure (I4/mmm; Z = 2). The M element has a tetrahedral coordination with respect X atom. In the Ni-containing compounds there is a tendency for square planar ination, although a perfectly square planar P(or Si) coordination of the Ni atom t be achieved in the $ThCr_2Si_2$-type structure. The A(Ln) atom is surrounded by d 8X atoms in the Th-containing compounds, the coordination number reaches tead of 16. Phosphorous atoms exist as pairs (P_2) whereas in $EuCo_2P_2$, the large istance indicates the existence of isolated P^{3-} ions (Marchand and Jeitschko Lanthanide contraction is apparent in the unit cell volumes of $LnNi_2P_2$ ounds which also indicates that Ce, Eu and Yb may be present in an intermediate e state. Intermediate valence of Eu in $EuNi_2Pi_2$ has been verified recently by ajan *et al* (1981, 1983) and Sampathkumaran *et al* 1982). Mixed valence of Eu lso be a feature in the arsenide and antimonide phases. As expected, the unit cell e increases on going from P to As to Sb for a given LnM_2X_2-system. Based on the tomic distance and unit cell volumes of the Co and Ni-containing phosphides, ko proposed an ionic formulation of the type $Eu^{2+}(Co^{2+}Co^{2+})\ P^{3-}P^{3-})$ and $Ni^{1+}Ni^{1+})\ (P_2)^{4-}$ where the M element is present in a low oxidation state. ailed physical property studies of the pnictide phases with the $Zr_2Fe_{12}P_7$- and Si_2-type structures are yet to be made. In view of the fact that metallic behaviour uperconductivity have been discovered in the related ternary phosphides P_{12} (M = Fe, Ru), it is possible that superconductivity may be exhibited by these excess ternary system of compounds as well.

rnary oxides

ry oxides with the perovskite (ABO_3-type) and spinel (AB_2O_4-type) structure are to be not very conducive to high T_c superconductivity (Nb-doped or reduced $_3$ has a $T_c \leq 1$ K; copper containing chalcogenide spinels, $CuRh_2X_4$, Se, have $T_c \leq 5$ K). However, one isolated example in each of the above structure s now known with $T_c \sim 11$–13·5 K: (i) $BaPb_{1-x}Bi_xO_3$ ($x = 0{\cdot}05$–$0{\cdot}3$) and $_{1+x}Ti_{2-x}O_4$ ($x = 0{\cdot}1$–$0{\cdot}3$). The compounds are type II superconductors. ght *et al* (1975) discovered that the orthorhombic $BaPbO_3$ and monoclinic $_3$ perovskites form complete series of solid solutions and superconductivity is induced for $x = 0{\cdot}05$–$0{\cdot}30$ in $BaPb_{1-x}Bi_xO_3$ whereas the end members ($x = 0$ a are metallic and semiconducting respectively. Later studies by Khan *et al* (1 Gilbert *et al* (1978, 1982) and Suzuki *et al* (1980) confirmed the above observatio samples in the bulk and thin-film form. Studies also showed that T_c increases about 9 K for $x = 0{\cdot}05$ to a maximum of about 13 K at $x = 0{\cdot}3$. For $x \geqslant 0{\cdot}3$ superconductivity is destroyed and in fact the phases are semiconducting in nature significant to note that T_c is maximum for that value of x which is slightly belo value where the metal-to-semiconductor transition sets in. One feature of perovskite system is that the superconducting transitions are broad (1–2 K widt measured by the Meisner effect. Initial experiments on alkali metal doping (at th site) indicated an improvement in the sharpness of the transition width wit affecting the T_c value for a given value of x. Later experiments showed that a excess of Pb (over the nominal x) also produces the same effect showing thereby th broad transition may be related to non-random distribution of Pb and Bi at site perovskite structure.

Since there are no d electrons in $BaPb_{1-x}Bi_xO_3$, the conduction band co overlapping Pb 6s and O 2p bands. Sleight *et al* (1975) proposed a schematic e level diagram to explain the observed properties.

$Li_{1+x}Ti_{2-x}O_4$ ($0{\cdot}1 < x \leqslant 0{\cdot}3$) was first synthesized by Johnston *et al* (1973) found to be superconducting with a high T_c ranging from 10–12 K. The homoge range for the spinel structure varies from $x = 0{\cdot}33$ ($a = 8{\cdot}36$ Å) to approxim $x = -0{\cdot}2$ ($a = 8{\cdot}4$ Å). The superconducting compositions are in the vicinity o metal-to-semiconductor transition since for $x \sim 0$–$0{\cdot}1$, the samples are metalli those with $x \approx 0{\cdot}15$–$0{\cdot}33$ are semiconductors. Maximum T_c is found for $x =$ drops abruptly for $x \approx 0{\cdot}05$–$0{\cdot}1$ to a value less than 1·5 K. Magnetic suscepti (Johnston 1976; Murphy *et al* 1982), heat capacity (McCallum *et al* 1976) and c field measurements (Roy *et al* 1977; Foner and McNiff 1976) confirm that superco tivity is a bulk property of the $LiTi_2O_4$ compound and the Ti 3d electron responsible for the observed behaviour.

9. Ternary chalcogenides

9.1 *Ternary molybdenum chalcogenides (Chevrel phases)*

The ternary molybdenum chalcogenides $A_xMo_6Ch_8$ (A = metal; $x = 0$–4; Ch = Te) represent a family of isostructural METS compounds with remarkable chemica physical properties. Many of them are high T_c ($\leqslant 15$ K) and high critical magneti ($H_{c2} \sim 600$ kOe) superconductors. Originally discovered in 1971, they have extensively investigated in recent years. The structure and chemistry of these phas well understood to a certain extent but a complete understanding of the ph properties including superconductivity, exciting new possibilities and phase eq rium relationships need a lot more future research. Excellent reviews are available literature and hence only a brief account will be presented here (Fischer 1978; 1979; Schöllhorn 1980, 1983a, b; Umarji 1980; Shenoy *et al* 1981; Subba Ra Shenoy 1981; Corbett 1981; Maple and Fischer 1982; Fischer and Maple 1982; C and Sergent 1982; Pobell *et al* 1982; Simon 1981; Poppe 1980).

9.1a *Structure and stoichiometry*: The compounds, $A_xMo_6Ch_8$, possess a hexa mbohedral crystal structure ($a \sim 6{\cdot}5$ Å; $\alpha \sim 90°$). The structure essentially consists rhombohedral stacking of Mo_6Ch_8 units in such a way that the A atoms occupy the ›ty channels. Each Mo_6Ch_8 unit consists of an octahedral cluster of Mo atoms osed in a slightly deformed cube of Ch atoms (figure 18). The intracluster and rcluster Mo–Mo distances are small (intra, 2·7 Å, same as that in Mo-metal; inter Å) with the result that strong metal–metal bonding exists within the cluster and ciently strong interactions exist between intercluster Mo–Mo atoms. The A atoms mostly the electropositive elements of the periodic table (figure 19). The :hiometry x in $A_xMo_6Ch_8$ and the site occupancy depends on the ionic radius of the etal. Small ionic radii elements (*e.g.*, Cu, Ni, Co etc) occupy the so-called off-channel tions (with essentially tetrahedral coordination of Ch atoms) and x can vary from On the other hand, large ionic radii elements (*e.g.*, Pb, Sn, La, Eu, Yb) occupy the ral channel positions (figure 18; essentially 8-fold coordination) and x is fixed and

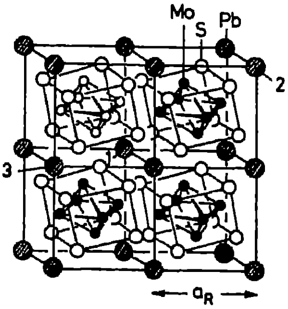

Figure 18. Structure of $PbMo_6S_8$. Mo_6S_8 unit is turned by ~27° with respect to rhombohedral cell vectors. Pb occupies the channel position.

Be											B	C	N	O	F
▨ Mg											▨ Al	Si	P	S	Cl y
▨ Ca	▨ Sc	▨ Ti	▨ V	▨ Cr	Mn	▨ Fe	▨ Co	▨ Ni	▨ Cu s	▨ Zn	▨ Ga	Ge	As	Se	Br y
▨ Sr	▨ Y	Zr	Nb x	Mo	Tc	Ru x	Rh x	▨ Pd	▨ Ag s	▨ Cd	▨ In	▨ Sn s	Sb	Te	I y
▨ Ba	▨ La s	Hf	Ta	W	Re x	Os	Ir	Pt	Au	▨ Hg	▨ Tl	▨ Pb s	Bi	Po	At
Ra	Ac														

▨ Ce	▨ Pr	▨ Nd	Pm	▨ Sm	▨ Eu	▨ Gd	▨ Tb	▨ Dy	▨ Ho	▨ Er	▨ Tm	▨ Yb s	▨ Lu
▨ Th	Pa	▨ U	▨ Np	▨ Pu	▨ Am	Cm	Bk	Cf	Es	Fm	Md	No	Lw

Figure 19. Partial periodic table showing the A elements (shaded) which form the $A_xMo_6Ch_8$ (Ch = S, Se) phases. s indicates the phases which have T_c between 8–15 K. Symbols x and y indicate that partial substitution is possible with these elements at the Mo and Ch site respectively (After Fischer 1978 with some modification).

close to 1. The A atoms effect an electronic charge transfer to the Mo_6Ch_8
essence, to the Mo-4*d* conduction band) (Fischer 1978; Ramasamy *et a*
Yashonath *et al* 1981; Freeman and Jarlborg 1982). Chevrel phases are ar
to chemical substitution at the A, Mo and Ch sites. In addition
$(A_{1-x}A'_x)Mo_6Ch_8$-type solid solutions, isostructural phases (Mo_2F
(Mo_4Ru_2)Se_8, ($Mo_{6-x}M_x$)Se_8, (M = Nb, Rh), $Mo_6Ch_6X_2$ (X = Cl,
$Cu_xMo_6S_6I_2$ and $Li_2Mo_6S_6Br_2$ have been isolated and studied (Fische
Radhakrishnan *et al* 1981; Umarji *et al* 1981a, b; Sankaranarayanan *et al* 1982
et al 1980; Behlok and Robinson 1983; Alekseevskii *et al* 1978, 1982). Inter
enough, and true to the nature of the channel structure, the A atoms, when small
Cu, Co, Ni), can be leached out by a simple mineral acid treatment or electroc
oxidation to give rise to the binary Mo_6Ch_8 compounds. Of course, the reverse
of insertion of foreign metal atoms into the channels of Mo_6Ch_8 to give ternarie
possible and has been studied (Fischer 1978; Schöllhorn 1980; Umarji *et al*

9.1b *Superconductivity and related properties*: The binary Mo_6Ch_8 anc
ternaries, $A_xMo_6Ch_8$ exhibit metallic behaviour, but with fairly high re
($\rho \sim 10^{-3}$ ohm cm). For A = alkali metal, post transition metal or rare ear
ternaries exhibit superconductivity. T_c values between 8–15 K are encounte
A = Pb, Sn, Cu, Ag, La and Yb. Binary Mo_6Se_8 has a T_c of 6·3 K whereas M
superconducting below 1 K and Mo_6Te_8 does not become superconducting u
lowest temperatures. $Mo_6S_6X_2$ (X = Br and I) exhibit a T_c of 13–14 K. M
susceptibility, heat capacity data and theoretical band structure calculations sh
there exists a large density of states at the Fermi level in $A_xMo_6Ch_8$ and the met
superconducting behaviour are exclusively due to the Mo-4*d* electrons (Fisch
Freeman and Jarlborg 1982; Andersen *et al* 1982). The number of electrons p
cluster (NEC) is an important parameter in determining the properties
it determines the occupancy of the 4*d*-conduction bands. For Mo_6S_8, NE
((6 × 6) – (2 × 8) and it becomes 21, 22 or 23 depending on the valency of A i
AMo_6S_8 (Ag, 20 + 1; Pb, 20 + 2; La, 20 + 3 etc) but the 4*d*-conduction ban
partially filled in these cases. Metallic and superconducting behaviour can
explained. Band structure calculation and also simple chemical bonding arg
predict that the 4*d*-subband will be completely filled for an NEC of 24 (a
Mo–Mo intracluster bonding, 12 edges in the Mo_6-octa cluster require 12 ×
electrons to form electron-pair bonds) and the material should exhibit semico
behaviour (because the upper lying Mo-4*d* subband is separated by an en
1–1·5 eV). Indeed, the compounds $Mo_2Re_4S_8$, $Mo_2Re_4Se_8$, Mo_4Ru_2S
$Cu_4^{1+}Mo_6S_8$ which possess an NEC of 24 are found to exhibit a semico
behaviour.

According to the McMillan-Allen-Dynes formalism of the original BCS theor
origin of superconductivity in a metal, T_c is directly dependent on the de
electronic states at the Fermi level, the electron-phonon interaction and phonor
of states, the latter being proportional to the Debye temperature. Measurem
todate show that the Chevrel phases satisfy all the criteria and no exotic mec
other than the phonon (BCS) mechanism need be invoked to explain the super
tivity. However, in the rare earth containing Chevrel phases, $LnMo_6S_8$, whic
antiferromagnetically at low temperatures, the superconducting state seem
modified to a non-BCS type due to a possible change in pairing (Ishikawa *et al* 1

sal correlation between T_c and known structural, chemical or physical parameters to exist in the Chevrel phases examined so far. A somewhat rough correlation xist between T_c and hexagonal lattice parameter ratio (c/a) in a related series of ounds but efforts to raise T_c beyond 15 K have not been successful. A detailed ation for the existence of very large critical fields in Chevrel phases has been led recently by Decroux and Fischer (1982).

Coexistence of superconductivity and magnetic order and the reentrant our: Rare earth Chevrel phases, $LnMo_6Ch_8$ (Ch = S, Se; Ln = rare earth or Y), t superconductivity (except for Ln = Ce, Eu) despite the fact that they contain tom % paramagnetic ions (*e.g.*, Ln = Tb, Dy, Ho, Er). This indicates that the tion of the *f*-electron spins with the Mo–4*d* conduction electrons is not much. etic susceptibility and other studies have shown that the rare earth is present as ion in $LnMo_6Ch_8$ phases (except Eu and Yb which are present in 2 + state) and nany of these support a large magnetic moment, there exists the possibility of ange magnetic order developing at low temperatures and still retain the onducting behaviour. Detailed studies by a variety of techniques including n diffraction have indeed shown that antiferromagnetism (with Néel temp., T_N) perconductivity (with transition temp. , T_c) in many of the Ln-Chevrel phases t with $T_N < T_c$ (table 3). The compound $HoMo_6S_8$ exhibits the interesting re- t behaviour similar to $ErRh_4B_4$ and other ternary systems (table 4). Neutron tion studies (Lynn 1983; Lynn *et al* 1981; 1983b) have shown that a sinusoidally ated magnetized state (with a period of 250 Å) coexists with superconductivity ove T_{c2} in $HoMo_6S_8$ analogous to the case of $ErRh_4B_4$. Coexistence of onductivity and ferromagnetism has been realized by Ishikawa *et al* (1982) in the ternary system $Ho_{1-x}Eu_xMo_6S_8$ (see table 4). Reentrant behaviour can be d in $DyMo_6S_8$ and $GdMo_6S_8$ to some extent by the application of magnetic imilar to the case of $LnRh_4B_4$ antiferromagnetic superconductors.

ondensed molybdenum cluster phases

y molybdenum compounds containing (Mo_9Ch_{11}), ($Mo_{12}Ch_{14}$) or $_2Ch_{6/2}$) (Ch = S, Se, Te) units resulting from a linear condensation of the dral Mo_6 clusters have been recently synthesized and studied. Representative unds are: $Ag_xMo_9Se_{11}$ ($x \approx 4$) (Gougeon *et al* 1983), $A_2Mo_9S_{11}$ (A = K, Tl), $_{15}S_{19}$, $A_2Mo_{15}Se_{19}$ (A = K, Ba, Tl), $In_xMo_{15}Se_{19}$ (x = 2·9–3·4) (Chevrel *et al* Chevrel and Sergent 1982), AMo_3S_3 (A = K, Rb, Cs) (Huster *et al* 1983) and Ch_3 (A = In, Tl; Ch = Se, Te) (Hönle *et al* 1980). The compounds crystallize with gonal symmetry. The *a* lattice parameter is ~ 9 Å but the *c* parameter varies with o_xCh_y content and decreases to a low value (~ 4·5 Å) for $x:y = 3:3$. The re of the $A_xMo_{15}Se_{19}$ phases is characterized by the presence of Mo_6Se_8 and $_{11}$ units, the latter resulting from a fusion of two Mo_6 octahedra along a on face, but all the Mo atoms have the same chalcogen environment as existing in evrel phases. The intracluster distance is small (~ 2·7 Å as in Chevrel phases) but uster distance is large (~ 3·4–3·5 Å). The indium and other A atoms are situated ree-dimensional network of channels similar to the $A_xMo_6Ch_8$ compounds (see All the phases examined so far are metallic and superconducting but T_c values are low (≤ 4·3 K). The $In_{2.9}Mo_{15}Se_{19}$ phase has been found to possess a relativ value of H_{c2} of 210 kOe.

10. Summary and conclusions

Metal excess ternary system (METS) of compounds are usually stoichiometric, l can be nonstoichiometric compounds (one of which is a nonmetal) occupy a dis or sets of crystallographic lattice sites and only a part of the valence electron metals are involved in chemical bonding with nonmetallic atom. The excess e are delocalized and whenever there is a strong metal–metal bonding (metallic bc compound exhibits a metallic behaviour. This is a necessary condition exhibition of superconductivity by any METS compound. Only a few of the large of known METS have been examined in detail till to-date. However, it is clear tha specific crystal structures and a specific type of bonding between the atoms in favourable for high T_c superconductivity. In fact Matthias and others have poi earlier that the high T_c exhibited by the $LnRh_4B_4$ and $A_xMo_6Ch_8$ phases is du presence of Rh and Mo clusters respectively. Similarly, the carbon atoms when inside an octahedra of metal atoms in the METS carbides give rise to superconductivity. However, from the preceding sections we note that high obtained whenever there is an inter-penetration of different types of clu condensation of metal atom clusters within the structure. Hence, the pre isolated metal atom and/or non metal atom clusters is favourable to superconductivity. Also, high crystal symmetry (cubic, rhombo or tetra) of the s appears to favour high T_c compared to the less symmetric structures compounds. The two isolated examples of the oxide systems show that electro perhaps also the crystal structure) instability induced by the compositional var a factor which governs the high T_c behaviour. Presumably this line of a extended to the METS may yield fruitful results in the search for new high T_c m Finally, we note that from the limited studies conducted on Co and Fe-co stannides and phosphides, the 3*d* transition metals need not be counted ou possible METS in the search for high temperature superconductivity.

Acknowledgements

Thanks are due to the Department of Science and Technology, Government New Delhi for the award of a research grant.

References

Adrian H, Müller R, Behrle R, Saemann-Ischenko G and Voit G 1981 Physica **B108** 1281
Alexkeevskii N E, Mitin A V, Bazan C, Dobrovolskii N M and Ronczka B 1978 *Sov. Phys.-JE*
Alexkeevskii N E, Mitin A V, Bazan C, Gren B and Folcik L 1982 *Solid State Commun.* **41** 56
Andersen O K, Klose W and Nohl H 1982a in *Superconductivity in ternary compounds I* (eds) Ø F
M B Maple (New York: Springer Verlag), Vol. 32
Andres K, Remeika J P, Espinosa G P and Cooper A S 1981 *Phys. Rev.* **B23** 1179
Ballestraci R 1976 *C.R.* (*Paris*) **282** 291
Barz H 1980 *Mater. Res. Bull.* **15** 1489
Barz H, Ku H C, Meisner G P, Fisk Z and Matthias B T 1980 *Proc. Natl. Acad. Sci. USA* **77**
Behlok R J and Robinson W R 1983 *Mater. Res. Bull.* **18** 1069

ı D J and Jeitschko W 1980a *J. Solid State Chem.* **32** 357

ı D J and Jeitschko W 1980b *J. Less Common Metals* **72** 147

ı D J and Jeitschko W 1980c *J. Less Common Metals* **76** 33

ı H F 1981 in *Ternary superconductors* (eds) G K Shenoy, B D Dunlap and F Y Fradin (New York lsevier: North Holland) p. 225

ı H F and Segre C U 1980 *Solid State Commun.* **35** 735

ı H F and Segre C U 1981 in *Ternary superconductors* (eds) G K Shenoy *et al* (New York: Elsevier North olland), p. 239

ı H F, Segre C U, Acker F, Rosenberg M, Dey S and Deppe P 1981 *J. Magn. Mag. Mater.* **25** 117

n H F, Yvon K and Braun R M 1980 *Acta. Crystallogr.* **B36** 2397

vski L N, Rusinov A I and Kulic M 1979 *Solid State Commun.* **30** 59

ion J D, Shenoy G K, Niarchos D, Viccaro P J and Falco C M 1980 *Phys. Lett.* **A79** 454

ion J D, Shenoy G K, Niarchos D, Viccaro P J, Aldred A T and Falco C M 1981 *J. Appl. Phys.* **52** 2180

avas J, Hodeau J L, Collomb A, Marezio M, Remeika J P and Vandenberg J M 1981 in *Ternary uperconductors* (eds) G K Shenoy, B D Dunlap and F Y Fradin (New York: Elsevier North Holland), 219

alier B, Cole A, Lejay P and Etourneau J 1981 *Mater. Res. Bull.* **16** 1067

alier B, Cole A, Lejay P, Vlasse M, Etourneau J, Hagenmuller P and Georges R 1982a *Mater. Res. Bull.* 7 251

alier B, Lejay P, Cole A, Vlasse M and Etourneau J 1982b *Solid State Commun.* **41** 801

alier B, Lejay P, Etourneau J and Hagenmuller P 1983 *Mater. Res. Bull.* **18** 315

alier B, Lejay P, Etourneau J, Vlasse M and Hagenmuller P 1982e *Mater. Res. Bull.* **17** 1211

alier B, Lejay P, Etourneau J, Vlasse M and Hagenmuller P 1982d *Proc. VII Intl. Conf. Solid Compds. ransition Elem., Grenoble, France*

alier B, Lejay P, Vlasse M, Etourneau J and Hagenmuller P 1982c *Proc. II Intl. Conf. on Solid State hemistry, Netherlands*

rel R, Sergent M and Prigent J 1971 *J. Solid State Chem.* 3 515

rel R, Potel M and Sergent M 1981 in *Ternary superconductors* (eds) G K Shenoy B D Dunlap and F Y radin (New York: Elsevier, North Holland) p. 7

rel R and Sergent M 1982 in *Superconductivity in ternary compounds I* (eds) Φ Fischer and M B Maple New York: Springer Verlag) p. 25

per A S 1980 *Mater. Res. Bull.* **15** 799

ett J D 1981 *J. Solid State Chem.* **39** 56

oux M and Fischer Φ1982 in *Superconductivity in ternary compounds II* (eds) M B Maple and Φ Fischer New York: Springer Verlag)

S K, Malik S K, Vijayaraghavan R and Wallace W E 1983 *J. Less Common Metals* **94** 266

hue P C and Bierstedt P E 1969 *Inorg. Chem.* **8** 2690

ıosa G P 1980 *Mater. Res. Bull.* **15** 791

ıosa G P, Cooper A S, Barz H and Remeika J P 1980 *Mater. Res. Bull.* **15** 1635

ıosa G P, Cooper A S and Barz H 1982 *Mater. Res. Bull.* **17** 963

r I and Nowik I 1983 *Solid State Commun.* **47** 831

l R A, Bhattacharjee J K and Bagchi A 1979 *Phys. Rev. Lett.* **43** 154

ıer Φ 1978 *Appl. Phys.* **16** 1

ıer Φ and Maple M B 1982 (eds) *Superconductivity in ternary compounds I* (New York: Springer Verlag)

Z, Lambert S E, Maple M B, Remeika J P, Espinosa G P, Cooper A S, Barz H and Oseroff S 1982 *Solid tate Commun.* **41** 63

r S and McNiff Jr E J 1976 *Solid State Commun.* **20** 995

man A J and Jarlborg T 1982 in *Superconductivity in ternary compounds II* (eds) M B Maple and Fischer (New York: Springer Verlag)

ert L R, Messier R and Roy R 1978 *Thin Solid Films* **54** 129; 1982 *Mater. Res. Bull.* **17** 467

geon P, Potel M, Padiou J and Sergent M 1983 *Compt. Rend* (*Paris*) **296** 351

nside H S, Blount E I and Varma C M 1981 *Phys. Rev. Lett.* **46** 49

tner A and Yvon K 1979 *Acta Crystallogr.* **B35** 451

ıaker H C, Woolf L D, Mackay H B, Fisk Z and Maple M B 1979 *Solid State Commun.* **32** 289

ıaker H C and Maple M B 1981 in *Ternary superconductors* (eds) G K Shenoy, B D Dunlap and Y Fradin (New York: Elsevier North Holland) p. 201

ıaker H C, Ku H C and Maple M B 1982 *Solid State Commun.* **43** 455

Hodeau J L, Chenavas J, Marezio M and Remeika J P 1980 *Solid State Commun.* **36** 839

Hönle W, Von Shnering H G, Lipka A and Yvon K 1980 *J. Less Common Metals* **71** 135

Hovestreydt E, Engel N, Klepp K, Chebot B and Parthe E 1982 *J. Less Common Metals* **85** 247

Hull G W, Wernick J H, Geballe T H, Waszczak J V and Bernardini J E 1981 *Phys. Rev.* **B24** 6715

Hulliger F 1981 in *Structure and bonding in crystals* (New York: Academic Press) Vol. II

Huster J, Schippers G and Bronger W 1983 *J. Less Common Metals* **91** 333

Ishikawa M, Sergent M and Fischer Φ 1981 *Phys. Lett.* **A82** 30

Ishikawa M, Fischer O and Muller J 1982 in *Superconductivity in ternary compounds II* (eds) M B Maple
O Fischer (New York: Springer Verlag)

Jacobson R A 1983 *J. Less Common Metals* **92** 177

Jaric M V 1979 *Phys. Rev.* **B20** 4486

Jaric M V 1980 *Phys. Rev.* **B22** 463

Jeitschko W and Braun D 1977 *Acta Crystallogr.* **B33** 3401

Jeitschko W, Braun D J, Ashcraft R H and Marchand R 1978 *J. Solid State Chem.* **25** 309

Jeitschko W and Jaberg B 1980 *J. Solid State Chem.* **35** 312

Jeitschko W, Nowotny H and Benesovsky F 1963 *Monatsch. Chem.* **94** 247, 332

Johnson V and Jeitschko W 1972 *J. Solid State Chem.* **4** 123

Johnston D C 1976 *J. Low Temp. Phys.* **25** 145

Johnston D C 1977 *Solid State Commun.* **24** 699

Johnston D C 1981 *Physica* **B108** 755

Johnston D C 1982 *Solid State Commun.* **42** 453

Johnston D C and Braun H F 1982 in *Superconductivity in ternary compounds II* (eds) M B Maple
Φ Fischer (New York: Springer Verlag) p. 11

Johnston D C, Prakash H, Zachariasen W H and Viswanathan R 1973 *Mater. Res. Bull.* **8** 777

Johnston J, Toth L, Kennedy K and Parker E R 1964 *Solid State Commun.* **2** 123

Khan Y, Nahm K, Rosenberg M and Willner H 1977 *Phys. Status Solidi* **39** 79

Klepp K and Parthe E 1982 *Acta Crystallogr.* **B38** 1541

Ku H C 1980 Ph.D. Diss., Univ. Calif. San Diego USA

Ku H C and Acker F 1980 *Solid State Commun.* **35** 937

Ku H C, Acker F and Matthias B T 1980 *Phys. Lett.* **A76** 399

Ku H C, Johnston D C, Matthias B T, Barz H, Burri G and Rinderer L 1979 *Mater. Res. Bull.* **14**

Ku H C, Meisner G P, Acker F and Johnston D C 1980 *Solid State Commun.* **35** 91

Ku H C and Meisner G P 1981 *J. Less Common Metals* **78** 99

Ku H C and Shelton R N 1980 *Mater. Res. Bull.* **15** 441

Ku H C and Shelton R N 1981 *Solid State Commun.* **40** 237

Kumagai K, Inoue Y, Kohori Y and Asayama K 1981 in *Ternary superconductors* (eds) G K Shenoy,
Dunlap and F Y Fradin (New York: Elsevier, North Holland), p. 185

Kuz'ma, Yu B and Bilonizhko N S 1972 *Sov. Phys. Crystallogr.* **16** 897

Kuz'ma, Yu B, Kripyakevich P I and Bilonizhko N S 1969 *Dopavidi. Akad. Nauk. Ukr. RSR Ser.* A(10

Kuz'ma, Yu B, Bilonizhko N S, Mykhalenko S L, Stepanchikova G F and Chaban N F 1979 *J. Less. Co*
Metals **67** 51

Lambert S E, Fisk Z, Hamaker H C, Maple M B, Woolf L D, Remeika J P and Espinosa G P 19
Ternary superconductors (eds) G K Shenoy, B D Dunlap and F Y Fradin (New York: Elsevier,
Holland), p. 247

Lander G H, Sinha S K and Fradin F Y 1979 *J. Appl. Phys.* **50** 1990

Lejay P, Chevalier B, Etourneau J, Hagenmuller P and Peshev P 1981a *Synth. Metals* **4** 139

Lejay P, Chevalier B, Etourneau J and Hagenmuller P 1981b *J. Less Common Metals* **82** 193

Lynn J W, Shirane G, Thomlinson W and Shelton R N 1981 *Phys. Rev. Lett.* **46** 368

Lynn J W 1983 *J. Less Common Metals* **94** 75

Lynn J W, Pynn R, Joffrin J, Ragazzoni J L and Shelton R N 1983a *Phys. Rev.* **B27** 581

Lynn J W, Shelton R N, Horng H E and Glinka C J 1983b (to be published)

Machida K and Matsubara T 1979 *Solid State Commun.* **31** 791

Mackay H B, Woolf L D, Maple M B and Johnston D C 1980 *J. Low Temp. Phys.* **41** 639

Mahanti S D, Sinha K P and Atre M V 1981 *J. Low Temp. Phys.* **44** 1

Malik S K, Dhar S K, Vijayaraghavan R and Wallace W E 1982 *J. Appl. Phys.* **53** 8074

Maple M B 1976 *Appl. Phys.* **9** 179

Maple M B and Fischer Φ 1982 *Magnetic superconductors in Superconductivity in ternary compoun*

:s *in Current Phys.* (eds) M B Maple and O Fischer (New York: Springer Verlag) **34**
ɅI B, Hamaker H C and Woolf L D 1982 in *Superconductivity in ternary compounds II* (eds)
Maple and Φ Fischer (New York: Springer Verlag)
ıd R and Jeitschko W 1978 *J. Solid State Chem.* **24** 351
oto H, Umezawa H and Tachiki M 1979 *Solid State Commun.* **31** 157
ȝ B T, Geballe T H and Compton V B 1963 *Rev. Mod. Phys.* **35** 1
s B T, Corenzwit E, Vandenberg J M and Barz H 1977 *Proc. Natl. Acad. Sci.* (*USA*) **74** 1334
ȝ B T, Marezio M, Corenzwit E, Cooper A S and Barz H 1972 *Science* (*USA*) **175** 1465
ım R W, Johnston D C, Luengo C A and Maple M B 1976 *J. Low Temp. Phys.* **25** 177
G P 1981 *Physica* **B108** 763
G P, Ku H C and Barz H 1983 *Mater. Res. Bull.* **18** 983
n D E, McWhan D B, Eckert J, Shirane G and Thomlinson W 1977 *Phys. Rev. Lett.* **39** 1164
n D E, McWhan D B, Schmidt P H, Shirane G, Thomlinson W, Maple M B, Mackay H B, Woolf L D,
Z and Johnston D C 1980 *Phys. Rev. Lett.* **45** 2060
ɩ, Shelton R N, Richardson Jr J W and Jacobson R A 1983 *J. Less Common Metals* **92** 177
D W, Greenblatt M, Zahurak S M, Cava R J, Waszezak J V, Hull Jr G W and Hutton R S 1983 *Rev.*
'him. Miner. **19** 441
ın R, Sampathkumaran E V, Gupta L C, Vijayaraghavan R, Prabhawalkar V, Bhaktdarshan and
lia B D 1981 *Phys. Lett.* **A84** 275
ın R, Sampathkumaran E V, Vijayaraghavan R and Shenoy G K 1983 *J. Less Common Metals* **94** 265
V and Ott H R 1979 *Phys. Lett.* **A70** 480
Odoni W, Fisk Z and Remeika J P 1981 in *Ternary superconductors* (eds) G K Shenoy, B D Dunlap
F Y Fradin (New York: Elsevier, North Holland), p. 251
, Chevrel R, Sergent M and Fischer Φ 1980 *J. Solid State Chem.* **33** 43
, Sergent M and Prigent J 1973 *C.R. Acad. Paris* **C277** 465
, Rainer D and Wühl H 1982 in *Superconductivity in ternary compounds I*, Chapter 7 (eds) Φ Fischer
M B Maple (New York: Springer Verlag)
J 1980 Ph.D. Thesis, JÜL-Report 1635, West Germany
ishnan T S, Janawadkar M P, Devare S H, Devare H G, Pillai T, Janaki R, Umarji A M and Subba
G V 1981 in *Ternary superconductors* (eds) G K Shenoy, B D Dunlap and F Y Fradin (New York:
ier North Holland), p. 91
shnan T V and Varma C M 1981 *Phys. Rev.* **B24** 137
ny S, Nagarajan T, Umarji A M and Subba Rao G V 1981 *Phys. Lett.* **A81** 71
J P, Espinosa G P, Cooper A S, Barz H, Rowell J M, McWhan D B, Vandenberg J M, Moncton D E,
Z, Woolf L D, Hamaker H C, Maple M B, Shirane G and Thomlinson W 1980 *Solid State Commun.*
23
979 *Monatsh Chem.* **110** 235
980 *Monatsh Chem.* **111** 517
Das Gupta A and Koch C C 1977 *IEEE Trans. on Magnetics* **MAG-13** 836
ınd Jeitschko W 1979 *Mater. Res. Bull.* **14** 513
ıst S and Nawapong P C 1966 *Acta Chem. Scand.* **20** 2250
ist S and Tansuriwongs P 1967 *Acta Chem. Scand.* **21** 813
Tachiki M, Koyama T, Matsumoto H and Umezawa H 1981 *Phys. Rev.* **B24** 3830
ıkumaran E V, Gupta L C and Vijayaraghavan R 1982 *Phys. Lett.* **A88** 180
narayanan V, Rangarajan G, Srinivasan R, Umarji A M and Subba Rao G V 1982 *Cryogenics* **22** 305
ırn R 1980 *Angew. Chem. Int. Ed. Engl.* **19** 983
ırn R 1983a in *Inclusion compounds* (eds) J L Atwood, D E D Davies and D D MacNicol (New York:
emic Press)
ırn R 1983b *Comments in Inorg. Chem.* **2** 271
U and Braun H G 1981 *Phys. Lett.* **A85** 372
U, Braun H F and Yvon K 1981 in *Ternary superconductors* (eds) G K Shenoy, B D Dunlap and F Y
in (New York: Elsevier North Holland), p. 243
M, Fischer Φ, Decroux M, Perrin C and Chevrel R 1977 *J. Solid State Chem.* **22** 87
R N 1978 *J. Less Common Metals* **62** 191
R N and Johnston D C 1978 in *High pressure and low temperature physics* (eds) C W Chu and J A
am (New York: Plenum) p. 409
R N, Karcher B A, Powell D R, Jacobson R A and Ku H C 1980a *Mater. Res. Bull.* **15** 1445

Shelton R N, Segre C U and Johnston D C 1980b *Solid State Commun.* **33** 843

Shenoy G K, Dunlap B D, Fradin F Y, Sinha S K, Kimbal C W, Potzel W, Probst F and Kalvi
Phys. Rev. **B21** 3886

Shenoy G K, Dunlap B D and Fradin F Y 1981 (eds) *Ternary superconductors* (New York: El
Holland)

Shenoy G K, Probst F, Cashion J D, Viccaro P J, Niarchos D, Dunlap B D and Remeika J P 198
Commun. **37** 53

Shenoy G K, Noakes D R and Meisner G P 1982 *J. Appl. Phys.* **53** 2628

Shoemaker C B and Shoemaker D P 1965 *Acta Crystallogr.* **18** 900

Simon A 1981 *Angew Chem. Int. Ed. Engl.* **20** 1

Sinha S K, Crabtree G W, Hinks D G and Mook H 1982 *Phys. Rev. Lett.* **48** 950

Sleight A W, Gillson J L and Bierstedt P L 1975 *Solid State Commun.* **17** 27

Stewart G R, Meisner G P and Ku H C 1982 in *Superconductivity in d- and f-band metals,* (eds)
W Weber *Kernforschungszentrum Karlsruhe GmbH, Karlsruhe,* p. 331

Subba Rao G V and Shenoy G K 1981 in *Current trends in magnetism* (eds) N S Satyamurthy and
Rao, *Indian Phys. Assoc. Bombay*

Suhl H 1978 *J. Less Common Metals* **62** 225

Suzuki M, Murakami T and Inamura T 1980 *Jpn. J. Appl. Phys.* **19** 72

Suzumura Y and Nagi A D S 1982 *Solid State Commun.* **41** 413

Toth L E 1967 *J. Less Common Metals* **13** 129

Umarji A M 1980 Ph.D. Thesis, IIT Madras (Unpublished)

Umarji A M, Subba Rao G V, Janawadkar M P and Radhakrishnan T S 1980 *J. Phys. Chem.*

Umarji A M, Subba Rao G V, Janawadkar M P and Radhakrishnan T S 1981a *Solid State C*

Umarji A M, Subba Rao G V, Sankaranarayanan V, Rangarajan G and Srinivasan R 1981
superconductors (eds) G K Shenoy, B D Dunlap and F Y Fradin (New York: Elsevier North
91

Vandenberg J M 1980 *Mater. Res. Bull.* **15** 835

Vandenberg J M and Barz H 1980 *Mater. Res. Bull.* **15** 1493

Vandenberg J M and Matthias B T 1977 *Proc. Nat. Acad. Sci. USA* **74** 1336

Woolf L D, Johnston D C, Mackay H B, McCallum R W and Maple M B 1979 *J. Low Temp.*

Yashonath S, Hegde M S, Sarode P R, Rao C N R, Umarji A M and Subba Rao G V 1981 *Solid St*
37 325

Yvon K 1979 in *Current topics in Materials Science* (eds) E Kaldis (Amsterdam: North Holl

Yvon K and Grüttner A 1980 in *Supercondictivity in d- and f-band metals* (eds) H Suhl and M B
York: Academic Press), p. 515

Yvon K and Johnston D C 1982 *Acta Crystallogr* **B38** 247

ater. Sci., Vol. 6, No. 2, May 1984, pp. 317–325. © Printed in India.

electric materials

M R SRINIVASAN

Materials Science Group, Tata Institute of Fundamental Research, Bombay 400005, India

Abstract. This paper presents a review of pyroelectric materials. The physics of pyroelectric materials is described. Various pyroelectric materials are compared for their efficiency in the detection of radiation. Current trends in pyroelectric material technology are highlighted.

Keywords. Pyroelectricity; ferroelectricity; piezoelectricity.

ntroduction

been known for a long time that some crystals exhibit electric polarization when
emperature is changed. This phenomenon is known as pyroelectricity and arises
the temperature dependence of spontaneous polarization in these crystals. The
lectric polarization, however, does not persist for a long time and gets neutralized
imperfect insulation and the presence of free charges in the crystal. While all the
lectric crystals are necessarily pyroelectric, the converse need not be true. A built-
mmetry in the crystal structure hindering the polarization reversal or a high
ve field exceeding the limit of electrical breakdown might prevent a pyroelectric
being a ferroelectric.

antitatively, the pyroelectric effect could be described by the equation

$$\Delta P_i = p_i \Delta T,$$

ΔT denotes the change in temperature, $\Delta P_i (i = 1, 2, 3)$ are the changes in the
onents of polarization P in the three-dimensional space and p_i are the
ponding pyroelectric coefficients. p is a vector property and by Neuman's
ple ought to remain invariant under all the symmetry operations of the crystal
1962). Hence pyroelectricity can be exhibited only by crystals belonging to the ten
classes 1, 2 m, 2 mm, 3, 3 m, 4, 4 mm, 6 and 6 mm.

ay be pointed out here that in some crystals polarization may appear under the
nce of hydrostatic pressure and this is a special case of piezoelectric effect. Since
static pressure is a scalar-like temperature this polarization linearly proportional
hydrostatic pressure can also be treated on par with pyroelectricity. Thus the
lectric effect under hydrostatic pressure can occur only in the above mentioned
lar classes. In general the piezoelectric effect has the mathematical character of a
rank tensor and is restricted only to 20 non-centrosymmetric classes excluding the
432. Thus the symmetry permits all the pyroelectric crystals to be piezoelectric
the converse is not true. Therefore it is possible to imagine two possible
butions to pyroelectricity in the following way. Experimentally to observe
lectricity one can heat the crystal and observe the change in polarization. The
iment could be performed in two ways. Either the shape and size of the crystal can

be kept fixed during the heating or the crystal may be released so that th expansion can occur quite freely. Obviously the magnitude of the effect observed i two cases will be different. In the first case the crystal is clamped and the observed may be regarded as the primary pyroelectricity. In the second case, in addition t primary effect, there is pyroelectric effect due to the variation of piezoelectri induced polarization with temperature. This is known as the secondary pyroelect The secondary pyroelectricity is found to contribute substantially to the total e

Hence for a free crystal the total pyroelectric effect could be written as

$$(\mathrm{d}P/\mathrm{d}T)_{\sigma,E} = (\mathrm{d}P/\mathrm{d}T)_{S,E} + (\mathrm{d}P/\mathrm{d}S)_{T,E}(\mathrm{d}S/\mathrm{d}T)_{\sigma,E}$$

where σ, S and E denote the stress, strain and electric field respectively. Equatic could be written as

$$\begin{aligned} p^{\sigma,E} &= p^{S,E} + (\mathrm{d}P/\mathrm{d}\sigma)_{T,E}(\mathrm{d}\sigma/\mathrm{d}S)_{T,E}(\mathrm{d}S/\mathrm{d}T)_{\sigma,E} \\ &= p^{S,E} + \mathrm{d}^{T,E}_{ijk} C^{T,E}_{jklm} \alpha^{\sigma,E}_{jk}, \end{aligned}$$

where $p^{\sigma,E}$ is the total pyroelectric coefficient; $p^{S,E}$ is the primary pyroelectric coeffi d_{ijk}, C_{jklm} and α_{jk} denote respectively the piezoelectric moduli, elastic compl coefficients and coefficients of thermal expansion. Clearly the secondary pyroel coefficient is given by the product of d_{ijk}, C_{jklm} and α_{jk}. Though secor pyroelectricity is due to piezoelectricity, only those piezoelectric crystals which b to the ten polar classes are permitted by crystal symmetry to exhibit secor pyroelectricity.

So far we have tacitly assumed that the temperature of the crystal is the same points. Uneven heating causes temperature gradients, which by thermal expansior rise to non-uniform stresses and strains. Under such conditions it is possibl piezoelectric crystals like α-quartz, which does not belong to the ten polar class exhibit secondary pyroelectricity. This secondary pyroelectricity due to non-uni heating is called the tertiary pyroelectric effect. The tensorial pyroelectricity ref the production of quadrupole or higher electric moments on heating.

2. Theory of pyroelectricity

In principle, in order to understand pyroelectricity in any material, one has to con the various mechanisms of the spontaneous polarization (such as ionic, elect orientational or surface charge) and study their variation with temperature. pyroelectric behaviour is fully described by the temperature variation of pyroel coefficient. Actually, it is convenient to consider the temperature variation of pri and secondary pyroelectric coefficients separately. The temperature variatic secondary pyroelectric coefficient is governed by those of piezoelectric moduli, e compliance constants and thermal expansion coefficients. Both piezoelectric m and elastic compliance constants are not strong functions of temperature, in crystals which do not undergo any phase transition. Hence the temperature variati secondary pyroelectric coefficient is akin to those of thermal expansion coeffic Conceptually, the origin of primary pyroelectric effect and its variation temperature is more difficult to visualise and has invoked considerable discussion i literature.

'he lattice dynamical theory of primary pyroelectricity for the case of ionic crystals first formulated by Max Born in the year 1945 (Born 1945). In this paper, Born had icated that primary pyroelectric coefficient would be proportional to T, though in his r treatise on lattice dynamics he predicted the T^3 law for the pyroelectric coefficient rn and Huang 1954). Recently Szigeti has brought out clearly many salient features he theory, especially the role of mechanical and electrical anharmonicity in primary ɔelectricity which in fact was overlooked by Born (Szigeti 1975, 1976).

ı the case of ionic crystals, there are two important mechanisms of polarization. ; being responsible for absorption in the infrared *i.e.* the lattice or ionic polarization the other in the ultraviolet *i.e.* the electronic polarization. In the very simplest and le model known as the rigid ion model, the electron cloud around the ion is assumed e rigid and consequently there is no contribution from electronic polarization. For ı a model, the total dipole moment of the crystal is given by

$$M = \sum_a \alpha_a Q_a,$$

re Q_a are the active normal coordinates *i.e.* those which produce uniform ırization in the direction of M., α_a are suitable normalizing constants.

[owever, in reality the electrons are deformed during the lattice vibrations as they ɜrience short range forces and also the dipolar field due to ions. The electron ›rmation is not just linearly proportional to lattice displacements but involves ıer terms as well. Hence when one takes into consideration the electronic ırization also, the dipolemoment of the crystal is given by

$$M = \sum_a \alpha_a Q_a + \sum_{jj'} \beta_{jj'} Q_j Q_{j'} + . \tag{3}$$

important point to note is that α_a includes both the effects due to lattice lacements and also the first order effects due to electron deformation. The above 'ession for the dipolemoment clearly implies the presence of electrical anharmo- :y in the crystal.

or the case of harmonic crystal, the potential energy is proportional to the square of normal coordinates. In reality crystals are not harmonic and the mechanical ırmonicity has to be taken into account. For such a crystal the potential energy ›lves the cubic and higher powers of the normal coordinates

$$W = \tfrac{1}{2} \sum_j \omega_j^2 Q_j^2 + \sum_{jj'j''} b_{jj'j''} Q_j Q_{j'} Q_{j''} + . \tag{4}$$

he primary pyroelectric coefficients $p^{S,E}$ could be expressed in terms of coefficients ɔh appear in the expansion of dipolemoment and potential energy (*i.e.* (3) and (4)).

$$p^{S,E} = \sum_j \left(\beta_{jj} - \sum_a \frac{\alpha_a b_{ajj}}{\omega_a^2} \right) \frac{C_j}{\omega_j^2}. \tag{5}$$

ɜ C_j is the contribution of the jth mode to the specific heat and is given by $(\partial \bar{n}_j / \partial T)$, $\bar{n}_j$ being the average occupation number of the phonons with energy $\hbar\omega_j$. rom the above expression, it could be shown that under Debye's approximation ıch actually involves invoking some properties of β_{jj} and b_{ajj} in the long wavelength t), the primary pyroelectric coefficient obeys T^3 law. But as has been rightly pointed out by Szigeti, in the case of complex polyatomic crystals, optic modes can hav low frequencies and hence the T^3 behaviour is observed only at very low tempera At this stage, it is also necessary to emphasize the role of both electrical and mech anharmonicity in primary pyroelectricity. Since the primary pyroelectric effect do involve thermal expansion, for quite some time, it was regarded that only the ele anharmonicity was responsible for primary pyroelectricity. It may be mentione thermal expansion is the result of mechanical anharmonicity. However, fro expression for primary pyroelectric coefficient, it is evident that the part pla mechanical anharmonicity cannot be neglected.

3. Pyroelectric detector and the figure of merit of pyroelectric materials

If the temperature change in a pyroelectric material is caused by the absorpt radiation, the observation of pyroelectric effect is equivalent to the detection radiation (Lecomte 1948). Basically, a pyroelectric detector consists of pyroelectric crystal oriented with the electrode surface normal to its polari vector. On absorbing the incident radiation the temperature of the pyroelectric m changes, which in turn changes the electric polarization. Thus pyroelectric m forms a capacitive element, the capacitance varying with temperature. The ca will deliver a current

$$i = pA\,(\mathrm{d}T/\mathrm{d}t),$$

where P is the pyroelectric coefficient, A is the electrode surface area and $(\mathrm{d}T/\mathrm{d}t$ rate of temperature change.

Since the pyroelectric current is proportional to the rate of temperature chan device gives a steady output only if there is continuous variation in the tempera the pyroelectric crystal due to modulation, pulsing or chopping of incident rad When the incident radiation is not modulated, pulsed or chopped, the device g output only till the time the pyroelectric crystal attains a steady temperature.

It must be noted that if the input radiation is slow compared to the t relaxation time of the crystal, the temperature essentially remains constant a current response is low. For input frequencies higher than the thermal rela frequency full current response results because the absorbed energy goes in heating of the crystal. The thermal relaxation frequency is given by

$$f_{\text{thermal}} = G/2\pi H,$$

where G is the thermal conductance between the crystal and the surroundings a the total heat capacity of the crystal. For a given crystal material and size, the t relaxation frequency is governed by conductance. Since the pyroelectric dete made to respond to rate of change of temperature, it differs from other t detectors. The fact that the crystal does not have to come to thermal equilibriu the case of thermocouples and thermistors allows the pyroelectric detector to r faster than other thermal detectors and still be sensitive to a wide spectrum of ra wavelengths.

The performance of the pyroelectric detector is usually described by responsivity (*i.e.* the pyroelectric voltage output per unit energy of incident rad and detectivity (*i.e.* the inverse of noise equivalent power (NEP) where NEP is def cident energy required to produce a signal equal to that of detector noise). The ;e responsivity as well as the detectivity depend not only on the particular lectric material but also on the characteristics of the amplifier employed for :ing the pyroelectric voltage. The detailed theory of pyroelectric detector has been ›sed by several workers (Lang 1971; Liu 1978). It is sufficient for our purpose to that the voltage responsivity is proportional to $p(\varepsilon c)^{-1}$ while the detectivity is ›rtional to $p(c(\varepsilon \tan\delta)^{1/2})^{-1}$, where p is the pyroelectric coefficient, ε is the tric constant, $\tan\delta$ is the loss tangent and c is the specific heat. Hence $p(\varepsilon c)^{-1}$ and $\tan\delta)^{1/2})^{-1}$ could be regarded as the figures of merit of pyroelectric materials. ly, in the case of pyroelectric materials which are also ferroelectric the dielectric ınt and the pyroelectric coefficient are strong functions of temperature and so is figure of merit. It could be shown that the figure of merit is maximum at the :rature corresponding to the stability limit of the ferroelectric phase (Liu 1978).

'yroelectric materials

ıportant component of pyroelectric detector technology pertains to the prepar- of suitable pyroelectric materials. Since every pyroelectric material has its own ıtages as well as disadvantages, a wide choice of pyroelectric materials is necessary ›nly for improving the detector performance but also to cater to specific :ations of detectors. With the discovery of ferroelectricity in a large number of ials, the choice of pyroelectric materials has increased. In the beginning, the ials that were examined for pyroelectric detection included triglycine sulphate arium titanate, which were among the few well-known ferroelectrics at that time. ent years, a number of titanates, niobates, tantalates, zirconates, germanates and ıers have been studied for pyroelectric detection.

ırt from the study of new pyroelectric materials, another aspect of material ɔlogy pertains to the modification of material properties with a view to enhance :tector performance. Dielectric constant and dielectric loss are quite sensitive to ıts and also to radiation damage and hence can be monitored to some extent. nts also increase the coercive field and thus can be employed for obtaining single in crystals, which are superior to multidomain ones. A number of mixed lectric materials like strontium barium niobate, potassium tantalate niobate, lead ıate titanate etc exhibit ferroelectricity over a wide range of composition of their tuents. In these crystals, it is possible to alter the curie temperature and lectric coefficient by varying the composition. This property also has been made f for improving the detector efficiency. Table 1 summarises the pyroelectric ials studied so far along with their figures of merit for voltage responsivity and :ivity.

: choice of the pyroelectric material is mainly determined by (a) its figure of merit, ıe detector size, (c) availability and durability of the pyroelectric material, ıvironment in which the material has to operate, (e) the radiation levels to be :ed, (f) the purpose for which the detector is employed, (g) the maximum :nt temperature of operation and the range over which stable operation is desired. : importance of factors (b) and (c) in the choice of pyroelectric material does not nuch of an explanation. It should be possible to grow large crystals of pyroelectric ial and fabricate them into thin slices. The durability is also an important factor.

Table 1. Figure of merit for various pyroelectric materials.

Material	T(°C) (1)	ε (2)	p ($\times 10^{-8}$) (3)	c (4)	s (5)	ρ (6)	FM-R ($\times 10^{-10}$) (7)	FM-D* ($\times 10^{-4}$) (8)	I
TGS (T_c = 49°C)	0	20	1·3	2·3	—	$2{\cdot}4 \times 10^{10}$	2·8	8·8	Bee
	25	35	4·0	2·5	1·66	$1{\cdot}7 \times 10^{10}$	4·6	20·9	(19
	40	100	12.0	2·8	—	$1{\cdot}6 \times 10^{9}$	4·3	17·1	
	−25	20	0·44	—	—	$1{\cdot}1 \times 10^{10}$	0·96	2·0	
DTGS (T_c = 61°C)	0	12	0·84	2·4	—	$5{\cdot}0 \times 10^{10}$	2·9	7·8	Bee
	25	18	2·7	2·5	1·7	$5{\cdot}0 \times 10^{10}$	6·0	24·2	(19
	50	60	10·0	2·8	—	$1{\cdot}2 \times 10^{10}$	6·0	39·2	
	−25	11	0·42	—	—	$1{\cdot}8 \times 10^{10}$	1·6	2·4	
LATGS (T_c = 49·5°C)	30	35	7·0	2·55	1·7	—	7·8	—	Ga Sha
DLATGS (T_c = 49·2°C, 61·2 °C)	25	22	2·5	2·55	1·7	—	4·4	—	Ga Sha
TGFB (T_c = 73·8°C, (73 °C)	30	15	2·1	1·68	1·66	—	8·3	—	Ga Sha
DTGFB (T_c = 74·5°C)	25	12	2·5	1·87	1·7	—	11·1	—	Ga Sha
TGSE (T_c = 22°C)	21	400	3·0	1·79	1·7	—	0·4	—	Ga Sha
$BaTiO_3$ (T_c = 135°C)	25	135	1·9	—	—	—	0·47	—	Bee
	60	200	7·0	3·0	6·0	$6{\cdot}0 \times 10^{6}$	1·17	0·57	(19
	100	400	20·0	—	—	—	1·67	—	
$PbTiO_3$ (T_c = 492°C)	25	142	2·7	3·2	7·78	$5{\cdot}3 \times 10^{8}$	0·59	1·90	Bee (19
$PbTiO_3$ (Matsuohita) (T_c = 470°C)	25	200	6	3·2	7·78	—	0·93	—	
$LiNbO_3$ (T_c = 1210°C)	25	30	0·4	—	—	$9{\cdot}8 \times 10^{10}$	0·48	—	Bee
	100	31	0·5	2·8	4·64	6×10^{10}	0·58	4·5	(19
	−25	51	2·1	3·0	—	$5{\cdot}3 \times 10^{10}$	1·4	16·1	
$LiTaO_3$ (T_c = 618°C)	0	52	2·2	3·0	—	$4{\cdot}4 \times 10^{10}$	1·4	15·4	Bee
	25	54	2·3	3·16	7·45	$3{\cdot}6 \times 10^{10}$	1·35	13·8	(19
	50	56	2·5	3·3	—	$2{\cdot}9 \times 10^{10}$	1·3	12·9	
	100	60	2·7	3·5	—	$2{\cdot}0 \times 10^{10}$	1·3	10·9	
PZT4 (clevite)	25	1400	3·7	3·0	7·5	$3{\cdot}2 \times 10^{8}$	0·087	2·2	Bee (19
(T_c = 328°C)	−25	1410	4·6	—	—	$6{\cdot}2 \times 10^{7}$	0·109	1·21	
PZTG-1306 (Gulton) (T_c = 290°C)	0	1570	4·6	—	—	$5{\cdot}9 \times 10^{7}$	0·098	1·18	Bee
	25	1730	4·6	3·0	7·6	$5{\cdot}7 \times 10^{7}$	0·089	1·16	(19
	50	1900	4·6	—	—	$5{\cdot}4 \times 10^{7}$	0·081	1·13	
	100	2330	4·6	—	—	$4{\cdot}9 \times 10^{7}$	0·066	1·07	
PZT.HST-41 (T_c = 270°C)	25	1800	2·0	3·0	7·6	$4{\cdot}5 \times 10^{7}$	0·037	0·45	Bee
	−25	640	4·0	—	—	$7{\cdot}8 \times 10^{7}$	0·24	1·36	(19
PZT5 (T_c = 365°C)	—	2100	4·7	3·0	7·75	—	0·075	—	Ga Sh

Table 1. (*contd*)

l	(1)	(2)	(3)	(4)	(5)	(6)	(7)	(8)	(9)
5) 0°C)	—	515	3·5	—	8·0	—	—	—	Garn and Sharp (1974)
5) 0°C)	—	600	3·9	—	7·95	—	—	—	Garn and Sharp (1974)
	0	740	4·8	—	—	$4{\cdot}8\times10^{7}$	0·25	1·28	Beerman (1975)
))	25	870	5·6	2·6	7·85	$3{\cdot}0\times10^{7}$	0·25	1·18	
8°C)	50	1020	6·3	—	—	$2{\cdot}0\times10^{7}$	0·24	1·09	
	100	1400	7·6	—	—	$1{\cdot}3\times10^{7}$	0·21	1·06	
) 5°C)	—	680	5·2	—	7·90	—	—	—	Beerman (1975)
35) 5°C)	25	1400	10·0	2·6	7·83	$5{\cdot}1\times10^{7}$	0·23	2·8	Beerman (1975)
) 5°C)	—	1860	13·0	—	7·82	—	—	—	Garn and Sharp (1974)
))°C)	—	3800	17·0	—	7·80	—	—	—	Garn and Sharp (1974)
$_x\mathrm{Nb_2O_6}$									Beerman (1975)
°C)	25	380	6·5	2·1	5·2	$1{\cdot}6\times10^{8}$	0·81	4·0	
C)	25	1800	11	—	—	$1{\cdot}2\times10^{8}$	0·29	5·8	
	−25	1600	5·6	—	—	$9{\cdot}0\times10^{7}$	0·17	2·5	
C)	0	2500	12·0	—	—	$5{\cdot}1\times10^{7}$	0·23	4·1	
	25	5000	37·0	—	—	$1{\cdot}9\times10^{7}$	0·32	7·7	
	50	12000	10·0	—	—	$6{\cdot}5\times10^{6}$	0·04	1·2	
$_x)_{1-(3y/2)}\,\mathrm{R}_y\mathrm{Nb_2O_6}$ (R: SBN) where $x \simeq 0{\cdot}5$ and $y = 0{\cdot}02$									Liu (1974)
C)	25	1630	11·7	2·61	5·328	$1{\cdot}15\times10^{8}$	0·27	4·72	
C)	25	1600	11·8	2·66	5·326	$1{\cdot}76\times10^{8}$	0·28	5·94	
C)	25	1050	9·2	2·39	5·323	$1{\cdot}79\times10^{8}$	0·37	5·19	
C)	25	854	8·35	2·34	5·328	$3{\cdot}21\times10^{8}$	0·42	6·42	
C)	25	448	5·3	2·45	5·327	$4{\cdot}74\times10^{8}$	0·48	4·68	
$_2$O	−25	12·1	1·0	—	—	$1{\cdot}3\times10^{11}$	3·6	16·0	Beerman (1975)
	0	12·2	1·07	—	—	$1{\cdot}1\times10^{11}$	3·8	15·7	
	25	12·3	1·17	2·3	2·06	$9{\cdot}8\times10^{10}$	4·1	15·9	
	50	12·4	1·6	—	—	$6{\cdot}6\times10^{10}$	5·6	17·9	
$_{11}$ C)	—	40	1·1	—	—	$5{\cdot}10^{11}$	—	—	Watton *et al* (1976)

Table 1. (*contd*)

Material	(1)	(2)	(3)	(4)	(5)	(6)	(7)	(8)
$Pb_{4\cdot75}Ba_{0\cdot25}Ge_3O_{11}$ (T_c = 101°C)		60	2·0	—	—	10^{14}	—	—
$Pb_{4\cdot70}Ba_{0\cdot3}Ge_3O_{11}$ (T_c = 70°C)		81	3·2	—	—	10^{14}	—	—
Na NO_2 (T_c = 163°C)	25	7·4	0·5	2·1	2·2	—	3·2	—
Polyvinyl-chloride (PVC)	—	5·33	0·01	—	—	—	—	—
Polyvinyl fluoride (PVF)	—	5·0	0·10 0·18	2·3	1·38	—	0·87	—
Polyvinylidene fluoride (PVF_2)	—	11·0	0·30	2·4	1·76	—	—	—
Polyacryl-nitrile (PAN)	—	7·7	0·005–0·01	—	—	—	—	—
Poly (4-nitro-styrene) atactic	—	6·2	0·006	—	—	—	—	—
Polyacry-lamide (PAA)	—	—	0·01	—	—	—	—	—

(1) T(°C): Temperature in °C at which measurements are made; (2) ε: Dielec
(3) p: Pyroelectric coefficient in Coul/cm^2/K°; (4) c: Volume specific heat
(5) s: Density in g/cm^3; (6) ρ: AC resistivity in ohm-cm; (7) FM-R: Figure of me
responsivity given by $p(\varepsilon c)^{-1}$; (8) FM-D*: Figure of merit for detectivity given
(9) Ref.: Reference

Table 1 clearly indicates that TGS and $Li_2SO_4 \cdot H_2O$ are good materials for p detection. But the main problem is their hygroscopic nature, which re operating conditions. Therefore $LiTaO_3$ is generally preferred. The proble crucial for vidicon applications, where the material ought to be not only phy chemically stable in the temperature and pressure conditions of the tube bu low thermal diffusivity, to obtain good spatial resolution. That is why PVF_2 much attention for vidicon applications on account of its low thermal di compared to that of TGS and $LiTaO_3$, and also the ease with which thin targe can be prepared.

Similarly for application in laser optics, the choice of the material is gove vulnarability to radiation damage. Invariably crystals like TGS are not Materials with high curie temperature are found to be resistant to radiatic The phenomenon of surface damage by laser pulses is not very well unders the $LiTaO_3$ detector is found to be satisfactory in the 1 mW–3 W average p from 10·6 μm C.W CO_2 laser, but is damaged by a single 1/3 J pulse with a 200 msec. But a PZTG 1306 detector is not damaged even after fifty pulses. observed that polycrystalline ceramic pyroelectric materials are more r radiation damage than single crystals. Strontium barium niobates are anot pyroelectric materials which are extensively employed in laser detection.

The temperature at which the detector has to be operated also determine of the pyroelectric material. For better sensitivity of the detector, the curie t e as close to that of the operating temperature (in such a case, it also becomes ary to take special care to avoid depoling in the material). In this sense, it is useful e pyroelectric materials whose curie temperature could be changed by changing mposition, doping etc. This accounts for the interest in materials like SBN, KTN, e_3O_{11}, TGS-TGSE and PLZT ceramics. Of late ceramic-plastic composites and per ferroelectrics are found to have good potential of becoming efficient ectric materials. (Harrison and Liu 1980; Newnham *et al* 1980; Shaulov *et al* The PZT-plastic composite has a figure of merit six times more than that of PZT. sence of dielectric divergence in improper ferroelectrics makes it possible to have figure of merit. The rare earth molybdates, propionates and boracites are found superior to TGS.

wledgement

uthor is thankful to Prof R Vijayaraghavan and Dr M S Multani for their kind t.

nces

n H P 1975 *Infrared Phys.* **15** 225

1945 *Rev. Mod. Phys.* **17** 245

and Huang K 1954 *Dynamical theory of crystal lattices* (Oxford: Clarendon Press)

E and Sharp E J 1974 *IEEE Trans. Parts Hybrids Package* **PHP10** 208

n W B and Liu S T 1980 *Ferroelectrics* **27** 125

B 1971 *Source book on pyroelectricity* (New York: Gordon and Breach)

J 1948 *Proc. Indian Acad. Sci.* **A28** 339

1974 *J. Electr. Mater.* **3** 91

1978 *Proc. IEEE* **66** 14

m R E, Skinner D P, Klicker K A, Bhalia A S, Hardimar B and Gururaja T R 1980 *Ferroelectrics* 9

1962 *Physical properties of crystals* (Oxford: Clarendon Press)

A, Smith W A, Loiacano G M, Bell M T and Tauo Y H 1980 *Ferroelectrics* **27** 117

3 1975 *Phys. Rev. Lett.* **35** 1532

3 1976 *Phys. Rev. Lett.* **37** 792

R, Smith C and Jones G R 1976 *Ferroelectrics* **14** 719

ater. Sci., Vol. 6, No. 2, May 1984, pp. 327–338. © Printed in India.

rphous state ferroelectricity, magnon scattering and phase lity in microparticle materials

M S MULTANI, P AYYUB, V R PALKAR, M R SRINIVASAN,
V SARASWATI, R VIJAYARAGHAVAN and D O SHAH*

Materials Research Group, Tata Institute of Fundamental Research, Bombay 400 005, India.
*Department of Chemistry, University of Florida, Gainesville, Florida 32611, USA.

Abstract. Microparticles and micrograin ceramics show features distinct from the usual-sized polycrystalline materials. Amorphous state material combined with microparticle size for $Pb(Zr_{0.51}Ti_{0.49})O_3$ mimics the dielectric behaviour of crystalline ferroelectricity in ABO_3 compounds. Fine-grained $Y_3Fe_5O_{12}$ (YIG) synthesized by pressure sintering of YIG microparticles exhibit spinwave relaxation due to transit time across grain diameter. Applying microemulsion techniques for microparticle synthesis, γ-Fe_2O_3 has been synthesized. The phase stability fraction γ-Fe_2O_3/α-Fe_2O_3 is found to be a function of particle size. At very small sizes γ-Fe_2O_3 becomes amorphous, leading to interesting Mössbauer studies.

Keywords. Microparticle; microemulsion; ferroelectricity; ferrimagnetism; magnon scattering; lead zirconate titanate; yttrium iron garnet; gamma-Fe_2O_3; Mössbauer spectroscopy.

norphous and microparticle $Pb(Zr_{0.51}Ti_{0.49})O_3$

electric behaviour of amorphous microparticle $Pb(Zr_{0.51}Ti_{0.49})O_3$ has been .. The dielectric properties indicate the presence of a polar glassy phase transition C and has been interpreted in terms of the ferroelectric glass model described by 1977, 1978).

troduction

hous solids are derived from prototype crystalline structures which have ntly metallic, covalent or ionic character for chemical bonding. The first two ave been studied extensively but the ionically-bonded ones have not received ttention. The main difference which arises on going from the crystalline to the ous state is the tendency of the coordination to decrease for the covalently-l materials, to increase for the metallic-bonded ones, and to remain unchanged ionic-bonded.

Mössbauer and EPR data it has been established that the bonding in the ABO_3 ctrics is mainly of ionic character (Bhide and Multani 1965 and references). Also, Lines (1977, 1978) has proposed a model for an ABO_3 ferroelectric glass alysed the possibility of dielectric anomalies in such a system. Subsequently, $_3$ and $LiTaO_3$ (Glass *et al* 1977a), $Pb_5Ge_3O_{11}$ (Glass *et al* 1977b), $PbTiO_3$ ige and Nakamura 1980) have been prepared in the amorphous state and their ic behaviour has been well-studied.

the practical point of view polycrystalline $Pb(Zr_{0.51}Ti_{0.49})O_3$ (PZT) has found a ge application because of the high d_{33} piezoelectric constant and high k_p, the electromechanical coupling factor.

1.2 *Experimental*

PZT in the amorphous state was prepared by the sol-gel technique. $Pb(NO_3)_2$,
and $TiCl_4$ were used for synthesis. The solutions of the above salts were mixe
proportion required to achieve correct stoichiometry. The solutions were mix
presence of NH_4NO_3 to avoid the formation of insoluble $PbCl_2$. W
homogeneous solution was added to NH_4OH and stirred, lead, zirconium and
got co-precipitated as hydroxides. The complex formed in this step was allowed
and the supernatant decanted out. The precipitate was repeatedly washed in
remove salts like NH_4Cl and NH_4NO_3 as well as the excess alkali. The stable s
complex was then prepared and dried. It was then subjected to DTA and TG
which indicated that the complex hydroxide decomposed into PZT. That this wa
step process is evident from the following arguments. The TGA showed a we
about 20 % which is in good agreement with the value of 15 % expected for the
of the complex $Pb(Zr_{0.51}Ti_{0.49})O_3$. $(OH)_6$ into PZT. Furthermore, the DT
complex showed a single sharp peak at 280°C indicating that the decompositi

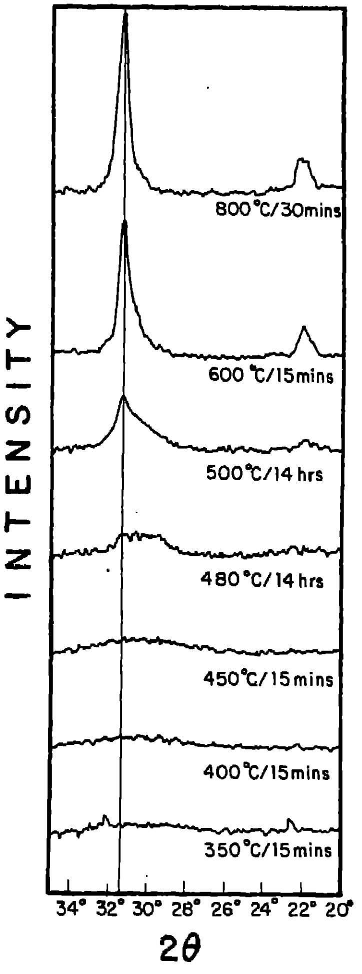

Figure 1. X-ray diffractogram in
amorphous-to-crystalline transitio

lex occurred in a single step. In contrast, the DTA for the conventional method of ration indicates three peaks corresponding to the following reactions.

$PbO + TiO_2 \rightarrow PbTiO_3$ at 610–710°C,
$PbTiO_3 + PbO + ZrO_2 \rightarrow PbO$ (solid solution) at 710–790°C,
PbO (solid solution) $+ PbTiO_3 \rightarrow Pb(Zr_xTi_{1-x})O_3$.

ay diffraction clearly showed that the PZT so formed was in the amorphous state. quivalent spherical diameter of the particles was calculated to be 40 nm from e area analysis using the Brunauer-Emmett-Teller technique. Thus the particle as not small enough to produce appreciable broadening of the XRD lines. The lline PZT could be obtained by suitable heat treatment at higher temperature as in figure 1.

Results and discussion

ielectric constant of the amorphous PZT was measured on pressed pellets of about diameter and 0·1 cm thickness. The capacitance was measured using a Wayne Kerr alance universal bridge. Figure 2 shows the temperature dependence of the tric constant. The dielectric constant shows a broad peak at 230°C and a sharp at 460°C. The latter peak was identified to be due to the crystallization on the basis DTA results which showed a broad exothermic peak at this temperature. DTA data ndicated that the transition at 230°C was of the second order. It was found that the dielectric peak persisted even on repeatedly cycling the material below the llization point, indicating that the peak did not arise from local relaxations. In the quent heating cycles up to 500°C both the dielectric peaks at 230 and 460°C peared. Instead there was a single peak at 325°C corresponding to the ferroelectric lectric transition in crystalline PZT.

e concept of a ferroelectric glass was initially investigated by Lines under the nption that the system was far below the crystallization temperature (Lines 1977). theory was later modified to include the effects of the intrinsic glass softening s 1978). The glassy phase is supposed to contain frozen-in dipoles with random itudes and orientations. These are formed by the distortion of dielectrically soft type units (*e.g.* BO_6 octahedra in the ABO_3 type compounds) which presumably their identity even in the glassy phase. As the crystallization temperature (T_{cr}) is oached from below, the tendency of these dipoles to become de-frozen leads to a dielectric anomaly at or near T_{cr}. It is important to note that the above described aly would be found in any material with such dielectrically soft units, irrespective ether it is a ferroelectric. In figure 2 the peak at 460°C can be identified with such an aly. The anomaly at 230°C may be considered to be analogous to a regular lectric-ferroelectric phase transition that occurs in crystals due to the cancellation ort range stabilizing forces and long range dipolar forces.

nes (1978) assumed a simple 2-parameter form for the local mode frequency $\omega(T)$ the temperature dependence of the dielectric response function is obtained in the field approximation

$$\varepsilon = 4\pi\alpha\theta/(1 - V\alpha\theta): \quad \text{non-polar phase,} \tag{1a}$$

$$\varepsilon = 4\pi(1{\cdot}5 - V\alpha\theta)/V(V\alpha\theta - 1): \quad \text{polar phase,} \tag{1b}$$

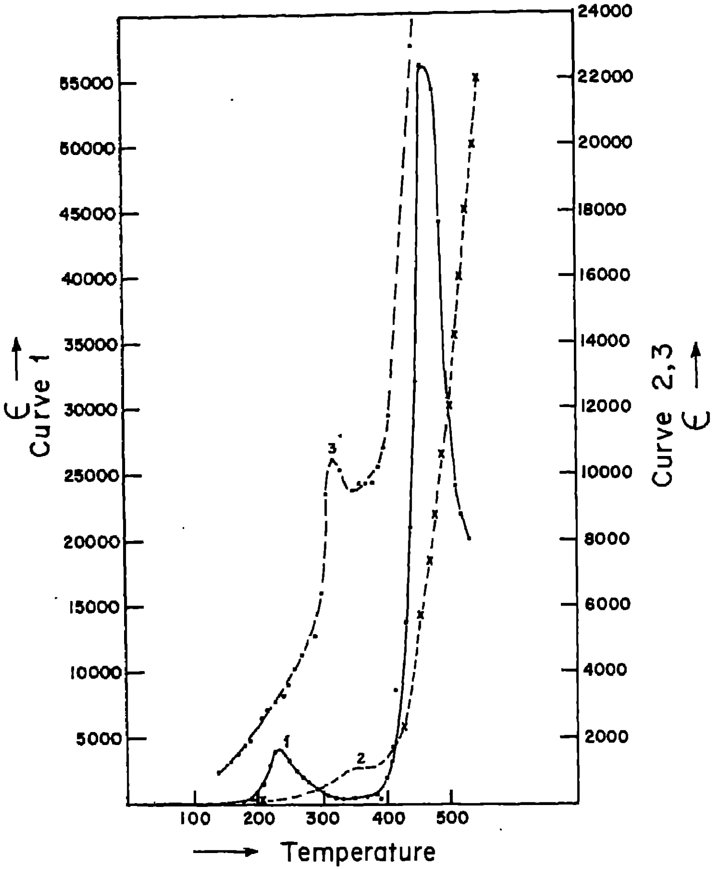

Figure 2. Temperature dependence of the dielectric constant in amorphous PZ

where $V = 4\pi/3$,

α = soft unit polarizability,

$\theta = 1 + a.\exp[-p(1-t)] - bt$ with $t = T/T_{cr}$,

$a = S^2\Delta/\alpha\omega^2$, is a measure of the mode softening

$b = 12AS^2kT_{cr}/\alpha\omega^6$, is a measure of anharmonicity.

The dielectric behaviour can be qualitatively studied by investigating the t ture dependence of the function $(\theta - 3/4\pi\alpha)$ where the second term is consta $(d^2\theta/dt^2)$ is necessarily positive it is impossible to obtain the dielectric b observed by us. At best one can obtain two singularities; one at T_{cr} and ano temperature below but close to it, but not a finite maximum at a tem considerably below T_{cr}. In any case the above theory should not be expected quantitatively over a wide temperature range.

wever, precisely because the two peaks are comparatively well-separated it is le to adopt the following approach. We can fit the higher dielectric peak with (1)) which describe the nature of anomalies close to T_{cr}. Since in the present case the aly occurs at $T = T_{cr}$, we can express in terms of a and b:

$$3/4\pi\alpha = \theta_{cr} = 1 + a - b.$$

us it is possible to determine the temperature-independent material constants a and the parameter p from the data. The lower dielectric peak may then be studied the approach of Lines where the local mode frequency and the mean square static cement of the ions from the prototype symmetry are assumed to be temperature endent (provided $T \ll T_{cr}$). Under this approximation a ferroelectric phase tion is predicted to occur at:

$$T_c^{glass} = T_{cr}(\alpha - 3/4\pi)/\alpha b. \qquad (3)$$

s possible to fit (1) with reasonable accuracy to the higher dielectric peak taking ·0100, $b = 0{\cdot}0272$ and $p = 2{\cdot}5$. We then consider a dielectric glass for which the nts a and b (and hence α) are known and try to find the temperature (if any) at it may undergo a ferroelectric-paraelectric transition. Thus from (3) we find that

$$T_c^{glass} = 190°\mathrm{C}$$

is reasonably close to the low temperature dielectric peak that was found in the e at $T = 230°\mathrm{C}$. This finding also seems to be in accordance with two other tions of Lines (1977), *viz*. that, in general

$$T_c^{glass} < T_c^{cryst}\ (325°\mathrm{C})$$

hat for a material with symmetric prototype units T_c^{glass} should not be too far T_c^{cryst}.

s important to stress here that the PZT studied is not only amorphous but particle as well. The studies of Känzig *et al* (1954) Känzig (1955), our recent work vasan *et al* 1983 and references therein) have repeatedly shown that the aneous strain and the dielectric anomaly decrease substantially, while T_c increases the crystalline ABO_3 ferroelectric is reduced in size from 1000 nm to 10 nm.

agnon scattering in fine-grained YIG

Introduction

m iron garnet (YIG) is a microwave ferrite and owing to the existence of grains and boundaries has specific characteristics. Fine-grained ferrites (of average diameter or less) have become technologically significant in making devices due to their ncy in handling microwave power (Hudson 1970). The microstructure is largely mined and controlled by preparation procedures. We have succeeded in obtaining y dense (above 99 % theoretical density) YIG of submicron and micron size using l method for the preparation of YIG powder and sintering of the compacts at high ures (~ 2000 kg/cm^2). The grain size dependence of the microwave properties studied, Our observations on ferrimagnetic resonance linewidths, magnetization, ptibility and spin wave instability threshold fields are reported herein.

2.2 *Experimental results*

The YIG powder was made by the sol-gel technique (Multani *et al* 1981) usi
and iron oxides of five-nine purity to avoid fast relaxing rare earth impuri
cold-pressed compacts were sintered in oxygen atmosphere for 2 hr at 140
compacts had grains of average size 2·5 μm, assuming the distribution to be l
The densities as measured by loss of weight in water were better than 5·14 (
density of YIG is 5·17). Fine-grain samples were obtained by hot pressing the c
a silicon carbide die at 1100°C (inside die) at a pressure of 1800–2000 k
soaking times of 10, 20, 30 and 60 min. These have been numbered as HP_5,
and HP_2 respectively. The grain size as (average) measured from scannin
microphotographs were 1·1, 0·9, 1·2 and 1·34 μm, respectively. The densities
to be good—higher than 5·14 and close to 5·16 g. cm^{-3} in one of them. The
magnetization values, which also reflect on the densities, were estimated u
loop tracer. These were close to the single crystal values. In polished, spheri
of size ~ 0·5 to 1 mm, ferrimagnetic resonance measurements were carrie
frequency of 9·25 GHz. The uniform precession linewidths ΔH and magneti
are given in table 1. The log-log plot of linewidth *vs* grain size gives a
dependence $a^{-0.6}$ where a is the average grain diameter (figure 3). DC
susceptibility and T_N measurements were conducted using Bruker instrum
fields 100 and 250 Oe in annealed spherical samples and irregular annealed
expected, susceptibility values reduced on annealing and increased with
field.

As YIG is an ordered ferrimagnet at room temperature even at low fields
250 Oe, the sample gets attracted to the pole piece and there is difficulty in ad
balance weight in the susceptibility instrument. In small, spherical sampl

Table 1. Characterization data on YIG

Samples	Grain size (μm)	Density (g/cc) ρ	Magnetization (gauss) $4\pi M_s$	FMR line width (Oe) ΔH	Remarks
A (1400°/2 hr)	2–3	5·12	1700	90–100	Narrows to 5 annealing 110
B (repeated A 1400°/8 hr)	3	5·13	1750	100	Does not narr ling for 10 hr 2 hr at 1200°C
C (1400°/8 hr)	2	5·14	1700	90	
Four-nine purity sol-gel sample	5	5·1	1700	120	
Thomson-CSF YIG	8		1780	25	
HP_2	1·34	5·12	1805	200	
HP_3	1·2	5·13	1805	200	
HP_4	0·9	5·14		220	
HP_5	1·1	5·16	1760	260	This sample h grain size dist compound to

On annealing 1100°C/30 min (6–9) do not show change in width.

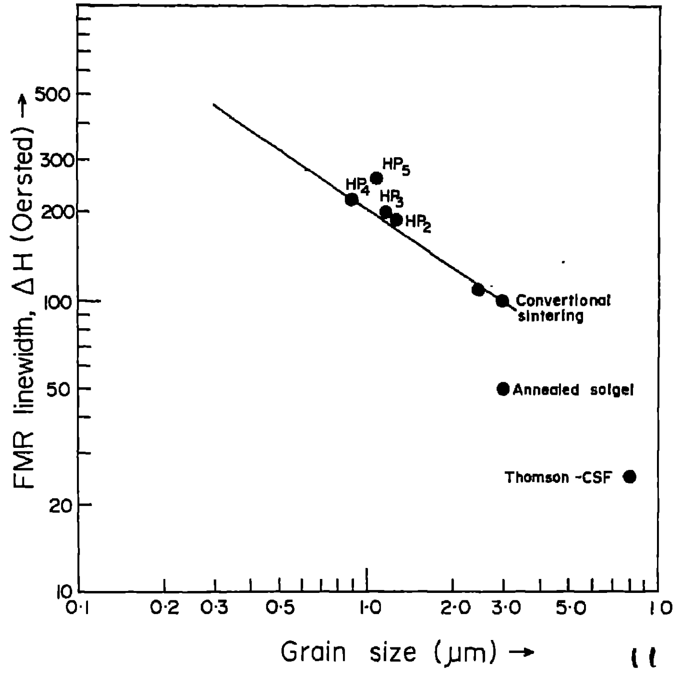

Figure 3. Uniform precession linewidth as a function of average grain diameter in polycrystalline YIG.

›lem is reduced but this also reduces the pull and thereby error is increased. It was ›rved that with decreasing grain size susceptibility increased. This trend is not ›rstood as one would expect a decrease in susceptibility with decreasing grain size ›g to reasons: (i) as the grains become finer superparamagnetism might set in as the ple tends to reduce the wall energy and approaches single domain, (ii) increase in ace area as grain sizes decreases gives more uncoupled spins on the surface.

össbauer measurements in fine powders (of sizes < 0·1 μm) did not show any ›rparamagnetism. Two sets of six-finger hyperfine patterns corresponding to hedral and tetrahedral sites were obtained. There was no change in hyperfine field uadrupolar interaction on wet-milling the powder for 30 hr in alcohol as the cle. Hence superparamagnetism in the sizes involved here can be ruled out. HP_5 has n size higher than HP_4 as seen in scanning electron micrographs. This was ›orted by the susceptibility and critical field measurements, but uniform precession h ΔH for HP_5 is higher than HP_4. The discrepancy we think, could be due to the ›r grain size distribution in HP_5. Parallel pumping of microwave power at a uency 9·6 GHz enabled us to measure the instability threshold critical fields, h_{crit} ›re 4). h_{crit} is found to be inversely dependent on grain size (figure 5). In samples of n sizes of a micron or less, the instability curve (h_{crit} *vs* H) does not have a marked imum as the instability sets in gradually. This leads to the difficulty of estimating the minimum accurately.

Discussion

FMR linewidths. We have observed (figure 3) that there is a grain-size

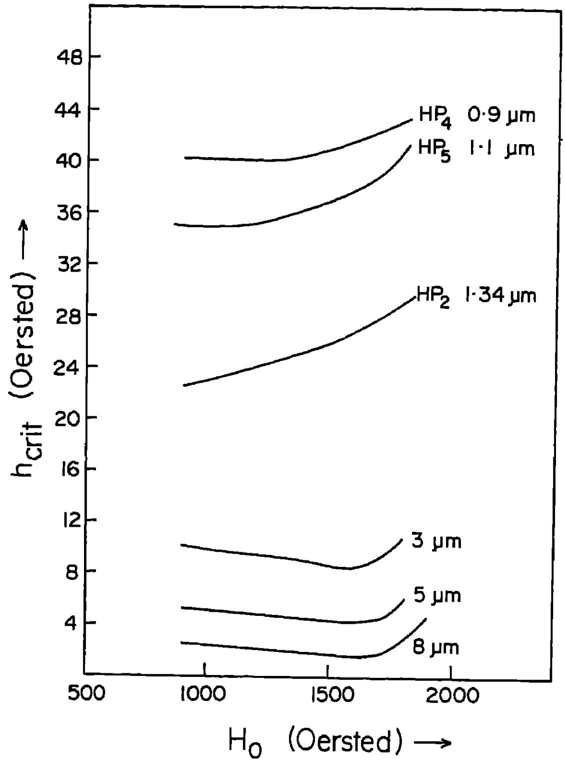

Figure 4. Spinwave instability threshold h_{crit} as a function of static external magn for parallel pumping at 9·6 GHz.

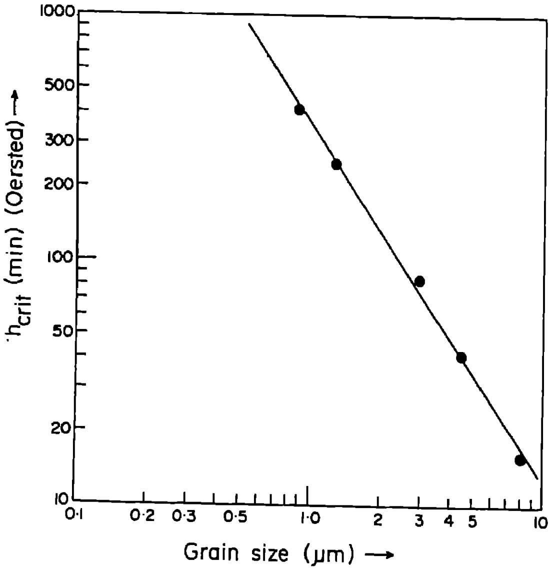

Figure 5. Spinwave instability threshold h_{crit} at the butterfly minimum as a fun average grain diameter in poly-crystalline YIG.

lence of linewidths. The only other grain-size dependent linewidth for uniform sion was observed by Inui *et al* (1975) at a resonance frequency of 2/3 ω_m where $\gamma 4\pi M_S$, M_S being saturation magnetization. This uniform precession frequency ie top of the magnon manifold (ω_k *vs* k curves for $\theta = 0$ and $\theta = (\pi/2)$. Inui *et al* had measured the widths in Sn-substituted Ga-V garnets of grain sizes varying :n 8 and 30 μm. No explanation was given for this and other parameters like γ and magnetization were also not held constant. Ferromagnetic resonance)adening is related to the polycrystalline nature of ferrites since a single crystal ıdth in YIG is only 0·5 Oe. For a polished, spherical sample of small dimensions ım) contributions of linewidth are essentially due to: (i) anisotropy in the nly-oriented, densely-packed crystallites and (ii) porosity, including regions :n crystallites, inclusions and second phase constituents.

he resonance linewidth determines the insertion loss, bandwidth and phase shift :vice, one desires the width to be minimal. Our materials have fine grains and y a high threshold h_{crit} but are limited by the broad widths. If one can realise the it would become possible to overcome it and make it best suited for devices. resonance linewidth at uniform precession can be written as

$$\Delta H_{UP} = \Delta H_i + \Delta H_{AN} + \Delta H_P, \tag{4}$$

ΔH_i is the intrinsic linewidth (of a crystal), ΔH_{AN} is the width arising due to :opy and ΔH_P is the width due to porosity. As the samples have high density, orated also by the high saturation magnetization, one can neglect ΔH_P presently. :ing 0·5 Oe can also be safely neglected. Thus the width appears to be essentially ıined by anisotropic field which arises owing to crystallites having their own axis gnetization. The coercive field, which is also a measure of anisotropy has been to depend upon grain size (Globus and Guyot 1972). Thus, a grain-size lent contribution to linewidth of uniform precession can arise through opy. The log-log plot of FMR width *vs* grain size follows the $a^{-0.6}$ law, similar to ective linewidth. As Fe^{3+} is an S-state ion with no spin-orbit effects and with low e fields, the condition $H_A \ll 4\pi M_S$ is valid *i.e.* anisotropy field is less than the :ion magnetization field and one can talk within the framework of spinwave ıch. For fine grains, in the low anisotropy limit, the dipolar coupling between lites is much greater and they tend to resonate collectively. The anisotropy line :ning should be from anisotropy field H_A but dipole-narrowed by a factor of M_s.

ömann (1958) gives for spherical sample linewidths of

$$\Delta H_{AN} \simeq (H_A^2/4\pi M_s)\,(8\pi\sqrt{3}/21). \tag{5}$$

ropy field $H_A \simeq (2k_1/M_s) \simeq 100$ Oe substituting, $\Delta H_{AN} \simeq 16$ Oe is the contri- due to anisotropy. Schlömann's (1958) theory also gives 26 Oe/percent for ty width in YIG at 10 GHz. For sample with porosity $< 0{\cdot}8\,\%$ (our worst sample is dense)

$$\Delta H_P \simeq 20\,\mathrm{Oe}$$

$$\Delta H_{UP} = \Delta H_{AN} + \Delta H_P + \Delta H_i \simeq 36{\cdot}5\,\mathrm{Oe}. \tag{6}$$

$_i$ also increases with increasing spinwave linewidth (as for fine grain samples) the m precession width is bound to be higher than the above value, but the)ancy is large. In a fine-grain sample the spin-wave picture is modified (in our samples of $< 1\,\mu m$, $k = 10^3\,cm^{-1}$, dipolar contributions are larger than e the occurrence of magnetostatic modes, giving rise to discrete spectrur relaxation and an increase in width is possible owing to this. Furthermor contribution could come from the magnetoelastic or magnetostrictive effe stress is introduced in the sample during sintering, compacting, grinding an Annealing for 10 hr at 1100°C after making the sphere or before has not pr change in the widths observed. Stress could also come in the pressure sinter inevitable in the preparation of a fine-grained materials. Röschmann (197 the conclusion of another undefined relaxation process while explaining th some ferrites. The concept of two-magnon scattering could be valid wavelengths are small compared to sample dimension, which condition is fine-grained samples.

2.3b *Critical field thresholds*: The critical field h_{crit} measured in a pa experiment shows that a decrease in grain size increases the field h_{crit}. The in size dependence of h_{crit} was observed by Vrehen *et al* (1969) and Patton gave the transit-time model as the most satisfying explanation. The life excited spin wave is limited by the transit time for the mode across an indi *i.e.* $\tau_k \simeq a_0/|v_g|$ where v_g is the spinwave group velocity and a_0 is the av diameter. Spinwave linewidth ΔH_k is given by

$$\Delta H_k \simeq \frac{1}{\gamma \tau_k} \simeq \frac{|v_g|}{\gamma a_0}.$$

A log-log plot of experimental ΔH_k extrapolated to $k = 0\,(\Delta H_{k \to 0})$ as a funct diameter showed

$$\Delta H_{k \to 0} \propto a_0^{-1}.$$

This model subsequently modified by Scotter (1972) and Sawado (1981) in pore sizes and by Borghese (1977) with grain size distribution has reasonabl the high k regions particularly for large sizes. The theoretical fit becomes p grains and k values $< 10^4\,cm^{-1}$. Patton (1970) doubts the relevance of parallel pump data ΔH_k from the transit-time model, because for grains in and submicron range magnetostatic modes become important and excha tions are small. Our experimental 'butterfly' curves follow the results of fine-grained samples had a gradual shifting up of instability with no marke The threshold fields were found to be high for the fine-grained samples. T desirable property for high power devices but as the uniform precession lin also large one has to strike a balance between the loss that can be allowed an handled.

3. Amorphous and microcrystalline Fe_2O_3

Gamma ferric oxide continues to be one of the most important mater magnetic recording devices. A very large number of patents cover the proce to γ-Fe_2O_3.

3.1 *Experimental*

Numerous methods have evolved for microparticle synthesis. We have dev iod based on microemulsions which have become very important in the past few s (Saffran and Turkevich 1983). In the thermodynamic equilibrium state of three-ponent microemulsion, the optically isotropic mixture consists of globular or ainlike regions of oil and water (~ 100 A) with surfactant molecules at the faces (Shah 1981). The surfactant molecules have hydrophilic polar heads and ophobic hydrocarbon tails.

ie systems we have used consist of an aqueous solution of ferric nitrate, 2-ethyl-nol and sorbitol-mono-oleate. The stable microemulsions were prepared for rent concentrations of ferric nitrate solutions by agitating ultrasonically. Each oemulsion sample was then treated with NH_4OH solution, resulting in ferric oxide precipitate. Now the system consisted of ferric hydroxide microparticles rsed in an organic phase. The surfactant prevented the coagulation of the oparticles.

ie microparticles were allowed to settle and then the solution was dried under red radiation. TGA of the dried material showed the decomposition loss between 250°C. Thus, all samples were calcined at about 260°C. The concentrations of nitrate solutions and the corresponding x-ray size are given in table 2.

Results and discussions

e 2 gives the details also of the susceptibility data at various fields. From the x-ray action intensities it is clear that the γ phase increases in proportion to the α phase ı the solution concentration is reduced. At very low concentrations the material mes x-ray amorphous. The particle sizes according to the Scherrer formula are also ı in table 2. TEM photographs showed spherical microparticles, with nominal ement of physical size with x-ray size.

ie gamma phase can be represented as a spinel structure, $(\square_{1/3}Fe^{3+}_{2/3})\,Fe^{3+}_2\,O_4$. eda and Morrish (1977) have shown that the cation vacancies order for large cles but the ordering (as seen from the presence of superlattice lines in x-ray action) disappears below about 200 A. In our pure gamma samples we did not rve the superlattice peaks.

ı interesting observation is through Mössbauer spectroscopy of the 150 A γ-Fe_2O_3 oparticles and x-ray amorphous Fe_2O_3 microparticles of 59 A (see figure 6). The room-temperature spectra, taken much above the superparamagnetic blocking erature, show two resonances. They correspond to the quadrupole splitting of the

Table 2. X-ray size and DC susceptibility

nitrate on conc. it %	γ-Fe_2O_3/α-Fe_2O_3 from x-ray diffraction	Particle size from Scherrer formula (A)	χ_m 400 Oe	χ_m 8 kOe	χ_m 15 kOe emu/g
	0·7	614	0·005	0·00085	0·00057
	1·0	250	—	—	—
	1·4	190	—	—	—
	Only γ-Fe_2O_3	140	0·006	0·000748	0·00043
	”	80	0·004	0·000686	0·00044
	”	59	0·0015	0·000225	0·00014
	Amorphous Fe_2O_3	?	0·0007	0·000048	0·000042

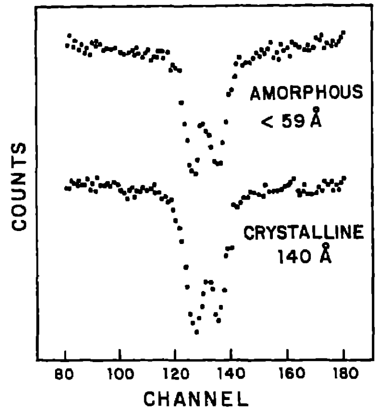

Figure 6. Mössbauer spectra superparamagnetic blocking te (A) 140 Å γ-Fe_2O_3 microparticles, phous Fe_2O_3 microparticles < 14 corresponds to 127·95 channel, nel = 0·109 mm. sec^{-1}, v is ne channel below 128. Co^{57}: Rh sourc + 0·33 mm. sec^{-1}.

Fe^{3+} ($3d^5$) state in the spinel octahedral and tetrahedral sites. The asymmetry due to the Goldanskaii-Karyagin effect.

Detailed Mössbauer studies are in progress.

Acknowledgements

We are grateful to the Department of Electronics for supporting the micr programme.

References

Bhide V G and Multani M S 1965 *Phys. Rev.* **A139** 1983
Borgese C 1977 *J. Physique* **38** 261
Glass A M, Lines M E, Nassau K and Shiever 1977a *J. Appl. Phys. Lett.* **31** 249
Glass A M, Nassau K and Shiever 1977b *J. Appl. Phys.* **48** 5213
Globus A and Guyot M 1972 *Phys. Status Solidi* **52** 427
Haneda K and Morrish A H 1977 *Solid State Commun.* **22** 779
Hudson A S 1970 *J. Phys. D:* **3** 251
Inui T, Takamizawa H, Ogasawara and Fuse T 1975 *AIP Conf. Proc.* **24** 483
Känzig W, Anilkar M and Brugger H R 1954 *Helv. Phys. Acta* **27** 99
Känzig W 1955 *Phys. Rev.* **98** 549
Lines M E 1977 *Phys. Rev.* **B15** 388
Lines M E 1978 *Phys. Rev.* **B17** 1984
Multani M S, Sharma D K, Palkar V R, Gokarn S G and Gurjar A 1981 *Mater. Res. Bull.* 1
Patton C E 1970 *J. Appl. Phys.* **41** 1637
Röschmann P 1976 *AIP Conf. Proc.* **34** 253
Safran S A and Turkevich L A 1983 *Phys. Rev. Lett.* **50** 1930
Sawado E 1981 *Proc. International Conf. on Ferrites, University of Tokyo Press, Tokyo* p. 818
Schlömann J 1958 *J. Phys. Chem. Solids* **6** 632
Scotter D G 1972 *J. Phys. D:* **6** 93
Shah D O 1981 *Surface phenomena in enhanced oil recovery,* (New York, Plenum Press)
Srinivasan M R, Multani M S, Ayyub P and Vijayaraghavan R 1983 *Ferroelectrics* (to appea
Takashige M and Nakamura 1980 *J. Phys. Soc. Jpn* **49B** 143
Vrehen Q H F, Beljers H G and DeLau J G M 1969 *IEEE Trans.* **MAG-5** 617

ater. Sci., Vol. 6, No. 2, May 1984, pp. 339–367. © Printed in India.

ation effects in nuclear reactor materials—Correlation with ture

P RODRIGUEZ, R KRISHNAN* and C V SUNDARAM
Reactor Research Centre, Kalpakkam 603 102, India
* Metallurgy Division, Bhabha Atomic Research Centre, Trombay, Bombay 400 085, India

Abstract. A review of radiation effects in nuclear reactor materials has been made; the irradiation effects have been correlated with the crystal structure of the materials. Five phenomena, irradiation hardening, irradiation embrittlement, irradiation creep, irradiation growth and void swelling that occur in materials by neutron irradiation in a reactor environment have been discussed with a view to explaining the physics of the phenomena and the engineering consequences. Metallurgical approaches for improving the irradiation performance of materials and for developing new alloys with better resistance to radiation damage have been pointed out.

Keywords. Nuclear reactor materials; irradiation effects; radiation damage; irradiation hardening; irradiation embrittlement; helium embrittlement; irradiation creep; irradiation growth; void swelling; stainless steels; zirconium alloys; uranium; nickel alloys.

troduction

ubject of radiation effects in materials is a vital area of relevance to reactor
ering as well as a large field for basic materials research. In this paper we shall
s neutron irradiation effects in a nuclear reactor environment in structural
als. Two effects are known to occur in non-fissile materials in the intense neutron
nment of a nuclear reactor. One is the extensive displacements of the atoms from
attice sites due to elasic interactions with the impinging neutrons. The second is
rmation of impurity atoms in the materials by transmutation reactions. Both
effects, the displacement of atoms from their lattice sites and the consequent
ction of various types of defect structures as well as the production of impurity
due to transmutation reactions can influence important macroscopic properties
ength, ductility and dimensional stability which are the most important features
practical application of the structural materials. The changes brought about by
tion on these properties are quite often unfavourable and adverse, justifying the
ce of radiation on materials being referred to as "radiation damage". In this paper
enomena, irradiation hardening, irradiation embrittlement, irradiation creep,
tion growth and void swelling that occur in materials due to neutron irradiation
actor environment will be discussed. We will also attempt to correlate the
tion effects with the crystal structure of the various materials.

radiation hardening

eneral effects of neutron irradiation on the mechanical behaviour are (i) an
e in the yield strength (irradiation hardening); (ii) an increase in the ultimate

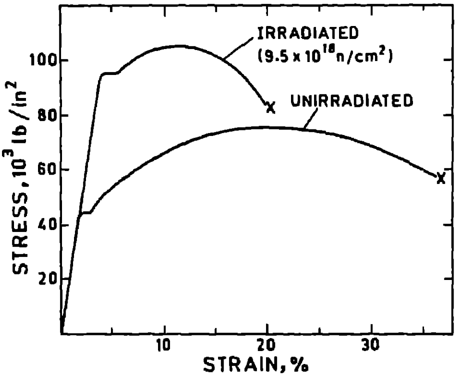

Figure 1. Change i
temperature tensile prope
steel produced by neutron
(Little 1976).

tensile strength which is less strong than the increase in the yield strength; (iii)
in the rate of work hardening and (iv) a reduction in the uniform and total el
These effects are illustrated in the typical example for mild steel (Little 197
figure 1.

The strengthening or irradiation hardening is caused by microstructu
introduced by irradiation. In pure metals, the impediment to dislocation m
originate directly from radiation-induced lattice defects whereas in alloy
effects like radiation-induced precipitation are also possible. The defects intr
irradiation can vary from single vacancies and interstitials of one atom diam
voids and helium bubbles as large as 3 to 30 nm in diameter or higher. Th
defects generated are point defects (interstitials and vacancies). At low tem
where the mobilities of these defects are limited they combine to form mul
defects, for example di-vacancies, tri-vacancies etc., or clusters of point
complexes with solutes which are a few atom diameter in size. As the i
temperature increases, planar defects like the depleted zones which can ev
into planar vacancy clusters and vacancy loops form. At temperatures betv
$0{\cdot}3T_m$ (T_m is the melting point in K) the interstitials are mobile and they can
by combining with immobile vacancies; annealing of interstitials at vacancy
other sinks also occur. Interstitials also agglomerate to form clusters of inte
still higher temperatures between 0·3 and $0{\cdot}5T_m$, the vacancies also beco
which cause their annihilation by recombination with interstitials; anneali
interstitials and vacancies at various sinks like loops, dislocations etc also tak
interstitial clusters further agglomerate to form interstitial type dislocation
an excess concentration of vacancies is produced which coalesce to form voi
and above $0{\cdot}5T_m$ volume diffusion becomes possible and if helium has been r
transmutation product helium bubbles form. A list of the various defect
(with their sizes) that can be produced in materials at different irradiation te
are given in table 1.

There have been two approaches to explain irradiation hardening (Die
earlier attempts, irradiation hardening was considered to be source harder
enhancement of the stresses necessary to activate dislocation sources
considered to be pinned by the irradiation-produced defects attached t
second approach has been the dispersed barrier hardening approach whic
impediment of dislocation motion in irradiated materials by localise

Table 1. Defects produced by irradiation

Temperature T/T_m	Defect	Size
0		
	Point defects: Vacancies and interstitials	One atomic diameter
0·1		
	Multiple point defects Clusters of point defects Complexes of vacancies and interstitials with solutes	a few atomic diameter
	Vacancy clusters and loops	diameter < 7 nm
0·3		
	Interstitial loops	diameter > 7 nm
	Rafts (agglomerates of clusters and small loops)	6–10 nm thick, 100–200 nm in length and width
	Voids	10–60 nm
0·5		
	Helium bubbles	3–30 nm
	Transmutation atoms (produced at all temperatures but agglomerates at $T/T_m > 0.5$)	

domly distributed in the lattice. The latter approach based on the theory of rmally activated-dislocation motion has gained considerable experimental and oretical support particularly in view of the fact that the approach has been ensively proved to be valid in unirradiated materials also.

he basis of the theory of thermally activated deformation (for recent reviews, see cks *et al* 1975; Li and Mukherjee 1972; Rodriguez and Dasgupta 1972; Evans and vlings 1969) is that the barriers to dislocation motion may be divided into two egories, short range and long range obstacles depending on the magnitude of the ance over which the force exerted by the obstacle extends. The shear flow stress τ can s be considered to consist of two components τ_μ and τ^*. τ_μ called the athermal or rmal or long range stress arises from interaction of moving dislocations with tacles whose force extends over distances of the order of ten atomic diameters or re. (For example the forces due to dislocations on parallel slip planes, grain ndaries or large obstacles such as second phase particles). τ_μ depends on perature only through the shear modulus μ. τ^* is the effective or thermal component low stress and arises from interaction of moving dislocations with short range tacles like solute atoms, clusters, point defects, forest dislocations, alternate low and energy configurations of the dislocation core (for example Peierls-Nabarro barrier non-planar dislocations) etc. τ^* is influenced by both temperature and strain rate.

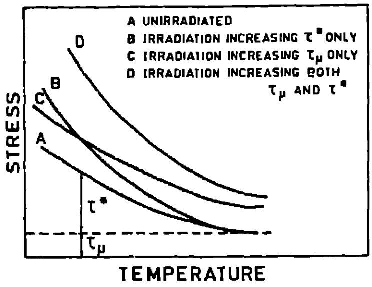

Figure 2. Schematic illustration of changes in thermal and athermal com of flow stress due to irradiation (R 1977).

The variation of flow stress with temperature and strain rate showing partitio the thermal and athermal stress components is shown in figure 2 (Rodriguez 197 various defect structures produced by irradiation (table 1) can have both long ran short range interactions with dislocations. An irradiation-induced defect can b rate-controlling when the short range energy barrier presented by it exceeds the l barrier in the unirradiated condition and thus alters the temperature dependenc flow stress. Schematic illustrations of possible changes in τ_μ and τ^* by irradiati also shown in figure 2. Curve A is the flow stress *vs* temperature curve unirradiated condition. Curve B is obtained when irradiation increases o thermal component of flow stress. When irradiation hardening is purely athe nature, the flow stress *vs* temperature curve is just shifted up along the stre resulting in curve C. Curve D represents the situation when irradiation increas the components of flow stress. Most of the experimental results rule out situa consistent with the fact that most of the defects introduced by irradiation hav

Table 2. Summary of results of dislocation dynamics in irradiated materials (Rod 1977)

Lattice type	Rate-controlling obstacle	
	Un-irradiated (Rodriguez and Dasgupta 1972)	Irradiated
BCC	P–N barrier Interstitial solutes	P–N barrier Solutes Solute-defect complexes Clusters or loops Divacancies (Little 1976; Arsenault 1976)
FCC and HCP, $c/a >$ ideal (basal slip)	Intersection of forest dislocations	Depleted zones (Diehl 1970) Faulted loops (Koppenal and Arsenault 1971)
HCP $c/a <$ ideal (prism slip)	Interstitial solutes	Interstitial solutes (Hamad *et al* 1975)
	P–N barrier	Irradiation-induced defects (Kayano *et al* 1977)

range and short range interactions with dislocations and hence the athermal onent of flow stress will invariably be increased by irradiation irrespective of ıer the rate-controlling mechanism is altered (D) or not (C).

ritical summary of the results indicating that the effects mainly depend on the l structure and the operative slip system is given in table 2 (Rodriguez 1977). ent reviews giving details of the results are available for fcc metals (Diehl 1970; enal and Arsenault 1971) and bcc metals and alloys (Little 1976 Arsenault 1976). imental studies on hcp materials on the other hand have been very few (Hamad *et* '5 and Kayano *et al* 1977).

cc metals

3 (Little 1976) is illustrative of the conflicting results obtained in parallel igations on bcc metals. Figure 3a giving results on polycrystalline α-iron is typical a (Ohr *et al* 1968) showing that irradiation produces no detectable change in the rature dependence of yield or flow stress, but gives rise to temperature-insensitive ion hardening. Data demonstrating other results that reveal an increase in the rature dependence is exemplified by the results for single crystal α-iron of two s, irradiated to a range of neutron doses shown in figure 3b (Diehl *et al* 1968). The two observations refer principally to tests performed below room temperature. A set of results on an aluminium-grain-size-controlled mild steel (Little 1967), in the test temperature range was extended up to 523 K demonstrates that the ion hardening is temperature-dependent above room temperature but tempera-nsensitive below (figure 3c). Since the strong temperature dependence of the

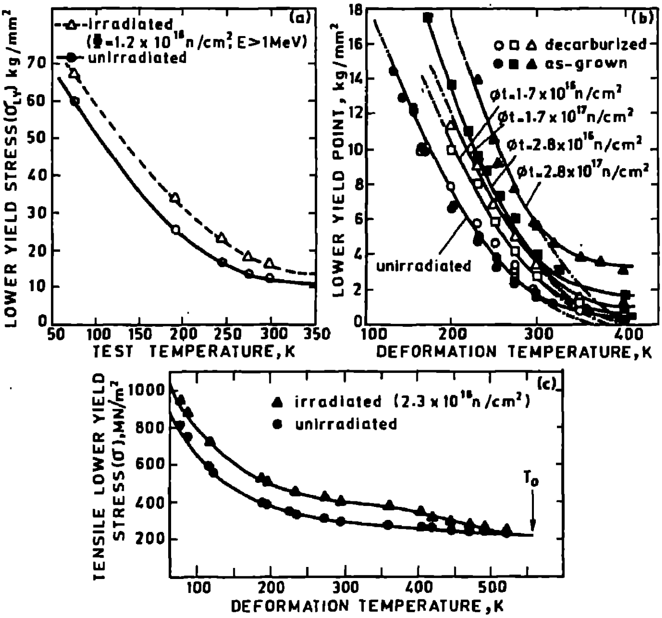

Figure 3. Conflicting results obtained in parallel investigations on bcc metals (Little 1976); (a) polycrystalline α-Fe (Ohr *et al* 1968); (b) α-Fe single crystals (Diehl *et al* 1968); (c) aluminium grain size controlled steel (Little 1967).

unirradiated yield stress also ceases at about room temperature, Little (1967 that thermally-activated overcoming of radiation-produced defects occu temperatures above which the unirradiated rate-controlling mechanism athermal; in the absence of the latter, the defects introduced by irradiation w been rate-controlling even at lower temperatures.

Seidel (1969) has explained the differences in the observations on irradiati in polycrystals and single crystals of α-iron (figures 3a and b) as arising opposing influences of irradiation on the two parameters σ_i and K in the we Hall-Petch relationship $\sigma = \sigma_i + Kd^{-1/2}$ relating strength σ to grain diamete unirradiated condition, the temperature dependence of flow stress is mainly in the Hall-Petch intercept σ_i. Since irradiation is found to increase the ten dependence of the single crystal flow stress (figure 3b) it is to be inferred temperature dependence of σ_i is increased by irradiation. The absence of any the temperature dependence of the polycrystal flow stress therefore indi irradiation has an opposing influence on the Hall-Petch slope K, and parti variation with temperature. Diehl and Seidel (1969) has cited in support of explanation, the results of Chow *et al* (1969) indicating a decrease ir temperature after irradiation which nullifies the increase in the temperatu dence of σ_i such that the temperature dependence of the overall flow stres unaffected.

Before closing the discussion on BCC metals, two important facts should b out. One is the existing controversy regarding the rate-controlling obstacle metals in the unirradiated condition itself (Rodriguez and Dasgupta 1972; K 1975; Li and Mukherji 1972; Evans and Rawlings 1969; Arsenault 1976); wh the Peierls-Nabarro barrier or the interstitial solutes? The second is the interstitial solute content on the change in τ^* due to neutron irradiati 1976; Arsenault 1976). Closely associated with the latter are the phenomena o anneal hardening (Little 1976; Wechsler 1972; Arsenault 1973) and radiation (Arsenault 1973, 1976), which are also influenced by the interstitial solut These effects are a consequence of the irradiation damage (vacancies, in divacancies, diinterstitials and clusters) acting as trapping sites or sinks for i solutes and *vice versa.*

2.2 *FCC metals*

Compared to BCC metals, the agreement among the experimental results on is much better (Diehl 1970; Koppenal and Arsenault 1971). The te dependence of flow stress is increased by irradiation and the intersectior dislocations is replaced by irradiation-produced defects as the rate-c obstacle. While there is agreement in the experimental results, the interpr results has not been free from controversies. One disagreement is regarding th the interaction of the rate-controlling defects with dislocations. Koppenal Koppenal and Arsenault (1965, 1971) have concluded that the rate-controllir is faulted loops and that the results conform to the model of Fleischer strengthening by the tetragonal distortion around defects. On the other h also been claimed (Diehl 1970; Diehl and Seidel 1969), that the results ar agreement with the model of Seeger (1958) of dislocations cutting through dispersed barriers (depleted zones) if it is assumed that an obstacle size spect erefore a unique temperature-independent activation energy does not exist. :r point of disagreement between the two groups has been on the contributions liation hardening to the thermal and athermal components of flow stress. The on FCC metals correspond to curve D of figure 3 which as discussed earlier should rpreted as increases in both the thermal and athermal components of flow stress .diation. Arsenault and Koppenal have adopted this view and the analysis of was accordingly made. Diehl and coworkers, on the other hand, have assumed is unaffected by irradiation and therefore the difference between the irradiated tress and the τ_μ for the unirradiated condition was taken as the thermal nent of flow stress for the irradiated state.

CP *metals*

; of dislocation dynamics in irradiated HCP metals have been very few. Hamad *et* 5) in a systematic study of quench-hardening and neutron-irradiation hardening mium have concluded that the defects produced by quenching or irradiation lead y athermal hardening; the rate-controlling obstacle, which is the interstitial , remains unaltered by irradiation. More recent work by Matta *et al* (1977) has ned these findings.

ano *et al* (1977), on the other hand, found that in titanium, another HCP metal to zirconium in its deformation characteristics, the thermal activation :ters of deformation were altered by irradiation. Irradiation-produced defects, all to be observed by electron microscopy, were considered to be related to the l component of stress.

:adiation embrittlement

imary issues in mechanical metallurgy are of course strength and ductility. It is ell established that all factors or treatments that strengthen metals also cause a se in ductility (the effect of grain size is the only known exception). It comes as no ;e therefore, that radiation hardening is almost always accompanied by a ;e in ductility though the enhanced fracture susceptibility caused by irradiation is)ly the most severe and most dramatic of all the hardening mechanisms. The ion in ductility measured by the decrease in the uniform or total elongation in a test or in the fracture toughness evaluated from impact tests or fracture nics tests or even as the area under the stress-strain curve is referred to as tion embrittlement. Four types of irradiation embrittlement have been identi- ı radiation embrittlement in BCC metals and alloys that undergo a ductile-brittle ion; (ii) radiation embrittlement in normally ductile metals like FCC metals; (iii) :mperature grain boundary embrittlement arising from the formation of helium :s from (n, α) reactions and (iv) embrittlement due to the formation of other ıutation products.

·radiation embrittlement in BCC *metals and alloys*

:tals and alloys undergo a transition in fracture mode from ductile behaviour to fracture as the temperature is decreased; below the transition temperature called the nil ductility transition temperature (NDTT), fracture occurs by cleavag energy required for fracturing a specimen in an impact test is negligible.

Irradiation has two effects on BCC metals and alloys, firstly it increases the secondly it brings down the fracture energy of the material even in the duct (so-called upper shelf energy). Irradiation embrittlement and the increase in serious engineering problems in nuclear reactors since the materials chosen fo vessels and containment vessels of reactor systems are made of ferritic steels w BCC crystal structure and undergo the ductile to brittle transition. By cod ments, the operation of the reactor is permissible only if the NDTT of the co material is atleast ~ 37°C below the operating temperature of the compo

The influence of neutron irradiation on the NDTT of ASTM A203 Grade D s alloy ferritic steel containing approximately ~ 3.5% nickel) is shown in figure Raj *et al* 1983). The results have been obtained from charpy-V half size specim steel. Using the criterion of 30J energy to determine the NDTT, in the un condition (curve A) the steel has NDTT of −91°C and an upper shelf energy 100 J. Irradiation to a fluence level of 3.5×10^{19} n.cm^{-2} (curve B) increases th around 150°C while bringing down the upper shelf energy to as low as 40 J. A fluence of 5×10^{18} n.cm^{-2} (curve C) the NDTT is shifted to only about −10° upper shelf energy is about 50 J. The curve D shows the impact energy transi for the material that has been annealed at 300°C for 15 days following irradi fluence level of 3.5×10^{19} n.cm^{-2}. That is it shows the recovery in properties t obtained, by annealing at higher temperatures in specimens that have been irr a brittle condition corresponding to curve B. It is seen that the NDTT has bee down to −10°C and the upper shelf energy has increased to about 80 J. Thi annealing at higher temperatures offers the possibility of using *in situ* an reactor components to remove at least a portion of the irradiation dama reduce the NDTT to acceptable levels in those cases where the shift has become (Mansur and Bloom 1982; Steele 1975; Spitznagel *et al* 1976).

The ductile brittle transition in BCC metals is associated with the strong te dependence of the yield strength in these materials which has already been di § 2.1. According to the Ludwig-Davidenkov criterion (Grant and Fort Wechsler 1976) for the NDTT illustrated in figure 5, the ductile-to-brittle

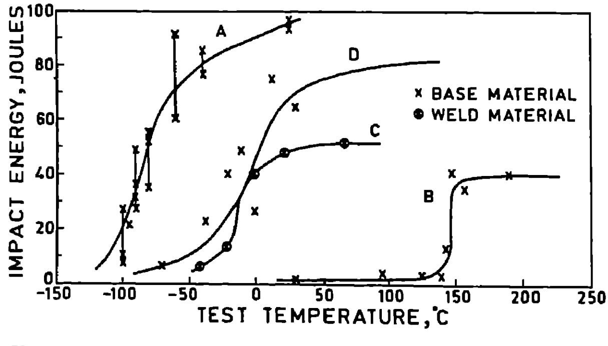

Figure 4. Impact energy *vs* temperature curves for ASTM A 203 grade D steel (R *al* 1983); A = Unirradiated; B = Irradiated to a fluence of $3{\cdot}5 \times 10^{19}$n.cm^{-2}; C = Ir fluence of 5×10^{18}n.cm^{-2}; D = Annealed at 300°C for 15 days after irradiation to $3{\cdot}5 \times 10^{19}$n.cm^{-2}.

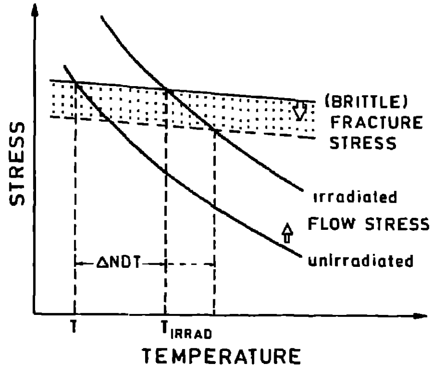

Figure 5. Schematic illustration of the Ludwik-Davidenkov criterion for NDTT and its shift with irradiation.

at a temperature where the yield stress, due to its strong increase with decrease in ature reaches the critical stress for cleavage fracture which is much less ature-dependent. Furthermore the cleavage fracture stress is relatively in- lent of microstructural features such as the defect clusters introduced by tion. The yield stress however increases drastically upon irradiation thereby g the NDTT to higher values as shown in figure 5. To explain the decrease in the shelf energy with irradiation it has been suggested (Ehrlich 1980) that the ge fracture stress could be reduced by irradiation-induced defects; the dashed line re 5 illustrates this situation which also results in a larger shift in the NDTT.

dual elements in ferritic steels are found to have a very significant effect on the of irradiation embrittlement (Bement 1972). Two elements that have the most ious effect are phosphorous and copper. Studies by Brenner *et al* (1978) using n microscope to determine the structure on an atomic level have shown that and phosphorous can stabilise a high concentration of very small microvoids ^{21} voids/m^3 with a mean diameter of 0.6 nm). These stabilised microvoids would e the increased flow stress and the associated shift in NDTT. Notwithstanding the ce of residual elements on radiation defect stabilisation, there are other intrinsic of these elements on impact behaviour which may prove to be important in the vity to radiation embrittlement. Those residual elements which restrict cross-slip, ignificant matrix strengthening, and reduce surface energy are primarily suspect.

Table 3. Effects of residual elements on sensitivity to irradiation embrittlement of steel (Bement 1972)

t	Increases NDTT	Reduces ductile shelf	Forms precipi-tate	Reduces surface energy	Increases flow stress	Restricts cross slip
	√(S)	—	√	√(S)	√(S)	√(S)
	√(S)	—	—	√	√(S)	√
	—	√(S)	√(S)	√(S)	—	—
	√(M)		√	√	√	√
	√ (S)	Increases	√(S)	√	√	√
	√ (M)	√ (M)	√(S)	√	√	√

S—strong effect; M—mild effect.

Some of the elements that fall in this category are listed in table 3 (Bement seen that phosphorous contributes strongly to all the three processes, coppe solution hardener and silicon, vanadium, aluminium and cobalt diminish cross-slip.

The preceding discussion on the low temperature embrittlement in BCC alloys have been restricted to a few qualitative remarks aimed at explaining of the phenomenon. The literature on the subject is very extensive an discussions on the influence of chemical composition, metallurgical var irradiation variables (neutron dose, dose rate, neutron spectra and temperature) on the influence of irradiation on NDTT have been well docume literature (Wechsler 1967; Steele 1975; Nichols and Cowan 1971; Ehrlich

3.2 *Irradiation embrittlement in normally ductile metals and alloys*

Figure 6 shows the effect of neutron irradiation on the tensile stress-strain b a normally ductile metal like FCC copper (Makin 1967). The essential featu effects are: (i) increase in yield strength (ii) increase in the ultimate tensile str smaller extent than the increase in yield stress; (iii) decrease in the ra hardening; and (iv) decreases in the uniform and total elongations. Thes irradiation on the shape of the tensile stress-strain curve for copper ap broadly representative of ductile metals of all the three crystal structures (F HCP) and of pure metals and complex alloys alike. For example it may be see in a material like mild steel which shows the ductile-brittle transition the e stress-strain curve at room temperature at which mild steel is ductile (figur similar to the effect in face centred cubic copper.

The reductions in ductility caused by irradiation in normally ductile ma been attributed to the phenomenon of dislocation channelling, whic exhibited by irradiated or quenched FCC, BCC and HCP metals (Wechsler radiation-produced defect clusters are apparently removed when slip dislo set in motion along the slip plane in the earlier stages of deformation. The then continues by the motion of subsequent slip dislocations along the sam preference to the nucleation of a new band in an adjacent region of the c result, the deformation becomes considerably more localised than is t

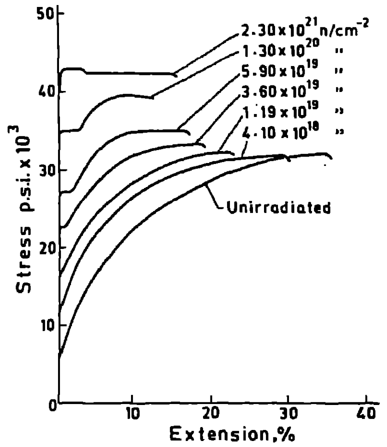

Figure 6. Stress-strain curve talline copper tested at 20°C afte the doses indicated (Makin 19

diated metals. Due to the dislocation channelling deformation takes place in the ands in a catastrophic manner and leads to plastic instability localised in the els or slip bands at a strain "averaged over the gauge length" which is smaller than mogenous deformation. The phenomenon of dislocation channeling is also able lain the reduction in work hardening rate due to irradiation in ductile metals. The al of irradiation-produced obstacles by the moving dislocations will result in a ion in the enhancement of flow stress with strain and consequently in a reduced hardening rate. It has been pointed out (Diehl 1977) that the reduced work ning and dislocation channeling are essentially the same phenomenon on nt scales (macroscopic and microscopic). On a macroscopic scale plastic ility and necking always set in when in a tensile test, within a small strain interval, rease in stress due to work hardening is too small to compensate the reduction in section so that the applied load remains constant or even decreases. A general ion in work hardening will always therefore result in premature necking and values of uniform and total elongations. On a microscopic scale the tendency of materials to become less ductile after irradiation is related to the mechanisms by defect clusters produced by irradiation are eliminated by the moving slip ations. The various proposed mechanisms whereby slip dislocations interact with move radiation-produced dislocation loops and other defects have been reviewed mmarised by Wechsler (1976).

elium embrittlement

onically generated helium has a strong effect on the elevated temperature fracture iour of metals and alloys above $0{\cdot}4T_m$. At these temperatures, grain boundary becomes prominent and intergranular fracture occurs by wedge cracking at boundary junctions or by the fracture of continuous brittle grain boundary itates or by cavitation. Helium produced by the various transmutation reactions reactor environment causes intergranular embrittlement by stabilising the s and the wedge cracks; the growth and coalescence of helium bubbles have also uggested as a possible mechanism for helium embrittlement. Another suggested nism is that helium reduces the grain boundary energy relative to the matrix aneously strengthening the matrix relative to the boundary by dislocation g.

problem of helium embrittlement has come to the fore with the advent of the fast r reactors which operate at high temperatures of the order of 500 to 700°C at grain boundary sliding becomes predominant in the structural materials. The mportant material of application in fast breeder reactors is stainless steels and f the data on the phenomenon of helium embrittlement have been generated on ass of materials. In stainless steels helium is generated from the $B^{10}(n, \alpha)Li^7$ n which has a high thermal neutron cross-section or from (n, α) reactions n fast neutrons and elements present in the steels like nickel, chromium, nitrogen on. Most of the helium produced is heterogeneously distributed in the tructure due to boron segregation and carbon replacement in MC and $M_{23}C_6$ itates. It is the segregation of helium at the grain boundaries that is the deciding in promoting helium embrittlement. The phenomenon of helium embrittlement tenitic stainless teels is illustrated in figure 7 (Harries 1979) which shows the of fast reactor irradiaion on the tensile properties of solution-annealed 316

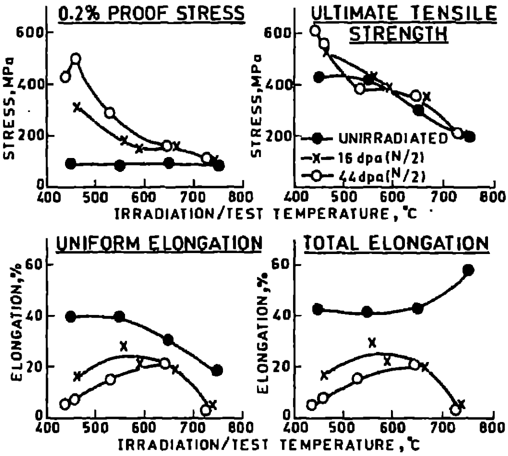

Figure 7. Effects of fast reactor irradiation on the tensile properties of so
316 stainless steel (Harries 1979).

stainless steel in the temperature range 400 to 750°C. The effects of irrad
0·2% yield stress, ultimate tensile strength, uniform elongation and total el
given in this figure. In the temperature range 400–650°C, the yield stren
with increase in dose; however the ultimate tensile strength is not significa
by irradiation. The ductilities, both uniform elongation and total elo
found to be significantly reduced by irradiation and the decrease in ducti
with increasing dose. However, two distinct temperature regions an
ductilities can be discerned from these results. Upto 650°C where irradiati
is prevalent as seen from the effects on yield strength, the ductility reduc
caused by the phenomenon of dislocation channelling which has already b
in the previous section. Above 650°C both uniform elongation and tot
show a drastic reduction reaching almost negligible values at temper
700°C. This high temperature irradiation embrittlement is associated w
tendency for fracture to occur along the grain boundaries and is a
production of helium and the stabilisation of cavities and wedge cracks b
fracture mode in the unirradiated material which is mixed trans-and i
changes to entirely inter-granular in the irradiated specimens.

The mechanisms for helium embrittlement have been critically review
(1972) and Harries (1979). Many of the fundamental features of helium e
are well understood and corrective actions can be arrived at. Among these
refinement (Harries and Roberts 1967), alloy adjustment to form preci
grains for trapping helium (Bloom and Weir 1967), improved melting pra
concentrations of boron and other neutronic helium formers (Standrin
thermomechanical treatments to strengthen boundaries and adjacent zo
Wheeler 1967; Bhanu Sankara Rao *et al* 1981) and heat treatments
stabilisation against recovery or recrystallisation during irradiation (
Kawasaki 1969).

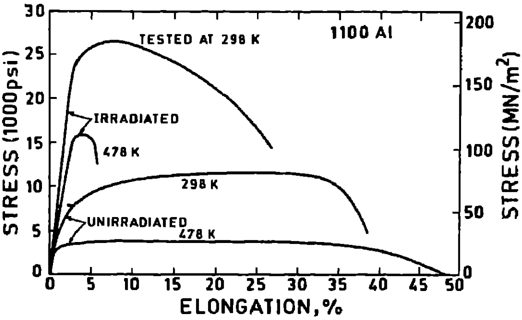

Figure 8. Effect of neutron irradiation (fluence 2·7 × 10^{22}n.cm^{-2} at 323 K) on the tensile curves of 1100 Al at 298 and 478 K (Farrell and King 1973).

mbrittlement due to other transmutation products

›ssible that the mechanical properties of structural materials can be altered by utation products other than helium as well. One known example is the case of ium (Farrell and King 1973) in which neutron irradiation damage when ted to high fluences at about 323 K was found to consist of the fine precipitate of utation produced silicon and the associated dislocation network and very few These defects were responsible for the large increase in the mechanical strength mercial purity aluminium as shown in figure 8. When tested at 298 K significant y loss was observed in this material which has been attributed to the production rittling silicon coming from the nuclear reaction,

$$^{27}\mathrm{Al}(n, \gamma) \rightarrow {}^{28}\mathrm{Al} \rightarrow {}^{28}\mathrm{Si} + \beta^{-}.$$

longation which was of the order of 38 % in the unirradiated condition at 298 K ɔwn to about 27 after irradiation. More important is the reduction in the uniform :ion which reduces from about 32 % to about 7 %. It is also seen that the ons in ductility at a higher temperature of 478 K are more severe with the total :ion decreasing from ~ 48 % to about 6 % after irradiation and the uniform :ion becoming as low as about 3 %. This embrittlement at the higher temperature K has been shown to be due to the phenomenon of grain boundary :lement by helium which was discussed in § 3.3. (In aluminium helium is ed from (n, α) reactions of Li and B present as impurities as well as from Al(n, α) ns).

adiation creep

s the time-dependent deformation that a material undergoes at a constant stress mperature. It is interesting to recall that the first radiation effect on the ıical properties of metals to be reported was, that the creep rate of single crystals mium increased on bombardment with alpha particles (Andrade 1945). :ed creep in a reactor environment was first observed in uranium in 1955 by s and Cottrell (1956). The observed creep was explained on the basis of internal ; developed by the neighbouring crystals undergoing anisotropic irradiation (see § 5). With regard to irradiation creep observed in isotropic materials the original thinking was that the normal thermal creep mechanism of dislocatio controlled glide gets enhanced by the large concentration of vacancies prod irradiation. Based on this, it was postulated (see for example, Rodriguez 1973 low temperatures below approximately $0{\cdot}3T_m$ where dislocation glide is t controlling mechanism there will be a reduction in creep rate under irradiation from irradiation hardening due to the defect clusters. At higher temp irradiation will increase the creep rate since climb-controlled glide is th mechanism and this can be assisted by the excess concentration of vacancies. O of the increased concentration of vacancies due to irradiation is to bring d temperature range at which creep due to dislocation climb can occur. It realised that at very high temperatures ~ 0·6 to $0{\cdot}7T_m$ where the concentr vacancies produced by irradiation is small compared to the thermal equ concentration of vacancies itself, irradiation will not have any significant effect and thermal creep would predominate. Now it is recognised that in add enhancement of climb and development of internal stress due to anisotropic there can be new mechanisms of irradiation creep. For example, the mecha stress-induced loop nucleation or loop alignment of interstitial clusters (SIPN) (1962) of stress-induced preferential absorption (SIPA) of interstitials at disl (Heald and Speight 1974; Wolfer and Ashkin 1975) have as a common feature formation or growth of interstitial loops and absorption of defects at the dislocations depend upon their orientation with respect to the external st therefore cause a macroscopic creep strain. Mansur (1979) has introduced th the stress-induced preferential absorption and emission of radiation-generate into the climb-glide model and this has been called PAG creep. Indeed tho experimental results on irradiation creep have been limited there have been m mechanisms proposed to account for the phenomenon. Excellent revie summaries on the theories and mechanisms of irradiation creep are available 1971; Gilbert *et al* 1977; Bement 1972; Ehrlich 1981; Mansur and Reiley 1980). the experimental results on irradiation creep have been generated on austenitic steels and zirconium alloys, the two major core component materials in thermal reactors respectively. In the following we present some of the typical r these two groups of materials.

4.1 *Irradiation creep in stainless steels*

Irradiation creep results from pressurised tubes of 20% cold worked 316 stain irradiated in EBR II are presented in figure 9 (Gilbert *et al* 1977). The cree (nominal hoop strain) that have been accumulated in the material after irradi 4138 h to a dose of 15 dpa (displacements per atom) at hoop stresses of 34, 69, 207 MPa are shown in the figure for the temperature range 370–620°C. The creep lines represent creep data obtained from pressurised tubes which were furnace for the same time that the irradiation specimens were irradiated. In ge a constant stress, the creep rate is dominated by irradiation creep process temperatures and eventually swamped out by normal thermal creep at high tures. There is a mild temperature dependence for the irradiation creep Irradiation creep is increased by a factor of approximately 2·5 as the ir temperature is increased from 400 to 575°C. Figure 10 is an example of the which has been obtained to date to support the contention that irradiation

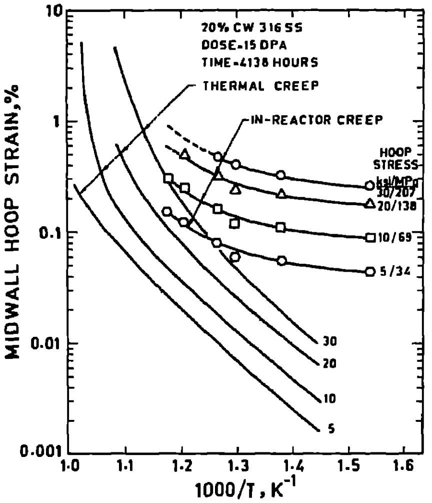

Figure 9. Irradiation creep results from pressurised tube of 20% cold-worked 316 stainless steel (Gilbert *et al* 1977).

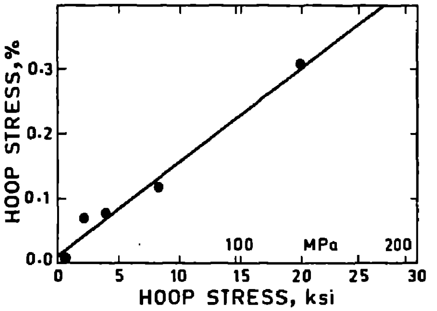

Figure 10. Linear stress dependence of irradiation creep in 316 stainless steel at 520°C and a fluence of 3 × 10^{22}n.cm^{-2}.

stress (these data were also obtained from pressurised tubes). Indeed it is this pendence in stress that distinguishes irradiation creep from the thermal creep h the stress dependence has an exponent of 3 to 5.

diation creep in zirconium alloys

ous reactor structural components that are made out of zirconium alloys at a temperature below 300°C, which is low relative to the melting point and at an operating stress which is below one half of the yield stress (except for). Thus one would expect the creep deformation to be insignificant. However, r creep tests have demonstrated that neutron irradiation substantially the creep rate of zirconium alloys by a factor of upto 10 times (Fidleris and 1966). Subsequently it became known that irradiation creep in zirconium anisotropic (Fidleris 1978). Thus efforts were made to correlate the observed n creep data with several parameters such as crystallographic texture, cold-in size and microstructure. Effect of neutron flux, dose, temperature and stress radiation creep behaviour was also taken into account in explaining the in-reep behaviour of zirconium alloys. An excellent review on this subject has tributed by Hurst *et al* (1976).

A knowledge of out-of-pile thermal creep of zircaloys is necessary to ha understanding of irradiation creep. Much of the early work was aimed at de the effect of cold-work on the creep properties of zircaloy-2. Zirconium all annealed condition have shown more primary creep and also a higher secon rate, upto about 10,000 hours. At larger times, it has subsequently been sho low stresses, within the temperature range of 300–400°C, cold work has littl the secondary creep rate (Van Echo and Poremka 1965). For sheet sampl (1957) has shown that creep properties in both the longitudinal and directions were virtually identical, which is strange for a notoriously a material like zircaloy-2. However, later studies by Bell (1962) have shown t stresses and at a temperature of 300°C, the creep rate of specimens taken tr from a tube is somewhat lower than that of longitudinal specimens. This has been attributed to a greater proportion of grains being available for sli tudinal specimens, assuming that most slip occurs on the $(10\bar{1}0)$ prism pla $\langle 11\bar{2}0 \rangle$ directions. Bell also showed that the creep rate generally decreases ruling out self-diffusion as a major creep mechanism at this temperature. As s proved difficult to produce a simple creep equation to include the va temperature and stress to predict the creep behaviour of zircaloy-2.

Fidleris and Williams (1966) were the first to show the significant increase i rate due to irradiation. A typical curve showing the accelerated effect of irra the creep rate is shown in figure 11. There is a general agreement that at flux le order of 10^{13} n/cm^2/sec, the creep rate is directly proportional to flux. It ta dose of about 1×10^{20} n/cm^2 to reach the steady state creep. The steady s showed an increase with increasing temperature. However, as the cre dependent on the stress level and flux, it is not possible to extrapolate the obtained at one temperature, to describe the behaviour at some other tem

At temperatures around 300°C, it has been found that the effect of stress o rate is dependent on the absolute stress level. However, it is likely that the effe on creep rate may be a complex one so that any extrapolation to stress levels b limit of the test data may be unreliable.

Fabrication procedures affect the texture, grain shape and dislocation st zirconium alloy tubes. Thus different manufacturing procedures can proc with different dimensional behaviours. Pressure tubes are normally manuf extrusion and cold drawing processes. Increased extrusion ratio leads to incre pole densities in the tangential direction (F_t). Subsequent drawing or

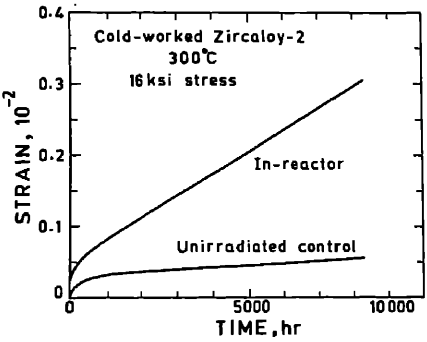

Figure 11. Accelerate creep in zircaloy-2 (Wood 1969).

ns tend to rotate the basal poles into the radial direction (F_r). The density of
les in the axial direction is almost zero.

nsional data are now available for cold-worked zircaloy pressure tubes
tured by eight different routes and irradiated in the Hanford N Reactor, CANDU
at Pickering and Douglas Point and the Winfrith SGHWR. These data show that
be desirable to have a higher F_t (achieved by a high extrusion ratio) which
ve a higher creep strength in the transverse directions. However, too high an F_t
y also pose a practical problem from length increase considerations.

1979) has shown that there is only a weak dependence of creep on dislocation
This is in agreement with the stress relaxation tests on extruded and cold-
Zr-2·5 wt % Nb (Coleman *et al* 1975). The excellent correlation of the model
d by Holt and Ibrahim (1979) and the pressure tube data obtained by Holt
now that the underlying physical assumption of Holt and Ibrahim (1979)
hat the strain producing mechanism for irradiation creep is glide, predomi-
f $b = 1/3 \langle 11\bar{2}0 \rangle$ dislocations on $(10\bar{1}0)$ planes, but with some contri-
rom another type of glide, probably of dislocations with $b = 1/3 \langle 11\bar{2}0 \rangle$
) planes. Thus the creep strains can be related to crystallographic texture
del based on variations in the amount of cross-slip of dislocations of the
$\langle 11\bar{2}0 \rangle$ from prism to basal planes. Such an attempt has recently been made
y (1981).

diation growth

n growth is defined as a change in dimensions during irradiation in the
of any applied stress; dimensional change under zero stress distinguishes
' from 'creep' which occurs under a stress. Irradiation growth occurs in single
nd textured polycrystals of anisotropic metals and alloys by the unequal
ion of interstitial and vacancy loops on different crystallographic planes. In the
we shall present the results and models available for the phenomena in
n alloys (HCP structure) used for core components in thermal reactors and in
uranium (orthorhombic) used as a fuel in research reactors.

diation growth in zirconium alloys

n growth occurs in all zirconium alloys and is anisotropic. It is known to
n the crystallographic texture and substructure of the material (Fidleris 1975;
1977; Holt and Ibrahim 1979; Murgatroyd and Rogerson 1979). In general,
n growth is assumed to be a constant volume process, although the hypothesis
me change during growth has also been proposed (Dollins 1975) and recently
nges in density in zircaloy have been observed after irradiation (Harbottle and
1980).

ences above about 1×10^{25} n.m^{-2} ($E > 1$ MeV), growth strains were shown
se with irradiation temperature upto about 573 K but were observed to
at higher temperatures.

le data clearly indicate strong differences in the magnitude of irradiation
r recrystallized and coldworked/stress-relieved zircaloy. The mechanisms of
re also thought to be substantially different for these two metallurgical
s (Fainstein-Pedraza *et al* 1978; Northwood 1977).

Adamson *et al* (1981) have shown that the growth strains for both annealed
cold-worked zircaloy exhibited a strong dependence on irradiation temperatu
range of 644–723 K), upto fluences between 1·4–6·3 × 10^{25} n.m^{-2}. The rate of
in growth with temperature in the annealed longitudinal material was fou
higher than the rate in 20% cold-worked material. In general the growth beha
these two cases were similar suggesting a common mechanism of growth ope
both types of material at the applicable damage rates and irradiation temp

Growth strains in a given direction in zircaloy are determined by the crystall
texture *i.e.* proportional to $(1 - f_d^c)$ where f_d^c is the fraction of basal poles,
direction *d*.

It appears that the high growth strains in annealed zircaloy are governe
formation of dislocation arrays which then climb. This is a change in
mechanism from that applying at lower irradiation temperatures and is simil
mechanism for cold-worked materials. Thus irradiation growth is dependent
on texture but also on dislocation density as reported by Holt (1979).

5.2 *Irradiation growth in metallic uranium fuel*

The dimensional instability of alpha uranium under reactor irradiation is o
earliest known forms of radiation damage. During irradiation below about
single crystal of uranium extends in ⟨010⟩ direction, and contracts in th
direction. There is no noticeable extension or contraction in the ⟨001⟩ directi
is no change in the volume of the material. Polycrystalline uranium with a
orientation thus changes its shape during irradiation. It has been proposed
"growth" results from the large number of vacancies and interstitials create
passage of a fission fragment through the crystal. Above about 500°C, self-di
sufficiently rapid for these point defects to be annihilated, but at lower tem
they aggregate into flat mono-layer plates which can be observed by tran
electron microscopy (Hudson *et al* 1962). Stresses due to anisotropic thermal e
in the fission spike force, the vacancies and interstitials to aggregate on differe
planes (Buckley 1962). Elongation, which is due to interstitial clusters, is theref
direction of minimum thermal expansion, ⟨010⟩, and contraction, which
collapsed vacancy clusters, is in the direction of maximum thermal expansion
This correlation of the direction of irradiation growth with the direction of r
thermal expansion has been observed in other anisotropic lattices also (Buckl
This mechanism suggests no simple way to eliminate the basic growth proces
remedy for changes in shape is sought in producing uranium of small grain
total preferred orientation. However, grains in uranium are notoriously impe
become more so during irradiation. Thus the presence of sub-boundaries m
mask the effect of the nominal grain size.

Irradiation swelling is another phenomenon which takes place in metallic
fuel. There is a net volume increase due chiefly to the gaseous fission produ
and krypton which at reactor operating temperatures tend to precipitate to
bubbles. The inert gases are extremely insoluble in solids and precipitate
embryo gas bubbles on any suitable nuclei, *e.g.* dislocations, grain boundaries
boundaries. There is the additional possibility that the gas nucleates 'homoge

Since swelling is least when the gas pressure is high, *i.e.* when the bubbles
swelling would be reduced by increasing the number of heterogeneous nucl

subsequent coarsening. The gas bubbles can grow only when vacancies are le and these are plentiful above about 450°C. However, the limitation to bubble will be the ability of the gas to redistribute within the metal.

n boundaries like dislocations, will tend to adhere to gas bubbles because this the total surface energy. A moving grain boundary will also tend to drag the s and owing to the greater binding force, the grain boundary will be able to drag ıch larger bubbles than a dislocation. Hence if recrystallisation or grain growth small bubbles in the matrix will be swept and will undergo rapid coalescence. the number of gas bubbles is kept to a maximum, swelling will be minimum, by ing their migration.

s been found that minor alloying additions and impurities play a significant role cing swelling. Carbon, which is present in most commercial uranium in amounts -1 000 ppm, has a marked effect in reducing volume increases (Loomis and 1962). The greatest individual effect in reducing swelling was produced by 00 ppm of aluminium, which was further enhanced by the presence of about n of iron and 600 ppm of carbon (Bellamy 1962; Pugh 1961). For producing this however, it is necessary to quench the uranium from the beta phase and ently anneal it in the alpha phase. Uranium of this composition and heat nt has been developed by UKAEA and is known as adjusted uranium and is to have minimal irradiation growth effects.

d swelling

while carrying out electron microscopic examination of specimens of stainless adiated in the Dounreay fast reactor (DFR) Cawthorne and Fulton (1967) found pherical cavities in the material which seemed to contain nothing except a small of gas. In addition to being a new and curious scientific discovery, it was very preciated that the development of void in a material meant that the density of erial would decrease and its physical size would increase and this can have very nt implications to the design of a fast reactor core. In the last 17 years the of void swelling has received intensive research leading to a physical anding and quantifying of the phenomenon (Norris 1972; Johnston *et al* 1976; 1981; Mansur 1982; Bates and Powell 1981).

netric swelling caused by void formation has become a generally observed enon for metals and alloys after neutron irradiation or heavy ion bombard- the temperature range 0·30 to 0·60T_m. The basic ideas behind the formation of ın irradiation produced defect have already been described in § 2. The primary produced by irradiation are vacancies and interstitials and void formation occur temperatures higher than 0·30T_m where both vacancies and interstitials are Void growth requires specifically three conditions: firstly that there is a uration of vacancies; secondly the vacancies migrate to voids before being ted by interstitials and thirdly that more vacancies than interstitials arrive at clei. The last condition is satisfied by the fact that other defects like dislocations bias for interstitials and absorb more interstitials than vacancies. The second n is met if the temperature is high enough for vacancy mobility. The first n is met when the temperature is low enough for the thermal equilibrium ation of vacancies to be significantly lower than irradiation-induced concentration. Thus void formation occurs in a limited temperature range, of 0·3 t

Although there are important differences in detail the general nature formation for a variety of metals and alloys is similar. The voids are usually pol and in FCC metals commonly take the shape of a truncated octahedron bounc square [001] faces and 8 hexagonal [111] faces (Bement 1972). Void shapes and can be irregular however depending upon temperature and purity (Stieg 1969). Faulted interstitial loops are also generally observed in metals and alloy a low stacking fault energy (prismatic loops for high stacking fault energy) and with the voids account for a population balance between interstitials and v generated by neutron irradiation. Visible voids in stainless steels range in diame about 5 to 35 nm with the greatest number sized about 20 nm. Void formation several high purity metals and alloys of different crystal structures are summ tables 4 and 5 (Bement 1972). Reference to the tables reveals that voids ha observed in FCC (Ni, Al, Cu, Pt), BCC (Mo, Fe, B, Nb, W) and HCP (Re) metals wi irradiation temperature range 0·3 to $0{\cdot}6T_m$. Zirconium and titanium are exceptions in that they exhibit large vacancy loops and a general absence of v fluence of 3×10^{21} n/cm^2 (Brimhall *et al* 1971).

Most of the data on void swelling available are on austenitic stainless st nickel-base alloys because of their immediate interest as core component mat fast reactors. Also much of the progress towards evaluating and controlli swelling has been made possible by the use of charged particle bombardn accelerators to rapidly simulate the damage that occurs in a reactor. Howe damage produced by heavy ion bambardment in accelerators could give different from actual in-reactor irradiation. One major difference is that becau higher dose rate and the larger rate of defects production by ion bombardment temperature of swelling gets shifted to a higher temperature. For austenitic steels this shift is about 150°C (Johnston *et al* 1976) as illustrated in figure quantify damage produced by ion irradiation the damage dose is calcul represented as the number of times a lattice atom is displaced: displacements or dpa). It has also been demonstrated that prior implantation of helium with particle beam is necessary when heavy ion irradiation is carried out to simulate

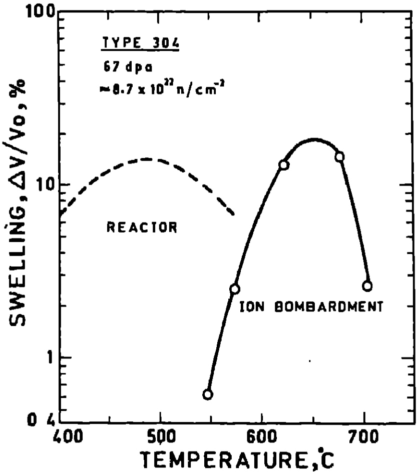

Figure 12. Temperature dence of swelling in 304 stai during reactor and ion ir (Johnston *et al* 1976).

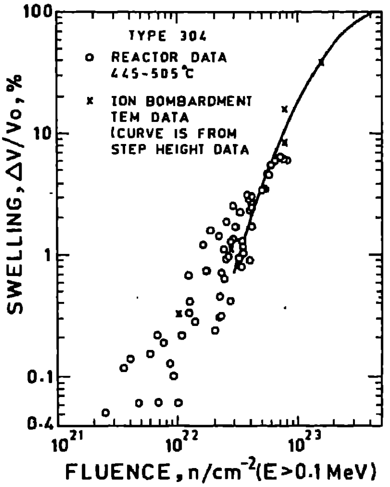

Figure 13. Dose dependence of swelling in 304 stainless steel by reactor and ion irradiation at the respective peak swelling temperatures (Johnston *et al* 1976).

ım in stabilising voids in reactor irradiation. However, a good correlation can be ›d between swelling and fluence in reactor and ion irradiations when the swelling the respective peak swelling temperatures are compared as illustrated in figure ınston *et al* 1976) where the swelling *vs* fluence data for two types of irradiation ›wn and the ion dose has been converted to fluence by taking 10^{23} n/cm^2 as ent to 77 dpa. The main point that emerges from the accelerated test using ion rdment is that at the fluences of 2 to 3 × 10^{23} n/cm^2 which is the target fluence ımercial fast reactors, the swelling can be as large as 20 to 30 %. It may be seen gure 13 that there is a threshold fluence below which no appreciable swelling The value of the threshold fluence is of the order of 10^{21} n/cm^2, which ›onds to a value of approximately 6 dpa.

ling rates as a function of irradiation temperatures for M316, M316L, FV 548 ›nonic PE 16 alloy irradiated in DFR to fast fluences up to 8·7 × 10^{22} n/cm^2 in the ature range 300–650°C are shown in figure 14 (Bramman *et al* 1971). The g rate in M316L is only half that in M316. Also peak swelling rates are observed rent temperatures. M316 shows peak swelling rate at 600°C while in the case of 'er carbon M316L, peak swelling occurs around 500°C. The peak swelling in at 600°C is associated with the precipitation of $M_{23}C_6$ carbides in this ature range. These results suggest that control of carbon level is important in ining void swelling. For both M316 and 316L cold work is found to drastically the swelling rate. It has been shown that with a very high initial dislocation in the cold worked condition the nucleation of both interstitial dislocation ınd voids is inhibited as a consequence of dominance of point defect ›ination at the dislocation sinks (Little *et al* 1980). FV 548 in both solution ›d and cold-worked conditions shows lower swelling rates than M316. FV 548 s higher carbon level (0·06 to 0·09 %) than M316 (0·05 %) but has a niobium level ıs specified as 8 times the carbon content. This suggests that inhibition of ınular $M_{23}C_6$ precipitate by the addition of MC carbide forming elements is › in reducing void swelling. The beneficial effect of carbide stabilising elements titanium or niobium in reducing void swelling has been demonstrated by many (Bloom and Stiegler 1970; Ehrlich and Gross 1974). Figure 13 also shows that

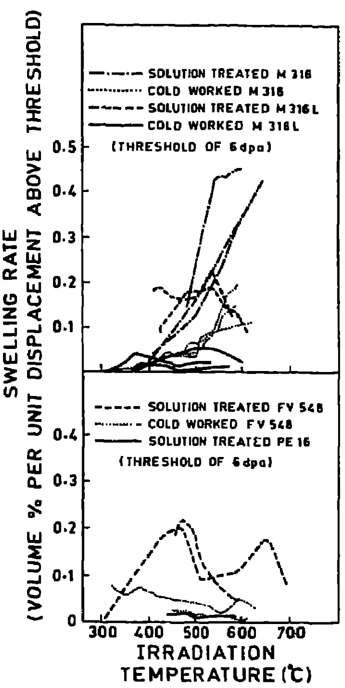

Figure 14. Swelling rates in
FV548 and PE16 alloys (Brammar

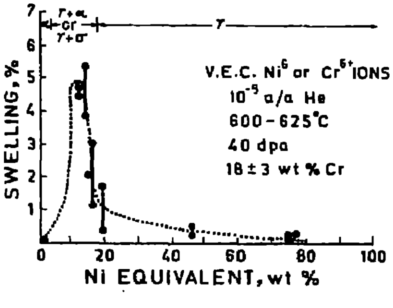

Figure 15. Void swelling in ste
base alloys as a function of nic
(Harries 1974).

Nimonic alloy PE 16 has a very low swelling rate relatively insensitive t
temperature compared to stainless steels.

The void swelling in various steels and nickel-base alloys, as a functi
equivalent contents, is shown in figure 15 (Harries 1974). The void swellin
zero for the ferritic steel (approximately 2% nickel equivalent), relativ
variable for the austenitic stainless steels (3–18% nickel equivalent) a
progressively at higher nickel contents. A similar dependence of void
austenitic stainless steels and nickel-base alloys with nickel content h
observed by other workers (Johnston *et al* 1976).

Nickel-base alloys like Nimonic PE 16, though attractive from the poi
low swelling, have a greater tendency for helium embrittlement discus
because of the higher production of helium due to the nickel (n, α) reaction
the very low swelling resistance of ferritic steels a number of ferritic/mar
have come to the fore as candidate materials for core components for

. Among these must be mentioned the HT9 and D57 two high strength ferritic 'hich are candidate materials for potential applications in the fast breeder :ores in the US (Chin *et al* 1982) and the FV 448 martensitic stainless steel being / considered and studied in the UK programme (Little *et al* 1980). The sms of swelling suppression in alpha iron and ferritic steels have been ised by Little (1979) who has emphasised the key role played by both interstitial ititutional solutes in inducing enhanced mutual recombination of point defects trapping processes and also in lowering dislocation mobility and bias for tial self-interstitial capture in these materials and thereby controlling their void response. Based on careful transmission electron microscopic studies of ıs irradiated in a high voltage electron microscope Little *et al* (1980) have :d that the suppression of void formation in the FV 448 martensitic stainless to be attributed to the simultaneous formation of $a\langle 100\rangle$ interstitial on loops in addition to the $a/2\langle 111\rangle$ interstitial dislocation loops. Loops

Table 4. Voids in pure metals (Bement 1972)

Metal	Temperature range voids observed T/T_m	Minimum reported fluence ($\times 10^{-19}$ n/cm^2)	Maximum reported volume fraction of voids (%)
Ni-FCC	0·31–0·60	0·11	0·64
Al-FCC	0·35	3	high
Mo-BCC	0·30–0·49	3	0·28
Cu-FCC	0·39	12	0·17
Re-HCP	0·39–0·41	50	0·10
Fe-BCC	0·40	300	0·12
V-BCC	0·30–0·41	490	1·77
Nb-BCC	0·26–0·40	2500	—
Zr-HCP	0·42	300 (voids not observed)	
Ti-HCP		300 (voids not observed)	

Table 5. Voids in alloys (Bement 1972)

Alloys		Temperature range voids observed (T/T_m)	Minimum reported fluence ($\times 10^{-19}$ n/cm^2)	Maximum reported volume fraction of voids (%)
304 ss (annealed)	FCC	0·38–0·55	14	4·1
316 ss (annealed)		0·38–0·51	500	3
304 ss (cold-worked)		0·40	2800	0·1
316 ss (cold-worked)		0·41–0·58	2300	0·02
V-20% Ti	BCC		1400 (Voids not yet observed)	

Table 6. Relative probabilities for the formation of *a* ⟨100⟩ dislocation loops in a range of BCC metals (Little *et al* 1980)

Metal	Relative probabilities
Nb	$4{\cdot}3 \times 10^{-5}$
V	$5{\cdot}5 \times 10^{-5}$
Fe	$5{\cdot}7 \times 10^{-9}$
Ta	$7{\cdot}9 \times 10^{-11}$
Mo	$1{\cdot}9 \times 10^{-19}$
W	$1{\cdot}4 \times 10^{-27}$

with $b = a/2 \langle 111 \rangle$ are the predominant loop type nucleated. However ther
probability of about $5{\cdot}7 \times 10^{-9}$ at 420°C for the nucleation of $a \langle 100 \rangle$ lo
both types of loops are present $a/2 \langle 111 \rangle$ network acts as a vacancy sink in
and absorbs the net vacancy flux created by the growth by preferential
capture of the isolated a 100 loops. This explanation seems to be quite reaso
the tendency for void suppression or swelling resistance should be goven
probability of $a \langle 100 \rangle$ loop formation relative to that for $a/2 \langle 111 \rangle$ loop forn
values of this probability for the various BCC metals which include the techı
important metals such as niobium, molybdenum, tungsten, vanadium and ta
shown in table 6. It can be seen that relative to alpha Fe, V and Nb are more
with respect to $a \langle 100 \rangle$ loop formation while Mo, W and Ti are less favoura
it may be inferred that V and Nb are likely to exhibit relatively high swelling r
irradiated in the cold-worked condition, whereas tantalum, molybdenum an
would show higher susceptibility for void formation than iron and ferritic
susceptibility increasing in the order tantalum, molybdenum, tungsten.]
cited earlier (tables 4 and 5) tend to support this explanation since molybc
found to show void formation whereas voids could not be observed in V

The role of major elements like nickel, in iron-chromium-nickel alloys
pointed out already. The swelling of iron-chromium-nickel alloys can be si
reduced by one or two orders of magnitude by minor elements. It has alı
pointed out that commercial stainless steels containing stabilisers such as tit
niobium are found to swell less than the unstabilised stainless steels. Bloom
have reported that the additions of silicon and titanium to type 316 stee
appreciable reduction in swelling. Bates (1975) investigated the effects of
minor element content in a type 316 stainless steel on in-reactor swelling (fig
17). Individual additions of many of the elements that are normally added to
made to a base alloy of Fe-15 Cr-20 Ni. Only silicon, titanium, zirconium ar
caused an appreciable reduction in swelling with zirconium being the most
a per atom basis. Boron, carbon, phosphorous molybdenum, mang
aluminium either had little effect or caused a slight increase in swelling. Th
have confirmed the observation of Bloom *et al* (1976) that combination of
titanium appears to be more effective in reducing swelling than the simple
the individual effects would suggest. The temperature dependence of swe

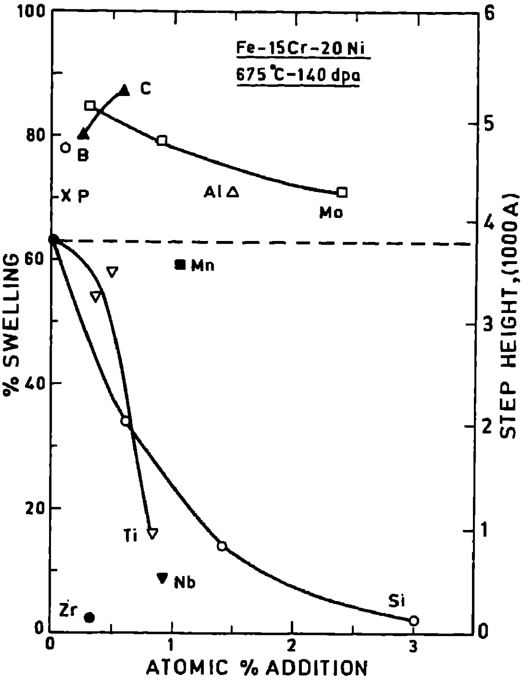

Figure 16. Effects of individual minor element additions on the swelling of Fe-15 Cr-20 Ni steel (Johnston *et al* 1976)

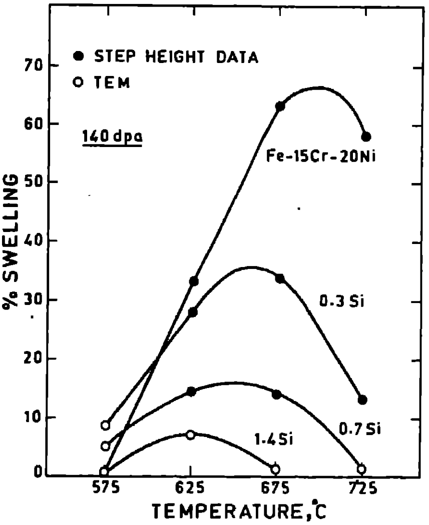

Figure 17. Effect of Si additions on swelling in Fe-15 Cr-20 Ni steel (Johnston *et al* 1976).

Fe-15Cr-20Ni alloy with additions of silicon is shown in figure 16 suppression is greater at higher temperatures. Also there is a tendency t swelling temperature towards a lower temperature region.

The phenomenon of void swelling has engineering implications fo core components in a fast breeder reactor. It increases the diameter of th is considered to be partly beneficial since it helps to reduce fuel-cl interaction by making more room available inside the pin for the fuel to pin swelling could restrict coolant passages in the assembly leading to well as increasing the pumping power needed to maintain the coolant the amount of swelling expected this may not be a serious problem f performance *per se*, difficulties may arise because of the differential sw the fuel pin, the wire wrap on the fuel pin or the grid supporting t hexagonal wrapper holding the assembly of fuel pins. The most seriou swelling is on the subassembly wrapper. As void swelling depends temperature the wrappers will elongate by different amounts dependin position within the core. The wrapper is a long stiff structure whic locations is irradiated more on one side than the other. This causes the v so that its top end moves away from the core centre. This problem c bowing is important when the subassemblies are unrestrained, and one o measures is to alter the design by using the constrained core concept in of the subassemblies is accommodated by elastic and creep strains in th deflection of wrappers between the support points. In fact, irradiation cr enhances deformation capability of the material during irradiation is u the stresses developed due to swelling. Other solutions within the un concept itself are operational and include periodic rotation of the sub the adoption of the use of wrapper materials resistant to void swelling. economics of the fast breeder reactor it is considered necessary tha wrapper materials should have void swelling not exceeding 6% in the tar 20% cold-worked 316 type stainless steel with 0·4 to 0·6 wt% silicon and titanium additions of 0·3 to 0·5 wt% is considered to meet this requir been used in EBR II in USA and Superphenix in France and is the p material in our own programme for building fast breeder power reacto

7. Summary

A review of radiation effects in nuclear reactor materials has been made; effects have been correlated with the crystal structure of the materials. Fi irradiation hardening, irradiation embrittlement, irradiation creep, irra and void swelling that occur in materials by neutron irradiation environment have been discussed. There is definitive evidence that in F slip HCP metals (Zn, Cd), irradiation produced defects become rate-contr deformation. In the case of BCC metals and prism slip HCP metals (Zr, hardening appears to be athermal in nature. In all cases irradiatio accompanied by irradiation embrittlement manifested by reduced work lowered ductility. This type of embrittlement caused by irradiation in n metals arises from localised deformation due to dislocation channeling BCC metals and alloys which undergo ductile to brittle transition at low shifts the transition temperature to higher temperatures and lowers the ergy in the ductile region (upper shelf energy at high temperatures). The ls chosen for pressure vessels and containment vessels of reactor systems ystal structure and it is necessary to limit the residual elements and to have a ize in these steels so that the ductile-brittle transition temperature and its irradiation are minimised. Helium embrittlement becomes important at peratures $> 0{\cdot}4T_m$ where grain boundary slidings become predominant; of helium bubbles from (n, α) transmutations at grain boundaries promotes ar fracture by stabilising wedge cracks and grain boundary cavities. ent due to other transmutation products can also occur as exemplified by of Si in Al. The influence of irradiation on creep depends on temperature. peratures where irradiation hardening predominates creep rate is reduced. -produced vacancies enhance climb and thereby lowers the temperature at by climb-controlled glide can occur. In addition to such enhanced thermal iation also causes creep due to new mechanisms which arise from stress-entation/alignment of dislocation loops and stress-induced absorption of at dislocations. Irradiation growth (change in dimensions under zero stress) nisotrophic materials like Zr (HCP) and U (orthorhombic) by the unequal of interstitials and vacancy loops on different crystallographic planes. Void n phenomenon that occurs at temperatures between 0·3 and $0{\cdot}6T_m$ and at ation doses typical of fast reactors. HCP metals like Zr, Ti and BCC refractory ferritic/martensitic steels are less prone to void swelling than the austenitic els and nickel-base alloys. Nickel-base alloys have better void swelling than eels but their greater susceptibility to helium embrittlement offsets this Stainless steels with controlled Si additions stabilised with Ti/Nb cold about 20% are found to have acceptable swelling rates for fast reactor s.

1977 in *Zirconium in the nuclear industry* (Philadelphia: American Society for Testing and
ASTM STP 633, pp. 326
Tucker R P and Fidleris V 1981 in *Fifth International Conference on Zirconium in the Nuclear*
l.) D. Franklin (Philadelphia: American Society for Testing and Materials) ASTM STP 754
1945 *Nature* (*London*) **156** 119
ed.) 1973 *Proc. Int. Conf. Defects and Defect Clusters in BCC Metals and their Alloys; Nucl.*
629
976 in *Treatise on materials science and technology. Vol. 6. Plastic deformation of materials* (ed.)
rman (New York: Academic Press) pp. 83
siviswanathan K V and Rodriguez P 1983 in Activity Report of Metallurgy Programme 1981
Kalpakkam: Reactor Research Centre) RRC-60, pp. 67
in *Properties of reactor structural alloys after neutron or particle irradiation* (Philadelphia:
ociety for Testing and Materials), ASTM STP 570 pp. 369
Powell R W 1981 *J. Nucl. Mater.* **102** 200
Report AECL 1456 (Chalk River: Atomic Energy of Canada Ltd.)
962 Inst. of Metals Symposium on Uranium and Graphite, London
972 *Rev Roum Phys* **17** 505, 519, 607, 619
Rao K, Seetharaman V, Mannan S L and Rodriguez P 1981 *J. Nucl. Mater.* **102** 7
d Stiegler J O 1970 *J. Nucl. Mater.* **35** 244
iegler J O, Rowcliffe A F and Leitnaker J M 1976 *Scripta. Met.* **10** 303

Bloom E E and Weir J R (Jr) 1967 in *Irradiation effects in structural alloys for thermal and fast reactors* (Philadelphia: American Society for Testing and Materials) ASTM STP 456 pp. 241

Bramman J I, Bagley K Q, Cawthorne C, Fulton E J and Sinclair W D J 1971 in *Voids formed by irradiation of reactor materials Proc. BNES Conf.* (eds) S F Pugh, M H Loretts and D I R Norris (London: British Nuclear Energy Society) pp. 27

Brenner S S, Wagner R and Spitznagel J A 1978 *Metall. Trans.* **A9** 1761

Brimhall J L, Kulcinski G L, Kissinger H E and Mastel B 1971 *Rad. Eff.* **9** 273

Buckley S N 1962 in *Properties of reactor materials and the effects of radiation damage* (ed.) D J Litter (London: Butterworths) pp. 413

Causey A R 1981 *J. Nucl. Mater.* **98** 313

Cawthorne C & Fulton E J 1967 *Nature* (*London*) **216** 575

Chin A B, Neuhold R J and Straalsund J L 1982 *Nucl. Technol.* **57** 426

Chow J G Y, McRickard S and Gruinsky D H 1969 in *Radiation damage in solids* (Vienna: International Atomic Energy Agency) Vol. 1, pp. 277

Coleman C E, Causey A R and Fidleris V 1975 Report AECL-5042 (Chalk River: Atomic Energy of Canada Ltd)

Diehl J 1970 in *Vacancies and interstitials in metals* (eds) A Seeger, D Schumacher, W Schilling and J Diehl (Amsterdam: North-Holland Co) pp. 739

Diehl J 1977 in *Proc. Indo-German Seminar on Radiation Damage* (Kalpakkam: Reactor Research Centre) pp. 336

Diehl J and Seidel G P 1969 in *Radiation damage in reactor materials* (Vienna: International Atomic Energy Agency) Vol. 1 pp. 209

Diehl J, Siedel G P and Weller M 1968 *Suppl. Trans. Jpn Inst. Metals* **9** 219

Dollins C C 1975 *J. Nucl. Mater.* **59** 61

Ehrlich K 1980 in *Proc. Joint JEN-KFK Seminar on Materials for Reactor Vessels and Components*, Paper No. 7, Madrid, November 1980

Ehrlich K 1981 *J. Nucl. Mater.* **100** 149

Ehrlich K and Gross R 1974 in *Proc. Symp. on Fuel and Fuel Elements for Fast Reactors* (Vienna: International Atomic Energy Agency) Vol. 2, p. 179

Evans A G and Rawlings R D 1969 *Phys. Status Solidi* **34** 9

Fainstein-Pedraza D, Savino E J and Pedraza A J 1978 *J. Nucl. Mater.* **73** 151

Farrell K and King R T 1973 *Metall. Trans.* **4** 1223

Fidleris V 1975 *Atomic Energy Rev.* **13** 61

Fidleris V 1978 Paper presented at Int. Conf. Reactor Materials Science, Alushta, USSR May 1978

Fidleris V and Williams C D 1966 *Electrochem. Technol.* **4** 258

Fleischer R L 1962 *Acta Metall.* **10** 835

Fleischer R L 1962 *J. Appl. Phys.* **33** 3504

Gilbert E R 1971 *Reactor Technol.* **14** 258

Gilbert E R, Straalsund J L and Wire G L 1977 *J. Nucl. Mater.* **65** 266

Grant S P and Fortner E 1972 *Metals Engg. Q.* **12** 17

Hamad A M, Sharma B D and Rodriguez P 1975 *Trans. Indian Inst. Metals* **28** 231

Harbottle J E and Herbillon F 1980 *J. Nucl. Mater.* **90** 249

Harries D R 1979 *J. Nucl. Mater.* **82** 2

Harries D R and Roberts A C 1967 in *Effects of radiation on structural materials* (Philadelphia: American Society for Testing and Materials) ASTM STP 426, pp. 21

Heald P T and Speight M V 1974 *Philos. Mag.* **29** 1075

Hesketh R V 1962 *Philos. Mag.* **7** 1417

Holt R A 1979 *J. Nucl. Mater.* **82** 419

Holt R A and Ibrahim E F 1979 *Acta Metall.* **27** 1319

Hudson B, Westmacott K H and Makin M J 1962 *Philos. Mag.* **7** 377

Hurst P, Nichols R W, Pickles B, Watkins B and Wood D S 1976 *Atomic Energy Rev.* **14** 439

Johnston W G, Lauritzen T, Rosolowski J H and Turakalo A M 1976 *J. Metals* **28** 19

Kayano H, Higashiguchi Y and Yagima S 1977 *J. Nucl. Sci. Technol.* **14** 117

Kocks U F, Argon A S and Ashby M F 1975 *Progress in Mater. Sci.* **19** 1

Koppenal T J 1965 *Philos. Mag.* **11** 1257

Koppenal T J and Arsenault R J 1965 *Philos. Mag.* **12** 951

Koppenal T J and Arsenault R J 1971 *Metall. Rev.* **157** 175

Levy I S and Wheeler K R 1967 in *Effects of radiation on structural materials* (Philadelphia: American Society for Testing and Materials) ASTM STP 426, pp. 458

Li J C M and Mukherji A K (eds) 1972 *Proc. John E. Dorn Memorial Symposium on Rate Processes in Plastic Deformation* (Metals Park OH: American Society for Metals)

Little E A 1967 *Phys. Status Solidi* **A3** 983

Little E A 1976 *Int. Metals Rev.* **21** 25

Little E A 1979 *J. Nucl. Mater.* **87** 11

Little E A, Bullough R and Wood M H 1980 UKAEA Report AERE-R 9678 (Harwell: Atomic Energy Research Establishment)

Loomis B A and Pracht D W 1962 USAEC Report ANL-6532 (Argonne: Argonne National Laboratory)

Makin M J 1967 in *Radiation effects* (ed.) W F Sheely (New York: Gordon and Breach) pp. 627

Mansur L K 1979 *Philos. Mag.* **A39** 497

Mansur L and Bloom E E 1982 *J. Metals* **34** 23

Mansur L K and Reiley T C 1980 *J. Nucl. Mater.* **90** 60

Matta M K, Batra I S and Sharma B D 1977 *Trans. Indian Inst. Metals* **30** 240

Murgatroyd R A and Rogerson A 1979 *J. Nucl. Mater.* **79** 302

Nagasaki S and Kawasaki S 1969 in *Radiation damage in reactor material* (Vienna: International Atomic Energy Agency) Vol. 2, pp. 161

Nichols R W and Cowan A 1971 *Atomic Energy Rev.* **9** 1

Norris D I R 1972 *Rad. Effects* **14** 1

Norris D I R 1972 *Rad. Effects* **15** 1

Northwood D O 1977 *Atomic Energy Rev.* **15** 547

Ohr S M, Tucker R P and Wechsler M S 1968 *Suppl. Trans. Jpn Inst. Metals* **9** 187

Pugh S F 1961 *J. Nucl. Mater.* **4** 177

Roberts A C and Cottrell A H 1956 *Philos. Mag.* **1** 711

Rodriguez P 1973 in *Radiation damage in reactor materials* (Kalpakkam: Reactor Research Centre) RRC-1, pp. 135

Rodriguez P 1977 in *Indo-German Seminar on Radiation Damage* (Kalpakkam: Reactor Research Centre) pp. 353

Rodriguez P and Dasgupta P 1972 in *Recent developments in metallurgical science and technology* (New Delhi: Indian Institute of Metals) pp. 47

Rogerson A and Murgatroyd R A 1979 *J. Nucl. Mater.* **80** 253

Seeger A 1958 *Proc. Second Int. Conf. Peaceful Uses of Atomic Energy* (New York: United Nations) **6** 250

Seidel G P 1969 *Rad. Effects* **1** 177

Shober F R 1957 Report BMI 1168 (Columbus: Battelle Memorial Institute)

Spitznagel J A, Shogan R P and Phillips J A 1976 in *Irradiation effects on the microstructure and properties of materials* (Philadelphia: American Society for Testing and Materials), ASTM STP 611, pp. 434

Standring J, Bell I P, Tickle H and Glendinning A 1967 in *Irradiation effects in structural alloys for thermal and fast reactors* (Philadelphia: American Society for Testing and Materials) ASTM STP 456, pp. 414

Steele L E 1975 Neutron irradiation embrittlement of reactor pressure vessel steels, technical report Series No. 163 (Vienna: International Atomic Energy Agency)

Stiegler J O, Farrell K, Dubose C K H and King R T 1969 in *Radiation damage in reactor materials* (Vienna: International Atomic Energy Agency) Vol. 2, pp. 229

Van Echo J A and Poremka S W 1965 Report BMI-X-10113 (Columbus: Battelle Memorial Institute)

Watkins B and Wood D S 1969 in *Applications related phenomena in zirconium and its alloys* (Philadelphia: American Society for Testing and Materials) ASTM STP 458, pp. 226

Wechsler M S 1967 *Nucl. Safety* **8** 461

Wechsler M S 1972 in *Defects in refractory metals* (eds) R de Batist et al (Mol, Belgium: Studiecentrum voor Kernenergie) pp. 235

Wechsler M S 1976 in *Proc. Int. Conf. on Fundamental Aspects of Radiation Damage in Metals* (eds) M T Robinson and F W Yong Jr, USERDA Report CONF 751006, Vol. 2, pp. 991

Wolfer W G and Ashkin M 1975 *J. Appl. Phys.* **46** 547

Bull. Mater. Sci., Vol. 6, No. 2, May 1984, pp. 369–393. © Printed in India.

Structural disorder and solid state transformations in single crystals of $Zn_xCd_{1-x}S$ and $Zn_xMn_{1-x}S$

M T SEBASTIAN and P KRISHNA

Physics Department, Banaras Hindu University, Varanasi 221 005, India

Abstract. Single crystals of $Zn_xCd_{1-x}S$ and $Zn_xMn_{1-x}S$ were grown from the vapour phase at 1100°C in the range $x = 0{\cdot}9$ to 1. X-ray characterization shows that polytypes and disordered structures occur in $Zn_xCd_{1-x}S$ for $x \geqslant 0{\cdot}94$, whereas $Zn_xMn_{1-x}S$ displays disordered and polytype structures in the entire range $x = 0{\cdot}9$ to 1. It is observed that $Zn_xCd_{1-x}S$ and $Zn_xMn_{1-x}S$ undergo a 2H–6H solid state transformation on annealing in vacuum around 600°C. Experimental analysis of the intensity distribution along the $10 \cdot L$ reciprocal lattice row as recorded on a single crystal diffractometer from partially transformed crystals shows that the mechanism of the transformation cannot be explained in terms of the one-parameter models of non-random faulting reported earlier. A two-parameter theoretical model with α representing the probability of random insertion of a fault in the 2H structure and β representing the probability of the growth of the 6H nucleus, is developed both for a deformation mechanism and a layer displacement mechanism. It is found that the theoretical model of non-random deformation faulting with $\beta \gg \alpha$ approximates the actual mechanism of transformation in these crystals.

Keywords. Structural disorder; single crystals; polytype structures; theoretical models.

1. Introduction

In recent years there has been considerable interest in the study of mixed crystals of the type $Zn_xCd_{1-x}S$ and $Zn_xMn_{1-x}S$ and the characterization of their physical properties. The possibility of obtaining a systematic variation of photoelectronic properties simply by adjusting the solid solution composition has given rise to an interest in optoelectronic applications of $Zn_xCd_{1-x}S$ crystals, mainly luminescence applications (Brodin *et al* 1970; Kawaguchi *et al* 1976; Yoshikawa and Sakai 1976) and heterojunctions for photovoltaic energy conversion (Burton and Hench 1976; Domeus *et al* 1977). Manganese-doped ZnS (ZnS : Mn) provides an efficient system for high field electroluminescence (Theis 1981) and the electroluminescent devices exhibit (Inouguchi *et al* 1974) characteristics which are especially attractive for use in flat panel refreshed matrix displays with high peak luminescence-voltage response. Such devices can be operated (Inouguchi *et al* 1974) at high brightness for tens of thousands of hours at constant voltage with little loss of luminescence.

It is therefore of considerable interest to examine the defects present in such crystals and study their influence on device properties. It is well known that single crystals of ZnS when grown from the vapour phase at temperatures above 1050°C show a variety of polytype structures with considerable random disorder. On the other hand CdS which is isostructural with ZnS does not exhibit polytype structures and the related disorder effects (Chandrasekharaiah and Krishna 1969). Zinc sulphide and cadmium sulphide both display two polymorphic structures—wurtzite (2H) and sphalerite (3C).

Manganese sulphide on the other hand exists in three polymorphic forms—a stable green α-MnS with the rock salt structure and two pink metastable adamantine structures β-MnS (sphalerite type) and γ-MnS (wurtzite type). The β and γ-forms are metastable at room temperature and convert (Mehmed and Heraldson 1938; Schnaase 1933) into α-MnS on heating at 200°C. β-MnS is also known to convert into α-MnS at high pressure (Roomians 1963).

CdS and ZnS are known to form solid solutions of the type $Zn_xCd_{1-x}S$ for all values of x (Cherin *et al* 1970). MnS and ZnS on the other hand form a continuous series of solid solutions only in the range $x = 0$ to 0·52 (Schnaase 1933; Kröger 1939; Juza *et al* 1956; Lutz and Becker 1977). The present investigation was undertaken to study (i) the variation of the disorder effects in single crystals of $Zn_xCd_{1-x}S$ and $Zn_xMn_{1-x}S$ with change of composition and (ii) the effect of composition on the wurtzite-sphalerite (2H-3C) phase transformation which is known to give rise to defect structures in these materials.

2. Crystal growth, characterization and annealing behaviour of $Zn_xCd_{1-x}S$

Single crystals of $Zn_xCd_{1-x}S$ $(1 > x > 0{\cdot}90)$ were grown (Sebastian and Krishna 1983) from the vapour phase at 1100°C in the presence of H_2S gas. Needle-shaped crystals ranging in length from 0·5–8 mm and in width from 0·1–0·5 mm were obtained. For $x = 0{\cdot}95$ we observed dendritic growth with large sword-shaped dendrites branching and rebranching at 60° angles as seen in figure 1(a). The $Zn_{0\cdot95}Cd_{0\cdot05}S$ dendrites grew as needles along the $\langle 10\bar{1}0\rangle$ directions and finally merged to form a platelet perpendicular to [0001]. Figure 1 shows the dendrites at four different stages of growth.

The structure of as-grown $Zn_xCd_{1-x}S$ crystals was examined (Sebastian and Krishna 1983) by x-ray diffraction by recording 15° c-axis oscillation photographs. The crystals showed different structures depending on the amount of cadmium present in the crystal. All the crystals with a composition $x \leqslant 0{\cdot}93$ were free of stacking faults and had a perfect 2H structure. For $x \geqslant 0{\cdot}94$ the crystals were found to contain 2H, 3C, 2H + 3C, polytype and disordered structures. The dendrites observed at $x = 0{\cdot}95$ were single crystals containing 2H + 3C + disorder in their structure.

Needle-shaped crystals of 2H $Zn_xCd_{1-x}S$ were annealed in vacuum at successively higher temperatures in the range 400–1100°C for 1 hr each and then quenched in cold water to arrest the structural transformations induced in them. During annealing the crystals were kept immersed in ZnS powder in a silica tube to prevent the crystal from vapourising at high temperatures. After each annealing run the crystals were quenched by immersing the silica tube in cold running water. The structure of the crystals was re-examined by x-ray diffraction after each annealing followed by quenching. The crystals were also examined under an optical microscope before and after annealing to detect any macroscopic kinks characteristic of crystals undergoing transformation by the periodic slip mechanism.

It is found that the transformation behaviour of the 2H $Zn_xCd_{1-x}S$ crystals depends on the value of x. The crystals with the composition $x > 0{\cdot}98$ transformed to a disordered twinned 3C structure in a manner similar to that reported earlier for ZnS (Sebastian *et al* 1982, 1983a). The 2H crystals in the composition range $0{\cdot}98 > x > 0{\cdot}95$ on annealing transformed to a disordered 6H structure around 600°C.

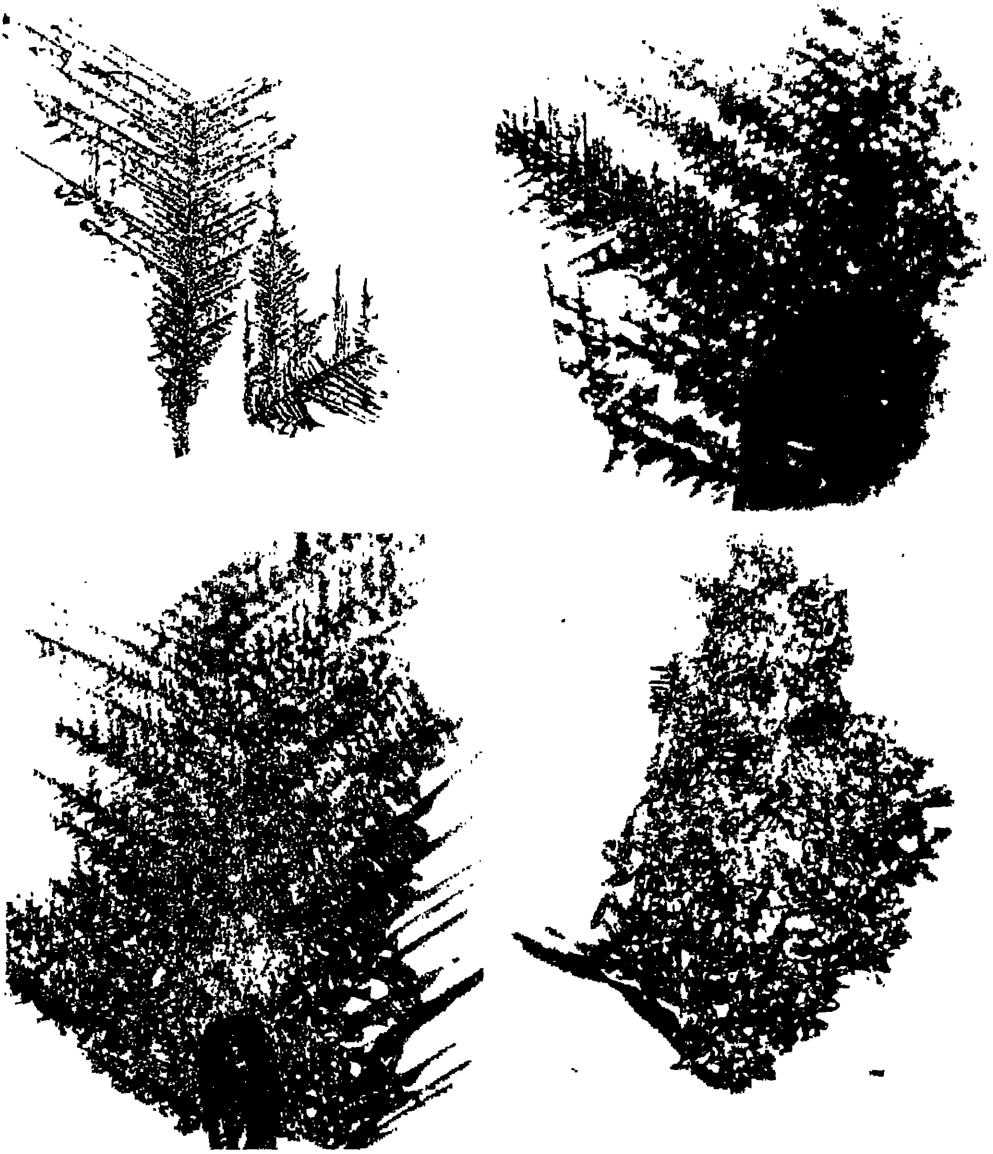

Figure 1. Optical micrographs showing the progress of dendritic growth of $Zn_{0\cdot95}Cd_{0\cdot05}S$ crystals. The axis of the dendrites is found to be along $[10\bar{1}0]$ with the *c*-axis nearly perpendicular to the plane of the figure. The dendrites appear to merge into a platelet as the growth proceeds (× 20).

These crystals on further annealing, at higher temperatures transformed to a disordered twinned 3C structure around 800°C. The crystals in the range $0\cdot95 \geqslant x > 0\cdot93$ behave differently. Nearly 30% of the crystals studied transformed to a disordered 6H structure and the rest to a disordered 2H structure around 600°C. These crystals on further annealing at higher temperatures do not transform to a 3C structure. Figure 2 shows the $10 \cdot L$ reciprocal lattice row of a $Zn_{0\cdot94}Cd_{0\cdot06}S$ crystal before and after annealing at 800°C. The crystals with $x < 0\cdot93$ do not undergo any structural transformation and remain as perfect 2H in the temperature range up to 1100°C indicating that the addition of CdS to ZnS stabilizes the 2H phase in the solid solution.

3. Growth, characterization and annealing behaviour of $Zn_xMn_{1-x}S$ crystals

Single crystals of $Zn_xMn_{1-x}S$ were grown in a manner similar to that described for $Zn_xCd_{1-x}S$. Polycrystalline ZnS and MnS were mixed in calculated proportions for different values of x ($0\cdot9 \leqslant x < 1$). The crystals obtained were needle-shaped, up to 5 mm in length and 1 mm thick. The crystals were examined by x-ray diffraction and were found to contain perfect 2H, disordered 2H, 2H + 3C, polytypes and disordered structures. The 6H structure was encountered more frequently than in $Zn_xCd_{1-x}S$ crystals.

Needle-shaped crystals of $Zn_xMn_{1-x}S$ were annealed in vacuum in the temperature range 400–1100°C for 1 hr each and quenched in the manner described earlier for $Zn_xCd_{1-x}S$ crystals. The structure of the crystals was re-examined by x-ray diffraction after each annealing run. It was observed that nearly 75% of the 2H $Zn_xMn_{1-x}S$ crystals transformed to a disordered twinned 3C structure in a manner similar to that observed for pure ZnS (Sebastian *et al* 1982). In the remaining 25% crystals disordered 6H structure was observed around 500°C as an intermediate state. On further annealing at higher temperatures this disordered 6H structure transformed to a

Figure 2. The $10.L$ reciprocal lattice row of a 2H $Zn_{0\cdot93}Cd_{0\cdot07}S$ crystal recorded (a) before annealing (b) after annealing at 800°C for 1 hr. The crystal has transformed partially to a 6H structure. (Camera radius 3 cm, CuK radiation × 4).

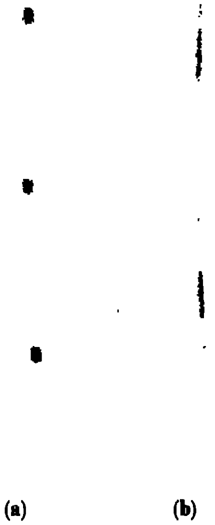

(a) (b)

Figure 3. The 10.L reciprocal lattice row of a 2H $Zn_{0{\cdot}9}Mn_{0{\cdot}1}S$ crystal recorded (a) before annealing (b) after annealing at 600°C for 1 hr. The 2H reflections have nearly disappeared and diffuse reflections have developed in positions of 3C and 6H reflections. (Camera radius 3 cm, CuK radiation. × 3).

disordered twinned 3C structure. All the crystals transformed back to a disordered 2H structure on annealing above 1050°C. Figure 3 shows the 10 · L row of a perfect 2H $Zn_{0{\cdot}9}Mn_{0{\cdot}1}S$ crystal before and after annealing at 600°C for 1 hr. Most of the crystals which transformed to the twinned 3C structure showed an enhancement of intensity at positions of 6H reflections along the 10 · L row. After each annealing run the crystals were examined under an optical microscope to detect any change in the shape of the crystals. No kinks or other macroscopic changes in the shape of the crystals were observed after transformation.

4. Mechanism of the 2H-6H transformation

Daniels (1966) and Mardix and Steinberger (1966) proposed a periodic slip mechanism to explain the 2H-3C transformation in ZnS and for the formation of long period polytypes. This envisages the expansion of stacking faults around an axial screw dislocation causing them to occur with a period equal to the Burgers vector of the screw dislocation. However, periodic slip caused by the expansion of a single deformation fault around a screw dislocation of 6 layered Burgers vector in a 2H structure would give rise to an 18R structure as shown below

initial structure:

A B A B A B|A B A B A B A B A B A B A B A B A B A B . . . . .
C A C A C A|C A C A C A C A C A C A . . . . .
B C B C B C|B C B C B C . . . . .
A B A B A B| . . . . .

resulting structure:

$$ABABABCACACABCBCBCABABAB\ldots\ldots = 18\text{R}$$
$$(1113)_3$$

The transformation to a 6H structure is only possible if two partial dislocations of opposite signs occur at three layer separations and expand simultaneously around a screw dislocation of 6-layered Burgers vector. Moreover, crystals undergoing a 2H-6H transformation by the periodic slip mechanism should develop macroscopic kinks. The absence of such kinks and the strong diffuse intensity observed on x-ray diffraction photographs along the $10\cdot L$ reciprocal lattice row indicate that the transformation has occurred by the non-random nucleation of stacking faults at three-layer separations (Secco d'Aragona *et al* 1966; Sebastian *et al* 1982). In this case the Burgers vector of the partial dislocation bounding each stacking fault can be in any of three symmetry related directions. Since each fault nucleates independently, the three directions would occur with equal probability producing no macroscopic kinks. Even in crystals which do not contain a screw dislocation, the faults can nucleate preferentially at 3-layer separations in order to effect the 2H-6H transformation. A similar transformation from the 2H to the 6H structure has been observed earlier by Krishna and Marshall (1971) in SiC and possible mechanisms were investigated in detail by Pandey *et al* (1980).

4.1 *Theoretical models*

The 2H to 6H transformation in close-packed structures can occur by two different mechanisms involving the non-random insertion of either layer displacement faults or deformation faults (Pandey *et al* 1980) in the 2H structure. If layer displacement faults nucleate at three-layer separations the 2H structure would convert to a 6H structure as shown below

initial structure: $AB\underline{A}BA\underline{B}\;AB\underline{A}BA\underline{B}\;AB\ldots\ldots$
resulting structure: $AB\underline{C}BA\underline{C}\;AB\underline{C}BA\underline{C}\;AB\ldots\ldots$

The layers indicated by underlining have changed their positions. The same transformation can also be effected by the insertion of deformation faults at three layer separations as depicted below

initial structure: $A\;B\,|\,A\;B\;A\;B\;A\;B\;A\;B\;A\;B\ldots\ldots$
$C\;A\;C\,|\,A\;C\;A\;C\;A\;C\;A\ldots\ldots$
$B\;A\;B\,|\,A\;B\;A\;B\ldots\ldots$
$C\;A\;C\,|\,A\ldots\ldots$
$B\ldots\ldots$

resulting structure: $ABCACBABCACB\ldots\ldots$

Pandey *et al* (1980) have theortically calculated the diffraction effects that would be expected from crystals undergoing transformation by both the mechanisms on the assumption that faults do not occur at less than three layer separations but otherwise have the same probability of occurrence at all layers. On the basis of this one-parameter model the main differences in the diffraction effects expected from crystals undergoing

2H-6H transformation by the layer displacement and deformation mechanisms are as follows

(i) The reflections $H-K \neq 3n$ and $L = 0, \pm 1$ (mod 2) of the 2H structure remain sharp and unbroadened throughout the transformation for the layer displacement mechanism while these are considerably broadened for transformation by the deformation mechanism

(ii) For transformation by the layer displacement mechanism a diffuse reflection develops initially around the position $L = \pm \frac{1}{2}$ (mod 2) and then splits into two reflections which migrate towards the $L = \pm \frac{1}{3}$ (mod 2) and $L = \pm \frac{2}{3}$ (mod 2) positions as the transformation proceeds towards 6H. At an intermediate stage of transformation the new 6H reflections are thus shifted towards each other *i.e.*, towards the $L = \pm \frac{1}{2}$ (mod 2) position. For transformation by the deformation mechanism, the new reflections characteristic of the 6H structure appear initially near positions $L = \pm \frac{1}{6}, \pm \frac{5}{6}$ (mod 2) and then approach towards $L = \pm \frac{1}{3}, \pm \frac{2}{3}$ (mod 2) as the transformation progresses towards the 6H structure. At an intermediate stage of transformation these reflections are thus shifted away from each other *i.e.*, away from the $L = \pm \frac{1}{2}$ (mod 2) positions.

Therefore the nature of stacking faults involved in the structural transformation can be determined by studying the peak broadening and peak shifts of x-ray diffraction maxima recorded from partially transformed crystals.

4.2 *Analysis of the observed intensity profiles and comparison with the one-parameter model*

The point intensity distribution along the $10 \cdot L$ reciprocal lattice row of several partially transformed crystals in different stages of transformation was recorded on a four-circle computer-controlled single crystal diffractometer using the method described earlier by Pandey and Krishna (1977). MoKα radiation was used to record the intensity diffracted by the crystal. The crystal and the counter were held stationary during each observation and the crystal was oriented by the computer to diffract the $10 \cdot L$ row for different values of L (in steps of $\Delta L = 0{\cdot}01$) into the counter. The divergence of the incident beam was adjusted to cover the mosaic spread in the crystal. The sharp reflections $H - K = 0$ (mod 3) were used to orient the crystal and to define the hexagonal unit cell. Figure 4 shows the diffractometer record of intensity along the $10 \cdot L$ reciprocal lattice row as recorded from a 2H $Zn_{0{\cdot}93}Cd_{0{\cdot}07}S$ crystal after annealing at 800°C for 1 hr. The crystal is in the initial stage of transformation and the 6H peaks have just begun to appear. The 2H reflections are quite sharp and the new 6H reflections are shifted from their correct positions. Figure 5 shows a similar intensity record obtained from a $Zn_{0{\cdot}94}Cd_{0{\cdot}06}S$ crystal at a more advanced stage of the 2H-6H transformation. The 6H peaks are more clearly developed and are much less shifted from their correct positions. Similar diffractometer records were obtained on annealing 2H crystals of $Zn_xMn_{1-x}S$ at different stages of transformation. The intensity profiles obtained experimentally from partially-transformed crystals show that the new 6H reflections appear at an earlier stage of transformation and are shifted in the direction predicted by the deformation mechanism. However, the 2H and 6H peaks are much sharper than what is expected on the basis of the one-parameter model and the shift of

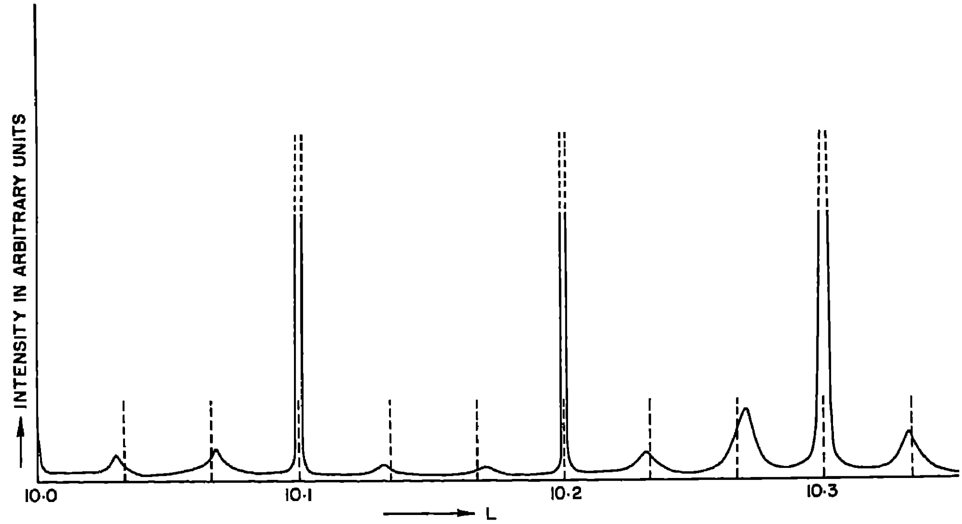

Figure 4. Single crystal diffractometer plot of intensity versus L along the $10\cdot L$ reciprocal lattice row recorded after annealing a perfect 2H $Zn_{0.93}Cd_{0.07}S$ crystal at 800°C for 1 hr. Vertical dashed lines indicate the correct 6H positions from which the new 6H peaks are clearly shifted. The 2H peaks are very sharp and intense and the crystal is in an early stage of transformation.

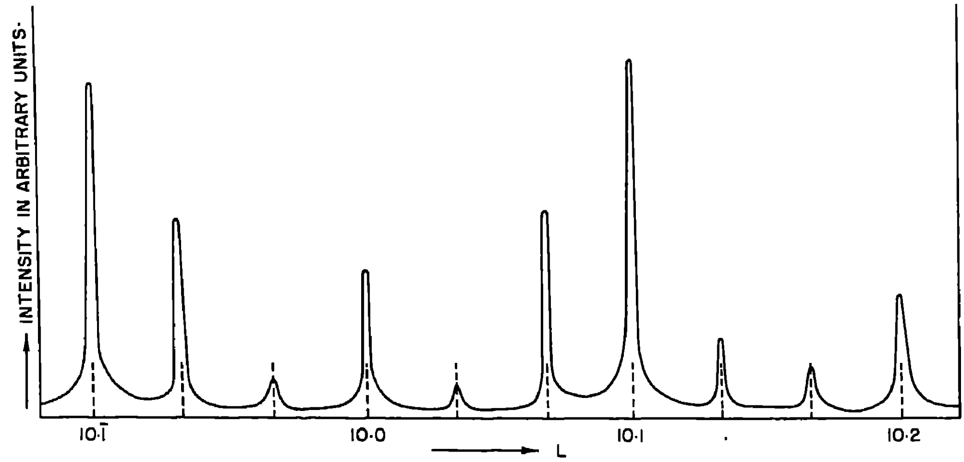

Figure 5. Single crystal diffractometer plot of intensity versus L along the $10\cdot L$ reciprocal lattice row recorded after annealing a perfect 2H crystal of $Zn_{0.94}Cd_{0.06}S$ at 800°C for 1 hr. Vertical dashed lines indicate the correct 6H positions. The crystal is at a more advanced stage of transformation.

the 6H reflections is also much smaller. Therefore it is evident that the 2H-6H transformation in $Zn_xCd_{1-x}S$ and $Zn_xMn_{1-x}S$ crystals does not take place in accordance with the one-parameter model proposed by Pandey *et al* (1980).

5. Development of a two-parameter model

From the experimental results described above it appears that the probability (β) of faults nucleating at 3-layer separations is much larger than the probability (α) of their occurrence at larger separations. The former (β) corresponds to the probability of the growth of a 6H nucleus within the 2H phase and the latter (α) to the probability of fresh nucleation of a fault in the 2H structure. It is possible to develop the theory of x-ray diffraction from 2H crystals undergoing transformation to the 6H structure by (i) the deformation mechanism and (ii) the layer displacement mechanism using two parameter model. A choice between the two mechanisms can then be made from a comparison of the theoretically-predicted diffraction effects with those actually observed provided only one of the mechanisms is operative in the crystal at a time. The need for a two parameter model for ZnS was recognized by Jagodzinski (1949), Müller (1952) and Singer (1963). More recently Lele and Pandey (1982) employed a 2-parameter model to theoretically investigate the 3C–2H transformation in cobalt.

We develop below the theory of x-ray diffraction from crystals undergoing the 2H-6H solid state transformation by (i) the deformation mechanism and (ii) the layer displacement mechanism under the following assumptions:

(i) The crystal is infinite in size and free of distortions.
(ii) The scattering power for all the layers is the same.
(iii) There is no change in the layer spacings at the faults.
(iv) The faults extend right across the crystal boundaries.
(v) The faults occur preferentially at 3-layer separations with a fault probability β which is different from the probability α of random nucleation at larger separations. The probability of faults occurring at less than 3 layer separations is negligible.

5.1 *The theory of x-ray diffraction from crystals undergoing the 2H–6H solid state transformation by the deformation mechanism*

In the perfect 2H structure we distinguish two types of layers with subscripts 0 and 1 according as the stacking offset vector is $+S_i$ or $-S_i$ where S_i denotes $S_1 = \frac{1}{3}a\,[1\bar{1}00]$, $S_2 = \frac{1}{3}a\,[01\bar{1}0]$ and $S_3 = \frac{1}{3}a\,[\bar{1}010]$. The perfect 2H structure can thus be written as

$$A_0B_1A_0B_1A_0B_1A_0B_1\ldots.$$

There are six other types of layers in a 2H crystal undergoing transformation to the 6H structure by the deformation mechanism. Let the subscripts 0^1 and 1^1 denote the first layer of the slipped stack according as it follows a 0 type or 1 type layer. It is assumed that the next two layers after a 0^1 or 1^1 type layer are unfaulted. Therefore the layer following a 0^1 or 1^1 layer is designated as 0^2 or 1^2. The next layer after this is denoted as 0^3 or 1^3 in order to distinguish it from 0 or 1, since there is a probability β that the growth of a 6H nucleus may commence from these layers. We can now compute the probability $P_{(m,j)}$ of arriving at the mth layer with the subscript j ($j = 0, 1, 0^1, 1^1, 0^2, 1^2, 0^3$ and 1^3) with the help of the following probability trees which consider the transitions from $(m-1)$th layer to the mth layer with each type of layer at the origin (Sebastian and Krishna 1983b):

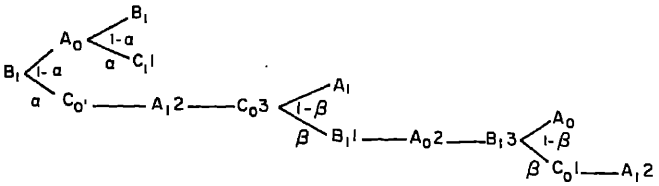

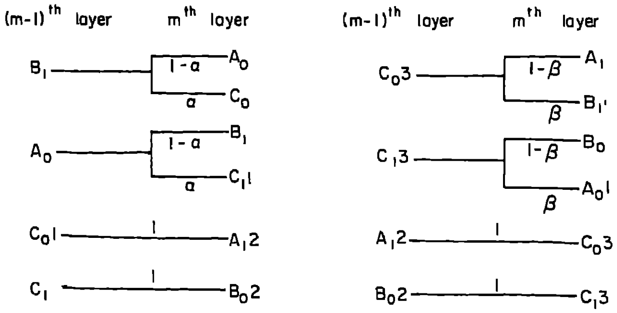

As shown in the probability trees, the layer type following B_1 (or A_0) layers in the absence of a deformation fault is A_0 (or B_1) and occurs with the probability $(1-\alpha)$. Therefore in the presence of a deformation fault the layer following B_1 (or A_0) is C_{0^1} (or C_{1^1}).

The probability $P_{(m,j)}$ may now be computed as follows

$$P_{(m,0)} = (1-\alpha)P_{(m-1,1)} + (1-\beta)P_{(m-1,1^3)}, \tag{1}$$

$$P_{(m,1)} = (1-\alpha)P_{(m-1,0)} + (1-\beta)P_{(m-1,0^3)}, \tag{2}$$

$$P_{(m,0^1)} = \alpha P_{(m-1,1)} + \beta P_{(m-1,1^3)}, \tag{3}$$

$$P_{(m,1^1)} = \alpha P_{(m-1,0)} + \beta P_{(m-1,0^3)}, \tag{4}$$

$$P_{(m,0^2)} = P_{(m-1,1^1)}, \tag{5}$$

$$P_{(m,1^2)} = P_{(m-1,0^1)}, \tag{6}$$

$$P_{(m,0^3)} = P_{(m-1,1^2)}, \tag{7}$$

$$P_{(m,1^3)} \; P_{(m-1,0^2)}. \tag{8}$$

The function $J_{(m,j)}$ can be written (Prasad and Lele 1971) as

$$J_{(m,j)} = \exp(i\phi_m)_j = \sum P_{(m,j)} \exp(i\phi_m)_j, \tag{9}$$

where
$$\exp(i\phi_m) = \exp(i\phi_{m-1})\exp(\pm i\phi_0), \tag{10}$$

and $\phi_0 = 2\pi/3$ is the phase difference between the $(m-1)$th and mth layers and takes plus or minus sign depending on the layer sequence being cyclic $A \to B \to C \to A$ or anticyclic $A \to C \to B \to A$. Using (1) to (10) and putting

$$\exp(+i\phi_0) = \omega_1 \text{ and } \exp(-i\phi_0) = \omega_2$$

we get

$$J_{(m,0)} = (1-\alpha)J_{(m-1,1)}\omega_2 + (1-\beta)J_{(m-1,1^3)}\omega_2, \tag{11}$$
$$J_{(m,1)} = (1-\alpha)J_{(m-1,0)}\omega_1 + (1-\beta)J_{(m-1,0^3)}\omega_1, \tag{12}$$
$$J_{(m,0^1)} = \alpha J_{(m-1,1)}\omega_1 + \beta J_{(m-1,1^3)}\omega_1, \tag{13}$$
$$J_{(m,1^1)} = \alpha J_{(m-1,0)}\omega_2 + \beta J_{(m-1,0^3)}\omega_2, \tag{14}$$
$$J_{(m,0^2)} = J_{(m-1,1^1)}\omega_2, \tag{15}$$
$$J_{(m,1^2)} = J_{(m-1,0^1)}\omega_1, \tag{16}$$
$$J_{(m,0^3)} = J_{(m-1,1^2)}\omega_2, \tag{17}$$
$$J_{(m,1^3)} = J_{(m-1,0^2)}\omega_1. \tag{18}$$

Let the solution of the system of difference equations (11) to (18) be of the form

$$J_{(m,j)} = C_j \rho^m, \qquad m \geqslant 0, \tag{19}$$

where C_j and ρ are functions of α and β. Substituting in equations (11) to (18) and eliminating the various C's we finally get the so-called characteristic equation

$$\rho^8 - (1-\alpha)^2\rho^6 + \alpha(1-\beta)\rho^4 - \beta^2\rho^2 + (\alpha^2 + \beta^2 - 2\alpha\beta) = 0. \tag{20}$$

Holloway (1969) obtained an analytic solution for the diffracted intensity in terms of coefficients and boundary conditions of the characteristic equation. His intensity expression is

$$I = f^2 C \left[\left(\frac{1}{2} + \frac{\sum\limits_{j=1}^{n-1} \sum\limits_{k=0}^{j-1} a_{n-k} T_{j-k} \exp{(n-j)\, i\pi L} - a_0}{\sum\limits_{j=0}^{n} a_j \exp{(j i\pi L)}} \right) + \text{C.C.} \right], \tag{21}$$

where a_n is the coefficient of ρ^n in the characteristic equation, T's are the boundary conditions, C is a scale factor and

$$f^2 = f_{\text{Zn}}^2 + f_{\text{S}}^2 + 2 f_{\text{Zn}} f_{\text{S}} \cos\frac{3\pi L}{4}.$$

In the present case

$$n = 8,\ a_8 = 1,\ a_6 = -(1-\alpha)^2,\ a_4 = \alpha(1-\beta),$$
$$a_2 = -\beta^2 \text{ and } a_0 = (\alpha - \beta)^2,$$
$$a_7 = a_5 = a_3 = a_1 = 0.$$

The boundary conditions (T's) can be found out by the following method. First we find the probability W_j of finding a layer with subscript j on passing through an arbitrary region of the crystal. From the probability tree we get

$$W_0 = (1-\alpha)W_1 + (1-\beta)W_{1^3},$$
$$W_1 = (1-\alpha)W_0 + (1-\beta)W_{0^3},$$
$$W_{0^1} = \alpha W_1 + \beta W_{1^3} = W_{1^2} = W_{0^3},$$
$$W_{1^1} = \alpha W_0 + \beta W_{0^3} = W_{0^2} = W_{1^3},$$
$$W_0 + W_1 + W_{0^1} + W_{1^1} + W_{0^2} + W_{1^2} + W_{0^3} + W_{1^3} = 1.$$

Solving the above equations we get

$$W_0 = W_1 = \frac{1-\beta}{2-2\beta+6\alpha} \tag{22}$$

$$W_{0^1} = W_{1^1} = W_{0^2} = W_{1^2} = W_{0^3} = W_{1^3} = \frac{\alpha}{2-2\beta+6\alpha}. \tag{23}$$

The boundary condition (which is the sum of the product of the phase factor and the probability factor from all the origins) can now be obtained by considering all possible sequences starting with layers of each type 0, 1, 0^1, 1^1, 0^2, 1^2, 0^3 and 1^3 at the origin and writing T_m in each case *i.e.*,

$$T_m = \sum_j W_j \langle \exp(i\phi_m)_j \rangle.$$

Thus

$$T_1 = -\tfrac{1}{2}, \qquad T_2 = \frac{2-2\beta}{2(1-\beta+3\alpha)},$$

$$T_3 = -\frac{1-\beta.}{2(1-\beta+3\alpha)}, \qquad T_4 = \frac{(1-3\alpha)(1-\beta)}{1-\beta+3\alpha},$$

$$T_5 = -\frac{1-3\alpha-\beta-3\alpha^2+6\alpha\beta+3\alpha^2\beta}{2(1-\beta+3\alpha)},$$

$$T_6 = \frac{2-12\alpha-2\beta+12\alpha^2+18\alpha\beta-6\alpha^3-12\alpha^2\beta+6\alpha^3\beta}{2(1-\beta+3\alpha)},$$

$$T_7 = -\frac{1-6\alpha-\beta+3\alpha^2+12\alpha\beta-3\alpha^2\beta-3\alpha\beta^2-3\alpha^4+3\alpha^4\beta}{2(1-\beta+3\alpha)}.$$

Substituting the coefficients (a's) and the seven boundry conditions(T's) in (21) and carrying out the summations we get the intensity expression as

$$\begin{aligned} I = f^2C\{[\tfrac{1}{2} &+ (T_1 \exp(7i\pi L) + T_2 \exp(6i\pi L) + (T_3 + a_6T_1)\exp(5i\pi L) \\ &+ (T_4 + a_6T_2)\exp(4i\pi L) + (T_5 + a_6T_3 + a_4T_1)\exp(3i\pi L) \\ &+ (T_6 + a_6T_4 + a_4T_2)\exp(2i\pi L) + (T_7 + a_6T_5 + a_4T_3 + a_2T_1) \\ &\times \exp(i\pi L) - a_0)/(a_0 + a_2\exp(2i\pi L) \\ &+ a_4\exp(4i\pi L) + a_6\exp(6i\pi L) + \exp(8i\pi L))] + \text{C.C.}\}. \end{aligned} \tag{24}$$

On simplifying (24) we get the final intensity expression for a 2H crystal undergoing solid state transformation to the 6H structure as

$$I = f^2C\left(1 + \frac{x}{y}\right), \tag{25}$$

where

$$\begin{aligned} x = {} & B_1R_1 + a_0B_1R_7 + a_2B_1R_5 + a_4B_1R_3 + a_6B_1R_1 + \\ & B_2R_2 + a_0B_2R_6 + a_2B_2R_4 + a_4B_2R_2 + a_6B_2 + \\ & B_3R_3 + a_0B_3R_5 + a_2B_3R_3 + a_4B_3R_1 + a_6B_3R_1 + \\ & B_4R_4 + a_0B_4R_4 + a_2B_4R_2 + a_4B_4 + a_6B_4R_2 + \end{aligned}$$

$$B_5R_5 + a_0B_5R_3 + a_2B_5R_1 + a_4B_5R_1 + a_6B_5R_3 +$$
$$B_6R_6 + a_0B_6R_2 + a_2B_6 + a_4B_6R_2 + a_6B_6R_4 +$$
$$B_7R_7 + a_0B_7R_1 + a_2B_7R_1 + a_4B_7R_3 + a_6B_7R_5 +$$
$$B_8R_8 + a_0B_8 + a_2B_8R_2 + a_4B_8R_4 + a_6B_8R_6.$$

$$y = G_1 + G_2R_2 + G_3R_4 + G_4R_6 + G_5R_8 + G_6R_2$$
$$+ G_7R_4 + G_8R_6 + G_9R_2 + G_{10}R_4 + G_{11}R_2$$

$$B_1 = 2T_1, \quad B_2 = 2T_2, \quad B_3 = 2(T_3 + a_6T_1), \quad B_4 = 2(T_4 + a_6T_2),$$
$$B_5 = 2(T_5 + a_6T_3 + a_4T_1), \quad B_6 = 2(T_6 + a_6T_4 + a_4T_2),$$
$$B_7 = 2(T_7 + a_6T_5 + a_4T_3 + a_2T_1), \quad B_8 = -2a_0,$$

$$R_1 = \cos \pi L, \quad R_2 = \cos 2\pi L, \quad R_3 = \cos 3\pi L,$$
$$R_4 = \cos 4\pi L, \quad R_5 = \cos 5\pi L, \quad R_6 = \cos 6\pi L,$$
$$R_7 = \cos 7\pi L, \quad R_8 = \cos 8\pi L,$$

$$G_1 = 1 + a_0^2 + a_2^2 + a_4^2 + a_6^2, \quad G_2 = 2a_2a_0,$$
$$G_3 = 2a_0a_4, \quad G_4 = 2a_0a_6, \quad G_5 = 2a_0, \quad G_6 = 2a_2a_4,$$
$$G_7 = 2a_2a_6, \quad G_8 = 2a_2, \quad G_9 = 2a_4a_6, \quad G_{10} = 2a_4, \quad G_{11} = 2a_6.$$

5.1a *Prediction of diffraction effects.* The variation of the diffracted intensity with $L(h_3)$ along the $10 \cdot L$ reciprocal lattice row for different values of α and β as calculated from (25) in steps of $\Delta L = 0{\cdot}01$ are depicted in figure 6a, b, c, d, e and f. The x-ray diffraction effects from a 2H crystal undergoing transformation to the 6H structure by the deformation mechanism are as follows

(i) Reflections with $H - K = 0 \pmod 3$ and $L = 0 \pmod 2$ are unaffected by the transformation and remain sharp throughout the transformation.

(ii) The following diffraction effects are predicted for reflections with $H - K \neq 0 \pmod 3$.

  (a) Reflections with $L = 0, \pm 1 \pmod 2$ are broadened. These correspond to the positions for the 2H structure.

  (b) There are changes in the integrated intensities of different reflections.

  (c) For small values of $\alpha(\alpha = 0{\cdot}02\text{–}0{\cdot}06)$ the 2H reflections remain sharp and the new 6H peaks appear as β increases to a value between 0·4 and 0·6. The 6H peaks which are initially broad become sharper as β increases to 0·9. For this range the resulting final structure shows considerable intensity at the 2H positions in comparison with the intensity at the 6H positions. The final resultant structure ($\beta = 0{\cdot}9$) shows the co-existence of the 2H and the 6H structures.

  (d) For $\alpha = 0{\cdot}1$ to 0·2. The 2H reflections are broad and the new 6H peaks start appearing when $\beta = 0{\cdot}4$. The 6H peaks at $L = \pm \frac{1}{3}, \pm \frac{2}{3} \pmod 2$ are shifted away from each other. As β increases these 6H peaks gradually move from the shifted positions to the positions $L = \pm \frac{1}{3}, \pm \frac{2}{3} \pmod 2$ and all the reflections become sharper.

  (e) For $\alpha = 0{\cdot}3\text{–}0{\cdot}4$. The 2H reflections are heavily broadened with a dip in the middle of the reflection. When β increases to 0·4 each reflection splits into three and as β increases above 0·4 two of them move away from the central peak to the normal 6H positions.

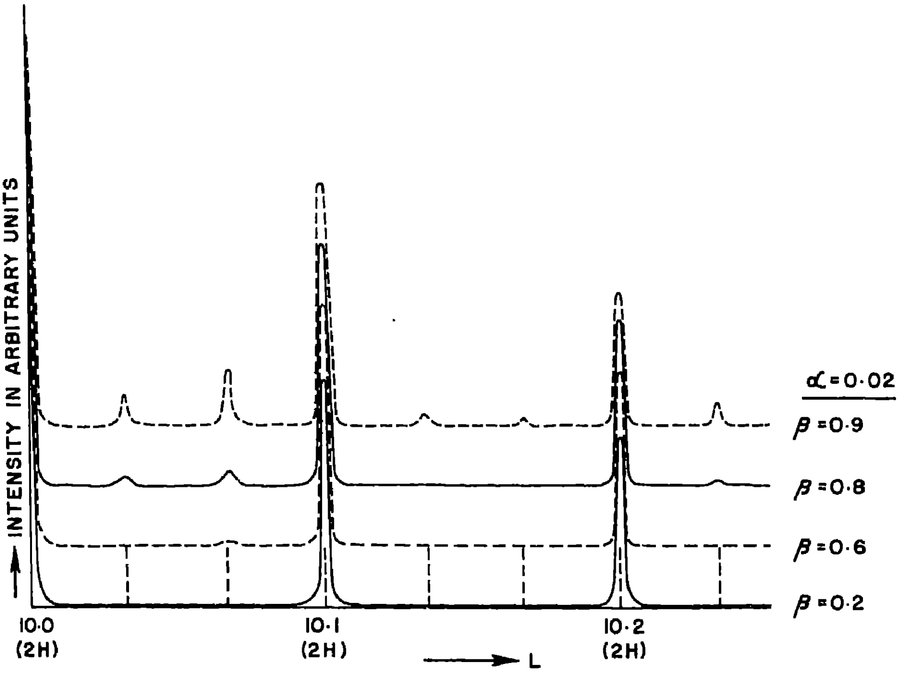

Figure 6(a).

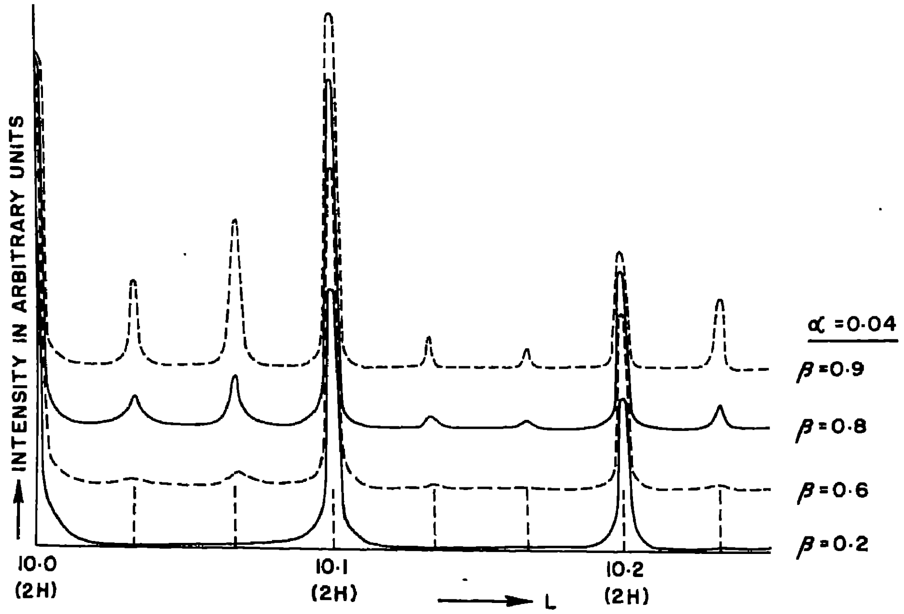

Figure 6(b).

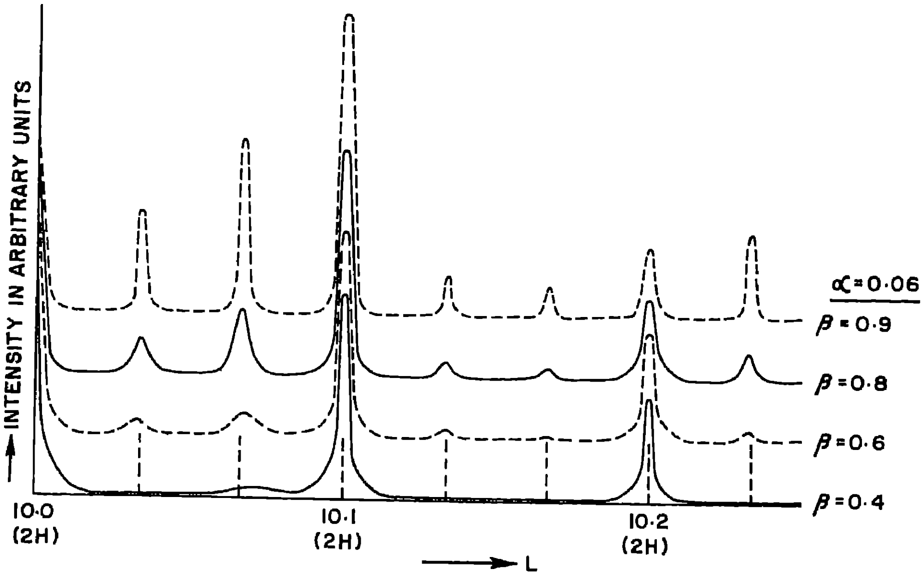

Figure 6(c).

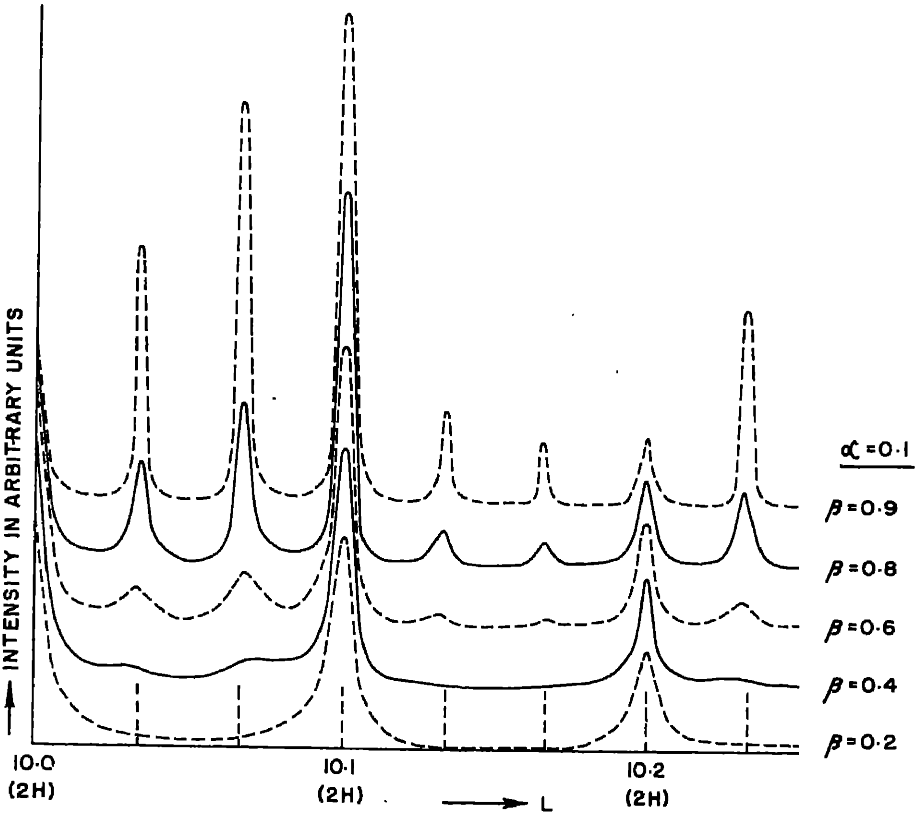

Figure 6(d).

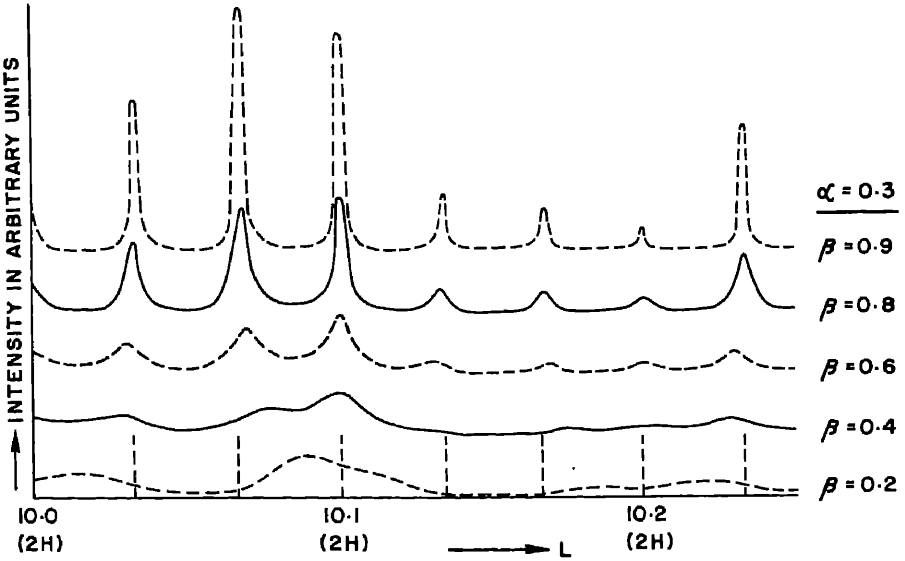

Figure 6(e).

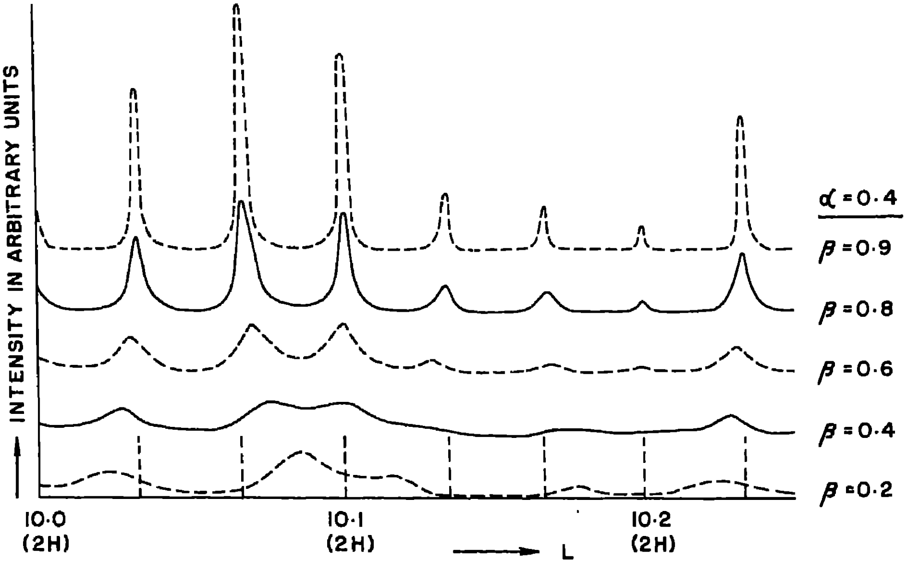

Figure 6(f).

Figure 6. Calculated variation of the diffracted intensity along the 10·L reciprocal lattice row for a crystal undergoing transformation by the deformation mechanism with $\beta = 0{\cdot}2, 0{\cdot}4, 0{\cdot}6, 0{\cdot}8$ and $0{\cdot}9$. The dashed vertical lines indicate the correct 6H positions. The calculated curves have been shifted vertically for different values of β for clarity. (a) $\alpha = 0{\cdot}02$, (b) $\alpha = 0{\cdot}04$, (c) $\alpha = 0{\cdot}06$, (d) $\alpha = 0{\cdot}1$, (e) $\alpha = 0{\cdot}3$, (f) $\alpha = 0{\cdot}4$.

5.2 *The theory of x-ray diffraction from 2H crystals undergoing solid state transformation to the 6H structure by the layer displacement mechanism*

Employing the notation described in the previous section the probability tree for the layer displacement mechanism can be written as follows for the two-parameter model

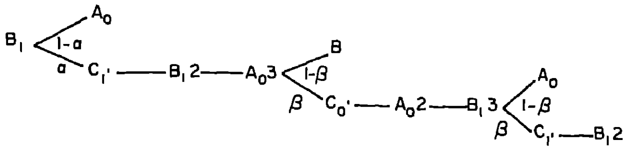

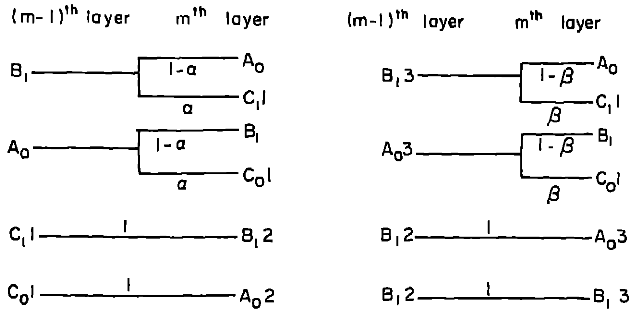

To compute the probability $P_{(m,j)}$ of arriving at the mth layer with the subscript $j(j = 0, 1, 0^1, 1^1, 0^2, 1^2, 0^3$ and $1^3)$ with the help of the probability trees, we consider the transitions from the $(m-1)$th layer to the mth layer starting with each type of layer (*i.e.* $0, 1, 0^1, 1^1, 0^2, 1^2, 0^3$ and 1^3) at the origin. Thus we have

$$
\begin{aligned}
P_{(m,0)} &= (1-\alpha)P_{(m-1,1)} + (1-\beta)P_{(m-1,1^3)},\\
P_{(m,1)} &= (1-\alpha)P_{(m-1,0)} + (1-\beta)P_{(m-1,0^3)},\\
P_{(m,0^1)} &= \alpha P_{(m-1,0)} + \beta P_{(m-1,0^3)},\\
P_{(m,1^1)} &= \alpha P_{(m-1,1)} + \beta P_{(m-1,1^3)},\\
P_{(m,0^2)} &= P_{(m-1,0^1)},\quad P_{(m,1^2)} = P_{(m-1,1^1)},\quad P_{(m,0^3)} = P_{(m-1,1^2)},\\
P_{(m,1^3)} &= P_{(m-1,0^2)}.
\end{aligned}
$$

Following the procedures described earlier for the deformation mechanism we get the following difference equations

$$J_{(m,0)} = (1-\alpha)J_{(m-1,1)}\omega_2 + (1-\beta)J_{(m-1,1^3)}\omega_2, \tag{26}$$

$$J_{(m,1)} = (1-\alpha)J_{(m-1,0)}\omega_1 + (1-\beta)J_{(m-1,0^3)}\omega_1, \tag{27}$$

$$J_{(m,0^1)} = \alpha J_{(m-1,0)}\omega_2 + \beta J_{(m-1,0^3)}\omega_2, \tag{28}$$

$$J_{(m,1^1)} = \alpha J_{(m-1,1)}\omega_1 + \beta J_{(m-1,1^3)}\omega_1, \tag{29}$$

$$J_{(m,0^2)} = J_{(m-1,0^1)}\omega_1, \tag{30}$$

$$J_{(m,1^2)} = J_{(m-1,1^1)}\omega_2, \tag{31}$$

$$J_{(m,0^3)} = J_{(m-1,1^2)}\omega_2, \tag{32}$$

$$J_{(m,1^3)} = J_{(m-1,0^2)}\omega_1. \tag{33}$$

Let the solution of the system of difference equations (26) to (33) be of the form

$$J_{(m,j)} = C_j \rho^m \qquad m \geqslant 0. \tag{34}$$

Substituting this value of $J_{(m,j)}$ in (26) to (33) and eliminating the various C's we finally obtain the characteristic equation

$$\rho^8 - (1-\alpha)^2 \rho^6 - 2\alpha(1-\beta)\rho^4 - \beta^2\rho^2 + (\alpha-\beta)^2 = 0. \tag{35}$$

Adopting the method described earlier we get from the probability tree

$$\begin{aligned} W_0 &= (1-\alpha) W_1 + (1-\beta) W_{1^3}, \\ W_1 &= (1-\alpha) W_0 + (1-\beta) W_{0^3}, \\ W_{0^1} &= \alpha W_0 + \beta W_{0^3} = W_{0^2} = W_{1^3}, \\ W_{1^1} &= \alpha W_1 + \beta W_{1^3} = W_{1^2} = W_{0^3}. \end{aligned}$$

But $W_0 + W_1 + W_{0^1} + W_{1^1} + W_{0^2} + W_{1^2} + W_{0^3} + W_{1^3} = 1$.

Solving the above equations we get

$$W_0 = W_1 = \frac{1-\beta}{2-2\beta+6\alpha},$$

$$W_{0^1} = W_{1^1} = W_{0^2} = W_{1^2} = W_{0^3} = W_{1^3} = \frac{\alpha}{2-2\beta+6\alpha}.$$

Proceeding in the manner described earlier for the deformation mechanism, we get the following boundary conditions

$$T_0 = 1, \quad T_1 = -\frac{1}{2}, \quad T_2 = \frac{2-2\beta}{2-2\beta+6\alpha},$$

$$T_3 = -\frac{1-\beta+3\alpha-3\alpha\beta}{2-2\beta+6\alpha}, \quad T_4 = \frac{2-2\beta+6\alpha^2-6\alpha^2\beta}{2-2\beta+6\alpha},$$

$$T_5 = -\frac{1-\beta+3\alpha-3\alpha^2+3\alpha^3+3\alpha^2\beta-3\alpha^3\beta}{2-2\beta+6\alpha},$$

$$T_6 = \frac{2-2\beta+6\alpha^2-12\alpha^3+6\alpha^4-6\alpha^2\beta+12\alpha^3\beta-6\alpha^4\beta+6\alpha\beta^2}{2-2\beta+6\alpha},$$

$$T_7 = -\frac{1-\beta+3\alpha-3\alpha^2+9\alpha^3-9\alpha^4+3\alpha^5-3\alpha^2\beta-9\alpha^3\beta+9\alpha^4\beta-3\alpha^5\beta+6\alpha^2\beta^2}{2-2\beta+6\alpha}.$$

The applicability of Holloway's method is restricted by the condition that none of the roots of the characteristic equation has unit modulus. In the present case two of the roots have unit modulus as shown below.

Equation (35) can be written as

$$(\rho^2-1)[\rho^6 + (2\alpha-\alpha^2)\rho^4 + (-\alpha^2+2\alpha\beta)\rho^2 + (-\alpha^2+2\alpha\beta-\beta^2)] = 0. \tag{36}$$

Therefore two of the roots have unit modulus *i.e.*

$$\rho_6 = 1 \text{ and } \rho_7 = -1,$$

and $$a_6 = 1,\ a_4 = 2\alpha - \alpha^2,\ a_2 = -\alpha^2 + 2\alpha\beta,$$
$$a_0 = -\alpha^2 + 2\alpha\beta - \beta^2,\ a_5 = a_3 = a_1 = 0.$$

Recently Lele (1980) obtained an analytical solution for the diffuse diffracted intensity when the characteristic equation found from the difference equation has roots with unit modulus. In this method we obtain a self-consistent set consisting of the characteristic equation and the boundary conditions which do not have the effect of any roots with unit modulus and thus can be used as input for the calculation of the diffracted intensity by Holloway's method. The diffracted intensity corresponding to the roots with unit modulus consists of sharp peaks and has to be superposed on the diffuse intensity corresponding to the roots with non-unit modulus.

Multiplying the terms inside the square bracket (36) with $(\rho+1)$ and $(\rho-1)$ respectively we get

$$\begin{aligned}\rho^7 + \rho^6 + (2\alpha-\alpha^2)\rho^5 + (2\alpha-\alpha^2)\rho^4 + (-\alpha^2+2\alpha\beta)\rho^3 + (-\alpha^2+2\alpha\beta)\rho^2 \\ + (-\alpha^2+2\alpha\beta-\beta^2)\rho + (-\alpha^2+2\alpha\beta-\beta^2) = 0,\end{aligned} \tag{37}$$

and

$$\begin{aligned}\rho^7 - \rho^6 + (2\alpha-\alpha^2)\rho^5 - (2\alpha-\alpha^2)\rho^4 + (-\alpha^2+2\alpha\beta)\rho^3 - (-\alpha^2+2\alpha\beta)\rho^2 \\ + (-\alpha^2+2\alpha\beta-\beta^2)\rho - (-\alpha^2+2\alpha\beta-\beta^2) = 0.\end{aligned} \tag{38}$$

From (37) and (38) we get the following coefficients

$$b_6 = 1,\ b_5 = 2\alpha-\alpha^2,\ b_4 = 2\alpha-\alpha^2,\ b_3 = -\alpha^2+2\alpha\beta,\ b_2 = -\alpha^2+2\alpha\beta,$$
$$b_1 = -\alpha^2+2\alpha\beta-\beta^2,\ b_0 = -\alpha^2+2\alpha\beta-\beta^2,$$
$$b'_6 = -1,\ b'_5 = 2\alpha-\alpha^2,\ b'_4 = -(2\alpha-\alpha^2),\ b'_3 = (-\alpha^2+2\alpha\beta),$$
$$b'_2 = -(-\alpha^2+2\alpha\beta),\ b'_1 = -\alpha^2+2\alpha\beta-\beta^2,\ b'_0 = -(-\alpha^2+2\alpha\beta-\beta^2).$$

Following Lele (1980),

$$C_0 = \frac{T_{m-1} + b_{n-2}T_{n-2} \ldots + b_1T_1 + b_0T_0}{\rho_0^{n-1} + b_{n-2}\rho_0^{n-2} \ldots + b_1\rho_0 + b_0},$$

we get

$$C_6 = \frac{T_7 + b_6T_6 + \ldots + b_0T_0}{\rho_6^7 + b_6\rho_6^6 \ldots + b_1\rho_6 + b_0}.$$

Substituting the values of T's and b's and $\rho_6 = 1$ we get

$$C_6 = \frac{1-\alpha-\beta-\beta^2+\beta^3-\alpha\beta^2+2\alpha\beta}{4(1-\beta+3\alpha)(1+2\alpha+4\alpha\beta-3\alpha^2-\beta^2)}.$$

Similarly,

$$C_7 = \frac{T_7 + b'_6T_6 + \ldots + b_{1}'T_1 + b'_0T_0}{\rho_7^7 + b'_6\rho_7^6 + \ldots + b'_1\rho_7 + b'_0}$$
$$= \frac{3-3\beta+9\alpha-3\beta^2+6\alpha\beta-15\alpha\beta^2+24\alpha^2\beta-12\alpha^3+3\beta^3}{4(1-\beta+3\alpha)(1+2\alpha+4\alpha\beta-3\alpha^2-\beta^2)}.$$

The boundary conditions which no longer have the effects of any roots with unit modulus are given by

$$K_m = T_m - \sum_{j=n-p}^{n-1} C_j\rho_j^m,$$

where the roots, $\rho_j, j = (n-p)$ to $(n-1)$ have unit modulus. Thus we have

$$\begin{aligned} K_1 &= T_1 - (C_6\rho_6 + C_7\rho_7) = T_1 - (C_6 - C_7) \\ K_2 &= T_2 - (C_6 + C_7), \quad K_3 = T_3 - (C_6 - C_7), \\ K_4 &= T_4 - (C_6 + C_7), \quad K_5 = T_5 - (C_6 - C_7). \end{aligned}$$

Substituting the five boundary conditions (K's) and the coefficients (a's) of the characteristic equation in Holloway's expression

$$I = f^2 C \left\{ \left[\frac{1}{2} + \frac{\sum_{j=1}^{n-1} \sum_{p=0}^{j-1} a_{n-p} K_{j-p} \exp(n-j) i\pi L - a_0}{\sum_{j=0}^{n} a_j \exp(ji\pi L)} \right] + \text{C.C.} \right\},$$

where C.C. stands for the complex conjugate, we get

$$\begin{aligned} I = f^2 C \{ (\tfrac{1}{2} + [&K_1 \exp(5i\pi L) + K_2 \exp(4i\pi L) + (K_3 + a_4 K_1) \exp(3i\pi L) \\ &+ (K_4 + a_4 K_2) \exp(2i\pi L) + (K_5 + a_4 K_3 + a_2 K_1) \exp(i\pi L) \\ &- a_0] / (a_0 + a_2 \exp(2i\pi L) + a_4 \exp(4i\pi L) + \exp(6i\pi L))) + \text{C.C.} \} \end{aligned}$$

On simplifying we get the final intensity expression for a 2H crystal undergoing solid state transformation to the 6H structure by the layer displacement mechanism as

$$I = f^2 C \left(1 + \frac{x}{y} \right), \tag{39}$$

where

$$\begin{aligned} x = {} & B_1R_1 + a_4B_1R_1 + a_2B_1R_3 + a_0B_1R_5 + \\ & B_2R_2 + a_4B_2 + a_2B_2R_2 + a_0B_2R_4 + \\ & B_3R_3 + a_4B_3R_1 + a_2B_3R_1 + a_0B_3R_3 + \\ & B_4R_4 + a_4B_4R_2 + a_2B_4 + a_0B_4R_2 + \\ & B_5R_5 + a_4B_5R_3 + a_2B_5R_1 + a_0B_5R_1 + \\ & B_6R_6 + a_4B_6R_4 + a_2B_6R_2 + a_0B_6, \end{aligned}$$

$$\begin{aligned} y = {} & 1 + a_0^2 + a_2^2 + a_4^2 + 2a_0a_2R_2 + 2a_0a_4R_4 \\ & + 2a_0R_6 + 2a_2a_4R_2 + 2a_2R_4 + 2a_4R_2. \end{aligned}$$

$$\begin{aligned} B_1 &= 2K_1, \quad R_1 = \cos \pi L, \\ B_2 &= 2K_2, \quad R_2 = \cos 2\pi L, \\ B_3 &= 2(K_3 + a_4K_1), \quad R_3 = \cos 3\pi L, \\ B_4 &= 2(K_4 + a_4K_2), \quad R_4 = \cos 4\pi L, \\ B_5 &= 2(K_5 + a_4K_3 + a_2K_1), \quad R_5 = \cos 5\pi L, \\ B_6 &= -2a_0, \quad R_6 = \cos 6\pi L. \end{aligned}$$

5.2a *Prediction of diffraction effects.* The variation of the diffracted intensity along the $10 \cdot L$ reciprocal lattice row for different values of α and β (calculated from (39) in steps of $\Delta L = 0{\cdot}01$) is depicted in figure 7a, b, c. The intensity corresponding to roots with unit modulus consists of sharp peaks and has to be superposed on the diffuse intensity shown in the figure. The diffraction effects from 2H crystals undergoing transformation

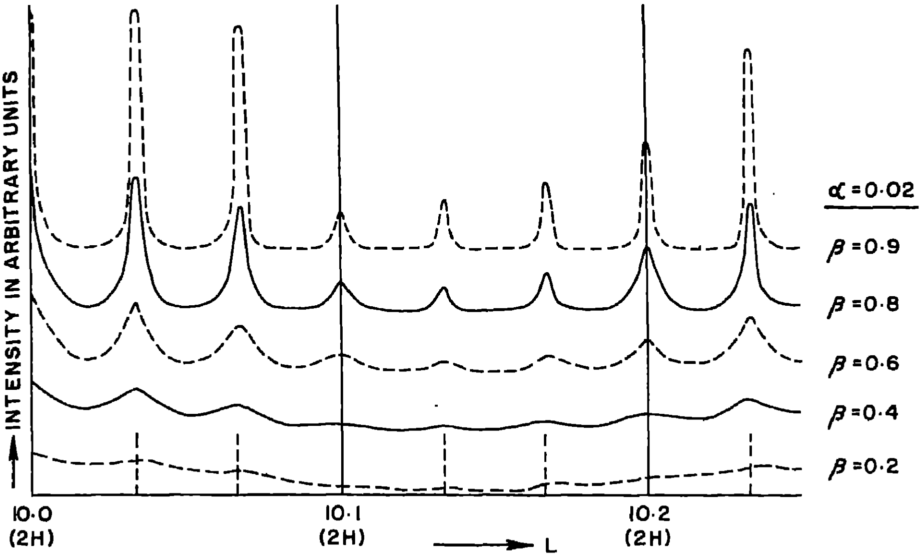

Figure 7(a).

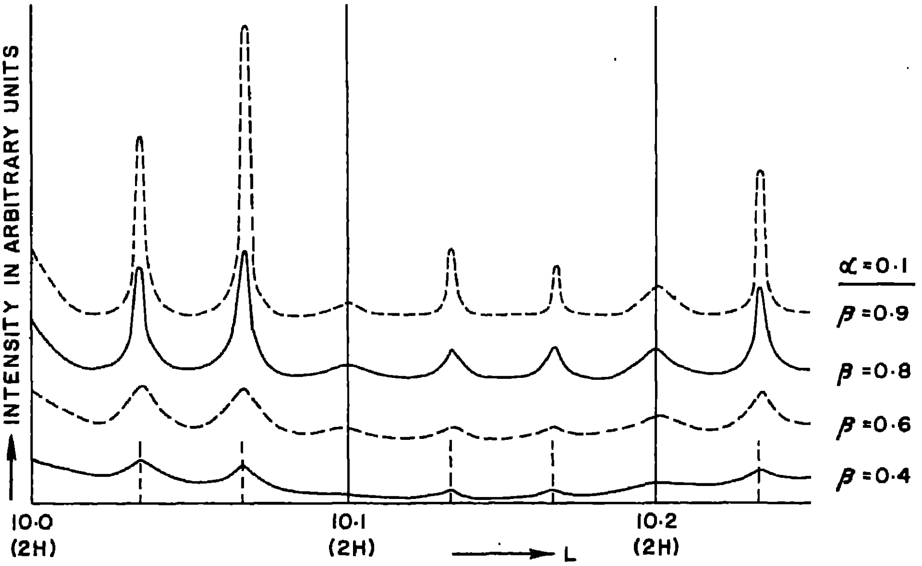

Figure 7(b).

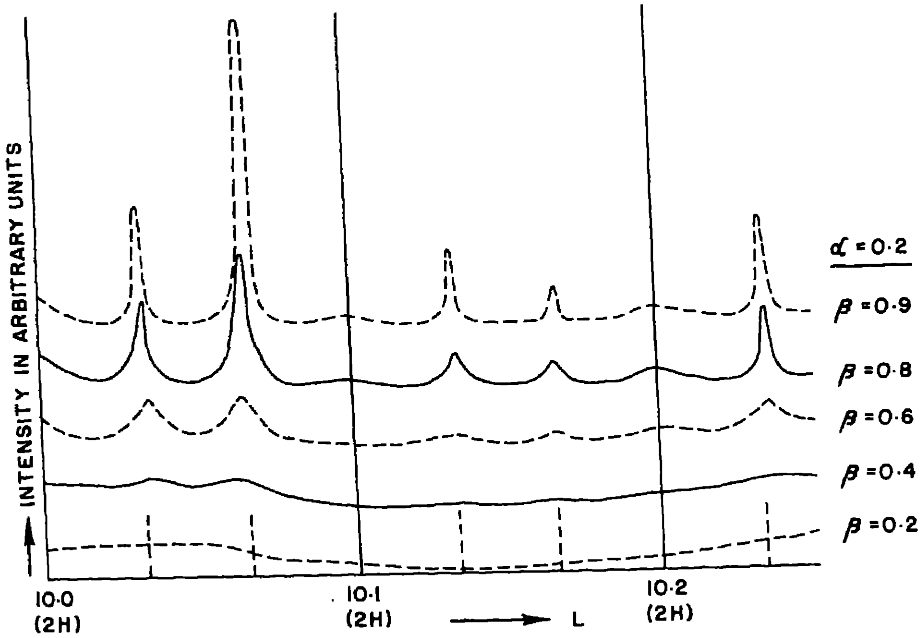

Figure 7(c).

Figure 7. Calculated variation of the diffracted intensity along the 10·L reciprocal lattice row for a crystal undergoing transformation by the layer displacement mechanism with $\beta = 0{\cdot}2$, 0·4, 0·6, 0·8 and 0·9. The dashed vertical lines indicate the correct 6H positions. The calculated curves have been shifted vertically for different values of β for clarity. (a) $\alpha = 0{\cdot}02$, (b) $\alpha = 0{\cdot}1$, (c) $\alpha = 0{\cdot}2$.

to the 6H structure by the layer displacement mechanism may be summarised as follows

(i) The reflections with $H - K = 0$ (mod 3) and $L = 0$ (mod 2) are unaffected by the transformation and remain sharp throughout the transformation.

(ii) The following diffraction effects are predicted for the reflections with $H - K \neq 3n$

- (a) reflections with $L = 0, \pm 1$ (mod 2) are not broadened,
- (b) There are changes in the integrated intensities of the different reflections.
- (c) For $\alpha = 0{\cdot}02$ to $0{\cdot}1$: The new 6H peaks appear at $L = \pm \frac{1}{3}, \pm \frac{2}{3}$ (mod 2) when β increases to a value of about 0·2. Initially these reflections are broad and as β increases to 0·9 they become sharper.
- (d) For $\alpha = 0{\cdot}2$ to 0·4: When $\beta = 0{\cdot}2$ new heavily broadened peaks appear at $L = \pm \frac{1}{2}$ (mod 2). When β increases to a value between 0·4 and 0·6 these peaks broaden and split into two. As β increases to a still larger value (0·6–0·9) these reflections which have split into two peaks move away from each other towards the normal 6H positions, viz. $L = \pm \frac{1}{3}, \pm \frac{2}{3}$ (mod 2) and become sharper.
- (e) The 2H peaks are present throughout the transformation as in the case of deformation mechanism. The one-parameter model does not show such a co-existence of 2H and 6H peaks.

6. Comparison of theoretically predicted diffraction effects with those experimentally observed

A study of the x-ray photographs and the corresponding intensity profiles of the crystals in different stages of the transformation shows that the transformation commences with a broadening of the 2H reflections. This broadening is small when α is small but quite considerable for larger values of α. The experimentally obtained intensity profiles (diffractometer records of intensity) approximate to the theoretical profiles computed for the deformation mechanism. In many crystals the new 6H peaks are observed to be shifted away from each other at the initial stages of transformation in accordance with the predictions of the deformation mechanism. For transformation by the layer displacement mechanism the 2H reflections would have remained sharp and the new 6H peaks would be shifted towards each other in partially transformed crystals. The range of α and β values for two typical crystals obtained by comparing the experimental profiles (figures 4 and 5) with the theoretically calculated profiles for the deformation mechanism are

$\alpha = 0\cdot06$–$0\cdot1$, $\beta = 0\cdot6$–$0\cdot8$ (figure 4),
$\alpha = 0\cdot06$–0.1, $\beta = 0\cdot8$–$0\cdot9$ (figure 5).

7. Discussion of results

It is found that the phenomena of polytypism and one-dimensional disorder cease to occur in $Zn_xCd_{1-x}S$ crystals for $x < 0\cdot94$. Only perfect 2H structure occurs for $x \leqslant 0\cdot93$. This is in agreement with earlier studies performed on melt grown crystals (Kozielski 1976). A higher cadmium content stabilizes the 2H phase. Similar studies performed with ZnS and ZnSe which form solid solutions of the type $ZnS_{1-x}Se_x$ over the entire composition range from $x = 0$ to 1, have shown (Kozielski 1976) that polytypes and disordered structures occur only in the range $0 < x < 0\cdot3$. The hexagonality of the crystals increases with increasing selenium content. Melt grown solid solutions of the type $ZnS_{1-x}Te_x$ are also known to display (Kozielski 1976) polytypes and one-dimensional disordered structures. Apparently in all these systems the stacking fault energy (SFE) is a function of composition and disorder effects cease when SFE becomes greater than a certain critical value.

It is known (Sebastian *et al* 1982) that 2H ZnS transforms to a disordered twinned 3C structure on annealing and that deformation faults nucleate the transformation. Shachar *et al* (1968) have reported that the 2H ZnS crystals transform to a disordered 3C + 6H structure on applying external stresses by a needle or a knife edge. Consequently it is expected that deformation faults are also involved in the 2H–6H solid state transformation observed in $Zn_xCd_{1-x}S$ and $Zn_xMn_{1-x}S$ crystals. The transformations occur by the non-random insertion of deformation faults but the one-parameter model developed (Pandey *et al* 1980) for a similar transformation in SiC s not applicable to these materials. The two-parameter model described above does xplain the observed intensity distribution approximately for $\beta \gg \alpha$. The peak shift and peak broadening of the reflections with $H - K \neq 3n$ depend on the relative magnitudes f α and β. The partially transformed $Zn_xCd_{1-x}S$ and $Zn_xMn_{1-x}S$ crystals are found to ossess a small value of α ($\alpha = 0\cdot02$ to $0\cdot2$) and a large value of β ($\beta = 0\cdot4$ to $0\cdot9$) during the 2H–6H transformation. This implies that the 2H–6H transformation in these materials commences with the random insertion of a few deformation faults (small α) which quickly develop into 6H nuclei by preferred faulting at 3-layer separations (large β). For larger values of α the reflections with $H-K \neq 3n$ and $L = \pm \frac{1}{3}, \pm \frac{2}{3}$ will become broadened and show peak shifts. The case when $\alpha = \beta$ corresponds to the one-parameter model developed by Pandey *et al* (1980). For $\alpha \ll \beta$, a small number of 6H nuclei would grow into thick 6H regions. Therefore the 6H reflections would appear at an early stage of transformation and the 2H reflections will not broaden considerably. This is what we observe in the case of the 2H–6H transformation in $Zn_xCd_{1-x}S$ and $Zn_xMn_{1-x}S$.

The diffractometer records in figure 5 show an enhancement of intensity at 3C positions which is observed in many crystals. It indicates that there is a finite probability of faults occurring also at two-layer separations. The assumption that the probability of faulting at less than three-layer separations is zero, is therefore an approximation and the actual faulting in such a system is more complicated.

Acknowledgements

The authors are grateful to the Department of Science and Technology, New Delhi, for providing financial assistance. Thanks are also due to Dr S Lele for helpful discussions. One of us (PK) is grateful to Prof. H Schulz for providing single crystal diffractometer facilities at the Max-Planck Institute (FKF), Stuttgart, W. Germany.

References

Brodin M S, Budnik P I, Vitrikhoski N I and Zakreveskii S V 1970 *Sov. Phys. Semiconductors* **4** 435
Burton L C and Hench T L 1976 *Appl. Phys. Lett.* **29** 612
Chandrasekharaiah M N and Krishna P 1969 *J. Cryst. Growth* **5** 213
Cherin P, Lind E L and Davies E A 1970 *J. Electrochem. Soc.* **117** 233
Daniels B K 1966 *Philos. Mag.* **14** 487
Domeus P, Cadene M, Cohen C W and Martinuzzi S 1977 *Photovoltaic solar energy conversion, Proc. Conf., Luxemburg*, p. 168
Holloway H 1969 *J. Appl. Phys.* **40** 4313
Inouguchi T, Takeda M, Kakihara Y and Yoshira M 1974 *Stable high luminescence thin film electroluminescent panels in Dig. SID Int. Symp., Los Angeles, CA. Soc. for Inf. Disp.* p. 86
Jagodzinski H 1949 *Acta Crystallogr.* **2** 208
Juza V R, Rabenau A and Pascher G 1956 *Z. Anorg. Allg. Chem.* **285** 611
Kawaguchi H, Ito H and Inaba H 1976 *Opt. Commun.* **16** 6
Kozielski M J 1976 *J. Cryst. Growth* **30** 86
Krishna P and Marshall R C 1971 *J. Cryst. Growth* **9** 319, *ibid* **11** 147
Kröger F A 1939 *Z. Kristallogr.* **A 100** 132 *ibid* 543
Lele S 1980 *Acta Crystallogr.* **A36** 584
Lele S and Pandey D 1982 *Proc. Int. Conf. on Solid to solid phase transformations. AIME Warandale*, p. 1487
Lutz H P and Becker W 1977 *J. Solid State Chem.* **20** 183
Mardix S and Steinberger I T 1966 *Isr. J. Chem.* **3** 243
Mehmed F and Heraldson H 1938 *Z. Anorg. Chem.* **235** 193
Müller H 1952 *News Jahrb. Miner. Abh.* **84** 43
Pandey D and Krishna P 1977 *J. Phys.* **D10** 2057
Pandey D, Lele S and Krishna P 1980 *Proc. R. Soc.* (*London*) **A369** 435, 451, 463
Prasad B and Lele S 1971 *Acta Crystallogr.* **27** 54

Roomians C J M 1963 *J. Inorg. Nucl. Chem.* **25** 253
Schnaase H 1933 *Z. Phys. Chem.* **B20** 89
Sebastian M T, Pandey D and Krishna P 1982 *Phys. Status Solidi* **71** 633
Sebastian M T and Krishna P 1983 *Solid State. Commun.* **48** 879
Sebastian M T and Krishna P 1983a *Bull. Mater. Sci.* **5** 257
Sebastian M T and Krishna P 1983b *Phys. Status Solidi* **79** 271
Secco d'Aragona F S, Delavignette P and Amelinckx S 1966 *Phys. Status Solidi* **K14** 115
Shachar G, Mardix S and Steinberger I T 1968 *J. Appl. Phys.* **39** 2485
Singer J 1963 *Acta Crystallogr.* **16** 601
Theis D 1981 *J. Lumines.* **23** 191
Yoshikawa A and Sakai Y 1976 *Jpn. J. Appl. Phys.* **15** 1861

Bull. Mater. Sci., Vol. 6, No. 2, May 1984, pp. 395–403. © Printed in India.

The pressure-volume relation of ytterbium up to 9 GPa

S USHA DEVI and A K SINGH

Materials Science Division, National Aeronautical Laboratory, Bangalore 560017, India

Abstract. The pressure-volume relation of ytterbium has been determined up to 9 GPa using tungsten carbide opposed anvil high pressure x-ray camera. The fcc phase of ytterbium is observed between one atmosphere and 4 GPa and the bcc phase above 3·5 GPa. The bcc phase can be metastably retained down to 1 GPa by gradually decreasing the pressure from a region where only bcc phase alone is observed. The bulk modulus, B_0, at zero pressure and the pressure derivative of the bulk modulus, B'_0, are determined by fitting Murnaghan equation to the pressure-volume data. The following values were obtained: $B_0 = 16{\cdot}3$ GPa and $B'_0 = 3{\cdot}6$ for the fcc phase, and $B_0 = 14{\cdot}7$ GPa and $B'_0 = 1{\cdot}5$ for the bcc phase. Based on the present data it is suggested that the thermodynamic equilibrium pressure for fcc $\rightleftharpoons$ bcc transformation in ytterbium is below 3·5 GPa. The valence change under pressure has been discussed.

Keywords. Equation of state; high pressure; x-ray diffraction; ytterbium.

1. Introduction

Ytterbium has a face-centred cubic (fcc) structure at room temperature and pressure, and transforms to a body-centred cubic (bcc) structure at 3·9 GPa (Hall *et al* 1963). The equation of state up to 4 GPa was measured by several investigators (Bridgman 1954; Hall and Merrill 1963; Stephens 1964). Though the results obtained by these investigators show an overall agreement, the finer features of the pressure-volume data differ. Further, these measurements were made with piston-cylinder apparatus which had ~ 4 GPa as the upper limit of attainable pressure. As a result, no measurements could be made on the bcc phase and even the measurements of volume change of the transformation are incomplete.

The equation of state of ytterbium up to 9 GPa has been measured using tungsten carbide opposed anvil x-ray apparatus, and the results are reported in this paper. The bulk modulus and its pressure derivative in the fcc phase have been compared with the results available in the literature. Some results on the bcc phase metastably retained much below the transformation pressure are also reported.

2. Experimental details

A tungsten carbide opposed anvil set-up with boron-epoxy gasket and epoxy pressure transmitting medium was used to record the x-ray diffraction patterns at elevated pressures. A small piece of 99·9% pure ytterbium supplied by Rare Earth Products Limited, USA was thinned down to 0·04 mm by pressing it between two flat surfaces and subsequent polishing on 600 grade emery paper. A piece measuring approximately 0·3 × 0·2 × 0·04 mm was cut from the thinned piece, and placed in the central hole of the boron-epoxy gasket such that the smallest dimension was parallel to the gasket surface. The rest of the space in the hole was filled with epoxy resin, which acted as the pressure transmitting medium. The epoxy resin was allowed to set; the excess epoxy was removed by polishing on 600 grade emery the gasket and specimen assembly. The gasket with the specimen at the centre was placed on the anvil such that the incident x-ray beam was normal to the 0·3 × 0·2 face of the specimen. The gasket was compressed to a nominal pressure of 2 GPa and brought back to room pressure. The gasket was reloaded in steps of about 0·5 GPa, and the diffraction patterns recorded using MoK α radiation and a cylindrical film cassette. The hydraulic pressure of the ram, p_r was noted for each experiment.

The pressure on the specimen, p_s was determined by calibrating the hydraulic pressure of the ram, p_r in terms of the pressure experienced by the specimen. For this purpose, separate runs were made with sodium chloride samples mixed with epoxy resin (in the ratio 1:4). The diffraction patterns from NaCl were recorded at various ram pressures. The specimen pressure was calculated from the observed unit cell volume and the theoretically calculated equation of state of NaCl (Decker 1971). The typical $p_r - p_s$ plots are shown in figure 1. These calibration curves were used to determine the specimen pressure at any ram pressure. The calibration curve was found to depend markedly on the gasket thickness and the ratio of boron and epoxy in the gasket. For the high degree of reproducibility of the $p_r - p_s$ relation, the gasket thickness was maintained within 0·01 mm. The compression of the gasket and specimen assembly prior to gathering the data further improves the reproducibility of the $p_r - p_s$ relation. A precise control of boron-epoxy ratio while making the gaskets is difficult. It becomes necessary to calibrate each batch of gaskets separately. The freshly prepared

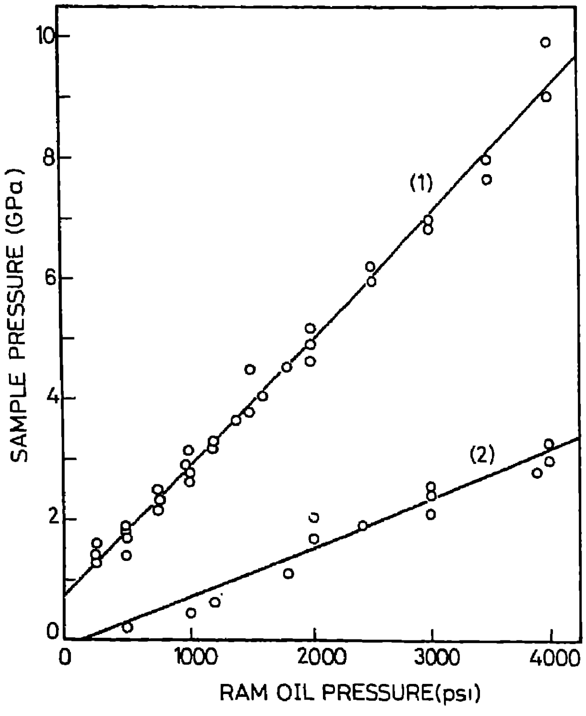

Figure 1. Plot of specimen pressure against hydraulic ram pressure. (1) 3 mm anvil (2) 5 mm anvil.

gaskets often showed larger scatter in the $p_r - p_s$ plot than the gaskets which were stored for sometime after preparation. The gaskets were therefore stored at room temperature for nearly a month before use. The other relevant experimental details are given elsewhere (Singh and Kennedy 1976).

The error in the specimen pressure for a given error in the ram pressure can be reduced to some extent by using anvils with larger faces. For this reason the anvils with 5 mm face diameter were used up to 4 GPa and 3 mm face diameter up to 9 GPa.

The volume changes during the reverse transformation (bcc → fcc) were studied by the following procedure. The pressure was increased in steps until the x-ray diffraction patterns indicated the presence of bcc phase alone. The pressure was then decreased in steps and x-ray patterns recorded after each decrement. The specimen was found to remain in fully bcc phase until the pressure was reduced to $\approx$ 1 GPa. The diffraction patterns from the coexisting fcc and bcc phases were recorded. The pressure on the specimen was calculated by using the observed cell volume of the fcc phase and the experimentally determined equation of state.

The quality of x-ray diffraction patterns was reasonably good. Normally, five lines from the fcc phase and four lines from the bcc phase could be recorded. When the two phases coexisted, the quality of the diffraction pattern was poorer. This was reflected in a large scatter in the pressure-volume data.

3. Results and discussion

The pressure-volume data are shown in figure 2. The bulk modulus at one atmosphere, B_0 and its pressure derivative, B'_0 were determined by fitting to the pressure-volume data Murnaghan equation of the form,

$$V/V_0 = \left(1 + \frac{B'_0 p}{B_0}\right)^{-1/B'_0},$$

where V_0 and V denote the volumes of the unit cell respectively at one atmosphere and

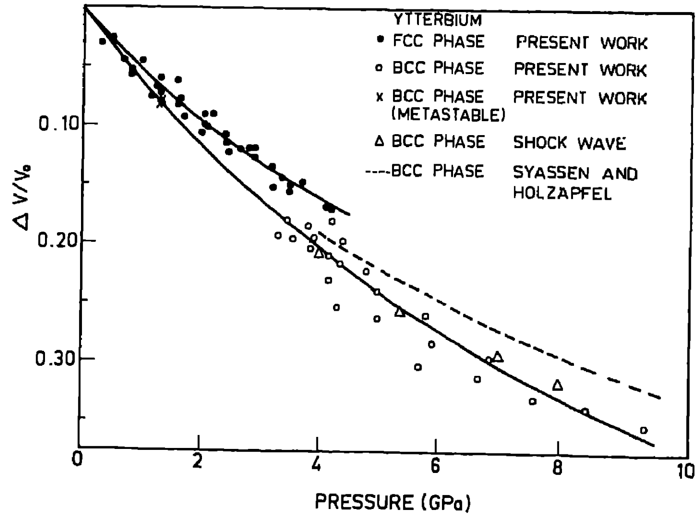

Figure 2. Pressure-volume data.

at a pressure p. The pressure-volume data up to 3·5 GPa were used to obtain the values of B_0 and B'_0 of the fcc phase. The values of B_0 and B'_0 of the bcc phase were obtained using data in the pressure range 4–9 GPa. Assuming the error to be in the measurement of (V/V_0) alone, the standard deviation in (V/V_0) was calculated and found to be 0·008. These errors are nearly twice as large as those in some of the best experimental devices which employ liquid pressure transmitting medium and *in situ* pressure measurement using ruby fluorescence technique or NaCl pressure marker.

3.1 *Fcc phase*

The values of B_0 and B'_0 of the fcc phase as obtained from the present data along with those obtained by the other investigators are listed in table 1. The values of B_0 reported by the various investigators range from 13 GPa to 17 GPa. The present value agrees well with those reported by Hall and Merrill (1963), Stephens (1964), and Gust and Royce (1973). The value reported by Bridgman (1954) appears to be too low. The values of B_0 obtained from the measurement of ultrasonic sound velocity (Smith *et al* 1957; Rosen 1971) are significantly lower than the present value, but agree well with Bridgman's (1954) value. The present value of B'_0 is significantly larger than the values reported by Bridgman (1954) and Stephens (1964). However, B'_0 for most solids is closer to 4, as indicated by the validity of Birch equation of state, the present value of B'_0 appears realistic.

The measurements by Hall and Merrill (1963) indicated a break in slope of the pressure-volume curve at 1·8 GPa. This was, however, not supported by other experiments made with similar apparatus (Stephens 1964). The reported change in slope (Hall and Merrill 1963) is too small to be detected in the present experiments.

It is interesting to compare the bulk modulus of ytterbium with those of the other rare earths. This can be done with the help of a $\log B_0 - \log v_0$ plot (Anderson and Nafe 1965), where v_0 is atomic volume. Such a plot for compounds having similar bonding characteristics results in a straight line, indicating that the bulk modulus increases exponentially as the atomic volume decreases. The $\log B_0 - \log v_0$ plot for rare earth elements is shown in figure 3. The solid line is a least-squares fit to the data for rare earths. It is seen that the ytterbium point falls much below this line.

A similarity between the high pressure behaviour of ytterbium and alkaline earth elements specially strontium has long been noted (Jayaraman *et al* 1963). Strontium, like ytterbium, has a fcc structure at one atmosphere and transforms to bcc phase at ~ 4 GPa. These similarities prompted a comparison of the bulk modulus of ytterbium with the bulk moduli of alkaline earth elements. The data for calcium, strontium and

Table 1. Compression parameters of ytterbium (fcc phase) in the pressure range (0–4 GPa)

B_0(GPa)	B'_0	Method	Reference
13·3	1·22	Piston-cylinder	Bridgman (1954)
17·2	—	-do-	Hall and Merrill (1963)
15·3	1·57	-do-	Stephens (1964)
13·8	—	Ultrasonic	Smith *et al* (1957)
13·5	—	-do-	Rosen (1971)
15·0	—	-do-	Gust and Royce (1973)
16·3	3·6 ± 0·9	X-ray	Present results

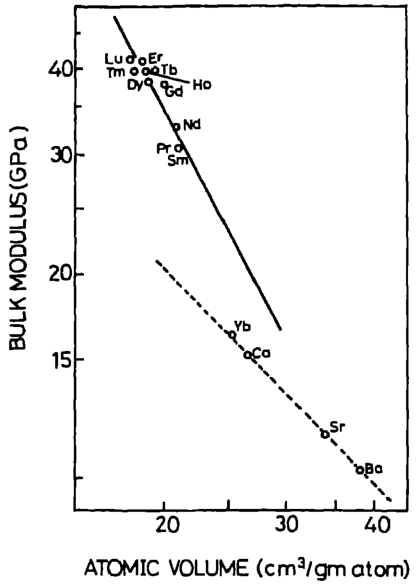

Figure 3. A log $B_0 - \log v_0$ plot. The B_0-value for ytterbium is from the present experiments and for others from Gschneidner (1964).

barium are also plotted in figure 3. It is seen that the points fall on a straight line suggesting a strong similarity between ytterbium and alkaline earth elements so far as the dependence of bulk modulus on atomic volume is concerned.

3.2 *Bcc phase*

The values of B_0 and B'_0 of the high pressure phase (resulting from a transformation) cannot be obtained by fitting to the pressure-volume data an equation of state in standard form, because often a discontinuous volume change is associated with the transformation. This difficulty is simply overcome by shifting the origin of co-ordinates to (p_t, V_t), where p_t and V_t are respectively the observed pressure of transformation and the volume at p_t; any equation of state in standard form can then be used. The equation fitted in this manner indicates that $V \neq V_0$ at $p = 0$. This physically means that the room pressure density of the starting material is different from the density of the high pressure phase at room pressure. The volume measurements on the metastable bcc phase at ~ 1 GPa indicate that the situation in the case of bcc ytterbium is different. The volume difference between the fcc and bcc phases decreases rapidly with decrease in pressure and seems to vanish at $p = 0$. The pressure-volume curve thus passes through the origin of co-ordinates. A Murnaghan equation was therefore fitted to pressure-volume data in the pressure range 4–9 GPa. The value of B_0 and B'_0 were respectively 14·7 GPa and 1·5.

Syassen and Holzapfel (1979) determined the pressure-volume relation for the bcc phase of ytterbium up to nearly 30 GPa using a diamond anvil camera. The values of B_0 and B'_0, however, were not reported. On fitting Murnaghan equation to the data the following values were obtained: $B_0 = 14{\cdot}7$ and $B'_0 = 2{\cdot}49$. The value of B_0 agrees very well with the present value, but the B'_0 value is significantly larger than the present value. This is also reflected in the fact that the overall volume compression obtained by Syassen and Holzapfel (1979) is smaller than that obtained in the present experiments.

Table 2. Compression parameters of ytterbium (bcc phase) in the pressure range (4–9GPa)

B_0(GPa)	B'_0	$(\Delta V/V_0)_t^*$ at 4 GPa	Reference
—	—	−0·032	Hall *et al* (1963)
12·0	2·71	—	Gust and Royce (1973)
14·7	2·49	—	Syassen and Holzapfel (1979)
14·7	1·50	−0·043	Present results

* $(\Delta V/V_0)_t$ is the volume change associated with the fcc-bcc transformation.

Table 3. The fcc → bcc transformation pressure (start pressure) in ytterbium

Transformation pressure (GPa)	References
4·0	Bridgman (1954)
4·0	Hall *et al* (1963)
4·0	Souers and Jura (1963)
3·8	Stager and Drickamer (1963)
4·0	Hall and Merrill (1963)
4·0	Jayaraman (1964)

The present pressure volume data for the bcc phase, however, lie closer to those obtained in shockwave experiments (Gust and Royce 1973). The compression parameters derived from the data of various investigators are listed in table 2. The volume change associated with the transformation is −0·043, and is marginally higher than the value obtained by Hall *et al* (1963).

The volume compression of ytterbium is much larger than that of the other rare earths. It is only above 15 GPa that the volume compression of ytterbium becomes comparable to that of the other rare earths (Syassen and Holzapfel 1979). Further, the present data indicate that the bulk modulus of the fcc phase is larger than that of the bcc phase at the same pressure. For example, at 4 GPa the bulk moduli are 30·7 GPa and 20.7 GPa respectively for the fcc and bcc phases. The anomalous compression of bcc ytterbium and its relation to a possible electronic transition will be discussed in § 3.4.

3.3 *Pressure of transformation*

The fcc → bcc transformation pressure has been reported by many investigators (table 3). The pressures reported were the pressures at which the transformation was found to start in experiments wherein either the pressure was continuously increased or the pressure was increased in small steps with a reasonable waiting period (a few min) between the steps. It is seen in table 3 that the start pressure of the transformation was close to 4 GPa in most experiments. Souers and Jura (1963) noted the fcc ⇌ bcc transformation was characterized by a large hysteresis and felt that the equilibrium pressure was close to the start pressure for the fcc → bcc transformation. The present data indicate that bcc phase could often be observed around 3·5 GPa in the experiments wherein pressure was increased in steps and held constant during the x-ray exposure. In the experiments with decreasing pressure, the bcc phase was metastably retained down to pressures as low as 1 GPa.

A transformation can proceed only if the applied pressure is more than the equilibrium pressure. Since the fcc → bcc transformation was found to occur even at 3·5 GPa, the equilibrium pressure is expected to be much below 3·5 GPa. In fact, the study by resistometric method of the kinetics of the fcc → bcc transformation under isobaric-isothermal conditions indicated that the kinetics of the transformation became slower at lower pressures, and the fcc → bcc transformation was found to occur even at 3·3 GPa (Singh *et al* 1982, 1983; Singh 1983; Divakar *et al* 1984). It is certain that the transformation will occur at pressures below 3·3 GPa if sufficient time is allowed. These data and also the present results indicate that the equilibrium pressure for fcc $\rightleftharpoons$ bcc transformation in ytterbium is much below 3·3 GPa and not close to 4 GPa as many earlier investigators believed.

The fcc → bcc transformation in ytterbium under isobaric conditions exhibits incubation period which decreases exponentially with increase in pressure (Divakar *et al* 1984). The start pressure of the transformation is close to the pressure at which the incubation time becomes small as compared with the loading time. Because of the exponential nature of the pressure-dependence of the incubation time, large changes in the incubation time can be brought about by relatively small changes in pressure. Thus, the experimentally observed start pressure is not very sensitive to the rate of loading. This, together with the fact that the rates of loading employed by various investigators do not vary widely, explains why highly reproducible values for the start pressure (table 3) were obtained by the various investigators, even though the transformation can occur over a wide range of pressures under isobaric conditions.

3.4 *Electronic transition*

The electrical resistivity of ytterbium increases with increase in pressure reaching a maximum near 4 GPa (Bridgman 1954; Stager and Drickamer 1963), followed by a large decrease. Lawson (1956) suggested that this decrease in resistance was due to a transfer of a 4*f* electron to the conduction band. Hall and Merrill (1963) established that the decrease in resistance was associated with the fcc → bcc transformation. Hall *et al* (1963) observed that the experimentally determined radius (1·75 A) of ytterbium in the bcc phase at 4 GPa was close to that of trivalent ytterbium at one atmosphere. On this basis it was concluded that the fcc → bcc transformation was accompanied by a change in valency of ytterbium from 2+ to 3+.

The fcc → bcc transformation in ytterbium was compared with a similar structural transformation in strontium (Jayaraman *et al* 1963; McWhan and Jayaraman 1963; Jayaraman 1964). There are no 4*f*-electrons in strontium, and as such the 4*f*-electrons are not involved in the transformation of its structure, and therefore in ytterbium also 4*f*-electrons are not involved in the structural transformation.

McWhan and Jayaraman (1963) suggested that the decrease in ionic radius observed by Hall *et al* (1963) in fact could be accounted for by incorporating a correction for the change in co-ordination number, when the structure changes from fcc to bcc. The radius in the bcc phase at 4 GPa is 1·75 A and becomes 1·80 A after applying a correction for the change in coordination number (Gschneidner 1961). It was argued that the difference between this value (1·80 A) and the observed value (1·82 A) in the fcc phase at 4 GPa was not significant. Therefore, it was concluded that the metallic radii were same in both fcc and bcc phases, and that there was no electronic transition involved in the fcc → bcc transformation in ytterbium.

It is to be noted that the volume per atom with a radius of 1·8 A in the fcc phase is less than that with a radius of 1·82 A by 3·2 %. This is exactly equal to the change in volume observed at the structural transformation (Hall *et al* 1963). Thus, even though the radius in the bcc phase is corrected for the change in the co-ordination number, still there is 3·2 % decrease in volume. This is to be expected for the following reason. The correction for the change in co-ordination number has been derived by Gschneidner (1961) by considering a few temperature-induced structural transformations in elemental solids. The transformations considered show a change in co-ordination number but practically no change in volume. Since most structural transformations under pressure result in a decrease in volume, the atomic radius in the high pressure phase even after the correction for co-ordination number change will be smaller than the radius in the low pressure phase at the same pressure. Thus, the changes under pressure in the atomic radius cannot be used as an indicator of the valence change.

It has been suggested by Coqblin and Blandin (1968) and Coqblin (1971) that since trivalent ytterbium has 13*f*-electrons, the unpaired spin should order magnetically. Katzman and Mydosh (1972) measured the temperature dependence of electrical resistivity down to 1·3 K and at pressures between 5–16 GPa. These experiments did not indicate the presence of superconductivity or magnetic effects and it was concluded that bcc ytterbium is not in trivalent state. The theoretical calculations of Johansson and Rosengren (1975) and Rosengren and Johansson (1976) suggest a valence transition near 14 GPa. The LIII-absorption edge studies made by Syassen *et al* (1981) with diamond-anvil cell and x-rays from synchroton source suggest that the valency of ytterbium changes from 2+ to 3+ continuously over the pressure range 3–33 GPa.

It is certain that the fcc → bcc transformation in ytterbium does not involve a change in valency. The evidences for change in valency even at higher pressures are not clear cut. The *s*, *p*, *d* band structure model (Souers and Jura 1963; McWhan *et al* 1969) which attempts to explain the behaviour of ytterbium in terms of the shift of 5*d* band with respect to 6*s*, 5*p* bands is an alternative model. However, the role of 4*f* electron in ytterbium cannot be ignored altogether because the existence of 4*f* level close to the Fermi level is suggested by optical (Broden *et al* 1970) and x-ray photoemission (Hagstrom *et al* 1970) experiments.

References

Anderson O L and Nafe J E 1965 *J. Geophys. Res.* **70** 3951
Bridgman P W 1954 *Proc. Am. Acad. Arts Sci.* **83** 1
Broden G, Hagström S B M and Norris C 1970 *Phys. Rev. Lett.* **24** 1173
Coqblin B 1971 *J. Physique* **32** C1-599
Coqblin B and Blandin A 1968 *Adv. Phys.* **17** 281
Decker D L 1971 *J. Appl. Phys.* **32** 3239
Divakar C, Mohan M and Singh A K 1984 *J. Appl. Phys.* (to be published)
Gschneidner K A Jr 1961 *Rare earth alloys* (New York: Van Nostrand)
Gschneidner K A Jr 1964 *Solid State Phys.* **16** 275
Gust W H and Royce E B 1973 *Phys. Rev.* **B8** 3595

Hagström S B M, Hedén P O and Löfgren H 1970 *Solid State Commun.* **8** 1245
Hall H T, Barnett J D and Merrill L 1963 *Science* **139** 111
Hall H T and Merrill L 1963 *Inorg. Chem.* **2** 618
Hedén P O, Löfgren H and Hagström S B M 1971 *Phys. Rev. Lett.* **26** 432
Jayaraman A 1964 *Phys. Rev.* **A135** 1056
Jayaraman A, Klement W and Kennedy G C 1963 *Phys. Rev.* **132** 1620
Johansson B and Rosengren A 1975 *Phys. Rev.* **B11** 2836
Katzmann H and Mydosh J A 1972 *Z. Phys.* **256** 380
Lawson A W 1956 in *Progress in metal physics* (eds) B Chalmers and R King (New York: Pergamon) Vol. **6** p. 1
McWhan D B and Jayaraman A 1963 *Appl. Phys. Lett.* **3** 129
McWhan D B, Rice T M and Schmidt P H 1969 *Phys. Rev.* **177** 1063
Rosen M 1971 *J. Phys. Chem. Solids* **32** 2351
Rosengren A and Johansson B 1976 *Phys. Rev.* **B13** 1468
Singh A K and Kennedy G C 1976 *J. Appl. Phys.* **47** 3337
Singh A K, Divakar C and Mohan M 1982 23*rd High Pressure Conference of Japan*, Kyoto p. 100.
Singh A K, Mohan M and Divakar C 1983 IX AIRAPT International High Pressure Conference, Albany, NY, USA
Singh A K 1983 *Bull. Mater. Sci.* **5** 219
Smith J F, Carlson C E and Spedding F H 1957 *J. Metals* **9** 1212
Souers P C and Jura G 1963 *Science* **140** 381
Stager R A and Drickamer H G 1963 *Science* **139** 1284
Stephens D R 1964 *J. Phys. Chem. Solids* **25** 423
Syassen K and Holzapfel W B 1979 *in High pressure science and technology* (eds) K D Timmerhaus and M S Barber (New York: Plenum) Vol. **1**, p. 223
Syassen K, Wortmann G, Feldhaus J, Frank K H and Kaindl G 1981 in *Physics of solids under high pressure* (eds) J S Schilling and R N Shelton (Amsterdam: North-Holland) p. 319

Bull. Mater. Sci., Vol. 6, No. 2, May 1984, pp. 405–413. © Printed in India.

Some recent advances in materials technology

S RAMASESHAN and N BALASUBRAMANIAN*

Indian Institute of Science, Bangalore 560012, India.
*Everest Building Products, R&D centre, Peenya II, Bangalore 560058, India.

Abstract. Recent advances in five key areas of materials technology are discussed. Structural and non-structural composites, electrically-conducting polymers, materials obtained by rapid quenching, new developments in hydraulic cements and photothermal solar energy conversion are reviewed.

Keywords. Composites; conducting polymers; metglasses; macroscopically defect free cement; selective surfaces.

1. Introduction

Recent years have seen vast strides in materials technology. The application of fundamental principles has improved materials by orders of magnitude and enabled them to meet contradictory requirements. For instance, permanent magnets with maximum energy product $(BH)_{\max}$ up to 240 kJ per cubic meter are commonplace today but in 1950, only one fourth of this value had been attained. To cite another example one can now talk of making springs with cement. The methods of fabrication have also become sophisticated. In an effort to obtain more transistors per chip and larger computer memories at lower costs, the silicon technology has been improved to such an extent that it can now meet the threat from alternative technologies such as Josephson devices and magnetic bubbles. In the present review five growth areas are commented upon; the choice of topics to a certain extent depended upon the research interests of the authors.

2. Composite materials

2.1 *Structural applications*

The composite materials present the designer unique opportunities because of the possibility of (i) combining two or more phases with interesting properties and (ii) lamination of several plies to generate a laminate of optimum properties. The first topic is known as micromechanics (in the context of mechanical properties) and the second, as the laminated plate theory. Starting from the properties of the unidirectional composite where all the fibres are oriented along the direction of stress, the properties of off-axis composites and of laminates consisting of plies at different orientations can be calculated. In the case of elastic constants Q_{ij}, the calculations make use of the transformation relations for the fourth order tensors (Tsai 1983). The elastic constants of the laminate are obtained by applying the rule of mixtures relation to the elastic constants of the plies. For symmetric laminates which are thin, a 3 × 3 symmetric matrix of elastic constants is required to describe the elastic behaviour but for specially orthotropic laminates the number of constants required reduces to 4.

The strength properties of anisotropic materials such as composites are described by a surface in strain (ε) space (Tsai and Hahn 1980).

$$G_{ij}\varepsilon_i\varepsilon_j + G_i\varepsilon_i = 1. \tag{1}$$

The coefficients of (1) can be calculated from simple tests such as longitudinal tension and compression, transverse tension and compression and shear and the elastic constants discussed previously. The failure surfaces for plies with various orientations using (1) are shown in figure 1 for a graphite-epoxy composite. The inner envelope represents the minimum strength properties of this material. The use of such failure surfaces in the optimal design of composite laminates has been discussed elsewhere (Balasubramanian 1983). For a biaxial loading condition where the longitudinal tensile stress is twice the transverse one *i.e.*, $\langle 2, 1, 0 \rangle$, the optimum laminate will have 11 plies at 0° and 5 plies at 90° and will withstand $\langle 462, 231, 0 \rangle$ MPa before the first crack occurs. If glass-epoxy were used, 14 plies of 0° and 4 plies of 90° will be required. Such a laminate will withstand $\langle 108, 54, 0 \rangle$ MPa (Balasubramanian 1984). The decision to use one or the other can be made after taking into account costs, densities, thicknesses etc.

Such an ability to tailor the material along with the inherently high strength and stiffness of fibres and the easy processability of resins have led to the widespread use of composites. The Lear Fan 2100 uses carbon and Kevlar based composites which account for 70 % of its weight (Noyes 1983). In the wing, cover skins, spars and ribs are made of carbon fibre woven fabrics. In the fuselage, main skin panels, pressure bulkheads, flooring and frames are made of fabrics and unidirectional tapes. The empennage contains horizontal and vertical stabiliser skins, main spars and ribs of carbon-composites. Aileron skins and spars, elevator skins and spars and flap skins contain Kevlar fabrics. For the same cost, the number of miles travelled on Lear fan 2100 is nearly 3·5 times that on Cessna citation. A number of other aerospace and engineering applications especially in India were reviewed earlier (Ramaseshan and Balasubramanian 1977).

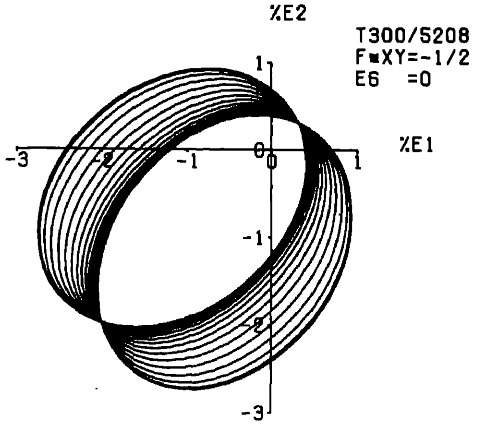

Figure 1. Failure surfaces of graphite-epoxy composite.

2.2 Non-structural applications

Composite materials have interesting electrical, magnetic optical and thermal properties (Albers 1976). One class of materials is similar to the structural materials discussed above in which the constituents contribute proportionally. The second class consists of materials in which the physical output of one phase becomes the input for the second phase. Such properties have been called product properties (van Suchtelen 1972) or operator properties (Ramaseshan and Balasubramanian 1977). One example is a composite consisting of a piezomagnetic phase A and a piezoelectric phase B. In such a composite, the application of a magnetic pulse induces a change in the shape of A. Since A and B are bonded together, B is also strained and being piezoelectric consequently develops an electric pulse. Thus, a magnetic pulse is converted into an electric pulse by the composite. The composite is the unidirectionally-solidified eutectic of barium titanate ($BaTiO_3$) which is the piezoelectric phase and the mixed nickel-iron oxide (NiO-Fe_2O_3) which is the piezomagnetic phase. Composites with operator properties can have entirely new properties or can give a known conversion but with a higher yield.

For optical applications, sodium fluoride-sodium chloride (NaF-NaCl) eutectics can be solidified unidirectionally so that NaF rods are parallel to the axis of the specimen grown. The composite then has image transmission properties similar to those of fibre-optic materials. The spacing between the rods can be controlled by the conditions of solidification. In fact, the solidification in this system was studied under zero-gravity conditions in a space-processing experiment and the inter-rod spacing was found to be more uniform compared to the eutectic composites solidified on earth. The controlled eutectic can then act as a far infrared transmitting medium for wavelengths longer than the inter-rod distance (typically 6 μm). Other examples of non-structural composites include aligned indium antimonide-nickel antimonide eutectics which are currently in use as magneto-resistive and infrared materials (Weiss and Wilhelm 1963).

In structural applications one phase is used in fibre form (one-dimensional) and the other in bulk form (three-dimensional). In non-structural applications, interesting variations in properties are obtained by using the phases in various forms (powders, layers etc). The ceramic fabrication processes permit such variations (Newnham *et al* 1980). These authors use a coral skeleton characterised by (i) a narrow pore size distribution (ii) a pore volume which equals the volume of the solid phase and (iii) complete interconnectivity of pores.

The skeleton is machined to the desired geometry and vacuum-impregnated by wax. The skeleton is then leached out leaving the wax negative. The PZT slip (containing PZT, 2 μm size, water and polyvinyl alcohol) is forced into the wax negative by vacuum impregnation. When the wax is burnt off, PZT in coral structure is obtained (this is the lost wax process, well-known in metallurgy). PZT is then filled with high purity silicone rubber and a composite of PZT/silicone is obtained. The composite has a longitudinal piezoelectric coefficient $\bar{d}_{33}$ of 160 pCN^{-1}. If now a biaxial compression is applied such that the sample height is reduced by 80% in one direction and by 20% in the perpendicular direction, the electric flux path through the piezoelectric is greatly reduced and the permittivity, $\bar{\varepsilon}_{33}$ is reduced. However $\bar{d}_{33}$ is reduced much less and the ratio between the two, the longitudinal piezoelectric voltage coefficient $\bar{g}_{33} = (\bar{d}_{33}/\bar{\varepsilon}_{33})$ becomes very high, 300×10^{-3} $Vm\, N^{-1}$. This is 15 times the value for the homogeneous PZT transducer.

The other examples of non-structural applications are wear-resistant composite coatings obtained by electroless and electrodeposition (Indira Rajagopal 1983) and ablative composites of high silica and phenolic (Ramachandran *et al* 1980).

3. Conducting polymers

Polymers are known for their processability, fracture toughness and low cost. They could provide cheaper alternative to metallic conductors if the polymers could be made conducting by the use of dopants. A list of conducting polymers produced this way is given in table 1 along with the data on their electrical conductivity. These materials are of considerable theoretical and practical interest (Heegar 1981; Mort 1980). Figure 2 shows the structure of polyacetylene, a non-pendant-group polymer with an unsaturated chain. Undoped polyacetylene (PA) is a semiconductor with a conductivity of 10^{-5} to 10^{-6} $\text{ohm}^{-1}\,\text{cm}^{-1}$. The conductivity is of the *p* type as shown by thermopower measurements and the activation energy of the conductivity is 0·3 eV. Its band gap as deduced from optical absorption is 1·4 eV. When PA is doped by reacting the polymer with a strong oxidising or reducing agent, an excess of positive or negative charge is

Table 1. Conducting polymers

Polymer	Dopant	Conductivity ($\text{ohm}^{-1}\,\text{cm}^{-1}$)
Polyacetylene	Arsenic pentafluoride	1200
Poly-*p*-phenylene	Arsenic pentafluoride	500
Polypyrrole	Iodine	100
Polypyrrole	Perchlorate	40
Polyaluminophthalocyanine fluoride	Iodine	4·5
Polyphthalocyaninealloraine	Iodine	1·4
Polyphenylene sulfide	Arsenic pentafluoride	1
Mercury	—	10^4
Copper	—	6×10^5

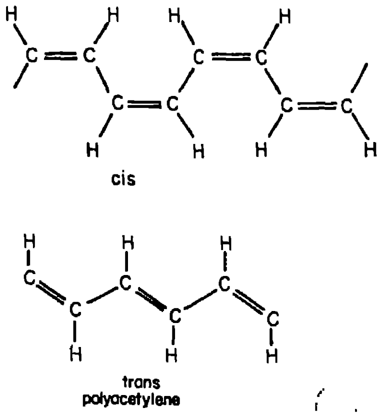

Figure 2. Structure of polyacetylene.

produced on the polymer. The charge is free to move through the polymers because of the inter linking of double bonds. Specifically, PA doped with AsF_5 or with iodine (electron acceptors) has a conductivity of 1000 ohm^{-1} cm^{-1}. Doping with sodium napthalide (electron donor) leads to *n*-type material with similar conductivity. The behaviour is concentration-dependent. At low doping levels, the material is a semiconductor and at 1 to 3 atomic % of doping, transition to metallic behaviour takes place. There are two proposed models. According to the first, the transition is due to percolation of $(CH)_x$ chains. These constitute the conducting particles in an insulator and after sufficient doping, interconnections between conducting particles occur (Zallen 1978). In the second model soliton (solitary wave solutions to nonlinear problems) theory of electrical conduction is used. At low doping levels, it is energetically more favourable for the charge from the dopant molecule to bind itself to the soliton rather than enter the conduction or valence bands (Su *et al* 1979). At higher doping levels solitons become so numerous that they overlap to form a continuous metallic state. ESR spectra of trans-PA confirm the presence of one neutral soliton for every 3000 bonds.

The practical applications of conducting polymers include (1) photoreceptor elements (2) photovoltaic cells and (3) commercial batteries. However, there is need for considerable development work. New ways of doping have to be found to assure the stability of conductors in air. The structural irregularities in the resin affect conductivity and will have to be minimised. There is also evidence that the solutions of lithium iodide in dimethoxyethane (DME), intended for use in light weight batteries leach out the triiodide ions I_3 (produced by the action of I_2 on PA) from PA. When this happens the conductivity of the iodine-doped PA drops by eight orders of magnitude. The same phenomenon occurs while charging the battery. Hence a barrier coating which prevents leaching without affecting the conductivity will have to be developed.

4. Materials by rapid solidification

Duwez and coworkers (Klements *et al* 1960) showed that some alloys could be cooled fast enough (10^6 °C sec^{-1}) to yield glasses (Metglasses). These are now produced commercially. The liquid metal can be passed through a nozzle with a thin slit that lies in close proximity to a cold rotating wheel. As the metal flows from the slit it is very quickly quenched into a glass (Narasimhan 1979). This process can, in principle, produce any desired width. Metglasses mostly contain an early or late transition metal and a metalloid (Suryanarayana *et al* 1980) or an early transition metal and a late transition metal (Suryanarayana 1980). Fast cooling can produce new crystalline phases or amorphous alloys. The high pressure annealing of amorphous alloys can yield new crystalline phases which are not obtained by annealing at ambient pressures. Rapid solidification processing eliminates forging, rolling, drawing etc., and is much faster compared to the conventional processes. However, the heat extraction must be rapid which limits the shape of articles produced to ribbons, wires and thin sheets. They also are unstable at high temperatures. The corrosion rate of Metglasses is 1000 times smaller than that of stainless steels. Ferrous glasses are easily magnetized and exhibit high saturation magnetizations. The loss factor is very low (Luborsky *et al* 1978). Although a number of structural applications (Gilman 1980) have been suggested including reinforcements in composites (Strife and Prewo 1981; Yeow 1980) Metglasses are important from the point of view of magnetic properties. The use of metallic glass cores in power transformers will reduce core losses and result in energy savings. The use of lasers to melt only the surface of the material or laser glazing is an interesting development. A laser melts the surface of a bulk material which rapidly solidifies when the incident beam is removed. The otherwise conventional material now has a surface layer 1 to 10 mm thick which is amorphous or microcrystalline in nature.

5. Macroscopically defect-free (MDF) cement

Cement and steel are the most widely used construction materials. But our understanding of cement is much poorer than that of steel. This situation is changing as a result of interdisciplinary research devoted to cement. The hydraulic cements (ordinary portland cement and its modifications, calcium aluminate cement etc.) are inert, non-combustible and cost less energy to produce them than metals or plastics. It is easy to shape them into finished parts because the setting takes place at room temperature. However the tensile strength and strain to failure and fracture toughness are low compared to other materials. This is why cement is used in compression. The limitations of cement have been overcome by the modification of their structure (Birchall *et al* 1981, 1982). The conventional cement has a porosity of 25 to 35% and pore sizes of 10^{-9} to 10^{-3} m. It was previously thought that the low strength of cement could be explained entirely by the porosity dependence of strength (Feret 1897). It is now realised that the pore acts like a Griffith flaw and the pore size affects the strength more strongly (Kendall *et al* 1983). Simple equations to quantify these ideas have been available in the literature for a long time. The strength (σ) dependence on flaw size (c) is given by the Griffith (1920) formula

$$\sigma = (ER/\pi c)^{1/2}, \tag{2}$$

where E is the Young's modulus and R the fracture energy. For a solid of porosity p

$$E = E_0(1-p)^3, \tag{3}$$

and

$$R = R_0 \exp(-kp), \tag{4}$$

where k is a constant. Hence

$$\sigma = \left(\frac{E_0 R_0}{\pi c}\right)^{\frac{1}{2}} [(1-p)^3 \exp(-kp)]^{1/2}. \tag{5}$$

Equation (5) suggests that the strength can be improved by (i) reducing porosity p (ii) reducing the pore size, c and most importantly, (5) shows that the reduction of porosity by 30% can increase the strength by a factor of 2, but the reduction of pore size from 1 mm to 0·01 mm (10 μm) increases the strength by a factor of 10.

By the addition of a polymer, dough mixing and air removal it is possible to produce cement with pore size less than 15 μm. Such a cement is known as the Macroscopically Defect Free cement (Birchall *et al* 1981). The properties of such cement are shown in table 2 along with those of ordinary cement for comparison. The data show that the MDF is not only vastly superior to the conventional cement but can compete with aluminium and steel in many applications.

The following water-soluble polymers have been used in making the MDF cement:

Table 2. Properties of MDF compared to ordinary cement

	Ordinary cement	MDF cement
Flexural strength, MPa	10	40–150
Young Modulus, GPa	20	35–50
Compressive strength, MPa	40	100–300
Fracture energy ($J\,m^{-2}$)	20	40–200
Electrical breakdown ($kV\,mm^{-1}$)	0·1	6–13
Gas permeability ($mol\,m^{-1}\,sec^{-1}\,Pa^{-1}$)	10^{-12}	10^{-16}

(i) hydroxy propylmethyl cellulose (ii) polyacrylamide (iii) polyvinyl alcohol and (iv) polyvinyl acetate.

A typical composition is given by 100 parts (by mass) cement, 7 parts polymer and 10 parts water. This materials is thoroughly mixed by applying shear. The polymer attaches to the cement particles and acts as a lubricant promoting the sliding of the cement particles so that they can be closely packed. By applying a low pressure (5 MPa) air bubbles can be removed. The space available for the growth of hydration products is restricted due to close packing in MDF cement paste and calcium hydroxide is present as a platlet, 10 mm thick and larger crystals may act as flaws and reduce the strength. The MDF cement will find many applications in the building industry in the form of sheets, pipes, rods, *T*-sections etc. With fibre reinforcement (*e.g.* Kevlar) further improvements in fracture toughness are possible.

6. Surfaces for selective absorption of solar energy

Efforts are being made to convert solar energy into useful heat. The simplest device which does that is the flat plate collector, which has a black surface painted on it. But the radiation losses from such a surface are considerable. Hence a spectrally selective surface which absorbs solar energy without radiating heat is efficient. For efficient photothermal conversion of solar energy, the absorbing surface should ideally exhibit zero reflectance over the solar range ($0{\cdot}3 \lesssim \lambda \lesssim 2\ \mu m$) and unit reflectance over the thermal range ($2 \lesssim \lambda \lesssim 20\ \mu m$) (figure 3). The reflectance should change at a wavelength λ_c of say 3 μm. An example of a material with such selective absorption is $Zr\,B_2$.

More frequently a composite of a semiconductor and metal is used. The short

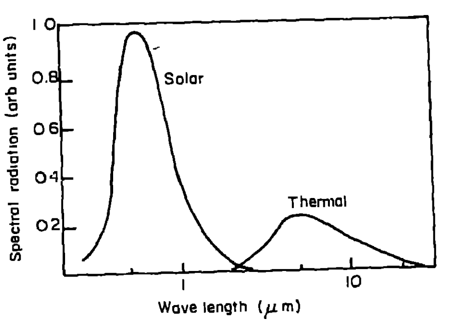

Figure 3. Solar and thermal spectra.

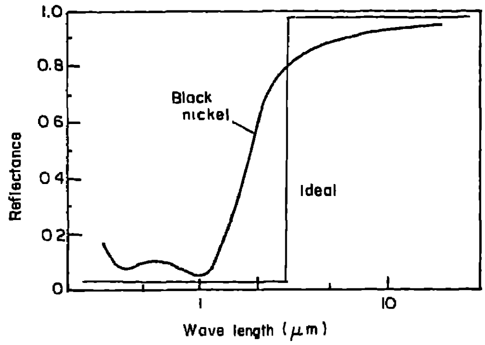

Figure 4. Spectral reflectance of the ideal and an actual selective surface.

wavelength radiation can be absorbed by the semiconductor of appropriate bandgap ($\approx 0{\cdot}5$ eV) and the metal substrate has a low thermal emittance. Figure 4 shows the behaviour of such a composite along with that of the ideal selective surface.

The most widely used surfaces are: (i) "black chrome". This is a Cr–Cr_2O_3 composite produced by electroplating. (ii) Nickel, pigmented Al_2O_3. This is a Ni–Al_2O_3 composite produced by the electrolytic colouration of anodized aluminium sheet. This surface has a solar absorptance of 92 to 97 % and thermal emittance of 10 to 26 %. (iii) Ni-NiO composite produced by chemical conversion of nickel foil. A co-evaporated Mo-Al_2O_3 composite layer coated with Al_2O_3 and deposited on to molybdenum has a solar absorptance of 99·2 % and normal thermal emittance below 8 %. The promising coatings for photo thermal energy conversion must be assessed for long term durability in operating environments (Bogaerts and Lampert 1983).

7. Concluding remarks

While commenting on the frontier technologies, one must be aware that threats could come out of the blue and cause panic. This happened in the case of graphite-epoxy composites when the moisture problem arose and again when the graphite fibres released from the composite caused electrical short-circuits. In both cases the probability of failure was shown to be low. In the case of fibre-optic cables, hydrogen was found to diffuse through the nylon and steel cladding and concentrate inside the cable. It could diffuse into the quartz fibre and attenuate light especially at long wavelengths. This danger is present in submarine cables where the protective steel cladding could set up a galvanic cell with the sea water and produce hydrogen. It was discovered that the caulking compound used to seal the under water joints also had the property of blocking the hydrogen gas. The areas we have chosen to discuss are the ones where science and technology have progressed together and where it is difficult to halt the progress merely because of the fear of the unknown.

References

Albers W 1976 *Composite materials, Proc. Int. Conf.* (ed.) E Scale (New York: AIME) Vol 2
Balasubramanian N 1983 *Curr. Sci.* **52** 1171
Balasubramanian N 1984 to be published

Birchall J D, Howard A J and Kendall K 1981 European Patent No. 021682

Birchall J D, Howard A J and Kendall K 1982 European Patent No. 0055035

Birchall J D 1983 *Philos. Trans. R. Soc. London* **A310** p 31

Bogaerts W F and Lampert C M 1983 *J. Mater. Sci.* **10** 2847

Feret R 1897 *Bull Soc. Encour. Ind. Natl Paris* **II** 1604

Gilman J J 1980 *Science* **80** 856

Griffith A A 1920 *Philos. Trans. R. Soc. London* **A221** 163

Heeger A J 1981 *Commun. Solid State Phys.* **10** 53

Indira Rajagopal 1983 *Bull. Mater. Sci.* **5** 323

Kendall K, Howard A J and Birchall J D 1983 *Philos. Trans. R. Soc. London* **A310** 139

Klements W, Willens R H and Duwez P 1960 *Nature* (*London*) **187** 869

Luborsky F E, Frischmann P G and Johnson L A 1978 *J. Magn. Mater.* **8** 318

Mort J 1980 *Science* **80** p 819

Narasimhan D 1979 *U S Patent* 4 **142** 571

Newnham R E, Bowen L J, Klicker K A and Cross L E 1980 *Mater. Eng.* **2** 93

Noyes J V 1983 *Composites* **14** 129

Ramachandran B E, Pai B C and Balasubramanian N 1980 *J. Am. Cer. Soc.* **63** 1

Ramaseshan S and Balasubramanian N 1977 *Sci. Today* Sept. Issue

Strife and Prewo K M 1981 *Comp. Tech. Rev.* **3** 76

Su W P, Schrieffer J R and Heeger A J 1979 *Phys. Rev. Lett.* **42** 1698

Suryanarayana C 1980 *Rapidly quenched metals—A bibliography* 1973–79 (New York: IFI/Plenum)

Suryanarayana C, Inoue A and Masumato T 1980 *J. Mater. Sci.* **15** 1993

Tsai S W 1983 ICM-4 (eds) J Carlsson and N G Ohlson (New York: Pergamon) Vol 4 p 103

Tsai S W and Hahn H T 1980 *Introduction to composite materials* (Pennsylvania: Technomic)

Van Suchtelen J 1972 *Phillips Res. Rep.* **27** 28

Weiss H and Wilhelm M 1963 *Z. Phys.* **176** 399

Yeow Y T 1980 *Comp. Tech. Rev.* **2** 17

Zallen 1978 *Proc. 13th IUPAP Conf. on Statistical Physics* (eds) C G Kuper and I Riess (Bristol: Hilger)

FOREWORD

The last two decades have witnessed tremendous advancements in the instrumentation, techniques and applications of electron microscopy and micro-analysis. It is now possible to obtain structure images with a spatial resolution of about 0·1 nm and to carry out micro-chemical analysis of phases/constituents with a mean size of 5 nm. With a view to taking stock of the subject of electron optical techniques as a whole and its applications to the fields of metallurgy and materials science, a seminar on 'High Resolution and Analytical Microscopy' was organised at the Reactor Research Centre, Kalpakkam during February 18–20, 1982 under the joint auspices of the Metals Sciences Division of the Indian Institute of Metals and the Reactor Research Centre, Kalpakkam.

The Seminar was inaugurated by Shri C V Sundaram, Director, Reactor Research Centre and President, Indian Institute of Metals. The Seminar was a great success in terms of both the technical content and participation. The technical presentations, discussions and the concluding panel discussion were very lively and hopefully, provided a good stimulus for research and development efforts in high resolution and analytical microscopy in this country. I wish to thank Prof. A K Seal, and Prof. M K Banerjee, Chairman and Secretary of the Metals Sciences Division, respectively for their support and guidance in organising this Seminar. I also take this opportunity to thank my fellow members of the National Steering Committee, viz. Dr S Banerjee, Prof. T R Ramachandran, Prof. S Ranganathan, Prof. C N R Rao, Prof. C Suryanarayana and Dr V S Raghunathan for their valuable advice and cooperation.

The Proceedings of the Seminar brought out as an issue of the Bulletin of Materials Science contains 10 invited papers and 6 contributed papers. I am sure that the readers will benefit from these Proceedings as the participants did by attending the Seminar. I wish to convey my appreciation to my colleagues Dr V S Raghunathan, Dr V Seetharaman, Shri D Sundararaman and Shri P Kuppuswamy for assisting me in editing and processing the manuscripts of all the papers. Finally I am grateful to the Indian Academy of Sciences for bringing out the Proceedings of the Seminar as a special issue of the Bulletin of Materials Science.

PLACID RODRIGUEZ
Chairman
National Steering Committee

Bull. Mater. Sci., Vol. 6, No. 3, July 1984, pp. 417–452. © Printed in India.

High resolution electron microscopy of long range ordered alloys

S AMELINCKX[†], G VAN TENDELOO and J VAN LANDUYT

Rijksuniversitair Centrum Antwerpen, Groenenborgerlaan 171, B 2000-Antwerpen, Belgium

[†] Also at: SCK, B 2400 - MOL, Belgium

Abstract. In this paper a survey is given of the application of high resolution electron microscopy and selected area electron diffraction to the study of long range ordered alloys. The characteristic features of the diffraction effects and of the imaging of ordered alloys are discussed. Group theoretical considerations allow prediction of microtexture of such alloys. A number of simple alloy structures are imaged and it is shown, by means of simulated images, that under suitable diffraction conditions the columns of minority atoms are represented as bright dots. The columns of majority atoms are only visible at very small thicknesses. Subsequently a number of one- and two-dimensional long period superstructures derived from these simple structures are analysed, using high resolution micrographs. Finally the observed microtexture of the same alloy superstructures is compared with the predictions of group theory. Strongly non-conservative antiphase boundaries are found to dissociate in APB's which are as close to conservative as is compatible with the FCC lattice.

Keywords. High resolution electron microscopy; long range order; superstructure; modulated structure; antiphase boundries; domain structures.

1. Introduction

Single crystals of long range ordered alloys are usually highly fragmented in a large number of symmetry-related domains. The x-ray diffraction pattern of such a "single" crystal consists of the superposition of diffraction patterns due to all orientation variants. In structures with low symmetry the number of orientation variants may be as large as 12 or even 24. It is then in general difficult, if not impossible, to unscramble such a pattern into single domain patterns. Usually one can therefore only use x-ray powder diffraction methods with their well known limitations to determine the structures of the ordered alloys.

On the other hand when using selected area electron diffraction, combined with high resolution electron microscopy one can often select a single domain, as seen on the image, and obtain a monodomain diffraction pattern from it. In cases where the domain size is too small, even for selected area electron diffraction, one can sometimes obtain useful information from the optical diffraction pattern of a single domain on a high resolution image.

Long period interface modulated superstructures derived from simpler basic superstructures produce diffraction patterns which have characteristic geometrical features, which allow determination of modulated structure provided the basic structure can be identified.

Whereas x-ray diffraction is the most suitable method to determine the basic structure, electron diffraction, assisted by high resolution electron microscopy, is the most powerful technique to determine modulated structures. We shall illustrate this by means of a number of case studies of long range ordered alloys and their modulated derivatives (Amelinckx 1978–79).

2. Diffraction effects due to translation interface modulated structures

Structures which are derived from a basic structure by the periodic insertion of identical parallel translation interfaces, produce characteristic diffraction effects which we shall now discuss. Let $\bar{R}$ be the displacement vector of the parallel interfaces, d their distance and $\bar{n}$ their unit normal. The introduction of these interfaces produces a long period superstructure (figure 1). Let $\bar{g}$ represent vectors of the reciprocal lattice of the basic structure and $\bar{H}$ those of the superstructures, it was then shown (Amelinckx 1979, De Ridder *et al* 1972) that

$$\bar{H} = \bar{g} + \frac{1}{d}(m - \bar{g}\cdot\bar{R})\bar{n}, \qquad (1)$$

where m is a (small) integer. This expression proves that the diffraction pattern of the superstructures consists of linear sequences of equidistant spots (one for each value of m) associated with each basic spot $\bar{g}$. The spots within a sequence are separated by a distance $1/d$, and furthermore the sequence is shifted, with respect to the position of the basic spot from which the sequence is derived, by a fraction of the interspot distance given by $\bar{g}\cdot\bar{R}$. The intensity of the spots further decreases with increasing value of m.

This formula can easily be generalised to two-dimensional interface modulated structures. Let the interface distances be d_1 and d_2 respectively with unit normals $\bar{n}_1$ and $\bar{n}_2$ and $\bar{R}_1$ and $\bar{R}_2$ as displacement vectors. The reciprocal lattice vectors of the superstructures are then given by

$$\bar{H} = \bar{g} + 1/d_1(m_1 - \bar{g}\cdot\bar{R}_1)\bar{n}_1 + 1/d_2(m_2 - \bar{g}\cdot\bar{R}_2)\bar{n}_2, \qquad (2)$$

where m_1 and m_2 are integers. Formula (2) shows that the superstructure can be completely characterised by using information derived from the geometry of the diffraction pattern once the basic structure is known. By considering the variation of the intensity in the linear sequences it is in most cases possible to locate the basic spots and hence to identify the basic structure. The interspot distance within the sequences determines the distance d between the interfaces, which furthermore are perpendicular

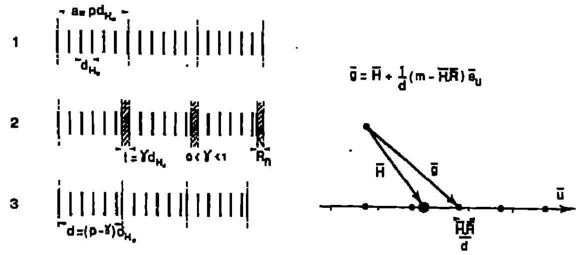

Figure 1. One-dimensional model of interface modulated structure and the associated diffraction pattern. 1. Basic structure with period d_{H_0}. 2. A slice of thickness γd_{H_0} is periodically removed. 3. Resulting modulated structure with period $d = (p-\gamma)d_{H_0}$. The diffraction vectors of the basic structure are represented by $\bar{H}$ and those of the modulated structure by $\bar{g}$.

to the direction of the sequence. The fractional shifts, with respect to the positions of the basic spots, determine the projection of $\bar{R}$ along the considered zone. Two zones are required to determine $\bar{R}$ completely but in many cases the projection is sufficient. We shall discuss examples of the determination of one and two-dimensional superstructures using this method.

If different interface spacings occur in a strictly periodic succession a new period results and is thus revealed in the diffraction pattern. However, if the spacing between interfaces varies discontinuously in a relatively narrow interval, *i.e.* if a mixture of two or three different spacings occurs in an aperiodic manner the diffraction pattern will reveal the average spacing (Fujiwara 1957). It is then possible that arrays of superlattice spots associated with different basic spots do not match where they meet and give rise to what is sometimes called a "spacing anomaly".

It is furthermore possible that the modulating interfaces are systematically ledged or jogged in such a way that their average orientation encloses a small angle with a simple direction of the basic structure (Van Tendeloo and Amelinckx 1977). This situation gives rise in the diffraction pattern to what is sometimes called an "orientation anomaly". The arrays of superlattice spots associated with the different basic reflections are then no longer parallel with a simple direction of the basic reciprocal lattice, but enclose a small angle with it. Diffraction patterns containing spacing and (or) orientation anomalies are sometimes called *pseudo-incommensurate* in contrast with the truly incommensurate patterns observed in deformation-modulated transition metal dichalcogenides (Van Landuyt *et al* 1974a,b, 1978; Williams *et al* 1974; Wilson *et al* 1974, 1975; Scruby *et al* 1975; Williams 1976) and related compounds (Van Tendeloo *et al* 1977; Cornellisen *et al* 1978).

3. Imaging in ordered alloys

3.1 *General considerations*

The structure of a binary alloy, derived from a known basic structure, is established once the positions of the minority atoms are known. The minority atoms determine in fact the unit cell size. The superlattice reflections can be thought of as resulting from scattering by the arrangement of the minority atoms only, provided the latter are attributed a scattering amplitude equal to the difference of the scattering amplitudes due to the minority and majority atoms respectively. This difference is positive if the minority atoms are also the lighter atoms, otherwise it is negative. Using superlattice reflections only for image formation thus reveals the positions of the minority atoms, which may be sufficient for a number of purposes. If an image of the basic structure is also needed, we must include the basic reflections in the set of image-forming beams.

These considerations have led us to the use of several imaging methods, depending on the objective pursued and on whether or not two-dimensional images are required.

3.2 *One-dimensional images*

If only a one-dimensional representation of the structure is required, for instance because the structure is a long period one-dimensional superstructure, one can use the following imaging techniques: (figure 2)

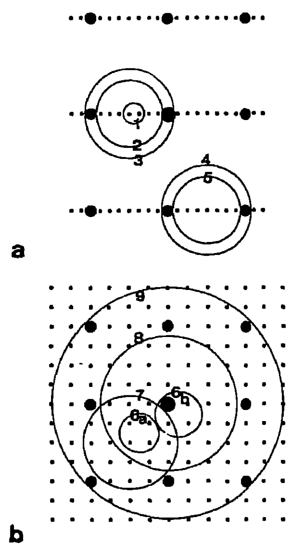

Figure 2. Schematic representation of different modes of beam selection referred to in the text. **a.** for one-dimensional long period structures; the second row is the "central" row. **b.** for two-dimensional long period structures; the centre of the pattern corresponds with the incident beam.

Mode 1: One can select two neighbouring superstructure reflections belonging to the same basic spot in a row of spots passing through the origin, *i.e.* in a central row. One uses only one Fourier component and consequently the image, only reveals the long spacing (Menter 1956).

Mode 2: If all superstructure reflections belonging to a central row are used, excluding the basic reflections in the row, one obtains the distribution of long spacings. (Van Landuyt *et al* 1974).

Mode 5: One can also use a sequence of superlattice reflections from a non-central row. This is a useful mode if one wants to reveal polysynthetic sub-unit cell twinning (Van Landuyt *et al* 1974).

Mode 3: If one selects basic reflections as well as superlattice reflections in a central row (3) or a non-central row (5) one images also the set of lattice planes of the basic structure which is parallel with the periodic interfaces that produce the superstructure. Any variability of the long spacing is now imaged in terms of the spacing of the basic lattice.

If orientation and spacing anomalies occur in the diffraction pattern it is possible to produce images by collecting a pair of spots belonging to arrays associated with different basic reflections (De Ridder *et al* 1975, 1976). The so-formed images have a moiré like aspect; neither their direction nor their spacing is constant.

3.3 *Two-dimensional images*

Mode 6: If only the superlattice needs to be imaged it is sufficient to include only pairs of neighbouring superlattice spots in two directions. This can be done either in the dark field (6a) or in the bright field (6b). In the latter case the image is formed by the direct beam and the first shell of superlattice reflections around it.

Mode 7: All superlattice reflections are selected which are present within one mesh of the reciprocal lattice of the basic structure, excluding the direct beam and the basic reflections. This is clearly a multiple beam dark field image. The Fourier components contributing to the image are in general just sufficient to locate the positions of the minority atoms (Van Tendeloo *et al* 1978).

Mode 8: Except for the direct beam all other basic reflections are excluded but as many shells of superlattice reflections as feasible are admitted (Van Tendeloo and Amelinckx 1978; Van Tendeloo *et al* 1980; Hiraga *et al* 1980). The number of Fourier components required to image the columns of minority atoms is now redundant; however such columns will therefore be imaged as sharper dots than in the previous mode 7.

Mode 9: All beams originating from the basic as well as from the superstructure reflections are selected, provided they do not correspond to spacings which are smaller than the instrumental resolving power of the microscope (Iijima *et al* 1974; Iijima 1975). For most current instruments this means that up to the first or possibly up to the second shell of reflections, due to an FCC matrix, can usefully be included. In our subsequent discussion we shall refer to these different modes and discuss examples of applications.

4. High resolution studies of basic alloy structures

4.1 *General*

A number of simple binary alloy superstructures of the FCC structure have been imaged in high resolution electron microscopy (Van Tendeloo *et al* 1978, 1981; Den Broeder *et al* 1981; Van Tendeloo and Amelinckx 1979). The separation of minority atoms in binary alloys is in many cases at least of the order of 2 Å, a distance which can conveniently be resolved.

Along certain zones the structure consists of columns, which contain only one atomic species, *i.e.* minority and majority atoms occur in separate columns. The distance between columns of minority atoms is then relatively the largest and it determines the unit mesh of the reciprocal lattice of the superstructure along this zone. Such zones are the most informative ones; along these it is possible to image only the minority atom columns by collecting superlattice reflections in the contrast aperture (mode 8). We shall say that the structure is a "column structure" along such rows.

4.2 *The Ni_4Mo structure* (Van Tendeloo *et al* 1978)

The alloy Au_4Mn which is isomorphous with Ni_4Mo (figure 3a) is a particularly suitable object for high resolution electron microscopy, using the dark field superlattice mode (mode 7). The reciprocal lattice as viewed along the c-direction, is shown in figure 4a, for a single variant. The diffraction conditions can then be chosen in such a manner that the projection of the centre of Ewald's sphere coincides with the centre of the octagon of superstructure reflections produced by the two coaxial variants (mode 6). Under these conditions all beams contributing to the images of coaxial variants enclose the same angle with the optical axis of the microscope and thus aberration-induced phase differences cancel. Particularly well-defined images result under these conditions.

The four beams collected in each variant provide the minimum number of Fourier components that allow to generate the pattern of minority atoms, without any redundant information.

Figure 5a shows an example of the Au_4Mn perfect structure observed in this mode (mode 7); along the [001] zone, the Au_4Mn structure is a column structure.

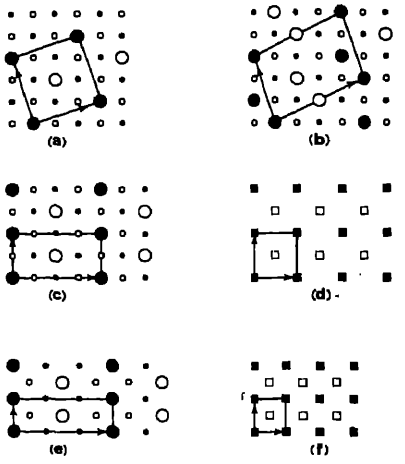

Figure 3. Schematic representation of different ordered structures derived from the FCC and the BCC structure. Large dots represent minority atoms. **a.** Au_4Mn structure viewed along the tetragonal c-axis. **b.** Monoclinic Au_5Mn_2 structure viewed along the twofold axis. **c.** Tetragonal DO_{22} structure (Au_3Mn) as viewed along the a-axis. **d.** The same structure viewed along the tetragonal c-axis. These three structures are derived from the FCC structure. **e.** Tetragonal Cr_2Al structure viewed along the a-axis (Au_2Mn has the same structure). **f.** The same structure viewed along the c-axis. This structure is based on a BCC lattice.

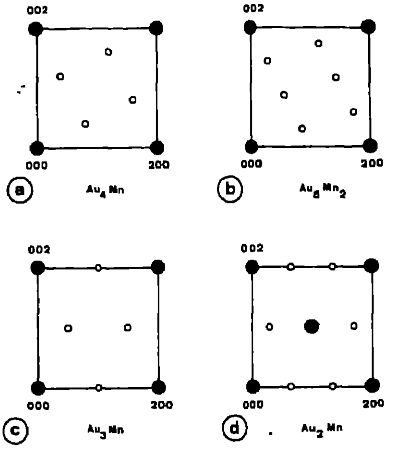

Figure 4. Reciprocal lattice sections of the structures represented in figure 3: In all cases a cube zone is shown. The full dots represent basic reflections, the open dots superstructure reflections.

We have also used the bright field basic lattice mode (mode 9). We now collect all beams within four unit meshes of the basic FCC reciprocal lattice, as well as the basic reflections themselves. The image now clearly contains information on the basic FCC structure, as well as on the superstructure. An image of a wedge shaped crystal obtained using this mode, is reproduced in figure 5b. It is clearly seen that in the thin part of the wedge the basic FCC structure is revealed. In the thicker parts, on the other hand, striking white dots reveal the positions of manganese columns. It is then possible to verify directly that the manganese columns occupy the positions with respect to the FCC lattice represented in the model of figure 3a. The interpretation of the bright dots as marking the positions of the manganese columns is justified on the basis of computer-simulated images, using the method described in §4.6.

4.3. *The DO_{22} structure* (Van Tendeloo *et al* 1983)

A model of the DO_{22} structure is represented in figure 3. Figure 3c and figure 3d are views along the *a*-axis and the *c*-axis respectively. It is clearly a tetragonal superstructure of the FCC superstructure with an ideal c/a ratio of 2, its ideal composition is A_3B. The reciprocal lattice as viewed along the a-direction is represented in figure 4c.

In specimens with nominal composition Au_3Mn, extensive regions of DO_{22} structure were obtained, as judged from the diffraction pattern. Images were obtained using the imaging mode 8. A view along the a-direction is reproduced in figure 5e whereas an image taken along the c-direction is shown in figure 5f. From the two projections, the structure can be determined unambiguously.

Like Au_4Mn viewed along the c-direction, the DO_{22} structure is a column structure when viewed along the a-direction, but not along the c-direction. The bright dots in figure 5e have the geometry and scale of the configuration of manganese columns in figure 3c as viewed along the a-zone. Along this zone there are in fact two types of manganese columns which differ in level by $a/2$; they are imaged in the same way however, suggesting that the projected charge density is to a good approximation all that matters in determining the image. The gold columns are not imaged at all.

Along the c-direction on the other hand the structure is not a column structure; all manganese containing columns are mixed and have the composition AuMn. Apart from a relative shift of $c/2$ in the c-direction they are all identical. One finds in fact that all such columns are imaged in the same way; the observed configuration of bright dots in figure 5f can be compared with the scheme of figure 3d. There is apparently very little doubt left that under the conditions used, the manganese columns in the DO_{22} structure have been imaged.

4.4 *The Au_5Mn_2 structure* (Van Tendeloo *et al* 1978; Van Tendeloo and Amelinckx 1979)

The Au_5Mn_2 structure is a monoclinic superstructure of the FCC structure; it is represented in projection of figure 3b; whereas the (010) section of the reciprocal lattice is shown in figure 4b.

When viewed along the two-fold axis it is a column structure; the configuration of manganese columns is in fact shown in figure 3b. The distance between the components of a pair is only 0·25 nm. In our most recent instrument we have been able to image the two columns in a pair as clearly separated bright dots (figure 5d) whereas in an earlier instrument we have only obtained elongated bright dots imaging a column pair (figure 5c).

The Au_5Mn_2 structure can in fact be described as an interface-modulated superstructure of the DO_{22} structure. When introducing periodic *APB*'s on (101) planes, with a displacement vector $1/4\,[201]_{DO_{22}}$, and with a period of ~ 0·62 nm, one obtains the Au_5Mn_2 structure.

We shall discuss in § 6.2 other related interface-modulated superstructures of the DO_{22} structure.

4.5 *The Cr_2Al structure* (Van Tendeloo *et al* 1981; Den Broeder *et al* 1981)

The Cr_2Al structure is based on a BCC lattice. It is a tetragonal superstructure with an ideal c/a ratio of 3; its unit cell contains three BCC unit cells (figure 3e). The ideal composition is clearly A_2B. Also Au_2Mn has a similar structure. Views along the a- and c-directions are shown in figure 5 g, h. The structure is a column structure along the [100], [010] and [111] zones, and obviously not along the [311] or [001] directions.

We have obtained clearly-defined structure images of Cr_2Al viewed along the [100] direction (figure 5g). The c/a ratio deduced from the image is about 2·9 in fair agreement with that deduced from x-ray diffraction. Along the c-axis all columns are identical and have the macroscopic composition A_2B. The reciprocal lattice, as viewed along the a-direction, is shown in figure 4d.

4.6 *Image simulation* (Spence 1981; Van Dyck 1978)

It is worth noting that in this paper we have intentionally and systematically used images which allowed a direct interpretation in terms of structure models. Such images can be obtained by making through focus series, but also more efficiently with an appropriately adapted microscope. Our instrument is equipped with an image intensifier system, making it possible to obtain the image on a television monitor at a magnification of 10^7 × . Under these conditions it is possible to observe visually the bright dot pattern of minority atoms. This has made it possible to select systematically focusing conditions and thicknesses which produce this type of patterns, avoiding the need for through focus series.

In all cases so far studied, we could produce images such that the pattern of bright dots had the same scale and geometry as the arrangement of columns of minority atoms, strongly suggesting that we were in fact representing such columns as bright dots.

Moreover we have also shown that under the same imaging conditions, the coincidence columns of minority atoms along the inclined interface between two orientation variants are revealed as bright dots (Van Tendeloo and Amelinckx 1978). This can be considered as an experimental proof of our suggestion.

Along zones where all columns have the same but mixed composition, *i.e.* the macroscopic composition, all columns are represented by bright dots of the same intensity.

All these observations strongly suggest that the bright dots do represent columns of minority atoms along zones where minority and majority atoms occur in separate columns (so-called column structures). Nevertheless it is desirable to verify this interpretation by means of computed images, following a "trial and error" scheme. This is in any case required if we want to make sure that the bright dots occur at the sites of the minority atom columns and are not merely reproducing the correct configuration at a shifted position, however. It is perhaps an academic question if we want to obtain

---

Figure 5. High resolution images of different basic ordered structures all at the same magnification. In all cases the bright dots reveal the columns of minority atoms; their configurations can be compared with figure 3. The unit cell is outlined. **a.** Au_4Mn structure viewed along the tetragonal c-axis. **b.** Wedge shaped crystal of the Au_4Mn structure. In the thin part only the FCC structure ($a_0 \sim 0{\cdot}2$ nm) is revealed; in the thicker parts the bright dots reveal the manganese columns. **c.** Monoclinic Au_5Mn_2 structure as viewed along the two-fold axis. The elongated dots represent close neighbour pairs of manganese columns. **d.** Monoclinic Au_5Mn_2 structure as viewed along the two-fold axis. The pairs of columns of manganese atoms are now revealed as separated dots. **e.** Tetragonal Au_3Mn (DO_{22}) structure ($c/a = 2$) as viewed along the a-axis. Only manganese columns are revealed. **f.** Tetragonal Au_3Mn (DO_{22}) structure as viewed along the c-axis. All columns are equivalent; they have a mixed composition. **g.** Tetragonal Cr_2Al structure (also Au_2Mn) viewed along the a-axis ($c/a = 3$). In the thin part of the specimen the body-centered basic structure is revealed. Only minority atom columns are visible in the thicker part. **h.** Tetragonal Au_2Mn structure viewed along the c-axis. Faults in (110) and $(1\bar{1}0)$ are invariably present in Au_2Mn.

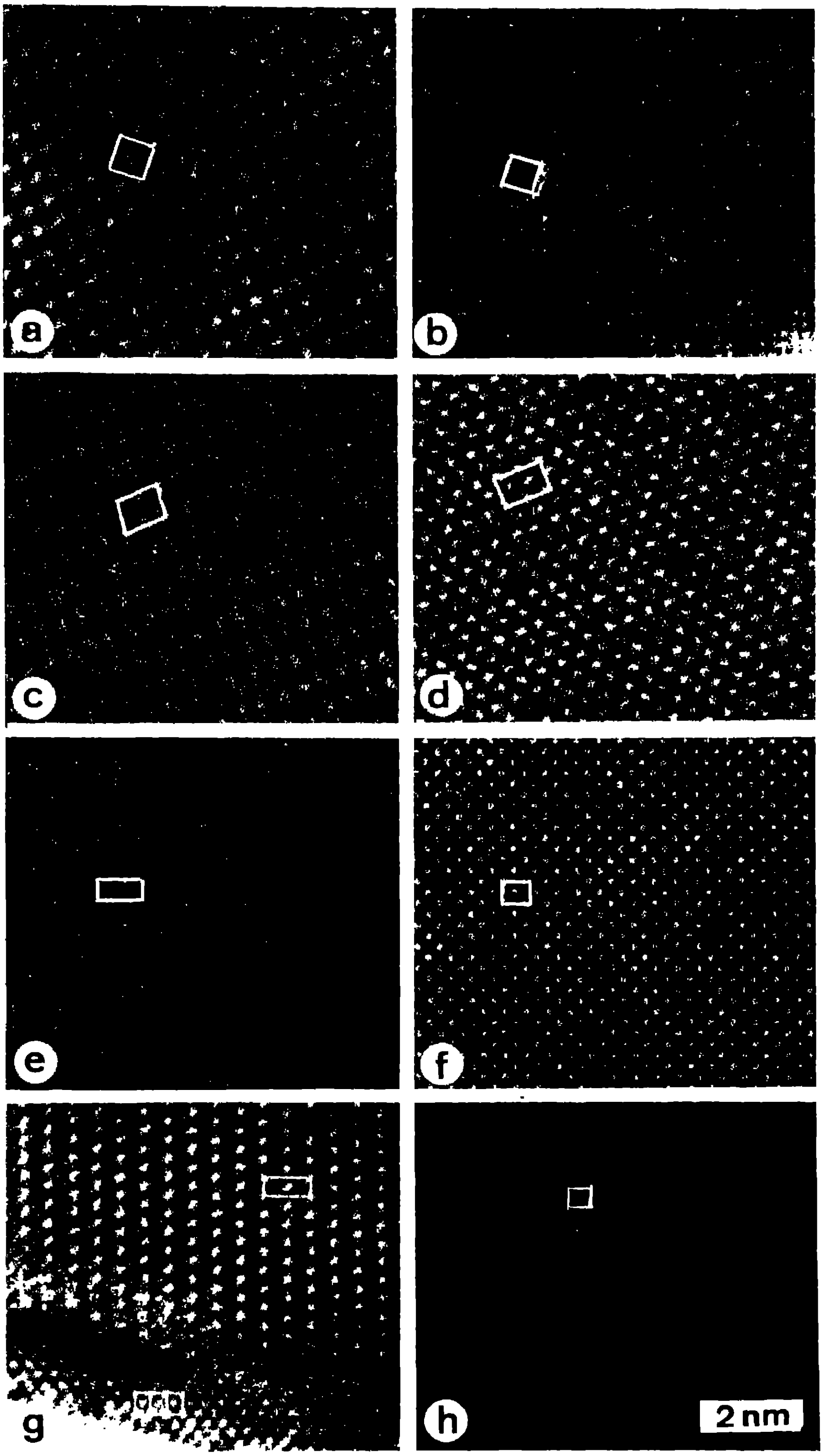
a
b
c
d
e
f
g
h
2 nm

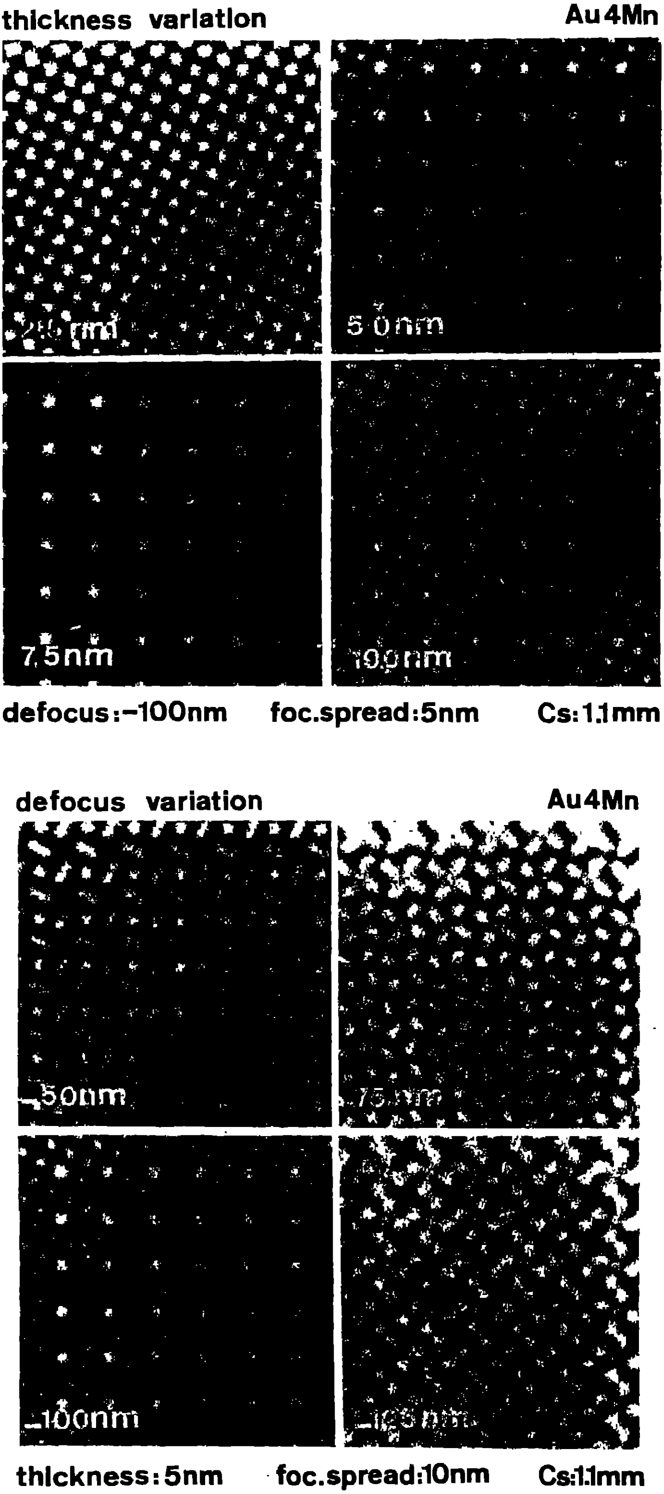

Figure 6. Computer-generated images of Au_4Mn (c_s = 1·1 mm) (Courtesy Van Dyck).

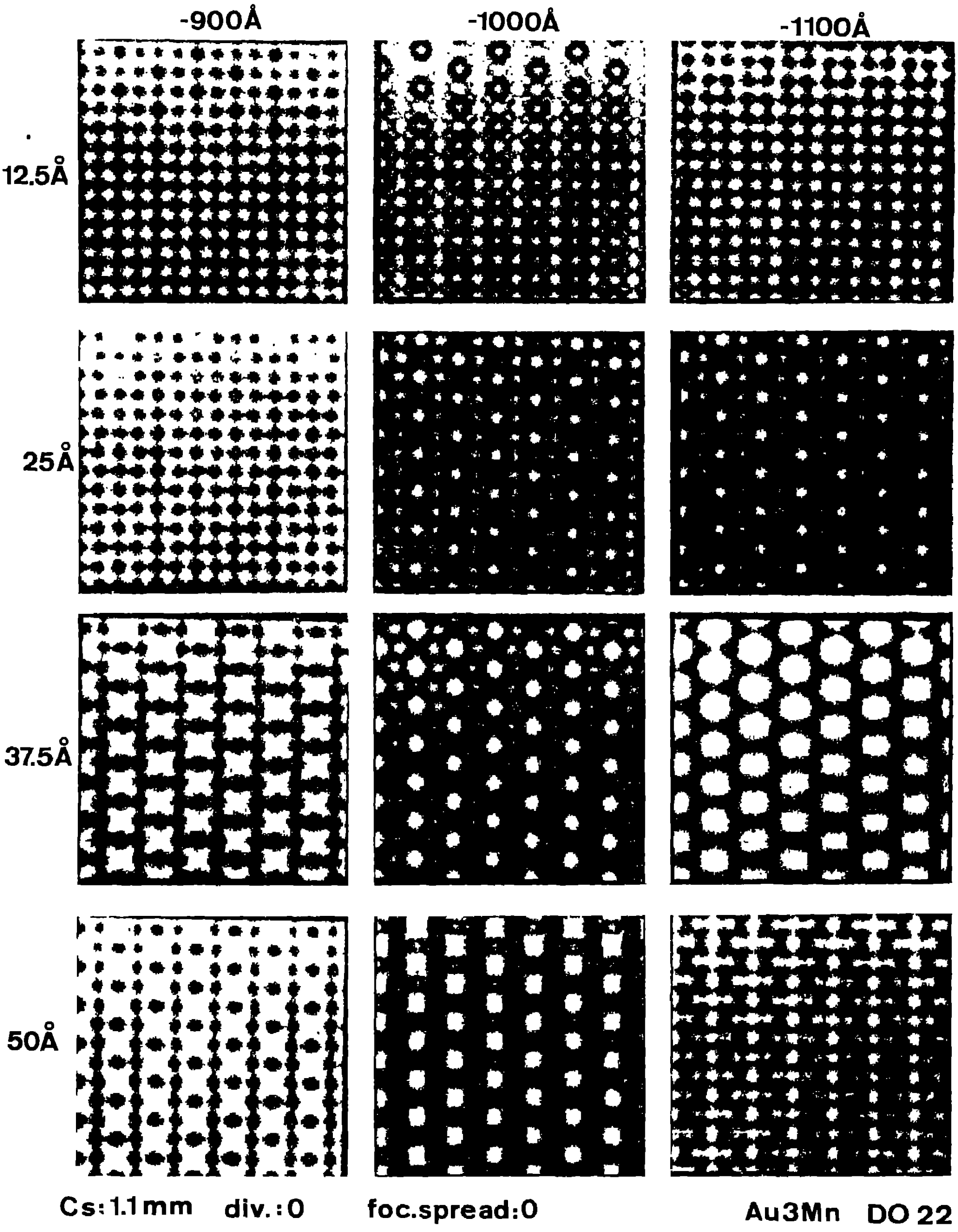

Figure 7. Computer-generated images of the Au_3Mn (DO_{22}) structure.

information on the perfect structure or even on translation interfaces; this is no longer so if we study the interface between orientation variants or other defect structures such as dislocations.

In order to make this verification, it is necessary to produce computed images and compare these with the observations. The computation method used here is an improved version of the multislice method originally proposed by Cowley and Moodie (1957) and further developed by Van Dyck (1980). It fully takes into account multiple beam dynamical scattering in the crystal, as well as the phase shifts introduced by the aberration of the electron optical system and by defocussing ($c_s = 1.1$ mm in our microscope). The final result of the calculation is plotted on a cathode ray screen and photographed, producing in this manner an image of the same nature as the electron micrograph.

We have computed a number of images of different basic structures, viewed along different directions, for a number of thicknesses and defocusvalues. We shall discuss here briefly two examples Au_4Mn and Au_3Mn (DO_{22} structure). The images were calculated on the assumption that the incident beam is parallel to the atom columns and that the superstructure spots as well as the first shell of basic spots are admitted through the objective aperture (mod 9).

The sequence of computed images in figure 6 refers to Au_4Mn. For easy reference the left bottom corner of the frame was occupied in the model by a manganese column. The brightest dots clearly occur at the sites where manganese columns are located according to the model at least for a defocus value of -1000 to -1200 Å and a thickness in the range of 50 Å.

At small thicknesses the sites of the gold atoms are marked by weaker dots; at larger thicknesses the gold images become vanishingly weak (figure 6). This thickness behaviour is in agreement with the observation (figure 5b).

A similar sequence of computed images referring to the DO_{22} structure of Au_3Mn is reproduced in figure 7. Again in this model a manganese column was placed in the left bottom corner of the frame. From the computed images we can conclude that in this case also the manganese columns are represented as bright dots in sufficiently thick foils. In thinner foils the gold atoms are also visible, as weaker dots however.

Qualitatively the contrast behaviour as a function of thickness can be understood by noting that the intensity of the superstructure beams builds up much more slowly as a function of thickness than the intensities of the beams due to the basic structure. Stated otherwise the depth variation of the intensities of the basic reflections is different from that of the superstructure reflections. At certain thicknesses the intensities of the basic beams may thus be weak whilst the superstructure beams may be relatively strong.

5. **Domain structure in alloys** (Van Tendeloo and Amelinckx 1974; Gaymont *et al* 1977)

5.1 *Orientation variants*

Long range ordering usually leads to a decrease in symmetry, the point group of the superstructure being a subgroup H of the point group G of the basic structure.

The superstructure can thus be formed in different orientations, related by symmetry operations of G, which were lost in the ordering process and which can thus no longer be present in H. Such orientation variants are *a priori* equally probable in a specimen formed in an isotropic environment.

The number of orientation variants is given by $n =$ order of $G/$order of H. In many cases the set of operations relating the different orientation variants form a group by themselves; the variant generating point group V. If V exists one can often choose different variant generating groups, which generate of course the same set of variants of the superstructure. The group V has to be a subgroup of G, of order n, and which has no element in common with any of the different orientations of H, except for the unit element. Let for instance $G = \left(\frac{4}{m}\bar{3}\frac{2}{m}\right)$ (order 48) and $H = 4/m$ (order 8) then one can choose as variant generating groups $V_1 = 32$ or $V_2 = 3m$ both of order 6.

The relation between H and V for a given group G is reciprocal, *i.e.* H is the variant generating group if the superstructure has the point group V.

The interface between different orientation variants will be called a "twin" boundary. An operation of V relates the domains on either side of the interface. Two interfaces with separate pairs of domains of which the components are related by the same operation of G will be considered as crystallographically equivalent. One pair of orientation variants can thus be brought into coincidence with the other pair by a symmetry operation of G. Crystallographically different interfaces will have associated operations of V belonging to different classes of G. In the above mentioned example the operations of $V_1 = 32$ belong to two classes: (i) perpendicular twins: the two domains on either side of the interface are related by a rotation over 120° about the three-fold axis along [111]; (ii) anti-parallel twins having the same four-fold axis (coaxial twins); the two domains are now related by a rotation of 180° about a two-fold axis along a [110] direction perpendicular to [111]; in terms of the alternative variant generating group $V_2 = 3m$ the second type of interface (anti parallel twins) separates domains related by a mirror passing through the threefold axis.

The DO_{22} structure occurs in three orientation variants represented schematically with respect to the basic FCC cube in figure 8c. The Au_4Mn structure can be formed in six orientation variants from any FCC matrix (figure 8a). Finally the Au_5Mn_2 structure occurs in 12 orientation variants (figure 8b) based on the same FCC basic lattice (table 1).

5.2 *Translation variants*

During the ordering process also translation symmetry is lost, the Bravais lattice of the basic structure being a sublattice of the Bravais lattice of the superstructure, neglecting small deformations of the basic lattice resulting from ordering. A number of lattice vectors of the basic structure are no longer lattice vectors of the superstructure. All vectors describing such translations are obtained by connecting one lattice node of the

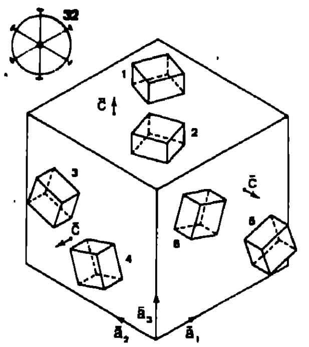

Figure 8a

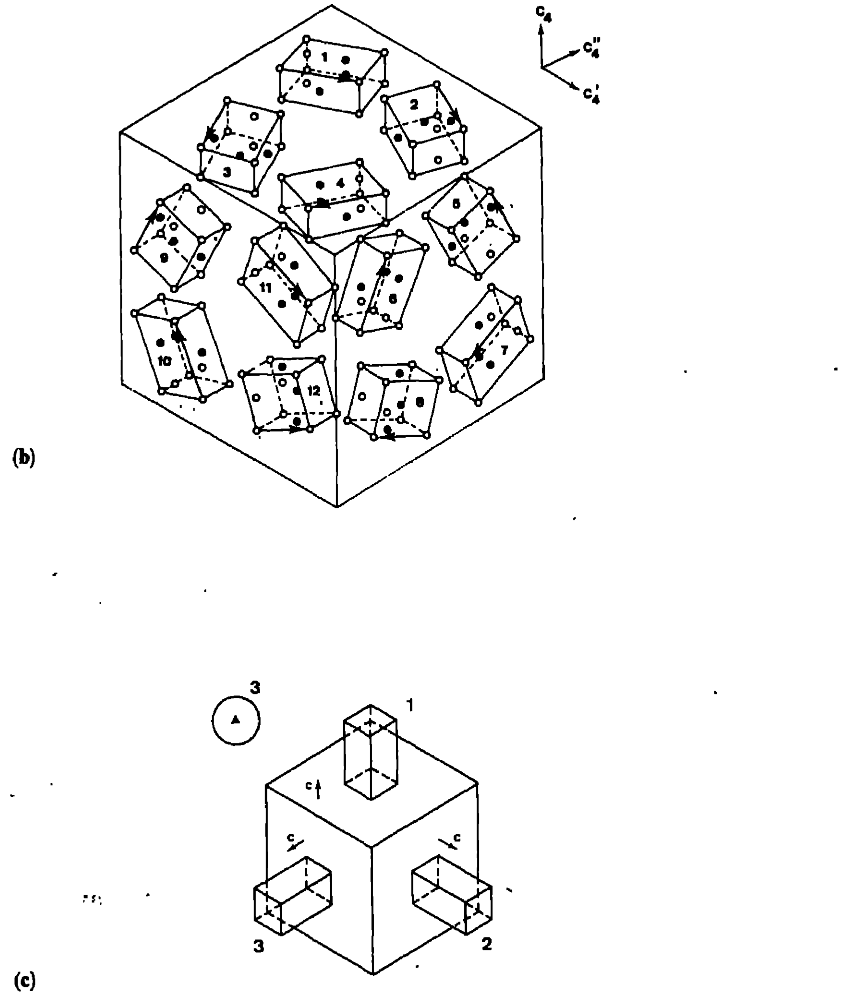

Figure 8. Unit cells of the orientation variants of three different ordered alloys represented with respect to the FCC cube. **a.** The 6 variants of the tetragonal Au_4Mn structure. The variant generating group is 32 with the three-fold axis along [111]. **b.** The 12 variants of the monoclinic Au_5Mn_2 structure. There is no variant generating group. **c.** The 3 variants of the tetragonal DO_{22} structure ($c/a = 2$). The variant generating group is 3, with the three-fold axis along the [111] direction of the FCC structure.

superlattice with all nodes of the basic lattice contained within one primitive unit cell of the superlattice. The number of such translations m is thus given by

$$m = \frac{\text{volume of primitive unit cell of superstructure}}{\text{volume of primitive unit cell of basic structure}}.$$

The symmetry translations lost during the ordering process are possible displacement vectors for the interfaces separating translation variants. Such interfaces, called anti-phase boundaries, result because the superstructure can, with equal *a priori* probability, nucleate in different parallel positions related by these vectors.

Taking again the Au_4Mn structure as an example one finds in this case $m = 5$, *i.e.* there are four different types of anti-phase boundaries; they are represented in figure 9.1.

In Au_5Mn_2 there are seven translation variants and hence six different types of anti phase boundaries (figure 9.2).

In the DO_{22} structure only four translation variants occur and hence three different APB's (figure 9.3).

The different geometrically allowed APB's need not all be actually present since in general their interfacial energies will be different. Moreover their energy also depends on the relative orientation of the displacement vector $\bar{R}$ and of the interface characterised by its unit normal $\bar{n}$.

Table 1. Different types of variants operating in ordered superstructures.

Structure	G (order 48)	H	Orientation variants n	Translation variants m	Total number of variants
Au_4Mn	$\frac{4}{m}\bar{3}\frac{2}{m}$ (FCC)	$4/m$	6	5	30
$Au_3Mn(DO_{22})$	$\frac{4}{m}\bar{3}\frac{2}{m}$ (FCC)	$4/m$ $2/m$ $2/m$	3	4	12
Au_5Mn_2	$\frac{4}{m}\bar{3}\frac{2}{m}$ (FCC)	$2/m$	12	7	84
$Au_2Mn(Cr_2Al)$	$\frac{4}{m}\bar{3}\frac{2}{m}$ (BCC)	$4/m$ $2/m$ $2/m$	3	3	9

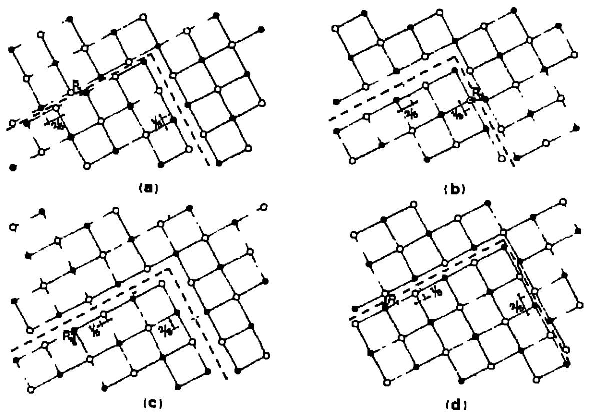

1.

Figure 9

2

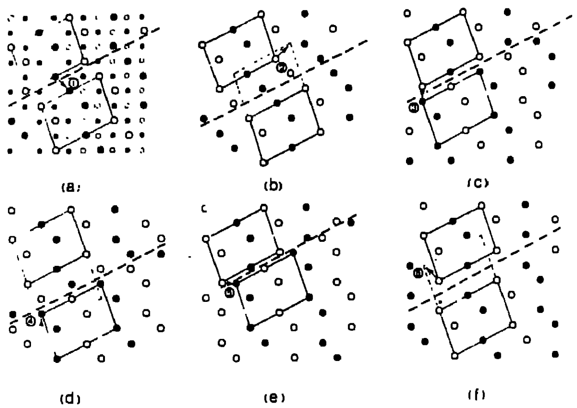

(a) (b) (c) (d) (e) (f)

2.

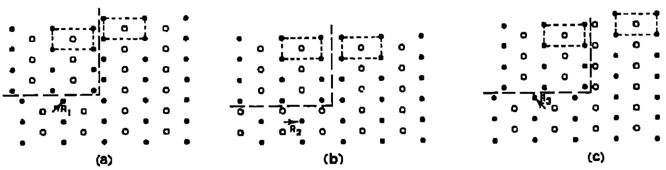

(a) (b) (c)

3.

Figure 9. Outlines of the unit cells of different ordered structures illustrating the geometrically possible anti-phase boundaries. 1. The Au_4Mn structure occurs in 5 translation variants. Four different anti-phase boundaries are geometrically possible. 2. The Au_5Mn_2 structure occurs in seven translation variants. Six different anti-phase boundaries are geometrically possible. 3. The DO_{22} structure can form in 4 different translation variants, leading to three different anti-phase boundaries.

6. One-dimensional long-period superstructures

6.1 *General*

For certain composition ranges and after suitable heat treatments a number of alloys adopt a one-dimensional long-period superstructure. Such structures have for instance been studied in the following alloy systems: CuAu (Scott 1960) Au-Zn (Schubert *et al* 1955; Iwasaki *et al* 1960; Iwasaki 1962; Van Tendeloo and Amelinckx 1977, 1978), Au-Mn (Van Tendeloo and Amelinckx 1978, 1981; Van Tendeloo *et al* 1978, 1979, 1980) AgMg (Fujiwara *et al* 1958; Schubert *et al* 1955). Cu-Sn (Schubert *et al* 1955; Van Sande *et al* 1978). We shall discuss three representative systems in order to illustrate the methods of interpretation and some characteristic features of such structures.

6.2 *The gold-manganese system*

In $Au_{4-x}Mn$ the one-dimensional long-period structure, derived from the Au_4Mn structure, (figure 10b), was found (Van Tendeloo and Amelinckx 1981). The diffraction pattern is reproduced in figure 11a, and represented schematically in figure 11b. From this scheme it is obvious that short sequences of equidistant superlattice spots along [110] directions are associated with the positions of the Au_4Mn spots; the sequences are shifted with respect to such positions over fractions of the interspot distance, as indicated in table 2. The displacement vector $\bar{R} = \frac{1}{10}[3\bar{1}5]$ is consistent with all fractional shifts as can easily be verified in table 2 by comparing calculated and observed values. The interspot distance leads to an interface spacing of ~ 1·1 nm, the interfaces being parallel with the (110) planes. These data suggest the model represented in figure 12a, when assuming that the white dots represent manganese columns. The structure is monoclinic with an ideal composition of $Au_{33}Mn_9$; it can be formed in twelve variants, four of which have their twofold axis parallel with the same cube direction. We call them *co-axial variants*. Each Au_4Mn variant can give rise to two variants of the one-dimensional superstructure.

A number of one-dimensional long-period superstructures derived from the DO_{22} structure were found in alloys in the composition range $Au_{3+x}Mn$. (Van Tendeloo *et al* 1978; Wolf *et al* 1978; Van Tendeloo and Amelinckx 1983).

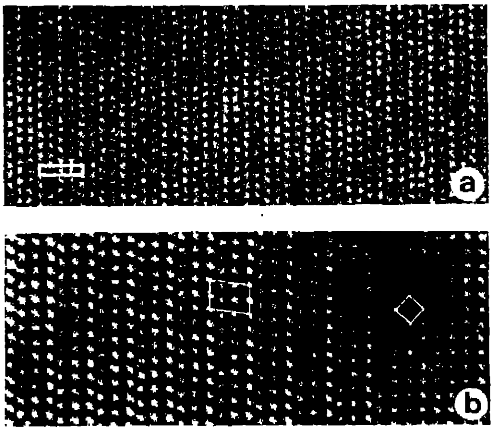

Figure 10. One-dimensional superstructures. **a.** Orthorhombic one-dimensional superstructure in Au_3Zn. The stacking sequence is $2\,\bar{2}\,2\,\bar{2}\ldots$ The bright dots represent zinc columns. (courtesy Schrijvers). **b.** Monoclinic one-dimensional superstructure derived from the Au_4Mn structure. In the right part of the micrograph a small area of Au_4Mn structure is still present. The bright dots reveal manganese columns.

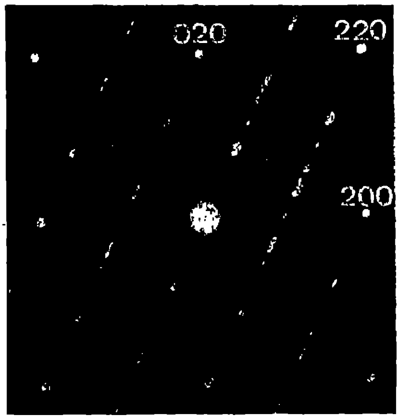

(a)

Figure 11

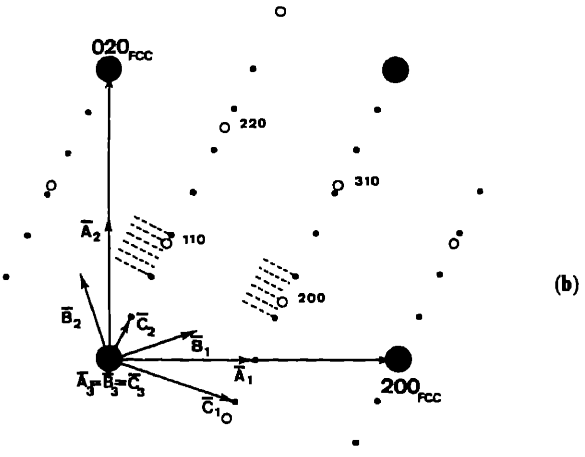

Figure 11. Diffraction pattern of the one-dimensional long-period superstructure of Au_4Mn. a. observed pattern. b. schematic representation. The Au_4Mn spots are represented as open dots.

Table 2. Fractional shift of the superlattice diffraction spots.

$\bar{g}$ (Au_4Mn)	Calculated fractional shift $\bar{R} = 1/10[3\bar{1}5]$ $\bar{g}\cdot\bar{R}$	Observed fractional shift
(1) 110	1/5	1/5 (or 4/5)
(2) 220	2/5	2/5 (or 3/5)
(3) 200	3/5	3/5 (or 2/5)
(4) 310	4/5	4/5 (or 1/5)
(5) $3\bar{1}0$	0	0 (or 1)

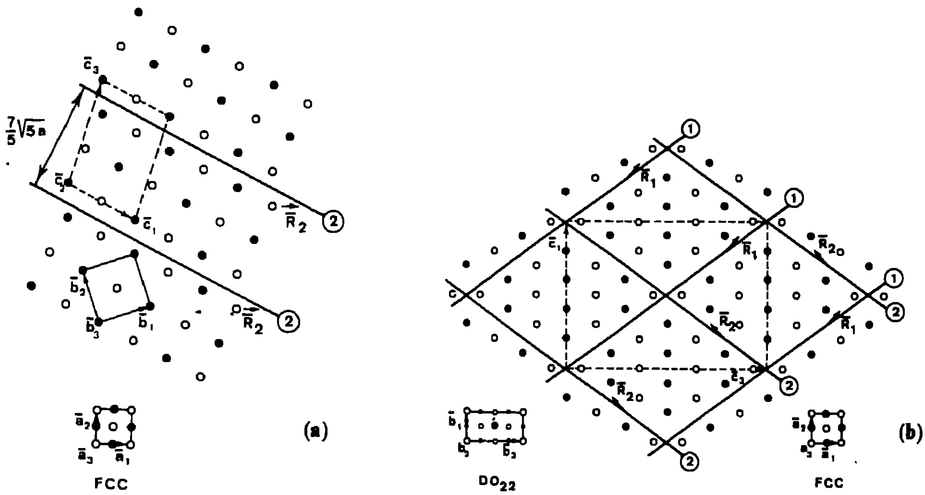

Figure 12. a. Model of the one-dimensional long-period superstructure of Au_4Mn (cf. figure 10b). b. Lozenge-shaped island superstructure of the DO_{22} structure (cf. figure 27).

An orthorhombic superstructure with a long period of about 20 Å, as observed at high resolution is shown in figure 13a together with its diffraction pattern. This superstructure results from the DO_{22} basic structure by the periodic introduction on

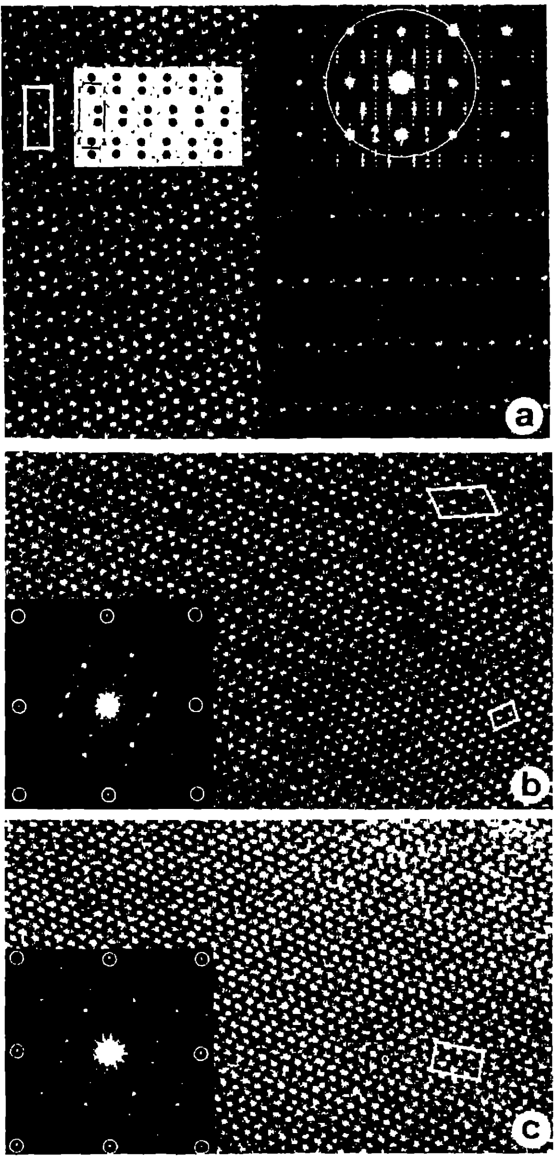

Figure 13. One-dimensional superstructures derived from the DO_{22} structure. **a.** Orthorhombic superstructure imaged under two different diffraction conditions; the right one emphasizing the 20 Å spacing; the left one shows all atom columns with the same contrast. The insets show the diffraction pattern and the selected beams. Also the structure is represented in inset; only manganese columns are shown. **b.** Monoclinic long-period superstructure with anti-phase boundaries along (302) planes. The unit cell is outlined. The inset shows the optical diffraction pattern. In the right bottom part a region of Au_5Mn_2 structure is visible. **c.** Monoclinic long period superstructure with anti-phase boundaries on (201) planes. The unit cell is outlined. The inset shows the optical diffraction pattern.

(100) planes of APB's which have alternatively displacement vectors 1/4 [201] and $1/4\,[20\bar{1}]$ and which have a 10 Å spacing. All these structural features can be obtained from the geometry of the diffraction pattern as described in § 2 and illustrated in the previous paragraph. A schematic model based on these considerations is reproduced in figure 14a, b; it can be compared with the high resolution image reproduced in figure 13a. Assuming the bright dots to represent the sites of manganese columns, excellent correspondence is obtained with the proposed model. The structure could also be considered as polysynthetically twinned. The anti-phase boundaries occurring in this structure are conservative; the ideal composition thus remains the same as that of the DO_{22} structure, *i.e.* Au_3Mn, unless the atomic positions along the APB's are not all occupied by manganese in the manner assumed in the model. It is unlikely that in this case the formation of the superstructure is composition driven.

The orthorhombic structure is apparently generated from the DO_{22} structure by the propagation of hairpin shaped APB's. Figure 15 shows the interface between an area of DO_{22} structure and an area of long-period orthorhombic structure; hairpin shaped APB's are quite apparent. This configuration suggests that the atomic rearrangements required to generate the orthorhombic structure from the DO_{22} structure take place preferentially along the APB's and in particular at the tip of the hairpin.

For slightly different compositions we have found two monoclinic long period superstructures of the DO_{22} structure. The displacement vectors are now the same for all interfaces; they are again of the type 1/4 [201] for both superstructures. However the orientations and spacings of the APB's are different for the two structures. In one case the APB's are in [302] planes and in the other in (201) planes (figure 13b, c) whereas the spacings are respectively ~ 0·8 nm and ~ 0·9 nm. Models for both structures are represented in figures 16a, b, whereas figures 13b, c are the corresponding high resolution images. The imaging conditions were again chosen in such a way that the minority atoms are represented as bright dots. The correspondence between the models and the high resolution images is quite striking.

6.3 *The gold-zinc system*

We have studied the one-dimensional superstructures in the gold-zinc system at different levels of resolution. The average distance between anti-phase boundaries as deduced from the diffraction pattern varies between 2 and 2·33 FCC unit cells.

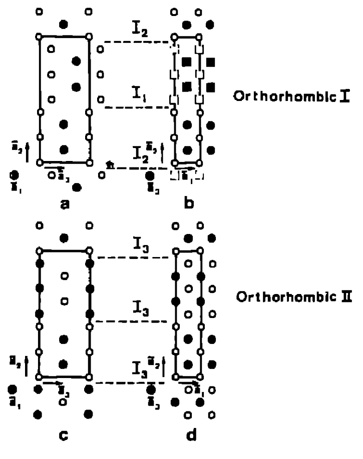

Figure 14. Models of two one-dimensional long-period superstructures of the DO_{22} structure. All anti-phase boundaries are conservative in the ideal structure. Figure 14a can be compared with figure 13a. The structure corresponding with figure 14c has been observed as well, but it is not reproduced here.

Line resolution of the long period have demonstrated that this is due to the presence of a mixture of APB spacings equal to two and three FCC unit cells. In some cases the mixture is quite regular and structures, which can be represented schematically by means of the symbols $2\,\bar{2}\,3\,\bar{2}\,2\,\bar{3}$ or $2\,\bar{2}\,2\,\bar{3}\,2\,\bar{2}\,2\,\bar{3}$, may result (figure 17). (The number indicates the width of successive domain strips in terms of zinc columns; the minus sign indicates a displaced strip). After long annealing the spacing tends to become uniform; the structure symbol then becomes $2\ \bar{2}\ 2\ \bar{2}$. An atomic resolution picture of this structure is reproduced in figure 10a. The antiphase boundaries are conservative and the ideal composition thus remains Au_3Zn.

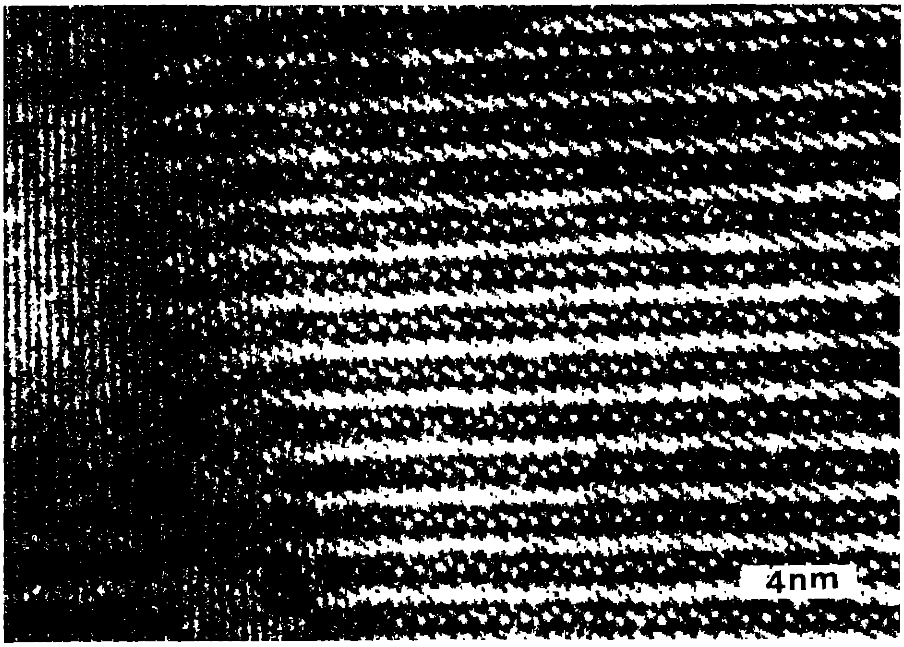

Figure 15. Interface between region of DO_{22} structure (left) and a region of orthorhombic I structure. The anti-phase boundaries propagate into the area of DO_{22} structure as hairpins.

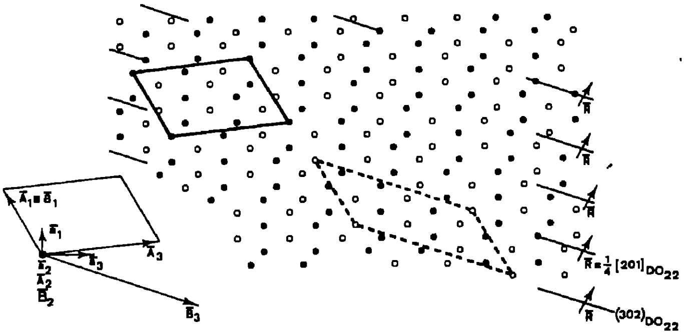

Figure 16a

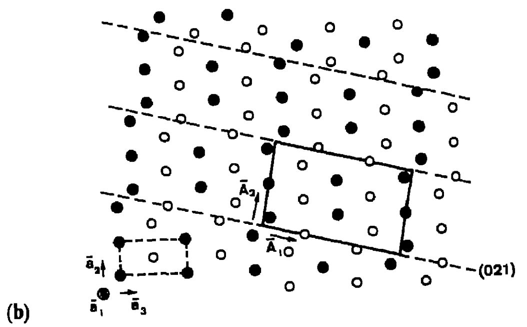

Figure 16. Models for monoclinic one-dimensional long-period superstructures of the DO_{22} structure. **a.** the APB's are on (302) planes. **b.** the APB's are on (201) planes. The displacement vector is the same in both cases.

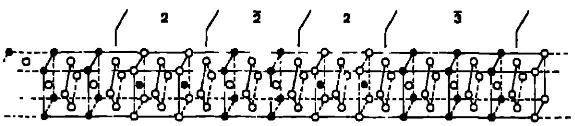

Figure 17. Model for the one-dimensional long-period superstructure in $Au_{3+x}Zn$.

After short annealing treatments at 250°C gold-zinc alloys with a composition of $Au_{3+x}Zn$ produce pseudo-incommensurate diffraction patterns, *i.e.* superstructure spot arrays associated with different basic spots do not match where they meet. Moreover the spot arrays often enclose a small angle with the cube direction. Lattice fringes reveal that the first effect is due to the presence of a mixture of spacings of 2 and 3 FCC unit cells wide; the diffraction pattern only reveals the average spacing. The second effect has to be attributed to systematic ledging of the anti-phase boundaries, causing the average orientation of the APB's to deviate slightly from the cube plane. This is represented schematically in figure 18. Presumably on further annealing the ledges migrate along the APB's producing in fact a lateral displacement of the APB's over a distance equal to the height of the ledge. This is possibly the mechanism by which, on annealing, the spacings become uniform. High resolution images show that the ledges do not have an abrupt structure, as suggested by the schematic of figure 18, but have a rather more gradual shape (figure 19).

Peculiar static configurations of anti-phase boundaries have been interpreted in terms of the formation and (or) elimination mechanism of long period APB structures (Van Tendeloo and Amelinckx 1977, 1978)

6.4 *The alloy Cu_3Sn*

The structure of Cu_3Sn is a periodic anti-phase boundary structure derived from an orthorhombic superstructure which is itself based on the hexagonally close packed structure (Schubert *et al* 1955). The lattice parameters of the long period superstructure a_s, b_s and c_s are given in terms of the lattice parameters of the basic orthorhombic structure by the relation

$$a_s = 2a_0,\ b_s = 8 - 10\,b_0,\ c_s = c_0.$$

The observations prove that the b_s parameter may be varied by the addition of aliovalent impurities such as Ni and Zn.

The structure is represented in figure 20; it was assumed that $b_s = 10\, b_0$. The APB's are in (010) planes and the displacement vector is $\bar{R} = 1/2\,[100]$. The observations on this alloy illustrate how the selection of an appropriate set of beams affects the final image and allows one to obtain the information best adapted to specific purposes. A

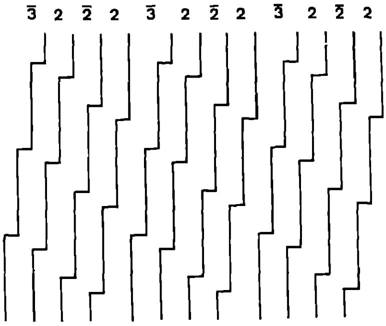
$\bar{3}$ 2 $\bar{2}$ 2 $\bar{3}$ 2 $\bar{2}$ 2 $\bar{3}$ 2 $\bar{2}$ 2

Figure 18. Systematic ledging of the anti-phase boundaries leads to a change in their average orientation. The strips with a width of 3 units are distributed more uniformly after ledging than before.

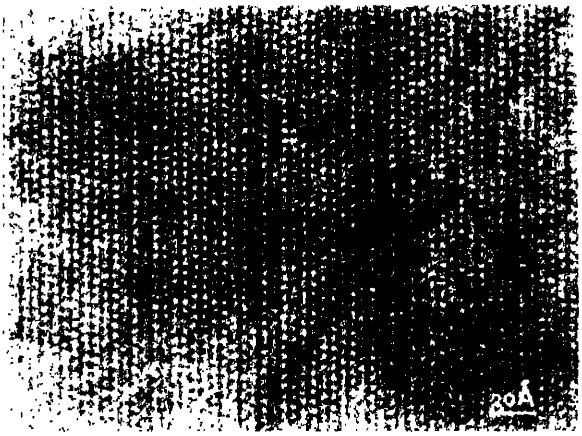

Figure 19. High resolution image of ledged APB's in Au$_{3+x}$Zn. The real structure of the ledges is much more gradual than in the schematic representation of figure 18 (courtesy Schrijvers).

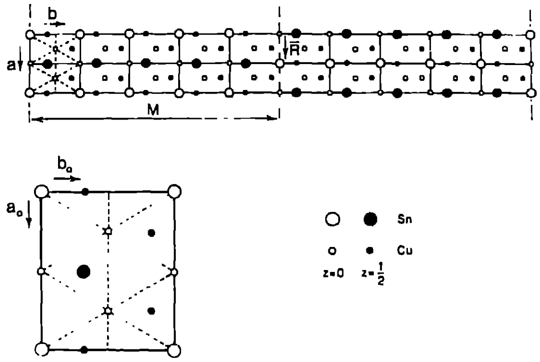

Figure 20. Model for the long period structure in Cu$_3$Sn. Also the basic structure derived from a HCP stacking is shown.

typical diffraction pattern is reproduced in figure 21a and represented schematically in figure 21b, after omission of double diffraction spots (Van Sande *et al* 1978).

A rudimentary lattice image is obtained by collecting a sequence of satellite spots of the row $h = 1$ in the objective aperture. Such dark field images only reveal the APB's as fine straight lines (figure 22a). Apart from occasional isolated faults the spacing is quite constant in well-annealed specimens; it corresponds to half the spacing deduced from a diffraction pattern; this is in accord with the model, since, the repeat distance contains two APB strips (figure 20). In nominally stoichiometric specimens the line spacing is $5\,b_0$; we shall represent the long-period structure by the symbol $5\,\bar{5}$, (the minus sign means displaced; the numbers indicate the width of the strips).

When collecting in the objective aperture the basic spots along the linear arrays of superlattice spots, lattice fringes due to the basic structure can be revealed as well.

It is then possible to observe directly the width of the domain strips in terms of unit cells of the basic structure (figure 22b).

When collecting beams belonging to at least two neighbouring arrays of satellite spots, as shown in the inset of figure 22c, one obtains a two-dimensional representation of the structure such as the one reproduced in figure 22c. Darker bands now mark the

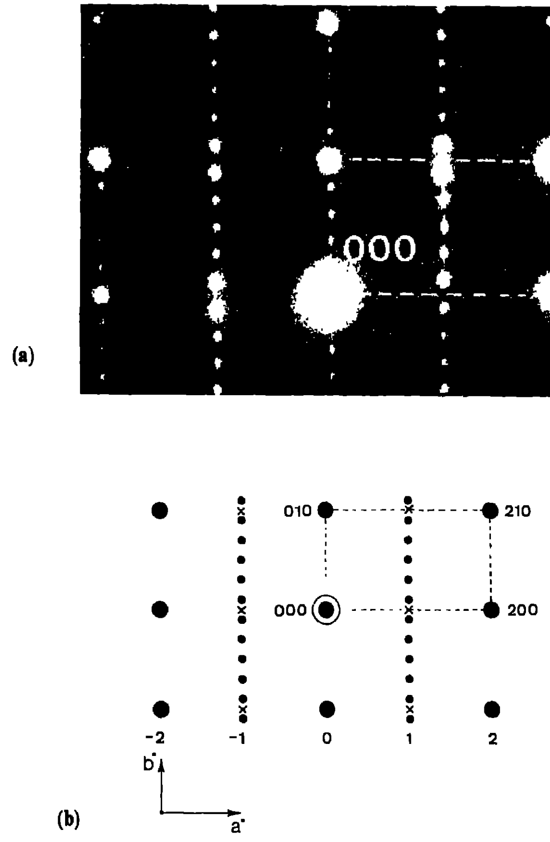

Figure 21. Electron diffraction pattern of Cu_3Sn. **a.** observed pattern. **b.** schematic representation.

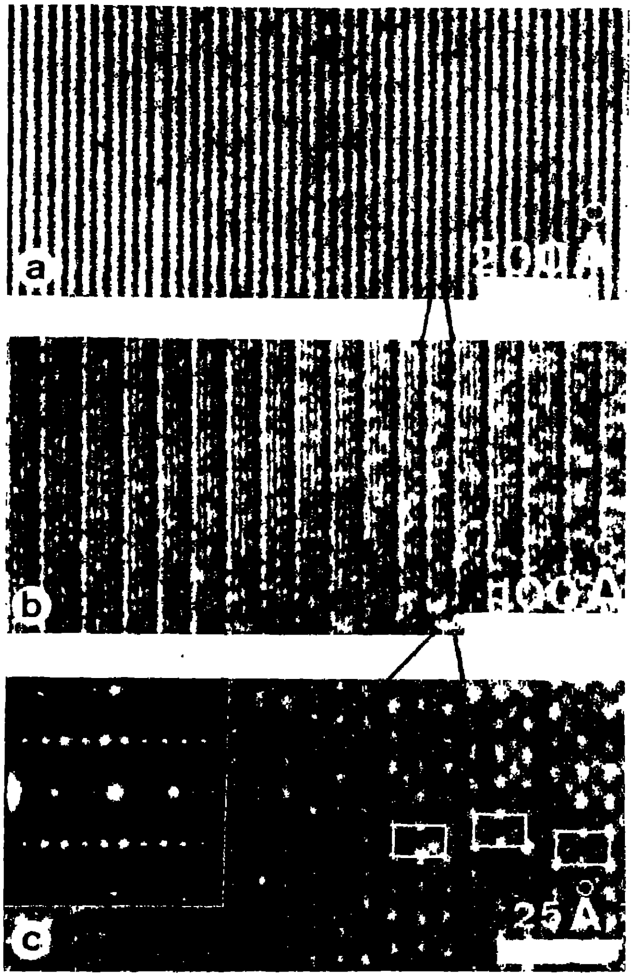

Figure 22. Images of the Cu_3Sn structure at different levels of resolution. **a.** one-dimensional image: the long spacing is revealed (mode 1). **b.** one-dimensional image: the spacing of the basic structure is revealed (mode 3). **c.** two-dimensional image (mode 8). The minority atoms are revealed as bright dots.

APB's. The scale and configuration of the white dots within the domains are the same as those of the minority atoms (Sn). The shift of the structure along the APB's is quite evident and in agreement with the model of figure 20.

The different levels of the resolution have been used for different purposes. The simple superlattice fringes have been used to study orientation variants; since the fringe orientation reveals directly the three possible directions of the *b*-directions with respect to the hexagonal basic structure. The lattice fringes of the basic structure have been used to study the changes in superperiod in alloys with addition of zinc and nickel; in particular the distribution of superlattice spacings becomes immediately evident. The diffraction pattern allows on the other hand to determine the average spacing. In quenched specimens the distribution is quite irregular. The "atomic" resolution image finally exhibits directly the configuration of atoms along APB's, and reveals the shift of the structure along them.

7. Two-dimensional island structure

7.1 *Derivatives of the Cu_3Au structure*

Several types of two-dimensional long period superstructures have been described in the literature (Terasaki and Watanabe 1981). A number of them is derived from the Cu_3Au ordered structure, which is based on an FCC lattice. The anti-phase boundaries are situated in mutually perpendicular cube planes giving rise to square or rectangular islands of Cu_3Au structure. One family of APB's is usually conservative and the other one non-conservative; both have a displacement vector of the type 1/2 $[110]_{FCC}$. A representative example of this type of structure is found in Cu_3 in which the islands contain somewhere between 2 × 3 and 4 × 6 palladium columns, depending on the exact composition of the alloy. It is represented in figure 23 whereas an observed example is reproduced in figure 24 (Watanabe *et al* 1955; Schubert *et al* 1955).

Similar structures with different island sizes have been observed in Au_3Mg (Airo 1978; Terasaki and Watanabe 1979), Au_3Zn (Van Tendeloo and Amelinckx 1978a; Wilkens and Schubert 1957; Iwasaki *et al* 1960; Vanderschaeve 1980; Iwasaki 1962).

7.2 *Derivatives of the Au_4Mn structure* (Van Tendeloo *et al* 1980; Hiraga *et al* 1980; Van Tendeloo and Amelinckx 1981)

A quite different square island structure was found in alloys with composition $Au_{4-x}Mn$. It is derived from the Au_4Mn structure (figure 25).

The antiphase boundaries with a displacement vector of the type 1/2 $[110]_{FCC}$ are situated in mutually perpendicular planes, consisting of segments of (110) and $(1\bar{1}0)$ planes, their average orientation enclosing a small angle with these planes. As yet only one such structure, with islands containing 3 × 3 manganese columns has been found (figure 26). Both families of anti-phase boundaries are non-conservative; the ideal composition of this phase is $Au_{31}Mn_9$. This structure is in fact the two-dimensional analogue of the one-dimensional structure described in § 6.2.

7.3 *Derivatives of the DO_{22} structure*

A third type of two-dimensional long period structure derived from the DO_{22} structure consists of parallelogram or lozenge shaped islands containing 3 × 3, 3 × 4 and 4 × 4

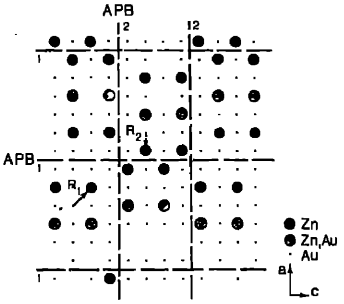

Figure 23. Schematic representation of the Cu_3Pd-type of two-dimensional long period superstructure; the structure shown refers actually to $Au_{3+x}Zn$. The vertical APB's are conservative, whereas the horizontal ones are non-conservative.

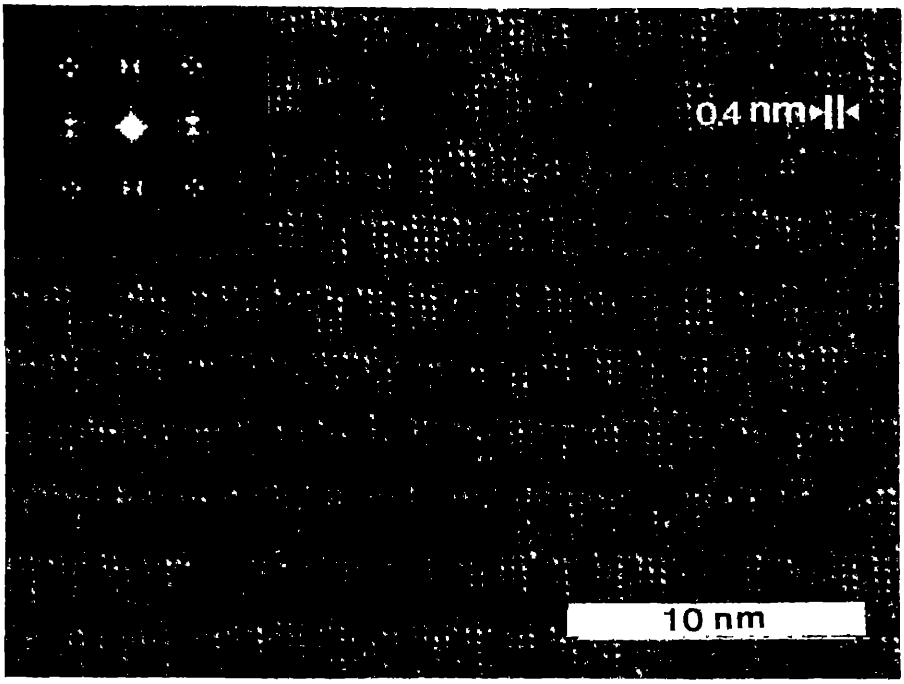

Figure 24. Orthorhombic Cu_3Pd structure consisting of islands containing 4 × 6 columns of minority atoms. The inset shows the part of the diffraction pattern used for imaging.

manganese columns (figure 27a, b). The displacement vectors of the anti-phase boundaries are 1/4 [201] and 1/4 [$20\bar{1}$]. The islands are limited by segments of {101} type planes; the average orientations of the anti-phase boundaries however deviate somewhat from these planes; they enclose an angle of 71°–77° (figure 12b). The ideal composition depends of course on the island size; for a 3 × 3 island size it is $Au_{31}Mn_9$.

In $Au_{4-x}Mg$ a monoclinic island structure with ideal composition $Au_{15}Mg_4$ was discovered (figure 28). It can be described as being derived either from the DO_{22} structure or from the Cu_3Au structure. It consists of rows of square islands, limited by cube planes, containing 2 × 2 magnesium columns. The average orientations of the anti-phase boundaries are (201) and (1 0 10).

Recently a new type of periodic anti phase boundary structure, derived from the DO_{22} structure, was found in an alloy with nominal composition $Au_{77.5}Mn_{22.5}$. The non-conservative APB's are now on (001) planes and the displacement vector is 1/4 [201]; the domain strips contain one DO_{22} unit cell. Its ideal composition is Au_7Mn_3. (Van Landuyt *et al* 1984).

8. Observations of domain structures

We shall now briefly discuss three examples of domain structures in the ordered alloys Au_4Mn, Au_3Mn (DO_{22}) and Au_5Mn_2 (figure 29). In the two coaxial variants of the Au_4Mn structure all manganese columns are parallel with the common four-fold axis. It is therefore possible to image the two orientation variants simultaneously.

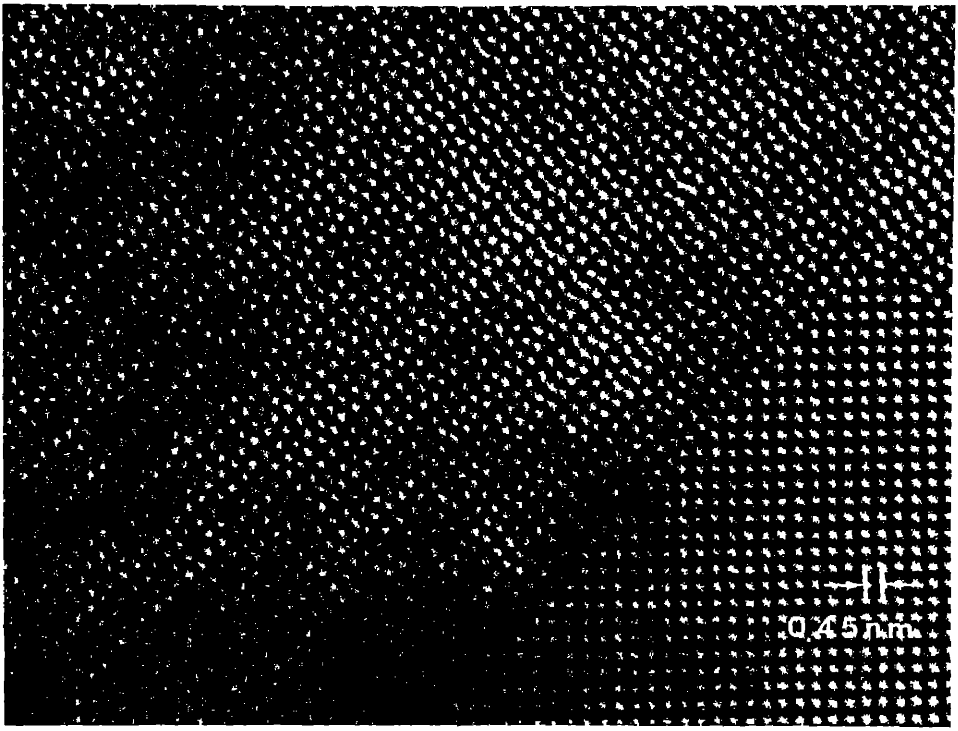

Figure 25. Tetragonal square island structure with composition Au_3Mn_9 derived from the Au_4Mn structure. In the right bottom corner an area of Au_4Mn structure is visible. In the right top corner a small strip of one-dimensional structure is visible as well.

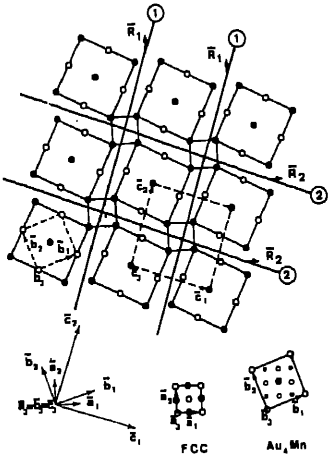

Figure 26. Model for the square island superstructure derived from the Au_4Mn structure (*cf.* figure 25).

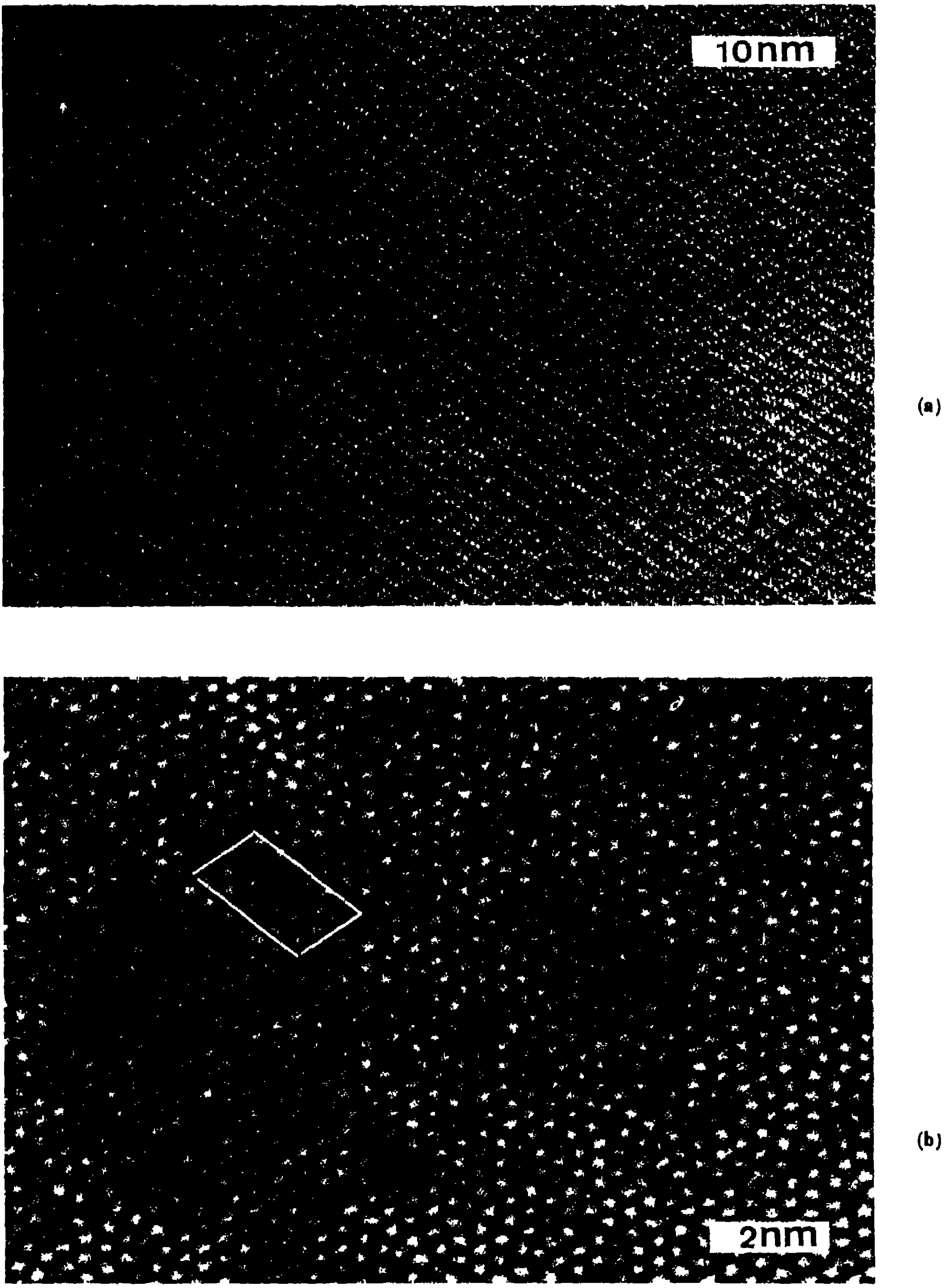

Figure 27. Parallelogram shaped island structure based on the DO_{22} structure. (*cf.* figure 12). **a.** superstructure dark field mode (mode 7). **b.** same type of structure imaged using mode 9.

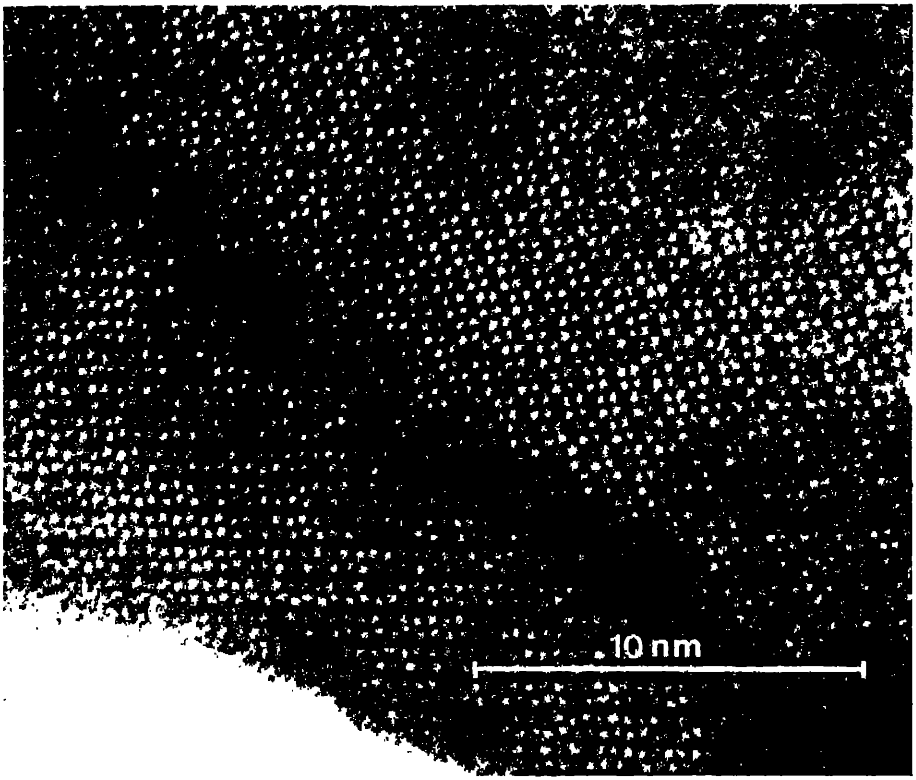

Figure 28. Monoclinic square island structure with ideal composition $Au_{15}Mg_4$. The bright dots image magnesium columns.

Figure 29b is a dark field superlattice image (mode 7), where orientation as well as translation variants are quite clearly revealed. In the particular case of Au_4Mn the imaging conditions are especially favourable. The eight superlattice spots due to the two variants are situated on a circle whose centre coincides with that of one square mesh of the reciprocal lattice of the basic FCC structure. It is possible to tilt the specimen in such a way that the projection of the centre of Ewald's sphere coincides with this point and moreover the objective aperture can be chosen in so as to admit only superlattice reflections. Under these conditions all image forming beams enclose the same angle with the optical axis of the microscope. As a result the angle dependent phase shifts introduced by the instrument, are same for all beams, ensuring optimum conditions for faithful image reconstruction.

The interface between coaxial variants is often inclined with respect to the common four-fold axis. Under the imaging conditions described above striking square arrays of bright dots are observed in the region of overlap (figure 30). It was demonstrated (Van Tendeloo and Amelinckx 1978) that this pattern is formed by the manganese columns which are continuous across the interface, *i.e.* the white dots form an image of the coincidence manganese columns. This observation supports the interpretation of the bright spots as images of manganese columns also in the other cases.

In Au_5Mn_2 the manganese columns are parallel to the two-fold axis in common to the four coaxial variants. The four types of domains can therefore be imaged under identical conditions. Such an image is reproduced in figure 29c; it was made using the dark field mode collecting all superlattice spots originating from the four orientation variants situated within one mesh of the reciprocal lattice of the FCC structure (mode 7). It is clear that the majority of interfaces are coherent twins situated in cube planes. Also translation variants can be recognised. The resolution of the instrument used to make the image was not sufficient to resolve close pairs of manganese columns; these are imaged as single elongated dots. Images of this type are nevertheless sufficient to study in great detail the microtexture of this alloy, which can be formed in 84 variants within a single FCC matrix. In particular it has been possible to identify all interfaces predicted on group theoretical grounds.

In the DO_{22} structure of Au_3Mn, image in figure 29a one can distinguish two orientation variants with their c-axis in the foil plane. An antiphase boundary is present as well.

9. Fine structure of antiphase boundaries

As mentioned in §5.2 all geometrically conceivable antiphase boundaries need not actually be present because the interfacial energy may be too large. In the gold-manganese system, for alloys with a composition in the vicinity of Au_4Mn we noted a strong preferential orientation of the APB's in well annealed specimens; they tend to be situated in $\{110\}$ planes of the Au_4Mn structure. Moreover all observed single APB's have a displacement vector which encloses with the interface normal the largest angle which is compatible with the FCC lattice i.e. they are of the type represented in the left part of figure 9.1(a)

Such APB's are as close as possible to conservative. As represented in the same figure a change in orientation over 90° causes the same APB to become strongly non-conservative. A number of such angular configurations has been observed in Au_4Mn (figure 31a) in each case one leg of the angle was simple and the other one was dissociated in two components being now of the same type as the simple leg (figure 31b). This is considered to be evidence for the instability of the strongly non-conservative APB's in an alloy of this composition.

Less strongly non-conservative APB's such as the one represented in figure 9.1(c), (left leg) and also in figure 32*a* were found to split up in two adjacent APB's of the stable type (figure 32b) giving rise to a small strip consisting of DO_{22} structure.

10. Conclusions

The combination of high resolution electron microscopy and selected area electron diffraction has made it possible to study in great detail the micro-texture of long range ordered alloys. It is clear that this micro-texture is much more complicated than diffraction experiments alone would suggest.

High resolution electron microscopy of alloy systems present a number of characteristic features which make this method particularly suited to determine also the basic structures. By a suitable choice of the imaging conditions one can reveal preferentially the minority atoms in a binary alloy, at least along certain zones.

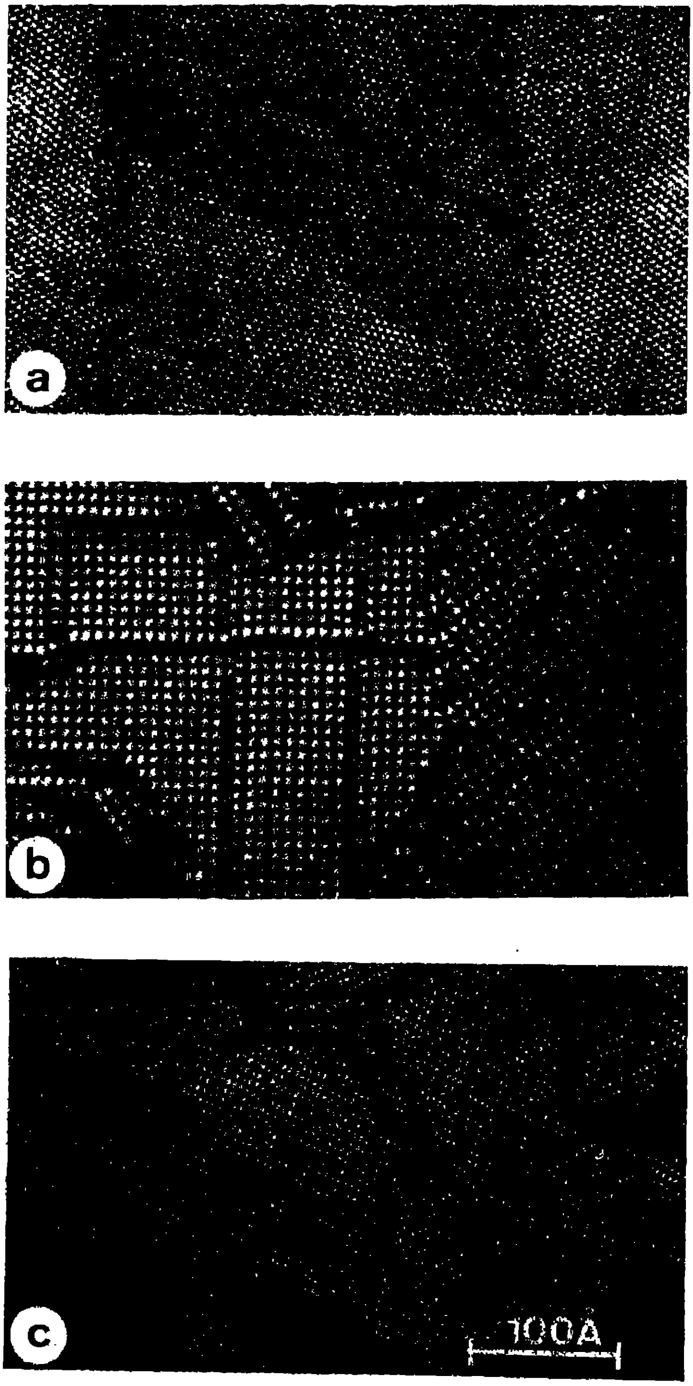

Figure 29. Domain structures in three basic structures. **a.** two orientation variants of the DO_{22} structure. The unit cells are outlined; an APB is visible as well. **b.** two coaxial variants of the Au_4Mn structure. Also anti-phase boundaries are present. **c.** Several coaxial orientation variants in the Au_5Mn_2 structure; also APB's are present.

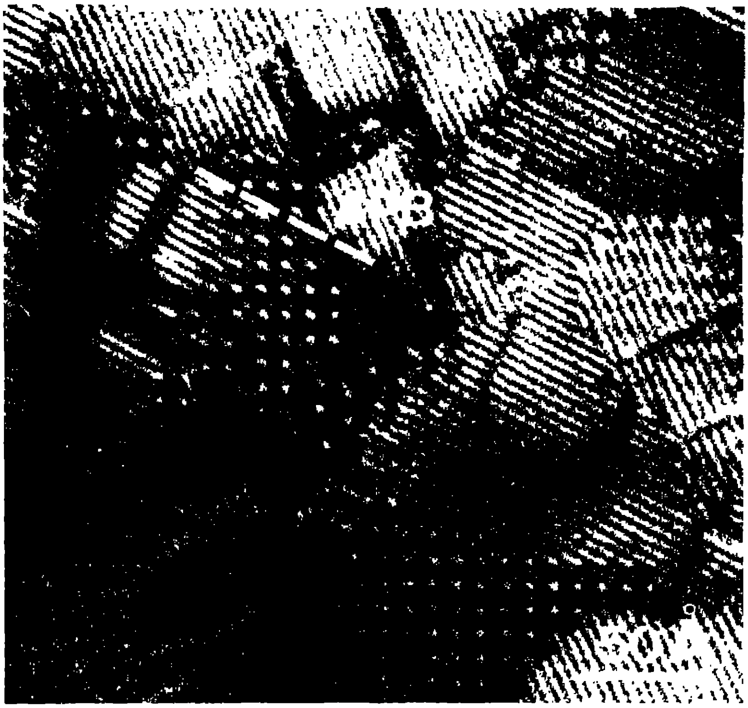

Figure 30. Pattern of coincidence columns along the inclined interface between two overlapping coaxial variants in Au_4Mn. The bright dots reveal the columns which are continuous across the interface.

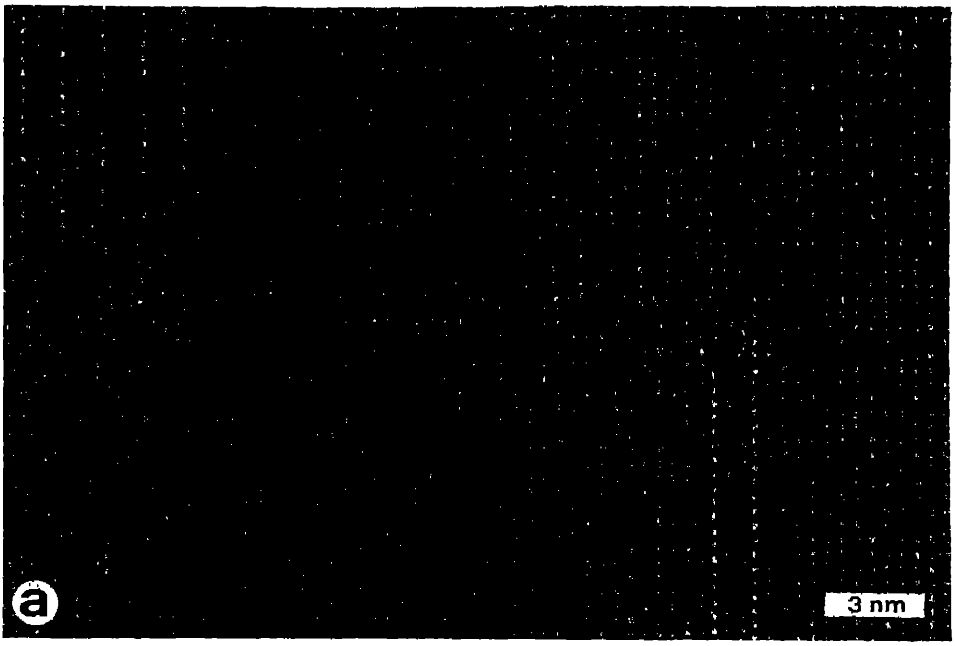

Figure 31

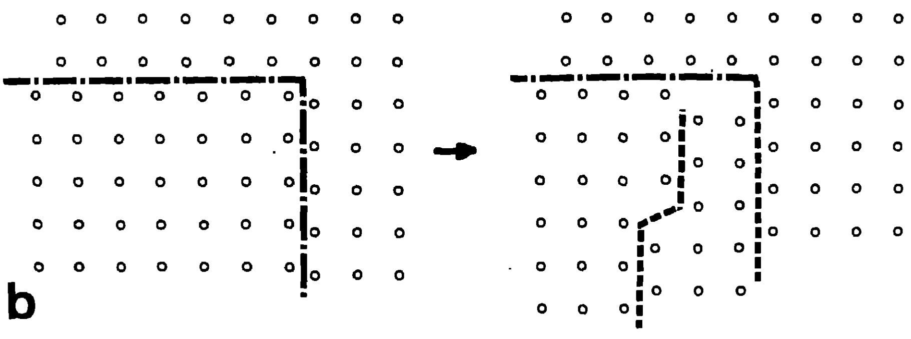

Figure 31. a. Rectangular arrangement of APB's in Au$_4$Mn. One "leg" is simple, the other one is dissociated in two components separated by three manganese columns. b. Analysis of the observed configuration (a) in terms of manganese columns.

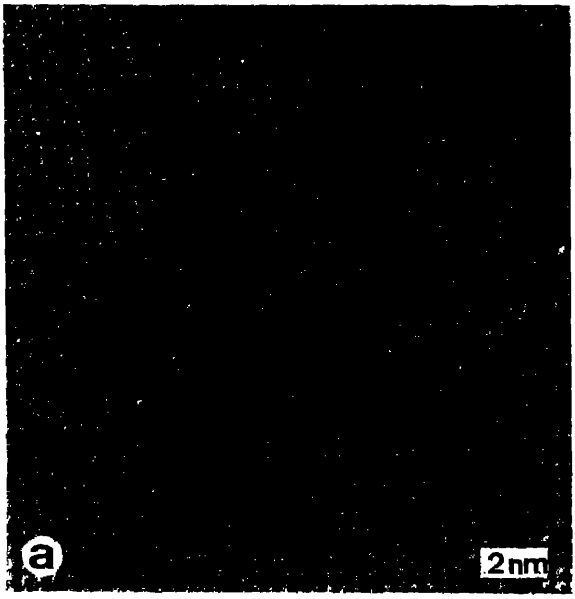

Figure 32

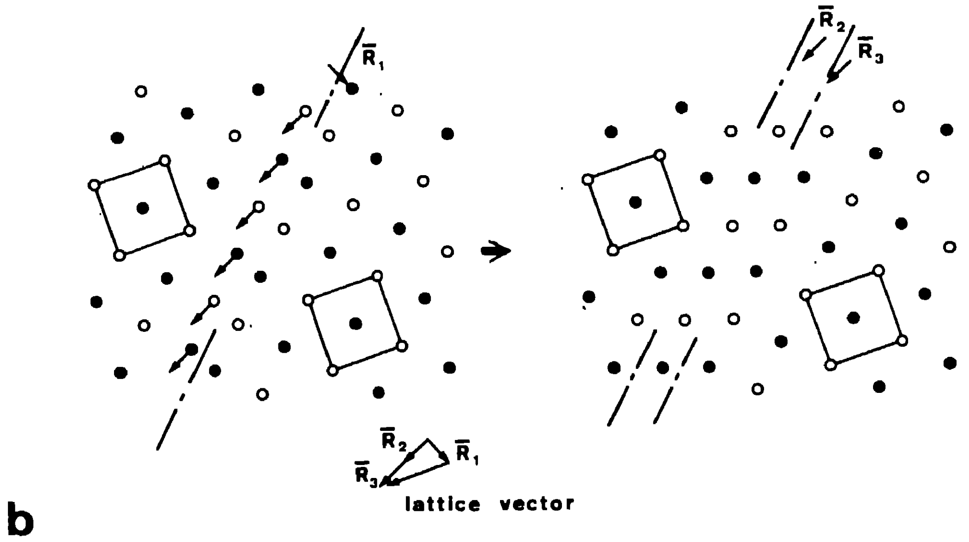

Figure 32. **a.** Dissociated antiphase boundary in Au_4Mn, intersecting a family of parallel antiphase boundaries. **b.** Analysis of the observed configuration **a** in terms of manganese columns.

A number of modulated alloy structures have been discovered first by the use of these methods.

Acknowledgements

This work was performed under the auspices of the association RUCA-SCK, with financial help from IIKW NFWO.

References

Airo P 1978 *Phys. Status Solidi* **47** K107

Amelinckx S 1978–79 *Chemi. Scr.* **14** 197

Amelinckx S 1979 *AIP Conf. Proc. n°* **53** 102

Cornellisen T, Van Tendeloo G, Van Landuyt J and Amelinckx S 1978 *Phys. Status Solidi* **48** K5

Cowley J M and Moodie A F 1957 *Acta Crystallogr.* **10** 609

De Ridder R, Van Landuyt J and Amelinckx S 1972 *Phys. Status Solidi* **9** 551

De Ridder R, Van Tendeloo G and Amelinckx S 1975 *Phys. Status Solidi* **30** K9

De Ridder R, Van Tendeloo G and Amelinckx S 1976 *Phys. Status Solid* **33** 383

Den Broeder F J, Van Tendeloo G, Amelinckx S, Hornstra J, De Ridder R, Van Landuyt J and Van Daal H J 1981 *Phys. Status Solidi* **67** 233

Fujiwara K 1957 *J. Phys. Soc. Jpn* **12** 7

Fujiwara K, Hirabayashi M, Watanabe D and Ogawa S 1958 *J. Phys. Soc. Jpn* **13** 167

Gaymont M, Gratias D, Portier R and Fayard M 1977 *J. Phys.* **C7** 47

Hiraga K, Shindo D and Hirabayashi H 1980 *Electron Microscopy* (eds) P Brederoo and J Van Landuyt 4 170

Iijima S 1975 *J. Solid State Chem.* **14** 52

Iijima S, Kimura S and Gotto M 1974 *Acta Crystallogr.* **A30** 251

Iwasaki H 1962 *J. Phys. Soc. Jpn* **17** 1620

Iwasaki H, Hirabayashi M, Fujiwara K, Watanabe D and Ogawa S 1960 *J. Phys. Soc. Jpn* **15** 1771
Menter J W 1956 *Proc. R. Soc.* **A236** 119
Schubert K, Kiefer B, Wilkens M and Haufler R 1955 *Z. Metallk.* **46** 692
Scott R E 1960 *J. Appl. Phys.* **31** 2112
Spence J 1981 *Experimental high resolution electron microscopy* (Oxford: Clarendon)
Terasaki O and Watanabe D 1981 *Jpn J. Appl. Phys.* **20** 381
Terasaki O and Watanabe D 1979 *AIP Conf. Proc. n°* **53** 253
Van Dyck D 1978 *Diffraction and imaging techniques in materials science* (eds) S Amelinckx, R Gevers and J Van Landuyt (North Holland Publ. Co) 1 355
Van Dyck D 1980 *J. Microsc.* **119** 141
Van Landuyt J, Kohn J A, Eckart D W and Amelinckx S 1974 *J. Solid State Chem.* **9** 104
Van Landuyt J, Van Tendeloo G and Amelinckx S 1974a *Phys. Status Solidi* **26** 259
Van Landuyt J, Van Tendeloo G and Amelinckx S 1974b *Phys. Status Solidi* **26** 585
Van Landuyt J, Van Tendeloo G and Amelinckx S 1984 *Phys. Status Solidi* (to be published)
Van Landuyt J, Wiegers G A and Amelinckx S 1978 *Phys. Status Solidi* **A46** 479
Vanderschaeve 1980 *Rev. Phys. Appl.* **15** 711
Van Sande M, De Ridder R, Van Tendeloo G, Van Landuyt J and Amelinckx S 1978 *Phys. Status Solidi* **A48** 383
Van Tendeloo G and Amelinckx S 1974 *Acta Crystallogr.* **A30** 431
Van Tendeloo G and Amelinckx S 1977 *Phys. Status Solidi* **A43** 553, K137
Van Tendeloo G and Amelinckx S 1978a *Phys. Status Solidi* **A47** 555
Van Tendeloo G and Amelinckx S 1978b *Phys. Status Solidi* **A49** 337
Van Tendeloo G and Amelinckx S 1978c *Phys. Status Solidi* **A50** 53
Van Tendeloo G and Amelinckx S 1979 *Phys. Status Solidi* **A51** 141
Van Tendeloo G and Amelinckx S 1981 *Phys. Status Solidi* **A65**, 73, 431
Van Tendeloo G and Amelinckx S 1983 *Phys. Status Solidi* **A** (to be published)
Van Tendeloo G, De Ridder R and Amelinckx S 1978a *Phys. Status Solidi* **A49** 55
Van Tendeloo G, Den Broeder F J, Amelinckx S, De Ridder R, Van Landuyt J and Van Daal H J 1981 *Phys. Status Solidi* **A67** 217
Van Tendeloo G, Van Landuyt J and Amelinckx S 1977 *Phys. Status Solidi* **A** K137
Van Tendeloo G, Van Landuyt J and Amelinckx S 1980 *Electron Microscopy* (eds) P Brederoo and G Boom 1 226
Van Tendeloo G, Van Landuyt J and Amelinckx S 1983 *Phys. Status Solidi* **A** (in press)
Van Tendeloo G, Van Sande M and Amelinckx S 1979 *Phys. Status Solidi* **A55** 681
Van Tendeloo G, Wolf R, Van Dyck D and Amelinckx S 1978b *Phys. Status Solidi* **A** 105
Van Tendeloo G, Wolf R, Van Landuyt J and Amelinckx S 1978c *Phys. Status Solidi* **A47** 539
Watanabe D, Hirabayashi M and Ogawa S 1955 *Acta Crystallogr.* **8** 510
Wilkens M and Schubert K 1957 *Z. Metallk.* **48** 550
Williams P M 1976 *Crystallography and Crystal Chemistry of Materials with Layered Structures* (ed) F Levy (Dordrecht: Reidel Publ.) 51
Williams P M, Parry G S and Scruby C B 1974 *Philos. Mag.* **29** 695
Wilson J A, Disalvo J and Mahayan S 1974 *Phys. Rev. Lett.* **32** 882
Wilson J A, Disalvo J and Mahayan S 1975 *Adv. Phys.* **24** 117

Bull. Mater. Sci., Vol. 6, No. 3, July 1984, pp. 453–458. © Printed in India.

High resolution electron microscopy of superconductors

C S PANDE

Naval Research Laboratory, Washington D.C. 20375, USA

Abstract. Until recently, in the field of superconductivity, electron microscopy has played only a minor role in studies of structure and properties of existing superconductors (except Nb and its alloys) and in the development of new and improved superconductors. This situation has changed in recent years. Electron microscopy is now being extensively used to study the growth, microstructure, and kinetics of many superconductors, especially of A15 type. Electron microscopy has also contributed to the understanding of the nature of radiation damage in these materials. These contributions will be reviewed with selected examples.

Keywords. Electron microscopy; super conducting materials; radiation damage; defect structure.

1. Introduction

Electron microscopy has now developed as one of the most powerful techniques available to metallurgists and solid state physicists. It is capable of very high resolution ((0·2–0·3 nm) lattice resolution, or ~ 0·5 nm point to point resolution is routine in modern conventional electron microscopes). Electron microscopes with a lattice resolution as fine as 0·06 nm is now available commercially. Crystal lattice of virtually most of the materials can now be resolved at least in principle by these instruments. However, an alternative mode of operation, *i.e.* the diffraction contrast is the most popular technique in use. This images the lattice defects in the lattice with a poorer resolution (~ 10 nm). However, the use of the weak beam technique has pushed this limit to ~ 2 nm. In addition, most electron microscopes display electron diffraction information. In recent years an attachment to the conventional microscope has been developed that can be used to convert it to a scanning electron microscope with a electron beam as fine as 1·5 nm. (This is in addition to dedicated scanning transmission electron microscopes (STEM) which are now commercially available with electron beam capabilities as fine as atomic dimensions. With the use of such a fine beam, individual atoms of some heavy elements have been photographed for the first time.) The availability of the fine electron beam in these instruments has opened up new possibilities, such as the use of energy dispersive x-ray spectroscopy and electron energy loss spectroscopy to obtain chemical analysis of regions as small as 5 nm. All these techniques can often be used for the same region of the specimen leading to a complete characterization of the given material (Hren *et al* 1979).

In spite of the availability of all these techniques, electron microscopy has, until recently, played only a minor role in studies of the structure and properties of existing superconductors and in the development of new and improved superconducting materials. Until 1974, most of the published work in this field related to the studies in Nb and its alloy, including the commercial material Nb-Ti. Very little attention has been paid to A15 compounds such as Nb_3Sn which are now beginning to replace Nb-Ti in technological applications. One possible reason for this was the difficulty of preparing thin film specimens from bulk for many superconducting materials as they are very brittle. Section 2 describes in some detail specimen preparation techniques followed by the applications of high resolution electron microscopy to high T_c (superconducting transition temperature) materials especially A15 materials. Some applications of high resolution electron microscopy to specimens cooled below T_c in the electron microscopes will also be mentioned.

2. Specimen preparation

For conventional (100 kV) transmission electron microscopy the specimens have to be less than 200 nm. It is, therefore, often necessary to obtain foils of such thickness from bulk. (Superconductors have also been prepared by vacuum evaporation or sputtering where in many cases one can deposit the right thickness directly avoiding any need for thinning.) For elemental superconductors such as Nb and its alloys, the conventional techniques such as electrolytic thinning, or chemical thinning, gives excellant specimens. These techniques are, however, not suitable for most of the high T_c superconductors. For these materials the most suitable technique is ion milling. Ion milling is essentially a way of thinning specimens by bombardment with inert heavy ions such as Argon ions. Care, however, is required in minimizing radiation damage and surface roughness. Typically the ion damage extends to about 5 mm below the surface of the specimen. (For full details of the technique see the review by Pande 1979a).

3. Application of high resolution transmission electron microscopy

3.1 *Niobium and its alloys*

High resolution transmission electron microscopy of ductile type II superconductors such as Nb, NbBi and Nb-Zr have been mostly directed towards understanding the flux pinning behaviour of these materials. Flux pinning and hence, critical current J_c, is very dependent on the interaction between the Abrikosov vortices (present in these materials in superconducting state) and the lattice defects, such as dislocations and precipitates. TEM has been used to characterize the defect structure. For example, Narlikar and Dew-Hughes (1966) showed that when the dislocations are uniformly distributed in Nb and its alloys (as observed by TEM) they have only a weak effect on J_c due probably to weak pinning of flux lines. Stronger pinning was observed when the dislocations were clustered into walls enclosing dislocation free regions (such as obtained after cold working). This result was also true for drawn superconducting filaments. The size of these cells (enclosed by the dislocation walls) was also significant. Neal *et al* (1971) found that in Nb-Ti highest J_c can also be increased by second phase precipitation. TEM showed that J_c is highest when the precipitate dispersion was finest. Further, it was found by Milne and Finlayson (1972) that the J_c value in Nb-Zr alloys depended on the volume fraction of the precipitates. Hillmann and Hauck (1972) using TEM discovered an interesting effect, the so-called "matching effect." J_c was highest when there was a matching between the flux line lattice spacing and the distance between the pinning sites.

3.2 *A15 superconductors*

3.2*a* *Martensitic phase transformations:* One of the earliest applications of TEM in the study of A15 compounds was the direct observation of martensitic phase transformation in V_3Si. The transformation was observed as a thinned V_3Si specimen cooled below 20 K in a liquid helium stage inside an electron microscope. Twin-related lamellae with thicknesses as small as 10 nm were observed (Goringe and Valdre 1966). A similar though not as extensive observation was made in V_3Ga (Nembach and Tachikawa 1970).

3.2*b* *Flux pinning by grain boundaries:* The high J_c of A15 compounds has been ascribed to fine grain size in these materials. Figure 1 shows fine grains in bronze processed Nb_3Sn. The first experimental correlation between grain size and J_c on the basis of TEM observation, was given by Nembach and Tachikawa (1970) in V_3Ga, and by Scanlan *et al* (1975) in Nb_3Sn. Extensive TEM on bronze processed Nb_3Sn showed that the grain size in this material could be as small as 40 nm (Pande unpublished). There were no other major pinning centres such as dislocations and precipitates, even at the grain boundaries. Figure 1 shows transmission electron micrograph showing typical grains in bronze processed Nb_3Sn. It is, therefore, concluded that the pinning in this material is mostly by the grain boundaries. A theory based on this idea has been proposed by Pande and Suenaga (1976).

3.2*c* *Stacking faults:* Essmann and Zerweck (1973) have predicted stacking faults on $\{111\}$ planes in A15 structure. In actual practice stacking faults are only observed if a small amount of carbon is added to A15 material (Uzel and Diepers 1973). This presumably implies that interstitial impurities are needed to form these faults.

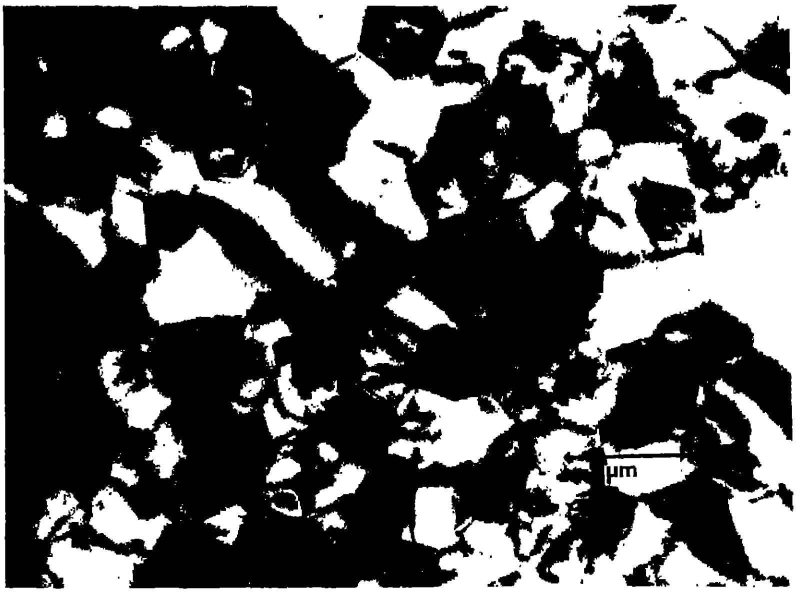

Figure 1. Transmission electron micrograph of bronze processed Nb_3Sn, showing that the most prominent defects are just grain boundaries as pinning centers.

3.2*d* *Radiation damage:* Radiation damage in high T_c superconducting materials is of technological concern because of the possible use of superconductors as magnets in fusion reactors. The nature of the damage in A15 compounds due to high energy nuclear radiation has been a subject of much controversy. The defects introduced by these radiations affect both J_c and T_c in these materials. A systematic high resolution electron microscopy of neutron irradiation of Nb_3Sn has now clearly revealed (Pande 1979b) the nature of this defect. Figure 2 shows a transmission electron micrograph imaged in superlattice reflection. This reflection "maps" the region of low disorder. The micrograph shows regions of "disorder" of size ~ 3·5 nm in a more or less ordered matrix. These regions were also regions of strain as proved by imaging these defects in fundamental reflections. The defects were coherent with the matrix. A detailed theory of T_c degradation based on these observations is given by Pande (1977).

It is not out of place to mention here that early electron microscopes (Ca 1965) had already given some indications of the existence of these disordered regions, although their exact nature could not be ascertained (Cody, Private Communication). These observations were, however, ignored leading to much confusion and controversy.

3.2*e* *Grain growth in multifilamentary superconductors:* Multifilamentary superconductors have been increasingly used in recent years. The nature of grain growth in these superconductors is important since it determines the J_c value (figure 3). These specimens are difficult to thin, except by ion milling. Pande (unpublished) has made an extensive study of the growth of grains as a function of annealing time and temperature.

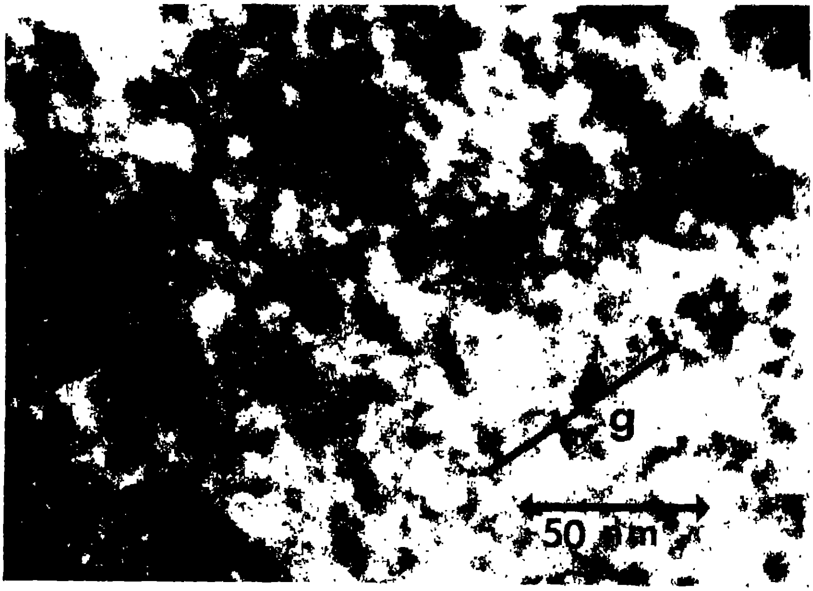

Figure 2. Electron micrograph in superlattice reflection $g = 011$ showing small disordered regions of size 3·5 nm in fast neutron irradiated Nb_3Sn.

Figure 3. Electron micrograph of filamentary superconductor showing Nb-Nb_3Sn and Sn-Nb_3Sn interface as well as individual grains. The grains near the interface are elongated.

3.2*f* *Dislocations in A*15 *compounds:* The dislocations in A15 compounds do not play any major role. However, the nature of dislocations in these materials is of theoretical interest. TEM observations indicate that Burgers vector of many of the dislocations are of the type $b = [100]$.

3.2*g* *Electron diffraction studies:* The electron diffraction studies of A15 have contributed a great deal of information regarding imperfections, etc. Schmidt *et al* (1976) have postulated the existence of charge density waves in these materials. However, a detailed study by Pande (unpublished) showed no evidence of such waves. However, some of the electron diffraction patterns are similar to that obtained by them (see figure 4).

3.2*h* *Direct resolution of flux lines without decoration:* Finally, we would like to mention another use of TEM, which has as yet not been successful, *i.e.* the direct

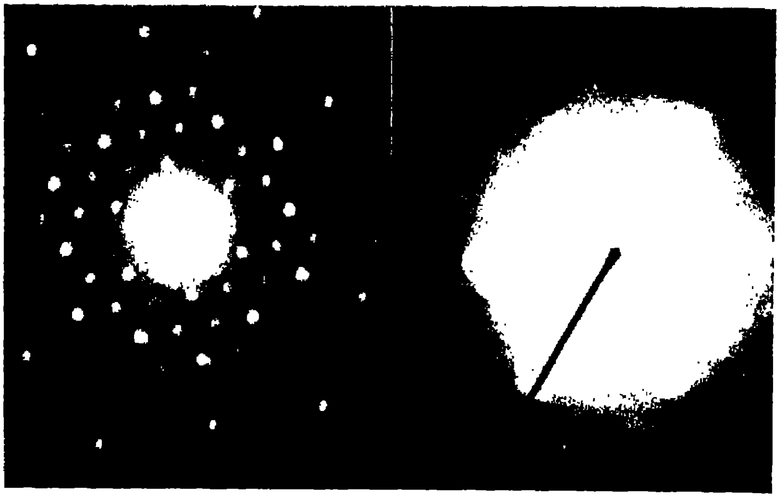

Figure 4. Electron diffraction from a well ordered (left) and heavily disordered (during growth) (right) specimens.

observation of flux line lattice, although thin film techniques have been combined with "decoration" techniques to give good indications of deflect flux line interactions (Herring 1974).

It is hoped that the examples presented here have demonstrated the usefulness of electron microscopy in a study of A15 superconductors. Much valuable information has already been obtained. It is expected that high resolution electron microscopy will be increasingly used in characterizing and developing technologically important superconductors.

References

Cody G D Private communication

Essmann U and Zerweek G 1973 *Phys. Status Solidi* **B57** 611

Goringe M J and Valdre U 1966 *Proc. R. Soc. (London)* **A295** 869

Herring C 1974 *Phys. Lett.* **A47** 105

Hillmann H and Hauck D 1972 *Appl. Superconductivity Conf.*, (New York: Institute of Electrical and Electronics Engineers) 429

Hren J J, Goldstein J I and Joy D C 1979 *Introduction to analytical electron microscopy* (New York: Plenum Press)

Milne I and Finlayson T R 1972 *Appl. Superconductivity Conf.* (New York: Institute of Electrical and Electronics Engineers) 425

Narlikar A V and Dew-Huger D 1966 *J. Mater. Sci.* 1317

Neal D F, Barber A C, Woolcock A and Gidley J A F 1971 *Acta Metallur.* **19** 143

Nembach E and Tachikawa K 1970 *Philos. Mag.* **21** 869

Pande C S 1977 *Solid State Commun.* **24** 241

Pande C S 1979a Superconductivity and electron microscopy in *treatise on material science and technology* **14** 171

Pande C S 1979b *Phys. Status. Solidi* **A52** 687

Pande C S (Unpublished work)

Pande C S and Suenaga M 1976 *Appl. Phys. Lett.* **29** 443

Scanlan R M, Fietz W A and Kich E F 1975 *J. Appl. Phys.* **46** 2244

Schmidt P H, Spencer E G, Joy D C and Rowell J M 1976 *2nd Conf. Superconductivity in d- and f-band Met.* (ed) D H Douglas (New York: Plenum Press) 431

Uzel Y and Diepers H 1973 *Z. Phys.* **258** 126

Bull. Mater. Sci., Vol. 6, No. 3, July 1984, pp. 459–475. © Printed in India.

High resolution electron microscopy as a tool for structural investigations

G SINGH and R S RAI

Department of Physics, Banaras Hindu University, Varanasi 221 005, India.

Abstract. Lattice imaging technique has been used to study an unknown high period polytype structure of SiC. A known structure like 6H has been studied by tilted beam two-dimensional images to determine optimum conditions for deriving structural information. The technique has then been used to determine a new structure (411R and its intergrowth structures), and the lattice imaging technique as a tool for structural investigation has been critically evaluated.

Keywords. High resolution electron microscopy; silicon carbide; lattice imaging; structural investigation; C-periodicity; stacking sequence; polytype in SiC.

1. Introduction

Lattice imaging in the electron microscope has emerged in the recent past as an important high resolution electron microscopy (HREM) technique for the study of ultra-microstructure of crystals. The most valuable capability of HREM concerns the study of local structural variations arising due to non-stoichiometry, stacking faults, etc. Further, it provides an opportunity to study the crystallography of materials directly in the real space compared to available information from diffraction techniques which are in reciprocal space. A number of mixed layer compounds, minerals and complex oxides have been studied by this technique (Van Landuyt *et al* 1973; Van Landuyt *et al* 1974; Cowley and Iijima 1972; Allpress and Sanders 1973; Buseek and Iijima 1974). Lattice imaging technique has been extended to two-dimensional crystal structure images by Allpress (1970), Iijima (1971) and Iijima *et al* (1973) and others who showed that image contrast could be directly correlated with structural details. However, the utility of this fascinating technique in structure determination is limited to only those materials which have high thermal stability under the impact of electron beam and have preferably large cell parameters. SiC is one such material which is known to crystallize into several polytype structures of extremely large periodicities.

In SiC, usually large period cells consist of regular stackings of unit cells of more common structure types like 6H, 15R, 4H and 21R which are periodically interrupted by stacking faults (Verma and Krishna 1966). Structures of large c-periodicities are thus generated. Therefore, it has become a common practice to describe any large period structure in terms of stackings of smaller unit cells. The utility of low resolution lattice images has already been established in the structural investigations of SiC structures of large cell parameters (Dubey and Singh 1978; Singh and Singh 1980; Singh *et al* 1981; Yessik *et al* 1975). The information available from one-dimensional lattice images is able to reduce the number of probable structures drastically and enables one to determine the correct structure.

It has been shown recently by Jepps *et al* (1979) that two-dimensional high resolution pictures are capable of revealing directly the stacking sequence of Si-C double layers. A common feature of most of the lattice imaging work reported in literature has been that they either involve intuitive interpretation or require *n*-beam image contrast calculations which require the knowledge of crystal structure and experimental parameters like foil thickness, defocus etc which are not easily known. During the present investigation a different approach has been adopted in the sense that crystals are first studied by x-ray diffraction and then by HREM technique so that the structural inferences drawn from the lattice images may be verified by establishing a match between observed and calculated x-ray intensities.

An attempt has been made to determine unknown SiC polytype structures with the help of lattice imaging which also provides an opportunity for critical evaluation of this technique in structural investigations.

2. Experimental details

The structures of SiC are often found in syntactic coalescence and those of large periodicities are usually in the form of very thin lamellae and it becomes very difficult to get even minute pieces of a crystal which is exclusively a large period structure. Therefore, samples suitable for electron microscope examination are prepared usually by crushing the coalesced crystals into powder form and dispersing the tiny fragments on a holey carbon grid. The lattice images have been taken on JEM 100 CX electron microscope. The most common cleavage plane in SiC is (0001). However, cleavage parallel to prismatic planes $\{11\bar{2}0\}$ is also found though less frequently and thin foils produced due to such cleavages are found suitable for lattice resolution studies.

As all the SiC structures are built up by three-dimensional network of tetrahedrally bonded Si and C atoms, they can be described by stacking sequence of either SiC tetrahedra or SiC double layers in terms of close-packing of equal spheres. Figure 1 shows six-layered hexagonal structure (6H) as viewed along *b*-axis. Si or C atoms

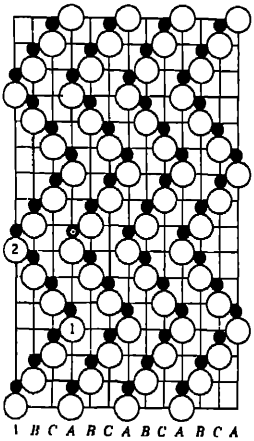

Figure 1. Zigzag sequence of Si and C atoms in the $(11\bar{2}0)$ plane of the 6H polytype of SiC.

corresponding to a cyclic sequence of layers $A \rightarrow B \rightarrow C$ and those in anticyclic sequence $A \rightarrow C \rightarrow B$ lie in the tetrahedral face planes ($\{10\bar{1}2\}$ and $\{10\bar{1}\bar{2}\}$ in 6H structure) which are mutually rotated by π. Since all the polytype structures consist of some combination of cyclic and anticyclic sequence of layers, the Si or C atoms always lie on either of the tetrahedral face planes which are inclined equally at 109° 28′ with *c*-axis. That means $\{10\bar{1}l\}$ and $\{10\bar{1}\bar{l}\}$ planes inclined at this angle with *c*-axis or very near to this in any polytype structure have high reticular density in different parts of the unit cell depending on the layer sequence. Of course the basal planes ($000l = \pm n$) for any *nH* or *nR* polytype also have high reticular density making these reflections invariably strong.

Now in a zone axis orientation if the objective aperture allows reflections of a two-dimensional reciprocal lattice net, the resulting image is a crude projection of the structure along the zone axis. When the incident beam is tilted to place the optic axis midway between $000l$ and $10\bar{1}l$ rows so as to allow equivalent reciprocal lattice vectors through the aperture, crossed lattice image may be formed from reflections of high reticular density planes *viz* basal stacking planes and tetrahedral face planes. Due to thickness variation of the sample the distribution of diffracted intensity of the allowed beam varies from one place to another giving rise to images of varying sharpness in terms of relative dominance of basal and inclined fringes. Optimum conditions are searched when chevron-shaped contrast presumably representing reticular density of tetrahedral face pair in projection is achieved. These chevrons along with basal fringes corresponding to individual stacking planes may enable one to uniquely read the stacking sequence of the entire unit cell.

3. Two-dimensional lattice images

3.1 *6H SiC*

Let us consider the structure image correlation in a simple case of 6H whose structure is fully known. Figures 2a, b show a two-dimensional lattice image taken under tilted beam illumination along with the diffraction pattern. The main features of the lattice image are: (i) the *c*-period blocks (1·5 nm) of 6H structure consist of two parts appearing in distinct dark and light contrast. The two parts are of equal width in comparatively thinner regions (top portion of the image) while at other places respective widths vary becoming 1 : 2 at the bottom portion, (ii) the chevron-shaped fringes in the two parts of the unit cell correspond to orientation and periodicity of $(10\bar{1}2)$ and $10\bar{1}\bar{2})$ planes.

These features may be understood in terms of contributions of the individual diffracted beams giving rise to a sinusoidal distribution of the charge density in the image plane. The wave fronts of this sinusoidal distribution are parallel to those lattice planes that may be supposed to produce the diffracted beam by reflection and its wavelength is equal to the *d*-spacing of these planes. Figure 3 shows the traces of contributing $(10\bar{1}l)$ planes which also represent the wavefronts of the sinusoidal charge distribution in the image. It may be noted that all the wavefronts coincide along equally-spaced lines parallel to *b*-axis which intersect the *a*-axis at spacings of 3·08 Å (*a*-parameter). Depending on the phase of the component sinusoidal distributions superposed on these points, pronounced dotted contrast should occur along lines perpendicular to *c*-axis at intervals of *c*-repeat period (1·5 nm) as is seen in figure 4. Taking into account the wavefronts of the relevant $(000l)$ planes also, it can be realized

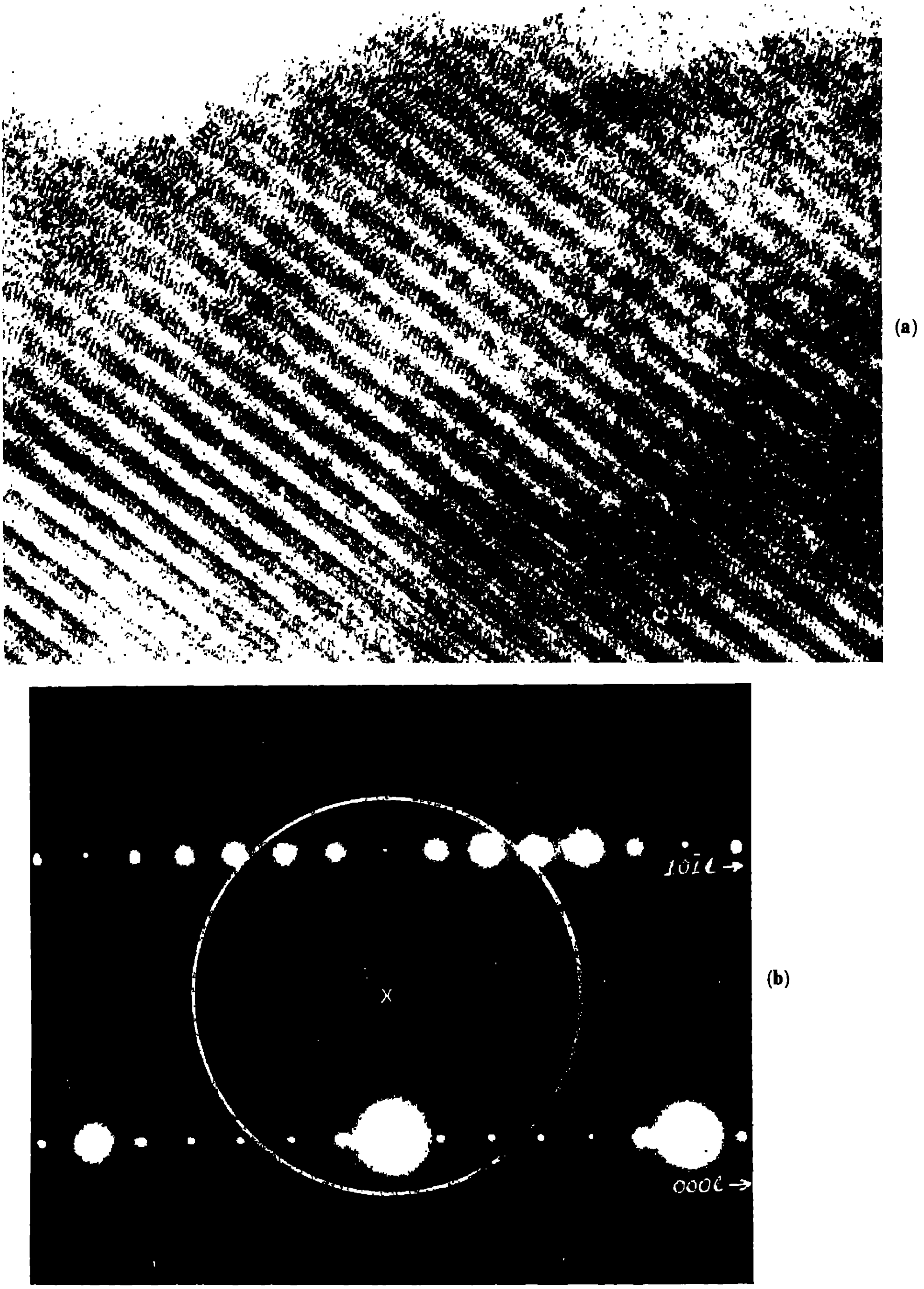

Figure 2. **a.** Tilted illumination lattice image of a 6H SiC. The beam is tilted midway between $10\bar{1}0$ and $000l$ so that $10\bar{1}2$ and $10\bar{1}\bar{2}$ reflections are included in the aperture. The inclined fringes forming chevrons are parallel to $(10\bar{1}2)$ and $(10\bar{1}\bar{2})$ planes (d spacing ≈ 0·25 nm). **b.** The corresponding diffraction pattern showing the position of optic axis by a cross and objective aperture by circle.

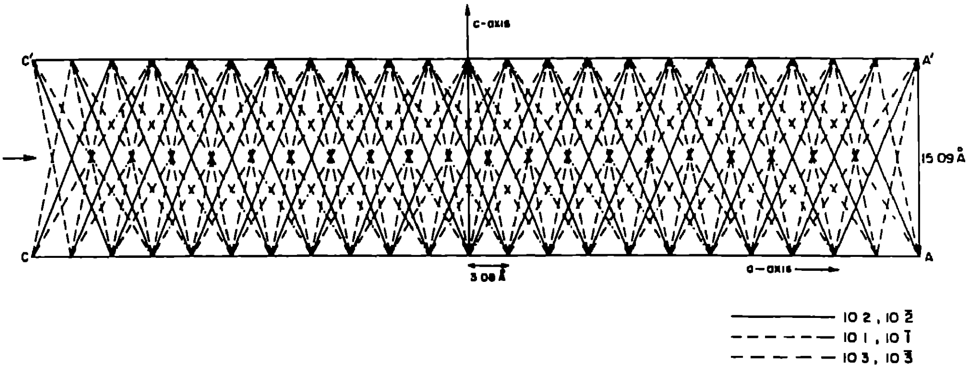

Figure 3. Traces of some 10$\bar{1}l$ lattice planes of the 6H polytype whose Bragg reflected beams pass through objective aperture. Traces of (000l) planes have not been drawn to avoid overcrowding.

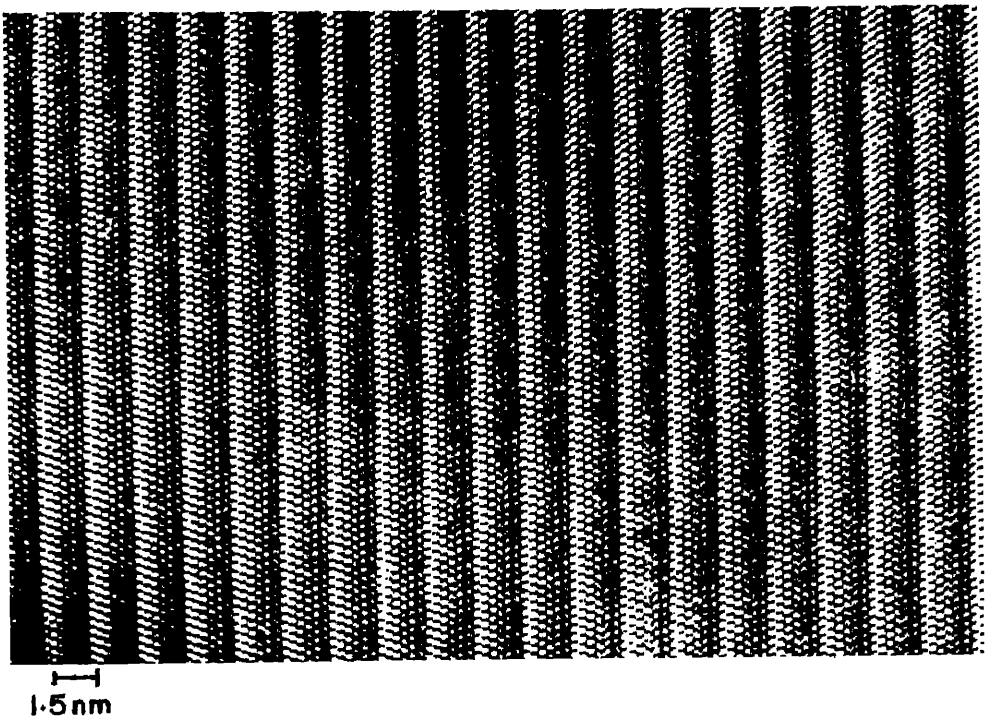

Figure 4. Tilted beam lattice image of 6H SiC taken under optimum condition showing pronounced dotted contrast of both the sets of fringes (basal as well as inclined).

that superposition of wavefronts to a lesser degree also takes place along lines normal to c-axis at intervals of interlayer separation (0·25 nm) throughout the unit cell resulting in subsidiary fringes. Therefore fringes representing fundamental interlayer separation along c-axis may be obtained under appropriate conditions provided the instrumental resolution of the microscope allows it. Figure 5 shows these fringes in a bright field

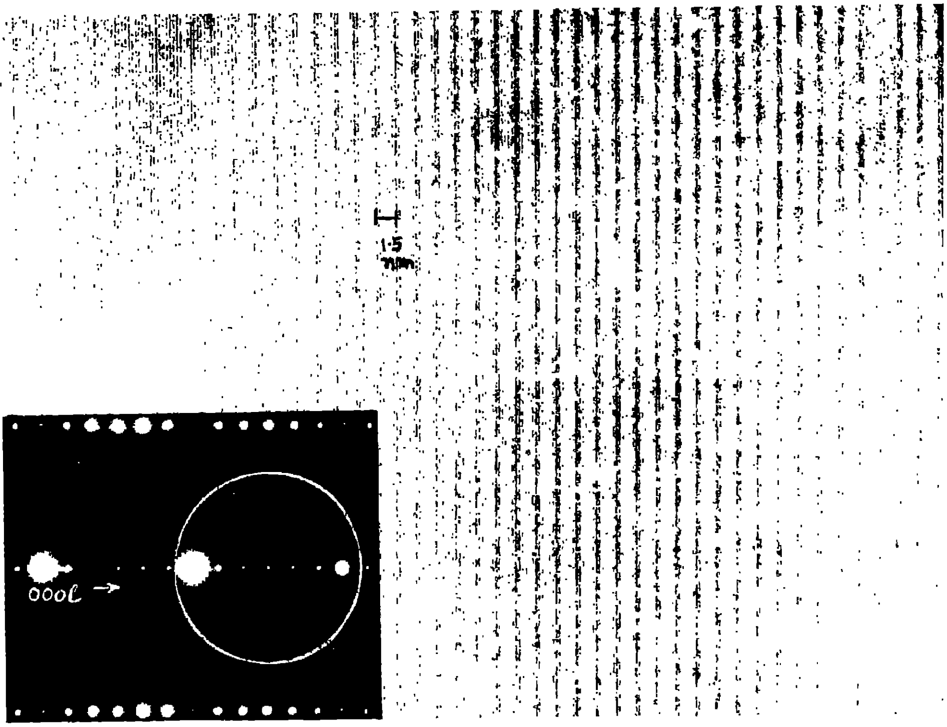

Figure 5. Bright field lattice image showing resolution of (0006) planes (representing inter-layer spacing ~ 0·25 nm) in 6H SiC. Fringe modulations at 1·5 nm periodicity characterize the *c*-repeat period. The corresponding diffraction pattern is shown as inset.

image formed by symmetrical $000l$ reflections and they can as well be obtained from a dark field image formed by $10\bar{1}l$ reflections. In tilted beam illumination pictures, these fringes can appear only under special experimental conditions. Out of these subsidiary fringes in tilted beam pictures which divide the unit cell into six parts, one at the middle is expected to be comparatively strong as can be seen from the traces of $(10\bar{1}l)$ planes in figure 3. This is because the $10\bar{1}l$ reflections are stronger than $000l$ reflections which appear only due to double diffraction.

Figure 2a shows a tilted beam image of a 6H foil where all the linear fringes of 0·25 nm periodicity do not appear while chevron-shaped fringes of almost the same periodicity are in good contrast and well resolved. If chevron-shaped fringes arise due to dominance of $10\bar{1}2$ and $10\bar{1}\bar{2}$ reflections, one would expect a cross grating pattern of the two sets of fringes. The chevron-shaped contrast can be understood only in terms of crude Fourier projection of the structure along *b*-axis because the image is formed by a limited of reflections of this zone. As can be seen from structure model (figure 1) each plane of the family $(10\bar{1}2)$ in one half of the unit cell and that of $(10\bar{1}\bar{2})$ in the other half consist of a closely-spaced pair of silicon and carbon planes. In a crude projection along *b*-axis these pairs of Si-C atomic planes project forming chevrons of certain width. Since atomic resolution in the used experimental set-up was out of question, the chevron-shaped contrast bears a close correlation with the projected charge density of the closely-spaced SiC planes.

The relative dominance of linear and inclined fringes in the image depends on the distribution of diffracted intensity, which may vary from position to position depending on thickness. Optimum conditions may be looked for, when both the sets of fringes are reasonably pronounced. Figure 4 shows an image taken under optimum condition.

Now the layer sequence of the 6H structure can be read from chevron-shaped fringe of figure 2a. In Zdhanov notation, the layer sequence read from the upper part of the image is 33 while that from the lower part is 24. This variation arising due to thickness changes introduces uncertainty in the structure which can be resolved only by confirming the structure either by establishing a match between observed and calculated x-ray intensities or between observed and calculated image contrast. In contrast, the linear fringe modulations at spacings of *c*-periodicity (1·5 nm) are not affected with respect to their periodicities by thickness variations to the same extent as chevron shaped fringes are. As a result, the derived structural information remains ambiguous unless confirmed by other means. Therefore, we have made use of HREM (two-dimensional lattice imaging) and x-ray diffraction as a complimentary tool in solving the structural details of a new polytype 411R of SiC and its intergrowth structures which is described below.

4. A new polytype of SiC 411R and its intergrowth structures

4.1 *X-ray diffraction characteristics*

A bluish black crystal of platelet shape (3 × 2 × 0·35 mm) having well-developed basal faces {0001} was chosen from a batch of SiC crystals grown from vapour phase (Lely's method). The *c*-axis oscillation photographs in two ranges of oscillation of this crystal (figures 6a, b) show spots of a 137-layered polytype superimposed over faint streak along $10\bar{1}l$ reciprocal lattice row. Unique identification of the polytype was not possible at this stage because spots on one side of the zero-layer line are absent due to absorption. This indicates that high period polytype exists in a thin lamellar form on the platelet of 6H structure and it was not possible to isolate its smaller piece for detailed x-ray examination. A detailed investigation of this crystal was subsequently done by lattice imaging in symmetric bright field and tilted illumination modes with twin purpose of deriving the structure as well as assessing the capability of chevron-shaped fringes for structural investigations.

4.2 *Lattice imaging studies*

After examining the crystal by x-ray diffraction, suitable samples for electron microscopic investigation were prepared by crushing the crystal, as discussed earlier. A thin crystal flake was brought in zone axis orientation giving *hoil* reflections as shown in figure 7a. Figure 7b is a bright field image obtained from symmetrical $000l$ reflections. The lattice image reveals a superperiodicity of 145·5 nm (figure 7b). Each superperiod consists of a sequence of four blocks of smaller periods of periodicities 34·5, 33, 34·5 and 43·5 nm respectively. A dark field picture taken with only $101l$ reflections also reveals similar pattern of periodicities. The same pattern of fringes occur over an extended area in the sample and figure 7b shows only a part of it. It may be seen that most of the fringe spacing correspond to 6H periodicity of 1·5 nm. The formation of four sub-periods and the superperiod essentially takes place due to insertion of faults in

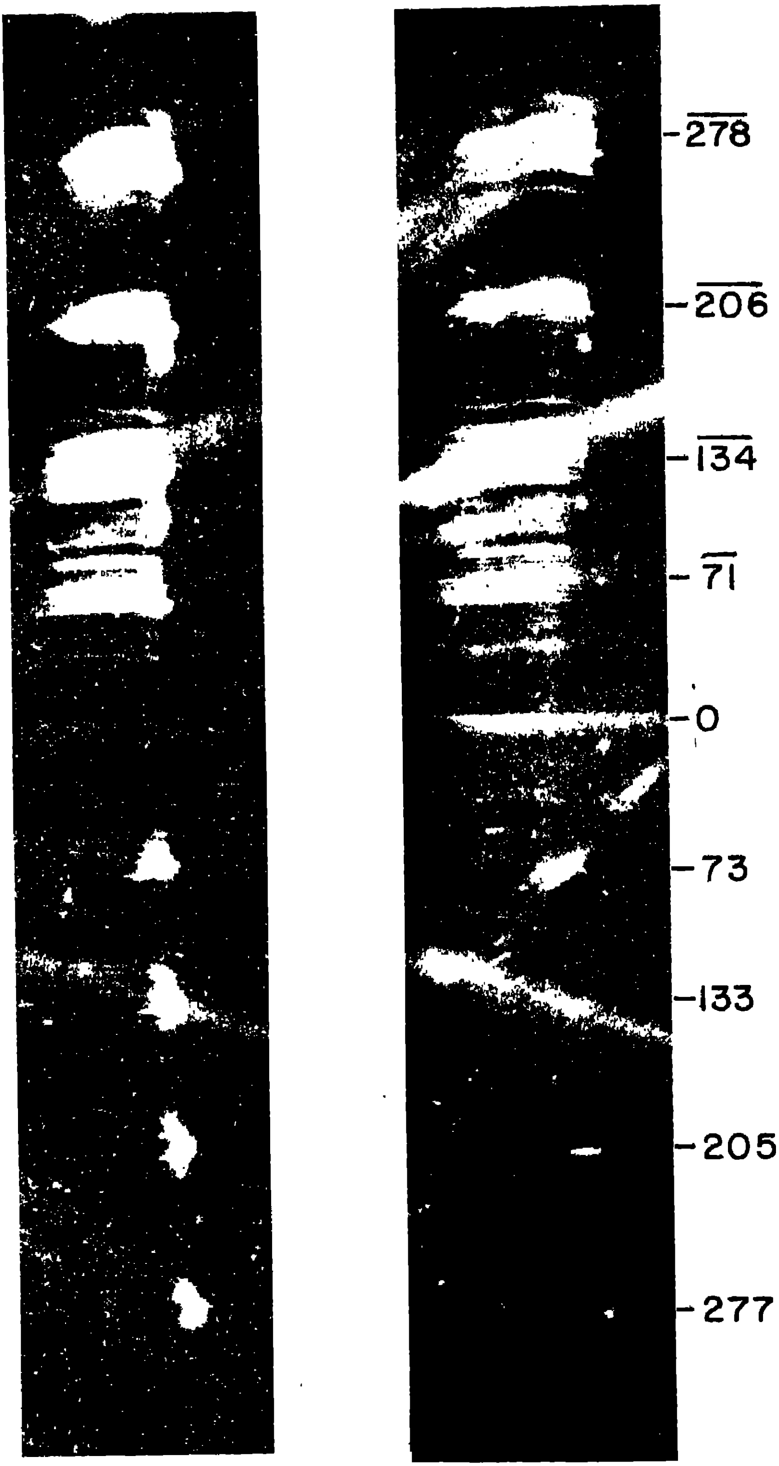

$\overline{278}$
$\overline{206}$
$\overline{134}$
$\overline{71}$
0
73
133
205
277

(a) (b)

a regular sequence of the 6H matrix. A periodicity as large as 145·5 nm cannot be normally detected by x-ray diffraction and therefore the faint streak in the x-ray pattern can be easily assigned due to this super-periodicity. The periodicity revealed by x-ray diffraction (figure 6b) corresponds to the periodicity of 34·5 nm which occurs twice in the superperiod block.

A two-dimensional lattice image (figure 8a) was taken under tilted beam illumination by including encircled reflections (figure 8b). To show at least one complete superperiod block this image has not been sufficiently magnified to clearly show two-dimensional features. Pictures were taken at different defocus values and one of them showing chevron-shaped fringes in good contrast is shown in figure 8a. As discussed earlier, the chevron-shaped fringes may be assumed to represent the layer stacking sequence of the structure. The magnified pictures of the three sub-units of the superperiod from figure 8a are shown in figures 9a, b, c. The stacking sequence read from this image for 34·5 nm block (figure 9a) in Zhdanov notation is $3223332223(33)_2$ $433332(33)_9$ $22(33)_4$. However, the stacking sequence read in this fashion is not unambiguous in the sense that some of the asymmetric units like 43 (marked in figure 9a) are not manifested very clearly. The stacking sequence read from pictures taken at a slightly different defocus value from figure 8a reveals a different stacking sequence. It is this extreme sensitiveness of these fringes which introduce uncertainty in the structural information derived from them. Therefore, lattice image information must be confirmed by other means.

The above layer sequence read from the lattice image has $n_+ - n_- \neq 3r$ (where n_+ represents the total number of layers in the cyclic sequence, n_- that of anticyclic sequence in the structure and r is any positive or negative integer including zero) and thus it corresponds to rhombohedral lattice and has to be repeated thrice to complete the hexagonal unit cell. The complete structure is given as:

$$[3223332223(33)_2\ 433332(33)_9\ 22(33)_4]_3.$$

Thus the polytype will be identified as 411R if this structure is correct. It is sufficient to compare the calculated and observed intensities of $10\bar{1}l$ reflections alone to determine the correctness of a proposed structure of any SiC polytype (Verma and Krishna 1966; Dubey and Singh 1978; Singh and Singh 1980; Singh *et al* 1981; Yessik *et al* 1975; Jepps *et al* 1979; Ramsdell 1944). Accordingly, the intensities of $10\bar{1}l$ reflections were calculated for the above structure and corrected for Lorentz and polarization factors. Though the full range of $10\bar{1}l$ reflections is not experimentally available due to reasons discussed earlier, the match between the calculated and observed x-ray intensities for the available reflections is quite good. This amply confirms the structure which was already read from the two-dimensional image with some reliability. The atomic positions of Si and C atoms can be derived from the Zhdanov symbol of the 411R structure.

Figure 6. **a.** The $10\bar{1}l$ reflections as recorded on a 15°, c-axis oscillation photograph of the parent SiC crystal. Polytype reflections along c^* are superimposed over faint streak (× 7). **b.** The $10\bar{1}l$ reflections as recorded on a 15°, c-axis oscillation photograph of the same crystal in a different range of oscillation. Spots are better resolved showing a periodicity of 137H or 411R polytype. Spots on one side of the zero-layer line are absent due to adsorption (× 7), CuKα radiation.

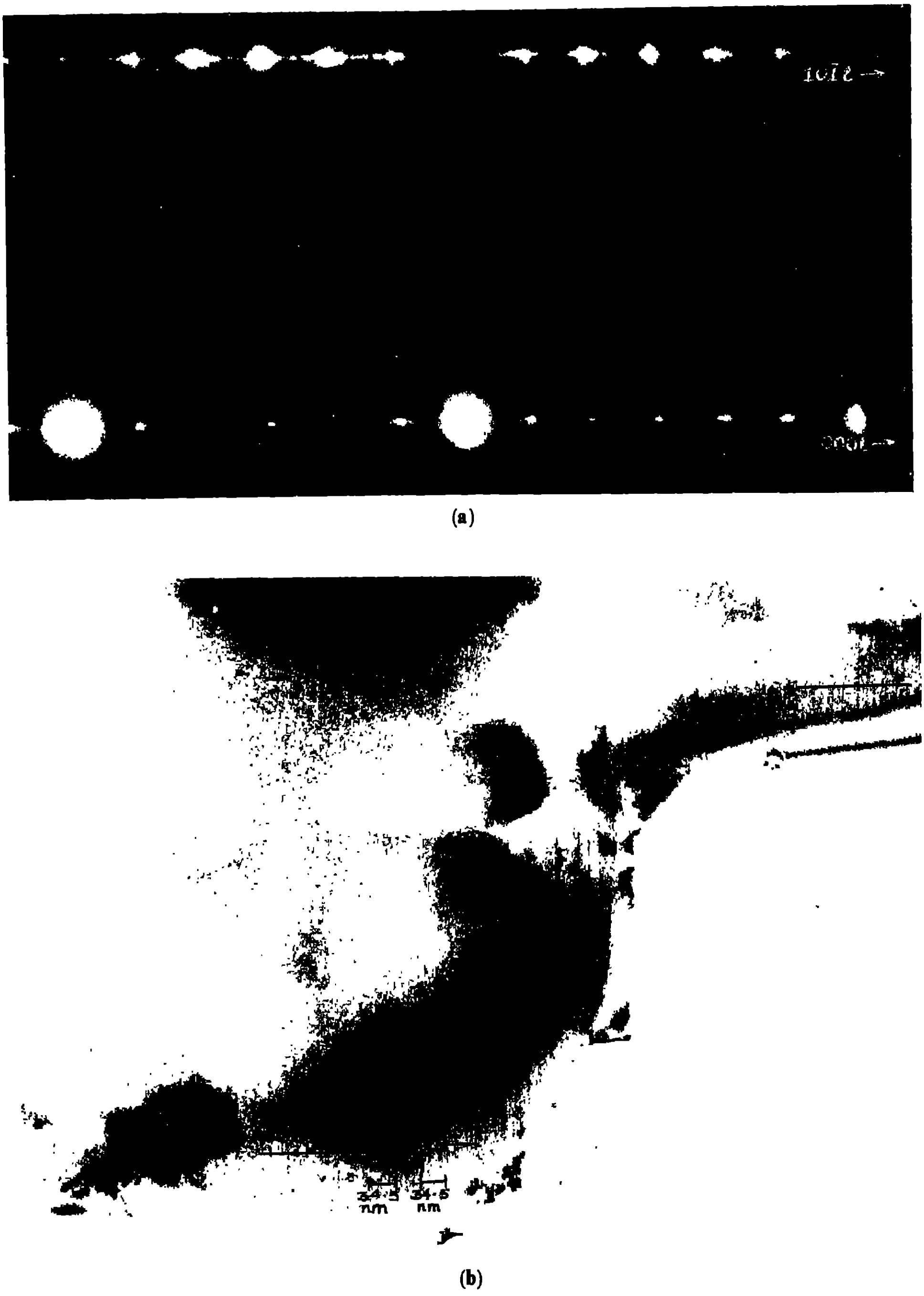

Figure 7. **a.** Electron diffraction pattern showing the *hoil* reciprocal lattice net of the same crystal as in figure 6b. **b.** A bright field lattice image, taken with symmetrical 000*l* reflections. Super-period blocks of 145·5 nm periodicity are marked. Each block consists of intergrowth of 34·5, 33, 34·5 and 43·5 nm blocks. The 34·5 nm blocks correspond to periodicity inferred from x-ray diffraction.

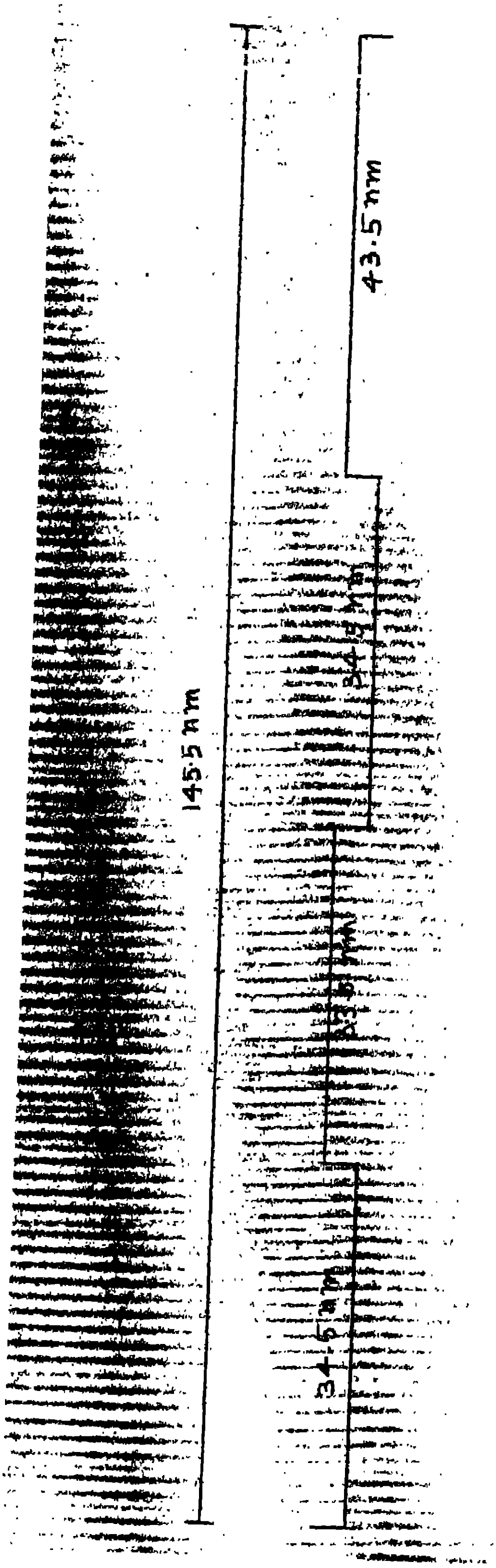

Figure 8 a.

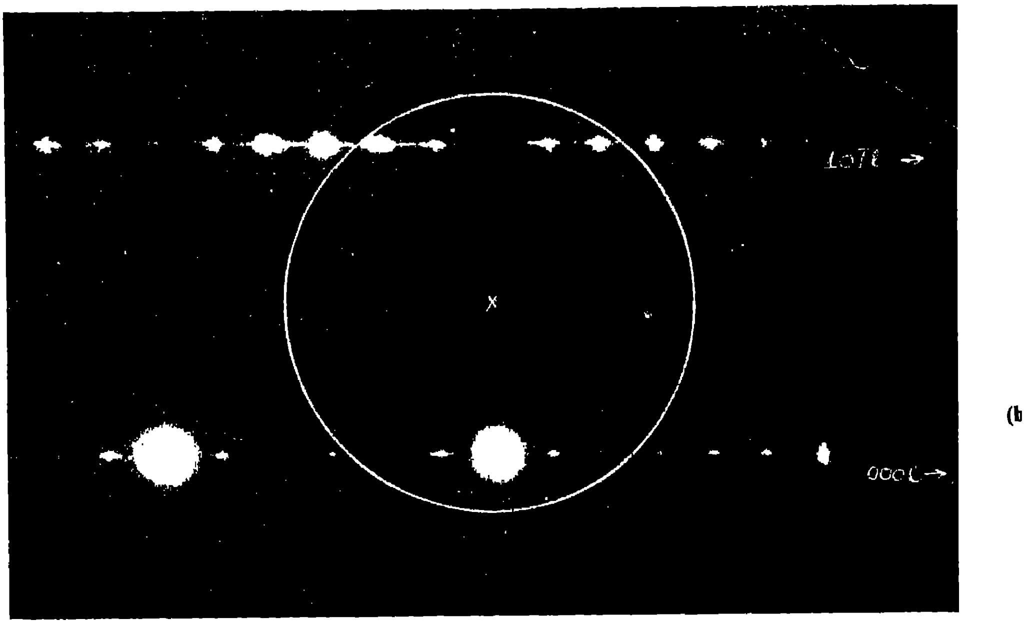

Figure 8. a. Two-dimensional lattice image taken under tilted beam illumination of the same crystal. Objective aperture symmetrically includes $000l$ and $10\bar{1}l$ reflections. b. Corresponding diffraction pattern, position of aperture and optic axis are marked.

4.3 *Intergrowth structures of* 411*R*

It has been seen from figures 7b and 8a that the super-period structure is built up of sub-units of periodicity 43·5 and 33 nm in addition to those of 411R. Since it has been possible to derive the layer sequence of 411R units from the chevron-shaped fringes, the structures of other intergrowth units can also be derived with reliability.

It can be seen from figure 9c that the layer sequence in 43·5 block is similar to that of 411R except that it contains a block of successive 15 fringes of 6H periodicity in place of nine such fringes in 411R unit cell. On the other hand, the 33 nm wide block has again similar layer sequence as in 411R except that it has eight successive fringes of 6H periodicity in place of nine in 411R unit (figure 9b).

4.4 *Super-period structure*

After decoding the layer sequence of constituent units, which intergrow coherently to form a super-period structure, one can write the full layer sequence of this structure in Zhdanov notation as

$$[\{3223332223(33)_2\ 433332(33)_9\ 22(33)_4\}\ \{3223332223(33)_2$$
$$433332(33)_8\ 22(33)_4\}\ \{3223332223(33)_2\ 433332(33)_9\ 22(33)_4\}$$
$$\{3223332223(33)_2\ 433332(33)_{15}\ 22(33)_4\}].$$

This represents a rhombohedral structure having 1734 SiC double layers in the

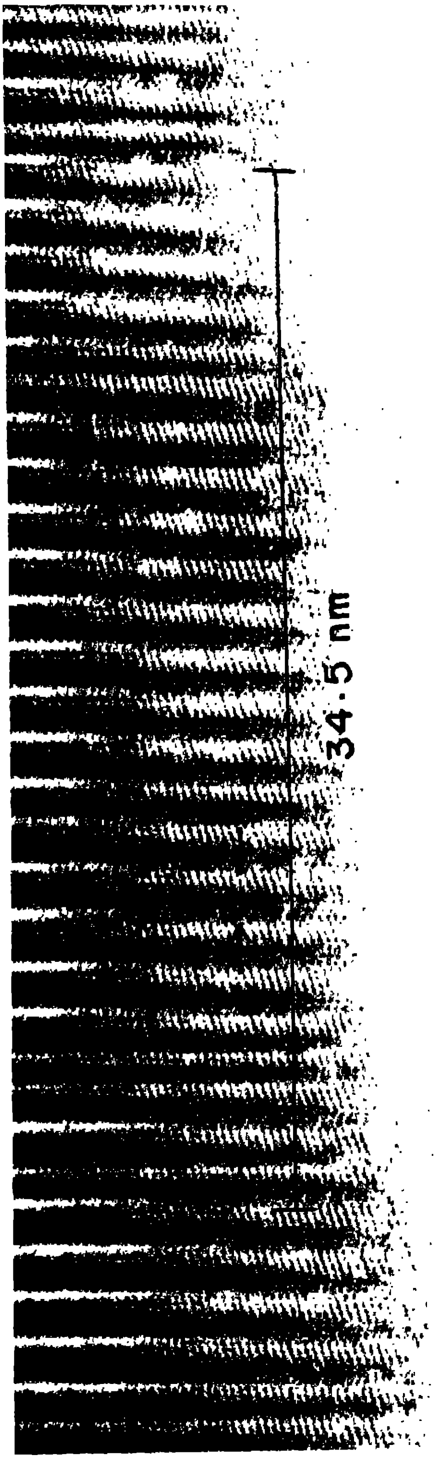

Figure 9a.

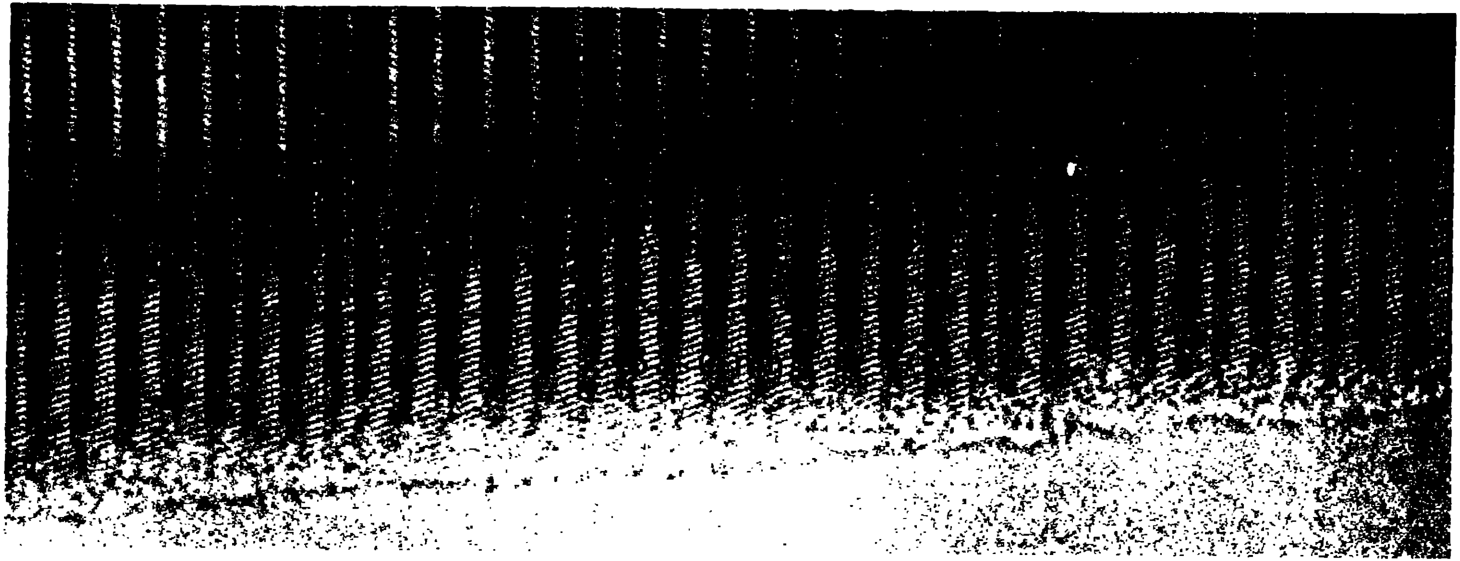

Figure 9b.

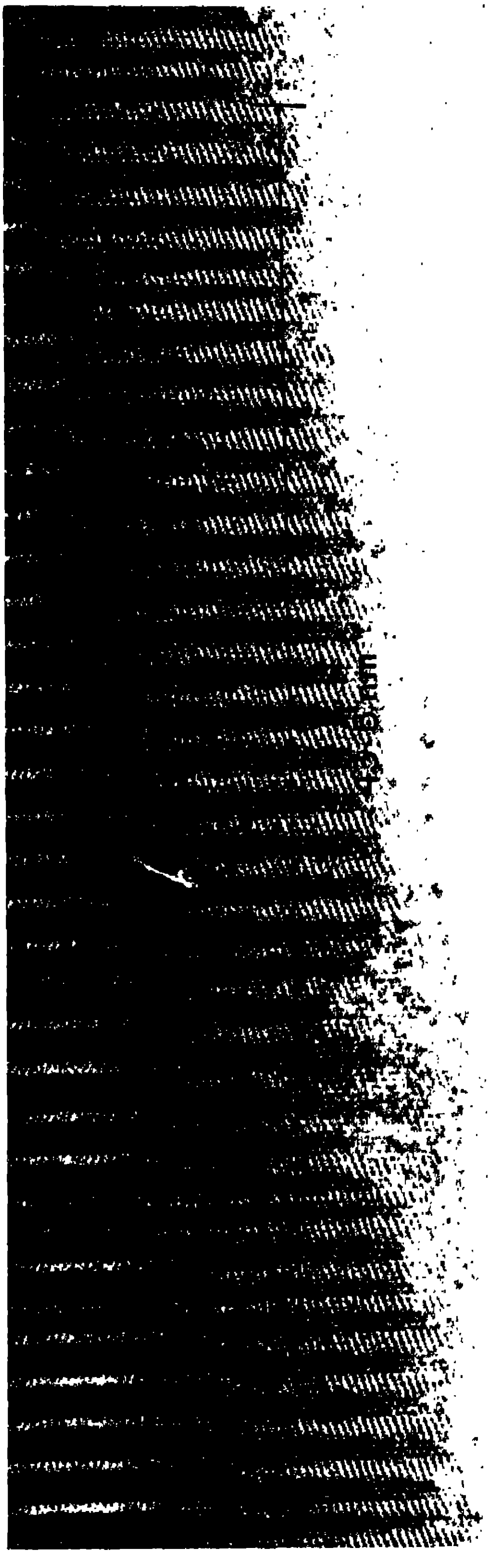

Figure 9. **a.** Enlargement of one 34·5 nm wide block of figure 8a. Layer stacking sequence may be read from the chevron shaped fringes. A stacking sequence of 43 corresponding to 21R is marked by arrows. **b.** Enlargement of the 33 nm wide block of figure 8a. **c.** Enlargement of 43·5 nm wide block of figure 8a.

hexagonal unit cell. Therefore, it is identified as 1734R and the complete structure is derived by repeating the above Zhdanov sequence three times.

5. Discussion

It has been seen from the above examples that tilted beam two-dimensional lattice images taken under suitable conditions contain direct information about the stacking sequence of layers in SiC structures. In 6H SiC by including highly excited $10\bar{1}2$ and $10\bar{1}\bar{2}$ reflections in the image formation, which are Bragg reflected from high reticular density planes forming chevron shaped surfaces in the structure, it is possible in principle to read the layer stacking sequence of the structure from chevron shaped fringes. However, chevron-shaped fringes simulating the layer stacking sequence are extremely sensitive to experimental parameters. As a result of this, the derived structural information remains ambiguous unless confirmed by other means. The reason for this state of affairs lies in the limited number of reflections used for obtaining these pictures.

For a real simulation of stacking reversal of layers we need details at the level of 0·25 nm in the image. This in turn requires inclusion of additional higher orders of diffraction spectra in the image formation, which are excluded, to avoid image deterioration due to spherical aberration. Therefore, a two-dimensional image will resemble a crude projection of the structure only when the foil is thin enough to behave as a phase grating and the image is taken under Scherrer defocus condition.

In contrast to chevron-shaped fringes, the linear fringes normal to *c*-axis arise essentially due to interference of different reflections of individual reciprocal lattice rows along c^*, like $000l$ or $10\bar{1}l$. An image formed by reflections of only one reciprocal lattice row can give the structure projected along a line. This gives rise to fringe modulations at spacings of *c*-periodicity of common polytypes which is of the order of 1 nm or more. Since the order of diffraction maxima along c^* allowed through the objective aperture is sufficient to give spatial frequencies in the image up to 0·25 nm, the series truncation errors are comparatively less and fringe modulations at the level of 1 nm or more become comparatively less sensitive to experimental parameters. Thus though the structural information available from one-dimensional fringes contains less details it is reliable. Therefore, wherever possible a combination of linear fringe spacings and chevron shaped fringes should be utilized to derive the structural information.

In 411R polytype let us consider only linear fringe spacings along *c*-axis. The unit cell contains fringe spacings expressed in terms of number of interlayer separation in the following sequence:

$$5, 5, 6, 4, 5, (6)_2, 7, 6, 5, (6)_9\, 4(6)_4.$$

This sequence may be converted into Zhdanov symbol by converting a 5 layer spacing into 32 or 23, a seven layer spacing into 43 and 34 and those of six and four layer spacing by 33 and 22 respectively. If the number of such spacings in the unit cell are large, the number of most probable structures even after taking a lattice image remains large. A good two-dimensional image in such complicated cases can lead straightaway to the correct structure, as shown by the present example. The structure determination of this polytype highlights the ambiguity in deriving structural information from lattice images unless properly confirmed by other means.

The details of the nature of intergrowth revealed by lattice imaging are characteristic of the power of this technique. In x-ray diffraction, characteristic spots of only 34·5 nm periodicity were observed whereas the real structure was built by regular intergrowth of three sub-units slightly different from each other. Therefore, the average structure observed by x-rays is only that of 411R. The super-periodicity of 145·5 nm simply gives rise to faint streaks due to lack of resolution. The nature of intergrowth observed in this example is not an isolated case. Similar intergrowths have also been observed in 150R and 40H (Singh and Singh 1980; Singh *et al* 1981) and this seems to be a general trend connected with the formation of large period polytypes in SiC. This aspect has come to light in greater detail only as a result of lattice imaging studies.

Acknowledgement

The authors are grateful to Prof. K H Jack of the Crystallography Laboratory, University of Newcastle upon Tyne, UK for providing experimental facility of JEM 100 CX.

References

Allpress J G 1970 *J. Solid State Chem.* **2** 78
Allpress J G and Sanders J V 1973 *J. Appl. Cryst.* **6** 165
Buseck P R and Iijima S 1974 *Am. Miner.* **59** 1
Cowley J M and Iijima S 1972 *Z. Naturforsch. Tiel* **A27** 445
Dubey M and Singh G 1978 *Acta Crystallogr.* **A34** 116
Iijima S 1971 *J. Appl. Phys.* **42** 5891
Iijima S, Cowley J M and Donnay G 1973 *Tschermaks.* Miner. Petogr. Mitt **20** 216
Jepps N W, Smith D J and Page T F 1979 *Acta Crystallogr.* **A35** 916
Ramsdell L S 1944 *Am. Miner.* **29** 431
Singh S R and Singh G 1980 *Acta Crystallogr.* **A36** 779
Singh S R, Singh G and Van Tendeloo G 1981 *Acta Crystallogr.* **A37** 625
Van Landuyt J, Amelinckx S, Kohn J A and Eckart D W 1973 *Mater. Res. Bull.* **8** 1173
Van Landuyt J, Amelinckx S, Kohn J A and Eckart D W 1974 *J. Solid State Chem.* **9** 103
Verma A R and Krishna P 1966 *Polymorphism and Polytypism in Crystals,* (New York)
Yessik M, Shinozaki S and Sato H 1975 *Acta Crystallogr.* **A31** 764

Bull. Mater. Sci., Vol. 6, No. 3, July 1984, pp. 477–490. © Printed in India.

Scanning transmission electron microscopy and microdiffraction techniques

J M COWLEY

Department of Physics, Arizona State University, Tempe, Arizona 85287 USA

Abstract. At the moment scanning transmission electron microscopy (STEM) instruments are not competetive with conventional TEM instruments for high resolution bright field imaging. For studies of the structure and defects of crystalline materials, their special virtues lie in the application of dark field imaging modes combined with observations of microdiffraction patterns from regions of diameter comparable with the microscope resolution limit (currently about 5 Å). They also offer capabilities for microanalysis by use of energy dispersive x-ray spectroscopy (EDS) or electron energy loss spectroscopy (ELS). In principle the spatial resolution of these microanalysis methods is comparable to that of the imaging modes but in practice it is limited by poor signal-to-noise ratios or by the nonlocalized nature of the inelastic scattering process.

The capabilities for microdiffraction are illustrated by sequences of diffraction patterns obtained as the incident beam is moved within the unit cell of a crystal of large (20 Å) periodicity. Applications of more immediate practical significance include diffraction studies of small crystallites of gold 20 to 50 Å in diameter and of the near-amorphous, thin oxide layers formed on chromium and iron films at room temperature.

Microdiffraction, combined with reflection electron microscopy and ELS analysis, provides a powerful new approach to the study of the surface structure of crystals, including bulk samples, and the investigation of surface reactions. In particular, if a beam of small diameter (10–20 Å) is made to run along the face of a small crystal, the diffraction pattern and ELS curves are very sensitive to the form of the potential distribution at the surface and the excitations of the surface states of the crystal.

Keywords. Convergent beam electron diffraction; microdiffraction; surface studies.

1. Introduction

For many areas of application of electron microscopy, STEM does not offer any particular advantage over the conventional TEM. When only bright field images or dark-field images of the standard type are required from specimens which are not too thick, use of STEM is inconvenient because the instruments have not been developed commercially to the same extent, specimen interchange takes longer because of the requirements for better vacuum and the images tend to be noisy and of limited size relative to the resolution, *i.e.* the number of usable picture elements per image is relatively small.

On the other hand the use of STEM has opened up an important new range of possibilities which are having increasing impact in electron microscopy, providing information previously inaccessible and allowing new approaches to a number of important problems of solid state science. New bright field and dark field imaging modes are available, largely because with the STEM configuration it is possible to choose any selected part or parts of the diffraction pattern to form the image. Several different image signals can be obtained simultaneously and combined to emphasize particular types of information concerning the specimen (Crewe *et al* 1970; Cowley and Au 1978). The STEM imaging mode lends itself particularly well to digital recording of data so that with a minicomputer coupled to the system it is possible to perform a variety of image processing procedures on-line or else the images may be stored conveniently for off-line processing (Strahm and Butler 1981).

For many areas of solid state science, the most important innovations associated with STEM are those which depend directly on the fact that at any one time the specimen is irradiated by an electron probe of very small diameter. For every probe position a microdiffraction pattern is produced from an area of the specimen of diameter comparable with the resolution limit of the STEM images. The energy losses of the transmitted electrons may be observed as a basis for microanalysis by the EELS techniques or microanalysis may be performed by detection of the emitted characteristic x-rays using EDS. Other signals which may be used to provide information on chosen parts of the specimen or else to form images include the emitted light, secondary electrons and acoustic waves. In each case the spatial resolution which can be achieved depends on the nature of the electron-specimen interaction, the efficiency of production of the detected signal and the efficiency of the detection system. At least in microdiffraction and ELS for small energy losses, spatial resolutions approaching 5 Å have recently been reported.

In this review we concentrate our attention on these techniques having high spatial resolution and their relationship to the high resolution STEM imaging modes and provide a few examples to illustrate the potential of these methods for the solution of problems of immediate relevance for research in solid state science.

2. Bright fields and dark field images

In order to obtain the STEM equivalent of the high resolution bright field TEM images of thin crystals, which are proving increasingly valuable for crystallographic studies, it is necessary to illuminate the specimen with a large objective aperture angle (figure 1). The beam which converges on the specimen must be coherent, *i.e.* the illumination falling on the objective aperture must come from a source which is so small that the coherence width is greater than the objective aperture diameter. According to the reciprocity relationship, the detector aperture must be small in order that the geometry be equivalent to TEM with a well-collimated incident beam. Hence only a very small proportion of the incident electrons can be detected and consequently, in order to produce a strong enough signal to form an image in a conveniently short time, it is

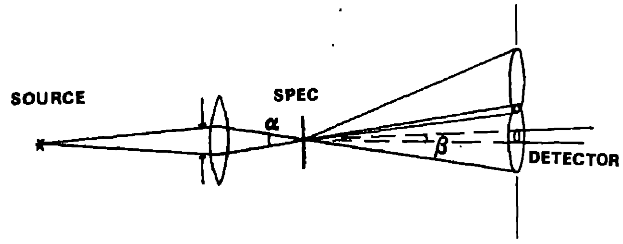

Figure 1. Diagram showing the objective aperture and detector aperture angles for STEM.

necessary to use a very bright, small source such as is given by a cold field emission gun.

For the currently available commercial STEM instrument, the HB5 from VG Microscopes Limited, England, the pole piece dimensions for the objective lens have been made relatively large in order to accommodate an EDS detector. Hence the bright field image resolution is about 4·5 Å as compared with 3 Å for contemporary 100 keV TEM instruments. Figure 2c is a bright field STEM image of the thin edge of a crystal of $Ti_2Nb_{10}O_{29}$ with the incident beam parallel to the short (3.8 Å) *b* axis. The crystal was aligned by observation of the microdiffraction patterns, such as figure 2a obtained using a small (10 μm) objective aperture. Then the objective aperture of the correct diameter for optimum bright field image resolution (60 μm) was inserted and the scan was switched on. The small black spot in figure 2a is the detector aperture which is actually a small mirror in the optical system attached to our HB5 instrument (Cowley and Spence 1979).

The resolution in figure 2c is noticeably poorer than that in the historically significant images of the same material taken by Sumio Iijima (1971), in which the rows of metal atoms parallel to the beam and separated by 3·8 Å (figure 2b) were clearly resolved. This is consistent with the results of calculations of image intensities made using the spherical aberration coefficients of the objective lenses used in the two cases (O'keefe *et al* 1978).

It is interesting to note that in the dark field STEM image of figure 2d obtained with an annular dark field detector, these atom rows, 3·8 Å apart, are clearly resolved as white spots and the representation of the structure is good. This is in striking contrast to the dark field images formed in TEM with the usual "high resolution" tilted-beam dark field geometry. For such images, although some fine detail is visible, the structure of the crystal projection is not reproduced in a recognizable form and even the symmetry of the image is strongly perturbed in a manner depending on the tilt of the incident beam (Sumio Iijima, private communication).

It has been argued by Crewe *et al* (1970) and Hanssen and Ade (1976) that dark field images from annular detectors have better resolution than bright field images. These arguments are valid for very thin, weakly scattering objects for which the weak phase object (kinematic scattering) approximation (the WPOA) applies, although modifications of the theory are necessary for imaging near the resolution limit (Cowley 1976). By extension of this theory it has been argued (Cowley 1978) that the same improvement of resolution should apply for thin, strongly scattering objects such as the crystal used for figure 2, for which the strong phase object approximation (POA) is valid. The symmetry of the experimental annular aperture configuration ensures that, in contrast to the TEM case, the symmetry of the dark field image will be maintained.

It seems clear that when, in the near future, the same ultra-high resolution pole pieces are used in STEM as in TEM instruments, important advances in the imaging of crystal structures will be possible.

3. Resolution enhancement by holography and coherent CBED

In his original paper on holography, Gabor (1949) proposed that a very small source of electrons should be placed close to a thin specimen to form a highly magnified shadow image which could be regarded as a hologram from which the object would be reconstructed, with correction of the aberrations of the lenses forming the source. This idea was abandoned because sufficiently small electron sources of the necessary

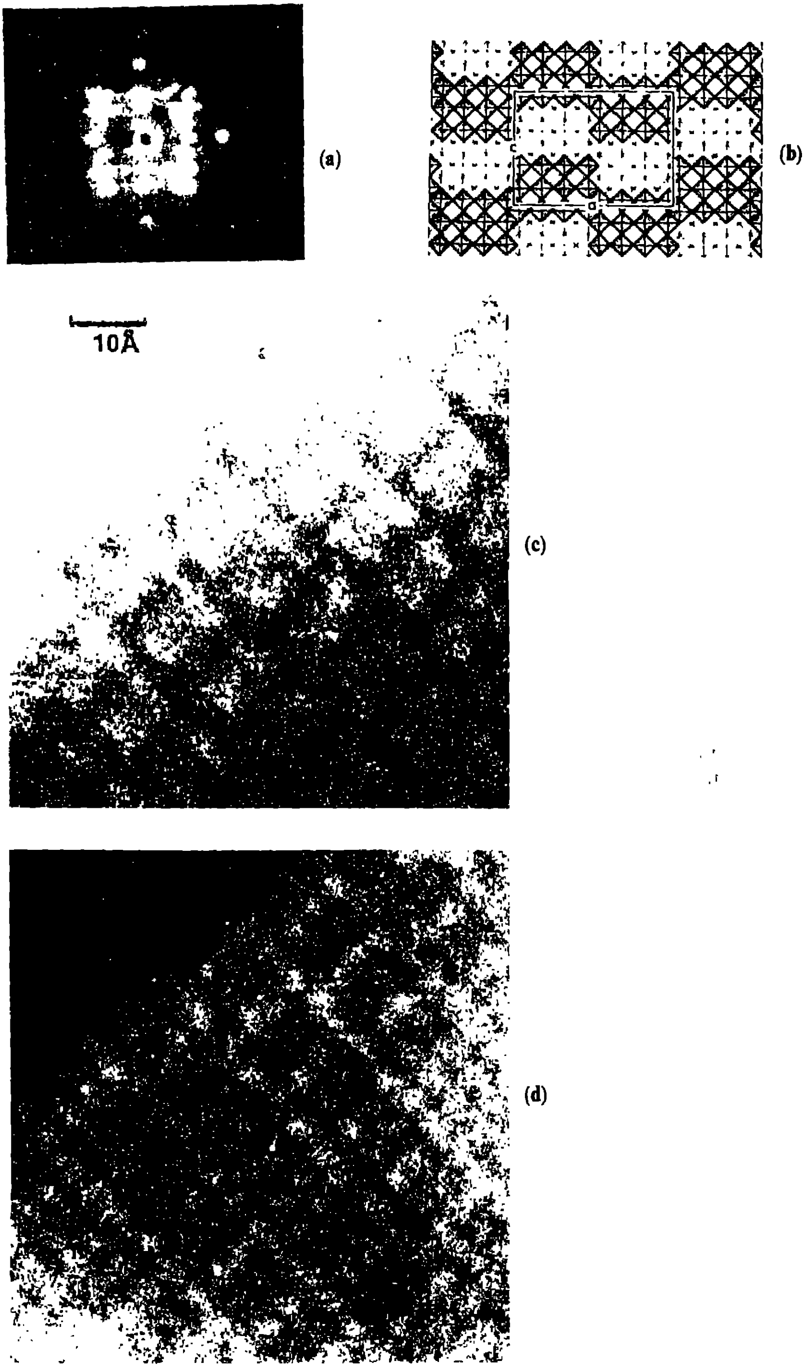

Figure 2. **a.** Convergent beam diffraction pattern from a thin crystal of $Ti_2Nb_{10}O_{29}$. **b.** A diagram of the structure of $Ti_2Nb_{10}O_{29}$, projected down the *b*-axis. The squares are oxygen octahedra, surrounding metal atoms, on two different levels indicated by the line width. **c.** A bright-field STEM image obtained with a small detector aperture. **d.** A dark-field STEM image obtained using a large annular detector excluding the zero beam.

brightness could not be formed at that time. Recently with the use of field emission guns and efficient two-dimensional detector systems, the proposal has become more nearly feasible. Shadow images formed in a STEM instrument have demonstrated that the essential requirements have been met (Cowley 1980).

Figure 3, for example, shows a series of shadow images of the thin edge of a MgO smoke crystal. The prominent fringes are given by the (200) lattice plane spacings ($d_{200} = 2{\cdot}1$ Å). The shapes of the fringes result from the effects of spherical aberration and defocus. Astigmation would distort the shapes but has been corrected to high accuracy by removing this distortion. The shapes are similar to those of the Ronchigrams used for the detection of aberrations of large telescope mirrors and observed when a diffraction grating is placed near the focus of the mirror (Ronchi 1964). The fringe patterns observed when thin crystals are placed near the focal point of an electron lens have therefore been named "electron Ronchigrams".

When the shadow images such as those of figure 3 are observed on the TV screen, movements of the Ronchi fringes are clearly seen for movements of the incident beam or of the crystal by much less than 1 Å. The shadow images, regarded as holograms, therefore contain information on a scale of small fractions of 1 Å and this information could in principle be retrieved by a suitable reconstruction process. Suggestions have been made on methods by which the reconstruction process could be carried out in practice (Cowley and Walker 1981).

For thin crystals having large unit cell dimensions when projected in the direction of the incident electron beam, it is interesting to observe the transition from the convergent beam microdiffraction patterns (CBED) (figure 2a) to the shadow image as the objective aperture size is increased and, as a consequence, the diffraction spots become larger. As the spots begin to overlap, strong interference effects become apparent in the regions of overlap. When the objective aperture size is so large that many diffraction spots overlap at any point of the diffraction pattern, the distinction between spots is no longer clear. At this stage, the diameter of the electron probe on the specimen is much smaller than the unit cell dimensions. Only a small part of the unit cell is illuminated and the diffraction pattern intensities reflect the arrangement and symmetry of the group of atoms in the beam. Then, as the electron beam is moved across the unit cell, the changes in the diffraction pattern can be observed and recorded (figure 4).

The extent of the diffraction pattern is such that it contains information on spacings as small as 0·5 Å or less. Interpretation of the patterns would allow structure analysis showing details in this scale.

4. Practical microdiffraction

While the large-aperture CBED patterns and shadow images have great potential which may be realized in the future, the patterns obtained with smaller objective apertures have immediate practical applications and are increasingly used for gathering data on small specimen areas not otherwise attainable. Patterns such as those of figure 2a and figure 5 have relatively large and poorly defined spots, as compared with the sharply-focussed selected area diffraction patterns commonly obtained with TEM instruments and cannot be used in the same way to give accurate measurements of lattice parameters. Nor can they show the same enormous range of relative intensities, ranging from strong sharp Bragg peaks to weak diffuse scattering. On the other hand, they can

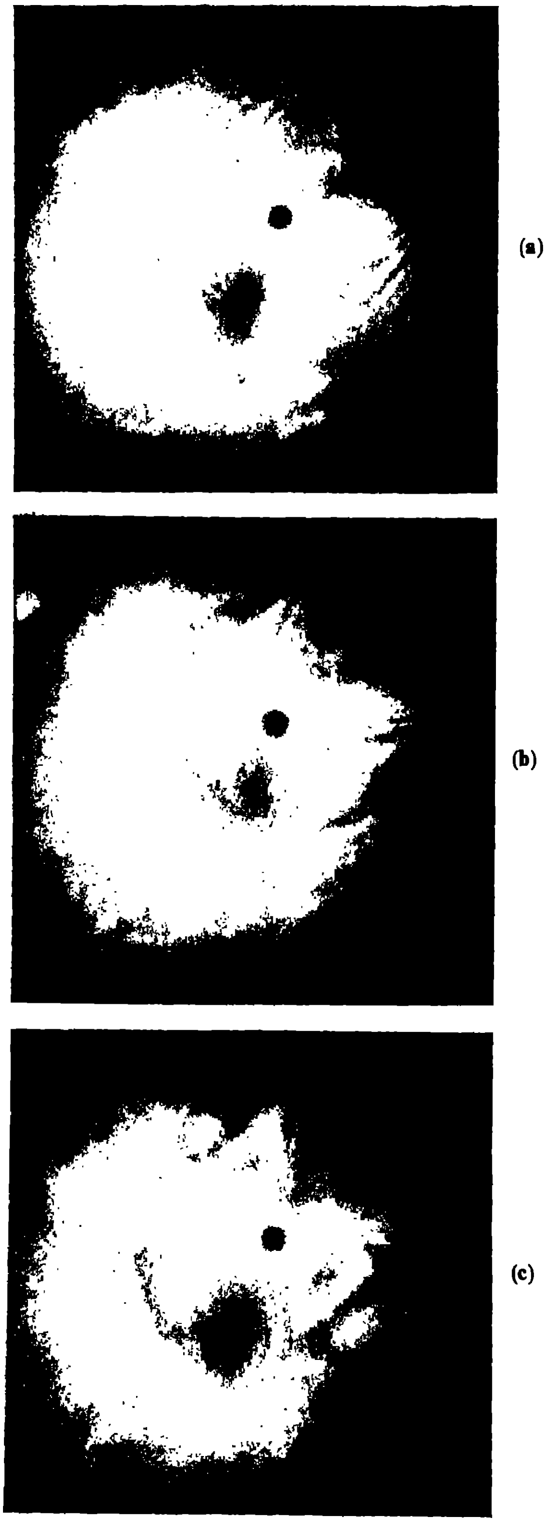

Figure 3. Shadow images of a thin crystal of MgO showing Ronchi fringes due to the 200 lattice planes ($d = 2{\cdot}1$ Å) taken from a through-focus series.

be obtained from specimen regions only 10–20 Å in diameter and provide information otherwise inaccessible on the structures of very small particles, the ordering in local domains of near-amorphous materials and the environments of individual crystal defects.

Small particles of face-centred cubic metals having diameters less than 100 Å are currently being investigated intensively because of their role in catalysts. Various electron imaging and diffraction techniques have been used to show that the particles are usually not single crystals but are multiply twinned on (111) planes, forming assemblies which commonly contain five or twenty tetrahedral regions related in this way. The evidence on these structures is reasonably clear for the size range down to about 50 Å. Information on smaller particles is needed to confirm the theoretical predictions that this multiply twinned form is in fact the equilibrium form for the smallest sizes and provides the nuclei from which larger particles grow.

The possibility of obtaining diffraction patterns from regions less than 20 Å in diameter is therefore significant in this context. Patterns have been obtained from gold particles formed by cósputtering with polyester or alumina and having diameters of 20 to 30 Å (Cowley and Roy 1981) (figure 5). The incident beam may lie completely within one single crystal region, (figure 5a) or include a single twin plane or two twin planes (figure 5b, c). The relative intensities and shapes of the spots may be used within limits to derive detailed information on the configurations (Cowley and Roy 1981). Series of patterns taken as the incident beam scanned over a particle could be applied to make complete analysis of its form. It is anticipated that this method of analysis may be extended to the 15–20 Å size range, beyond which difficulties arise because the individual single crystal regions between the twin planes are too small to give clearly recognizable patterns.

In another application of the method (Fumio Watari and Cowley 1981), it has been shown that single crystal patterns may be obtained from the microcrystals in the oxide layers formed when chromium is heated in air. The oxide layers give only very blurred arcs or rings in selected area diffraction patterns so that detailed analysis has previously not been possible. Single crystal microdiffraction patterns from individual microcrystals revealed that in addition to the known rhombohedral Cr_2O_3, a second form of oxide exists, forming a very thin layer on the surface and having a spinel-type structure which was previously unknown for chromium.

The epitaxial relationship in which this oxide grows on chromium could be established and, from this, models for the growth process could be proposed. It was deduced that the spinel crystallites never grow to more than about 10 Å thick or 50 Å wide but form an intermediate stage in the oxidation which is later dominated by the growth of the rhombohedral form as the oxide layer thickness increases.

Microdiffraction shows that the thin protective oxide layer formed on chromium in air at room temperature is almost completely amorphous (Fumio Watari 1983), having less local order than other so-called amorphous materials such as the amorphous forms of silicon or carbon for which the microdiffraction patterns from 15 Å diameter regions show considerable spottiness, reflecting the extent of the local positional correlations of the atoms (Cowley 1981). Comparison of the pattern from the chromium oxide, (figure 6a) with that from amorphous silicon (figure 6b) suggests that the degree of order in the former is much less.

This comparison of spottiness of the microdiffraction patterns provides at best a very qualitative and subjective measure of the degree of local ordering. However con-

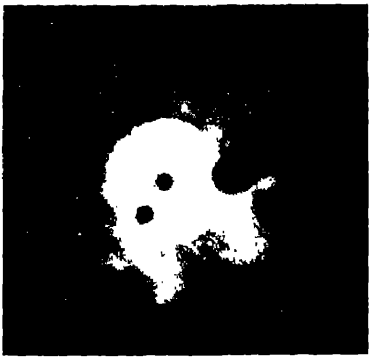

4(a)

4(b)

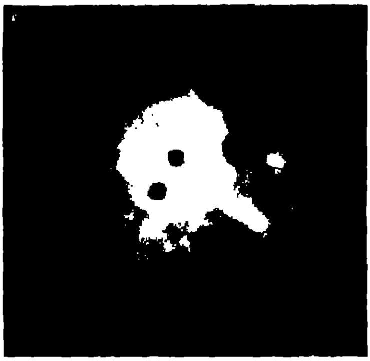

4(c)

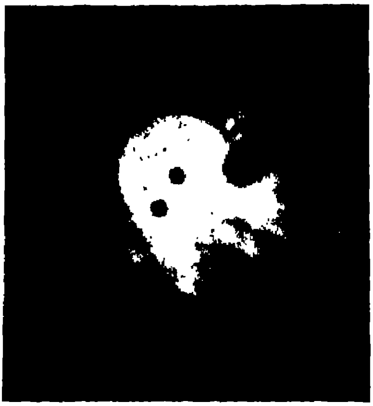

4(d)

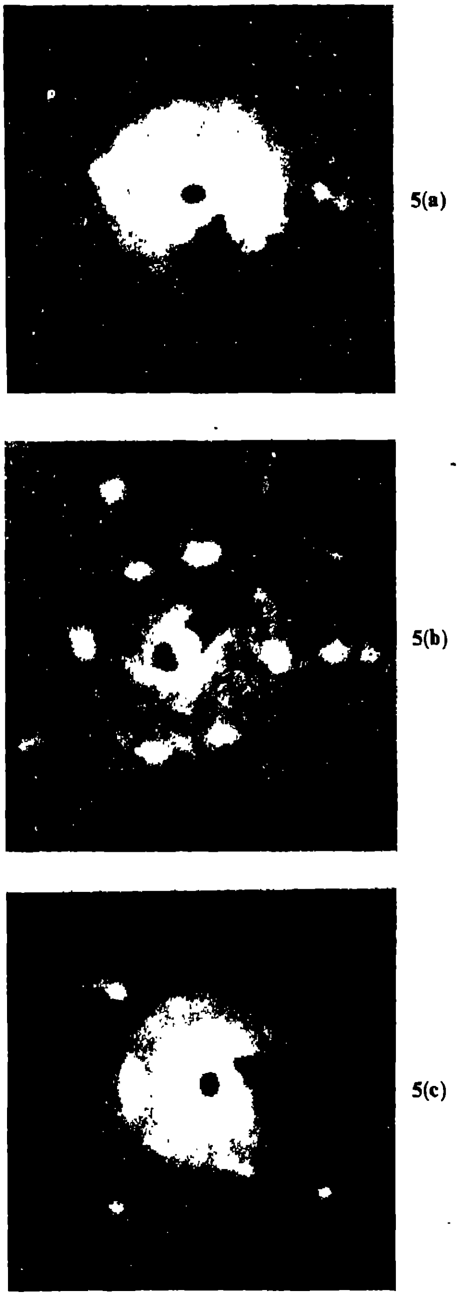

Figure 5. Microdiffraction patterns from small particles of gold, 20 to 50 Å in diameter showing the effects of twinning. The incident beam of diameter 15 Å illuminates no twin plane in **a**, one twin plane in **b** and two planes in **c**.

Figure 4. A series of microdiffraction patterns obtained as an electron beam of diameter 5 Å is moved across one unit cell of a $Ti_2Nb_{10}O_{29}$ crystal. The black spots and the other features are mirrors and a beam stop in the optical system.

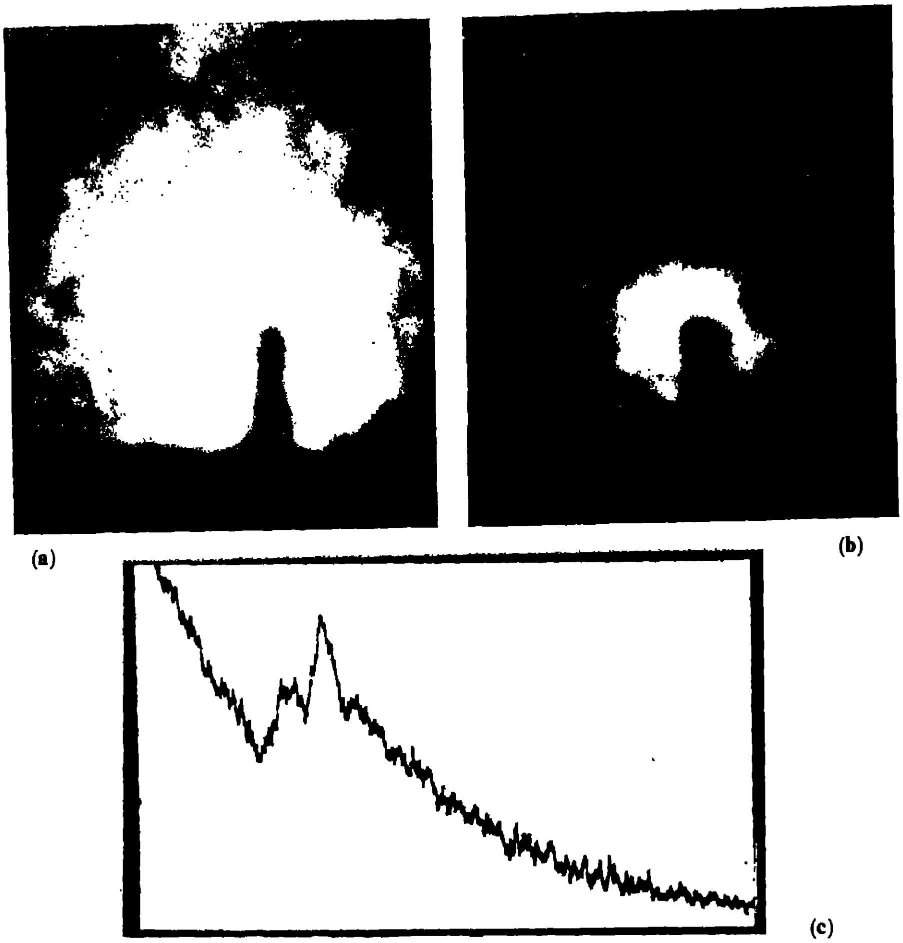

Figure 6. a. Microdiffraction pattern from a region 15 Å diameter of a thin oxidized chromium film. b. Similar microdiffraction pattern from a thin film of amorphous silicon. c. ELS spectrum from a thin oxidized chromium film showing the oxygen K edge and the chromium L edge.

siderable conceptual and operational problems have, to date, prevented the development of a more satisfactory, quantitative basis for measurement of the relevant parameters.

Further information may be derived concerning the thin amorphous protective layer on chromium by use of the STEM instrument in that the ELS method provides some indications as to its composition. The ELS curve of figure 6c shows the adjacent peaks due to the oxygen K-edge and the chromium L-edge. From observations of the ratios of the heights of these peaks for oxides of known composition and for films of different thicknesses it is possible to conclude that the oxide layer has a thickness of 10 Å on each side of the chromium and has a composition in the chromium-rich side of Cr_2O_3 (Fumio Watari 1981). Parallel determinations have been made for the thicker oxide layer which forms on iron.

5. Surface studies

To some extent all TEM and STEM studies of very thin specimens can be regarded as studies of surfaces since the surface layers constitute a large proportion of the sample. For special specimens and imaging modes the information on surface structure is explicitly sought and clearly obtained. Such cases include the imaging of atom-high surface steps (Moodie and Warble 1971), the observation of the movements of single heavy atoms on the surface (Crewe 1978; Iijima 1977) and the study of the structure and reactions of surface monolayers (Yagi *et al* 1979).

For most transmission specimens the scattering of electrons by the internal structure dominates the image. For these and for bulk specimens an alternative method for high resolution surface study has been found in reflection electron microscopy (REM). The initial experiments with this method were made with TEM instruments (Nielsen and Cowley 1976) and spectacular results on the surfaces of semiconductors have been obtained when an ultra-high vacuum instrument, with facilities for specimen treatment, has been used (Osakabe *et al* 1981).

STEM instruments have special capabilities for this type of surface research in that the imaging by scanning reflection electron microscopy (SREM) may be correlated with microdiffraction and microanalysis from any chosen small part of the imaged region (Cowley 1980). The vacuum in the specimen chamber is good enough for some surface work (10^{-9} torr or better) and allows surfaces to be kept reasonably clean and free from contamination.

The microdiffraction patterns obtained from surfaces in this mode are similar to the well-known RHEED (reflection high energy electron diffraction) patterns with the incident beam making glancing angles with the plane of the surface. With a convergent incident beam, the diffraction spots become lines and these are frequently seen to be doubled (figure 7a). The outer component of each spot is given by transmission through projections or crystal edges. The inner component comes from flat surface areas and so is displaced by refraction at the surface. By placing the collector aperture in a STEM instrument on one or other of these components, the transmission and reflection images can be formed separately. Figure 7b, for example, is the image of the surface of a small octahedral NiO crystal having overall dimensions of about 1 μm. The image is strongly foreshortened because the incident beam makes an angle of about 5×10^{-2} rads with the surface but a useful picture of the surface structure may be obtained. In such images surface steps of height 2–3 Å have been detected and a lateral resolution of about 10 Å has been achieved (Cowley 1982). The technique has obvious applications for the study of surface reactions and the effects on surfaces of various treatments.

In principle the diffracted beams from a surface may be used for ELS microanalysis or microanalysis may be achieved by spectroscopy of the emitted x-rays. Since, when a strong diffracted beam is produced, the penetration of the electrons into the surface may be as little as 10–20 Å, these methods should provide an important new possibility for the chemical analysis of thin surface layers. As yet these methods are not well developed.

Some striking results have been observed with a slightly different geometry. If a crystal such as that of figure 7 is turned so that the face of the crystal is exactly parallel to the incident beam, a diffraction pattern is produced which suggests that electrons have been channelled along the surface. They are deflected towards the crystal by the

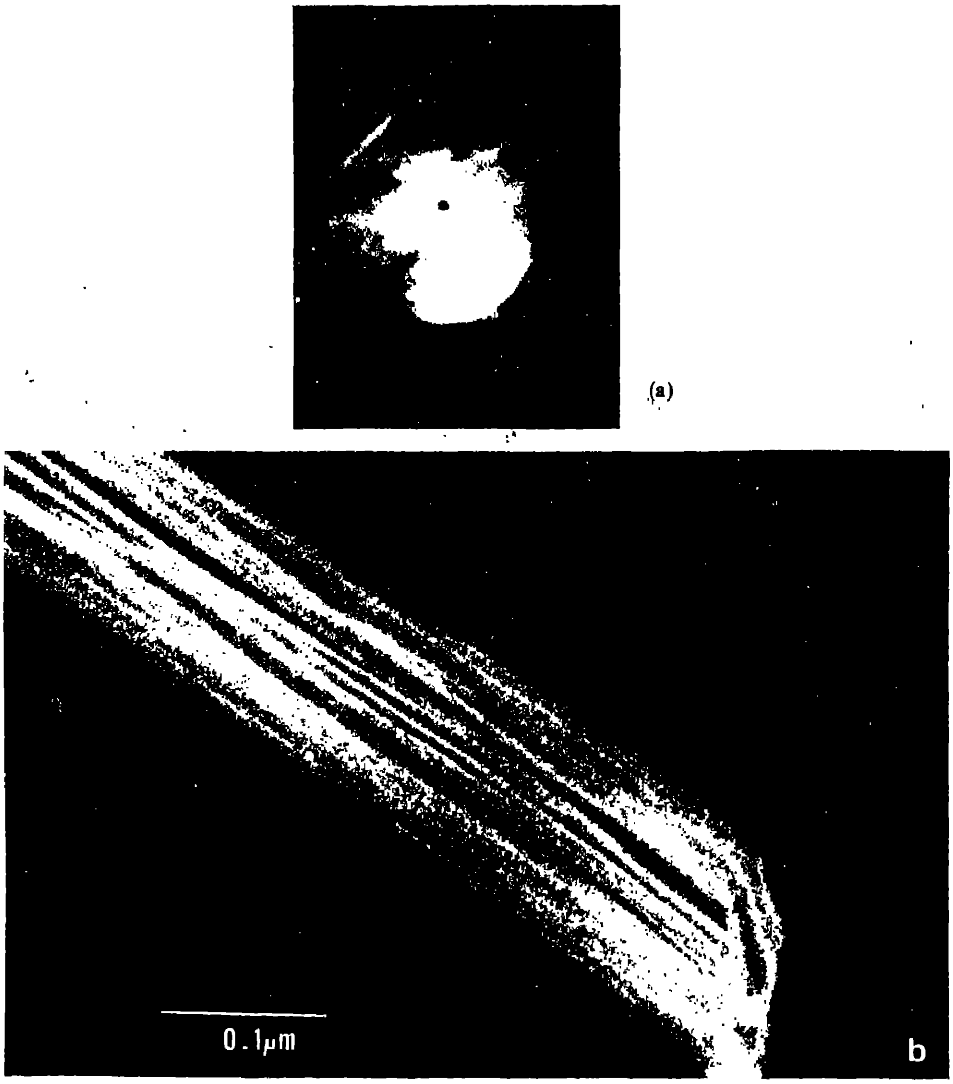

Figure 7. **a.** Convergent beam microdiffraction pattern from the surface of a crystal of MgO showing the doubling of diffraction spots due to refraction effects. **b.** Scanning reflection electron microscopy image of the (111) face of a small octahedral NiO crystal using the (444) reflection.

potential field extending from the crystal into the vacuum. Then in striking the crystal they are reflected out by Bragg diffraction but cannot escape the potential field and so continue in an oscillatory path along the surface (Cowley 1981a).

Because electrons which have been channelled in this way have travelled for large distances close to the surface they show strong peaks in the energy loss spectra corresponding to the electronic excitations and radiations generated at surfaces. For example figure 8 shows an ELS spectrum obtained by transmission through the edge of a crystal of NiO and spectra obtained when the electrons traverse a crystal face. For the

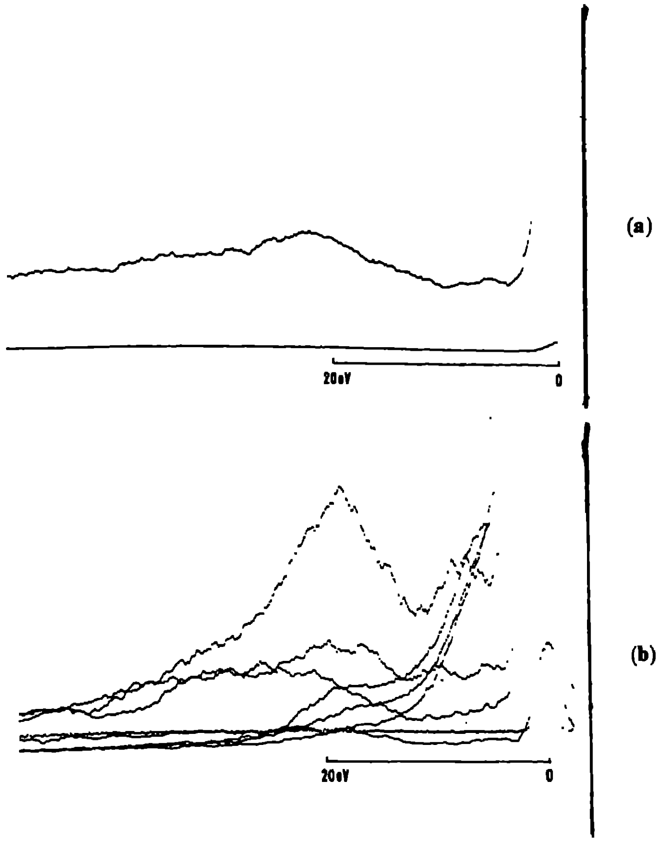

Figure 8. **a.** ELS spectrum obtained in transmission through a NiO crystal. **b.** Series of ELS spectra obtained as a beam of about 15 Å diameter, running parallel to the flat face of a NiO crystal, is moved successively closer to the face. The total lateral movement of the beam is about 50 Å.

latter, the energy losses associated with bulk excitations are scarcely visible. Instead there are strong new peaks in the 0–30 eV energy loss range.

Some of these peaks are undoubtedly due to the excitation of surface electronic states. Others, and especially the prominent peak at about 14 eV energy loss have been attributed to the generation of transition radiation at a frequency corresponding to the periodic oscillations of the electrons in and out of the surface as they are channelled along the face (Cowley 1981b). Transition radiation has been observed in other contexts and is associated with the fluctuation of the polarization field created by a charged particle at the surface of a dielectric. Its generation at a particular frequency due to an oscillatory motion is, however, a new and interesting phenomenon.

It now appears that the use of high voltage electrons in TEM and STEM instruments will provide a valuable new range of techniques for the study of surfaces, complementing the established methods of LEED, AES, SIMS, etc. In comparison with these well-known techniques, high spatial resolutions are possible, on the Å or nm scale rather than the μm scale. So far the interpretation of the high energy reflection diffraction intensities has not progressed as far as for LEED and the sensitivity of the surface microanalysis techniques does not match those of the established techniques but the fact that some diffraction and analytical data can be derived from very small areas of a surface and can be related to information from images of quite high resolution suggests that efforts to refine and develop these techniques will be amply rewarded in the near future.

Acknowledgement

The examples used to illustrate this review have been drawn from work which made use of the Facility for High Resolution Electron Microscopy, supported by the National Science Foundation.

References

Cowley J M and Au A Y 1978 *Scanning electron microscopy* (ed) Om Johari (Illinois: SEM Inc.) 53
Cowley J M and Spence J C H 1979 *Ultramicroscopy* 3 433
Cowley J M 1976 *Ultramicroscopy* **2** 3
Cowley J M 1978 *J. Crystallogr. Soc. Jpn* **20** 241
Cowley J M 1980 *Micron* **11** 229
Cowley J M and Walker D J 1981 *Ultramicroscopy* **6** 71
Cowley J M and Roy R A 1981 *Scanning electron microscopy* (in press)
Cowley J M 1980 *Microbeam analysis* (ed) D B Wittry (San Francisco Press) 33
Cowley J M 1981a 39*th Ann. Proc. Electron Microscopy Soc. Am.* (ed) G W Bailey (Baton Rouge: Claitor's Pub. Div.) 212
Cowley J M 1981b *Ultramicroscopy* 7 181
Cowley J M 1982 *Diffraction studies of non-crystalline substances* (eds) Hargittai and W J Orville-Thomas (Budapest: Akadimia Kiado)
Cowley J M *Surf. Sci.*(in press)
Crewe A V, Wall J and Langmore J 1970 *Science* **168** 1338
Crewe A V 1978 *Chem. Scr.* **14** 17
Fumio Watari and Cowley J M 1981 *Surf. Sci.* **105** 240
Fumio Watari 1983 *Surf. Sci.* (in press)
Fumio Watari 1981 *Proc. Microbeam Analysis Society Colorado* (in press)
Gabor D 1949 *Proc. R. Soc. London* **A197** 454
Hanssen K J and Ade G 1976 *Optik* **44** 237
Iijima S 1971 *J. Appl. Phys.* **42** 5891
Iijima S 1977 *Optik* **48** 193
Moodie A F and Warble C E 1971 *J. Cryst. Growth* **10** 26
Nielsen P E H and Cowley J M 1976 *Surf. Sci.* **54** 340
O'Keefe M A, Buseck P R and Iijima S 1978 *Nature* (*London*) **274** 322
Osakabe N, Tanishivo Y, Yagi K and Honjo G 1981 *Surf. Sci.* **109** 353
Ronchi V 1964 *Appl. Opt.* **3** 437
Strahm M and Butler J H 1981 *Rev. Sci. Instrum.* **52** 840
Yagi K, Takanayagi K, Kobayashi K, Osakabe N, Tanishivo Y and Honjo G 1979 *Surf. Sci.* **86** 174

Bull. Mater. Sci., Vol. 6, No. 3, July 1984, pp. 491–501. © Printed in India.

Applications of scanning transmission electron microscope microanalysis in the study of materials

GARY R PURDY

Department of Metallurgy and Materials Science, McMaster University, Hamilton, Ontario, Canada

Abstract. The dedicated STEM equipped with field emission electron source, affords opportunities for the acquisition of microchemical and microstructural data on a scale approaching the nanometer level. In this presentation, a number of applications of microchemical analysis and microdiffraction to engineering materials will be discussed, with major emphasis on high-strength low-alloy steels, steels for high formability in automotive applications, and aluminium alloys. Some advantages and limitations of the technique are noted, especially for application to analysis of electrochemically prepared thin foils, and to the analysis of extracted particles.

Keywords. STEM; microanalysis; dual phase steels; high strength and low alloy steels.

1. Introduction

In the two years since the joint McMaster-Toronto STEM facility was established, a number of experimental programmes have been undertaken, and a few brought to conclusion. This paper reviews selectively those examples of STEM microanalysis which have been most fruitful in establishing working, or "effective" limits on instrument performance, given a multi-user environment. In general, the problems have been chosen with a particular scientific or engineering objective in mind, rather than for optimum instrumental performance. Hence, they serve to demonstrate the potential of the STEM for providing useful microchemical information to complement that derived from more conventional studies.

2. The instrument

The instrument is a "dedicated" vacuum generator HB-5 STEM, with field emission electron source, energy-dispersive x-ray, and electron energy loss spectrographic capabilities. In addition, it is possible to record diffraction patterns using well-focussed beams of varying convergence. The overall performance of the instrument is essentially as specified by the supplier, but certain development programmes have been undertaken to improve the energy loss spectrometer performance, and the microdiffraction recording capability.

3. Studies of thin-foil specimens

3.1 *Dual phase steels*

The problem of austenite growth in the intercritical annealing of dual phase steels has been treated analytically by Speich *et al* (1981) and Wycliffe *et al* (1981). The results of the two treatments are at variance, largely because of the type of local equilibrium tha is assumed to hold at the austenite-ferrite interface during growth. Speich *et al* (1981 assume a partial or paraequilibrium (Hillert 1960; Gilmour *et al* 1972) for initi growth, followed by a transition to particular interfacial tie-line representative of glob equilibrium within the specimen. In contrast, the analysis of Wycliffe *et al* (1981 presumes that a full local equilibrium is attained during initial growth, and that a serie of tie-lines representing successive local equilibria are determined as part of th solution of the diffusion equations (figure 1).

The test of these hypotheses requires that high-resolution microanalyses b performed on well-characterized specimens of previously homogenized steel quenched from isothermal treatments in the intercritical temperature range.

Two techniques were adopted to study the manganese profiles in austenite and ferrit after intercritical annealing: The first was conventional microprobe analysis, usin deconvolution techniques (Gilmour *et al* 1972) to enhance the spatial resolution to th point where it was limited by statistical and instrumental factors. Figure 2 shows convolution of the predicted Mn profile through an austenite (martensite) particle wit the experimentally determined microprobe intensity distribution function. Note tha this specimen was annealed for 50 hr at 1023 K. While the agreement is satisfactory, it i seen that this represents an upper limit to the capability of the microprobe analyser, an does not relate decisively to the more interesting short-time intercritical treatments

The same specimen was sectioned and examined in the STEM (figure 3). It is clear tha the increased spatial resolution of the STEM allowed a more nearly complete and direc determination of the maximum manganese concentration at the austenite-ferrit interface, in spite of the somewhat greater statistical error (discussed below). Fo shorter times, *e.g.* 100 sec the STEM allowed the detection of a manganese-enriched rin in the austenite, as shown in figure 4. These results for short times, and others like then

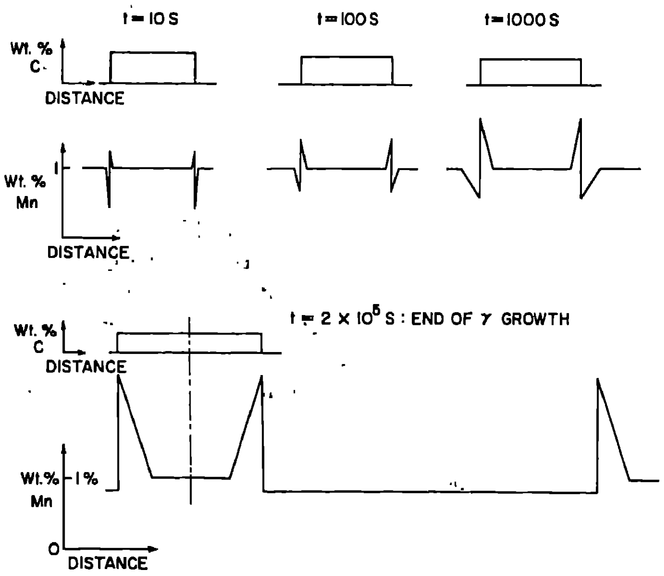

Figure 1. Computed carbon (C1) and manganese (C2) profiles for a 1 % Mn dual phase ste annealed for 50 hr at 1023 K, assuming a spherical austenite particle initially 1 μm in radiu

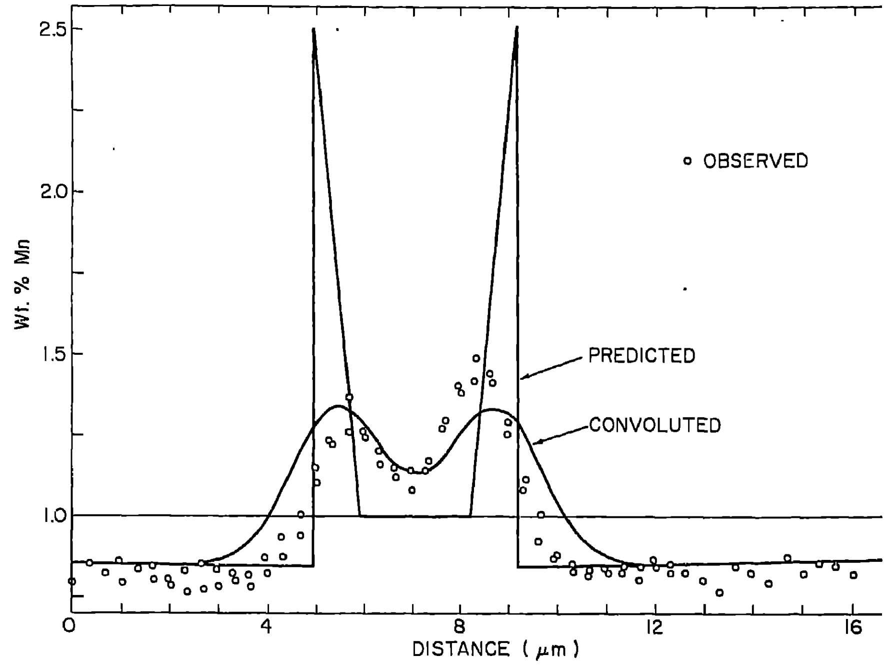

Figure 2. A predicted concentration profile is compared with an expected microprobe trace and compared with experimental points for an Fe-0·08 % C-1 % Mn alloy annealed for 50 hr at 1023 K.

lend credence to the full local equilibrium analysis as applied to intercritical annealing times typical of continuous processing routes. The longer time heat treatments are relevant to batch processing.

The sources of error in these analyses are of interest (Wycliffe 1981). It was determined that x-ray absorption in the specimen should have negligible effect on characteristic or background intensities, for the range of foil thickness and take-off angles employed. The major problems in obtaining precise information about the distribution of manganese in these rather dilute alloys are therefore statistical in origin, and involve precision in the measurement of both peak and background intensities; a schematic x-ray spectrum is shown in figure 5. The background intensity was estimated by extrapolating normalized integrated counts in the windows W1, W2, W3, and W4 (as a linear regression in $1/E$) to the manganese window. In treating the data in this way, Wycliffe encountered a systematic error, which is tentatively attributed to a low-energy (non-gaussian) contribution from the adjacent iron line. This detector characteristic was not suspected previously.

The austenite particles are approximately spherical; thus sectioning effects can distort the concentration profiles even when statistical factors are fully optimised. In an extreme case, a section through the manganese-enriched rim of an austenite particle would suggest uniform enrichment. In the more usual case, the interface is inclined to the foil and the net effect is a reduction in amplitude and a broadening in space of the interfacial concentration variation.

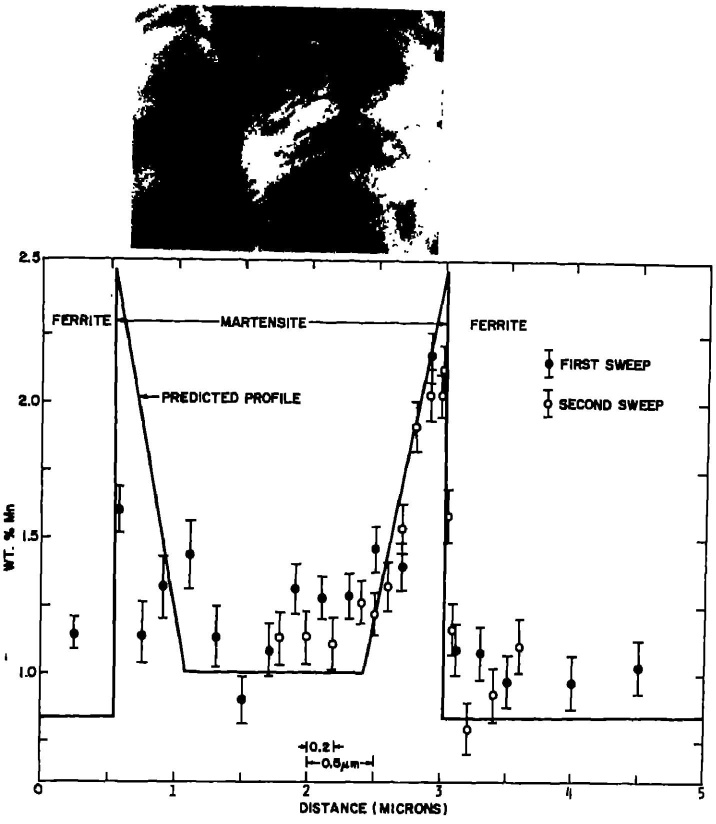

Figure 3. STEM microanalytical results are compared with a predicted concentration profile. Fe-0·08 % C-1 % Mn, 50 hr at 1023 K. The greater thickness at the left hand side of the particle caused broadening of the apparent concentration peak.

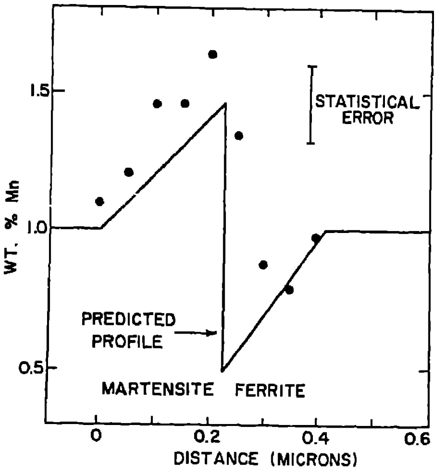

Figure 4. STEM analysis for the interfacial concentration profile from a specimen annealed for 100 sec at 1023 K.

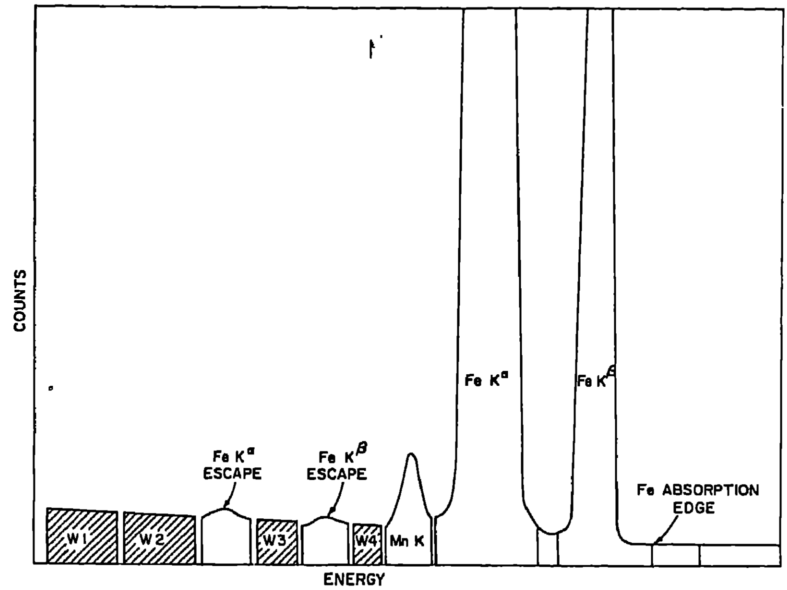

Figure 5. Schematic of an x-ray spectrum. The shaded regions were used in a linear regression of the normalized Mn background on $1/E$.

It is expected that beam spreading (Goldstein 1979) is the other chief source of loss of spatial resolution in these iron-base alloys; for a typical foil thickness of 100 nm, the estimated beam-spreading contribution to source size is 20 nm compared with the original probe diameter of approximately 1 nm. Deconvolution techniques can be applied to deal with this problem for some systems. They are not, however, justified for the present case.

Thus the technique of STEM x-ray microanalysis has proven valuable in the study of dual-phase steels. However, it should be noted that spectrometer and specimen limitations restrict the detectability of alloying element variations of lesser amplitude. A search for transformation-induced moybdenum segregation in a series of Fe–C–Mo alloys was less conclusive (Brown *et al* unpublished) mainly because the expected amplitude of segregation is at the margin of detectability.

4. Studies of aluminium alloys

The discontinuous-precipitation reaction in Al-Zn alloys is of fundamental as well as practical interest. Here a departure from local equilibrium is expected and necessary, and the solute (Zn) distribution at the transformation front is of interest from several points of view. A knowledge of the solute profile across the Al-rich regions is capable of analysis to yield the diffusion coefficient in the moving interface and a measure of the residual supersaturation left behind the moving front. In addition, the value of the composition in the depleted α immediately adjacent to the Zn-rich phase is required for a full analytical description of the process. Solorzano–Naranjo and Purdy (unpublished) have studied the composition profiles left behind the front, using

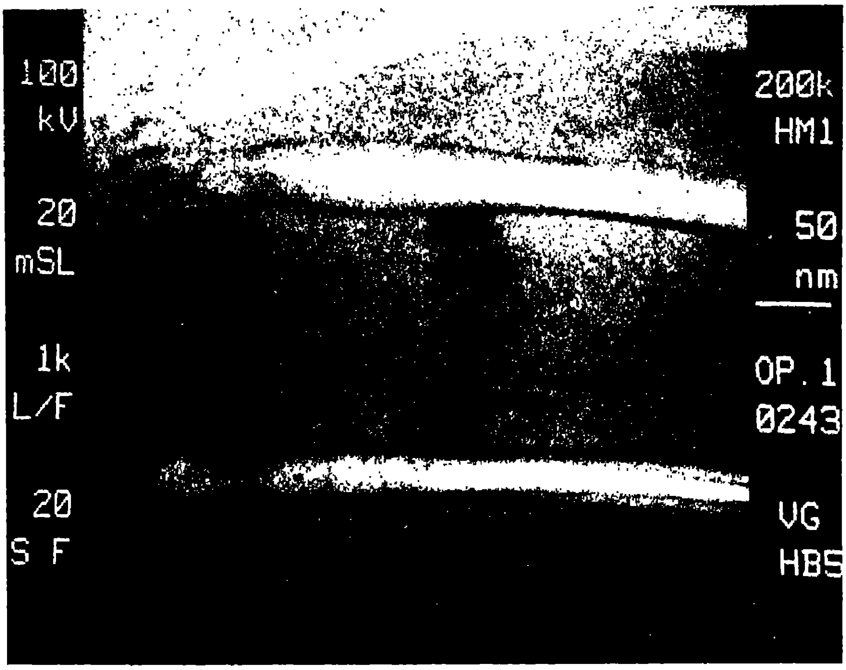

Figure 6. A STEM micrograph of the transformation front in an Al-28 at % Zn alloy, 10 min at 433 K. Scans across the depleted matrix are indicated by contamination traces.

electrolytically prepared foils from which the zinc-rich phase has been dissolved (figure 6). The results obtained to date suggest that these profiles are consistently and remarkably flat, allowing the assignment of a lower limit only to the interfacial diffusion coefficient.

A second example of the application of the STEM to aluminium-base system is that of θ' precipitation in Al-4 % Cu. Here, it is possible to obtain microdiffraction information from individual θ' plates (on edge) and to image individual growth ledges (figure 7). The solute field in the vicinity of the plates is accessible*, and it would be particularly interesting to map the copper distribution around an individual growth ledge. Current research (Perovic *et al* 1984) aims to compare the theory of ledge migration with experimental microchemistry.

5. Studies of isolated or extracted particles

The thin foil technique, although extremely useful in the study of gradients near interfaces, is limited in its application to the study of small particles, which are often obscured by matrix effects. Here, as an alternative, the study of extracted particles, supported on thin carbon (or other innocuous) substrates, has value.

The main example considered here, from the work of Houghton *et al* (unpublished)

---

* It is found that a brief treatment in an ion-thinning device is a useful precaution before examining electrochemically prepared Al-Cu foils.

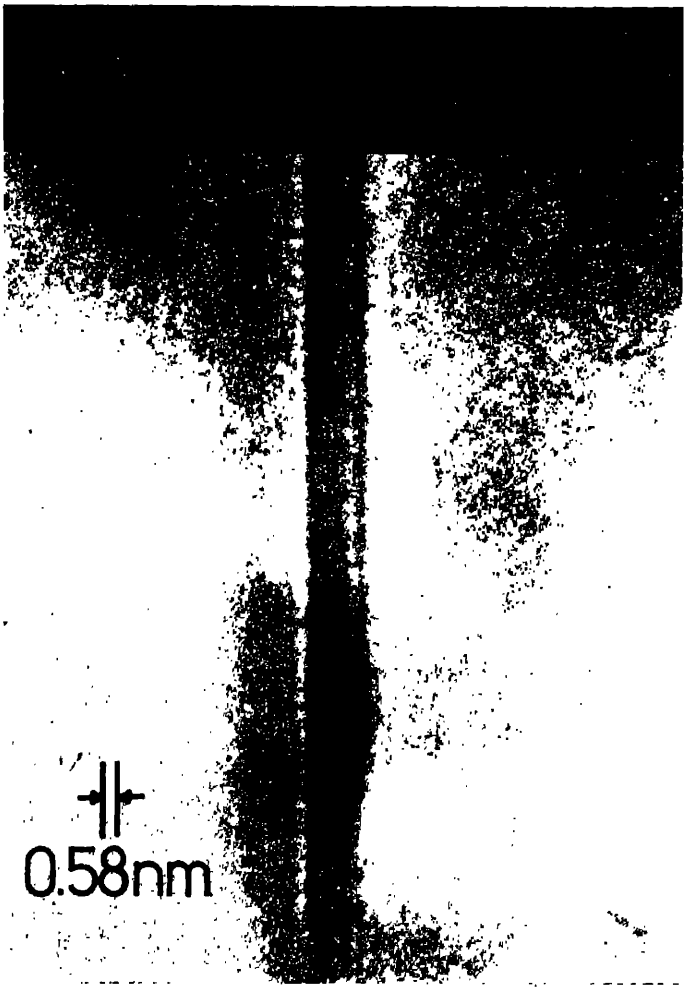

Figure 7. A θ' plate, imaged edge-on, to show a growth ledge.

was particularly useful to study precipitation sequences in high-strength low-alloy steels, subject to complex thermomechanical processing. The steels studied contained approximately 0·065 C, 2% Mn, 0·3% Si, 0·3% Mo, 0·003% S, 0·005% Nb and had varying titanium and nitrogen levels, from 0·011 to 0·039% and from 0·005 to 0·010% respectively (all concentration values in wt%). They were examined in the as-cast, reheated and control-rolled condition. In addition, several specimens were given thermal cycles designed to simulate the thermal history of the heat affected zone in a submerged arc welding process.

In conjunction with other metallographic techniques, the STEM proved most useful in identifying small carbonitride particles, and in establishing precipitation sequences. Figure 8 is a schematic histogram showing the size, shape and chemical composition of a typical precipitate distribution for a control-rolled alloy, along with probable formation temperatures. Figure 9 shows a STEM image, x-ray spectra, and micro-

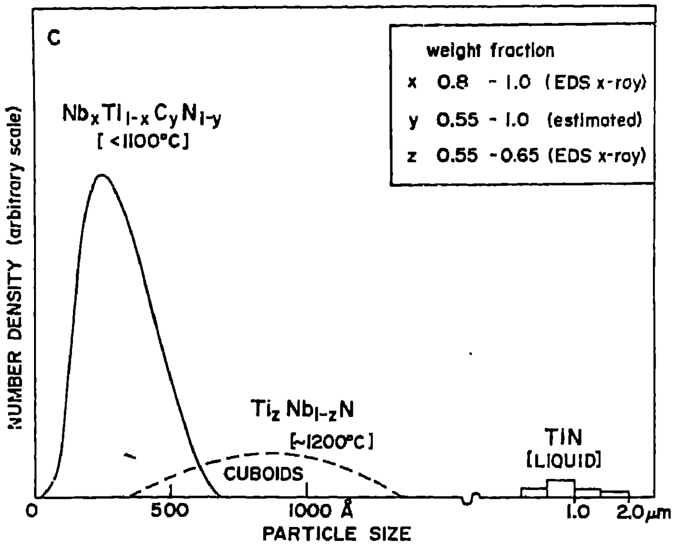

Figure 8. A schematic histogram showing the size, shape and chemical compositions of a typical precipitate distribution and probable formation temperatures.

diffraction patterns from a non-uniform particle, showing that epitaxial niobium-rich caps formed heterogeneously on the titanium-rich cubic central region of the particles.

By combining STEM-derived information with CTEM lattice parameter determinations (used to determine *C/N* ratios) and the solubility-product data of Narita (1975), it was made possible to establish predictive, simplified models for the precipitation sequence. The stable precipitate in austenite responsible for grain boundary pinning was identified in this work as $Ti_xNb_{1-x}N$, where x is of order 0·6; precipitates developed in control-rolled microstructures are of two major species: High temperature $Ti_xNb_{1-x}N$, formed during soaking; and carbonitrides of the general form $Nb_xTi_{1-x}(C_yN_{1-y})$. The latter precipitates were frequently found to be inhomogeneous (figure 9).

A final example of the utility of the STEM in the study of supported particles is in the study of the annealing behaviour of sputtered films (Lowden and Houghton (unpublished)). An unexpected result for Cu–Cr films containing a few percent chromium was the development of large-faceted copper crystals, which grow out of the plane of the foil (figure 10). The STEM is used here both as a microanalytical tool and as a high-resolution scanning electron microscope to image the copper crystals and to demonstrate their three-dimensional faceted morphologies in a manner not possible in the transmission mode. The details of the growth of these crystals are not yet clear, but it appears that they are essentially the result of abnormal grain growth in an inherently fine-grained initial thin foil. The experimental details and theoretical analysis of this most interesting effect await fuller study.

6. Conclusions

Some examples of the application of STEM microanalysis to the study of materials have been reviewed. It is clear from the experience gained to date that the STEM offers the

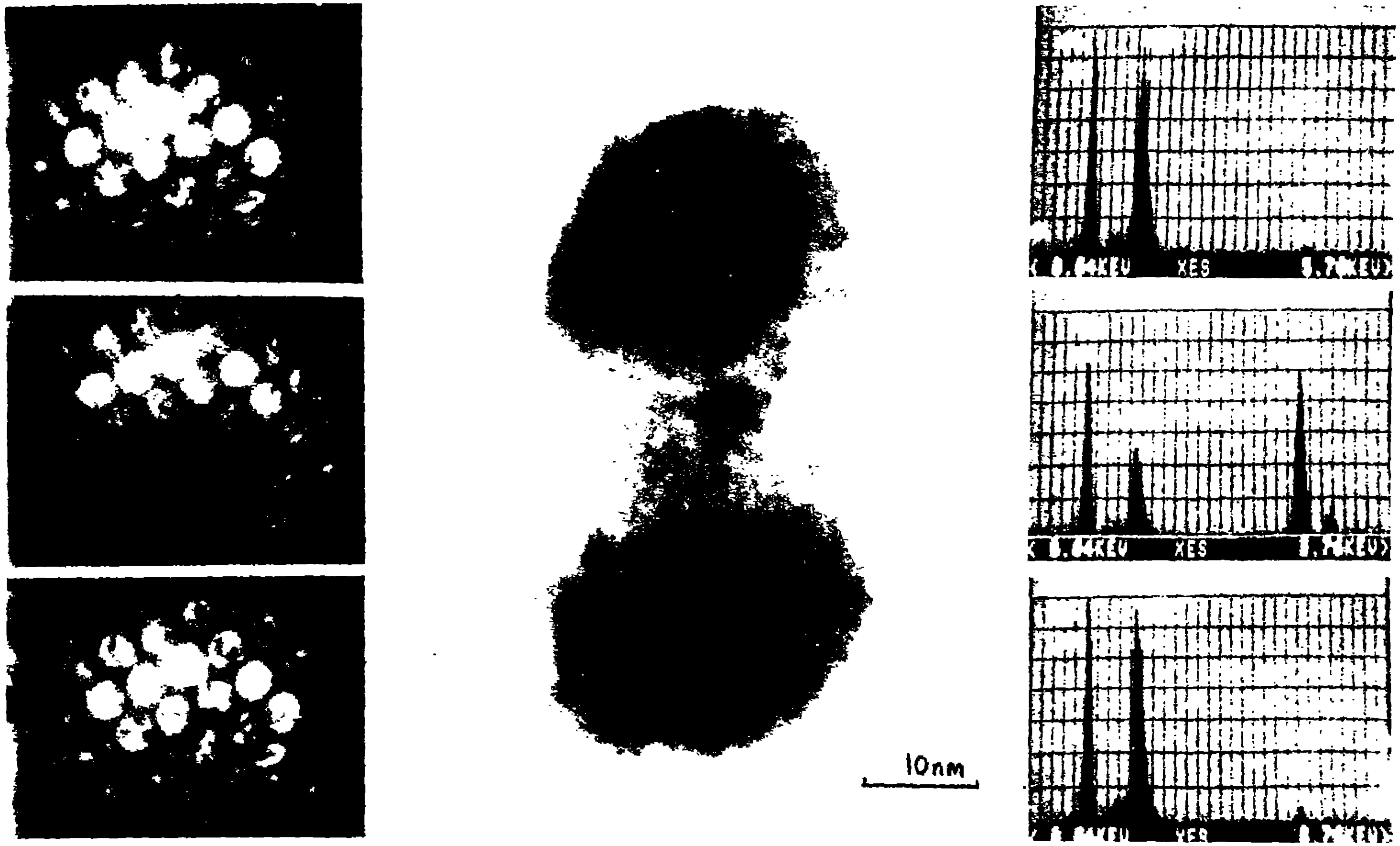

Figure 9. STEM micrograph of an extracted heterogeneous particle typical of those found in control-rolled microstructures, with x-ray spectra and micro diffractions from the various parts of the precipitate (Houghton *et al* (unpublished)).

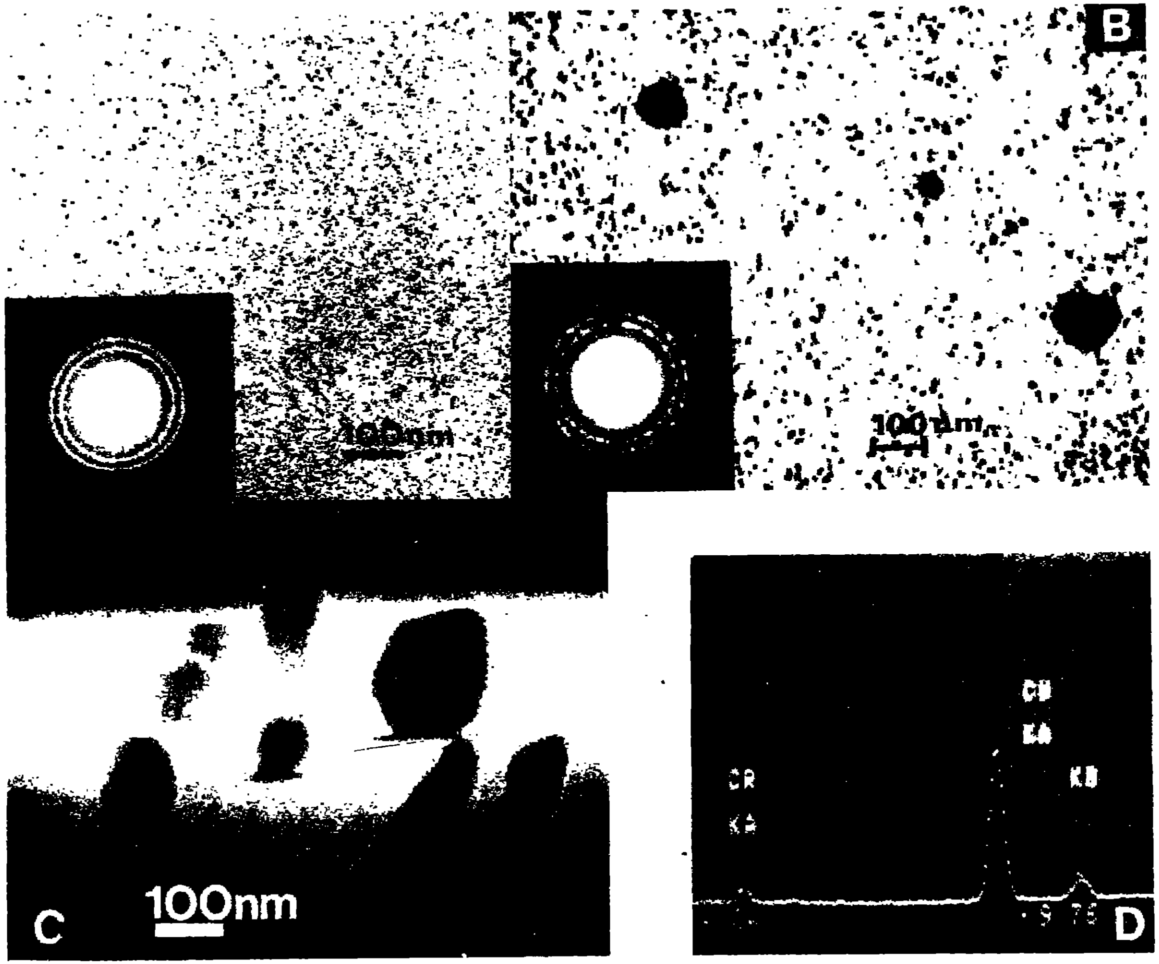

Figure 10 Stages of copper crystal growth from a sputtered Cu-6% Cr foil. The faceted growth morphologies are imaged in the

prospect of obtaining simultaneous microstructural and microchemical data on an unprecedented scale. It is equally clear that problems in specimen preparation generally exist and must be overcome by careful experimental design if the full potential of the instrument is to be realized as an aid in the study of engineering materials.

Studies currently underway at the McMaster-Toronto facility aim to exploit this potential for such diverse materials as crystalline ceramics, glasses, polymers, metallurgical coke, non-metallic inclusions and minerals, as well as a wide variety of metallic systems of interest to physical metallurgists. The unparalleled combination of analysis techniques and imaging modes offered by the STEM allows access to a new level of experimental information, and it is expected that this, in turn, will stimulate a new generation of thought in the science of materials.

Acknowledgements

The author is indebted to his colleagues at McMaster and Toronto for many stimulating discussions. Two senior research associates directly associated with the STEM, Dr Brian Robertson and Dr Derek Houghton, have contributed much to its development and application. The research was supported by grants from Energy, Mines and Resources, Canada and The Natural Sciences and Engineering Research Council, Canada.

References

Brown R, Badekas H and Purdy G R (to be published)
Gilmour J B, Purdy G R and Kirkaldy J S 1972 *Met. Trans.* 3 1455, 3213
Goldstein J I 1979 *Introduction to analytical electron microscopy* (ed) J J Hren *et al* (New York: Plenum Press) 83
Hillert M 1960 *Paraequilibrium* Internal Report of the Swedish Institute for Metals Research
Houghton D C, Weatherly G C and Embury J D (to be published)
Lowden P and Houghton D C (unpublished)
Narita K 1975 *Trans. I.S.I.J.* 15 147
Perovic V, Purdy G R and Weatherly G C 1984 (research in progress)
Solorzano-Naranjo I G and Purdy G R (unpublished)
Speich G R, Demarest V A and Miller R L 1981 *Met. Trans.* 12A 1419
Wycliffe P A, Purdy G R and Embury J D 1981 *Fundamentals of dual phase steels* (ed) R A Kot and B L Bramfitt (AIME) 59
Wycliffe P A 1981 Ph.D. Thesis, McMaster University, Hamilton, Canada

Bull. Mater. Sci., Vol. 6, No. 3, July 1984, pp. 503–512. © Printed in India.

X-ray microanalysis in the transmission electron microscope

G W LORIMER

Joint University of Manchester/UMIST, Department of Metallurgy, Grosvenor Street, Manchester, M1 7HS, England.

Abstract. The technique of x-ray microanalysis of thin specimens in the transmission electron microscope is well established. Quantitative analyses can be obtained by converting observed x-ray intensity ratios into weight fraction ratios by incorporating suitable correction factors.

Flourescence corrections in thin specimens are always significantly less than in bulk specimens and, except where strong characteristic radiation fluorescence enhancement is predicted in the bulk, can be safely ignored. As analysis probes less than 100 Å diameter have become available, the beam spreading has become an important parameter in determining the spatial resolution for analysis.

Present developments are directed at improving the quality of the analyses which can be obtained. This requires the generation of high quality correction factors, particularly for $Z < 13$, rapid and accurate methods of determining sample thickness, so that absorption corrections can be made, and the development of reliable procedures for determining the shape of the activated volume in a thin specimen.

Keywords. X-ray microanalysis; transmission electron microscopy; quantitative model; fluorescence and absorption corrections; intensity ratio; beam broadening.

1. Introduction

In a thin specimen the spatial resolution for chemical analysis is dramatically improved, compared to the bulk; the large, bell-shaped region produced by the diffusion of the electron probe beneath the surface of the specimen, from which majority of the x-rays are produced in a bulk sample, is absent in a thin foil (figure 1). If the sample is sufficiently thin to carry out quantitative transmission electron microscopy at 100 kV the activated volume is approximately a cylinder equal to the beam diameter.

2. Quantitative analysis: thin film approximation

Characteristic x-ray fluorescence and x-ray absorption in thin specimens is less than in bulk samples (figure 1). To a first approximation x-ray absorption and fluorescence can be neglected and the ratio of two observed x-ray intensities, I_A/I_B, can be related to the corresponding weight-fraction ratio, C_A/C_B, by the equation

$$C_A/C_B = k_{AB}(I_A/I_B), \tag{1}$$

where k_{AB} is a constant at a given accelerating voltage and is independent of specimen thickness and composition. k_{AB} values can be determined experimentally (Cliff and Lorimer 1975) or calculated (Goldstein *et al* 1977), by

$$k_{X\mathrm{Si}} = \frac{A_X(Q_K\omega_K a)_{\mathrm{Si}}\exp(-\mu_{\mathrm{Be}}^{\mathrm{Si}}\rho t)}{A_{\mathrm{Si}}(Q_K\omega_K a)_X\exp(-\mu_{\mathrm{Be}}^{X}\rho t)}, \tag{2}$$

where A_X and A_{Si} are atomic weights, Q_K the Green and Cosslett (1961) values of the K shell ionization cross-sections, ω_K the fluorescence yield, a the $K_\alpha/(K_\alpha+K_\beta)$ ratio (equal to one for $Z < 19$) and μ^X_{Be} and μ^{Si}_{Be} the 'effective' mass-absorption coefficients of Si and the element X in the detector window (the Be window, Si dead layer and Au contact film) of density ρ and thickness t. The ionization cross-section was assumed to be constant along the electron trajectory. A normalisation procedure, *e.g.* $\Sigma C_n = 1$, must be used to convert the ratios of the weight fractions into weight percentages. In some specimens assumptions must also be made concerning oxidation states: *e.g.* it is impossible to differentiate between Fe_3O_4 and Fe_2O_3 if ratios are measured, and oxygen cannot be detected.

The agreement between the experimental and calculated k_{AB} values is satisfactory for $Z >$ Si, (figure 2), and for these elements it would appear to be sufficient merely to

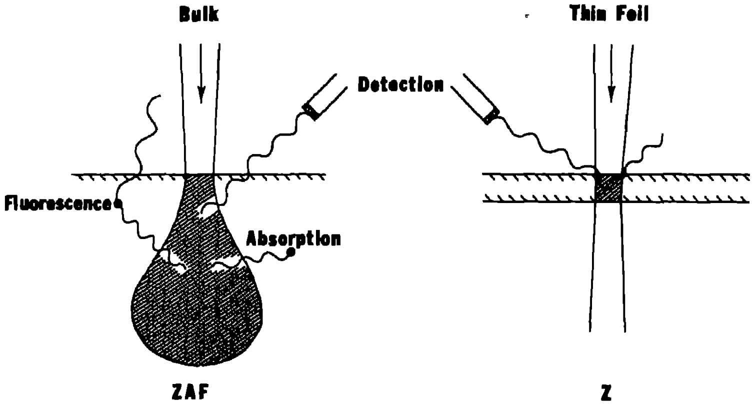

Figure 1. Schematic representation of the interaction of a high-energy electron beam with a bulk and thin-specimen. To a first approximation absorption and fluorescence effects can be ignored in the thin specimen.

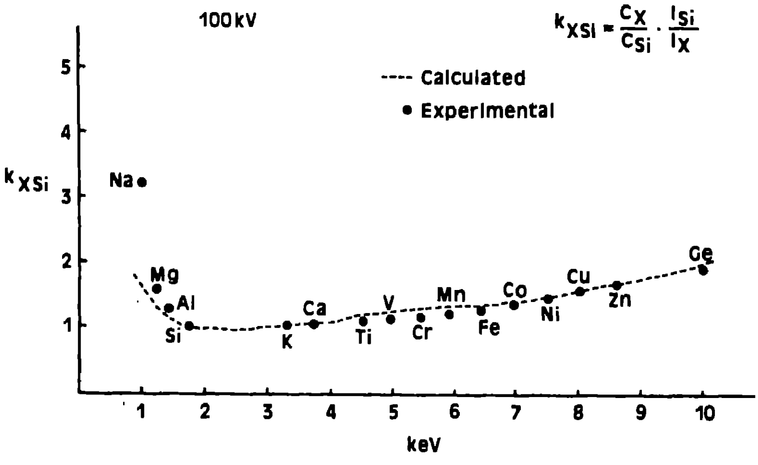

Figure 2. Comparison of calculated, Goldstein *et al* (1977), and experimental, Cliff and Lorimer (1975), k_{XSi} values at 100 kV.

calculate k_{AB} values for a given detector and accelerating voltage. The origin of the divergence between experiment and theory at low Z is not clear, but for elements Na → Si theory is particularly sensitive to parameters such as fluorescence yield (ω_K), Be window thickness etc., which are only approximately known. Another problem encountered is the loss of light elements during electron irradiation in the microscope. Figure 3 is from the work of McGill and Hubbard (1981) and shows the variation in the apparent k_{NaSi} value for a thin specimen of feldspar as a function of irradiation time.

Tables 1 and 2 are compiled from the experimental work of Wood *et al* (1981) and McGill and Hubbard (1981). They contain as good quality $k_{X\mathrm{Si}}$ values as are currently available. The McGill and Hubbard values have been extrapolated to zero time.

3. X-ray absorption in the specimen

The most important modification to the "thin film approximation" is where x-ray absorption follows the exponential law

$$I = I_0 \exp(-\mu\sigma x), \tag{3}$$

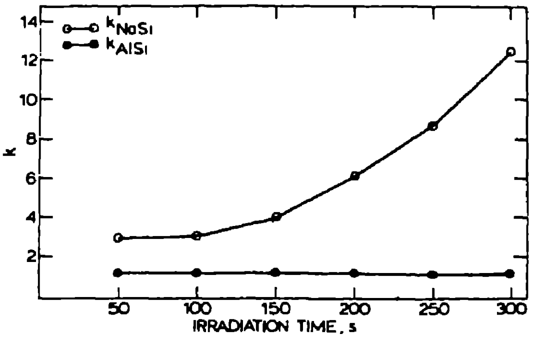

Figure 3. Variation in k_{NaSi} and k_{AlSi} with irradiation time for a feldspar (Amelia Albite). AEI EM6G, 100 kV, beam current 200 μA, beam diameter 3 μm. From McGill and Hubbard (1981).

Table 1. Comparison of experimental, I and calculated, II, $k_{A\mathrm{Si}}$ data at 120 kV.

Element	Z	I	II	Element	Z	I	II
Na	11	3·57	1·83	Ti	22	1·12	1·17
Mg	12	1·49	1·31	Cr	24	1·46	1·24
Al	13	1·12	1·14	Mn	25	1·34	1·32
Si	14	1·00	1·00	Fe	26	1·30	1·36
P	15	0·99	1·04	Ni	28	1·67	1·48
S	16	1·08	1·07	Ca	29	1·59	1·65
K	19	1·12	1·05	Mo	42	4·95	4·68
Ca	20	1·15	1·04	Ag	47	12·4	7·08

Calculated values assume $t_{\mathrm{Be}} = 7{\cdot}5\ \mu$m, $t_{\mathrm{Au}} = 0{\cdot}02\ \mu$m and $t_{\mathrm{Si}} = 0{\cdot}1\ \mu$m. From Wood *et al* (1981).

where I is the transmitted x-ray intensity, I_0 the initial x-ray intensity, μ the mass-absorption coefficient of a material of density ρ and path length x. When the *ratio* of characteristic x-ray intensities is considered, the *difference* in x-ray absorption coefficients is the important parameter. If two characteristic x-rays have similar values of μ they will be absorbed equally and their intensity ratio will be unaffected.

If t is the sample thickness and α the angle between the line of the detector and the sample surface, the x-ray intensity ratio I_A/I_B recorded by the detector will be modified by absorption in the specimen from the ratio recorded for an infinitely thin specimen, I_{0_A}/I_{0_B} (no absorption), as given in (4). The x-ray path length x is shown in figure 4.

$$\frac{I_A}{I_B} = \frac{I_{0_A}}{I_{0_B}} \frac{\mu_B\,[1-\exp(-\mu_A \rho t \csc\alpha)]}{\mu_A\,[1-\exp(-\mu_B \rho t \csc\alpha)]}, \tag{4}$$

where μ_A and μ_B are the mass absorption coefficients of the characteristic radiation in the sample of density ρ. The predicted effect of absorption in the specimen on the x-ray intensity ratios for orthopyroxene, a silicate mineral, is shown in figure 5.

In order to make an absorption correction it is necessary to know the x-ray path length within the specimen. There are various methods of determining the thickness of a sample, but it may be difficult to determine the x-ray path length with any degree of accuracy. This is particularly true for electrolytically or ion-beam-thinned samples which can be irregularly wedge-shaped. This problem has been discussed in detail by Goldstein and Williams (1981) who illustrated the large errors which could arise during the analysis of a NiAl sample if the shape of the foil and its orientation relative to the x-ray detector were not known (figure 6).

Table 2. Comparison of experimental and calculated $k_{A\mathrm{Si}}$ data at 100 kV.

Element	Z	I	II	III
Na	11	3·2	2·85	2·02
Mg	12	1·6	1·67	1·39
Al	13	1·2	1·15	1·16
Si	14	1·0	1·00	1·00
K	19	1·0	1·10	1·08
Ca	20	1·0	1·08	1·11

I. Cliff and Lorimer (1975); II. McGill and Hubbard (1981); III. Calculated values. These assume $t_{\mathrm{Be}} = 8\ \mu\mathrm{m}$, $t_{\mathrm{Au}} = 0{\cdot}02\ \mu\mathrm{m}$ and $t_{\mathrm{Si}} = 0{\cdot}1\ \mu\mathrm{m}$.

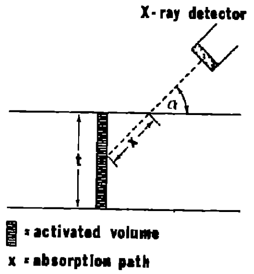

Figure 4. Geometry used for the calculation of absorption in the specimen. X is the absorption path length.

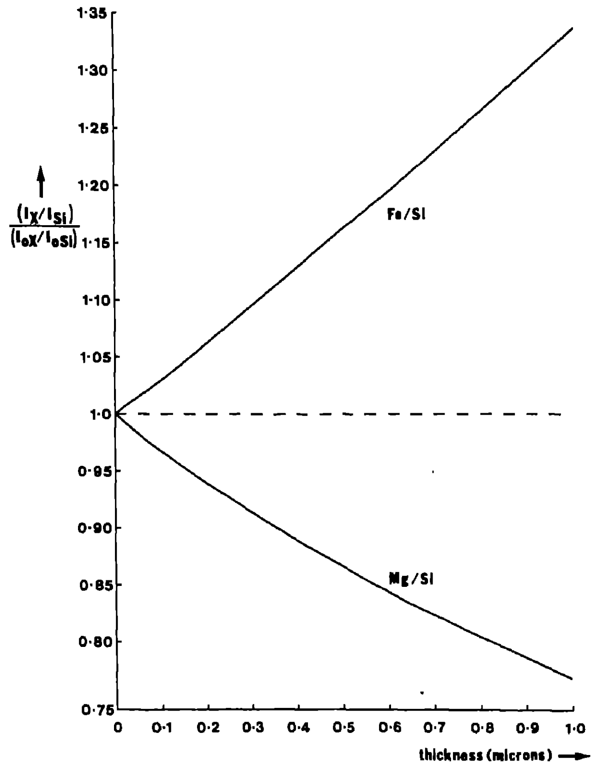

Figure 5. Effect of specimen thickness on x-ray intensity ratios for an orthopyroxene, $MgFeSi_2O_6$.

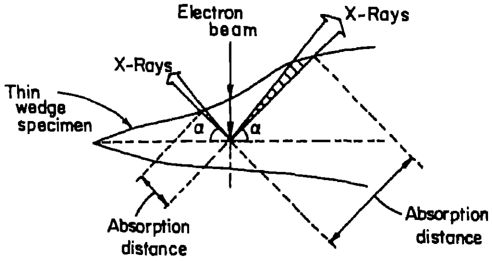

Figure 6. Possible absorption path lengths, depending on the position of the x-ray detector. From Goldstein and Williams (1981).

Figure 7 shows the observed variation in $\ln(I_{\mathrm{SiK}}/I_{\mathrm{FeK}\alpha})$ as a function of specimen thickness for a 2 wt% Si eutectoid steel which had been quenched to produce a martensitic microstructure of uniform composition. The line has a slope, as determined from least squares analysis, equal to 2090 $cm^2\ g^{-1}$. This is the approximate difference between the x-ray mass-absorption coefficients of iron (2502 $cm^2\ g^{-1}$) and silicon (710 $cm^2\ g^{-1}$) x-rays in the specimen, a value that is in agreement with that predicted in (4).

4. Effects of fluorescence in the specimen

Fluorescence due to the continuum, generally ignored in bulk samples, can be similarly ignored in thin foils, moreover it is usually safe to assume that characteristic fluorescence is also very small. However, when strong characteristic fluorescence is predicted in an equivalent bulk specimen, it is necessary to account for it in the thin specimen as well. Fluorescence in thin specimens has been discussed by Philibert and Tixier (1975), Lorimer *et al* (1977) and Nockolds *et al* (1979).

The model used by Nockolds *et al* (1979) for calculating the fluorescence correction is shown in figure 8. This predicts that in a thin, binary specimen AB the intensity of A radiation $\mathrm{d}I_F^A$ fluoresced in the annulus by B radiation from point P is given by

$$\mathrm{d}I_F^A = \frac{I_B}{T} C_A \mu_B^A \frac{r_A - 1}{r_A} \omega_{K_A} \exp(-\mu_B \sec\phi\rho z) \tan\phi \, \mathrm{d}s \, \mathrm{d}\rho z \, \mathrm{d}\phi. \tag{5}$$

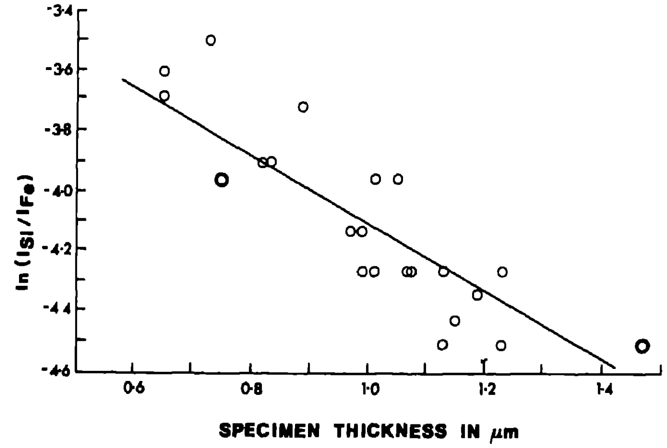

Figure 7. $\ln(I_{\mathrm{Si}K}/I_{\mathrm{Fe}K\alpha})$ *vs* thickness for a 2 wt % Si steel. From Lorimer *et al* (1977).

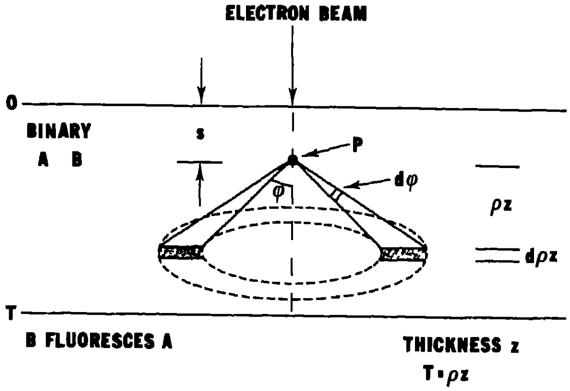

Figure 8. Model used for fluorescence correction. From Nockolds *et al* (1979).

Assuming symmetry about the centre of the foil, integration over the mass thickness T (g cm^{-2}) gives the total intensity I_F^A

$$I_F^A = I_B \frac{T}{2} |0{\cdot}923 - \ln(\mu_B T)| C_A \mu_B^A \omega_{K_A} \frac{r_A - 1}{r_A}, \qquad (6)$$

μ_B^A and μ_B are the mass absorption coefficients of X-radiation from element B in element A and the specimen, respectively. C_A is the weight fraction of element A, ω_{K_A} is the fluorescence yield of element A and r_A is the absorption-edge jump-ratio. The ratio of characteristic x-ray intensities I_A and I_B can be calculated using the formula for K-shell ionisation cross-sections proposed by Green and Coslett (1961), and used to modify (6) to give the fluorescence enhancement ratio for A radiation I_F^A/I_A in a thin foil

$$\frac{I_F^A}{I_A} = C_B \cdot \omega_{K_B} \cdot \frac{r_A - 1}{r_A} \cdot \frac{A_A}{A_B} \cdot \mu_B^A \cdot \frac{U_B \ln U_B}{U_A \ln U_A} \cdot \frac{T}{2} |0{\cdot}923 - \ln(\mu_B T)|, \qquad (7)$$

where U_A and U_B are the overvoltage ratios for elements A and B respectively, and A_A and A_B are the relevant atomic weights. (Note that if the sample is tilted through an angle α then expression (7) must be multiplied by sec α to allow for the resultant increase in I_B).

It is possible, using (7), to evaluate the fluorescence contribution from many fluorescing elements in the specimen. Thus by summing the individual contributions the total fluorescence enhancement of a particular element can be calculated and the necessary correction can be made.

5. Surface films

The work of Morris *et al* (1977) and others on aluminium alloys has clearly shown that during electropolishing solute-rich layers can be formed on the surface of the specimen, and that these will produce a marked change in the I_X/I_{Al} ratio near the edge of the specimen. Similar effects have been observed also on electropolished samples of steels. Figure 9 shows the effect in a thin martensitic specimen of 2 wt % Si eutectoid steel. The

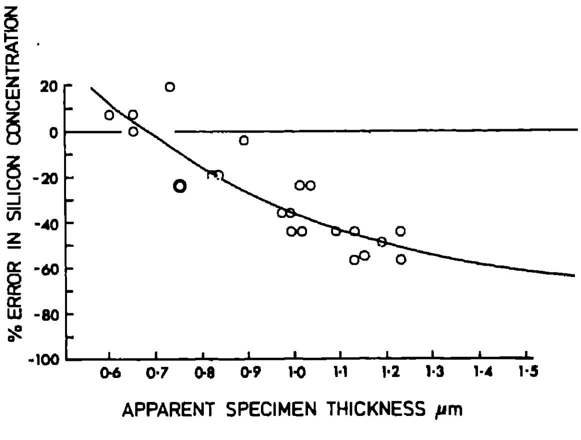

Figure 9. Error in measured concentration of silicon as function of specimen thickness for martensitic foil of 2 wt % Si eutectoid steel. The apparent increase in Si concentration at edge of foil is due to presence of Si-rich surface film. From Ridley and Lorimer (1981).

apparent silicon concentration is less than 2 % in the thicker regions of the foil, due to the preferential absorption of Si K radiation (discussed above) but near the edge of the sample the effect is reversed: *i.e.* the apparent silicon content is greater than 2 wt %.

In this and other steel specimens it has been found that the solute-rich layer can be removed by exposing the electropolished specimen to a 10–15 min treatment in an ion beam thinning apparatus (4 kV, 20 to 25° inclination).

6. Beam broadening in the specimen

Beam spreading in thin foils is currently a lively topic of both experimental investigation and theoretical analysis (refer Goldstein and Williams 1981; Doig *et al* 1981; Cliff and Lorimer 1981 which summarize the present state-of-the art).

A simple approach to the problem of beam spreading has been proposed by Goldstein *et al* (1977) who assumed that a single, elastic scattering event occurred at the centre of the foil and defined the x-ray source size as that volume in which 90 % of the electron trajectories lie. The beam broadening b, from a point probe is given by:

$$b = 6{\cdot}25 \times 10^5 \frac{Z}{E_0}\left(\frac{\rho}{A}\right)^{1/2} t^{3/2}\ \text{cm}, \tag{8}$$

where Z is the atomic number, E_0 the accelerating voltage, ρ the density, A the atomic weight and t the sample thickness. Equation (8) was derived for a single scattering event, and hence is strictly valid for only very thin foils, but it agrees moderately well with the Monte-Carlo calculations of Kyser (1979), Geiss and Kyser (1979) and Newbury and Myklebust (1979) and the few experimental measurements of beam broadening, Hutchings *et al* (1979) and Cliff and Lorimer (1981). Cliff and Lorimer (1981) have shown that the expression of Goldstein *et al* (1977) corresponds exactly to one limit predicted by plural scattering theory, that of a Gaussian distribution of scattering events, while the other limit, a single scattering event, predicts less broadening and coincides with Monte-Carlo calculations.

It is essential to know the electron intensity distribution in the incident probe if beam broadening in the specimen is to be calculated and the activated volume for x-ray microanalysis to be determined. The electron intensity distribution in the probe is often assumed to be Gaussian (Doig *et al* 1981), but this is often not the true situation. Figure 10 shows a microdensitometer trace of a micrograph of the analysis probe in a Philips EM400T operating in the TEM nanoprobe mode, 100 kV, eucentric position, spot size 6. A Gaussian distribution is superimposed on the experimentally measured profile. The experimental probe has a long, non-Gaussian, tail which, in the illustration, contains a significant proportion of the total current (the true three-dimensional ratio of 'tail' to 'probe' current is larger than the apparent ratio in the two-dimensional profile shown in figure 10.* The ratio of the electron intensity distribution in the 'tail' to that in the 'probe' depends on the convergence angle of the beam. A highly convergent beam, which produces the smallest possible 'probe', for a given set of operating conditions, also produces a large 'tail'. With a less convergent beam the 'tail' can be dramatically reduced, although the 'probe' diameter is increased. The origin of the 'tail'

---

* This distribution of electron intensity in the analysis probe is not unique to the EM400T. It is an inherent characteristic of any highly convergent probe-forming system.

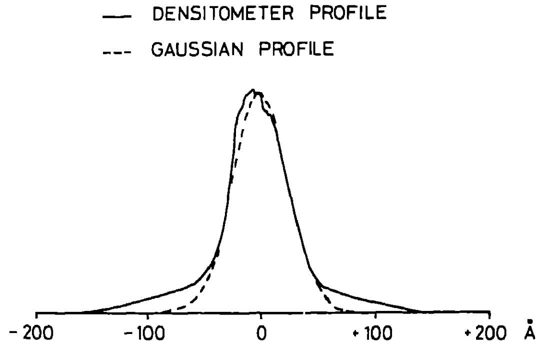

Figure 10. Microdensitometer profile of a focussed probe with a Gaussian profile superimposed. From Lorimer (1981).

is thought to be due to a combination of the high degree of illumination convergence and spherical aberration.

7. Summary

The physics of x-ray production, absorption and detection is moderately well-understood, and it has been applied to develop a model for the quantitative x-ray microprobe analysis of thin specimens. The major correction to the simple 'ratio' technique is that of x-ray absorption within the specimen, and this can be made if the sample thickness is known. With the availability of analysis probes of less than 10 nm in diameter, beam spreading within the specimen provides the ultimate limit to spatial resolution for chemical analysis. If 'true' concentration profiles on the nm scale are to be determined it is important to know the electron intensity distribution within the analysis probe, a distribution which may not be Gaussian.

References

Cliff G and Lorimer G W 1975 *J. Microsc.* **103** 203

Cliff G and Lorimer G W 1981 *Quantitative microanalysis with high spatial resolution* (eds) G W Lorimer, M Jacobs and P Doig (London: Metals Society) p. 47

Doig P, Lonsdale D and Flewitt P E J 1981 *Quantitative microanalysis with high spatial resolution* (eds) G W Lorimer, M Jacobs and P Doig (London: Metals Society) p. 41

Geiss R H and Kyser D 1979 *Ultramicroscopy* **3** 397

Goldstein J I, Costley J L, Lorimer G W and Reed S J B 1977 *Quantitative x-ray analysis in the electron microscope, Proc. Workshop on Analytical E M* (ed) O Johari (Chicago: IITRI) p. 315

Goldstein J I and Williams D B 1981 *Quantitative microanalysis with high spatial resolution* (eds) G W Lorimer, M Jacobs and P Doig (London: Metals Society) 5

Green M and Cosslett V E 1961 *Proc. Phys. Soc.* **71** 1206

Hutchings R, Loretto M H, Jones I P and Smallman R E 1979 *Ultramicroscopy* **3** 401

Kyser D F 1979 *Introduction to analytical electron microscopy* (eds) J J Hren, J I Goldstein and D C Joy (New York: Plenum) p. 199

Lorimer G W, Al-Salman S A and Cliff G 1977 *Developments in Electron Microscopy and Analysis* (ed) D C Misell (London: Institute of Physics) 369

Lorimer G W 1981 *Developments in electron microscopy and analysis* (ed) M J Goringe (London: Institute of Physics) p. 147

McGill R J and Hubbard F H 1981 *Quantitative microanalysis with high spatial resolution* (eds) G W Lorimer, M Jacobs and P Doig (London: Metals Society) 30

Morris P L, Davies N C and Treverten J A 1977 *Developments in electron microscopy and analysis* (ed) D C Misell (London: Institute of Physics) 374

Newbury D E and Myklebust 1979 *Ultramicroscopy* **3** 391

Nockolds C, Nasir M J, Cliff G and Lorimer G W 1979 *Developments in electron microscopy and analysis* (ed) T Mulvey (London: Institute of Physics) 417

Philibert J and Tixier R 1975 *Physical aspects of electron microscopy and microbeam analysis* (eds) B M Siegel and D R Beaman (New York: Wiley) 333

Ridley N and Lorimer G W 1981 *Quantitative microanalysis with high spatial resolution* (eds) G W Lorimer, M Jacobs and P Doig (London: Metals Society) 80

Wood J, Williams D B and Goldstein J I 1981 *Quantitative microanalysis with high spatial resolution* (eds) G W Lorimer, M Jacobs and P Doig (London: Metals Society) 24

Bull. Mater. Sci., Vol. 6, No. 3, July 1984, pp. 513–535. © Printed in India.

Analytical electron microscopy of aluminium alloys

T R RAMACHANDRAN*, D C HOUGHTON and J D EMBURY

Department of Metallurgy and Materials Science, McMaster University, Hamilton, Ontario, Canada

*Department of Metallurgical Engineering, Indian Institute of Technology, Kanpur 208 016, India

Abstract. X-ray microanalysis and electron energy loss spectroscopy of thin foils constitute the important techniques of high resolution chemical analysis using the electron microscope. The technique of x-ray microanalysis is discussed in this paper with particular emphasis on the study of aluminium alloys using a dedicated scanning transmission electron microscope (STEM).

The principle of determining chemical composition from observed x-ray peak intensities including the absorption of x-rays and beam broadening in thin foils are considered. The accuracy of peak intensity measurement and detection limits in x-ray microanalysis are illustrated with reference to Al-Mn alloys. The Cliff-Lorimer (*k*) factors for manganese, iron and copper with respect to aluminium were obtained from standard samples. Identification of phases in 1100 and 1200 aluminium and 3008 (Al-Mn-Zr) alloy were carried out from measured intensities of x-ray peaks. The experimental results emphasize the value of developing techniques for extracting the particles from the aluminium matrix. The transition phases formed in Al-6 % Zn-3 % Mg and Al-4 % Cu were investigated by micro-diffraction and x-ray microanalysis.

Keywords. High resolution analysis; x-ray microanalysis; aluminium alloy; phase identification; metastable phases.

1. Introduction

High resolution chemical analysis of thin foils examined in the electron microscope is carried out by the detection and quantitative characterization of x-rays and inelastically scattered electrons. X-ray microanalysis involves the detailed study of the energy (or wavelength) and intensity of characteristic x-rays while electron energy loss spectroscopy is concerned with the determination of characteristic energy losses suffered by the primary electrons as they pass through the specimen. The energy loss arises from a number of excitation processes amongst which electrons causing plasmon excitation and inner shell ionization are useful in providing chemical information. The important parameters in chemical analysis are the intensity of signals arising from the interaction of the electron beam with the specimen and the volume of the specimen from which these signals are excited. The former influences the accuracy and sensitivity of analysis while the latter determines the spatial resolution. High sensitivity and high resolution chemical analysis, therefore, requires the use of a high intensity small diameter electron probe. This is obtained by the use of a scanning attachment to the TEM or a dedicated STEM. The use of a highly convergent probe also allows the formation of microdiffraction patterns which provide crystallographic information from regions of the specimen illuminated by the probe.

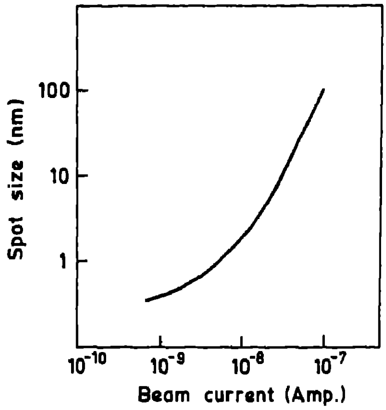

Figure 1. Relationship between beam current and beam diameter in the HB5 STEM.

The dedicated STEM makes use of a field emission gun. The gun brightness of this source is high ($\sim 10^{13}$ A/m^2/Sr) and it is thus possible to form an extremely fine probe carrying enough current to excite detectable signals from the specimen. The relationship between beam current and beam diameter in the VG HB5 STEM is shown in figure 1 (Williams 1980). A probe of ~ 2–5 nm diameter carries a current of ~ 5 nA sufficient to produce significant signal count rates. It should, theoretically, be possible to carry out chemical analysis with the same spatial resolution as the probe size. However, complications due to beam broadening (to be discussed later) affect the resolution. Microdiffraction patterns can be obtained from regions of ~ 2 nm diameter using the fine probe of the dedicated STEM. This topic has been covered at length by Cowley (1982) at this conference.

The principles of x-ray microanalysis are considered briefly in this paper followed by experimental results on phase identification and the nature of metastable phases in aluminium-base alloys.

2. Theoretical principles

2.1 *The ratio technique*

X-ray microanalysis involves the measurement of the intensity I_A of a characteristic x-ray peak and relating it to the total number of atoms, N_A, in the irradiated volume of the specimen exciting this particular radiation. I_A and N_A are related by the expression (Joy 1981),

$$I_A = I_0 N_A Q_A a_A w_A F, \tag{1}$$

where I_0 is the incident electron intensity, Q_A is the scattering cross-section for x-ray excitation, w_A is the fluorescent yield, a_A is the ratio of the number of $K\alpha$ (or $L\alpha$) x-ray photons to the sum of the total number of photons of the K (or L) series and F is the detection efficiency. It is assumed in (1) that the sample is so thin that absorption and fluorescence effects can be neglected. These two assumptions constitute the thin film criterion. N_A can be expressed in terms of the weight fraction C_A, atomic weight of A, A_A, thickness t of the foil and ρ the density of the foil—(1) can then be written as

$$I_A = \frac{(\text{Constant})\,(C_A Q_A a_A w_A F)}{A_A}. \tag{2}$$

If the intensities of two peaks due to elements A and B are simultaneously measured, the intensity ratio can be expressed by the equation,

$$\frac{I_A}{I_B}=\frac{C_A Q_A a_A w_A A_B}{C_B Q_B a_B w_B A_A}=\frac{C_A}{C_B}(k_{AB})^{-1}, \tag{3}$$

where k_{AB} (commonly referred to as the Cliff-Lorimer factor) is a constant independent of sample thickness, orientation and composition but dependent on accelerating potential. Equation (3) forms the basis of the ratio technique for the determination of composition from observed intensity ratio of the peaks (Philibert and Tixier 1968; Cliff and Lorimer 1975).

2.2 *Absorption of x-rays*

The thin beryllium window, the gold contact layer and the inactive silicon layer on the detecting crystal can absorb a significant proportion of the incident x-rays (particularly the soft x-rays). A correction for absorption in the beryllium window can be made by using the expression,

$$\frac{I_A}{I_B}=\frac{C_A Q_A w_A a_A A_B}{C_B Q_B w_B a_B A_A}\left[\frac{\exp-(\mu/\rho)^B_{\mathrm{Be}}\rho_{\mathrm{Be}}t_{\mathrm{Be}}}{\exp-(\mu/\rho)^A_{\mathrm{Be}}\rho_{\mathrm{Be}}t_{\mathrm{Be}}}\right], \tag{4}$$

where $(\mu/\rho)^A_{\mathrm{Be}}$ and $(\mu/\rho)^B_{\mathrm{Be}}$ are the mass absorption coefficients of the characteristic x-rays in beryllium, ρ_{Be} is the density of beryllium and t_{Be} the thickness of the window (typically 7 μm).

When the thin film criterion is not valid, absorption correction can be made by the use of the expression (Tixier and Philibert 1969; Goldstein *et al* 1977)

$$\frac{C_A}{C_B}=k_{AB}(I_A/I_B)_{TK}\left[\frac{(\mu/\rho)^A_{\mathrm{sp}}}{(\mu/\rho)^B_{\mathrm{sp}}}\right]\left[\frac{1-\exp-(\mu/\rho)^B_{\mathrm{sp}}\rho t\operatorname{cosec}\psi}{1-\exp-(\mu/\rho)^A_{\mathrm{sp}}\rho t\operatorname{cosec}\psi}\right] \tag{5}$$

where $(\mu/\rho)^A_{\mathrm{sp}}$ and $(\mu/\rho)^B_{\mathrm{sp}}$ are the mass absorption coefficients of the characteristic x-rays in the specimen, ρ is the specimen density, t is the specimen thickness and ψ is the x-ray take-off angle. In the VG HB5 STEM ψ varies from 15 to 42 depending on the use of the non-tilt—or double tilt cartridge. The ratio $(I_A/I_B)_{TK}$ measured in thick specimens defines the constant K^{thick}_{AB} which is related to K_{AB} by the expression,

$$\frac{C_A/C_B}{(I_A/I_B)_{TK}}=K^{\mathrm{thick}}_{AB}=K_{AB}\left[\frac{(\mu/\rho)^A_{\mathrm{sp}}}{(\mu/\rho)^B_{\mathrm{sp}}}\right]\left[\frac{1-\exp-(\mu/\rho)^B_{\mathrm{sp}}\rho t\operatorname{cosec}\psi}{1-\exp-(\mu/\rho)^A_{\mathrm{sp}}\rho t\operatorname{cosec}\psi}\right] \tag{6}$$

The ratio of K^{thick}_{AB} to K_{AB} is plotted in figure 2 for the compounds $\mathrm{Al_6Mn}$, $\mathrm{Al_2Cu}$ and $\mathrm{Al_3Fe}$ using the data for mass absorption coefficients from Heinrich (Heinrich 1966). The absorption correction is significant when the thickness exceeds ~ 200 nm and also for low take-off angle.

2.3 *Beam broadening effects*

The spatial resolution for x-ray microanalysis is influenced by the probe size and the broadening of the probe in the specimen. Goldstein *et al* (1977) have considered elastic scattering of a point source of electrons by atomic nuclei at the middle of the foil and

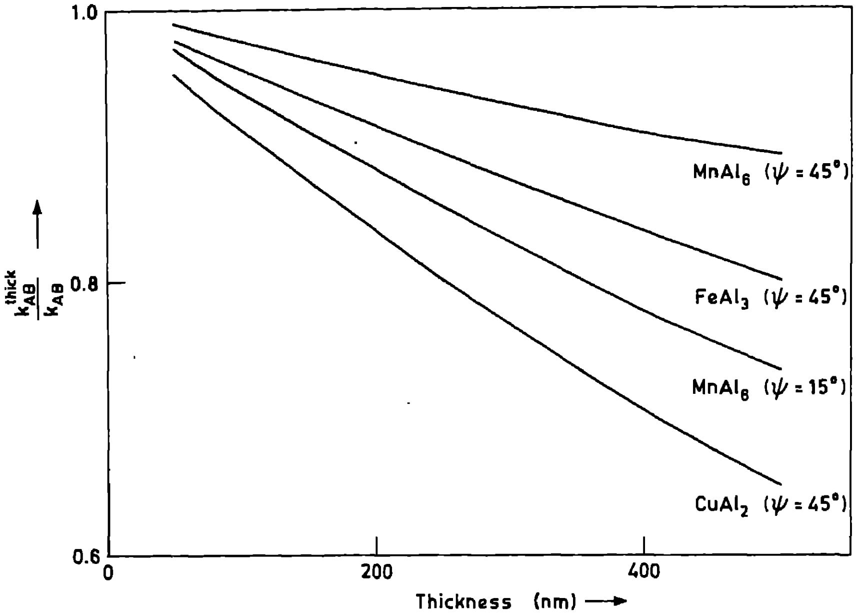

Figure 2. Relationship between $K_{AB}^{\rm thick}/K_{AB}$ and thickness of the foil for Al_6Mn, Al_3Fe and Al_2Cu. The effect of varying the take off angle is illustrated for Al_6Mn.

arrived at the following expression for beam broadening (*b*)

$$b = 625\,(Z/E)\,(\rho/A)^{1/2}t^{3/2} \tag{7}$$

where *b* and *t* are in cm and *Z* is the atomic number. A plot of beam spread against thickness is shown in figure 3 for aluminium. When the specimen thickness exceeds 200 nm, the spatial resolution for chemical analysis is ~ 30 nm. It is, therefore, clear that the advantage of using a fine probe as in the STEM may be counteracted by the use of relatively thick specimens. Beam spread has also been determined by using Monte-Carlo calculations (Keyser 1979) involving the simulation of individual electron trajectories. The results obtained are in excellent agreement with those predicted in (7) when the specimen thickness is less than 100 nm.

2.4 *Precision and detection limits*

The error in estimating the net intensity of an x-ray peak, I_A^n, can be expressed by the standard deviation, $\sigma(I_A^n)$, as

$$\sigma(I_A^n) = (I_A^t + I^b)^{1/2} \tag{8}$$

where I_A^t represents the total intensity collected in a predefined energy window and I^b is the background intensity. The relative error ε for 95 % confidence limit can be expressed as

$$\varepsilon = \frac{2\sigma(I_A^n)}{I_A^n} = 2\left[\frac{1}{I_A^n}\left(1+\frac{2}{P/B}\right)\right]^{1/2}, \tag{9}$$

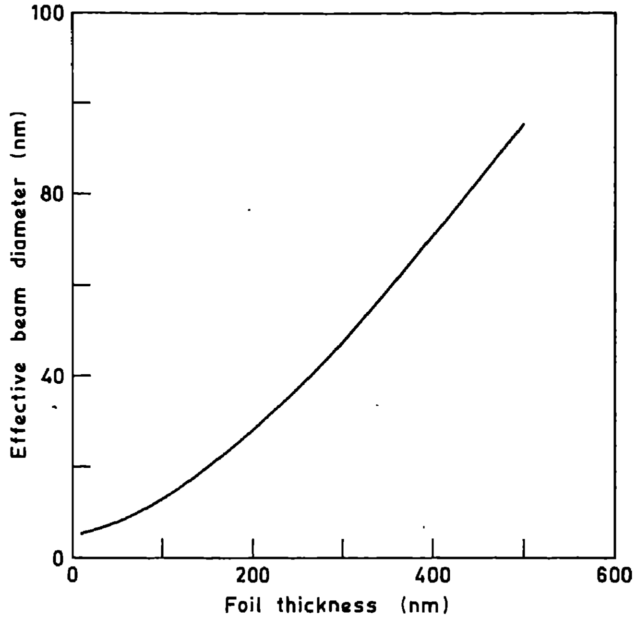

Figure 3. Variation of beam spread with foil thickness using the elastic scattering approximation.

where P/B is the net peak to background intensity ratio. The total relative error in the measurement of net intensities of two characteristic peaks ε_{AB} is then given by

$$\varepsilon_{AB} = 2\left[\frac{1}{I_A^n}\left\{1+\frac{2}{(P/B)_A}\right\}+\frac{1}{I_B^n}\left\{1+\frac{2}{(P/B)_B}\right\}\right]^{1/2}. \tag{10}$$

The total relative error in the measurement of peak intensities of manganese and aluminium is plotted in figure 4 as a function of peak to background ratio, for two values of aluminium peak intensities. The relative error is large (~ 13 %) for an aluminium count of 1000. A counting time of 100 sec gives rise to peak intensities of aluminium of ~ 10000 in the HB5 STEM; under these circumstances the error in peak intensity measurement is ~ 4 %.

The sensitivity limits for chemical analysis are defined by the minimum detectable mass (MDM) and minimum mass fraction (MMF). MDM represents the sensitivity in analyzing fine particles on extraction replicas or sputtered thin films. It is inversely proportional to the x-ray count time and electron current density. The electron current density in STEM is 10^4 A/cm^2 for a 10 nm probe (Oppolzer and Knauer 1979). This is about 2 to 3 orders of magnitude larger than that obtained with a conventional tungsten filament. Hence the MDM is much smaller in the STEM. The minimum mass fraction is a measure of the sensitivity of detecting one element in the presence of another. It is important in analyzing precipitates or composition gradient. MMF is limited by the continuous radiation arising from the excited volume. In order to distinguish a peak from the background the peak intensity I_A must be greater than

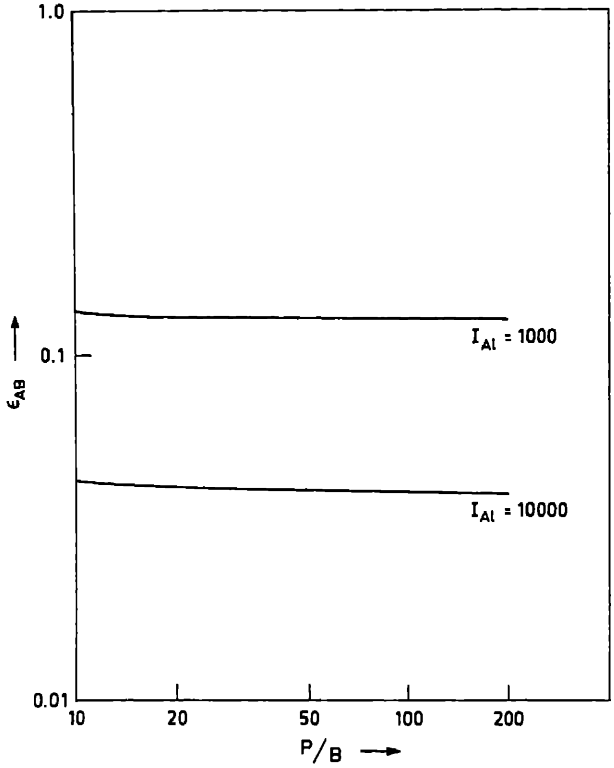

Figure 4. Dependence of the total relative error in the measurement of peak intensities on the peak to background (P/B) ratio. The mean value of 0·35 is used in the calculations for $I_{\mathrm{MnK}\alpha}/I_{\mathrm{AlK}\alpha}$.

$3(2I_A^b)^{1/2}$ where I_A^b is the background intensity in the energy region containing the peak of element A. Hence MMF can be expressed as,

$$(C_A/C_B)_{\min} = k_{AB}\frac{3(2I_A^b)^{1/2}}{I_B^n}. \tag{11}$$

Assuming that $I_B^b \simeq I_A^b$ (*i.e.* a constant background in the energy interval containing the peaks due to A and B),

$$(C_A/C_B)_{\min} = 3(2I_B^n \cdot P/B)^{-1/2} k_{AB}. \tag{12}$$

Using (12) the minimum weight fraction of manganese detectable in aluminium is plotted in figure 5 for total counts of aluminium of 5000, 10000 and 50000 as a function of peak to background ratio. A value of 0·97 is used in the calculations for $k_{\mathrm{Mn\text{-}Al}}$. For typical P/B values of 50–100 and total aluminium counts exceeding 10000, the minimum detectable weight fraction of manganese in aluminium is ~ 0·2–0·4%.

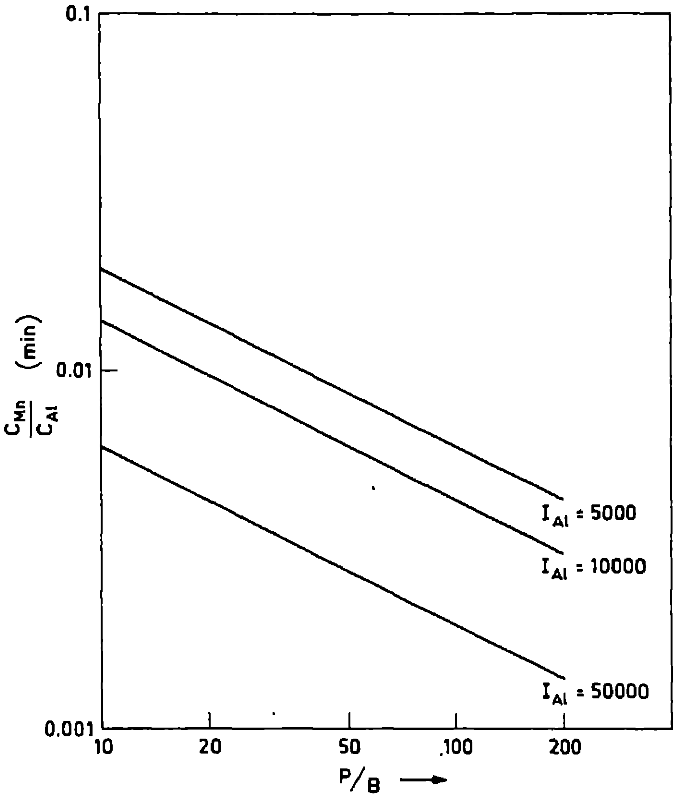

Figure 5. Variation of the minimum weight fraction of Mn detectable in Al with the peak to background ratio.

3. Experimental procedure

Cliff-Lorimer factors have been measured on a set of standard Al-Mn, Al-Fe and Al-Cu alloys supplied by the Alcan Laboratories, Kingston. Phase identification has been carried out on cold-rolled (~ 90%) and annealed (at 873 K) 1100 Al, 1200 Al and 3008 aluminium alloy. The composition of these alloys and the treatments given are shown in table 1. The nature of metastable phases has been studied in Al-6% Zn-3% Mg and Al-4% Cu alloys. Details of thermal treatments to which these alloys were subjected are also shown in table 1. The samples were chemically thinned in a mixture of orthophosphoric acid, sulphuric acid and nitric acid followed by electropolishing in a Struers Tenupol unit using methanol (90% by vol) and perchloric acid (10% by vol). They were heated for 300 sec at 373 K in the prevacuum of the STEM prior to examination. X-ray spectra were obtained from the phases using a typical count time of 100 sec.

The results of x-ray microanalysis can be complicated by surface films on thin foils or the appearance of 'systems peaks'. Surface films lead to abnormal intensity ratio near the edge of the foil. This effect has been observed in a number of aluminium-base alloys.

Table 1. Composition and thermal treatment of aluminium alloys.

System	Composition	Treatment
1100 Al	Fe 0·55% Si 0·15% Al 99·0% min.	Hunter cast – Cold rolled 90% annealed at 873 K for 1 h
1200 Al	-do- + small amount of chromium	-do-
3008 alloy	Mn 1·38%, Fe 0·46% Si 0·12%, Zr 0·29% Cu 0·09%, Ti 0·016% balance Al.	-do-
Al-Zn-Mg	Al-6% Zn-3% Mg	Solution treated at 748 K 1 hr quenched to 473 K for 1 min. and then maintained at 294 K for 1 min., aged at 448 K
Al-Cu	Al-4% Cu	Solution treated at 798 K for 24 hr in vaccum, quenched in water and aged at 513 K for 4 h.

Careful examination of the standard samples and commercial aluminium alloys reveal no significant difference in intensity ratio at the foil edge. The origin of 'systems peaks' and the methods of minimizing them are discussed in detail by Zaluzec (1979), X-ray counts from holes present in the particles show that the total hole count is less than 1% of that measured in the thinnest region of the particle—consequently complications due to system peaks can be ignored.

4. Results

4.1 *Determination of K values*

The microstructure of the standard Al-Mn and Al-Cu alloys and the x-ray spectra from the particles are presented in figures 6 and 7. The Al-Mn alloy reveals irregularly-shaped particles while those in Al-Cu are in the form of discs or are irregularly shaped. The intensity ratio, $I_{\mathrm{MnK}\alpha}/I_{\mathrm{AlK}\alpha}$ is constant in the various regions of the particle and also for a large number of particles. The mean value of the intensity ratio is $0{\cdot}35 \pm 0{\cdot}01$. Selected area diffraction patterns obtained in the TEM and STEM reveal that these particles are Al_6Mn. These two results are used to obtain a k value (the Cliff–Lorimer factor) of $0{\cdot}97 \pm 0{\cdot}03$. The results obtained from the Al-Cu and Al-Fe alloys show considerable scatter possibly because of the fact that the particles do not occupy the entire thickness of the foil. Analysis of selected area diffraction patterns indicates that the particles are $CuAl_2$ and $FeAl_3$. The k values obtained in this study are presented in table 2 along with other available data based on theoretical calculations and experimental measurements. The results are in good agreement with the theoretical calculations by Goldstein *et al* (1977) and Zaluzec (1979) and experimental measurements of Cliff and Lorimer (1975) and Woods *et al* (1981).

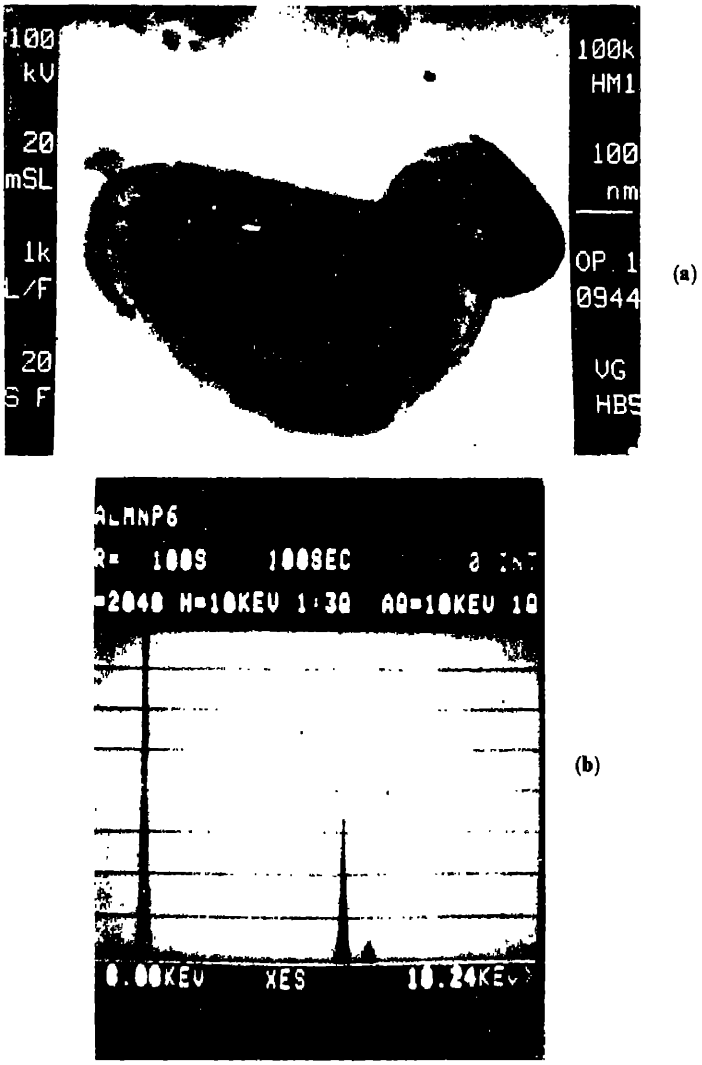

Figure 6. **a.** Typical STEM micrograph of Al_6Mn particle in the standard Al-Mn alloy. **b.** X-ray spectrum from the particle showing AlK, MnKα and MnKβ peaks.

4.2 *Phase identification*

Commercially pure aluminium contains the following binary and ternary phases (Porter and Westengen 1981); Al_3Fe (monoclinic), Al_6Fe (C-centred orthorhombic), Al_mFe (body-centred tetragonal), Al_2Fe (unknown structure characterized by highly irregular diffraction patterns), α-AlFeSi (b.c.c.), α' AlFeSi (hexagonal), α'' AlFeSi (tetragonal) and β' AlFeSi (monoclinic).

X-ray spectra from one of the particles and the matrix in 1200 aluminium are shown in figure 8. The particle shows prominant peaks due to Al, Si, Cr and Fe. Several particles show only Al, Cr and Fe peaks. The intensity ratios, *viz* $I_{SiK\alpha}/I_{AlK\alpha}$, $I_{CrK\alpha}/I_{AlK\alpha}$ and

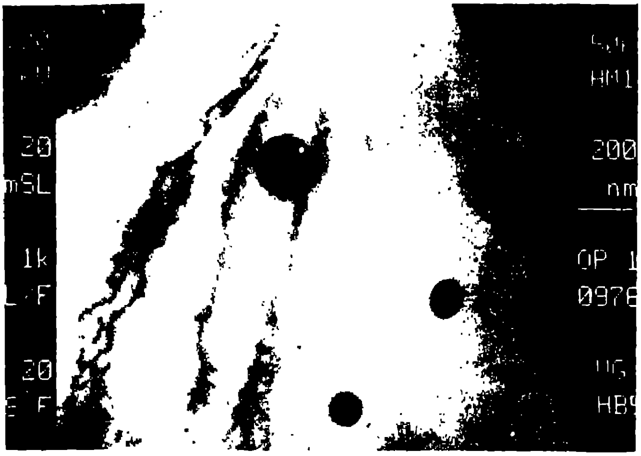

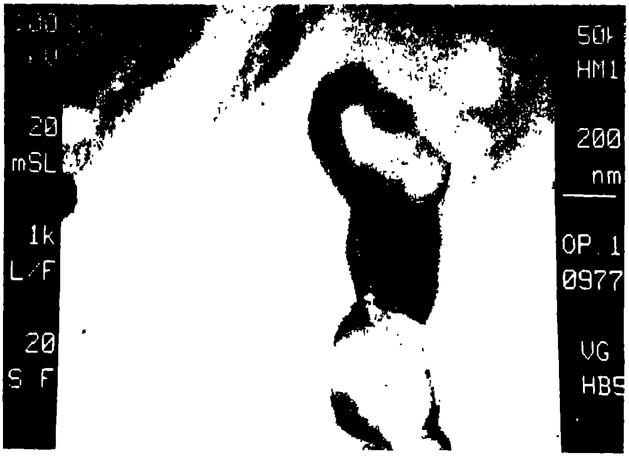

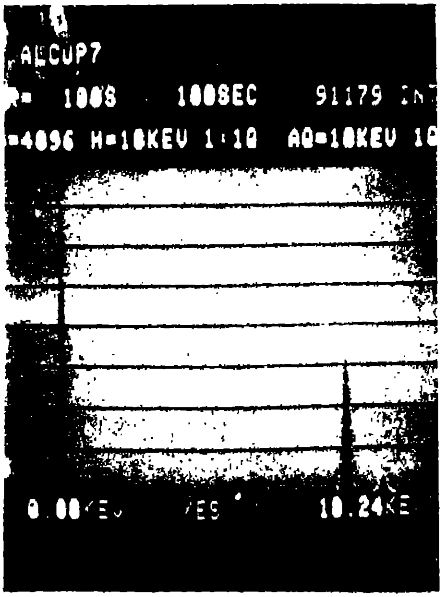

Figure 7. **a, b**: Typical STEM micrograph of $CuAl_2$ particles in the standard Al-Cu alloy. **c**. x-ray spectrum from one of the $CuAl_2$ particles showing AlKα, CuKα and CuKβ peaks; the small peak to the left of aluminium is probably due to noise in the system.

Table 2. Cliff–Lorimer (*k*) factor for Mn, Fe and Cu with respect to Al.

System	Present work	Goldstein *et al* (1977)	Zaluzec (1979)	Schreiber and Wims (1981)	Cliff and Lorimer (1975)	Woods *et al* (1981)
		k values				
Mn-Al	0·97 ± 0·03	1·17	1·23	0·67	0·86	1·20
Fe-Al	1·15 ± 0·1	1·19	1·28	0·78	0·89	1·16
Cu-Al	1·60 ± 0·15	1·42	1·60	0·96	1·11	1·42

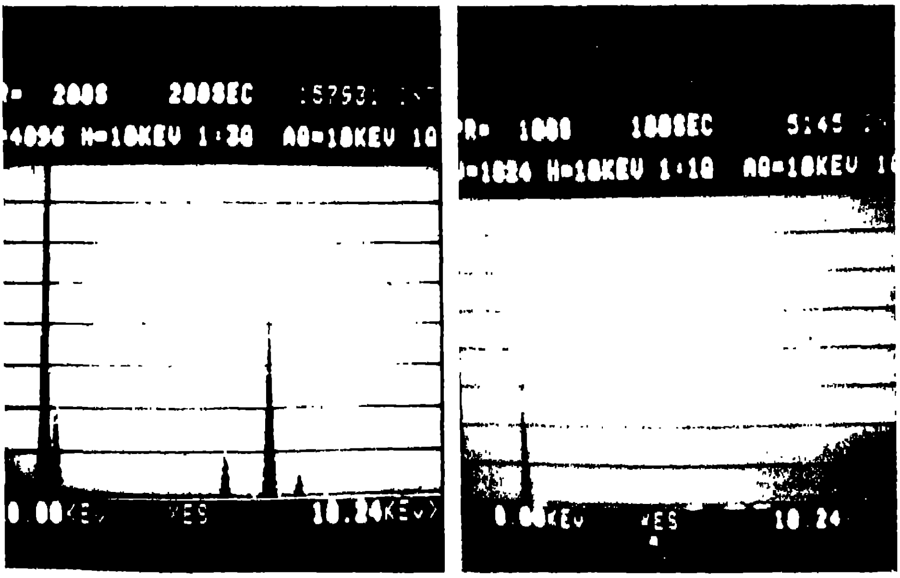

(a) (b)

Figure 8. X-ray spectra from **a.** a particle in 1200 aluminium showing AlK, SiK, CrKα, FeKα and FeKβ peaks and **b.** the matrix showing only the AlK peak.

$I_{FeK\alpha}/I_{AlK\alpha}$ show considerable scatter possibly due to improper orientation of the foil with respect to the electron beam and due to the fact that the particles do not occupy the entire depth of the foil. This problem has been overcome by carrying out x-ray microanalysis on the particles sticking to the edge of the foil (figure 9). Analysis from these particles should minimize contribution from the aluminium matrix. The results of analysis from 4 different regions of the particle in figure 9 are summarized in table 3. The SiKα to AlKα and CrKα + FeKα to AlKα intensity ratio are about the same; it is to be noted that CrKα + FeKα to SiK ratio is also nearly the same. Another method of overcoming this problem is to extract the particles using a mixture of 8-hydroxy quinoline, methanol, chloroform and benzoic acid (Cogan *et al* 1978; Hodgson and Parker 1981). This method is currently being tried for the extraction of particles. Two typical x-ray spectra from particles in 1100 aluminium are shown in figures 10a, b

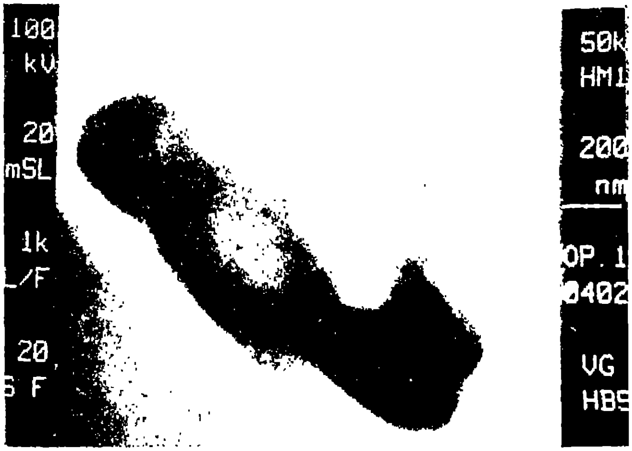

Figure 9. Typical STEM micrograph of a particle in 1200 aluminium sticking to the edge of the foil.

Table 3. Intensity ratio from various regions of the particle shown in figure 9.

Region	Ratio		
	$I_{SiK\alpha}/I_{AlK\alpha}$	$I_{CrK\alpha}/I_{AlK\alpha}$	$I_{FeK\alpha}/I_{AlK\alpha}$
1	0·13	0·05	0·43
2	0·12	0·05	0·44
3	0·14	0·07	0·43
4	0·16	0·10	0·46

revealing prominent peaks due to Al, Fe, Mn and Cu; convergent beam diffraction pattern obtained from the second particle is shown in figure 10c, the pattern corresponds to cubic AlFeSi. The intensity ratio obtained for particles showing Al and Fe peaks matches well with that obtained for Al_3Fe in the standard Al-Fe alloy. A few $CuAl_2$ particles have also been identified.

Typical microstructures of the constituents in the 3008 alloy are shown in figure 11a, b and the diffraction pattern from one of these particles in figure 11c. The pattern corresponds to Al_6Mn. It was not possible to identify any coarse zirconium-rich particles by diffraction. Typical x-ray spectra from the particles are shown in figure 11d, e with prominent Al and Mn or Al, Mn and Fe peaks. The ratio of Fe + Mn to Al intensity is constant within the limits of experimental error for a large number of particles irrespective of their morphology. The x-ray spectrum from the matrix shows only an aluminium peak (figure 11f). Careful examination of the sample reveals very fine zirconium-rich particles; a typical micrograph is shown in figure 12a and the x-ray spectrum in figure 12b revealing prominent AlKα and ZrLα peaks. The intensity ratio of zirconium to aluminium is 0·22.

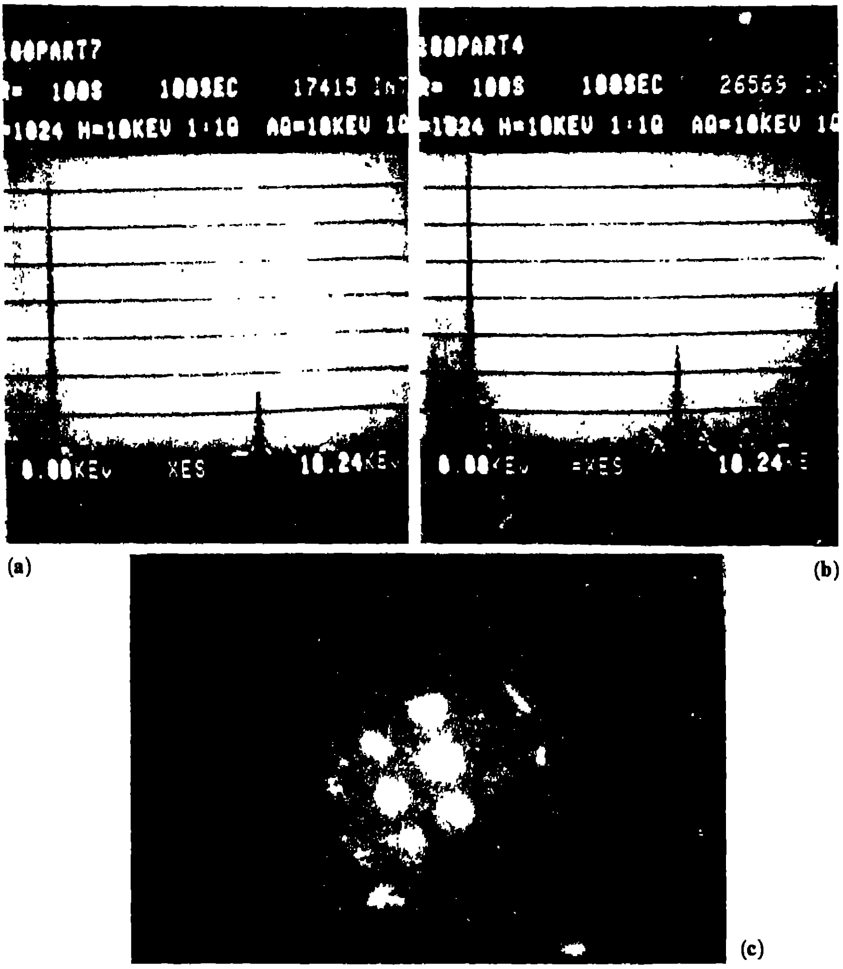

Figure 10. X-ray spectra from particles in 1100 aluminium showing **a.** AlKα, FeKα and FeKβ peaks and **b.** AlKα, SiKα, MnKα, FeKα, FeKβ, CuKα and CuKβ peaks, **c.** Convergent beam diffraction pattern from the particle in (b).

4.3 *Formation of metastable phases*

The transition phases formed in the Al-Zn-Mg and Al-Cu alloys were investigated by x-ray analysis and microdiffraction. Figure 13 is a bright field micrograph of metastable phases in Al-Zn-Mg formed by step quenching. The needles form along the $\langle 100 \rangle$ directions of Al. The selected area diffraction pattern from the area is shown in figure 13(a) while figure 13b, c, d represent microdiffraction patterns from the precipitate at approximate illumination half angles (α) of 8, 4 and 1·7 mrad respectively. The compositional difference between the metastable and equilibrium precipitates is clearly brought out in figure 14. The micrograph shows both needle-like metastable precipitates (marked as 2) and equilibrium precipitates (marked as 1) η-MgZn$_2$. The x-ray spectrum from the equilibrium precipitates shows ZnLα and AlKα peaks. The difference in the relative enrichment of the peaks is evident.

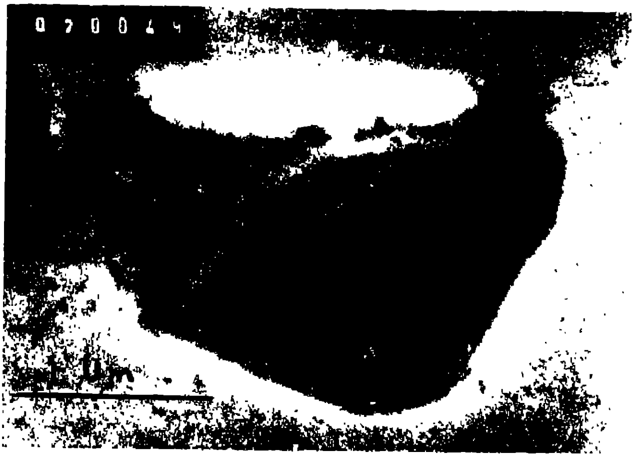

(a)

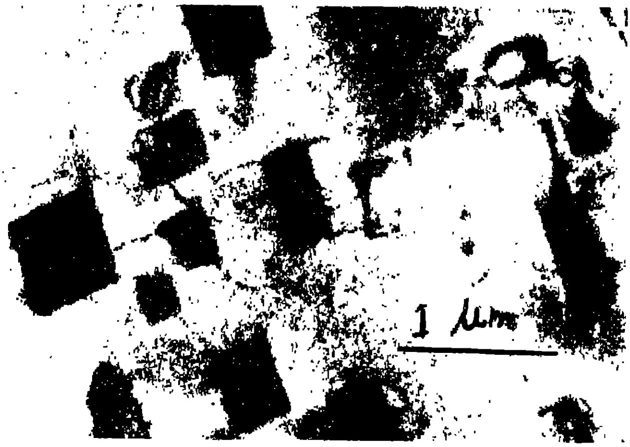

(b)

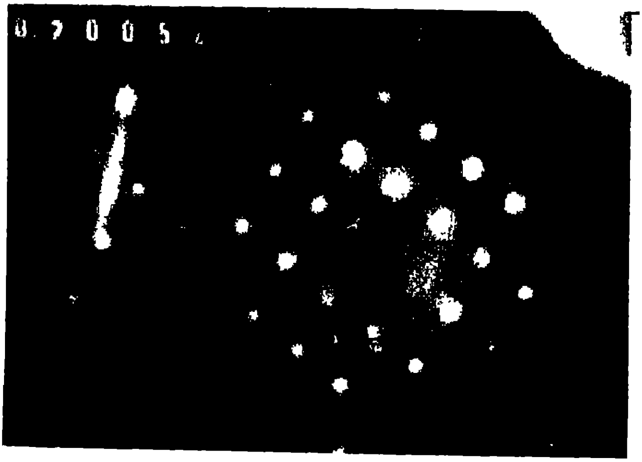

(c)

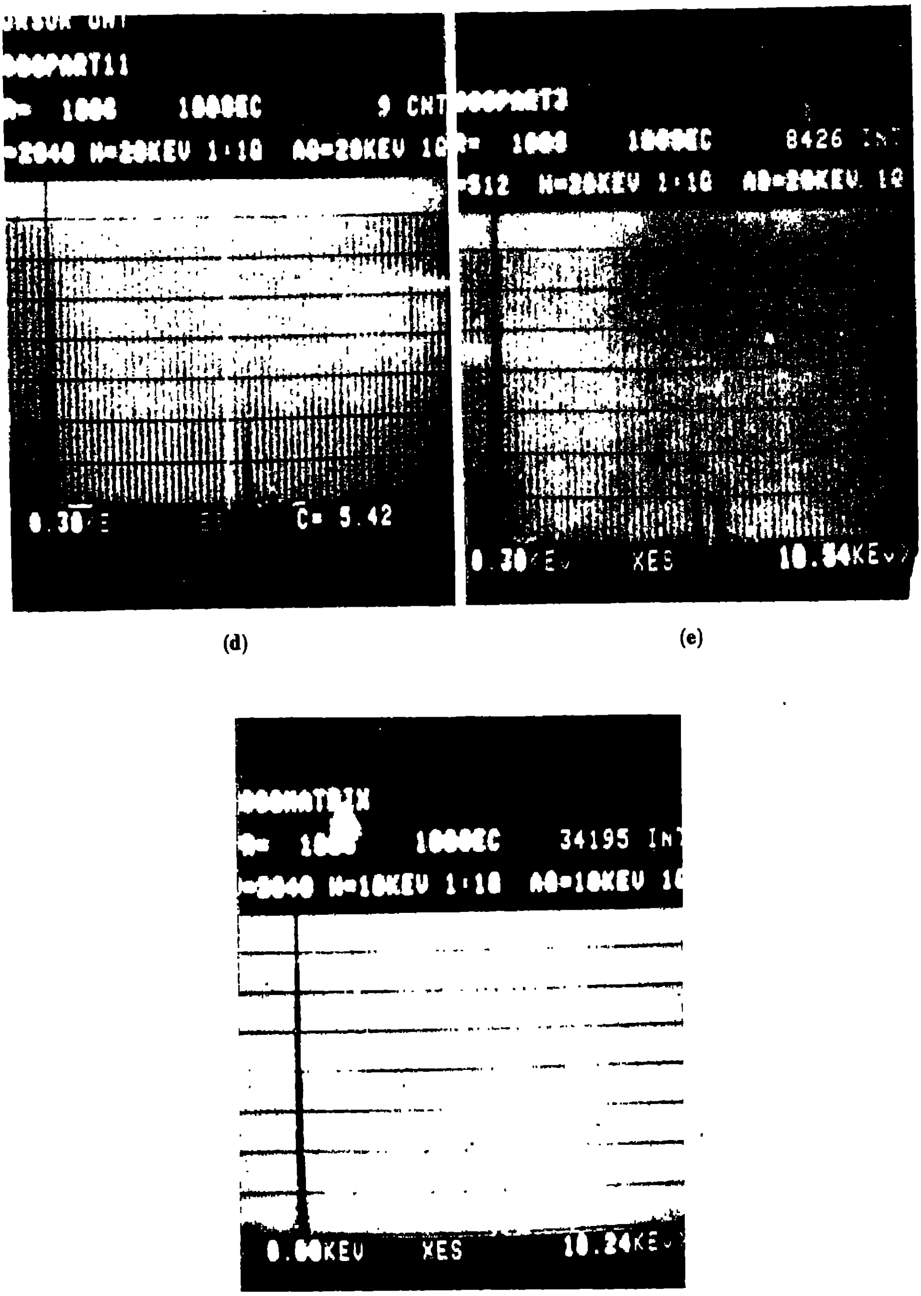

(d)

(e)

(f)

Figure 11. **a, b.** Microstructures of particles in the 3008 alloy. **c.** SAD pattern from one of the particles, Al_6Mn beam direction [112]. **d, e.** X-ray spectra from the particles showing AlKα, MnKα and Kβ and FeKα and Kβ peaks. **f.** X-ray spectrum from the matrix showing only the AlKα peaks.

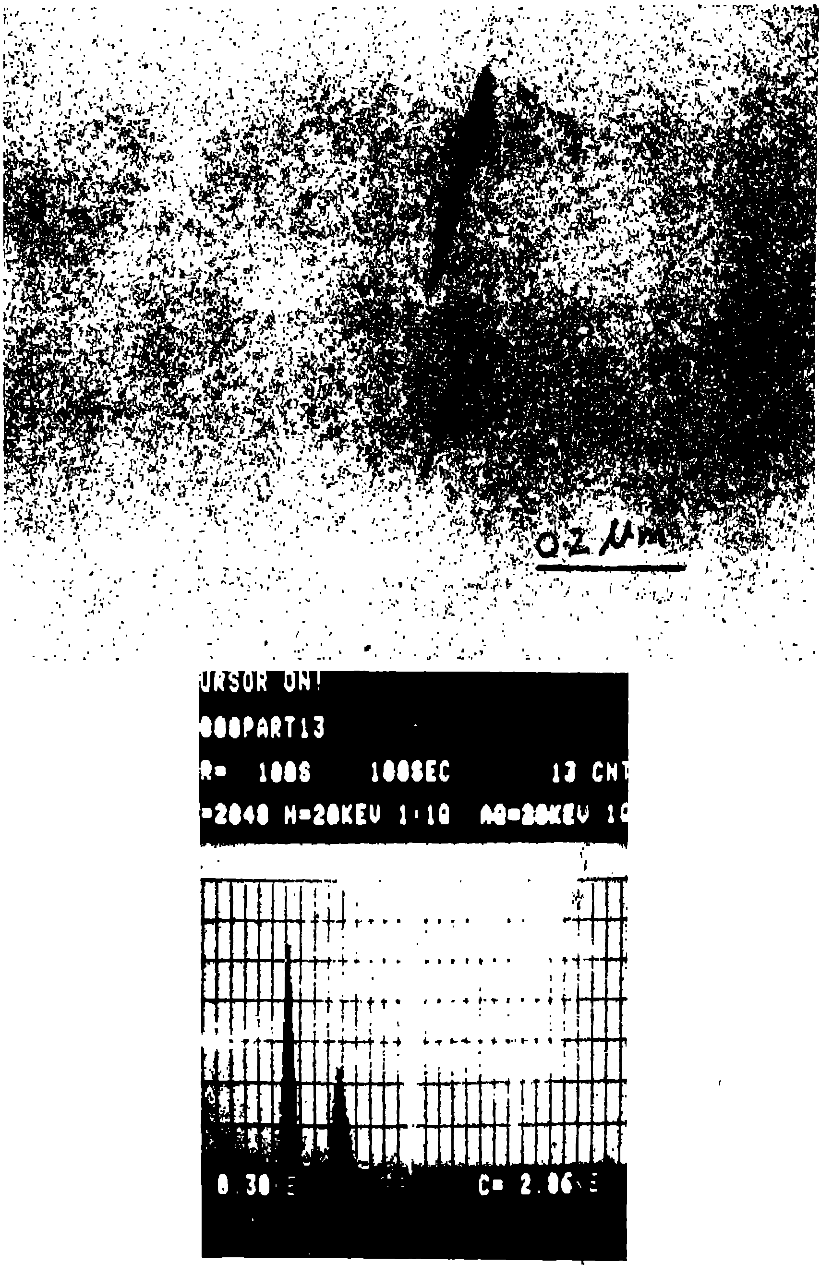

Figure 12. **a.** STEM micrograph of zirconium-rich particles in the 3008 alloy **b.** X-ray spectrum from one of the particles in (a) showing AlKα and ZrLα peaks.

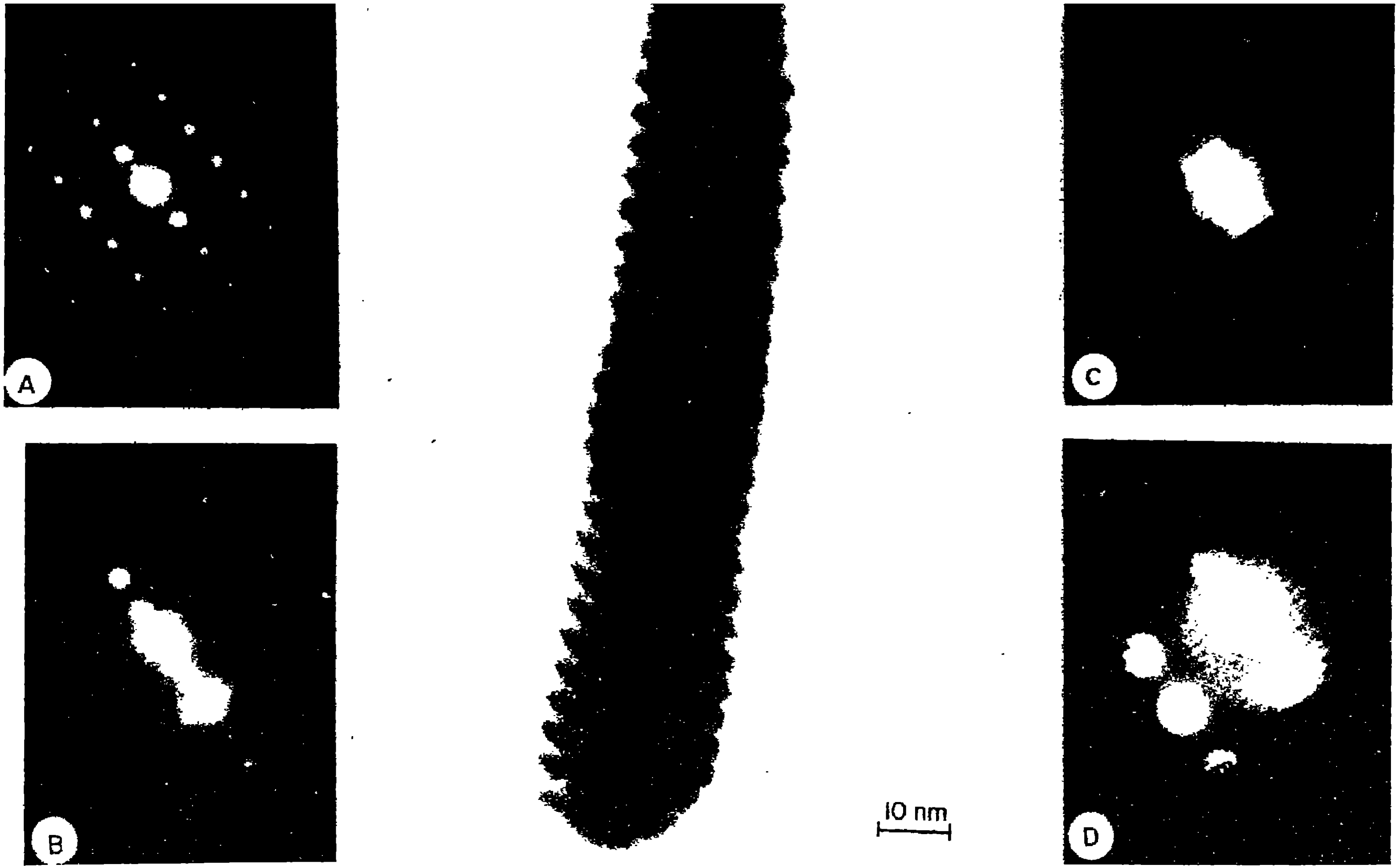

Figure 13. Bright field micrograph of the metastable phase in Al-Zn-Mg alloys. **a.** SAD pattern from the precipitate. **b–d.** Convergent beam diffraction patterns with illumination half angles of 8, 4 and 1·7 mrad respectively.

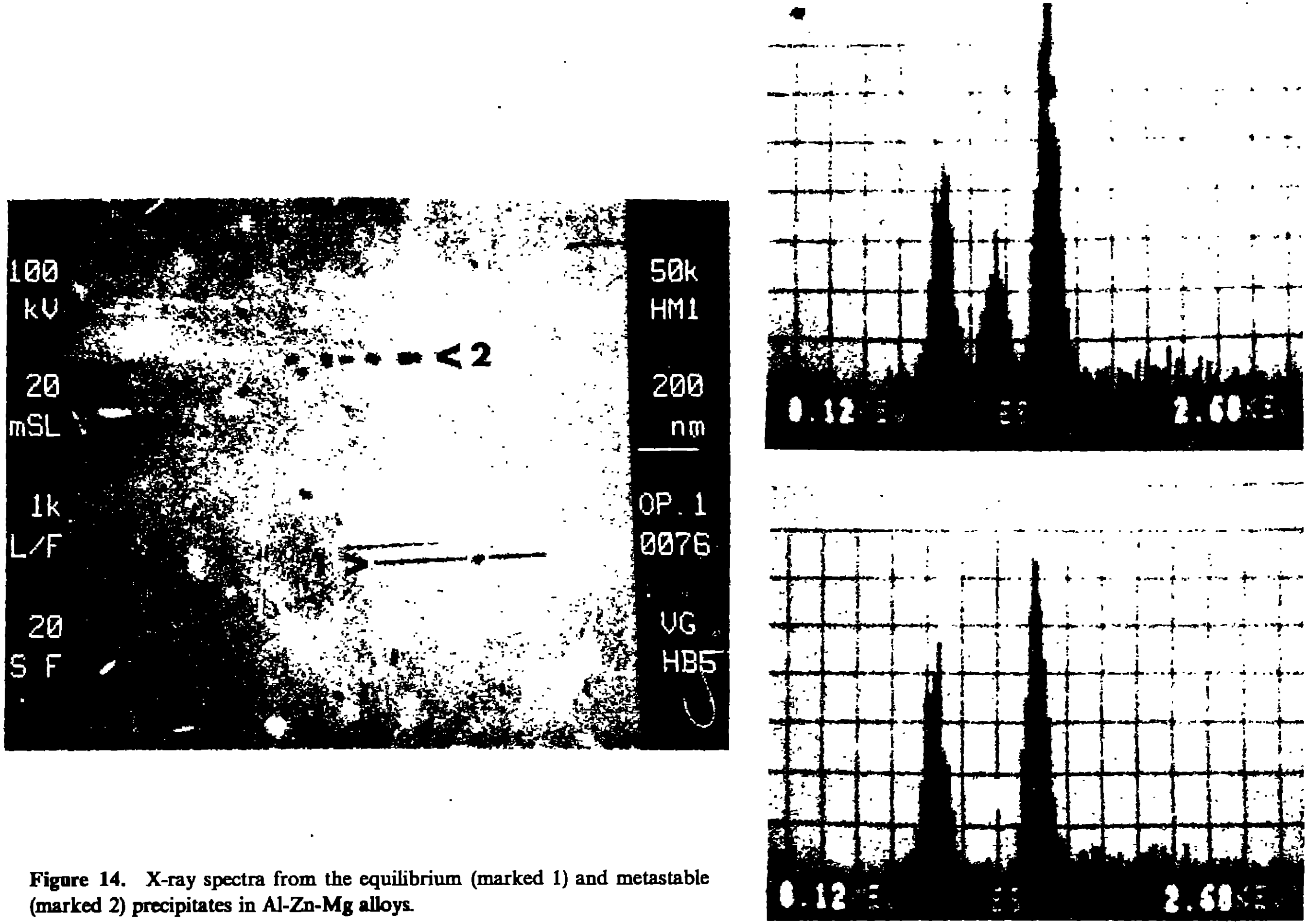

Figure 14. X-ray spectra from the equilibrium (marked 1) and metastable (marked 2) precipitates in Al-Zn-Mg alloys.

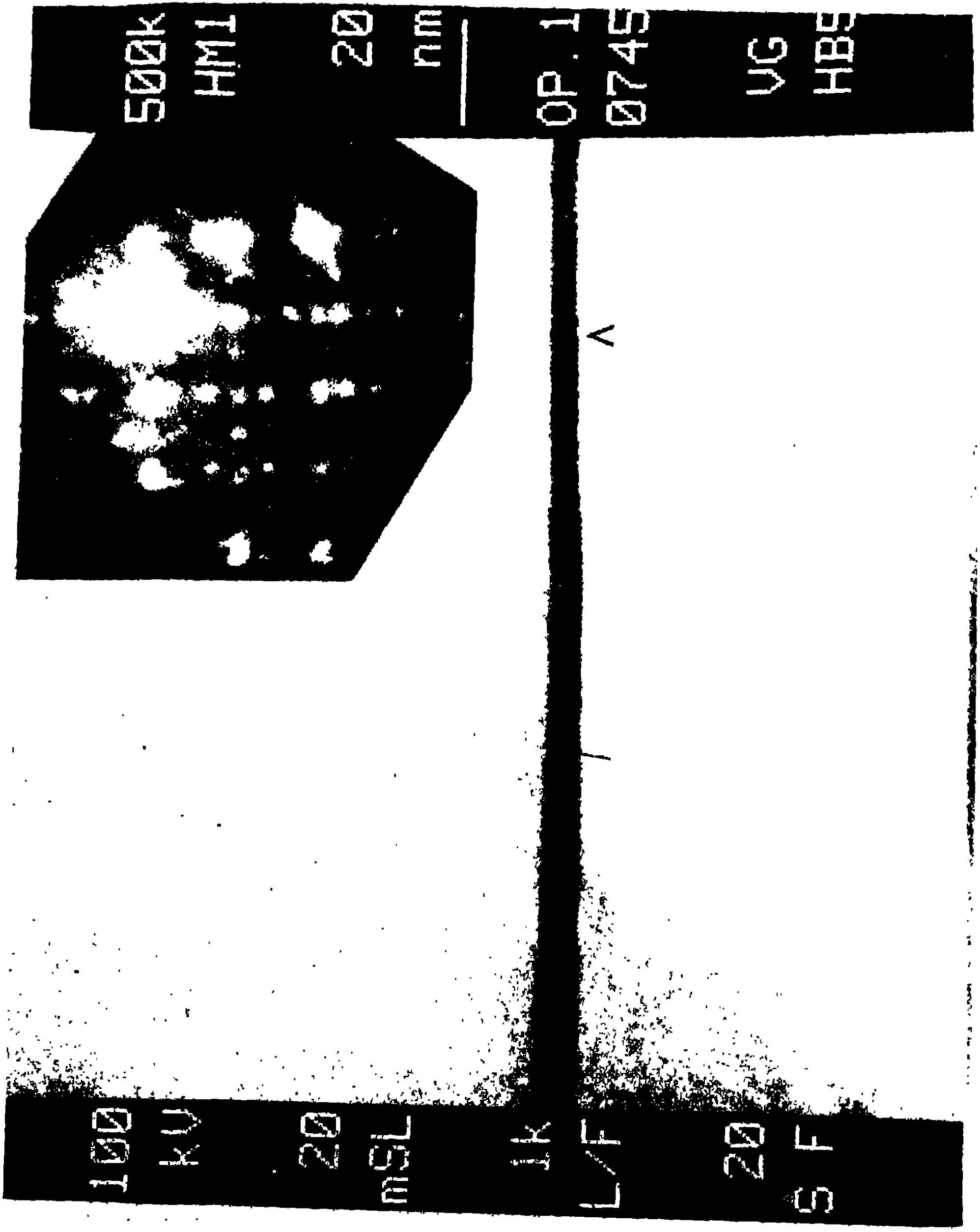

Figure 15a.

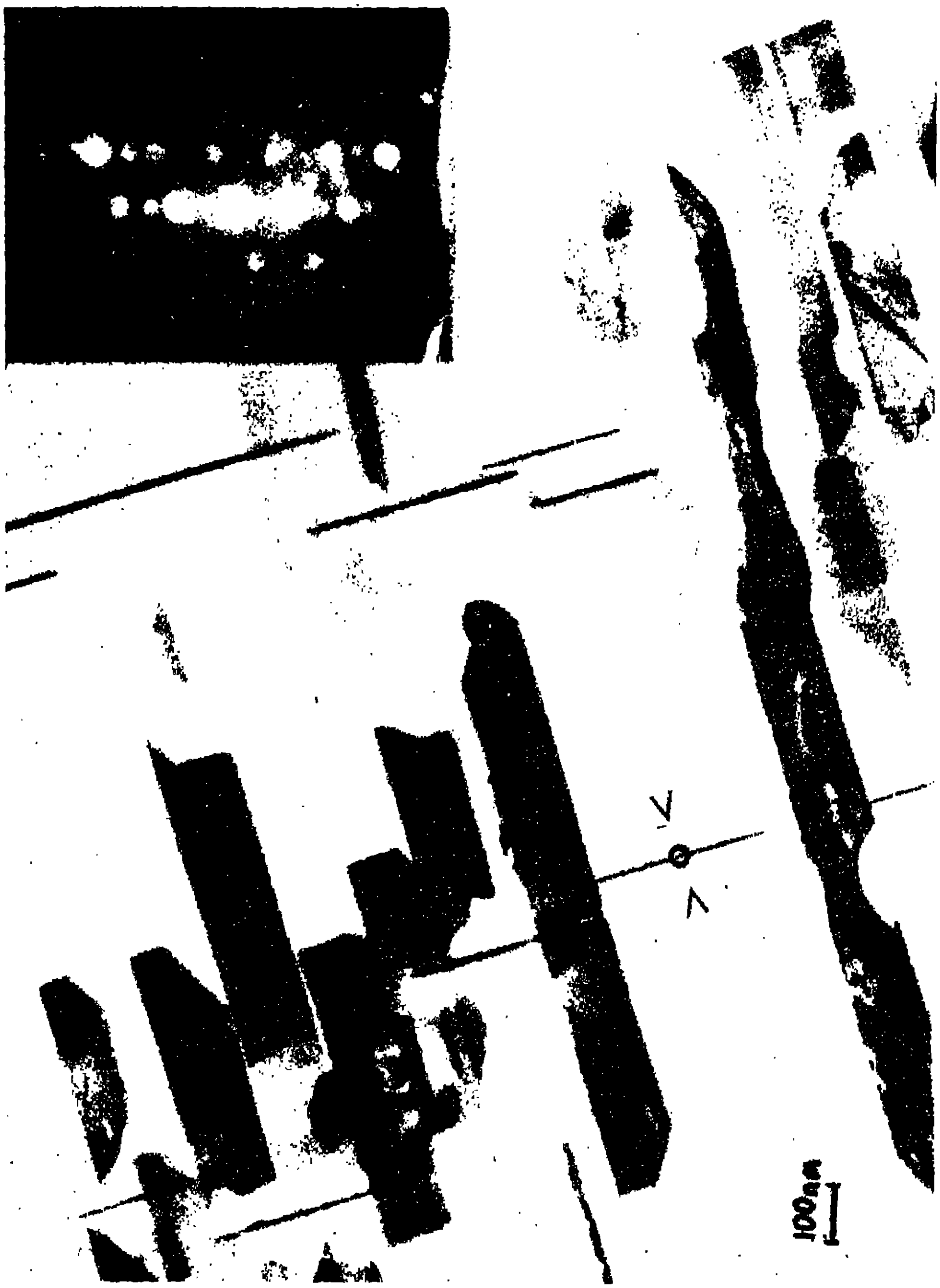
100nm

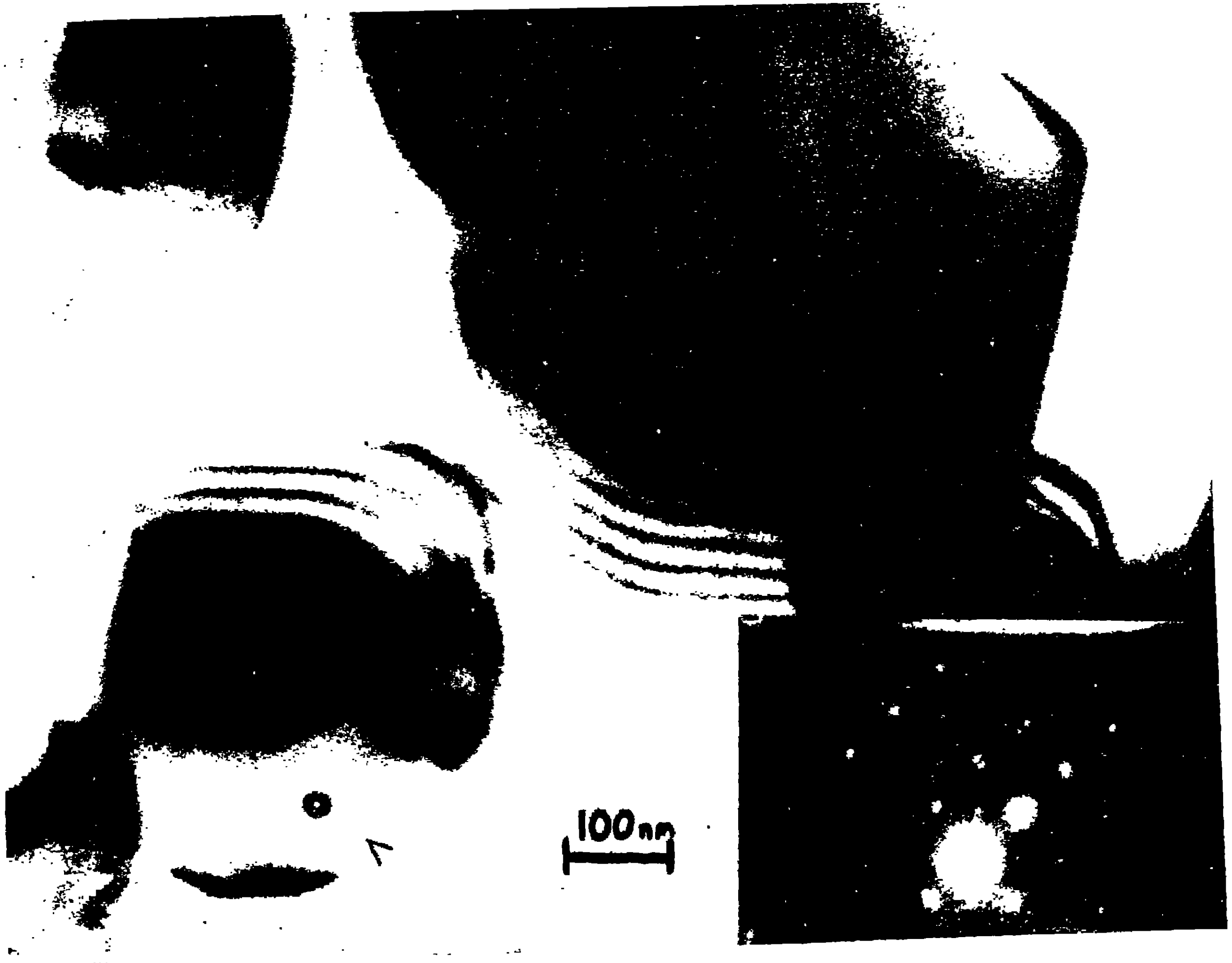

Figure 15. **a.** θ' platelets in Al-Cu alloy; the inset shows micro-diffraction pattern from the region indicated with illumination half angle of 1·7 mrad. **b.** θ' precipitates viewed with beam direction close to matrix [110] and microdiffraction patterns from one of the platelets. **c.** θ' platelets viewed normal to the large faces; SAD pattern obtained from a region of ~ 10 nm diameter using zero objective lens excitation current.

θ' platelets in Al-4% Cu alloys are shown in figure 15. The matrix has a cube orientation with a single θ' precipitate viewed edge on. The inset microdiffraction pattern has been obtained from the region indicated using α of 1·7 mrad. An array of θ' precipitates viewed θ' with beam direction close to matrix $[110]_\alpha$ is shown in figure 15b. The microdiffraction pattern obtained from an approximately 3 nm area centred on a θ' platelet at the portion indicated using α of 1·7 mrad is shown in the figure 15b. Figure 15c shows a stack of θ' platelets viewed normal to their large faces. The SAD pattern was taken at the position shown from an isolated θ' platelet using zero objective lens excitation. The beam diameter in the plane of the specimen in this mode is ~ 10 nm. The θ' reflections are seen near the forbidden (110) matrix reflections.

5. Conclusions

(i) The principles of x-ray microanalysis using the dedicated STEM are presented in this paper with particular emphasis on absorption correction to be applied when examining particles, beam broadening in foils of aluminium, precision of intensity measurements and detection limits; (ii) Hole count measurements indicate that the systems background effect can be ignored while examining the specimens in the VG HB5 STEM. (iii) The Cliff-Lorimer factor for converting the observed intensity ratio into weight fraction ratio has been measured for Mn, Fe and Cu with Al as the base as 0·97 ± 0·03, 1·15 ± 0·1 and 1·60 ± 0·15 respectively. These values are in good agreement with other experimental measurements and theoretical calculations. (iv) The peak intensity ratio obtained from a number of particles show a wide scatter possibly due to the contribution from the aluminium matrix. However, consistent results are obtained when particles at the edge of the foil are considered. The results also focus on the necessity of carrying out x-ray microanalysis on extracted particles. (v) The following phases have been identified in 1100 and 1200 Al and 3008 alloys: Al_3Fe, cubic AlFeSi, $CuAl_2$, Al_6Mn and possibly $ZrAl_3$. (vi) Microdiffraction and x-ray microanalysis have been used to study the structure and composition of metastable phases in Al-Cu and Al-Zn-Mg alloys.

Acknowledgements

The authors are grateful to Dr D Lloyd of Alcan, Kingston, Canada, for valuable discussion and to NSERC (Canada) for research support.

References

Cliff G and Lorimer G W 1975 *J. Microsc.* **103** 203
Cogan S F, Gayle F W, Klein J D, Cocks F H and Shepard M L 1978 *J. Mater. Sci.* **13** 2687
Cowley J M 1982 *National Seminar on high resolution and analytical microscopy* (Kalpakkam)
Goldstein J I, Costley J L, Lorimer G W and Read S J B 1977 (ed) O Johari (Chicago: IITRI) p. 315
Heinrich K F J 1966 *The electron microprobe* (eds) T D McKinley, K F J Heinrich and D B Wittry (New York: Wiley) p. 296
Hodgson P and Parker B A 1981 *J. Mater. Sci.* **16** 1343
Jones I P and Loretto M H 1981 *J. Microsc.* **124** 3
Joy D C 1981 *J. Microsc.* **124** 37

Keyser D F 1979 *Introduction to analytical electron microscopy* (eds) J J Hren, J I Goldstein and D C Joy (New York: Plenum Press) p. 199

Oppolzer H and Knauer V 1979 *Scanning electron microscopy* (ed) O Johari (Chicago: SEM Inc) 111

Philibert J and Tixier R 1968 *J. Appl. Phys.* 1 685

Porter D A and Westengen H 1981 *Quantitative microanalysis with high spatial resolution* (London: Metals Society) p. 94

Schreiber T P and Wims A M 1981 *Ultramicroscopy* **6** 323

Tixier R and Philibert J 1969 *Proc. 5th int. conf. on x-ray optics and microanalysis* (eds) G Molleustedt and K H Garukler (Berlin: Springer Verlag) p. 180

Williams P M 1980 *Chem. Phys. Solid Sur.* **8** 84

Woods J, Williams D B and Goldstein J I 1981 *Quantitative microanalysis with high spatial resolution* (London: The Metals Society) p. 24

Zaluzec N J 1979 *Introduction to analytical electron microscopy* (eds) J J Hren, J I Goldstein and D C Joy (New York: Plenum) p. 121

Bull. Mater. Sci., Vol. 6, No. 3, July 1984, pp. 537–547. © Printed in India.

Electron microscopy of defect clusters produced by radiation damage

S BANERJEE

Physical Metallurgy Division, Bhabha Atomic Research Centre, Bombay 400 085, India

Abstract. The methods of characterization of different types of radiation-induced defect clusters by TEM have been reviewed. Point defects produced in irradiated materials agglomerate in two or three dimensional clusters to reduce the strain energy associated with them. Two-dimensional clusters assume the configuration of vacancy or interstitial type dislocation loops which can be resolved if the size of the loops is large compared to the extinction distance associated with the imaging reflection. The small loops give rise to a black dot contrast under the kinematical and a black-white contrast under the dynamical imaging conditions. The method of characterization of dislocation loops which include the determination of the nature of the loop, the Burgers vector and the loop plane normal is discussed taking examples from the work done on the ion irradiated Ni_4Mo samples. A summary of available experimental results on the characterization of dislocation loops in different metals and alloys having fcc, bcc and hcp structures is presented. The contrast from stacking fault tetrahedra which form in some fcc metals and alloys after a certain degree of annealing is also discussed. The optimum conditions for imaging three-dimensional clusters or voids are derived on the basis of the contrast theory proposed for such defects. Special reference is made to the usefulness of "through focus analysis" in the imaging of very small cavities (with diameters as small as about 10 Å).

It is shown that the formation of disordered zones resulting from displacement cascades in the ordered matrix can be utilized in determining the shape and the volume of cascades in the virgin state. The importance of different contributing factors like the strain contrast and the structure factor contrast in producing the overall contrast from the disordered zones is discussed. Detailed observations on the shape of the disordered zones are shown to be important to establish the occurrence of the replacement collision sequence and the formation of sub-cascades.

Keywords. Radiation damage; electron microscopy; point defect clusters; disordered zones.

1. Introduction

Energetic particle irradiation of metals causes permanent displacement of atoms if the recoil energy transferred from the incident particles to the target atoms exceeds the displacement energy. Depending on the momentum and the energy, an incident particle can produce either a Frenkel type defect consisting of a single vacancy-interstitial pair or a cascade of displacements. The latter process results in creating a depleted zone having a vacancy-rich core surrounded by a region with a high density of interstitials. Such a depleted zone structure is not stable due to the high strain energy associated with it. A substantial part of the strain energy is released when vacancies in the core of the depleted zone collapse into a two dimensional cluster assuming the configuration of a vacancy type dislocation loop. When irradiation causes production of isolated point defects, their concentrations build up and depending on the extent of supersaturation, they tend to cluster as point defect agglomerates (PDA). Isolated point defects are not observable in TEM at the present time, but PDAS which assume configurations like dislocation loops, stacking fault tetrahedra, cavities etc give rise to specific contrast effects on TEM images. The present paper deals with the methods of characterization of PDAS by studying the details of their contrast.

As mentioned earlier, the formation of a dislocation loop at the core of a cascade involves migration of point defects and also annihilation of defects through the vacancy-interstitial recombination. As a result, dislocation loops do not truly represent the cascades associated with them in their virgin state. A better imaging of cascades has been possible in ordered alloys in which the cascade volumes are disordered by incident particles. This novel technique of imaging cascades will also be discussed here.

2. Contrast from small dislocation loops

Earlier investigations have shown that radiation damage in metals causes formation of defects, which appear as black dots of irregular shape when the sample is imaged in the kinematic bright field condition *i.e.* when no low order reflection is strongly excited. It was not possible to derive any crystallographic information regarding the nature and the geometry of the radiation induced defects from such black dot contrast. Essman and Wilkens (1964), for the first time, detected that the black dots in neutron irradiated copper revealed a characteristic black-white contrast when the samples were imaged under two-beam dynamical contrast condition (with excitation error, $s \approx 0$). From a systematic study of such black-white contrast, both theoretical and experimental, the methods of finding out various crystallographic parameters such as the nature of the loop, the Burgers vector, the loop plane normal associated with a defect cluster have now been established mainly from the work carried out by Wilkens and coworkers in Stuttgart and Eyre and his coworkers in Harwell. This subject has been dealt with extensively by Eyre (1972), Ruhle (1967a,b) and Wilkens (1970, 1973).

Some of the theoretical results based on which defect analysis can be done are summarised as follows: (i) Only those defects which lie within a distance of about 1·5 times ξ_g from the top and the bottom surfaces of the foil give rise to the black-white contrast under the two beam dynamical imaging condition with $\mathbf{g} \cdot \mathbf{b} \neq 0$ where $\mathbf{g}$ is the operating reflection and $\mathbf{b}$ the Burgers vector. The disappearance of the black-white contrast from small loops located at distances exceeding 1·5 ξ_g is due to anomalous absorption. The factor ξ'_g/ξ_g where ξ'_g is the anomalous absorption length provides a guide line for determining the maximum depth up to which a defect produces a black-white contrast. (ii) For loops in the middle region of the foil, *i.e.* outside the region of observable black-white contrast, a black dot contrast is expected. (iii) As mentioned earlier, dislocation loops located near the surfaces of the foil reveal a black-white contrast when $\mathbf{g} \cdot \mathbf{b} \neq 0$ and $s \approx 0$. If a vector $\mathbf{l}$ is so defined that it points from the centre of the black lobe to the centre of the white lobe of the contrast figure in the positive print, then the sign of $\mathbf{g} \cdot \mathbf{l}$ oscillates with depth as shown schematically for vacancy loops in figure 1. The orientation of $\mathbf{l}$ remains independent of the direction of g and lies parallel to $\mathbf{b}$ or its projection on the image plane. This statement is, however, valid only for angles between g and $\mathbf{b} \lesssim 55$ to 60° (Ruhle 1967 a,b). Image simulation results for the case of $\frac{1}{2}\langle 110\rangle$ and $\frac{1}{2}\langle 111\rangle$ edge loops in a bcc crystal show that $\mathbf{l}$ deviates from $+\mathbf{b}$ (or its projected direction) by an amount that increases as α, the angle between $\mathbf{b}$ and $\mathbf{g}$ (Eyre 1972). (iv) Eyre (1972) has shown that for fairly large values of $\mathbf{g} \cdot \mathbf{b}$ ($\gtrsim 4/3$) a fine structure is developed at the separation line between the black and the white lobes. (v) When $\mathbf{g} \cdot \mathbf{b} = 0$, a contrast figure often described as a butterfly contrast (Wilkens *et al*

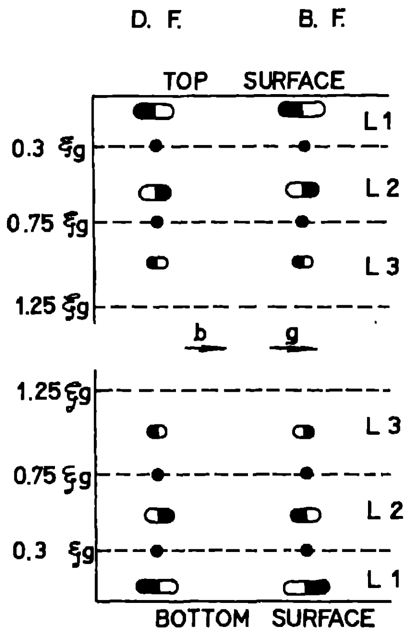

Figure 1. Schematic illustration, of the black-white contrast from small dislocation loops of vacancy type located at different depths of the sample. Bright (BF) and dark field (DF) image characteristics as seen on positive prints. For interstitial type loops the same image characteristics are seen for **g** pointing in the reverse direction.

1970) which contains three black and three white lobes is observed. (vi) Under the kinematical imaging condition *i.e.* for large excitation errors ($|s| \cdot \xi_g \gg 1$) only black dot contrast remains for all loop positions. Since the diameter of the black dot contrast, measured for instance at 20% image width, closely corresponds (within about 10% error) to the projected loop width, such kinematical images are very useful in the quantitative determination of the loop size.

Based on the aforementioned principles of image formation, it is possible to identify the nature of a small dislocation loop (*i.e.* either vacancy or the interstitial type) and determine the Burgers vector and the loop plane normal. The method is illustrated taking examples from a recent experimental work on ion irradiation induced damage in Ni_4Mo. (Banerjee *et al* (unpublished)).

2.1 *The sign of the misfit volume*

The vacancy and the interstitial type loops with misfit volumes, $\Delta V < 0$ and $\Delta V > 0$ respectively can be distinguished from the sign of $\mathbf{g} \cdot \mathbf{l}$ provided the depth position of the defect is determined accurately by the stereomicroscopic method. In Au^{++} ion irradiation on Ni_4Mo, the range of the incident ion was such that almost all defects were formed within the layer, L1 (refer figure 1). Therefore, in the present case, it was not necessary to find out the depth positions of these defects. Comparing figures 1 and 2 it can be seen that these defects are all vacancy loops, that **l** vectors for different loops are pointing along different directions and all are certainly not along the g vector. This observation clearly demonstrates that the strain field around these defects are not

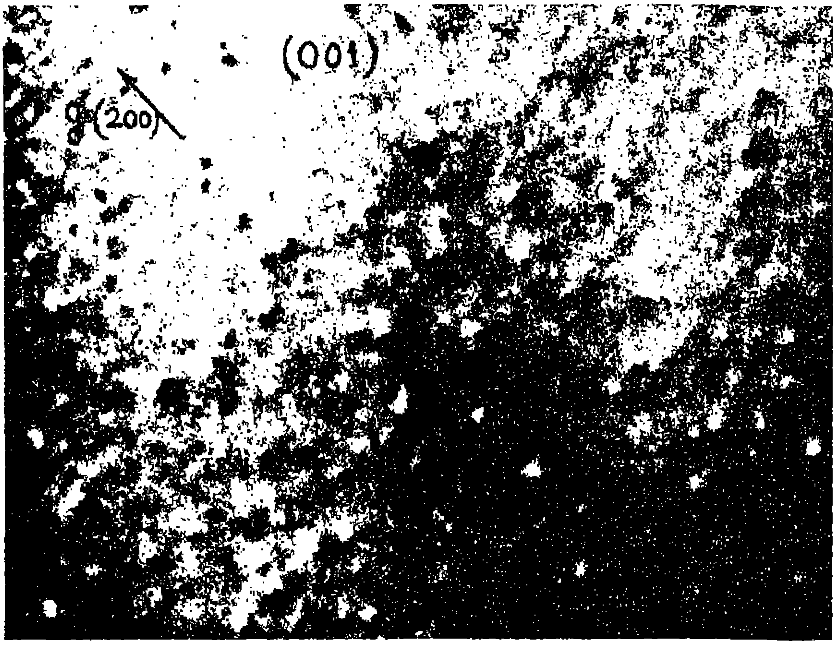

Figure 2. Black-white contrast from vacancy type dislocation loops produced in Ni_4Mo irradiated with 60 keV Au^{++} ions. Note that all **l** vectors are not parallel to **g**.

spherically symmetric because in that case the **l** vector is expected to be always parallel to **g**. Analysis of contrast figures of defect clusters in Nb_3Sn (Jenkins *et al* 1982) has shown such contrast character and they suggested the formation of amorphous disordered zones in the ordered matrix which results in the production of spherically symmetric strain centres.

2.2 *Burgers vector and plane normal* **n** *of a small dislocation loop*

The method of determining the Burgers vector **b** and the loop plane normal of a resolvable dislocation loop involves finding out a suitable *g* for which contrast extinction occurs and tilting experiments to bring the loop plane parallel to the electron beam direction. For the unresolved loops, a careful comparison of the contrast figure from a given set of dislocation loops under different imaging reflections enables one to determine these parameters unambiguously. Strictly speaking, a comparison between computer simulated images of dislocation loops with different **b** and **n** under various conditions of imaging (**g** and foil plane normal) is necessary. The analysis, however, turns out to be simpler in many cases where possible Burgers vectors are restricted by crystallographic arguments. Figure 3 illustrates one such example where loops are grouped into three types A, B and C depending on the contrast figures exhibited by them under different **g** all on the same foil plane (001). The **l** vectors are seen to be along A, B and C vectors which are along projections of different $\langle 110 \rangle$ and $\langle 111 \rangle$ directions. Table 1 shows that if **b** for A, B and C types of dislocation loops are taken to be those indicated in the last column of the table 1, the observed contrast figure

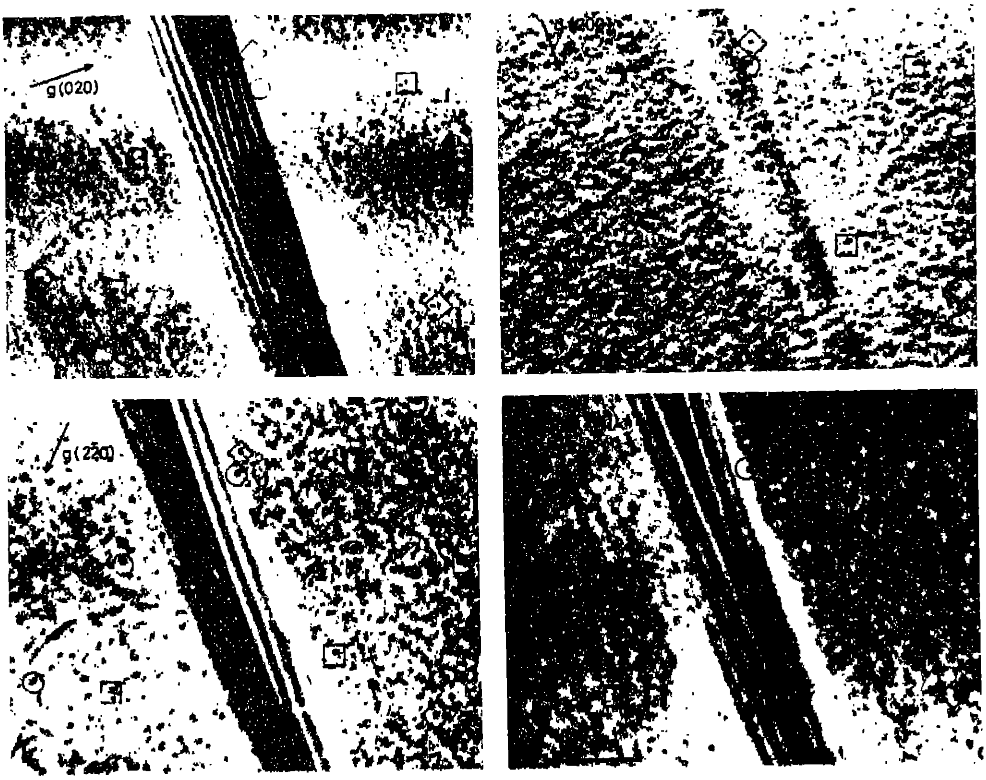

Figure 3. Analysis of Burgers vector of small dislocation loops. Based on the contrast character (as listed in table 1) under different operating reflections loops are grouped into three types A, B and C marked by circle, square and diamond markers.

matches with what is expected from theoretical considerations. Based on this observation, it has been concluded that apart from the Frank loops, some perfect loops are also formed in the ion irradiated ordered Ni_4Mo alloy. Figure 4 illustrates the details of the contrast figure of perfect and Frank loops under different imaging conditions with increasing magnitude of $\mathbf{g}.\ \mathbf{b}$. The internal contrast at the centre of the black-white figure is clearly visible when $\mathbf{g}.\ \mathbf{b}$ is close to 2.

Experimental work on several fcc metals has established that a great majority of small dislocation loops are of the Frank type which have pure edge character. The rule that the $\mathbf{l}$ vector is parallel to $\mathbf{b}$ or the projection of $\mathbf{b}$ is valid in such cases and therefore unambiguous identification of these loops is possible using this property of the loop contrast. However, this property alone is not sufficient to determine $\mathbf{b}$ and $\mathbf{n}$, particularly for shear loops.

In bcc metals, Eyre and Bullough (1965) have shown from theoretical consideration that small loops are nucleated on $\{110\}$ planes and in a subsequent shear process the Burgers vector $\mathbf{b} = \frac{1}{2}\ \langle 110 \rangle$ is converted into $\mathbf{b} = \frac{1}{2}\ \langle 111 \rangle$ or, less probably, into $b = \langle 100 \rangle$. Experimental work on ion irradiated Mo and on W (Eyre *et al* 1977) have shown that a majority of the loops in bcc metals have $\mathbf{b} = \frac{1}{2} \langle 111 \rangle$ and $\mathbf{n} = \langle 110 \rangle$. No evidence for loop with $\mathbf{b} = \langle 100 \rangle$ was found in W.

In Co (Wilkens 1978) nearly all loops could be indexed with $\mathbf{b} = 1/3\ \langle 11\bar{2}0 \rangle$ and $\mathbf{n} = \langle 10\bar{1}0 \rangle$. No radiation induced loops on the basal plane could be detected.

Table 1. Image characteristics of loops shown in figure 3.

Type (Marker)		g $[020]$	$[200]$	$[\bar{2}\bar{2}0]$	$[2\bar{2}0]$	b
	1		A	A	A	
A (Circle)	shape	butterfly	BW	BW	BW	$\frac{1}{2}[101]$ or
	g·b.	0	1	1	1	$\frac{1}{2}[10\bar{1}]$ or
	1	B	B		B	
B	shape	BW	BW	butterfly	BW	$1/3[\bar{1}\bar{1}1]$ or
(square)	g·b	2/3	2/3	0	4/3	$1/3[1\bar{1}\bar{1}]$
	1	C	C	C		
C	shape	BW	BW	IS	butterfly	$\frac{1}{2}[110]$
(Diamond)	g·b.	1	1	2	0	

A parallel to projection of $[101]$ and $[10\bar{1}]$;
B parallel to projection of $[1\bar{1}1]$, $[1\bar{1}\bar{1}]$ and $[1\bar{1}0]$;
C parallel to projection of $[111]$, $[11\bar{1}]$ and $[110]$. B W represents black-white contrast with no prominent internal structure. I S represents black white contrast with prominent internal structure.

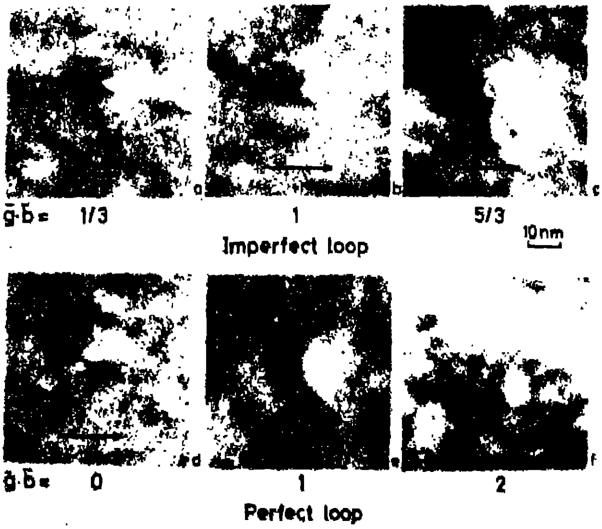

Figure 4. The influence of the magnitude of g·b on the details of the loop contrast.

3. Contrast from voids

Theoretical contrast calculations have been carried out by many investigators and on the basis of these results, Eyre (1972) has listed the Following image characteristics for voids:

(i) Voids give rise to strain contrast absorption contrast and phase contrast and relative magnitude of each of these very strongly depends on the void size, the thickness of the sample and the imaging condition. (ii) In a two-beam dynamical image, the largest contribution to in-focus images comes from absorption contrast except for very small cavities which produces strain contrast to a significant extent. (iii) When absorption contrast is predominant, contrast is dictated by foil thickness. The optimum contrast is obtained in a narrow region at the front of the first and second dark thickness fringe (figure 5). It has been demonstrated that cavities exhibit positive contrast at the bright and negative contrast at the rear or dark fringes in bright field, the reverse being true in the dark field. (iv) In thicker foils, anomalous absorption damps out the oscillation in intensity and all cavities exhibit above background contrast, due to a change in the normal absorption. (v) The contrast from very small voids can be obtained only in out of focus imaging, *i.e.* when objective lens is focussed on a plane at a distance, ζ (about 1 μm) from the bottom layer of the specimen. By this technique, cavities with diameters 10 Å or less can be made visible. Ruhle (1971) have shown that cavities degenerate with increase in thickness into pure phase objects in the electron optical sense. Such phase objects are invisible under in-focus conditions. The phase shift is given by ΔV, the difference between the mean inner potentials inside the cavity and in the crystalline matrix. The contrast figure obtained in the defocus mode consists of a central region which in bright or dark depending on the sign of ΔV and ζ and a number of Fresnel fringes of alternating sign surrounding the central region. 'Through focus imaging' technique can also be used, in principle, to establish ΔV because the contrast depends on the sign and the magnitude of ΔV for cavities which are large enough to be detectable under the in-focus imaging condition.

4. Contrast from disordered zones

In pure metals and disordered alloys the size of the vacancy loops produced by the collapse of vacancies at the core of displacement cascades gives a measure of the cascade size. The loops, however, do not truly represent the cascades because only the vacancies which survive in a cascade core make up a dislocation loop and vacancies undergo a considerable degree of rearrangement during the collapsing process. When displacement cascades are produced in ordered alloys, random displacements and replacements of atoms destroy the order within the cascade. Dark field image taken with a strongly excited superlattice reflection then shows a distribution of disordered zones embedded in the ordered matrix. The contrast arises primarily due to the difference in the structure factor for the superlattice reflections between the disordered zone and the ordered matrix. When such disordered zones are associated with dislocation loops, additional contribution from strain contrast also appears. Different factors which influence the image contrast of disordered zones have been evaluated by Jenkins *et al* (1976 a, b) both theoretically and experimentally on the Cu_3Au alloy. More recently, experiments on disordered zones in Ni_4Mo (Banerjee *et al* unpublished) have confirmed earlier findings. The results of these investigations can be summarized as follows:
(i) The contrast was a sensitive function of foil thickness. Figure 6 shows the intensity relative to the background (I/I_0) *vs* foil thickness for disordered zones in Ni_4Mo imaged under 1/5 (420) and 3/5 (420) reflections (Banerjee *et al* unpublished). For the 1/5 (420) superlattice reflection, the image intensity of the disordered zone is below the

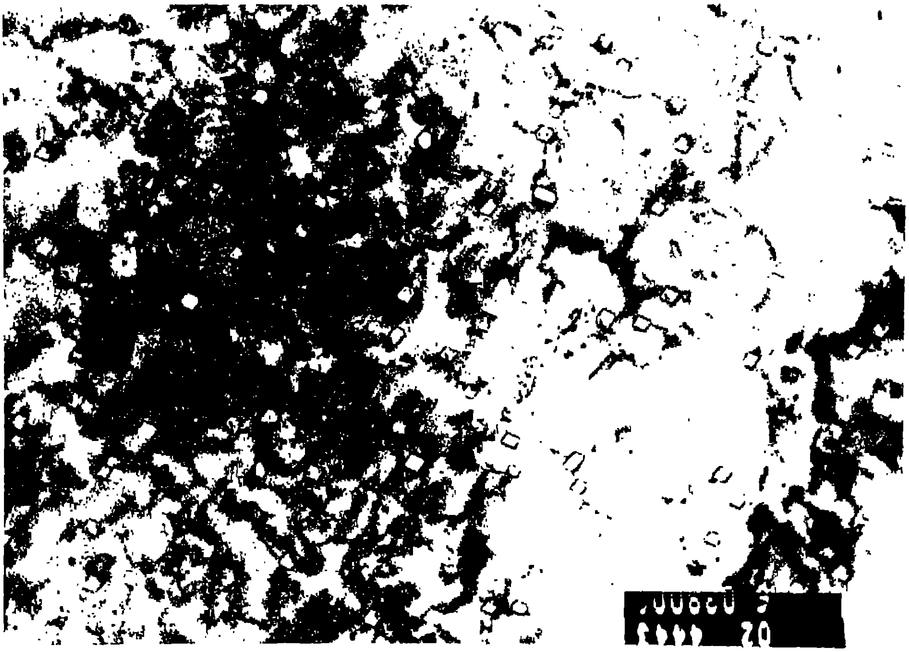

Figure 5. Contrast from voids in 316 stainless steel produced by MeV proton irradiation (courtesy S K Khera)

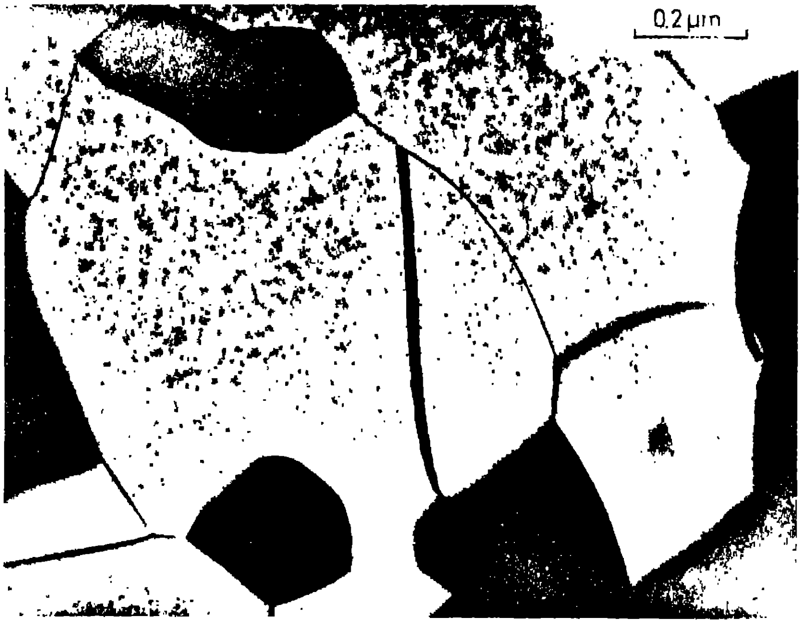

Figure 6. The calculated superlattice dark field contrast from a disordered zone of 5 nm in the matrix of the fully ordered Ni_4Mo. The influence of the degree of order(S) within the disordered zone and the specimen thickness on the contrast is shown. Calculation is based on twelve beams in a systematic row of reflections along ⟨420⟩ real vectors with $\mathbf{g} = 1/5\ \langle 420\rangle$.

background when the sample thickness is less than 850 Å while for the 3/5 (420) reflection the image intensity remains below the background for practically all electron transparent samples. The contrast, however, becomes very feeble as the sample thickness exceeds about 500 Å and therefore disordered zones do not remain visible in thick regions of the sample. Figure 7 illustrates the contrast observed from disordered zones in Ni_4Mo imaged under 1/5 (420) reflection. (ii) The thickness of the disordered zone is another factor which strongly influences the contrast. Numerical calculations (Jenkins *et al* 1976 a) have shown that the contrast falls below the 10 % level, commonly accepted as the visibility limit, for the disordered zone thickness smaller than about 20 Å. (iii) The contrast has been found to be linearly dependent on the long range order parameter, S within the disordered zone. (iv) The contrast has been shown to be fairly insensitive to the extent of deviation from the exact Bragg orientation and also to the depth at which the disordered zone is located in a sample. It may be noted that the superlattice dark field contrast from disordered zones located at depth Z_0 is the same as that for disordered zones located at depth $(t - Z_0)$ where t is the foil thickness. (v) Based on the calculations made by Jenkins *et al* (1976 a,b) in which contributions from both structure factor and strain constant are taken into account, it can be stated that the total contrast is dominated by the structure factor contribution for small disordered zones associated with dislocation loops (typically the loop diameter being less than about 40 Å for Cu_3Au imaged under (110) reflection). Even for larger disordered zones the size and the shape of the total contrast are fairly well represented by the contrast arising out of the structure factor contribution alone.

Because of the faithful reproduction of the shape of a cascade in the superlattice dark field image of the disordered zone associated with it, the details of the contrast figure

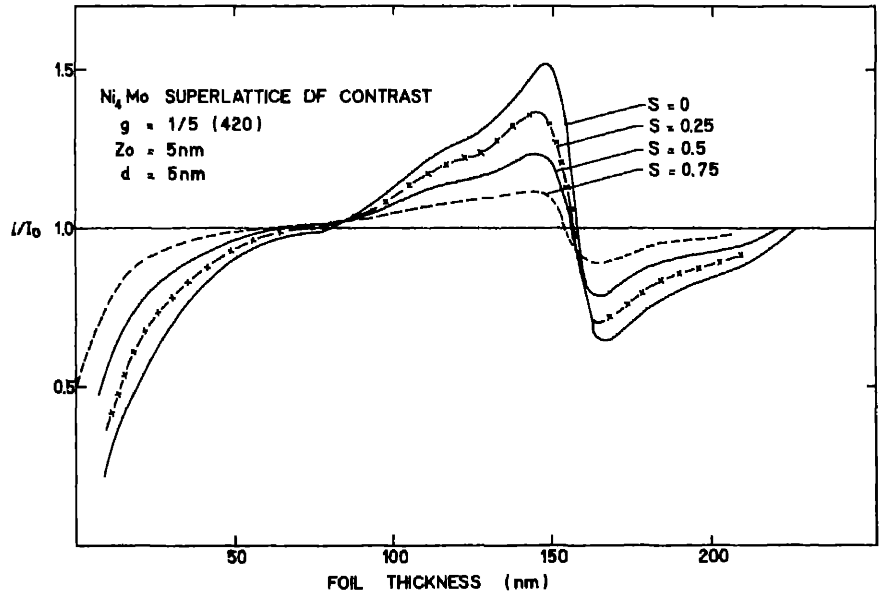

Figure 7. Dark field image with 1/5 ⟨420⟩ reflection to show disordered zones in the matrix of ordered Ni_4Mo irradiated with 60 KeV Au^{++} ions. Dark grains correspond to ordered domains related with bright domains by anti parallel twin relation.

have been studied to explore the mechanism of displacement and replacement of atoms within the cascade volume. From the measurement of size of the cascades and assigning a distribution of disorder within the cascades the number of replacements, n_r within a single cascade required to introduce the disorder can be computed. When this number is compared with the estimated number of atomic displacements, n_d ($\simeq E/2Ed$, where E is the energy of the incident ion and E_d is an average displacement energy), one obtains n_r/n_d to be in the range of 10 to 20. This suggests that disordering is caused largely due to the replacement process. It has been envisaged that disordering may occur by the following processes to different extents: (i) formation of thermal spikes (ii) collapse of vacancies to form vacancy loops, and (iii) replacement collision sequence (RCS). To assess the role of RCS, detailed observation on the morphology of disordered zones has been made by Jenkins *et al* (1976b) and they have reported splitting up of disordered zones into two or more distinct dots and extrusions of the disordered zone into the matrix. Attempt has been made to examine whether these extrusions coincide with the close packed $\langle 110 \rangle$ directions along which focussed RCS is expected to occur. But the results are not convincing enough to be certain that these extrusions are the path along which RCS has occurred. However, such a mechanism of propagation of RCS to produce sub-cascades in case of high incident ion energies ($>$ 30 keV) still appears very probable.

5. Concluding remarks

At present TEM methods are well developed for complete crystallographic characterization of point defect agglomerates produced by radiation damage. The lattice resolution technique has not yet found any significant application in analysing these defect structures. With the availability of high resolution TEMS and growing interest in lattice resolution microscopy one may forsee some suitable applications of lattice resolution microscopy in this area in the near future.

Acknowledgements

The author is indebted to Dr M Wilkens for many helpful discussions. The unpublished results included in this review were obtained during the author's stay at the Max-Planck-Institut fur Metallforschung as an Alexander-von-Humboldt fellow.

References

Banerjee S, Katerbau K-H and Wilkens M (to be published)
Essman U and Wilkans M 1964 *Phys. Status Solidi* **4** K 53
Eyre B L and Bullough R 1965 *Philos. Mag.* **12** 31
Eyre B L 1972 *Defects in refractory metals* (eds) R de Batist, J Nihoul and L Stals SCK/CEN Mol 311
Eyre B L, Loretto M H and Smallman R E 1977 *Vacancies* '76 (London: The Metals Society) 63
Jenkins M L, Katerban K H and Wilkens M 1976a *Philos. Mag.* **34** 1141
Jenkins M L and Wilkens M 1976b *Philos. Mag.* **34** 1155
Jenkins M L, Roller G, Katerban K H and Wilkens M 1982 *J. Nucl. Mater.* **108, 109** 603
Ruhle M 1967a *Phys. Status Solidi* **19** 263
Ruhle M 1967b *Phys. Status Solidi* **19** 279
Ruhle M 1971 *on Radiation induced voids in metals, Proc. Int. Conf*, Albany, New York

Wilkens M 1970 *Vacancies and interstitials in metals* (eds) A Seeger, D Schumacher, W Schilling and J Diehl (Amsterdam: North Holland) 485
Wilkens M 1973 *Applications of ion beams to metals* (eds.) S T Picraux, E P Eer- Nisse and F L Vook (New York: Plenum Press) 441
Wilkens M 1978 *Modern diffraction and imaging techniques* (eds) S Amelinckx, R Gevers and J Van Landuyt (Amsterdam: North Holland Publ. Co.)

Bull. Mater. Sci., Vol. 6, No. 3, July 1984, pp. 549–567. © Printed in India.

Electron microscopy of layered single crystals grown by direct vapour transport method

M K AGARWAL, P D PATEL, J V PATEL and J D KSHATRIYA

Department of Physics, Sardar Patel University, Vallabh Vidyanagar 388 120, India

Abstract. Besides interesting properties such as optical, transport, structure, etc. possessed by crystals of transition metal dichalcogenides, they have also been found to have a potential application in the fabrication of PEC solar cells. These crystals are normally grown by carrier gas transport technique but are always contaminated by carrier gases. A new method of direct vapour transport has been developed and successfully applied to grow these crystals including those of off-stoichiometric varieties.

The crystals thus grown have been characterized structurally using the techniques of x-ray powder, rotation and Weissenberg photographs and electron diffraction. Perfection studies have been made by techniques like chemical etching and electron microscopy.

This review describes the electron microscopic studies made on the single crystals of the layered compounds. High resolution technique of weak beam has been employed to study dislocation pattern. Dissociated dislocations have been used to estimate stacking fault energy. Such measurements have also been carried out at different temperatures and the variation of stacking fault energy with temperature has been worked out. Interesting information regarding phase transformation for TaS_2 and W_3Se_4 in the temperature range 109 to 580 K has been derived from the electron diffraction studies and the implications have been discussed.

Keywords. Electron microscopy; transition metal dichalcogenides; growth technique; x-ray diffraction; stacking fault energy; phase transformations.

1. Introduction

In the last two decades the materials of the family of transition metal dichalcogenides have received a rapidly growing attention. Many compounds of this family having a layered structure occupy a central position in the class of layered compounds due to their various important applications such as solid lubricants, energy converters, semiconductors, switching devices and model substances for testing and exploring photo-emission methods. Moreover, their polytypic and anisotropic behaviour in the past few years has become an intensively investigated field in the study of solid state research.

These compounds have the general formula TX_2 where T is a transition metal from IV B, V B or VI B group of the periodic table and X is one of the chalcogens sulphur, selenium or tellurium. The basic structure of loosely coupled X-T-X sheets make such materials extremely interesting such that, within a layer, the bonds are strong, while between the layers they are remarkably weak.

Some of the transition metal dichalcogenides have recently found application in the construction of photoelectrochemical (PEC) solar cells. Visible and near IR radiation absorbed by these compounds produces a *d-d* excitation of electrons, which does not involve the breaking up of essential crystal bonds. This leads to the generation of holes which do not directly lead to a photoelectrochemical corossion of the substrate. Both *n*-

type and *p*-type layer compounds can therefore be favourably used to construct regenerative electrochemical solar cells.

Normally the crystals of transition metal dichalcogenides (TMDC) are grown by using the chemical vapour transport method in which invariably iodine or bromine is used as the transporting agent. It has been observed that when TMDC crystals grown by bromine transport method are used to fabricate PEC cells, intercalation of bromine into the van der Waal's gap of these crystals react with the holes and traps them, which affects the efficiency of the cell. Thus the purity of crystals is of utmost importance in cell preparation.

Moreover, when such crystals are used for optical and electrical measurements, the presence of transporting agents in them makes them so different from sample to sample that the results are not at all reproducible. In order to avoid the contamination of the transporting agents a direct vapour transport method has been established for the growth of TMDC crystals. A brief description of the method of growth and the single crystals thus grown has been given below.

Since TMDC crystals possess a layered structure they easily lend themselves as ideal specimens for transmission electron microscopic (TEM) studies because one can easily prepare as thin specimens as desired by simply using the repeated cleavage method, for which one only needs a good quality adhesive tape and pure chloroform to prepare specimens in a matter of few minutes.

TEM studies of some of the TMDC crystals grown by us which has revealed very interesting information, has been described in this article.

2. Growth technique

The chemical vapour transport (CVT) technique has been widely used for the growth of single crystals of metal dichalcogenides. This technique using iodine or bromine as transport agents certainly gives very large crystals, sometimes of the order of 1 cm in basal extension. However, these transporting agents always contaminate the growing materials as already mentioned. Growing crystals without any contamination therefore requires a process in which no transporting agent is used. Such method was used by Al Hilli and Evans (1972) to grow single crystals of certain TMDC. This method of growth of crystals known as the direct vapour transport (DVT) method has been used to grow a number of TMDC crystals not grown so far.

A tubular furnace capable of reaching high temperatures (1173–1373 K) with required temperature gradient over the length of about 25 cm was used for the growth. Transparent quartz tubes with internal diameter of 2.2 cm and of length 20 cm were most adequate for the purpose.

The preparation of the starting materials for growth was done by filling the stoichiometric proportion of the materials in a quartz tube and then sealing it under evacuation of 10^{-5} torr. The tube was then heated in a furnace to about 1000 K for about 70 hr. After this firing, the tube contained a fine free flowing black powder which was then thoroughly shaken for proper mixing. The tube was again placed in the furnace for the actual growth of the crystals. The preparation and growth procedures of the different crystals grown by us have been summarised in table 1.

The stoichiometry of the grown crystals was verified by making the EDAX analysis on the Philips EM 400 microscope.

For the transmission work, cleavage flakes of sufficient thickness (700 Å) were prepared by repeated cleavage using an adhesive tape. The microscope (Philips EM 400) has a built-in facility for taking the weak beam pictures.

X-ray powder diffraction data were obtained using Debye Scherrer powder patterns of the crushed crystals/whiskers at 293 K. The oscillation and the Weissenberg photographs were taken.

3. Characterisation of the grown crystals

The as-grown crystals were characterised by x-ray diffraction technique using powder diffraction patterns, the oscillation and Weissenberg photographs of the single crystals. The crystal structure data of the compounds grown have been summarised in table 2.

Majority of the TX_2 layer dichalcogenides grown by us arise from the stacking of hexagonally packed planes. The basic co-ordination unit for crystals having a MoS_2-type structure is the trigonal prism. Their structure consists of hexagonal stacking of X-T-X sheets in which every T atom is surrounded by six X atoms in the trigonal prism. Figure 1 presents a schematic view of the structure. The stacking sequence of layers in TX_2 can be symbolised as $A_B B_A A_B B_A \ldots$ where A_B means a X-T-X sheet with X atoms in the B position and B_A means a sheet with X atoms in the B position and T atoms in the A positions.

The normal structure of TX_2 crystals having a MoS_2 type structure, is hexagonal, with two molecules per unit cell; atoms are in special positions of space group $P6_3/mmc$ with cations at $\pm(\frac{1}{3}, \frac{2}{3}, \frac{1}{4})$ and anions at $\pm(\frac{1}{3}, \frac{2}{3}, 4)$, $\pm(\frac{2}{3}, \frac{1}{3}, \frac{1}{2})$ positions. A second form of TX_2 crystals is known to be rhombohedral in space group R3m with atoms at sites $(0, 0, 0)T$ and $(0, 0, \frac{1}{2})$, $(0, 0, 5/12)X$.

In contrast to the majority of crystals possessing a MoS_2 type structure, TaS_2 crystals belong to a CdI_2 structure, (figure 2) which has a hexagonal unit cell containing a single molecule, with cations at special positions $(0, 0, 0)$ and anions at positions $(\frac{1}{2}, \frac{2}{3}, u)$ and $(\frac{2}{3}, \frac{1}{3}, -u)$ of space group $P\bar{3}m\,1$, where u is approximately $\frac{1}{4}$. The crystal structure analysis carried out on the crystals of TaS_2 in the present work shows that they are basically 1T type.

4. Electron microscopy of TMDC crystals

The advantage of using the weak beam method of electron microscopy for analysing dislocation system is illustrated in figures 3a, b, which are the BF and WB pictures respectively. Figure 3b represents the electron micrograph of a TaS_2 crystal taken in the $(2\bar{1}0)$ diffracted beam with the crystal oriented close to the exact Bragg reflection condition. The pattern shown in the hexagon $ABCDEF$ (figure 3a) is not clearly resolved. As a matter of fact it is difficult to interpret the pattern. On the contrary, the weak beam picture clearly shows that the pattern is formed from extended nodes.

The high resolution obtained with the weak beam technique has been used to observe two-fold ribbons in WS_2 and TaS_2 crystals. The value of the separation of the partials obtained in this way has been used to estimate the stacking fault energy γ. By applying isotropic theory in an infinite crystal the stacking fault energy follows from

$$\gamma = \frac{\mu b^2}{8\pi d_0}\left[\frac{2-\nu}{1-\nu}\right], \tag{1}$$

Table 1. Charge preparation and crystal growth technique.

Compound	Charge preparation procedure	Crystal growth details Temp. range (T_1-T_2) K in which the ampoule was kept in the furnace	Rate at which the temp. is increased from room temp. to the temp. range (T_1-T_2) K/30 min	Time for which the ampoule was kept in the temp. range (T_1-T_2) days	Rate at which the ampoule was brought from the temp. range (T_1-T_2) to the room temperature	Crystal size (mm³)
1	2	3	4	5	6	7
WS_2	Directly heating stoichiometric proportions of 99.5% pure tungsten and 99·9999% pure sulphur in the quartz ampoule at 1123 K for 70 hr	1. 1373–1353	50	8	20 K/30 min	10 × 4 × 0·12
		2. 1328–1308	50	8	20 K/30 min	15 × 10 × 0·25
		3. 1293–1273	50	8	20 K/30 min	12 × 7 × 0·12
$MoSe_2$	Directly heating stoichiometric proportions 99·5% pure molybdenum powder and specpure Selenium pellets in quartz ampoule at 1013 K for 72 hr	1. 1293–1268	50	3	50 K/30 min	11 × 7 × 0·05
		2. 1293–1268	50	10	50 K/30 min	14 × 8·5 × 0.1
WSe_2	Directly heating stoichiometric proportions of 99·9% pure tungsten and specpure selenium pellets in quartz ampoule at 1073 K for 72 hr	1. 1323–1303	50 size of ampoule length 215 mm I.D. 20 mm	10	50 K/30 min	18 × 6.5 × 0.6
		2. 1323–1293	50 size of ampoule length 215 mm I.D. 22 mm	10	50 K/30 min	17 × 12 × 0·4
MoS_2	Directly heating stoichiometric proportions of 99·45% pure molybdenum and 99·9999% pure sulphur powders in quartz ampoule at 973 K for 36 hr	1. 1413–1333	20	16	20 K/30 min	15 × 14 × 0·1
$Mo_{0.85}W_{0.15}Se_2$	Directly heating stoichiometric proportions of 99·95% pure molybdenum 99–95% pure tungsten and 99·999% pure selenium powders in quartz ampoule at	1193	50	10	40 K/hour	9 × 5 × 0·15
+						
$Mo_{0.8}W_{0.2}Se_2$	at 1023 K for 40 hr	1173	50	9	40 K/hour	15 × 11 × 0·2
$Mo_{0.7}W_{0.3}Se_2$	at 1003 K for 40 hr	1133		8	40 K/hour	6 × 5 × 0·2
$Mo_{0.6}W_{0.4}Se_2$	at 993 K for 40 hr	1098	50	9	40 K/hour	12 × 9 × 0·15

$Mo_{0.5}W_{0.5}Se_2$	at 973 K for 40 hr	1093	50	6	40 K/hour	17 × 14 × 0·2
$Mo_{0.6}W_{0.4}Se_2$	at 993 K for 40 hr	1113	50	7	40 K/hour	14 × 9 × 0·2
$Mo_{0.7}W_{0.3}Se_2$	at 1003 K for 40 hr	1143	50	8	40 K/hour	15 × 16 × 0·15
$Mo_{0.8}W_{0.2}Se_2$	at 993 K for 40 hr	1113	50	7	40 K/hour	20 × 13 × 0·2
$Mo_{0.9}W_{0.1}Se_2$	at 783 K for 40 hr	1123	50	8	40 K/hour	12 × 7 × 0·15
$WS_{1.16}Se_{0.84}$	Directly heating mixture of polycrystalline powders of WSe_2 and WS_2 in quartz ampoule	1293	30	8	20 K/30 min	11 × 9 × 0·2
$WSe_{1.99}$	Directly heating stoichiometric proportions of 99·95% pure tungsten and 99·999% pure selenium powders in quartz ampoule at 1073 K for 72 hr	1223–1273	50	10	20 K/30 min	20 × 17 × 0·07
$WSe_{1.97}$	at 1073 K for 72 hr	1193–1253	50	10	20 K/30 min	20 × 15 × 0·06
$WSe_{1.96}$	at 1073 K for 72 hr	1193–1253	50	10	20 K/30 min	22 × 22 × 0·06
$WSe_{1.93}$	at 1073 K for 72 hr	1213–1273	50	10	20 K/30 min	21 × 20 × 0·05
$WSe_{1.90}$	at 1073 K for 72 hr	1213–1273	50	10	20 K/30 min	20 × 19 × 0·05

Table 2. Structure type and lattice parameters.

Compound	Character and colour	Space Group	Parameter (A)		Density (g/cm^3)	Polytype
			a	*b*		
1	2	3	4	5	6	7
WS_2	*p*-type semiconductor	$P6_3/mmc$	3·148	12·34	7·5	2*H*
	Grey black shining		3·162	18·35		3*R*
$MoSc_2$	*p*-type semiconductor	$P6_3/mmc$	3·286	12·87	6·9	2*H*
	Covalent character		3·281	19·05		3*R*
WSe_2	*p*-type semiconductor	$P6_3/mmc$	3·286	12·97	9·0	2*H*
	Grey black		3·281	13·06		
MoS_2	Covalent character	$P6_3/mmc$	3·160	12·960	4·8	2*H*
	Blue grey black		3·160	18·33		3*R*
$Mo_{0.15}W_{0.85}Se_2$	*p*-type semiconductor Blue opaque	D_{6h}^4	3·268	12·851	7·440	2*H*
$Mo_{0.2}W_{0.8}Se_2$	Black opaque	$P6_3/mmc$	3·270	12·858	7·522	2*H*
$Mo_{0.3}W_{0.7}Se_2$	Black shining	$P6_3/mmc$	3·274	12·874	7·762	2*H*
$Mo_{0.4}W_{0.6}Se_2$	Blue opaque	$P6_3/mmc$	3·278	12·890	8·022	2*H*
$Mo_{0.5}W_{0.5}Se_2$	Black opaque	$P6_3/mmc$	3·281	12·905	8·212	2*H*
$Mo_{0.6}W_{0.4}Se_2$	Bluish opaque	D_{6h}^4 $P6_3/mmc$	3·284	12·922	8·425	2*H*
$Mo_{0.7}W_{0.3}Se_2$	Brown opaque	D_{6h}^4 $P6_3/mmc$	3·288	12·938	8·668	2*H*
$Mo_{0.8}W_{0.2}Se_2$	Black opaque	D_{6h}^4 $P6_3/mmc$	3·291	12·960	8·814	2*H*
$Mo_{0.9}W_{0.1}Se_2$	Bluish opaque	D_{6h}^4 $P6_3/mmc$	3·293	12·961	9·040	2*H*
$WS_{1.16}Se_{0.84}$	Grey black Shining	$P6_3/mmc$	3·1996	12·6119	8·251	2*H*
$WSe_{1.99}$	*p*-type semiconductor	$P6_3/mmc$	3·296	13·04	7·9931	2*H*
	Grey black		±0·02	±0·02		
$WSe_{1.97}$	*p*-type semiconductor	$P6_3/mmc$	3·301	13·14	7·8755	2*H*
	Grey black		±0·02	±0·02		
$WSe_{1.96}$	*p*-type semiconductor	$P6_3/mmc$	3·312	13.19	7·7715	2*H*
	Grey black		+0·02	±0·02		
$WSe_{1.93}$	*p*-type semiconductor	$P6_3/mmc$	3·328	13·30	7.5800	2*H*
	Grey black		±0·02	±0·02		
$WSe_{1.90}$	*p*-type semiconductor	$P6_3/mmc$	3·342	13·46	7·3750	2*H*
			±0·02	±0·02		

Group: VI d^4; coordination of the metal atom: trigonal prism.

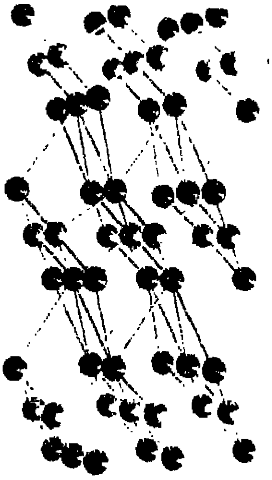

1.

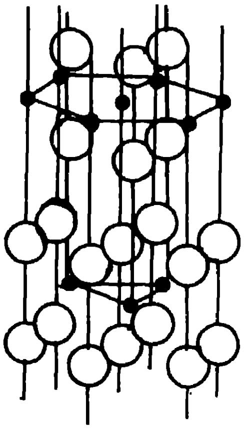

2.

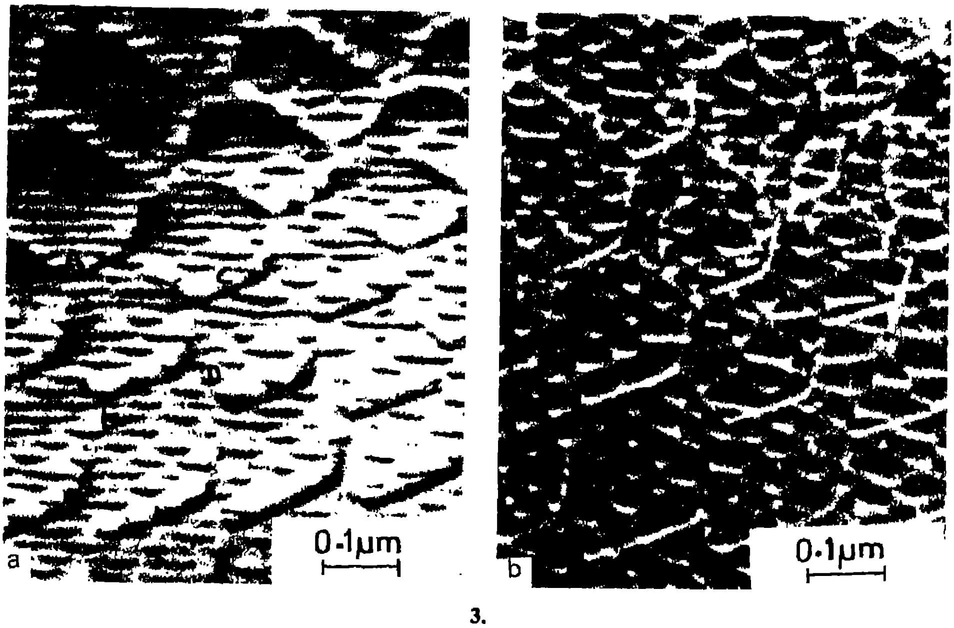

3.

Figures 1–3. **1.** Schematic view of MoS_2 type structure; **2.** Cadmium iodide layer structure. Small circles Cd, large circles I; **3a.** Bright field picture showing network pattern of the extended nodes; **3b.** Corresponding weak beam picture of 3a.

where d_0 expresses the equilibrium separation of the partials, d_0 is calculated from the formula

$$d = d_0 \left\{ 1 - \frac{2\nu}{2-\nu} \right\} \cos 2\phi \qquad (2)$$

where d is the distance between the partials in a ribbon; b, the Burgers vector of the partial; ϕ, the angle between the total burgers vector and ribbon; μ, the shear modulus; and ν, the Poisson's ratio.

Figure 4 shows a high resolution $2\bar{2}0$ weak beam dark field micrograph of a dislocation in WS_2 with Burgers vector $\frac{1}{2}[1\bar{1}0]$ with $s_{2\bar{2}0} = 2{\cdot}57 \times 10^{-2}$ Å^{-1}, showing two peaks in the image.

Also shown in figure 4 is the SADP from the area imaged, showing the weak $[2\bar{2}0]$ reflection and strong [220] reflection. Measurement of the separation of the peaks made using a micro-densitometer gave the separation value as 27 Å.

Using this value, γ/μ was determined from (1) and is found to be $4{\cdot}88 \times 10^{-11}$ cm. The corresponding value obtained from isolated ribbons in TaS_2 crystals is $5{\cdot}5 \times 10^{-11}$ cm.

Symmetrical three-fold ribbons can also be used to estimate the stacking fault energy γ. According to Aerts *et al* (1962) for ribbons, consisting of three partials with the same Burger's vectors

$$\gamma_1 = A\left(\frac{1}{x} + \frac{1}{x+y}\right), \tag{3}$$

$$\gamma_2 = A\left(\frac{1}{y} + \frac{1}{x+y}\right), \tag{4}$$

where
$$A = \beta \cos^2 \phi + \alpha \sin^2 \phi$$
$$\beta = \mu b^2/2\pi; \quad \alpha = \mu b^2/2\pi(1-\nu),$$

x and y are the widths of the ribbons, γ_1 and γ_2 are the stacking fault energies in the regions x and y respectively, b is the Burgers vector, ν is the Poisson's ratio, μ is the shear modulus, ϕ is the angle made by the Burgers vector with the partials.

An example of three-fold ribbons observed in some of the specimens of WSe_2 crystals is shown in figure 5. It was seen that the three partials comprising the three-fold ribbons go out of contrast simultaneously, proving that their Burgers vectors are the same. The ribbons widths x and y shown in figure 5 are used to calculate γ_1/μ and γ_2/μ since μ for WSe_2 is not known. For actual measurements the region shown in figure 5a was photographed in weak beam (figure 5b and γ_1/μ and γ_2/μ computed on the ribbons as shown in this figure.

Using the x and y values from figure 5b, γ_1/μ and γ_2/μ have been estimated as $56{\cdot}27 \times 10^{-12}$ cm and $46{\cdot}11 \times 10^{-12}$ cm respectively.

Since our microscope has built-in facility to vary the specimen temperature, a region showing three-fold ribbons (figure 6a) at 109 K was heated up to 319 K as shown in figure 6b. A comparison of the two figures clearly reveals that the width of the partials forming the three-fold ribbons marked XX in figure 6a has considerably increased.

As mentioned above, γ_1/μ and γ_2/μ were computed from the width of the ribbons in figure 6a. The region shown in figure 6a was heated at different temperatures. Sufficient time was given at each temperature for its stabilisation. γ_1/μ and γ_2/μ were computed from the width of the ribbons at each stage. These values are shown in table 3. A plot showing the variation of γ_1/μ and γ_2/μ with temperature is shown in figure 7.

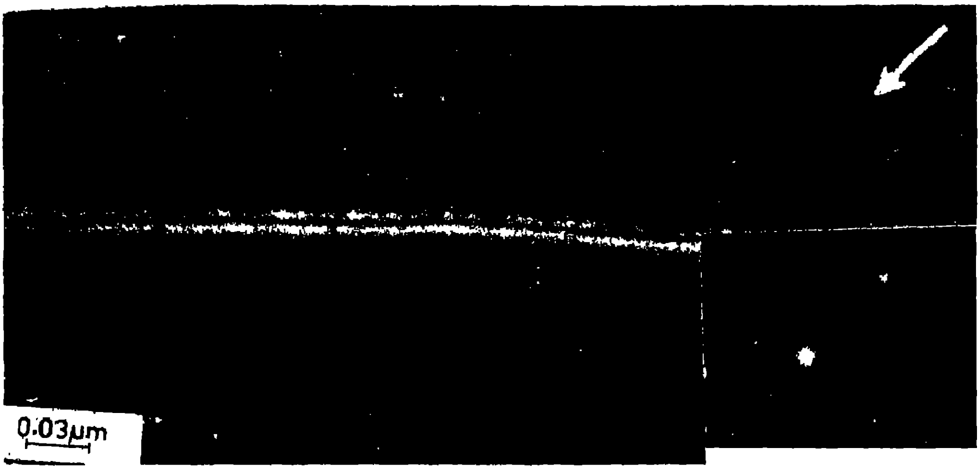

4.

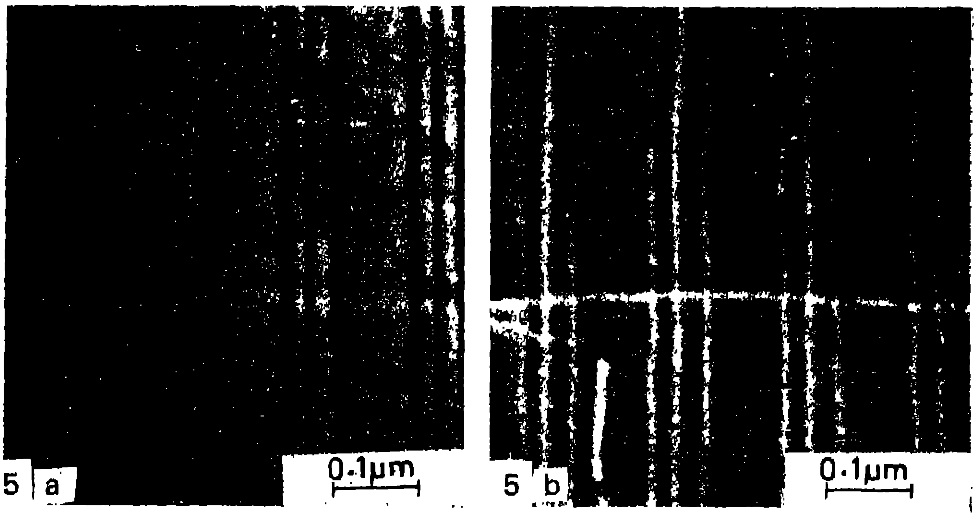

Figures 4–5. **4.** Weak beam dark field picture of two-fold ribbons in WS_2; **5a.** Bright field electron micrograph showing three-fold ribbons in WSe_2; **5b.** Corresponding weak beam picture of **5a.**

5. Studies of phase transformations

5.1 1*TTaS*$_2$

5.1a *Phase transformations from physical properties.* Disalvo *et al* (1974) and Thomson *et al* (1971) have studied a number of physical properties of 1*T*-TaS_2 crystals and have reported a number of phase transformations. They have particularly found that the electrical resistivity changes abruptly at 350 K and 190 K. The transition at

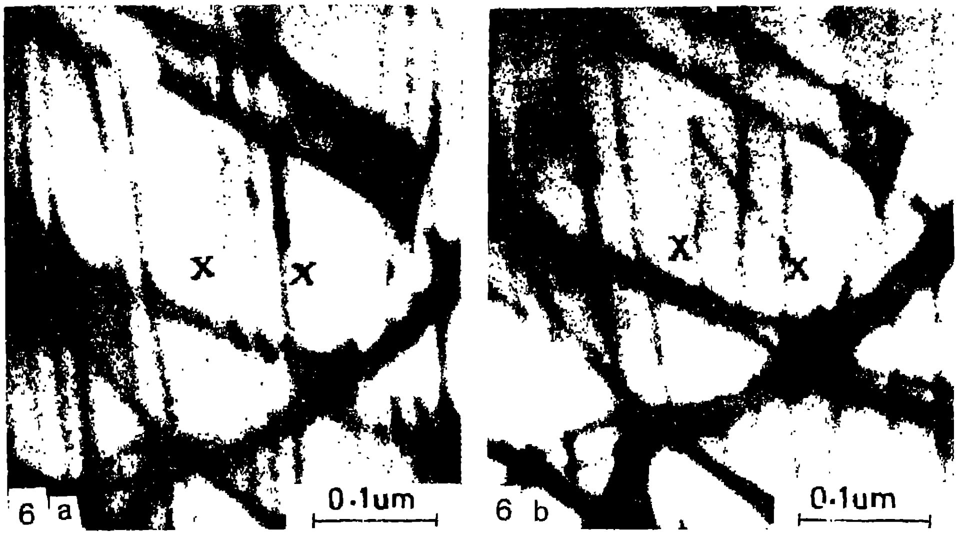

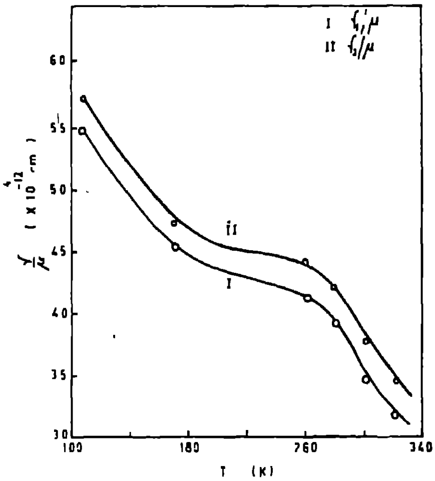

7.

Figures 6–7. **6a.** A region showing three-fold ribbons at 437 K; **6b.** Same region as figure 6a at +46 K; 7. Plots showing variation of γ_1/μ and γ_2/μ with temperature.

Table 3. Variation of γ/μ with temperature.

Temperature (K)	$\gamma_1/\mu(10^{-12}$ cm)	$\gamma_2/\mu(10^{-12}$ cm)
109	54·872	57·455
169	45·640	47·427
260	41·400	44·413
278·5	39·184	42·081
299	34·659	37·898
319	31·937	34·666

190 K is accompanied by a large hysteresis covering a temperature range of about 100 K. On increasing the temperature it occurs at 240 K, whereas with decrease in temperature it takes place at 145 K. The transition at 350 K shows little hysteresis and corresponds to a metal-semiconductor transition, whereas the 190 K transition corresponds to a change in the basal gap of the semiconducting phase. The magnetic susceptibility also shows a change at 350 K, the material however remaining paramagnetic. Similar type of hysteresis as found from electrical resistivity also occurs in the magnetic susceptibility.

5.1b *Phase transformations from electron diffraction:* Amelinckx (1976) proposed the existence of α, β, γ and δ phases in $1T$-TaS_2 crystal by studying the diffraction patterns at different temperature. Phases similar to β and δ were also observed by Williams *et al* (1974) and they proposed to call them $1T_1$, $1T_2$ and $1T_3$. Our observations regarding β and δ phases are shown in figure 8.

It is seen that at a temperature of nearly 586 K a pattern shown in figure 8a is obtained. Upon decreasing the temperature to 478 K a pattern as shown in figure 8b is obtained. Upon further decreasing the temperature to 350 K the pattern shown in figure 8c is obtained. The onset of β phase can be noted in this figure.

At 320 K the pattern suddenly changes reversibly into that shown in figure 8d. This pattern is actually a characteristic of the γ-phase. This transition temperature of 320 K coincides more nearly with the magnetic transition temperature (315 K). This observations differs from the observation of Amelinckx (1976) who observed this transition temperature as 350 K.

Further there is a large disagreement in reporting the exact temperature at which the pattern changes from incommensurate γ-phase to the commensurate δ-phase. In the case of Williams *et al* (1974) this temperature is 150 K while for Amelinckx (1976) it is 190 K. In the present studies also it is very difficult to pinpoint the exact temperature from the observation of the diffraction patterns alone, since the intensity of the six first order reflections surrounding the central spot goes on increasing as one lowers the temperature from 290 K to 85 K. The exact onset of the δ-phase is difficult to recognise. However, it appears that the phase occurs at 139 K (figure 8e).

The discrepancies reported in the literature concerning the relationship between changes in diffraction pattern and phase transitions as observed by discontinuities in the physical properties may be attributed to the error resulting from the measurement of the specimen temperature in the heating holder of an electron microscope.

It was generally seen that when crystals were heated from a temperature of 94·5 K to higher temperatures, the phases occurred in the sequence δ-γ-β. However, the exact temperatures at which the transitions occurred were only slightly different from those reported by earlier workers. In one case however observations quite different from those reported so far have been made and are described below.

A crystal heated from 94·5 K showed the occurrence of δ, γ and β phases but, at a temperature of 528 K all the superlattice spots disappeared and the crystal transformed completely to a 2H phase (figure 9). This crystal was then heated up to 617 K (figure 10) and then slowly cooled. At a temperature of 441 K superlattice spots reappeared (figure 11) but this time all the superlattice spots were exactly at the centre of the basic matrix spots, i.e.—the pattern formed a $2a_0$ hexagonal superstructure.

This pattern remained up to room temperature (figure 12). When the crystal was reheated the phase remained up to 540 K but then started disappearing. Upon cooling

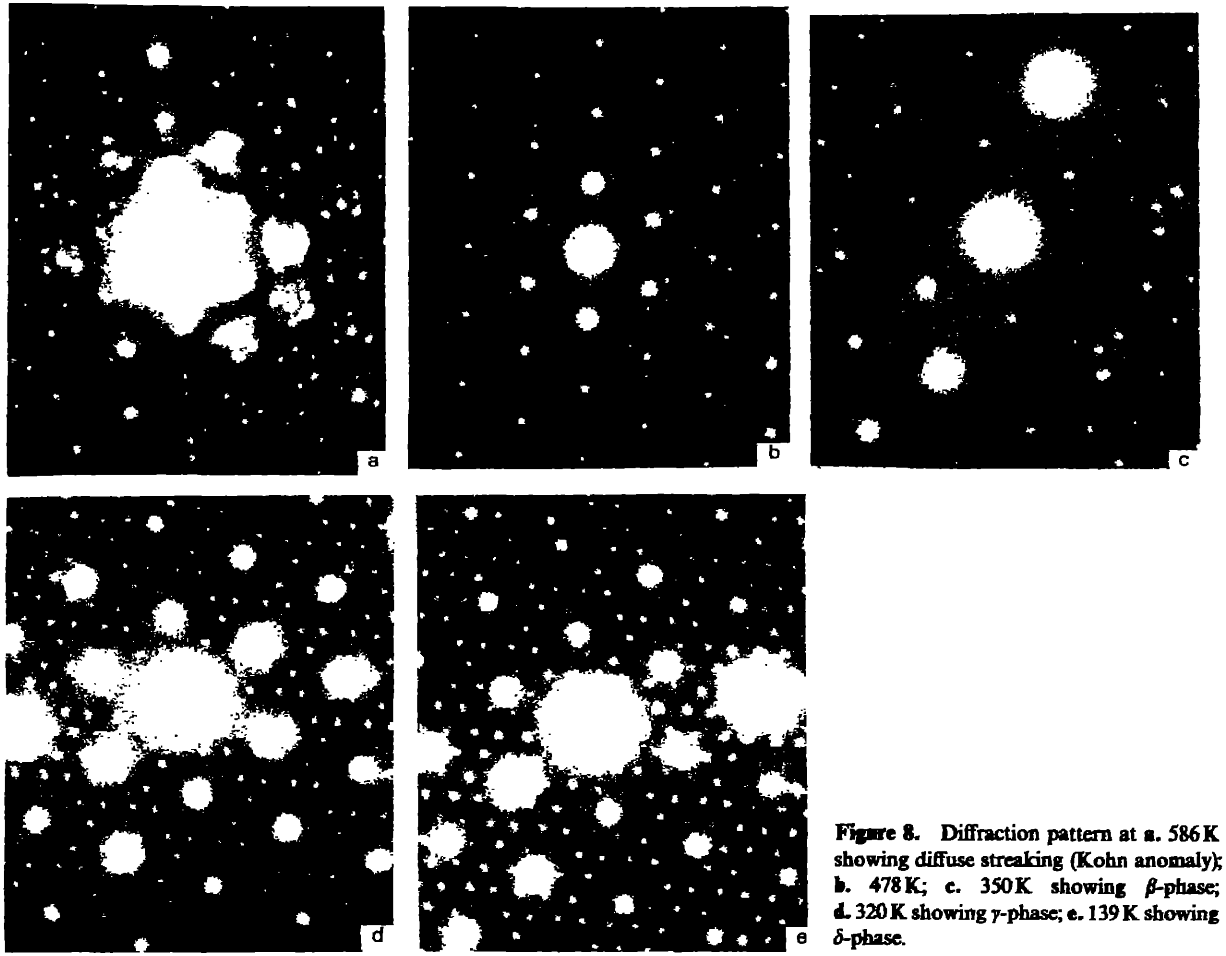

Figure 8. Diffraction pattern at **a.** 586 K showing diffuse streaking (Kohn anomaly); **b.** 478 K; **c.** 350 K showing β-phase; **d.** 320 K showing γ-phase; **e.** 139 K showing δ-phase.

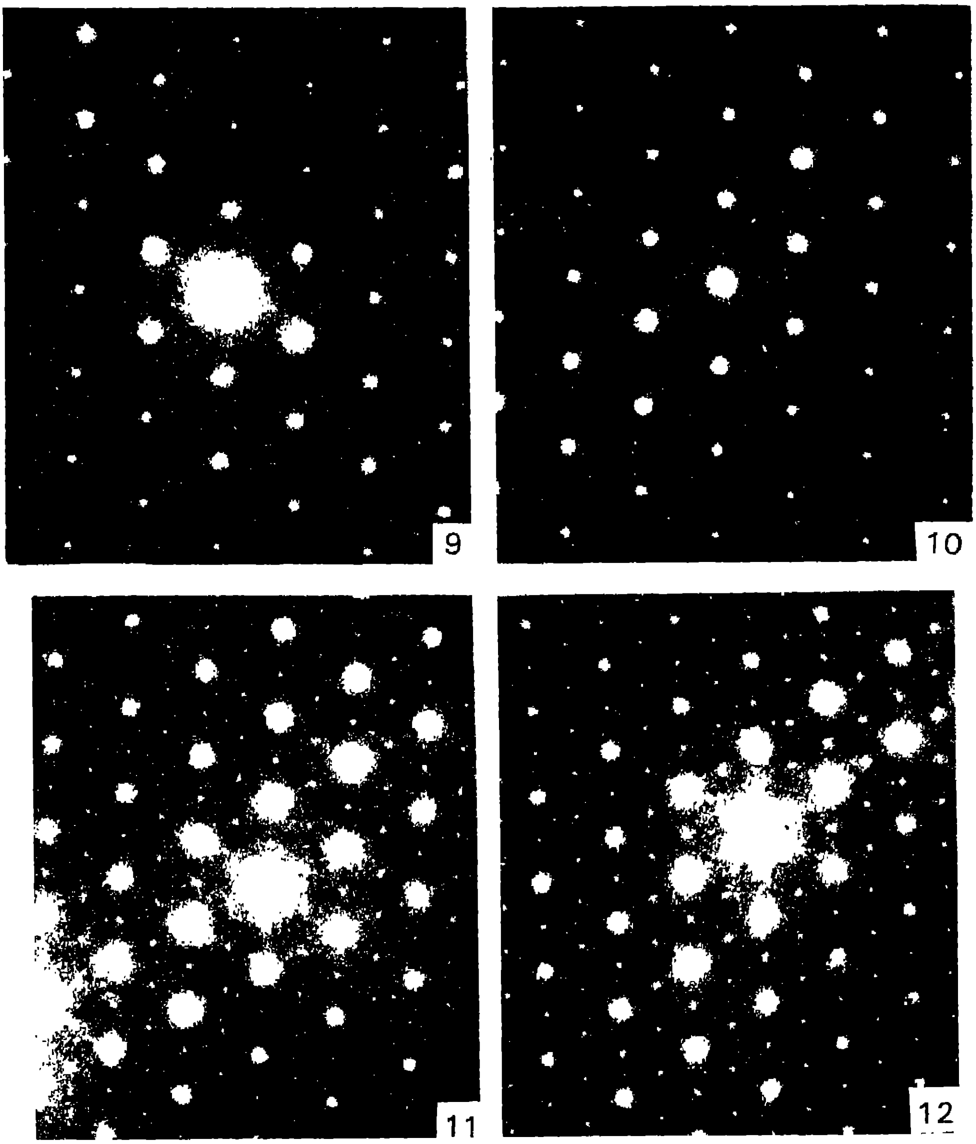

Figures 9–12. **9.** Electron diffraction pattern of TaS_2 showing 2H-phase at 528 K; **10.** Same diffraction pattern as figure 9 at 616 K; **11.** Diffraction patterns at 441 K (i.e. after slow cooling) at which the superlattice spots seem to reappear. **12.** Same diffraction pattern as figure 11 at 300 K.

the specimen again to room temperature the phase reappeared. Thus it can be concluded that the phase shown in figure 12 is reversible in the temperature range 300 to 540 K.

Diffraction patterns obtained from TaS_2 crystals intercalated by copper (De Ridder *et al* 1976, 1977; van Tendeloo *et al* 1976) are exactly similar to the one reported above. Moreover, these patterns are also having a reversible phase occurring over a certain temperature range.

Comparing the similarity of our patterns with those of De Ridder *et al* (1976, 1977) and van Tendeloo *et al* (1976), it is quite plausible to attribute the occurrence of the reversible phase in our specimen to some type of intercalation. Since the crystals were free from any kind of impurity it is more reasonable to consider autointercalation, which is quite probably due to Ta atoms, since when TaS_2 crystals are grown by direct vapour transport, along with the single crystals of TaS_2 one also observes needles or whiskers.

Diffraction pattern taken from these whiskers at and just below room temperature (figures 13 and 14) exhibit very faint streaks of diffuse intensity parallel to the close rows of Bragg reflections. The similarity of these diffraction patterns with those of TaS_3 suggests that the whiskers are not of TaS_2 but are in fact of TaS_3. That this is indeed the case can be seen from x-ray diffraction studies described below.

The powder diffraction pattern for the whiskers is shown in figure 15. When *d* values computed from this photograph are compared with the *d* values for TaS_3 in the ASTM data (table 4), it is seen that there is a remarkable degree of correspondence between the two data, thus indicating that the whiskers are due to TaS_3. The additional *d* values which do not correspond with the data for TaS_3 are in fact due to TaS_2. This is quite logical since the whiskers of TaS_3 grow along with the crystals of TaS_2.

The whisker growth indicates that some tantalum atoms which are in excess can sit between the TaS_2 layers and thereby lead to autointercalation.

This conjecture is further supported by the EDAX analysis of the regions showing the superlattice spots and the regions devoid of superlattice spots. It is conclusively seen from this study that regions showing superlattice spots show excess of tantalum in them.

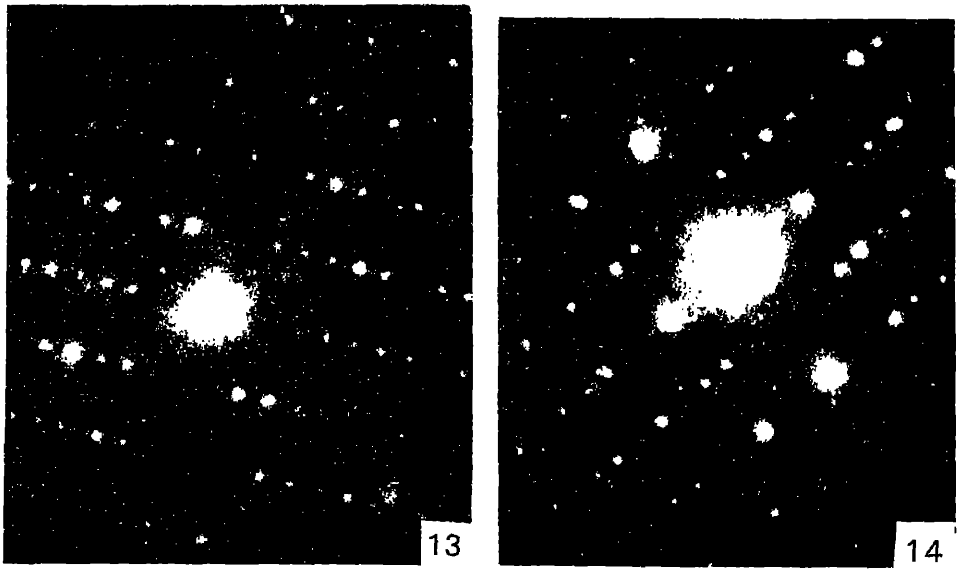

Figures 13, 14. Diffraction patterns taken from TaS_2 whiskers.

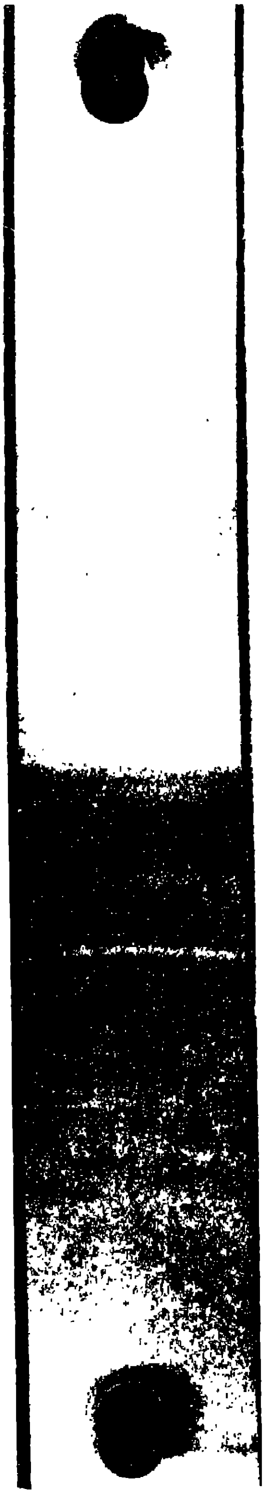

Figure 15. Powder diffraction pattern taken from TaS_2 whiskers.

Table 4. *d* values for TaS_3 whiskers.

d observed (Å)	*d* ASTM-data (Å)
9·252	9·20
7·565	7·01
5·9643	4·77
4·793	4·68
3·888	4·60
3·537	3·79
3·372	3·51
3·257	3·31
3·123	3·07
2·946	2·981
2·747	2·931
2·652	2·900
2·398	2·780
2·347	2·546
2·222	2·385
2·091	2·338
1·976	2·321
1·904	2·242
1·847	2·211
1·757	2·166
1·656	2·066
1·616	1·941
1·594	1·897
1·419	1·848

5.2 W_3Se_4

5.2a *Phase transformations indicated from diffraction patterns*: Reversible phase transitions similar to TaS_2 also occur in W_3Se_4 crystals grown by taking tungsten and selenium in stoichiometry by a direct vapour transport method.

A diffraction pattern obtained at room temperature from a thin specimen prepared from W_3Se_4 crystals is shown in figure 16. This pattern clearly resembles figure 12. Here also one sees a $2a_0$ hexagonal superlattice pattern.

Different diffraction patterns that are produced with decreasing temperatures are shown in figures 17a-d at 249, 175, 158 and 109 K respectively. A careful study of these figures reveals the following features: (i) All the patterns show a $2a_0$ hexagonal superlattice pattern (ii) Starting from room temperature, as the temperature is lowered, faint streaks start appearing along the line joining the superlattice spots. The intensity of this streaking goes on increasing with the decrease in temperature (iii) At a temperature of about 175 K a new phase starts appearing in the form of superlattice spots lying exactly midway between the superlattice spots formed earlier. The intensity of these spots goes on increasing as the temperature is lowered (iv) In figures 17b-d, it can be noted that around each matrix spot all the superlattice spots lie on a circle of

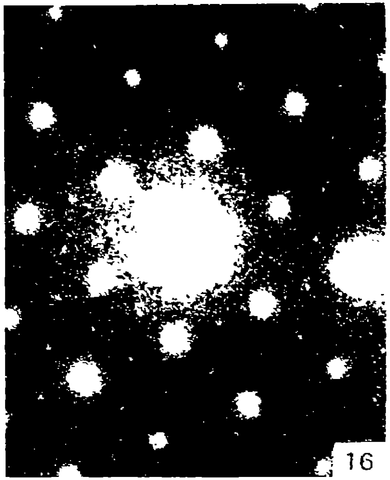

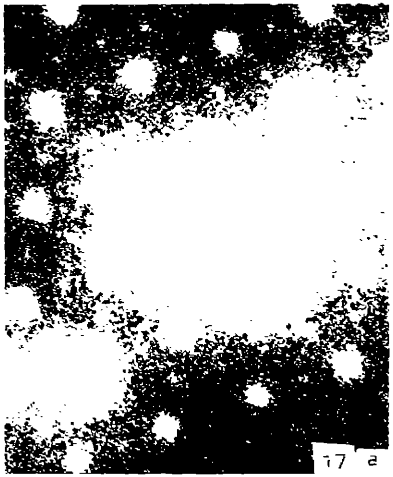

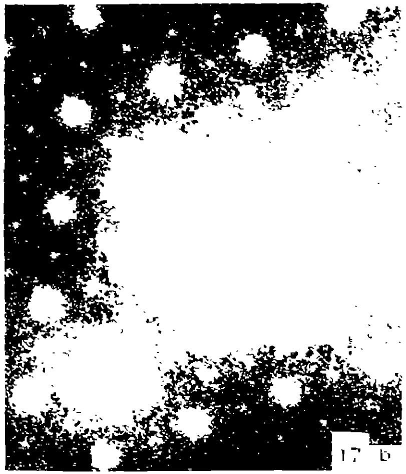

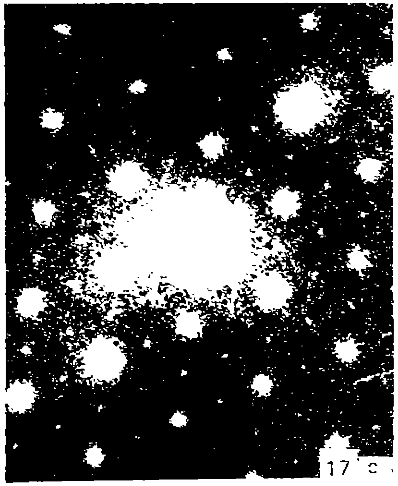

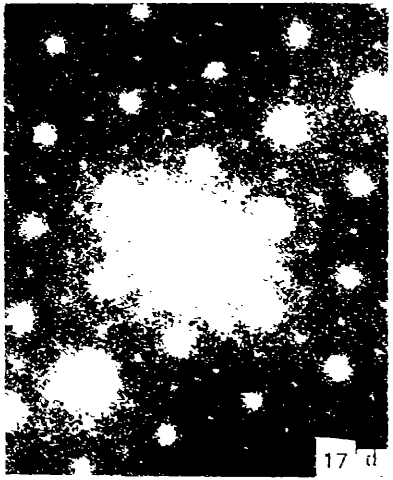

Figures 16–17. **16.** Electron diffraction patterns (while cooling) from W_3Se_4 at 298 K. **17.** Electron diffraction patterns (while cooling) of W_3Se_4 at **a.** 298 K, **b.** 249 K, **c.** 175 K, **d.** 158 K, **e.** 109 K.

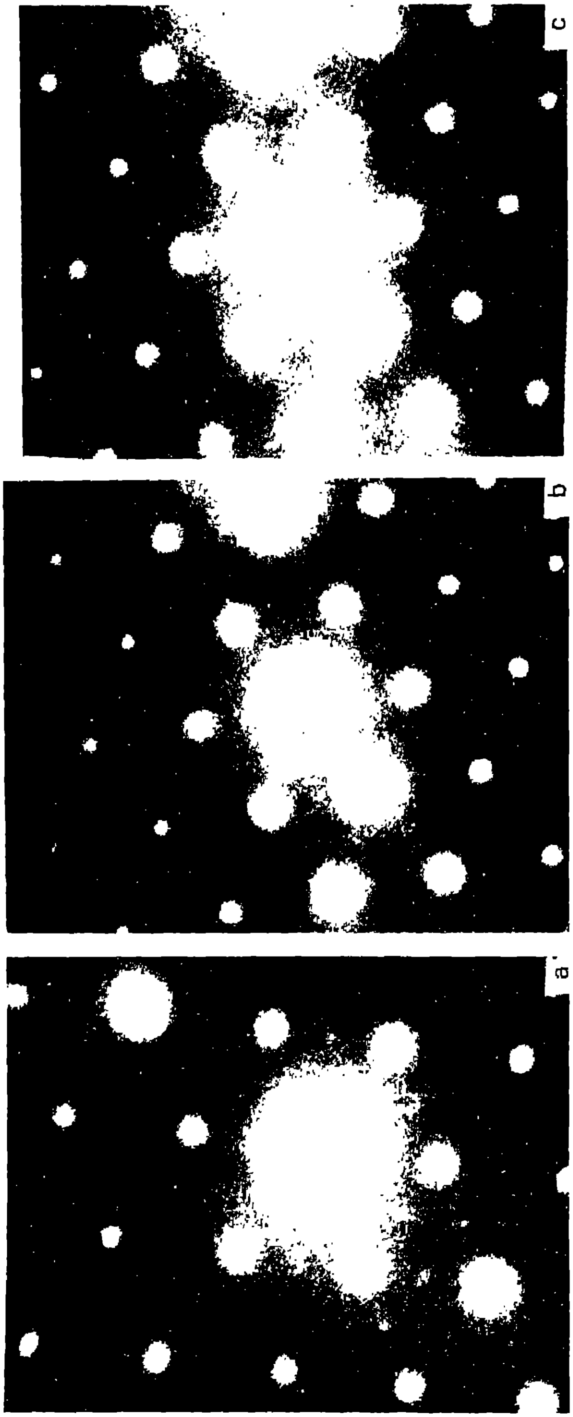

Figure 18. Electron diffraction patterns (while heating) of W_3Se_4 at a. 313 K, b. 426 K, c. 496 K.

diffuse intensity (v) The superlattice spots appearing at the temperature of 175 K are not very sharp and have a slight elongation. Similarly the diffraction patterns obtained on heating the specimen at 313, 426 and 496 K from room temperature are shown in figures 18a-c respectively.

It can be noticed from these patterns that the intensity of the superlattice spots goes on decreasing and finally at 459 K, they completely disappear giving rise to only the basic 2H structure.

The order depicted by the superlattice spots can be due to the presence of ordered domains in the structure. In order to verify this conjecture we tried to make dark field images with the superstructure spots. In such images if the order is because of domains, then different areas of the region from which the image is being formed will show different contrast. In the present case it was observed that the contrast is uniform, practically all areas of the region show uniform shade contrast.

In order to study the *c*-axis of the superstructure the specimen stage was tilted to bring other sections of the reciprocal lattice in view. In the diffraction patterns so obtained one notices continuous streaking along the *c*-axis which indicates a large amount of disorder in this direction.

Since the order represented by the superlattice spots is not because of ordered domains, it can be due to autointercalation. In some regions atoms of either W or S occupy positions between the Se-W-Se layers and give rise to the intercalation. Such intercalated specimens can give rise to an ordered diffraction pattern observed above.

The fact that the order goes on increasing as the temperature is lowered and vanishes completely as the crystal is heated can be easily attributed to the thermal vibrations of the intercalated atoms.

The appearance of a new phase at 175 K is predicted by the streaking of the spots in the diffraction pattern.

Acknowledgement

The authors are thankful to Prof. A R Patel for encouragement and his interest in the work.

References

Aerts E, Delavignette P, Siems R and Amelinckx S 1962 *J. Appl. Phys.* **33** 3078

Al Hilli A A and Evans B L 1972 *J. Crystal Growth* **15** 93

Amelinckx S 1976 *J. de Phys.* **37** 1976

De Ridder R, van Tendeloo G, van Landuyt J, van Dyck D and Amelinckx S 1976 *Phys. Status. Solidi* **A37** 591

De Ridder R, van Dyck D, van Tendeloo G, van Landuyt J and Amelinckx S 1977 *Phys. Status. Solidi* **A39** 383

Di Salvo F J, Maines R C and Waszczak J V 1974 *Solid State Commun.* **14** 497

Thomson A H, Gamble F R and Revelli J F 1971 *Solid State Commun.* **9** 981

van Tendeloo G, De Ridder R, van Dyck D, van Layduyt J and Amelinckx S 1976 *Phys. Status. Solidi* **A38** 185

Williams P M, Parry G S and Scruby C B 1974 *Philos Mag.* **29** 695

Bull. Mater. Sci., Vol. 6, No. 3, July 1984, pp. 569–572. © Printed in India.

Details of an imaging atom probe

V R SESHADRI, K NEELAKANTAN, E MOHANDAS and
V S RAGHUNATHAN

Reactor Research Centre, Kalpakkam 603 102, India

Abstract. An imaging atom probe has been incorporated in a conventional field ion microscope in our laboratory. The principle and instrumentation of the probe has been discussed.

Keywords. Field ion microscope; imaging atom probe; high voltage pulser.

1. Introduction

An alternative to the field ion microscope atom probe (FIMAP) is the imaging atom probe (IAP) (Panitz 1974). An IAP allows the estimation of chemical composition over a large area of a field ion specimen, while maintaining the excellent spatial resolution of the original atom probe developed by Muller *et al* (1968). This makes the IAP very much suitable in cases where the composition changes rapidly over a distance of few atom diameters—a situation often encountered at interphase interfaces, grain boundaries with segregation and other lattice inhomogenities. Section 2 gives the principle of an IAP. Section 3 describes the instrumentation and section 4 presents the experimental observations.

2. Principle

In a conventional FIM the atoms of the specimen surface can be field evaporated as ions by applying high voltage pulses of few nsec width over the standing d.c. potential. The disorbed species drift towards the detector at a velocity determined by their mass to charge ratio and the total applied potential to the specimen for field evaporation. The detector is then gated on after a delay which corresponds to the drift time of a particular species. The image on the screen then gives the distribution of the selected species over the specimen surface.

3. Instrumentation

Figure 1 shows the schematic of an IAP. The microscope is a conventional FIM comprising of a stainless steel vacuum chamber, vacuum pumping system, cryostat for cooling the specimen and a CEMA for image intensification.

The heart of the special instrumentation for IAP is the high voltage pulsers, shown schematically in figure 2. Unlike the conventional pulsers using krytrons or mercury-wetted relays these pulsers use a novel method for generating pulses of $\approx 1{\cdot}1$ kV

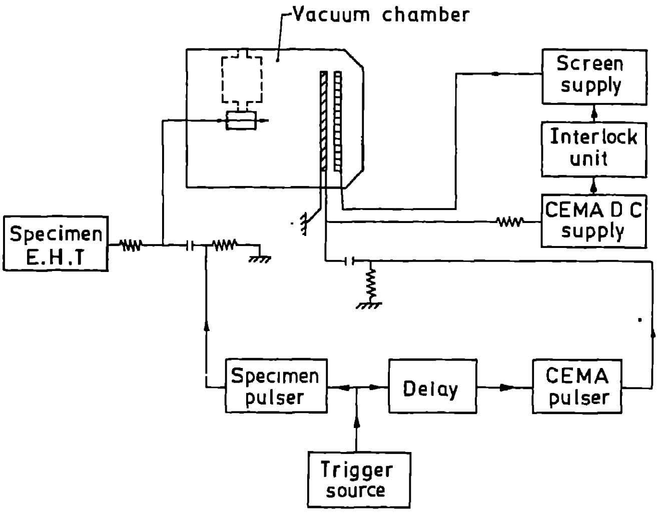

Figure 1. Block diagram of IAP.

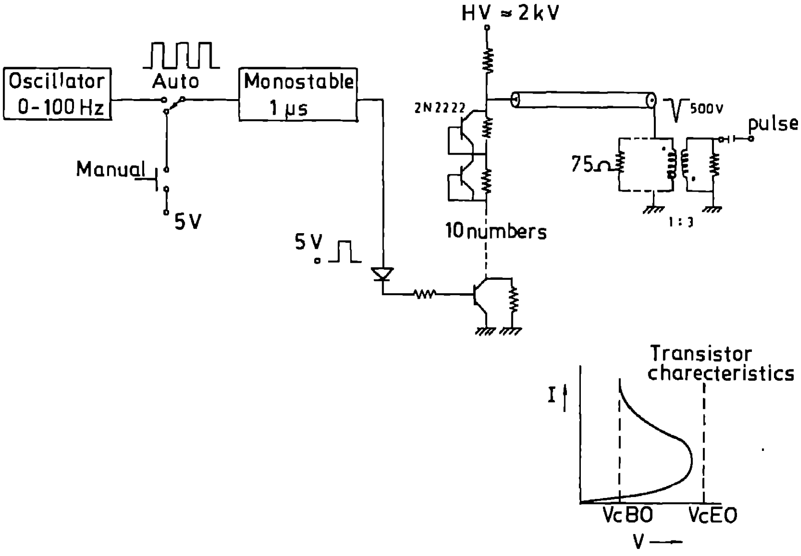

Figure 2. Schematic of high voltage pulser.

amplitude with pulse widths of a few nsec. The circuit is completely solid state and uses the controlled avalanche breakdown of a chain of *n-p-n* transistors. Ten transistors (2N2222) are connected in cascade as shown in figure 2. The circuit is biased by a 1·5–2 kV power supply through a 120 k Ω resistor in such a manner that the V_{CE} of the individual transistors are very close to the collector-base break down voltage. When a TTL (5 V) pulse is applied to the base of the transistor, at the bottom of the chain it saturates and the applied voltage gets redistributed among the remaining transistors.

This redistributed voltage is arranged to be greater than the breakdown voltage so that the entire chain goes into the avalenche breakdown mode. The sustaining V_{CE} of the transistors under avalanche breakdown is less than the breakdown voltage itself, because the transistor characteristics fold over (Millman and Taub 1965). Thus a negative pulse appears at the collector of the transistor at the top of the chain. This pulse is too wide to be used directly and is about 1 kV in amplitude. The rise time of the pulse is also quite large though fall time is to the order of a few nsec. This pulse is then shaped by a delay line differentiator and then stepped up by a 1 : 2 pulse transformer to obtain a positive pulse of up to 1·1 kV amplitude with a rise time and fall time of ≈ 5 nsec.

Two such pulse generators are used and sequentially triggered. The trigger pulses to the pulse generators are delayed by means of a delay generator which uses a monoshot to generate delays upto 1 nsec in steps of 10 nsec. The two generators are isolated and completely shielded from each other to prevent spurious triggering of second pulser. The CEMA pulser has to drive a capacitance load of approximately 400 pF and hence appropriate compensation networks are also incorporated in the design. The high voltage pulses with delay are shown in figure 3.

4. Experimental observation

The pulses have been connected to the system to achieve the following results:

(i) By applying the pulse to the specimen, superimposed on the operating d.c. voltage, controlled field evaporation has been observed. This helps primarily in shaping the specimen to get the field evaporated end form without specimen failure as is often the case with uncontrollable d.c. field evaporation.

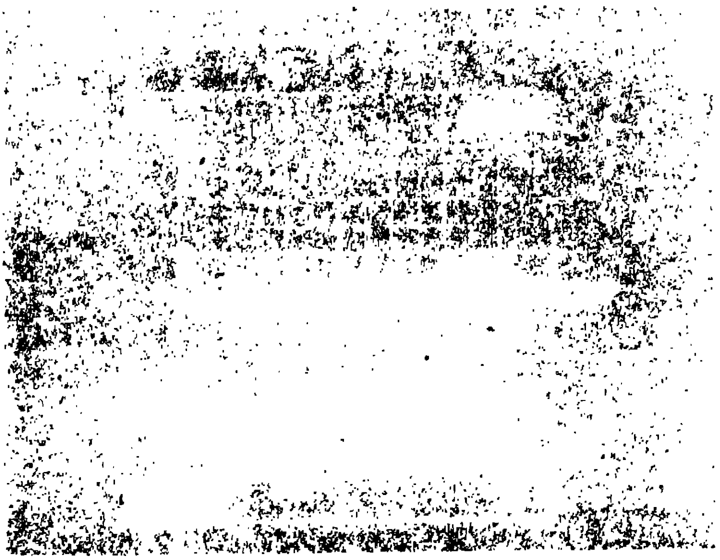

Figure 3. High voltage pulses showing the main pulse (top one at the beginning) and the delayed one (bottom). The main pulse is ≈ 1·5 kV and delayed pulse ≈ 500 V. The delay is 200 nsec/div.

(ii) With pulse applied to CEMA, gated FIM image has been observed with extremely low gas pressure. Further experiments to get IAP pictures were not successful due to poor detector performance.

5. Conclusion

A new method of producing high voltage pulser has been described. Application of these pulsers for construction of an IAP is discussed.

References

Millman J and Taub H 1965 *Pulse, digital and switching wave forms* (Kagakusha: McGraw Hill)
Muller E W, Panitz J A and Mclane S B 1968 *Rev. Sci. Instrum.* **39** 83
Panitz J A 1974 *J. Vac. Sci. Technol.* **11** 206

Bull. Mater. Sci., Vol. 6, No. 3, July 1984, pp. 573–577. © Printed in India.

Field ion microscopic observations of LaB_6 on tungsten

D B JOAG, P L KANITKAR, M M KANITKAR and V M SHUKLA

Department of Physics, University of Poona, Pune, India

Abstract. The importance of field ion microscopy as a unique surface microscopic technique has been pointed out with particular reference to the lanthanum hexaboride (LaB_6)-deposited refractory metal cathodes. In the core, field ion microscopic observations of LaB_6 deposited tungsten are described. The observations are discussed in relation to the field electron emission microscopy of LaB_6/W system. The paper ends with a few comments on the scope of further study of this or a similar system using the field ion microscopy and the atom probe field ion microscope.

Keywords. Field ion microscopy; lanthanum hexaboride; tungsten field evaporation; atomistic behaviour.

1. Introduction

In the studies of atomic adsorption on a substrate lattice, it is usually difficult in practice to define the structure of the substrate on atomic scale. The field ion microscope (FIM) allows us to observe individual atoms on an atomically smooth surface on various crystallographic planes in a single experiment (Muller and Tsong 1969).

Lanthanum hexaboride (LaB_6) has been a material of interest because of its excellent electron emissive properties (Lafferty 1951). Field electron emission properties of LaB_6-deposited tungsten have been investigated earlier (Dharmadhikari *et al* 1977, 1979). The adsorbed species were observed to agglomerate on the regions around $\{111\}$ and $\{001\}$ planes of tungsten. The work function of the composite surface also reduced, as in any other case of electropositive adsorption in general. Studies on coadsorption of lanthanum and boron by Okuno *et al* (1978) by field emission microscopy also suggested that lanthanum is located outside the substrate surface, boron remaining intermediate. It was, therefore, important to study the adsorption of LaB_6 on tungsten using FIM in order to shed more light on the atomistic behaviour.

2. Experimental

An all-metal bakeable chamber, evacuated to 10^{-8} torr by a combination of oil diffusion pump and a sputter ion pump, was used for this purpose. The specimen was mounted on a specimen manipulator and cooled to liquid nitrogen temperature by means of a copper braid. The microscope was equipped with a microchannel plate image intensifier and a fluorescent screen. The LaB_6 source was made by cataphoretic deposition of LaB_6 powder onto a clean tungsten spiral. The source was mounted on a three pin feed-through to facilitate resistive heating. A molybdenum cylinder around the source served as a mask to avoid unwanted deposition on insulating parts. The source was degassed thoroughly in vacuum prior to deposition. Helium was used as an imaging gas, which could be admitted through an all-metal valve. The tungsten wire was annealed at 1500°K in vacuum, before making the tip by electrochemical etching.

Initially, the tip was imaged and field evaporated to obtain the end form. The chamber was then re-evacuated to 10^{-8} torr and the specimen was manipulated to face the source. The adsorbate dose was pre-fixed by choosing the heating current and the duration of heating. The tip could be heated to a desired temperature by resistive heating in order to equilibrate the adsorbate over the surface. It was then manipulated back and the image was observed by re-admitting the imaging gas to a pressure of 10^{-5} torr. Temperatures of the tip and the source, when heated, were measured by optical pyrometer.

3. Results

3.1 *Clean tungsten*

Figure 1(a) shows the FIM of field evaporated tungsten surface cooled down to liquid nitrogen temperature, imaged at the helium pressure of 10^{-5} torr, in static mode.

3.2 *In situ deposition*

The adsorbate source was heated to 2100°K for 10 sec with the tip held at liquid nitrogen temperature. During deposition, the tip temperature was expected to rise by not more than 50°K. Figure 1(b) shows clusters of the adsorbate atoms, randomly deposited on tungsten.

3.2a *Substrate heated to 1200°K for 30 sec:* Three more doses, equivalent to the first one, were deposited onto the tip which was subsequently heated to 1200°K for 30 sec. The pattern in figure 1(c) appeared at the *best imaging voltage* (BIV) 2·3 kV. This pattern shows clusters of adsorbate on regions surrounding {121} planes of the substrate.

3.2b *Substrate heated to 1650°K for 30 sec:* Lanthanum hexaboride was again evaporated from the source and the substrate tip heated to 1650°K for 30 sec. The specimen was manipulated to bring one of the {001} planes in the field of view, as seen in figure 1(d). Clearly, growth is observed on {111} and {001} planes. Due to migration of the substrate tungsten atoms, the tip got blunted.

3.3 *Field evaporation*

As the field evaporation was carried out, the BIV rose steadily, the pattern remaining stable after the removal of every layer. However, the evaporation voltage was always only slightly higher than the imaging voltage and less when compared with the evaporation voltage for clean tungsten. Figure 1(e) shows the adsorbate covered surface with a few layers of adsorbate removed. Epitaxially grown layers on the {111}, {001} planes and the terraces joining {111} and {121} planes are clearly depicted. Figure 1(f) shows the field evaporated surface with a few interstitial atoms, particularly in the {011} planes. A few displaced atoms are also seen. The surface structure becomes more and more ordered after subsequent field evaporation.

At this stage, the {011} and the {111} and {001} planes had different BIV.

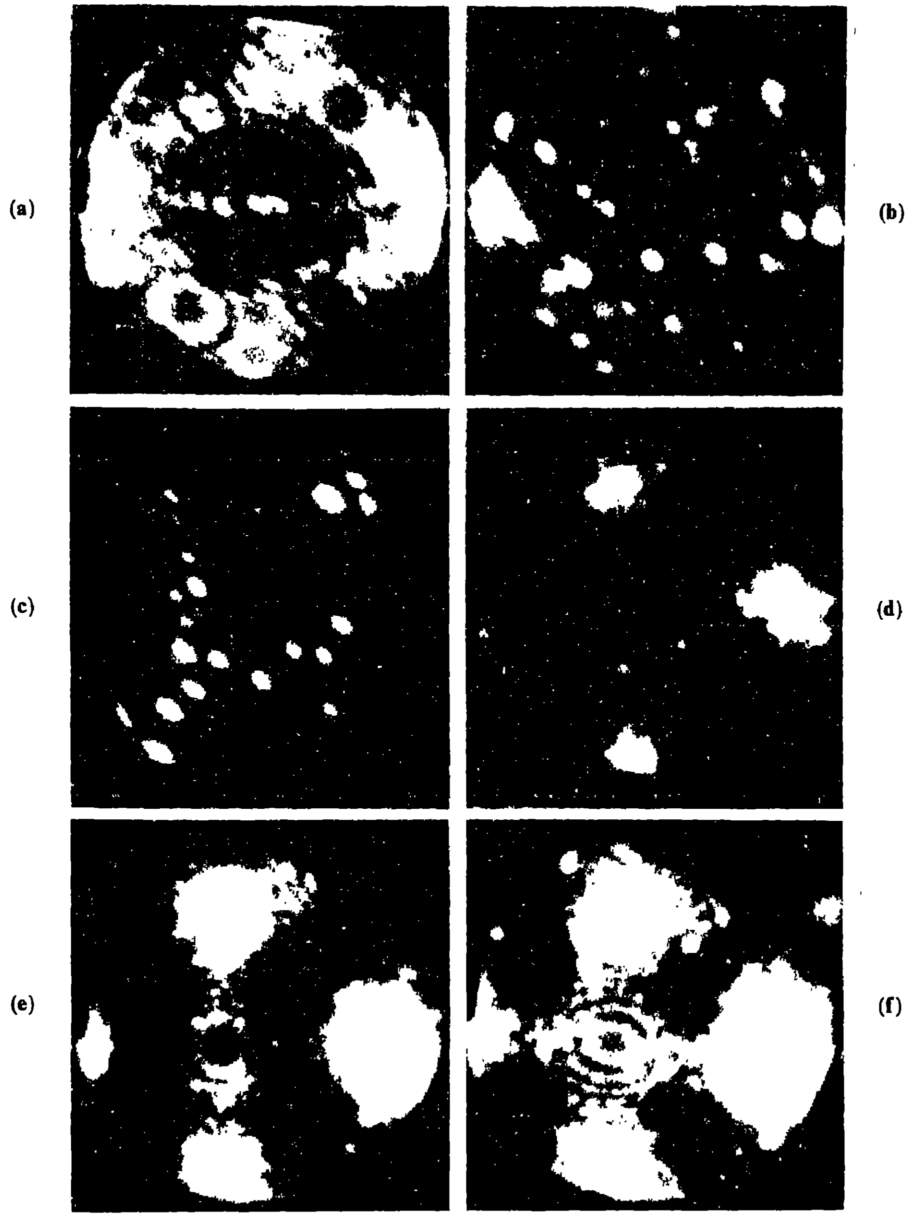

Figure 1a–f. **a.** Image of the field evaporated tungsten surface cooled down to liquid nitrogen temperature at the helium pressure of 10^{-5} torr (BIV 2·76 kV). **b.** Clusters of the adsorbate atoms (LaB_6), randomly deposited on tungsten (BIV 2.5 kV). **c.** Clusters of adsorbate on regions surrounding 121 planes of the substrate. Substrate heated to 1200 K for 30 sec at BIV 2·3 kV. **d.** Image of the blunted tip showing the segregation on {111} and {001} planes (substrate heated to 1650 K for 30 sec, BIV 3·66 kV). **e.** Image of the adsorbate covered surface with a few layers of adsorbate removed (BIV 4·4 kV). **f.** The field evaporated surface with a few interstitial atoms, particularly in the {011} planes.

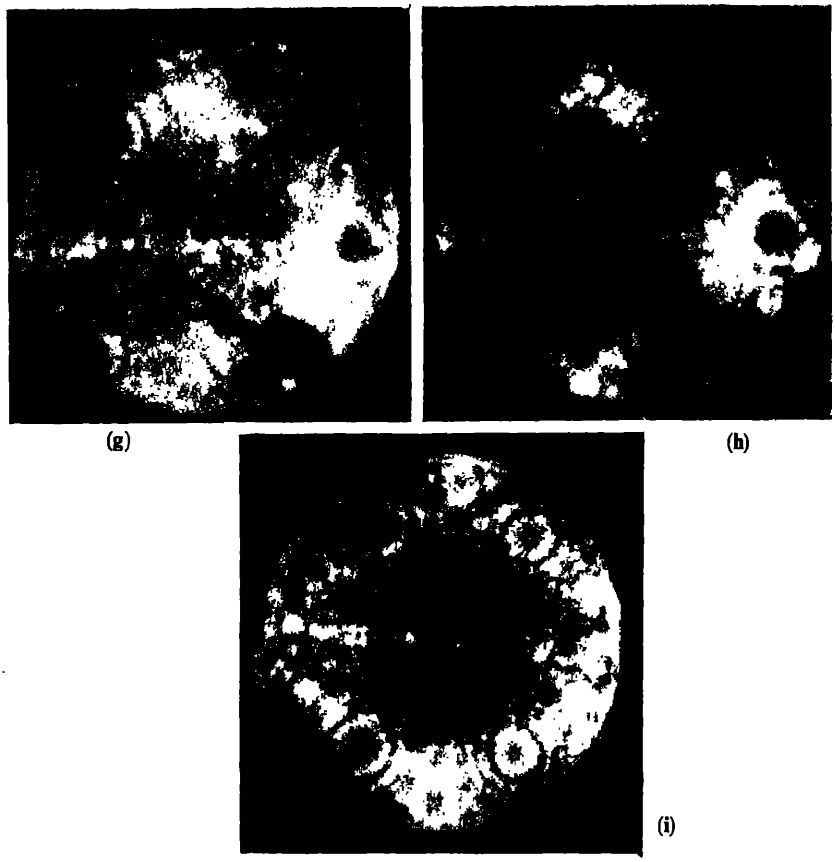

Figures 1g–i. **g.** Dependence of field evaporation on BIV ({011} planes best imaged; BIV 5·2 kV). **h.** Dependence of field evaporation on BIV ({111} and {001} planes best images; BIV 4·4 kV). **i.** Image of the clean tungsten pattern after continued field evaporation (BIV 5 kV).

Figures 1 (g, h) depict this difference. This could be attributed to the difference in local curvatures.

Continued field evaporation led to the clean tungsten pattern seen in figure 1(i).

3.3a *Further heating of the tip:* It was observed that heating the tip in vacuum at 1200°K did not result into blunting phenomenon. Also the adsorbate deposited on the tip shank migrated to the {111} and {001} planes due to heating and the same sequence of patterns during field evaporation was observed.

4. Discussion

4.1 *Epitaxial growth*

Reproducible epitaxial layers are formed on {001} and {111} planes and terraces between {001} and {121} planes. The BIV dropped to a low value as compared to tungsten. The observed growth was compatible with our earlier investigations using field electron emission microscopy.

4.2 *Substrate-adsorbate interface*

The tungsten surface stripped off all the adlayers shows deformed atom rings. This could be caused by the lattice deformation on heating the substrate to a temperature at which migration of substrate atoms sets in. This results in the reconstruction observed in these patterns (Bassett 1965). It was observed that the removal of three to four $\{111\}$ layers again resulted into well-ordered tungsten pattern.

4.3 *The imaged species*

Field evaporation from the overgrown regions occurred at voltages well below that required to remove tungsten atoms from the otherwise clean surface. Thus, the adlayers proved to be marginally stable for the helium ion microscopy at 78°K. The behaviour of the adlayers is typical of metallic adsorbates. Electronegative adsorbates usually are not imaged (Forbes 1971). Lanthanum is known to be electropositive and boron electronegative with respect to tungsten. The co-adsorption studies of lanthanum and boron on tungsten (Okuno *et al* 1978) and our earlier results using field electron emission microscopy of LaB_6/W system (Dharmadhikari *et al* 1977, 1979), indicated that lanthanum layer at the co-adsorbed surface is responsible for the observed lowering of work function of the composite surface. Also, the ionization probability is higher at the sites of enhanced positive charge. Geometrically, boron atoms being smaller in diameter as compared with tungsten, can fill the surface interstitials, while the lanthanum atoms being large in diameter as compared with the other two, remain outside the surface contributing to the observed image. All these factors tend to suggest that the imaged species are lanthanum atoms.

Acknowledgement

The authors acknowledge with thanks financial assistance from CSIR, New Delhi.

References

Bassett D W 1965 *Proc. R. Soc. (London)* **A286** 191
Dharmadhikari C V, Joag D S and Kanitkar P L 1977 *Phys. Status Solidi* **A42** K 99
Dharmadhikari C V, Joag D S and Kanitkar P L 1979 *J. Phys.* **D12** 809
Forbes R G 1971 *Surf. Sci.* **27** 659
Lafferty J M 1951 *J. Appl. Phys.* **22** 299
Muller E W and Tsong T T 1969 *Field ion microscopy: Principles and applications* (New York: Ann. Elsevier Pub) 99
Okuno K, Sasaki T, Kim H, Inoue T and Sugata E 1978 *Jpn J. Appl. Phys.* **17** 719

Bull. Mater. Sci., Vol. 6, No. 3, July 1984, pp. 579–594. © Printed in India.

Metallic glasses

C SURYANARAYANA

Centre of Advanced Study in Metallurgy, Department of Metallurgical Engineering, Banaras Hindu University, Varanasi 221 005, India

Abstract. Metallic glasses are a new class of materials produced by rapidly quenching the melts at rates often exceeding a million deg/sec. These have been found to display an optimum combination of properties such as high strength, good bend ductility, improved corrosion resistance and excellent soft magnetic properties. Thus, metallic glasses are emerging as economically viable competitors to conventional engineering materials.

A clear understanding of the atomic structure of metallic glasses and its change during annealing are of prime importance. Although techniques such as field-ion microscopy (FIM) x-ray diffraction and small angle x-ray scattering have been employed for this purpose, high resolution electron microscopic (HREM) investigations conducted during the last few years aided greatly in deriving information on the atomic scale. Availability of high-voltage high-resolution electron microscopes has been mainly responsible for this happy situation.

Studies on several metallic glasses have revealed that HREM images contain well-defined pattern of fringes over local regions, even though the diffraction pattern is that of a typical amorphous structure. The details of structure in the early stages of crystallization derived through HREM, FIM and analytical microscopic techniques are presented and discussed.

Keywords. Metallic glasses; glass-forming ability; melt quenching; rapid solidification techniques; crystallization behaviour; high-resolution microscopy; analytical microscopy.

1. Introduction

Metallic glasses are a new class of potential engineering materials which have come into prominence during the 1970s (Anantharaman 1982; Gilman 1980; Chen 1980). These are glassy in the sense that the atomic arrangement is random (non-crystalline), but differ from the conventional glasses in that they are not transparent, are not brittle and do not contain borates, silicates etc. Although non-crystalline solids can be prepared by methods such as vapour deposition (Chopra 1969), sputtering (Dahlgren 1978), laser treatment (Poate and Brown 1982), electrodeposition (Brenner 1963; Simpson and Brambley 1971), ion implantation (Grant 1978; Borders 1979; Picraux and Choyke 1982) and rapid quenching from the liquid state (Duwez 1967, 1979; Cahn 1980), purists reserve the term '*metallic glasses*' only to those that are produced by rapid quenching from the melt. The present article deals with the high resolution and analytical microscopic studies of metallic glasses with a view to understand their structure and its effect on the properties.

2. Classification of metallic glasses

The first metallic glass was produced in 1960 by Professor Pol Duwez and his colleagues at the California Institute of Technology, Pasadena, USA (Klement *et al* 1960). A few milligrams of the Au-25 at. % Si eutectic alloy were rapidly quenched from the molten state by the "gun" technique. In this method, a molten droplet is atomised and allowed to solidify instantaneously in the form of a *thin film* on a *good heat conducting substrate* such as copper so that heat is removed rapidly through the process of *conduction* (Duwez and Willens 1963). Since this pioneering effort, literally several thousands of alloy compositions have been quenched into the glassy state (Jones and Suryanarayana 1973; Takayama 1976; Suryanarayana 1980b). Even though it is a formidable task to classify these metallic glasses in a systematic way, traditionally they are broadly grouped under two categories *viz* (i) metal-metalloid and (ii) metal-metal.

The metal-metalloid category can be represented by the general formula $A_{75-85}B_{15-25}$, where A represents the metal and B the metalloid. The metal can be either an early transition metal (Ti, Zr, . . .), a late transition metal (Fe, Co, Ni, . . .) or a noble metal (Au, Pd, Pt, . . .) while the metalloid can be either B, C, P, Ge or Si. Combinations of metals constituting about 80 at.% and combinations of metalloids constituting about 20 at.% can also be used. Some of the famous and useful compositions are $Pd_{80}Si_{20}$, $Fe_{80}B_{20}$, $Fe_{40}Ni_{40}B_{20}$, $Fe_{40}Ni_{40}P_{14}B_6$, $Fe_{80}P_{13}C_7$, while an exotic composition is $W_{35}Mo_{20}Cr_{15}Fe_5Ni_5P_6B_6C_5Si_3$. In the above alloys and in many others, the ratio of metal to metalloid is almost always 80:20. Recently, however, metal-metalloid glasses with a metalloid content much higher than 20% have also been detected (Inoue *et al* 1979).

The metal-metal category, on the other hand, contains only metals. The metals can be either (a) transition metals, (b) rare-earth metals, (c) alkali-metals or (d) uranium, neptunium or plutonium (Suryanarayana 1980a). An important difference of this group from the commercially more useful metal-metalloid category is that glasses in the metal-metal category are formed in a wide composition range from as low as 10 at.% to as high as 50 at.%. Typical compositions of this category are $Co_{90}Zr_{10}$, $Hf_{80}Ni_{20}$, $La_{76}Au_{24}$, $Ca_{73}Zn_{27}$, $Zr_{64}Ni_{36}$, $U_{60}Cr_{40}$. Some well-investigated compositions include $Cu_{50}Zr_{50}$, $Mg_{70}Zn_{30}$ and $Ni_{60}Nb_{40}$.

3. Glass-forming ability

A pure metallic melt has not been so far quenched into the glassy state, even though hundreds of binary, ternary and more complex alloys could be made glassy. To form a glass, a metallic melt must be solidified sufficiently rapidly, exceeding a critical rate R_c, such that spontaneous crystallization is avoided. The value of R_c can vary from as low as 10^2 ksec^{-1} for $Pd_{40}Ni_{40}P_{20}$ to as high as 10^8 ksec^{-1} for $Fe_{90}B_{10}$. In principle, *any alloy* can be made glassy if the critical cooling rate is exceeded. However, with the presently available cooling rates, only some alloys could be quenched to form glasses.

Based on the experimental observations, several criteria have been suggested to indicate easy glass formation. The most used criterion is the reduced glass temperature, T_{gr} representing the ratio of the glass transition temperature T_g to the melting point of the alloy T_m. The higher the value of T_{gr} the easier it is for the alloy to form a glass. Since T_g varies much less rapidly with composition than T_m, alloys at the eutectic composition will have very low T_m and consequently very high T_{gr}. The observation that several alloy compositions around deep eutectics can be easily made glassy lends support to this criterion (Nielsen 1979). Other criteria proposed include (i) a minimum disparity of atomic sizes between the two constituents (more applicable to metal-metalloid glasses);

the ratio of atomic radii should be in the range of 0·59–0·88, (ii) a high hole formation enthalpy (Buschow 1982), (iii) chemical short-range order in the melt such that the local composition in the melt differs substantially from any stable crystalline species (Sommer 1982). In addition, an electronic criterion that $2k_F = K_p$ where k_F is the Fermi energy wave vector and K_p is the position of the first peak in the diffuse x-ray scattering curve, has been proposed by Nagel and Tauc (1977). In spite of these several criteria, it has not been possible to explain the glass-forming ability of the various alloy systems. It appears that different criteria may apply to different systems. Cahn (1983) has recently published a review on this aspect.

4. Methods of production

The gun technique referred to earlier (Duwez and Willens 1963) gives the highest cooling rates attainable amongst the melt-quenching techniques. However, this method suffers from the disadvantage that it produces porous foils of irregular cross-section. As such these products are not amenable to property studies. Furthermore, only small quantities can be produced at a time (in other words, this is a batch process) and thus industrial applications cannot be visualised for these products. The piston-and-anvil technique (Pietrokowsky 1963), though again produces *only small quantities* at a time, yields large foils of uniform cross-section and has been used quite extensively. These limitations prompted the development of methods for *continuous production* of foils, tapes and wires of uniform cross-section. The popular methods of today include the twin-roller (Chen and Miller 1970), melt spinning (Hubert *et al* 1973), melt extraction (Maringer and Mobley 1974) and planar flow casting (Narasimhan 1979). Figure 1 shows the principles of these four methods. In the twin-roller technique, a stream of

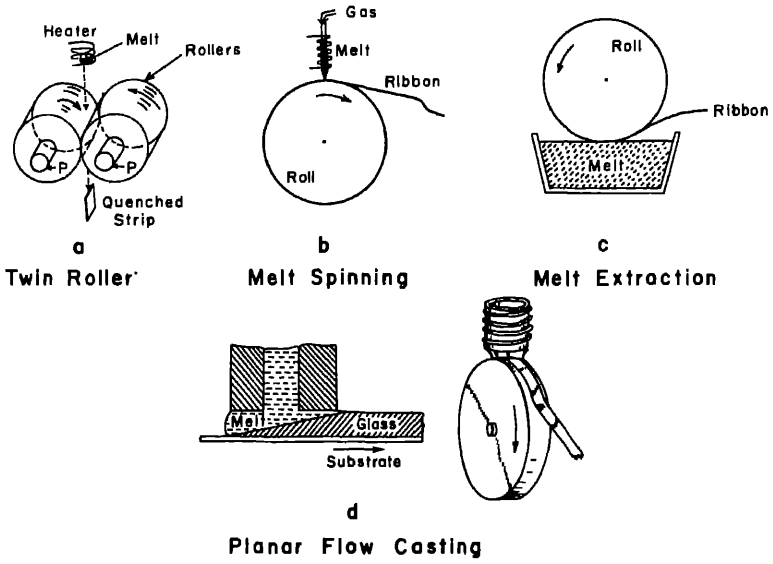

a Twin Roller

b Melt Spinning

c Melt Extraction

d Planar Flow Casting

Figure 1. Diagrams showing the principles of the four common and popular melt-quenching techniques.

molten metal is rolled into a sheet or tape between two conducting rolls rotating in opposite directions. In melt spinning, by far the most popular of the rapid quenching methods of today, a stream of liquid metal is made to strike the outer rim of a fast-rotating disc. The centrifugal force acts to throw the ribbon off the disc. The tapes produced have a width of a few millimeters and a thickness of 50–100 μm. Melt extraction is slightly different from melt spinning in that the melt source is stationary, and the edge of a rotating disc or wheel picks up the melt to form filaments. The planar flow casting process employs a nozzle with a slotted orifice and positioned to be almost in contact with the surface of the rotating disc. Ribbons up to 15 cm in width have already been produced by this technique and it is claimed that ribbons with 30 cm width will be produced in the near future.

Since the thickness of the tapes produced by all the above methods is at least about 50 μm, these have to be electrolytically thinned for TEM investigations.

5. Properties of metallic glasses

The main reason for intensive worldwide activity in the field of metallic glasses is that these materials have the best combination of physical, chemical and mechanical properties.

Metallic glasses are very hard (with a hardness value as high as 1300 kg/mm^2 for $Fe_{75}B_{25}$ and 1700 kg/mm^2 for $Fe_{55}Mo_{40}B_5$) and very strong. For example, the tensile strength of $Fe_{60}Cr_6Mo_6B_{28}$ glass is 4800 MPa while that of an ausformed crystalline 18 % Ni steel is only 2000 MPa. The bend ductility is fairly high, although in tension, they withstand only about 1 % strain. This high bend ductility is maintained almost up to the crystallization temperature in many glasses. Since alloys containing light metals such as Ti and Be can also be made strong glasses, the strength to weight ratio is much higher than is possible in crystalline alloys (for a comprehensive recent review on mechanical properties of metallic glasses please see Li 1981).

Because of the random atomic arrangements, metallic glasses have electrical resistivity 2–3 times higher than their crystalline counterparts. In addition, the temperature coefficient of resistivity is small and often negative (Cote and Meisel 1981). The phenomenon of superconductivity is also observed in metallic glasses; the highest transition temperature recorded is only about 9 K. But, they have a high critical field and their properties can be modified by suitable heat treatment (Johnson 1981; Inoue and Masumoto 1981; Suryanarayana 1983).

Another interesting feature of metallic glasses is their high corrosion resistance. Alloys containing additions of Cr and P have been found to have better corrosion resistance than even stainless steels (Masumoto and Hashimoto 1980; Waseda and Aust 1981). Certain glasses can also act like selective catalysts (Brower *et al* 1983).

Metallic glasses have outstanding magnetic properties. They are magnetically soft, have a reasonably high saturation magnetization, very low coercivity, zero magnetostriction and high electrical resistivity. Further, because of the absence of crystallinity, metallic glasses are magnetically isotropic. In view of this excellent combination of properties, applications for these materials in transformer cores, tape recorder heads, magnetic shielding, motors, transducers, amplifiers, etc are being seriously considered (Luborsky 1980; Masumoto and Egami 1981).

In spite of the superior properties achieved in metallic glasses, during annealing they undergo drastic changes. For example, after crystallization (sometimes even before) they are very brittle. The magnetic and electrical properties also show substantial changes even before the onset of crystallization. All these are expected to be related to the modifications in the glassy structure of the alloy and thus high resolution electron and field-ion microscopic studies will aid in understanding these changes due to low temperature annealing.

6. Structure

A crystalline solid is characterised by a periodic distribution of the constituent atoms in three dimensions. The diffraction patterns from crystals consist of a series of sharp spots (single crystals) or rings (polycrystalline samples). While the positions of these spots/rings give an idea of the dimensions and angular relations of the unit cell, the intensities help in determining the precise locations of the constituent atoms. Metallic glasses, on the other hand, possess a disordered structure and their diffraction patterns show two or three broad diffuse rings. From these, it becomes experimentally impossible to derive complete information regarding the atomic arrangements in metallic glasses.

From the intensity data, one can, however, calculate the radial distribution function (RDF), which is equal to $4\pi r^2 \rho(r)$, where $\rho(r)$ is the average number density of atoms at a distance r from any atom chosen as the origin. The RDF provides an *average* structure and indicates the approximate distance r (peak positions) and numbers (peak areas) of first, second, etc nearest neighbours. It does not, however, indicate the angular positions of the neighbours, wherein lies the lack of detail (Cargill 1975).

An alternative representation of the structure is provided by the reduced RDF, $G(r) = 4\pi r[\rho(r) - \rho_0]$, where ρ_0 is the density of the glass. Figure 2 shows this function for a variety of metal-metalloid glasses. Analysis of the first peak indicates that the number of first nearest neighbours is of the order of 11·5 to 13 and that the near neighbour distance is about 2% greater than the respective 12-coordinated Goldschmidt diameter of the metal species. From these results it appears that metallic glasses are close-packed materials. Figure 2 further shows that the relative positions and heights of higher order peaks are approximately the same and that the second peak is *always* split, with the higher spacing peak diminished relative to the first. The split in the second peak distinguishes the RDF's of metallic glasses from those of liquids, where the split is absent. It is important to note here that the curves do not provide any information concerning the environment of a metalloid atom. Thus, in order to more fully characterise an n-component glass, one must perform separate scattering experiments utilising $n(n+1)/2$ different wavelength radiations. This has been done only in a few cases (see for example, Waseda 1980, 1981) and the results clearly indicate that no two metalloid atoms can be nearest neighbours.

The next step in the analysis of the structure is to start with a model, calculate the theoretical RDF from this (with the help of a computer) and compare it with the experimental RDF. Recently, Livesey and Gaskell (1982) introduced the concept of a figure of merit for evaluating the accuracy of RDF's.

The concept of dense random packing of hard spheres (DRPHS) introduced by Bernal and developed by Finney (1979), originally to explain the structure of liquid metals, has found favour for the structure of metallic glasses as well. This is natural because metallic glasses can be considered as frozen-in liquids and so their structures are expected to be similar. Figure 3 shows the remarkable agreement between the experimental and calculated RDF's for $Ni_{76}P_{24}$. In spite of this, the model takes into account the presence of only the metal atoms in the alloy and the packing fraction is only about 0·63, which is about 10% less than the value computed from measured densities. To overcome this limitation Polk (1972) proposed that the metal atoms form essentially a DRPHS structure and the metalloid atoms occupy the larger holes characteristic of the DRPHS structure, which was contested by Gaskell (1979) on the ground that to accommodate, *without*

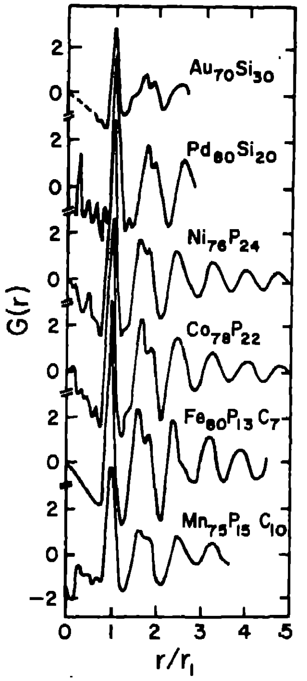

Figure 2. Reduced radial distribution functions for several metal-metalloid glasses (Cargill 1975). Here r_1 is the position of the first peak maximum.

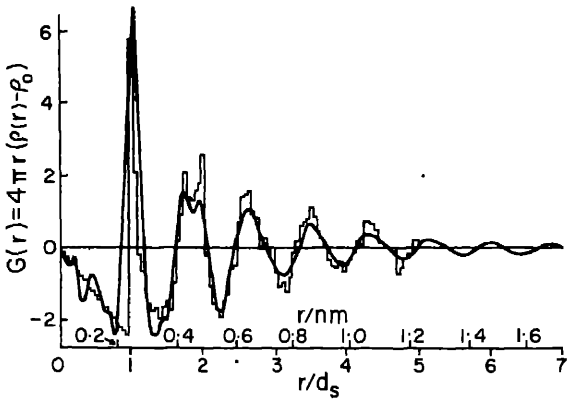

Figure 3. Comparison of reduced radial distribution functions $G(r)$ for Finney's DRPHS structure and for amorphous $Ni_{76}P_{24}$ (Cargill 1975).

distortion, 20% of metalloid atoms even in the largest holes, the diameter of the metalloid atom must be ⩽ 0·48 of the metal atom diameter. And this is true of only boron and carbon and not of other metalloids. Turnbull (1981) points out that the size of the metalloid is reduced to fit the available interstitial space. In other words, the metalloid atoms adjust to the environment. Modifications to the DRPHS model include relaxation (Boudreaux and Gregor 1977) of *soft* spheres, which gives a packing factor of 0·69–0·7, in agreement with values deduced from density measurements.

Fujita (1982) proposes intermediate-range ordering in amorphous solids and works out the diffraction theory for $Fe_{80}B_{20}$ (Hamada and Fujita 1982) and shows that there is excellent agreement between the model and the experiment.

Another model which finds favour at present seems to be the one proposed by Gaskell (1979). The origin of this model lies in the observation that during HREM of amorphous alloys, structural units as large as 1·5–2 nm are observed (Gaskell *et al* 1979). The 'microcrystalline' model will be insufficient to explain this. Further, this would require a large amount of boundary volume and an accompanying density deficit larger than the 1–2% observed (Cargill 1970, 1981). Thus, Gaskell (1979, 1982) proposes the existence of structural units (containing 200–400 atoms) in which the atoms are *crystallographically* defined and twinning planes, in three dimensions, comprise the interface. These units are packed to give essentially *random* long-range structures. These structural units have been identified to be trigonal prisms, which can be dissected (distorted) into tetrahedra and octahedra similar to those existing in crystalline interstitial phases. Thus, the local and, perhaps, medium-range structure of metallic glasses resemble *in detail* the structure of the corresponding crystalline phase. Experimental confirmation of this model is provided by Mehra *et al* (1983) from their studies on Ru-Zr-B alloys, where they show that irregular prismatic packing based on Ru_2B crystal gives good fit of the observed RDF's, while the DRPHS model cannot give even a moderate agreement.

All the above models have been proposed specifically for the metal-metalloid glasses. The Polk model ably explains the 80:20 ratio of metal to metalloid atoms based on DRPHS model. The model of Gaskell also is in a position to explain the composition ranges of 15–25 at.% metalloid on the basis of the existence of crystalline compounds of the type A_3B and A_4B. However, very few models have been proposed for metal-metal glasses. These pose more problems in view of the wide range of compositions where glasses form. Wang (1979) proposed a model, involving random stacking of interpenetrating Kasper polyhedra, which successfully explained the observations made on sputtered W-Fe. Ni-Nb, etc amorphous alloys produced at equiatomic compositions. Finney (1979) raised doubts about its applicability in three dimensions.

It must be emphasised, however, that the problem of the structure of metallic glasses is far from solved. Other techniques such as small-angle x-ray scattering (Osamura *et al* 1979, 1981, 1982) Mössbauer spectroscopy (Fujita 1981), nuclear magnetic resonance (Durand 1981), extended x-ray absorption fine structure studies (Hayes *et al* 1978) and HREM techniques can also aid in determining the structure of metallic glasses and efforts are being made in this direction.

7. Crystallization behaviour

Since the crystalline form of alloys is the lowest energy configuration, metallic glasses can be considered metastable. On continuous heating, metallic glasses will first lower their energy by relaxing to a more stable glassy state and then at still higher temperatures (above the crystallization temperature), they crystallize into the most stable phases (Scott 1980). The crystallization temperature depends on the alloy system under consideration and can vary from as low as 380 K (for $Mg_{70}Zn_{30}$) to as high as 1225 K (for a complex tungsten-base alloy). The crystallisation temperatures can be determined with the aid of a differential scanning calorimeter. Irrespective of whether it is a metal-metalloid or a metal-metal glass, the decomposition behaviour can be represented by the general sequence (Masumoto and Maddin 1971; Suryanarayana 1980a).

Amorphous → amorphous′ → MS I → MS II → stable phases where amorphous′ represents the relaxed amorphous structure and MS I and MS II represent metastable phases. While the Japanese workers prefer the above representation, Köster and Herold (1981) proposed that crystallization reactions can be classified into three groups:
(i) *Polymorphous crystallization* in which the metallic glass crystallizes without any change in composition into a supersaturated solid solution or a metastable or stable crystalline compound; (ii) *Primary crystallization*, in which the first crystals to form will have a composition different from that of the glass; and (iii) *Eutectic crystallization* where simultaneous crystallization of two crystalline phases occurs by a discontinuous reaction.

It is possible to relate these two classifications. Polymorphous crystallization is rare, but can be considered as equivalent to the formation of MS I or directly the stable phase. This is possible only in concentration ranges encompassing a stable compound in the equilibrium diagram. Primary crystallization is equivalent to the formation of MS I followed by MS II containing higher solute contents. Eutectic crystallization is equivalent to simultaneous formation of MS I and MS II from the amorphous matrix.

8. High-resolution and analytical studies

HREM, field-ion microscopy and analytical microscopic techniques are helpful to determine the structure of metallic glasses (so far, this had only limited success) and to characterize the products of early stages of decomposition.

8.1 *As-quenched structure*

Electron micrographs recorded from metallic glasses at 100 kV do not show any contrast at normal resolution level (figure 4). The selected area diffraction pattern shows only a diffuse halo. This observation brings out the limitation, that even if microcrystals were to be present, the resolution limit of 100 kV instruments is insufficient to bring these out (Gaskell *et al* 1979). Observations made with a 500 kV electron microscope reveal a 'droplet' structure for the as-quenched amorphous Pd-Si alloy (Gaskell and Smith 1980), even though the diffraction pattern continues to show only diffuse haloes. High-resolution micrographs of these droplets reveal fringe patterns with a spacing of about 0·23 nm. While the fringes are very clear in thin films, only edges show the fringe pattern in thicker foils. This is a reflection of the decreased probability of overlap with disordered regions or with ordered domains not at the Bragg angle. Further, the fringes have only a low contrast (even though higher than that observed in amorphous semiconductors, which have a low intensity first peak in the

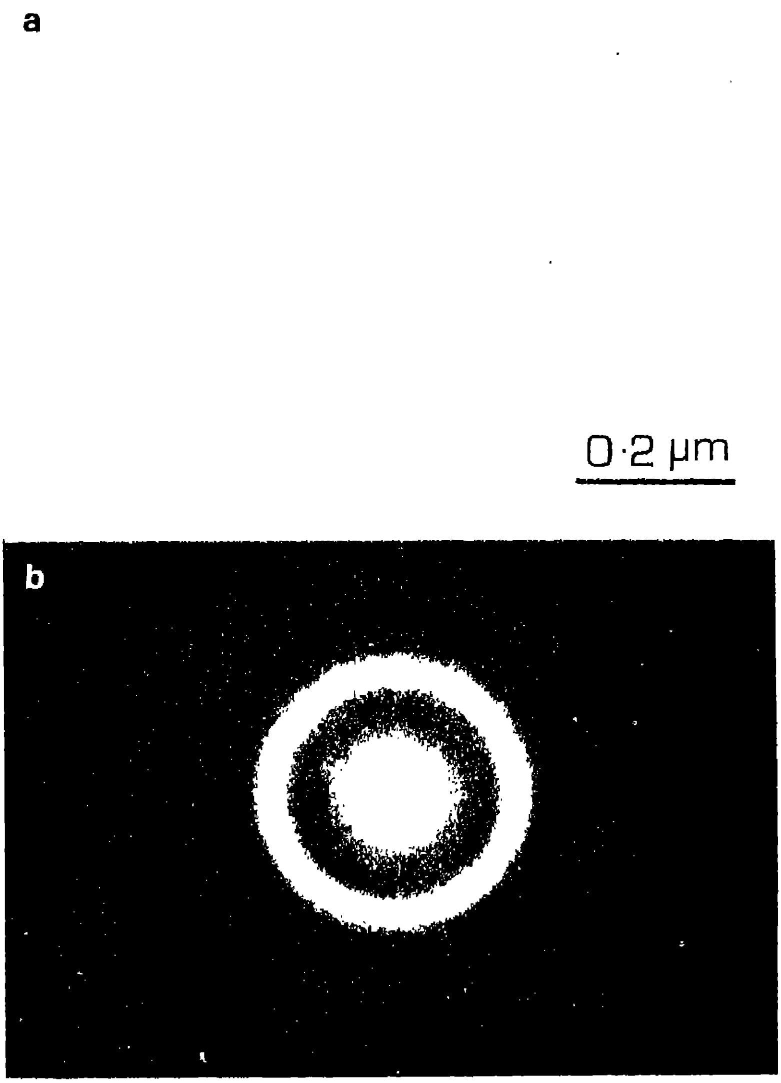

Figure 4. **a**. An electron micrograph representing a typical as-quenched glassy structure. No contrast can be observed. The selected area diffraction pattern showing a broad diffuse halo is shown in **b**.

structure factor curve) and there are several apparently independent fringe systems per particle. Gaskell and Smith (1980) claim that these particles are characteristic of the glassy structure and suggest that the diffuse interface present distinguishes them from crystalline particles nucleated during annealing. (Fujita *et al* 1980, however, show that low temperature annealing at 563 K of an $Fe_{83}B_{17}$ alloy, precipitates α-Fe crystals having a diffuse interface with the matrix). Apart from the nature of the interface, the size of the crystal formed during thermal decomposition is larger. These fringe patterns in the droplets (particles) have been shown to conform to the polytetrahedral packing mentioned earlier in §6.

A point of caution here is that the above results refer to flash-evaporated or sputtered films, and similar results are not reported in many melt-quenched glasses so far. In fact, through-focal series on several melt-quenched metallic glasses do not show any fringe patterns (Fujita *et al* 1980; Imura *et al* 1982; Fukamichi *et al* 1979, 1982), but only the presence of coherently scattering domains 0·5–2 nm in size (probably due to limitations of resolution). High-voltage electron microscopy studies of these alloys have been carried out by Ishida *et al* (1982). They find that the as-quenched structure varies depending on the composition, quenching method and quenching conditions. Figure 5(a) shows an electron micrograph of a sputter-deposited $Co_{94}Zr_6$ alloy indicating that it is microcrystalline. Even though the diameter of the crystals is only 10–20 atomic diameters, the density of microcrystals increases with the thickness of the foil. However, when the Zr content is increased to 11 at.% a truly random structure without the presence of any fringe structure is produced (figure 5b). It is interesting to note here that the $Co_{94}Zr_6$ alloy has the best magnetic properties (better than even $Co_{89}Zr_{11}$) even though it contains some microcrystallites.

High-resolution electron micrographs of *melt-quenched* $Fe_{40}Ni_{40}P_{14}B_6$ (METGLAS 2826) and wide $Pd_{80}Si_{20}$ ribbon specimens are shown in figure 6(a) and (b), respectively. Although the selected area diffraction patterns from both the samples show only diffuse rings, the $Fe_{40}Ni_{40}P_{14}B_6$ alloy has a true amorphous structure, while the $Pd_{80}Si_{20}$ alloy shows some lattice fringes. It is suggested that these fringes may arise due to the lower cooling rate (specimen width ~ 15 mm). From these results, Ishida *et al* (1982) conclude that the details of the structure of the amorphous phase may differ from system to system.

It was pointed out earlier (Ranganathan and Suryanarayana 1972) that field-ion microscopy can play an important role in understanding the structure of metallic glasses. Cotterill and Kragh (1977) observed a $Pd_{80}Si_{20}$ glassy sample in a field-ion microscope at 78 K and reported the absence of any wide-spread crystallinity. They reported that in some regions they could detect small clusters of atoms that are suggestively regular. However, other recent investigations (Jacobaeus *et al* 1980; Inal *et al* 1980, 1981; Arise *et al* 1982) clearly indicate a random distribution of atoms in the as-quenched state. The interpretation of field-ion images is made difficult due to the fact that only one species of atoms is visible. There are additional problems in concentrated alloys (Müller and Tsong 1969).

Jacobaeus *et al* (1980) imaged specimens of $Fe_{80}B_{20}$ and $Fe_{78}Mo_2B_{20}$ (METGLAS 2605 and 2605A, respectively) in a field-ion microscope and found no dissimilarities in configurations in the as-quenched state. By careful plotting of the co-ordinates of the image points (representing the iron atoms), the triplet correlation of atomic positions was produced. This may represent the first step in the quest to remove the ambiguities inherent in the exclusive use of pair distribution functions in the study of the non-crystalline state. It is also possible that this type of approach will help to shed some light on the question of the microstructure of metallic glasses.

8.2 *Early stages of crystallization*

High-resolution and analytical microscopic investigations have been more useful in understanding the intricacies of the early stages of crystallization. Quite a few detailed studies have been undertaken in this direction in recent times.

One of the detailed investigations concerns the crystallization behaviour of Fe-B and

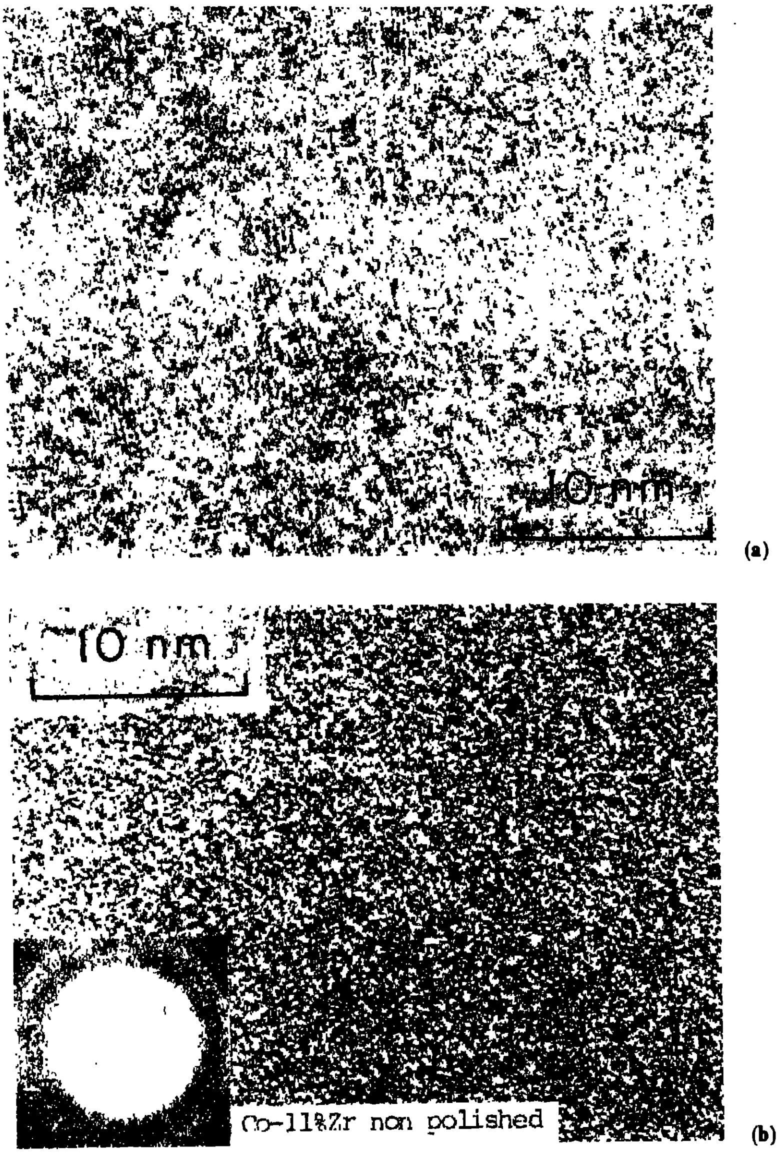

Figure 5. **a.** An axial HREM of sputter-deposited $Co_{94}Zr_6$ alloy. Microcrystals are seen, **b.** Micrograph of the $Co_{89}Zr_{11}$ alloy. No lattice fringe is seen (Courtesy: Yoichi Ishida).

Ni-B glasses (Fujita *et al* 1980). Crystallization starts with the precipitation of α-Fe microcrystals (primary crystallization) which have a diffuse interface with the matrix. These microcrystals contain further fine structures several nanometres in size. These crystals have a rhombic shape whose diagonal axes are parallel to the $\langle 110 \rangle_{Fe}$ direction. Lattice imaging of the crystals confirmed that they are α-Fe and that they contain fine crystallites as evidenced by the presence of boundaries and Moiré patterns. The microcrystals were found to grow only when the interface became sharp. Annealing at higher temperatures resulted in the formation of the Fe_3B crystals.

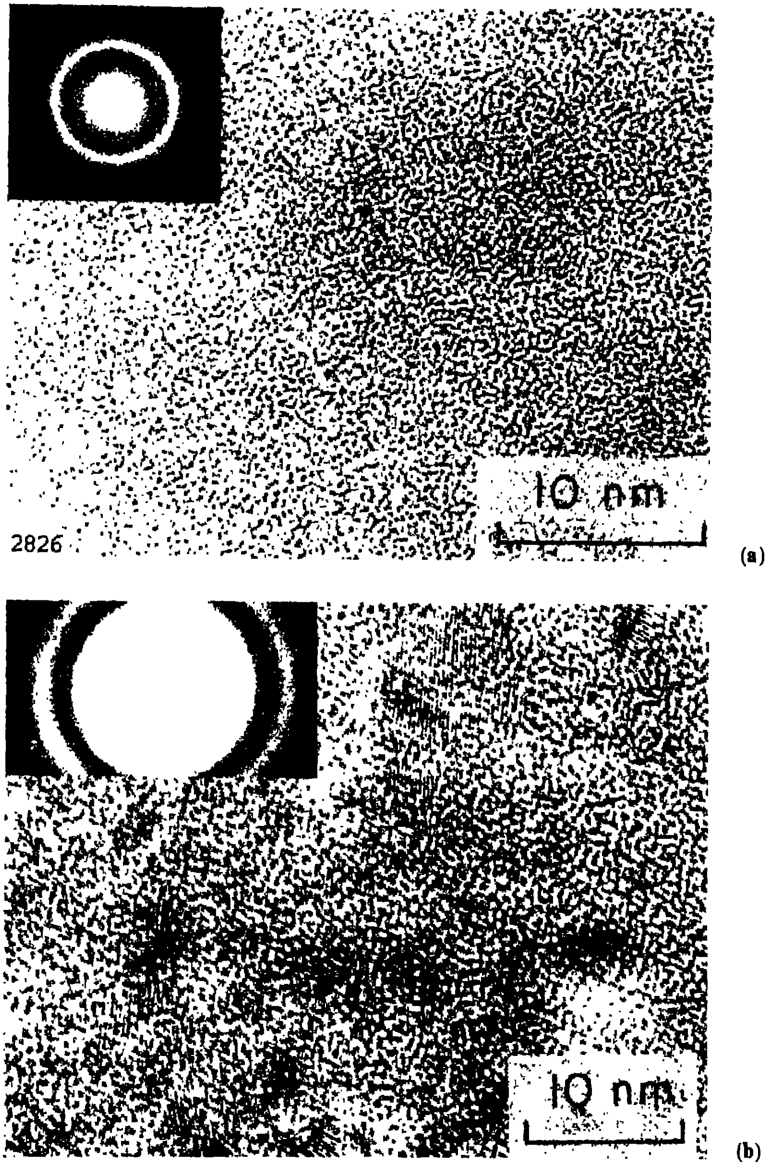

Figure 6. **a.** HREM of a melt-quenched $Fe_{40}Ni_{40}P_{14}B_6$ sample. Notice the true amorphous nature. **b.** Micrograph from melt-quenched $Pd_{80}Si_{20}$ wide ribbon. Lattice fringes can be seen in some areas (Courtesy: Yoichi Ishida).

In a very interesting and thought-provoking paper, Piller and Haasen (1982) reported results on an atom-probe field-ion microscopic study of a $Fe_{40}Ni_{40}B_{20}$ glass and observed that the glass on annealing at 643 K decomposes into two amorphous phases $(FeNi)_3B$ and FeNiB of low boron content. (It was indicated that the formation of the $(FeNi)_3B$ supports the glass model of Gaskell 1979). Another interesting observation made by them was that 70 ± 10 % of the image spots are due to boron atoms (while

Jacobaeus *et al* (1980) assumed that only iron atoms were imaged!). Piller and Haasen (1982) had also analysed the kinetics of decomposition and concluded that kinetics seem to be governed by long-range diffusion of boron in the glassy state. A glass containing more than 18 % boron was found to be brittle.

Inal *et al* (1980) investigated the crystallization behaviour of glassy $Fe_{80}B_{20}$ by combined x-ray diffraction and field-ion microscopy (FIM) techniques. They showed that FIM was more potent in revealing the presence and distribution of crystalline particles in the early stages of decomposition. As an example, they observe that while a sample annealed at 1053 K for 15 min shows the presence of only Fe_3B compound in the x-ray patterns, FIM investigations show the presence of α-Fe particles and Fe_3B even on annealing for 45 sec at 1053 K. This is understandable because x-ray patterns show the average picture and may not show the presence of a phase present in very small quantities, while FIM can show the presence of even very small volume fractions of a phase. However, the usefulness of FIM in the last stages of crystallization is limited owing to the large size of the crystalline particles. An FIM study of laser-induced phase transformations in $Fe_{80}B_{20}$ also revealed features similar to the above with the proviso that the laser beam impingement area corresponded to longer periods of anneal, and the regions removed from this zone show the same phase structure obtained with shorter periods of annealing (Inal *et al* 1981).

Vitek *et al* (1975) report the high-resolution electron microscopic study of the crystallization of a metal-metal glass ($Cu_{60}Zr_{40}$). In the early stages of crystallization, small crystals of a $Cu_{10}Zr_7$ phase were detected which consisted of subgrains 30–50 nm in size. Since lattice fringes were not terminating inside a subgrain, it was concluded that the subgrains were free from dislocation arrays.

Only a few analytical microscopic investigations have been reported in the literature so far. It is needless to emphasise that HREM coupled with analytical techniques can give a wealth of information which can resolve many of the controversies existing today.

As mentioned earlier, precipitation of an MS I phase takes place on annealing the glass at the crystallization temperature. This MS I phase may have a composition which is the same or different from the glass composition. Diffraction patterns recorded from the crystals were used to measure the lattice parameter (accuracy is not very high) and estimate the solute content of the crystal. This can decide whether the crystallization is of the primary type or polymorphous type. However, energy dispersive spectroscopy (EDS) techniques, now-a-days commonly available as attachment to transmission electron microscopes, can readily evaluate the composition of the crystal and decide the type of crystallization. Such a type of investigation was reported by Heimendahl and Oppolzer (1978) on $Fe_{32}Ni_{36}Cr_{14}P_{12}B_6$ (METGLAS 2826A). They showed that this glass undergoes a primary crystallization, since the crystal to form first had much less Cr and P and higher Fe content than the glass (B could not be analysed). A similar investigation was undertaken on $Fe_{40}Ni_{40}P_{14}B_6$ (METGLAS 2826) and the results showed that the phase first precipitating was $(FeNi)_3PB$ (Tiwari and Heimendahl 1981).

Since metallic glasses are non-crystalline, formation of voids is difficult to understand. Free volume exists in metallic glasses, but aggregation of this to form voids is again doubtful. However, Morris (1980) reports the observation of voids in METGLAS 2826 ribbons annealed at 653 K. This was questioned by Tiwari and Heimendahl (1981), but Morris (1981) insists that under suitable kinetic conditions the formation of such metastable aggregates might occur. He supports the observation by the fact that the voids (very small, round, featureless objects) (i) show an orientation-dependent contrast and (ii) show through-focus contrast variations similar to those expected of small voids.

9. Concluding remarks

It has been shown that metallic glasses have outstanding physical, chemical and magnetic properties. In fact, the combination of properties is so excellent that it is difficult to think of a better engineering material. In addition, metallic glasses are produced directly from the liquid state into the net shape in a *single step* and thus the process is much cheaper than the conventional methods and so economically viable. These factors are responsible for the intensive activity throughout the world to see that metallic glasses replace the existing crystalline materials at least in some spheres. Some progress has already been made in this direction in Japan.

The nature of the metallic glasses, their structure and its influence on the properties (the so-called structure property correlations) are beginning to be understood only now. The difficulties being encountered are enumerated in the preceding sections; but it is hoped that the advent of new techniques and sophistication of the existing techniques and methods will aid in overcoming the difficulties. Urgent attention is required to be focussed on resolving the many *different results* obtained on the *same alloy*. This may be due to changes in quenching methods, quenching conditions (thickness of specimen, cooling rate, atmosphere) or even local changes in composition. Thus, it will be fruitful if investigations are carried out by producing the glassy structure in *one alloy* under controlled conditions by *different methods* and correlate the structure with the properties. Until this is done we will continue to have a large body of unrelated results on various alloys.

Acknowledgements

The author expresses his gratitude to Prof. T R Anantharaman for his constant encouragement. The author was exposed to the excitement of working in this field of metallic glasses during his stay at Tohoku University, Sendai, Japan. He would deem it a pleasure and privilege to thank Prof. Tsuyoshi Masumoto of this University for the opportunity provided to him. Finally, he thanks Dr Yoichi Ishida for supplying the high resolution electron micrographs.

References

Anantharaman T R 1982 Presidential Address, Indian Science Congress (69th Session), Mysore
Arise T, Lu H, Nakamura M, Suzuki Y, Yamamoto R and Doyama M 1982 in *Proc. Int. Conf. Rapidly Quenched Metals* (ed) T Masumoto and K Suzuki (Sendai: The Jpn. Inst. Metals) 1 435
Borders J A 1979 *Annu. Rev. Mater. Sci.* **9** 313
Boudreaux D S and Gregor J M 1977 *J. Appl. Phys.* **48** 152, 5057
Brenner A 1963 *Electrodeposition of alloys* (New York: Academic Press)
Brower W E, Mazyjaszezyk M S, Pettit T L and Smith G V 1983 *Nature* (*London*) **301** 497
Buschow K H J 1982 *Solid State Commun.* **43** 171
Cahn R W 1980 *Contemp. Phys.* **21** 43
Cahn R W 1983 in *Proc. 5th Int. Conf. on Phys. of Non-Crystalline Solids* (ed) J Zarzycki (Orsay: Les Editions de Physique)

Cargill G S 1970 *J. Appl. Phys.* **41** 12

Cargill G S 1975 *Solid state phys.* (eds) F Seitz, D Turnbull and H Ehrenreich (New York: Academic Press) **30** 227

Cargill G S 1981 in *Atomic energy rev. suppl.* 1 (Application of nuclear techniques to the study of amorphous metals) (ed) U Gonser (Vienna: IAEA) 63

Chen H S 1980 *Rep. Prog. Phys.* **43** 353

Chen H S and Miller C E 1970 *Rev. Sci. Instrum.* **41** 1237

Chopra K L 1969 *Thin film phenomena* (New York: McGraw-Hill)

Cote P J and Meisel L V 1981 in *Glassy metals I: Ionic structure, electronic transport and crystallization* (ed) H J Güntherodt and H Beck (Berlin: Springer-Verlag) 141

Cotterill R M J and Kragh F 1977 *Scand. J. Metall.* **6** 191

Dahlgren S D 1978 in *Rapidly quenched metals III* (ed) B Cantor (London: The Metals Society) **2** 36

Durand J 1981 in *Atomic energy rev. suppl.* 1 (Application of Nuclear Techniques to the study of amorphous metals) (ed) U Gonser (Vienna: IAEA) 143

Duwez P 1967 *Trans. Am. Soc. Metals Qly.* **60** 607

Duwez P 1979 *Proc. Indian Acad. Sci.* **C2** 117

Duwez P and Willens R H 1963 *Trans. Met. Soc. AIME* **227** 362

Finney J L 1979 *Nature (London)* **280** 847

Fujita F E 1981 in *Atomic energy rev. suppl.* 1 (Application of nuclear techniques to the study of amorphous metals) (ed) U Gonser (Vienna: IAEA) 173

Fujita F E 1982 in *Proc. 4th Int. Conf. on Rapidly Quenched Metals* (ed) T Masumoto and K Suzuki (Sendai: The Jpn. Inst. Metals) **1** 301

Fujita H, Hashimoto K and Tabata T 1980 *Mater. Sci. Eng.* **45** 221

Fukamichi M, Hoshimoto K and Yoshida H 1979 *Scr. Metall.* **13** 807

Fukamichi M, Hoshimoto K and Yoshida H 1982 in *Proc. 4th Int. Conf. on Rapidly Quenched Metals* (ed) T Masumoto and K Suzuki (Sendai: The Jpn. Inst. Metals) **1** 417

Gaskell P H 1979 *J. Non-cryst. Solids* **32** 207

Gaskell P H 1982 in *Proc. 4th Int. Conf. on Rapidly Quenched Metals* (ed) T Masumoto and K Suzuki (Sendai: The Jpn. Inst. Metals) **1** 247

Gaskell P H and Smith D J 1980 *J. Micros.* **119** 63

Gaskell P H, Smith D J, Catto C J D and Cleaver J R A 1979 *Nature (London)* **281** 465

Gilman J J 1980 *J. Phys. Colloq.* **41** C8-811

Grant W A 1978 *J. Vac. Sci. Technol.* **15** 1644

Hamada T and Fujita F E 1982 in *Proc. 4th Int. Conf. on Rapidly Quenched Metals* (ed) T Masumoto and K Suzuki (Sendai: The Jpn. Inst. Metals) **1** 319

Hayes T M, Allen J W, Tauc J, Giessen B C and Hauser J J 1978 *Phys. Rev. Lett.* **40** 1282

Heimendahl M V and Oppolzer H 1978 *Scr. Metall.* **12** 1087

Hubert J C, Mollard F and Lux B 1973 *Z. Metall.* **64** 835

Imura T, Doi M, Makiyama M and Itoh Y 1982 in *Proc. 4th Int. Conf. on Rapidly Quenched Metals* (ed) T Masumoto and K Suzuki (Sendai: The Jpn. Inst. Metals) **1** 605

Inal O T, Keller L and Yost F G 1980 *J. Mater. Sci.* **15** 1947

Inal O T, Murr L E and Yost F G 1981 *Mater. Sci. Eng.* **51** 101

Inoue A, Kitamura A and Masumoto T 1979 *Trans. Jpn Inst. Metals* **20** 404

Inoue A and Masumoto T 1981 *Sci. Rep. Res. Inst. Tohoku Univ.* **A29** 305

Ishida Y, Ichinose H, Shimada H and Kojima H 1982 in *Proc. 4th Int. Conf. on Rapidly Quenched Metals* (ed) T Masumoto and K Suzuki (Sendai: The Jpn. Inst. Metals) **1** 421

Jacobaeus P, Madsen J U, Kragh F and Cotterill R M J 1980 *Philos. Mag.* **B41** 11

Johnson W L 1981 in *Glassy metals I: Ionic structure, electronic transport and crystallization* (ed) H J Güntherodt and H Beck (Berlin: Springer-Verlag) 191

Jones H and Suryanarayana C 1973 *J. Mater. Sci.* **8** 705

Klement W, Willens R H and Duwez P 1960 *Nature (London)* **187** 869

Köster U and Herold U 1981 in *Glassy metals I: Ionic structure, electronic transport and crystallization* (ed) H J Guntherodt and H Beck (Berlin: Springer-Verlag) 225

Li J C M 1981 in *Ultrarapid quenching of liquid alloys* Vol. 20 of *Treatise on materials science and technology* (ed) H Herman (New York: Academic Press) 325

Livesey A K and Gaskell P H 1982 in *Proc. 4th Int. Conf. Rapidly Quenched Metals* (ed) T Masumoto and K Suzuki (Sendai: The Jpn. Inst. Metals) **1** 335

Luborsky F E 1980 in *Ferromagnetic materials* (ed) E P Wohlfarth (Amsterdam: North-Holland) **1** 451

Maringer R E and Mobley C E 1974 *J. Vac. Sci. Technol.* **11** 1067

Masumoto T and Egami T 1981 *Mater. Sci. Eng.* **48** 147

Masumoto T and Hashimoto K 1980 *J. Phys. Colloq.* **41** C8-894

Masumoto T and Maddin R 1971 *Acta Metall.* **19** 725

Mehra M, Williams A R and Johnson W L 1983 *Phys. Rev.* **B27**

Morris D G 1980 *Scr. Metall.* **14** 879

Morris D G 1981 *Scr. Metall.* **15** 813

Müller E W and Tsong T T 1969 *Field ion microscopy: principles and applications* (New York: American Elsevier)

Nagel S R and Tauc J 1977 *Solid State Commun.* **22** 129

Narasimhan M C 1979 *U.S. Patent* 4 142, 571

Nielsen H J V 1979 *Z. Metall.* **70** 180

Osamura K, Shibue K, Shingu P H and Murakami Y 1979 *J. Mater. Sci.* **14** 945

Osamura K, Shibue K, Suzuki R, Murakami Y and Takayama S 1981 *J. Mater. Sci.* **16** 957

Osamura K, Suzuki R and Murakami Y 1982 in *Proc. 4th Int. Conf. Rapidly Quenched Metals* (eds) T Masumoto and K Suzuki (Sendai: The Jpn. Inst. Metals) **1** 431

Picraux S T and Choyke W J 1982 (ed.) *Metastable Materials Formation by Ion Implantation* (New York: Elsevier Sci. Pub. Co.)

Pietrokowsky P 1963 *Rev. Sci. Instrum.* **34** 445

Piller J and Haasen P 1982 *Acta metall.* **30** 1

Poate J M and Brown W L 1982 *Phys. Today* (June) 24

Polk D E 1972 *Acta Metall.* **20** 485

Ranganathan S and Suryanarayana C 1972 in Proc. Symp. on *Recent developments in metallurgical science and technology* (Calcutta: The Indian Inst. Metals), Physical Metallurgy, 155

Scott M G 1980 *Metals Technol.* **7** 133

Simpson A W and Brambley D R 1971 *Phys. Status Solidi.* **B43** 291

Sommer F 1982 in *Proc. 4th Int. Conf. on Rapidly Quenched Metals* (eds) T Masumoto and K Suzuki (Sendai: The Jpn. Inst. Metals) **1** 209

Suryanarayana C 1980a in *Structure and properties of amorphous Metals II* (ed.) T Masumoto and T Imura (Sendai: Suppl. Sci. Rep. Res. Inst. Tohoku Univ.) **A28** 143

Suryanarayana C 1980b *Rapidly quenched metals—A bibliography* 1973–1979 (New York: IFI Plenum)

Suryanarayana C 1983 in *Metallic glasses* (ed) T R Anantharaman (Aedermannsdorf: Trans Tech)

Takayama S 1976 *J. Mater. Sci.* **11** 164

Tiwari R S and Heimendahl M 1981 *Scr. Metall.* **15** 809

Turnbull D 1981 *Metall. Trans.* **A12** 695

Vitek J M, Vander Sande J B and Grant N J 1975 *Acta Metall.* **23** 165

Wang R 1979 *Nature* (*London*) **278** 700

Waseda Y 1980 *The structure of non-crystalline materials* (New York: McGraw Hill)

Waseda Y 1981 *Prog. Mater. Sci.* **26** 1

Waseda Y and Aust K T 1981 *J. Mater. Sci.* **16** 2337

Mater. Sci., Vol. 6, No. 3, July 1984, pp. 595–602. © Printed in India.

gh voltage electron microscope irradiation and observations in tallic glasses

R V NANDEDKAR and A K TYAGI

Materials Science Laboratory, Reactor Research Centre, Kalpakkam 603 102, India

Abstract. High voltage electron microscope (HVEM) has been extensively used to produce radiation damage and to study the characteristics of defects so produced in crystalline solids. To understand the defect production in metallic glasses and to evaluate the influence of such defects on physical properties like crystallisation temperature etc., high voltage microscopy and subsequent *in situ* heating and observation has been extremely useful technique. This paper gives a qualitative overview of such work performed in metallic glasses. In particular results obtained on a nickel based metallic glass using a HVEM and an electron accelerator are presented. The advantages and limitations of HVEM irradiation are highlighted.

Keywords. Accelerator irradiation; metallic glass; defect characteristics; high voltage electron microscopy; crystallization temperature.

Introduction

use of high voltage electron microscope (HVEM) as an electron irradiation facility to
te displacement damage in crystalline samples is well known (Makin 1971).
tron irradiation will produce Frankel defects in metallic samples which will cluster
a complicated structure such as dislocation loops and voids which can simul-
ously be observed when the irradiation is in progress. This technique has been
lied very successfully to simulate fast reactor damage and get a quick estimate of the
nt of damage that would occur in the fast reactor (Norris 1972a, b).

etallic glasses have gained considerable interest both in basic and applied sciences.
ar as 'defects' in amorphous systems in general and metallic glasses in particular are
cerned, very little is so far known. A lot of experimental work backed with
retical modelling has to be done before 'defects' in such systems could be
lerstood. The study of production of defects, their recovery and influence on the
hanical, physical properties and crystallisation behaviour in metallic glasses can
an insight of the structure of amorphous materials. It is also suggested (Chang and
1977) that because of the nature of amorphous state, no more disorder can be
oduced into metallic glasses by irradiation and if it be the case, these alloys are
ential candidates for the nuclear energy applications. However radiation damage
cts such as swelling (Chang and Li 1977) and blistering (Nandedkar and Tyagi
1a) has been observed in the metallic glasses. The interesting area of research is the
uence of these defects on the crystallisation behaviour. As already mentioned, HVEM
rs a two-in-one, in the sense that one can produce and observe damage
ultaneously. The effect of these defects on the crystallisation temperature T_c can be
nd out by using the heating-stage and study the electron diffraction pattern as a
ction of temperature after irradiation.

In this paper we give a qualitative survey of HVEM irradiation and accelerator irradiation work done to study defects and its influence on the crystallisation temperature of metallic glasses. The advantages and limitations are highlighted along with the results on a nickel based metallic glass ($Ni_{45}Fe_5Co_{20}Cr_{10}Mo_4B_{16}$) using a HVEM and an electron accelerator. These results are discussed by comparing with other experimental results.

2. Survey of the earlier work

Neutron irradiation (Lesueur 1970, 1975; Krammer *et al* 1979; Doi *et al* 1979) and charged particle (Richtin *et al* 1978; Schumacher *et al* 1980) irradiation experiments of metallic glasses so far have been able to establish the irradiation induced defects in metallic glasses. In these experiments techniques used were mainly wide-angle x-ray scattering, electrical resistivity, transmission electron microscopy etc. These techniques especially wide-angle scattering and resistivity have shown that irradiation produces 'vacancy type' of defects in metallic glasses. Another technique which is very sensitive to the presence of defects in the crystalline samples is positron annihilation. This technique includes positron lifetime and two-photon angular correlation measurements. This technique is very sensitive to very small vacancy concentration ranging from 10^{-4} to 10^{-7}. Chen (1976) exploited this technique for electron irradiated (electrons from an accelerator) Pd-Ni-Si sample and the lifetime measurement did not show any evidence of vacancy like defects. Even two-photon angular correlation experiment(Chaung *et al* 1978) on electron irradiated Pd-Ni-Si showed no vacancy-like defects. Very recent experiments (Moser *et al* 1981) on positron lifetime measurements of low temperature electron irradiated metallic glasses show that lifetime increases after irradiation and comes back to original value after isochronal annealing. This experiment suggests that irradiation produces cavities of different sizes. These cavities are produced in the neighbourhood of the compressed regions of the metallic glasses. The recovery is explained on the basis of recombination of cavities with compressed regions. Electrical resistivity of low temperature (4·6 K) irradiated $Pd_{80}Si_{20}$ with electron of energy 3 MeV is found to increase (Klaumunzer and Petri 1982; Klaumunzer *et al* 1981). The change in the resistivity is proportionate to radiation-induced defect concentration. Thermal recovery of $Pd_{80}Si_{20}$ is continuous from 10 K to 500 K. These experimental results have been analysed by characterising the defects as excess free volume (vacancy-like defect) and negative free volume or compressed region (interstitial like defect). These results also indicate that the two types of defects have to be separated by a minimum distance of ~ 10 Å otherwise the stress field would overlap and give rise to spontaneous recombination.

The experiments above have so far shown that vacancy-type defects are produced. What influence will these 'defects' have on the crystallisation temperature T_c? Not much work has been done in the field of electron irradiation and its effect on T_c. However, people have effectively used HVEM in combination with heating-stage for T_c determination. Kiritani *et al* (1977, 1978) studied the structure and crystallisation process of amorphous Au-Si, Fe-B and CoFeSiB after electron irradiation in a HVEM. Only Au-Si was prepared by vacuum deposition whereas other samples were prepared by melt quenching. They observed a lowering in the crystallisation temperature. In other words, the process of crystallisation is accelerated. This may be possible due to enhanced nucleation triggered off on account of radiation damage. The results are explained on the basis of variable latent vacancy mechanism of diffusion in amorphous materials (Kiritani and Yoshiie 1978). Doi *et al* (1976) have studied splat-cooled Fe-P-C and Fe-P in a HVEM with various energy levels from 100 keV up to a dose of 1×10^{23} e/cm^2. They observed no appreciable change in the transmission electron diffraction pattern at room temperature. They observed that crystallisation is retarded or T_c is enhanced. They explained the retardation on the basis that during splat quenching, clusters less than 10 Å in size (atomic assemblies which are short range in order) are supposed to be present. These clusters act as nuclei for crystallisation. Irradiation destroys these nuclei and therefore there will be a low probability for forming the clusters or nuclei in the irradiated region and hence retardation in crystallisation. However the same authors have observed acceleration of crystallisation in FeBSi, NiBSi, NiBSiC, NiPB and NiP alloys and no effect in NiPC (Doi and Imura 1978, 1980). Metallic glasses 2826 ($Fe_{40}Ni_{40}P_{14}B_6$) and 2826 A ($Fe_{32}Ni_{36}Cr_{14}P_{12}B_6$) have been studied by Von Heimendahl (1981) after irradiation in HVEM which was operated at 1 MeV and 1.1 MeV to a dose of 4×10^{23} e/cm^2. It was observed that there is an acceleration in T_c of 2826 A in the irradiated region. No actual T_c measurement was done. In contrast, 2826, no effect of irradiation was visible. The explanation, which is rather qualitative, is put forward on the basis that 2826 A has low activation energy for nucleation of crystal (350 kJ/mol) as against that of 2826 (740 kJ/mol). The lower value of 2826 A explains the higher sensitivity to local rearrangements of atoms and therefore acceleration in T_c.

3. Electron irradiation of a nickel based metallic glass

HVEM offers many advantages to study samples over a conventional transmission electron microscope. Higher energy of electrons will give greater penetration (~ 1 μm) and therefore the information obtained is closer to a bulk sample. Due to higher beam energy one gets better practical resolution and a very good resolution in thinner samples. It also offers as mentioned earlier, electron irradiation facility to study radiation damage.

Although these advantages look rather attractive some limitations are there due to higher beam energy. Radiation damage poses some problems which are not desirable. It gives a greater danger to the operator from x-radiation from different parts of the microscope. It has poor response to the viewing screen, lower contrast, poor photographic emulsion and of course the high cost.

When used as irradiation facility to study and observe irradiation damage, it has limitations from the thickness. It is well known that the surfaces act as sink for the point defects produced during irradiation. In thin samples surfaces act as sinks and therefore it gives serious limitations when one wants to simulate neutron damage. Again electron irradiation will produce Frenkel pairs as against cascades in neutron and charged particle irradiation. One cannot irradiate in HVEM under controlled conditions on the sample such as temperature, stress. Therefore the only advantage it gives is to accumulate higher damage in shorter time due to high beam intensity. In an electron accelerator irradiation, one can have control over the specimen parameters such as temperature and stress. Thicker samples which are more representative of bulk can be used in an electron accelerator irradiation.

In studying the effect of irradiation on T_c of metallic glasses in HVEMS, the only technique one can employ is the *in situ* heating in the hot-stage. The temperature of the sample is measured with a platinum-platinum rhodium thermo-couple which is attached to the holder and not to the sample. Depending upon the thermal contact of the specimen with the holder and the thermal conductivity of the sample, the temperature of the sample will be different from what is actually measured.

Judging all these limitations of HVEM irradiations we have irradiated a nickel-based metallic glass both in an electron accelerator to low doses and in a HVEM to a high dose. This metallic glass with composition $Ni_{45}Fe_5Co_{20}Cr_{10}Mo_4B_{16}$, is in the form of a long ribbon about 40 μ thick and 4 mm wide. Samples were irradiated to doses ranging from 1×10^{14} e/cm^2 to 4×10^{16} e/cm^2 with 3·5 MeV electrons at room temperature using a water cooled target holder in a linear accelerator at Tata Institute of Fundamental Research, Bombay. For a high dose of 2×10^{21}/cm^2, electron transparent samples were irradiated with 1 MeV electrons in a JEM 125 HVEM of University of Antwerp, Belgium. The current density during HVEM irradiation was kept 1×10^{21} e/cm^2 min which roughly corresponds to a dose rate of 18 dpa/hour. The rise in temperature due to beam heating was estimated to be $\sim$ 50 K.

The crystallisation temperature T_c is the temperature at which the process of crystallisation starts. This temperature T_c was determined for both as-received and accelerator irradiated samples using resistometry, hot-stage electron microscopy and differential scanning calorimetry (Nandedkar and Tyagi 1981b; Nandedkar *et al* 1981). T_c of HVEM irradiated sample was determined by heating the sample *in situ* in the hot stage of HVEM. Transmission electron microscopy samples for hot stage were prepared using 10% H_3PO_4 and 90% H_2SO_4 at 6 V and examined in hot-stage of Philips EM 400 operated at 100 kV. It was rather difficult to control the rate of heating but it is estimated to be about 15–20 K/min. HVEM samples were directly heated *in situ* after irradiation and the electron diffraction patterns were taken at different temperatures. The temperature at which the pattern changes from amorphous to crystalline is recognised as the crystallisation temperature. Figure 1 shows a typical hot-stage electron diffraction pattern of the accelerator irradiated sample. The crystallisation begins at 653 ± 20 K in both as-received and accelerator irradiated samples. Figure 2 shows the typical micrograph and diffraction pattern of HVEM irradiated sample before and after the onset of crystallisation. The crystallisation was observed at a temperature 653 ± 20 K. Table 1 summarises the results on crystallisation temperature for as-received, accelerator irradiated and HVEM irradiated metallic glass.

All the earlier studies on the effect of electron irradiation on crystallisation behaviour of metallic glasses were performed in HVEMs. Koster and Herald (1981) have pointed out that although *in situ* observation of crystallisation in hot-stage of a TEM will give

Table 1. Crystallisation temperature (in K) of electron irradiated metallic glasses.

	As-received	Accelerator irradiated	HVEM irradiated
Resistometric	390 ± 15 K	663 ± 15 K	
Hot-stage electron microscopy	653 ± 20 K	663 ± 20 K	653 ± 20 K
D.S.C.	673 ± 5K	676 ± 5 K	

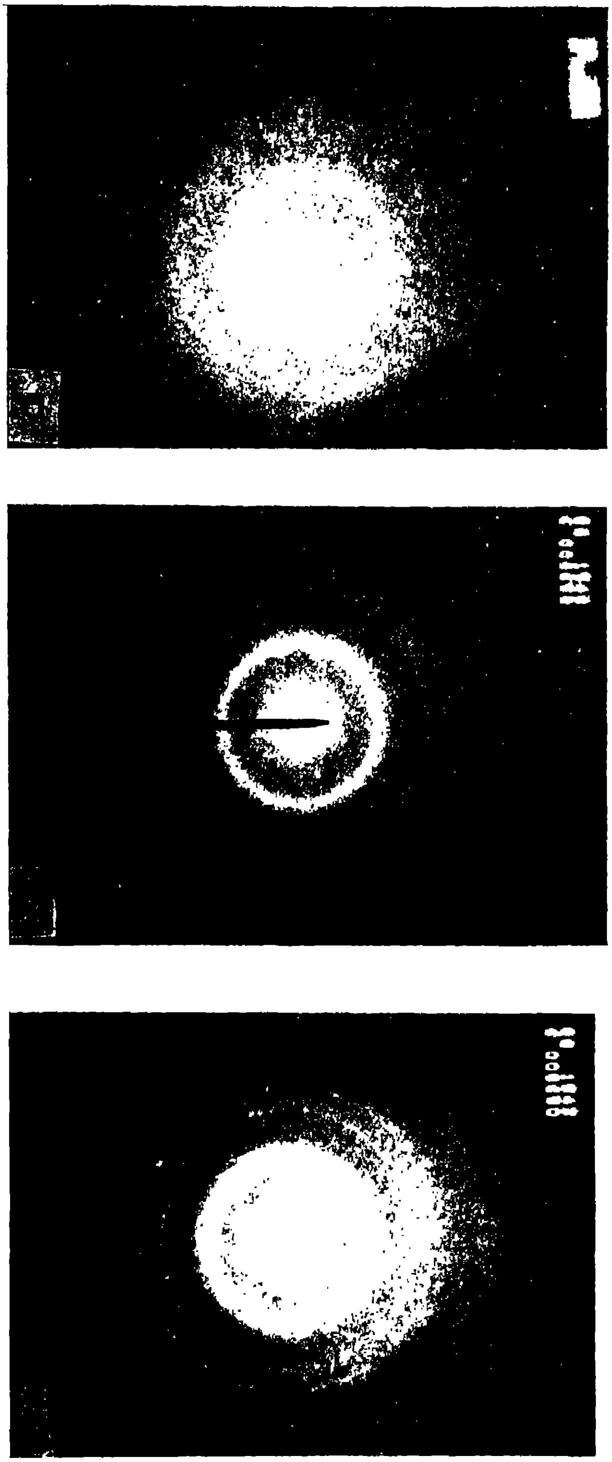

Figure 1. Electron diffraction pattern of electron irradiated (accelerator) metallic glass at **a**. room temperature **b**. 653 K and **c**. 703 K. The crystallisation begins at 653 K.

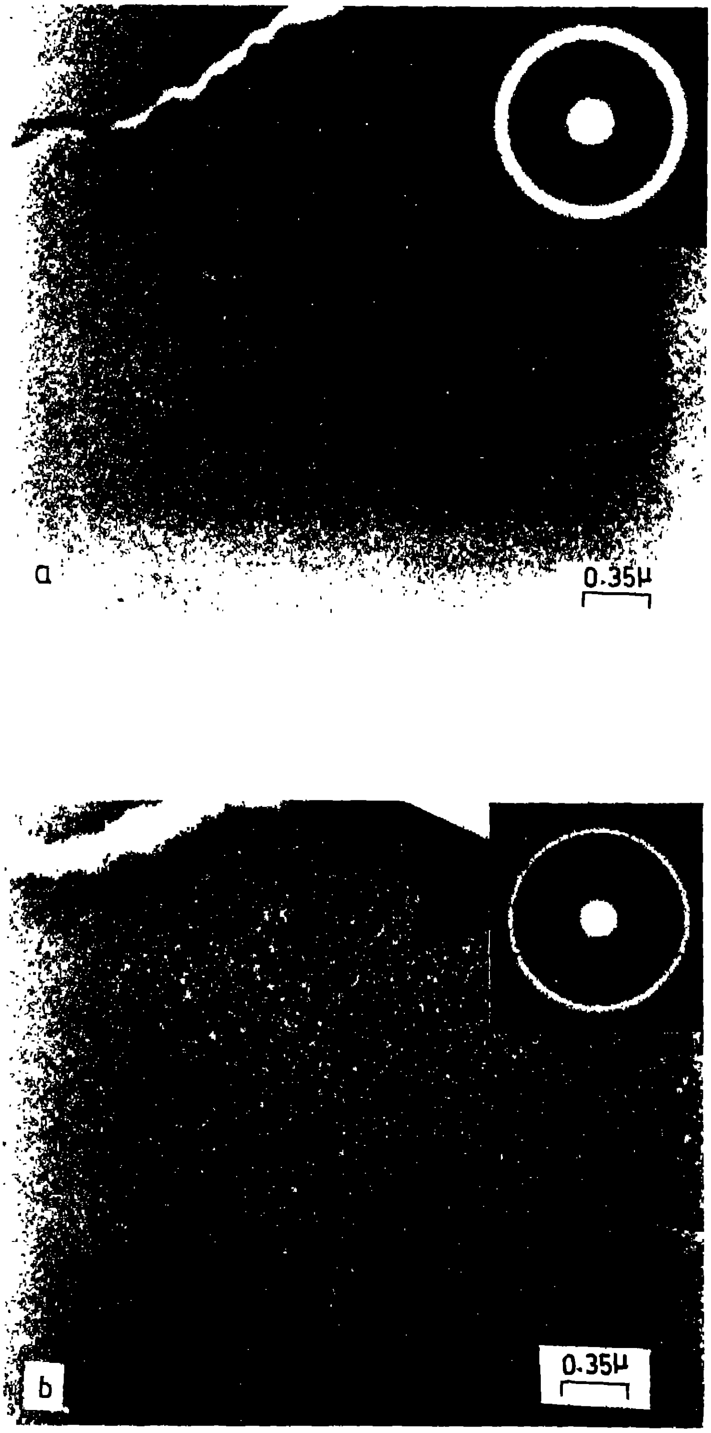

Figure 2. Microstructure and diffraction pattern of HVEM irradiated sample; dose 2×10^{21} e/cm^2 **a.** at room temperature and **b.** when heated *in situ*. The crystallisation begins at 653 K.

valuable information about the micromechanism of the reactions, the crystallisation can be drastically different from that of bulk. We, therefore, irradiated samples in an accelerator and it was observed that crystallisation temperature determined from the bulk measurements such as resistometry were not drastically different from that of their foil measurements.

Comparing our results with those of earlier workers, no definite conclusion about the effect of defects on crystallisation can be drawn. However we can only say that the effects of electron irradiation on T_c are closely related to both irradiation conditions and metal-metalloid combination.

Conclusion

HVEM is being effectively used to study damage in metallic glasses and its influence on the crystallisation temperature using heating-stage of HVEM. However, a HVEM has certain limitations which can be overcome by supplimenting HVEM results with those of irradiation from an electron accelerator. Results on a specific nickel-based alloy $Ni_{45}Fe_5Co_{20}Cr_{10}Mo_4B_{16}$ have been discussed and it has been observed that electron irradiation from both HVEM and accelerator has no significant effect on crystallisation temperature.

Acknowledgements

It is our pleasure to thank K Varatharajan for his association with this work. Our thanks are due to Dr Ray for providing the metallic glass sample.

References

Chang B T and Li J C M 1977 *Scr. Metall.* **11** 933
Chaung S Y, Tsand P K, Tan G J and Chen H S 1978 *Phys. Status Solidi* **40** K 181
Chen H S 1976 *Phys. Status Solidi* 34 K127
Doi K, Ayan T and Kawamura K 1979 *Non-Cryst. Solids* **34** 405
Doi M and Imura T 1978 *3rd Int. Conf. on Rapidly Quenched Metals*, Brighton (UK) 2 372
Doi M and Imura T 1980 *J. Mater. Sci.* **15** 3701
Doi M, Yoshida M, Nanoyama M, Imura T, Masumato T and Yoshio Y 1976 *Mater. Sci. Eng.* **23** 169
Kalumunzer S, Rentzsch S, Schumacher G and Vogl G 1981 *Yamada conference on point defects and defect interactions*, Kyoto (Japan)
Kalumunzer S and Petri W 1982 *Phys. Lett.* **A87** 314
Kiritani M and Yoshiie T 1978 *Suppl. Sci. Rep.* Research Institute of Tôhoku University, Japan A63
Kiritani M, Yoshiie T and Fujita F E 1977 *Proc. V Int. Conf. on High Voltage Electron Microscopy*, Kyoto (Japan)
Kiritani M, Yoshiie T and Fujita F E 1978 *Proc. III Int. Conf. on Rapidly Quenched Metals*, Brighton (UK) 2 308
Koster U and Herald U 1981 *Glassy metals I* (eds) H J Guntherodt and H J Beck (Berlin: Springer-Verlag) 225
Kramer E A, Johnson W L and Cline C 1979 *Appl. Phys. Lett.* **35** 815
Lesueur D 1970 *Fizika* 2 Suppl. 2 131
Lesueur D 1975 *Radiat. Eff.* **24** 101
Makin M J 1971 *Electron microscopy in materials science* (ed) U Valdre (New York and London: Academic Press) 388
Moser P, Hautojarvi P, Yli-Kaupilla J and Chamberrod A 1981 *4th Int. Conf. on Rapidly Quenched Metals*, Sendai (Japan)

Nandedkar R V and Tyagi A K 1981a *Radiat. Eff. Lett.* **58** 91
Nandedkar R V and Tyagi A K 1981b *Scr. Metall.* **15** 1175
Nandedkar R V, Tyagi A K and Varatharajan K 1981 *4th Int. Conf. on Rapidly Quenched Metals*, Sendai (Japan)
Norris D I R 1972a *Radiat. Eff.* **14** 1
Norris D I R 1972b *Radiat. Eff.* **15** 1
Richtin M, Van der Sande J and Baldo P M 1978 *Scr. Metall.* **12** 639
Schumacher G, Klaumunzer Rentzsch S and Vogl G 1980 *Z. Phys.* **B40** 19
Von Heimendale 1981 *Scr. Metall.* **15** 1145

Bull. Mater. Sci., Vol. 6, No. 3, July 1984, pp. 603–609. © Printed in India.

High resolution electron microscopic studies of $HoAl_3$, $Er_{0.5}Gd_{0.5}Al_3$ and $Y_{0.91}Er_{0.09}Al_3$ in thin film form

ANAND KUMAR SINGH, AJAY KUMAR SINGH, M S GUPTA* and O N SRIVASTAVA

Department of Physics, Banaras Hindu University, Varanasi 221 005, India
* Philips India Limited, Bombay 400 018

Abstract. Rare earth trialuminides (RAl_3) exhibit an interesting series of structures changing from 2H to 3C in the bulk form. Many of the rare earth trialuminides have been recently found to exhibit curious structural characteristics such as the occurrence of the modulated phases. A detailed investigation of the formation synthesis and characterization of some binary and ternary alloys of the rare earth-aluminium system has been carried out. High resolution microscopic technique has been employed to study the modulated phases for some alloys *e.g.* $HoAl_3$, $Er_{0.5}Gd_{0.5}Al_3$ and $Y_{0.91}Er_{0.09}Al_3$. With the help of lattice imaging technique, several new modulated phases have been investigated. A possible mechanism for the formation of these phases has been suggested. The details of the results obtained by lattice imaging technique are discussed.

Keywords. High resolution electron microscopy; structural characterisation; modulated phases; Al–rare earth system; lattice imaging.

1. Introduction

About half a century ago a classic example of superlattice formation in CuAu was reported by Johannson and Linde (1936). Since then, several other modulated phases have been discovered in a variety of materials ranging from metallic to dielectrics through semi-metallics. The occurrence of modulated phases have been curious to crystallographers and also to materials scientists since these phases exhibit interesting properties and many times correspond to potentially important materials from the applied aspect. These alloys have drawn considerable attention in view of the fact that they absorb hydrogen exothermically, nonstoichiometrically and reversibly which has already been recognized as a future fuel. Rare earth metals and alloys are further known to exhibit interesting magnetic properties and are very promising materials for memory devices in computers.

The present communication deals with the occurrence and stabilisation of modulated phases in binary and ternary rare earth metal trialuminides such as $HoAl_3$, $Er_{0.5}Gd_{0.5}Al_3$ and $Y_{0.91}Er_{0.09}Al_3$.

The modulated phases discovered in the present investigation originate in a novel way—they result as a consequence of amorphous to crystalline transformation. Often intergrowth of several modulated phases occurs. The profuse occurrence of random and ordered stacking faults suggests that the polytype-like modulated phases are formed through creating and ordering of stacking faults. Evidences and arguments have been put forward to show that the driving force for the modulated phases is the lowering of electronic energies which offsets the increase in energy due to creation of stacking faults. It has been shown that even slight variations in electron concentration (size of the Fermi surface) may lead to the genesis of several modulated phases.

2. Experimental techniques and results

The binary and ternary rare earth metal trialuminides were made by homogenising the stoichiometric mixture of rare earth metal/metals and aluminium in vacuum ($\approx 10^{-6}$ torr) at a temperature ranging between 823 and 873 K for about 20 hr. The initial agglomerate of the alloys so formed were tested by x-ray diffraction through Guinier focussing camera. These agglomerates correspond to the reported bulk structure of the material, *e.g.* 15R for $HoAl_3$. Thin films from these agglomerates were formed by vacuum ($\approx 10^{-7}$ torr) thermal vapour deposition. The as-grown thin films were amorphous as evidenced by the featureless electron micrographs and the diffraction patterns exhibiting haloes, obtained from them. These as-grown thin films underwent amorphous to crystalline transformation when they were heated with focussed electron beam at a temperature of about 500°K for about 30 sec. The resulting crystalline phase consisted of isolated crystals. These single crystal regions often contained heavy density of planar faults. An extensive analysis of electron diffraction patterns taken from the transformed phase revealed that the most abundant phase in thin film form for $HoAl_3$ and $Y_{0.91}Er_{0.09}Al_3$, were their reported structural phases *viz.* 15R with $a = 6{\cdot}052$ Å; $c = 35{\cdot}93$ Å and 9R with $a = 6{\cdot}185$ Å, $c = 21{\cdot}14$ Å. However, in $Er_{0.5}Gd_{0.5}Al_3$ the most abundant phase was 3C with $a = 4{\cdot}1$ Å unlike its bulk phase 9R. In addition to their bulk structures in all the cases the non-basal diffraction patterns containing a^*c^* reciprocal lattice network revealed the presence of modulated phases where the a lattice periodicity was invariant but the c periodicity differed from one phase to the other. The c periodicity in all cases was integral multiples of interlayer spacing of close packed layers in their bulk structures e.g. 2·39 Å for $HoAl_3$. The different modulated phases discovered are 4H, 5H, 15R, 30R, 42R and disordered 60R for $HoAl_3$; 3C, 4H, 6H, 9R, 12R, 15R, 16H, 24H, 42R and several other disordered structures for $Er_{0.5}Gd_{0.5}Al_3$ and 9R, 4H and 16H for $Y_{0.91}Er_{0.09}Al_3$. Although the characterisation of diffraction patterns revealed the presence of the modulated phases they alone could not lead to unambiguous results regarding the state of disorder and inter-growth of various phases. Also for the case of high period structures when the resolution of diffraction spots become questionable the diffraction analysis does not lead to an unambigous structural characterisation. Keeping this in view high resolution transmission electron microscopy was resorted to unravel the details of the structural features of the modulated phases. Figure 1 shows the bright field high resolution electron micrograph employing direct beam and 00·3 spots. This figure clearly reveals the presence of a twin boundary at A. The two crystal regions were confirmed to correspond to 42R as was cleared from the crossed diffraction pattern of the region containing the boundary. The diffraction pattern is also shown and the spots 00·42 are indexed for both the crystals. The blocks of 42R were found to consist of two fringe spacings corresponding to 5 layers, followed by a fringe spacing corresponding to 4 layers. Several lattice images were recorded for the structural variants in $Er_{0.5}Gd_{0.5}Al_3$ thin films. Figure 2 represents a dark field lattice image formed by 00·9 spot including two other neighbouring spots of 00·*l* row. Here the fringe spacing comes out to be 7·04 Å. Since

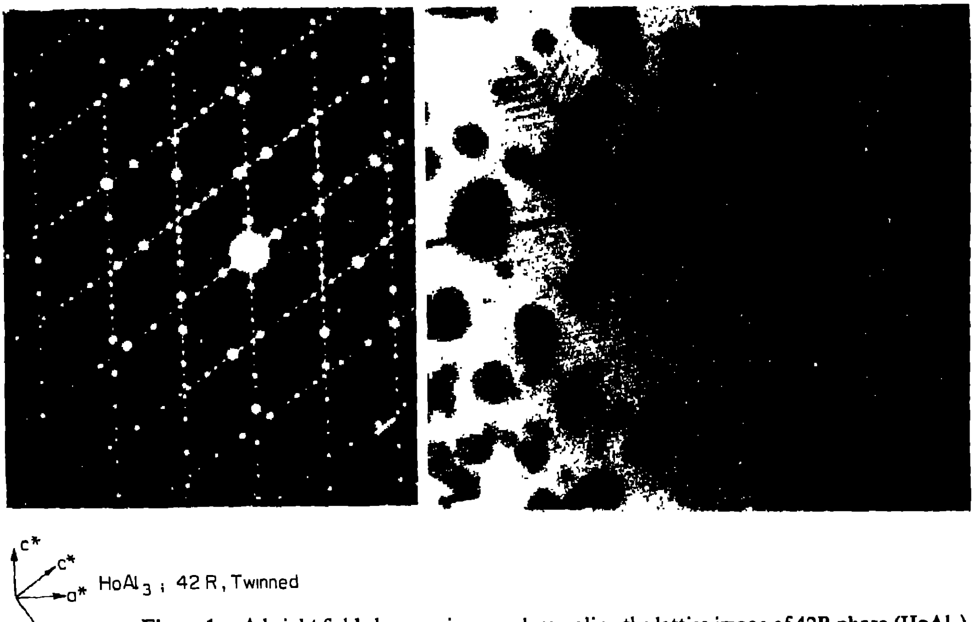

Figure 1. A bright field elecronmicrograph revealing the lattice image of 42R phase ($HoAl_3$) and corresponding diffraction pattern. Twin boundary can be noticed. Unit cell of 42R phase consists of fringes of 4H, 15R and 15R (i.e. 4H + 15R + 15R). Unit cell width corresponds to ≈ 33·4 Å.

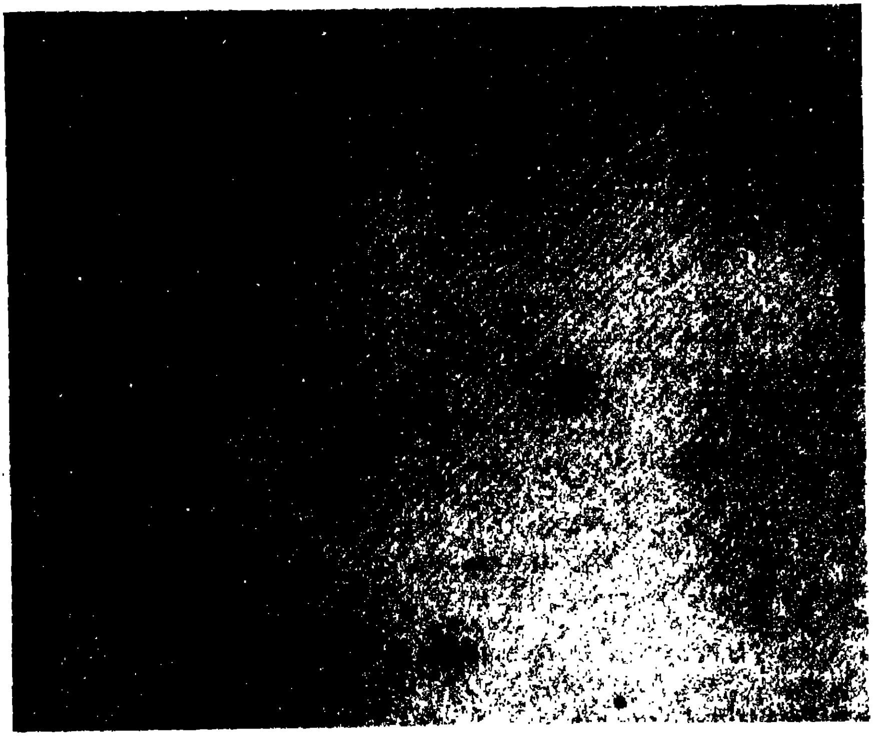

Figure 2. Dark field lattice image of 9R phase of $Er_{0.5}Gd_{0.5}Al_3$ alloy. Fringe spacing corresponds to 7·04 Å.

the diffraction pattern revealed the phase to be 9R the actual periodicity of the lattice is $3 \times 7{\cdot}04 = 21{\cdot}12$ Å. This agrees very well with the known periodicity 21·14 Å of 9R phase. Figure 3 shows the lattice fringes of 4H. Fringe spacing directly gives the c periodicity of 4H modulated phase which corresponds to $\approx 9{\cdot}4$ Å. The heavy strips marked as s represent stacking faults. Figure 4 shows a typical lattice resolution in bright field from a disordered region. Growth of several modulated phases such as 6H, 15R and of 14 layer (42R) can be noticed. Random stacking faults are also clearly seen. The alteration of background intensity with lattice images of periodic structures yield evidence of the presence of twins. Several other modulated phases have been observed with the help of high resolution electron microscopy which could not be identified by means of electron diffraction alone. These results are summarized in the following table.

The electron microscopic studies of $HoAl_3$, $Er_{0.5}Gd_{0.5}Al_3$ and $Y_{0.91}Er_{0.09}Al_3$ thin films reveal the existence of modulated phases in these films. The observed modulated phases for these trialuminides are given below:

Rare earth trialuminides	Modulated phases
$HoAl_3$	4H, 5H, 15R, 30R, 42R and disordered 60R
$ER_{0.5}Gd_{0.5}Al_3$	3C, 4H, 6H, 9R, 12R, 15R, 16H, modulated phases with periodicity of 7, 9, 13, 18, 22, 24, 32 and 46 layers and some disordered structures.
$Y_{0.91}Er_{0.09}Al_3$	9R, 4H, 16H, some disordered structures and the existence of some high period modulated phases.

3. Discussion

The mystery behind the occurrence of modulated phases has been generally too intriguing to be unravelled in a satisfactory way. In the present case which is akin to the phenomenon of polytypism the already proposed mechanisms for the formation of polytypism which explains the formation of polytypes during growth is not applicable since in the present case the modulated phases are formed during an amorphous to crystalline transformation. However, as is well-known in metallic systems the electronic energy plays an important role in stabilising the modulated phases (Sato and Tooth 1963; Sato *et al* 1967). An explanation for the formation and stabilisation of the modulated phases has been proposed by Singh *et al* (1981) for $GdAl_3$, on the basis of reduction of electronic energy elaborated in terms of contacts of Fermi surface and Brillouin-zone. In this the authors presume that slight variation in the Fermi surface scanning vector $2k_f$ may occur on the basis of valency fluctuations of rare earth metal involved and/or stoichiometric variation. It has been shown on the basis of geometrical scheme that even a slight variation in Fermi scanning vector may suffice to stabilise the modulated phases. The case of $Er_{0.5}Gd_{0.5}Al_3$ is shown in figure 5 (Singh *et al* 1981). The case of $Y_{0.91}Er_{0.09}Al_3$ is under consideration.

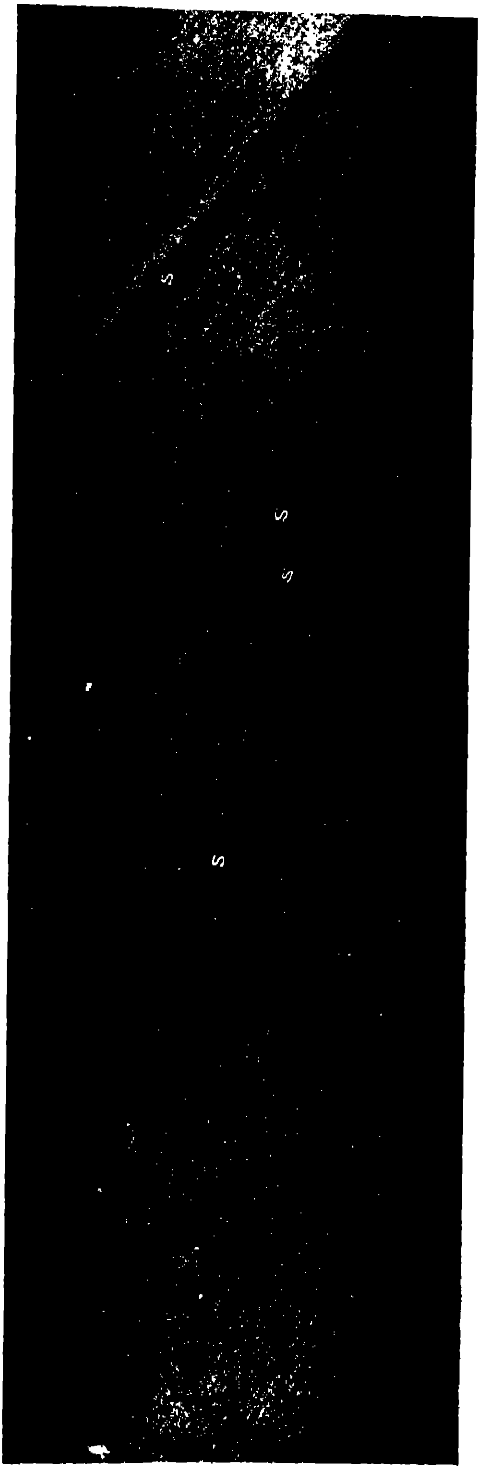

Figure 3. Lattice planes of 4H phase of $Er_{0\cdot5}Gd_{0\cdot5}Al_3$. Faults marked '*s*' can also be noticed. Fringe spacing corresponds to 7·04 Å.

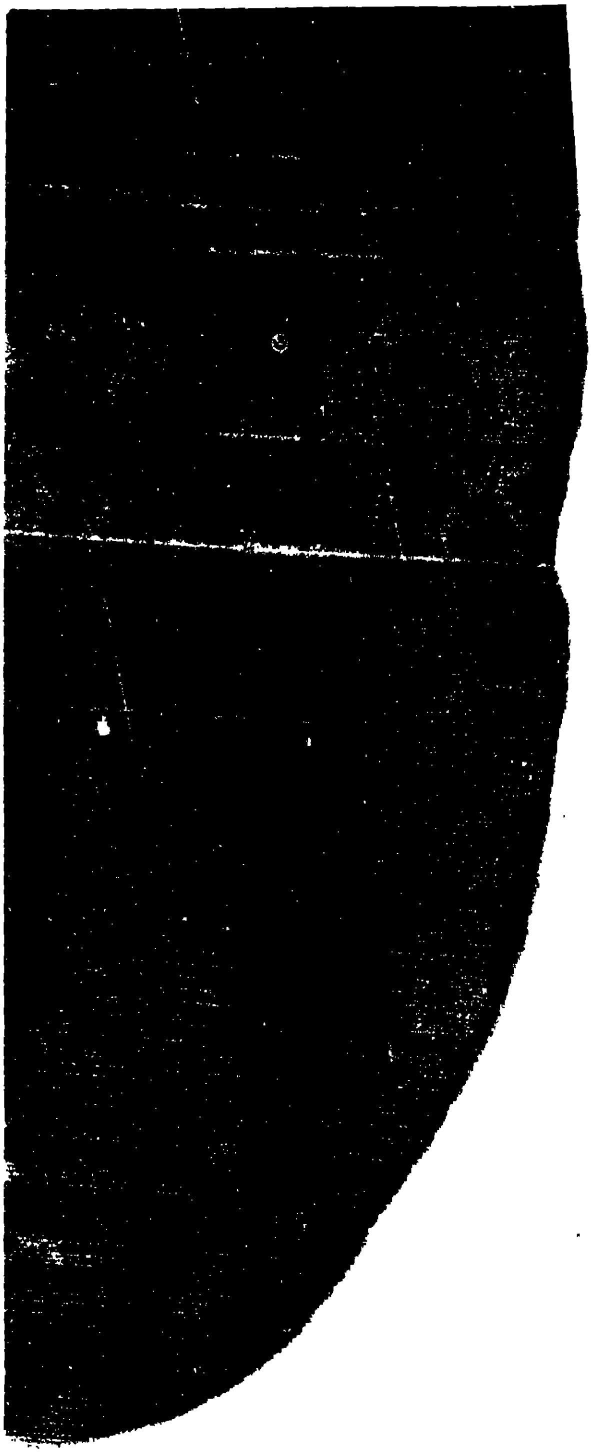

Figure 4. Bright field lattice image revealing the inter-growth of different modulated phases such as 6H, 15R and 14H (42R) of $Er_{0.5}Gd_{0.5}Al_3$.

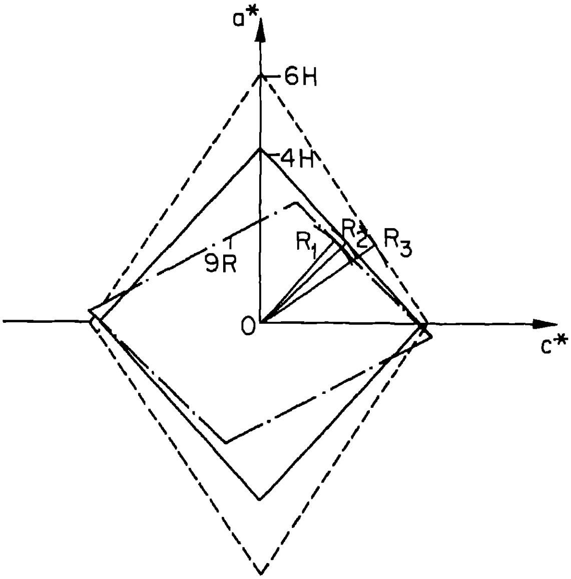

Figure 5. The Fermi surface Brillouin zone interaction exhibiting the stabilization of 4H, 6H and 9R modulated phases in $Er_{0.5}Gd_{0.5}Al_3$.

Acknowledgements

Two of the authors (AKS and AKS) are greatly indebted to CSIR, for the award of a fellowship. Authors wish to thank Dr G Van Tendeloo, Belgium for his help in electron microscopy.

References

Johannson C H and Linde J O 1936 *Ann. Phys.* **25** 1

Sato H and Toth R S 1963 *Alloying behaviour and effects in concentrated solid solution* (ed) T B Massalski (New York: Gordon and Breach) 295

Sato H, Toth R S and Honjo G 1967 *J. Phys. Chem. Solids* **28** 137

Singh A K, Acharya S and Singh A K 1981 *Indian J. Pure Appl. Phys.* **19** 941

Bull. Mater. Sci., Vol. 6, No. 3, July 1984, pp. 611–616. © Printed in India.

Electron diffraction analysis of antimony films

P D PRABHAWALKER and AMARJIT SINGH*

Regional Sophisticated Instrumentation Centre Indian Institute of Technology, Powai, Bombay 400 076, India
* Department of Physics, University of Bombay, Vidyanagari, Bombay 400 098, India

Abstract. Antimony films of about 3000 Å thickness are grown on NaCl substrate at various substrate temperatures. The films were subsequently analysed for electron diffraction and for grain size on electron microscope. At lower substrate temperatures, the film showed a single crystalline growth, and the crystal grain size was small. However at higher substrate temperatures a cubic phase along with hcp phase was found to exist and also the enlargement of the grain size was observed.

Keywords. Electron diffraction; antimony film; metastable crystalline states; phase changes.

1. Introduction

Recently the studies of semi-metal films particularly antimony films, have been a matter of considerable interest. Antimony films exhibit interesting thermoelectric properties (Boyer *et al* 1981), and also crystallographically, a number of metastable crystalline states are observed in liquid quenched or vapour-deposited antimony films (Dilshad Akhter *et al* 1979). Antimony is known to exist in a simple cubic structure ($a = 2{\cdot}96$), and in hcp structure ($a = 3{\cdot}33$ Å and $c/a = 1{\cdot}58$) at pressures of 50 and 90 kbar respectively (Kabalkina and Mylov 1964). In the present work, a systematic study on antimony films deposited at various substrate temperatures has been carried out. Its subsequent effect on the microstructure and the crystal structure of antimony films has been studied by electron microscopy.

2. Experimental

Antimony of high purity (99.99 %) was evaporated from a tungsten boat at a pressure 2×10^{-6} torr. Initially an attempt was made to use glass as a substrate, however it was rather inconvenient to remove thin antimony films of the order of 300 Å from the substrate. Hence compressed sodium chloride pellets were prepared and they were transferred immediately from the desiccator to the evaporater. The pellets were kept in close contact with the substrate heater. The thickness of the films was estimated from the amount of antimony evaporated as well as by a thickness monitor. It was ensured that the deposition took place on dry pellet at the desired temperature. After the deposition was complete, the thin films were taken out by dissolving the pellet in water. The thin films were examined on a Phillips-EM 301 transmission electron microscope. The microscope was operated at 60 kV accelerating potential and at a magnification of × 40,000.

3. Results

For the sake of better comparison, the same accelerating voltage has been maintained (60 kV) throughout the experiment, which gives the wavelength of the incident radiation as 0.0487 Å. Since the same camera constant is used, it is possible to compare the spots/rings of one figure with that of the other.

Figures 1a,b show the electron micrograph and the electron diffraction pattern respectively of the film deposited at room temperature. The electron micrograph shows formation of small granular structures indicating formation of crystalline state. The electron diffraction pattern had a number of rings. The diameter of these rings given in table 1 shows that the ratios of d^2 for the outer ring to the next ring in order is a constant

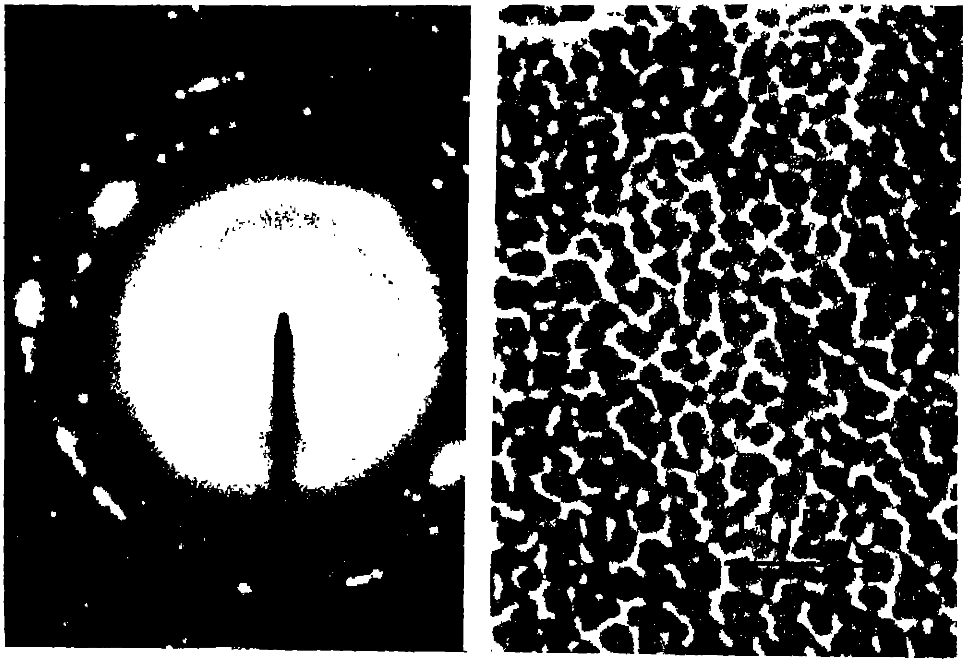

(a) (b)

Figure 1. a. Electron diffraction pattern **b.** Electron micrograph of the antimony film deposited at room temperature

Table 1. Diameter of electron diffraction rings and the ratio of their squares, substrate being at room temperature.

Ring No.	d_n = diameter of the ring n	d_n^2	$\sum = (d_n/d_{n-1})^2$
1	3.07	9.43	—
2	3.92	15.37	1.63
3	4.94	24.40	1.59
4	6.22	38.69	1.59
5	7.83	61.31	1.59

1·59. Reference to the camera geometry and Bunn charts reveals that the structure is hcp and the distance corresponds to $(10\bar{1}0)$ plane. The constants of the hcp crystal were according to the previous literature, *i.e.* $a = 3{\cdot}33$ Å and $c/a = 1{\cdot}58$ (Dilshad Akhter *et al* 1979).

Figures 2a,b show the diffraction patterns and the electron micrograph respectively of the films deposited at 323 K. It has been observed that the grain size has become larger and the crystal structure has started changing. The electron diffraction pattern corresponds to a spot pattern showing (110) planes of a cubic structure and some traces of the previous ring pattern are also seen.

At further elevated temperatures i.e. at 373 K, the cubic pattern becomes predominant and large crystals are formed. The previous ring pattern is faintly visible (figures 3a,b).

At 423 K the pattern becomes more complicated and absolutely polycrystalline (figures 4a,b). We get a number of rings in the diffraction pattern. Nine rings which were predominantly seen were taken for comparison. Starting from the outermost ring, squares of the ratios of the diameters of the inner ones were taken and are shown in table 2.

A close look at the table shows that the ratios 9/7, 8/6, and 6/4 are around 1·59. Since the magnification, incident radiation and camera constant have remained the same, it can be concluded that these rings resemble the previous hcp structure with $a = 3{\cdot}33$ Å and $c/a = 1{\cdot}58$. The second commonly occurring ratio is between 6/5, 5/4, 4/3 and 9/8 and is 1·12.

Excepting these two ratios there are no more ratios which are repeating. We can

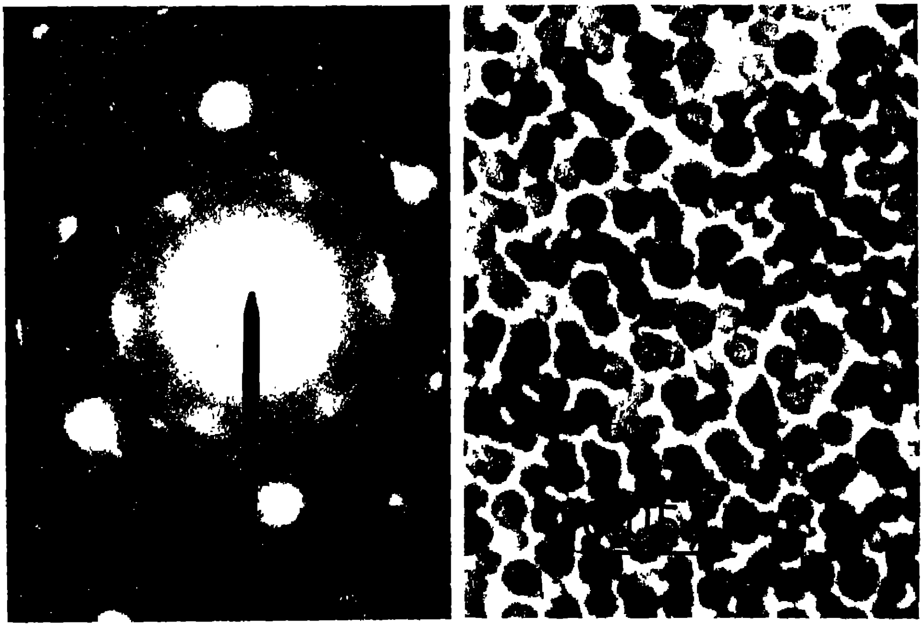

(a) (b)

Figure 2. a. Electron diffraction pattern **b.** (×44000) Electron micrograph deposited at 323K.

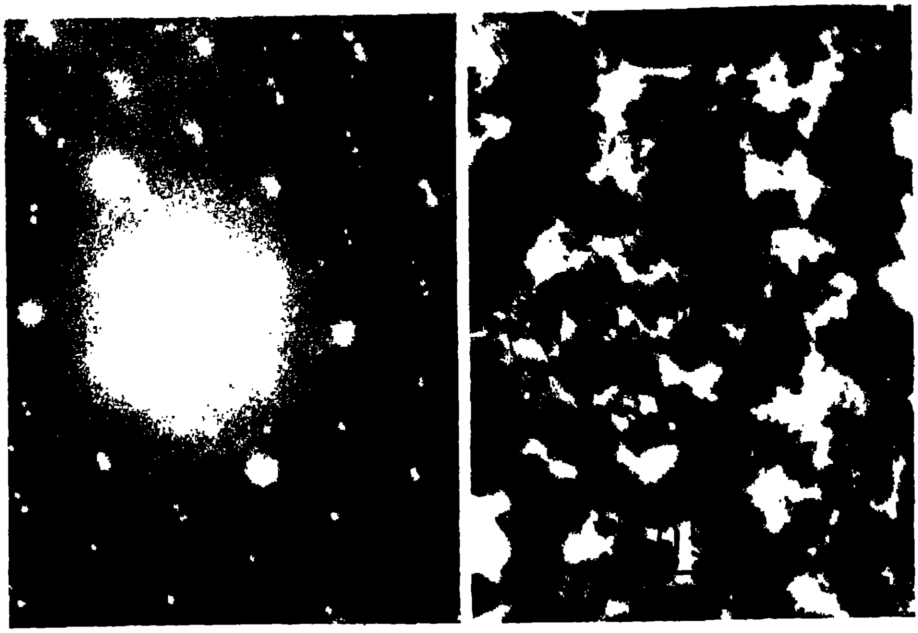

(a) (b)

Figure 3. a. Electron diffraction pattern **b.** (×44000) Electron micrograph of the film deposited at 373K.

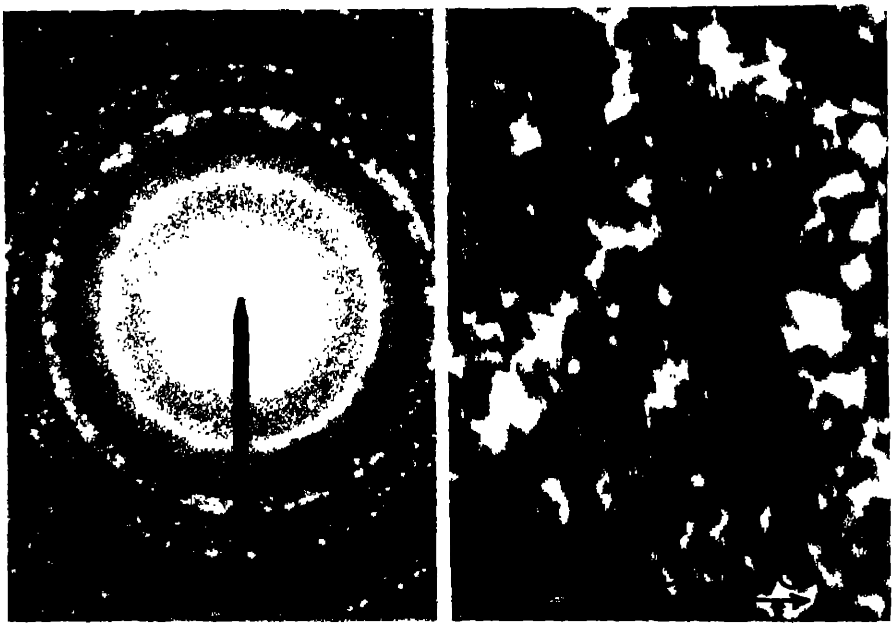

(a) (b)

Figure 4. a. Electron diffraction pattern **b.** (×44000) Electron micrograph of the film deposited at 423K.

Table 2. Squares of the ratios of the outer diameter to the inner one.

Ring No.	Value for various ratios $\sum = (d_{ni}/d_{Nj})^2$							
	$N = 98$	7	6	5	4	3	2	1
9	−1·14	1·57	2·25	2·48	3·11	3·93	6·90	13·08
8	—	1·43	1·67	1·84	2·33	2·92	5·14	9·73
7	— —	—	1·57	1·98	2·50	3·10	4·39	8·31
6	— —	—	—	1·12	1·59	1·75	2·78	5·27
5	— —	—	—	—	1·12	1·45	2·80	5·30
4	— —	—	—	—	—	1·12	1·76	3·32
3	— —	—	—	—	—	—	1·76	3·32
2	— —	—	—	—	—	—	—	1.89

attribute this second ratio to the cubic phase seen in the previous figures. Other ratios may be due to the metastable phases of other crystals in the process of formation or might be some other reflections of the existing crystals. They were not considered as they were not significant in number.

Since the photographs were taken under the same magnification and since we know that the cubic plane is (110), and the hexagonal one is $(10\bar{1}0)$, the interatomic distance of the cubic phase is estimated to be 3·4 Å.

4. Discussion

The present study shows that because of the variation of the substrate temperature a number of additional phases are developed in the vapour-deposited antimony film. If the series of the diffraction patterns are observed carefully, it is found that the sample gradually changes from a polycrystalline hcp to crystalline cubic and then back to polycrystalline hcp and cubic mixture. In figure 3 the hcp structure has almost vanished. Similarly it is also expected that at some temperature between 373 and 423 K this hcp structure may reappear again. The study of this point is worth undertaking; however it would need a better control of substrate temperature. The cubic phase observed has a larger interatomic distance *i.e.* 3.4 Å. In previous studies by splat cooling (Dilshad Akhter *et al* 1979), such a structure with $a = 3.16$ was observed.

5. Conclusions

(i) hcp phase of antimony is observed by vapour deposition also. (ii) By increasing the substrate temperature, the cubic phase is also observed. (iii) The cubic phase has larger interatomic distances than usual. (iv) At intermediate substrate temperature hcp phase vanished and reappeared at higher temperatures. (v) At the substrate temperature of 423 K both hexagonal and cubic phases become polycrystalline.

Acknowledgments

Thanks are due to Dr C S Harendranath for making the TEM facility available. The authors also thank Mr Nageshwar Rao and Miss Mruga H Joshi for help in the use of TEM.

References

Boyer A, Des B, Chacht and Groubert 1981 *Thin Solid Films* **76** 119
Dilshad Akhtar Venkar V D and Chopra K L 1979 *Thin Solid films* **58** 327
Kabalkina S S and Mylov V P 1964 *Sov. Phys-Dokl* **8** 917

Bull. Mater. Sci., Vol. 6, No. 3, July 1984, pp. 617–623. © Printed in India.

Formation of lamellar $M_{23}C_6$ on and near twin boundaries in austenitic stainless steels

B SASMAL

Department of Metallurgical Engineering, Indian Institute of Technology, Kharagpur 721 302, India

Abstract. Thin foil electron microscopy studies were made on the precipitation of lamellar $M_{23}C_6$ during aging at 973 K and 1073 K in water-quenched specimens of two austenitic stainless steels. After the precipitation on incoherent twin boundaries $M_{23}C_6$ formed on coherent twin boundaries and in the regions adjacent to incoherent twin boundaries. These precipitates showed lamellar morphology and were aligned in a specific manner with respect to the twin boundaries. Such lamellar precipitates were absent in the specimens which were isothermally treated at 1073 K after being transferred from the solution treatment temperature. The lamellar morphology of $M_{23}C_6$ is suggested to be developed by the influence of residual specific stress field around twin boundaries resulted from quenching.

Keywords. Electron diffraction; lamellar $M_{23}C_6$; precipitation morphology; twin boundaries.

1. Introduction

Precipitation of $M_{23}C_6$ in austenitic stainless steels was studied by many investigators. In quenched and aged conditions $M_{23}C_6$ precipitates (Lewis and Hattersley 1965; Wolff 1966; Beckitt and Clark 1967; Singhal and Martin 1967; Wilson 1971; Weiss and Stickler 1972) on incoherent twin boundaries after the precipitation on grain boundaries. During the later stages of aging, precipitation occurs on coherent twin boundaries and within the grains. The precipitates adjacent to an incoherent twin boundary grow as plates on both sides of the boundary, which are parallel to the coherent twin boundaries (Lewis and Hattersley 1965; Beckitt and Clark 1967; Singhal and Martin 1967; Hattersley 1964 and Lewis 1964).

Two models have been put forward to explain the formation of these lamellar precipitates. Beckitt and Clark (1967) suggested that the stress generated due to growth of precipitates nucleated on an incoherent twin boundary drives the twinning dislocations out of the boundary. These dislocations have been attributed to act as sites for nucleation continuously as they move out into the matrix and thus to form the plates of $M_{23}C_6$ on the $\{111\}$ (twinning) planes. Singhal and Martin (1967) however observed the stacking faults formed possibly by bowing of the twinning dislocation out of the incoherent twin boundary after the precipitation on the boundary. They have suggested that $M_{23}C_6$ precipitation occurs by nucleation along the bounding Shockley dislocation and by growth across the stacking fault to form a sheet of carbide. Shockley partial might again be repelled by the precipitate and the repetition of the precipitation process might cause further growth of the plate.

In order to examine these models a detailed electron microscopy study was made on the formation of lamellar $M_{23}C_6$ adjacent to incoherent twin boundaries and on the precipitation at coherent twin boundaries.

2. Experimental

The chemical composition of two austenitic stainless steels (AISI 316L and DIN 4981, hereafter referred to A and B respectively) studied are given in table 1. The cold-rolled sheet specimens (about 150 μm thick) were solution-treated (5·4 Ksec (1 hr 30 min) at 1433 K for steel A and 1·8 Ksec (30 min) at 1550 K for steel B) inside sealed silica tubes in argon atmosphere and quenched in water. The quenched specimens were then aged at 973 K and 1073 K inside evacuated silica tubes for various durations from 3·6 Ksec (1 hr) to 14·4 Msec (4000 hr). A few bulk specimens ($10 \times 5 \times 3$ mm) of A after being solution-treated were transferred to 1073 K, held for 360 Ksec and 1·8 Msec and then cooled in air. Thin foils for electron microscopy examination were prepared by twin-jet electrolytic polishing with a mixture of 10 % perchloric acid and 90 % acetic acid.

3. Results and discussion

Steel A was fully austenitic in the as-quenched condition, while B contained a considerable amount of undissolved NbC particles. $M_{23}C_6$ was the only carbide to be precipitated in A during aging at 973 K and 1073 K. In B both NbC and $M_{23}C_6$ formed. Because of the precipitation of NbC in very fine form on grain boundaries, on dislocations, in association with stacking faults and as dot-like particles, the precipitation of $M_{23}C_6$, in general, was appreciably low and was delayed in B (Sasmal 1980). $M_{23}C_6$ first precipitated on grain boundaries and later on incoherent twin boundaries followed by intragranular precipitation on continued aging. After the precipitation on incoherent twin boundaries a preferential precipitation of $M_{23}C_6$ was noted in the regions adjacent to these boundaries (figure 1). Precipitation on coherent twin boundaries also occurred simultaneously. In B, though the intragranular precipitation was rarely observed, a new mode of precipitation of $M_{23}C_6$ around undissolved NbC particles was noted. This is reported earlier (Terao and Sasmal 1978, 1981).

Electron diffraction analysis showed that the $M_{23}C_6$ precipitates were face-centred cubic and had almost the same lattice parameter in both the steels: $a = 10.7$ Å. They were found to grow at all the sites with the cube orientation relationship with austenite matrix, *i.e.*

$$\{100\}_{M_{23}C_6} \parallel \{100\}_\gamma,$$
$$\langle 100\rangle_{M_{23}C_6} \parallel \langle 100\rangle_\gamma.$$

Table 1. Chemical analysis of steels.

Steel	Composition, wt. %								
	C	Ni	Cr	Mn	Mo	Si	Nb	B	Fe
A	0·014	11·5	17·3	1·15	2·2	0·56	—	—	Balance
B	0·057	15·8	16·2	1·12	1·84	0·41	0·77	0·0003	„

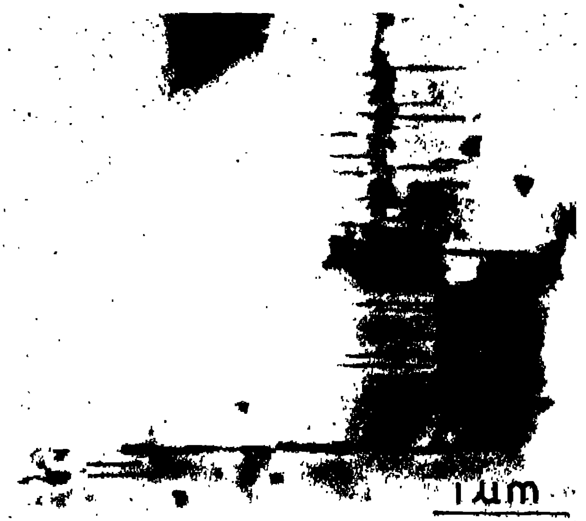

1

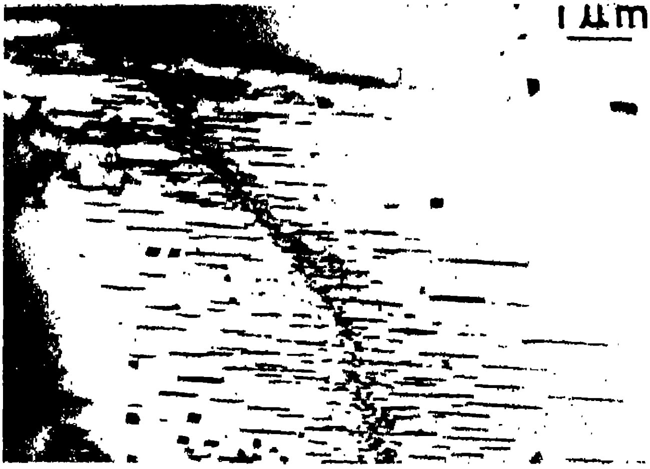

2

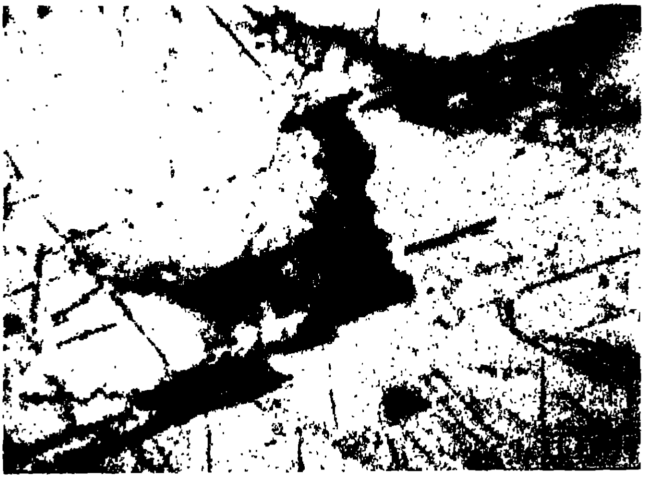

3

Figures 1–3. Steel A, aged for 28·8 Ksec (8 hr) at 1073 K. Lamellar $M_{23}C_6$ formed close to incoherent twin boundaries and on coherent twin boundaries. **2.** Steel A, aged for 1·80 Ksec (50 hr) at 1073 K. $M_{23}C_6$ plates increased in number on both sides of the incoherent twin boundary. The specimen foil is nearly parallel to the (110) of the matrix and the twin axis is $[\bar{1}11]$. **3.** Steel B, aged for 14·4 Msec (4000 hr) at 1073 K. $M_{23}C_6$ plates formed on coherent twin boundaries and adjacent to incoherent twin boundaries, but considerably less in number.

The results agree with those reported earlier (Lewis and Hattersley 1965; Weiss and Stickler 1972; Singhal and Martin 1968). The morphology of these precipitates after a long aging period, however, depends on the precipitating sites (Sasmal 1980). Whatever may be the morphology of these particles, their interfaces always consist of $\{111\}$ and $\{110\}$ types of planes. This result confirms the suggestion made by Beckitt and Clark (1967).

In the adjacent regions of an incoherent twin boundary $M_{23}C_6$ grew as plates into the austenite matrix on both sides of the boundary (figure 1). The plates grew in a direction parallel to the coherent twin boundaries. On longer aging, more and more lamellar $M_{23}C_6$ formed in a similar fashion and gradually grew away from the incoherent twin boundaries (figure 2). The number of lamellae however decreased progressively with increase in distance. On the coherent twin boundaries also, $M_{23}C_6$ grew as similar plates which on longer aging joined one another making almost a continuous layer of precipitates. In B, $M_{23}C_6$ plates also formed on coherent twin boundaries and in the vicinity of incoherent twin boundaries, but to a lesser extent, (figure 3). A few examples of morphology of the lamellar precipitates in the vicinity of an incoherent twin boundary are shown schematically in figure 4. The large planes of these plates are parallel to the twinning planes. A detailed study of the characteristics of these lamellar precipitation has been reported elsewhere (Terao and Sasmal 1980). The

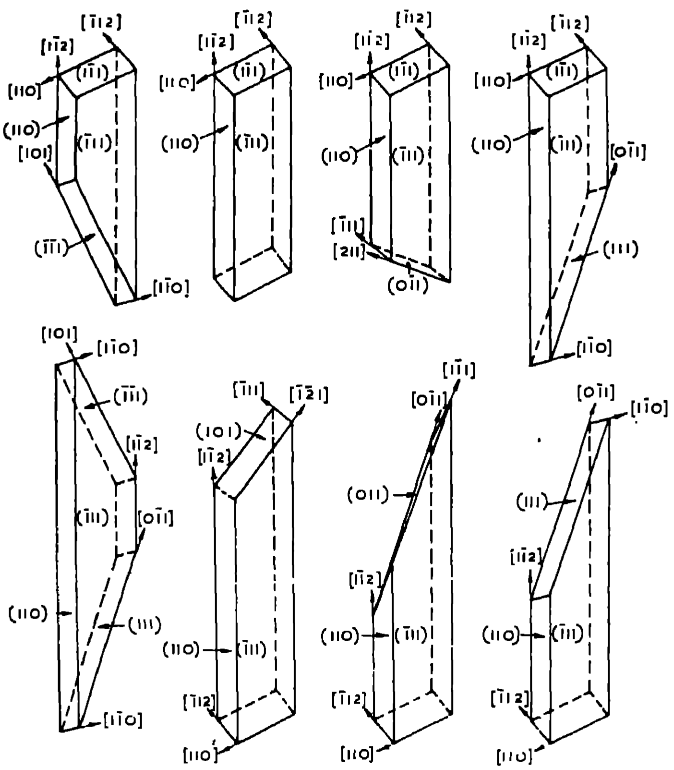

Figure 4. Several examples of morphology of $M_{23}C_6$ lamellae formed adjacent to an incoherent twin boundary, the twinning plane being $(\bar{1}11)$.

specific features of the formation of these $M_{23}C_6$ lamellae were observed to vary from one twin to another.

The lamellar $M_{23}C_6$ precipitates, as reported by the previous investigators (Beckitt and Clark 1967; Singhal and Martin 1967) were assumed to result from emanation into the grains of the precipitates nucleated earlier, on incoherent twin boundaries. On the basis of this assumption in the mechanisms suggested for their formation the glide of the twinning dislocations possibly repelled from the incoherent twin boundaries by the stress field of growing particles at the boundaries has been proposed to play the most important role. The plate morphology has been attributed to result by a repeated nucleation (Beckitt and Clark 1967) on these gliding Shockley particles, or by the formation of stacking faults, nucleation on the outer particals and subsequent growth across the stacking faults (Singhal and Martin 1967). A close examination (by tilting the thin foils about different axes) of these lamellae, however revealed that most of them stood separate from the precipitates formed on incoherent twin interfaces, having no contact whatsoever. On the other hand, if any one of these mechanisms were operative, the lamellar $M_{23}C_6$ might not form in B since dislocations are more preferable sites for precipitation of NbC. Further, none of these mechanisms is able to explain the lamellar precipitation on coherent twin boundaries.

To examine further the validity of these models another experiment was made. A few bulk specimens of A were held at 173 K for sufficiently long periods, after being transferred directly from the solution-treatment temperature. As shown in figure 5, $M_{23}C_6$ precipitated in these specimens only on incoherent twin boundaries. No lamellar precipitation occurred either on coherent twin boundaries or in the regions adjacent to the incoherent twin boundaries. These observations indicated that quenching from the solution-treatment temperature is essential to induce lamellar precipitation during aging, and the existing models have no provisions to accommodate this fact.

Due to differential contraction between cooler and hotter parts of a metallic body, quenching from a high temperature induces pronounced stress. The state of stress inside a specimen becomes complicated in the vicinity of a barrier such as grain boundaries, twin boundaries and undissolved particles. The effect of the quenching stress near twin boundaries would, however, be different from that near a grain boundary owing to the inherent difference in characteristics of these two types of boundaries. In this respect coherent twin boundaries would once again behave differently from incoherent twin boundaries. Quenching stress produces residual stresses in the specimens, the maximum value of which has been calculated (Lang 1965) to be

$$\sigma_{\max} = \frac{E\alpha\Delta T}{1-\nu} \cdot \frac{S^2}{3a\,t_0},$$

where E = Young's modulus; α = coefficient of thermal expansion; ΔT = temperature range $(T_q - T_{\text{room}})$; ν = Poisson's ratio $(= 0.3)$; $2S$ = thickness of the plate; a = thermal diffusivity in cm^2/sec; t_0 = total transient time.

The change of orientation of a crystal in a specific manner across twin boundaries is expected to induce a specific stress field around the boundaries since the elastic constants of a material are different along different directions. In these regions, $M_{23}C_6$ which always nucleates on $\{111\}$ austenite planes, because of least misfit (Beckitt and Clark 1967) across these interfaces has to choose one of the possible habits in order to

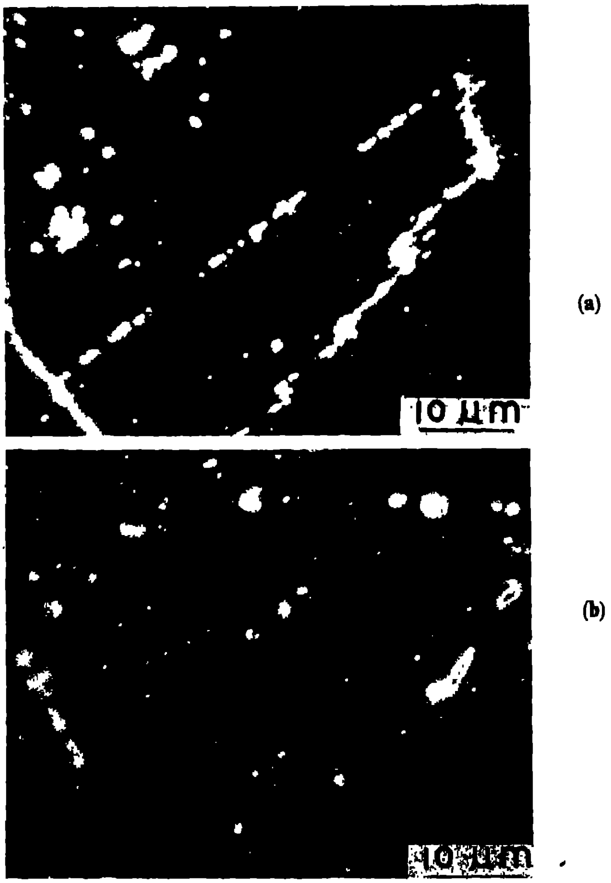

Figure 5. Dark-field optical micrographs of steel A. **a.** Water quenched and aged at 1073 K for 1·8 Msec (500 hr). $M_{23}C_6$ precipitated on incoherent and coherent twin boundaries and also in the regions adjacent to incoherent twin boundary. **b.** Quenched to 1073 K and held for 1·8 Msec (500 hr). Coherent twin boundaries and regions close to the incoherent twin boundaries are free from lamellar $M_{23}C_6$.

minimise the coherency strain. This is in conformity with the observations made. It is therefore, proposed that the presence of a residual specific stress field around twin boundaries in the quenched specimens is responsible for the formation of lamellar $M_{23}C_6$ precipitates on coherent twin boundaries and in the regions close to incoherent twin boundaries. Possibly vacancies play an important role in the process of their nucleation.

4. Conclusions

The lamellar $M_{23}C_6$ precipitates on coherent twin boundaries and near incoherent twin boundaries form during aging in the quenched samples only. The morphology and the specific orientation of these precipitates are influenced by the residual stress developed around twin boundaries due to quenching. The nucleation of these precipitates is aided by vacancies.

References

Beckitt F R and Clark B R 1967 *Acta Metall.* **15** 113
Hattersley B and Lewis M H 1964 *Philos. Mag.* **10** 1075
Lang W 1965 *Keruforschungzentrom Karlsruhe Report No* 274
Lewis M H and Hallersley B 1965 *Acta Metall.* **13** 1159
Sasmal B 1980 Ph.D. Thesis, Indian Institute of Technology, Kharagpur
Singhal L K and Martin J W 1967 *Acta Metall.* **15** 1603
Singhal L K and Martin J W 1968 *Acta Metall.* **16** 1159
Terao N and Sasmal B 1978 *C. R. Acad. Sci. (Paris)* **C287** 487
Terao N and Sasmal B 1980 *Metallography* **13** 117
Terao N and Sasmal B 1981 *Trans. Jpn. Inst. Metals* **22** 379
Weiss B and Stickler R 1972 *Met. Trans.* **3** 851
Wilson F G 1971 *J. Iron Steel Inst.* **209** 126
Wolff V E 1966 *Trans. MS-AIME* **236** 19

FOREWORD

The mechanical behaviour of materials is of vital interest to many branches of engineering and technology. Although at one time physicists were interested in this subject, at present its study is pursued mainly by metallurgists and mechanical engineers. However, the recent focus on topological defects etc., made some of us wonder whether the time was ripe for physicists to renew their interest in mechanical properties. In order to explore this, a Discussion Meeting was held at the Reactor Research Centre, Kalpakkam on February 7, 8 and 9, 1983. The Meeting was sponsored by the Indian Academy of Sciences, the Department of Science and Technology, the Defence Metallurgical Research Laboratory and the Department of Atomic Energy. About 70 scientists belonging to various disciplines took part.

We present in this volume the written version of the talks given at the Meeting, the record of the discussions that followed the oral presentations, and of the Panel Discussion that took place in the concluding session. Owing to restrictions of space, and in the interests of reasonable uniformity of style and notation, we have been forced to make (generally minor) editorial changes in the manuscripts submitted by the speakers, and on occasion, prune the material in places. While great care and pains have been taken to preserve the essential spirit of every point the authors have intended to make, we do accept the responsibility for the changes necessitated by the reasons stated.

The Meeting itself was quite lively and absorbing, with a variety of views expressed by people with varying specializations. In offering the Proceedings we hope that the excitement of the Meeting would be shared by a wider audience, and enthuse at least some physicists to enter this area.

The task of preparing the Proceedings for publication has been quite strenuous and could not have been accomplished but for the unstinted help and cooperation we have received from many. Particular mention should be made of G Ananthakrishna, B Purniah, Radha Ranganathan, V Sridhar, P Subba Rao and T D Sundarakshan. We also would like to express our personal indebtedness to Prof. S Ramaseshan for support and encouragement in organising the Discussion Meeting.

February, 1984
C N R Rao
Editor of Publications,
Indian Academy of Sciences

Guest Editors
V BALAKRISHNAN
G VENKATARAMAN

Bull. Mater. Sci., Vol. 6, No. 4, September 1984, pp. 627–631. © Printed in India.

Observations on the physical basis of mechanical behaviour

S RAMASESHAN
Indian Institute of Science, Bangalore 560 012, India

1. General remarks

It gives me great pleasure to participate in this Discussion Meeting. This is perhaps the first time that physicists, materials scientists and metallurgists in India have planned a meeting to understand each other and to see whether phenomena not completely comprehended by one group can be looked into by another or jointly. The motivations are so praiseworthy that I am sure something will come out of such meetings. If these meetings are to be successful many obstacles have to be surmounted. The first, of course, is that of language. Each person here must understand the jargon of the other. The second is to make a conscious attempt to change one's attitudes.

The metallurgists and physicists today appear to be two different animals. The purpose of this meeting is to see that the barriers that have been artificially raised are removed. One has only to read the fascinating books by Cyril Stanley Smith, *From Art to Science* and *A Search for Structure* to realise that metallurgy which has been an empirical science for a long time has been eminently successful; and yet what is common to the village blacksmith is very mysterious to the physicist. Science was injected into metallurgy only recently. Most metallurgists, like chemists, are pragmatists. They reduce many sophisticated theories to thumb rules which work and which have advanced the fields most spectacularly. However, there is a tendency among many of them not to go too deeply into the fundamentals of the phenomena they observe. The physicist, on the other hand, choose rather simple ideal systems and model them. As this approach has been rather successful in physics he feels that by using a similar one he can "clean" up many of the problems which the metallurgist does not understand. In this connection, I must recall what Prof. Andrew Huxley—a physicist himself who entered biology and distinguished himself—said when he lectured at the Indian Institute of Science, Bangalore on Physical Sciences and Biology. Biology, according to him, is inherently complex. Simplistic models sometimes hinder rather than advance the subject. It is the complexity and the basis of this complexity that one must try to understand and describe. The physicist, if he is to be useful at all, must enter biology with great humility, with a genuine intent to understand the subject and its spirit. What Huxley said of biology is, in my view, applicable to metallurgy and materials science.

In each field of science when sufficient knowledge accumulates, a great step is usually taken which throws new light and opens up new vistas. This happened to biology about 25 years ago when biologists and crystallographers combined to unravel the structure of DNA and caused a revolution which biology is still experiencing.

For metallurgy there was one such great flash in 1934 when the theory of dislocation was put forward by physicists which opened the gates for the understanding of the mechanism of strengthening, crystal growth etc. Fifty years have now passed and one feels that a coming together of scientists in related fields may possibly help is taking another important step even if it is not as revolutionary as the dislocation theory. Being an experimenter myself I must stress the importance of experiments. Unfortunately the experimental approach is sometimes neglected by physicists in India. Experiment forms the backbone of progress is any field. I am told that Prof. Mott often stressed that every theoretical paper or idea must suggest a clean interesting experiment which can be *performed*. I do hope that at the end of this meeting crucial experiments will be suggested which will help to bring about the proper understanding of some of the puzzling phenomena in this field.

If such meetings are held often they would create a community of scientists interested in mechanical behaviour of materials. They may also provoke individuals or groups with complementary competences to collaborate. One hopes that the theorists and experimenters would join hands to look into some of the exciting problems in this field. Following the spirit advocated by the organisers of this Meeting, in this inaugural talk I shall mention a few experiments which I and my group have performed (many of which are unpublished) and others which are not so well-known, that have come my way. I shall also raise some questions which have troubled me particularly those connected with crack generation, hardness and its variation, friction, wear, surface states and the nature of grain boundaries.*

2. Welding of surfaces and generation of cracks

In some experiments done in 1944 I noticed that diamond surfaces freshly cleaved in vacuum (10^{-5} torr) do not rejoin when brought together almost immediately after cleaving. It was also possible to show by studying the Jamin effect (*i.e.* by ellipsometric methods) that a thin film is formed on the cleaved surface. In 1948 Gwathemay showed that cleaved copper single crystal welded together in vacuum (10^{-8} torr) a phenomenon now common in space.**

At the surface of a metal due to discontinuity there would be a spill-over of electrons and the consequent charge imbalance is prevented by the electrons collectively conspiring to set themselves into oscillations. When two clean metal surfaces are brought close to each other these oscillations in each piece (which are independent) can become coupled and they go backwards and forwards from one piece to the other, bonding the two surfaces. Another crucial question is: Can stress concentration in a metal cause an instability in the electron oscillations so that decoupling can take place causing the formation of two surfaces (i.e. a crack?) These are topics of great interest worthy of some thought and discussion.***

---

* No attempt is made to pad it up to make it more intelligible!

** I am not aware of any experiments done in space attempting to join or weld diamonds. It is not clear to me why diamond surfaces should not also weld as copper surfaces do. The dangling bonds in diamond may help to *chemisorb* atoms to form a thin film. In metals also thin films are formed by physical adsorption. One wonders whether the difference in the magnitude of the energies of chemisorption and physisorption is the real cause of the two types of behaviour.

*** Some may disagree with the conjecture that two metal surfaces weld together in vacuum because the surface plasmons go backwards and forwards from one piece to another. It is strange that the magnitude of the surface energy is very close to the contribution of the correlation part of the electron energy. Does this imply that for some reason there is a cancellation of some of the very large terms like the lattice contribution, the kinetic energy of the electron etc? Similarly, when one considers the cohesive energy (next section) is there also a cancellation of the Madelung term, corresponding to the kinetic energy of the electron so that the electrons are mostly responsible for the cohesive energy.

Crude measurements (by us) of the stress optic coefficients of metals indicate that stress has considerable effect on the electrons. Stress distorts the lattice and due to this there are two optical effects. Firstly, the anisotropic distribution of the polarisable atoms in the strained lattice alters the index (n) and absorption (k) tensors. Secondly, electrons moving in the strained lattice can also alter the n and k tensors. The latter effect appears to be quite large and is opposite to that of the former.

3. Do electrons contribute to the hardness of metals?

Since electrons do contribute so much to the cohesive energy of a solid, it seems very probable (at least to me) they contribute to the hardness of a metal.[†]

Some compounds like rare earth chalcogenides (example SmS which has the NaCl structure) are semiconductors and become metals under pressure, undergoing isostructural semiconductor-to-metal transformation. There is a volume change and the resistance drops by five to six orders of magnitudes. These are peculiar metals which have positive and negative ions inside with 'free electrons" in them. By measuring the hardness of the two phases one can get an idea as to whether electrons do contribute to hardness or not. To make measurements at high pressures is not easy although the method mentioned in the next section could be adopted for this purpose. The effect of the density change on hardness must also be taken into account.

A similar isostructural semiconductor-metal-transition can be effected by adding adequate amounts of rare earth metal which simulates the effects of pressure (*e.g.* SmS is a semiconductor while $Sm_{0.85}$, $Gd_{0.15}S$ is a metal). The hardness of the metal is much higher than that of the semiconductor. But one cannot be certain whether this increase is due to the electrons, the change of density or the additional Gd atoms in the substance.

4. The hardness pendulum—The measurement of the variations of hardness

The hardness pendulum, devised by experimentors in USSR, in which a loaded cylinder oscillates on the surface under study can be used to measure hardness of the metal under a variety of conditions. The hardness is estimated from the rate of damping of the oscillations. Liquids can be placed between the surface and the cylinder to study the effects of adsorption and hardness. With an electrolyte, variation of hardness can be studied with varying potentials applied on the system. The hardness of the material increases with increasing potential and becomes maximum when the charge on the surface is zero and it decreases as the surface becomes progressively negatively charged. In fact, this curve is very similar to the variation of the interfacial tension of Hg solution interface with applied voltage indicating clearly that the surface energy (which changes with the application of potential) is involved in the phenomenon of hardness. By analogy with the Hg solution interface the effect of atoms absorbed on the surface was studied. Many patents on additives to increase the machining rates have resulted from this work.

[†] I am not at all happy using the word 'electron' in this loose manner as I am aware that there are several contributions to the energy from electrons themselves and they even have opposite signs.

[‡] To my mind the question "do electrons" contribute to the hardness of metals is an important one and deserves further theoretical and experimental investigation.

It is also found that the effect of absorption of neutral atoms decreases the hardness. It is also a known fact that the work function $W(\phi)$ of a refractory transition metal is lowered by as much as 4 eV by a monolayer of Cs. This is possibly the reason why adsorption can decrease hardness. Theoretical calculations of the electron distribution on the surface have also been done. When a tin crystal is coated with liquid gallium the crystal becomes brittle. Laue photographs show that a single crystal becomes polycrystalline. It is thought that the grains are held together by surface tension forces of the liquid. The strength of the solid decreases considerably although its ductility is not affected.

5. Friction, surface roughness and surface states

The second law of friction discovered by the great Leonardo da Vinci (which states that the coefficient of friction (μ) is independent of the surface area) appears mysterious to many when they first come to know of it. To explain this experimental law one must seek a phenomenon by which a true area of contact is proportional to load (the first law states that the $\mu \propto$ load). The real surface of any material consists of microscopic hills and valleys (asperities). When two surfaces touch, the area of contact being small the stress is very large. An elastic deformation takes place first and this is followed by a plastic one till the total area of contact increases to a value which can support the load. This phenomenon can be elegantly demonstrated by observing intensively the total internal reflection in a right angle prism. When the surface (with its asperities) is laid on the hypotenuse of the prism wherever there is a real contact there is no total internal reflection, and where there is no contact, evanescent wave returns into the medium of the prism. The intensity of the totally reflected beam decreases with load.

The existence of the asperities has also been demonstrated by measurements of the AC surface resistance (at very high frequencies 24000 MHz when the skin depth is as low as 0·4 μ) and this surface resistance is much greater than the DC resistance. If the surface is bathed in carbon monoxide, the AC resistance increases considerably indicating that the electrons are trapped in the surface states created by CO.

6. Electrons and metals

There are many other questions which require consideration. What is the submicroscopic beilby layer which forms when one metal is rubbed against another? And which spalls off during wear producing hard particles? Why is it harder and more brittle than the parent metal—although it is said to have the same composition? Has the metal turned amorphous due to the high temperatures and pressures produced during wear? Does the contribution of the electron to cohesive energy increase in amorphous metals, making them harder and corrosive resistant? Electron micrographs definitely indicate that the boundaries in large angle polycrystalline metals and alloys are extremely thin (about 3 to 5 atomic layers). Are these really "amorphous" regions with coordination polyhydra postulated by Bernal for "liquids"? Are polycrystals stronger than the monocrystals because dislocation cannot wander across the grain boundaries or is it because electron "lattice" interactions at the grain boundaries contribute to the cohesive energy?

We know that the dislocation theory has been very successful but are we leaning a bit too heavily on it, relegating the effect of free electrons on the mechanical properties, to the background?

Soon after the discovery of the quantum theory, it was appreciated that the physical basis for the optical and magnetic properties of solids must be found at the microscopic level. Unfortunately, the physical basis of mechanical behaviour was relegated as engineering. Only some outstanding scientists like Mott and Pierls appreciated that one must look at microscopic phenomena to understand mechanical behaviour also. Soon after the advent of the dislocation theory, their interest shifted to other problems and physicists have been very reluctant to contribute to this complex but important field. It is a bit ironical because the most dramatic and obvious property of a solid is, of course, its mechanical strength. This meeting clearly shows that we in India have a unique opportunity to make some important contributions before the rest of the world wakes up, so to say.

Bull. Mater. Sci., Vol. 6, No. 4, September 1984, pp. 633–641. © Printed in India.

Shocks and high velocity deformation

R CHIDAMBARAM

Physics Group, Bhabha Atomic Research Centre, Bombay 400085, India

Abstract. The shock Hugoniot curves of a large number of materials up to a few Mbar have been obtained experimentally. Metallurgical examination and physical measurements on metallic and other samples recovered after shock loading up to several 100 kbar indicate the existence of large concentrations of point, line and planar defects. Dislocation mechanisms have been invoked to explain shock wave propagation and the phenomena related to the quick homogenisation of stress and strain behind the shock front. Computer simulation models using molecular dynamics calculations have also been used to understand some aspects of shock wave propagation at an atomistic level. For very strong shocks, the material is expected to melt under shock heating, but the experimental evidence regarding this is inconclusive. A combination of shock temperature measurement and theory may be able to answer this question.

Keywords. Shock propagation; shock deformation; shock melting.

1. Introduction

During the last decade or two, our understanding of the mechanical effects of shock waves on materials has advanced considerably. There is now a wealth of metallurgical information on samples recovered after being subjected to shock loading. Active measurements of physical parameters such as the electrical resistivity have also been attempted in a few cases. Physical phenomena like shock deformation, phase transformations under shock loading and shock melting have been understood to a somewhat smaller extent at the microscopic level. We shall discuss some of these aspects in this paper.

If the shock wave propagating in a material is considered to be a sharp discontinuity in stress, then, using the laws of conservation of mass, momentum and energy, it can be shown that the undisturbed state is related to the shocked state at the shock front as follows:

$$U_s\rho_0 = \rho_1(U_s - U_p), \tag{1}$$

$$P_1 - P_0 = \rho_0 U_s U_p, \tag{2}$$

$$E_1 - E_0 = \tfrac{1}{2}(P_1 + P_0)(V_0 - V_1), \tag{3}$$

where U_s is the shock front velocity, U_p is the particle velocity in the compressed region; P, E, ρ and $V(=1/\rho)$ are respectively the pressure, specific internal energy, density and specific volume: the suffixes 1 and 0 represent quantities in the shocked and the unshocked regions respectively.

If the equation of state $E = E(P, V)$ of the material is also known, we can use (3) to write P as a function of V (for all practical purposes, $P_0 \simeq 0$). The locus of all states (P, V) which can be obtained by a single shock from an initial state (P_0, V_0) is known as the Rankine-Hugoniot curve or simply the Hugoniot curve (figure 1).

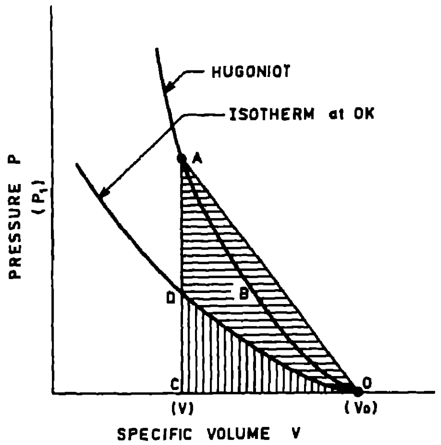

Figure 1. The Hugoniot curve. The vertically-hatched area is a measure of the cold compressive energy. The horizontally-hatched area is a measure of the heat energy in the shocked sample.

It is evident from (3) that the internal energy deposited in the compressed body is the area of the triangle *OAC*. If the compression is carried out isothermally at 0°K to the same final volume *V*, the material will be at the point *D*. The area of the curved triangle *ODC* therefore represents the "cold" elastic energy. The difference between the areas of *OAC* and *ODC* is a measure of the heat energy deposited by the shock in the compressed sample; the contribution from defects created by the shock, such as vacancies and dislocations, is relatively negligible. To give some numbers, a shock pressure of 1 Mbar* will compress a sample of aluminium from a density of 2·78 to 4·30 g/cm^3 and heat it to 3540 K. The corresponding shock velocity is 10·1 mm/μsec and the particle velocity is 3·6 mm/μsec.

After the shock wave has passed, the sample will unload along the curved path *ABO* doing work on the surroundings represented by the area of the curved triangle *OBAC*. (For simplicity we assume that the terminal specific volume $\simeq$ the initial value V_0, which would be true in the absence of porosity in the initial sample, etc.) The difference in the areas *OAC* and *OBAC* represents the (waste) heat deposited in the terminal sample. In aluminium, the residual temperature is 1440 K. If the amount of waste heat exceeds the enthalpy of vaporization (or melting), the terminal sample will be in the vaporised (or molten) state. In peaceful nuclear explosions (*e.g.*, see Chidambaram and Ramanna 1975), when a nuclear explosive is detonated underground in a rock medium, about 20% of the explosive energy is utilised in vaporising approximately 70 tons of rock, and another 20% in melting approximately 300 tons of rock for every kton of yield.

2. Range of shock pressures achieved experimentally

By keeping chemical explosives (usually in the form of lenses and pads) in contact, shock pressures of a few 100 kbar can be transmitted into materials. Alternately, a metal plate (flyer plate) can be accelerated by a contact explosive or a gas gun, and can subsequently be made to deliver its momentum to a target plate by impact. Pressures up to several Mbars can be achieved in this manner, though the pressure pulse widths are smaller (typically a few mm in space); still higher pressures can be obtained using curved rather than plane geometries. Exploding foils and rail guns can also be used to accelerate flyer plates. The highest shock pressures achieved to date have been through laser—or nuclear explosive-driven shocks and are in the range of tens of Mbars (for a more detailed discussion see Godwal *et al* 1983a). The metallurgical and physical observations to be discussed below have generally been on samples shocked to pressures less than about 1 Mbar.

---

* 1 Mpa = 10 bar, 1 Gpa = 10 kbar, 1 Tpa = 10 Mbar.

3. Finite elastic-plastic deformation by shock waves

When a plane shock wave propagates through a material, the change in density occurs—from a macroscopic point of view—through uniaxial compression. Consider a volume element of cross-sectional area A (perpendicular to the direction of shock propagation) and length L. During shock compression, A remains unchanged while L decreases in direct proportion to the decrease in the specific volume (see figure 2). If the element were allowed to expand from the final compressed state without lateral constraints it would reach normal density at the boundaries shown by the broken lines, provided it had been in a state of hydrostatic strain and stress in the compressed state. This gives us the elastic and plastic strain components in the direction of shock propagation and in the lateral directions, as indicated in the figure.

The time scales involved in shock propagation are typically in the μsec region, while the rise times are well below a nsec. Are conditions of hydrostatic stress and strain achieved behind the shock front, and, if so, how quickly? The answer to this question comes from the beautiful flash x-ray diffraction experiments of Johnson and Mitchell (1980) with single crystals of LiF, Al and graphite. Specific Bragg reflections were recorded using a Mo x-ray pulse synchronised with the duration of the shock compression of the crystal. These authors concluded that: (a) single crystals transform to the hydrostatically-compressed state within less than 20 nsec—there is no immediate conversion to a polycrystalline state; (b) the unit cell volume compression is in agreement with the conventional macroscopic volume compression data to within 1 %, independent of crystal orientation (shocks of strengths between 400 kbar and 1·1 Mbar were propagated along [100] and [111] in LiF). In related experiments at Trombay (Gupta 1980) we shocked polycrystalline samples of zirconium (hexagonal crystal

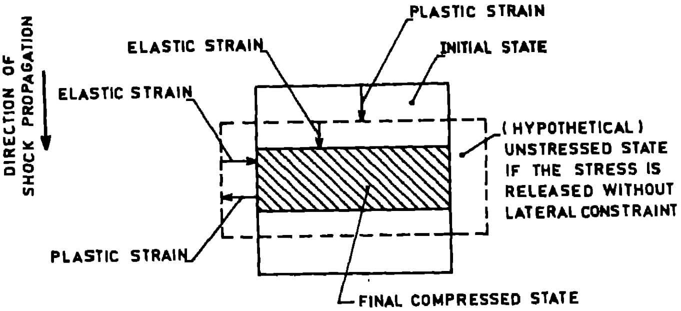
DIRECTION OF SHOCK PROPAGATION
PLASTIC STRAIN
ELASTIC STRAIN
INITIAL STATE
ELASTIC STRAIN
(HYPOTHETICAL) UNSTRESSED STATE IF THE STRESS IS RELEASED WITHOUT LATERAL CONSTRAINT
PLASTIC STRAIN
FINAL COMPRESSED STATE

Figure 2. Finite elastic-plastic deformation created by a shock wave.

system) which showed a prominent texture ({100} planes preferentially normal to the axis of the cylindrical sample). The texture was retained to a substantial extent in the terminal sample, after shock loading to about 150 kbar.

At very low pressures, the unit cell of the crystal may be expected to respond by one-dimensional compression. Correspondingly, in the Hugoniot curve, there is a pressure value known as the Hugoniot elastic limit (HEL) below which the response of the material to the shock pressure is nearly linear; the Hugoniot really begins to curve (concave upwards) from this point. The HEL is related to the shear strength of the material; one may expect that, for shock pressures lower than this limit, no rearrangement of the crystal lattice occurs (unlike in strong shocks discussed below). However, Jamet (1980) found, in some recent flash x-ray experiments with NaCl single crystals (HEL = 280 bar), that the one-dimensional deformation must be taken into account even for shock pressures above 10 kbar. Some experiments on the measurement of triaxial stress components using piezo-resistive gauges for shock pressures below, around and above the HEL are now being carried out for several materials (see, *e.g.* Chartagnac 1982).

Computer simulation of shock propagation in crystal lattices has also been attempted (Tsai and Macdonald 1976). Shock compression is initiated in a semi-infinite lattice by moving the lattice along the x-axis towards the origin with (mass) average velocity corresponding to the particle velocity U_p defined in (1)–(3), and making it collide with its image at $x = 0$. Many effects are correctly predicted by these molecular dynamics calculations including the achievement of thermal equilibrium and a state of hydrostatic stress, and also the right temperature. However, the strain in the compressed state turns out to be far from hydrostatic! This is related, we believe, to the computer limitation that necessitates a small-sized crystal lattice without scope for the generation of dislocations. As we shall see, the introduction of mobile-dislocation mechanisms is unavoidable in the description of shock propagation in solids.

4. Defect-generation during shock propagation

A variety of point, line and planar defects can be induced by shocks. Solid samples are usually examined after recovery following shock loading, and there is always the question of the relation of the residual defects to those present during the different stages of shock loading. On the one hand, shock heating may anneal out defects; on the other, the shock unloading process may lead to further plastic deformation. The former may be prevented to some extent by doing the experiment at liquid nitrogen temperatures, and then ejecting and storing the sample also at the same low T; electrical resistivity annealing measurements in copper shock-loaded (70–380 kbars) in this manner yield typical vacancy concentrations $\sim 10^{-4}$ (Mogilevskii 1970). The vacancy concentrations estimated from active resistance measurements in shock-loaded silver foils are perhaps ten times higher (Dick and Styris 1975; Graham 1981). Similarly, the density of dislocations in metals increases with shock pressure-approximately as $P^{1/2}$, according to Murr and Kuhlmann-Wilsdorf (1978). This density is about 10^{10}–10^{11} cm^{-2} in recovered samples shock-loaded up to 100–200 kbar, although once again the dislocation density could be much higher *during* shock propagation (Graham 1981; Svensson 1981).

In the original model of Smith (1958) for shock wave propagation, an interface of dislocations was postulated between the shocked and unshocked regions so that the deviatoric stresses arising from the shock could be relieved. The dislocation interface separates two lattices with different parameters. This interface of dislocations would, according to Smith, move with the shock front. If the dislocations move on a slip plane making an angle ϕ with the shock-front plane, the velocity of the dislocations becomes $U_s \operatorname{cosec} \phi$ which produces the necessary plastic strain. Such supersonic dislocations are, however, unacceptable for several reasons (Meyers and Murr 1981). This had led Meyers to postulate a new model whose essential features are as follows: (a) Dislocations are homogeneously at (or close to) the shock front by the deviatoric stresses set up by the state of uniaxial strain; the generation of these dislocations relaxes the deviatoric stresses. Adjacent dislocation layers are made up of dislocations with Burgers vectors of opposite signs; (b) The dislocations move short distances at subsonic speeds; (c) New dislocation interfaces are generated as the shock wave propagates through the material.

This model qualitatively explains many experimental results. Meyers and Murr also believe that the rarefaction part of the wave (corresponding to shock unloading) plays only a minor role in dislocation generation.

The shock front has a width W extended over a few lattice spacings, *i.e.*, $W \sim 10^{-6}$ cm. The strain rate $\dot{\varepsilon}$ can be written as (Gilman 1979)

$$\dot{\varepsilon} \simeq \frac{U_s}{2W} \frac{(\rho_1 - \rho_0)}{\rho_0}. \tag{4}$$

If the shock velocity is taken to be 1 cm/μsec and a density compression of 2 is achieved by the shock, $\dot{\varepsilon} \approx 10^{12}\ \mathrm{sec}^{-1}$, which is enormous. What is the mechanism of the transport of momentum down the steep velocity gradient? It is through atoms and dislocations, and the dislocation velocity may be expected to be proportional to U_s. The drag pressure D, which acts in opposition to the driving pressure P and equals it under steady motion conditions, can be written as a product of an effective viscosity η and the strain rate $\dot{\varepsilon}$. Gilman finds that the value of the viscosity that arises from the dislocations is of the order of 1 poise. As both η and $\dot{\varepsilon}$ are proportional to U_s, $D \sim U_s^2$, and hence can be very large for strong shocks. I have discussed this aspect in detail to emphasize the complexity that a first-principle calculation of shock wave structure, shock width, etc., would entail. The heating of the material by the shock wave can, however, be calculated using (1)–(3) and condensed matter theory, because the contribution of the various defects produced by the shock wave propagation to the free energy of the material is small.

What about shock propagation in liquids? One has to re-interpret the mobile-dislocation mechanisms in this case, taking into account the short-range order in liquids on the one hand, and the narrow width of the shock front on the other. To the best of my knowledge, no work has been done along these lines.

5. Phase transformations and melting under shock

Most phase transitions observed under static pressures are also observed under shock pressures. In fact, many sluggish phase transitions are readily observed under shock conditions because the deviatoric shear stress provides a driving force to overcome any activation barrier. The phase transformation is best examined in terms of U_s and U_p, rather than the conventional variables P, V. The plot of U_s vs U_p is (surprisingly) linear for a given phase (up to pressures of several megabars), and shows a discontinuity and change of slope upon the occurrence of a phase transformation. There is one important point which must be kept in mind when discussing shock-induced phase transformations: unlike static pressures, shock pressures also induce heating, and the rise in temperature may influence or inhibit the transformation. For example, in the alpha (hcp) to omega (simple hexagonal) phase transformation in Ti, the amount of ω-phase formed increases continually with pressure in the 'static' case; in contrast, under shock this amount first increases and then decreases as the shock pressure is increased. The reason for this behaviour is the change in temperature (Sikka *et al* 1982).

As one keeps on increasing the shock pressure, does the shock heating lead to melting in the compressed state, and, if so, what is the melting temperature? There is still considerable controversy with regard to this point. This is because the slope changes in the $U_s - U_p$ curves are either small or else have an alternative interpretation in terms of certain electronic changes. The shock-Hugoniot measurements show, for example, the existence of a relatively less-compressible high-pressure phase (beyond 300 kbar) in all members of the rare-earth series. This 'stiffening' of the Hugoniot curves has been identified with melting by Carter *et al* (1975), but Gust and Royce (1973) attribute it to the onset of a repulsive interaction between the noble-gas atomic cores. McMahan *et al* (1981), on the other hand, have analysed this phenomenon in terms of the completion of $s-d$ transfer in La. Again, in Pb, the various estimates of shock melting pressures range from 220 kbar to 1·24 Mbar (Duvall and Graham 1977).

The melting temperature under shock compression increases as indicated schematically in figure 3. We feel that the onset of shock melting may be established by a combination of shock temperature measurement and theoretical considerations (Godwal *et al* 1983b). The Hugoniot curves obtained by equation-of-state calculations in the solid and liquid states are quite distinct in the $T-P$ plane, as shown schematically in figure 3. There is a mixed solid-liquid region in the middle. (We have done these calculations for Al and Pb by the pseudopotential method. At $\rho_1/\rho_0 = 1{\cdot}8$ in Al, for example, the temperatures predicted are 12500 K and 8100 K respectively using the corresponding solid and liquid state theories.) Thus, a measurement of shock temperatures over a range of shock pressures will presumably yield information of the type shown in figure 3, so that the onset of melting may be discerned clearly.

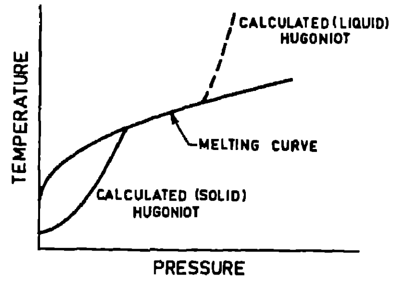

Figure 3. Schematic phase diagram for melting by shock heating.

6. Conclusions

There are many problems in the shock deformation of metals which are not yet fully understood. Most of the metallurgical studies have been on terminal samples shock-loaded to a few 100 kbar or less. Large concentrations of a variety of defects are found in these samples. These concentrations are presumably even greater during the various stages of shock propagation, since shock heating is supposed to anneal out many of the defects. The generation and motion of dislocations are essential in explaining shock front propagation which leaves behind a shocked region in a state of essentially hydrostatic strain (at least for strong shocks). Some computer simulation studies on atomistic models have also been attempted, but they do not account for all the experimental facts. Evidence for the melting of materials under very strong shocks is still in some doubt and may need a combination of theory and shock temperature measurement in order to be established conclusively. Much theoretical and experimental work still remains to be done in the field of shock deformation and related effects in materials.

Acknowledgements

The author thanks Dr S K Sikka and Dr B K Godwal for many helpful discussions.

References

Carter W J, Fritz J, Marsh S P and McQueen R G 1975 *J. Phys. Chem. Solids* **36** 741
Chartagnac P F 1982 *J. Appl. Phys.* **53** 948
Chidambaram R and Ramanna R 1975 *Proc. Tech. Commun. PNE IV* (Vienna: International Atomic Energy Agency) p 421
Dick J J and Styris D L 1975 *J. Appl. Phys.* **46** 1602
Duvall G E and Graham R A 1977 *Rev. Mod. Phys.* **49** 523
Gilman J J 1979 *J. Appl. Phys.* **50** 4059
Godwal B K, Sikka S K and Chidambaram R 1983a *J. Phys. Rep.* (under publication)
Godwal B K, Sikka S K and Chidambaram R 1983b (unpublished)
Graham R A 1981 in *Shock waves and high-strain-rate phenomena in metals* (eds) M A Meyers and L E Murr (New York: Plenum Press) p 375
Gupta S C 1980 Ph.D Thesis, University of Bombay (unpublished)
Gust W H and Royce E B 1973 *Phys. Rev.* **B8** 3595
Jamet F 1980 in *High pressure science and technology* (eds) B Vodar and Ph Marteau (Oxford: Pergamon Press) Vol 2 p 974
Johnson Q and Mitchell A C 1980 in *High pressure science and technology* (eds) B Vodar and Ph Marteau (Oxford: Pergamon Press) Vol 1 p 977
McMahan A K, Skriver H L and Johanseen B 1981 *Phys. Rev.* **B23** 5016
Meyers M A and Murr L E 1981 *Shock waves and high strain-rate phenomena in metals* (eds) M A Meyers and L E Murr (New York: Plenum Press) p 487
Mogilevskii M A 1970 *Combustion, explosion and shock waves* Vol 6 p 197
Murr L E and Kuhlmann-Wilsdorf D 1978 *Acta Met.* **26** 847
Sikka S K, Vohra Y K and Chidambaram R 1982 *Prog. Mater. Sci.* **27** 245
Smith C S 1958 *Trans. AIME* **212** 574
Svensson T 1981 *Shock waves and high strain rate phenomena in metals* (eds) M A Meyers and L E Murr (New York: Plenum Press) p 547
Tsai D H and Macdonald R A 1976 *High Temp. High Pressures* **8** 403

Discussion

C K Majumdar: Entropy production is not taken into account satisfactorily in any essentially hydrodynamics-based formalism. Eckart's work (1945) may perhaps indicate how this aspect should be incorporated into the description of shocks.

K Srinivasa Raghavan: There is nothing unusual about nonhydrostatic strain due to hydrostatic stress, because one is dealing with nonhomogeneous structures.

R Chidambaram: The question here is whether, in Tsai's molecular dynamics calculation on a bcc crystal, unit cells can be strained nonhydrostatically under hydrostatic stress. This has been achieved here by 'buckling' of neighbouring cells—akin to twinning. This picture appears to be somewhat artificial to me, the problem arising from the neglect of mechanisms of plastic deformation.

K A Padmanabhan: Can the amount of explosive charge be estimated, when, say, a hollow cylinder of Al is cald on to a hollow inner cylinder of steel?

Chidambaram: The attenuation behind the shock front is related to the ratio of the mass of the metal to the mass of the explosive. In the problem of explosive welding one has to strike a balance between having too little explosive (the attenuation is then too high) and having too much explosive (the metal cylinder is then damaged).

A P Pathak: Can channeling by charged particles be used to extract information about the defects while experiments on mechanical properties (including shock wave propagation) are in progress?

Chidambaram: I think the penetration of charged particles into the specimen could pose problems, as the diameter of the metal plates under study $\gtrsim$ 1 cm

R Krishnan: In uniaxial tensile testing, an increased strain rate is equivalent to a reduction in test temperature. Is this so also for hydrostatic stress?

Chidambaram: For shock induced deformation, a higher strain rate implies a higher shock pressure which would lead to increased shock heating.

S Ramaseshan: How long does the rise in T due to the shock wave take to cool down?

Chidambaram: The fall from the high temperature in the compressed state to the residual temperature after shock unloading usually occurs in μsec. The cooling beyond that is by normal mechanisms.

Ramaseshan: How are boundary conditions specified in the molecular dynamics study of the shock front? How does this method differ from the finite element approach?

Chidambaram: As in usual solid state theory, cyclic boundary conditions were used by Tsai and Macdonald. The finite element method is a more general mathematical technique that is useful even in problems where there are no periodic lattices.

P Rodriguez: What is an ideal powder?

Chidambaram: In the context of diffraction, it is one in which there is no preferred orientation of the grains.

Rodriguez: For melting to occur, the dislocation density must be of the order

$10^{13}/\text{cm}^2$, but experimentally it is $10^{11}/\text{cm}^2$. How is this discrepancy explained?

Chidambaram: The high temperatures prevailing probably cause annealing of some of the dislocations, reducing their density.

Rodriguez: The high strain rates used in shock experiments are also used in metallurgical techniques like explosive forming and welding. The physical basis of these methods needs to be understood.

Rodriguez: In the flyer plate method used for welding and forming the interface is wavy. Could you comment on this?

Chidambaram: The uniformity with which one can produce a plane wave or shock wave by any of these methods is about 100 nsec. Within this time a non-uniformity of the order of 0·1–1 mm sets in. This has to be carried through.

D Kumar: In the energy diagram, a part of the triangle is the recoverable elastic energy and a part is the dissipated heat energy. Does the rest go into the formation of dislocations?

Chidambaram: The energy required to create dislocations is small and is generally ignored in the book-keeping.

S N Bandopadhyay: What is the evidence that the *strain* is hydrostatic?

Chidambaram: Flash x-ray diffraction experiments on cubic crystals indicate that the crystal behind the shock front reaches a state of hydrostatic strain within 20 nsec.

Bull. Mater. Sci., Vol. 6, No. 4, September 1984, p. 643. © Printed in India.

Computer simulation of tensile testing*

V SRIDHAR

Materials Science Laboratory, Reactor Research Centre, Kalpakkam 603 102, India

Abstract. A brief overview of the molecular dynamics method, with emphasis on the work of Parrinello and Rahman, is presented. Molecular dynamics is a method for studying classical statistical mechanics of well-defined systems through a numerical solution of Newton's equations. A set of N particles with coordinates r_i ($i = 1, \ldots, N$) and confined in a cell are allowed to interact through a potential. The bulk is usually simulated by periodically repeating the cell in space. Newton's equations are then solved numerically and the statistical averages of dynamical properties are calculated as temporal averages over the trajectory of the phase space. This method has already been used to simulate a liquid. Now, based on a Lagrangian formulation, it is possible to study systems under the most general conditions of externally applied stress. Unlike the earlier calculations, in this procedure, shape and size are governed by equations of motion obtained from the Lagrangian. Thus it allows us to study structural transformations which may be brought about by an interplay of external and internal stresses. By applying this technique to a single crystal of Ni, Parrinello and Rahman observe that the stress-strain relations obtained confirm with reported results. Under compressive loading it is found that Ni shows a bifurcation in its stress-strain relation and the system changes from cubic to hexagonal close packing. Such a transformation could perhaps be observed under extreme conditions of shock. Finally the scope of computer simulation is highlighted and the limitations of employing such a method are pointed out.

---

*only summary of the talk

Bull. Mater. Sci., Vol. 6, No. 4, September 1984, pp. 645–651. © Printed in India.

Instabilities in yielding

G VENKATARAMAN

Reactor Research Centre, Kalpakkam 603 102, India

Abstract. This paper addresses itself to instabilities observed during tensile testing, and complements the papers of Rodriguez and Ananthakrishna presented at this Meeting. The work of Caglioti *et al* on the elastic to plastic transformation is first reviewed. The work of Kubin *et al* on the serrated (repeated) yielding observed at liquid helium temperatures is then discussed in brief. Finally, our own work relying on electronic simulation is described. We conclude with some brief remarks on a few important questions that merit attention in the future.

Keywords. Tensile testing; yielding; instabilities; electronic simulation.

1. Introduction

Yielding observed during a tensile test is being discussed by several speakers at this Meeting. While metallurgists are by and large interested in the deformation mechanisms, for physicists the nonlinearities and the instabilities arising thereof are perhaps attractive avenues for investigation. Dr Rodriguez will present the metallurgist's point of view while Dr Ananthakrishna will discuss how he views the phenomena as a physicist. My talk will deal with some work on the subject that is pertinent to the present Meeting but not touched upon by them.

2. Elastic to plastic transition

The work done by Prof. Caglioti and coworkers (Boffi *et al* 1980) who address themselves to the instability associated with the elastic to plastic transition is first reviewed. They adopt a hydrodynamic approach, and their basic idea is as follows. One starts with the Helmholtz free energy F expressed as a function of the temperature T and strain ε, since these are quantities which can be measured in real time during an experiment. $F(T, \varepsilon)$ is expanded in a series in ε and $\theta = (T-T_0)/T_0$, $F(T_0, 0)$ being the free energy of the undeformed solid at temperature T_0, assuming that a uniaxial tension is applied. By differentiating $F(T, \varepsilon)$ appropriately with respect to the state variables, expressions are deduced for the entropy S and the equilibrium stress σ_e. These are substituted in the space- and time-dependent partial differential equations representing entropy and momentum balance. This is the starting-point for the subsequent stability analysis, the procedure up to this point being identical to what is normally done in hydrodynamics.

We are interested in the question of stability as the material deforms through the elastic region. Let us suppose that the applied (constant) strain rate is $\dot{\varepsilon}_a$. To investigate the stability of a particular state $\varepsilon_a (= \dot{\varepsilon}_a t$, t being the elapsed time) and temperature θ,

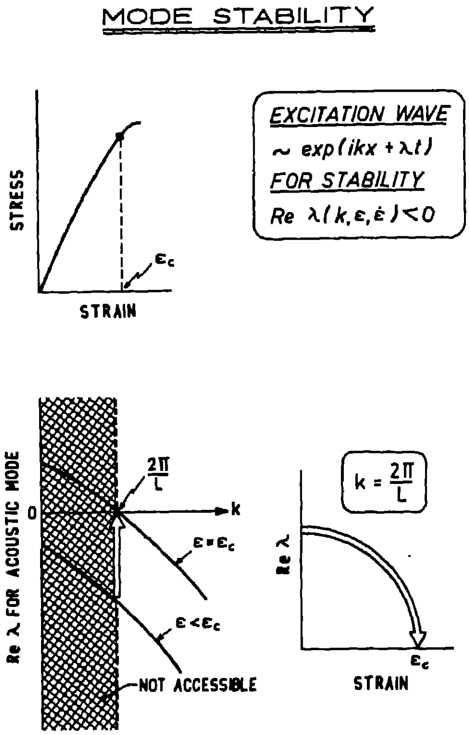

Figure 1. Instability of acoustic mode as $\varepsilon \to \varepsilon_c$. Owing to finite size of the specimen, the shaded region is not accessible.

one imposes small fluctuations $\delta\varepsilon$ and $\delta\theta$ around the reference state. Linearization yields a set of three coupled first-order equations for the quantities $\delta\theta$, $(\delta\dot{\varepsilon}/\varepsilon_a)$ and $\delta\varepsilon$, on which the standard normal-mode analysis may be performed. (In fluid dynamics, one would obtain the Rayleigh and Brillouin modes in this manner.) For a given mode to be stable, it is necessary that $\mathrm{Re}\,\lambda(k) < 0$, where λ is the corresponding eigenfrequency and k is the wavevector. It turns out that all the modes are stable as long as ε_a is smaller than a critical strain ε_c. At the critical strain, the acoustic mode with the longest wavelength (*i.e.*, $k \approx 2\pi/L$ where L is the length of the sample) becomes unstable (figure 1). There is an obvious analogy with phase transitions; Boffi *et al* (1980) have indeed drawn a parallel with the nonequilibrium transition in the laser. As yet there is only partial experimental confirmation of these ideas, but I understand (Bottani, private communication) that efforts are in progress to monitor the transition more completely by measuring the associated temperature fluctuations.

3. Repeated yielding

Let us consider next the instability aspects of serrated yielding. Dr Rodriguez in his presentation offers a comprehensive survey of the various mechanisms responsible for repeated yield drop. Dr Ananthakrishna considers one of these models, namely, that due to Cottrell, and analyzes how instabilities can arise. I shall complete the picture by discussing the work of Kubin *et al* and some of our own work.

3.1 *Low-temperature yielding*

Kubin and coworkers (Estrin and Kubin 1981; Kubin *et al* 1982, 1983) are concerned with repeated yield drops observed at liquid helium temperatures. These arise due to thermomechanical instabilities for which a model is proposed. The stability analysis is rather similar to that carried out by Boffi *et al* (1980) (the applied stress and the temperature are now chosen as the state variables characterizing the material undergoing deformation). These two variables are coupled through two nonlinear differential equations, the mechanical equation and the equation describing heat removal, in which the experimental conditions are suitably introduced. Linearization, stability analysis, etc., are then performed as usual, and contact is made with elementary bifurcation theory (Haken 1977).

The parameters that enter into the thermomechanical model of Kubin and coworkers (Estrin and Kubin 1981; Kubin *et al* 1982, 1983) are: the specimen dimensions, the applied strain rate, the combined elastic modulus of the specimen and the machine, the specific heat of the specimen and the coefficient of heat transfer. These parameters are combined into three dimensionless quantities $\dot{\Sigma}_a$ (the reduced elastic slope of the straining curve), α (the reduced activation volume) and ν (representing, apart from a factor, the ratio of the elastic and thermal energies). These are the control parameters. Figure 2 shows the $(\nu/\alpha, \dot{\Sigma}_a\alpha)$ plane in control parameter space. The different regions represent qualitatively different kinds of mechanical behaviour, the nature of which is amplified in figure 3. The types of trajectories in the phase space (σ, θ) associated with the various regions in figure 2 are sketched in figure 3a, and the corresponding yield curves are shown in figure 3b. While one has an asymptotic steady state in region II, one obtains serrations in region III. The crossing of the II-III boundary corresponds to a hard-mode instability. (A similar instability is discussed by Ananthakrishna with reference to his model.) To sum up, the work of Kubin *et al* demonstrates that it is possible to predict whether plastic deformation at low (cryogenic) temperatures will be smooth or jerky, depending on the values of a specified set of mechanical, geometric and thermal parameters, by using bifurcation theory and stability analysis.

3.2 *Electronic simulation*

I now turn to the work on serrated yielding which Neelakantan and myself (1983) have been engaged in recently. Our work was triggered by a fascinating paper by Franck

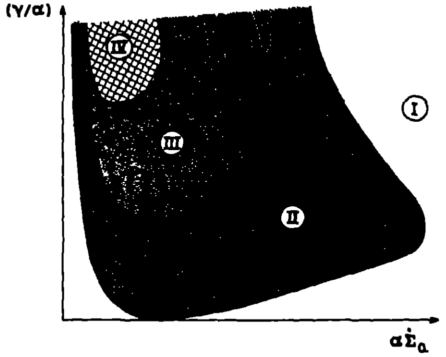

Figure 2. Regions of different types of mechanical behaviour in the parameter plane $(\dot{\Sigma}_a\alpha, \nu/\alpha)$ (Kubin *et al* 1983).

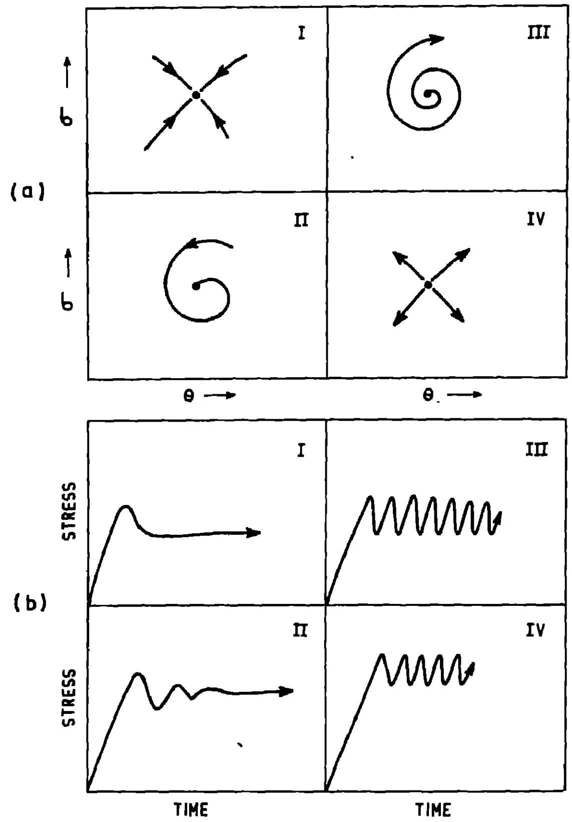

Figure 3. **a.** Phase space plots corresponding to the different regions shown in figure 2. **b.** Stress *vs* time curves corresponding to the different regions of figure 2 (Kubin *et al* 1983).

(1974) which gives an overview of feedback oscillations occurring in widely different chemical and biological systems. According to Franck, these diverse systems exhibit very similar behaviour because they share an underlying "negative resistance" feature. In serrated yielding, it is well known that at least for one class of models, *viz*., the Cottrell-Bilby model (1949) (see also the paper by Rodriguez at this Meeting), there *is* such a negative resistance feature. We (Neelakantan and Venkataraman 1983) therefore explored how some of the observed features of repeated yielding could be understood along the lines indicated by Franck. It was most convenient to map the problem onto an equivalent electronic problem, and essentially carry out an analog simulation.

Skipping the details, the essential idea underlying our work may be understood by referring to figure 4. Shown here is a typical negative resistance characteristic, the detailed nature of which is dependent (in the physical problem under consideration) on parameters such as the dislocation density, temperature, etc. The applied strain rate prescribes the *load line*; the behaviour of the specimen during the test depends on where the load line cuts the characteristic curve. If the intersection is in the negative resistance region, then there is instability and oscillations (in stress) ensue.

Now, in contrast to the situation obtained usually in an electronic device, the characteristic curve itself evolves during the test for a specimen undergoing plastic

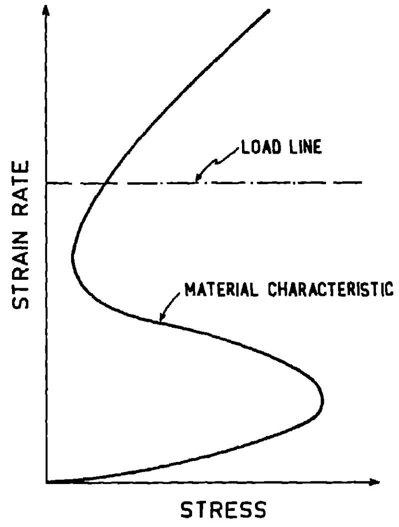

Figure 4. Schematic plot of the strain rate *vs* stress curve for a material exhibiting serrated yielding. (For examples of such curves in the Fe-C system, see Neelakantan and Venkataraman 1983). The negative resistance feature arises due to dislocations breaking away from their atmospheres.

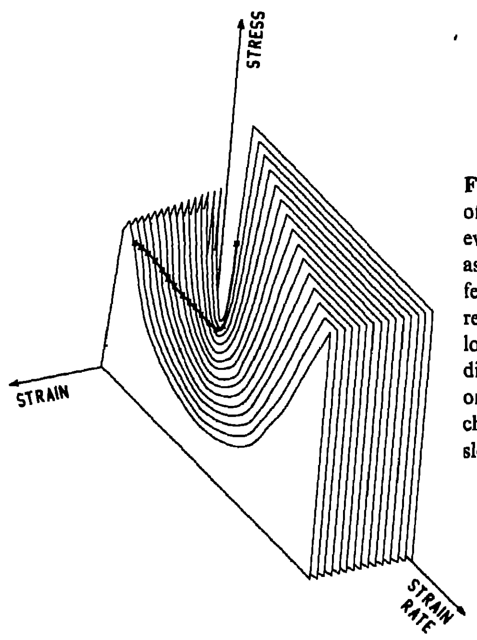

Figure 5. Perspective plot of a family of characteristic curves, simulating the evolution during an actual test. The valley associated with the negative resistance feature is seen to widen as the test progresses. The trajectory obtained by the load line method is also partially indicated. Serrations occur during the test only when the load line intercepts the characteristic in a region of negative slope.

yields. Thus, at a fixed temperature, and for the *same* material, the intersection of the load line and the characteristic may occur in a region of positive slope at one instant and in a region of negative slope at the next. The general form of the characteristic also suggests why serrations occur only in a certain region of the test curve. Figure 5 shows a schematic plot of a family of evolving characteristic curves for a material at a particular temperature. The trajectory resulting from the load line is also indicated, and one can see that instability can occur in certain ranges of the strain and not in others.

Our approach demonstrates that numerous aspects of tensile test curves observed in practice are readily reproduced and studied under convenient, controlled conditions in a suitably constructed analog device. One can begin to understand some of the observed trends in depth. For example, it is known that at a given temperature, serrations are absent both at very high and low strain rates; likewise, at a given strain rate, serrations appear only in a certain temperature band. There is therefore a well-defined region in the $\dot{\varepsilon}-T$ plane within which serrations occur. Our study shows that such a bounded region is indeed to be expected.

4. Conclusions

One common feature of all the models cited is that they tacitly assume the medium to respond homogeneously during repeated yielding. There are, however, reasons to believe that the deformation is in fact spatially inhomogeneous. This aspect has not received the attention it deserves in theoretical studies of the phenomenon, and one hopes that in the years to come this will be set right.

Another relatively neglected aspect is the important role played by noise: a considerable amount of irregularity exists in the observed serrations. Ananthakrishna discusses the effects of fluctuations to some extent in his paper. In our work, too, some thought has been given to the matter. Our preliminary finding is that when noise is included, the simulated tensile test curves begin to resemble real-life curves such as, *e.g.*, those found in Hall (1970). This work is still in progress. One's experience with the study of fluctuations in other areas of physics suggests that here, too, such an analysis would be a fruitful avenue of investigation.

References

Boffi S, Bottani C E, Caglioti G and Ossi P M 1980 *Z. Phys.* **B39** 135

Cottrell A H and Bilby B A 1949 *Proc. Phys. Soc.* **A62** 49

Estrin Y and Kubin L P 1981 in *Deformation of polycrystals Proc. 2nd Risø Int. Symp. Metal. Mat. Sci.*, (eds) N Hansen, A Horserrell, T Leffers and H Lilholt p. 179

Franck U C 1974 in *Physical chemistry of oscillatory phenomena Symp. Faraday Soc.* No. 9, p. 137

Haken H 1977 *Synergetics* (Berlin: Springer)

Hall E O 1970 *Yield point phenomena in metals and alloys* (New York: Plenum)

Kubin L P, Spiesser Ph and Estrin Y 1982 *Acta Metall.* **30** 385

Kubin L P, Estrin Y and Spiesser Ph 1983 preprint, Low temperature plastic deformation of metals and bifurcation theory (to appear in *Res. Mechanica*)

Neelakantan K and Venkataraman G 1983 *Acta Metall.* **31** 77

Discussion

G Srinivasan: The introduction of noise seems to produce bands. Is it that you are seeing some kind of a beat phenomenon?

G Venkataraman: We have not explored all the possibilities to say something at this stage.

R Ramaswamy: The kind of bunching phenomenon that occurs does have a practical analogue. This is the phenomenon of intermittency—shortly before the onset of a truly turbulent phase, long range periodicity appears in bursts.

K R Rao: Referring to Caglioti *et al*'s work, in the yield instability region, the soft mode may go to zero giving rise to an incommensurate phase reciprocal lattice point. Has this been experimentally observed?

Venkataraman: It has not been observed. This is only a model.

Bull. Mater. Sci., Vol. 6, No. 4, September 1984, pp. 653–663. © Printed in India.

Serrated plastic flow

P RODRIGUEZ

Metallurgy Programme, Reactor Research Centre, Kalpakkam 603 102, India

Abstract. This paper attempts an assessment of the current understanding of the phenomenon of "serrated plastic flow", which manifests itself as serrations, load drops, jerkiness or other discontinuities in the stress-strain curves obtained in constant extension rate tensile tests, and as sudden bursts of strain in constant loading rate tests and in constant load (stress) creep tests (the so called staircase creep). Though one can identify at least seven physical processes that can cause serrations, the discussion here is restricted mainly to serrated yielding in tension tests originating from dynamic strain ageing (DSA). The characteristics of the five types of serrations that have been identified so far and the experimental conditions under which they occur are discussed. The various models of serrated flow that have been put forward are reviewed critically. Some recent results on 316 stainless steel are presented to illustrate the effects of grain size, temperature and strain rate on serrated flow. Manifestations of DSA other than serrations such as a negative strain rate sensitivity, positive temperature dependence for flow stress and work hardening, and the ductility minimum are also discussed. Finally the various issues to be resolved are enumerated.

Keywords. Serrated flow; dynamic strain ageing; continual mechanical twinning; flow stress; work hardening peaks; ductility minimum.

1. Introduction

The organisers of this discussion meeting in their invitation requested that I should present here the metallurgist's viewpoint of 'serrated plastic flow'. At the outset let me state that whatever I say in the following should be considered as my own understanding of the phenomenon. There will be many materials scientists and engineers (including those with both physics and metallurgy backgrounds) who may not agree with all the views propounded here; there must also be an equally large number of physicists and metallurgists who may find common ground with the interpretations offered. It is interesting to note that in a recent international conference on deformation, two different treatments of the phenomenon, both by metallurgists have been given. One is based on a strain ageing mechanism involving the diffusion of solute atoms to temporarily arrested dislocations (McCormick 1983) and the other interprets it as an example of catastrophe theory in physical metallurgy (Strudel 1983).

The objective of the present paper is an assessment of the current understanding of the phenomenon of serrated plastic flow. We start with a brief description of the methodology of the tensile test. The physical processes that can cause serrated flow are then identified. Subsequent discussions are restricted to serrations due to dynamic strain ageing (DSA) or the Portevin-Le Chatelier (PL) effect (Portevin and Le Chatelier 1923) arising from interactions between diffusing solute atoms and mobile dislocations. The characteristics of five types of serrations observed under conditions of DSA are then discussed. The various quantitative models for serrated flow that have been put forward are then critically reviewed. Some recent results on 316 stainless steel are presented to illustrate the effects of grain size, temperature and strain rate on the DSA behaviour. This is followed by a discussion of the various manifestations of DSA in tensile test results. Finally, the various issues to be resolved are considered and catalogued.

2. Phenomenology

In a tension test, (the specimen suitably gripped between two crossheads, one moving and the other fixed) is deformed at a constant nominal strain rate determined by the velocity of the moving crosshead. At any instant of time, the total strain ε, the plastic strain ε_p in the specimen, and the elastic strain ε_e of the specimen-machine system are related by

$$\varepsilon = \varepsilon_p + \varepsilon_e, \tag{1}$$

$$\dot{\varepsilon} = \dot{\varepsilon}_p + \dot{\varepsilon}_e. \tag{2}$$

Equation (2) can be rewritten as

$$\dot{\varepsilon} = \dot{\varepsilon}_p + \frac{1}{E_s}\dot{\sigma}, \tag{3}$$

where σ is the stress and E_s the elastic modulus of the specimen-machine system. The condition for serrations or load drops is that the plastic strain rate $\dot{\varepsilon}_p$ exceeds the imposed strain rate $\dot{\varepsilon}$, *i.e.* whenever there is a sudden increase in $\dot{\varepsilon}_p$, a load drop occurs.

The phenomenon can also occur in creep tests in which strain in a specimen under a constant stress is measured as a function of time. Sudden bursts of plastic strain occur periodically, with the result that the creep curve has the shape of a staircase (hence the name 'staircase creep'). This manifestation of DSA in creep tests is discussed in another paper (Ananthakrishna 1983) presented at this Meeting.

3. Physical processes that can cause serrated flow

A survey of the literature shows that we can identify at least seven physical processes that can lead to serrations in the flow curve:

(i) The plastic strain rate under dislocation glide is given by

$$\dot{\varepsilon}_p = \rho_m b \bar{v}, \tag{4}$$

where ρ_m is the mobile dislocation density, $\bar{v}$ the average velocity of dislocations and b the Burgers vector. Serrations will therefore occur whenever there is an instantaneous increase in ρ_m or in $\bar{v}$ or in both.

(ii) Interaction of moving dislocations with DSA can lead to sudden increases in ρ_m and/or $\bar{v}$ and we shall be mainly examining this particular phenomenon.

(iii) In alloys undergoing order-disorder transformations, gradients or modulations in order encountered by moving dislocations can cause serrated flow (Mannan and Rodriguez 1972; Samuel and Rodriguez 1975, 1980).

(iv) Another phenomenon that can cause serrations is continual mechanical twinning as has been reported for an Fe-25 at% Be alloy (Bolling and Richman 1965). Twinning is characterised by a positive temperature dependence and a negative strain rate sensitivity for the flow stress which are also obtained under conditions of DSA.

(v) A sudden increase in the specimen temperature due to adiabatic heating is another possibility (Ramachandran 1983; Ramachandran *et al* 1970; Kubin *et al* 1982). This has been found to occur in tests at cryogenic temperatures. Dissipiation of the heat of deformation becomes difficult since the specimen surface is covered by a layer of gas molecules of the cryogenic liquid. The resultant increase in specimen temperature satisfies the condition for a load drop since a higher plastic strain rate can now occur at the applied stress level.

(vi) Phase transformations induced by stress and strain can also cause serrated flow. This aspect is covered in another paper presented at this Meeting (Seetharaman 1983).

(vii) Weertman (1967) has pointed out that yielding across fracture surfaces in brittle materials when tested under both hydrostatic pressure and triaxial non-hydrostatic stresses can cause serrations.

4. Types of serrations

Five types of serrations due to DSA termed A, B, C, D and E have so far been identified (figure 1). Types A, B and C are well-known and their characteristics are also well documented (Russel 1963; Macherauch and Munz 1966; Solar-Gomez and McG-Tegart 1969; Brindley and Worthington 1970; Cuddy and Leslie 1972) whereas serrations of types D and E have been referred to only relatively recently (Pink and Grinberg 1981; Wijler *et al* 1972). The characteristics of the different types of serrations and the experimental conditions that produce them are as follows.

(i) Type A serrations are periodic serrations from repeated deformation bands initiating at the same end of the specimen and propagating in the same direction along the gauge length. These are considered as locking serrations, characterised by an abrupt rise followed by a drop to below the general level of the stress-strain curve. They occur in the low temperature (high strain rate) part of the DSA regime.

(ii) Type B serrations are oscillations about the general level of the stress-strain curve that occur in quick succession due to discontinuous band propagation arising from the DSA of the moving dislocations within the band. (This contrasts with the smooth propagation of the band that occurs after initiation with a type A load drop). Type B

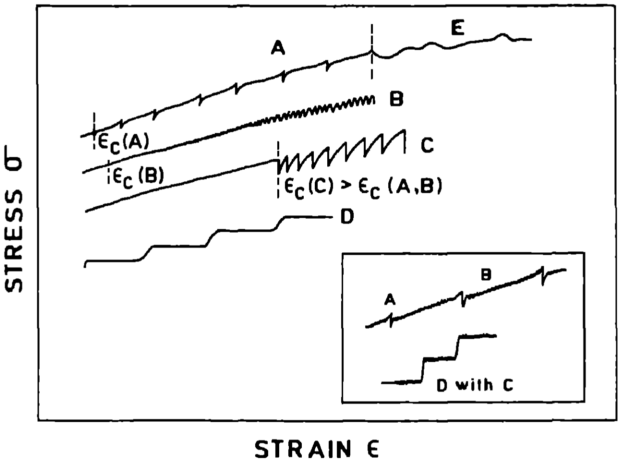

Figure 1. Types of serrations.

serrations often develop from those of type A with increasing strain (figure 1 inset) or occur at the onset of serrated yielding at high temperatures and low strain rates.

(iii) Type C serrations are yield drops that occur below the general level of the flow curve and are therefore considered to be due to dislocation unlocking. They occur at higher temperatures and lower strain rates than in the case of types A and B serrations.

(iv) Type D serrations are plateaus in the σ-ε curve due to band propagation similar to Luders band with no work hardening or strain gradient ahead of the moving band front. Like type A serrations, they can occur alone or with type B serrations during the band propagation (figure 1 inset). In Au-Cu 14 wt % alloy, Wijler *et al* (1972) produced type D serrations by homogeneous prestraining at high temperatures.

(v) Type A serrations change over to type E serrations at high strains. The latter are similar to type A serrations, but with little or no work hardening during band propagation.

5. Models for serrated flow from DSA

Any theory or model for serrated flow should account for the different types of serrations that appear in different alloys and for the influence of temperature, strain and strain rate on these various types. For the onset of serrations in substitutional alloys, a critical strain ε_c is required. The ε_c value is dependent on both $\dot{\varepsilon}$ and the temperature T (figure 2). At high strain rates and low temperatures where the first serrations are of type A or B, ε_c increases with increasing strain rate and decreasing temperature. At high temperatures and low strain rates, where serrations of type C are observed, ε_c increases with increasing temperature and decreasing strain rate. While current theoretical models are unable to account for this latter behaviour, the variation of ε_c with T and $\dot{\varepsilon}$ in the low temperature (high strain rate) regime has been rationalized by a number of theoretical models based on the interaction of diffusing solute atoms and mobile dislocations.

5.1 *Interpretations of* ε_c

The oldest quantitative model for serrated yielding is due to Cottrell (1953) in which the mobile solutes are assumed to interact with quasi-viscously moving dislocations; serrations are attributed to repeated locking and unlocking of dislocations in solute atmospheres, which occurs when $\bar{v}$ equals the drift velocity of the solutes in the stress field of the dislocations. In subsequent modifications of this model that integrate it with the theory of thermally activated deformation processes, it was recognised (Sleeswyk

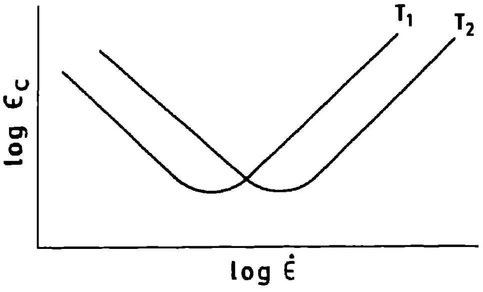

Figure 2. Effect of strain rate and temperature on critical strain; $T_2 > T_1$.

1958; McCormick 1972) that the "ageing" of the dislocations would take place during the waiting time of the dislocations at discrete obstacles rather than during their actual motion. When the diffusion coefficient is high enough to saturate the dislocation with a solute atmosphere during the waiting time, serrated yielding will start. In the model of van den Beukel (1975) though the same picture of solute-dislocation interaction was adopted, ε_c was chosen (following the ideas of Sleeswyk 1958; Penning 1972) to be the strain at which the strain rate sensitivity $\gamma = \partial\sigma/\partial \ln \dot{\varepsilon}$ became negative. In all the three approaches, the final result is that at ε_c

$$\rho_m^{(c)} C_v^{(c)} = K_1 \dot{\varepsilon} \exp(E_m/kT), \tag{5}$$

where C_v is the vacancy concentration E_m is the vacancy migration energy and T the absolute temperature. The three models yield widely different values for the constant K_1 (the value in the original Cottrell model does not account for the experimental values of ε_c). The vacancy concentration is enhanced due to the strain (Van Bueren 1955) according to

$$C_v = A\varepsilon^m. \tag{6}$$

Similarly, the strain dependence of ρ_m can be expressed as

$$\rho_m = B\varepsilon^\beta. \tag{7}$$

From (5), (6) and (7) we get

$$\varepsilon_c^{m+\beta} = K_2 \dot{\varepsilon} \exp(E_m/kT). \tag{8}$$

DSA due to interstitial solutes (8) reduces to

$$\varepsilon_c^\beta = K_2' \dot{\varepsilon} \exp(E_m/kT). \tag{9}$$

Experimental results in the low temperature-high strain rate region have given reasonable values for m, β and E_m. Typical $(m+\beta)$ values are between 2 and 3 for substitutional alloys; for interstitial alloys (Van den Beukel 1980), β lies between 0·5 and 1.

It has generally been observed that the critical strain ε_c increases with increasing grain size (Brindley and Worthington 1970; Charnock 1968, 1969; Mannan 1981; Mannan *et al* 1983). Relating this increase to the grain size dependence of ρ_m, Charnock (1968, 1969) has shown that (8) can be modified to include the grain size dependence of ε_c according to

$$\varepsilon_c = K_3 d^p \dot{\varepsilon}^q \exp[E_m/kT(m+\beta)] \tag{10}$$

where $p = n''/(m+\beta)$, $q = 1/(m+\beta)$ and the parameter n'' arises from the $\rho_m - d$ relationship of Conrad and Christ (1963): $\rho_m = N\varepsilon^\beta/d^{n''}$.

5.2 *Some results on* 316 *stainless steel*

The flow curves obtained in the temperature range 523–923 K at a strain rate of $3 \times 10^{-4}\,\text{sec}^{-1}$ for 316 stainless steel of two different grain sizes (0·04 and 0·125 mm) are shown in figures 3 and 4 (Mannan 1981; Mannan *et al* 1982, 1983). (The serration types are labelled as in §4). The observed effects of the grain size on DSA are the following: (a) The DSA temperature region gets shifted to higher temperatures with increasing grain size; (b) For all grain sizes (8) is valid with $(m+\beta) = 2{\cdot}3$, β was estimated to be $\simeq 0{\cdot}9$, in

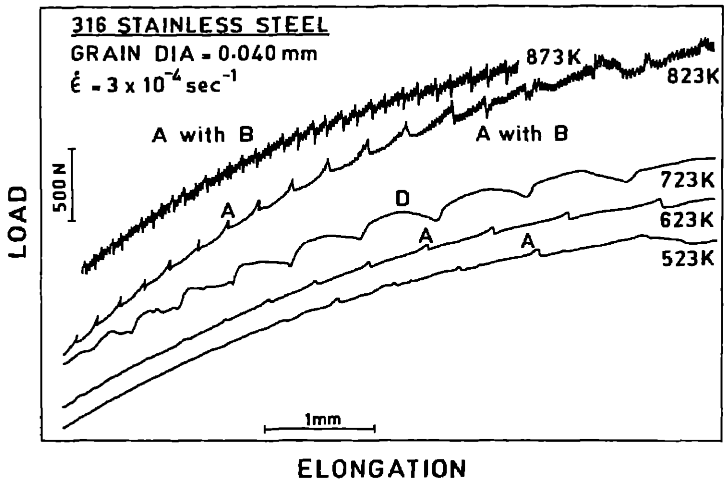

Figure 3. Serrated plastic flow in 316 stainless steel with grain size $d = 0{\cdot}04$ mm.

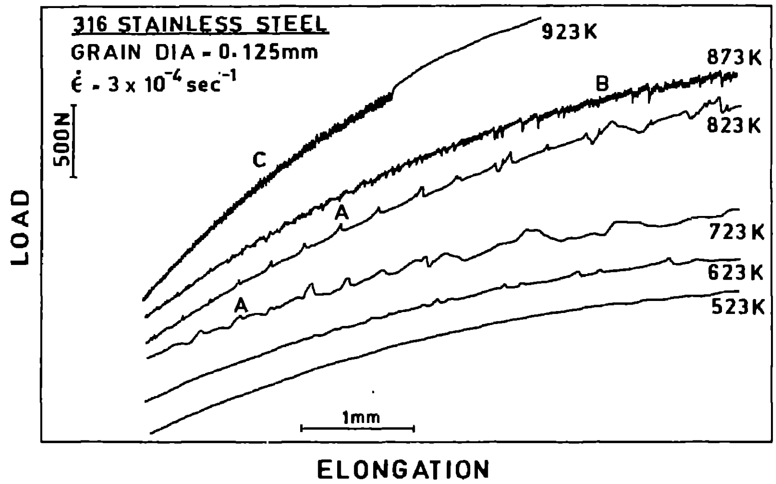

Figure 4. Serrated plastic flow in 316 stainless steel with grain size $d = 0{\cdot}125$ mm.

good agreement with the prediction of $\beta = 1$ for a linear increase in dislocation density with strain; (c) The relationship between ε_c and d follows (10) with $p = 0{\cdot}6$; (d) An apparent activation energy for DSA of 255 kJ/mol is obtained for all grain sizes from the variation of ε_c with T, (8); (e) A fit to the Hall-Petch equation for the variation of the flow stress σ_ε with grain size d, namely, $\sigma_\varepsilon = \sigma_{0\varepsilon} + K_\varepsilon d^{-1/2}$ where K_ε and $\sigma_{0\varepsilon}$ are constants (called the Hall-Petch slope and intercept respectively), yields a monotonic decrease of $\sigma_{0\varepsilon}$ with temperature; whereas K_ε though it generally decreases with temperature, shows a peak in the temperature region 523–723 K. This indicates that grain boundary regions are preferred sites for dynamic strain ageing (Armstrong 1968); (f) A peak in the variation of work hardening with temperature is also obtained but towards the upper

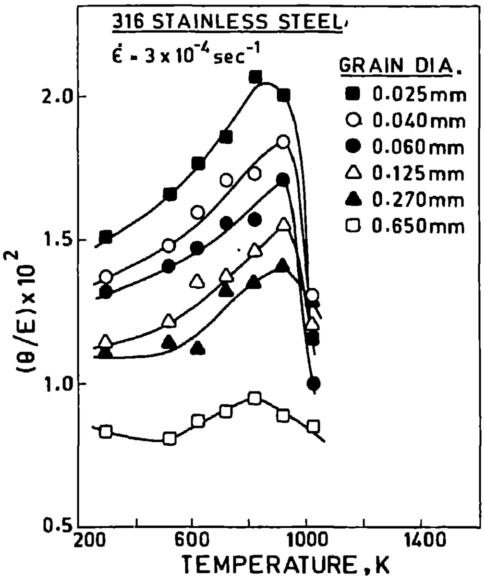

Figure 5. Variation in work hardening with temperature for 316 stainless steel with different grain sizes. E is the Young's modulus. $\theta = \Delta\sigma/\Delta\varepsilon$, $\Delta\sigma$ is the flow stress increment over the strain interval $\Delta\varepsilon$ from $\varepsilon = 0{\cdot}005$ to $\varepsilon = 0{\cdot}05$.

end of the DSA temperature range (figure 5). Consistent with the fact that this temperature range represents conditions for strong pinning and accordingly the most rapid and strongest dislocation immobilisation, leading to an increased rate of dislocation accumulation (Reed-Hill 1974), the DSA peak for work hardening also becomes more pronounced with decreasing grain size.

5.3 *Other interpretations of serrated flow*

Equation (4) allows serrations to occur for sudden increases in ρ_m or in $\bar{v}$ or in both of them. The models discussed in §5·1 assume that the average velocity is unchanged, and that serrations occur due to changes in ρ_m owing to the locking and unlocking of dislocations during deformation. It has also been pointed out that the solute atmospheres formed could be dragged along with the moving dislocations, and that such atmospheres would exert a drag stress on the dislocation which varies with dislocation velocity as schematically illustrated in figure 6(a) (Hirth and Lothe 1968; Schmidt and Miller 1982). With this drag stress contribution included, the normal stress-velocity variation for dislocations shown in figure 6(b) assumes the shape shown in figure 6(c). Nabarro (1967) has suggested that serrations will occur in the strain rate (dislocation velocity) region between the points B and D in this figure since the dislocation velocity is a multivalued function of stress in this region; for a given value of the applied stress it is possible for the velocity to increase suddenly to a higher value. The region between C and D where the moving dislocation requires a lower stress for a higher velocity (negative strain rate sensitivity) is more commonly identified with the dynamic instability of plasticity leading to the PL effect (Sleeswyk 1958; Sleeswyk and Verel 1972; Wilcox and Rosenfield 1966; Yoshinaga and Morozumi 1971; Penning 1972; Malygin 1973). Suggestions have also been made that serrated yielding could be considered as a manifestation of 'chaotic' behaviour (Neelakantan and Venkataraman 1982) or as an example of a 'catastrophe' in plastic deformation (Strudel 1983) arising from the negative-resistance feature between C and D.

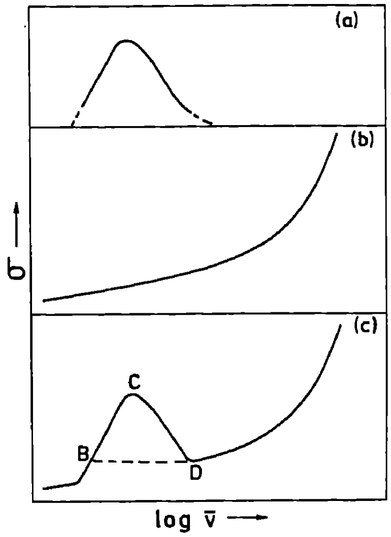

Figure 6. (a) The solute drag stress on a dislocation as a function of dislocation velocity. (b) Normal stress-velocity relation for dislocation in the absence of the drag stress. (c) Actual stress-velocity variation due to the presence of a drag stress at intermediate velocities.

That negative strain rate sensitivity is a crucial factor for the PL effect is now recognised in all the models. The treatment of McCormick (1983), for example, points out that the critical strain for the onset of serrated flow can be rationalised by matching the critical velocity (for negative resistance) with the solute diffusion coefficient. In the models of Van den Beukel (1975, 1980) and of Mulford and Kocks (1979) it is held that any solute mobility makes a negative contribution to the total strain rate sensitivity and that this contribution increases with strain; when the total strain rate sensitivity becomes negative plastic flow becomes unstable. In arriving at the strain dependence of the strain rate sensitivity, Van den Beukel retains the notions of a strain-dependent solute diffusion coefficient and strain-dependent mobile dislocation density from the older models. Mulford and Kocks (1979), on the other hand, describe the strain rate sensitivity in terms of the flow stress σ which is the sum of two components—the friction stress σ_f and the dislocation flow stress σ_d; solute mobility affects σ_d, the strain-hardening component of the flow stress. More recently, Van den Beukel and Kocks (1982) have arrived at a unified approach which enables the negative strain rate sensitivity to arise as a consequence of the influence of solute mobility on both the friction stress (by decreasing the obstacle spacing along the dislocation) and forest hardening (by increasing the strength of dislocation junctions).

In a paper that has not received the attention that it deserves, Weertman (1967) has suggested that the PL effect occurs as a result of an instability of the dislocations in going back and forth between a slow moving state and a fast moving state due to dynamic frictional stress drops. The effect occurs because of the inherent instability of the position that separates the fast slip region from the slow slip region in the slipped zone. The similarity between earthquakes and the behaviour of groups of dislocations in a slip band when the frictional force is reduced for any reason has also been pointed out: "Earthquakes are merely, the PL effect exhibited in a sample whose dimensions happen to have a grand scale".

Mention should also be made of attempts to understand serrated yielding through mechanical and electronic models. Dry friction models that simulate the strain bursts in staircase creep (Bodner and Rosen 1967) and the load drops in tensile tests (Rosen and Bodner 1969) have been devised which consider some of the features of DSA such as the negative strain rate sensitivity, work hardening and deformation by band propagation. Similar electronic analogs for the tensile test situation have also been demonstrated (Neelakantan and Venkataraman 1983).

6. Other manifestations of DSA

As we have mentioned earlier, serrations represent only one of the manifestations of dynamic strain ageing. In figure 7 the various other anomalies associated with DSA are illustrated schematically. These are (i) a peak in the variation of σ with T (ii) a peak in the variation of the work hardening $\theta = \Delta\sigma/\Delta\varepsilon$ with T, (iii) a peak in the variation of the Hall-Petch slope K_ε with T, (iv) a minimum in the variation of the ductility with T and (v) a minimum in the strain rate sensitivity $\gamma = \Delta\sigma/\Delta \ln \dot{\varepsilon}$ with γ going negative in the temperature region of serrated flow. The variations in γ with stress and strain at different temperatures are also shown in figure 7. The types of serrations normally observed in the different temperature regions are also indicated.

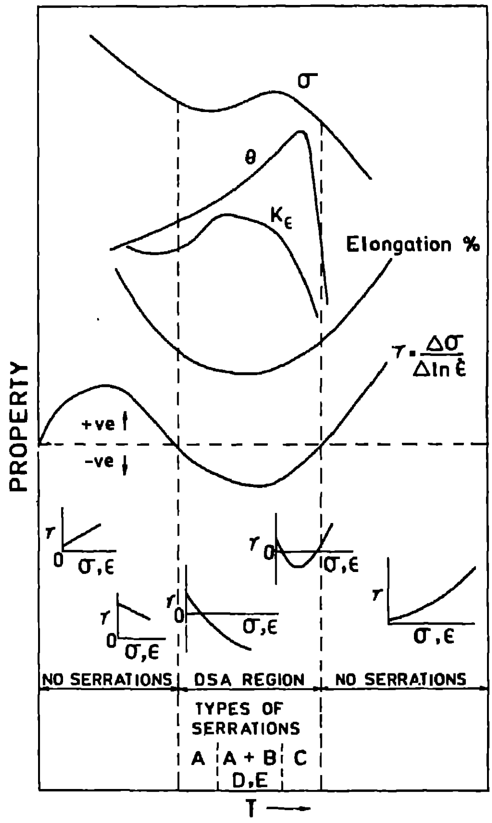

Figure 7. Schematic illustration of the various manifestations of dynamic strain ageing.

7. Issues to be resolved

(i) The main issue to be resolved unambiguously is whether the load drops are caused by a sudden increase in ρ_m or in $\bar{v}$ or in both. We are handicapped by the fact that we do not so far have an experimental technique to measure ρ_m or $\bar{v}$ during deformation. Acoustic emission measurements hold out promise as a potential method of attack on this problem.

(ii) Deformation during serrated flow is inhomogeneous and localised in bands. The actual strain rate in the deformation band is much higher than the imposed or assumed strain rate. Measurements and analysis of deformation band parameters such as the band velocity, band strain, band width and the average strain rate in the band should therefore receive greater attention than they have hitherto (McCormick 1983).

(iii) Current theoretical models are unable to account for the inverse effects (ε_c increasing with increasing temperature and decreasing strain rate) observed in the high temperature-low strain rate region in which type C serrations are observed.

(iv) Most of the models are incomplete in that they make *ad hoc* assumptions or use empirical relationships; there is no detailed understanding either experimentally or theoretically of the effect of strain on diffusion, of the dependence of mobile dislocation density on strain or of the effect of a solute atmosphere on dislocation–dislocation interactions.

(v) Though it is often recognised that only short range diffusion in dislocation core (pipe diffusion) is involved in many manifestations of DSA, we are handicapped by the lack of an adequate knowledge of the appropriate diffusion coefficients.

(vi) In analysing the dependence of σ on $\dot{\varepsilon}$ and T, is the splitting of the flow stress into additive contributions from forest interactions, solutes, lattice friction, justified? How is such an approach reconciled with the idea that the obstacle with the highest energy barrier will be rate-controlling?

This list is evidently not an exhaustive one, but it does highlight some of the aspects of DSA that deserve greater attention from both experiment and theory in future.

References

Ananthakrishna G 1984 *Bull. Mater. Sci.*

Armstrong R W 1968 in *Dislocation dynamics* (eds) A R Rosenfield, G T Hahn, A L Bement and R I Jaffee (New York: McGraw Hill) p. 293

Bodner S R and Rosen A 1967 *J. Mech. Phys. Solids* **15** 63

Brindley B J and Worthington P J 1970 *Met. Rev.* **15** 101

Bolling G F and Richman R H 1965 *Acta Metall.* **13** 709, 723, 745

Charnock W 1968 *Philos. Mag.* **18** 89

Charnock W 1969 *Philos. Mag* **20** 209

Conrad H and Christ B 1963 in *Recovery and recrystallization of metals* (ed) L Himmel (New York: Interscience) p. 124

Cottrell A H 1953 *Philos. Mag* **44** 829

Cuddy L J and Leslie W C 1972 *Acta Metall.* **20** 1157

Hirth J P and Lothe J 1968 *Theory of crystal dislocations* (New York: McGraw-Hill)

Kubin L P, Spiesser Ph and Estrin Y 1982 *Acta Metall.* **30** 385

Macherauch E and Munz D 1966 *Z. Metall.* **57** 552

Malygin G A 1973 *Phys Status Solidi* **A15** 51

Mannan S L 1981 *Influence of grain size on the flow and fracture in AISI type* 316 *stainless steel at elevated temperatures* Ph.D. Thesis, Indian Institute of Science, Bangalore

Mannan S L and Rodriguez P 1972 *Philos. Mag.* **25** 673

Mannan S L, Samuel K G and Rodriguez P 1982 in *Proc. 6th Int. Conf. Strength of Metals and Alloys,* Melbourne, Aug. 1982 (ed) R C Giffkins (New York: Pergamon Press) Vol 2 pp. 637–642

Mannan S L, Samuel K G and Rodriguez P 1983 *Trans. Indian Inst. Metals* **36** 313

McCormick P G 1972 *Acta Metall.* **20** 351

McCormick P G 1983 in *Deformation—All aspects, Int. Conf. on Metal Sci., ICMS,* Ranchi (Calcutta: Indian Institute of Metals)

Mulford R A and Kocks U F 1979 *Acta Metall.* **27** 1125

Nabarro F R N 1967 *Theory of crystal dislocation* (Oxford: University Press) p. 431

Neelakantan K and Venkataraman G 1983 *Acta Metall.* **31** 77

Penning P 1972 *Acta Metall.* **20** 1169

Pink E and Grinberg A 1981 *Mater. Sci. Eng.* **51** 1

Portevin A and LeChatelier F 1923 *CR Acad. Sci.* **176** 507

Ramachandran V 1983 in *Deformation—All aspects, Int. Conf. on Metal Sci., ICMS,* Ranchi (Calcutta: Indian Institute of Metals)

Ramachandran V, Baldwin D H and Reed-Hill R E 1970 *Metall. Trans.* **1** 3011

Reed-Hill R E 1974 *Rev. High Temp. Mater.* **2** 214

Rosen A and Bodner S R 1969 *Mater. Sci. Eng.* **4** 115

Russel B 1963 *Philos. Mag.* **8** 615

Samuel K G and Rodriguez P 1975 *Trans. Indian Inst. Metals* **28** 323

Samuel K G and Rodriguez P 1980 *Trans Indian Inst. Metals* **33** 285

Schmidt C G and Miller A K 1982 *Acta Metall.* **30** 615

Seetharaman V 1984 *Bull Mater. Sci.* **6**

Sleeswyk A W 1958 *Acta Metall.* **6** 598

Sleeswyk A W and Verel D J 1972 *Scr. Metall.* **6** 1972

Solar-Gomez A J R and McG Tegart W J 1969 *Philos. Mag.* **20** 507

Strudel J L 1983 in *Deformation—All Aspects, Int. Conf. on Metal Sci., ICMS,* Ranchi, (Calcutta: Indian Institute of Metals)

Van Bueren H G 1955 *Acta Metall.* **3** 519

Van den Beukel A 1975 *Phys Status Solidi* **A30** 197

Van den Beukel A 1980 *Acta Metall.* **28** 965

Van den Beukel A and Kocks U F 1982 *Acta Metall.* **30** 1027

Weertman J 1967 *Can. J. Phys.* **45** 797

Wijler A, Schade Van Westrum J and Van den Beukel A 1972 *Acta Metall.* **20** 355

Wilcox B A and Rosenfield A R 1966 *Mater. Sci. Eng.* **1** 201

Yoshinaga H and Morozumi S 1971 *Philos. Mag.* **23** 1351, 1367

Bull. Mater. Sci., Vol. 6, No. 4, September 1984, pp. 665–676. © Printed in India.

Repeated yield drop phenomena as a cooperative effect

G ANANTHAKRISHNA

Materials Science Laboratory, Reactor Research Centre, Kalpakkam 603 102, India

Abstract. We present a theoretical model of repeated yielding (RY) which reproduces many experimentally observed features, apart from showing how the temporal behaviour of the phenomenon emerges as a consequence of the cooperative behaviour of defects. We first consider the case of step-like creep curves. Our model leads to a coupled set of nonlinear differential equations which admit limit cycle solutions, and thence jumps on the creep curve. Approximate closed form solutions for the limit cycles and the steps on the creep curve are obtained. The model is then extended to the constant strain rate experiment by including the machine equation. The temporal ordering of RY is shown to follow, as well as several other features characteristic of RY. Chaotic flow is also exhibited: the model has a sequence of period-doubling bifurcations with an exponent equal to that of the quadratic map. Finally, we have analysed the fluctuations during the onset of RY using nonlinear Langevin equations. Fluctuations in the periodic (RY) phase are also investigated. We conclude that RY is another example of a dissipative structure.

Keywords. Repeated yield drop; defects; cooperative behaviour; limit cycle solutions; nonlinear Langevin equations.

1. Introduction

There have been numerous phenomenological treatments of repeated yielding (RY) in the metallurgical literature (Bell 1973; Bodner and Rosen 1967; Cottrell 1953; McCormic 1972; Penning 1972; van den Beukel 1975, 1980). The best known model is Cottrell's dynamic strain-ageing model and its extensions (McCormic 1972; van den Beukel 1975, 1980). In these models, expressions are derived for such quantities as the critical strain, the critical strain rate, the dependence of the flow-stress on the strain rate, etc. Little attention has been paid to relating these quantities to the basic dislocation mechanisms such as cross glide, the Frank-Read mechanism, the formation of dislocation locks, etc. Also, there has been no attempt to investigate how the temporal behaviour of repeated yielding could arise naturally as a consequence of the basic dislocation mechanisms. From this point of view Cottrell's model is essentially static in character.

The transition from a single yield drop to a situation where RY occurs when certain 'drive' parameters (*e.g.*, the strain rate, temperature, etc.), are varied has the physical features of a nonequilibrium phase transition. (For examples of such transitions which arise only when the system is driven away from equilibrium, see Nicolis and Prigogine 1977; Haken 1978). We have constructed dislocation-dynamical model (Ananthakrishna and Sahoo 1981; Ananthakrishna and Valsakumar 1982; Valsakumar and Ananthakrishna 1983) which exhibits most of the experimentally observed features of RY and demonstrates that RY is a nonequilibrium phase transition. Needless to say, we consider somewhat idealized conditions, and further do not attempt to fit any actual data. In § 2, we start with the simplest case, namely, steps on the creep curve. Based on well-known dislocation mechanisms, we introduce a model which transforms one type of dislocation into another, giving rise to a set of coupled nonlinear differential equations for the corresponding densities. For a range of values of the rate constants, these equations are shown to admit *limit cycle* solutions. These lead immediately to jumps on creep curves. The model predicts a temperature range in which these jumps appear. In §3, we outline how approximate closed form solutions for the limit cycles and the steps on the creep curve are obtained. The results are shown to agree with experiments on zinc (Zagorukuyko *et al* 1977). Section 4 contains the extension of the model to the constant strain rate case by coupling the equations of §2 to the machine equations. The temporal ordering of RY is shown to follow (Ananthakrishna and Valsakumar 1982). Also demonstrated are several important features typical of RY such as bounds on the strain rate, bounds on the concentration of solute atoms, the negative strain rate dependence of the flow stress, the dependence of the amplitude on the strain rate and strain, etc.

Our model also exhibits chaotic flow, which finds some support from experiments. We find a sequence of period doubling bifurcations (Ananthakrishna and Valsakumar 1983) with an exponent identical to that for a quadratic map. This is presented in §5. Section 6 is devoted to the study of fluctuations during the onset of RY using nonlinear Langevin equations. We have used the Monte-Carlo and Gaussian decoupling methods (Valsakumar *et al* 1983). As the strain rate approaches its critical value, the variance not only diverges, but also shows the periodic nature of the fluctuations. Fluctuations within the periodic phase (RY) are also investigated. Our entire analysis shows that RY is another example of a dissipative structure (Nicolis and Prigogine 1977). In the final section, some unresolved problems are discussed.

2. Steps on the creep curve

2.1 *The model*

Perhaps the simplest manifestation of instability in plastic flow, from a conceptual point of view, is a creep curve with steps. However, there are not many instances of measurements where stepped response has been observed (Ardley and Cottrell 1953; Navratil *et al* 1974; Stejskalova *et al* 1981; Zagorukuyko *et al* 1977; Da Silveira and Monteiro 1979; Lubahn and Felgar 1961). There appears to be no detailed theory for the phenomenon. The model we propose (Ananthakrishna and Sahoo 1981; Valsakumar and Ananthakrishna 1983) is a natural extension of our earlier work (Sahoo and Ananthakrishna 1982) where a theory of creep was developed under the assumption that mobile dislocations (denoted by *g*) and immobile dislocations (denoted by *s*) transform into each other and are in dynamical balance. In the present case, we introduce a third species of dislocations (denoted by *i*) which are surrounded by clouds of solute atoms. These are dislocations moving much slower than the mobile species, ultimately becoming immobile. The introduction of this species is reminiscent of the basic feature of Cottrell's (1953) theory, so that the model is in keeping with the essential spirit of Cottrell's theory.

Let N_g, N_s and N_i denote the densities of the *g*, *s* and *i* species respectively. The rate equations for these quantities are (a dot denotes the time derivative):

$$\dot{N}_g = \theta V_g N_g - \mu N_g^2 - \mu' N_g N_s + \lambda N_s - \alpha N_g, \tag{1}$$

$$\dot{N}_s = k\mu N_g^2 - \mu' N_g N_s - \lambda N_s + \alpha' N_i, \tag{2}$$

$$\dot{N}_i = \alpha N_g - \alpha' N_i. \tag{3}$$

Here V denotes the dislocation velocity. We assume that θ, $\bar{\mu}$, μ', α, α', and λ are constants for a given stress at a given temperature. The first term in (1) corresponds to the production of dislocation by the cross glide mechanism; the second corresponds to the immobilization of two mobile dislocations and the annihilation of pairs of dislocations at a rate $(l-k)\mu$; the third corresponds to the annihilation of a mobile dislocation with an immobile one; and the last arises from solute atoms gathering around dislocations. Once a certain number of solute atoms gather around a moving dislocation, its mobility is reduced, and it becomes a type i dislocation (hence the source term αN_g in (3)). As the size of the solute atom cloud increases, the dislocation eventually becomes immobile (hence the source term $\alpha' N_i$ in (2)). The term λN_s comes from the (thermal or athermal) activation of immobile dislocations. The parameter α is expected to depend on the diffusion constant of the solute atoms, their concentration and the velocity of dislocations of type i. The parameter α' is the rate of immobilization, and hence should be expected to depend on the critical velocity (k is a parameter close to unity).

It is convenient to make equations (1)–(3) dimensionless by setting

$$x = (\mu/\lambda)N_g, \quad y = (\mu/\theta V_g)N_s, \quad z = (\mu\alpha'/\lambda\alpha)N_i. \tag{4}$$

Then

$$dx/d\tau = (l-a)x - bx^2 - xy + y, \tag{5}$$

$$dy/d\tau = b(kbx^2 - xy - y + az), \tag{6}$$

$$dz/d\tau = c(x - z), \tag{7}$$

where

$$\lambda = \theta V_g t, \quad a = \alpha/\theta V_g, \quad b = \lambda/\theta V_g, \quad c = \alpha'/\theta V_g. \tag{8}$$

(We have set $\mu = \mu'$ in order to reduce the number of parameters.)

2.2 *Stability analysis and existence of limit cycles*

Equations (5)–(7) form a nonlinear system. Under well-known conditions (Minorsky 1962), these admit periodic solutions called limit cycles for a certain range of values of the parameters a, b, c and k. Although the method of investigation is well known, for the sake of completeness we briefly outline the procedure used. Limit cycles are special classes of solutions which are isolated closed trajectories in the phase space (x, y, z) such that any trajectory which is sufficiently close to it either approaches it or recedes from it. Such closed trajectories can arise only in nonlinear systems. The search for limit cycles is generally preceded and aided by an investigation of the properties of the system around the steady state values x_a, y_a, and z_a. The stability of the system is decided by the nature of its singular points—node, focus, saddle point or centre. Linearising the set of equations around (x_a, y_a, z_a), one obtains an equation of the form

$$d\boldsymbol{\psi}/d\tau = \boldsymbol{W}\boldsymbol{\psi}, \tag{9}$$

where $\boldsymbol{\psi}$ is the column vector with components $(x - x_a)$, $(y - y_a)$, $(z - z_a)$, and $\boldsymbol{W}$ is a 3×3 matrix. A node arises when all three eigenvalues of $\boldsymbol{W}$ are of the same sign, and a saddle point when only two of these are of the same sign; a focus occurs when there are two complex conjugate eigenvalues, and a centre when one eigenvalue is identically zero and the other two are pure imaginary. (In the last case the nature of the singular point may have to be analysed more carefully; see Minorsky 1962).

An attractive limit cycle exists if there is a surface surrounding an unstable focus into which all trajectories enter: in the present case, we first look for a domain in the parameter space (a, b, c, k) when two of the eigenvalues are complex with at least one of them having a positive real part, and then show that such a surface exists (Ananthakrishna and Sahoo 1981). The only constraints that we have on the values of the parameters are $a < 1$ (which arises because the total rate of production of dislocations is positive); $k < 1$; and $a, b, c > 0$. (N_g, N_s and N_l are obviously positive).

2.3 *Staircase creep*

An analytical solution of (5)–(7) for arbitrary values of the parameters, and valid for all times, is difficult. To obtain numerical solutions, V_g must be known as a function of $N = N_l + N_s + N_g$ and $\sigma^*(N)$, where σ^* is the effective stress. For simplicity we assume V_g to be constant. Although this assumption is not physical, it can be argued that it will not alter the qualitative features of staircase creep (Ananthakrishna and Sahoo 1981). The creep curve obtained by integrating the Orowan equation is shown in figure 1. The steps on the creep curve appear only in the secondary region, which is consistent with the existing experimental results (Zagorukuyko *et al* 1977; Da Silveira and Monteiro 1979).

Our model also predicts a feature which is in agreement with experiment, namely, that there are upper and lower bounds for the asymptotic creep rates for which staircase creep occurs. These arise because the frequency of oscillation $\sim V_g \mathrm{Im}\, \omega_1$, where ω_1 is one of the two complex conjugate eigenvalues of $\boldsymbol{W}$. Bounds can be put on $\mathrm{Im}\, \omega_1$,

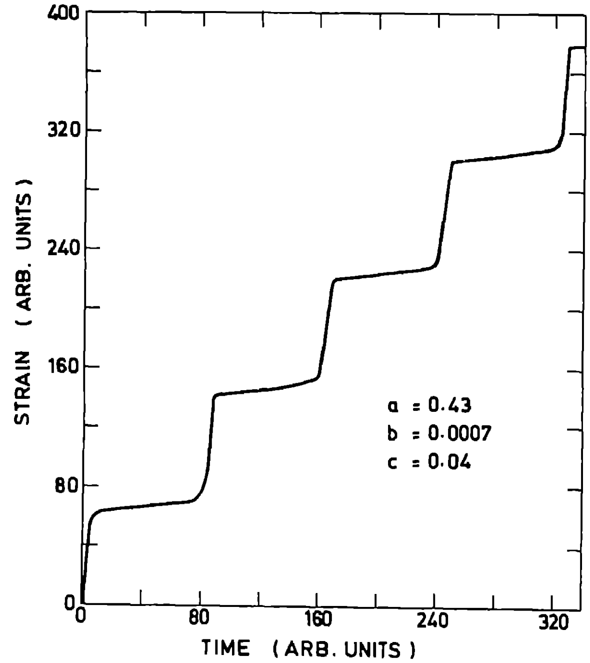

Figure 1. Staircase creep for typical values of the parameters a, b and c.

depending on the basic mechanism prevailing in the system. This implies corresponding bounds on V_g in order to have *observable* steps on the creep curve. This in turn implies that the phenomenon can only be observed over a finite range of $\dot{\varepsilon}$ (in practice, somewhat less than three orders of magnitude). Moreover, since V_g is temperature dependent (for a fixed stress), this phenomenon can only occur over a fixed range of temperature, as corroborated by the experimental results of Zagorukuyko *et al* (1977).

3. Approximate solutions

We outline an analytic procedure for obtaining asymptotic solutions to our equations. This is essential if one wants to relate the theoretical rate constants to accessible parameters such as the applied stress σ_a, temperature T, concentration of solute atoms C, etc. Our method follows that of Tyson (1977) for the Belousov-Zhabotinski oscillating chemical reaction. The main point is to identify a fast mode and adiabatically eliminate it to obtain a reduced set of two coupled equations from the original set of three equations (5)–(7). Approximate solutions are then obtained by using the method of relaxation oscillations (Minorsky 1962; Tyson 1977). Defining $X = x - X_a, Y = y - y_a, Z = z - z_a$, and $\tau' = b\tau$, (5)–(7) may be re-written in the form

$$b\dot{X} = -[\alpha X + \beta Y + bX^2 + XY], \tag{10}$$

$$\dot{Y} = -[\gamma X + \delta Y - bX^2 + XY - aZ], \tag{11}$$

$$\dot{Z} = \frac{c}{b}[X - Y], \tag{12}$$

where the dot now refers to differentiation with respect to τ'. Further, the constants $\alpha, \ldots, \delta$ are

$$\alpha = a + 2bx_a + y_a - 1,\ \beta = x_a - 1,\ \gamma = y_a - 2bx_a,\ \delta = x_a + 1 \tag{13}$$

(The constant α used here is distinct from that appearing in (1) of §2.) Since $b \ll a, c$, we see that $|\dot{X}| \to \infty$ as $b \to 0$ unless the right side in (10) vanishes identically. This amounts to saying that X must change with a characteristic time $\sim b$ to maintain the condition

$$\alpha X + \beta Y + bX^2 + XY = 0 \tag{14}$$

Thus X is a fast variable that can be adiabatically eliminated from (10)–(12), and the resulting pair of independent equations used for further analysis.

We use the results of stability analysis and further express $\alpha, \beta, \gamma, \delta, x_a, y_a$ and z_a as power series in b. We then determine the 'null clines'

$$\dot{Y} = 0 \leftrightarrow Z_1 = Z(Y) = X(Y) + \frac{2}{a}[x_a + X(Y)]Y, \tag{15}$$

and

$$\dot{Z} = 0 \leftrightarrow Z_2 = X(Y), \tag{16}$$

and again express $Z(Y)$ in powers of b. To find the limit cycles, we look for the intersection of the null clines in the region of negative slope. From the expressions for the null clines Z_1 and Z_2 we obtain a reasonable idea of the phase portrait. For $a < 1/3$ and for $1/\sqrt{2} < a < 1$, the steady state is stable. For $1/3 < a < 1/\sqrt{2}$, the null clines intersect in the negative slope region, which means that a limit cycle exists. Figure 2

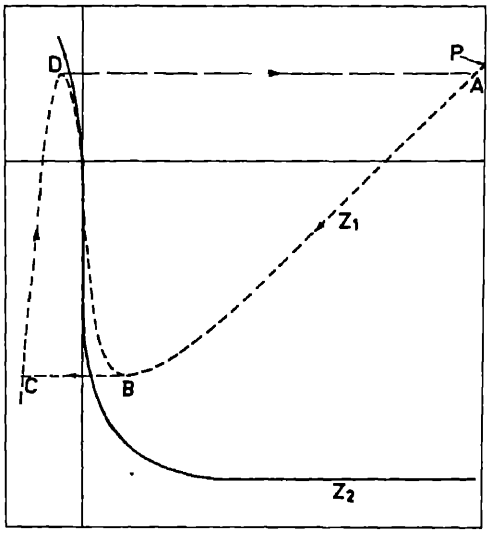

Figure 2. Phase plane portrait (the null clines Z_1 and Z_2 plotted as a function of Y) in the case $1/3 < a < 1/2$. The limit cycle is ABCDA.

shows a typical phase portrait for $1/3 < a < 1/2$. Starting from an arbitrary point, the trajectory moves along the null cline $\dot{Y} = 0$ until it reaches the turning point D, from where it almost instantaneously jumps to A. Thereafter it moves along the branch $\dot{Y} = 0$ (slowly) until it reaches the second turning point B from where it jumps to C, and the process continues. Thus the trajectory is a closed one and the limit cycle is $A \rightarrow B \rightarrow C \rightarrow D \rightarrow A$. From the expressions for Z_1 and Z_2, it is possible to calculate also the period, the amplitude and the wave form of the limit cycle solution. Finally, as already stated, we can integrate the Orowan equation to obtain the steady state creep curve which exhibits steps (Valsakumar and Ananthakrishna 1983).

Although the results of the model (in its present form) are not directly applicable to the detailed results on zinc (Zagorukuyko *et al* 1977), they still permit qualitative comparison. That the steps are seen only in the secondary creep region is obviously consistent with our theory, since the latter predicts a bifurcation from the steady state solution to a periodic one. Zagorukuyko *et al* (1977) report a rapid monotonic increase of the magnitude of the step in the strain as a function of σ_a; a weak, decreasing dependence of the period of the jump on σ_a; and a decrease of the magnitude of the jump in strain with increasing T. All these features are consistent with our work.

4. Repeated yield drop

Our model can be extended to a constant strain rate experiment by augmenting equations (1)–(3) with the machine equation representing the load sensed by the load cell, namely

$$\dot{\sigma}_a = K[\dot{\varepsilon} - b_0(N_g + \gamma N_i)V_g(\sigma^*)], \tag{17}$$

where a dot denotes the time derivative. Here $\dot{\varepsilon}$ is the imposed strain rate, K is the effective compliance, b_0 is the Burgers vector and σ^* is the effective stress. The second term on the right in (17) is the plastic strain rate $\dot{\varepsilon}_p$. We assume the power law $V_g = V_0(\sigma^*/\sigma_0)^m$, with $\sigma^* = \sigma_a - HN^{1/2}$, where H is a constant characteristic of hardening and m is a velocity exponent. Following a procedure similar to that of § 2, it can be shown that there is a domain in the space of the relevant parameters for which limit cycle solutions exist. Choosing values of the parameters in the domain of instability so as to be consistent with the expected values of the dislocation densities and the yield drops, numerical solutions of the system of equations may be obtained, and various characteristic features of the RY exhibited may be studied. These appear to be generally consistent with the experimental results. (Note that the latter are in the nature of averages over the sample dimensions.) We list these salient features: (a) There is a range of $\dot{\varepsilon}$ over which serrations are seen. (b) The model exhibits the negative strain rate behaviour of the flow stress at a fixed value of the plastic strain. The inset in figure 3 shows a typical plot of σ_a *vs* $\dot{\varepsilon}_p$, with a minimum in σ_a at a point $\dot{\varepsilon}_p = \dot{\varepsilon}_{\min}$. Curves corresponding to larger ε_p are displaced successively upwards. This feature has been both theoretically (Penning 1972; van den Beukel 1975) and experimentally verified (Bodner and Rosen 1967). (c) Figure 3 shows a typical plot of serrated yielding. The serrations are asymptotically periodic. Since it is not possible to identify them (from the plot itself) as serrations of type A or type B, a strain rate change test (Wijler and van Westrum 1971) must be carried out, from which it is found that beyond $\dot{\varepsilon}_{\min}$ the serrations are of type B. (d) The amplitude of the serration increases up to $\dot{\varepsilon}_{\min}$ and decreases thereafter. (e) The amplitude increases and saturates as a function of ε, consistent with experiments (McCormic 1971). (f) There are upper and lower bounds on the parameter α of (1) within which serrated yielding occurs. Since α depends on the concentration of solute atoms, this implies that there is a range of the solute atom concentration in which the phenomenon occurs. (g) ε_c (the critical strain), as a function of $\dot{\varepsilon}$, first decreases and then increases (McCormic 1971). (h) Beyond the range of $\dot{\varepsilon}$ where serrated yielding occurs, the 'normal' behaviour of $\sigma_a(\varepsilon)$ is resumed.

It should be pointed out that there has so far been no attempt to derive the negative strain rate behaviour of flow stress (which is crucial for any meaningful description of the phenomenon) starting from dislocation *interactions*. In the existing theories this is either assumed (Penning 1972) or derived (van den Beukel 1975) through a phenomenological treatment of waiting times involving in any case only individual dislocations. In contrast, this property emerges naturally in the present model from a consideration of dislocation interactions.

We have shown that the new temporal order represented by serrated yielding is the consequence of a bifurcation from a temporally homogeneous steady state plastic flow

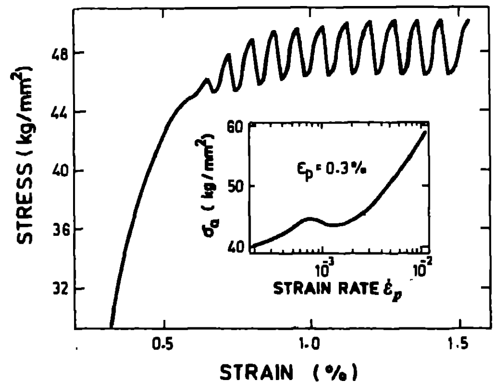

Figure 3. Calculated stress-strain curve showing repeated yielding. The inset is a graph σ_a *vs* $\dot{\varepsilon}_p$ for the same values of the parameters.

beyond some critical values of the parameters. This order is a result of a balance between the energy input (in the form of dislocation multiplication) and dissipation (annihilation, immobilisation and other processes). The phenomenon is obviously a far-from-equilibrium situation and is an example of a dissipative structure (Nicolis and Prigogine 1977).

5. Chaotic flow

We now turn to the chaotic flow exhibited by our model over a certain range of a drive parameter, the applied strain rate. (There is also some experimental evidence for such a flow, which will be discussed subsequently in brief). This adds to the growing list of models and physical situations exhibiting chaos (Ott 1981; Eckmann 1981; Lauterborn and Kramer 1981; Jefferies 1982). The model has an infinite sequence of period-doubling bifurcation eventually leading to chaos. The region over which chaos is exhibited is very small compared to the range of $\dot{\varepsilon}$ over which RY is seen (RY is considered to be periodic). We have calculated the value of the associated exponent and found it to be the same as the exponent for the quadratic map. We have also obtained the associated one-dimensional map. As the parameter of interest is the applied strain rate $\dot{\varepsilon}$, we fix the values of all the other parameters within the instability region and study the bifurcation sequence with respect to the parameter $e = \dot{\varepsilon}(\mu/\lambda V_0 b_0)$. The region where the period doubling bifurcation occurs is small, and is located near the upper end of the range of e (the dimensionless strain rate) over which RY is observed. For the chosen values of the parameters, the first bifurcation from the periodic state with period T to a state with a period $2T$ occurs at $e_1 = 159{\cdot}98444$, while the successive bifurcation to states with period 2^2T, 2^3T, . . ., occur at $e_2 = 173{\cdot}7178$, $e_3 = 175{\cdot}8974$, ... The exponents $\delta = \lim(e_n - e_{n-1})/(e_{n+1} - e_n)$ appears to be very close to that obtained by for the quadratic map (Grossman and Tnomae (1977), Feigenbaum (1978)). The estimated value of e_∞ is 176·4669, beyond which we find chaotic motion. Figures 4 and 5 show the variation of the stress σ_a with time (equivalently, the strain) for $e = 174{\cdot}679$ (motion with period $4T$) and $e = 178{\cdot}205$ (chaotic motion) respectively. A log-log plot of the projection of the strange attractor in the $N_g - \sigma_a$ plane is shown in figure 6. The associated one-dimensional map is shown in figure 7. Unlike the corresponding map for the Lorenz model (Ott 1981), our map has a smooth rounded maximum similar to the quadratic map except that it is very much skewed.

The fact that our model can exhibit chaotic flow has prompted us to look for experimental evidence for the plots of repeated yield drops. (Of course, the value of the parameter which controls the magnitude of the variation in σ_a, *i.e.*, the magnitude of the yield drop, has to be appropriately chosen). Even though we are constrained by the fact that the *average* stress level remains constant in our model, we have found evidence (Hall 1970) in support of such flows. Experimentally, too, this occurs towards the end of the $\dot{\varepsilon}$ range for which RY is seen. If we subtract the normally observed slow increase in the base level of the stress, there appear to be many more situations which perhaps correspond to chaos (Rosen and Bodner 1969).

6. Fluctuations during the onset of repeated yielding

We have discussed so far the possibility of a new temporal phase arising as a drive parameter (here, $\dot{\varepsilon}$) is varied. The situation corresponds to a *hard mode instability* in

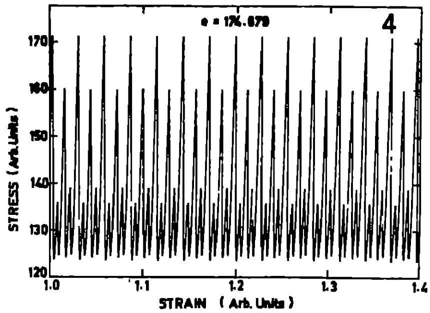

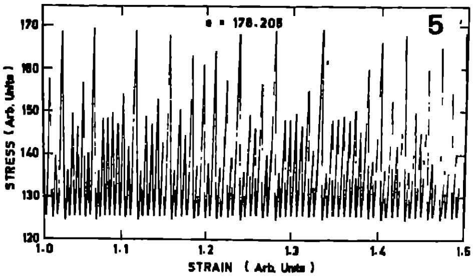

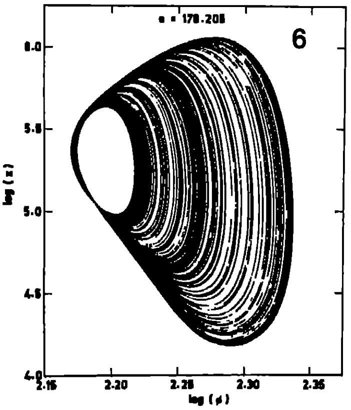

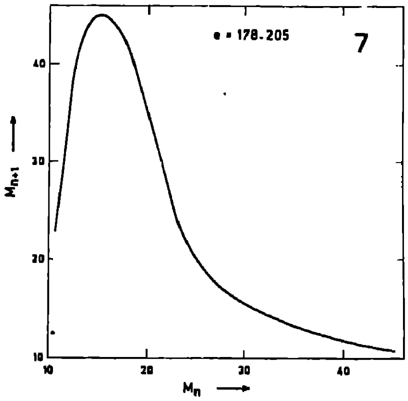

Figure 4. Stress-strain curve for $e = 174{\cdot}679$ with period 4T.

Figure 5. Stress-strain curve for $e = 178{\cdot}205$, *i.e.*, in the chaotic region.

Figure 6. A log-log plot of the projection of the strange attractor for $e = 178{\cdot}205$ in the $x-\phi$ plane. Here $x = (\mu/\lambda)\, N_g$ and $\phi = \sigma_a/\sigma_0$.

Figure 7. The one-dimensional map associated with chaotic flow in the model.

which the real part of complex conjugate modes changes sign (from negative to positive) in the frequency plane, as the drive parameter crosses its critical value. The foregoing analysis is completely deterministic. We now analyse the nature of the fluctuations when the parameter is in the neighbourhood of its critical value.

Our analysis begins with the nonlinear Langevin equations obtained by adding Gaussian white noise terms to the deterministic equations. We have used both the Monte Carlo technique and a Gaussian decoupling method (Valsakumar *et al* 1983) to study the fluctuations. (However, in the present context the second method can be applied only in the special case $H = 0$; otherwise powers of $N^{1/2}$ are present, which cannot be handled without further approximations). It is convenient to discuss the general features of the fluctuations with the help of the equivalent Fokker-Planck equation. The standard form of the Fokker-Planck equation is

$$\frac{\partial \pi}{\partial t}(\xi,t) = \frac{\partial}{\partial \xi}[(K(t)\cdot \xi \pi(\xi,t))] + \frac{1}{2}\frac{\partial^2}{\partial \xi^2}[D(t)\pi(\xi,t)], \tag{18}$$

where

$$K(t) = \frac{\partial C_1(y)}{\partial y}, \; D(t) = C_2(y), \tag{19}$$

and

$$\frac{dy}{dt} = C_1(y) \text{ and } \xi = \varepsilon^{-1/2}[x - y]. \tag{20}$$

Here, x is the random variable, y its mean, $C_1(y)$ the first jump moment and $C_2(y)$ the second moment. (*K* is the regression matrix.) ε is the (system-size) expansion parameter. To identify the onset of the periodic state beyond the critical value of the drive parameter, it is convenient to use the concept of the 'irreversible circulation of fluctuation' defined by (Tomita and Tomita 1974; Tomita *et al* 1974)

$$\alpha = \tfrac{1}{2}[(K\sigma)^T - K\sigma] \tag{21}$$

where σ is the variance (T represents the transpose). K and σ are related by

$$\tfrac{1}{2}\sigma = \alpha + K\sigma + \tfrac{1}{2}D. \tag{22}$$

If a periodic state occurs as a result of the hard mode instability both α and σ diverge; the instability is incurred through α, which becomes increasingly large as the transition point is approached from below.

Our preliminary investigations reveal that as $\dot{\varepsilon} \to \dot{\varepsilon}_c$ from below, the fluctuations show an overall growth which is indicative of the divergence of the variance, in addition to exhibiting a near periodic modulation which is indicative of the approach to a periodic state. For $\dot{\varepsilon} > \dot{\varepsilon}_c$, the fluctuations have the normal characteristics expected when limit cycle solutions are supported. The details of this study will be reported elsewhere.

7. Concluding remarks

We have shown that the state of temporal order represented by steps on the creep curve or by repeated yield drops is a consequence of a bifurcation from a temporally homogeneous, steady-state plastic flow. (A similar approach has been used by Kubin *et al* (1984) for low temperature RY.) A major criticism that can be raised is that the theory does not take into account the inhomogeneous deformation that normally accompanies the phenomenon. (Although, to the best of the author's knowledge, experiments do not show which is the cause and which is the effect, *i.e.*, whether an inhomogeneous deformation is the cause and a yield drop is the effect, or *vice versa*. We believe that it is not possible to disentangle the two. Nor is there any theory that takes the inhomogeneous deformation into proper account. The closest is that of Penning (1972) in which the feature is simply assumed). However, we argue (Ananthakrishna and Valsakumar 1982) that if the space dependence is properly taken into account, the inhomogeneity of the deformation should follow automatically. The point is that such an extended model would still exhibit the negative strain rate behaviour of the flow stress (which has been assumed by Penning (1972) to show that hopping and propagating band type solutions are supported). Attempts are underway to demonstrate explicitly that such solutions indeed occur when appropriate space dependence is included.

Another possible criticism could be that the model merely 'mimics' the effects of the waiting of dislocations at obstacles which van den Beukel (1975) has used to derive $\sigma(\dot{\varepsilon}_p)$. However, this work deals with individual dislocations whereas what is observed in an actual experiment is an ensemble average over participating dislocations. Therefore, for such a theory to hold good, there must be a 'phase coherence' between the dislocations, if the effects are to manifest themselves at a gross level. Further, it is known that the negative strain rate behaviour is essential for RY. (For a detailed analysis of various tensile test conditions using the negative strain rate behaviour, see Neelakantan and Venkataraman 1983). Our analysis shows that this behaviour is a consequence of the competition between different dislocation interaction mechanisms. We have also checked (Ananthakrishna and Sahoo 1981) that the incorporation of certain other basic dislocation mechanisms (pile up, pinning and depinning of dislocations from obstacles) leads to similar results.

Finally, it should be pointed out that several materials like nylon (Schultz 1974), metallic glasses (Takayama 1979), wood, etc. are known to show RY. The present work suggests that the *mathematical mechanism in all these cases must be the emergence of limit cycle solutions which are characteristic of non-linear systems. As plastic flow is basically nonlinear, such solutions are an intrinsic possibility.* The basic microscopic physical mechanisms of course are bound to be different in different materials.

Acknowledgement

The author thanks Dr G Venkataraman for arousing his interest in this problem.

References

Ananthakrishna G and Sahoo D 1981 *J. Phys.* **D14** 2081
Ananthakrishna G and Valsakumar M C 1982 *J. Phys.* **D15** L171
Ananthakrishna G and Valsakumar M C 1983 *Phys. Lett.* **A95** 69
Ardley G W and Cottrell A H 1953 *Proc. R. Soc.* **A219** 328
Bell J F 1973 *Handbuch der Physik Band* VIa/I (Berlin: Springer-Verlag)
Bodner S R and Rosen A 1967 *J. Mech. Phys. Solids* **15** 63
Cottrell A H 1953 *Philos. Mag.* **44** 829
Da Silveira T L and Monteiro S N 1979 *Met. Trans.* **A10** 1795
Eckmann J P 1981 *Rev. Mod. Phys.* **53** 643
Feigenbaum M J 1978 *J. Stat. Phys.* **19** 25
Grossman S and Tnomae S 1977 *Z. Naturforsch.* **32a** 1353
Haken H 1978 *Synergetics* (Berlin: Springer-Verlag)
Hall E O 1970 *Yield point phenomena in metals and alloys* (Macmillan: London)
Jefferies D J 1982 *Phys. Lett.* **A90** 317
Kubin L P, Estrin Y and Spiesser Ph 1984 *Res. Mechanica* **10** 25
Lauterborn W and Kramer E 1981 *Phys. Rev. Lett.* **47** 1445
Lubahn J D and Felgar R P 1961 *Plasticity and creep of metals* (New York: John Wiley)
McCormic P G 1971 *Acta Metall.* **19** 463
McCormic P G 1972 *Acta Metall.* **20** 351
Minorsky N 1962 *Nonlinear oscillations* (New Jersey: Van Nostrand)
Navratil V, Hammersky M and Blazkova 1974 *Czech. J. Phys.* **B24** 907
Neelakantan K and Venkataraman G 1983 *Acta Met.* **31** 77
Nicolis G and Prigogine I 1977 *Self organization in non-equilibrium systems* (New York: Wiley)
Ott E 1981 *Rev. Mod. Phys.* **53** 643
Penning P 1972 *Acta Metall.* **20** 1169

Rosen A and Bodner S R 1969 *Mater. Sci. Eng.* **4** 115
Sahoo D and Ananthakrishna G 1982 *J. Phys.* **D15** 1439
Schultz J 1974 *Polymer materials science* (New Jersey: Princeton-Hall)
Stejskalova V, Hammersky M, Luckac P, Vostry P and Sprusil B 1981 *Czech J. Phys.* **B31** 195
Takayama 1979 *Scr. Met.* **13** 463
Tomita K, Ohta T and Ohta H 1974 *Prog. Theor. Phys.* **52** 1744
Tomita K and Tomita H 1974 *Prog. Theor. Phys.* **51** 1731
Tyson J J 1977 *J. Chem. Phys.* **66** 905
Valsakumar M C and Ananthakrishna G 1983 *J. Phys.* **D16** 1055
Valsakumar M C, Murthy K P N and Ananthakrishna G 1983 *J. Stat. Phys.* **30** 637
van den Beukel A 1975 *Phys. Status Solidi* **A30** 197
van den Beukel A 1980 *Acta Metall.* **20** 965
Wijler A and van Westrum S 1971 *Scr. Metall.* **5** 531
Zagarukuyko L N, Ostasky A L and Soldatov V P 1977 *Phys. Met. Metallogr.* **43** 156

Discussion

P Rodriguez: You cited some results on zinc. In your model, the Cottrell type of solute locking is envisaged. What was the solute species?

G Ananthakrishna: Zinc is a poor example (the dislocations are actually produced due to inhomogeneities at the surface).

Rodriguez: Many of the conclusions with respect to the critical strain, the magnitude of the strain burst, the delay time for the strain burst to occur, etc., follow automatically once Cottrell locking is introduced. It is therefore not surprising that the model gets these right.

Ananthakrishna: Cottrell locking is not manifest in the equations of the model.

N Kumar: You get period doubling bifurcations even though your maps are not discrete. Is this because of the higher dimensionality of the system of equations?

Ananthakrishna: One-D are the simplest of systems which exhibit chaos. Coupled system of differential equations also exhibit such a behaviour. The associated 1-D map can be obtained.

C K Majumdar: It would be interesting to examine the structure of your set of equations from the point of view of catastrophe theory.

Bull. Mater. Sci., Vol. 6, No. 4, September 1984, pp. 677–687. © Printed in India.

Mechanisms and empirical equations for deformation and some principles of alloy design

T BALAKRISHNA BHAT

Defence Metallurgical Research Laboratory, Kanchanbagh, Hyderabad 500 258, India

Abstract. Some aspects of the deformation behaviour of solids at very high, moderately high and low strain rates are discussed. In the very high strain rate region, deformation equations and the physics of the shock front are analysed to propose a route to lower energy dissipation at the shock front. In the moderately high strain rate region, alloy design principles for maximizing the deformation resistance are outlined. In the low strain rate region, an analysis of the physical basis for the power law creep equation is presented. Some physical arguments are presented as a rationale for the high stress exponents and activation energies often observed in particle-strengthened alloys. The additivity of strain rates by various mechanisms is also briefly discussed.

Keywords. Deformation mechanisms; empirical equations; dislocation dynamics; shock front; impact resistance; alloy design.

1. Introduction

The behaviour of solids under deformation depends on the operating stress level, the temperature, and many material properties such as the elastic modulus, the microstructure and the properties of the individual constituents. The behaviour is indeed complex and can be described only by semiquantitative and quasi-empirical relations. In the very high strain rate region where shock waves predominate in the flow process, the microstructure and initial temperature are relatively unimportant. The crystalline state and basic material properties such as the modulus and density are important in this region. In the lower strain rate region such as that observed in the ballistic testing of materials, the stress-strain diagrams, the glide resistances, the phonon drag and the temperature play important roles. In the low strain rate region as in creep, the operating temperature and stress are most important. A smaller but significant role is also played by the microstructure. The regimes of deformation rates and stresses of interest in the present discussion are shown in figure 1.

2. Deformation at very high pressures and strain rate

Pressure impulses injected into materials generate shock waves. At low pressures the shock front consists of purely elastic strains and the wave propagates over large distances with relatively little attenuation. A typical example of such a wave is that of sound waves generated by gentle knocks on any solid. More intense waves such as those generated during hollow charge collisions or in implosions intended for thermonuclear fusion generate high nonelastic strains at the wave-fronts. Such waves suffer large drags and tend to get dissipated. This drag is in some cases undesirable, for example in

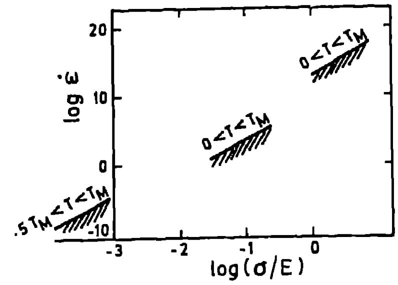

Figure 1. Stress-strain rate regimes considered in this paper.

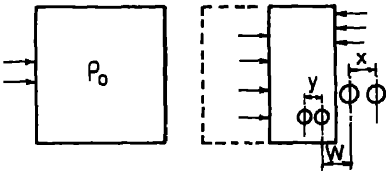

Figure 2. Schematic diagram illustrating the strain at a shock front: $\varepsilon = (x-y)/x$.

thermonuclear experiments. We may therefore analyse the drag mechanisms in terms of a specific question, namely, how to reduce the drag.

At the shock front a low density phase is transformed to a high density phase. This transition induces both bulk and shear strains at the front (Gilman 1979). Figure 2 illustrates the situation at the shock front. The strain there may be written as

$$\varepsilon = (\rho - \rho_0)/\rho_0, \tag{1}$$

where ρ_0 is the initial density and ρ is the shocked density. The power dissipated at the moving front is

$$G = B\dot{\varepsilon} = Bv_{\text{sh}}/W, \tag{2}$$

where B is the drag coefficient, v_{sh} is the speed of the shock front, and W is the width of the transition region between the shocked and the unshocked state. The power dissipated at the shock front is thus controlled by the parameters B and W.

In crystalline solids the shock front moves *via* the coordinated motion of atoms. The interface between the shocked and the unshocked regions is thought to consist of a set of interface dislocations and a compressed zone (figure 3). The areal density of dislocations, ρ_{dis}, depends on the compression ratio according to

$$\rho_{\text{dis}} = \frac{1}{\sqrt{2}b}[1-(\rho_0/\rho)^{1/3}], \tag{3}$$

where b is the Burgers vector. Figure 4 is a plot of this dependence. The dislocation spacing approaches b at high compression ratios. The shear strain rate at those dislocations (which travel with the shock front) becomes $\dot{\varepsilon} = v_{\text{sh}}/b$. Typical values are $v_{\text{sh}} \simeq 10^7$ cm/sec and $b = 2{\cdot}5 \times 10^{-8}$ cm, so that $\dot{\varepsilon} \simeq 4 \times 10^{14}$ sec^{-1}. At such a high strain rate, even in a material as fluid as water (viscosity $\sim 10^{-2}$ poise) the drag becomes 4×10^4 kg/mm^2! Shock pulses therefore attenuate extremely rapidly. One way to reduce this drag pressure would be the use of metallic glasses which have a liquid-like structure on either side of the shock front. The intense localisation of strains arising from the smallness of the Burgers vector of the dislocations is then avoided.

3. Deformation at moderately high strain rates

At lower stress levels (the middle shaded region in figure 1), the deformation front advances at subsonic speeds. A typical example in this range of strain rates is the

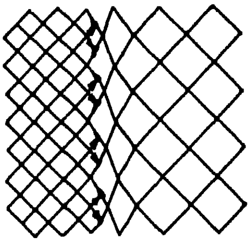

Figure 3. Schematic illustration of the interface structure at shock fronts in crystalline materials.

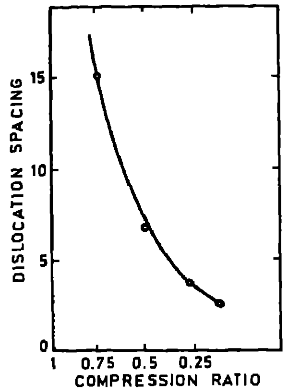

Figure 4. Variation of dislocation spacing (in units of b) at the shock front as a function of the compression ratio.

deformation armour under ballistic attack. Strain in this regime normally occurs by dislocation movement. The flow is governed by high-velocity dislocation dynamics. The equation of motion for a dislocation line is of the form (Kocks *et al* 1973)

$$M\ddot{y}+B\dot{y}=b(\sigma-\tau), \tag{4}$$

where M is the 'mass' of the dislocation, B is the viscous drag coefficient, σ is the applied stress, and τ is the lineglide resistance of the dislocation element against slow glide. Clearly, M, B and τ must be maximised for increasing the strength of the material. The 'mass' M of the dislocation can be shown to be

$$M=U/v_s^2=1/2\,b^2\rho, \tag{5}$$

where U is the line energy per unit length of the dislocation, v_s is the velocity of sound, and ρ is the material density of the material. Hence high density materials (*e.g.*, steel) and materials with large Burgers vectors (*e.g.*, intermetallics) offer greater resistance to dynamic flow. The drag coefficient B is controlled by the Peierls potential and the phonon-dislocation interaction. Dissipation of energy occurs when dislocations interact with phonons. In addition, shear-stress fluctuations due to phonons cause dislocations to flutter. Nonlinear elastic strains near dislocations also scatter phonons because of local changes of modulus and density (and hence of the speed of elastic waves). These mechanisms retard moving dislocations. Further, a moving dislocation has to build up and relax elastic strains, and this process is also retarded by the interaction with phonons. All these factors lead to a drag coefficient of the form (Kocks *et al* 1973)

$$B=k_BT/\Omega\omega, \tag{6}$$

where Ω is the atomic volume and ω is the atomic frequency. In contrast to the other mechanisms resisting flow, the drag B increases with temperature. Moreover, there is also a rapid increase of B when the speed of the dislocation $\gtrsim 0{\cdot}5\,v_s$. This is because the strain field of the dislocation begins to be compressed into smaller volumes (for lack of time!) at any given location. However, the discrete nature of the atoms and the low compressibility of atomic cores puts an upper limit to this contraction and allows 'supersonic' speeds to be reached at high stress levels, as in the shock waves discussed earlier.

Turning to the parameter τ (the line glide resistance) in (4), we observe first that this resistance normally varies with the location on the glide plane. The Peierls resistance, for instance, varies periodically with a wavelength b. Solute atoms provide small discrete obstacles. Precipitates, interphase interfaces and cell or grain boundaries provide a coarser but stronger set of obstacles. Some of these obstacles are repulsive to dislocations, some are attractive and some are energy-storing. A schematic glide-resistance diagram is shown in figure 5. The spatial variation of the effective driving force on the dislocation results in an oscillatory motion superposed on its steady state motion. This induces radiation of elastic energy from the moving dislocation into the crystal. As this energy must also be supplied by the applied stress, the hills and valleys in the glide-resistance diagram contribute to the drag. The varying effective driving force also causes rapid acceleration or deceleration of the dislocation as it moves in the glide plane. The dislocation may then be able to overcome an obstacle on its path at least in part through its inertia. Attractive obstacles are specially prone to this phenomenon, for the energy picked up in the 'downhill' motion of the dislocation can facilitate its subsequent travel 'uphill'. Similarly, many small obstacles met with after passage through a large repulsive obstacle can be overcome dynamically. It is also possible for a moving dislocation to interact with near-by dislocations and transfer energy to them. Thus, under dynamic conditions obstacles incorporated in the matrix begin to lose their individuality and efficacy and the macroscopic concepts of flow stress may no longer be valid.

The onset of this dynamic behaviour is influenced by many factors. Higher values of the viscosity and larger obstacles sizes or spacing postpone the onset to higher dislocation velocities. Larger values of M and b favour an early transition. For obstacles of width smaller than a few Burgers vectors, dynamic effects emerge when (Kocks *et al* 1973)

$$(\sigma/G) > (k_B T/\Omega G)^2, \qquad (7)$$

where σ is the stress level and G is the shear modulus. A rationale for specifying low-T impact properties for armour materials is hidden in this above equation, because low temperatures bring out the dynamic effects at lower stresses and strain rates. This also suggests that the results of low-T tensile tests may correlate better with ballistic performance when the highest suitable test temperature is chosen by the onset of simultaneous decrease in strength and ductility.

Certain alloy design criteria (for good ballistic performance) also emerge from this discussion. A material that must resist flow at the strain rates, presently under

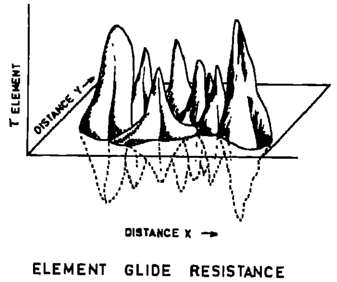

Figure 5. Schematic glide-resistance diagram in multiphase materials.

consideration, should not exhibit significant dynamic weakening. Thus, a high Peierls stress is particularly detrimental. Also undesirable are microstructures with precipitates that almost touch each other, as are attractive precipitates, even when they are strong. Long range barriers such as subgrains, martensite lath boundaries, strong and large (> 2000 Å) repulsive precipitates, or repulsive-type solute elements would be the ideal candidates for the purpose at hand.

4. Deformation at low stresses and strain rate

Even at low stresses materials can deform provided the temperature is sufficiently high to permit thermal activation of certain microscopic processes. This deformation mode, called creep, has been extensively studied over the years and a variety of equations, mechanisms and explanations have been proposed by various workers.

One particular widely-used semi-empirical equation is the 'power law', according to which the creep rate $\dot{\varepsilon}$ can be expressed as the product of a (small) power of the stress and an exponential function of T:

$$\dot{\varepsilon} = A(Gb/KT)\,(\sigma/G)^n D_0 \exp(-Q/RT). \tag{8}$$

Here A is a constant, D_0 is the preexponential in the diffusion coefficient, R is the gas constant and Q is the activation energy for diffusion. This equation has been shown to work for simple metals and ionic solids (Bird *et al* 1969). Nevertheless, many difficulties and unexplained modes of behaviour persist. The magnitude of the creep rate predicted by (8) is often incorrect (Evans and Knowles 1981). The index n lies anywhere between 1 and 6 and sometimes can be as high as 40 (Benjamin and Cairns 1971). The observed activation energy for creep often deviates significantly from that for diffusion, and in addition varies with T and σ (Poirier 1978). Moreover, even if there is a correlation between the activation volumes for self-diffusion and creep, one cannot unequivocally conclude that the creep is diffusion-controlled, because it can be shown that any process that depends on the pressure through the modulus will also have the same activation volume (Beyeler 1969). In spite of the large literature extant on the subject, a generally-agreed upon theory is lacking as yet.

4.1 *The stress exponents and the creep deformation mechanisms*

The index n is unity for viscous flow in solids, as in fluids. This is a characteristic of microscopically homogeneous or structureless flow. Diffusional flow as in polycrystalline materials at elevated temperatures also exhibits a linear stress dependence. Basically, the applied stress serves only to generate higher point defect concentrations on grain boundaries under tensile stress relative to boundaries under no stress. The concentrations are exponential functions of $(\sigma\Omega/k_B T)$ which approximate to linear functions of σ at low stress levels (Nabarro 1948; Coble 1963).

Several anomalies exist in the dislocation creep region. Stocker and Ashby (1973) have used a heuristic statistical analysis to prove that $n = 3$ is the most probable value for dislocation creep. A simple way to see this is as follows: The dislocation density $\propto \sigma^2$, while the dislocation velocity $\propto \sigma$, in a viscous flow picture. Orowan's equation then directly leads to $\dot{\varepsilon} \propto \sigma^3$. The same conclusion can also be reached if we treat the creep as being controlled by the coarsening of dislocation networks (Evans and Knowles 1981).

Dislocation creep that is controlled by recovery processes generally has a larger stress exponent. One such process is the mutual annihilation of dislocations with opposite Burgers vectors (or their segments) when they meet each other. If ρ_+ and ρ_- denote the densities of dislocations with Burgers vectors of opposite signs, the annihilation can be considered as a second order reaction with a rate given by $\dot{\rho} = K_1 v \rho_+ \rho_-$ where ρ is the total dislocation density and K_1 is a reaction constant. The rate of reaction, and hence of recovery, is evidently greater the higher the dislocation velocity. The strain rate associated with the recovery can be written as $\dot{\varepsilon} = \dot{\rho} bs$ where s is the average distance travelled by a dislocation before annihilation. Substituting a quadratic dependence of the dislocation density on σ and a linear dependence of v on σ, we get

$$\dot{\varepsilon} \sim \sigma^4. \tag{9}$$

This recovery strain rate leads to a proportional but larger glide strain rate, which is the observed strain rate. Thus, recovery-controlled creep is expected to have a stress exponent equal to four.

One may be tempted to combine such power laws into a general functional form

$$\dot{\varepsilon} = \sum_n a_n (\sigma/G)^n, \tag{10}$$

where the a_n are independent of σ, a particular mechanism being associated with each distinct n value. Equation (10) implies that the control of the creep rate shifts to the mechanisms corresponding to higher n values with increasing stress. Often, however, this is not the case. One plausible conclusion from this is that the index n has no specific connection with any mechanism. Alternatively, one may invoke a back stress concept, such that the effective stress for creep is given by

$$\sigma_{\text{eff}} = \sigma - \sigma_b = \sigma - f_n(\sigma),$$

where σ is the applied stress and the function f_n depends on the specific mechanism concerned. The back stress can be considered as a measure of the energy spent on athermal steps that are essential for creep but do not directly lead to any significant creep strain. A specific illustration of the use of back stress concept is in the creep behaviour of particle-strengthened systems. Unusually large n values are often observed in both diffusional creep and dislocation creep regions (Benjamin and Cairns 1971). Recently, we have shown how the anomalous stress exponents in TD Nichrome and Mar M·200 superalloys fall in line with that for nickel once the back stress arising from strong dislocation-particle interactions is taken into account (Balakrishna Bhat and Arunachalam 1980; Balakrishna Bhat 1981). When the particles are attractive, the back stress appears as a threshold stress; when they are repulsive, the back stress increases with applied stress, reaching a limiting value as shown in figure 6. The back stress for diffusion creep is believed to be associated with the interaction of grain boundary dislocations with particles at the grain boundaries. It must be mentioned that the term 'back stress' has also been used in several different contexts. For example, it has been identified with the internal stress which includes the average stress field of the dislocation structure together with the cell boundaries (Pahutova and Cadek 1973; Argon *et al* 1981). In reality, the power law discussed earlier is the result of the interaction of defects among themselves and with the background stress field; the average stress field of the other defects is therefore already taken into account, and it is incorrect to include it once again in the back stress.

4.2 *Activation energy for deformation*

4.2a *Activation energy and the bulk modulus*: The activation energy can be considered as the work a solid under load has to perform on itself in temporarily expanding against its own bulk modulus to accommodate the moving unit of flow. Figure 7 is a plot of $Q/[\Omega(1-P_f)]$ *vs* the bulk modulus for various metals. (P_f is the packing factor for the crystal). The approximately linear fit is noteworthy. It is interesting to note also that the activation energy is the energy that gets stored in the empty space $\Omega(1-P_f)$ as the solid momentarily dilates or contracts!

4.2b *Activation energy for dislocation creep and the creep mechanism*: A power law for creep presupposes that the activation energy for creep is equal to that for diffusion. However, the observed value of the activation energy is not constant. It increases with T

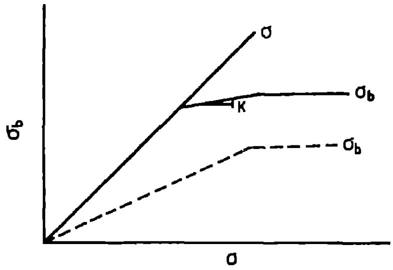

Figure 6. Schematic variation of back stress σ_b with applied stress σ in particle-strengthened alloy systems.

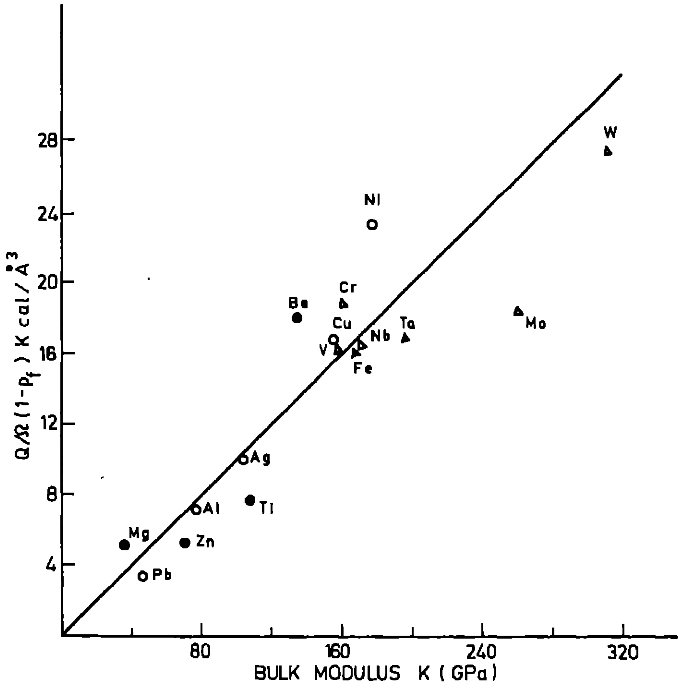

Figure 7. Dependence of $Q/[\Omega(1-P_f)]$ on bulk modulus for metals.

to match the activation energy for diffusion only in some small range of homologous temperature which, moreover, is different for each material (Poirier 1978). In particle-strengthened systems anomalously high and variable activation energies have often been reported.

It has often been suggested that the variation of the elastic modulus with temperature should account for the anomaly (Shewfelt and Brown 1974). However, this is not very convincing. Consider a force-displacement diagram between the atoms in a crystal as shown in figure 8. The elastic modulus reflects the rate of energy storage for infinitesimal displacements from the equilibrium value whereas the activation energy reflects the energy needed for a displacement equal to a lattice parameter which is more like the *area* under the curve. The inadequacy of the effect of T on E as a measure of its effect on Q is obvious.

The apparent activation energy for creep in particle-strengthened systems also depends on the back stress and its variation with temperature. This contribution to the apparent activation energy is given by (Balakrishna Bhat 1981)

$$\Delta Q = [nRT^2/(\sigma - \sigma_b)]\,[\partial\sigma_b/\partial T]. \tag{11}$$

For diffusion creep with low n and σ_b, the contribution is relatively small. For dislocation creep with large n and σ_b (as in TD nichrome), the contribution can be large. Further, σ_b varies an order of magnitude more rapidly with T than is predicted by the variation of the elastic modulus alone. The reason for this difference is not clear at the moment. Perhaps, with increasing T dislocation climb increases exponentially, facilitating the selection of easier flow paths by a sampling of the field of glide resistance along all three axes. The effective glide resistance (which one may call the 'volume glide resistance') or the back stress for creep will be different from the 'plane glide resistance' derived for a planar distribution of obstacles and a largely in-plane overcoming of obstacles by the dislocations. During creep, dislocations accumulate in difficult-to-glide locations and direct the other dislocations to climb over to easier regions of flow. When once climb has become possible, the back stress changes only slowly with temperature (figure 9).

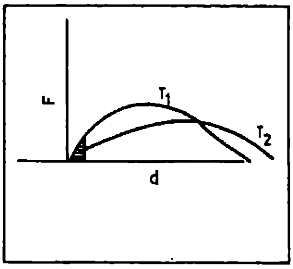

Figure 8. Atomic force-displacement diagram for two different temperatures.

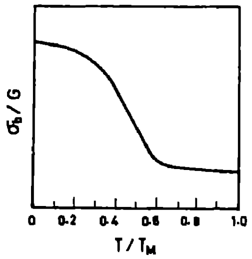

Figure 9. Temperature dependence of the back stress in particle-strengthened alloys.

A consequence of the volume-sampling hypothesis is that high n and high Q are not necessarily coupled. Even at high temperatures, σ_b in ODS alloys can be relatively large, giving a large effective n. The volume-sampling process reaches saturation above a particular temperature and the back stress then drops slowly with further increase of T. The apparent activation energy would then be small in spite of a large n value. Indeed, the results of Benjamin and Cairns (1971) on ODS alloys show a modulus-compensated activation energy close to that for self-diffusion in spite of a high apparent stress exponent of 32·8 at $T = 1350°\mathrm{C}$. At a lower temperature, a lower n value is obtained, but Q is still twice the activation energy for self-diffusion. Another consequence of volume-sampling is that there will be no influence of particle shape on the T-dependence of σ_b for a random distribution of obstacles, since the T-dependence arises primarily from the climb-controlled volume-sampling of weaker regions from the same random distribution of obstacles, and not from climb around individual particles. This observation is substantiated by the experiments of Shewfelt and Brown (1974). It would be of interest to perform a computer simulation of this volume-sampling glide process during the creep of particle-strengthened systems, in order to optimize the particle size and distribution for effective resistance to creep flow.

5. Additivity of creep rates

An unsolved problem in creep relates to the additivity of creep rates through various mechanisms. The expansion of (10) presupposes such additivity. All theoretical treatments to date have also made this assumption. However, the basic physical processes involved cast a doubt on the validity of this assumption.

Consider for instance diffusion creep and grain boundary sliding. Diffusion creep elongates the grains; when added over all the grains, this leads to directional elongation. However, grain sliding events as in superplastic flow introduce new directions for diffusional creep, with the net result of eliminating diffusion creep on the average.

Then again, dislocation creep pre-empts diffusion creep by consuming vacancies en route as they move from one grain boundary to the other. Dislocation creep also generates ledges on grain boundaries and hinders both diffusion creep and grain boundary sliding. On the other hand, diffusion creep tends to retard the onset of grain boundary sliding by generating nonequiaxed grains. It also retards dislocation creep by not allowing large stress concentrations to build up at the grain boundaries. Thus, each mechanism appears to possess an intrinsic inhibiting effect on the others, which may explain why one obtains well-delineated deformation mechanisms in creep experiments. The opposite can also happen in some cases. For example, dislocation glide and climb favour each other. Dislocation activity at the grain boundary zone can enhance grain boundary diffusivity and hence superplastic strain rates. Computer simulation of the deformation process should be of help in understanding these coupled processes.

6. Summary

Our discussion above may be summarized in the form of the following specific questions:

(a) Will metallic glasses exhibit low damping of shock waves? (b) Can low temperature tensile and compressive tests be used to design alloys for good ballistic performance?

(c) Will attractive precipitates prove inferior to repulsive precipitates in the context of ballistic resistance? (d) Can the Arrhenius term in the creep rate be rewritten as a combination of the bulk modulus, the atomic volume and the packing factor? (e) Is the back stress concept relevant, and is it correct to subtract internal stresses due to defects which move to cause strain? (f) Can a microstructure suitable for optimal creep resistance be designed using the concept of volume glide resistance? (g) Can the strain rates arising from different mechanisms be considered to be additive, even though some of them appear to be mutually inhibiting?

Acknowledgements

The author acknowledges many useful and inspiring discussions with Dr V S Arunachalam and Prof. K Srinivasa Raghavan during the course of this work. He is also grateful to Dr P Rama Rao for inspiring him to write this article. The curves in figure 9 are a result of discussions with Shri A K Gogia.

References

Argon A S, Print F and Moffatt W C 1981 in *Creep and fracture of engineering materials and structures* Proc. Int. Conf., Swansea, U.K.
Balakrishna Bhat T and Arunachalam V S 1980 *J. Mat. Sci.* **15** 1614
Balakrishna Bhat T 1981 *Effect of second phase on microstructural development and engineering properties* Ph.D. Thesis, Indian Institute of Technology, Madras
Balakrishna Bhat T 1983 *Principles for protection* Trans. I.I.M. (to be published)
Benjamin J S and Cairns R L 1971 in *Modern developments in powder metallurgy* (ed) H Hausner (New York: Plenum) 5 47
Beyeler M 1969 Report CEAR 3715
Bird J E, Mukherjee A K and Dorn J E 1969 in *Quantitative relations between properties and microstructure* (eds) D G Brandon and A Rosen, (Jerusalem: Israel University Press) p 255
Coble R L 1963 *J. Appl. Phys.* **34** 1679
Evans H E and Knowles G 1981 in *Creep and fracture of engineering materials and structure* Proc. Int. Conf. at Swansea, U.K. (eds) B Wilshire and D R Owen J. p 169
Gilman J J 1979 *J. Appl. Phys.* **50** 4059
Kocks U F, Argon A S and Ashby M F 1973 *Thermodynamics and kinetics of slip* (Illinois: Argonne National Laboratory)
Malu M and Tien J K 1975 *Scr. Met.* **9** 1117
Nabarro F R N 1948 Report of a Conference on the strength of solids 1963 The Physical Society, London 1.
Pahutova M and Cadek 1973 *J. Mater. Sci. Eng.* **11** 151
Poirier J P 1978 *Acta Metall.* **26** 629
Shewfelt A S W and Brown L M 1974 *Philos. Mag.* **30** 1125
Stocker R L and Ashby M F 1973 *Scr. Met.* **7** 115

Discussion

K A Padmanabhan: Your statement that dislocations could move as fast as the shock front does not appear to tally with the detailed analysis of J D Eshelby on dynamical effects on dislocations. Moreover, as in special relativity, the mass of a dislocation increases with its velocity. Incidentally, Dr Chidambaram's observation that the density of dislocations at the shock wave front is $\sim 10^{11}$ cm^2 also indicates that the total strain arises from a larger *number* of dislocations rather than a few moving at extremely high speeds.

N Kumar: In his book, Frank describes what led him to the theory of the Frank-Read mechanism: the realization that the velocity of a dislocation could never exceed the velocity of sound.

Bhat: When the width and amplitude of the incident impulse are large, shock waves travelling at speeds higher than the speed of sound develop. The strain gradients at the front have to be established in the short duration of the passage of the front, so that the strain rate becomes high. This strain rate can be achieved by either or both the terms in the classical equation $\dot{\varepsilon} = \rho b v + \dot{\rho} b s$ where the symbols are as explained in the text. Clearly, movement of the dislocations is required, v being associated with ρ and s with $\dot{\rho}$. If quasistatic dislocations alone account for the shock front, the shocked stress state would acquire permanence in the material. When shock waves can travel faster than the speed of sound, dislocations too can do the same. Physically both share the same important characteristics—strains and strain gradients in their vicinity.

S N Bandhopadhyay: The basic equations of plasticity like those for the velocity field, strain field, localized modes of deformation etc., do not appear to be taken care of properly in the finite element modelling of deformation.

Bhat: I think that the finite element method specialises in taking care of localized modes of deformation *without* sacrificing the basic equations of plasticity.

K A Padmanabhan: Did you measure the back stress in your experiment by either the stress reduction or stress relaxation method? Otherwise you are just introducing an adjustable variable.

Bhat: The existence of the back stress has not been experimentally established, and it cannot be measured directly. It is felt only by the dislocation that is moving in a structure. Even though the back stress is an adjustable empirical variable it has a certain consistency associated with it. When we introduce this parameter in order to bring the stress exponents to normal values, the anomalous activation energies in such materials automatically come down to normal values for diffusion. This certainly suggests that back stress is a parameter that has some fundamental significance associated with it.

V Balakrishnan: Regarding the computer simulation results on deformation, if you begin with empty spaces between grains, should you not expect further cavitation to occur? Or do you have hydrostatic stress, and the cavities just get filled in?

Bhat: We apply hydrostatic or uniaxial compressive loading in order to simulate hot pressing conditions.

V Balakrishnan: Within a single grain or element, what sort of compatibility conditions do you put in to ensure that no holes are formed?

Bhat: Strain compatibility conditions are put in to ensure that any particular mode has a unique displacement. Regarding your observations on the additivity *vs* interdependency of various creep mechanisms, another interesting example is provided by grain boundary sliding and diffusion creep. Grain boundary sliding occurs via the climb as well as glide of dislocations at the boundary. Climb generates vacancies which can in turn lead to vacancy creep.

Bull. Mater. Sci., Vol. 6, No. 4, September 1984, pp. 689–698. © Printed in India.

Superplasticity

K SRINIVASA RAGHAVAN

Department of Metallurgical Engineering and Department of Physics, Indian Institute of Technology, Madras 600036, India

Abstract. Superplasticity is the phenomenon of extraordinary ductility exhibited by some alloys with extremely fine grain size, when deformed at elevated temperatures and in certain ranges of strain rate. To put the phenomenology on a proper basis, careful mechanical tests are necessary. These are divided into (i) primary creep tests, (ii) steady state deformation tests, and (iii) instability and fracture tests, all of which lead to identification of macroscopic parameters. At the same time, microstructural observations establish those characteristics that are prerequisites for superplastic behaviour. Among the macroscopic characteristics to be explained by any theory is a proper form of the equation for the strain rate as a function of stress, grain size and temperature. It is commonly observed that the relationship between stress and strain rate at any temperature is a continuous one that has three distinct regions. The second region covers superplastic behaviour, and therefore receives maximum attention. Any satisfactory theory must also arrive at the dependence of the superplastic behaviour on the various microstructural characteristics. Theories presented so far for microstructural characteristics may be divided into two classes: (i) those that attempt to describe the macroscopic behaviour, and (ii) those that give atomic mechanisms for the processes leading to observable parameters. The former sometimes incorporate micromechanisms. The latter are broadly divided into those making use of dislocation creep, diffusional flow, grain boundary deformation and multimechanisms. The theories agree on the correct values of several parameters, but in matters that are of vital importance such as interphase grain boundary sliding or dislocation activity, there is violent disagreement. The various models are outlined bringing out their merits and faults. Work that must be done in the future is indicated.

Keywords. Superplasticity; ductility; stress and strain rate; grain boundary; dislocation creep; diffusional flow.

1. Introduction

Structural superplasticity is a high-homologous-temperature phenomenon exhibited by some metals and alloys which suffer extended or anomalous ductility under restricted circumstances. Elongations amounting to a few thousands per cent have been reported. When the conditions of deformation are changed, the same material does not possess the same ductility, and this has led to serious inquiries into the fundamental reasons for this behaviour. The technological off-shoot of this research, *viz.*, the development of many commercial alloys as well as forming processes, has not lagged behind. The aim of this paper is to summarize the observations made on superplastic materials and to identify their characteristics, to list the most important mechanisms identified as responsible for this behaviour, and to outline the more important models/theories presented so far. For recent reviews, see Edington *et al* (1976), Gifkins (1982), Hazzledine and Newbury (1976) and Padmanabhan and Davies (1980). Some points of controversy, which needs to be eliminated, are indicated.

2. Observations

The first systematic study on low-melting eutectics displaying superplasticity (Pearson 1934) is by now familiar. Observations on superplastic materials may be divided broadly into two classes: (i) those involving macroscopic aspects, from mechanical deformation studies; and (ii) those involving microscopic aspects, from microstructural observations.

2.1 *Macroscopic observations*

The variables are stress, strain, strain rate and temperature. However, a curve as shown in figure 1 is most common, showing the relationship between the flow stress σ and the strain rate $\dot{\varepsilon}$. This relationship can be mathematically written as

$$\sigma = A\dot{\varepsilon}^m, \tag{1}$$

where A is a constant and m is the strain rate sensitivity index (on a log-log plot, the slope of the curve). Three regions can be recognized which may conveniently be labelled I, II and III. Region II is the one of interest, where superplasticity is displayed. The peak values of m in this region coincide with maximum elongation, indicating a direct, if not linear, relation between them. In the superplastic region, m has values from 0·3 to 0·9. It may be mentioned here that all the three regions of figure 1 may not be found with a single experimental set-up.

The steady state strain rate in region II may be expressed in the familiar form of a diffusion-controlled process according to

$$\dot{\varepsilon} \propto \frac{Gb}{k_B T}(b/d)^p\,(\sigma/G)^n\,\mathrm{D}_0 \exp(-Q/RT), \tag{2}$$

where G is the shear modulus, b is the magnitude of the Burgers vector, and d the grain size. D_0 and Q denote a pre-factor and activation energy, respectively, while p and n are indices to be determined. Alternative equations to describe the behaviour of $\dot{\varepsilon}$ are also available in the literature. Their relative merits will be discussed in a later section.

The (thermal) activation energy in (2) may be determined by three different methods (Langdon 1982): (i) changing the temperature very rapidly during a test on a single

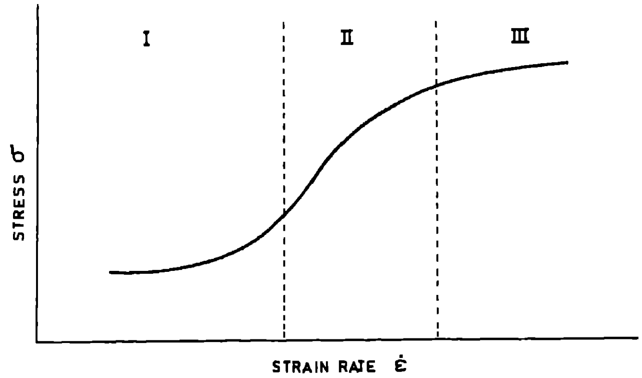

Figure 1. Flow stress plotted against strain rate.

specimen at constant stress; one finds

$$Q = \frac{R \ln (\dot{\varepsilon}_2 G_2^{n-1} T_2)\,(\dot{\varepsilon}_1 G_1^{n-1} T_1)}{[(T_2 - T_1)/(T_1 T_2)]}, \tag{3}$$

where $\dot{\varepsilon}_1$ and $\dot{\varepsilon}_2$ are the strain rates before and after the increase in temperature, and G_1 and G_2 the values of the shear modulus at the respective temperatures. (ii, iii) data from different specimens tested to steady state flow yield either

$$Q_\sigma = -R\left(\frac{\partial \ln \dot{\varepsilon} G^{n-1} T}{\partial(1/T)}\right)_{d,\sigma}, \tag{4}$$

or, in another version,

$$Q_{\dot{\varepsilon}} = R\left(\frac{\partial \ln (\sigma^n / G^{n-1} T)}{\partial(1/T)}\right)_{d,\dot{\varepsilon}}. \tag{5}$$

We shall assume the equality of these two versions. Typical values of Q for the three regions suggest an activation energy for self-diffusion, Q_{SD}, in region I, an activation energy for grain boundary diffusion in region II, and an activation energy equal to or lower than Q_{SD} in region III.

The different activation energy values led to the belief that several mechanisms were operative. It must be noted here that $m\,(=1/n)$ varies with strain rate at different temperatures. The index m itself can be measured in several ways (Edington *et al* 1976). With the experimental values of n and Q, the grain size index p can be obtained by plotting $\dot{\varepsilon}$ *vs* the grain size at constant stress and temperature. A p value between 2 and 3 is typical of a number of superplastic materials in region II.

2.2 *Metallographic observations*

The microstructural study of superplastic materials includes surface observation through optical microscopy, replica electron microscopy and scanning electron microscopy, and internal structure determination through transmission electron microscopy. On a few specimens, fracture and cavitation have also been studied. Of great importance is the relative contribution of grain boundary sliding to the total strain. Microstructural observations made on specimens undergoing superplastic deformation show that: (i) there is no massive recrystallisation, (ii) there is grain rotation (both ways), (iii) a new surface is created, (iv) texture is generally reduced: (a) texture weakens continuously with strain; (b) texture weakens to a steady distinct lower level; (c) texture generally weakens, while retaining some components. (In some cases, new texture is introduced). (v) there is little dislocation activity, (vi) there is deformation near grain boundaries, (vii) grain boundary sliding takes place, (viii) there is diffusional flow in region I.

It is clear that any model proposed to explain superplastic behaviour must satisfactorily account for these observations. It must also lead to the proper constitutive equations to give the activation energy, strain rate sensitivity index and the grain size index. The general conclusions that may be drawn from the results of metallographic observations are listed in the next section.

3. Characteristics of superplastic materials

From the various observations made, the following general conclusions may be drawn (Sherby and Ruano 1982): (i) The superplastic material must have a fine grain size ($\leqslant 10\ \mu$m), which must remain so, (ii) the presence of a second phase is necessary to inhibit grain growth, (iii) the mechanical strength of the second phase must generally be of the same order as that of the matrix, (iv) the second phase, if harder, should be finely distributed within the matrix, (v) the grain boundaries between the matrix grains should be of the high angle kind, (vi) the grain boundaries should be mobile so as to reduce stress concentration at triple points, (vii) the grains should be equiaxed in order to enable a grain boundary to experience a shear stress, allowing grain boundary sliding to occur, (viii) the grain boundaries must resist tensile separation.

4. The role of grains

Noting that superplasticity is confined to materials with fine grains which remain fine-grained and equiaxed, one can conclude that the grain centres must move as if the material were deforming homogeneously (Hazzledine and Newbury 1976). Thus it is necessary that the grains slide past one another during deformation. Sherby and Ruano (1982) have considered two phenomenological equations

$$\dot{\varepsilon} = 10^9 \frac{D_{\mathrm{GB}} b}{d^3} (\sigma/E)^2 \tag{6}$$

when grain boundary diffusion is thought to be the rate-controlling step, and

$$\dot{\varepsilon} = 10^8 \frac{D_{\mathrm{latt}}}{d^2} (\sigma/E)^2, \tag{7}$$

when lattice diffusion is considered to be the rate-controlling step. Experimentally a plot of $(\dot{\varepsilon} d^3/bD_{\mathrm{GB}})$ *vs* (σ/E) gives the correct exponent, namely, 2. Grain boundary sliding is therefore conceded to be the dominant mechanism.

Grain boundary sliding has been sought to be explained as brought about either by the motion of dislocations or by diffusion. In the dislocation model, crystal dislocations gliding to a grain boundary confine their subsequent motion to its vicinity. Special grain boundary dislocations whose Burgers vector is different and is related to a particular boundary may also move conservatively with the grain boundary. In this model, the strain-rate sensitivity m could be manipulated to be less than one, but then the grains would have to be elongated, which is not observed. On the other hand, the diffusion model considers the easy sliding of grains on smooth portions. If further sliding is opposed by irregularities, the rate of sliding is controlled by the movement or elimination of irregularities by diffusion. Such sliding could take place also at interphase boundaries. (These are classical notions and have been questioned by Padmanabhan and Davies 1980). However, since the strain rate is directly proportional to the applied stress, m will have a value of 1, which is at variance with experimental values. It would therefore appear that changes in the grain shape must also be taken into account.

4.1 *Grain strain*

Since structural continuity must be preserved, the grains must undergo some strain. This can be thought of in two different ways. Vacancy diffusion in the bulk can result in a change of shape, when the path of diffusion is fully across the grain. This Herring-Nabarro creep is given by the expression

$$\dot{\varepsilon} = (20\,D_{\text{latt}}\,\Omega)/(k_B T d^2), \tag{8}$$

where Ω is the atomic volume. When the diffusion path is confined to the grain boundary region, one has Coble creep, given by

$$\dot{\varepsilon} = 50\,D_{\text{GB}}\,\Omega\delta/(k_B T d^3). \tag{9}$$

Here δ is the width of the diffusion path. It may be noted that in both the above expressions, $m = 1$.

On the other hand, matter can be moved by conservative and non-conservative motion of dislocations. Nabarro (1967) has given two expressions, the first being a power dependence $\dot{\varepsilon} \propto \sigma^3$; the second for pipe-diffusion along the cores of dislocations, leads to $\dot{\varepsilon} \propto \sigma^5$. It may be mentioned that the grain size does not figure in these expressions. Friedel creep envisages a pile-up of dislocations against a grain boundary, from which the leading dislocation climbs into the grain boundary. The process is controlled by the climb rate of dislocations. This has been utilized to yield a relation $\dot{\varepsilon} \propto \sigma^2$. However, it is clear that grain elongation is unavoidable, and that as the grains elongate, the process must be exhausted. There is nothing in this picture to indicate the rotation of the grains. Moreover, no dislocation pile-ups have been observed in superplastic alloys.

4.2 *Interaction between grain strain and grain boundary sliding*

It is commonly believed that neither of the above can take place without the other, as they must together produce strain rates compatible with one another. The amount of strain produced by grain sliding is usually measured by surface markers, even though there is considerable controversy about the measurement. However experimentally the value $(\varepsilon_{\text{GBS}}/\varepsilon_{\text{tot}})$ varies between wide limits. It may be pointed out here that such measurements have been made at a strain of about 0·2, which is not typical of superplastic deformation. Stevens (1971) puts an upper limit of 0·62 to this ratio. Hazzledine and Newbury (1976) point out that at any instant the strain *rate* due to sliding is of the same order as the *rate* of strain of the grain.

Nevertheless, the idea has persisted that the strain due to grain boundary sliding must necessarily be less than the total strain. Consequently, an overwhelming majority of the mechanisms suggested invoke some process or the other to accommodate grain boundary sliding. It is against this background that different mechanisms are outlined in the next section. It is instructive to reproduce the figure from Edward and Ashby (1979) illustrating the different accommodation processes (figure 2).

5. Atomic mechanisms for superplasticity

It has been pointed out earlier that mechanisms employing diffusion creep or slip are unable to account for many of the observations satisfactorily, in particular for the large

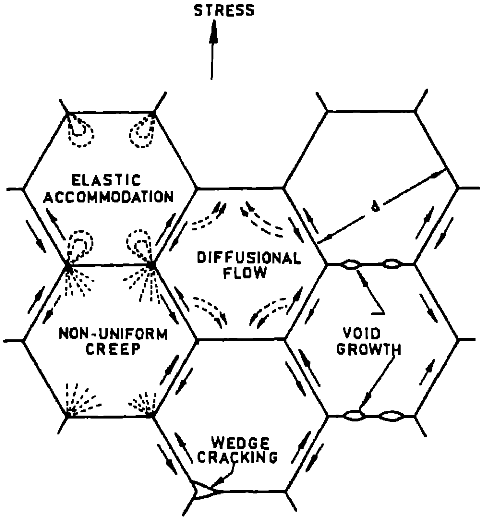

Figure 2. Consequences of grain boundary sliding (After Edward and Ashby 1974).

amount of grain boundary sliding. In this section, some more mechanisms will be listed where grain boundary sliding (GBS) is considered along with some accommodating processes.

5.1 *GBS accommodated by dislocation motion*

Ball and Hutchison (1968) put forward the idea that several groups of grains slide at once. When there is an unfavourably oriented grain, a stress concentration results which can be relieved by dislocation motion. The dislocations, which are necessarily in a pile-up, prevent further sliding until the lead dislocation climbs. Mukherjee (1971) contended that the grains move individually. Again a pile-up is invoked because dislocations are produced by irregularities in the grain boundaries. This itself is a major difficulty since, as mentioned earlier, no pile-ups have been seen. Moreover, the same dislocation motion will be rate controlling in region III too, and it would be impossible to distinguish between the two.

5.2 *GBS and diffusion creep*

Ashby and Verral (1973) proposed a grain switching event as central to their model. A group of four grains reacts to a tensile stress, sliding past each other and changing their shape to maintain continuity. These switching events occur randomly throughout the specimen with various clusters in different stages of the process. The accommodation strain is accounted for by bulk and boundary diffusion. While the model, which considers the topological aspects of the sliding process, satisfactorily explains most of the observations, there are large variations in the predicted values of parameters.

Hazzledine and Newbury (1976) have used the concept of grain emergence: as a group of adjacent grains slide, a grain from the layer below emerges at a location where a fissure would otherwise open up. Grain boundary migration occurs at the same time to restore the dihedral angles, resulting in the rounding off of the emergent grain and the curvature of all other grain boundaries. Having conceded that the phenomenon is too complicated for analysis, Hazzledine and Newbury proceed to give a viscoelastic model of superplasticity with several dashpot elements representing Nabarro, Coble and Friedel creep, as well as grain boundary and interphase sliding. The general conclusion is that a single comprehensive mechanism is not possible.

5.3 *GBS and core-mantle theory*

Gifkins (1976) proposed for each grain a non-deforming core surrounded by a mantle in which flow occurs. While the core contains statistically stored dislocations, the mantle, which is a few per cent of the grain diameter, contains geometrically necessary dislocations. The grain boundary dislocations piled-up against a triple edge are responsible by their movement for grain boundary sliding. The stress concentration of the pile-up is regarded as that of a freely slipping crack. By climb and glide the lead dislocations accommodate grain boundary sliding. Gifkins arrived at an appropriate equation to account for the observed parameters. Since the widths of the core and mantle are adjustable parameters, the experimental verification has been criticised as "an exercise in curve fitting". Further, no single mechanism has been identified as responsible for superplasticity.

Arieli and Mukherjee (1980) have also criticised this model on the ground that the deformation will slow down in time and eventually come to a stop, since many dislocations will be lost by annihilation. Also the stress concentration has been calculated by the Eshelby, Frank and Nabarro method, which does not apply to climb or any other deformation process.

Arieli and Mukherjee themselves employed a modified mantle behaviour. The small number of pre-existing dislocations are attracted to the boundary under the action of the applied stress and their own line-tension. The individual dislocations climb the short distance to the boundary and, in the process, create new dislocations by the Bardeen-Herring mechanism. At the boundary, the dislocations are annihilated. The eventual stress concentration created by the dislocations climbing into the boundary are relaxed by grain boundary diffusion. It may be noted here that there has been no experimental evidence for the Bardeen-Herring mechanism.

5.4 *Micromultiplicity*

As the grain boundary network has alternate sets of shear paths, the deformation continues even if grain boundary sliding is obstructed locally. In other words, the local stress conditions would alternatively enhance or decrease the importance of the obstacles. A number of processes, mentioned above, could be appropriately combined to give the total strain rate. It is obvious that this is also merely a curve-fitting exercise since the arbitrary constants of the constitutive equations can be adjusted appropriately.

5.5 *Unaccommodated GBS*

There has been considerable controversy as to whether grain boundary sliding is independent of diffusional strain. The work of Raj and Ashby (1972), Speight (1975) and Beere (1976) has shown that specimen strain can only develop when both sliding and diffusion can operate simultaneously. Therefore the deformation can be attributed to either sliding or diffusion, and can be described as diffusion-accommodated sliding or sliding-accommodated diffusion; in no sense can they contribute independently (Burton 1977).

Accordingly, Padmanabhan (1977) regards the upper limit of 60–65 % placed on the contribution from sliding to be a consequence of the assumption that both diffusion and sliding are present as separate steps. It is also held that the ideas concerning sliding in coarse-grained materials were not necessarily relevant to sliding in ultrafine-grained alloys, and that superplastic deformation is a result of pure grain boundary sliding of non-deformation grains that require no accommodation. Starting from the fundamental rate equation one arrives at a constitute equation

$$\dot{\varepsilon} = C\frac{\delta}{d^2}\sigma^n \exp(-Q_0/RT), \tag{10}$$

where C is a constant and δ is the jump distance in the grain boundary region. The stress exponent n may be recognized as the inverse of the strain-rate sensitivity index, m, and is shown to be a function of stress, grain size and temperature. Excellent agreement with experimental results is achieved, as is a demonstration of the transition to the region III in which climb-controlled motion of dislocations occurs.

6. The activation energy for superplasticity

The activation energy Q has been introduced in (2). It was mentioned there that different values are obtained for Q in the three regions of figure 1. This is done by treating the sigmoidal curve as a combination of three linear curves. The assumption of the equality of Q_σ and $Q_{\dot{\varepsilon}}$ ((4) and (5)) has also been mentioned. Padmanabhan (1981) has objected to the procedure on the grounds that (2) is empirical, that for each range a constant but different n value is assumed, and that within each range the activation energy is assumed to be independent of the temperature and the stress level of its evaluation. He has pointed out that the evaluation of the activation energy from an equation that has no physical basis is bound to lead to erroneous results, and that since n is continuously variable, there is no justification for treating this as a constant. At the junctions of region II with regions I and III the n value becomes ambiguous. Topologically and microstructurally regions I and II are not different. Only region III indicates a change of mechanism. Another serious objection is the treatment of an expression containing a T-dependent pre-factor as a true Arrhenius form. Padmanabhan (1981) has derived expressions for Q_σ and $Q_{\dot{\varepsilon}}$ (the values corresponding to the shear mode) and has pointed out that the best estimates of the real activation energy are only attained when data pertaining to the range in which m is large (~ 1) are used. It is regrettable that many of the leading workers in the field have not recognized the force of these arguments.

7. The role of dislocations in superplasticity

Even though many of the models invoke dislocations to explain superplasticity, there has been no direct experimental evidence to support dislocation activity. However, Edington *et al* (1976) have argued, taking Nicholson's (1972) experiments as an example, that dislocations might have been active or that they might have been obstructed by precipitates. Padmanabhan (1980) has argued that this was unlikely. He has further held that any dislocation seen was the residue of the initial configuration or the existence of local stress concentrations or a favourable strain rate at which dislocation motion commences. *In situ* experiments have also failed to reveal substantial quantities of dislocation.

Melton and Edington (1973) have maintained that since (i) statistically significant differences in the angular distance of the dislocations from their nearest possible glide planes were found as a function of the deformation rate; (ii) the Burgers vector distribution changed as a function of strain rate; (iii) increasing the initial density by cold working prior to superplastic deformation did not produce any detectable differences in the Burgers vectors and densities after superplastic deformation; (iv) there is an equilibrium dislocation density typical of superplastic flow and (v) dislocations are also observed at strain rates an order of magnitude less than that corresponding to $m_{\max}$, one must conclude that crystallographic slip plays a small but significant role in superplasticity. Padmanabhan (1980) has countered these arguments by citing experimental results accepted by Melton and Edington themselves. It therefore appears that the available experimental evidence could support either point of view. Lücke (1974) has pointed out that any sequence of deformation processes leading to a given strain tensor will give the same texture. Hence the operating mechanisms cannot be deduced solely from texture results. TEM has provided no evidence for dislocation activity.

8. Future work

To set at rest the controversy regarding the mechanism of superplasticity, work is required along the lines indicated below: (i) a better understanding of the structure of grain boundaries and interphase boundaries, (ii) a correct analytical form for the flow stress as a function of strain rate, temperature and grain size, (iii) unequivocal experimental evidence to support or discount dislocation activity, (iv) an understanding of the role of the stacking fault energy, (v) an unambiguous interpretation of experimental curves such as the double sigmoidal plot of figure 1.

It is to be hoped that there will be a happier conclusion to superplasticity than in the case of work hardening, in which field the workers have apparently agreed not to agree.

Acknowledgements

The author is indebted to Prof. K A Padmanabhan of IIT, Madras for many valuable clarifications.

References

Arieli A and Mukherjee A K 1980 *Mater. Sci. Eng.* **45** 61
Ashby M F and Verral R A 1973 *Acta Metal.* **21** 149
Ball A and Hutchison M M 1968 *Met. Sci. J.* **3** 1
Beere W B 1976 *Met. Sci. J.* **10** 133
Burton B 1977 *Diffusional creep in polycrystalline materials* (Ohio: Trans Tech Publications)

Edington J W, Melton K N and Cutler C P 1976 *Prog. Mater. Sci.* (eds) B Chalmers, J W Christian and T B Massalski (Oxford: Pergamon Press) Vol. 21 p. 61
Edward G and Ashby M F 1979 *Acta Metal.* **27** 1505
Gifkins R C 1976 *Met. Trans.* **A7** 1225
Gifkins R C 1982 in *Superplastic forming of structural alloys* (eds) N E Paton and C H Hamilton, The Metallurgical Society of AIME 3–26
Hazzledine P M and Newbury D E 1976 in *Grain boundary structure and properties* (eds) G A Chadwick and D A Smith (New York: Academic Press) Chap. 7
Langdon T E 1982 in *Superplastic forming of structural alloys* (eds) N E Patson and C H Hamilton, The Metallurgical Society of AIME 27–40
Lücke K 1974 *Can. Metall. Q.* **13** 261
Melton K N and Edington J W 1973 *Met. Sci. J.* **7** 172
Mukherjee A K 1980 *Mater. Sci. Eng.* **8** 83
Nabarro F R N 1967 *Philos. Mag.* **16** 231
Nicholson R B 1972 in *Electron microscopy and structure of materials* (ed) G Thomas (University of California) 682
Padmanabhan K A 1977 *Mater. Sci. Eng.* **29** 1
Padmanabhan K A 1980 *Met. Sci.* **14** 506
Padmanabhan K A and Davies G J 1980 *Superplasticity* (Berlin: Springer Verlag)
Padmanabhan K A 1981 *J. Mater. Sci. Lett.* **16** 531
Pearson C E 1934 *J. Inst. Met.* **54** 111
Raj R and Ashby M F 1972 *Met. Trans.* **3** 1937
Sherby O D and Ruano O A 1982 in *Superplasticity forming of structural alloys* (eds) C E Paton and C H Hamilton, The Metallurgical Society of AIME 241–256
Speight M V 1975 *Acta Metall.* **23** 779
Stevens R N 1971 *Philos. Mag.* **23** 265

Bull. Mater. Sci., Vol. 6, No. 4, September 1984, pp. 699–700. © Printed in India.

Grain boundary-dislocation interactions*

S RANGANATHAN

Department of Metallurgy, Indian Institute of Science, Bangalore 560012, India

Abstract. Our current understanding of the structure of grain boundaries will be described first. The structure of low angle boundaries can be rigorously described in terms of arrays of dislocations. The structure of high angle boundaries continues to defy a complete and rigorous description. A model has been developed based on coincidence site lattices. This model postulates the presence of grain boundary dislocations even at high angles of misorientation to accommodate the deviation from exact coincidence conditions. The Burgers vectors of such grain boundary dislocations can be found by the translation vectors of the DSC lattice. An interesting point is that the Burgers vectors are not lattice translations. Hence the dislocations are confined to the surface of the boundary and cannot move into the grain. Alternative descriptions of the structure of grain boundaries make appeal to the Bernal type of polyhedral voids that occur in metallic glasses. A brief discussion of the strength of this approach will be outlined. Dislocations at grain boundaries can affect both grain boundary migration and sliding. The possible mechanisms for these phenomena will be described. The importance of understanding these mechanisms to explain deformation of metals at high temperatures will be stressed.

Discussion

M Youssuff: Is it possible to include vacancies in the approach you have described?

S Ranganathan: This is an important question; the answer is not known.

P Rodriguez: How do you explain migration with the help of imprisoned grain boundary dislocations?

Ranganathan: It is easy to explain this migration in a framework similar to Aronson's theory of the growth of precipitates. For example, in cases where the ledge mechanism operates, the ledges move along the plane in which the precipitate is growing.

Rodriguez: If we provide energy in the form of stress, is it possible that the smaller grain boundary dislocations combine to form larger mobile lattice dislocations?

Ranganathan: It should be possible, but no clear evidence is available.

S Ray: Can only certain lattice vectors be split into DSC vectors?

Ranganathan: Any lattice vector can be broken into DSC vectors, since the DSC lattice consists of both the lattice positions.

Ray: Are ledges inherited from the energetics of growth? Are these a common feature?

Ranganathan: They need not be inherited from the growth. Yes, they are a reasonably common feature.

---

* Only a summary is presented.

S Ramaseshan: Why is a polycrystalline material stronger than a real single crystal?

Ranganathan: In a polycrystalline material, the dislocations are stopped at the grain boundaries, thereby impeding their movement.

Ramaseshan: In the Bernal picture, could a polycrystalline material be considered as a composite of grains and grain boundaries?

Ranganathan: One could think of the polycrystalline material as a two phase material—the grain boundaries and the grains. The idea, though found in the literature, has no validity. We have to consider the boundary as a whole.

T V Ramakrishnan: Is there any evidence for the existence of dislocations and their movement?

Ranganathan: We can actually see dislocations by etch, pit techniques, field-ion microscopy, electron microscopy, etc.! There is no doubt about the movement of the boundary of a bicrystal when it is loaded in the form of a cantilever.

G Srinivasan: Should not the energetics contain all sorts of things, including contributions from the electrons?

Ranganathan: I am tempted to agree with this since all existing theories seem to be succeeding only up to a point. There seems to be something basic that is missing.

Srinivasan: Could the unique microscopic properties shown by a metallic glass (*e.g.*, the electronic properties and ductility) be translated to a microscopic description of grain boundary sliding?

Ranganathan: One would indeed like to do that. However we are rather ignorant about both these areas and hence not much progress has been made.

Srinivasan: Is this analogy being used only with reference to structure?

Ranganathan: Right now, for the structure and the geometry.

K R Rao: As the dislocation structure can change owing to a variety of factors, it appears that the structure of the specimen is really transient—how does one ensure reproducible conditions in this sense?

Ranganathan: The underlying structures are not as transient as appears at first sight, but careful investigation of this point is certainly in order.

A P Pathak: Is there a study of the variation of the strength with respect to the orientation of the boundaries?

Ranganathan: I think this has been done for bicrystals, but not for polycrystals.

Bull. Mater. Sci., Vol. 6, No. 4, September 1984, p. 701. © Printed in India.

Instabilities in first order phase transitions*

S BANERJEE

Metallurgy Programme, Bhabha Atomic Research Centre, Bombay 400085, India

Abstract. Majority of the metallurgical phase transformations are first-order transitions which occur by the nucleation and growth process near equilibrium conditions. In recent years, homogeneous transformation has been reported in some of these cases at conditions significantly away from those of equilibrium. In this paper some of these transformations will be discussed. In the first part of the presentation the thermodynamic and the mechanistic distinctions between first and higher order phase transformations will be discussed and a comparison made between homogeneous and heterogeneous modes of phase transformations and those of deformation. Based on Landau's free energy *vs* generalised order parameter plots, an instability temperature is defined for first order phase transformations below which the transformation can occur by a continuous amplification of a concentration or a strain fluctuation. In the second part experimental evidence in support of the continuous mode of transformations in two ordering reactions are presented. These are: (i) a transition from the short range to the long range chemical order in Ni_4Mo (Dla structure) and (ii) a hybrid displacive-replacive ordering in Zr_2Al ($B8_2$ structure). In order to make the continuous mode operative in these first order transformations (which is possible at a high "supercooling"), radiation in the former and rapid quenching in the latter were employed. In the last part, the martensitic transformation and the shape memory effect is described in terms of Landau's plots and the mechanical and thermodynamical consequences of the model are discussed.

Discussion

M Youssuff: What is the criterion by which we can distinguish whether the development of long-range order is by nucleation and growth or by a continuous mechanism?

S Banerjee: The only criterion is whether we are below T_0 or not. Also, not all ordering can be described in terms of compositional modulations.

V K Wadhawan: What is order parameter in Ni_4Mo?

Banerjee: The population density of Mo atoms on a given lattice site.

V C Sahni: Is there any example where there is a formation volume and the transformation is homogeneous?

Banerjee: It is possible that the volume change is very small like in Ni_4Mo.

Sahni: How is the expansion of free energy in terms of the order parameter justified in a first order phase transition (since the OPM is discontinuous)?

Banerjee: It cannot be justified.

---

* Only a summary is presented.

Bull. Mater. Sci., Vol. 6, No. 4, September 1984, pp. 703–716. © Printed in India.

Deformation and martensitic transformation

V SEETHARAMAN

Metallurgy Programme, Reactor Research Centre, Kalpakkam 603 102, India

Abstract. The influence of applied stresses and imposed plastic deformation on the martensitic transformation of a parent phase is described. Changes in mechanical properties such as flow stress, work hardening rate, fracture toughness, etc brought about by strain-induced martensitic transformation are briefly examined. In the absence of appreciable dislocation glide, atomic displacements associated with glissile boundaries are highly ordered and reversible modes of (plastic or nonlinear pseudoelastic) deformation. Such processes lead to large strains and are encountered in deformation twinning, martensitic transformations and in the reorientation of martensite units. The reversibility leads to phenomena such as elastic twinning, thermoelastic martensites, superelasticity, shape memory and two-way shape memory effects, and rubber-like behaviour. These are discussed using a unified approach based on thermoelastic equilibrium. The shape memory effect suggests several potential applications of the martensitic transformations in non-ferrous alloys in which the effect is most commonly observed. Recent developments in this area are reviewed with special reference to the prerequisites for the effect and the influence of metallurgical processing on the extent of shape recovery.

Keywords. Plastic deformation; pseudoelasticity; shape memory effect; martensitic transformation.

1. Introduction

A martensitic transformation is a first-order solid-state structural transformation that is diffusionless, involves relative atomic motion by amounts smaller than the interatomic spacing, and exhibits a lattice correspondence between the parent and product structures. The transformation is generally adiabatic, athermal and exhibits hysteresis. It proceeds by a shear mechanism, and the net macroscopic distortion of the crystal can be regarded as an invariant plane strain. This implies that the interface between the parent phase and the growing martensite crystal is a plane of zero average macroscopic distortion. This feature has been verified in several experiments on the surface relief effect produced by the transformation. According to the phenomenological theories proposed by Wechsler *et al* (1953) and by Bowles and Mackenzie (1954) it is possible to consider the invariant plane strain as a superposition of the following components: a lattice strain (Bain strain), a lattice-invariant shear, a rotation and a dilation. The lattice-invariant shear required can manifest itself as slip, twinning or faulting of the martensite units. Besides, the different variants of martensite units formed from a parent phase crystal are generally arranged as three dimensional self-accommodating groups such that the total macroscopic strains are minimised.

Martensitic transformations can be induced by the application of external stress or by lowering the temperature. The former possibility arises because the free enthalpies of the parent phase and the martensite, and their equilibria, depend not only on the temperature and the composition but also on the stress; moreover, the nucleation and growth processes are associated with shear strains and these couple to the internally or externally applied stresses. This paper deals with the relationship between martensitic transformations and deformation (both recoverable and nonrecoverable). We first consider the thermodynamic and kinetic aspects of stress-assisted and strain-induced martensitic transformations. This is followed by an account of an experimental study of the influence of plastic deformation at cryogenic temperatures on the martensitic transformation in an austenitic stainless steel. Next, we deal with the phenomenon of transformation-induced plasticity and its applications. Finally, a series of related phenomena including thermoelasticity, pseudoelasticity and the shape memory effect are discussed from a unified point of view based on the reversibility of the deformation caused by the migration of glissile interfaces.

2. Stress-assisted and strain-induced martensitic transformations

The driving force for the spontaneous martensitic transformation is the difference ΔG^c in the chemical free energy between the parent and the martensite phases. It is known that the transformation does not set in at the equilibrium temperature T_0 ($\Delta G^c(T = T_0) = 0$). Instead, it requires substantial undercooling, and commences at a temperature $M_s < T_0$. If the parent phase is stressed at a temperature $T (T_0 > T > M_s)$, a mechanical driving force, U, is added to the chemical driving force; stress-assisted martensitic transformation occurs at T if

$$|\Delta G^c(T)| + U \geqslant |\Delta G^c(M_s)|. \tag{1}$$

U is a function of the stress and the orientation of the martensite crystal with respect to the parent phase. Patel and Cohen (1953) have shown that

$$U = \tau\gamma_0 + \sigma\varepsilon_0, \tag{2}$$

where τ is the shear stress resolved along the transformation shear direction on the habit plane, γ_0 is the transformation shear strain, σ is the dilatational stress resolved normal to the habit plane, and ε_0 is the normal component of the transformation strain. If a single crystal of the parent phase is stressed according to the geometry shown in

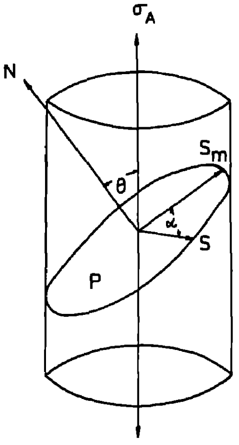

Figure 1. Geometry of stressing in a single crystal. P is the habit plane having N as its normal. S is the shear direction and S_m is the maximum shear direction of the applied stress on the habit plane. (The other symbols are explained in the text).

figure 1, τ and σ can be expressed for any given orientation of the martensite plate as

$$\left.\begin{aligned}\tau &= 0{\cdot}5\,\sigma_A \;\sin 2\theta\cos\alpha \\ \sigma &= \pm 0{\cdot}5\,\sigma_A(1+\cos 2\theta)\end{aligned}\right\} \tag{3}$$

where σ_A is the absolute value of the applied stress, θ is the angle between the axis of the applied stress and the normal to the habit plane, and α is the angle between the shear direction of the transformation and the maximum shear direction of the applied stress on the habit plane (the sign of σ specifies whether the stress is tensile or compressive). If the chemical driving force (ΔG^c) decreases linearly with an increase in temperature above M_s, it is logical to expect that the critical applied stress for martensite formation should increase linearly with temperature. In practice, it is observed that the critical stress shows a linear dependence only between M_s and M_s^σ (figure 2). Beyond M_s^σ the stress required would exceed the flow stress of the parent phase and thus cause plastic deformation of this phase. Olson and Cohen (1972) have postulated that in the temperature range $M_s^\sigma < T < M_d$ the nucleation of martensite is aided by the large number of defects caused by the plastic deformation, and hence the transformation is considered to be strain-induced (M_d is the highest temperature at which the

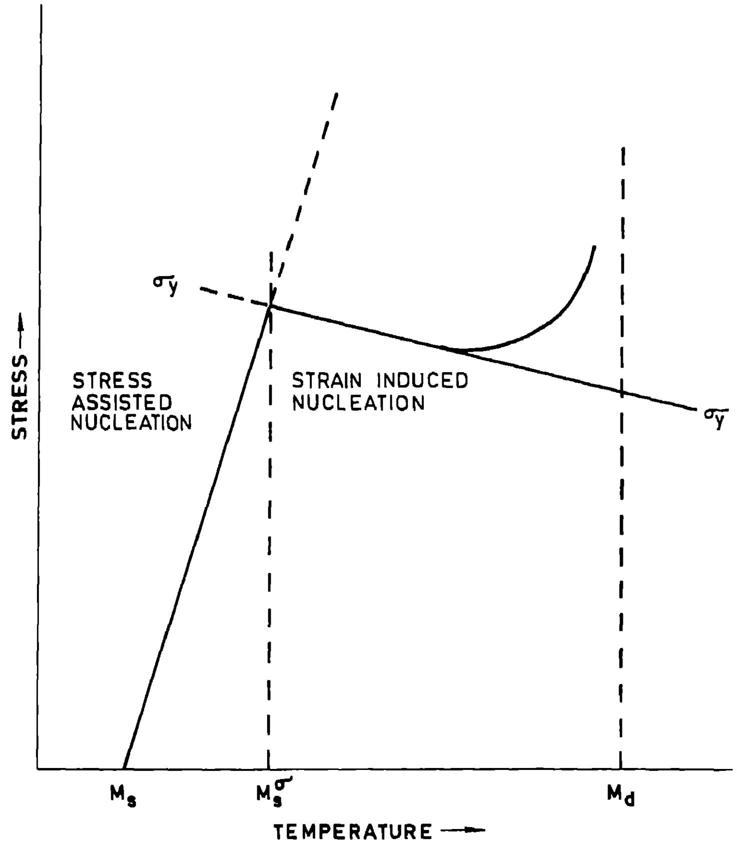

Figure 2. Variation of the critical stress required for the onset of the transformation at different temperatures. (The regimes of stress-assisted and strain induced transformation are indicated.)

transformation can be induced; $M_d < T_0$). There is thus a fundamental difference between stress-assisted and strain induced transformations.

The volume fraction f of the martensite formed at any given level of plastic strain ε_p is given by (Olson and Cohen 1975; Murr *et al* 1982)

$$f = 1 - \exp\{-\beta[1 - \exp(-\alpha\varepsilon_p)]^n\} \tag{4}$$

where α, β and n are temperature dependent parameters. Recently, Tamura (1982) has suggested that the transformation kinetics should be based on the stress rather than the strain, and has proposed a different expression for f that depends on σ_A, γ_0 and ε_0. The role of plastic deformation in the strain-induced nucleation of martensite has been a subject of controversy. Olson and Cohen (1972, 1976) firmly believe that the intersection of slip bands produced as a result of plastic deformation acts as a nucleation site for martensite. In contrast, Suzuki *et al* (1977) and Onodera and Tamura (1979) have expressed the view that the local stress concentration near the grain boundaries due to the pile-up of dislocations would raise the applied stress to values obtained by the extrapolation of the straight line in figure 2 well beyond M_s^σ.

3. Strain-induced martensitic transformation in a type 316 austenitic stainless steel

Type 316 austenitic stainless steel does not transform to martensite spontaneously even when it is cooled down to 77 K. In contrast, plastic deformation at low temperatures leads to the formation of two different types of martensites: ε martensite with an hcp structure and α martensite with a bcc structure. Figure 3 illustrates the variations in the volume fractions of these phases with plastic strain at 77 K. The main conclusions that can be drawn from this plot are: (i) With increasing plastic strain, the amount of ε phase present increases to a maximum and then decreases gradually, (ii) Detectable amounts of the α phase are formed only beyond a certain minimum value of the plastic strain, beyond which its volume fraction increases continuously with the plastic strain. These results imply that the α martensite forms at the expense of the ε martensite.

Plastic deformation of the austenite (γ) at temperatures below 220 K leads to the progressive formation of wide stacking faults, clusters of overlapping stacking faults, and finally, thin sheets the ε martensite. Transmission electron microscopy of the deformed samples reveals a large number of shear bands on $\{111\}_\gamma$ planes. These bands

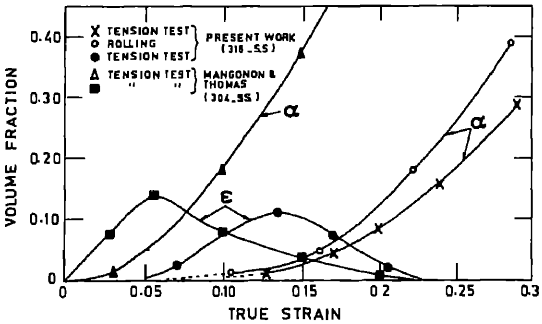

Figure 3. Variation of the volume fraction of the ε and α martensites in a type 316 stainless steel as a function of the true strain at 77 K. The results of Mangonon and Thomas (1970) in a type 304 stainless steel are shown for comparison.

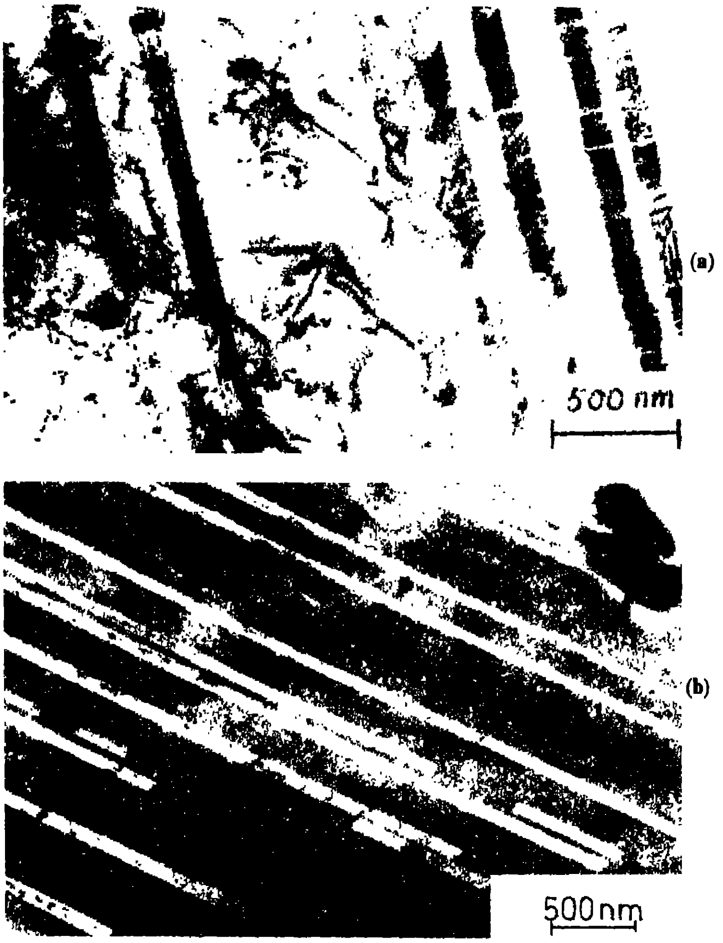

Figure 4. Transmission electron micrographs of type 316 stainless steel deformed at 77 K up to 5 % strain. (a) wide stacking faults forming on the $\{111\}_\gamma$ planes, (b) dark field micrograph showing one of the variants of the deformation bands.

consist of overlapping faults, deformation twins and the ε martensite, the relative proportions of which vary with the temperature, strain rate and the extent of deformation. Typical examples of the microstructure obtained after tensile deformation at 77 K up to 5 % strain are shown in figure 4. When the austenite is subjected to strains larger than 15 % at 77 K, tiny crystals of α are observed at the intersections of two different variants of the shear bands. On continuing the deformation, the α nuclei grow along the cylinderical axes of the rod-shaped volumes comprising the intersections of these bands. The above experimental evidence obtained by x-ray diffraction and electron microscopy techniques proves conclusively that the ε martensite forms as an intermediate phase in the $\gamma \rightarrow \alpha$ transformation, the sequence being representable as $\gamma \rightarrow \varepsilon \rightarrow \alpha$ (Seetharaman 1976; Seetharaman and Krishnan 1981).

4. Transformation-induced plasticity (TRIP)

As already mentioned, martensitic transformation can be considered as a mode of plastic deformation of the parent phase that competes with other modes such as slip and twinning. Therefore, if martensite forms dynamically during the mechanical testing of any alloy, the mechanical properties of the alloy would inevitably be altered considerably. Figure 5 shows the stress-strain curves of the Fe-29 Ni-0·26 C austenitic alloy deformed in tension at different temperatures (Tamura *et al* 1970a). The values of M_s and M_d for this alloy are 213 K and 298 K, respectively. The large serrations observed in the curves at 223 K and 203 K are due to the formation of stress-assisted martensite. On the other hand, the curves corresponding to 243 K or 263 K exhibit very fine serrations and also substantial tensile elongation: the samples corresponding to these curves show evidence of the presence of strain-induced martensite. Such an enhancement in the ductility of an alloy owing to the onset of strain-induced martensitic transformation is known as ‘transformation-induced plasticity (TRIP).

The tensile properties of three different austenitic steels in the temperature range $M_s^\sigma < T < M_d$ are shown in figure 6 (Tamura *et al* 1970b). The inverse temperature dependence of the 0·2 % proof stress observed between M_s^σ and M_s (figure 6a) is due to the transformation strain caused by the stress-assisted martensite formed before the yielding of the parent austenite phase. The total elongation exhibits a maximum at temperatures just above M_s^σ. Such an enhancement in elongation has been attributed to the suppression of the necking phenomenon. This, in turn, is due to the increase in the work-hardening rate caused by the strain-induced martensitic transformation. Similar increases in the work-hardening rates have also been encountered in austenitic stainless steels (Angel 1954; Ludwigson and Berger 1969; Seetharaman 1976). The hardness of the martensite increases with increase in the carbon content of the steel. It follows that, for a given volume fraction of martensite, the increase in the work-hardening rates will be high for high carbon steels. Thus the TRIP phenomenon will be dominant in austenitic steels containing high levels of carbon.

Although ductility can be enhanced markedly by TRIP, strengthening must be achieved by other methods. Zackay *et al* (1967) developed an ultra-high-strength steel called TRIP steel in which the ductility is enhanced by the TRIP of the retained austenite

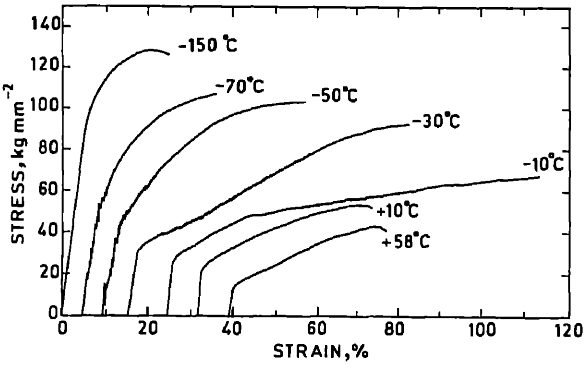

Figure 5. Stress strain curves of Fe-29Ni-0·26C austenitic alloy deformed in tension at different temperatures.

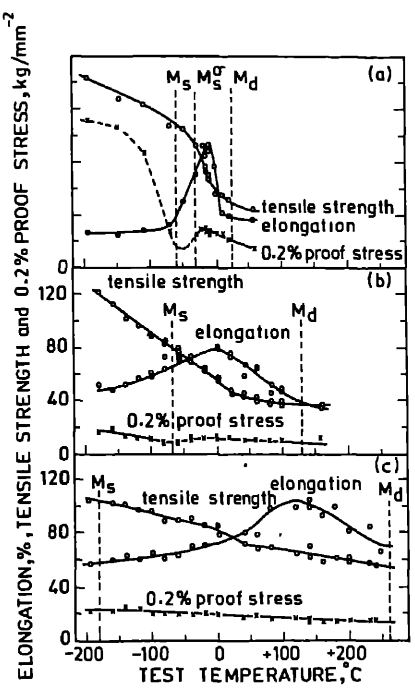

Figure 6. Effect of test temperature on tensile properties in three different types of metastable austenitic steels (a) Fe-29Ni-0·26C, (b) Fe-19-Cr-11Ni, (c) Fe-24Mn-0·26C.

while the strength is increased by the ausformed martensite. TRIP steels exhibit good properties at low temperatures because of the retained austenite, and are therefore suitable structural materials for chemical plants, containers for liquified gases, armour plates and earthquake dampers. Furthermore, the TRIP phenomenon is very effective in improving the formability, particularly the deep drawability, of austenitic stainless steels (Divers 1964).

5. Thermoelasticity, pseudoelasticity and shape memory effect

The thermodynamics of the growth of the martensite plate can be represented by the following energy balance:

$$G_T^c + U \gtreqless \tau_0\gamma_0 + \sigma_0\varepsilon_0 + S_M A + \xi\gamma_0, \tag{5}$$

where τ_0 is the intrinsic shear resistance of the parent phase against the shear strain γ_0, σ_0 is the intrinsic tensile resistance of the parent phase against ε_0, S_M is the specific surface energy of the parent-martensite interface, A is the shape factor of the martensite, and is a dissipation factor. Let us exclude the trivial case of the stoppage of a growing plate by a grain boundary or some equivalent obstacle. Then an equality in (5) implies that any small change in the thermal or mechanical components of the driving force will cause growth or shrinkage of the martensite plate. This equilibrium condition forms the basis of the thermoelastic martensitic transformation. A thermoelastic martensite forms and grows continuously as the temperature is lowered, and shrinks and vanishes as the temperature is raised. Figure 7(a) gives a schematic representation of this transformation indicating the increase in the internal stress σ_i and the volume fraction f of the martensite, these being measures of the progress of the transformation.

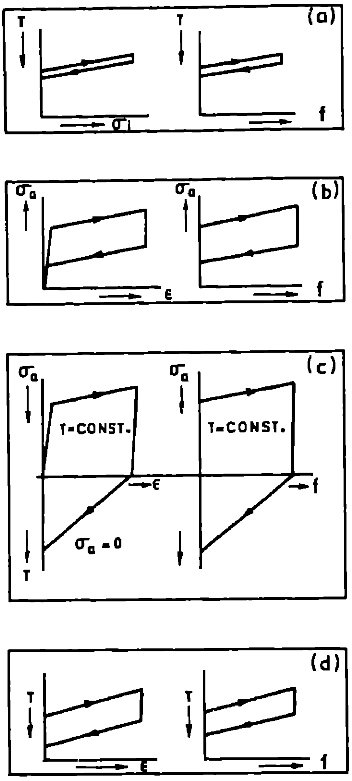

Figure 7. Schematic representation of (a) thermoelasticity (b) pseudoelasticity (c) shape memory effect and (d) two-way shape memory effect.

There is no sudden appearance or disappearance of large groups of martensite plates (the burst phenomenon).

Pseudoelastic behaviour (figure 7b) is a complete mechanical analogue of the thermoelastic transformation. In this case, the transformation proceeds continuously with increased applied stress. The 'plastic' strain is caused by the shape strain accompanying the formation of martensite. Recovery of the shape strain therefore occurs when the transformation is reversed. This type of pseudoelastic behaviour is obtained when the material is stressed at temperatures higher than the finish temperature A_f for the reverse transformation. Pseudoelasticity can also occur by the reorientation of the existing martensite variants (Krishnan *et al* 1974). Other terms such as superelasticity, ferroelasticity, rubber-like behaviour etc. have sometimes been used to describe pseudoelastic behaviour.

The shape memory effect arises if a macroscopic deformation is accompanied, as before, by a martensitic transformation which is not reversed on removal of the applied stress; in a second step the reverse transformation and a concomitant reversal of the macroscopic deformation are induced by heating. Figure 7(c) shows this behaviour schematically. The upper half represents the response of the specimen to the isothermal variation of the applied stress, while the lower half pertains to the effect of subsequent heating. The idealised curves shown in figure 7(a–c) suggest close interrelations between these processes. If the stress hysteresis in a pseudoelastic transformation is so large that the reverse transformation is incomplete at $\sigma_a = 0$, then the residual martensite can be reverted by heating, *i.e.*, by employing the shape memory effect. This clearly demonstrates the interchangeability of stress and temperature as state variables.

A two-way shape memory effect occurs when the specimen deforms spontaneously during the cooling half-cycle and recovers during the heating half-cycle (figure 7d). An alloy which exhibits the one-way or normal shape memory effect can often be converted into a reversible memory alloy by "training" with a few cycles of the one-way type, or (more effectively), a few pseudoelastic cycles above M_s (Christian 1982). The maximum strains of the reversible effect are normally much smaller than those of the simple shape memory effect for a given alloy.

6. Common characteristics of materials exhibiting the memory effect

On the basis of extensive investigations conducted on Au-Cd, In-Tl, Ni-Ti, Cu-Zn, Fe-Pt and Cu-Al-Ni alloys, Wayman and Shimizu (1972) have concluded that the following conditions are necessary for an alloy to exhibit the shape memory effect: (i) The martensitic transformation should be a thermoelastic one; (ii) the parent phase and the martensite should be ordered; (iii) the lattice-invariant shear must occur by twinning rather than by slip.

While the first two conditions hold good for all the alloys investigated so far, the last condition, namely, the internal twinning of martensite does not appear to be very general. In fact, there is ample evidence in the literature to show that martensites in silver- and copper-based ordered alloys contain extensive and periodic faulting in the stacking sequence of the close packed planes, and these alloys do exhibit the shape memory effect to a significant extent.

6.1 *Thermoelastic martensites*

A thermoelastic martensite is generally characterised by (i) a small driving force, (ii) a small shear component of the shape strain, (iii) a small volume change, and (iv) a matrix with a high elastic limit (Dunne and Wayman 1973; Tong and Wayman 1975). It is clear that a thermoelastic martensite crystal must have a perfectly coherent interface with the surrounding matrix and that the coherence must be maintained during the whole process of growth or shrinkage. This is possible only if the volume change associated with the transformation is small. Furthermore, the small value of the thermal hysteresis is a direct consequence of the smallness of the driving force.

6.2 *Effect of ordering*

It is found that some degree of ordering (usually, long range ordering) is present in all parent phases which are known to transform thermoelastically. As a case in point, the ordered Fe_3Pt alloy undergoes a thermoelastic martensitic transformation and also exhibits the shape memory effect, while disordered specimens of the same composition display neither.

According to the phenomenological theory of martensitic transformation (Wayman 1964), the habit plane is a plane of zero average distortion. However, localised distortions still persist at the interface though they are macroscopically arranged out by the lattice-invariant shear. This fine-scale distortion is not expected to exceed the elastic limit of the matrix in ordered alloys (because of the order-hardening effects), but in

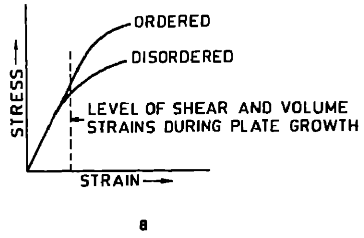

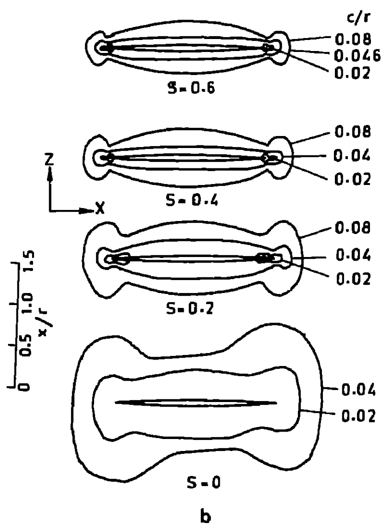

Figure 8. (a) Schematic stress-strain curves for the disordered and ordered states of the parent phase. (b) Matrix yield stress contours around an oblate spheroidal plate of an Fe-Pt alloy. The plate is in the x-y plane and the contours are drawn for varying values of the long range order parameter, S and the aspect ratio, c/r.

disordered alloys the elastic limit is evidently exceeded and the interface eventually becomes incoherent. This is explained with the help of the hypothetical stress-strain curves shown in figure 8(a). Ling and Owen (1979) have re-examined the plastic deformation around a growing thermoelastic plate, and have predicted the size of the plastic zone around plates of various shapes and in materials with varying long-range order (figure 8b). In the disordered alloy (longrange order parameter $S = 0$), general yielding has occurred all around the isolated plate with an aspect ratio $c/r = 0{\cdot}02$. However, when $S > 0{\cdot}4$, such yielding is confined to a small volume near the radial edge. It is therefore clear that the primary role of ordering is to strengthen the parent and the martensite phases without affecting significantly the value of the shear modulus, μ, thereby increasing the ratio σ_y/μ of the yield strength to μ.

The ordered arrangement of atoms is also important when one considers the reverse transformation upon heating. If a material is to exhibit the shape memory effect, it is essential that all the martensite plates formed in a single crystal of the parent phase should revert as a unit to the original orientation of the parent phase. When an ordered parent phase transforms to an ordered martensite, the arrangement of atoms, though ordered, exhibits a lower symmetry in the latter phase (following the deformation of the lattice). Considering that another lattice distortion must be operative during the inverse transformation, it follows that the number of reverse lattice correspondences is more limited than in cooling transformation, one imposes the restriction that the original ordered arrangement in the parent phase be recovered. In fact, in Cu-Al-Ni alloys it has been shown that there is only one lattice correspondence between the parent and the martensite phases which maintains the original order (Wayman and Shimizu 1972). Accordingly, the ordered martensite is obliged to revert to the original orientation of the parent phase in this case.

6.3 *Lattice softening*

Shape memory alloys exhibit interesting and anomalous behaviour with respect to the temperature dependence (near M_s) of the electrical resistivity, elastic constants, etc. Moreover, 'extra' reflections appear in the x-ray and electron diffraction patterns taken at temperatures just above M_s. The damping capacity of these alloys increases anomalously to reach a maximum near M_s. Among all these pre-martensitic phenomena, the most important and striking feature is that the temperature derivative of the elastic shear constant $\mathrm{d}C'/\mathrm{d}T$ (where $C' = (C_{11} - C_{12})/2$) is large and positive. Zener (1947) has explained the low values of $C_{11} - C_{12}$ observed in β-brass for $T \approx M_s$ on the basis of the instability of the bcc lattice with respect to a $(110)\,[1\bar{1}0]$ shear. Thus it is suggested that the very low value of the thermodynamic driving force required at M_s is due to the assistance by long wavelength phonon instabilities of the nucleation of martensite in a soft lattice. As with ordering, it is probable that the major, and certainly the most direct consequence, of lattice softening in the nature of martensite growth would be with regard to the ratio σ_y/μ. A decrease in μ increases the magnitude of the shear strain which can be accommodated elastically.

6.4 *Mechanisms for the shape memory and related effects*

The most remarkable consequence of deformation by interface migration is that the substantial strains produced this way are often completely recoverable when the chemical or mechanical driving force is removed. This 'shape recovery' is a consequence of the highly ordered nature of the atomic displacements during thermoelastic interface deformation. It contrasts with the irreversibility of the plastic deformation produced by dislocation glide or by the formation of martensite plates or deformation twins with an accompanying dislocation deformation. The most important mechanisms based on interface migration which have been put-forward for the effects under consideration include (i) the stress-assisted reversible growth of martensite; (ii) the reorientation of the martensite plates under an applied stress; (iii) inter-twin growth; and (iv) martensite-to-martensite transformation under stress. We now discuss these mechanisms in brief.

6.4a *Stress-induced reversible growth of martensite:* The essential feature of this mechanism is that those plates of martensite grow which have orientation and shear directions favoured by the dominant shear due to the imposed macroscopic change in shape; while other less favourably oriented variants shrink. The growth must be mechanically reversible (and hence thermoelastic) if the shape is to be completely recoverable. The martensite plates which participate in this mechanism may be nucleated under the action of the applied stress, in which case only the favourably-oriented variants will be produced; or they may be plates which may have been formed athermally before the external stress is applied.

6.4b *Reorientation of martensite plates:* Macroscopic shape deformation can be achieved by an externally applied stress through the growth of martensite plates favourably oriented in the stress field at the expense of less suitably oriented plates. It is to be noted that when the martensite interface moves, the habit plane itself remains unchanged, suggesting that ratio of the thickness of alternate segments of transformation twins within the plates remains unchanged. A special and specific mechanism whereby martensite plates can be reoriented under stress has been proposed by Wasilewski (1975). It is described as a 'stress-assisted double transformation'. When a stress is applied at a temperature between A_d and M_f, the martensite transforms to the β'-phase by the stress-assisted reverse transformation; (M_f is the martensite finish temperature during cooling and A_d is the lowest temperature at which martensite reverts to austenite under deformation) and then, because it is both thermally unstable and subject to an external stress, it transforms instantaneously to a martensite variant more favourably oriented with respect to the applied stress field than the original plate. However, there is no experimental evidence as yet for the transitory existence of an intermediate β'-phase.

If the specimen is fully martensitic and consists of self-accommodating groups of martensite, then on the application of external stress, movements of the existing plate boundaries or creation of new ones together with changes in internal structure will occur. Because no untransformed parent phase is present, no invariant plane strain conditions need to be satisfied; only a three-dimensional strain minimisation is necessary.

6.4c *Inter-twin growth:* Macroscopic deformation by change in the thickness of two twin variants under an applied stress was first reported by Olander (1932) and studied in detail in Au-Cd and In-Tl alloys by Chang and Read (1951). This mechanism does not involve any movement of the martensite-martensite interfaces. On applying a stress the twin boundaries move so as to thicken those twins which are favourably oriented with respect to the applied stress. On removal of the stress, the twin boundaries return (relatively slowly) to their original positions, and the specimen recovers its original shape. The strains thus recoverable may be as large as 0·08 in Au-Cd.

6.4d *Martensite-to-martensite transformation under stress:* In Cu-Ni-Al alloys two different martensites β'_1 and γ'_1 form from the parent β_1. It is reported that the β' martensite can be transformed partially to γ'_1 by applying a stress below M_s. Similarly, athermally formed β'_1 martensite in Cu-Al alloys can transform either to an fcc or hcp structure by deformation. Delaey and Warlimont (1975) have demonstrated a similar martensite-to-martensite-transformation in a Cu-Zn-Al alloy.

The different possible routes in a pseudoelastic cycle and a shape memory cycle are illustrated in figure 9 (Cook 1981). This diagram compares the changes involved in a shape memory cycle (VABCDEZ) with those in a pseudoelastic cycle (VWXYZ). If the same martensite phase is produced in the two cycles, the structure at X is identical with that at C and D, and the state X may be converted into D by cooling at a constant strain.

7. Applications of the shape memory effect

One of the earliest applications of the shape effect was the introduction of tubing or pipe couplings that shrink during heating. Ni-Ti alloy couplings are used for connecting aircraft hydraulic lines. These are expanded by 4% in the martensitic

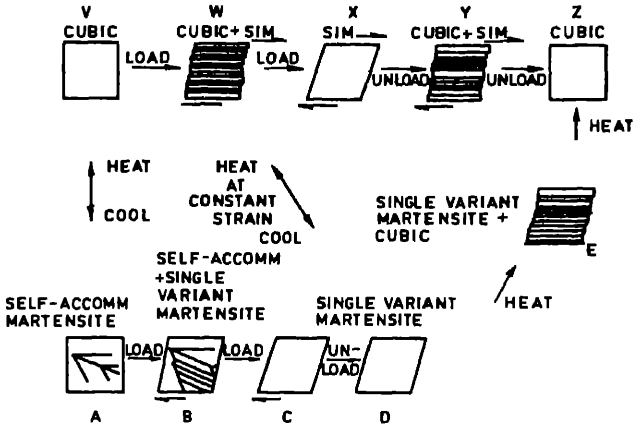

Figure 9. Schematic structural changes during a pseudoelastic cycle VWXYZ and a shape memory cycle VABCDEZ.

condition at liquid nitrogen temperatures, and placed around the tubes to be joined. Warming at room temperature produces a tight seal. Substantial developments have taken place in the field of copper-based shape memory alloys, particularly the Cu-Zn-Al alloys, with emphasis on their applications as thermostats, automotive control devices and actuators. Applications in the field of medicine include the use of such materials for orthodontic dental arch wires, blood clot filters and orthopaedic devices.

References

Angel T 1954 *J. Iron Steel Inst.* **177** 165
Bowles J S and Mackenzie J D 1954 *Acta Metall.* **2** 129
Chang L C and Read T A 1951 *Trans. Met. Soc. AIME* **191** 47
Cook J M 1981 Ph.D. Thesis, Cambridge University (unpublished)
Christian J W 1982 *Met. Trans.* **A13** 509
Delaey L, Krishnan R V, Tas H and Warlimont H 1974 *J. Mater. Sci.* **9** 1521
Delaey L and Warlimont H 1975 *Proc. conf. shape memory effects in alloys*, (eds) J Perkins (New York: Plenum Press) p. 59
Divers C K 1964 *Met. Prog.* **86** 115
Dunne D P and Wayman C M 1973 *Met. Trans.* **4** 137
Krishnan R V, Delaey L, Tas H and Warlimont H 1974 *J. Mater. Sci.* **9** 1536
Ling H S and Owen W S 1979 *Proc. int. conf martensitic transformation* (ICOMAT 1979), (Cambridge: MA) p. 368
Ludwigson D C and Berger J A 1969 *J. Iron Steel Inst.* **207** 63
Mangonon Jr P L and Thomas G 1970 *Met. Trans.* **1** 1587
Murr L E, Staudhammer K P and Heeker S S 1982 *Met. Trans.* **A13** 627
Olsen G B and Cohen M 1972 *J. Less Common Metals* **28** 107
Olsen G B and Cohen M 1975 *Met. Trans.* **A6** 791
Olsen G B and Cohen M 1976 *Met. Trans.* **A7** 1905
Olander A 1932 *J. Am. Chem. Soc.* **54** 3819
Onodera H and Tamura I 1979 US-Japan seminar on *Mechanical behaviour of metals and alloys associated with displacive transformation*, (Troy, NY) p. 24
Patel J R and Cohen M 1953 *Acta Metall.* **1** 531
Seetharaman V 1976 *Effect of thermomechanical treatments in stainless steels* M.Sc. (Tech) Thesis, University of Bombay

Seetharaman V and Krishnan R 1981 *J. Mater. Sci.* **16** 523
Suzuki T, Kojima H, Suzuki K, Hashimoto T and Ichihara H 1977 *Acta Metall.* **25** 1162
Tamura I 1982 *Met. Sci.* **16** 245
Tamura I, Maki T and Hato H 1970a *Trans. Iron Steel Inst. Jpn* **10** 163
Tamura I, Maki K, Hato H, Tomoto Y and Okada M 1970b *Proc. ICSMA* 3, (ASM, Metals Park Ohio) p. 900
Tong H C and Wayman C M 1975 *Acta Metall.* **23** 209
Wasilewski R J 1975 *Met. Trans.* **A6** 1405
Wayman C M 1964 *Introduction to the crystallography of martensitic transformation* (London: Macmillan)
Wayman C M and Shimizu K 1972 *Met. Sci. J.* **6** 175
Wechsler M S, Lieberman D S and Read T A 1953 *Trans. AIME* **197** 1503
Zaekay V F, Parker E R, Fahr D and Busch R 1967 *Trans. ASM* **60** 252
Zener C 1947 *Phys. Rev.* 71 846

Discussion

V K Wadhawan: What is the role of the superlattice structure in the shape memory effect?

V Seetharaman: Ordering of the parent and martensite phases has two consequences. (i) It increases the yield strength of the parent and product phases by the 'Fisher's order hardening mechanism' (ii) It reduces the number of variants available for the reverse transformation so that strain recovery can occur efficiently.

S Ray: Does the shape memory effect occur only in isothermal martensite systems (through mode softening) or is it possible in athermal martensites also?

Seetharaman: It is seen in athermal martensites though the mode may not soften completely.

R Krishnan: Are there examples of transformation induced plasticity in ceramic materials?

Seetharaman: I know only a few examples of these. The material must have a residual plasticity before we can introduce TRIP.

Bull. Mater. Sci., Vol. 6, No. 4, September 1984, pp. 717–732. © Printed in India.

Strength and electronic structure

K GOVINDA RAJAN

Materials Science Laboratory, Reactor Research Centre, Kalpakkam 603 102, India

Abstract. The main attribute of a solid is its resistance to deformation, or its 'strength'. We discuss first the interpretation of the strength parameter. The current situation with regard to the central problem of providing a microscopic description of the strength parameter is briefly reviewed. Electrons in metals provide the cohesion, so that an understanding of the role played by electronic structure in the strength attribute should lead to practical hints for building stronger materials. The useful 'aircraft alloy' (Ti + Al + V) illustrates one such important relationship, *viz*., that the addition of a non *d*-character metal to a *d*-electron host strengthens the latter. Again, metals are distinguished from non-metals by the Fermi surface they possess, and it is interesting to examine any possible relationship between the anisotropy of the Fermi surface with the observed anisotropy in hardness (or yield strength). Next, we turn to cleavage, and point out that the assumption that it is the exact opposite of cohesion faces objections. Cohesion is an average property, whereas cleavage is a crack-tip phenomenon. Finally, among the processes familiar to the metallurgist wherein a metal is hardened, electron-moderated mechanisms have been identified in at least two cases, and we conclude with a brief account of these.

Keywords. Strength; cohesive energy; electronic energy; electron-mediated interactions; strengthening mechanisms.

> "... merely corroborative details to lend an aspect of verisimilitude to what would otherwise be a bald and unconvincing narrative ..."
>
> Gilbert and Sullivan—The Mikado

1. Introduction

A solid is characterized by its resistance to deformation, or its strength. In particular, the ability of a solid to resist shearing forces is used to distinguish it from a fluid. Three broad characteristics can be recognized when the meaning of 'strength' is considered. Resilience or elasticity, when subjected to transient forces—that is, how strongly does the solid attempt to regain its original shape if a force is applied to it for a time and then removed? The Young's modulus, which is a measure of such resistance, varies over three orders of magnitude (10^{10}–10^{13} dyn/cm^2). Resistance to flow is the next characteristic and it concerns the question: how much applied force is required to obtain a particular rate of flow? Flow resistance varies even more—from 10^5 to 10^{12} dyn/cm^2—and the measured rates of flow vary over 12 orders of magnitude. Third, by applying sufficient tension, solids can be pulled apart into two pieces. How much applied force is required to fracture a solid? Fracture resistance is the resistance of a material to crack propagation. It is measured in terms of the fracture surface energy, which may be as little as 10 dyn/cm or as high as 10^8 dyn/cm, *i.e.*, varies over 7 orders of magnitude.

Owing to these diverse and variable aspects, the problem of strength is one of great complexity. Strength depends on the collective response of a crystal to applied stress, so that its description is quite involved. That is, strength depends on the behaviour of aggregates of particles, and the central problem in the science of strength has been to learn how to describe mechanical behaviour in terms of the fundamental properties of matter, so that the shapes of stress-strain or strain-time curves and their dependence on loading conditions can be predicted from a small number of experimental relationships (Gilman 1969).

Turning to metals, we know that the properties of metals arise from the behaviour of the free electrons, and their interaction with the metallic ions. Much attention has therefore been directed to the properties of electrons (in particular, the free electrons) in metals, and features such as electrical conduction, magnetic properties and structure in metals have been understood. This success provides the motivation to look into the question of whether progress with regard to the strength attribute too can be made using this approach.

2. Perfect cleavage

We begin by discussing how the strength of a solid is calculated in order to understand the role of electronic structure.

The separation of a crystal into two or more parts by the propagation of a geometrically plane crack through the solid is called cleavage. Perfect cleavage is portrayed in figure 1. A crystal is stressed in tension vertically to the point of theoretical cohesive strength (figure 1a), and then this stress is exceeded simultaneously at every one of the atomic bonds across the cleavage plane extending interminably and mathematically all the way across the stressed crystal (figure 1b), with no intermediate stages. The crystal goes directly from cohesion to cleavage with no crack propagation direction. The more recent, and present, concept of perfect cleavage is that the elastic bonds connecting the atoms are individually overcome one by one in chronological order, as shown in figure 1c. In this visualization, perfect cleavage is the propagation of an atomically sharp crack with the applied stress overcoming the elastic stresses in a purely elastic manner, and with the atoms separating in geometrically opposite directions, along the direction of the tensile stress.

2.1 *Ideal strength of a crystalline solid*

The maximum stress required to produce, in an ideal crystal, a perfect cleavage of the form imagined above is called the ideal strength or the theoretical strength of a solid

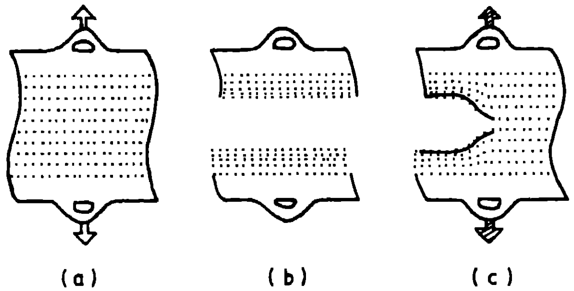
(a) (b) (c)

Figure 1. Perfect cleavage: (a) and (b) Original picture; (c) present concept of perfect cleavage.

(TS). Before the development of the dislocation theory of solids, this problem was of considerable interest because calculated values of the strength were typically greater than experimental values by a factor of 100 or more. Even at the present time, this problem is of theoretical and practical importance, as a knowledge of the TS is useful in determining the stress distribution and other properties in the region at the tip of a crack; in determining the dislocation core radii; in defining the point at which coherency breakdown occurs at a particle-matrix interface; and in providing insight into the phenomenon of melting. The reviews by Milstein (1982) and Macmillan (1972) exemplify these points. Macmillan also reviews the practical approach to the measurement of TS. The measurements are carried out either on specially grown whiskers or on single crystals of materials in which the dislocation density is very small ($\sim 10^1$–10^2 cm^2). Table 1 provides a comparison between the calculated and measured strength for a few solids.

A simple way of estimating the cleavage stress of a perfect crystal is as follows (Kelly 1973). It is assumed that the crystal is pulled at $T = 0$, and the restoring force per unit area between two adjacent atomic planes is assumed to vary with distance according to $\sigma = K \sin \pi/a\,(x - a_0)$, where a_0 is the equilibrium separation between the atomic planes, and a is the range of the interatomic force. The latter is evaluated by setting

$$2\gamma = \int_{a_0}^{a_0+a} \sigma \,\mathrm{d}x$$

at cleavage, γ being the surface energy of the solid; the factor 2 appears because a pair of surfaces is created when cleavage occurs. Thus $a = \pi\gamma/K$. The maximum value of σ is identified as the TS of the solid, so that we have simply $\sigma_{\max} = K$. K is evaluated from the definition of the Young's modulus Υ for the appropriate direction in the solid, namely, $\Upsilon = a_0\,\mathrm{d}\sigma/\mathrm{d}x$. For $x \simeq a$, this gives

$$\Upsilon = K\pi \frac{a_0}{a} \cos \frac{\pi}{a}(a - a_0) \simeq \frac{K\pi a_0}{a},$$

Table 1. Comparison of calculated and measured values of the strength of a few solids.

Calculated values of TS				Experimental data		
		Theoretical strength (calculated) × 10^{-11} dyn/cm^2				
Material	Tensile direction	equation (1)*	equation (2)	Material	Max. tensile stress $\sigma_{\max} \times 10^{-10}$ dyn/cm^2	$\frac{\sigma_{\max}}{\Upsilon} \approx$ strain
Ag	⟨111⟩	2·4 (0·20)	—	Whiskers		
Ag	⟨111⟩	2·7 (0·25)	—	Ag	1·73 ⟨100⟩ tension	0·040
Cu	⟨111⟩	3·9 (0·20)	3·796	Cu	2·94 ⟨111⟩ tension	0·028
Cu	⟨100⟩	2·5 (0·51)	3·60	Fe	13·10 ⟨111⟩ tension	0·049
W	⟨100⟩	6·1 (0·22)		Cd	2·80 ⟨1120⟩ tension	0·040
α-Fe	⟨100⟩	3.0 (0·34)				
α-Fe	⟨111⟩	4·6		Crystal		
C(dia)	⟨111⟩	20·5		Ge	7-12	0·05–
Si	⟨111⟩	3·2				0·08
Ni	⟨100⟩		2·3			

* Values indicated in parentheses are the calculated strains.

so that we have, finally,

$$\sigma_{\max} = (\Upsilon \gamma / a_0)^{1/2}. \tag{1}$$

This simple treatment indicates that the strength goes as $\sqrt{\Upsilon}$ and $\sqrt{\gamma}$. The values of strengths obtained from this approach are indicated in table 1.

2.2 *More exact calculations of* TS

After Born's work on the necessary conditions for the thermodynamic stability of a crystal lattice with respect to arbitrary (but small) homogeneous deformations, many attempts have been made to refine the calculations of the theoretical strength (Esposito *et al* 1980; Milstein 1982). The current approach is to proceed along the following lines: (a) The solid under consideration is defined by specifying its crystal structure, parameters of the unit cell, etc. (b) The interaction between the ions and electrons is specified next. For simplicity, pair potentials (Lennard-Jones, Morse, etc.) are used. However, for metals where there is a clear deviation from the Cauchy relation $C_{12} = C_{44}$, the pair potential approximation is not applicable. Recently, the so-called "*ab-initio* potential" method for the calculation of the TS has been developed to overcome the limitations of the pair-potential approximation (Carlsson *et al* 1980). (c) The Born stability criteria are applied, and the suitability of the potential is checked. (d) The cohesive energy per atom (or unit cell) is calculated as a function of the parameters of the potential and other geometric parameters. (e) The unit cell is stretched, and the energy is calculated as a function of the strain. (f) Considering for the moment a cubic crystal with lattice parameter a_0 (thus $a_1 = a_2 = a_2 = a_0$), it is clear that a stretch, for example along [100], will impart a tetragonal distortion. For computational ease the deformation is imagined to increase a_1 and decrease a_2 and a_3 in such a manner as to keep $a_2 = a_3$ and the transverse stress $\sigma_2 = \sigma_3 = 0$. In practice, this is achieved by an iterative technique. The relevant stress σ_1 is calculated from the expression

$$\sigma_1 = \frac{4}{a_0^3} \frac{\partial U}{\partial (a_1/a_0)}. \tag{2}$$

where U is the cohesive energy. The theoretical strength is identified as

$$\text{TS} = (\sigma_1)_{\max}. \tag{3}$$

Figure 2 gives an idea of the way σ_1 varies with extension along [100] in nickel. The maximum σ_1 value is the TS, and the corresponding a_1 value gives the strain at fracture. Obviously, the cleavage process is imagined to be the exact opposite of cohesion, with all bonds snapping simultaneously when σ_1 reaches $(\sigma_1)_{\max}$.

Further details may be found in the references listed at the end (*e.g.*, Milstein 1982). Table 1 also contains the TS values calculated by these more exact methods. It is interesting to note that even the naive calculations outlined in § 2.1 are already in reasonably good agreement with the observed values. The more exact calculations, in addition to improving this agreement, also help us in understanding the correlation between the electronic structure and strength of metals.

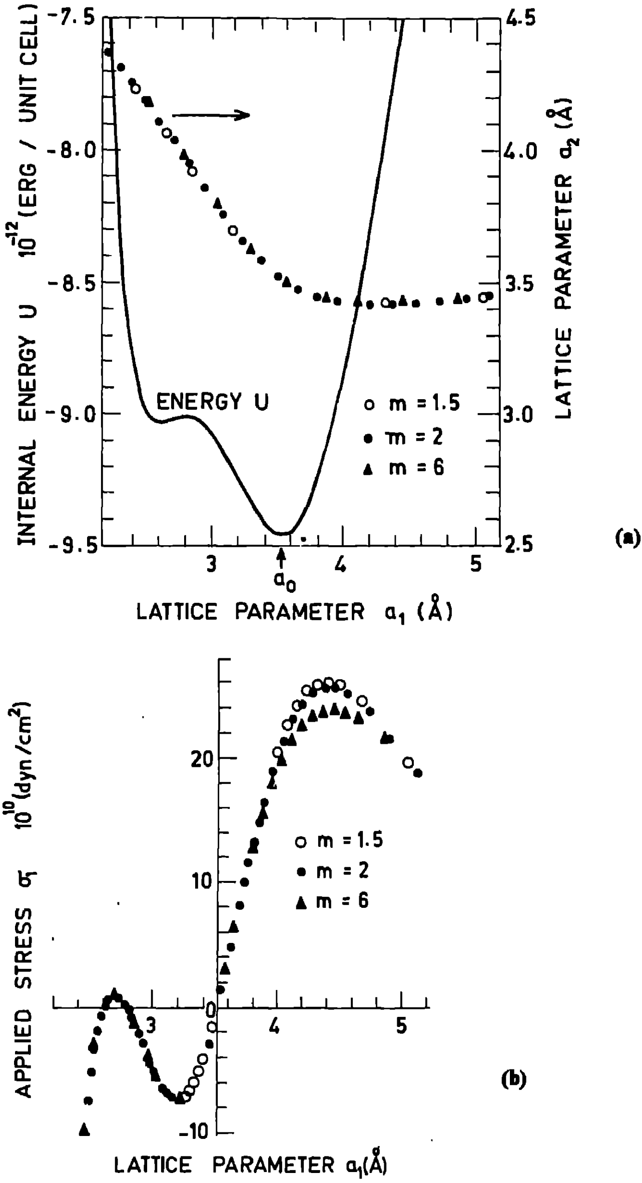

Figure 2. (a) The internal energy (cohesive energy) as a function of the axial lattice parameter a_1 for [100] uniaxial loading in fcc Ni. (b) Computation of the true axial stress σ_1 as a function of a_1 for [100] loading. The maximum value of σ_1 is the theoretical strength. The calculations were performed using a Morse potential $\phi(r) = D[\exp\{-2m\alpha(r-r_0)\} - 2\exp\{-m\alpha(r-r_0)\}]$. Results for a few values of m are shown (after Milstein 1982).

3. Cohesion and electronic structure

We have seen that in strength calculations, the cohesive energy of the solid has to be first determined. It therefore becomes necessary to see how the electronic structure enters the calculation of cohesive energy, for a better understanding of the relationship between strength and electronic structure (especially in metals).

The calculations of the total energy of a metallic structure is formulated as the determination of the energy of an assembly of N ions (each with volume Ω) at sites $\mathbf{r}_n$ arranged on a crystal lattice, and NZ valence electrons. The total energy U is first separated into the energy of the ions, which is purely potential and comes from their mutual repulsion, and that of the electrons, which contains both kinetic and potential terms. The energy of an electron with momentum k is given (to a second order of approximation) by

$$E(k) = \frac{\hbar^2 k^2}{2m} + V_0 + \sum_q{}' \frac{V_q^2}{E_k - E_{k+q}}, \tag{4}$$

in standard notation. To obtain the total energy of the electrons, we must sum $E(k)$ over all occupied states, *i.e.*, over all $k \leqslant k_F$, the Fermi momentum of the electrons. The first two terms on the right in (3) are free-electron terms, this being the zeroth approximation for the perturbation theory. All such terms are *structure-independent*. The first term is the kinetic energy of the free electron gas, and the second is the average value of the lattice potential. Both terms depend upon the total volume. All the structure dependence of $E(k)$ resides in the third term, which contains the strengths of atomic potentials expressed in some suitable form. If the potentials are weak, a second-order correction is adequate and this leaves $E(k)$ only slightly structure-dependent. The corresponding mechanical characteristic is softness; *e.g.*: Na, K, etc. As the strength of the atomic potentials in a sequence of metals increases more terms have to be added to $E(k)$, making it more and more structure-dependent. As a result, these metals fall into a sequence of increasing hardness (or strength). It has been suggested that the parameter E_g/Δ can also be used as a measure of atomic potential strength, where E_g is the width of a low-lying band gap at the zone boundary and Δ is the width of the energy band itself.

The cohesive energy of a metal can be written as a sum

$$U = U_0 + U_s \tag{5}$$

of a structure-independent part U_0, and a structure-dependent term U_s. The former is given by

$$\begin{aligned} U_0 &= U_e + ZV_0 + W_E \\ &= \frac{3}{5} ZE_F + ZV_0 - 0{\cdot}9 \frac{Z^2 e^2}{R}. \end{aligned} \tag{6}$$

The first two terms represent the free electron energy averaged over all the occupied states. (E_F is the free electron Fermi energy.) ZV_0 is the mean value of the pseudopotential in a sphere of Ω, *i.e.* the mean potential energy per electron multiplied by the number of electron per ion. W_E is the electrostatic energy of the ions in the uniform free electron gas. In determining its value, the ions are imagined to be spheres immersed in the electron gas. When crystal structures are taken into account, the geometric factor 0·9 is modified to other values very close to 0·9. Correction terms like

Table 2. Comparison between the observed values of the cohesive energy U with the calculated values of the structure independent part of U.

Element	$-U_0$ (in ry) calculated	Measured cohesive energy (ry)
Li	0·513	0·512
Na	0·457	0·460
K	0·369	0·388
Be	0·995	1·13
Mg	0·852	0·892
Zn	0·991	1·05
Cd	0·937	0·993
Al	1·32	1·38
Sn	1·69	1·77
Pb	1·73	1·81

the electrostatic self-energy, that is, the interaction of the electron gas with itself, also have to be considered. The structure-independent energy U_0 is thus

$$U_0 = \frac{3}{5} Z E_F + Z V_0 - 0{\cdot}9 \frac{Z^2 e^2}{R} - \frac{e^2}{2Z} \int \frac{\rho(\mathbf{r})(r)}{|\mathbf{r}-\mathbf{r}'|} \, d\mathbf{r} \, d\mathbf{r}'. \tag{7}$$

Further correction terms to allow for correlation and exchange effects among the conduction electrons and for the exclusion of conduction electrons from the core, enable U_0 to be determined more accurately.

A comparison (table 2) between the observed and calculated cohesive energies for a number of metals shows that the structure-independent energy dominates the volume dependence of the total energy; so that, by choosing a particular pseudopotential form, U_0 can be evaluated as a function of Ω. From this, the structure, compressibility and strength follow readily.

The structure-dependent energy U_s has the following terms:

$$U_S = U_{\mathrm{BS}} + \Delta W_E. \tag{8}$$

The band structure energy U_{BS} is the change in energy in going from the free electron model to one containing a periodic potential. ΔW_E is a structure-dependent correction to W_E. In one dimension, if the Fermi level lies just below a band gap, the effect of the band structure is a lowering of the energy below the free electron level. If the Fermi level were far above a band gap, the net effect would leave the free electron energy unaltered. However, the actual Fermi surfaces in metals and other crystals always lie close to the first few reciprocal lattice vectors so that the effect of the band gaps always decreases the total energy, *i.e.* U_{BS} is always negative. Figure 3 shows this schematically. This structure-dependent part of the electron energy can be expressed as

$$U_{\mathrm{BS}} = \sum_{k<k_F} \sum_{g}{}' \frac{V_g V_g^*}{E_k - E_{k+g}}. \tag{9}$$

This is a perturbation-theoretic result, and is not accurate close to the Brillouin zone boundary—it diverges when the Bragg condition is exactly satisfied. The way the structure controls U_{BS} can be seen by writing the final form of U_{BS} as

$$U_{BS} = \sum_{\substack{g \\ g \neq 0}}' [S(g)]^2 [V(q)]^2 \chi(q) \varepsilon(q), \tag{10}$$

where $S(g)$ is zero except at reciprocal lattice vector points and is thus the sole repository for the influence of the structure. The remaining factors are characteristic only of the nature of the atoms in question, and they are usually collectively termed the energy-wavenumber characteristic $F(q)$:

$$F(q) = V(q)^2 \chi(q) \varepsilon(q), \tag{11}$$

$F(q)$ has the form as shown in figure 4 for various metals.

The theory described so far has been used by metal physicists to understand the crystal structure of metals, to provide the basis for the Hume-Rothery rules, and to explain the stability of alloy phases at the absolute zero of temperature (Harrison 1966; Wilkes 1973). Calculation of the theoretical strength has been attempted only for copper and fcc iron. Once U is calculated the calculation of the strength proceeds on the lines explained in § 2.2. Table 3 indicates the values of theoretical strengths obtained for copper using three different potentials. Obviously, this approach of treating the

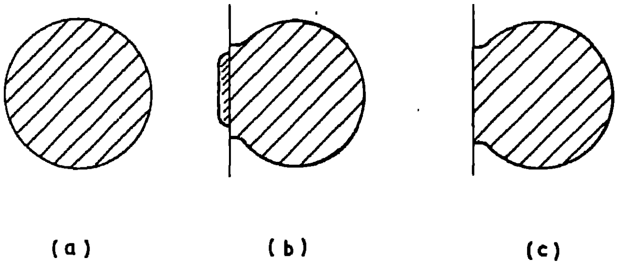

Figure 3. (a) Free electron Fermi surface—a sphere. (b) The Fermi sphere intersected by a Brillouin zone. This gives rise to little energy change. (c) Sphere touching plane—energy gain.

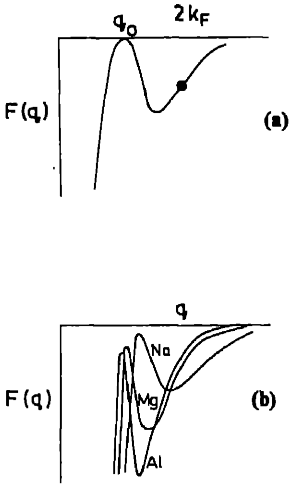

Figure 4. (a) Schematic diagram of energy-wavenumber characteristic. (b) Energy-wavenumber characteristic for some metals.

Table 3. The theoretical strength of copper calculated using three different model potentials.

Potential	Theoretical strength, σ_t (dyn/cm^2)	Strain $\varepsilon_t = \sigma_t/\Upsilon$
Nonself-consistent KKR	$5{\cdot}5 \times 10^{11}$ ($\Upsilon/2{\cdot}3$)	0·5
Self-consistent ASW with Ewald correction	3·6 ($\Upsilon/4{\cdot}0$)	0·3
Pair potential	3·6 ($\Upsilon/4{\cdot}0$)	0·5

electrons as nearly free cannot be used when dealing with transition and rare-earth metals, as these possess narrow *d* and *f* bands respectively.

It may be observed from tables 1 and 3 that while there is satisfactory agreement between the computed and observed σ_t values, the calculated values of the *strains* ε_t at failure are nearly an order of magnitude greater than those found experimentally. Brenner's (1956) early experiments on single crystal copper whiskers indicated for [111] tension, a maximum stress $\sim \Upsilon/40$, where Υ is the measured Young's modulus for polycrystalline copper, and a strain of only 0·03 (3 %). Brenner noticed that in his experiments, all the specimens did not cleave, but sheared apart. It might also be of interest to note that in another study (McQueen and Marsh 1962), flat single crystal samples of Cu were subjected to shock waves of sufficient intensity to cause fracture. Because of the geometry of the experiment, the transverse dimensions of the sample remain essentially fixed. For the [100] orientation, the yield strength obtained was $\Upsilon/7{\cdot}5$. However, the derivation of this value from the known shock-wave intensity involved the use of hydrodynamic equations and equations of state whose validity is difficult to assess.

The substantial difference between the calculated and the observed strains prompts us to examine closely how good the foregoing picture of cleavage is. It is true that in some experiments a shear yield rather than no clean cleavage was observed. Yet, this alone cannot account for the entire difference. It must be that, after all, fracture is not as simple as pure cleavage, which is just the antithesis of cohesion. Finally, it should be mentioned that the strength calculations have so far been performed for a simple cubic unit cell; it is not known at present just how complicated these calculations are for other lower symmetries.

4. Cohesion *vs* cleavage

Cohesion may be described as a process holding the atoms together and cleavage as a process parting the atoms, and it is tempting to imagine these processes being exactly opposite in character. In tensile tests crystals are held together by cohesion until a load is reached where cleavage (or other fracture) occurs. From the measured load and the cross-sectional area one can compute the average force per unit area which existed at the time of fracture. This is the fracture, or cleavage, stress. It is not the cohesive strength; up to the point of fracture, the crystal had cohesion, and every atomic bond across the future cleavage plane was certainly strained in something close to perfectly-elastic tension. The moment a crack formed, however, be it 10 Å or 2000 Å, a new condition came into being—the crack tip. In short, cleavage is a crack-tip phenomenon, whereas cohesion is an average property of a crystal. It is appropriate to quote Beachem (1978) here: "Cohesive energies, or cohesive forces, do account for the loads to which tensile or bend specimens can be subjected before they break. Once fracture starts, however, events become localized and average properties become less important than local stresses, general microstructures become less important than local crack-tip microstructures, and bulk environments become less important than local crack-tip environments. Those average macroscopic bulk properties which were used in predicting the forces to which the whisker (or other specimen) could be loaded, before fracture, no longer apply. Local properties and events become decisive. Once fracture starts, it is a whole new ball game."

5. Yield strength, hardness and related parameters

The hardness of materials is a very useful quantity from the practical viewpoint. It is an empirical parameter; depending on the material, and is measured on a suitable scale. Figure 5 shows how the Vicker's hardness varies across the periodic table for the various elements. The hardness of a crystalline material and its yield strength are proportional to each other (Gilman 1973; Havner 1979). Thus the same trend in variation is expected for the strength attribute. The first prominent peak at around $e/a \sim 7$ lies among the transition metals possessing narrow d-bands. The second, higher peak is found among the group IV metalloid elements. This latter peak in the

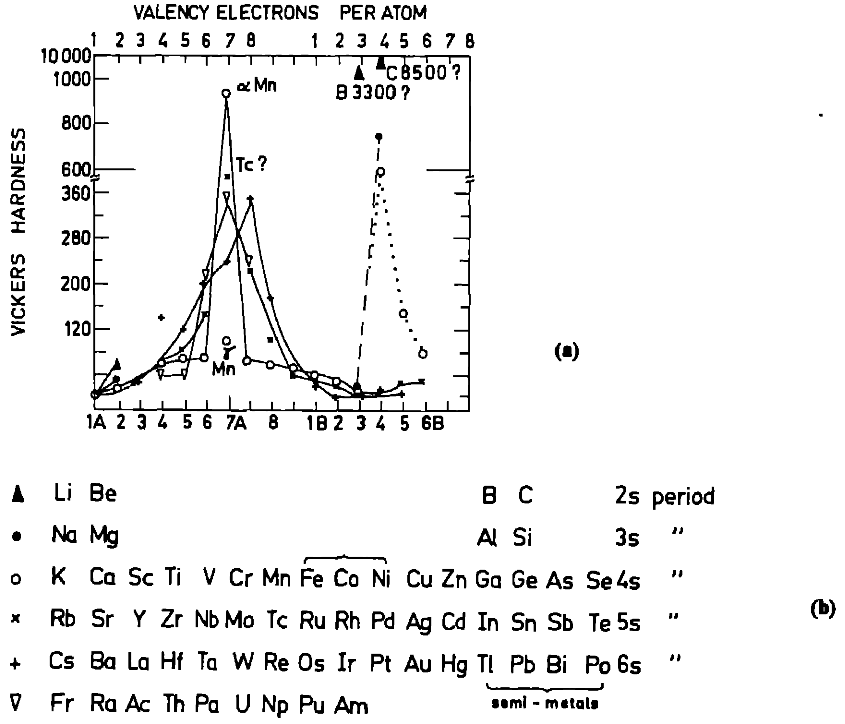

Figure 5. Vickers hardness at room temperature for various metals (after O'Neill 1967).

strength is interpreted in terms of the progressive changeover from metallic to covalent bonding. The second peak will *still* be there, even if one questions the validity of inclusion of diamond (metastable phase) in the figure.

Extensive data on the hardness of metals and alloys are available in the literature. In recent years, the microhardness parameter of metals and alloys has come to be regarded as the 'strength' microprobe (Westbrook and Conrad 1973). Two recent results concerning the behaviour of microhardness are relevant here and serve to illustrate the subtle interplay between the electronic structure and the strength. The first is the rather surprising correlation found between the microhardness and the semiconductor-to-metal transition pressure in group IV elements (Gerk and Tabor 1978). The hardness values of Ge, Si and C (diamond) were found to be 800, 1200 and 10^4 kg/mm^2 respectively. These values are remarkably close to the hydrostatic pressure values necessary to initiate semiconductor-to-metal transition in these elements (1000, 1550 and $\sim 10^4$ kg/mm^2). This indicates that plastic flow has been sustained (ductility indicates the presence of the metallic phase) in these brittle materials, and is probably because the indentation process involves a large component of hydrostatic stress inhibiting brittle failure. The second point concerns the now-established anisotropy with respect to crystallographic direction of the hardness of crystals. The elegant experiments of Tabor and his school, especially those of Brookes, have established the scratch hardness technique on an analytical basis, and data on the hardness along different crystallographic directions is available (Brookes 1981; O'Neill 1967; Westbrook and Conrad 1973). Results for copper appear in figure 6. One interprets the anisotropy in terms of the variation in the resolved shear stress for a specified indentor orientation, and therefore with the relevant active slip system. Since hardness and yield strength can be imagined to be directly related in metals, the question arises whether the

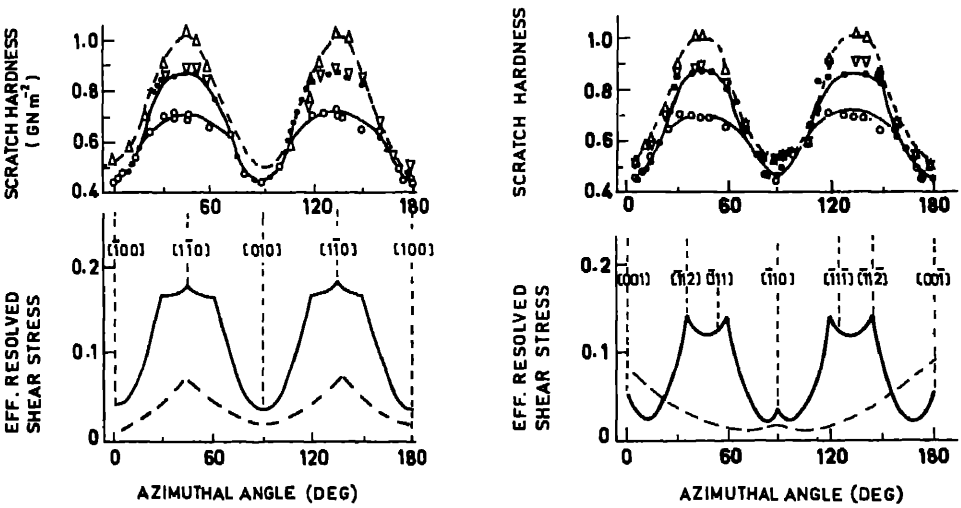

(a) (b)

Figure 6. The measured scratch hardness results for copper. The indentor used was diamond with a 120° cone and an edge-leading 136° pyramid, and with a normal load of 500 g. (a) (001) surface and (b) (110) surface. The bottom curves represent the calculated stress values along various directions, all lying in the plane on which measurements are made (Brookes 1981).

above anisotropy can emerge from the calculation of the cohesive energy. The structure-dependent term U_{BS} in the total energy (equation (9)) must therefore be subjected to a closer examination. This involves analysing the band structure and Fermi surface in the presence of an applied stress. A beginning has been made in Watts (1979). It appears that by calculating the electron density from these Fermi surface results, one can discuss the influence of external stress on the elastic constants and, consequently the hardness. It is suggested that this line of approach might help in the endeavour to correlate the anisotropy in hardness with the anisotropy in the Fermi surface.

6. Strengthening mechanisms: role of electron mediated processes

There are a number of processes, well-known to metallurgists, available for enhancing the strength of elemental metals. The chief methods are (Peckner 1967): (a) dislocation strengthening, (b) strain hardening, (c) solid-solution hardening, (d) precipitation hardening, (e) dispersed-phase strengthening, (f) diffusionless (martensitic) transformation strengthening, (g) superlattice strengthening, and (h) radiation hardening. If we ask whether a definite electron-mediated effect has been identified with the strengthening mechanism in any of the above processes, the answer is a tentative 'yes' for mechanisms (c) and (g). We therefore start with the discussion of solid-solution strengthening.

6.1 *Solid-solution strengthening*

The simplest method of strengthening or hardening is by alloying the host element with other suitable elements/impurities. According to Conrad (1981), the solubility of the impurities will have a different value in the vicinity of dislocations than in other regions, and that the solute distribution will be such as to minimize the energy of the alloy. As the dislocations move under external stress this minimum energy configuration of the impurities is disturbed, raising the energy; the impurities thus tend to act as pinning centres for dislocations. The actual detailed mechanism could either be elastic or electronic in origin. (Ultimately, of course, elastic energy can be traced to an electronic origin). The problem of solution hardening in alloy physics can be related to that of calculating the change in energy of an impurity as its nearest neighbours vary their relative positions. The impurities are assumed to be arranged such that the distortion around the impurity is part of a macroscopic and uniform distortion of the surrounding host. The distortion is produced by first considering a single impurity in the host, undistorted except for the elastic distortion produced by a possible size mismatch. Thus a macroscopic and uniform distortion ΔS is applied to the host so as to produce the desired distortion around the impurity. Changes in the energy of the system as a function of the distortion are calculated and ΔE_i, the part due to the presence of the impurity, is isolated. The interaction between the impurities is neglected (assuming the impurity to be sufficiently dilute). The magnitude of $\Delta E_i/\Delta S$ is a measure of the solution strengthening; the larger it is, the greater is the solution strengthening. Figure 7 shows the strengthening coefficient for a few Ti-based alloys (Collings and Gegel 1975). It can be deduced from these figures that the solid solution strengthening increases roughly in proportion to the distance between the columns in the periodic table of the solvent and solute. In Ti, when such an impurity is added, its lack of *d*-character causes a larger perturbation in the wave function of the system in its vicinity.

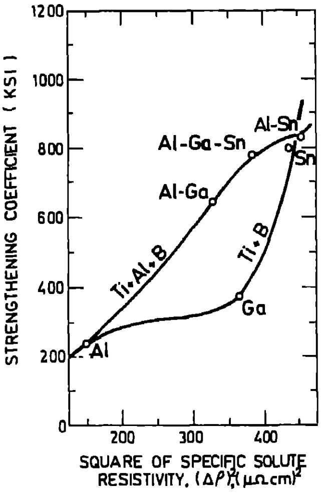

Figure 7. Correlation between the strengthening coefficient ($d\sigma/dC$) (equivalently, dE_i/da) and the electrical resistivity for a set of Ti + B alloys and a set of Ti + Al + B alloys (B = Ga, Sn, etc.) (Collings and Gegel 1975).

Assuming that the wavefunction in the vicinity of an atom is the same as it is in the atomic configuration, the problem is simplified by imagining the perturbation introduced by the impurity to be spherically symmetric and highly localized. This then permits the definition of phase shifts introduced by the presence of the impurity. The phase shift (for a general l-character: $l = s, p, \ldots$) has the form

$$\delta_l = \pi Z_l/(4l+2), \tag{12}$$

where Z_l is the difference in the number of valence electrons between the impurity and the host. The introduction of the impurity and the corresponding phase shifts disturbs the wave function in the vicinity of the impurity. The distortion is appreciable and causes a given Bloch state to scatter into other states and decay with time. This leads to electrical resistivity; and indeed, a significant correlation has been found in experimental studies between the increase in electrical resistivity $\Delta\rho$ and the solution hardening. It is of interest to look at the form of the final expression for the strengthening coefficient dE_i/da (Stern 1975)

$$\frac{dE_i}{da} = \frac{1}{6\pi}\frac{dW}{da}\left[E_i + \frac{2}{\pi}\int_{-\infty}^{0}\frac{\varepsilon_0 I(\varepsilon)\,d\varepsilon}{\{1-\varepsilon_0 R(\varepsilon)\}^2 + \{\varepsilon_0 I(\varepsilon)\}^2}\right]. \tag{13}$$

This is entirely equivalent to $d\sigma/dC$, the variation of the conductivity with the impurity concentration. In (13), W is the band width and a is the lattice parameter. (ε is the reduced energy parameter, E/W.) ε_0 is six times the ground state energy of the impurity in units of W. R and I are certain functions that involve the phase shifts. As dW/da in (13) is independent of the impurity, the variation of interest is the expression in square brackets. If the impurity forms a bound state level below the bottom of the band ($U_0 \ll -1$), then (dE_i/da) is proportional to U_0; thus larger the magnitude of U_0, greater is the dE_i/da, and greater the solid solution strengthening.

Thus, it seems that an impurity with an electronic structure very different from that of the host causes a large perturbation of the wavefunction of the latter, leading to large phase shifts and consequently to high solution hardening. It would be worthwhile to measure the changes in the various elastic constants of the alloy with impurity concentration, in particular to confirm the expected increase in elastic constants with the addition of impurities of the above type (Conrad 1981).

6.2 *Superlattice strengthening*

In a solid solution, the atoms of the different components of the alloy form a common crystal lattice, generally that of the solvent. The metallic type of bond is found in all metal-based solid solutions regardless of the type of bond peculiar to the solute in the solid state. Nonmetallic atoms (C, N, Si, etc.) do not change the metallic bond of metallic solid solutions. In a number of metallic systems (Cu + Au, Fe + Al, Fe + Si, Ni + Mn, etc.) the atoms of both components occupy entirely definite positions in the solid solution lattice if the alloy has been slowly cooled or has been heated for a long time at a definite temperature. Such ordered solid solutions are distinct from those in which the components assume statistically random positions in the lattice. This new order superimposed on the solvent lattice results in a structure called a ‘superlattice’. Ordered solid solutions occur when the ratios of the alloyed components (in atomic %) are equal to whole numbers, and are designated Cu_3Au, Fe_3Al etc. The formation of an ordered solid solution is accompanied by a sharp fall in electrical resistivity and a sharp increase in hardness and strength.

The ‘order-disorder’ compounds are regarded as intermediate phase between solid solutions and chemical compounds. Much work has been done on these alloys (Warlimont 1974), including the correlation between their mechanical properties (in particular, the strength) and their electronic structure. Experimentally, correlations are found between a typical strength attribute, namely, hardness, and the so-called short-range-order (SRO) parameter, which is related to the ordering energy $V(k)$. The SRO parameter can be determined from diffuse x-ray scattering measurements, as in these measurements one really probes the chemical nature of the nearest neighbours of an atom, and thus the SRO. Interesting Fermi surface effects giving rise to satellites in the diffuse x-ray scattering have been seen (Scattergood *et al* 1970), and thus the SRO and the Fermi surface effects in these compounds can be imagined to be related. If only the connection between any elastic constant (or any other suitable strength attribute) and the SRO parameter, can be established, the correlation between the strength and electronic structure in this mode of strengthening can be understood. This last step constitutes the lacuna in this area of investigation.

7. Summary

Elucidating the physical basis of one of the important mechanical attributes of a solid, namely, its strength, continues to be a challenging problem. Much success has, no doubt been achieved using the dislocation idea. We have examined the problem of understanding the strength of a crystalline solid on the basis of its electronic properties. The attempts that have been made so far adopted the view that cleavage can be regarded as the exact opposite of cohesion. This enables one to use in full the electronic theory of the cohesion of solids. The strength values calculated on this assumption agree by and large with the limited experimental values available. However, as pointed out in § 3, there is an order of magnitude difference between the calculated and measured strains at failure. Also, it is true that the way the unit cell is assumed to deform in calculating the strength is not realistic. There is scope for refinements here, both in terms of allowing for more realistic deformations as well as extending the calculation to non-cubic symmetries of the unit cell. Nevertheless, it appears that as far as the problem of cleavage is concerned, well-known dislocation mechanisms and dislocation-crack-tip interactions are adequate to account for the strength of materials. The electronic theory (in the form of a phase shift analysis) meets with reasonable success when applied to the solution-strengthening problem. Systematic measurements of the elastic constants of sequences of alloys with, say, titanium as the host metal will be valuable. In the case of order-disorder compounds, an analysis of the relationship between the short-range-order parameter and the elastic constants (and thus the strength) would be very desirable. We have not commented in this article on the possible correlations that may exist between the electronic structure and the other strengthening mechanisms listed in § 6.

Acknowledgement

The author thanks Dr G Venkataraman for suggesting this problem.

References

Beachem C D 1978 in *Proceedings of the Second International Conference on Mechanical Behaviour of Materials* (Ohio, Metals Park, ASM) 322ff

Brenner S S 1956 *J. Appl. Phys.* **27** 1484

Brookes C A 1981 *Philos. Mag.* **A43** 529

Carlson A E, Gelatt C D and Ehrenreich H 1980 *Philos. Mag.* **A41** 241

Collings E W and Gegel H L 1975 *Physics of solid solution strengthening* (New York: Plenum Press)

Conrad H 1981 *Prog. Mater. Sci.* **26** 2

Esposito E, Carlsson D D, Ehrenreich H and Gelatt C D (Jr) 1980 *Philos. Mag.* **A41** 251

Gerk A P and Tabor D 1978 *Nature* (*London*) **271** 732

Gilman J J 1969 *Micromechanics of flow in solids* (New York: McGraw Hill)

Gilman J J 1973 *J. Appl. Phys.* **44** 982

Hall E O 1970 *Yield phenomena in metals and alloys* (London: Macmillan and Co.)

Harrison W 1966 *Pseudopotentials in the theory of metals* (Massachussetts: Benjamin Inc.)

Havner K S 1979 *J. Mech. Phys. Solids* **27** 393

Kelly A 1973 *Strong solids* (Oxford: Clarendon Press)

Macmillan N H 1972 *J. Mater. Sci.* **7** 239

McQueen R G and Marsh S P 1962 *J. Appl. Phys.* **33** 654

Milstein F 1982 in *Mechanics of solids* (eds) H G Hopkins and M J Sewell (Oxford: Pergamon Press) 417ff

O'Neill H 1967 *Hardness measurement of metals and alloys* (London: Chapman and Hall)

Peckner D 1967 *The strengthening of metals* (New York: Reinhold Publishing Co.)

Scattergood R O, Moss S C and Bever M B 1970 *Acta Metall.* **18** 1087

Stern E A 1975 in Collings and Gegel (1975)

Warlimont H 1974 *Order-disorder transformations in alloys* (Berlin: Springer-Verlag)

Watts B K 1979 *J. Phys.* **F9** 1565

Westbrook J H and Conrad H 1973 *The science of hardness testing and its research applications* (Ohio, Metals Park, ASM)

Wilkes P 1973 *Solid state theory in metallurgy* (London: Cambridge University Press)

Discussion

K R Rao: Could you comment on the nature of the electronic systems you are considering and their relation to the strength of materials?

K Govinda Rajan: The kind of electrons being considered will be specified once the potential is specified. It may also be useful to think in terms of electron charge densities around ion cores and their distortion during loading to understand strength phenomena.

A P Pathak: Instead of talking about the "effects of electronic structure on strength", it appears to be preferable to consider the *correlation* of electronic and mechanical properties. After all, all cohesion in solids is due to electronic structure (either orbital core electrons or conduction/valence electrons), and strength must necessarily be due entirely to electronic structure. Evidently the strength does not depend simply or directly upon, say, the band gap or the conduction electron density (as do the electrical properties), but on combinations of these properties, the core electrons, and of course the structure of the solid. Would you like to comment on this?

Govinda Rajan: In the exhaustive review by K A Gschneider (Solid State Physics, Vol. 16), one finds graphs of electronic properties (resistivity, valence electrons per atom, etc.) *vs* mechanical properties (yield strength hardness) for elemental metals. No significant microscopic picture, however, has emerged. What I have attempted instead is to identify—from the plethora of mechanical properties—the "strength" attribute, and to discuss the role of electronic structure in this context. This is because the strength parameter is, in a sense, the final stage of the mechanical response of a solid, and thus should be amenable to simple calculations. Even this view in which, for instance, cleavage is imagined to be the exact opposite of cohesion has met with serious objection from the metallurgists, as I have taken care to point out

G Venkataraman: It might be interesting to measure the hardness of a semiconductor after pumping electrons into the conduction band by, say, using a laser. This would also have practical relevance to devices like GaAs diode lasers.

Bull. Mater. Sci., Vol. 6, No. 4, September 1984, pp. 733–753. © Printed in India.

Ferroelasticity

V K WADHAWAN

Neutron Physics Division, Bhabha Atomic Research Centre, Trombay, Bombay 400 085, India

Abstract. This paper surveys the present-day description of ferroelasticity in terms of the notion of symmetry descent. Based on the work of earlier authors, a symmetry classification of phase transitions is presented. A general classification of twinning in crystals is also attempted on the basis of this scheme. Most kinds of twinning fall into two broad categories: nonferroelastic and ferroelastic. The shape-memory effect associated with martensitic transitions is discussed briefly. The interesting possibilities of this effect in the case of ferroelectric ferroelastics, for which the electric field provides an additional control parameter, are also mentioned.

Keywords. Ferroelasticity; symmetry; phase transitions; twinning; ferroelectric ferroelastics.

1. Introduction

The elastic (or recoverable) response of a material to a small external stress can be nonlinear in general, although it is predominantly linear in a large number of crystalline substances, glass, and many cross-linked polymers. The elastic response is markedly nonlinear in cellular structures like wood and in "elastomers" like rubber, which consist of long, spaghetti-like, entwined molecules. The recoverable strain in materials of either the linear or the nonlinear type is usually a *single-valued* function of the small applied stress. There is, however, a technologically important class of materials for which the elastic response is neither linear nor single-valued. Ferroelastic materials belong to this class.

A good deal of our present understanding of ferroelastics has been obtained by considering them as the mechanical analogues of ferroelectric and ferromagnetic materials. In fact, the concept of ferroelasticity itself was introduced by direct analogy with ferroelectricity and ferromagnetism. In particular, one associates stress-strain hysteresis with a ferroelastic, which implies that the spontaneous strain is a double-valued function of stress, even for vanishingly small values of the stress (figure 1). The key to such mechanical behaviour lies in the domain structure of the ferroelastic. As we shall see, the most elegant and rational description of the domain structure of a crystal comes from considerations of broken symmetry at a real or hypothetical phase transition. A proper understanding of ferroelastic behaviour is hardly possible unless one pays attention to the ferroelastic phase transition.

The most significant factor contributing to this understanding has been the approach, initiated by Aizu (1970) and developed by a number of other workers, (Janovec *et al* 1975; Tolédano and Tolédano 1976, 1977, 1980, 1982), according to which ferroelastic phase transitions form part of the larger class of *ferroic phase transitions*: these are transitions which result in a change of the point-group symmetry of the crystal. A *ferroelastic* phase transition, by definition, entails not only a change of the

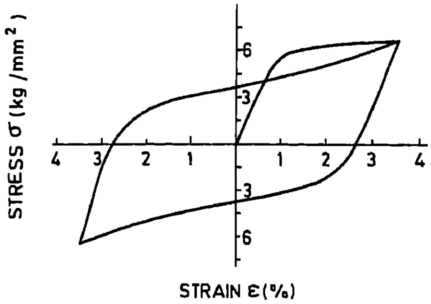

Figure 1. Stress-strain hysteresis curve for the ferroelastic $\beta' - Au_{26}Cu_{30}Zn_{44}$ martensite at 298 K (Nakanishi *et al* 1971).

point symmetry, but also a change of the crystal system (if we regard the hexagonal and trigonal crystal systems as a single system) (Tolédano and Tolédano 1980).

Ferroic behaviour of crystals encompasses not only ferroelasticity but also other, more subtle, types of mechanical properties like ferrobielasticity. Here I shall describe the salient features of the formalism of ferroicity, developed over the last decade and a half. It will be further argued that the notion of ferrocity also provides a very rational and fairly comprehensive description of the occurrence of twinning in crystals. Twinning, in its general sense, is a far more common feature of crystals than has been realized so far. Ferroelasticity itself is a type of mechanical twinning "with change in form" (Klassen-Neklyudova 1964).

2. Ferroelasticity

The term "ferroelasticity" has had a number of connotations, all similar, and yet not quite the same. It was first used in physical metallurgy by Frank in the early 1950's to describe the "rubber-like" memory effect in the gold-cadmium alloy (see Lieberman *et al* 1975). A piece of $Au_{1.05}$ $Cd_{0.95}$ or InTl, when deformed severely (with up to 10% strain) at room temperature, exhibits almost complete crystallographic and morphological recovery when the external stress is removed. As has been pointed out by Lieberman *et al* (1975), there is a tendency in the literature to use the term "ferroelasticity" somewhat indiscriminately in this context. It is important to distinguish clearly between two situations for describing this pseudoelastic behaviour, depending on whether the deforming stress is applied just above the phase transition temperature T_c, or at temperatures below T_c. Figure 2 depicts the two cases schematically. The first case represents "pseudoelasticity by transformation", and the second "pseudoelasticity by reorientation" (Warlimont 1976). In the first case the crystal is initially in the parent phase and the application of a deforming stress causes a reversible stress-induced phase transition. When the stress is removed, all parts of the specimen revert to the parent phase. This behaviour is also described as *superelasticity* (Wasilewski 1975; Barrett and Massalski 1980), or *martensitic thermoelasticity* (Lieberman *et al* 1975). But it must not be called ferroelasticity. Ferroelastic response does not involve any phase transition. Pseudoelastic recovery by reorientation, depicted on the right in figure 2, does correspond to ferroelasticity (Liberman *et al* 1975). The material is already in the lower-temperature, or ferroelastic phase. It is also capable of existing in more than one twin state or domain. The rubber-like pseudoelastic behaviour results from the reversible migration of the twin boundaries or

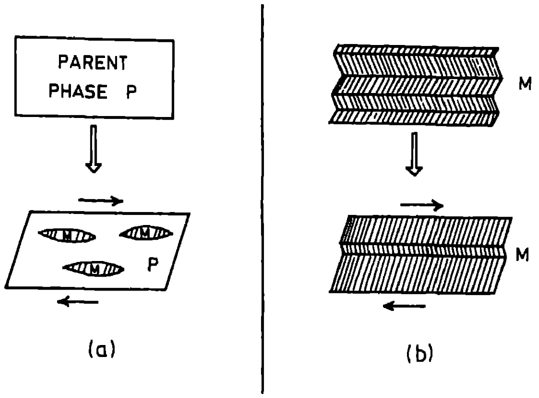

(a) (b)

Figure 2. (**a**) Pseudoelasticity by transformation (or superelasticity), and (**b**) pseudoelasticity by reorientation (or ferroelasticity).

domain walls. This property is also referred to as *piezomorphic memory* by Lieberman *et al* (1975). As we shall see presently, shape recovery or memory is not regarded by physicists as an essential feature of ferroelasticity; the shape recovery at temperatures below T_c results from a volume-dependent restoring force, which may not always be present in a ferroelastic crystal.

The stress-assisted double phase transition in TiNi also leads to a mechanical response which resembles ferroelasticity (Wasilewski 1975). However, in keeping with the usage in the rest of physics, the term "ferroelastic" should not be used for those switching phenomena which involve a stress-assisted or any other kind of *phase transition.*

The term "ferroelasticity" was introduced in 1969 (Alefeld *et al* 1969; Aizu 1969) and was used in quite different contexts. Alefeld and coworkers (see Alefeld 1971) were dealing with the problem of hydrogen and other point defects in metals like Nb and Pd, whereas Aizu viewed ferroelastic behaviour as resulting from the occurrence of domain structure (or "orientation states"), taking no note of the presence of any defects in the crystal. We first consider the question of hydrogen or other interstitial impurities in crystals in brief, followed by an exposition of Aizu's approach and its subsequent development by other workers.

Hydrogen occupies interstitial sites in metals and causes a displacement of the surrounding metal atoms, thus creating local strain fields, as well as a net macroscopic strain. Point defects like hydrogen which distort the host lattice are called *elastic dipoles* (see, *e.g.* Peisl 1978). In general the distortion may be anisotropic and one needs a second-rank polar tensor, (ε_{ij}^{d}), to describe the strain field around a defect. If a uniaxial stress is applied to such a system, a stress-induced diffusion of the interstitial defects to neighbouring sites occurs, resulting in a reorientation of the anisotropic elastic dipoles (figure 3). This time-dependent or anelastic relaxation is known as the *Snoek effect.* Obviously, a stress-strain hysteresis loop looking like the ferroelastic curve of figure 1, will result from such a process. If the defects are highly mobile, one observes the so-called *Gorsky relaxation,* in which the directed diffusion of the defects over many lattice distances occurs under a stress *gradient.* The strain field created by an elastic dipole is long-ranged and is felt by the other elastic dipoles in the metal. This "elastic interaction" is believed to be largely responsible for the $\alpha \rightarrow \alpha'$ phase transition in the H-Nb and H-Pd systems (see Wagner 1978). The reason is that Landau's mean field theory works well for this phase transition and it is known that this theory is good for transitions driven by long-range interactions.

Clearly, ferroelastic behaviour resulting from the presence of point defects will disappear in the absence of these defects. This is where Aizu's concept of ferroelasticity differs from that of Alefeld *et al.* In the former, ferroelastic properties arise from the pseudosymmetry resulting from a (real or hypothetical) structural phase transition, and not from the presence of defects. The concept of a *prototype symmetry* plays a central role here. The prototype is the highest supergroup symmetry attainable by, or conceivable for, a given crystal without requiring a rupture or reconstructive rearrangement of chemical bonds. A ferroelastic phase (more generally, a ferroic phase) emerges from the prototype symmetry owing to a small, spontaneous, symmetry-breaking "distortion" when some control parameter such as the temperature is varied. Figure 4 provides an illustration of this, where an orthorhombic symmetry *mmm* (D_{2h}) is assumed for the prototype. A phase transition to monoclinic symmetry can lead to two possible *orientation states*, S_1 and S_2, both of which are equally stable in the absence of an external force. Although the actual symmetry of the ferroelastic phase is monoclinic, it is also pseudo-orthorhombic because it differs only slightly from the prototype configuration. Since the two states S_1 and S_2 also differ only slightly from each other, it should be possible to switch S_1 to S_2 and *vice versa* by applying a small, suitably oriented, uniaxial stress, as shown in the lower part of figure 4. This possibility of the occurrence of more than one orientation state, (*i.e.*, the presence of domain structure), is what is responsible for ferroelastic behaviour, in particular the stress-strain hysteresis. Aizu (1969) defined a ferroelastic as a crystal which has two or more equally stable

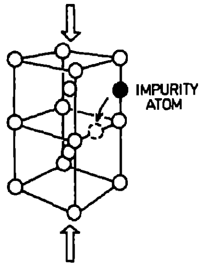

Figure 3. Stress-induced diffusion of an interstitial impurity (Snoek effect).

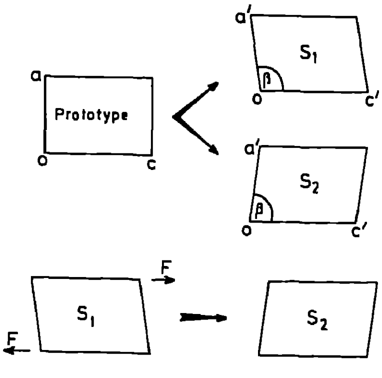

Figure 4. Schematic of an orthorhombic-to-monoclinic ferroelastic phase transition, giving two equivalent orientation states S_1 and S_2 in the lower-symmetry phase.

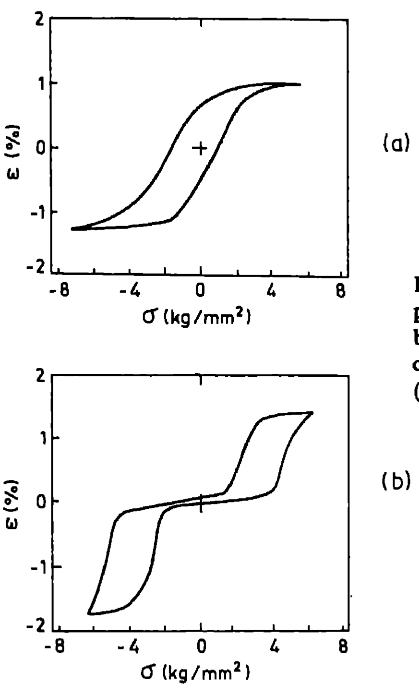

Figure 5. Illustrating the distinction made in physical metallurgy between (a) ferroplastic behaviour and (b) ferroelastic behaviour. The curves shown are for the alloy $Au_{1.05}Cd_{0.95}$ (Lieberman *et al* 1975).

orientation states, and which can be switched from one such state to another by the application of a suitable uniaxial stress. Since all the orientation states are equally stable, the system may not bounce back to the initial state when the stress is removed. It is clear from the above definition that what is called ferroelasticity by Aizu would be described as *ferroplasticity* by physical metallurgists (see Lieberman *et al* 1975). The distinction between ferroelastic and ferroplastic behaviour is illustrated in figure 5 for a gold-cadmium alloy. Very often this distinction is not made in physics, because the term "ferroelastic" is used to imply "ferromechanical", in the sense that the driving force conjugate to the 'order parameter' (strain) is mechanical or elastic in nature (and not electric or magnetic).

Aizu's definition of ferroelasticity also supersedes the earlier usage of this word in physics for describing magnetostrictive and electrostrictive distortions in ferromagnetic and ferroelectric crystals. It is possible for a crystal to be ferroelastic without also being ferroelectric or ferromagnetic. The present concept of ferroelasticity has led to the development of an elegant, symmetry-based, classification of a very large class of phase transitions, and we turn now to an outline of this scheme.

3. A symmetry classification of phase transitions in crystals

Figure 6 presents a symmetry classification of phase transitions in crystals based on the work of various authors (Tolédano and Tolédano 1982 and references therein). We exclude from this scheme reconstructive phase transitions like the graphite-to-diamond transition. We also exclude those martensitic and other phase transitions where the lattice distortion is so drastic that it results in a change of coordination number. An example of this is the transition occurring in CsCl, where the structure changes from

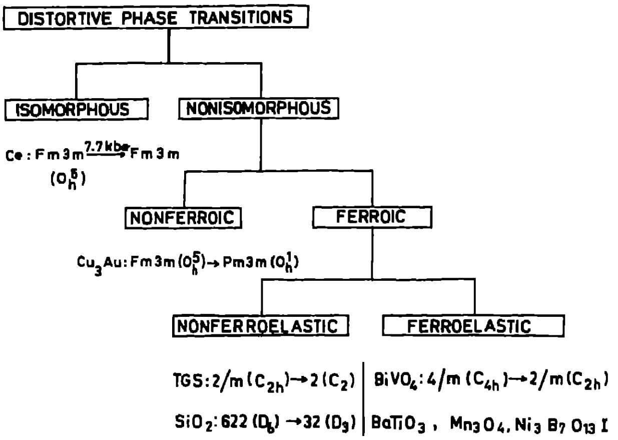
DISTORTIVE PHASE TRANSITIONS
ISOMORPHOUS
NONISOMORPHOUS
Ce : $Fm3m \xrightarrow{7.7\ \mathrm{kbar}} Fm3m$
(O_h^5)
NONFERROIC
FERROIC
Cu$_3$Au: $Fm3m\ (O_h^5) \rightarrow Pm3m\ (O_h^1)$
NONFERROELASTIC
FERROELASTIC
TGS: $2/m\ (C_{2h}) \rightarrow 2\ (C_2)$
SiO_2: $622\ (D_6) \rightarrow 32\ (D_3)$
$BiVO_4$: $4/m\ (C_{4h}) \rightarrow 2/m\ (C_{2h})$
$BaTiO_3$, Mn_3O_4, $Ni_3B_7O_{13}I$

Figure 6. A classification of phase transitions based on considerations of symmetry descent from a prototype symmetry.

simple cubic to fcc on heating through the phase transition at 733 K, resulting in a change of the coordination number from 8 to 6.

We use the term *distortive* for the phase transitions considered in figure 6, although even this term is not entirely adequate. It is intended to cover both displacive and order-disorder phase transitions (Muller 1981). The term "group-subgroup type phase transitions" would be perhaps more appropriate if we remember that a group permits the trivial possibility of being its own subgroup or supergroup. In this scheme, all phases of a crystal are regarded as derived from a certain supergroup symmetry called the *prototype* (Aizu 1981). The prototype is the highest conceivable crystallographic symmetry from which a given phase can result by a small distortion. Phase transitions in this classification are therefore not always between two consecutive phases, but between the prototype and the phase under consideration. All phase transitions in crystals can be divided into two categories: *isomorphous phase transitions and nonisomorphous phase transitions.* In the former, there is no change in the space-group symmetry of the crystal. A well-known example is the transition occurring in Ce at a pressure of 7·7 kbar (0·77 GPa), involving a volume collapse of about 14 %, but leaving the space-group symmetry unchanged as *Fm*3*m* (O_h^5). The change of space-group symmetry at a nonisomorphous phase transition can be of two types: *nonferroic* and *ferroic.* In a nonferroic phase transition there is a change in only the translational symmetry, but no change in the point-group symmetry (Tolédano and Tolédano 1982). Perhaps the best known example of this type is the order-disorder transition occurring in the alloy Cu$_3$Au at 667 K, where the symmetry changes from *Fm*3*m* (O_h^5) to *Pm*3*m* (O_h^1). The high pressure transition occurring in EuS at 215 kbar (21·5 GPa) is another example, involving the same symmetry change as Cu$_3$Au. Ferroic phase transitions involve a change of the point-group symmetry with or without a change of the translational symmetry. If there is a change of the point-group symmetry but no change of the crystal system (provided we do not regard the hexagonal and trigonal crystal systems as distinct for the purposes of this definition), the phase transition is defined as *nonferroelastic* (Tolédano and Tolédano 1976). Examples of nonferroelastic transitions include the ferroelectric transition in triglycine sulphate (symmetry changing from

$2/m(C_{2h})$ to $2(C_2)$), and the $\beta \rightarrow \alpha$ transition in quartz (symmetry changing from $622(D_6)$ to $32(D_3)$). With the above proviso about hexagonal and trigonal crystal systems, a change of crystal system becomes a necessary as well as a sufficient condition for a phase transition to be called *ferroelastic* (Tolédano and Tolédano 1980). A ferroelastic phase transition may be either purely ferroelastic, as in $BiVO_4$, or it may be simultaneously ferroelectric as in $BaTiO_3$, or simultaneously ferromagnetic as in Mn_3O_4. The Ni-I boracite undergoes a phase transition which is simultaneously ferroelastic, ferroelectric and ferromagnetic.

I have recently come across a statement by Fleury and Lyons (1981) according to which a centre of symmetry is always preserved across a ferroelastic phase transition. The rationale behind this statement is not entirely clear; in the cubic-to-tetragonal phase transition in $BaTiO_3$, for example, the centre of symmetry is not preserved even though the phase transition is ferroelastic; the fact that the order parameter of this transition does not have the symmetry of a strain component does not preclude the occurrence of ferroelasticity in the tetragonal and the other lower-symmetry phases of $BaTiO_3$ (see also Aizu 1972a).

4. Ferroic crystals

A ferroic crystal is one which can undergo a ferroic phase transition. The definition of a ferroic transition in terms of a change in the point-group symmetry has a deep significance. Among other things, it enables us to classify ferroic crystals in terms of their macroscopic physical properties like polarization, strain, etc. The reason for this is that these properties are described by the point group symmetry of the crystal, and a ferroic phase is derived, by definition, by deleting certain point-group operations of the prototype. The lowering of the point symmetry at a ferroic phase transition must necessarily be accompanied by the emergence of at least one new macroscopic tensor property component. If this component also has the symmetry of the order parameter, the corresponding response function becomes anomalously large in the vicinity of the transition. This is important in many of the device applications of ferroic crystals.

Let us imagine a crystal in a particular orientation state S_1, under the influence of an external electric field (E_i), a magnetic field (H_i) and a stress (σ_{ij}). The free energy density for this orientation state can be written as

$$d\Phi = SdT - P_i dE_i - M_i dH_i - \varepsilon_{ij}\, d\sigma_{ij}, \tag{1}$$

where S denotes the entropy, P_i the polarization, M_i the magnetization, and ε_{ij} the strain. P_i, M_i and ε_{ij} consist of a spontaneous part (if any) and an induced part owing to the presence of the external fields. One can integrate (1) to obtain the free-energy density Φ_1 for state S_1. Similarly, the free-energy density Φ_2 can be obtained for another orientation state S_2. The difference $\Delta\Phi = \Phi_2 - \Phi_1$ determines whether the crystal makes a state shift from S_1 to S_2, or vice versa under the action of the external forces. The final expression for $\Delta\Phi$ can be written as follows (see Wadhawan 1982 for details):

$$\begin{aligned} -\Delta\Phi = {} & \Delta P_i^0 E_i + \Delta M_i^0 H_i + \Delta\varepsilon_{ij}^0 \sigma_{ij} + \tfrac{1}{2}\Delta\kappa_{ij} E_i E_j + \tfrac{1}{2}\Delta\chi_{ij} H_i H_j \\ & + \tfrac{1}{2}\Delta s_{ijkl}\, \sigma_{ij}\sigma_{kl} + \Delta\alpha_{ij} E_i H_j + \Delta d_{ijk} E_i \sigma_{jk} + \Delta Q_{ijk} H_i \sigma_{jk} \\ & + \tfrac{1}{6}\Delta e_{ijk} E_i E_j E_k + \ \dots \end{aligned} \tag{2}$$

Here $\Delta P_i^0 = P_{2i}^0 - P_{1i}^0$ is the difference between the values of the ith component of the spontaneous polarization in the states S_2 and S_1. The other difference terms are defined similarly. κ_{ij}, χ_{ij} and s_{ijkl} are, respectively, the elements of the electric susceptibility tensor, the magnetic susceptibility tensor, and the compliance tensor. α_{ij}, d_{ijk} and Q_{ijk} are elements of the magnetoelectric, piezoelectric and piezomagnetic tensors respectively, and e_{ijk} stands for the components of the third-order electric susceptibility tensor. Equation (2) serves to define the various types of ferroic crystals. A ferroelectric crystal is defined as one for which at least one pair of orientation states exists such that $\Delta P_i^0 \neq 0$ for one or more values of i. Similarly, a ferroelastic crystal is one for which $\Delta \varepsilon_{ij}^0 \neq 0$ for at least one pair of orientation states. A ferromagnetic crystal is defined similarly. Ferroelectric, ferroelastic and ferromagnetic crystals are collectively called *primary ferroics*.

It is clear from (2) that other types of ferroicity are also possible. For example, if $\Delta s_{ijkl} \neq 0$ for one or more pairs of orientation states, the crystal is said to be a *ferrobielastic*. Quartz is a well-known example of a ferrobielastic crystal. The Dauphiné twins of α-quartz differ in the sign of the elastic compliance coefficient s_{1123} (as well as in the signs of other symmetry-related coefficients). Consequently, although the two twin states do not differ in spontaneous strain (and therefore quartz is not a ferroelastic), a difference in *induced* strain can be established between them under the action of a common uniaxial stress. A suitable stress can then act on this difference to cause switching from one twin state to the other. Lead germanate, $Pb_5Ge_3O_{11}$, is another crystal which can be expected to exhibit ferrobielastic and ferroelectric switching concomitantly. Hence, for applied stresses smaller than the elastic limit, crystals may exhibit elastic, ferroelastic and ferrobielastic (figure 7) mechanical response, or any combination of these.

Still other types of ferroic behaviour can be anticipated from (2). Differences in the piezoelectric tensor between two orientation states can result in *ferroelastoelectric* switching under the *combined* action of an electric field and a uniaxial stress. In an analogous manner, *ferromagnetoelastic* switching becomes possible through differences in the piezomagnetic tensor, and so on. Ferrobielasticity ($\Delta\Phi \sim \sigma^2$), ferrobielectricity ($\Delta\Phi \sim E^2$), ferrobimagnetism ($\Delta\Phi \sim H^2$), ferroelastoelectricity ($\Delta\Phi \sim \sigma E$), ferromagnetoelasticity ($\Delta\Phi \sim \sigma H$) and ferromagnetoelectricity ($\Delta\Phi \sim HE$) are the six types of *secondary ferrocity* possible in crystals (Aizu 1972a, 1973). Aizu (1970) has derived 773 possible "species" of ferroic crystals (a species is characterized by the point symmetry of the prototype and the point symmetry of the ferroic phase in question) by assuming that: (a) every time-symmetric point group can become the prototypic point group in some species of ferroic crystal; (b) when a prototypic point group is specified, every one of its proper subgroups can become the ferroic point group in some species with this prototypic point group; and (c) when a

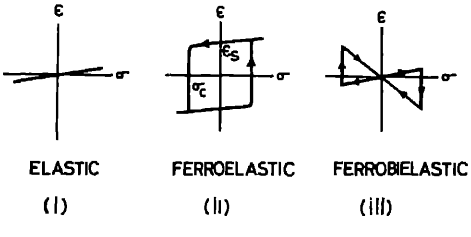

Figure 7. Typical curves illustrating the distinction between elastic, ferroelastic, and ferrobielastic response of crystals to external stress.

prototypic and a ferroic point group are specified, as many species are possible as the number of different ways in which the elements of the ferroic point group can be put in correspondence with the elements of the prototypic point group.

5. Domain structure

The mechanical behaviour of a ferroelastic is influenced in a crucial way by its domain structure. In fact, many of the applications of ferroelastics and other ferroic crystals depend on our ability to control the nucleation and mobility of their domain walls. The fracture-toughness achieved in zirconia by exploiting the ferroelastic phase transition is a case in point. A surprisingly large amount of information about the expected domain structure of a crystal can be obtained from symmetry considerations alone. Two or more domains or twin configurations become possible in a crystal because of the lowering of the prototype symmetry at a real or hypothetical phase transition. Regions of the crystal which were completely equivalent under the operations of the prototype symmetry group become nonequivalent either with respect to orientation, or with respect to mutual disposition, or both; this is what gives a crystal its domain structure.

In the spirit of the Landau theory, one holds the emergence of an order parameter responsible for the lowering of the prototype symmetry. The symmetry G of the daughter phase is determined by the symmetry G_0 of the prototype and the symmetry Γ of the order parameter. G can be obtained by the principle of superposition of symmetries, commonly known as the *Curie principle* (see Kopstik 1968). Shubnikov and Kopstik (1974) have stated a more updated version of it and called it the Neumann-Minnigerode-Curie principle, (NMC) principle. According to the Curie principle: "When several different natural phenomena are superimposed on one another, forming a single system, their *dissymetries* add up. As a result, only those elements of symmetry common to all the phenomena remain". If, for example, G_1 and G_2 denote the symmetry groups corresponding to two physical properties of a crystal, the symmetry G of the crystal cannot be higher than the intersection of G_1 and G_2. If we consider the symmetry groups G_i, $i = 1, 2, 3, \ldots$, of all possible physical properties of the crystal, the symmetry G of the crystal is given by the intersection of all these groups:

$$G = G_1 \cap G_2 \cap G_3 \ldots = \overset{i}{\cap} G_i \tag{3}$$

The more familiar Neumann's principle follows from the above as an inclusion relation:

$$G_i \supseteq G. \tag{4}$$

In other words, the symmetry element (G_i) of any physical property of a crystal include all the symmetry elements (G) of the crystal. G is contained in every G_i; in fact, it is a subgroup of every G_i. Equations (3) and (4) can be combined (Shubnikov and Kopstik 1974) to read

$$G_i \supseteq G = \overset{i}{\cap} G_i \tag{5}$$

In the context of a phase transition accompanied by the emergence of an order parameter having the symmetry group Γ, it follows that the symmetry group G of the resultant phase is given by

$$G = G_0 \cap \Gamma, \tag{6}$$

where G_0 is the symmetry group of the disordered phase. G is that maximal subgroup of G_0 which leaves the order parameter invariant (Janovec 1972).

The Curie principle can be applied not only to determine the compatibility or incompatibility of G, G_0 and Γ, but also to understand inter-domain relationships. Suppose a crystal undergoes a phase transition from symmetry G_0 to G on cooling, (that is, under the influence of a scalar control parameter, T); it follows that, in the lower-temperature phase, the macroscopic symmetry of the sample crystal *as a whole* would be the intersection of G_0 and the symmetry group of a scalar. The intersection of these two is G_0 itself. Thus, macroscopically speaking, the crystal *as a whole* has an average symmetry G_0 even in the daughter phase. But the microscopic symmetry has actually been reduced from G_0 to G. The two statements, taken together, imply that the crystal must split into domains in the lower phase. It also follows that, since the symmetry group of each domain is G, transformation operations which can map one domain to another are those which are *lost* at the phase transitions (Janovec 1976). These are called *Φ-operations* (Aizu 1974). In particular, mirror planes of symmetry lost at a phase transition can become domain walls separating two contiguous domains of the lower phase (Mallard's law). To quote Shubnikov and Kopstik (1974): "The whole process of a phase transition obeys the astonishing law discovered by philosophers—*the symmetry compensation law*: If symmetry is reduced at one structural level, it arises and is preserved at another!"

Let G'_0 and G' denote the point groups of the space groups G_0 and G respectively. If n_p and n_f are the orders of the groups G'_0 and G', the maximum possible number of orientation states or rotational domains possible in the ferroic phase is given by (Aizu 1970; Janovec 1972) $q' = n_p/n_f$. Any operation which is a symmetry operation of G'_0, but not that of G', is called an *F-operation*. An F-operation maps one orientation state to another. Choosing a common reference frame for all the orientation states, if G' is the point group for a particular orientation state S_1 and f is any F-operation from S_1 to another orientation state S'_1, the set of all F-operations from S_1 to S'_1 is equal to fG' (Aizu 1970; Janovec 1972). The point group G'_0 can be split into a sum of q' left cosets of the subgroup G':

$$G'_0 = f_1G' + f_2G' + \dots + f_{q'}G'. \tag{7}$$

Here a coset f_rG' comprises all operations mapping the domain S_1 to the domain S_r. There is a one-to-one correspondence between domains and left cosets. Extending the above considerations from point groups to space groups, if G is a subgroup of G_0 of index q, G_0 can be written as a sum of left cosets as follows

$$G_0 = \phi_1 G + \phi_2 G + \dots + \phi_q G. \tag{8}$$

Once again, there is a one-to-one correspondence between a left coset and a possible structural configuration called a *situation* or a *terrain* (Aizu 1974). The ϕ's are a representative set of Φ-operations from a particular situation to each of the q situations.

A single domain may consist of one or more terrains, but a uniterrain sample is necessarily unidomain also. The possible occurrence of more than one terrain in a domain is referred to as *domain degeneracy* (Janovec 1976). It can be determined with the help of *Hermann's theorem* (Hermann 1929), according to which, if G is a subgroup of a space group G_0, then one can always find a space group Z which contains G as a klassengleiche or equipoint-group subgroup, and which is also a maximal equi-translational subgroup of G_0 ($G \subseteq Z \subseteq G_0$). The index of Z in G_0 is also equal to $q'(= n_p/n_f)$. The number of terrains (also called translational domains or antiphase domains) possible in each (rotational) domain is given by the index m of G in Z. The domain degeneracy is m. It is also equal to the number of times by which the volume of the primitive unit cell of the daughter phase is nominally larger than that of the primitive cell of the prototype. The total number of situations, q, is related to the number of orientation states, q', through m:

$$q = q'm. \tag{9}$$

The fact that q is a finite number is a consequence of the discrete nature of crystallographic space groups. If the prototype symmetry G_0 is described only by a continuous symmetry group, the symmetry group G of the ordered phase may have an infinite index q. In such a case the domain structure is replaced by its dynamical counterpart, namely the occurrence of *Goldstone modes*, which are gapless excitations that tend to restore the prototype symmetry (Janovec 1976).

6. An unsolved problem of ferroelasticity

The elegant and powerful group-theoretical formalism developed by physicists for describing ferroelastic and other forms of ferroic switching in crystals in a unified way is not without a flaw. This was first pointed out by Laves (1975) by citing the example of mechanical twinning in hcp metals like Mg. Such metals have a point-group symmetry $6/mmm$ (D_{6h}), and apparently undergo ferroelastic switching by shearing along the planes $\{1\ 0\ \bar{1}\ 2\}$ in the directions $\langle\bar{1}\ 0\ 1\ 1\rangle$. This type of mechanical twinning results in a large reorientation (by 84°) of the slip plane (0001), and has a drastic influence on the plastic behaviour of these metals (Klassen–Neklyudova 1964). But this apparently ferroelastic twinning does not come within Aizu's formalism because it is not possible to conceive a *crystallographic* prototype symmetry, of which the symmetry $6/mmm$ of the ferroelastic phase is a subgroup.

Aizu (1970) gave a precise definition of prototype symmetry by demanding that the following two conditions be satisfied: (a) The point-group symmetry of the prototype should contain all the F-operations from each of the orientation states of the ferroic to all orientation states. (b) If any symmetry operation of the prototype point group is performed on any orientation state, the result must only be one of the possible orientation states, and none other.

The prototype group is also a proper supergroup of the ferroic point group. The example of Mg seems to indicate that ferroelasticity can also occur in materials with a symmetry such that only a subgroup of this symmetry is a subgroup of the prototype symmetry (Laves 1975). If a relaxing of the definition of a prototype is allowed so as to accommodate such a possibility, the prototype would not always contain *all* the symmetry elements of the point group of the ferroelastic phase. Such a modification of the theory does not look very appealing, particularly because it negates a good deal of the elegant description of domain structure of ferroelastic and other ferroic crystals (§ 5). It also goes against the spirit of the Landau theory of phase transitions. No really good solution of this problem is available at present.

7. Twinning

Before the development of x-ray crystallography, the classification of twinning in crystals was based mainly on morphological studies made by contact goniometry and optical goniometry (Friedel 1926). X-ray diffraction patterns, particularly those obtained with Buerger's precession camera, give us directly a picture of the reciprocal lattice of a twinned crystal. This has led to what may be called the second stage in the classification of twinning (Donnay and Donnay 1974). All twinned crystals are divided into two categories, depending on whether the diffraction pattern reveals a single orientation of the reciprocal lattice for the twins ("obliquity" $\omega = 0$), or two or more orientations with a common origin ($\omega \neq 0$). In the first case one talks of *twinning by twin-lattice symmetry* (TLS), and in the second case *twinning by twin-lattice quasi-symmetry* (TLQS). A further subdivision of each of these main categories is made in terms of the *twin index n*, defined as the ratio of the volume per node in twin lattice to the volume per node in crystal lattice. The twin lattice is the lattice with the smallest cell that is common to both members of the pair. The twin lattice is perfectly continuous across the twin wall for $\omega = 0$, but has a small deviation at the wall when $\omega \neq 0$. Twinning by TLS and by TLQS is also called, respectively, "twinning without change of form" and "twinning with change of form" (Klassen-Neklyudova 1964).

This description of twinning concerns itself mainly with geometrical features like orientational relationships of the lattices. Although many crystallographers have indeed dealt with twinning at the structural level, the descriptive terminology available at present does not make evident certain features such as electrical twinning in a ferroelectric crystal, or more subtle effects like differences in the piezoelectric tensor in the twin structure of a crystal like NH_4Cl. I think a stage has now been reached where a more comprehensive and informative classification of twinning can be made in terms of the ideas of symmetry descent discussed in §§3 and 5. We shall use the word "twinning" in a very general sense here, covering all electric, magnetic, elastic or other forms of domain structure possible in a crystal.

Twinning in a crystal implies that the structure can exist in two or more configurations that are energetically equivalent, but differ in mutual orientation, or mutual disposition, or both. The enthalpy barrier for changing one configuration to the other across a twin wall may be either reasonably low (as in Dauphine twins in α-quartz), or it may be extremely high, even exceeding the breakdown field or the fracture strength (as in Brazil twins in quartz, and also many growth twins). In the former case, barring exceptions like magnesium (§6), an F- or Φ-operation derived from an appropriately assigned prototype symmetry should always be definable. In the latter case, there are two possibilities:

(a) The twins across the interface are lawfully related by an F- or Φ-operation, and the enthalpy barrier just happens to be high; (b) a proper F- or Φ-operation is not definable for mapping one twin into the other; this may happen when, for example, the crystal is in a prototypic phase, and not a ferroic phase (see Aizu 1981).

Thus all twinning can be divided into two types (I and II, say). Type I twins are related by an F- or Φ-operation, whereas type II twins are not. For type I twins a prototype symmetry is always conceivable. In many cases of this type, even if switching from one twin to the other is not possible at room temperature, it may become possible at temperatures sufficiently close to the transition temperature. In any case, demonstration of switching is neither a necessary nor a sufficient condition for assigning a twin to type I; It is necessary and sufficient that an F- or Φ-operation, derived from an appropriate prototype symmetry, is definable. In this scheme, twinning in magnesium will be classified as type II (§6). A better example of type II twinning is provided by Brazil twins in quartz. They are related by a mirror operation, which is not a part of the

622 (D_6) of β-quartz. The symmetry 622 is prototypic for the symmetry 32
uartz, which can consequently exist in two orientation states related by an
n that is a two-fold rotation about the optic axis (Wadhawan 1982). These two
n states are just the Dauphiné twins. Unless a prototypic symmetry higher
an be conceived for this crystal (which is not possible because that would
drastic breaking and reassembling of the structure), Brazil twins do not
domains or terrains in the sense discussed in § 5. (The concept of the
has been discussed with great clarity by Aizu 1978, 1981.) .
I twins, a nonisomorphous phase transition to the prototypic phase either
xists, or can be imagined. In $BaTiO_3$, for example, the cubic phase is
to the tetragonal, trigonal and orthorhombic phases, whereas in
$_4$ the hexagonal prototypic phase is hypothetical (Sawada *et al* 1976; also
k 1978). A nonisomorphous phase transition can be either nonferroic or
ure 6). If it is nonferroic, twinning comprises antiphase domains only. About
undergoing nonferroic transitions have been listed by Tolédano and
(1982). This twinning is obviously of the TLS type, and the superlattice
resulting from it lead to a smaller primitive unit cell in the reciprocal lattice.
crystals, twinning can occur either by TLS or by TLQS, depending on whether
transition is nonferroelastic or ferroelastic (figure 6).

rroelastic twinning

ll nonferroelastic twinning will be dubbed as just twinning by TLS in the
ne of classification, the advantage of the new scheme suggested here can be
the fact that many further subdivisions are possible: We can have
ic twinning (as in TGS, SbSI and $LiNbO_3$), ferrobielastic twinning (as in
ferroelectric-ferrobielastic twinning (as in $Pb_5Ge_3O_{11}$), ferroelastoelectric
s in NH_4Cl, $CuCsCl_3$ and α-quartz), ferromagnetoelastic twinning (as in
NF_2 and $FeCO_3$), ferromagnetoelectric twinning (as in Cr_2O_3), and
tic twinning (as in $Cr_5(PO_4)_3Cl$ and the mineral elapsolite (K_2NaAlF_6)).
lomains observed in $Fe_{36}Cr_{22-x}(Ti, Mo)_x$, γ-brass, δ-NiMo, lithium ferrite
) (Amelinckx 1976) also constitute a subclass of nonferroelastic twinning.
oelastic twinning may indeed occur in ferroelastic crystals, in the so-called
oelastics, in which some twins are ferroelastically related and some are
astically related. Examples of the latter are the antiparallel (180°) domains in
TiO_3. A partial ferroelastic is that for which $\Delta\varepsilon^{0}_{ij} = 0$ in (2) for at least one
ot all pairs) of orientation states.

mely useful tabulation of the "orders" of state shifts in ferroic crystals has
by Aizu (1972a). The same tabulation can provide a very informative basis
g the "order" of twinning in a ferroic crystal. For example, ferroelectric
an be described as "first-order electrical twinning", and ferrobielastic
s "second-order mechanical twinning".

ing or zero-obliquity twinning has two subclasses: (i) *twinning by merohedry*,
e twin index $n = 1$, and (ii) *twinning by reticular merohedry*, for which $n > 1$.
ond case n is usually equal to 3, and very rarely equal to 5 (Donnay and
74). For purposes of crystal structure determination, twinning by meroh-
ts some special problems. Various procedures have been suggested to
e (Catti and Ferraris 1976; Rees 1982; Jameson 1982). Both Dauphiné and

Brazil twinning in α-quartz is described as twinning by merohedry in the old scheme of classification (Donnay and Donnay 1974), whereas, in the present scheme, Brazil twins are type II twins, while Dauphiné twins are type I ferrobielastic-ferroelastoelectric twins.

7.2 *Ferroelastic twinning*

This corresponds to twinning by TLQS in the old scheme. Only one further subdivision is made in the old classification: The twinning is said to be by *pseudomerohedry* if $n = 1$, and by *reticular pseudomerohedry* if $n > 1$ (Cahn 1954; Donnay and Donnay 1974). In the new scheme, the twinning is characterized as purely ferroelastic in $Pb_3(PO_4)_2$ and $BiVO_4$, ferroelectric-ferroelastic in $BaTiO_3$, ferromagnetic-ferroelastic in Mn_3O_4, and ferromagnetic-ferroelectric-ferroelastic in $Ni_3B_7O_{13}I$. The presence of any antiphase domains can also be adequately rationalized in terms of reduction of the translational symmetry of the prototype.

8. Ferroelastic phase transitions

Ferroelastic phase transitions are characterized by a change of the crystal system, subject to the proviso that hexagonal and trigonal crystal systems are not regarded as distinct for the purpose of defining ferroelastic transitions (§ 3). The lattice distortion responsible for the change of crystal system is embodied in the spontaneous strain accompanying such transitions.

8.1 *Proper ferroelastic transitions*

A further subdivision of these is sometimes made between *true-proper* and *pseudo-proper* ferroelastic transitions. For the former, the strain itself is the primary order parameter. For the latter, though the strain ε has the same symmetry as the order parameter Q, the order parameter is some other primary instability. In LaP_5O_{14}, for example, the driving force of the transition is an instability with respect to a Raman-active optical mode (Errandonea 1980). The strain arises because of a bilinear coupling term of the form $K_1 Q\varepsilon$. A typical Landau expansion of the free energy density in this case can be written as follows (Wadhawan 1982):

$$\Phi = \Phi_0 + \frac{a}{2}(T-T')Q^2 + \frac{b}{4}Q^4 + \frac{C_0}{2}\varepsilon^2 + \frac{B}{4}\varepsilon^4 + K_1 Q\varepsilon. \tag{10}$$

The elastic stiffness coefficient goes to zero (that is, the response function corresponding to ε diverges) at the phase transition temperature T_c given by the equation

$$T_c - T' = K_1^2/aC_0. \tag{11}$$

Here T' is the temperature at which the optical soft mode frequency *would* have gone to zero on cooling if the phase transition had not actually occurred at the higher temperature T_c. The distinction between true-proper and pseudoproper transitions disappears as $K_1 \to 0$. In any case most, if not all, proper ferroelastic transitions are of the pseudoproper type. Luthi and Rehwald (1981), who have listed a large number of them, make no distinction between the two types. Many other authors follow the same practice. The temperature shift ($T_c - T'$) can be as large as 160 K in LaP_5O_{14}, and 230 K in $BiVO_4$.

The Landau theory of phase transitions works well for systems for which the range of the interaction driving the phase transition is longer than the correlation length characterizing the critical fluctuations of the order parameter. The theory therefore provides a good description of proper ferroelastic transitions for which the critical fluctuations are the acoustic modes (Cowley 1976). (As already stated in § 2, the theory holds exactly also for the "ferroelastic" phase transitions in hydrogen-metal systems (Alefeld and Volkl 1978; Wagner 1978), the elastic interaction mediated via the distortion fields around interstitial hydrogen atoms being a long-ranged attractive interaction.)

8.2 *Improper ferroelastic transitions*

In these transitions, the spontaneous strain arises only as a secondary effect, through a nonlinear coupling with the order parameter. The Landau expansion therefore contains a coupling term proportional to $\varepsilon\eta^n$, where η is the order parameter modulus, and n is a finite integer called the *faintness index* (Aizu 1972b, c; Dvorak 1974). The spontaneous strain varies as the nth power of the order-parameter modulus, $\varepsilon_0 \sim \eta^n$. The higher the value of n, the smaller is the spontaneous strain. Since strain is no longer the order parameter, the elastic response function does not show very large anomalies at the phase transition. Barring a few exceptions, the Landau theory does not, in general, provide a good description of this class of ferroelastic phase transitions (Wadhawan 1982).

8.3 *Incommensurate phase transitions*

This fundamentally new class of phase transitions (new, that is, for nonmagnetic systems) is currently attracting a good deal of attention (Pynn 1979; Bak 1982). In the usual "commensurate" phase transitions, the pattern of static displacements of atoms in the lower-symmetry phase can be described by a frozen-in wave of wavevector **k**, which is a *rational* fraction of a prototype reciprocal-lattice vector **r*** along the same direction:

$$\mathbf{k} = (n_1/n_2)\mathbf{r}^*, \tag{12}$$

where $n_1 = 0, \pm 1, \pm 2, \ldots$ and $n_2 = \pm 1, \pm 2, \ldots$. For example, for a "zone-centre" phase transition $n_1/n_2 = 0$, and for a "zone-boundary" phase transition it is equal to 1/2. In an incommensurate transition, **k** is an *irrational* fraction of **r***, so that no two atoms have the same static displacement. In other words, in the incommensurate phase no translational symmetry exists in the direction of **k**. Therefore, the notion of antiphase domains or translational domains discussed in §5 does not apply any more for this direction. However, the incommensurate phase still has a well-defined point-group symmetry and the concepts of rotational domains or orientation states and of F-operations between them are still relevant.

In incommensurate transitions no finite-order coupling between the order parameter and any macroscopic property such as the strain or polarization is possible in the Landau expansion (Riste 1978). Consequently, no spontaneous strain or polarization can appear in the incommensurate phase. Such a polarization or strain gets averaged out to zero because of the zero-energy phase modulation of the displacement pattern.

However, as the temperature of the incommensurate phase is lowered, a point is reached where a "lock-in" transition occurs, at which the fraction connecting **k** to $\mathbf{r}^*$ becomes rational, and a finite-order nonlinear coupling between the order parameter and one or more macroscopic properties (each with a definite faintness index) can occur. The lock-in transition has been observed to be first-order in all the cases studied so far. The mechanical behaviour of a crystal near an incommensurate transition is influenced by the effect of the transition on its elastic constants. A number of studies of this have already been made, notably by ultrasonic techniques and include the following crystals listed by Luthi and Rehwald (1981): K_2SeO_4, Rb_2ZnCl_4, $(N(CH_3)_4)_2ZnCl_4$, $(NH_4)_2BeF_4$ and $K_2PbCu(NO_2)_6$.

It is pertinent to mention here a relatively new experimental technique, namely, γ-ray diffractometry (Schneider 1981) which is particularly well suited for studying ferroelastic phase transitions, and especially the critical behaviour of the order parameter. Because of the small wavelength involved ($\lambda = 0{\cdot}03$ Å usually), γ-ray diffractometry is a forward-scattering experiment (with scattering angles seldom exceeding 2°). The change $\Delta\theta$ in the Bragg angle is related to the change Δd in the interplanar d-spacing by equation

$$\Delta\theta = -(\Delta d/d)\tan\theta. \tag{13}$$

As θ is very small, it follows that changes in the d-spacings have a vanishingly small effect on the Bragg peak position, θ. Therefore, any significant shifts of the peak position in the "ω-scan" normally employed for recording the diffraction pattern can be attributed almost entirely to a tilting (reorientation) of the concerned lattice planes, with a negligible contribution from changes in their d-spacing. This is in marked contrast to the situation in conventional x-ray or neutron crystallography where in the back-scattering region ($\theta \simeq 90°$) normally preferred for lattice-parameter determination, $\Delta\theta$ is extremely sensitive to changes in the d-spacing. γ-ray diffractometry is therefore ideally suited for studying those phase transitions which entail spontaneous deformation of the crystal lattice, and the consequent tilting of the lattice planes. This is just what happens in ferroelastic phase transitions. The spectral width of the nuclear γ-rays used is extremely small ($\Delta\lambda/\lambda = 10^{-6}$ for the ^{198}Au source); this results in excellent angular resolution. A resolution of 1″ of arc can be achieved. Further, since the γ-rays are extremely penetrative, the presence of massive high-pressure cells, or elaborate arrangements for achieving a high degree of sample temperature control, do not present any serious problems. The technique looks very promising. Its applications in this direction have begun only recently (see Bastie and Bornarel 1979; Alkire and Yelon 1981).

9. The shape-memory effect

The shape-memory effect (SME) in alloys is associated with martensitic phase transitions, which are first order, diffusionless, structural phase transitions involving a distortion of the crystal lattice. Their closeness to ferroelastic phase transitions is obvious. The SME pertains to the shape recovery of a material on heating to a certain temperature, after it has been subjected to a deforming strain of as much as 10% at a lower temperature. As in pseudoelastic recovery (§ 2), two situations are possible for the "one-way" SME: by transformation or by reorientation (Warlimont 1976). In the former case, the deforming stress induces a phase transition to the martensitic phase, whereas in the latter case the material is already in the martensitic phase and the applied stress makes some domains grow at the cost of others. The shape recovery on heating in both cases involves a phase transition to the parent phase.

In a martensitic transition the parent and the martensitic phase coexist over a certain range of temperatures. For good shape recovery in the SME, it is necessary that the interface between the parent and the martensitic phases be created, annihilated or moved in a reversible manner. A number of conditions should be met for this (Nakanishi 1975; Wasilewski 1975). For example, plastic flow should not occur during deformation. Thus a high yield strength of the initial matrix is required. Also, the driving force required for the nucleation and/or growth of martensite plates should be low. The dominant term in the free energy barrier opposing the nucleation of martensite in the matrix can be written as $C\varepsilon_m^2$, where C is the relevant shear elastic constant of the matrix and ε_m is the effective martensitic strain. A low value of C would be favourable for the stress-induced nucleation of martensite, but it would also imply a lower yield strength. The optimization of these two requirements indicates that one should apply the deforming stress at a temperature close to M_f, the martensite finish temperature (Wasilewski 1975).

In a proper ferroelastic phase transition, some stiffness constant, or a combination of stiffness constants, necessarily tends to zero (§ 8). The presence of such a transition should therefore indicate the possibility of SME in the material (Nakanishi 1975).

Over the last few years, the Landau theory has been increasingly applied to martensitic transitions. The Landau theory was initially formulated for dealing with second-order phase transitions. Further, a Landau expansion like that of (10) presupposes that the order parameter is a slowly varying quantity. Martensitic transitions are first-order phase transitions. One has therefore to employ Devonshire's (1954) generalization of the Landau theory to deal with them. Further, a first-order transition normally exhibits thermal hysteresis. In the temperature range of the thermal hysteresis, the two phases coexist. In addition to this, there also are domain walls associated with the domain structure of the daughter phase. At the domain walls and in the coexistence range of T, the order parameter changes rapidly. This makes the usual Landau expansion of the free energy inadequate, and one must include terms involving the derivatives of the order parameter, in the spirit of Ginzburg's (1955, 1960) extension of the Landau theory.

For understanding the SME, one has to deal not only with the effect of temperature on the martensitic transition, but also that of stress. In fact, many workers believe that the SME is merely one of the manifestations of the effect of stress on a martensitic phase transition, the martensitic transition for systems exhibiting the SME being taken as just a first-order proper ferroelastic transition (Wasilewski 1975; Falk 1980). In other words, some suitably defined spontaneous strain can be taken as the order parameter of the transition. A very simple but fairly universal model Landau expansion of the free energy has been proposed by Falk (1980), which explains a large number of features in a whole group of alloys exhibiting the SME. Falk's calculation is the mechanical counterpart of Devonshire's (1954) treatment of first-order proper ferroelectric phase transitions driven by the temperature and the electric field. The martensitic alloys CuZn, CuAlNi, AgCd, $CuAuZn_2$, NiTi and NiAl are treated together in this phenomenological theory, ignoring their superlattice structure and the differences in the stacking sequence of their close-packed layers. After a suitable rescaling, the following ansatz is made for the free-energy:

$$f(e, t) = f_0(t) + (t + 1/4)e^2 - e^4 + e^6, \tag{14}$$

where f, e and t respectively denote the scaled values of the free-energy density, the shear strain (the order parameter), and the temperature. Equation (14) is a universal one for a large number of shape-memory alloys. The properties of specific materials enter through the scaling constants. All mechanical and thermodynamic properties are derived from (14). It is remarkable that this simplest of possible models leads to qualitative agreement with numerous experiments on shape-memory alloys; the stress-strain curves exhibiting elasticity, ferroelasticity and superelasticity in the appropriate temperature regions, the mode softening, the shape-memory effect, the occurrence of the stress-induced and temperature-induced phase transition, and the latent heat of the transition.

At the next level of complication, the electric field must also be brought in. From the point of view of theory, this is naturally a more difficult problem, but it also promises to present a richer variety of physical behaviour. One does not normally think of studying the effect of the electric field in alloys because of their high electrical conductivity. Especially interesting in this regard are materials such as PLZT and $BaTiO_3$ which are simultaneously ferroelastic and ferroelectric. The presence of ferroelectricity ensures that the spontaneous strain can be manipulated both by a mechanical stress and by an electric field. This is also important in applications of the SME because, by and large, electric fields are easier to apply in practice than mechanical stresses of appropriate magnitude and frequency. Experimental results on the effect of electric fields on the SME are just beginning to come in. Perhaps the first experiment of this type was that on PLZT ceramics (Wadhawan *et al* 1981). The composition of PLZT, that is (Pb, La) (Zr, Ti)O_3, is conveniently specified by the $x/y/z$ notation, where y/z indicates the Zr/Ti ratio, and x denotes the atomic percentage of La ions substituted for Pb. The composition $x/65/35$ has received a great deal of attention because of its closeness to the morphotropic phase boundary (Haertling and Land 1971; Haertling 1971). Its ferroelastic nature was first demonstrated by Meitzler and O'Bryan (1971). For $x > 4{\cdot}5$, this material possesses a property known as *penferroelectricity* (Meitzler and O'Bryan 1973), or *quasiferroelectricity* (Carl and Geisen 1973). There is a very interesting phase transition, called the $\alpha \to \beta$ transition by Keve and Annis (1973), which is similar in many ways to a martensitic phase transition. Whereas above a temperature T_c the material behaves like a normal paraelectric, the dielectric behaviour immediately below T_c, *i.e.*, in the α-phase, is not that of a normal ferroelectric. The α-phase is "quasiferroelectric" in which there are polar distorted microregions shorter than the wavelength of light. Application of an electric field between T_c and a lower temperature T_p changes the microdomains to macrodomains, which, however, revert back to randomly distributed microdomains (giving a macroscopically nonferroelectric state) when the electric field is switched off. The experimentally observed "slim" hysteresis loops constitute evidence in favour of this model (Carl and Geisen 1973). When the electric field is applied at a temperature below T_p, stable macrodomains indicative of long-range order are induced and the material behaves like a normal ferroelectric (as well as a ferroelastic), exhibiting "fat" hysteresis loops. Materials showing this type of diffuse phase transition are called "relaxor" ferroelectrics (Smolensky 1970). In the temperature range between T_c and T_p, microdomains of polar short-range order coexist with the paraelectric matrix, just as martensite coexists with the parent matrix over a certain temperature range.

The SME in PLZT ceramic of composition $x/65/35$, with $4 \leqslant x \leqslant 8$, was investigated in some detail by Kimura *et al* (1981), and the effect of an electric field on the SME in 6·5/65/35 PLZT was studied by Wadhawan *et al* (1981) by performing very simple bending experiments on thin bars of the ceramic. The modification introduced by the electric field on the SME could be interpreted in terms of the above microdomain model. In the temperature region in which the microdomains exist, the system is "electrically soft", but not "mechanically soft", and the load does not produce a large bending. However, when the electric field is switched on, it changes the microdomains to macrodomains, the material also becomes mechanically soft, and the load produces an additional bending. This was only a preliminary experiment. Much more work is needed to understand the phenomena involved in detail. Since ferroelectricity and ferroelasticity are coupled properties in the case of PLZT, it should be possible to produce changes in strain, including shape-memory bending, purely by electrical means, without the need for any mechanically-produced deformation. Electrically-produced SME would present challenging possibilities for both theory and experiment, as well as for device applications.

10. Concluding remarks

The subject of ferroelasticity has gained maturity being viewed as a part of the much larger subject of ferroicity. Much has been learnt or predicted about ferroelasticity by analogy with ferroelectricity. It appears that we can improve, considerably, our understanding of the physical basis of mechanical behaviour by drawing analogies with electrical phenomena (Alefeld 1971).

Based on the symmetry classification of phase transitions, a more rational-looking classification of twinning in crystals has been attempted. Two broad categories of twinning emerge: nonferroelastic and ferroelastic. Although this appears to run parallel to the existing division into twinning by merohedry and twinning by pseudo-merohedry, the advantage of the new scheme is that many finer features like piezoelectric twinning can also be distinguished.

As was brought out repeatedly, our present description of ferroelasticity is based on the concept of symmetry descent and the principle of superposition of symmetries (the Curie principle). In fact the Landau theory of phase transitions, which is so effective in explaining a large body of experimental facts, is itself based on the Curie principle. The Landau theory is being increasingly applied to martensitic phase transitions which have a substantial overlap with ferroelastic phase transitions. Although this is a promising development, a certain amount of caution is warranted because we are dealing with *first-order* phase transitions, many of them of so drastic a nature that a change of coordination number and "internal topology" is involved. In some of these transitions there is no group-subgroup relationship between the symmetries of the parent and the daughter phases. While the theoretical apparatus for dealing with second-order phase transitions is very well-developed, in first-order phase transitions only a beginning has been made in some respects (Aizu 1981).

References

Aizu K 1969 *J. Phys. Soc. Jpn* **27** 387
Aizu K 1970 *Phys. Rev.* **B2** 754

Aizu K 1972a *J. Phys. Soc. Jpn* **32** 1287

Aizu K 1972b *J. Phys. Soc. Jpn* **33** 629

Aizu K 1972c *J. Phys. Soc. Jpn* **33** 1390

Aizu K 1973 *J. Phys. Soc. Jpn* **34** 121

Aizu K 1974 *J. Phys. Soc. Jpn* **36** 1273

Aizu K 1978 *J. Phys. Soc. Jpn* **44** 683

Aizu K 1981 *Phys. Rev.* **B23** 1292

Alefeld G, Schaumann J, Tretkowski J and Volkl J 1969 *Phys. Rev. Lett.* **22** 697

Alefeld G 1971 in *Critical phenomena in alloys, magnets and superconductors* (ed) R E Mills (New York: McGraw-Hill) p 339

Alefeld G and Volkl J 1978 in *Hydrogen in metals, I: Basic properties* (eds) G Alefeld and J Volkl (Berlin: Springer-Verlag) p 1

Alkire R W and Yelon W B 1981 *J. Appl. Cryst.* **14** 362

Amelinckx S 1976 in *Developments in electron microscopy and analysis* (ed) J A Venables (London: Academic Press) p 417

Bak P 1982 *Rep. Prog. Phys.* **45** 587

Bastie P and Bornarel J 1979 *J. Phys.* **C12** 1785

Cahn R W 1954 *Adv. Phys.* **3** 363

Carl K and Geisen K 1973 *Proc. IEEE* **61** 967

Catti M and Ferraris G 1976 *Acta Cryst.* **A32** 163

Cowley R A 1976 *Phys. Rev.* **B13** 4877

Devonshire A F 1954 *Adv. Phys.* **3** 85

Donnay G and Donnay J D F 1974 *Can. Miner.* **12** 422

Dvorak V 1974 *Ferroelectrics* **7** 1

Dvorak V 1978 *Czech. J. Phys.* **B28** 989

Errandonea G 1980 *Phys. Rev.* **B21** 5221

Falk F 1980 *Acta Metall.* **28** 1773

Fleury P A and Lyons K 1981 in *Structural phase transitions I* (eds) K A Muller and H Thomas (Berlin: Springer-Verlag) p 9

Friedel G 1926 *Lecons de Cristallographie* (Paris: Berger-Levrault)

Ginzburg V L 1955 *Nuovo Cimento* **2** 1234

Ginzburg V L 1960 *Sov. Phys. Solid State* **2** 1824

Haertling G H and Land C E 1971 *J. Am. Ceram. Soc.* **54** 1

Haertling G H 1971 *J. Am. Ceram. Soc.* **54** 303

Hermann C 1929 *Z. Kristall.* **69** 533

Jameson G B 1982 *Acta Crystallogr.* **A38** 817

Janovec V 1972 *Czech. J. Phys.* **B22** 974

Janovec V, Dvorak V and Petzelt J 1975 *Czech. J. Phys.* **B25** 1362

Janovec V 1976 *Ferroelectrics* **12** 43

Keve E T and Annis A D 1973 *Ferroelectrics* **5** 77

Kimura T, Newnham R E and Cross L E 1981 *Phase Transitions* **2** 113

Klassen-Neklyudova M V 1964 *Mechanical twinning of crystals* (New York: Consultants Bureau)

Kopstik V A 1968 *Sov. Phys. Cryst.* **12** 667

Laves F 1975 *Acta Crystallogr.* **A31** S9

Lieberman D S, Schmerling M A and Karz R S 1975 in *Shape memory effects in alloys* (ed) J Perkins (New York: Plenum Press)

Luthi B and Rehwald W 1981 in *Structural phase transitions I* (eds) K A Muller and H Thomas (Berlin: Springer-Verlag) p 131

Meitzler A H and O'Bryan Jr H M 1971 *Appl. Phys. Lett.* **19** 106

Meitzler A H and O'Bryan Jr. H M 1973 *Proc. IEEE* **61** 959

Muller K A 1981 in *Structural phase transitions* I (eds) K A Muller and H Thomas (Berlin: Springer-Verlag) p 1

Nakanishi N, Murakami Y, Kanchi S, Mori T and Miura S 1971 *Phys. Lett.* **A37** 61

Nakanishi N 1975 in *Shape memory effects in alloys* (ed) J Perkins (New York: Plenum Press) p 147

Olson G B and Cohen M 1982 *Proc. Conf. Solid–Solid Transf.* 1981 ICOMAT 1982

Peisl H 1978 in *Hydrogen in metals I: Basic properties* (eds) G Alefeld and J Volkl (Berlin: Springer-Verlag) p 53

Pynn R 1979 *Nature* (*London*) **281** 433
Rees D C 1982 *Acta Crystallogr.* **A38** 201
Riste T (ed) 1978 *Electron-phonon interactions and phase transitions* (New York: Plenum Press)
Sawada A, Makita Y and Takagi Y 1976 *J. Phys. Soc. Jpn* **41** 174
Schneider J R 1981 *Nucl. Sci. Appl.* **1** 227
Shubnikov A V and Kopstik V A 1974 *Symmetry in science and art* (New York: Plenum Press)
Smolensky G A 1970 *J. Phys. Soc. Jpn* **28** Suppl 26
Suzuki T 1978 *J. Phys. Soc. Jpn* **45** 860
Tolédano P and Tolédano J C 1976 *Phys. Rev.* **B14** 3097
Tolédano P and Tolédano J C 1977 *Phys. Rev.* **B16** 386
Tolédano J C and Tolédano P 1980 *Phys. Rev.* **B21** 1139
Tolédano P and Tolédano J C 1982 *Phys. Rev.* **B25** 1946
Wadhawan V K, Kernion M C, Kimura T and Newnham R E 1981 *Ferroelectrics* **37** 575
Wadhawan V K 1982 *Phase Transitions* **3** 3
Wagner H 1978 in *Hydrogen in metals I: Basic properties* (eds) G Alefeld and J Volkl (Berlin: Springer-Verlag) p 5
Warlimont H 1976 *Mater. Sci. Eng.* **25** 139
Wasilewski R J 1975 in *Shape memory effects in alloys* (ed) J Perkins (New York: Plenum Press) p 245

Discussion

G Venkataraman: It is observed that to understand the domain structure, one has to use not only the symmetry of the ferroelastic phase, but also that of the parent phase. This is similar to what Mermin does when he classifies defects using G, the symmetry of the disordered phase, and H, the symmetry of the ordered phase.

N Kumar: Is ferroelasticity a noncentrosymmetric phenomenon?

V K Wadhawan: The spontaneous-strain is a second-rank polar tensor. Thus the presence or absence of a centre of symmetry does not effect the occurrence of ferroelasticity in a crystal.

N Kumar: Since there was no prototype group for magnesium, can it be ferroic?

Wadhawan: The D_{6h} symmetry of magneisum does not admit of a crystallographic prototype group. Therefore we are not able to assign this crystal a place in the existing classification of ferroic crystals.

N Kumar: In order to have one-to-one correspondence is it necessary to have distortion connected with displacement vectors which are not some multiples of lattice spacing?

Wadhawan: We are talking here about the *one-way* SME and I think the question of one-to-one correspondence is more relevant for the two-way SME.

Bull. Mater. Sci., Vol. 6, No. 4, September 1984, pp. 755–772. © Printed in India.

Effects of mechanical deformation: Exoemission

G MUKHOPADHYAY

Department of Physics, Indian Institute of Technology, Bombay 400 076, India

Abstract. An introduction to some of the physical effects (*e.g.* exoemission, acoustic emission and mechanoluminescence) associated with the mechanical deformation of solids is presented. Greater emphasis has been given to exoelectron emissions. Experimental information and plausible mechanisms for exoemission have been described briefly. In particular, exoelectron emission from metals and oxide-coated metals has been discussed at some length, with the hope of generating a common interest among physicists and metallurgists.

Keywords. Mechanical deformation; stress; defects; dislocations; electron emission.

1. Introduction

There exist a number of effects associated with the mechanical deformation of solids. One class of effects is the emission of particles (charged and/or neutral), light and sound, when a material is undergoing deformation or is subjected to a constant strain rate. The emission of particles (in particular, electrons) is called exoelectron emission. The emission of light usually occurs in the form of luminescence from those materials which contain luminescent sources, and such an effect when induced by mechanical deformation is called mechanoluminescence. The emission of sound or stress waves is known to occur from a variety of materials, and is usually called acoustic emission. We shall describe here these effects and their understanding at the present time, with particular emphasis on exoemission, especially from metals and metal oxides during mechanical deformation. We shall see that these effects have some common features, require a great deal of future study and promise to be excellent tools for applied research (especially for metallurgists) in the field of nondestructive testing.

2. Exoemission

The phenomenon of exoemission (EE) was reported quite a long time ago (McLennan 1902). However, it was mainly after the introduction of the Geiger tube in the 1920's that the effect was truly recognised. Freshly-prepared Geiger tubes gave high and irregular counting rates for the first few hours or days, before functioning normally, and this led to the discovery that freshly machined metal surfaces emit electrons. This phenomenon was first carefully investigated by Kramer (1950) and sometimes referred to as the Kramer effect. Kramer himself found that all freshly prepared metal surfaces gave off electrons and suggested that the electrons gained the required energy for coming out of a metal by acquiring some of the energy released in the exothermal processes occurring on the surface. The prefix 'exo-' originates from this explanation. Although our present understanding indicates that the actual explanation of the phenomenon is not as simple as this, the name has survived. It now appears that EE occurs for almost all materials in varying degree.

2.1 *Main features of EE*

The main features of EE occurring in various materials can be summarized as follows:

(i) The material exhibiting EE must be 'excited' externally to produce a perturbation in the form of a structural change. The external excitation may be in the form of cold working, irradiation by electromagnetic radiation (UV or higher frequencies), particle bombardment (α, β-rays, neutrons, protons, slow electrons, ions), exposure to gases, abrasion, mechanical deformation, etc.

(ii) The effect is strongly correlated with relaxation processes in the material, both causally and temporally, and it appears only after the generation of the perturbation. The observed time dependence can often be fitted by one or more decaying exponentials. The corresponding time constants reflect the presence of one or more relaxation processes, which normally depend strongly on the amount and nature of the defects in the system. It is this aspect of the EE process that makes it an attractive nondestructive technique of characterizing a material for its defect contents.

(iii) Unlike stationary effects, such as photoemission (PE) and thermionic emission (TE), EE is a nonstationary process, *i.e.* the EE flux is of transient character. Further, the effect is rather weak compared to PE or TE, with a EE flux typically in the range of 10^{-13} A/m^2.

(iv) The emission may be spontaneous or may require external stimulation, in addition to the external excitation. The stimulation may be in the form of increased temperature (thermally-stimulated exoemission (TSEE)) or electro-magnetic radiation (photo-stimulated exoemission (PSEE)), usually in the optical range. The EE observed without any photostimulation is usually referred to as 'dark emission'. Normally TSEE is observed non-isothermally, although it can also be observed isothermally. For PSEE, it is necessary that the photon energy is less than the work function of the material under study. Otherwise normal PE will accompany EE making data analysis rather difficult. PSEE can enhance a normal 'dark EE' intensity by a factor as large as 10^4 or more. Both TSEE and PSEE have been correlated with several other effects, such as thermally stimulated luminescence (TSL), electron-stimulated desorption (ESD), thermally stimulated conductivity (TSC), thermally stimulated depolarization currents (TSDC), and thermally stimulated desorption (TSD), depending on the material studied. Observations of these effects enhance the understanding of the EE process and are therefore generally desirable. There does not appear to have been any attempt as yet to correlate EE with acoustic emission or mechanoluminescence.

(v) The EE rate is strongly correlated with the work function ϕ of the system. This correlation is of major relevance for PSEE as well as TSEE, and it is necessary to measure the work function simultaneously by an independent method during an EE observation, to facilitate understanding of the EE process.

(vi) The EE effect has two components, one of which is volume dependent and the other, surface dependent. For a particular system one or both may occur depending on the material and its surface condition as well as its surrounding gas medium. The surface effect is strongly related to the surface condition, and in a controlled EE experiment it is often desirable to have an ultra-high vacuum ($\sim 10^{-10}$ Torr) to separate the surface effect from the volume effect. It is also desirable to have an experimental arrangement for characterizing the surface condition of the sample.

(vii) EE emission can occur continuously, or in large bursts, or with the latter superimposed over the former. It is usually believed that the continuous emission is related to the motion of defects in the sample, whereas the emission in bursts is related to the propagation of cracks (or micro-cracks). Thus the nature of the EE may reveal the nature of its source.

2.2 *Experimental arrangement*

The apparatus for measuring EE consists of an excitation unit, a stimulation unit and a detection unit, attached to an ultrahigh vacuum (UHV) chamber containing the sample. It should be equipped with an Auger spectrometer and a quadrupole mass analyzer for structural and chemical analysis of the surface of the sample and for the identification of the chemical composition of the residual gases in the chamber. A facility for measuring the work function (*eg.*, by the Kelvin or Fowler method) is desirable. In addition, a LEED facility may be used for characterization of the surface structure. A quartz window on the chamber will facilitate optical measurements (*e.g.* luminescence, optical absorption, etc.), which often prove valuable for understanding EE.

An apparatus and the technique for observing TSEE has been described by Glaefeke (1979). We describe here an apparatus for observing EE or PSEE (figure 1). This is perhaps one of the most sophisticated versions of this type, developed and used by Rosenblum *et al* (1977) for studying EE during the mechanical deformation of a dogbone shaped sample (marked S in figure 1) of Al, Ni or Ti, with and without oxidised layers. The details of their experimental arrangement are described briefly here. The excitation unit consists of an arrangement for producing uniaxial tensile strain at a constant rate. The sample placed inside an UHV chamber (part of a LEED apparatus) is clamped at both ends, with the fixed end attached to a load cell (LC) and the other end attached to a pulling rod coupled to a linear variable differential transformer (LVDT) for measuring the displacement and thereby the strain rate. Strain at a constant rate is applied at intervals, causing EE in bursts. The vacuum chamber (UHVC) is equipped with a ion-gun (IG) for *in-situ* cleaning of the sample surface. No stimulation unit was used by Rosenblum *et al* (1977), although a LiF window (W) is provided for the purpose of photostimulation. In such experiments the EE flux is usually weak (10^4-10^6 particles/sec/m^2) and it is desirable to have a single-event charged particle and photon

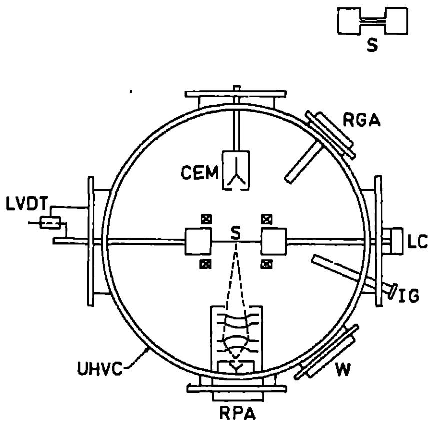

Figure 1. Schematic diagram for EE apparatus. (Rosenblum *et al* 1977).

detector as part of the detection unit. Rosenblum *et al* used a channel electron multiplier (CEM in figure 1) with an input cone (for focussing and accelerating the emitted particles into CEM) with an appropriate shielding and magnetic-discrimination scheme (for identifying the charged particles as electrons, or negative or positive ions). The shield ensured that the electrostatic field developed between the emitting surface and the cone was due to the CEM's biasing potential relative to the specimen rather than to the potential across the CEM. A retarding potential analyser (RPA) was used for Auger and photoelectron spectrometry for studying and characterizing the surface condition of the sample. For the detection of photons (presumably arising from the mechanoluminescence effect), a miniature single-photon counter tube (Bendix BX 754) was used in place of the (removable) RPA unit. For measuring the energy distribution, an electron spectrometer of high resolution (retarding grid potential analyser-RGA in figure 1) was specially designed to suit the way the strain was applied and the EE observed. However, the energy in the energy distribution could be measured only with respect to the Fermi level of the retarding grid, since the work functions of the oxides were uncertain, especially under mechanical strain. Figures 2–5 show the results of EE from Al with an oxide (Al_2O_3) layer, observed by Rosenblum *et al* (1977, 1977a). In figure 2, curves 1–3 correspond to electron emission intensity plotted against strain for samples with oxide thickness of 2000 Å, 250 Å and 50 Å respectively; the oxides for 2000 Å and 250 Å were grown anodically while the 50 Å thick oxide was grown naturally (*i.e.*, natural air-formed oxide). Curve-4 corresponds to negative ion emission from the 2000 Å thick oxide sample. Curve 5 is the stress-strain curve for the sample. In all cases a constant strain rate of $\dot{\varepsilon} = 2{\cdot}2 \times 10^{-4}\ \text{sec}^{-1}$ was used at an ambient pressure of 10^{-10} Torr. In figure 3, curve 1 corresponds to photon emission from the 2000 Å thick oxide sample

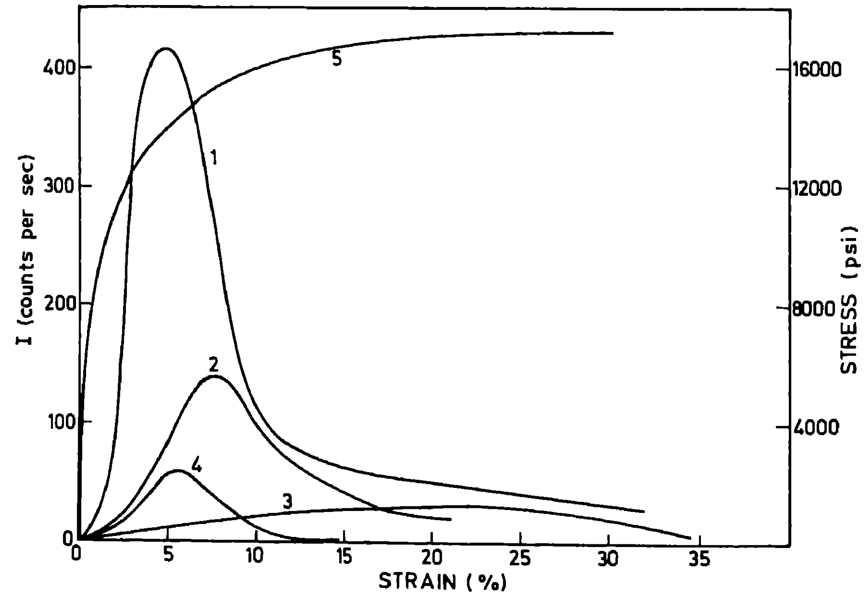

Figure 2. Electron emission intensity *vs* strain: 1. d (oxide thickness) = 2000 Å; 2. d = 250 Å; 3. d = 50 Å; Negative ion emission: 4. d = 2000 Å; stress-strain relation: 5. Strain rate $\dot{\varepsilon} = 2{\cdot}2 \times 10^{-4}\ \text{sec}^{-1}$ (Rosenblum *et al* 1977, 1977a).

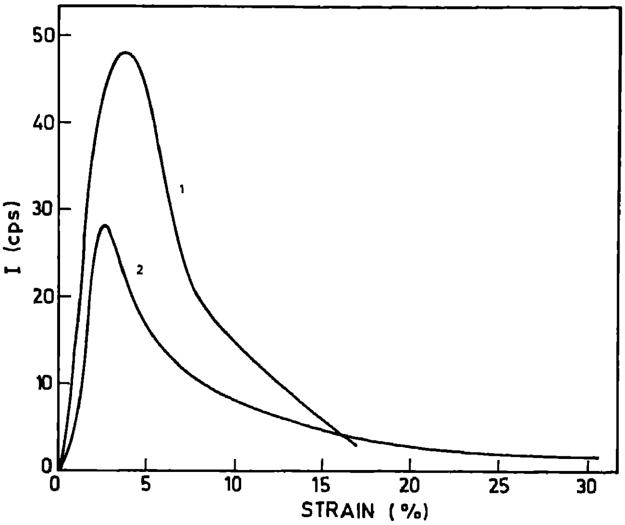

Figure 3. Photon emission intensity *vs* strain: 1. $\dot{\varepsilon} = 2{\cdot}2 \times 10^{-4}\ \mathrm{sec}^{-1}$. Positive ion emission: 2. $\dot{\varepsilon} = 5{\cdot}3 \times 10^{-4}\ \mathrm{sec}^{-1}$ $d = 2000$ Å (Rosenblum *et al* 1977, 1977a).

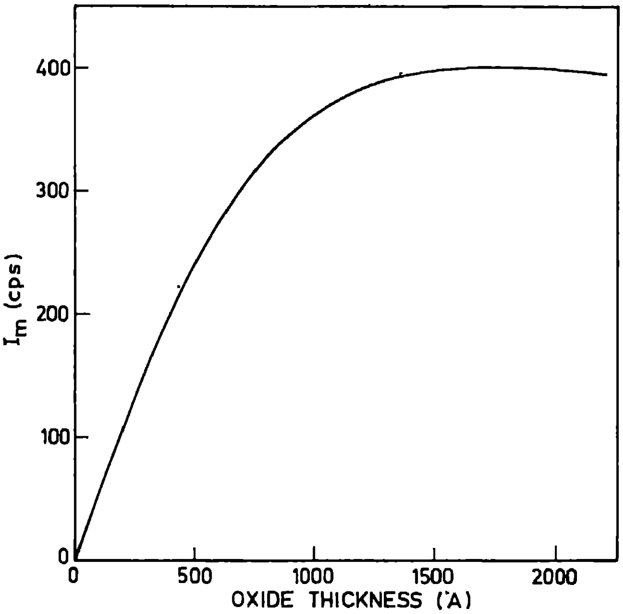

Figure 4. Maximum electron emission intensity *vs* oxide thickness: $\dot{\varepsilon} = 2{\cdot}2 \times 10^{-4}\ \mathrm{sec}^{-1}$ (Rosenblum 1977a).

for the same strain rate as above, while curve 2 corresponds to positively charged ion emission for the same sample at a strain rate of $5{\cdot}3 \times 10^{-4}\ \mathrm{sec}^{-1}$. The general features of the intensity as a function of strain are the same for the emission of electrons, positively or negatively charged ions, or photons. Figure 4 shows the peak electron

2.3 *Mechanism and general understanding*

The mechanisms for EE have always been a subject of controversy, partly because each worker or group of workers has tried to explain the experimental results through phenomenology suitable for that particular experimental situation (which is not easily reproduced), and mainly because of the very complex nature of the EE phenomenon. We now describe briefly some of the mechanisms based on observations under specific situations (see Glaefeke 1979 for further details).

2.3a *Excitations induced chemically:* Spontaneous EE can occur when chemically reactive gases interact with initially clean metal surfaces (Bohun 1961; Bohun *et al* 1965; Delchar 1967; McCarrol 1969; Gesell *et al* 1970; Brus and Comas 1971; Born and Linke 1976). The process involved here is adsorption, the subsequent emission occurring from the surface. An adsorption process can be either physical (physisorption) or chemical (chemisorption) in nature. In physisorption, the adsorption-desorption equilibrium (at constant T) is reached without activation. The heat of physisorption is typically of the order of 0·1 eV per species, which is too small to trigger EE. In contrast, chemisorption requires an activation energy and is preceded by physisorption. The heat of chemisorption is of the order of several eV per species, sufficient for EE. Compared to physisorption which is reversible and forms multilayers, chemisorption is partially irreversible and ceases at monolayer coverage unless the adsorbed species diffuses into the bulk of the substrate. Such diffusion does occur in the case of oxidation and growth of the oxide layer. The rate of chemisorption may be determined from the chemical kinetic rate equation when the chemical reaction velocity is rate-determining, or from Fick's law of diffusion when the diffusion process is rate-limiting. The EE rate is then assumed to be proportional to the rate of chemisorption. Analysis along these lines then indicates a maximum in the EE current as a function of time. When more than one species is chemisorbed, one would expect a maximum corresponding to each species. Thus, the two observed maxima in the EE from clean Mg surfaces exposed (by abrasion) to O_2 and H_2O in the dark have been attributed to the two different adsorbing species (Gesell *et al* 1970). It has also been found from a simultaneous measurement of the work function that the maximum in the EE corresponds to a minimum in the work function ϕ. Thus, the EE has been attributed to (a) the lowering of the work function due to adsorption with a dipole moment of the adsorbed complex favouring emission, and (b) transfer of the released heat of chemisorption to generate surface plasmons which in turn transfer their energy to electrons causing EE. For Al, a substantial decrease in the work function ϕ (with the minimum in ϕ coinciding with the maximum in dark EE) during adsorption of water has been reported (Born and Linke 1976, from 4·5 eV to 1·3 eV; Wortmann 1978).

Spontaneous EE can also occur during thermally stimulated desorption (TSD) without any preliminary excitation, and such TSEE is sometimes referred to as self-excited EE (Bohun 1961; Krylova 1976; Krylova *et al* 1976). For *e.g.*, highly hydrated oxides (Al_2O_3, MgO etc.) and alkali halides (NaCl etc.) show a strong gas desorption accompanied by EE (Krylova 1976). It is believed that the active species at the surface recombine with the sites which have become vacant through desorption due to thermal stimulation. The released recombination energy is then responsible for this TSEE (Krylova *et al* 1976).

TSEE has been observed during heterogeneous catalytic reaction, for example during catalytic oxidation of hydrogen and carbon monoxide on NiO, ZnO and platinum black (Krylova 1976). Since both TSEE and catalysis depend on chemical thermodynamics, a relationship between the two is to be expected. Indeed, a reproducible linear relation between the two has been demonstrated for catalytic oxidation (Krylova 1976).

2.3b *Excitation by UV and x-rays:* Some alkali halides (especially those with small electron affinity at the surface, *e.g.*, chlorides and fluorides), during exposure to UV light, exhibit PSEE when photostimulated with an additional UV light source. TSEE may be observed during thermal annealing. The mechanism for EE is believed to be a two-step photothermal process involving colour centres generated by the exciting UV light. The first step is the optical transition from the colour centre to the conduction band, and the second step is the thermionic emission from the conduction band to vacuum. The stimulation spectra (*i.e.*, PSEE as a function of the stimulating wavelength) have been studied extensively and found to give information about the colour centres similar to that yielded by their optical absorption spectra (Ford *et al* 1970; Bichevin *et al* 1971; Nink and Holzapfel 1973; Maiste *et al* 1973; Kortov *et al* 1982; Tale *et al* 1982).

TSEE has been reported after excitation with x-rays, and a correlation between TSL and TSEE established (Holzapfel and Krystek 1976). TSEE from oxides irradiated with x-rays has also been investigated (Rudolf and Glaefeke 1982). In most cases, a direct liberation of electrons from traps (produced by irradiation) is assumed to explain the EE.

2.3c *Excitation by electrons:* EE has been observed from materials during exposure to electron beams. However, this occurs only for insulators. So far, atomically clean metal surfaces have not exhibited EE on irradiation, and the presence of oxide or adsorbed species seems to be absolutely essential for EE observation here. This seems to be true also for semiconductors. The EE behaviour is strongly dependent on the energy of the exciting electron beam. For low energy electrons (0.2 to 30 eV) the adsorbed species on the surface and the surface states are affected and here EE is essentially a surface phenomenon. These EE spectra are similar to the UV-excited spectra, and electron-stimulated desorption (ESD) can occur. ESD can influence TSEE spectra appreciably. Concepts involving chemical reactions at the surface are utilized to correlate the two (Jakowski and Glaefeke 1976; Euler and Scharmann 1976; Brunsmann and Scharmann 1977; Kirihata and Akutsu 1979). For moderate energy electrons (several hundred to several thousand eV), volume states are excited, generating a complicated space charge inside the insulator. This in turn produces a positive-negative double layer whose electric field (as large as 10^6 V cm^{-1}) causes EE (Fitting *et al* 1979; Fitting 1981). Systems studied, among others, are Al_2O_3 (Krylova 1971; Schlenk 1976; Chrysson and Holzapfel 1980). ZnO (Krylova 1971; Hiernaut *et al* 1972; Kriegseis and Scharmann 1975), NiO (Krylova 1971; Hiernaut *et al* 1972), SiO_2 (Krylova 1971; Jakowski and Glaefeke 1976), BeO (Euler and Scharmann 1976; Scharmann and Wiessler 1980) and NaF (Brunsmann and Scharmann 1977).

2.3d *Excitation by nuclear radiation:* Reproducible EE has been observed from a number of substances using nuclear radiation as the source of excitation. Among the substances studied are alkali halides, alkaline-earth halides, sulphates, sulphides and a number of metal oxides. TSEE from BeO and LiF have been studied extensively because of their dosimetric applications (see Glaefeke 1979 for details). Simultaneous measurement of TSL and TSEE from the same emitter can discriminate between those types of radiation which cause bulk effects (TSL) and those causing surface effects (TSEE).

For example, both α- and soft β-irradiation yield high TSEE intensity (since the total energy is absorbed near the surface) but rather weak TSL, in BeO. On the other hand, γ irradiation causes very weak TSEE but a very strong TSL. Thus, TSEE and TSL from BeO can distinguish between α (or soft β) and γ doses. Fast neutrons can cause EE via recoil protons or α radiation, and the corresponding TSEE may be separated from the γ-ray TSEE by a subtraction procedure to determine the fast neutron dosage. BeO dosimeters based on these properties may have a dose response range from as low as 10^{-6} rad to 10^2 rad. Compared to conventional dosimeters, however, a TSEE-based dosimeter has some technical shortcomings, such as a strong dependence of the TSEE on the mechanical treatment and the ambient atmosphere of the detecting material. This may be responsible for its lack of commercial usage.

2.3e *Excitations through direct structural change:* EE has been observed from a number of materials in which excitation is brought about by direct structural changes. Such changes can be induced by external application of stress, or by generating stress internally through heat treatment of the material.

EE has been observed from metals with atomically clean surfaces in ultrahigh vacuum. Kortov *et al* (1971) observed EE during plastic deformation of Al. Mints *et al* (1973) tried to correlate EE with the process of recovery and recrystallization of metals. Mechanical deformation generates a high concentration of defects (vacancies and dislocations). The relaxation of the stress is accompanied by the diffusion of vacancies towards the surface and the recovery of dislocations. These defects can rearrange themselves exothermally, and the localized release of thermal energy may be taken up by electrons. However, emission of these electrons would require a substantial lowering of the work function ϕ, which is believed to be due to high roughness on a clean metal surface (Lewis 1954; Rhead 1977). Pardee and Buck (1977) and Buck *et al* (1977) considered the roughness-enhanced coupling of incident light with surface plasmons (which can transfer their energy to electrons) to explain PSEE.

EE from oxide covered metals has been observed both in the dark as well as with photostimulation during mechanical deformation. Since most metals in practical situations are oxidised at the surface, these EE observations are of considerable applied interest. The dark emission under UHV has been observed only during mechanical deformation or abrasion of oxide covered metals (Gieroszynski and Sujak 1965; Sujak *et al* 1965; Brotzen 1967; Sujak and Gieroszynski 1970; Linke 1970; Kortov *et al* 1970; Arnott and Ramsey 1971; Kortov and Myasnikov 1972; Kelly and Himmel 1976; Rosenblum *et al* 1977, 1977a). Photostimulated emission during abrasion or plastic deformation of oxide-coated metals can be very large as compared to the dark emission (by a factor of 10^4 or more) and a number of oxidised metals have been investigated exploiting this fact (Grunberg 1958; Von Voss and Brotzen 1959; Pimbley and Francis 1961; Mueller and Pontinen 1964; Claytor and Brotzen 1965; Gieroszynski and Sujak 1965; Sujak *et al* 1965; Sujak and Gieroszynski 1970; Baxter 1973; Shorshorov *et al* 1976; Baxter and Rouze 1978; Wortmann 1978; Dickinson *et al* 1978; Komai 1978). Among various oxide coated materials (*eg*., Al, Ni, Steel, Ti, Mo, etc.), the most widely studied one is Al_2O_3-coated Al. Qualitatively the same emission behaviour has been observed when the oxide covered metal is mechanically abraded or plastically deformed under tension. In the case of tensile strain, dark emission occurs only during a change in the strain and ceases abruptly when the deformation stops. Similarly, when photostimulated, considerable enhancement in electron emission occurs only during constant strain rate, the emission being regarded as burst emission, even though a continuous component (much smaller in magnitude) may be present. In case of burst emission, typically, for a constant strain rate, the emission increases to a maximum followed by a monotonic decrease with increasing deformation or strain (see figure 2). The emission depends on the strain rate as well as the oxide thickness (see figure 4). The burst emission has been associated with the propagation of cracks or micro-cracks. PSEE from thick oxide layers has been attributed to the propagation of cracks perpendicular to the stress direction, independently of the underlying micro-structure of the metal. In thin oxide layers, it has been attributed to fracture at slip steps (Baxter and Rouze 1978).

The continuous EE is believed to arise from two components, one controlled by the diffusion of point defects (generated by strain) towards the surface, and the other controlled by the relaxation of dislocations. One may dominate over the other, or both may be present. For example, Pimbley and Francis (1961) could explain EE from abraded oxidised Al through a model based on the diffusion of vacancies, while Claytor and Brotzen (1965) explained EE from mechanically deformed oxidised Al in terms of the diffusion of other point defects. On the other hand, Mueller and Pontinen (1964) studied EE from freshly abraded as well as from abraded and aged samples of oxidised Al and concluded against the defect diffusion mechanism. However, Shorshorov *et al* (1976) could correlate PSEE during plastic deformation with the generation of dislocations as well as vacancies by simultaneously studying the behaviour of these defects (using metallographic methods). They found no diffusion of vacancies but found relaxation of dislocations in molybdenum, while both phenomena occurred in α-iron.

The burst emission, especially in dark, is supposed to originate from cracks or microcracks which develop in the oxide as soon as the local surface strain in the underlying metal substrate exceeds the ultimate tensile strain of the oxide layer (Sujak 1964). Originally it was believed that the opposing surfaces of a propagating fissure (microcrack) become charged, providing a strong electric field that causes field emission (Gieroszynski and Sujak 1965). This so-called electrified-fissure model for EE was reinvestigated by Arnott and Ramsey (1971) who restricted its applicability to polar substances. For non-polar substances, they proposed to interpret EE in terms of rearrangement of dangling bonds created during the propagation of cracks. Rabinowicz (1977) has elucidated this model, but also questioned its feasibility. Rosenblum *et al* (1977a) believe that the release of strain energy in the vicinity (*e.g.* the tip) of a propagating crack results in local heating to a temperature (estimated to be ~ 3000 K for Al) sufficient to cause thermionic emission from the walls. However, they also observed emission of positive and negative ions, which indicates that field-assisted emission of electrons cannot be ruled out.

EE during heat treatment of materials (without external excitation) arises from the internal mechanical stress generated thermally due to the process of phase transformation. Thus EE has been observed during changes of the state of aggregation or modification (first order phase changes, *e.g.*, transition from the hexagonal to the cubic form in thallium, change or modification of hexagonal chromium and selenium, melting of ice, lead, tin, etc.) and during changes of orientation (second order phase changes, *e.g.*, the antiferromagnetic-paramagnetic transition in Ni + NiO and Cr + Cr_2O_3). The EE intensity is regarded as proportional to the defect content and a measure of the degree of completion of the phase change. The mechanism is believed to be the same as that for stress-induced EE. The emission has also been observed during second-order phase changes in crystalline pyroelectrics (*e.g.*, lithium niobate, BeO), where the mechanism is regarded as a thermally stimulated field effect (see Glaefeke 1979 for further details).

2.4 *Theoretical models for* EE

It is clear from the preceding description that EE is a rather complex phenomenon involving several intermediate steps, depending on the type of material and the actual experimental condition. However, there appear to be three broad steps in the electron emission mechanism: (i) External excitation generates defects and the relaxation of the response to the excitation is associated with the motion or relaxation of these defects. (ii) The defects transfer their energy either directly or via some other agent (*e.g.*, surface plasmons in metals, and possibly phonons) to the electrons by the process of annihilation, or rearrangement, or by chemical reactions (at the surface). (iii) Electrons gaining this energy escape the material in the form of EE when their energy exceeds the work function or the electron affinity, or when an electric field (in electrified fissures) assists the emission. The controlling factors here (*e.g.* work function, etc.) may themselves depend on the nature of the excitation and on the experimental conditions.

Glaefeke (1979) has discussed various theoretical models for the last two steps, especially for dielectrics. Following Kelly (1972), he has described the thermionic emission model, in which the electron concentration is determined by reaction kinetics controlled by the concentration of defects (electron traps) and the retrapping-recombination processes for electrons. The theory has been applied to TSEE with some success. A field-assisted emission model has been developed for space-charge-controlled EE from highly insulating materials (excitation induced by electron bombardment) with the transport and escape of electrons determined by a Monte-Carlo process. The model can explain the intensity, energy and angular distribution of EE, for example in BeO (Kortov and Zolnikov 1975; Fitting *et al* 1979).

In EE from metals with or without an oxide layer, most of the theoretical work has been devoted to step one. Early studies on EE were on the diffusion of vacancies or point defects towards the surface. The rate of arrival of the defects at the surface was determined by Fick's law. This was then assumed to be proportional to the rate at which the electron emitting centres were activated and thereby to the electron emission rate (Grunberg and Wright 1955; von Voss and Brotzen 1959; Pimbley and Francis 1961; Claytor and Brotzen 1965). More recently Nagornykh and Demin (1978) have incorporated into the diffusion equation the generation of vacancies during the straining of oxide coated metals. The diffusion of point defects from the metal into the oxide was matched by the diffusion of oxygen in the opposite direction. The formation of a filled electron trap (F-centre type) at the oxygen vacancy in the oxide was assumed. The electron emission rate was determined from the reaction kinetics involving thermal ionization of traps and recapture of electrons by the traps. The model was applied to EE from oxidised Al with some success.

The model for EE in bursts is based on crack propagation, and is more phenomenological than the model described above (Arnott and Ramsey 1971; Rosenblum *et al* 1977a). These however apply specifically to oxide coated metals. For surface-controlled EE, models based on chemisorption and Auger transitions have been evolved (Kasemo *et al* 1979). Models based on the stress dependence of thermionic emission have also been considered (Tinder 1968).

3. Acoustic emission

By acoustic emission (AE) one means the generation of stress waves during structural changes in a material. These may be generated internally (*eg.*, during phase transitions) or by an externally applied stress. The phenomenon is known to occur for almost all kinds of materials, and has been called by different names in different fields of research; for example, it is referred to as 'seismoacoustic activity' when observed in rocks under stress. AE usually refers to all kinds of stress waves even though the emitted frequencies may be far above the audible range. Extensive work has been done in this field, although to a somewhat applied nature (especially in relation to seismic studies of rocks), and some excellent review articles are available (Green 1969; Liptai *et al* 1971; Dunegan and Tatro 1971; Lord 1975). A brief description of the relevant parts of the subject follows:

The first systematic study of AE was by Kaiser in the 1950's, on polycrystalline zinc, steel, aluminium, copper and lead. He observed that AE was irreversible, *i.e.*, emission did not occur during reloading of a material until the stress exceeded its previous value—a phenomenon usually known as the 'Kaiser effect'. This memory effect applies to most metals but generally not to other materials. In 1961 Schofield reported AE from aluminium and zinc single crystals, commercial copper, aluminium, lead and 70–30 brass, and established correlation with dislocations, slips and grain boundary motion. Tatro and Liptai (1962) studied AE from polycrystalline aluminium and steel for various strain values, and from the observed dependence on the surface condition of the specimen, concluded that AE was a surface phenomenon. Later Schofield studied AE from aluminium single crystals, with and without the oxide layer, and found the surface condition to be of secondary importance except for influencing the strain locally at the point where AE commenced in a burst. It was found that the oxide coating was not a source of AE. Further work by Schofield has established AE as primarily a volume effect. The general features of AE derived from the work of several persons can be summarized as follows (Lord 1975).

AE occurs in two forms: continuously, and in bursts. Continuous emissions of rather high frequency ($\gtrsim 10^2$ kHz) and very low intensity usually occur in metals and metallic systems, and supposedly arise from mobile dislocations and possibly slip movements. Burst emissions occur with much higher intensity and are supposedly associated with failures such as twinning, microcracks, unpinning of dislocations from obstacles, and growth of already existing cracks; they occur at relatively large values of the plastic strain.

Figure 7 shows a typical experimental AE rate as a function of the tensile strain (Dunegan and Harris 1969). This particular result is remarkable in that it fits beautifully with Gilman's mobile dislocation model (Gilman 1966) which gives the mobile dislocation density N_m as a function of the plastic strain ε_p through the relation $N_m = m\varepsilon_p \exp(-\phi\varepsilon_p)$, where m is the dislocation breeding factor, and $\phi = H/\sigma$, where H is the hardening coefficient, and σ is the rms stress. The fit is shown in the dashed curve in figure 7 with $m = 1{\cdot}44 \times 10^7$ and $\phi = 70$ (Lord 1975). This shows that the AE rate is directly related to the mobile dislocation density, so that one may contemplate determining H, an important mechanical parameter, using the AE technique. Unfortunately such a fit of Gilman's formula does not work for many materials. This has been attributed to the inhomogeneity in the strain caused by the occurrence of Lüder's bands.

At present there does not seem to be any rigorous microscopic theory for the actual

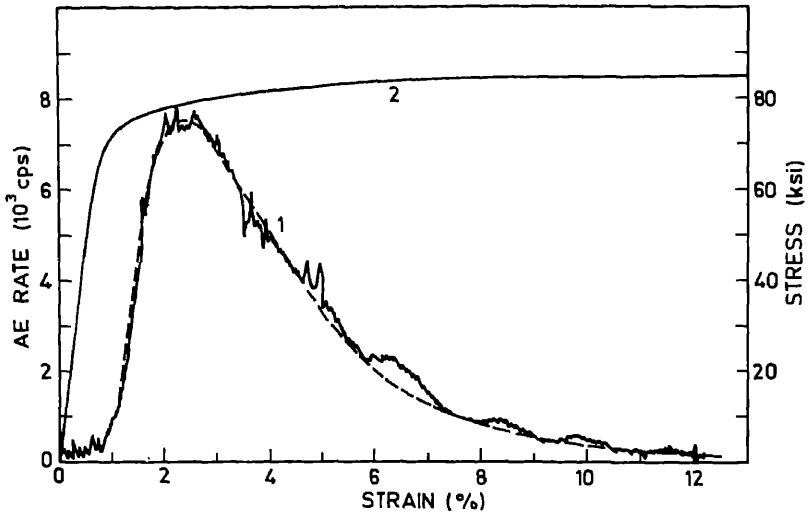

Figure 7. Acoustic emission intensity *vs* strain: 1. experimental: dashed curve. Gilman's relation. Stress *vs* strain: 2. (see Lord Jr 1975).

internal mechanism of AE. The major thrust in this area is in the direction of applied research, of establishing empirical relationships between AE and mechanical parameters (Lord 1975). Further, there has been no attempt to correlate AE with EE, although the typical emission intensity vs strain curves for Al are remarkably similar (compare figures 2 and 7).

4. Mechanoluminescence

Some materials emit light when subject to stress beyond a particular level. This phenomenon is broadly called mechanoluminescence (ML) or triboluminescence. (ML is preferred, to avoid confusion with thermoluminescence which is customarily denoted by TL). Extensive research has been done in this field on a very large number of materials, and the subject has been reviewed by a number of authors (Meyer *et al* 1970; Walton 1977; Zink 1978). Only a brief account of the relevant aspects is given here.

The most widely-studied materials are the alkali halides where the electron traps are the source of luminescence. ML spectra are similar to the TL spectra of a given material. Belyaev *et al* (1963) observed ML spectra during the growth of cracks in alkali halides under uniaxial strain, with photon emission in bursts, indicating that ML is associated with crack propagation. ML during fracture can be a hundred times more intense than TL, the concept of electrified fissures has been used to explain this (Belyaev *et al* 1966; Belyaev and Martyshev 1969). Observations on ML during abrasion or scratching of alkali halides have been correlated with the propagation of cracks and TL (estimated temperatures as high as 10^4 K) at the crack-tip (Meyer *et al* 1970). ML emission has been found to have a memory (analogous to the Kaiser effect) in activated alkali halides and ZnS. In experiments where the strain is repeated, no emission is observed in the elastic or plastic regions; and for a second application of strain, not until its magnitude exceeds that of the previously applied strain. This indicates that the ML intensity depends on the depinning of dislocations under stress (Alzetta *et al* 1970; Scarmozzino 1971). Simultaneous ML and AE have been observed during mechanical deformation of organic glasses, steel and copper plates, indicating a common origin (Sodomka *et al* 1980). ML during the deformation and fracture of metallic alloys has also been reported (Borisova *et al* 1975). Molotskii (1978) observed ML during the plastic deformation and fracture of copper. Zink and his coworkers have observed ML in many organic and inorganic crystals (Zink 1978; Chandra and Zink 1980). In many cases, explanations on the basis of piezo-electrification, cleavage electrification and triboelectrification, have been given (Meyer *et al* 1970; Walton 1977; Chandra 1981).

Intense ML has been observed from coloured alkali halides (coloured by x- or γ-ray irradiation) by a number of workers. The emission is thought to be a result of the interaction of dislocations with colour centres (Butler 1966; Shmurak 1969; Alzetta *et al* 1970; Guerrero and Alvarez-Rivas 1978; Chandra and Zink 1980). Recently ML emission during the application as well as the release of uniaxial compression in x-ray irradiated alkali halides have been reported by Chandra and Elyas (1978). They have also studied γ-irradiated alkali halides and ML emission from coloured alkali halides under repeated stress, and established a linear relationship between the ML intensity and the measured density of newly-created dislocations at the end of repeated-stress cycles (Elyas 1981). At present a proper theoretical understanding of ML emission, particularly from materials containing active luminescence centres, is still lacking, although some theoretical attempts have been made to understand ML in terms of electric field and pressure effects (Lin *et al* 1980). Studies correlating ML with EE or AE also seem to be inadequate.

5. Conclusions

We have tried to present an introduction to the subject of some special physical effects, especially exoelectron emission, in the context of the mechanical deformation of solids. For a better understanding of the exoelectron process, we have also discussed possible mechanisms for EE and two other related phenomena, AE and ML. While a number of possibly important references may have been inadvertently omitted, it is hoped that this article is sufficiently self-contained to generate interest in studying EE in a systematic manner. It can be safely said that, at present, a concrete theory of EE is lacking. Further, extensive, experimental study is required for understanding and correlating EE with AE and ML. For example, one should study more carefully the role of the work function, dislocations (the applicability of Gilman's theory or modification thereof), the mechanism of energy transfer to electrons, and the escape of electrons from metals and oxide-coated metals. On the applications side, one ought to study more extensively the growth of microcracks using spot scanners (PSEE, as in Baxter 1973) and establish empirical relationships with mechanical parameters in the same manner as has been done for acoustic emission studies.

Further references on EE are: Scharmann (1967), Becker (1972), Ramsey (1976), Krylova (1976) and Glaefeke (1979).

Acknowledgements

The author thanks Dr G Srinivasan and Prof. S Ramaseshan for bringing this subject to

his attention. Thanks are also extended to Mr C V Krishna Murthy for providing some of the material presented here.

References

Alzetta G, Chudacek I and Scarmozzino R 1970 *Phys. Status Solidi* **a1** 775

Arnott D R and Ramsey J A 1971 *Surf. Sci.* **28** 1

Baxter W J 1973 *J. Appl. Phys.* **44** 608

Baxter W J and Rouze S R 1978 *J. Appl. Phys.* **49** 4233

Becker K 1972 CRC *Crit. Rev. Solid State Sci.* **3** 74

Belyaev L M, Nabatov V V and Martyshev Yu N 1963 *Sov. Phys. Crystallogr.* **7** 464

Belyaev L M and Martyshev Yu N 1969 *Phys. Status Solidi* **34** 57

Belyaev L M, Nabatov V V, Pisarevskii Yu V and Shaldin Yu V 1966 *Sov. Phys. Crystallogr.* **10** 647

Bichevin V, Käämbre H and Lushchik Ch. 1971 *Phys. Status Solidi* **a5** 525

Bohun A 1961 *Czech. J. Phys.* **11** 819

Bohun A, Sak J and Psenickova M 1965 *Czech-Z-Phys.* **15** 667

Borisova E A, Glebova R D, Platonov A A and Skyarov N M 1975 *Sov. Phys. Dokl.* **20** 435

Born D and Linke E 1976 *Proc. 5th Int. Symp. on EE and Dosimetry* (eds) A Bohun and A Scharmann (Prague: Inst. Solid St. Phys. Acad. Sci.) p 265

Brotzen F R 1967 *Phys. Status Solidi* **22** 9

Brunsmann U and Scharmann A 1977 *Phys. Status Solidi* **a43** 519

Brus L E and Comas J 1971 *J. Chem. Phys.* **54** 2771

Buck O, Pardee W J, Szalkowski F J and Thompson D O 1977 *Appl. Phys.* **12** 301

Butler C G 1966 *Phys. Rev.* **141** 750

Chandra B P 1981 *Phys. Status Solidi* **a64** 395

Chandra B P and Elyas M 1978 *Kristall. U. Tech.* **13** 1341

Chandra B P and Zink J I 1980 *Phys. Rev.* **B21** 816

Chrysson E and Holzapfel G 1980 *Phys. Status Solidi* **a59** K49

Claytor R N and Brotzen F R 1965 *J. Appl. Phys.* **36** 3549

Delchar T A 1967 *J. Appl. Phys.* **38** 2403

Dickinson J T, Braunlich P, Larson L A and Marceau A 1978 *Appl. Surf. Sci.* **1** 515

Dunegan H L and Harris D O 1969 *Ultrasonics* **7** 160

Dunegan H L and Tatro C A 1971 *Techniques of metals research* (ed) R F Bunshah (New York: Wiley Interscience) Vol V p 273

Elyas M 1981 *Studies of mechanoluminescence produced during application and release of a uniaxial pressure in x-irradiated KBr, KCl, KI, LiF and NaCl crystals*, Ph.D. Thesis, The Ravishanker University, Raipur, India

Euler M and Scharmann A 1976 *Phys. Status Solidi* **a34** 297

Fitting H J 1981 *Phys. Status Solidi* **a63** K47

Fitting H J, Glaefeke H, Wild W and Lange J 1977 *Phys. Status Solidi* **a42** K75

Fitting H J, Glaefeke H, Wild W, Franke M and Müller W 1979 *Exp. Tech. Phys.* **27** 13

Ford L H, Holzapfel G and Kaul W 1970 *Z. Angew Phys.* **30** 259

Gesell T F, Arakawa E T and Calcott T A 1970 *Surf. Sci.* **20** 174

Gieroszynski A and Sujak B 1965 *Acta Phys. Pol.* **28** 311

Gilmann J J 1966 *Proc. 5th U.S. Nat. Congr. Appl. Mech.* 385

Glaefeke H 1979 *Topics in applied physics* (ed) P Bräunlich (Berlin: Springer-Verlag) Vol 37 p 224

Green A T 1969 *Nucl. Safety* **10** 4

Grunberg L 1958 *Br. J. Appl. Phys.* **9** 85

Grunberg L and Wright K H R 1955 *Proc. Roy. Soc. London* **A232** 403

Guerrero E and Alvarez-Rivas J L 1978 *Solid State Commun.* **28** 199

Hiernaut J P, Forier R P and Van Cakenberghe J 1972 *Vacuum* **22** 471

Holzapfel G and Krystek M 1976 *J. Phys. (Paris)* **37** C-7-238

Jakowski N and Glaefeke H 1976 *Thin-Solid Films* **36** 195

Kasemo B, Tornqvist E, Nørskov J K and Lundqvist B T 1979 *Surf. Sci.* **89** 554

Kelly P 1972 *Phys. Rev.* **B5** 749

Kelley P and Himmel L 1976 *Comm. Solid State Phys.* **7** 81

Kirihata H and Akutsu J 1979 *Phys. Status Solidi* **a51** K 109

Komai K 1978 *Trans. Jap. Inst. Met.* **19** 119

Kortov V S and Myasnikov I E 1972 *Phys. Status Solidi* **a9** 119

Kortov V S and Zolnikov P P 1975 *Phys. Status Solidi* **a31** 331

Kortov V S, Mints R I, Myasnikov I E and Gaprindoshvily A Y 1970 *Phys. Status Solidi* **a3** 13

Kortov V S, Mints R I and Teplov V G 1971 *Phys. Status Solidi* **a7** K89

Kortov V, Isakov V, Glaefeke H and Fitting H J 1982 *Phys. Status Solidi* **a73** K275

Kramer J 1950 *Der metallische zustand* (Gottingen: Vanderhoeck Ruprecht)

Kriegseis W and Scharmann A 1975 *Phys. Status Solidi* **a29** 407

Krishna Murthy C V 1982 *Exoelectron emission*, M.Sc. Thesis, Indian Institute of Technology, Bombay, India

Krylova I V 1971 *Phys. Status Solidi* **a7** 359

Krylova I V 1976 *Usp. Biol. Khimii* **45** 2138 (English Transl.: 1976, *Russ. Chem. Rev.* **45** 1101)

Krylova I V, Svitov V I and Konyushkina N I 1976 *Zh. Fiz. Khimii* **50** 933 (English Transl.: 1976 *J. Phys. Chem.* **50** 555)

Lewis T J 1954 *Proc. Phys. Soc.* **B67** 187

Lin S H, Wutz D, Ho Z Z and Eyring H 1980 *Proc. Natl Acad. Sci.* (*USA*) 77 1245

Linke E 1970 *Z. Angew Phys.* **29** 241

Liptai R G, Harris D O, Engle R B and Tatro C A 1971 *Int. J. Nondestruct. Test.* **3** 215

Lord A E Jr. 1975 *Physical acoustics* (eds) W P Mason and R N Thurston (Academic Press: New York) Vol. XI 289

McCarrol B 1969 *J. Chem. Phys.* **50** 4758

McLennan J C, 1902 *Philos. Mag.* **3** 195,

Maiste A, Sorkin B, Elango M and Käämbre H 1973 *Phys. Status Solidi* **a20** K83

Meyer K, Obrikat D and Rossberg M 1970 *Kristall. Tech.* **5** 5, 181

Mints R I, Melekin V P, Segal V M and Icolev I Yu 1973 *Sov. Phys. Solid State* **14** 2153

Molotskii M I 1978 *Sov. Phys. Solid State* **20** 956

Mueller R K and Pontinen K 1964 *J. Appl. Phys.* **35** 1500

Nagornykh S N and Demin Yu A 1978 *Phys. Met. Metall.* **46** 170

Nink R and Holzapfel G 1973 *J. Phys.* (*Paris*) **34** C-9-491

Pardee W J and Buck O 1977 *Appl. Phys.* **14** 367

Pimbley W T and Francis E E 1961 *J. Appl. Phys.* **32** 1729

Rabinowicz E 1977 *Sci. Am.* **236** 74

Ramsey J A 1976 *Progr. surface and membrane Sci.* (New York: Academic Press) Vol 11 p 117

Rhead G E 1977 *Surf. Sci.* **68** 20

Rosenblum B, Carrico J P, Bräunlich P and Himmel L 1977 *J. Phys.* **E10** 1056

Rosenblum B, Braunlich P and Himmel L 1977a *J. Appl. Phys.* **48** 5262

Rudolf G and Glaefeke H 1982 *Phys. Status Solidi* **a73** K253

Scarmozzino R 1971 *Solid State Commun.* **9** 1159

Scharmann A 1967 *Festkorperprobleme* (Berlin: Akad.-Verl.) Vol 6 p. 106

Scharmann A and Wiessler U 1980 *Phys. Status Solidi* **a60** 117

Schlenk W 1976 *Phys. Status Solidi* **a33** 217

Shmurak S Z 1969 *Sov. Phys. Solid State* **10** 1526

Shorshorov M Kh., Zhebynev D A and Alekhin V P 1976 *Proc. 5th Inter. Symp. on EE and Dosimetry* (ed) A Bohun and A Scharmann (Prague: Inst. Solid St. Phys. Acad. Sci.) p. 229

Sodomka L, Leistner M, Tessmar H and Karel F 1980 *Kristall. U. Tech.* **15** 1101

Sujak B 1964 *Acta Phys. Pol.* **26** 1033

Sujak B and Gieroszynski A 1970 *Acta Phys. Pol.* **A37** 733

Sujak B, Gieroszynski A and Pega E 1965 *Acta Phys. Pol.* **28** 61

Sujak B, Gieroszynska K and Gieroszynski A 1982 *Phys. Status Solidi* **a72** K177

Tale I, Kortov V and Popov V 1982 *Phys. Status Solidi* **a74** 395

Tatro C A and Liptai R G 1962 *Proc. Symp. on Physics and Non Destructive Testing* (Southwest Research Inst., San Antonio, Texas) p. 145

Tinder R F 1968 *J. Appl. Phys.* **39** 355

Von Voss W D and Brotzen F R 1959 *J. Appl. Phys.* **30** 1639

Walton A J 1977 *Adv. Phys.* **26** 887

Wortmann J 1978 *Phys. Status Solidi* **a50** 509

Zink J I 1978 *Acc. Chem. Res.* **11** 289

Discussion

M Yussouff: Has the velocity distribution of the emitted electrons been measured?

G Mukhopadhyay: Yes, it has, in some cases.

R Chidambaram: How does thermoluminiscence dosimetry compare with exoemission?

Mukhopadhyay: I am sorry, I can't give you a precise answer.

R Krishnan: If there are two or more processes of exoemission occurring simultaneously, can one separate one from the other?

Mukhopadhyay: Only by doing additional experiments.

G Venkataraman: Would the exoemission rate depend on the type of defect migrating to the surface?

Mukhopadhyay: Yes, it would—particularly the temperature dependence, because activation is involved.

C K Majumdar: How long before the actual crack occurs can one detect anything by the techniques you have described?

Mukhopadhyay: This depends on the material. In fatigue cycling with a large stress amplitude, very early detection is possible (at 0·7% of failure).

P Rodriguez: Is the exoemission phenomenon more amenable to measurement in fatigue cycling than in a uniaxial tensile test?

Mukhopadhyay: Not necessarily, but I think this depends on the experimentalist.

M Yussouff: Is exoemission a field emission process?

Mukhopadhyay: No, because the actual explanation depends on the type of sample and environment involved.

Bull. Mater. Sci., Vol. 6, No. 4, September 1984, pp. 773–774. © Printed in India.

Relevance of liquid state to solid state properties*

H R KRISHNA MURTHY and T V RAMAKRISHNAN

Department of Physics, Indian Institute of Science, Bangalore 560 012, India

Abstract. We outline in this talk the beginning of a new programme to study physical properties of crystalline solids. It is based on considering the latter, a broken symmetry phase, in terms of the higher symmetry liquid phase. The solid is a calculable perturbation on the fluid. This is exactly opposite to the standard approach which relates mechanical properties to the behaviour of defects (mainly dislocations) etc., in an otherwise perfect crystalline solid. However, most other broken symmetry phases (*e.g.* ferromagnets) are discussed starting from a symmetric Hamiltonian or a free energy functional, and earlier work by one of the authors shows that the liquid-solid transition is well described, qualitatively and quantitatively, by this approach. On the other hand, defect theories of melting have a long record of nonsuccess. In the first part of the talk, the density wave theory of freezing will be outlined, and it will be shown how properties such as Debye Waller factor, entropy change of freezing etc. can be calculated with no or one free parameter. The problem of calculating shear elastic constants and dislocation core structures as well as energies in terms only of observable liquid state properties will be set up, and results presented. The method will be contrasted with zero temperature 'atomistic' models which obscure the essential dependence on structure and flounder in a mass of detail. The concluding part will describe further proposed applications, some suggestive experimental results extant in the literature, and some speculations.

Discussion

G Venkataraman: Is something like the Josephson effect possible in this case of change of phase associated with ballistic motion or diffusion?

T V Ramakrishnan: This is a hard question to answer.

V Balakrishnan: What stabilizes the system against other possible μ_G's? How does the system choose, say, between the fcc and bcc structures?

Ramakrishnan: We examine the stability of the fluid with respect to a *given* structure.

V Balakrishnan: What is it in the system that kills fluctuations with other wavevectors?

Ramakrishnan: The correlation function $S(q)$ is strongly peaked at a particular q. Thus the energy to excite this mode is far less than that for any other mode.

G Ananthakrishna: How does one measure the three-point correlation?

Ramakrishnan: This can be estimated either by computer simulation or by doing light scattering experiments on colloidal crystals.

G Srinivasan: Could one find the pressure dependence of the two-point correlation?

Ramakrishnan: This does not give the quantity required here.

---

* Only a summary is presented.

K R Rao: Is it necessary that the three-point correlation measurement be done in solid state?

Ramakrishnan: No. A "combination" scattering experiment has to be done in the liquid state for information in the short-range region.

K R Rao: What is the difficulty in predicting the melting temperature?

Ramakrishnan: The difficulty is that μ_G and C_G are dimensionless quantities.

S Ranganathan: Can your theory take into account the liquid-glass transition?

Ramakrishnan: No. We are very far from it.

D Dhar: How is the effective potential you use related to the effective potential used in cell theories of melting?

Ramakrishnan: The two are not related to each other.

S R Shenoy: Can one use your theory to handle a crystal with frozen-in defects?

Ramakrishnan: Perhaps one could, depending on how perfect these crystallites are and also on how rapidly the phase changes.

R Chidambaram: Where is the entropy of melting in this model?

Ramakrishnan: We calculate the entropy of melting from the known thermodynamic functions.

G Ananthakrishna: How do you describe dislocations and vacancies in your model?

Ramakrishnan: I don't know how to describe vacancies, but dislocations can be described in a manner similar to vortices in a superconductor.

Bull. Mater. Sci., Vol. 6, No. 4, September 1984, pp. 775–798. © Printed in India.

Elastic continuum theories of lattice defects: a review

DEBENDRANATH SAHOO

Materials Science Laboratory, Reactor Research Centre, Kalpakkam 603 102, India

Abstract. The presently available elastic continuum theories of lattice defects are reviewed. After introducing a few elementary concepts and the basic equations of elasticity the Eshelby's theory of misfitting inclusions and inhomogeneities is outlined. Kovács' result that any lattice defect can be described by a surface distribution of elastic dipoles is described. The generalization of the isotropic continuum approach to anisotropic models and to Eringen's isotropic but non-local model is discussed. Kröner's theroy (where a defect is viewed as a lack of strain compatibility in the medium) and the elastic field equations (formulated in a way analogous to Maxwell's field equations of magnetostatics) are described. The concept of the dislocation density tensor is introduced and the utility of higher-order dislocation density correlation tensors is discussed. The beautiful theory of the affine differential geometry of stationary lattice defects developed by Kondo and Kröner is outlined. Kosevich's attempt to include dynamics in the elastic field equations is described. Wadati's quantum field theory of extended objects is mentioned qualitatively. Some potential areas of research are identified.

Keywords. Elastic continuum theory; lattice defects; inhomogeneities; dislocations; disclinations; dislocation density tensor; torsion tensor; curvature tensor; dislocation density correlations; elastic field equations; nonlocal elasticity.

1. Introduction

This paper is intended to survey the elastic continuum theories of lattice defects. The understanding of the behaviour of crystal defects is essential for studying such processes as anelasticity, plastic flow, rupture, fatigue and radiation damage, which play a crucial role in materials science. The lattice distortion produced by a defect can be calculated by using elastic models at sufficiently large distances from the defect. In many applications, a continuum theory offers precise analytic expressions for the stress fields of defects, their interaction energies, etc., and hence is of immense practical value. In contrast to this, a discrete atomistic approach (which is unavoidable at short distances from the defects) does not offer analytically convenient working relations, although it yields reliable numerical data.

At present there is no unified theory of defects in continuous media. Most theories are developed with a particular type of defect in view. Thus the methods applicable to point defects are different from those applicable to line defects—for dislocations, see *e.g.*, de Wit (1960), Nabarro (1967), Mura (1968); for volume defects (inclusions), see Eshelby (1957). Moreover, almost all theories are restricted to static defect problems. The dynamical theory of defects in continua is still in its infancy. This review presents a bird's eyeview of the various approaches to defects in a continuous medium.

2. Continuum modelling of defects

In the elastic continuum theory, defects are modelled following the procedure given by (See e.g. Eshelby 1956). In order to construct a defect, one marks out in the medium an appropriate surface S_C bounded by a curve C and makes a cut coinciding with C. Then a relative displacement $\delta\mathbf{u}$ is given to each pair of points on either side of S_C, scraping away material where there would be interpenetration and filling in the remaining gaps with additional material. In general, $\delta\mathbf{u}$ can be written as

$$\delta u_i = b_i + \Omega_{ij} x_j \quad (i, j = 1, 2, 3),$$

where x_j denotes the coordinates of the point, b_i the relative translation of this point, and $\Omega_{ij} (= -\Omega_{ji})$ describes the relative rotation of S_C. A general dislocation is thus described by six constants—in other words, it consists of six elementary (Volterra) dislocations. Each of the latter can be characterized by a single constant, the other five being set equal to zero. A rotational dislocation with $b_i = 0$ is actually a disclination. When $\Omega_{ij} = 0$, one has the usual (translational) dislocation with a Burgers vector $\mathbf{b}$. Some examples of defects created in this manner are shown in figure 1. Figure 1(a) shows an edge dislocation produced by cutting a ring-shaped cylinder across the surface S_C, choosing the axis of the cylinder as the curve C, and displacing the upper side of the surface S_C over the lower by an amount $\mathbf{b}$ perpendicular to the axis. In figure 1(b), a sector of the cylinder is cut defining the surface S_C and the axis as C, and both sides of the surface are pulled apart widening the angle of the sector so as to accommodate a larger sized sector. This produces a wedge disclination, $\mathbf{\Omega}$ being a rotation around the axis. Figure 1(c) shows the Somigliana prescription for creating a substitutional or an interstitial atom. A sphere is cut out of the matrix, its radius altered by adding or removing material, and the sphere is then reinserted in the matrix. This is the familiar misfitting sphere model. Note that there is no boundary curve C in this case. It can be shown that a knowledge of $\delta\mathbf{u}$ as a function of position x_i on the surface S_C, together with the boundary conditions at the surface of the body, completely determines the resulting state of internal stress.

3. Basic equations of elasticity theory

In the linear theory of elasticity, the condition of equilibrium is given by

$$\sigma_{il,l} + f_i = 0, \tag{1}$$

where σ_{il} is the stress tensor, f_i is the body force and the usual comma notation for derivatives and the convention of summation over repeated indices are used. σ_{ij} is related to the strain tensor e_{ij} by Hooke's law:

$$\sigma_{il} = C_{ilmn} e_{mn}, \tag{2}$$

where

$$e_{mn} = \tfrac{1}{2}(u_{m,n} + u_{n,m}), \tag{3}$$

is the symmetric part (sym) of the gradient (grad) of the displacement field $\mathbf{u}$: thus $e = \text{sym grad } \mathbf{u} \equiv \text{def } \mathbf{u}$. For an isotropic homogeneous medium

$$C_{ilmn} = \lambda \delta_{il} \delta_{mn} + \mu(\delta_{im} \delta_{ln} + \delta_{in} \delta_{lm}), \tag{4}$$

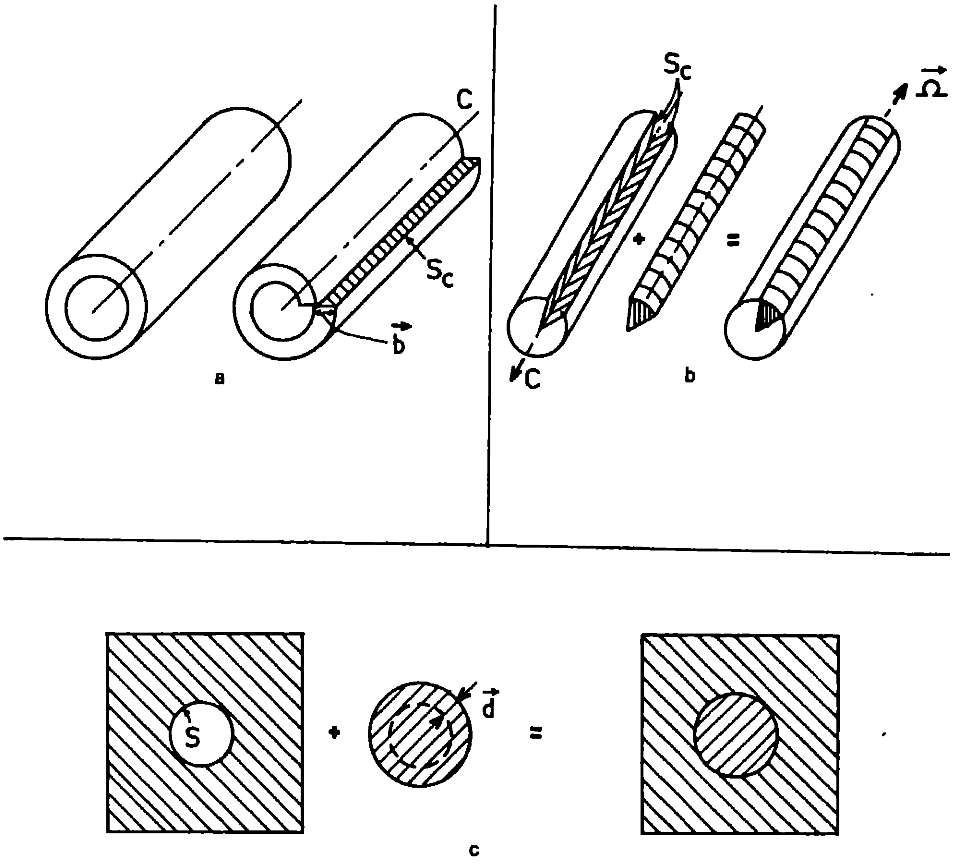

Figure 1. (a) Continuum model of an edge dislocation. (b) Continuum model of a wedge disclination. (c) Misfitting sphere model for a substitutional atom.

where λ is Lame's constant and μ is the shear modulus. Equations (1)–(3) imply the differential equations

$$C_{ilmn}u_{m,nl}+f_l=0 \tag{5}$$

for $\mathbf{u}$. Let G_{li} be the Green function tensor defined by the equation

$$C_{ijkl}G_{km,lj}(|\mathbf{r}|)+\delta_{im}\delta(|\mathbf{r}|)=0 \tag{6}$$

and the boundary condition $G_{km}(r\to\infty)=0$. Then

$$G_{km}(r)=\frac{1}{8\pi\mu}\left[\delta_{km}r_{,pp}-\frac{\lambda+\mu}{\lambda+2\mu}r_{,km}\right]. \tag{7}$$

The elastic field due to the body force $\mathbf{f}$ is given by

$$u_l(\mathbf{r})=\int f_i(\mathbf{r}')G_{li}(|\mathbf{r}-\mathbf{r}'|)\,\mathrm{d}^3r'. \tag{8}$$

The existence of a continuous single-valued displacement field u_l requires the incompatibility (inc) of the strain tensor to vanish, *i.e.*,

$$\mathrm{inc}\, \boldsymbol{e} = 0, \tag{9}$$

where, in component form,

$$(\mathrm{inc}\, \boldsymbol{e})_{ij} = -\varepsilon_{ikl}\varepsilon_{jmn} e_{ln,km} = [\mathrm{curl}\,(\mathrm{curl}\, \boldsymbol{e})]_{ij}, \tag{10}$$

ε_{ikl} denoting the completely antisymmetric Levi-Civita tensor or the alternator.

There are two broad ways of introducing defects into this picture. One is to start with (1) and assign an effective f_i, as is usually done in a point defect (Eshelby 1957). In line defects, one puts $f_i = 0$, but generalises (8) to include the contribution from the cut surface S_C (Mura 1968). In the second approach, one must recognise that when defects are present in the medium, the displacement field $\mathbf{u}$ is no longer a continuous single-valued function on S_C, and therefore the compatibility condition ought to be modified. This is achieved by generalizing (9) to include a source term η characterising the incompatibility distribution of the defect, *i.e.*, (9) is replaced by

$$\mathrm{inc}\, e = \eta. \tag{11}$$

In the next section we describe briefly the first approach which is due largely to Eshelby (1957).

4. The Eshelby approach

Volume defects such as precipitates, solute atoms, self-interstitials, etc contribute to the change in the elastic state of the medium. A self-interstitial is modelled as a misfitting homogeneous inclusion (MHI). It corresponds to matter of volume $V + \Delta V$ being forced into a cavity of volume V in the medium (see figure 2a). Both the inclusion (I) and the matrix (M) have the same elastic moduli. An MHI is created in a body because of internal stress, *i.e.*, some region I of volume V develops internal stress and is transformed to a different shape and size with a volume $V + \Delta V^C$ while remaining inside the matrix M (see figure 2b). Thus a constrained stress (σ_{ij}^C) or a constrained strain (e_{ij}^C) is developed both in I and M.

Now suppose M was absent and I alone were to undergo a transformation (see figure 2c). It would acquire a different shape and size, with volume $V + \Delta V^T$. Let σ_{ij}^T and e_{ij}^T be the stress and strain associated with the transformation. These *need not* be of elastic origin (they may arise from metallurgical transformations, for example). Thus, symbolically, $I \xrightarrow{T} I^T$, and $M \xrightarrow{T} M$. Eshelby has posed and answered the following questions:

(i) How can one relate σ_{ij}^C and e_{ij}^C to σ_{ij}^T and e_{ij}^T? (ii) What can one deduce about the behaviour of $\mathbf{u}^C$, $\boldsymbol{\sigma}^C$ and e^C, the dilation and the self-energy of an MHI of arbitrary shape? (iii) What is the interaction energy of an MHI with an applied stress field σ_{ij}^A?

After answering these questions Eshelby asks the same questions for an "inhomogeneity" (see figure 2d). The inhomogeneity is an inclusion having elastic constants (λ^*, μ^*) different from those of the matrix (λ, μ). Note that a perfectly-fitting inhomogeneity (PFI) does not perturb the stress field in the matrix. However, a misfitting inhomogeneity (MFI) would alter the stress field in M.

An MFI is an appropriate model for a foreign interstitial in a crystal. Eshelby shows how to reduce the problem of an MFI to an equivalent MHI problem. The problem of an MFI in the presence of an external stress σ_{ij}^A is of interest in many practical situations such as SIPA creep (Heald and Speight 1974), voids in strained metals, etc. In the presence of σ_{ij}^A, a PFI can undergo an induced transformation strain e_{ij}^T 'proportional' to the applied strain e_{ij}^A. To illustrate the Eshelby approach, consider an MHI for which the displacement field u_i^C is given by

$$u_i^C(r) = \int \mathrm{d}S_l' C_{jlmn} e_{mn}^T(\mathbf{r}') G_{ij}(|\mathbf{r}-\mathbf{r}'|). \tag{12}$$

Eshelby considers a spherical and an ellipsoidal MHI for which e_{mn}^T is constant, and, using (7) for the Green function, arrives at the familiar relations (for the spherical MHI):

$$\left.\begin{aligned} e_{ij}^C &= {}'e_{ij}^C + \tfrac{1}{3} e^C \delta_{ij} \\ &= \beta\, {}'e_{ij}^T + \tfrac{1}{3} \alpha e^T \delta_{ij}, \\ e^C &\equiv e_{ii}^C,\ {}'e_{ij}^C \equiv e_{ij}^C - \tfrac{1}{3} e^C \delta_{ij}, \\ \alpha &= \frac{1}{3}\left(\frac{1+\nu}{1-\nu}\right),\ \beta = \frac{2}{15}\left(\frac{4-5\nu}{1-\nu}\right). \end{aligned}\right\} \tag{13}$$

Here ${}'e_{ij}$ is the deviatioric part of e_{ij} and e is the scalar part. The general results for a PFI and an MFI under an applied load are given in Eshelby (1957).

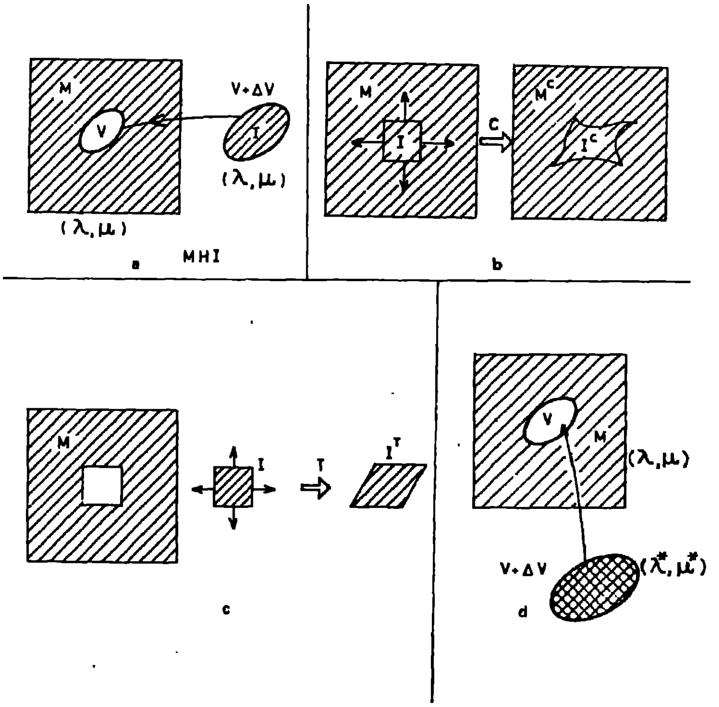

Figure 2. (a) A misfitting homogeneous inclusion (MHI). (b) The rectangular region I undergoing a constrained transformation in the matrix resulting in a curved shape. (c) The region I, detached from the matrix, undergoing a T transformation. (d) A misfitting inhomogeneity (MFI).

A significant feature of Eshelby's theory is the recognition of the important role of surfaces in defect problems. Eshelby was the first to show that the surface contribution to the change in volume of the medium, when defects are present, is quite significant. When defects (internal stresses) are present in a bounded medium, one must invoke image forces such that the boundary of the medium is kept free of stresses (the equilibrium condition), analogous to the method of images in electrostatics. As in the latter case, the image stress in the defect problem should have no internal sources in the medium. A well-known result derived by this method is that the volume change of a finite medium when a single spherical point defect is present is γ times the corresponding volume change in the infinite medium, where $\gamma = 3(1-\nu)/(1+\nu)$ is the famous Eshelby factor and ν is Poisson's ratio. If ν is taken as 1/3, then γ is as large as 3/2.

5. The elastic dipole tensor

Of central importance in the study of defects is the concept of the elastic dipole. Let a point force f_j be acting at a point $\mathbf{r}'$ in an elastic medium. The displacement u_j at a point $\mathbf{r}$ caused by the force is

$$u_j(\mathbf{r}) = f_l(\mathbf{r}')G_{lj}(|\mathbf{r}-\mathbf{r}'|). \tag{14}$$

Now suppose that in a small volume centred at $\mathbf{r}'$, N point forces $f_k^\alpha(\mathbf{r}'+\mathbf{s}^\alpha)$ are acting at the points $\mathbf{r}'+\mathbf{s}^\alpha$ ($\alpha = 1, \ldots, N$). Then (14) must be generalised to

$$\begin{aligned} u_l(\mathbf{r}) &= \sum_{\alpha=1}^{N} f_k^\alpha(\mathbf{r}'+\mathbf{s}^\alpha)G_{lk}(|\mathbf{r}-\mathbf{r}'-\mathbf{s}^\alpha|) \\ &= \left[\sum_{\alpha=1}^{N} f_k^\alpha\right] G_{lk}(|\mathbf{r}-\mathbf{r}'|) + \left[\sum_{\alpha=1}^{N} s_j^\alpha f_k^\alpha\right] G_{lk,j'}(|\mathbf{r}-\mathbf{r}'|) \\ &\quad + \frac{1}{2}\left[\sum_{\alpha=1}^{N} s_j^\alpha s_m^\alpha f_k^\alpha\right] G_{lk,j'm'}(|\mathbf{r}-\mathbf{r}'|). \end{aligned} \tag{15}$$

Here the second equality is obtained by expanding the Green function in a Taylor series about $(|\mathbf{r}-\mathbf{r}'|)$. (Note that $G_{lk,j'}$ stands for $\partial G_{lk}/\partial x_j'$). The first term in the expansion vanishes, because for physically realizable defects the invariance of the entire system under a rigid infinitesimal translation implies that

$$\sum_\alpha f_k^\alpha(\mathbf{r}'+\mathbf{s}^\alpha) = 0. \tag{16}$$

The elastic dipole (P_{jk}), tripole (P_{jkl}), etc are then defined as the quantities in parentheses in the successive terms that remain:

$$\begin{aligned} P_{jk} &= \sum_{\alpha=1}^{N} s_j^\alpha f_k^\alpha, \\ P_{jmk} &= \sum_{\alpha=1}^{N} s_j^\alpha s_m^\alpha f_k^\alpha, \text{ etc.} \end{aligned} \tag{17}$$

The displacement field due to a dipole is thus

$$u_l(\mathbf{r}) = P_{jk}G_{lk,j'}(|\mathbf{r}-\mathbf{r}'|) \text{ and } P_{jk} = P_{kj}. \tag{18}$$

It can be shown easily that a dipole is simulated by a body force according to

$$f_i(r) = P_{ik}\delta_{,k'}(r-r'). \tag{19}$$

The importance of the elastic dipole can be judged from the following result due to Kovács (1978): *Any lattice defect can be described by a surface distribution of elastic dipoles.* To establish this fact, consider a surface S in a medium, and let it undergo a transformation such that the surface element dS'_m at a position $\mathbf{r}'$ on the surface has a displacement $a_l(\mathbf{r}')$. Due to this transformation, the surface element dS'_m becomes a source of an elastic singularity with a dipole strength which can be defined by the expression

$$\mathrm{d}P_{ik} = C_{iklm}a_l\mathrm{d}S'_m. \tag{20}$$

The total strength of the defect is given by

$$P_{ik} = \int_S C_{iklm}a_l\,\mathrm{d}S'_m. \tag{21}$$

The displacement field of the defect is obtained by applying (18) and integrating over the dipole distribution

$$\begin{aligned} u_n(\mathbf{r}) &= \int G_{nl,k'}(\mathbf{r}-\mathbf{r}')\,\mathrm{d}P_l(\mathbf{r}') \\ &= C_{iklm}\int_S G_{nl,k'}(\mathbf{r}-\mathbf{r}')a_l\,(\mathbf{r}')\,\mathrm{d}S'_m. \end{aligned} \tag{22}$$

To apply this result to a dislocation, consider a cut in the medium over the surface S_C bounded by a closed curve C. The positive direction of the normal to S_C is related to C by the right hand rule. Now let each point on S_C be given a displacement $a_l(\mathbf{r}') = b_l$, $\mathbf{b}$ being a constant vector. Then we obtain the familiar Burgers (1939) result

$$u_n(r) = C_{iklm}b_i\int_{S_C} G_{ln,m}(r-r')\mathrm{d}S'_k, \tag{23}$$

which is the displacement field of a dislocation loop C of Burgers vector $\mathbf{b}$.

The displacement field of an MHI can be obtained by choosing for S a closed surface enclosing a volume $V \neq 0$ and considering the displacement $a_l(r')$ inside and outside S:

$$a_l(\mathbf{r}') = \begin{cases} u_l^T(r'), & \text{if } \mathbf{r}' \in V \\ 0, & \text{otherwise.} \end{cases} \tag{24}$$

Using (18) and applying Gauss's theorem, one obtains

$$u_n(\mathbf{r}) = \int_V C_{iklm}u^T_{l,m}G_{nl,k'}\,\mathrm{d}V' + \int_V C_{iklm}u^T_l G_{nl,k'm'}\,\mathrm{d}V'. \tag{25}$$

As the Green tensor is symmetric and satisfied the equation

$$C_{iklm}G_{nl,k'm'} = -\delta_{nl}\delta(\mathbf{r}-\mathbf{r}'), \tag{26}$$

we obtain

$$u_n(\mathbf{r}) = \begin{cases} \displaystyle\int_V \sigma^T_{ik} G_{ni,k'}\,\mathrm{d}V' - u^T_n, & \text{if } r \in V, \\ \displaystyle\int_V \sigma^T_{ik} G_{ni,k'}\,\mathrm{d}V', & \text{if } r \notin V, \end{cases} \tag{27}$$

where $\sigma^T_{ik} = C_{iklm} u^T_{l,m}$. This result is essentially the same as that obtained by Eshelby (1961) if we identify $\frac{1}{2}(u^T_{l,m} + u^T_{m,l})$ with the transformation strain e^T_{ml}. The total strength of this defect is

$$\begin{aligned} P_{ik} &= \oint_S C_{iklm} u^T_l \,\mathrm{d}S'_m \\ &= \int_V C_{iklm} u^T_{l,m} \quad \mathrm{d}V' = \int_V \sigma^T_{ik}\,\mathrm{d}V'. \end{aligned} \tag{28}$$

Thus an MHI can be interpreted as a space distribution of dipoles with a volume density σ^T_{ik}. A PFI can be treated similarly (Kovàcs 1978), and the results of Eshelby (1957) rederived.

The interaction energy U between the defect, a strain field e^A_{ik} and the associated force F^t_n acting on the defect are expressed by the following general relations:

$$\begin{aligned} U &= -\int e^A_{ik}(\mathbf{r}')\,\mathrm{d}P_{ik}(\mathbf{r}') \\ &= -\int_S C_{iklm} e'_{ik}(\mathbf{r}') a_l(\mathbf{r}')\,\mathrm{d}S'_m. \end{aligned} \tag{29}$$

$$\begin{aligned} F^t_n &= \int e^A_{ik,n}\,\mathrm{d}P_{ik} \\ &= C_{iklm} \int_S e^A_{ik,n}(\mathbf{r}') a_l(\mathbf{r}')\,\mathrm{d}S'_m. \end{aligned} \tag{30}$$

These equations are applicable to any type of defect. Thus, substituting in (30) the displacement appropriate for a dislocation and using Stokes' theorem, one recovers the Peach-Koehler (1950) expression for the force

$$F^{\mathrm{disl}}_n = \oint_C \varepsilon_{mnk} \sigma^A_{lm} b_l \,\mathrm{d}l'_k, \tag{31}$$

where σ'_{lm} is the stress field associated with the strain e'_{lm} and $\mathrm{d}l'_k$ is a line element along C.

6. Generalizations of elastic continuum models

An important step towards bridging the gap between the elastic continuum approach outlined in the previous sections and the more detailed atomistic calculations has been achieved on two different fronts: the anisotropic continuum approach and the nonlocal continuum approach.

6.1 *The anisotropic continuum models*

These models are well described in the recent book by Teodosiu (1982) which also contains an exhaustive set of relevant references. A point defect in a crystal lattice is better represented by an elastic dipole tensor which is *anisotropic*, conforming to the symmetry of the actual defect site in the lattice, whereas the host lattice may be modelled as an elastically isotropic medium. We mention as an example the calculation of the interaction energy between two point defects with cubic symmetry O_h by Siems (1968). He showed that two elastic dipoles do not interact, and that the principal singularity of the elastic interaction energy between two such defects is the dipole-octupole interaction. Models along these lines have been proposed for faceted voids in irradiated crystals (Evans *et al* 1972; Malen and Bullough 1971).

Another approach is to consider spherically symmetric point defects in a host medium that is elastically anisotropic. The major drawback of this approach is the nonavailability of a closed form analytic expression for the Green tensor. For symmetries other than hexagonal symmetry (Kröner 1953), the solutions are in the form of series, thus necessitating perturbation-type calculations. For these reasons of mathematical inconvenience, not much work has been done along these lines. (For point defects, see Eshelby 1956; for line defects in an anisotropic host medium, Teodosiu 1982; Steeds and Willis 1979).

6.2 *The nonlocal elastic continuum models*

Eringen and Edelen (1972) and Eringen (1972, 1976) have developed a new theory of elasticity called nonlocal elasticity. This theory makes use of nonlocal elastic constants (a closer approximation to the force constants of the atomistic theories). The basic equations of linear isotropic elastic solids, for the static case and vanishing body forces are:

$$\left.\begin{aligned}
\bar{\sigma}_{ik,k} &= 0,\\
\bar{\sigma}_{ik} &= \int_V \sigma_{ik}^{NL}(\mathbf{r},\mathbf{r}')\,\mathrm{d}^3r',\\
\sigma_{ik}^{NL} &= \alpha(|\mathbf{r}-\mathbf{r}'|)C_{iklm}e'_{lm},\\
e'_{lm} &= \tfrac{1}{2}(u_{l,m'}+u_{m,l'}).
\end{aligned}\right\} \qquad (32)$$

Here $\alpha(|\mathbf{R}|)$ attenuates rapidly as $R \to 0$, it is a continuous function which depends on a parameter a such that when $a \to 0$, $\alpha(R) \to \delta(R)$ and the classical equations of elasticity are recovered. Here $e'_{lm} \equiv e_{lm}(\mathbf{r}')$ and $u_{l,m'} = \partial u_l/\partial x'_m$. The stress $\sigma^{NL}(\mathbf{r})$ is the nonlocal stress in the sense that its value at $\mathbf{r}$ depends on the strain at all $\mathbf{r}' \in V$. Eringen has shown that the first equation in (32) is satisfied if and only if $(C_{iklm}e_{lm})_{,k} \equiv \sigma_{ik,k} = 0$ in V. This means that the *displacement* field remains the same in the nonlocal theory as in the classical theory. The *stresses* differ in the two theories.

Kovàcs and Vörös (1979) showed that the appropriate body force F_i to be included in the generalization of (32) is

$$F_i(\mathbf{r}) = \int \alpha(\mathbf{r}-\mathbf{r}')f_i(\mathbf{r}')\,\mathrm{d}V', \qquad (33)$$

where $f_j(\mathbf{r})$ is the body force in the classical theory (see (1)). The force acting on an elastic dipole is then

$$F_j(\mathbf{r}) = \mathbf{P}_{jk}(\mathbf{r}')\alpha_{,k'}(\mathbf{r}-\mathbf{r}') \tag{34}$$

and the interaction energy U between the elastic dipole and a displacement field u_i^A is

$$U(r) = -\int P_{jk}(\mathbf{r})\alpha(\mathbf{r}'-\mathbf{r})\mathbf{e}^A_{jk}(\mathbf{r}')\,\mathrm{d}V'. \tag{35}$$

Note that the interaction depends on the strain field at *all* points in the medium. The force acting on the dipole is

$$f_n = \int P_{jk}(\mathbf{r})\alpha(\mathbf{r}'-\mathbf{r})e^A_{jk,n}(\mathbf{r}')\,\mathrm{d}V'. \tag{36}$$

Note that (34)–(36) reduce to the corresponding equations of the classical theory, *i.e.* to (19), (29) and (30) when $\alpha(\mathbf{r}'-\mathbf{r}) \to \delta(\mathbf{r}'-\mathbf{r})$.

Since any defect can be described as a surface distribution of dipoles (discussed in § 5), it is interesting to generalise the results of the local theory for a surface distribution of dipoles. Kovács and Vörös (1979) have shown that (29) then generalises to the form

$$U = -\int_S \bar{\sigma}^A_{lm}(\mathbf{r}')a_l(\mathbf{r}')\,\mathrm{d}S'_m, \tag{37}$$

where

$$\bar{\sigma}^A_{ik}(\mathbf{r}) = \int_V \sigma^{NL,A}_{ik}(\mathbf{r},\mathbf{r}')\,\mathrm{d}V' = \int_V \alpha(|\mathbf{r}-\mathbf{r}'|)C_{iklm}e'^A_{lm}\,\mathrm{d}V' \tag{38}$$

and $a_l(\mathbf{r})$ and S are as defined in § 5. Similarly, (30) generalises to

$$f_n = \int_S \bar{\sigma}^A_{lm}(\mathbf{r}')a_l(\mathbf{r}')\,\mathrm{d}S'_m. \tag{39}$$

It is easy to show that the self-energy of the defect is

$$U_s = -\frac{1}{2}\int_S \bar{\sigma}^s_{lm}(\mathbf{r}')a_l(\mathbf{r}')\,\mathrm{d}S'_m, \tag{40}$$

where $\bar{\sigma}^s_{lm}$ is the stress field due to the defect alone.

As expected, the stress singularities and the embarassing infinite self-energies in the usual defect calculations are replaced by well-defined, finite quantities in the nonlocal theory. This is closer to physical reality, and the advantage of obtaining realistic defect properties without performing tedious atomistic calculations makes this approach very attractive. For lack of space, we quote a single result to substantiate this remark. The interaction energy U between two dilation centres of volume increments ΔV_1 and ΔV_2 is given by

$$U = 2\mu\frac{(1-\nu)}{(1-2\nu)}\Delta V_1 \Delta V_2 \alpha(R), \tag{41}$$

where R is the distance between the two defects. (Note that when $\alpha(R)$ is replaced by $\delta(R)$, $U \to 0$, since $R \neq 0$.) The self-energy U_s of a dilation centre of volume increment ΔV is

$$U_s = \tfrac{1}{2} P \Delta V \alpha(0) \tag{42}$$

A convenient representation of the kernel $\alpha(r)$ is the Gaussian

$$\alpha(R) = \frac{\pi^{3/2}k^3}{a^3}\exp(-k^2R^2/a^2). \tag{43}$$

It is natural to interpret the parameter a as the lattice parameter. The other parameter k is estimated by Eringen (1977a, b) from a consideration of the critical shear stress needed to create a dislocation. This leads to $k = 0{\cdot}94$ for fcc metals. In fcc metals $\Delta V = a^3\varepsilon/4$ where $\varepsilon = (V - V_0)/V_0$, the relative volume difference between the host and the alloying atoms. Then, using $\nu = 1/3$ and $k = 0{\cdot}94$, one obtains $U_s = 0{\cdot}56\mu a^3\varepsilon^2$. This is to be compared with the atomistic model calculation of Flinn and Maradudin (1962) which yields $U_s \approx 0{\cdot}54\mu a^3\varepsilon^2$.

Other examples of the application of the nonlocal theory include expressions for the stress field, strain energy, etc. of screw and edge dislocations (Eringen 1977a, b; Eringen and Balta 1979), as well as a nonsingular expression (Eringen *et al* 1977) for the stress-concentration function in the problem of an elastic plate with a sharp crack and subjected to a uniform tension (at infinity) perpendicular to the crack (the Griffith problem). These results show the potential utility of the nonlocal elastic models of defects which certainly needs to be explored much more elaborately. Moreover, calculations in nonlocal elastic theory are much simpler than the corresponding ones in the anisotropic elasticity approach briefly described in § 6.1.

7. The linear continuum theory of dislocations

Electron microscopic observations show that deformed crystals have numerous dislocation lines which are very often randomly tangled. A convenient way to describe these dislocations is via the *dislocation density tensor* $\alpha_{ij}(\mathbf{r})$ (Nye 1953). Consider an arbitrary point P in the material. In the neighbourhood of P, within a small area element $\mathrm{d}\mathbf{S}$, there are several dislocation lines with Burgers vector $\mathbf{b}^{(a)}$ ($a = 1, 2 \ldots n$) in the directions $\hat{\nu}^{(a)}$, as shown in figure 3. The effective Burgers vector $\mathrm{d}\mathbf{b}$ of n dislocations threading the surface $\mathrm{d}\mathbf{S}$ is then given by

$$\mathrm{d}S_i\alpha_{ij} = \sum_{a=1}^{n}(\hat{\nu}^{(a)}.\hat{\nu})b_j^{(a)} \equiv \mathrm{d}b_j, \tag{44}$$

where $\hat{\nu}$ is the unit vector at P defining the element $\mathrm{d}\mathbf{S}$. The scalar product $(\hat{\nu}^a, \hat{\nu})$ measures the threading of the surface $\mathrm{d}\mathbf{S}$ by the ath dislocation. In integral form, (44) is written as

$$\int_S \mathrm{d}S_i\alpha_{ij} = b_j = \oint_C \mathrm{d}u_j, \tag{45}$$

where C is the closed curve bounding the surface S. (Kröner 1964 and Noll 1967 have

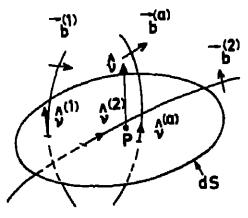

Figure 3. The area element dS showing the threading of dislocation lines.

defined α_{ij} somewhat differently; see Teodosiu (1982)). Now

$$\alpha_{ij} = \varepsilon_{ikl}\partial_k \beta_{lj} \quad (\text{or } \boldsymbol{\alpha} = \operatorname{curl} \boldsymbol{\beta}), \tag{46}$$

where $\beta_{ij}(\mathbf{r}) = u_{j,i}(\mathbf{r})$ is the gradient of the elastic displacement. Using (46) in (45) and invoking Stokes theorem, we find

$$\partial_i \alpha_{ij} = \alpha_{ij,i} = 0, \ (\text{or div } \boldsymbol{\alpha} = 0), \tag{47}$$

because the divergence of a curl vanishes. Physically this relation means that dislocations cannot end inside the medium. Another feature of the α-tensor is worth noting. The first index i of α_{ij} denotes the average direction of the dislocation lines whereas the second index j denotes the direction of the Burgers vector. Thus the diagonal components of $\boldsymbol{\alpha}$ correspond to screw dislocations and the off-diagonal elements to edge dislocations. Since the diagonal and nondiagonal components of a tensor are not invariant notions, *the classification of dislocations into edge and screw types is not to be taken too seriously.*

The introduction of the $\boldsymbol{\alpha}$-tensor has given impetus to the development of the beautiful differential-geometric theory (see § 9). The connection with geometry arises from the physical fact that dislocations involve a certain curvature or bending of the lattice network, thus imparting a curvature to the continuum (Nye 1953). To be more precise, the rotation tensor ω_{ij} defined as the antisymmetric part of β leads to an axial rotation vector $\omega_k = \frac{1}{2}\varepsilon_{ijk}\omega_{ij}$. The difference in ω between two points separated by an infinitesimal distance $d\mathbf{r}$ is given by

$$\mathrm{d}\omega_j = (\varepsilon_{jkl}\partial_k e_{li} + \kappa_{ij})\mathrm{d}x_i,$$

where

$$\kappa_{ij} = \alpha_{ij} - \tfrac{1}{2}\alpha_{kk}\delta_{ij} \tag{48}$$

is the Nye's curvature tensor (see also Kröner 1981). Thus, in the absence of elastic strains, the presence of a continuous distribution of dislocations alone leads to a rotation $d\theta$ between two points separated by a distance $d\mathbf{r}$ given by $d\theta_j = \kappa_{ij}\mathrm{d}x_i$. It is also straightforward to calculate the incompatibility tensor η associated with the presence of the dislocation distribution. We quote the final result (Kröner 1981):

$$\eta_{ij} = -\varepsilon_{ikm}\varepsilon_{jln}\partial_{kl}e_{mn} = \varepsilon_{ikm}\partial_k\kappa_{mj} = -\tfrac{1}{2}(\varepsilon_{iln}\partial_n\alpha_{jl})_{(ij)}, \tag{49}$$

$$\bar{\eta} = \operatorname{inc} \boldsymbol{e} = \operatorname{curl} \boldsymbol{\kappa} = (\boldsymbol{\alpha} \times \nabla)_{\text{sym}} = -\operatorname{curl} \boldsymbol{\alpha}^T.$$

It is evident that the divergence of η vanishes.

8. The internal stress problem and Kröner's theory

Defects are characterized by the incompatibility tensor η associated with them. For a continuous distribution of dislocations it is given by (49). A single dislocation is described as a limiting case of the continuous distribution with the help of delta functions:

$$\alpha_{ij} = t_i b_j \delta(p)\delta(q), \tag{50}$$

where t_i is the tangent to the dislocation line and p, q are suitable coordinates perpendicular to the dislocation line. For a spherical interstitial atom occupying a volume ΔV and located at $\mathbf{r}_0$, the incompatibility tensor is

$$\eta = \Delta V(\vec{\nabla} \times I \times \overleftarrow{\nabla})\delta(\mathbf{r} - \mathbf{r}_0), \tag{51}$$

where I is the unit tensor (δ_{ij}).

The main problem in defect theory is: given the tensor η as a function of $\mathbf{r}$, to calculate the internal stress and strain in the body. This is a boundary value problem for the equations $\partial_i \sigma_{ij} = 0$ (force equilibrium condition in the bulk) and $\sigma_{ij} n_j = 0$ on the surface S of the body (the traction boundary condition) together with the incompatibility equation $\operatorname{inc} e = \eta$. There are three ways of calculation of e.

(i) *The Eshelby-Eddington method*: Eshelby (1956) uses the fact that, because of the tensor identities

$$\operatorname{inc}(\operatorname{def} u) = 0 \text{ and } \operatorname{div}(\operatorname{inc} A) = 0, \tag{52}$$

any solution of the incompatibility equation can be written as

$$e = \operatorname{def} \mathbf{u} + \tilde{e}, \tag{53}$$

where $\tilde{e}$ is a particular solution of the equation and $\mathbf{u}$ is an arbitrary vector field. If we put $\eta = 0$ on the boundary S, then following the method of Eddington in the general theory of relativity, one can write

$$\tilde{e}(\mathbf{r}) = \frac{1}{4\pi} \int_V d^3\mathbf{r}' \frac{\eta(\mathbf{r}') - (\operatorname{Tr} \eta) I}{|\mathbf{r} - \mathbf{r}'|}. \tag{54}$$

Next, by substituting (53) into the other field equation and the boundary conditions, one obtains a traction boundary-value problem of classical elasticity theory where $\mathbf{u}$ plays the role of a displacement field, while the body forces and the surface forces are given by

$$f_k = C_{klmn} \tilde{e}_{mn,l}, \tag{55}$$

$$t_k = -C_{klmn} \tilde{e}_{mn} n_l. \tag{56}$$

(ii) *Mura's method*: This method make use of the elegant Green function technique. The working relation (derived in Mura 1968; Teodosiu 1982) for the calculation of the elastic deformation tensor is

$$\beta_{mr}(\mathbf{r}) = \int \mathrm{d}^3 r' C_{plqn} \varepsilon_{nrt} \alpha_{qt,l'}(\mathbf{r}') G_{mp}(|\mathbf{r} - \mathbf{r}'|). \tag{57}$$

(iii) *Kröner's method*: Kröner (1981) exploited the analogy of the elastic field with the magnetostatic field. The following is the correspondence between quantities and relations in both theories. (See Seeger 1961 for an excellent review where reference to Kröner's earlier work are given.)

Elasticity	*Magnetism*
vector quantity	scalar quantity
rank two tensor	vector
rank four tensor	rank two tensor
div	div
inc	curl

Elasticity	*Magnetism*
div inc $\equiv 0$	div curl $\equiv 0$
def	grad
inc def $\equiv 0$	curl grad $\equiv 0$
Burgers vector $\mathbf{b}$	current $\mathbf{I}$
incompatibility tensor η	current density $\mathbf{J}$
strain tensor e	magnetic intensity $\mathbf{H}$
stress tensor σ	magnetic induction $\mathbf{B}$
elastic constant C	permeability μ
$\sigma = C : e$	$\mathbf{B} = \mu\mathbf{H}$
div $\sigma = 0$	div $\mathbf{B} = 0$
inc $e = \eta$	curl $\mathbf{H} = \frac{4\pi}{c}\mathbf{J}$
tensor potential χ	vector potential $\mathbf{A}$
$\sigma =$ inc χ	$\mathbf{B} =$ curl $\mathbf{A}$

Another auxiliary tensor potential χ' is introduced ingeniously by Kröner. This is given by

$$\chi'_{ij} = \frac{1}{2\mu}\left(\chi_{ij} - \frac{\nu}{1+2\nu}\chi_{kk}\delta_{ij}\right), \tag{58}$$

the inverse relation being

$$\chi_{ij} = 2\mu\left(\chi'_{ij} + \frac{\nu}{1-\nu}\chi'_{kk}\delta_{ij}\right). \tag{59}$$

χ' satisfies the equations

$$\nabla^4\chi' = \eta \text{ and div } \chi' = 0. \tag{60}$$

Assuming that $\eta \to 0$ at the boundary of the infinite medium one calculates χ' from the relation

$$\chi'_{ij}(\mathbf{r}) = -\frac{1}{8\pi}\int \mathrm{d}^s\mathbf{r}'\,|\mathbf{r}-\mathbf{r}'|\,\eta_{ij}(\mathbf{r}'). \tag{61}$$

In principle this solves the internal stress problem, since σ can now be calculated using $\sigma =$ inc χ.

Kröner has also put the elastic theory of point defects in a broader perspective. According to him, the elastostatics of a continuum with extrinsic point defects (foreign interstitials) is analogous to electrostatics, whereas in intrinsic defects (vacancies, self-interstitials) the elasticity theory is analogous to magnetostatics:

Electrostatics	Elastostatics with extrinsic defects
div $\mathbf{D} = \rho$	div $\sigma = -\mathbf{f}$
curl $\mathbf{E} = 0$	inc $e = 0$
$\mathbf{D} = \varepsilon\cdot\mathbf{E}$	$\sigma = C : e$
$U = \frac{1}{2}\mathbf{D}\cdot\mathbf{E}$	$U = \frac{1}{2}\sigma\cdot e$

Magnetostatics	Elastostatics with intrinsic defects (internal sources)
div $\mathbf{B} = 0$	div $\sigma = 0$
curl $\mathbf{H} = \mathbf{J}$	inc $e = \eta$
$\mathbf{B} = \mu \cdot \mathbf{H}$	$\sigma = C:e$
$U = \frac{1}{2}\mathbf{B} \cdot \mathbf{H}$	$U = \frac{1}{2}\sigma:e$

The distinction between extrinsic and intrinsic defects is considered to be a most fundamental one, since this has deeper implications in terms of differential geometry. The terms 'diaelasticity' and 'paraelasticity' now acquire meanings by analogy with electro- and magnetostatics. Carbon atoms in iron are permanent elastic dipoles giving rise to paraelasticity; whereas, in diaelasticity, the induced elastic dipoles p_{ij}^{ind} arise only in the presence of an applied elastic strain e_{kl}, according to $p^{\mathrm{ind}} = \alpha : e$. The PFI leads to diaelasticity, while MFI leads to both para- and diaelastic effects. A quantitative measure of the para- or diaelasticity associated with a point defect is the corresponding polarizability. The calculation of this quantity is an important problem in the study of point defect relaxation as in the Snoek effect (see, *e.g.*, Leibfried and Breur 1978). There are also ferroelastic solids possessing permanent macroscopic elastic dipole moment along favoured directions (see, *e.g.* Wadhawan 1982).

9. Differential geometry of defects

The description of defects in the foregoing was confined to linearalized theories. When finite deformations are included, the language of differential geometry and tensor calculus becomes indispensable. A summary of these theories is given by Kröner (1981) and we follow his presentation. The nature of the differential geometry is decided by the degrees of freedom associated with the atoms or molecules of the crystal. For constituent particles of the same kind, each having only three translational degrees of freedom (a Bravais lattice), affine geometry seems to be appropriate; whereas for a non-Bravais lattice of molecules possessing rotational degrees of freedom in addition to translational ones, Finsler's geometry (Amari 1962) is required.

Consider for simplicity a cubic primitive Bravais lattice and choose the lattice lines as the Cartesian coordinate lines. The Cartesian coordinates of this defect-free, reference crystal are denoted by x^k. Let the crystal be deformed and let this configuration have coordinates z^k. The connection between infinitesimal increments in the coordinates in the two configurations is given by

$$dz^k = B_m{}^k dx^m, \quad B_m{}^k = \partial z^k / \partial x^m. \tag{62}$$

Now dx^m being the corresponding change in the undeformed configuration, the relative displacement is given by

$$du^k = (B_m{}^k - \delta_m{}^k)\, dx^m = \beta_m{}^k dx^m. \tag{63}$$

With the coordinates x^k we associate an 'external observer' (also called the Eulerian frame of reference). Consider another observer, the 'internal observer' (the Lagrangian frame of reference) whose reference coordinates are 'dragged along' in the process of deformation. As long as the crystal is defect-free and the deformation is compatible, the internal observer feels no deformation. Let the coordinates of this frame of reference be

$y^{k'}$. Then the square of the distance between two infinitesimally separated points

$$ds^2 = \delta_{k'l'}\,dy^{k'}\,dy^{l'} \tag{64}$$

is an invariant for this observer. In contrast, for the external observer, there is a change in ds^2 after a deformation takes place, given by

$$ds^2 - ds_0^2 = (g_{kl} - \delta_{kl})\,dx^k\,dx^l \equiv 2e_{kl}\,dx^k\,dx^l. \tag{65}$$

Here ds_0^2 is the value of ds^2 before deformation, and

$$g_{kl} = \delta_{mn} B_k{}^m B_l{}^n. \tag{66}$$

The strain tensor can be easily shown to be

$$e_{kl} = \tfrac{1}{2}(\beta_{kl} + \beta_{lk}) + \tfrac{1}{2}\beta_k{}^m \beta_l{}^n \delta_{mn}. \tag{67}$$

Next, let us establish a connection between dislocations and torsion. Cartan (1928) introduced the concept of 'torsion' in a purely mathematical context. Later, Frank (1951) constructed the Burgers circuit to define a dislocation. That there is a remarkable similarity between Cartan's procedure for introducing torsion in differential geometry and Frank's construction for a dislocation was noted by Kondo (1952, 1955), Bilby *et al* (1955) and Bilby (1960). Frank considers the nonclosed path $A'B'C'D'E'$ (see figure 4) around a dislocation in a crystal counting the steps (each step consists of one atomic spacing). The closer failure **A′E′** is the Burgers vector. Cartan transports a vector **CD** along the path **CB** from C to B and then a vector **CB** along the path from C to D. The vectors $\mathbf{CD} = \mathbf{d}_1\mathbf{x}(C)$, $\mathbf{BA} = \mathbf{d}_1\mathbf{x}(B)$, $\mathbf{CB} = \mathbf{d}_2\mathbf{x}(C)$ and $\mathbf{DE} = \mathbf{d}_2\mathbf{x}(D)$ are all of infinitesimal length. The law of parallel transport of $\mathbf{d}_1\mathbf{x}(C)$ along $\mathbf{d}_2\mathbf{x}(C)$ can be written as

$$d_1x^h(B) = d_1x^h(C) - \Gamma_{ml}{}^h d_1x^l(C) d_2x^m(C), \tag{68}$$

where $\Gamma_{ml}{}^h$ is the affine connection. Similar transport of $d_2\mathbf{x}(C)$ along $d_1\mathbf{x}(C)$ gives

$$d_2x^h(D) = d_2x^h(C) - \Gamma_{ml}{}^h d_2x^l(C) d_1x^m(C). \tag{69}$$

The closure failure is thus

$$\begin{aligned}(\mathrm{AE})^h &= d_1x^h(C) + d_2x^h(D) - d_2x^h(C) - d_1x^h(B)\\ &= \Gamma_{ml}{}^h(d_1x^l d_2x^m - d_2x^l d_1x^m)\\ &= -\Gamma_{ml}{}^h dS^{ml},\end{aligned} \tag{70}$$

where $dS^{ml} = (d_1x^m d_2x^l - d_1x^l d_2x^m)$ is the area element enclosed by the four infinitesimal vectors. The tensor dS^{ml} is related to the area vector dS_n by the relation

$$dS^{ml} = \bar{\varepsilon}^{nml}\,dS_n, \quad dS_n = \tfrac{1}{2}\bar{\varepsilon}_{nml}\,dS^{ml}, \tag{71}$$

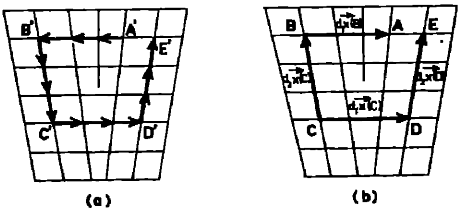

Figure 4. (a) Frank's circuit, (b) Cartan's circuit.

where $\bar{\varepsilon}^{nml} = g\bar{\varepsilon}^{nml}$, with $g = (\det(g_{lm}))^{1/2}$ (i.e., $\bar{\varepsilon}^{nml}$ is the contravariant Levi-Civita tensor, etc.). Note that only the antisymmetric part of the connection contributes to the vector $(\mathbf{AE})^h$ in (70). This is Cartan's torsion tensor,

$$T_{ml}{}^{h} = \tfrac{1}{2}(\Gamma_{ml}{}^{h} - \Gamma_{lm}{}^{h}). \tag{72}$$

Now, to establish contact with the dislocation density tensor α_{ij} defined in § 7, note that by definition the Burgers elemental vector is

$$\mathrm{d}b^k = \alpha^{nk}\mathrm{d}S_n \equiv \alpha_{ml}{}^{k}\mathrm{d}S^{ml}, \tag{73}$$

where

$$\alpha_{ml}{}^{k} = \tfrac{1}{2}\bar{\varepsilon}_{nml}\alpha^{nk},\ \alpha^{nk} = \bar{\varepsilon}^{nml}\alpha_{ml}{}^{k}. \tag{74}$$

On comparing $\mathrm{d}b^k$ with $(\mathbf{AE})^k$ we get

$$T_{ml}{}^{k} = -\alpha_{ml}{}^{k}. \tag{75}$$

This basic identification of the dislocation density tensor with the torsion tensor is the starting point of the differential geometric approach.

The presence of torsion leads to a non-Riemannian geometry. It is known (Schouten 1954) that if the metric is to satisfy the relation $\nabla_m g_{lk} = 0$ where ∇_m is the symbol for covariant derivative, then the most general form of the affine connection possible is related to the torsion as follows: writing $\Gamma_{ml}{}^{h} = g^{hk}\Gamma_{mlk}$, it turns out that

$$\Gamma_{mlk} = g_{mlk} + h_{mlk}, \tag{76}$$

where

$$g_{mlk} \equiv \tfrac{1}{2}(\partial_m g_{kl} + \partial_l g_{mk} - \partial_k g_{lm}) \tag{77}$$

and

$$h_{mlk} \equiv T_{mlk} + T_{kml} - T_{lkm}. \tag{78}$$

Here g_{mlk} is the Christoffel symbol of the second kind, and h_{mlk} is the *contortion tensor*. The earlier definitions of the distortion tensor β_{lk}, the strain tensor e_{lk} and the rotation tensor ω_{lk} are generalised to read

$$\left.\begin{aligned} \mathrm{d}\beta_{lk} &= \Gamma_{mlk}\mathrm{d}x^m, \\ \mathrm{d}e_{lk} &= \Gamma_{m(lk)}\mathrm{d}x^m, \\ \mathrm{d}\omega_{lk} &= \Gamma_{m[lk]}\mathrm{d}x^m, \end{aligned}\right\} \tag{79}$$

where (lk) and $[lk]$ respectively stand for symmetric and antisymmetric combinations of these indices. Equation (9) of the linearized theory, which can also be written as

$$\vec{\nabla} \times e \times \overleftarrow{\nabla} - \mathrm{sym}\{\boldsymbol{\alpha} \times \overleftarrow{\nabla}\} = 0 \tag{80}$$

is generalised in the nonlinear theory to the vanishing of the curvature tensor, *i.e.*,

$$R_{nmlk} = 0, \tag{81}$$

where $R_{nmlk} = g_{kh}R_{nml}{}^{h}$ and

$$R_{nml}{}^{h} = 2(\partial_n\Gamma_{ml}{}^{h} - \Gamma_{mp}{}^{h}\Gamma_{nl}{}^{p})[nm]. \tag{82}$$

Equation (81) is the *second basic law* of the differential geometric theory of lattice defects. Physically, this means that if a crystal has dislocations as the only defects in it during deformation, and if it does not develop cracks, then the dislocation distribution must be accompanied by elastic strains such that the curvature tensor vanishes.

The second basic identification states that elementary *extrinsic* defects (extra matter on interstitial sites, fission fragments, α-particles stuck in the medium, etc) cause a *rotation-like* curvature ($R_{nm[lk]} \neq 0$, $R_{nm(lk)} = 0$). According to the third basic identification, *intrinsic* point defects like self-interstitials and vacancies lead to a *non-metric* curvature ($R_{nm[lk]} = 0$, $R_{nm(lk)} \neq 0$). The non-metric situation is not as well understood in differential geometry as the metric connection. When extrinsic defects are present in addition to dislocations, a beautiful analogy emerges between the field equations of defects and Einstein's equations in the general theory of relativity. To see this, we note that the curvature tensor R_{nmlk} is antisymmetric in l and k for the metric geometry, and, by definition, it is also antisymmetric in n and m. Thus, without any loss of information, it can be replaced by a second rank tensor E^{ij} (called the Einstein tensor) given by

$$E^{ij} = \tfrac{1}{4}\bar{\varepsilon}^{inm}\bar{\varepsilon}^{jlk}R_{nmlk}. \tag{83}$$

It can be shown that, in the linear approximation, (83) reduces to

$$\boldsymbol{E} = -\operatorname{inc} \boldsymbol{e} + \operatorname{curl} \boldsymbol{\kappa}. \tag{84}$$

Note that when $R_{nmlk} = 0$, $E^{ij} = 0$. When extra matter is present, the Einstein tensor does not vanish and becomes equal to the matter tensor M^{ij} or $\boldsymbol{E} = \boldsymbol{M}$. This is analogous to the Einstein's field equation. Thus the defects in a crystal are analogous to matter in the universe. "Without matter, the universe is not interesting; without defects, a crystal is dead—" (Kröner 1981).

The approach to defect theories *via* differential geometry is undoubtedly an elegant one. There is a related approach by Wang (1967) and Noll (1967) which starts with the philosophy that the constitutive law of the continuum being fundamental, it must determine the geometry. There are attempts at constructing a Yang-Mills type of minimal coupling theory for materials with dislocations and disclinations (Kadić and Edelen 1982; Edelen 1980). The work of Julia and Toulouse (1979) and that of Dzyaloshinskii and Volovik (1978) are efforts in the same direction. There are further treatments of the differential geometry of defects by Gairola (1979), Zorawski (1967) and Marcinkowski (1979). Marcinkowski in several publications has applied differential geometric techniques extensively to dislocations on surfaces, grain boundaries, cracks, etc.

In spite of its mathematical elegance, the differential-geometric approach to defect problems has not helped much in the development of the phenomenological theory of plasticity. The reason is that, in contrast to the case of electric or magnetic lines of force in electromagnetic theory, dislocation lines almost always form very irregular interconnected networks. This is the main reason why the continuum theory of dislocations and the differential-geometric approach as such can never constitute a good macroscopic theory of plasticity. Dislocations piercing through an area element in the crystal usually appear with positive as well as negative signs so that their resultant Burgers vector is often zero or has a very small value. This results in a very small magnitude for the dislocation density $\boldsymbol{\alpha}$. To understand this, consider for example the configuration of dislocations shown in figure 5. All the dislocation lines are in the z direction; positive (⊥) and negative (T) dislocations have Burgers vectors $+b$ and $-b$, respectively. Let the domain be divided by a mesh as shown in the figure and let a^2 be the area of each small square. If we consider as the area ΔS_3 the rectangle AA'B'B, $\alpha_{31} = -b/a^2$; if ΔS_3 is the rectangle BB'C'C, $\alpha_{31} = +b/a^2$; whereas if area ΔS_3 = AA'C'C, $\alpha_{31} = 0$. Note that if we let $\Delta S_3 \to 0$ around the point P_1, then $\alpha_{31}(P) = \pm b_1 \delta(P - P_1)$, where the + sign is applicable if there is a positive dislocation at P_1, and

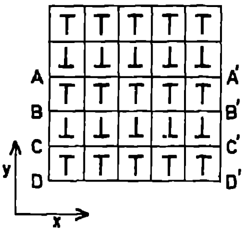

Figure 5. Positive and negative edge dislocations arrays piercing through a rectangular region.

the − sign if there is a negative dislocation. This means that the microscopic theory of dislocations is built into the formalism, but that in the process of coarse-graining over the distribution of dislocations, too much information seems to be lost.

Kröner (1970) has suggested the following way to rectify this deficiency. According to him, the random distribution of dislocations calls for the use of statistical mechanics. Information about the actual dislocation distribution may be given by n-point correlation tensor functions $\langle\alpha(\mathbf{r}_1)\alpha(\mathbf{r}_2)\ldots\alpha(\mathbf{r}_n)\rangle$ which give the probability of finding dislocation elements at $\mathbf{r}_1, \mathbf{r}_2 \ldots \mathbf{r}_n$. Thus one considers, instead of a single real specimen, a whole ensemble of crystals all filled with dislocation line elements in such a way that the ensemble represents all possible realizations of a given macroscopic dislocation state. One may impose extra conditions by prescribing the total energy, the total dislocation length, etc. These would correspond to various types of ensembles (analogous to the well-known microcanonical, canonical and grand canonical ensembles). Kröner (1970) shows that the information contained in the two-point correlation $\langle\alpha_{ij}(\mathbf{r})\alpha_{kl}(r')\rangle$ is quite extensive. For example, it gives information about the total dislocation length in a given volume element, the density of dislocation dipoles, etc. It is (obviously) suitable for describing planar dislocation networks, and, to some extent, dislocation pileups as well. Kröner and Teodosiu (1974) have made the important observation that the internal mechanical state, instead of being represented by the dislocation density tensor and its higher-order correlations, can also be specified by means of the fluctuations of the stress and elastic strain produced by the dislocations. This is of interest because it is the fluctuating stresses and strains that determine the deformation behaviour of materials. This line of approach is very attractive, but much work needs to be done. For example, if the dislocation elements are the basic entities of the system which we want to describe by statistical mechanics, what is the counterpart of Liouville's theorem that would guarantee that the known equations of motion of the dislocation line elements are satisfied? It is worth mentioning here that in another attempt to rectify the shortcomings of the dislocation density tensor, Kroupa (1962) has introduced the dislocation loop density as an additional variable. This approach too has not yet had any practical application.

10. Continuum mechanics of moving dislocations

Kosevich (1979) has generalised the basic equations of continuum mechanics taking into account the motion of dislocations during deformation. He has given a very simplified treatment under the (rather drastic) assumption that the energy conservation equation remains unchanged. (This is equivalent to assuming that no heat is generated in the process of dislocation motion). Thus, only the equations of continuity expressing the (local) conservation of mass and (linear) momentum are considered. One begins with the fundamental equation which introduces dislocations into elasticity theory, namely, (46). If dislocations remain static during the deformaton, then the velocity field $V_k(\mathbf{r})$ is related to the elastic distortion field $\beta_{ik}(\mathbf{r})$ by $\partial_i V_k = \partial_t \beta_{ik}$. However, when dislocations move, this equation must be generalized to

$$\partial_i V_k = \partial_t \beta_{ik} - j_{ik}. \tag{85}$$

Here $j_{ik}(\mathbf{r})$ is the dislocation flux tensor which must be so chosen that (85) is consistent with (46). Taking the curl of (85) and using (46), one obtains the (local) law of conservation for the Burgers vector

$$\partial_t \alpha_{ik} + \varepsilon_{ilm} \partial_l j_{mk} = 0. \tag{86}$$

If C is a closed curve bounding a surface S, then (86) can be expressed in the alternate form

$$\mathrm{d}b_k/\mathrm{d}t = -\oint_C j_{ik}\,\mathrm{d}x_i. \tag{87}$$

The total distortion β^T_{ik} is the sum of the elastic distortion β_{ik} and the plastic distortion β^P_{ik}. Since $\partial_i V_k = \partial_t \beta^T_{ik}$ by definition, we have evidently $\partial_t \beta_{ik} = -j_{ik}$. Hence

$$\partial_t e^P_{ik} = -j_{(ik)}, \tag{88}$$

which is the Orowan equation. For a continuous distribution of dislocations,

$$j_{ik} = \varepsilon_{ilm} \sum_a b_k V_m(\mathbf{r}, \hat{\nu}^{(a)}) \nu_l^{(a)}. \tag{89}$$

(compare with (46) which defines α_{ik}). The trace j_{kk} of the flux tensor j_{ik} is of special interest in connection with the continuity equation for mass. Noting that the relative change in density $\delta\rho$ is given by $e_{kk} = -\delta\rho/\rho$ (where ρ is the density of the medium) and using (85), one obtains

$$\partial_t \rho + \operatorname{div}(\rho \mathbf{V}) = -\rho j_{kk}. \tag{90}$$

The 'complete system' of dynamical equations can then be presented in the form

$$\left.\begin{aligned}
&\partial_i \sigma_{ik} = \rho \partial_t V_k \quad \text{(Newton's Law)},\\
&\sigma_{ik} = C_{iklm} \beta_{lm} \quad \text{(elastic constitutive Law)},\\
&\varepsilon_{ilm} \partial_l \beta_{mk} = -\alpha_{ik},\\
&\partial_i V_k = \partial_t \beta_{ik} - j_{ik},
\end{aligned}\right\} \tag{91}$$

where the tensors α_{ik} and j_{ik} must be specified. Note that α_{ik} and j_{ik} must satisfy (47) and (86).

We mention here that a lattice defect approach to plasticity and viscoplasticity has been proposed by Kröner and Teodosiu (1974), in which particular emphasis is laid on dislocations. These authors propose a complete set of equations which consist of the continuity equations including the law of conservation of energy, and the thermoelastic constitutive equations for the stress and the heat flux. However, the theory is rather formal and has not yet been tested on any practical problem.

11. The quantum field theory approach

Field theorists have recently been interested in defects in crystals. Defects (termed 'extended objects' to stress the generality of the formalism) are viewed as classical macroscopic objects in a quantum ordered state (a perfect crystal). They are a macroscopic manifestation of the local condensation of bosons associated with a quantum mechanical collective mode (the phonons). There is an efficient tool called the boson transformation technique which describes the condensation process mathematically. In high energy physics, the topological structure of extended objects has been of great interest, being connected with the problems of quark confinement and particle structure. The boson transformation approach to defects was motivated by the success of the theory of solitons. A soliton is a localized wave solution of a classical nonlinear equation which behaves like a particle. The search for soliton solutions in three space dimensions is a challenging problem in itself. Their localized nature suggests that dislocations, point defects, grain boundaries, etc. are somehow related to soliton-like objects in three-dimensions. As it would require a rather lengthy presentation of the field-theoretic background and the boson transformation formalism, we do not describe this approach here. It is best described in the review article of this theory by Wadati (1979). (See also: Umezawa *et al* 1982.) We mention also that Holz (1979, 1980) has given a microscopic Hamiltonian theory of dislocations in crystals.

12. Conclusion

The present review was intended to bring out the fact that there is as yet no single unified theory of all defects in crystals. The merits and drawbacks of the various theories available have been pointed out. To the reviewer the following areas seem to need urgent attention. The idea of Kröner (1970) that the loss of information in the coarse-graining process needed to define the dislocation-density tensor can be remedied with the help of higher-order correlation functions, needs to be pursued further. The alternate idea of Kröner and Teodosiu (1974) that it must be possible to describe the deformation behaviour of materials in terms of the fluctuations of the stress and strain (produced by dislocations) clearly suggests a stochastic approach to plastic flow. The difficulty here is the fact that even the deterministic equations needed to completely describe plastic flow are yet to be developed. In fact this was the spirit of the work of Kröner and Teodosiu (1974). Perhaps some extremely simple situations (like steady state creep) must be modelled first in terms of a stochastic description, and the relevant correlation tensors explicitly computed. Both Kosevich (1979) and Kröner and Teodosiu (1974) have proposed hydrodynamic equations for matter undergoing deformation. One testing ground for such hydrodynamic equations could be the work-hardening behaviour of materials. Cottrell (1953) has given a beautiful analogy between stage I of work-hardening and the laminar flow of a fluid, and between stage II and turbulent flow. However, one does not yet know what the ‘Reynold number’ is which would characterize the transition to ‘turbulence’ in the case of plastic flow. In the spirit of this analogy, it may be possible to introduce different types of dislocation density tensors to describe the transition from stage I to stage II of the work-hardening curve. It seems that much work remains to be done in developing a hydrodynamic theory of a continuous medium containing dislocations.

References

Amari S 1962 in *RAAG memoirs of the unifying study of the basic problems in engineering and physical sciences by means of geometry* (ed) K Kondo (Tokyo: Gakujutsu Bunken Fukyu-kai), Vol 3, p 193

Bilby B A 1960 in *Progress in solid mechanics* (eds) I N Sneddon and R Hill (Amsterdam: North-Holland), Vol 1, p 329

Bilby B A, Bullough R and Smith E 1955 *Proc. R. Soc.* (*London*) **A231** 263

Burgers J M 1939 *Proc. Acad. Sci. Amsterdam* **42** 378

Cartan E 1928 *Lecons sur la Gêométrie des espaces de Riemann* (Paris: Gauthier-Villars)

Cottrell A H 1953 *Dislocations and plastic flow in crystals* (Oxford: Clarendon Press)

de Wit R 1960 in *Solid state physics* (eds) F Seitz and D Turnbull (New York: Academic) Vol 10, p 249

Dzyaloshinskii I and Volovik G 1978 *J. Phys.* **39** 693

Edelen D G B 1980 *Int. J. Eng. Sci.* **18** 1095

Eringen A C 1972 *Int. J. Eng. Sci.* **10** 425

Eringen A C 1973 *Lett. Appl. Eng. Sci.* **1** 11

Eringen A C 1976 *Continuum Physics*, Vol IV, (New York: Academic)

Eringen A C 1977a *J. Phys.* **D10** 671

Eringen A C 1977b *Int. J. Eng. Sci.* **15** 177

Eringen A C and Balta F 1979 *Crystal Lattice Defects* **8** 73

Eringen A C and Edelen D G 1972 *Int. J. Eng. Sci.* **10** 233

Eringen A C, Speziale C G and Kim B S 1977 *J. Mech. Phys. Solids* **25** 339

Eshelby J D 1956 in *Solid state physics* (eds) F Seitz and D Turnbull (New York: Academic) Vol 3, p. 79

Eshelby J D 1957 *Proc. R. Soc.* (*London*) **A241** 376

Eshelby J D 1961 in *Progress in solid mechanics* (eds) I N Sneddon and R Hill (Amsterdam: North-Holland) Vol 2, p 89

Evans J H, Bullough R and Stoneham A M 1972 in *Radiation induced voids in metals* (eds) J W Corbett and L C Ianiello USAEC-CONF-71061

Flinn P A and Maraduddin A A 1962 *Ann. Phys.* **18** 81

Frank F C 1951 *Philos. Mag.* **42** 809

Gairola B K D 1979 in *Dislocations in solids* (ed) F R N Nabarro (Amsterdam: North-Holland) Vol 1, p 223

Heald P T and Speight M V 1974 *Philos. Mag.* **29** 1075

Holz A 1979 *Phys. Rev.* **A20** 2521

Holz A 1980 *Phys. Rev.* **B22** 3678

Julia B and Toulouse G 1979 *J. Phys.* **40** L-395

Kadić A and Edelen D G B 1982 *Int. J. Eng. Sci.* **20** 49, 433, 747, (see also Kadić A and Edelen D G B 1983 *A gauge theory of dislocations and disclinations* (Berlin: Springer-Verlag))

Kondo K 1952 On the geometrical and physical foundations of theory of yielding in *Proc. 2nd Japan Nat. Congr. Applied Mechanics*, Tokyo

Kondo K 1955 Non-Riemannian geometry of imperfect crystals from a macroscopic viewpoint, in *RAGG memoirs of the unified study of basic problems in engineering and physical sciences by means of geometry* (ed) K Kondo (Tokyo: Gakujutsu Bunken Fukyu-kai)

Kosevich A M 1979 in *Dislocations in solids* (ed) F R N Nabarro (Amsterdam: North-Holland) Vol 1, p 33

Kovács I 1978 *Physica* **B94** 177

Kovács I and Vörös G 1979 *Physica* **B96** 111

Kröner E 1953 *Z. Phys.* **136** 402

Kröner E 1964 *Phys. Kondens. Materie* **2** 262

Kröner E 1970 in *Inelastic behaviour of solids* (eds) M F Kanninen, W F Adler, A R Rosenfeld and R I Jaffee (New York: McGraw-Hill) p 135

Kröner E 1981 in Les Houches Session XXXV, 1980–*Physics of defects* (eds) R Balian *et al* (Amsterdam: North-Holland)

Kröner and Teodosiu C 1974 in *Problems of plasticity*, Int. Symp. on Foundations of Plasticity, Warsaw 1972, (ed) A Sawczuk (Leyden: Noordhoff Intl Publishing) p 45

Kroupa F 1962 *Czech. J. Phys.* **B12** 191

Leibfried G and Breur N 1978 *Point defects in metals* (Berlin: Springer-Verlag) Vol I

Malen K and Bullough R 1971 in BNES European Conf, Reading, England, March 1971

Marcinkowski M J 1979 *Unified theory of the mechanical behaviour of matter* (New York: Wiley)

Mura T 1968 *Adv. Mater. Res.* **3** 1

Nabarro F R N 1967 *Theory of crystal dislocations* (Oxford: Clarendon)

Noll W 1967 *Arch. Rational Mech. Anal.* **27** 1

Nye J F 1953 *Acta Metall.* **1** 153

Peach M and Koehler J S 1950 *Phys. Rev.* **80** 436

Schouten J A 1954 *Ricci-Calculus* (Berlin: Springer-Verlag)
Seeger A 1961 *Phys. Status Solidi* **1** 669
Siems R 1968 *Phys. Status Solidi* **30** 645
Steeds J W and Willis J R 1979 in *Dislocations in solids* (ed) F R N Nabarro (Amsterdam: North-Holland) Vol 1 p 33
Teodosiu C 1982 *Elastic models of crystal defects* (Berlin: Springer-Verlag)
Umezawa H Matsumoto H and Tachiki M 1982 *Thermofield dynamics and condensed systems* (Amsterdam: North-Holland)
Wadati M 1979 *Phys. Rep.* **50** 87
Wadhawan V K 1982 *Phase Transitions* **3** 3
Wang C C 1967 *Arch. Rational Mech. Anal.* **27** 33
Zorawski M 1967 *Théorie mathématique des dislocations* (Paris: Dunod)

Discussion

T V Ramakrishnan: What is the continuum local theory value for the self-energy of a point defect?

D Sahoo: For a mathematical point defect, it is infinity, but for a rigid 'point' defect occupying a volume ΔV, it is $\frac{2}{3}\mu\Delta V$, where μ is the shear modulus of the medium.

N Kumar: What is P in the nonlocal theory? Can you go to the local limit through some approximation?

Sahoo: P is the elastic dipole tensor, as in the local theory. It is the interaction between a dipole and a strain field which is nonlocal. Yes, one can go to the local limit by the replacement $\alpha(R) \rightarrow \delta(R)$.

H R Krishna Murthy: Is the nonlocal theory supposed to simulate the lattice?

Sahoo: Yes, it is intermediate between the local continuum theory and the discrete atomistic theory. The lattice appears through the parameter a occurring in the kernel $\alpha(R)$. This a is essentially the lattice constant.

Ramakrishnan: In that case, where is the dispersion?

Sahoo: Eringen (1972, 1973) has explicitly calculated the dispersion for a one-dimensional lattice. He has also calculated the dispersion curve for Rayleigh surface waves.

A S Parasnis: What exactly is it in the nonlocal theory that removes the infinities in the stress and strain at the core of a (screw) dislocation—a divergence which seems to be almost a necessity in a continuum theory?

Sahoo: It is essentially the replacement of all the δ functions by the finite kernel $\alpha(R)$. Being a smooth function like a Gaussian, this removes the infinities in the calculation of the integrals involved.

Parasnis: I have two comments: (i) I wonder if mere analogies, such as are implied in the attempt to have a 'unified' theory of defects, are likely to give physically significant theories and results. For example, two decades ago some mathematically-minded people drew an analogy between the closure failure *a la* the Burgers/Frank circuit and Ampere's law and built up a fair edifice. But this could *not* explain the simple fact that like-currents attract whereas like-dislocations repel. What is needed is a *physical* theory going beyond such analogies. (ii) The difference between a Burgers circuit and a Frank circuit is that since the latter closes in the dislocated crystal/medium, it refers to the Burgers vector in the undislocated reference crystal/medium. You called the circuit a 'Frank circuit' but opened it in the dislocated crystal!

G Srinivasan: I wonder whether in the multiple glide region, the analogy may be with a cross-linked polymer rather than with turbulence. The problem in the polymer case has been made tractable by de Gennes, Edwards and others. The analogy may be worth pursuing.

C K Majumdar: Dr Srinivasan is apparently referring to the calculation of the elastic property of rubber by Prof. S F Edwards. There is a linear part, a plateau and a nonlinear rising part—somewhat similar to the regions I and II you refer to. It is quite possible that this analogy is better than that with laminar and turbulent flow. Now, the rubber and the polymer problems are dominated by entropy. Entropy is always difficult to handle in a mechanistic or hydrodynamic model. This difficulty appears also in the treatment of shocks or grain boundaries discussed earlier. The entropy equation, if written down from the second law, is somewhat different in nature from the hydrodynamic equations or the electrodynamic or the elastic equations (compare for example, the entropy generation equation of Sommerfeld). Edward's calculation of rubber elasticity is statistical mechanical in character, because entropy is involved. (Hydrodynamic equations or electrodynamic equations in continuous media are also statistical in character, but entropy is not so easily expressed in mechanical terms—entropy has an integral character in phase space and is not easily expressed in a differential equation.) If the entropy equation could be written down, or rather, if the entropy could be woven into the framework, the analogy could be exploited—the insight of de Gennes and Edwards in random network problems may perhaps be useful here.

Bull. Mater. Sci., Vol. 6, No. 4, September 1984, pp. 799–804. © Printed in India.

Fracture of particulate composites

S RAY

Department of Metallurgical Engineering, University of Roorkee, Roorkee 247 672, India

Abstract. A thermodynamic analysis of the process of fracture in elastically deformable composites is formulated. The critical dimensions leading either to particle fracture or to matrix-particle decohesion are identified. Fracture in plastically deformable composites is discussed in the light of the experimental evidence regarding void or cavity nucleation. Models of void growth under the application of stress and the role of void growth in causing failure are described in brief.

Keywords. Fracture; composite; void nucleation; void growth; cavity.

1. Introduction

Particulate composites are materials containing one or more discontinuous phases dispersed in a matrix of a distinctly different phase, such that the length to diameter ratio of each dispersoid is of the order of unity. If the extent of the discontinuous phase (or phases) is small and the load shared by it is insignificant, the material is not effectively regarded as a composite because the mechanical property of the material does not reflect the characteristics of the discontinuous phase. However, many materials that are not originally designed as particulate composites may pick up discontinuous phases during processing in the form of particles of insoluble impurities or inclusions which subsequently exert an important influence on the fracture behaviour of these materials. Particulate composites can be divided into four basic classes depending on the mechanical properties of the continuous phase (the matrix) and the discontinuous phase (the particle). (a) brittle matrix-brittle particle, (b) brittle matrix-ductile particle, (c) ductile matrix-brittle particle, and (d) ductile matrix-ductile particle. The fracture behaviour of the first two classes will be analysed under the broad heading of elastically deformable composites in § 2, and fracture in the other two classes will be examined in § 3.

The first systematic approach to the process of fracture was developed by Griffith (1920) to explain the discrepancy between the ideal strength and the observed strength in a brittle material. The thermodynamics of the process of extension of an atomically sharp pre-existing crack of length $2c$ under an applied stress of σ was examined. When a crack extends, elastic energy is released due to relaxation of stress around the extended part of the crack; some energy is also expended by the system in creating a fresh crack surface. The extension of the crack becomes feasible only when the former energy exceeds the latter, thereby reducing the total free energy. The fracture stress, σ_0, calculated on the above basis is as given below.

$$\sigma_0 = (2\alpha E/\pi c)^{1/2}, \qquad (1)$$

where α is the specific energy of the crack surface and E is the Young's modulus.

Orowan (1949) provided a similar analysis for the extension of a crack under the plane stress condition. Sack (1946) and Sneddon (1946) modified the estimate of σ_0 in (1) by including the stress concentration effect around the crack. However, the original approach is based on the very general principles of thermodynamics and so provides a *necessary* criterion for the propagation of a crack leading to fracture. Here, we use this simple approach to examine the different possible fracture processes in the problem at hand, to gain an insight into the underlying essentials. Detailed stress calculations will not be of help in this regard because crack propagation is controlled by the local stress and strain which are inhomogeneous and dependent on the exact particle shape and distribution. These material parameters vary considerably from sample to sample, even for the same engineering material.

2. Elastically deformable composites

Any composite with a brittle matrix can be deformed only elastically irrespective of the nature of the reinforcing particle. To determine the fracture behaviour it is necessary to analyse the local stress distribution around the particles. When a particulate composite is deformed, the force is not directly applied to the particles but is transferred through the matrix. We consider the simple model of a particle embedded in a brittle matrix as given in figure 1. To simplify the mathematical treatment the following assumptions are made: (i) Poisson's effect is negligible; (ii) both the particle and the matrix have the same shear modulus. The elastic matrix is subjected to a tensile stress of σ_m. The forces acting on an element extending an angle $d\theta$ at the centre are shown in figure 1(b). If τ_θ is the shear stress acting at the particle-matrix interface, the elemental force balance in the direction of the applied stress gives

$$d\sigma/d\theta = 2\tau_\theta. \tag{2}$$

A special case (*i.e.*, equal elastic moduli for particle and matrix) of the general result derived by Sezawa and Miyazaki (1928) then yields, for the magnitude of the stress distribution τ_θ at the particle-matrix interface, the expression

$$\tau_\theta = (1/2)\sigma_m \sin 2\theta. \tag{3}$$

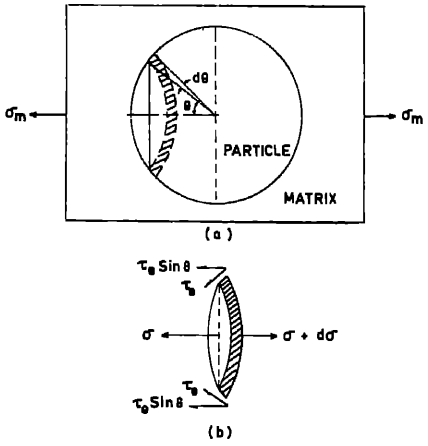

Figure 1. (**a**) Schematic representation of a single particle composite model. (**b**) Elemental force balance at a section of the particle.

Inserting this in (2) and integrating, the magnitude of the stress in the particle at a plane labelled by the angle θ is

$$\sigma_p = \sigma_m \sin^2 \theta. \tag{4}$$

Let $\bar{\sigma}_m$, $\bar{\sigma}_p$ and $\bar{\tau}$ be the fracture strengths of the matrix, particle and interface. Then the matrix, or the particle, or the interface fractures first, if $\bar{\sigma}_m$, or $\bar{\sigma}_p$, or $2\bar{\tau}$ is the smallest of the three quantities $\bar{\sigma}_m$, $\bar{\sigma}_p$, $2\bar{\tau}$. In the first case, the original analysis of Griffith and its subsequent modifications are applicable, after the inhomogeneous stress distribution is determined. In the second and third cases, a similar analysis brings out certain additional parameters of interest.

2.1 *Particle fracture*

When the particle has fractured at a plane whose angle of extension is 2θ at the centre, this crack will be able to propagate in the matrix provided it is thermodynamically feasible. If the particle has a radius r, the change in energy ΔE for an infinitesimal extension $\mathrm{d}r$ of the crack is given by

$$\Delta E = -4\pi r^2 \,\mathrm{d}r\, \sigma_m^2 (1-\nu_m)^2 \sin^2\theta / E_m + 2\pi r\,\mathrm{d}r\,\gamma_m \sin\theta, \tag{5}$$

where ν_m and E_m are Poisson's ratio and the elastic constant respectively of the matrix and γ_m is the surface energy of the matrix. For the crack to propagate spontaneously, ΔE should be negative, which implies that

$$r > r_c = E_m \gamma_m / [2(1-\nu_m)^2 \sigma_m^2 \sin^2\theta]. \tag{6}$$

Since the particle has fractured when $\sigma_p = \bar{\sigma}_p = \sigma_m \sin^2\theta$ the composite will at once satisfy the necessary condition for failure if

$$r > E_m \gamma_m \sin^3\theta / [2(1-\nu_m)^2 \bar{\sigma}_p^2]. \tag{7}$$

Otherwise, the load can be increased till it attains the value

$$\sigma_m = [E_m \gamma_m / 2r(1-\nu_m)^2 \sin^2\theta]^{1/2}. \tag{8}$$

The matrix will fail at a load different from that causing the fracture of the particles. As a *range* of particle size is involved in real-life composites, the estimate of σ_m given by (8) must be calculated using the largest value of the particle radius r that is involved.

2.2 *Interface fracture*

When the interface is weak, let a crack be initiated there at an angle θ. The crack will extend along the interface from an angle θ to $\theta + \mathrm{d}\theta$ if the corresponding change in energy is negative. This change is given by

$$\Delta E = -\pi r^3 \sigma_m (1-\nu_p)^2 \sin^4\theta \,\mathrm{d}\theta / E_p + 2\pi r^2 (\gamma_p + \gamma_m - \gamma_{pm}) \sin\theta \,\mathrm{d}\theta, \tag{9}$$

where ν_p and E_p are Poisson's ratio and the elastic constant, respectively, of the particle; γ_p is the surface energy of the particle and γ_{pm} is the particle-matrix interfacial energy. The debonding between the matrix and the particle will take place as long as $\Delta E < 0$, and will extend up to

$$\theta_c = \sin^{-1}\left[\frac{2(\gamma_p + \gamma_m - \gamma_{pm})E_p}{r(1-\nu_p)^2 \sigma_m}\right]^{1/2}. \tag{10}$$

Clearly, this crack can propagate into the matrix if the size of the particle is such that

$$r \geqslant E_m \gamma_m / [2(1-\nu_m)^2 \sigma_m^2 \sin\theta_c]. \tag{11}$$

If r is smaller than the quantity on the right, the load must be increased to the level given by (8) in order to fracture the matrix.

The surface energy of the particle, that of the matrix, and the particle-matrix interfacial energy play a vital role in determining the mode of fracture. The experimental determination of these energies is difficult and sometimes unreliable because of the segregation of impurities. The predictions of the above analysis may also become unreliable due to kinetic factors.

3. Plastically deformable composites

The phenomenon of fracture in a composite with a ductile matrix is commonly encountered in metals and alloys with inclusions. As composites contain a combination of phases, it is instructive to explore first the mechanism of fracture in a ductile single-phase material.

It is observed that cavities form in front of propagating cracks. It has therefore been assumed that vacancies in the highly strained region condense into voids. Under appropriate conditions of stress, these voids give rise to propagating cracks leading to the failure of the material. However, Balluffi and Siegel (1955) contend that the excess concentration of vacancies produced due to strain is not sufficient to lead to the homogeneous nucleation of voids, and that nuclei for void formation must pre-exist in the specimen. It is well known that cavities may also nucleate through a host of other mechanisms. For example, grain boundary sliding at low strain rates and intermediate temperatures gives rise to voids; and under such circumstances any factors preventing grain boundary sliding would also suppress the nucleation of cavities. Smith and Barnby (1967) have observed the nucleation of cavities at dislocation pile-ups, while Davies and Williams (1969) have observed this process taking place at twin-grain boundary intersections. All these mechanisms are operative at sites with large stress concentrations.

Such stress concentrations exist in the neighbourhood of the particles in a composite, and cavities form there either by cavity nucleation as in pure materials, or by mechanical decohesion of the matrix-particle interface as explained in § 2. Thermodynamic analysis (Greenwood and Harris 1965) shows that if $\gamma_{pm} < 10^{-3}\ \gamma_m$, mechanical decohesion is the most likely mode for cavity formation. Brown and Stobbs (1971) have estimated the critical strain for mechanical decohesion. A comparison of this estimate with the experimental value observed in a composite of silica particles dispersed in copper (Palmer and Smith 1968) indicates that the theoretical value is highly overestimated. This poses a problem, because a thermodynamic analysis provides *necessary* conditions and therefore *minimal* estimates in general. The discrepancy here may be attributed to the relaxation of stress observed around the smaller particles by the formation of prismatic loops. However, no such stress relaxation occurs around large particles and voids are readily formed there. Given a detailed understanding of the mechanisms of void creation, no quantitative theory of the fracture process under consideration is available, because the process is ultimately controlled by local stresses and strains, which in turn are governed by the shape and distribution of the particles in the matrix. Moreover, once voids are formed, the stress induces further growth and both the volume and the shape of the voids change, with the actual strain history exerting a significant influence.

Mcclintock (1968) proposed the first model for the growth of a cylindrical hole in a hardening plastic matrix. Subsequently, Rice and Tracey (1969) investigated another model for the growth of a spherical hole in a non-hardening plastic matrix and proposed a nonlinear relation between the radial velocity of the void surface and the applied strain field. Jalinier (1981) applied the linear version of the model to the damage observed in sheet metal. For a void caused by the decohesion of the particle-matrix interface as well as for a void generated by the cracking of the particle, $\varepsilon_i = B_i \varepsilon_i^{\infty}$, where ε_i is the relative extension of the void in the i-direction and ε_i^{∞} is the applied strain field far from the void. For decohesion, B_i is a function of the ratio $\varepsilon_2/\varepsilon_1$ of the principal strains, which for fragmentation is a constant ≈ 4. These theoretical results agree well with experimental observations.

The growth of the voids leads to failure by two possible mechanisms. The material between growing voids starts getting thinner till a necking instability sets in, resulting in the coalescence of the voids and eventual fracture. It is also possible that at some stage in the growth of the voids, conditions become ripe for cracks to originate from the voids, as explained in § 2.

4. Conclusions

Fracture in particulate composites is an important area in need of viable theories. The difficulties arise from the complexity of the stress distribution in an inhomogeneous material and the dependence of the fracture process on highly local stress and strain conditions. Estimates based on energy considerations have led to some understanding of the phenomena involved, but much remains to be done.

References

Balluffi R W and Siegel L L 1955 *Acta Metall.* **3** 170

Brown L M and Stobbs W M 1971 *Philos. Mag.* **23** 1201

Davies P W and Williams K R 1969 *J. Metal Sci.* **3** 48

Greenwood G W and Harris J E 1965 *Acta Metall.* **13** 936

Griffith A A 1920 *Philos. Trans. R. Soc.* **A221** 163

Jalinier J M 1981 Thesis, Univ. of Metz, France (unpublished)

Mcclintock F A 1968 *J. Appl. Mech.* **35** 363

Orowan E 1949 *Rep. Prog. Phys.* **12** 185

Palmer I G and Smith G C 1968 *Oxide dispersion strengthening* (New York: Gordon and Breach) p 253

Rice J R and Tracey D M 1969 *J. Med. Phys. Solids* 17 201

Sack R A 1946 *Proc. Phys. Soc.* **58** 729

Sezawa K and Miyazaki B 1928 *Proc. Jpn Soc. Mech. Eng.* **31** 625

Smith E and Barnby J T 1967 *J. Metal Sci.* **1** 1

Sneddon I N 1946 *Proc. R. Soc.* **A187** 229

Discussion

P Rodriguez: Why has the dislocation pile-up at the interface not been taken into account?

S Ray: Dislocation pile-up treatments are suspect. All these effects have been put into an experimental parameter ε_m.

V C Sahni: What is the implication if you have an interface of finite thickness?

Ray: I do not know the answer at present.

G Srinivasan: Is there an essential difference between the way a crack propagates in metals and insulators on the one hand, and in crystalline and amorphous materials on the other?

Ray: There is no appreciable difference.

K Srinivasa Raghavan: What about the possibility that the crack nucleates at the interface and goes into the matrix or the particle as decided by the relative moduli?
Ray: It is possible to treat this case along the same lines, but my interest has been in the problem of incipient cracking of the particle.

Bull. Mater. Sci., Vol. 6, No. 4, September 1984, p. 805–806. © Printed in India.

Experimental study of fluctuations in materials*

K R RAO

Nuclear Physics Division, Bhabha Atomic Research Centre, Bombay 400 085, India.

Abstract. Mechanical behaviour is decided by the structure and kinetics of defects in materials. External forces play an important role in determining the growth, decay and motion of defects. In addition there is an inherent fluctuation in the various microscopic characteristics of the system as the latter acts as a 'heat bath'. A disturbance that is set up in the system is affected by these fluctuations. The response of the system to external forces can be related to the behaviour of the system due to intrinsic fluctuations in the absence of impressed forces. This is the basis of relation between study of fluctuations in the system and various relaxation phenomena observed. It is proposed to discuss certain features of this subject in relation to various material properties.

Discussion

A P Pathak: What kind of information does one get about defects and defect structures from small angle neutron (or x-ray) scattering? For thin specimens charged particle scattering (channeling as well as backscattering) gives detailed information about all kinds of defects and defect structures. How do the two techniques compare as regards defect studies?

K R Rao: As I have explained in my talk, small angle scattering (x-ray or neutron) can give information on the *average* size, number and distribution of defects present in a solid (x-rays and neutrons give essentially similar information). Electron microscopy and charged particle scattering give useful information on point defects. Charged ionic particles in channeling experiments, for example, have helped one to decide whether certain impurities are substitutional or interstitial. However, such experiments generally require single crystals, and such studies have mostly been confined to 'ideal' defect studies. Small angle neutron scattering has the advantage that it can be used with bulk systems with large beam diameters, but the intensities are limited at present.

G Venkataraman: It seems to be of interest to consider, say, a creep experiment set up in a neutron beam. By studying the small angle scattering, one could perhaps learn something about the kinematics of defects during the course of deformation.

G Ananthakrishna: How do you measure the two-time correlation function in nonlinear systems?

Rao: I believe that *non-stationary* situations are the ones being investigated currently.

G Ananthakrishna: Binder remarks that coarse graining leads to fuzziness of the spinoidal boundary. How would one measure such an effect?

---

*Only a summary is presented.

Rao: My *guess* would be that perhaps one ought to start with compositions corresponding to the fuzzy boundary, and then carry out experiments quite similar to the ones I have already described.

Bull. Mater. Sci., Vol. 6, No. 4, September 1984, pp. 807–815. © Printed in India.

Elementary concepts in chaos and turbulence

RAMAKRISHNA RAMASWAMY

Tata Institute of Fundamental Research, Homi Bhabha Road, Colaba, Bombay 400 005, India

Abstract. The phenomenology of aperiodic or chaotic behaviour is described with reference to simple theoretical models and experiments. A brief description is given of the current understanding of how irregular dynamical motions can arise.

Keywords. Chaos; nonlinear dynamics; turbulence.

1. Introduction

In the past few years, an intense effort has been devoted towards the detailed study of intrinsically random phenomena. Random phenomena are plentiful; in this talk, I will attempt to give a brief introduction to the rather simple concepts that at present underlie a basic understanding of chaos or irregularity, and the onset of turbulence. Many of the ideas are novel and interesting; whether or not these concepts are directly applicable in the context of mechanical behaviour as discussed in this Meeting is not entirely clear, but that is more a problem of application. This talk will be primarily phenomenological and qualitative without much emphasis on the mathematics (although much of the insight in this field really comes from the mathematics). Rather than give explicit references through the text, I prefer to list in the bibliography several articles that discuss these concepts in greater detail.

It is of interest to examine families of (nonlinear) systems rather than particular cases, as this type of study is apt to reveal more of the general behaviour. Typically, such systems can be parametrized by some physical variable such as temperature, pressure, applied voltage, etc. In many situations, the following general pattern has been seen to occur as a function of the relevant control parameter:

Smooth behaviour ⟶ transitional range ⟶ erratic behaviour

periodic ⟶ ? ⟶ aperiodic

A few examples are given below.

(1) *Heart beats* are possibly the most familiar instance of regular, periodic behaviour. As a function of applied stress (for example during physical exertion), we can easily observe the period changing as the heart beats faster. When this exertion is now coupled with oxygen availability, when one is climbing a mountain, say, the period can change drastically, and in fact may become quite erratic. This has unfortunate physiological effects (death is likely), and emphasises the importance of a transition from regular to irregular behaviour under the variation of a control parameter.

(2) A less familiar example occurs in the study of *animal populations*. This assumes

importance in livestock farming or fishery management, where it is necessary to know the behaviour of the population as a function of time, typically from generation to generation. One can in fact write fairly simple equations (of the difference, differential, or differential-delay type) to describe the population, where the control parameters are the food supply and the reproductive ability. These simple equations can give rise to totally chaotic behaviour for some values of these parameters.

(3) An example that I will discuss later on has to do with the *onset of turbulence*. In the classic Rayléigh-Benard experiment, when a liquid is heated, convective motion is established within the liquid. As the rate of heating is increased, the motion can become quite irregular, leading eventually to the full scale turbulence which is seen in the boiling liquid.

(4) It is possible that in a material under stress, this kind of behaviour is present as well, as may be deduced from the equations that model *serrated yielding*, for some values of the applied strain.

There are several more examples that one could cite. What is important, however, is that chaos is a *dynamical* phenomenon, and is abundant, in that it occurs frequently in nonlinear situations. (Nonlinearity of the dynamical system is a necessary condition for chaos, but is not a sufficient one.)

2. Dynamics

We define a dynamical system in terms of one independent variable, such as time, t, one or more dependent variables, $x_i(t)$, and an external (control) parameter, μ. One requires a prescription to determine the evolution of the dependent variables. This is done via a system of differential equations,

$$\frac{\mathrm{d}}{\mathrm{d}t} x_i(t) = F_\mu(\mathbf{x}(t)), \tag{1}$$

or difference equations,

$$x_i(j+1) = F_\mu(\mathbf{x}(j)). \tag{2}$$

The index j plays the role of a discrete time in the latter case. The parametric dependence is contained in F_μ. Given these and a set of initial conditions, it is straightforward to obtain the time evolution of the dependent variables. This defines an *orbit*, and it is the behaviour of these orbits as a function of time that describes the dynamics. It is customary to examine the dynamics in the phase space of the variables $x_i(t)$, $i = 1, 2 \ldots$

We can simply define *regular* behaviour as motion, $x_i(t)$, which is predictable. That is, the dynamical variables are periodic functions of time, or combinations of periodic functions, *i.e.*, quasiperiodic functions. Irregular or chaotic motion is, in contrast, unpredictable, and therefore is given by an aperiodic function (equivalently, of infinite period). It is important to emphasize that these motions are discussed entirely in terms of deterministic evolution via (1) or (2). Chaotic motions arise independent of random noise or fluctuations. In fact, it is customary to label such intrinsic erratic behaviour as *self-generated chaos*.

The notions of regular and chaotic motion can be quantified in several ways. A direct and rather obvious means is through the spectral or Fourier analysis of the orbits.

Regular motion leads naturally to a discrete Fourier spectrum, since the motion is either periodic or quasiperiodic. The spectrum for chaotic motion must necessarily be continuous owing to the aperiodicity (*i.e.*, any and all frequencies—in particular, zero-frequency). Another means of distinction is based on the Liapunov instability of orbits. The euclidean distance between regular orbits can grow linearly; whereas, between chaotic orbits, it grows exponentially. It is also possible to examine the orbits themselves, to get an idea of how they develop in phase space. When there are n dependent variables, corresponding to m degrees of freedom, the phase space is of dimension n ($x_i(t)$; $i = 1, 2, \ldots, n$). Examining the motion in this n-dimensional space is a difficult task. One can, however, essentially accomplish this by examining the Poincare surface-of-section. This works best when the number of degrees of freedom is small, $m = 2$ or 3. To construct a surface of section, one chooses a particular plane in the phase space, and locates the point of intersection each time the orbit passes through this plane. If a given orbit is examined for a sufficiently long time, there are several points of intersection, and these give an idea of the geometry of the orbit. For regular motions, the points of the Poincare section lie on smooth curves, whereas for chaotic motions, these points are scattered apparently randomly in the plane (independent of which particular plane is chosen).

In discussing dynamical systems, it is useful to distinguish between conservative systems (where the volume of phase space is constant in time) and non conservative systems (where this volume changes with time). The behaviour is somewhat different in the two cases. In most physical situations one encounters dissipative, nonconservative systems, owing to the presence of frictional forces, and in that sense these systems are more important. It is however necessary for completeness to describe in brief the behaviour of conservative systems.

2.1 *Conservative (Hamiltonian) systems*

The most common examples of conservative systems are Hamiltonian systems, wherein one can define a Hamiltonian function, $H(\mathrm{x})$. As general dynamical systems, these have $n = 2m$ dependent variables for m degrees of freedom. Thus, the phase space is of dimension $2m$; m of these variables are 'coordinates', and m are their conjugate 'momenta'. Evolution is governed by Hamilton's equations. (In the discrete case, the requirement of constant phase space volume is replaced by the condition that the Jacobian of the transformation in (2) have the value ± 1). One can further separate such systems into two classes: integral systems and nonintegral systems. In the former class, it is possible to make a canonical transformation such that $H(x)$ is given in terms of m (in general, new) 'momentum' variables alone. These are constants of the motion, which is then constrained to lie on well-defined geometrical objects, namely, m-dimensional tori in the phase space of dimension $2m$. Thus the motion is *always* regular. We can regard nonintegrable Hamiltonians as arising from integrable ones by the addition of perturbation terms (depending on μ), such that H can no longer be expressed as a function of m momentum-like variables alone. There is then no guarantee that the motion will lie on m-dimensional tori. The powerful KAM theorem applies in such cases. Loosely speaking, this theorem states that, depending on the magnitude of the perturbation, some of the tori that exist in the integrable case get distorted, and some of them are destroyed. When the tori are merely distorted, the motion still remains regular; but when they are destroyed, the orbits are free to wander over all of phase space, and can therefore become highly irregular and chaotic. The phenomenology of Hamiltonian chaos is in fact extremely bizzare and involved; this erratic behaviour basically arises from the complicated interactions between internal resonances. The foregoing is a cursory description of the bare essentials of the matter. As a simple example, consider the discrete map

$$x_{i+1} = \mu x_i - (y_i - x_i^2)(1-\mu)^{1/2}, \tag{3}$$

$$y_{i+1} = x_i(1-\mu)^{1/2} + (y_i - x_i^2)\mu. \tag{4}$$

This roughly models the Poincaré surface of section of an $m = 2$ degree of freedom Hamiltonian system. Orbits are constructed by iterating points in the xy plane under the above transformations. Depending on where one starts, successive points in figure 1 can lie on a smooth curve (A) or on a set of smooth curves (B)—these correspond to regular motion on tori; or else the points can be scattered all over the plane (C)—this is a chaotic orbit and is not confined to any simple geometrical object. In general, the motion can be extremely complicated. This is both typical, in the sense that most nonlinear Hamiltonian systems are likely to be nonintegrable, and pathological, in the sense that for any nonzero value of μ, a nonintegrable Hamiltonian will exhibit *some* chaotic motions.

2.2 *Dissipative systems*

As already mentioned, dissipative systems are more common, and thus more pertinent. A typical example is provided by the forced-beam problem. A beam of length b is

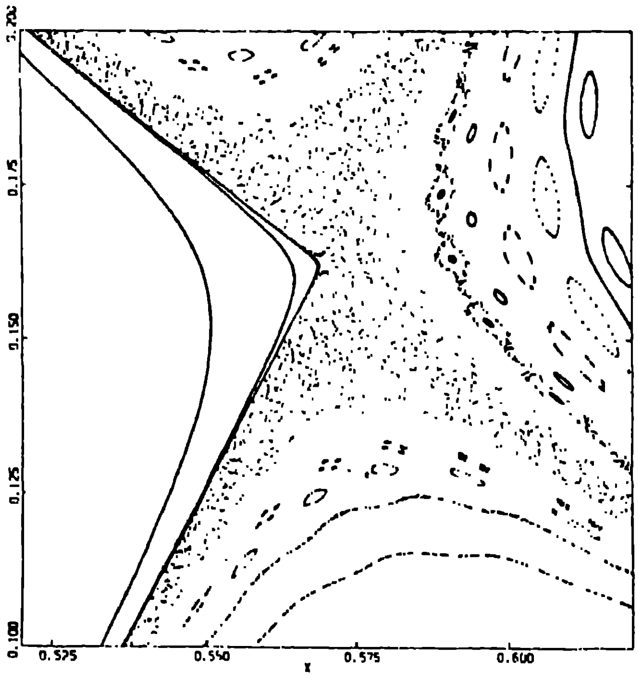

Figure 1. Orbits in the xy plane induced by the discrete transformation of equations (3)–(4). A and B are examples of regular motion, while the set of points C is typical of the Poincaré section of a chaotic orbit.

pinned at two ends, separated by distance l. When l is less than the beam length, the beam settles into one of the two symmetric equilibrium configurations. A sinusoidal force is applied at the ends, and the beam oscillates about the equilibrium position. As the excitation increases, however, the rod begins to snap back and forth between the two equilibria. If $w(x, t)$ is the lateral displacement,

$$w(x, t) = \xi(t)\sin(\pi x). \tag{5}$$

For small forcing amplitudes, $\xi(t)$ is a periodic function; but as the forcing amplitude increases, $\xi(t)$ can become quite chaotic. The problem can be properly formulated mathematically, and simplified to a more familiar problem, the Duffing equation. The latter describes a simple nonlinear forced oscillator with frictional damping,

$$\ddot{x}+\alpha\dot{x}+x+\beta x^3 = f\cos(\omega t). \tag{6}$$

This example is sufficient to illustrate much of the phenomenology. When $\alpha = \beta = f = 0$, (6) corresponds to the equation of motion of a simple harmonic oscillator of unit mass and frequency. The motion in phase space is extremely simple: a circle in the $x\dot{x}$ plane, given by the parametric equations,

$$x(t) = A\cos(\omega t+\phi);\ \dot{x}(t) = -A\sin(\omega t+\phi). \tag{7}$$

The motion is trivially regular. If damping is now introduced, keeping $\beta = f = 0$, one has damped harmonic oscillations; the motion now consists of orbits that spiral exponentially into a *sink* at $\dot{x} = x = 0$. When forcing is also included, one has a *limit cycle* behaviour, *i.e.*, orbits converge asymptotically onto a limiting structure in the phase plane, and the motion is periodic on this limit cycle.

The sink and the limit cycle are examples of simple *attractors*. When nonlinearity is included in the equation of motion, it is possible to have more complicated attractors—in particular, *strange*, or chaotic, aperiodic attractors. One early example of such an attractor was found by Lorenz in a 3-mode truncation of the Navier-Stokes equation

$$\begin{aligned}\dot{x} &= 10(y-x),\\ \dot{y} &= \mu x - y - xz,\\ \dot{z} &= xy - 8z/3.\end{aligned}$$

The strange attractor (SA) that occurs in this system is shown in perspective in figure 2. The orbit spends random amounts of time on the two distinct portions of the attractor.

SA's are crucial in one picture of the onset of chaos and turbulence, the Ruelle-Takens model. Here chaos is presumed to occur by the creation of SA's, and the mechanism is as follows. Solutions to (1) are studied. For small μ, some simple periodic motion is present; as μ increases, (Hopf) bifurcations occur; the motion is still regular, but now on m-dimensional tori, where $m > 1$. When two such bifurcations have occurred, then it can be (mathematically) proven that any small perturbation suffices to create a SA, and hence chaos.

Currently, there exist several such scenarios for the onset of chaos and turbulence, each applicable in different circumstances. In the so-called Feigenbaum picture, we consider systems described by (1) or (2). As a function of the parameter μ, the following behaviour pattern occurs. For $\mu < \mu_0$, there is some kind of a simple sink. At μ_0, a bifurcation takes place and an orbit of period τ becomes stable and attracting. (Technically, this is through a "pitchfork" bifurcation). As μ is increased beyond a certain

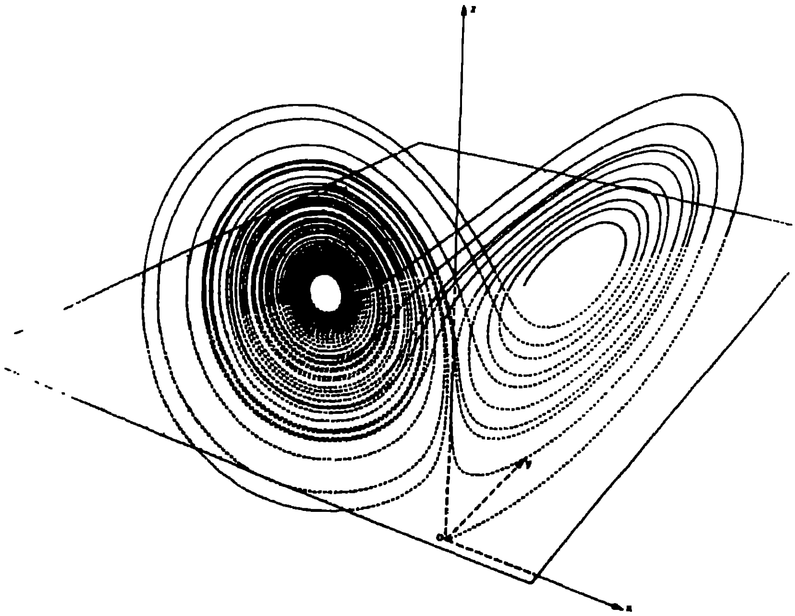

Figure 2. The strange attractor in the Lorenz system, equation (8), for $\mu = 28$. The attractor consists of two almost planar portions, and the orbit wanders chaotically from one side to the other.

value μ_1, the period $-\tau$ orbit loses stability, but one of period 2τ is born which is now stable and attracting. At a higher value μ_2 another bifurcation takes place, with the period-2τ orbit losing stability while a period-4τ orbit becomes stable. This process repeats itself: at μ_n, a period-$2^n\tau$ orbit becomes stable and attracting while the period-$2^{n-1}\tau$ orbit loses stability. In the limit, one has a $2^\infty\tau$-period orbit, *i.e.*, an orbit of infinite period, or chaos. The interesting thing is that μ_∞ is finite—the *period-doubling cascade* occurs quite rapidly, and furthermore, the rate of convergence of the bifurcation points,

$$\delta_n = \frac{\mu_n - \mu_{n-1}}{\mu_{n+1} - \mu_n} \tag{9}$$

logarithmically approaches $\delta = 4{\cdot}669201609 \ldots$ as $n \to \infty$. The most surprising fact is that the number δ is universal for a large general class of F_μ. The precise form of F_μ does not matter (within certain restrictions). Wherever the period-doubling route to chaos is found, the number δ that one computes from measurement is identical to that found by Feigenbaum (i.e., 4·669 . . .). Historically, this number was discovered in a study of the discrete one-humped map of the unit interval known as the logistic equation, namely,

$$\begin{aligned} &x(j+1) = \mu x(j)[1 - x(j)], \\ &0 \leqslant x \leqslant 1,\ 0 \leqslant \mu \leqslant 4. \end{aligned} \tag{10}$$

(In fact, there are several other universal constants that can be found within such a picture.) The period-doubling route to chaos has been seen to occur in a wide variety of cases—in abstract maps such as (10), in differential equations such as (8), in a variety of theoretical experiments modelling chemical reaction kinetics, in forced oscillator problems, in a seven-mode truncation of the Navier-Stokes equation, and even in the equations that model repeated yielding in mechanical behaviour. Most crucially, though, a number of physical experiments have also confirmed this picture. The Rayleigh-Bénard flow problem mentioned earlier is one such. In this experiment, liquid helium is heated at around 4 K, and the temperature at a point within the cell is monitored as a function of time. The Rayleigh number, R, plays the role of the parameter μ. For low R, convective rolls are formed in the experimental cell; the motion is periodic. As the temperature is raised, the motion begins to become turbulent. The Fourier transform of the temperature as a function of the time clearly shows the existence of a basic frequency, f, and the subharmonic bifurcations, which give rise to peaks at $f/2, f/4, f/8, f/16$, etc. (see figure 3). The Feigenbaum constant computed from this experiment turns out to be about 4·8, amply confirming the general theory.

It must also be mentioned that the Rayleigh-Bénard experiment prepared differently displays the Ruelle-Takens behaviour as well. There is yet another common mechanism, *intermittency*, through which chaos can occur, *via* "tangent" bifurcations. Prior to the onset of full-scale chaotic behaviour, there are long periods of time when the motion is perfectly regular, interspersed with short bursts of erraticity. This route too can be observed experimentally.

In dissipative systems, chaos comes about in a manner different from that in conservative systems. Essential ingredients are bifurcations and attractors. One can have either period-doubling bifurcations and a periodic attractor in the Feigenbaum scenario (thus only one independent frequency), or bifurcations from a period orbit to tori, followed by a strange attractor in the Ruelle-Takens picture (thus at most three independent frequencies).

3. Summary

This talk has only briefly touched upon the basic phenomenology of irregular motion. Much of the interest in nonlinear dynamics arises from the existence of a large component of the unexpected and the counterintuitive. I have tried to outline the

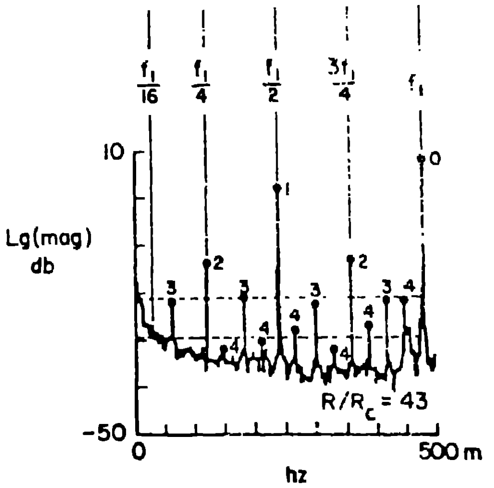

Figure 3. Period doubling subharmonics in the temperature power-spectrum of liquid helium in a Rayleigh-Benard experiment (from Maurer and Libchaber, *loc. cit.*).

various paths or routes to chaos; unavoidably, there are gaps in this short presentation.

Although much progress has been made, there are still several open questions. For example, there is no minimal (or maximal) degree of complexity necessary to ensure chaos—very nonlinear systems can be integrable, while even the simplest (cubic) nonlinearity can induce chaos. And at the microscopic level, which may or may not be of interest here, quantum effects occur, and there is no clear understanding of how this can modify classical chaos.

When it does occur, chaos can have important consequences. For one thing, it becomes possible to apply statistical methods to advantage, if the behaviour is sufficiently random-like. On the other hand, chaos may be an undesirable feature if one wishes to remain in the region of the precisely predictable—this situation is common, for example, in particle storage rings where particle losses occur via erratic orbits: It is then essential to minimise or totally avoid chaos. The very ubiquity of chaos makes it necessary to examine dynamical processes in greater detail, whatever the context—this can well include mechanical behaviour.

References

1. General references on chaos

1980 *Proc. Int. Conf. on Nonlinear Dynamics* (ed) R H G Helleman (Ann. N.Y. Acad. Sci. No. 603)
Jorna S (ed) 1978 *Topics in nonlinear dynamics* (Am. Inst. Phys. Conf. Proc., Vol. 46)
Helleman R H G 1970 in *Fundamental problems in statistical mechanics* (ed) E D G Cohen (New York: North-Holland Publ) Vol 5, p 165
Moser J 1978 *Math. Intell.* **1** 65
Ruelle D 1980 *Math. Intell.* **2** 126
May R M 1976 *Nature* (*London*) **261** 459
Hofstadter D 1981 *Sci. Am.* **245** 16

2. Conservative systems

Berry M V 1978 in *Topics in nonlinear dynamics* (ed) S Jorna Vol 46 (*Am. Inst. Phys. Conf. Proc.*)
Ramaswamy R 1981 *Phys. News* **12** 60

3. Dissipative systems

Eckmann J P 1981 *Rev. Mod. Phys.* **53** 665
Kumar D 1982 *Phys. News* **13** 109
Tomita K 1982 *Phys. Rep.* **86** 113
Crutchfield J, Farmer J and Humberman B 1982 *Fluctuations and simple chaotic dynamics Phys. Rep.* **92** 45

4. Some experimental references

Maurer J and Libchaber A 1979 *J. Phys. Lett.* **40** 419
Maurer J and Libchaber A 1980 *J. Phys.* **41** C3
Feigenbaum M 1979 *Phys. Lett.* **A74** 375
Gollub J P, Besons S V and Steinmann J 1980 *Proc. Int. Conf. nonlinear dynamics* (ed) R H G Helleman (Ann. N.Y. Acad. Sci. No. 203)

5. Other references

Lorenz E N 1963 *J. Atmos. Sci.* **20** 130
Ruelle D and Takens F 1971 *Commun. Math. Phys.* **20** 167
Feigenbaum M 1978 *J. Stat. Phys.* **19** 25
Feigenbaum M 1979 *J. Stat. Phys.* **21** 669

Discussion

G Ananthakrishna: Why is it often said that Landau's theory does not give a correct description of turbulence?

R Ramaswamy: The trouble with the Landau picture of turbulence is that as you vary a particular parameter, you have a series of bifurcations to the wrong geometrical object. These are in a certain sense bifurcations from a periodic orbit to a toroid, and thence a sequence of toroids. A limiting strange attractor does not appear.

G Ananthakrishna: Which route to the turbulent state is followed in the Rayleigh-Benard case?

Ramaswamy: It has been shown that all 3 routes may be followed.

G Ananthakrishna: Is there any algorithm to get the Poincare map for multi-dimensional systems?

Ramaswamy: It is a difficult process.

S R Shenoy: Can one make a statement about the minimum order of the differential equations and of the nonlinearity in them in order to get chaos?

Ramaswamy: This is difficult. We do not even have a clear way of predicting whether a system is going to be integrable or not. A minimum requirement for chaos is of course nonlinearity, but it is not easy to make a more exact statement of general applicability.

K R Rao: Does the central peak in a second order phase transition have anything to do with chaos?

Ramaswamy: There is no analogy at all between the onset of chaos/turbulence with any kind of phase transition.

M Youssuff: How does one develop a probabilistic description of the chaotic state?

Ramaswamy: One of the reasons for studying chaos is to determine when ergodic theory is valid. Clearly, at the very least, chaos is needed for ergodicity to occur.

Bull. Mater. Sci., Vol. 6, No. 4, September 1984, pp. 817–822. © Printed in India.

Fractals

D DHAR

Tata Institute of Fundamental Research, Bombay 400 005, India

Abstract. An elementary introduction to the concept of fractals is given. Some examples of fractals drawn from nature are briefly discussed. It is suggested that fractal geometry may be useful in characterizing the grain size and shape distributions in polycrystalline solids.

Keywords. Fractals; non-integral dimensions; grains.

1. Introduction

This talk is intended as an elementary introduction to the concept of fractals for non-experts. I shall try to concentrate on some of the qualitative geometrical features, and will not discuss more technical topics such as phase transitions on fractals.

The organization of the talk is as follows: In § 2 I shall briefly discuss the motivation for studying these unconventional geometrical objects. The intuitive notion of dimension is generalized in § 3 to include non-integral values of the dimension. Some illustrative examples are given in § 4. Section 5 contains some concluding remarks.

2. Motivation

Fractals are geometrical objects having an effective dimensionality which is non-integral. They are useful in modelling several quite different physical situations. It may not be unreasonable to hope that they would also be useful in describing certain aspects of the mechanical behaviour of matter.

This situation is not entirely like that of a biochemist who tries to sell a 'wonder drug' without quite knowing which ailment it cures. In our case, the drug is acknowledged to be 'neurosensitive'. Whether the effects are desirable or undesirable in a specific proposed application is not known beforehand. In some cases, for example in the understanding of the influence of dimensionality on critical phenomena near phase transitions, fractals have been found to be very useful.

The mechanical specification of a system involves the listing of the variables in terms of which the state of the system is described (kinematics), and of the laws of mutual interaction and time-evolution of these variables (dynamics). The choice of variables in terms of which we characterize the state is important: unnatural choices lead to convoluted descriptions. An example of a bad choice of variables is the Ptolemaic insistence on describing planetary motion in terms of a superposition of uniform circular motions. A comparatively more recent example is the phrase 'temperature-dependence of the Debye temperature' used by some physicists around 1910 to describe the non-agreement of the measured temperature-dependence of the specific heat of materials with Debye's theoretical predictions.

The introduction of fractals to describe the mechanical behaviour of matter has, first, a kinematical aspect. It has not yet been established that our difficulties in understanding the mechanical properties of solids are sufficiently acute to necessitate a substantial change from the conventional picture involving an ideal solid plus defects. However, the general trend of the discussions at this Meeting would seem to indicate that, near the plastic limit, the formalism is under stress. It may be useful to explore the possibility of alternative modes of description.

Most text books on the mechanics of solids start out by classifying the defects in solids as point-, line-, surface-, or volume-defects. It is not surprising that the classification scheme is geometrical, and is almost universally preferred over other possible schemes (alphabetical, historical, mobile/immobile defects, annealed/quenched defects, etc.). The geometrical characterization of defects captures some of their most important features. It cannot be the whole story, but it is a useful place from which to begin.

3. A definition of non-integer dimensionality

It is well-known that the strength of solids is a strong function of the grain size and grain shape. Earlier it has been emphasized by Ranganathan that grains in metals are quite irregular in shape (Ranganathan 1984). A schematic representation of possible grain shapes on a two-dimensional lattice is shown in figure 1. Clearly, a material with compact hexagonal grains (as in figure 1a) would be different, mechanically, from a material with very ramified grains (figure 1d). It would be useful to have a numerical characterization of these grain shapes to be able to specify whether the grains are compact objects with a few holes, or are ramified and stringy. Roughly speaking, a compact volume, a disc-like shape, and a string-like shape respectively would behave like three-, two- and one-dimensional objects. A numerical characterization of attributes such as 'stringiness' often gives rise to nonintegral answers, when applied to objects of complex geometrical shapes. Such objects may be said to have a non-integral dimension and are called fractals (Mandelbrot 1977, 1982).

What is meant by saying that an object has dimension 1·5? For that matter, what is meant by saying that an object is three-dimensional? Before giving a definition of dimension, which is generalizable to non-integral values, it is useful to remember that the dimension we assign to an object depends very much on our choice of its representation. A ball of wool may be represented as a point, or a sphere, or as a tangled line (having dimensions 0, 3, and 1 respectively) depending on our scale of description (Mandelbrot 1977). The dimension we assign actually pertains to the mathematical representation of the object, and not to the object itself.

In order to be useful, a definition of dimension must be simple, robust (insensitive to small changes in geometry), and should agree with our intuitive notion of dimension

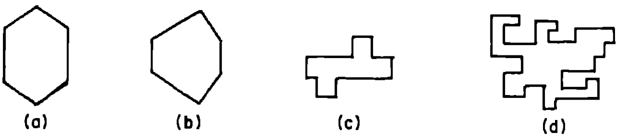

Figure 1. A sequence of increasingly complex grain shapes (schematic).

when applied to conventional spaces (like manifolds). Several such definitions may be found in the literature (Mandelbrot 1977, 1982; Dhar 1977; Engelking 1978). In the following, we consider only the simplest of these.

Consider a space in which the distance between two points, and a volume measure, are defined. Let $V(R)$ be the volume of the set of points whose distance from an arbitrarily chosen origin is less than R. If $V(R)$ varies as R^D for large R, for all choices of the origin, we define D to be the fractal dimensionality of the space. Formally,

$$D = \lim_{R\to\infty} [\log V(R)/\log R].$$

Clearly, using this definition, a straight line has dimension 1 and a plane has dimension 2. Now consider the triangular gasket shown in figure 2. It consists of an equilateral triangle, the mid-points of the sides of which are joined together and divide the triangle into four smaller, equal triangles (three upright, and the central one inverted). Each of the three upright second-generation triangles is divided similarly into four third-order triangles. The 3^2 upright triangles of the third generation are further divided to give 3^3 fourth order triangles, and so on, *ad infinitum*. The gasket consists of all the points in the plane which belong to at least one of the line segments used in this division procedure.

It is easy to see that the points belonging to the gasket have zero area, but that the total length of the line segments which constitute the gasket is infinite. It would thus seem reasonable to assign this set of points a dimensionality between 1 and 2. To determine the fractal dimensionality of the gasket we have to define the metric and a volume-measure for this case. The distance between two points is most simply defined as the Euclidean distance between them (alternatively, as the length of the shortest line joining them and lying completely on the gasket). The volume of an rth generation triangle with all inside points included is defined to be 3. Using these definitions, it is easy to see that

$$V(2R) = 3V(R).$$

Using the definition of D given earlier, this gives $D = \log_2 3 \approx 1{\cdot}54$. The triangular gasket is thus an example of a fractal.

4. Other examples

In the following we give some additional illustrative examples of fractals. For additional examples, and some very beautiful pictures, see Mandelbrot (1977, 1982).

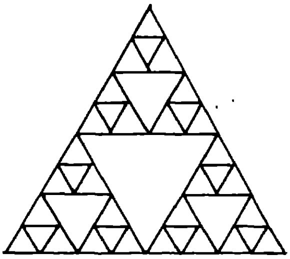

Figure 2. The triangular gasket. Only the edges belonging to the first, second, and third order triangles are shown here for clarity.

4.1 *Lattice animals*

Lattice animals are defined as connected clusters of sites embedded on a lattice (figure 3). The problem of the determination of the mean values of the properties of animals containing a given number of sites, given that all distinct shapes of such animals have equal statistical weights, is called the random animal problem. This assumption is not true for crystal grains, as compact grains have lower surface energy, and are favoured thermodynamically.

If a typical animal on a d-dimensional hypercubical lattice (d is an integer here) were compact, its maximum lateral extent R would vary as $n^{1/d}$, where n is the number of sites in the animal. It is found that random animals are typically stringy, and R varies as a *larger* power of n. In 3-dimensions, the dependence is $r \sim n^{1/2}$. Thus a random animal in 3-dimensions has a fractal dimension equal to 2 because $n \sim R^2$.

4.2 *Percolation clusters*

Consider a d-dimensional hypercubical lattice (d integral) in which each nearest-neighbour bond is, independent of others, unbroken (*i.e.*, connects the sites at its ends) with a probability p (figure 4). For small p values (p less than a critical value p_c), a site chosen at random is connected to only a finite number of other sites through occupied bonds. In this case, the effective dimension of the clusters may be defined to be zero. For $p > p_c$, the mutually connected sites constitute a finite fraction of the total number of sites of the lattice, and form a d-dimensional network (with some holes). When p is equal to the critical probability p_c, the incipient infinite cluster has zero fractional volume, and is very tenuous. However, if we construct a sphere of radius R about a point, the expected number of sites connected to the origin varies as R^D where $D \approx 1{\cdot}6$ for $d = 2$. The infinite cluster at the percolation threshold is an easily-realizable example of a fractal.

4.3 *Soap powder*

If we look at soap powder under a microscope, it is seen to consist of a large number of particles of varying sizes. As in the case of crystallites in metals, the average linear extent

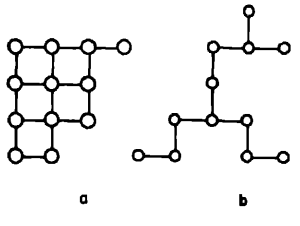

Figure 3. Animals on a square lattice. (a) is a compact cluster, while (b) is stringy.

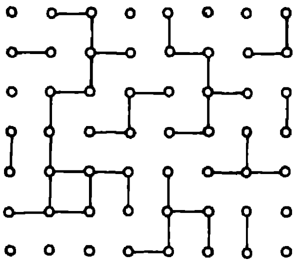

Figure 4. A random configuration of unbroken bonds on a square lattice.

of these powder particles grows faster than the cube root of their mass, and can be used to define an effective dimension of the powder. We should expect the fractal dimension of soap powder to be between 2 and 3. The precise numerical value may perhaps depend upon its chemical structure.

4.4 *The distribution of galaxies*

The precise nature of the large-scale structure of the distribution of matter in the universe is not very well-known. According to one view, the distribution of galaxies in the universe is essentially uniform. However, a different picture, in which the universe shows clustering at all scales of length, is also consistent with experimental data. According to this picture, galaxies typically reside in clusters of galaxies, which themselves are part of clusters of galaxies and so on. Each cluster contains about 3 subclusters on the average. The size of the cluster is appreciably smaller than inter-cluster distance, which implies that the number of galaxies in a sphere of radius R, centred at any particular galaxy, grows as R^D with $D < 3$. Thus the distribution of the galaxies in the universe shows a fractal structure.

4.5 *Coastlines*

The coastline of an island is typically a very zigzag line (figure 5), and its measured length depends very much on the size of the divider spacing (or calliper length) used to measure it (say, from a very detailed map). If we use a smaller divider spacing, we measure more of the small detours and turns that the line makes, and the measured length is larger. If the line is smooth at very short distances, then, as the divider spacing is decreased, the length will tend to a limiting finite value (which is defined to be the 'length of the line'). If, however, the line is rough at all length scales, we may find that $L(s)$, the length measured when the divider spacing is s, varies as s^{1-D}, where $D > 1$. This D may be called the fractal dimension of the coastline. For several actual coastlines $D = 1{\cdot}2$. For a Brownian motion path $D = 2$.

5. Concluding remarks

It should be clear from the preceding examples that fractals are not exotic, pathological objects dreamt up by mathematicians, but are very much a part of the world around us. They provide a natural description of the non-classical geometrical forms encountered in nature. It is this common geometrical character, and not the occurrence of fractional powers, which is the characteristic feature of fractals. Fractional power laws are, of course, encountered quite frequently in Nature. For two observables X and Y, if X varies as an integral power of Y (not equal to ± 1), then Y varies as a non-integral power of X. It is preferable not to use the term 'fractal' in the absence of a geometrical structure in the problem (as in, say, of stock-market prices). Fractals may also show up in the discussion of mechanical properties of matter in the context of dynamical response and the onset of chaos. A discussion of these aspects may be found elsewhere (Ramaswamy 1984). Additional references on fractals may be found in Dhar (1981).

Figure 5. A schematic representation of a coastline. The line will show further wrinkles and detours, if observed on an expanded scale.

References

Dhar D 1977 *J. Math. Phys.* **18** 577
Dhar D 1981 in *Current trends in magnetism* (Bombay: Indian Physics Association) p. 207
Engelking R 1978 *Dimension theory* (Amsterdam: North-Holland)
Mandelbrot B B 1977 *Fractals: form, chance and dimension* (San Francisco: Freeman)
Mandelbrot B B 1982 *The fractal geometry of Nature* (San Francisco: Freeman)
Ramaswamy R 1984 *Bull. Mater. Sci.* **6**
Ranganathan S 1984 *Bull. Mater. Sci.* **6**

Discussion

N Kumar: Are fractal dimensions and similar apparently geometrical concepts applicable to *dynamics*?

D Dhar: Yes, there are connections. An example is magnetisation creep.

G Venkataraman: These concepts have also been employed in describing turbulence.

R Ramaswamy: Strange attractors have been shown to have well-defined fractal dimensions.

S Ranganathan: Fractals may have some bearing on the shapes of second phase particles which influence mechanical properties.

Bull. Mater. Sci., Vol. 6, No. 4, September 1984, pp. 823–825. © Printed in India.

Summary and outlook

V BALAKRISHNAN

As we are running short of time, I will be brief. I would like to begin by repeating the platitude (or self-evident truth!) that, just as approaches to a certain problem can be different, so can the motivations. A person may be motivated to study a problem for purely aesthetic reasons, and not out of any practical considerations at all; but the person should have the freedom to do so. To paraphrase what has been said by many eminent scientists: If a fraction of time spent in a subjective argument over different approaches to a problem was spent in actual computation using any of the techniques under contention, there would perhaps be no need for the argument because the problem would be considerably closer to resolution! Similarly, I feel that there is no need here to debate the respective motivations of physicists and metallurgists, including the question of what constitutes a problem and what is meant by a solution to one. All techniques, however mathematical or however empirical, are acceptable and indeed essential to make any headway in a subject as complicated as the one we have been discussing.

I would now like to make two general comments, one taken from Prof. N Kumar and the other based on Dr K R Rao's talk. In any given subject, theorists generally like to have the broad paradigms brought out so as to have a framework for further development. The general paradigm that is used in the area of mechanical deformation is of course that of dislocations. Given a paradigm, the theoretical physicist then faces the interesting question of the adequacy or otherwise of the paradigm in the light of subsequent experimental information. A well-known example is that of the soliton which is the "paradigm of the 80's" in several branches of physics. When certain regimes of essential nonlinearity are reached, the traditional plane wave-cum-superposition principle is no longer adequate, and new basic entities like solitons (or more generally 'lumps') have to be introduced. So, in this sense, it is very relevant to ask whether, when we look at a practical problem like a large-angle grain boundary, the paradigm of the dislocation is still meaningful—notwithstanding the fact that in the limit of small angles, the boundary is describable in terms of an array of dislocations. Thus, a radical approach which gives up the idea of dislocations altogether would be worth examining further. Equally welcome are other approaches which bring out geometrical coincidences like the DSC lattice together with the idea of dislocations on *this* lattice.

My second general comment concerns the experimental side. A large number of possibilites were catalogued systematically this morning by Dr Rao. Some techniques like acoustic emission, which perhaps have not been emphasized sufficiently for lack of time, should be explored more systematically. Turning to questions for theoreticians arising out of experiment, consider, for example, spinoidal decomposition and the various nonlinear theories of diffusion associated with it. What light does experiment shed on the cut-off and truncation procedures employed in Cahn's theory and its various modifications to include 'higher order' nonlinearities? What are the experimental inputs needed for a critical discrimination between the various theories—in the manner, for example, critical experimental inputs to the theory of freezing were spelt out by Prof. Ramakrishnan in his lecture? You may recall that he pointed out how the shape of the structure factor really determines how good the approximation is and also serves as a self-consistency check. Something like that would be worth attempting for theories of spinoidal decomposition too. Perhaps this has already been done. I am tempted to recall a remark I came across once—I think it was made by Frauenfelder in the early days when many nuclear physicists were getting into solid state physics *via* the Mössbauer effect—that it is always a big surprise to a person getting into another field to realize that the "natives were not as stupid as they seemed from outside", and that all the obvious things had been done! I am sure all the physicists here have this realization about metallurgy.

There are some other points of interest which I should like to mention, although my list will surely reflect my personal bias as a theoretical physicist. Consider for example the general question of nucleation and discontinuous transitions. The diversity and richness of the phenomena encountered here were well brought out in the talk by Dr Wadhawan. It seemed to me that considerable work remained to be done to get the 'theory' here to the same stage of development as has been reached for continuous transitions. Another point which struck me relates to describing things in terms of disorder rather than order. For example, when one considers systems with quenched disorder, one starts with simple models, but pretty soon when the defect density becomes high, one introduces things like disorder variables. Starting from the high-temperature phase, one can then use duality properties, for instance, and get information on the ordered phase as well as on the defects in the ordered phase. This is more fruitful than attempting to start at the ground state and work one's way upwards. Perhaps when the dislocation density is very high, this kind of approach may be useful—indeed, I should think that recent ideas on 'solid-state turbulence' are preliminary steps in this direction. But a great deal of work remains to be done to 'quantify' the properties of random tangles of dislocations, etc. Starting from the theory of liquids is of course carrying the idea of coming in from the disordered phase to its ultimate, but this may be *too* basic for the purpose I have in mind here. The theory of *freezing* we heard about was aptly named, for it did not deal with the question of how to go from the solid to the liquid phase, *i.e.*, how to restore the broken symmetry. A complete picture of the transition should of course give us an idea of this obverse side of the coin, too.

I would also like to emphasize a point that Dr Ramaswamy made during his presentation. When one tries to apply ideas like chaos to mechanical behaviour (as has been initiated by Dr Ananthakrishna), it would be good to try and obtain first a *model-independent characterization of* the *basic* variables in the mechanical behaviour problem. It is very interesting to demonstrate that chaos appears in specific models of dislocation dynamics. Presumably the phenomenon is much more general. So one would like to know what the minimal set of relevant variables is, and so on, in order to extract model-independent information to the extent possible. This is all the more important in an area like chaos because we know that 'neighbouring' dynamical systems can have widely different behaviour. We should at least be able to put various models of dislocation dynamics into their appropriate 'universality' classes. Only then can one undertake a critical examination of the role of various physical parameters in inducing bifurcations, chaotic behaviour, etc.

Having mentioned chaos, I should also like to make a remark on the slightly older paradigm of solitons, nonlinearities, etc. It may be relevant to ask whether nonlinearities of the kind that arise in the continuum elasticity theory Dr Sahoo talked about, can help to stabilize nondissipative structures like solitons—and if so, what are these? Are they the analogues of dislocations in discrete models? This is no doubt an entirely theoretical kind of question, but I am sure that it would aid progress if we understood the basic reason why these objects get stabilized.

I realize I have essentially been conveying the prejudices of a theorist but that is because I am not really competent to say much about the experimental possibilities. However, I will emphasize that this is a field in which observation is prime. We want facts. However, I should like to heartily endorse a point made by Prof. Kumar. Given the plethora of facts and the very large number of variables involved in the field of mechanical behaviour, physicists generally find the going difficult since they like things to be presented in terms of basic features, or very general arguments and reasons. To snow a physicist with a mass of metallurgical details sounds a bit like French grammar where you list all the irregular verbs and exceptions *ad nauseum.* So, if I may make an appeal—it would be nice for the metallurgists to *intentionally oversimplify* the problems that they face when presenting them to a physicist. *After* he gets interested and starts answering questions, you can 'bring him down to earth', as Prof. Srinivasaraghavan said, by gradually including the complications; otherwise there is a tendency for him to get turned off right in the beginning. This approach will also help sift and place all the facts in order of importance and relevance, in itself a worthwhile and by no means trivial task. Fortunately, in the talks we have had during these three days, this has, by and large, been achieved. Many of us physicists have noted down at least some things that are general features, notwithstanding exceptions, and I am sure some of us will actually explore at least the simplified cases. In that sense, I think, this Meeting has worked out well.

Bull. Mater. Sci., Vol. 6, No. 4, September 1984, pp. 827–835. © Printed in India.

Panel discussion

Moderator:	Prof. S K Joshi, Department of Physics, Roorkee University
Panelists:	Dr R Krishnan, Metallurgy Division, Bhabha Atomic Research Centre Dr V C Sahni, Nuclear Physics Division, Bhabha Atomic Research Centre Dr S Ray, Metallurgy Department, Roorkee University Prof. N Kumar, Department of Physics, Indian Institute of Science

Prof. Joshi: We have had a busy and very fruitful Discussion Meeting. This is the last session, and we are gathered to hear the reactions of the panelists, as well as their suggestions. There are no restrictions or guidelines, and the panelists are completely free to express what they feel. I shall alternate between metallurgists and physicists, and will start with Dr Krishnan.

Dr Krishnan: During the past three days I have informally talked to many of the participants, and I have come to the conclusion that this Meeting has been a unique experience. I suggest it should continue as an annual feature—if not on the same subject, at least on topics of an allied nature.

A general remark I would like to make is that many of the theoretical papers have shown that it is necessary to take the theoretical aspects more seriously and also utilize mathematical and physical concepts in explaining some of the behaviour of materials. On the other hand, I also felt that perhaps it is not necessary to explain some of the well-accepted observations the metallurgists have made. It would be more useful to complement the metallurgists in a suitable manner.

One topic not fully discussed at this Meeting is fracture. Why are we interested in obtaining a better understanding of the physical basis of mechanical behaviour? Essentially it is so that one can design better materials which will withstand service conditions. For instance, one might be interested in designing a material with good fatigue resistance or good creep resistance. We know that materials can fracture in widely different ways—ductile, brittle, cleavage etc. On the opening day, Prof. Ramaseshan has already pointed out how important it is to know the stress corrosion cracking behaviour of materials under service environments.

Take the nuclear field as an example. The iodine produced as a fission product can interact with the zircaloy clad and make the clad susceptible to stress corrosion cracking. The basic question here is: What does iodine do under stress to the grain boundary? Is there a decohesion caused by a lowering of the cohesive energy of the grain boundary which is locally under stress? Is it possible to predict which atomic species (like iodine) are efficient in lowering the cohesive energy? Theoretical studies of this problem coupled with suitable experiments will go a long way in establishing interplay between physical concepts and metallurgical interests.

Another example, again from the nuclear industry, relates to the irradiation creep behaviour of zircaloy coolant tubes. While the reactor itself has a life span of about 30 years, one is forced at present to change these tubes once in every 12 yrs or so because of irradiation creep. To develop a material that will be good for the entire life span of the reactor, we must perhaps introduce new ideas. One should examine how the texture (*i.e.* the preferred orientation) and grain shape influence irradiation growth of the material. Perhaps, as Prof. Ranganathan suggested, one could use the concept of fractals to characterize grain shape topology— and thus have a better measure for studying and characterizing irradiation growth.

These are some examples of practical problems where there can be a meaningful dialogue between physicists and metallurgists. They involve finding real-time solutions to real-life problems based on an understanding of the basic behaviour of materials.

Prof Joshi: Thank you, Dr Krishnan, for pointing out some problems where physicists and metallurgists could come together. We now turn to Dr Sahni.

Dr V C Sahni: I would like to go back to the remark which Dr Venkataraman made on the opening day. He was looking at a certain matrix element and trying to find out whether it would be zero or non-zero at the end of the Meeting. Now metallurgists are essentially practitioners. In fact, you would have noticed this from Dr Krishnan's remarks. On the other hand, physicists are a different kind of people. They tend to look behind a phenomenon, try to understand it from an atomistic basis and so on.

An analogy comes to my mind at this point. Consider the automobile engine. Obviously there are (automobile) engineers who design such objects. But there are also people trying to understand the basics of the combustion process *via* tools like Raman scattering. The hope is that such basic studies can lead to the improvement of the efficiency of the engine.

Physicists cannot from the word go come up with solutions to the practical problems of metallurgists. The important thing is they try to analyze the microscopic basis for a particular type of behaviour. In turn, the metallurgist can build on this instead of relying on a phenomenological understanding of the situation. Of course this is the way science progresses.

So, coming back to the point Dr Venkataraman made about whether there is an overlap matrix element or not, I think we really have to look at the interface between the two disciplines. As Prof. Ranganathan's talk clearly brought out, a topic like the large-angle grain boundary is something which physicists can examine from an atomistic point. If some light is shed, then perhaps it will enable the metallurgists to come up with better materials. In short, physicists can *via* tools of their own (like fluctuation spectroscopy) explore microscopic processes which in turn can form inputs to the metallurgical aspects. So my own view is that the matrix element might not be as large as one would hope for, but it is not zero either. I am in agreement with Dr Krishnan that exercises like this Meeting should continue. Hopefully, if we repeat it a couple of times, we may converge on something significant and improve the matrix element in the future.

Prof. Joshi: Thank you, Dr Sahni. I think the value of the matrix element depends on the "frame" of reference just as Deepak Dhar pointed out that the length of a coastline depends on the length scale used for measurement. Locally the matrix element is sometimes positive and sometimes negative. What we must all do is to go to a scale where it becomes *globally* positive! I now request Dr Ray to give his views.

Dr Ray: Before we try to explain the mechanical behaviour of a material, we must first define the mechanical *state* of the material. Important in this context is a proper description of the grain boundary concerning which Prof. Ranganathan described a beautiful model. However, from the questions that were raised after that talk, I can see that there are limitations to that model. One wonders what the correct description of the situation at the grain boundary should be. May be something will emerge in the future.

One topic on which we did not focus is vacancies, especially their role in defining the mechanical state of matter. Vacancies play an important role as we know from annealing experiments on cold-worked samples. They are also pertinent to certain aspects of plastic deformation.

Next comes the grain shape. We all know that the grain shape is probably important but we do not yet know how to describe it quantitatively. Probably, the fractal concept might help us.

Let us now consider the transition from the elastic to the plastic regime. We used to think of this in terms of dislocations becoming mobile and multiplying. Now they are being described in terms of fluctuations, bifurcations, chaos and what not! Incidentally, I would like to point out that for bcc metals, there is a temperature below which this transition does not take place; for fcc metals however, this does not hold. All facts taken together, the picture to my mind is a bit puzzling. Is the elastic to plastic changeover really a transition or the emergence of a stable fluctuation of a particular kind?

Prof. Joshi: Thank you, Dr Ray. I now invite Prof. Kumar who has all along been making illuminating remarks from the floor, to give us his views as a panelist.

Prof. Kumar: I believe it is a part of conventional wisdom (which goes back to the Greek philosopher Lucretius) which says that a thing is explained only if it is done in terms of underlying microscopic objects (which, one presumes, exist). This may be a mental bias but no one seriously questions such an approach now. Certainly it is a part of our training as physicists. The question therefore is: What is the appropriate level of microscopy at which we want to discuss the present problems? Certainly you don't start with quantum mechanics if you want to build a house! There must be an "efficient" relationship between the microscopic world and the phenomenon we wish to understand. Of course all phenomena are not easily reducible to microscopic pictures. That we shall bear in mind. Now I shall get down to something specific.

Physicists often work with paradigms. For instance, if we are talking about a solid, we immediately imagine a perfect crystalline lattice and invoke Bloch's theorem. Everything is fine. Any departure from this idealization is a bit unfortunate but we take care of it in terms of a small perturbation. This is an example of an ideal picture that a physicist uses as a paradigm. On the other hand, a metallurgist, confronted as he is with *actual* metals, has his own paradigms. As I understand it now having come here, they mostly have to do with dislocations (which, I believe, live, multiply, climb, pile up and even die!). This is very nice. It is not necessary that dislocations exist; it is enough if they exist as paradigms! For example, quarks most probably do not exist but it is quite convenient to explain all matter in terms of quarks; it is a good mental picture. On the other hand, if we are going to discuss heavily deformed materials, is this paradigm based on dislocation as an elementary object convenient? True there are pictures showing dislocation— they are real objects and they certainly exist. We can even work out the mathematics of a single dislocation— no problem. I am told the two-body problem also can be done. But what if we have more than two, say 10, 20 or 10^{11}? That is where the problem lies. Near a large-angle grain boundary, do they retain their imitable integrity or not? If they don't, then we may have to look for something else in terms of which to describe these structures. Prof. Ranganathan did this by resolving the large deformation at the grain boundaries into a big part (DSC) plus a small part (described in terms of dislocation with Burger's vector taken from the DSC). I am happy with this picture. However, a doubt remains in my mind. In a metal, the large deformations at the grain boundaries must surely be sensed and felt by the electrons. If so, are we justified in ignoring the reactions of the electrons to such a heavy distortion? Even geometrically speaking, one wonders whether the dislocation concept is appropriate at a large angle grain boundary where there is such a pile up. Perhaps things are too amorphous-like in that region, and some alternate description should be tried (if not already done). So, the large-angle grain boundary appears to be a problem which physicists would be interested in because this is a case where one paradigm might give way to another.

Aside from this, there is a nontechnical matter that I raise on behalf of Prof. Ramakrishnan, which is: Where do we go from here? We obviously cannot meet time and again just to review work already available in books and journals. The important question is: Are we sure that there are sufficiently important, interesting, nontrivial open problems which physicists would be interested in? As of now, most of us physicists are *not* working on problems of mechanical behaviour. We are looking for the possibility of Discussion Meeting induced transitions. For something worthwhile to emerge, physicists must be willing to give more than 10% of their time. This is a practical issue if we mean business, and I suppose we do!

Prof. Joshi: Thank you Prof. Kumar. I now invite comments from the floor. Comments may please be restricted to broad issues or questions rather than matters of specific detail.

Dr G Venkataraman: As mentioned by you Prof. Joshi, I would like to make a few broad suggestions. The first of these arises out of a conversation I had with Prof. Ramaseshan at the time when the idea for the present Meeting took shape. Prof. Ramaseshan pointed out that while holding a meeting of this type was fine, everyone would go back and continue working on the same problems as before, instead of exploring the new grounds revealed at the Meeting. He emphasized that if fresh ground is to be broken, it would essentially have to be by young people who have not yet committed themselves to working in an already established area. I have been discussing this question informally during the last three days with several people, and the consensus appears to be that we must organize a regular, pedagogic school wherein young people can be given a systematic introduction that will orient them for research in this area.

Next I would like to point out that the Department of Science and Technology (DST) has identified this subject as a Thrust Area. If good proposals concerning experimental or theoretical research are made to DST, I am sure funds would be forthcoming.

Lastly, as regards future Meetings of this type, my sampling seemed to reveal that: (i) Future Meetings are necessary, (ii) they should not be large, and (iii) the topic of the Meeting should be more specific say like fracture, physics of large deformations etc.

Prof. Joshi: If we look at the growth of the interaction between physicists and metallurgists (in this country), we notice that some of it originated right here at RRC. In this Meeting, we heard on the first day a description of some experiments on serrated yielding performed by Dr Rodriguez's group. A theory of serrated yielding was also presented by a physicist from RRC. Maybe the theory was not explicitly motivated by those experiments but the interactions between the Materials Science group and the Metallurgy group must have had some influence. Some catalytic agent is definitely needed to promote such interdisciplinary interaction, may be in the form of an official directive!

I was having a conversation with Prof. Kumar wherein he remarked that when we return from this Meeting, most of us will go back to doing what we were doing earlier! What we do is, I suppose, decided by many factors but the value system is a key one. If one wants to encourage such interaction, then one must attach a value to it. I suggest that physicists and metallurgists in multidisciplinary Institutes like, for example BARC, should experiment in investing some percentage of their time to interdisciplinary activity of this kind. The outcome of such experiments could perhaps be reported at the next Meeting whenever we have it.

Anyway, as far as this Meeting is concerned, it has been a very fruitful one though, as some comments both from the panel and the floor indicate, a few aspects could have been better. But this Meeting has certainly had its utility, and we shall take advantage of whatever we have learnt to augment this interaction.

Prof. Kumar: I just want to add something. When I came here, I had a little misgiving in the sense that the subject obviously is an old one. I was aware that eminent physicists like Sir Charles Frank had worked on the subject. The point is that I had a feeling that around the World there must be many physicists working on metallurgy. Now as a physicist, I am not directly involved in this type of work and therefore I just don't know what has already been done. Unfortunately, no one here explicitly pointed that out, and also what has *not* been done. As someone remarked, the natives are not quite stupid! If we are not properly informed about what has already been done, we might end up reinventing the wheel!! Would someone like to comment?

Dr R Ramaswamy: I want to say a few things—probably in repetition, and some of them platitudinous perhaps! When a person like me comes to a Meeting like this, he does not necessarily come looking for problems. One comes, one listens to the problems aired, one says what one can, and one contributes. In that sense, I don't think it is valuable for us to seek where we are going *vis-a-vis* conferences of this type because such a conference serves precisely the purpose for which it was arranged *i.e.* to bring together people of different disciplines and see what each one can get out of it. *Of course* we will go back to doing whatever we were doing before. The hope is that the little one might have heard might make *the* difference. Undoubtedly there will be more conferences of this type in the future but whether they should be held or not are spontaneous questions. When Deepak and I go back to TIFR we might well say, "Why are we doing abstract problems? Let us get together with chemists etc". In that case we are the ones who would have benefited. One cannot induce such things; they happen reasonably spontaneously.

Prof. C K Majumdar: When I came here, I certainly did so with the purpose of hearing metallurgists because we physicists do not often hear people of other disciplines. It was certainly educative. The things learnt should not be viewed in terms of immediate return alone because they also broaden your outlook. Even if you go back to doing what you were doing before, your view point would have changed a little and that is a good thing.

Turning to specific suggestions, I think we should have another such Meeting, perhaps in three years. Time scales are a bit long in this country, and probably, it will be at least three years before we can really talk anything new— by new I mean results obtained in *our* laboratories.

Now there are not many places where interdisciplinary work of this type is being done. I for one do not even know where metallurgical work goes on, apart from organizations like RRC, BARC, HAL and the IIT's. Obviously there must be other organizations using at least some metallurgical skills, the State Transport Corporations for example. Judging from the conditions of the buses they ply, there is clearly scope for some technological improvement (!) which could perhaps be done by metallurgists. At the same time, the wayside auto shops seem to manage alright, and they appear to be having a way of accumulating empirical knowledge that is beneficial to their work. In all the training we talk about, we should not forget such people. Somehow they have to be exposed to modern developments. In other countries this is taken care of, and phenomena like exoemission are actually put to practical use by high-technology companies like Lockheed. Details of such applications are often not discussed in the open literature and we have to learn them on our own. History in fact shows that advanced civilizations often keep technology to themselves and do not allow it to percolate to other civilizations. In such cases therefore, we have to learn the hard way.

Not everything in science should be done just for publication or priority. Certain things, even if it means repetition, *have* to be done to make Society run better. Repetition may not actually be a bad thing for in the process one might actually improve on what is already known. I can give you an example. The Chinese apparently had ice cream long before the Europeans knew about it. Marco Polo brought ice cream knowhow from China to Europe, and later the Americans improved it! In short, there are aspects of technology which we have to develop on our own. In that sense, we should find a way of inducing some technologists also to attend such Meetings in the future.

The other thing I would like to comment on is the School that Dr. Venkataraman mentioned. The School should not just involve lectures alone; the students must also get exposed to some experiments. In that case, I think the School should be organized in places like this (RRC) or at the Indian Institute of Science, where there are appropriate facilities.

Dr K R Rao: My comments relate to the remarks made earlier by Prof. Kumar. I think many of us would like to go back and actually do something different instead of continuing to do the same thing we have been doing for the last 25 years or so. In this context, I think the identification of unsolved problems is very important. One example comes to mind and that relates to Atomic Data for Fusion Research prepared by the IAEA about four years ago. A huge report has been written identifying hundreds of problems. IAEA has followed up this effort with some funding, and has also been evaluating the data coming out of the various research Centres. Although we are not trying anything on that scale, I feel that if problems are identified and made known say through the Proceedings of this Meeting, it might lead to various people (including those not present here) picking up the strands. Particularly in the experimental field, there is no reason why some of us cannot try something new, provided new experiments or problems are identified by specialists.

Prof. V Balakrishnan: I wish to comment briefly on a point raised yesterday by Prof. Ramakrishnan. In his characteristic fashion, Prof. Ramakrishnan pointed out that it would be useful for solid state physicists to learn the basics of physical and mechanical metallurgy. This is being done in some places but perhaps the exercise could be made more systematic. It is certainly being done with respect to courses on materials science but not so much in the case of solid state physics. As far as the latter is concerned, if one can spend a lot of time on electronic properties then surely a chapter of mechanical properties is reasonable, especially as it will at least get the jargon straightened out for condensed matter physicists. This chapter need not be very long. I noticed that right here on the first day, many physicists expressed to me their concern about the jargon. They could not understand it, but repeated use of the term dislocation seems to have made it familiar enough to most people (rather like the way theorems are established in high energy physics, namely you repeat it often enough and it becomes a theorem)!

In a slightly more serious vein, I think that some simple experiments on mechanical behaviour should also be introduced in the undergraduate curriculum. And there are very dramatic experiments, like the one on work-hardening demonstrated by Bragg in his Royal Institution lectures. A similar one, perhaps already known to some of you, involves closing one end of an open cylinder with a tissue paper, filling it with sand, after which you put a metal rod and apply enormous load on it. We got this set up at IIT recently and I personally along with several other people put my full weight on the rod and the tissue paper did not break because the stress was distributed by those fine grains of sand. Experiments like this bring out beautifully the effect of interfaces, grain boundaries and so on. Perhaps we should spend some time generating ideas for such elementary but very effective demonstrations which will convey to physicists the basic concepts of metallurgy.

Dr R Chidambaram: I think what was unique about this Meeting was that it brought a small group of metallurgists and physicists together. Also, unlike other meetings where people come and either give invited talks or present contributed papers, I got the impression that one was expected in this Meeting to talk about problems one had not completely finished or one did not know enough about. Thus, for example, I did not talk about our work on the equation of state— something we know how to handle. Instead, I talked on something in which we had some doubts and in which some metallurgical concepts were involved. If you look at the matrix element which Dr Sahni was talking about, the value of that matrix element must be obtained, I think, by integrating over the personal responses from all the individual participants, as is being done here during the present Panel Discussion. With this in mind, I will tell you what I personally gained from this Meeting. Honestly, I did not expect that the metallurgists would ask the kind of questions they actually asked after my talk. Of course Dr Majumdar raised a point about the entropy equation which I had not written down. If one knew how to write it down, the problem of the structure of the shock front would be solved substantially, but the current state of the art is such that one does not know how to discuss entropy production in the case of shock propagation in solids. On the other hand, after listening to the large number of talks we had on dislocations and grain boundaries, I think I now have a better perspective on how to think about these physically, in relation to the propagation of a shock front. That way I think this Meeting has been very successful.

As regards the periodicity of such Meetings, I think a Meeting once in three years as Dr Majumdar suggested would be appropriate. And that should be interspersed with a School in which there are lectures both by physicists (theoretical as well as experimental) and metallurgists.

Prof. Joshi: Would a metallurgist from the floor like to react? Yes Dr Rodriguez.

Dr P Rodriguez: I would like to make a few observations and the first of these relates to Prof. Ramakrishnan's remark that before physicists deal with the real physical nature of problems in complex materials like alloys, they need to develop a better understanding of the basics of physical and mechanical metallurgy. As history shows, metallurgy has been enriched considerably by the work of the physicists, and in fact many physicists have contributed to the study of plastic deformation and the fracture of metals. For example there is the monumental work of Schmidt and Bose on the deformation behaviour of single crystals of fcc metals. Prof. Ramakrishnan showed a picture of such deformation behaviour, and quoting from Bell's work said that metallurgists ignore it but that is really first-year text book material for metallurgist! We start with the deformation behaviour of a fcc single crystal and then extend it to the polycrystal. That is my first point.

People have quoted many things, the old testaments, their heroes, etc!. I will quote George Santayana who said that those who do not learn history will be condemned to repeat it. So let us be careful about not repeating history! Particularly from some theoretical physicists, I got the impression that they would like to apply some newly discovered mathematical formalisms to explain already explained phenomena. I am not stating this as a criticism but it is important that before going ahead with applying a theory or a model one should take stock of the state of the art. This point was made by Prof. Kumar and it is important. One way of achieving this is to organize a course or even write a text book. We have beautiful books on physics for engineers, physics for metallurgists etc. May be it is time to write a book on metallurgy for physicists!

Another aspect that I would like to point out is that in the important area of deformation and fracture behaviour of materials, we have reached a stage of understanding wherein we can now *a priori* design an alloy. This topic, *i.e.* the relationship between microstructure and mechanical properties of alloys has been completely left out from this Discussion Meeting. By microstructure I mean the substructure for example, the distribution of second phases, their morphology, the dislocation density etc. We find that the total dislocation density *per se* is not always the controlling factor, rather the way the dislocations are arranged, *i.e.* whether they are tangled or have a cell-structure. This topic has been completely overlooked. Of course it is obvious that all topics could not have been covered in a Discussion Meeting like this. But this argument shows that there is enough scope to have more frequent Meetings, focussing attention on such specific topics.

Prof. Joshi: Since there is a time restriction, I am afraid I have to interrupt and cut short this interesting Discussion!

I will sum up by saying that there is a need for future Discussion Meetings as well as a tutorial School. The duration, the periodicity, the organization, the themes—all these could be left open at the moment.

Being the last speaker permit me to express our grateful thanks to the Organizers of this unique Meeting. I would also like to express our special thanks to our hosts who have taken such good care of us. Finally, I wish to thank the panelists, those who participated from the floor, and the audience in general for making this discussion lively. Thank you all once again!

Bull. Mater. Sci., Vol. 6, No. 5, September 1984, pp. 837–899. © Printed in India.

Phase transformations—a physicist's perception

G VENKATARAMAN
Reactor Research Centre, Kalpakkam 603 102, India

Abstract. Echoing a recent remark by Prof. Ramaseshan, a perspective review is made of the field of phase transformation, highlighting areas that might appeal to physicists. Prominent in this category are the study of ground state structures, the study of phase diagrams and the study of kinetic phenomena.

Enumeration of ground state structures calls for inputs from group theory as well as reliable potentials, and physicists are therefore well equipped to make significant contributions. The theoretical analysis of phase diagrams (concerning which much experimental information already exists) raises challenging questions in equilibrium statistical mechanics. Since the problems map to Ising models of varying complexity and their generalizations, there are also very interesting connections to magnetism. Lately, computer simulation has added a new dimension, opening up fresh vistas both for theory and experiments. The study of kinetics belongs to the newly emerging area of non-equilibrium statistical mechanics. The focus being on *temporal* phenomena, physicists can play a key role, particularly through the application of various types of relaxation spectroscopy. On the theoretical side too there are challenging problems, especially on account of the dominance of nonlinearities. Indeed if one is bold enough, one could even speculate on possible universalities underlying the complex microstructures invariably seen in late-stage evolution. In short, though the subject of phase transformations has thus far been nursed predominantly by metallurgists, there is enough room for physicists to make an independent entry and to make distinctive contributions.

Keywords. Phase transformations; phase diagrams; spinodal decomposition; ordering kinetics.

1. Introduction

The theme of this paper relates to a remark made by Prof. Ramaseshan at the Baroda Seminar on Thrust Areas in Physics, and it is perhaps relevant to begin by outlining the background.

Around 1980, the Department of Science and Technology (DST) initiated an intensive exercise to identify Thrust Areas in various scientific disciplines. As a part of this, a Seminar was organized in Baroda during November 1981 to which were invited a cross-section of active physicists in the country. Although the ostensible purpose of the Seminar was to aid the DST in identifying areas which it could fund selectively, Dr. Ramanna who presided made the suggestion that since there was a rare gathering of physicists with diverse interests, the occasion should in fact be utilized to draw up something like a National Plan for Physics. A part of this Plan could then be funded by the DST, and the balance by other appropriate agencies. This suggestion was greeted with enthusiasm, and several exciting proposals were unveiled by those present. Intervening in the discussion, Prof. Ramaseshan remarked that while large projects in areas like gamma-ray astronomy or high-energy physics were no doubt to be commended and also needed, some thought should also be given to researchers in small

---

This paper was originally prepared for the 60th birthday volume of Prof. S Ramaseshan.

universities, most of whom remained outside the orbit of "big science". He went on to emphasize that in drawing up a list of Thrust Areas, consideration must also be given to subjects like phase transformations which not only offered challenge but also did not require massive funding and could therefore be pursued by those with modest resources. I was quite delighted by this suggestion and the specific reference to Phase Transformations since I had just then begun to gravitate towards the subject myself.

Now the subject of phase transformations is well established amongst metallurgists. Physicists, on the other hand, have generally stayed away possibly because it appeared messy to them. However, in the light of many recent developments in physics (*e.g.* advances in the understanding of nonlinear phenomena), some of these so-called messier aspects have acquired an attraction of their own. The main purpose of this article therefore is to draw the attention of physicists to such aspects, and hopefully induce at least some of them to enter this area. The paper is thus essentially a perspective review addressed to physicists, keeping in mind the needs of those who may be totally unfamiliar with the subject. However, in the spirit of Prof. Ramaseshan's remarks, interspersed are several suggestions for further work for those adventurous enough to enter the area.

2. Preliminaries

2.1 *Some elementary facts*

To most physicists, a phase transition usually calls to mind a change of state like solid to liquid etc. Metallurgists on the other hand, are interested mainly in transformations *within* the solid state. Of the many variations possible even in this category, we restrict attention to order-disorder transformations associated with compositional fluctuations. In the interest of simplicity, we shall further confine ourselves to binary alloys $A_{1-x}B_x$ $0 \leqslant x \leqslant 1$ (*e.g.* Al-Zn or Cu-Au).

To fix our ideas, let us consider a Cu-Zn alloy (β-brass) with equiatomic composition *i.e.* $x = 0{\cdot}5$. Both at high as well as at low temperatures, there is a well-defined lattice (*viz* bcc) associated with this alloy. However, there is a difference in the way the atoms are distributed amongst the lattice sites. Above 468°C, the occupancy of the lattice sites by Cu and Zn atoms is statistical whereas below that temperature, there is a well-defined order in the arrangement (see figure 1). One can intuitively see that entropy considerations must dominate at high temperatures leading to disorder. On the other hand, interatomic forces assert themselves at low temperatures leading to an ordered structure as in figure 1b. The temperature 468°C represents a transition point for the order-disorder process.

In the example just discussed, every atom has an atom of the other species as a nearest neighbour in the ordered state, implying that the potential v_{AB} dominates over v_{AA} and v_{BB}. It could also happen that v_{AB} is not strong enough to achieve this in which case a different type of ordering ensues wherein, the material organizes itself into large crystalline domains rich in either A or B type atoms. Essentially, "birds of a feather flock together", and the phenomenon is often called *phase separation* or clustering.

Superficially, phase separation and an order-disorder transition (like the one in β-brass) appear different but if we associate a wavelength scale with the two processes as is schematically done for a 1-D example in figure 2, then we can discuss the two in the same framework, as is done for ferro- and antiferromagnetism. Phase separation being

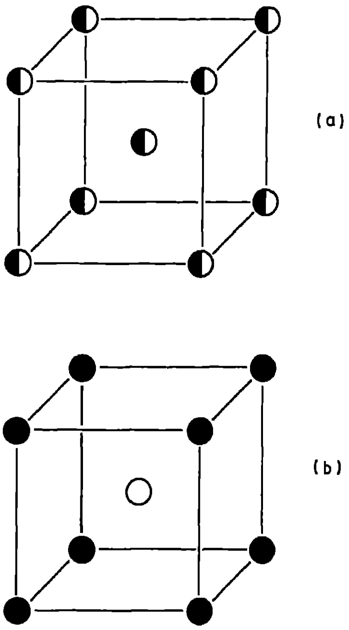

Figure 1. Schematic illustration of order-disorder in β-brass. The structure is bcc in both phases but in the disordered phase, the occupation of the lattice sites by the two species of atoms (shaded and full) is strictly statistical as in (a).

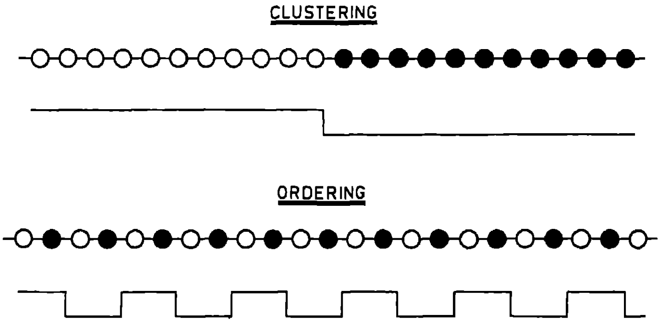

Figure 2. One-dimensional example to illustrate the different wavelength scales for clustering and ordering.

similar to ferromagnetic ordering will be associated with a wavevector $k \sim 0$ while order-disorder transition being similar to antiferromagnetism will be associated with a wavevector $k \sim$ zone boundary.

2.2 *Phase diagrams—a primer*

A study of phase transformations without some knowledge of phase diagrams is hardly possible. Most physicists are no doubt familiar with phase diagrams for monatomic systems but once one enters the world of multicomponent systems, phase diagrams can become quite complex, indeed even for binaries such as we shall be considering. A brief primer on phase diagrams is therefore useful.

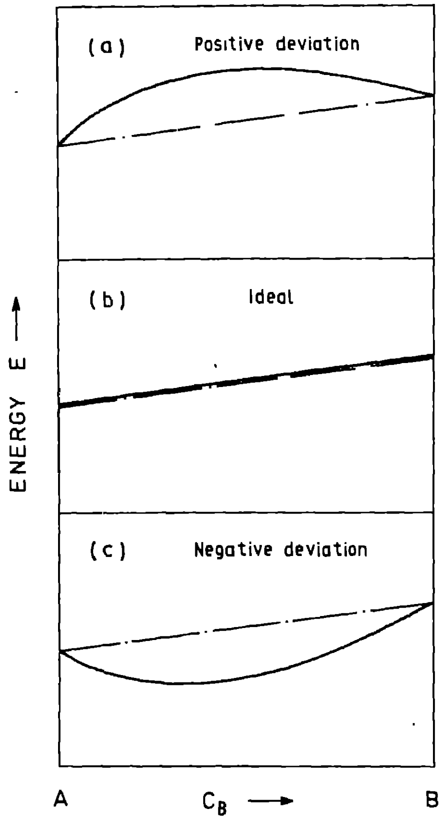

Figure 3. Schematic plot of energy as a function of composition for the three situations discussed in the text.

Broadly speaking, a phase is a state of aggregation. Our interest is in the various phases possible when two atomic species A and B are mixed together to form a solid at different temperatures and at different compositions. A phase diagram is therefore essentially a map of the various possible states of aggregation in the temperature-composition plane. From thermodynamics we know that the equilibrium state of a system is determined by the minimum of the free energy (FE) with respect to the appropriate thermodynamic variables. Accordingly, we direct attention now to the minimum of the FE at various temperatures and compositions. To start with we note that the free energy is given by

$$F = E - TS$$

where E is the internal energy*, T the temperature and S the entropy. In figure 3, E is plotted schematically as a function of composition (Wulff 1971). Here the dashed lines denote the energy before mixing and the solid lines that after the mixing. The 'ideal' situation is that shown in figure 3b where the energy does not change on mixing. More usually, one has either a positive or negative deviation from ideality as in figure 3a or c.

We next consider entropy, for which the situation prior to and after mixing will be as schematically depicted in figure 4. The results of the last two figures may now be

---

* Strictly speaking, we should have enthalpy $H(= E + pV)$ instead of E. However, most material processing is done around atmospheric pressure. From a practical point of view therefore H is well approximated by E.

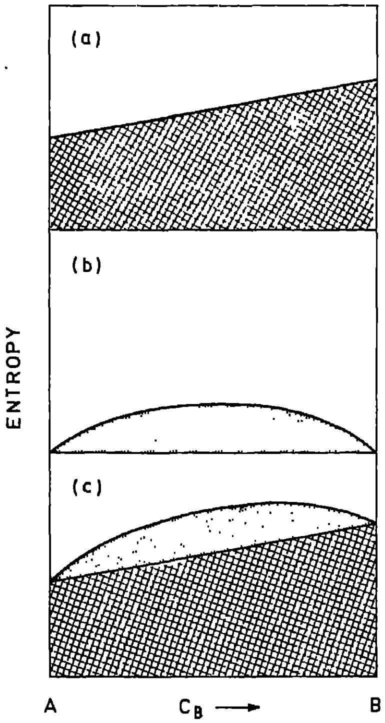

Figure 4. (a). entropy of the $A_{1-x}B_x$ system before mixing. (b). sketch of entropy of mixing. The total will then be as in (c).

combined to visualize how F varies with composition at a given T. Of the several possibilities, that corresponding to negative deviation from ideality is of particular interest to us and the free energy curve for this situation is sketched in figure 5. To find the most stable arrangement that results after mixing at the chosen temperature T we must obviously look for the minima in F. Using this criterion, it is clear from the figure that if we prepare a mixture of composition c_B, then this mixture will be unstable. It will seek stability by splitting into a mixture of two solutions of compositions c_B^1 and c_B^2. Observe that after such a separation, the F value diminishes from F_u to F_s.

The above scenario applies to all mixtures with composition in the range c_B^1 to c_B^2, and we conclude that for all compositions in this range, a *mixture of two phases* is the most stable state. This is the phase separation briefly mentioned earlier. When T is increased slightly, essentially a similar situation is obtained, with c_B^1 moving slightly away from the A end and c_B^2 moving slightly away from B. As T increases, c_B^1 and c_B^2 approach each other continuously, eventually merging at some temperature T_c. For $T > T_c$, segregation into two phases of different compositions no longer occurs; instead the solid solution itself is stable, and we have a one-phase region. Thus, the locus of c_B^1 and c_B^2 in the temperature-composition plane provides a boundary separating the one-phase and two-phase regions of the solid. Figure 6 shows a portion of the phase diagram of Al-Zn where such a two-phase region exists.

It is of course not necessary that when two atomic species are mixed, one should always get phase separation at low temperatures. Instead one could also obtain ordering, as *e.g.* in Cu-Au systems. We shall have more to say later about these two

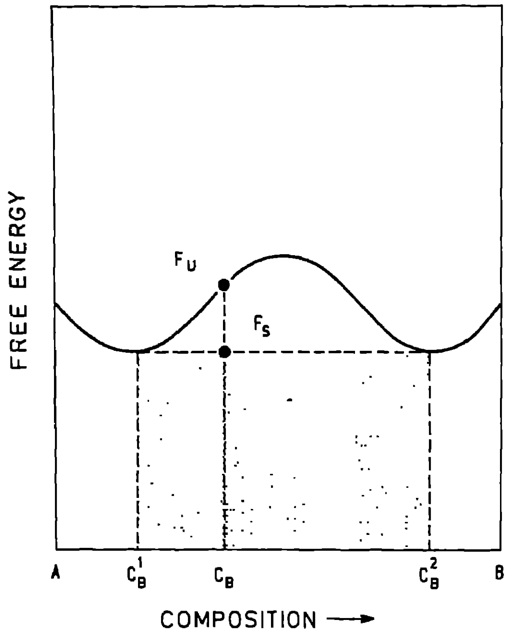

Figure 5. Free energy curve corresponding to a particular temperature for negative deviation from ideality. F_u is the value corresponding to the unstable state created immediately after mixing, while F_s is the value corresponding to the stable state. For every composition in the shaded region, the terminal state is a mixture of two phases of compositions c_B^1 and c_B^2.

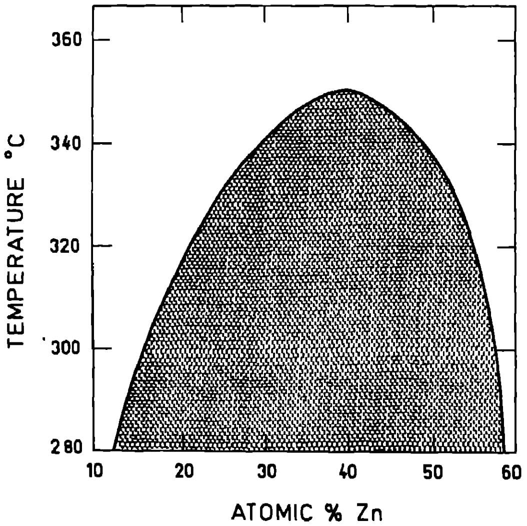

Figure 6. Portion of the Al-Zn phase diagram showing the two-phase region.

representative cases of phase separation and ordering.* For the nonce let us note that the solid mixtures we are considering are restricted to the substitutional type *i.e.* if we take a perfect *A* type solid and add *B* type atoms, the latter replace *A* at the lattice sites. For this to be possible, the following criteria must be broadly satisfied:

---

* Phase separation is *also* a type of ordering! Only the wavelength scale is different.

(i) The atomic radii of the two elements must be within 15% of each other. (ii) The crystal structures of *A* and *B* must be the same. (iii) The valence of *A* and *B* must not differ by more than unity. (iv) The electronegativity must be nearly equal.

While we have sketched the concept of the phase diagram from (elementary) theoretical considerations, we should remember that metallurgists often actually map phase diagrams by doing experiments. Indeed there is a wealth of such data (Hansen 1958), and, as we shall see later, a theoretical analysis of such diagrams is a possible avenue of interest for physicists.

2.3 *Areas of interest*

Given the fact that metallurgists have already contributed much to the subject, especially on the experimental side, it is natural to wonder whether there is any room for physicists (*e.g.* Chen *et al* (1979) point out that prior to the late sixties, there were at least 36 books and reviews on the subject. Also, there have been several major conferences held on the subject during the last decade). However, a careful appraisal does show that there are certain areas in this vast domain where physicists could bring to bear tools that are their specialities. Prominent among these areas are:

(i) The elucidation of ground state structures, (ii) Calculation of phase diagrams, and (iii) The study of kinetic phenomena.

Of the above, the calculation of phase diagrams belongs to the realm of equilibrium statistical mechanics, and, as we shall see in § 3, raises problems in the traditions of Onsager since one mainly deals with Ising models of various complexity. The study of kinetic phenomena on the other hand, takes one to the newly emerging area of nonequilibrium statistical mechanics. The presence of nonlinearities is an added attraction.

In terms of tools, apart from neutron and x-ray scattering which are already familiar, physicists could also exploit various types of relaxation spectroscopy. No doubt the scattering techniques have already been used to some extent in the past but there is considerable scope for enhancing their applications. Particularly in the case of x-rays, the recent availability of synchrotron radiation opens up many new exciting possibilities. Also, there are many technical innovations like position-sensitive detectors that have hardly been used for such studies. As far as relaxation spectroscopic studies are concerned, the field is literally wide open. Complementing all these is the powerful technique of computer simulation, used already to some extent, but admitting of considerably more exploitation. In short, there is plenty of scope for physicists to make a distinctive contribution of their own to the field, although they may be latecomers.

3. Equilibrium structures

3.1 *Ground state structures*

Given a disordered structure (say belonging to the fcc lattice), there arises the general question of the type of ordering that will occur at lower temperatures. In a simple situation as in β-brass (see figure 1), one could perhaps have made a good guess of the ordered structure purely from inspection. However, such guesses are not always easy, requiring, as they do, considerable crystallographic insight. A systematic approach to enumerating the possible ordered structures has been evolved by Soviet scientists, inspired largely by Landau's theory of phase transitions.

Before sketching the work of the Soviet School, we note first that the ground state structure is the atomic arrangement assumed by the solid at absolute zero of temperature. While it is the onus of theory to predict this structure fro.n first principles, a considerable body of information about the structures actually occurring in Nature has already been accumulated through diffraction experiments. Next we remark that ordering is essentially characterized by the appearance of a superlattice. The superlattice structure that emerges depends on (i) the structure of the parent lattice, (ii) the interatomic forces, and (iii) the atomic composition of the system. If, for example, we consider the fcc lattice, then several ordered structures based on it are possible some of which are illustrated in figure 7. The distribution of the various superlattices possible amongst the alloys realizable by combining various elements in the periodic table have been painstakingly compiled by Kozlov *et al* (1974) and the data is worth glancing through.

Returning to the enumeration of possible superlattice structures, the basic idea is the following: Let us first describe the atomic distribution by means of a function $n(\mathbf{r})$ which gives the probability of finding an atom of some definite kind at site $\mathbf{r}$ of the lattice. In a disordered alloy $n(\mathbf{r})$ is a constant c. On the other hand, when the system orders, $n(\mathbf{r})$ assumes m (say) different values $n_1, n_2, \ldots, n_m$ at the m sublattices are associated with the structure. In brass, *e.g.*, $m = 2$. Of course, $n(\mathbf{r})$ corresponding to a particular sublattice position has the same value in all the unit cells. The problem now is to determine the possible distribution $n(\mathbf{r})$ can have when ordering occurs. Khachaturyan (1974) approaches this by regarding $n(\mathbf{r})$ as being built up of *static* composition waves as follows:

$$n(\mathbf{r}) = C + \frac{1}{2}\sum_{\mathbf{k}} \{Q(\mathbf{k}) \exp(i\mathbf{k}\cdot\mathbf{r}) + \mathrm{C.C}\}. \tag{1}$$

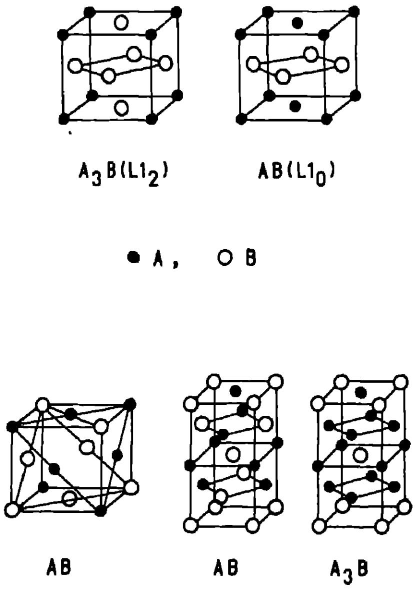

Figure 7. Some of the ordered structures observed in fcc lattices.

Here the summation over **k** runs over the first Brillouin zone of the disordered alloy. $Q(\mathbf{k})$ is the (complex) amplitude of the concentration wave of wavevector **k**. Following Landau, one now writes the sum over **k** as sums over various possible stars one can form in the Brillouin zone (see figure 8). With this regrouping,

$$n(\mathbf{r}) = C + \sum_s \eta_s \varepsilon_s(\mathbf{r}), \tag{2}$$

where

$$\varepsilon_s(\mathbf{r}) = \frac{1}{2}\sum_i \{\gamma_s(\mathbf{k}_i(\star s)) \exp i\, \mathbf{k}_i(\star s)\cdot \mathbf{r} + \text{C.C.}\}. \tag{3}$$

In (3), the summation runs over all the members i of the star s whereas in (2) the sum is over all the possible stars. Together, all the wavevectors in the Brillouin zone are accounted for. Comparing with (1)

$$Q(\mathbf{k}_i) = \eta_s \gamma_s(\mathbf{k}_i). \tag{4}$$

The quantities η_s are the long-range parameters which assume the value 0 in the disordered state, and the value 1 at 0°K. Since composition is conserved, the number of order parameters required to describe the ordered structure will be $(m-1)$. Later (in § 3.3) we shall see that the order parameters η_s are essentially the analogues of sublattice magnetizations.

Although formally the summation in (2) ranges over all the stars in the Brillouin zone, in practice (—and this is in the spirit of Landau's theory of phase transition) one

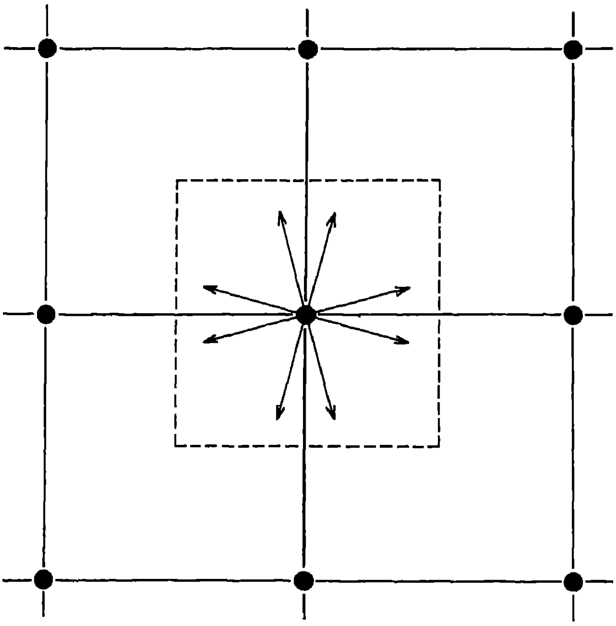

Figure 8. Illustration of the concept of star of the wavevector for a square lattice. The dots indicate the reciprocal lattice points, and the dashed line the central Brillouin Zone. The cluster of eight arrows represents a star. Starting from any one of these arrows, one can generate the entire cluster by a systematic application of the point group operations of the lattice.

supposes that a given ordering is associated uniquely with composition waves corresponding to a particular star. For illustration, let us consider ordering in Cu-Au alloys. X-ray experiments have revealed that ordering is linked to the appearance of superlattice {100} reflections (which, of course, are forbidden in the disordered state). It is reasonable therefore to suppose that the ordering is governed by the star of the wavevector [100] which comprises of the wavevectors [100], [010] and [001]. Thus (2) can be written as

$$n(\mathbf{r}) = C+\eta\{\gamma_1 \exp(i\mathbf{k}_1\cdot\mathbf{r})+\gamma_2 \exp(i\mathbf{k}_2\cdot\mathbf{r})+\gamma_3 \exp(i\mathbf{k}_3\cdot\mathbf{r})\}. \qquad (5)$$

where $\mathbf{k}_1$, $\mathbf{k}_2$ and $\mathbf{k}_3$ are the three wavevectors of the star. The lattice vector $\mathbf{r}$ can be expressed in terms of the (cubic) unit cell vectors $\mathbf{a}_1$, $\mathbf{a}_2$, $\mathbf{a}_3$ as

$$\mathbf{r} = x\mathbf{a}_1+y\mathbf{a}_2+z\mathbf{a}_3 \qquad (6)$$

with $(x+y+z)$ = constant. By letting $\mathbf{r}$ vary in (5), it is easily seen that $n(\mathbf{r})$ can take the following values

$$\begin{aligned} n_1 &= C+\eta(\gamma_1+\gamma_2+\gamma_3); & n_2 &= C+\eta(\gamma_1-\gamma_2-\gamma_3);\\ n_3 &= C+\eta(-\gamma_1+\gamma_2-\gamma_3); & n_4 &= C+\eta(-\gamma_1-\gamma_2+\gamma_3). \end{aligned} \qquad (7)$$

If now we invoke the fact that $(m-1)$ equals the number of distinct order parameters and remember that in this case there is only one order parameter, namely η, we are led to the fact that $m = 2$ for Cu-Au. Hence n can take only two values at the set of all sites (xyz) of the fcc lattice, leading to the two possibilities

$$\text{(i) } n_1 = n_4,\ n_2 = n_3; \quad \text{(ii) } n_2 = n_3 = (n_1+n_4). \qquad (8)$$

The first alternative arises if $\gamma_1 = \gamma_2 = 0$ whence

$$n(xyz) = C+\eta\gamma_3 \exp(2\pi i z) = C\pm\eta\gamma \qquad (9)$$

in alternate (001) planes. This is the so-called CuAu I structure. On the other hand, if alternative (ii) is to be realized, then we must have all the γ_i's equal whence

$$\begin{aligned} n(xyz) &= C+\eta\gamma\{\exp(2\pi i x)+\exp(2\pi i y)+\exp(2\pi i z)\}\\ &= \begin{cases} C+3\eta\gamma & \text{at the corners of the unit cell cube}\\ C-3\eta\gamma & \text{at the face centres.}\end{cases} \end{aligned} \qquad (10)$$

This is the Cu_3Au structure.

The above example shows how symmetry considerations may be applied a la Landau's theory to obtain some idea of the superlattice structures possible. Merely enumerating possible superlattice structures alone is not enough. This is somewhat similar to the exercise often done for ferroelectrics, where one uses group theory to enumerate the type of ordered structures that can arise. Symmetry thus picks out the various possibilities; which of these is actually favoured depends of course on the interatomic forces. To illustrate, we once again consider the fcc lattice, and direct attention now to the internal energy. The three potentials to be considered are, $v_{AA}(r)$, $v_{BB}(r)$ and $v_{AB}(r)$. In terms of these pair potentials, the internal energy E may be expressed as

$$\mathscr{E} = \frac{1}{2}\sum_{ij}\sum_{l\neq m} v_{ij}(l-m)\langle\sigma_i(l)\sigma_j(m)\rangle. \qquad (11)$$

Here i, j refer to the species A, B while l and m denote lattice sites. The quantity σ is an occupation operator defined by

$$\begin{aligned}\sigma_A(l) &= 1 \quad \text{if site } l \text{ is occupied by an A-type atom}\\ &= 0 \quad \text{if site } l \text{ is not occupied by an A-type atom.}\end{aligned} \tag{12}$$

$\sigma_B(l)$ is defined similarly. The bracket denotes an average (here over the ground state). The lattice energy will evidently be determined by the correlations of the σ's at the various sites, and the system will choose that atomic configuration for which $\mathscr{E}$ is a minimum.

It is convenient to introduce an operator $\gamma_i(l)$ which describes deviations from mean occupation by

$$\gamma_A(l) = \sigma_A(l) - c_A = \begin{cases} 1-c_A \\ -c_A \end{cases}; \tag{13}$$

where c_A is the concentration of A. Since $c_A + c_B = 1$, one has

$$\gamma_B(l) = -\gamma_A(l). \tag{14}$$

Using the γ's, the part of the internal energy that relates to occupation deviations can be written as

$$E = \frac{1}{2}\sum_{ij}\sum_{l \neq m} v_{ij}(l-m)\langle \gamma_i(l)\gamma_j(m)\rangle. \tag{15}$$

By elementary manipulation, this can be written as

$$E = \frac{1}{2}\sum_{lm} V(l-m)\langle \gamma(l)\gamma(m)\rangle, \tag{16}$$

where we have written γ for γ_A, and V is an effective potential defined by

$$V(\mathbf{r}) = 2v_{AB}(\mathbf{r}) - v_{AA}(\mathbf{r}) - v_{BB}(\mathbf{r}). \tag{17}$$

In terms of Fourier transforms

$$E = \frac{N}{2}\sum_{\mathbf{k}} V(\mathbf{k})|\Gamma(\mathbf{k})|^2 \tag{18}$$

where $\Gamma(\mathbf{k})$ is the transform of $\gamma(\mathbf{r})$.

The quantity $V(\mathbf{k})$ is periodic in reciprocal space reminiscent of, say, phonon dispersion curves, and will therefore have maxima, minima and saddle points (—the well-known van Hove (1953) singularities). The expectation now is that the state of order is governed primarily by where minima in $V(\mathbf{k})$ occur. One knows that barring unusual circumstances, minima of lattice periodic functions occur at points of high symmetry in the Brillouin zone (van Hove 1953). Thus, ordering is mainly associated with the build up of a compositional wave (also sometimes called concentration wave) with a wavevector corresponding to the special point where $V(\mathbf{k})$ has a minimum. This therefore is also the wavevector at which a superlattice reflection is seen in the diffraction pattern when ordering occurs. As may be expected, around the transition temperature there are critical fluctuations of the composition in this region of $\mathbf{k}$-space and consequently there is an enhancement of the scattering in the superlattice reflection region just prior to ordering. We shall say more about critical scattering later.

The potential $V(\mathbf{r})$ depends on the details of the electronic structure, and is often not known with sufficient accuracy for present purposes. It is therefore customary to parametrize pair interactions in terms of interactions up to a specified set of neighbours. One now examines minima in $V(\mathbf{k})$ as the ratio (V_2/V_1) is varied (where V_1 and V_2 denote the first and second neighbour interactions). The results can be succinctly paraphrased as in figure 9 due to Clapp and Moss (1968) who followed Villain (1959) who had earlier made such plots for magnetic structures. Incidentally, we see from figure 9 that in a certain range of ratios, ordering occurs for $k = 0$ leading to clustering of like atoms.

Mention should also be made of the work of Richards and Cahn (1971) and various Japanese workers (Katsura and Narita 1973; Kudo and Katsura 1976; Kanamori and Kakehashi 1977) who have studied ground-state structures using a real-space analysis. Recently some rigorous methods for describing low temperature structures of very general lattice systems have also been developed (Progov and Sinai 1975, 1976; Holsztynski and Slawny 1978; Slawny 1979).

Although some territory has no doubt been covered in the work of the various above mentioned authors, there is considerable scope for further work. One might wonder whether ground-state structures are not encompassed in a study of the phase diagram as a whole (§ 3.2). Indeed they are; however an independent knowledge of ground state structures does help phase diagram calculations and in that sense is a worthwhile, stand-alone activity.

Before leaving the subject, a brief reference must be made to off-stoichiometric structures. Suppose, for instance, we consider an alloy where, say, the concentration of A species is slightly less than 0·5. The question now is what happens in the ordered state. One's first guess would be that small deviations from stoichiometry would be absorbed as defects. However, when the deviations are substantial, the situation may not be that

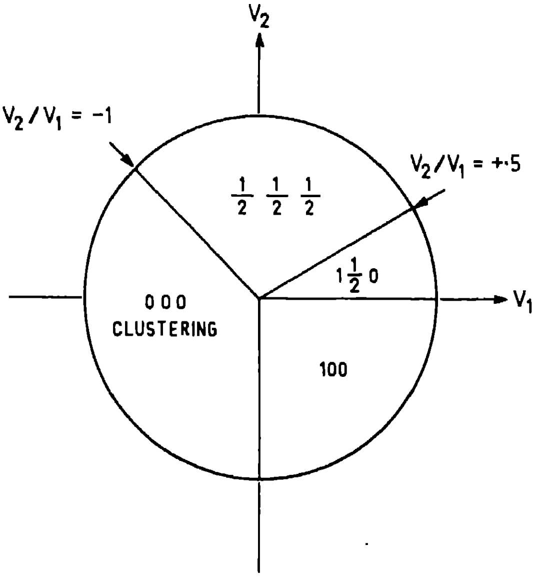

Figure 9. Location of minima of $V(k)$ as a function of the ratio V_2/V_1 for the fcc lattice. (After Clapp and Moss 1968).

simple. Krivoglaz and Smirnov (1965) suggested that at 0°K, an off-stoichiometric alloy decomposes into alloy of stoichiometric composition and a pure metal. It is not clear whether there is any experimental evidence in support of this suggestion. Kozlov *et al* (1974) have advanced the alternate idea that the excess atoms may undergo further ordering at suitable sites, leading to a new complex structure which they refer to as 'super-superstructure'. The experimental situation if assessed from the literature, can be quite bewildering to a physicist! When an alloy is prepared at high temperatures and cooled below the transition, it not only orders but develops a lot of microstructure; one has therefore to be quite careful in drawing the right conclusions.

One case worth mentioning explicitly is CuAu (nominal equiatomic composition). When this alloy is cooled from high temperatures, it transforms below 385°C into what is called the CuAu II structure illustrated in figure 10 (Ogawa 1974). There is an alternation every five cells, and the overall structure can be thought of as composed of antiphase domains of size $5b$. The oscillations are also referred to as long period oscillations (LPO). Such oscillations are reported for many ground state structures, and, in view of the extensive interest amongst physicists on charge density waves etc. are worth a close look (see also § 4.5). Returning to LPO's in Cu-Au alloys, there is evidence that the period $2M$ is not always an integral number (see figure 11) (Ogawa 1974). Noteworthy here is the fact that M varies with composition (which effectively alters the electron/atom ratio). There is also a lattice modulation of density related to the LPO. This, as well as the nonintegral values observed for M are interesting questions (Sato and Toth 1961) but unfortunately we cannot pursue them further here.

Another comment that needs to be made concerns the effective potential $V(r)$ in (17). Now an implicit assumption underlying (15) is that all ions always exactly occupy the lattice sites. In practice this is not so, and ions could deviate, *e.g.* on account of size. One must therefore allow for such 'positional relaxation', and evaluate the energy of the relaxed system. In effect, it amounts to modifying $V(k)$ as

$$V(k) \rightarrow V^{(1)}(k) = V(k) - \text{relaxation energy}. \qquad (19)$$

Of course if the potential is parametrised, then the parameters refer actually to the effective potential $V^{(1)}$. For further details concerning the relaxation energy, a recent article by de Fontaine (1979) may be consulted.

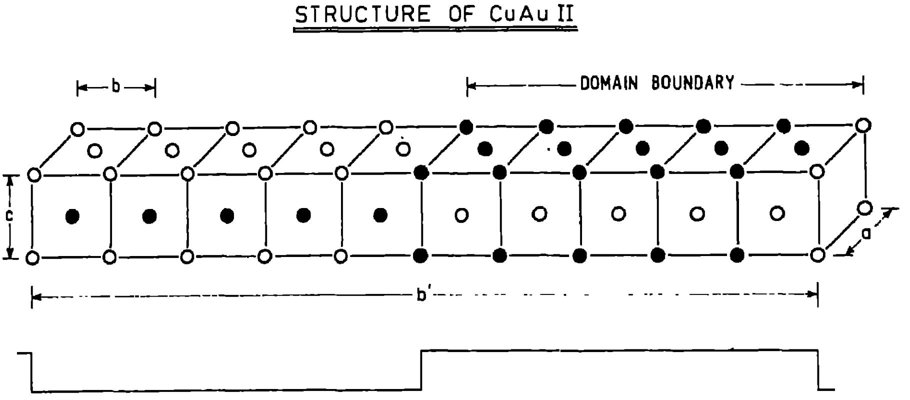

Figure 10. Illustration of the long-period oscillation in CuAu II. After every five cells, there is an alternation in the occupancy pattern (after Ogawa 1974).

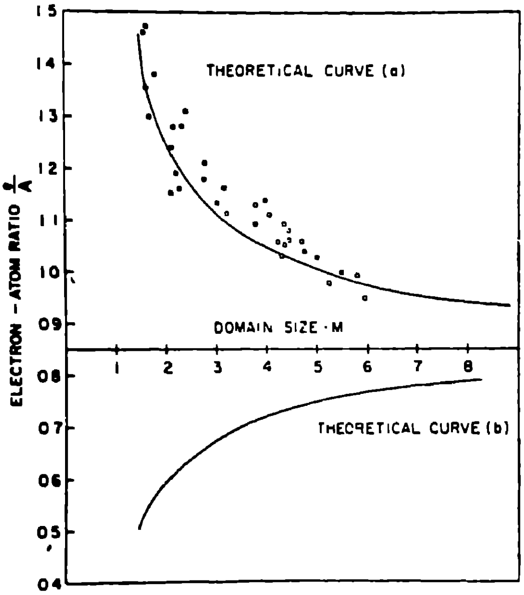

Figure 11. Variation of M with electron to atom ratio. The solid lines are theoretical curves (due to Sato and Toth 1961) corresponding to two assumptions (after Ogawa 1974).

3.2 *Calculation of phase diagrams*

The phase diagram problem is a logical extension of the ground state problem in that one now studies when order disappears.

It is convenient to discuss the problem in the language of Ising spins rather than in terms of the occupation operators σ introduced earlier. The Ising spin operator S_l associated to lattice site l is defined in terms of $\sigma_B(l)$ as

$$S_l = 1 - 2\sigma_B(l) = \begin{cases} +1 & \text{if site } l \text{ is occupied by an } A \text{ atom} \\ -1 & \text{if site } l \text{ is occupied by a } B \text{ atom.} \end{cases} \tag{20}$$

Observe that in terms of $\sigma_A(l)$,

$$S_l = 1 + 2\sigma_A(l). \tag{21}$$

Using the Ising spins to describe the Hamiltonian, the statistical mechanics of order-disorder can now be mapped into an appropriate Ising problem, establishing links with the rich traditions that already exist in this area.

Now at absolute zero of temperature, the spin system will be perfectly ordered. As the temperature is raised, some spins will flip (meaning A and B atoms will exchange places). Such flips no doubt cost energy but the entropy term $-TS$ in the expression for free energy provides the required compensation. However, the disorder cannot be increased indefinitely, and at every temperature there is an optimum disorder. If the disorder exceeds the optimum, then F increases due to increase of E whereas if it is less, then it again increases but due to inadequate cancellation from the entropy term. Equilibrium is thus dictated by the minimum of the free energy, and in the calculation of the phase boundaries, the computation of this minimum is an important step.

Given the range of interaction of the Ising spins, the calculation of E is straightforward (and is discussed further in § 3.3). Far more problematical is the entropy term, and to appreciate the difficulty let us consider a 1-D Ising chain. We assume first that the chain is fully ordered (!) with all spins up (say). The entropy is then zero. At the other extreme where each spin is completely free to flip, there are 2^N configurations possible (N is the number of spins), and the corresponding entropy is $S = k_B \log 2^N = Nk_B \log 2$. The question is how does one calculate the entropy for situations in between where there is intermediate order. If, for example, we *definitely* know two spins alone are down and all the rest up then the number of configurations possible is a simple matter to work out. But unfortunately, we cannot make definitive statements about exactly how many spins are up and how many are down. We can at best have only statistical information about the state of order embodied in the correlation functions

$$\xi_1 = \langle S_l \rangle; \quad \xi_2 = \langle S_l S_m \rangle; \quad \xi_3 = \langle S_l S_m S_n \rangle \ldots \tag{22}$$

The set $\{\xi_l\}$ must first be known and using it the entropy and indeed F itself must then be computed. Calculation of S in terms of the ξ's is precisely where problems enter, for one must in principle know and use all correlation functions up to ξ_N. This evidently is also the place for approximations to make their entry!

Before discussing the approximations, we call attention to Onsager's (1944) famous paper on the 2-D square lattice Ising problem where he calculated the partition function exactly. This is not only a *tour de force* but also a touchstone for evaluating various approximation schemes (as we shall soon see).

The approximation schemes alluded to, reduce in effect to using a suitable subset of the full set $\{\xi_l\}$ of the correlation functions. The subset is so chosen that the group of spins involved form a cluster which is consistent both with the geometry of the lattice and the range of interactions (usually restricted to near neighbours (*nn*) and next nearest neighbours (*nnn*)).

Figure 12 gives samples of some clusters used in the study of ordering in fcc Ising lattices. In figure 12a the cluster is a regular tetrahedron made up of *nn* spins. In figure 12b one has a *nn* regular tetrahedron and an octahedron consisting of *nn* and *nnn* spins. Within a cluster itself one can identify subclusters *e.g.* the triangle (123) in figure 12b, which is in the overlap of the tetrahedron and the octahedron. Likewise, the triangle (126) in figure 12c is a subcluster shared by two irregular tetrahedra.

The entire computational scheme based on cluster approximation is known as the cluster variation method (CVM). As formally developed by Morita (1972), it is based on the exact variational principle of equilibrium statistical mechanics. In any given implementation of the CVM, one first chooses the largest cluster L one is going to work with. One then considers all the subclusters l consistent with L. Corresponding to each subcluster l, one now considers the various possible arrangement of spins/atoms. For instance, the arrangement in the triangle (123) could be (AAA), (ABA), (BAB) etc. If J_l denotes a configuration such as above, then we next need to know $x_{J_l}(l)$ the concentration of this configuration in the cluster l. It is in the calculation of the cluster configuration that the correlation functions enter. To illustrate, we again consider the triangular subcluster (123). Let p_1, p_2 and p_3 denote the lattice sites. The correlation functions we then need are the single spin, two spin and three spin functions ξ_1, ξ_2, ξ_3

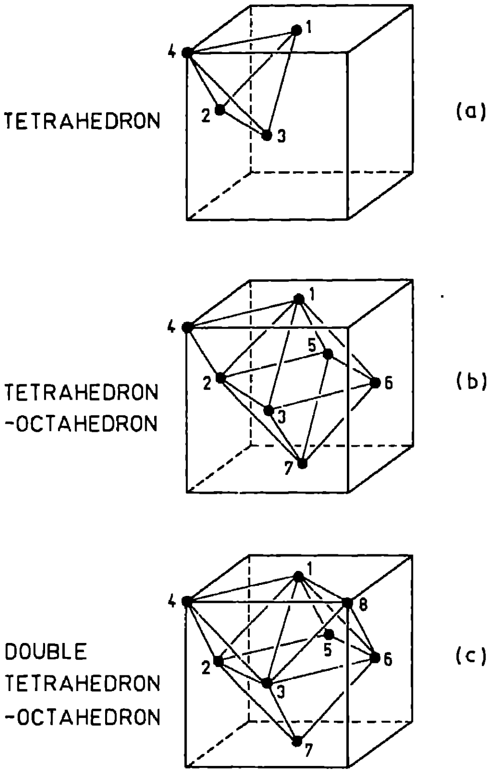

Figure 12. Some of the clusters used in CVM calculations for fcc lattices (**a**). tetrahedron used by Kikuchi *et al* 1980 (**b**) and (**c**) are larger clusters used by Sanchez and de Fontaine (1978, 1980, 1982).

respectively. In terms of these correlation functions, x_{AAB}, for example will be

$$x_{AAB} = \tfrac{1}{8}\{1+(+1+1-1)\xi_1+[(1\times 1)+(1\times -1)+(-1\times 1)]\xi_2 + (1\times 1\times -1)\xi_3\}. \tag{23}$$

The formal expressions for the cluster probabilities are:

$$\begin{aligned} x_i(p_1) &= \langle \sigma_i(p_1)\rangle = \tfrac{1}{2}\langle 1+iS_{p_1}\rangle, \\ x_{ij}(p_1p_2) &= \langle \sigma_i(p_1)\sigma_j(p_2)\rangle \\ &= \frac{1}{2^2}[1+i\langle S_{p_1}\rangle + j\langle S_{p_2}\rangle + ij\langle S_{p_1}S_{p_2}\rangle], \\ x_{ijk}(p_1p_2p_3) &= \langle \sigma_i(p_1)\sigma_j(p_2)\sigma_k(p_3)\rangle \\ &= \frac{1}{2^3}[1+i\langle S_{p_1}\rangle + j\langle S_{p_2}\rangle + k\langle S_{p_3}\rangle + ij\langle S_{p_1}S_{p_2}\rangle \\ &\quad + jk\langle S_{p_2}S_{p_3}\rangle \\ &\quad + ki\langle S_{p_3}S_{p_1}\rangle + ijk\langle S_{p_1}S_{p_2}S_{p_3}\rangle]\text{etc.} \end{aligned} \tag{24}$$

Here $i, j, k \ldots$ take on values ± 1 for each of the two components in the system. (Result (23) thus readily follows from above).

The entropy can now be expressed as a series in cluster probabilities as

$$S \approx Nk_B \sum_{l=1}^{L} \gamma_l \sum_{J_l} x_{J_l}(l) \log x_{J_l}(l) \tag{25}$$

where γ_l is an appropriate coefficient (Barker 1953). Once the clusters have been identified and their concentrations or probabilities evaluated, the rest is largely numerical, and will be described shortly.

Historically, one of the early attempts at explaining the order-disorder transformations is due to Bragg and Williams (1934, 1935). Domb (1981) narrates an interesting story concerning these famous papers. Apparently, Bragg gave a seminar in 1933 in Manchester during which he qualitatively described his thoughts on how ordering occurred in binary alloys. Williams, a member of the audience, presented Bragg with a mathematical outline of Bragg's theory at the end of the lecture. (The story of the Rushbrook inequalities is similar! See Stanley 1971). Bragg was impressed but felt that the calculation was so simple, it surely must have been published earlier. However, no such paper had yet appeared and so Bragg and Williams proceeded to publish their ideas!

In the CVM language, the Bragg-Williams theory retains only ξ_1 or point clusters. Next comes the Bethe approximation (1935) which includes pairs *i.e.* also ξ_2. From these early beginnings, the push has always been towards larger clusters. Modern applications of the CVM have been promoted largely by de Fontaine and coworkers, building upon schemes originally developed by Kikuchi (1951), Barker (1953) and van Baal (1973). Before describing some of these recent results, we refer to figure 13 which gives a feel for the improvements available in going to larger clusters in 2-D square lattice, where Onsager's exact result is available as a bench mark.

Turning now to phase diagrams calculations for real alloys, the main steps in the calculational schemes as implemented at present are as follows (de Fontaine 1982):

(i) Choose the basic lattice system, the range of interactions and the largest cluster to be used. Form then the ξ's.

(ii) Construct the thermodynamic potential Ω (also called the grand potential) defined by

$$\Omega = F - \tfrac{1}{2}(\mu_A - \mu_B)\sum_l S_l \tag{26}$$

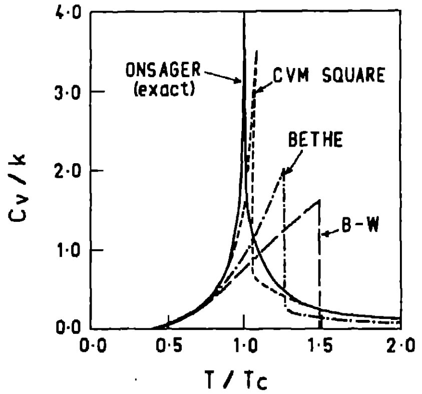

Figure 13. Specific heat variation for the square-Ising lattice. Onsager's result is the exact one. Observe the improvement in going from the Bragg-Williams approximation to the CVM square cluster approximation.

where the μ's are the chemical potentials of the two atomic species. The chemical potential term is required since we would like to permit concentration C_B to vary (while the total number of atoms is fixed).

(iii) For a fixed (T, $\mu \equiv 1/2(\mu_A - \mu_B)$), minimize Ω with respect to the ξ's considered *i.e.* the set of ξ's consistent with the largest cluster L chosen.

(iv) When Ω is minimized, it leads to a set of (nonlinear algebraic) equations for the ξ's. Solve these equations.

(v) Use the ξ's obtained in step (iv) to compute the equilibrium potential Ω_{eqbr}.

(vi) Plot Ω_{eqbr} *vs* T for fixed values of μ for the different phases. The point (T, μ) at which two curves cross is a point of phase coexistence. An example is given in figure 14.

(vii) Vary T and μ and establish the locus of phase coexistence *i.e.* the phase boundaries.

(viii) Every intersection between the Ω curves for two phases, α and β, say, gives two values of the point correlation function ξ_1. From these, determine the average concentrations c_B^α and c_B^β.

(ix) Assemble the results into phase diagrams in the (T, μ) and (T, c) planes.

Following Iliopoulos (1980), one might also add:

(x) Publish your result,

(xi) Choose another alloy system and GO TO (i)!

The CVM has been extensively applied by Kikuchi, de Fontaine and coworkers, from whose contributions we will now cite a few examples. Firstly in table 1 (de Fontaine 1979) we summarize some results obtained for Ising ferromagnets (which, incidentally, are isomorphous to AB binary solutions; recall earlier remarks about the correspondence between magnetic systems and alloy systems).

Next we consider results for ordering. Kikuchi *et al* (1980) have obtained the phase diagram for the Cu-Au system using *nn* interactions for the Ising spins, and a tetrahedron cluster. The calculated phase diagram is shown in figure 15b which is to be

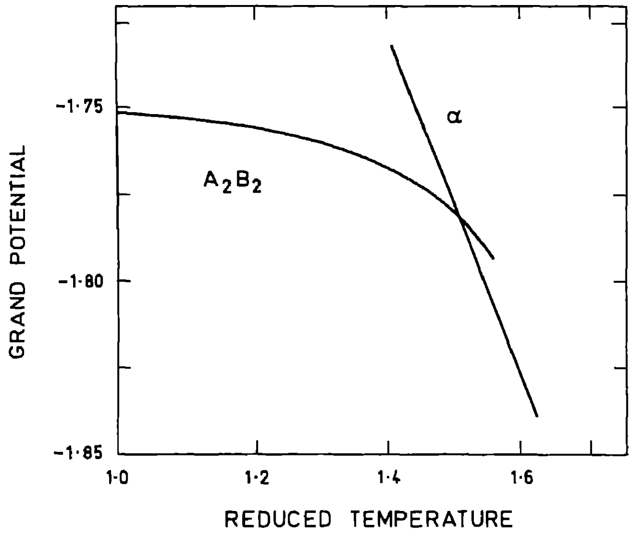

Figure 14. Variation of the grand potential with temperature for the A_2B_2 and disordered (α) phases, for zero chemical potential ($c_B = 0{\cdot}5$). The intersection gives the temperature value at which the two phases coexist. (after de Fontaine 1982).

Table 1. Calculated normalized transition temperature in units of k_BT/zJ where J is the strength of the nearest neighbour interactions and z the number of nearest neighbours (after de Fontaine 1979).

	2D Square lattice	2D Triangular lattice	3D Simple cubic	Remarks
z	4	6	6	
Bragg-Williams (point)	1·0	1·0	1·0	all refer to transition temperatures
CV Bethe (pair)	0·7212	0·8222	0·8222	
CV square or triangle	0·6057	0·62525	0·7683	
CV cube or tetrahedron	—	—	0·7628	
Exact (or best known)	0·567	0·6062	0·7522	

compared with the experimentally determined one (figure 15c) and that calculated by Shockley (1938) using the Bragg-Williams approximation (figure 15a). While those not used to phase diagrams may regard the agreement between CVM and experiment fair, the comparison is actually quite impressive given the approximations involved.

Sanchez and de Fontaine (1978) have gone beyond the tetrahedral approximation to the clusters illustrated in figure 12b and c, and investigated (Sanchez and de Fontaine 1980, 1982) the phase diagram for the ⟨1½0⟩ family of ordered superstructure *i.e.* lattices where ordering is associated with a ⟨1 ½ 0⟩ compositional wave. In addition to the usually considered *nn* interactions, the *nnn* interactions were also included. Results have been obtained for a range of values of the ratio of second-to-first-neighbour pair interactions in the range 0 to 0·5. The results are relevant for ordering in diverse systems like Ni-Mo, Ni-V etc. Incidentally, a knowledge of the ground state structure is very helpful in testing out a particular ordered state as in figure 14.

These calculations by de Fontaine and coworkers have shown the distinct superiority of the CVM over earlier models in yielding realistic results. For instance, in Cu-Au systems, the Bragg-Williams approximation predicts a first-order transition for Cu_3Au ($L1_2$ ordering) and a second-order transition for CuAuI ($L1_0$ ordering), whereas experimentally the transition is of first order for both the stoichiometric compositions. The Bethe approximation is even worse, and predicts no transition at all. The CVM does much better and predicts correctly a first order transition for both. The main advantage of the CVM is that reasonably accurate results are obtained without too much computational effort (—much of this has no doubt been due to the exercise of ingenuity in arriving at the practical computational scheme). In the results reported thus far, about 30 to 70 nonlinear algebraic equations had to be solved but it was not taxing. However, numerical difficulties were found at low temperatures where some of the cluster probabilities tended exponentially to zero. Where transition temperatures are concerned, the CVM does a respectable job, judging from the 3-D cubic Ising ferromagnet for which independent, reliable results are available from high-temperature expansion methods (table 1). But where exponents are concerned, CVM predicts only classical ones for higher-order transitions. This is not unexpected since the method is built around equilibrium correlation functions and does not include fluctuations. It is perhaps not out of place here to mention that Mahan and Claro (1977) have used the real-space renormalization-group approach to calculate a CuAu-type

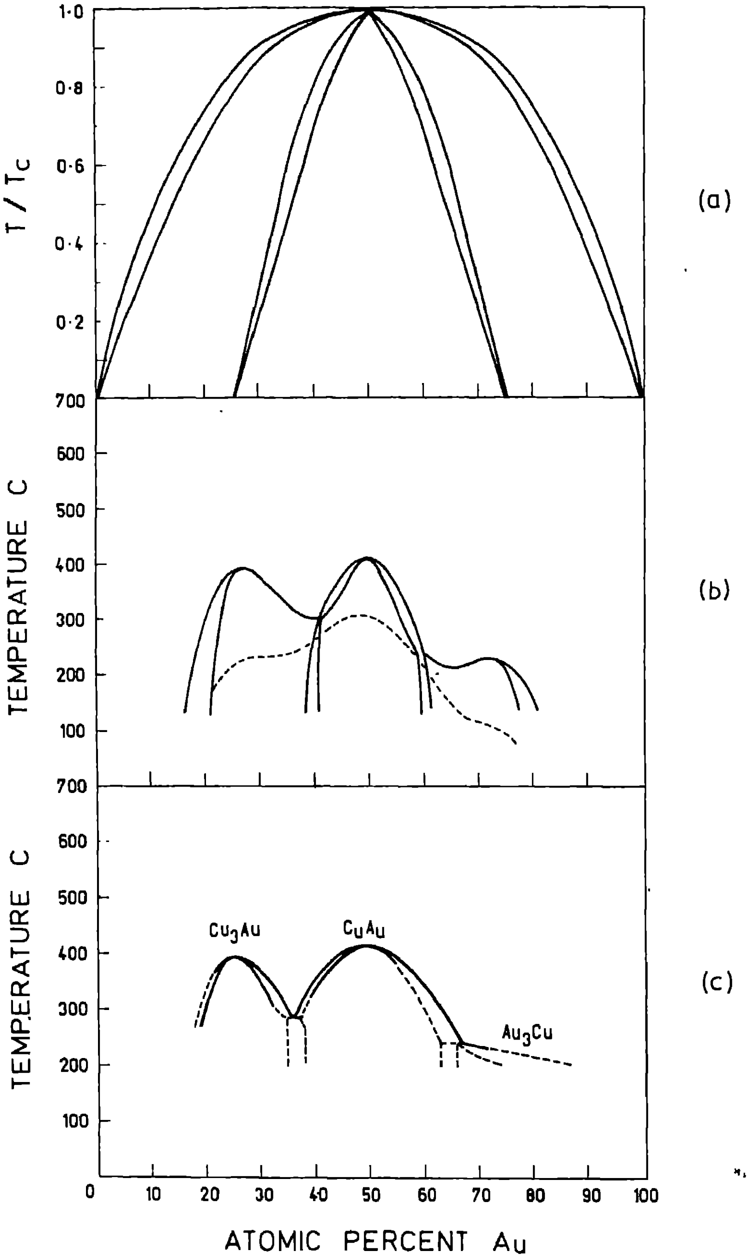

Figure 15. Phase diagram for the Cu-Au system (a). results obtained by Shockley (1938). (b). shows the CVM results of Kikuchi *et al* (1980). For comparison, the experimental results are given in (c) (Hansen 1958).

phase diagram. The results are however poor in that the ordering of CuAu ($L1_0$ ordering) is not predicted and the ordering of Cu_3Au ($L1_2$ ordering) is predicted to be of second order.

The stage is now set to consider a totally different approach to the calculation of phase diagrams *viz.*, that of computer simulation.

3.3 *Phase diagrams and computer simulation*

As in several other branches of physics, computer simulation has proved extremely useful in unveiling various subtle aspects relating to phase transformations. In this subsection, we review the work done in relation to phase diagrams while in a later section, we shall touch upon studies in kinetics.

The basic idea is to start with a representative Hamiltonian that describes configuration interactions, and then use a Monte Carlo technique to deduce the structure appropriate to specific thermodynamic conditions. Since the problem is formulated in the Ising-spin language, there are understandable links with many magnetic problems.

To obtain the desired Hamiltonian, we go back to (11), the expression for internal energy. Adding to it a chemical potential term $(\mu_A - \mu_B)\sum_l \sigma_B(l)$ as earlier, we have

$$\mathscr{H} = \frac{1}{2}\sum_{ij}\sum_{l \neq m} v_{ij}(l-m)\langle \sigma_i(l)\sigma_j(m)\rangle + (\mu_A - \mu_B)\sum_l \sigma_B(l). \tag{27}$$

Introducing Ising spins as in (20), the Hamiltonian in (27) can now be transformed (barring a constant term) as

$$\mathscr{H} = \sum_{l \neq m} J_{lm} S_l S_m - H\sum_l S_l, \tag{28}$$

where

$$J_{lm} = -\{v_{AA}(l-m) + v_{BB}(l-m) - 2v_{AB}(l-m)\}/4, \tag{29}$$

is the exchange integral for Ising spins, and

$$H = \frac{1}{2}\sum_{m(\neq l)}\{v_{AA}(l-m) - v_{BB}(l-m)\} + \frac{1}{2}(\mu_A - \mu_B), \tag{30}$$

is an 'external' field acting on the Ising spins.

As it stands, the spin at site l interacts with spins at all other sites m in the lattice. To make the problem tractable, one restricts, as earlier, the range to the nearest and next nearest neighbours so that $\mathscr{H}$ now is given by

$$\mathscr{H} = -J\sum_{(nn)} S_i S_j + \alpha J \sum_{(nnn)} S_i S_j - H\sum_i S_i. \tag{31}$$

The parameter $(-\alpha)$ is a measure of the relative strength of the *nnn* interaction.

One now takes a system of $N = 4L^3$ spins on a fcc lattice with periodic boundary conditions. In the actual simulation, N was ~ 15000. Next one specifies an initial configuration $X_0 = \{S_1, S_2, \ldots, S_N\}$, the choice of which will be discussed shortly. Using pseudo random numbers, one then generates a random change of configuration $X_0 \to X_1$. There are two ways of achieving this, depending on what ensemble one works with. If one is using a canonical ensemble, then the total 'up' spin as well as the total 'down' spin must be individually conserved. Hence $X_0 \to X_1$ is achieved by choosing at random a nearest neighbour AB pair and exchanging spins. This 'Kawasaki dynamics' (Kawasaki 1972) conserves the concentration c_B of the system. In the case of the grand canonical ensemble, the magnetic field is held constant and $X_0 \to X_1$ is implemented *via* the flip $S_i \to -S_i$ of a randomly chosen spin. These spin fluctuations are equivalent to fluctuations of c_B. As is well-known, both ensembles should yield results equivalent to each other in the thermodynamic limit $N \to \infty$. Working with finite N as in simulation experiments, it is important to verify that the results do not depend on the ensemble chosen. Having produced a change $X_0 \to X_1$, one now computes (in both cases) the energy change $\delta U = \mathscr{H}(X_1) - \mathscr{H}(X_0)$ resulting from the configurational change. The transition probability for such a change is

$$W = \exp(-\delta U/k_B T)/\{1 + \exp(-\delta U/k_B T)\}, \tag{32}$$

which is compared to a random number η chosen uniformly from the interval (0, 1). If $W > \eta$, the transition is performed; otherwise the old configuration is counted once more for the averaging, the attempted X_1 is rejected, and another transition is tried. The Monte Carlo steps (MCS) are repeated till an equilibrium distribution is obtained. To achieve convergence within a few thousand MCS, it is necessary to choose the initial state X_0 appropriately.

Two groups, namely that of Lebowitz and of Binder have been active in studying phase diagrams by simulation. Recently they merged their efforts to make a detailed study of a system that is a prototype for Cu-Au alloys (Binder *et al* 1981). Since this is the most comprehensive study to date, we shall present some results from it.

In this work, nearest neighbour interactions alone were considered *i.e.* α was set equal to zero. The initial state was variously chosen as ferromagnetically ordered state, a disordered state or an antiferromagnetic state, as appropriate. Runs using the canonical ensemble were done at various fixed compositions c_B, and for each composition, runs were taken at several temperatures (actually at several values of $k_B T/|J|$). The grand canonical ensemble runs were done for various fields corresponding to a fixed temperature, and the temperature was subsequently varied. The quantities monitored were, (i) the internal energy, (ii) the net magnetization m and (iii) the order parameter $\tilde{m}$. In terms of the sublattice magnetization m_ν (ν = 1,2,3,4) defined by

$$m_\nu = (1/N) \sum_{\substack{i \\ \text{over } \nu\text{th sublattice}}} \langle S_{i,\nu} \rangle, \tag{33}$$

m is given by

$$m = m_1 + m_2 + m_3 + m_4, \tag{34}$$

while $\tilde{m}$ is given by

$$\begin{aligned} \tilde{m} &= m_1 + m_2 - m_3 - m_4 \qquad && (AB \text{ structure}) \\ &= m_1 + m_2 + m_3 - m_4 \qquad && (A_3B \text{ structure}). \end{aligned} \tag{35}$$

Figure 16 shows a plot of magnetization as a function of the applied field. When H is zero, there is no magnetization. As H is increased, m also increases, and the increase would have been linear (dashed line) if the system were disordered. Instead, the m value stays below the dashed line indicative of order until a field H'_{C_1} is reached when it jumps. H'_{C_1} is thus a critical field required to derive the system to disorder. Order sets in again at H_{C_2}'' and disappears at H_{C_2}. The order parameter variations are also shown in figure 16, from which the field-induced transitions (at a fixed temperature) are clearly evident.

Figure 16 is what is termed 'raw data' by Binder *et al* (1981). For several such data, the phase diagram of the Ising antiferromagnet was constructed as in figure 17. Noting that $\sigma_B(l) = (1 - S_l)/2$, the average concentration C_B of B atoms in the alloy is related to m by $C_B = (1 - m)/2$. Therefore, the diagram of figure 17b which is the phase diagram

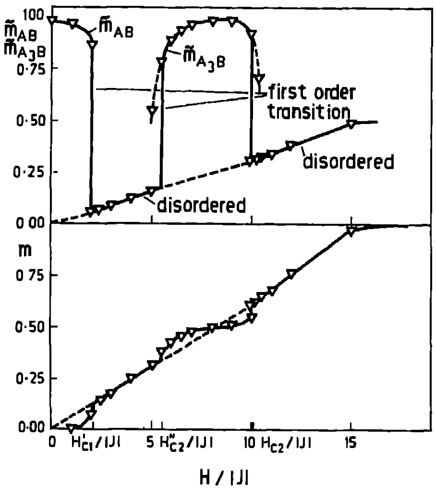

Figure 16. Order parameter (top) and magnetization (bottom) for the nearest neighbour Ising antiferromagnet plotted as a function of the field for the temperature $T_{k_B}/|J| = 1{\cdot}5$. Estimates for the three critical fields H'_{c_1} H''_{c_2} and H_{c_2} are also indicated. (after Binder *et al* 1981).

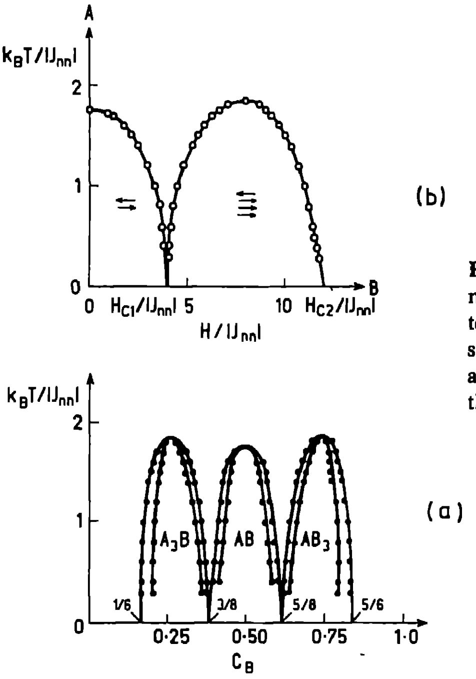

Figure 17. (a) Phase diagram of the nearest neighbour fcc lattice in the temperature-composition plane. Ordered structures are indicated. All transitions are of first order. (b) Phase diagram in the temperature-field plane.

for an Ising antiferromagnet in a magnetic field can be mapped to the temperature-composition plane as in figure 17a to yield a phase diagram appropriate to the alloy AB. The two-phase regions shown here arise from the fact that for certain values of the field, m is multivalued.

Recently, Binder (1981) has extended the above work to include *nnn* interactions also. The phase diagram is now considerably altered (see figure 18), a noteworthy feature being the occurrence of a multicritical point at $H = 0$. This is an interesting finding in view of a recent theoretical prediction that such a point arises out of a meeting of lines of 3- and 4-state Potts model-like transitions.

Returning to the implications for the alloy problem, the broad finding is that simulation corroborates CVM results as is explicitly brought out in figure 19. At stoichiometric compositions, the two methods come fairly close to each other. This has also been noted from limited simulations done for $\alpha = 0{\cdot}25$. The feeling therefore is that stoichiometric alloys are rather insensitive to the parameters of the model as well as the accuracy of the approximations used. Study of off-stoichiometric systems (both experimentally and theoretically) may be more worthwhile. In this context, Binder (1980a) has proposed that one could, for example, explore short-range order as a function of composition (see figure 20). Measurements of this type would provide a valuable test of whether a model faithfully represents a real system. Another useful hint to emerge from these studies is that the interaction parameters are probably composition dependent. In other words, the same exchange integral $J(r)$ cannot be used over the entire composition range. The possibility of 'frustration' is yet another interesting finding. To understand this, we refer to figure 21 which shows two neighbouring cells of the A_3B structure. Focussing attention on the spin at the centre of the common plane, it is found that four of its bonds to *nn* are energetically favourable while the other eight are unfavourable. Therefore at the critical field H'_{C_1}, this spin can be overturned at no cost. One has essentially a 'frustration-type' of situation here since the central spin is under conflicting orders. Binder *et al* (1981) therefore advocate improvements to theoretical methods so as to handle frustration.

As of now, the computer simulation method has some limitations. Being time consuming, it cannot be applied for wide ranging explorations as, for example, the CVM. Also the treatment of the configurational entropy is crude. However, there is no doubt that valuable insight has been gained from whatever has been done so far. And it is also

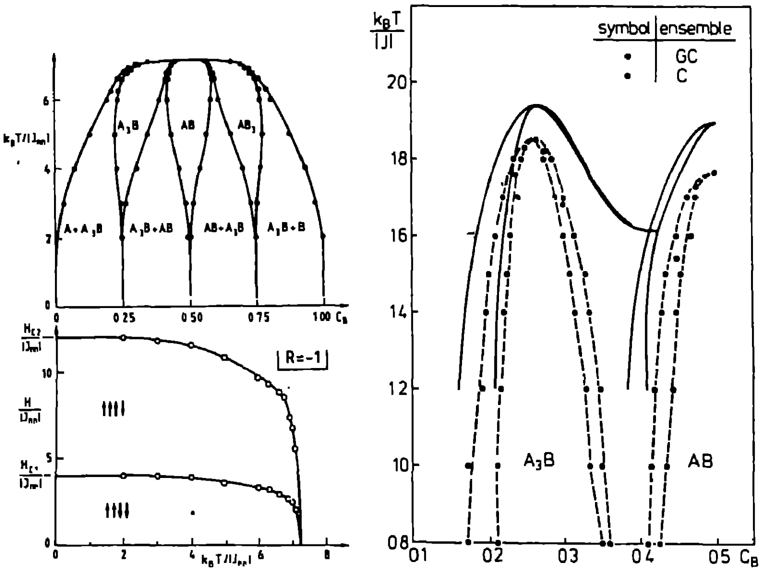

Figures 18–19. 18. (Left) Phase diagram of the next nearest neighbour Ising antiferromagnet in the T-field and T-composition planes. Observe that the simulated diagram is still far from experiment. (after Binder 1981). **19.** (Right) Comparison of the phase diagram for the fcc binary alloy as obtained by simulation and the CVM results (after Binder *et al* 1981).

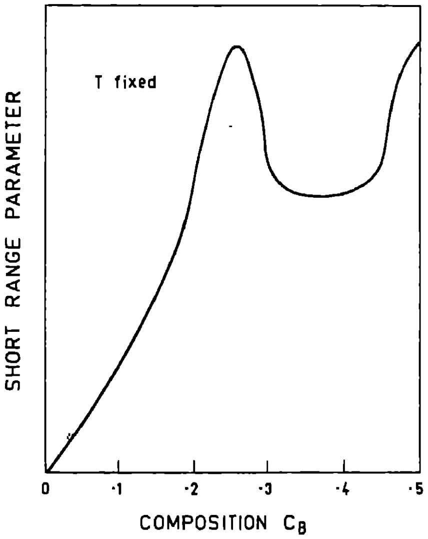

Figure 20. Schematic plot of the variation of the (Cowley) short-range order parameter as a function of concentration. The temperature is fixed, and below T_c. The sharp variations are related to the crossings of the phase boundaries. See also figure 45 (after Binder 1980a).

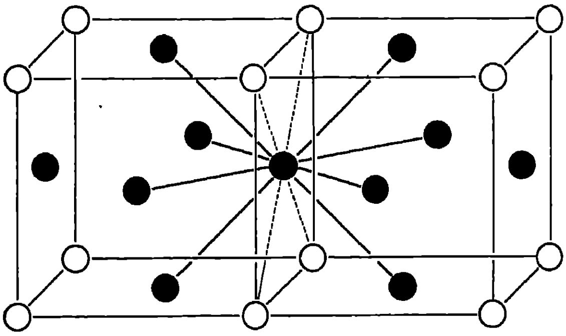

Figure 21. Illustration of the concept of a 'spin' under conflicting orders and thereby becoming 'loose' at the critical field. For explanations, see text. According to Binder *et al* (1981) such a 'conflict' leads to a frustration-type of situation as in spin glass (after Binder *et al* 1981).

clear that simulation will always be required both to complement as well as to continually spur experiment and theory.

4. Kinetic phenomena

We turn our attention now to phenomena that occur when one either approaches a phase boundary or crosses it. As is to be expected, there will be manifestations of critical phenomena in the neighbourhood of a transition across the boundary, and such critical effects have indeed been observed even in the twenties. For instance, Johansson and Linde (1928) found that the electrical resistivity of Cu_3Au rose sharply with increasing temperature around 390°C, the transformation temperature. One could therefore envisage extensive studies on critical exponents related to the vast variety of transformations possible. It is however unlikely that such studies while *very useful* will reveal anything fundamentally *new* concerning the *basic universalities* under lying critical phenomena since the cream has in a sense already been skimmed off. Far more interesting is the study of dynamic phenomena following a quench as it raises questions in nonequilibrium statistical mechanics, currently an active area.

In systems such as we are interested in, quenching (notionally) causes a step function change of temperature. However, although the phonons have readjusted, the atoms are unable to follow suit and occupy their new equilibrium positions with such rapidity. Positional readjustments involve large scale migration of atoms through diffusive processes, necessarily requiring some time. Thus, immediately after a quench, the system is left in a highly non-equilibrium state. It then coasts down (with the atoms readjusting their positions), eventually attaining equilibrium. Studies made during the coastdown can shed valuable light on the behaviour of systems far from equilibrium. The attendant nonlinearities make such investigations even more interesting.

In this Section, we shall review progress in the understanding of such kinetic phenomena and also indicate questions that still await solutions.

4.1 *Linear kinetics*

The broad question one faces is: What exactly happens after a quench? There is no simple universal answer to such a question for much depends on whether one is considering the early- or the late-stage behaviour, whether it is a clustering or an ordering system, etc. We shall deal with some of these complications as we go along. For the present we will offer a qualitative picture assuming the system responds linearly to the forces set up following the quench (—a bad assumption!).

Let c_B be the average concentration of the B species and $c(r,t)$ the distribution (of the B species) in the quenched alloy. It is convenient to consider $c(k,t)$ the Fourier transform of the composition fluctuation $[c(r,t)-c_B]$. $c(k,t)$ thus represents a compositional wave of wavevector k. If the system behaves linearly, then each Fourier component has an evolution history that is completely delinked from those of the others. The task now reduces to formulating an equation of motion for $c(k,t)$ and solving it. Thanks to the linearity assumption, one has (Cahn 1961, 1968)

$$c(k,t) \sim \exp[\alpha(k)t], \tag{36}$$

where $\alpha(k)$ depends on the forces acting in the quenched system. If α is negative, the fluctuations decay but if α is positive the fluctuations grow, in fact indefinitely, indicative of an instability in the system. The question therefore is: How does $\alpha(k)$ behave as a function of k, and, in particular, is it positive for certain values of k? The latter would depend of course on the instabilities.

Figure 22 shows some schematic plots of α both above and below the transition temperature for a clustering as well as an ordering system (Cook *et al* 1969). We notice that α becomes positive only below the transition temperature. Only then do certain fluctuations grow to giant proportions, driving the system to a totally new state altogether. For a clustering system α becomes positive near the zone centre, whereas for an ordering system it becomes positive in the neighbourhood of the superlattice position associated with the ordering process.

Now fluctuations cannot really grow in an unbounded manner, and such growth is in fact arrested by nonlinearities. Another way of saying this is that the different Fourier

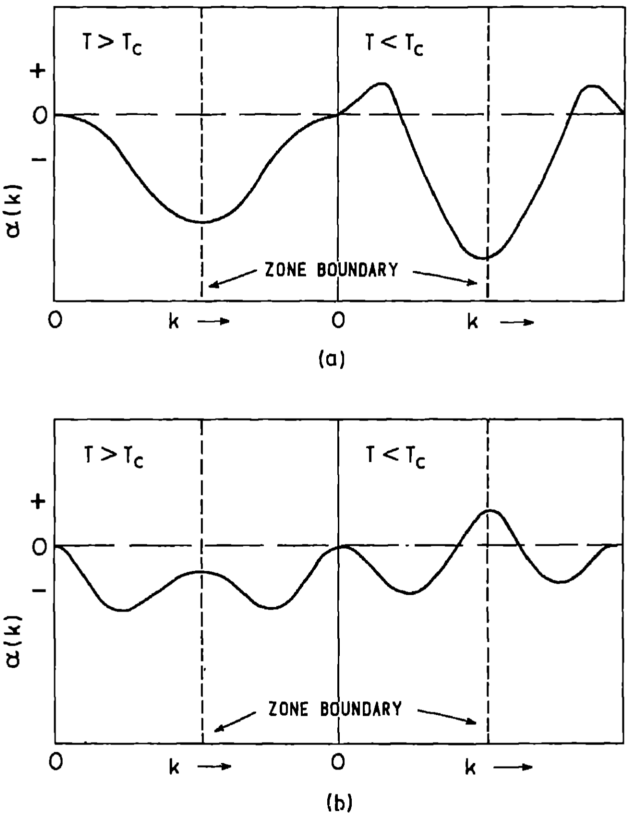

Figure 22. Schematic plot of α above and below the transition temperature T_c (a). situation for a clustering reaction, where α becomes positive below T_c around $k = 0$. In an ordering reaction on the other hand, α becomes positive in the region of the superlattice reflection. The region where α becomes positive is related to the region where $V(k)$ has a minimum (after Cook *et al* 1969).

components start interacting with each other, checking runaway growth. While the concept of a 'linear' amplification factor $\alpha(k)$ does become blurred to some extent in the presence of non-linearities, it certainly is meaningful in the disordered region at least.

Some interesting experiments on 'disordering kinetics' have been performed to obtain plots of $\alpha(k)$ and they are worth a brief mention (Paulson and Hilliard 1977). In these experiments, a multilayer film several thousand Angstroms thick was prepared by alternately depositing two elements (*e.g* Cu and Au) in the desired proportions. The as-deposited composition modulation produces satellite peaks in an x-ray diffraction pattern. One now upquenches the specimen, taking it into the one-phase region. The modulation then progressively disappears due to the interdiffusion of the atomic species. By monitoring the time-dependence of the intensity of the satellite peak, $\alpha(k)$ can be obtained. The wavelength of the modulation can be varied by controlling the deposition, and in this way $\alpha(k)$ can be studied as a function of k. A typical plot so obtained is shown in figure 23. We shall return again to the amplification factor for clustering systems in § 4.3.

Linear theories essentially provide first-order answers. They are reasonably adequate

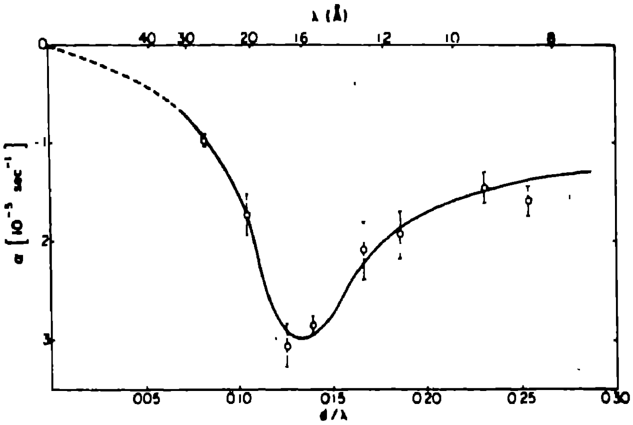

Figure 23. Amplification rates α *vs* λ observed at 225°C in thin films of Cu-16 at % Au (after Paulson and Hilliard 1977).

in the disordered region where *all* fluctuations decay, and one does not encounter runaway situations. However, such theories are inadequate as one approaches the critical region; and in the ordered region, they totally fail to describe the kinetics.

4.2 *Beyond linear theories*

For answers beyond linear theories one should look to nonequilibrium statistical mechanics, and presently we shall consider some general aspects. To provide a framework for the discussion, we shall suppose the free energy density f to be given by

$$f(x; a, b) = \tfrac{1}{2}ax^2 + \tfrac{1}{4}x^4 + bx. \qquad (37)$$

This is the Ginzburg-Landau form, together with a magnetic field term bx. The quantities a and b are the control parameters while x is the order parameter. Our f here is equivalent to the grand potential discussed in § 3.

Our first interest is in the minima of f, and the locus traced by them as a and b are varied. In the language of catastrophe theory (Gilmore 1981), the minima are the critical points of f. The various critical points of f are obtained as follows:

$$\begin{array}{lllll} \text{nondegenerate crit. pt.} & (\mathrm{d}f/\mathrm{d}x) = 0 & \text{i.e. } x^3 + ax + b & = 0 & \\ \text{two-fold degenerate} & & & & \\ \text{crit. pt.} & (\mathrm{d}^2f/\mathrm{d}x^2) = 0 & \text{i.e } 3x^2 + a & = 0 & \\ \text{three-fold degenerate} & & & & \\ \text{crit. pt.} & (\mathrm{d}^3f/\mathrm{d}x^3) = 0 & \text{i.e } 6x & = 0. & (38) \end{array}$$

It is easily seen from above that the locus of the doubly degenerate critical points is given by (Gilmore 1981)

$$(a/3)^3 + (b/2)^2 = 0. \qquad (39)$$

This 'fold curve' also called the separatrix is sketched in figure 24, and it divides the parameter space into two regions representing functions with one critical point and functions with three critical points. This feature is made explicit with representative

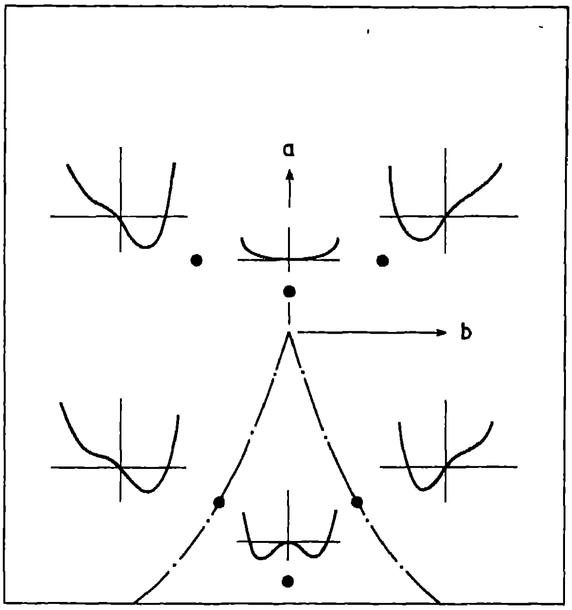

Figure 24. Sketch of the fold curve for f given by (37). Also shown are representative plots of f *vs* x for the various points in the (a, b) plane indicated by dots (after Gilmore 1981).

plots for f corresponding to various points in the a-b plane. The origin represents the function $f = (x^4/4)$, and corresponds to a three-fold degenerate critical point.

It is helpful also to have some idea of certain surfaces associated with f (Gilmore 1981; Kikuchi and de Fontaine 1976). These are (i) the critical manifold defined by $(\mathrm{d}f/\mathrm{d}x) = 0$, (ii) the critical value surface f_c made up by the values assumed by f when $\nabla f = 0$ and (iii) the critical curvature surface defined by $(\mathrm{d}^2 f/\mathrm{d}x^2) = 0$. Sketches of these surfaces are given in figure 25, and they aid the analysis of system behaviour following a disturbance to the system. Thus, for instance, the critical curvature surface is useful while discussing the stability of the system.

In nonequilibrium phenomena, the state of the system is governed by f which often changes for one reason or the other. In this changing situation, the system attempts to find a minimum appropriate to the prevailing conditions but when several minima are available, the question naturally arises regarding which minimum the system jumps to. Two extremes are possible as illustrated in figure 26. In figure 26a the system remains in a stable or metastable equilibrium state until that state disappears whereas in figure 26b the system always chooses the global minimum. Between these two limiting conventions, many other possibilities exist. Which of these conventions operate in a given situation depends on the relative values of the barrier height ΔE and the noise level N. If $N/\Delta E \ll 1$, then the delay convention is observed while if $N/\Delta E \gg 1$ the Maxwell convention operates (figure 27).

Another way of looking at a system evolution is *via* the probability distribution function $P(x, t)$. Figure 28a shows a schematic plot of $f(x)$ at some instant of time while figure 28b depicts $P(x, t)$ for that same instant. Notice P peaks away from the minimum, typical of a nonequilibrium situation. As time evolves, $P(x, t)$ will seek to attain a form appropriate to equilibrium. There are two characteristic times T_1 and T_2 associated with

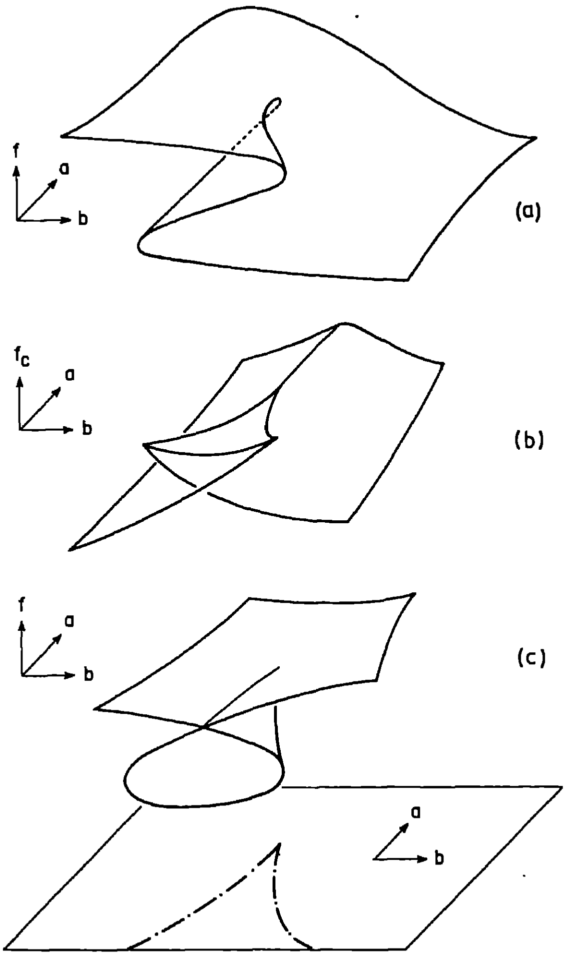

Figure 25. Schematic plots of various critical surfaces associated with the f of (37) (a). surface defined by $\nabla f = 0$. (b). critical value surface f_c which, for a given (a, b) gives the f value corresponding to the condition $\nabla f = 0$. The critical curvature surface $f'' = 0$ is sketched in (c). This is useful for discussing instabilities. At the bottom is projected the fold curve. The relationship of the latter to the various surfaces sketched above it should be clear (after Gilmore 1981).

this approach to equilibrium. Of these, T_1 is the time for relaxation to a local minimum and T_2 from a metastable minimum to a global minimum (see figure 28d). In transiting from a local minimum to a global minimum the system essentially drifts (in x space). Relaxation to a local minimum on the other hand is like a diffusive process.

The regime of the two conventions can also be spelt out in terms of T_1 and T_2. If $C = \{a, b, \ldots\}$ denotes the set of control parameters, then the delay convention operates if (Gilmore 1981)

$$T_1^{-1} \gg (\mathrm{d}C/\mathrm{d}t) \gg T_2^{-1}, \tag{40a}$$

while the Maxwell convention operates if

$$T_2^{-1} \gg (\mathrm{d}C/\mathrm{d}t). \tag{40b}$$

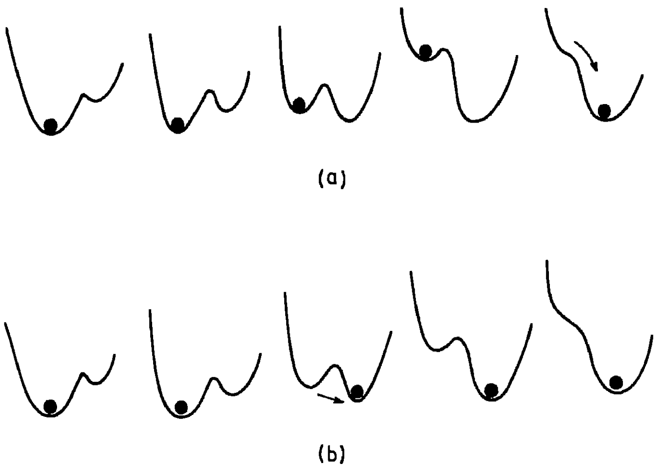

Figure 26. Illustration of the two conventions adopted for discussing change of state under nonequilibrium conditions. (**a**). Delay convention—the system remains in a stable or metastable state until that state disappears, (**b**). Maxwell convention—the system always chooses the global minimum (after Gilmore 1981).

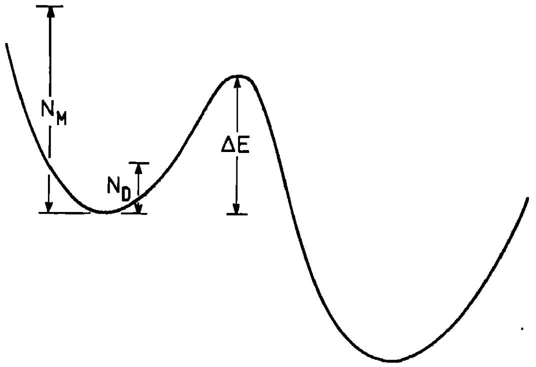

Figure 27. Illustration of the conditions under which the delay and Maxwell conventions are applicable.

To see the link between these two conventions and the topography of the critical manifold, we present in figure 29 the projections of the critical manifold on the (a, b) as well as the (a, x) plane. When the Maxwell convention is adopted, the critical manifold is a "soldered manifold" because the portions of the manifold $\nabla f = 0$ describing unstable critical points and metastable minima have been removed and replaced by a flat piece which interpolates between the two mimima. Later in § 4.3 when we consider phase separation, we will recognize the projections of the two manifolds on the (a, x) plane as the coexistence line and the spinodal respectively. The projections on the (a, b) plane are of special interest in a ferromagnet where one has the practical possibility of varying the magnetic field and inducing a phase transition. It is illuminating to follow the transitions (especially under nonequilibrium conditions), as trajectories on the critical manifold (see Gilmore (1981) for examples and details).

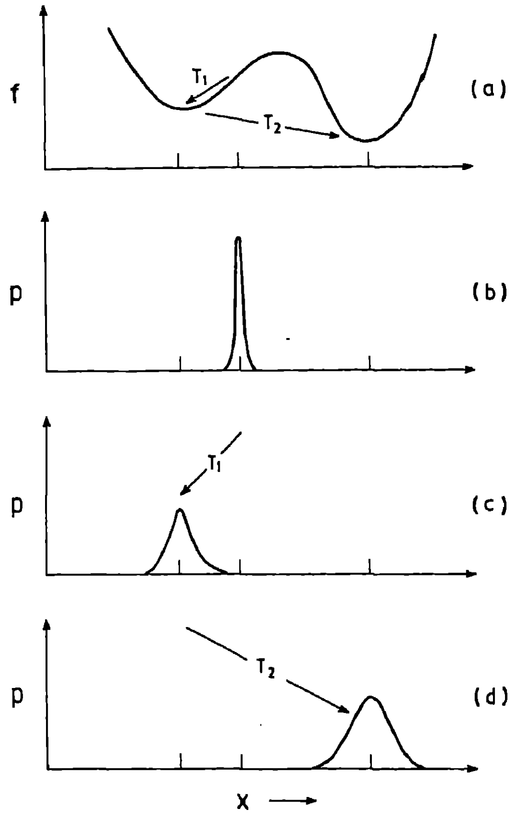

Figure 28. Description of the system evolution in terms of the probability distribution function $P(x; t)$. (a) and (b) depict $f(x)$ and $P(x, t)$ at some instant t, say (after Gilmore 1981).

The quantitative aspects of the approach to equilibrium revolve almost entirely around the probability distribution function $P(x, t)$. A quench, for example, creates a certain $P(x, 0)$. The system not being in equilibrium, P will naturally evolve approaching that appropriate to equilibrium. The questions in this context are: What is the equation that governs the evolution of P, how does one solve this question, and how does one use this knowledge of P to make predictions pertinent to specific experiments?

The evolution of P is governed by the well-known Fokker-Planck equation

$$\frac{\partial P}{\partial t} = -\frac{\mathrm{d}}{\mathrm{d}x}[K(x)P] + \frac{1}{2}D\frac{\mathrm{d}^2 P}{\mathrm{d}x^2}, \tag{41}$$

here D is the diffusion coefficient and $K(x)$ a drift force. In many problems, this drift force can be expressed as the gradient of a potential *i.e.*

$$K(x) = -[\mathrm{d}V(x)/\mathrm{d}x]. \tag{42}$$

In our problems, $K(x)$ will be related to the free energy.

The derivation of the Fokker-Planck equation from the more fundamental Master equation is too involved a question to be discussed here but fortunately good treatments are available in literature (—see, for example, Haken 1978; for a discussion

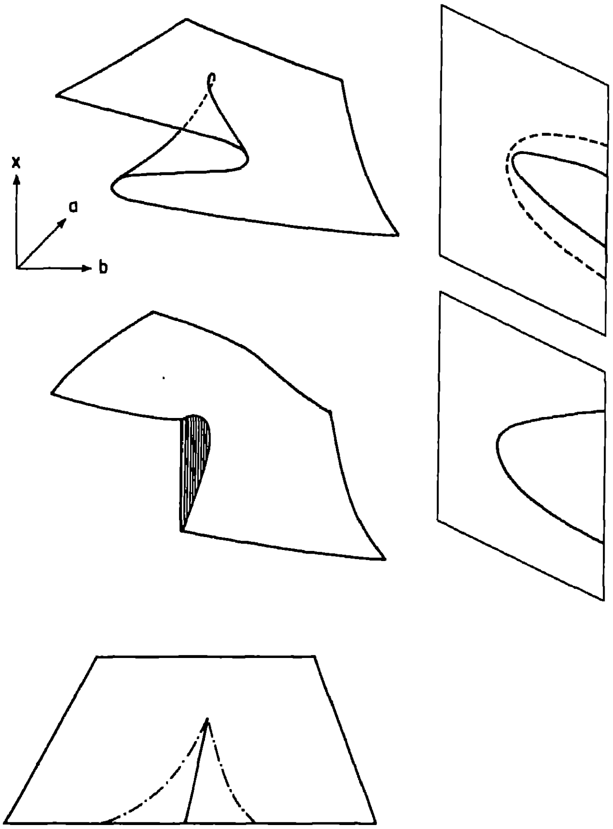

Figure 29. Projections of the critical manifold ($\nabla f = 0$) on the (a, b) and (a, x) planes.

vis-a-vis problems of materials science, see Venkataraman and Balakrishnan 1977; Venkataraman 1982).

The Fokker-Planck equation is sometimes written as a continuity equation i.e. as

$$\overset{\circ}{P}+\frac{\mathrm{d}}{\mathrm{d}x}j=0, \tag{43}$$

where j the probability current is given by

$$j=\left[K(x)\,P-\frac{1}{2}D\frac{\mathrm{d}P}{\mathrm{d}x}\right]. \tag{44}$$

In equilibrium statistical mechanics, one is interested in the stationary solutions of the Fokker-Planck equation; but in our kind of situations, it is the time-dependent solution that is of interest. In general, finding exact solutions is not possible, and one must resort to a suitable approximation scheme. A very readable account of these problems is available in the book of Haken (1978). Figure 30 shows a schematic plot of the evolution of P in a typical problem. Starting off as a δ-function, P drifts (which gives rise to the dotted line trajectory) and it also broadens (due to diffusion).

The probability density function we need for discussing clustering etc is somewhat

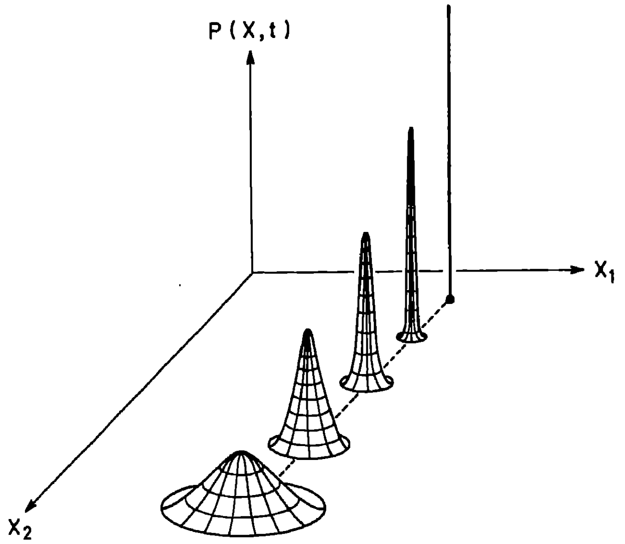

Figure 30. The concept of time evolution of $P(x,t)$ is discussed in this figure. For convenience x is assumed to be two dimensional and it is supposed that at $t = 0$, P starts off as a δ-function. With the passage of time, the state of the system *drifts* in x-space as indicated by the dotted trajectory. Simultaneously, due to fluctuations, the distribution function also broadens.

more general, being a functional of the form $P(\{\psi\},t)$. Here

$$\{\psi\} = (\psi_1, \psi_2, \ldots, \psi_n), \tag{45}$$

with ψ_r being the coarse-grained value of the order parameter ψ in the rth cell. *i.e*

$$\psi_r = \frac{1}{n_r} \sum_{l \in \text{cell } r} \psi(l) \tag{46}$$

There are n_r lattice sites l in cell r and there are n cells in all. $\{\psi\}$ comprehensively describes the state of the system.

Like $P(x,t)$ which we considered earlier, $P(\{\psi\},t)$ is also conserved. In the continuum limit (where sums over coarse-grained cells are replaced by integrals), the continuity equation is given by

$$\frac{\partial}{\partial t} P(\{\psi\},t) = -\int \mathrm{d}\mathbf{r} \frac{\delta J_r}{\delta \psi(\mathbf{r})}, \tag{47}$$

where J_r is the probability current, and δ signifies a functional differentiation.

The expression for J_r depends on whether the order parameter is conserved or not. The latter quantity is said to be conserved if the change $\psi_r \to \psi_r + \varepsilon$ in the cell r is accompanied by a compensating change $\psi_s \to \psi_s - \varepsilon$ in a neighbouring cell s. In clustering reactions, the order parameter is composition which obviously is conserved. On the other hand, in ordering reactions the order parameter is *not* conserved (—recall the examples of ferro- and antiferro magnets). Bearing these two possibilities in mind, the expression for J_r can be written as (Billotet and Binder 1979)

$$J_r(\{\psi\},t) = -C\left[\frac{\delta F\{\psi\}}{\delta \psi(\mathbf{r})} P(\{\psi\},t) + k_B T \frac{\delta P(\{\psi\},t)}{\delta \psi(\mathbf{r})}\right], \tag{48}$$

where $F\{\psi\}$ is the (coarse-grained) free energy functional. If the order parameter is conserved, then $C = -M\nabla_r^2$ where M is the mobility*, whereas if the order parameter is not conserved then C is simply a rate factor fixing the time scale.

Equations (47) and (48) are too formal and complex for practical use, and watered down versions are necessary. A common practice is to use the above equations to construct equations of motion for various moments of P. A few illustrative examples follow.

Consider the clustering problem, and let $c(\mathbf{r})$ denote the local concentration of B atoms. This is the order parameter, and being conserved

$$J_r(\{c(\mathbf{r})\}, t) = -M\nabla^2\left[\frac{\delta F\{c(\mathbf{r})\}}{\delta c(\mathbf{r})}P + k_BT\frac{\delta P(\{c(\mathbf{r})\}, t)}{\delta c(\mathbf{r})}\right]. \tag{49}$$

Multiplying both sides of (47) by $c(\mathbf{r})$ and integrating we get

$$\int \delta\{c(\mathbf{r})\}\, c(\mathbf{r})\frac{\partial}{\partial t}P(\{c(\mathbf{r})\},t) = -\int \delta\{c(\mathbf{r})\}\int \mathrm{d}\mathbf{r}' \times \frac{\delta J}{\delta c(\mathbf{r}')}c(\mathbf{r}). \tag{50}$$

After simplifications, this gives the *average* equation

$$\frac{\partial}{\partial t}\langle c(\mathbf{r})\rangle = -M\nabla^2\left\langle\frac{\delta F}{\delta c(\mathbf{r})}\right\rangle. \tag{51}$$

(M is assumed to be a constant *i.e* independent of $c(\mathbf{r})$). At this stage one makes the convenient assumption that P is *always* sharply peaked around $\langle c(\mathbf{r})\rangle$ *i.e*

$$P(\{c(\mathbf{r})\}, t) = \pi\delta(c(\mathbf{r}) - \langle c(\mathbf{r})\rangle) \tag{52}$$

This then leads to

$$\frac{\partial}{\partial t}\langle c(\mathbf{r})\rangle = -M\nabla^2\frac{\delta F\{\langle c(\mathbf{r})\rangle\}}{\delta c(\mathbf{r})}. \tag{53}$$

Being an average equation, the bracket $\langle\ \rangle$ can be dropped. The assumption (52) is crucial, for it implies that there are no fluctuations. In terms of figure 30 what it implies is a drift of a δ-function with no broadening. In § 4.3 we shall discuss an application of (53).

Our next example relates to ordering where, we must remember, the order parameter is *not* conserved. Binder (1973) has used the same steps as above for this problem. He starts with (47) which, after manipulations, takes the form

$$\frac{\partial P(\{\psi\}, t)}{\partial t} = -C\int \mathrm{d}\mathbf{r}\frac{\delta}{\delta\psi(\mathbf{r})}[K(\psi(\mathbf{r}))P] + C\int \mathrm{d}\mathbf{r}\frac{\delta^2 P}{\delta\psi(\mathbf{r})^2}, \tag{54}$$

where the drift force $K(\psi(\mathbf{r}))$ is given by

$$K(\psi(\mathbf{r})) = -\frac{\delta F\{\psi\}}{\delta\psi(\mathbf{r})}. \tag{55}$$

Equation (54) is the Fokker-Planck equation generalized to deal with a situation where P is a functional rather than a function; compare with equation (41). For F, Binder assumes the Ginzburg-Landau form. He then calculates the first moment as in (50), making an assumption similar to (52). The resulting equation for $(\partial \psi(\mathbf{r})/\partial t)$ is the time-dependent Ginzburg-Landau equation as applied to the alloy problem. Once again, because of the approximation (52), fluctuations are not included in the treatment.

---

* The mobility is related to the diffusion coefficient by the Einstein relation $D = Mk_BT$.

For comparison with experiment, one needs correlation functions involving the order parameter like

$$\langle \psi(\mathbf{r}, t)\psi(\mathbf{r}', t)\rangle = \int \delta\{\psi\}\, \psi(\mathbf{r}, t)\psi(\mathbf{r}', t) P(\{\psi\}, t). \tag{56}$$

Multiplying both sides of (47) by $\psi(\mathbf{r}, t)\, \psi(\mathbf{r}' t)$ and integrating, one obtains an equation of motion for the correlation function. This was essentially the starting point for Langer's theory (Langer 1969; Langer and Turski 1973; Langer *et al* 1975) of spinodal decomposition. Billotet and Binder (1979) also used a similar approach in their theory of ordering reactions. Suitable approximations were then introduced by the above authors to make the solution of the equation of motion tractable, for subsequent comparison with experiment. As we shall note in the following subsections such theories while including in some measure the nonlinearities (which the time-dependent Ginzburg-Landau equation does) and fluctuations (which the Ginzburg-Landau equation does not) do not yet give perfect agreement, signalling the need for improved approximations.

In brief, the usual starting point for problems involving nonequilibrium systems is the ('generalized') Fokker-Planck equation. From here, one must make one's way through suitable approximations to an equation which can form the basis for comparison with experiments. The latter aspects will be dealt with shortly.

For historical completeness we must mention that, Dienes (1955) and Vineyard (1956) wrote down by analogy with chemical reactions, a *rate* equation for the (long-range) order parameter $S \equiv \langle \psi \rangle$. Dienes (1955) calculated $\dot{S}$ numerically for both first order and second order transitions, and the trends obtained by him are sketched in figure 31. If $\dot{S}$ is positive for a certain value of S, then a fluctuation in the system corresponding to that particular S value will be unstable. Figure 31 will now show that in a second-order phase transition, the system is unstable to infinitesimal fluctuations whereas in a first-order transition, a large fluctuation (in S) is necessary. Qualitatively, this is often identified with a nucleation and growth mechanism (Yamauchi and de Fontaine 1974).

The Dienes-Vineyard approach to ordering kinetics has now been superseded by the more formal treatment based on the Fokker-Planck equation.

4.3 *Spinodal decomposition*

It was at one time believed that phase separation occurred only through a nucleation and growth process *i.e.* small pockets of A-rich and B-rich regions first formed scattered throughout the specimen which subsequently grew and coalesced, transforming the entire specimen to the ordered state. Experiments however revealed that under certain conditions of quenching, the approach to ordering was quite different being akin to "continuous" ordering that one usually associates with a second-order phase transition. This mode of decomposition is referred to as spinodal decomposition.

One picture being worth a thousand words (!) it is perhaps desirable at this stage to refer to figure 32 (Oki *et al* 1974) which, incidentally, gives some idea of the diversity of microstructure one can observe in such experiments.

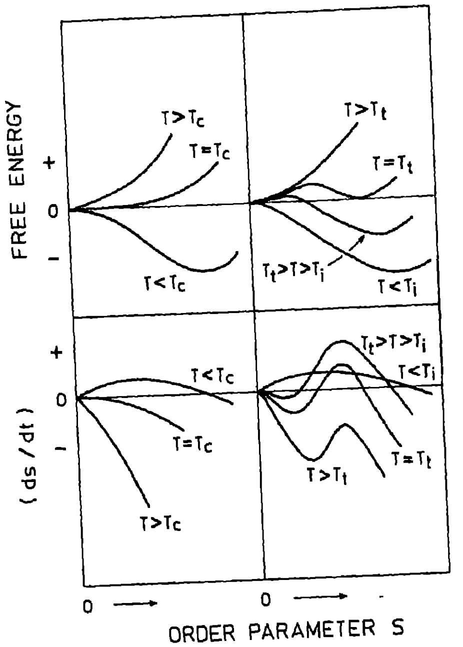

Figure 31. Schematic plots of $\dot{S}$ *vs* S based on the calculations reported by Dienes (1955). The top half of the figure shows sketches of the free energy as a function of the long-range order parameter S for a first- as well as a second-order phase transition. Sketched below are the variations of $\dot{S}$ at different temperatures.

The fact that ordering occurred (under certain conditions) simultaneously over large distances indicated that a large scale migration of atoms was involved; and yet when a diffusion model was tried, it failed. The first nontrivial insight into the processes actually occurring came from the work of Cahn (1961, 1962, 1968). To obtain his model, we go back to (53) and put

$$F\{c(\mathbf{r})\} = \int d\mathbf{r}(\tfrac{1}{2}K|\nabla c|^2 + f(c)), \tag{57}$$

with

$$f(c) = f_0 + \frac{A}{2}(c - c_B^{\text{crit}})^2 + \frac{B}{4}(c - c_B^{\text{crit}})^4, \tag{58}$$

thus obtaining

$$\frac{\partial c(r,t)}{\partial t} = M\nabla^2[-K\nabla^2 c + (\partial f/\partial c)_T]. \tag{59}$$

Writing $c(r,t) = c_B + \delta c(r,t)$ and linearizing,

$$\frac{\partial \delta c}{\partial t} = M\nabla^2[-K\nabla^2 + (\partial^2 f/\partial c^2)_{T,c_B}]\delta c. \tag{60}$$

Solving by Fourier transform,

$$\begin{aligned} c(k,t) &= F\cdot T \text{ of } \delta c(r,t), \\ &= c(k,0)\exp[\alpha(k)t], \end{aligned}$$

where

$$\begin{aligned} \alpha(k) &= -Mk^2(Kk^2 + f''), \\ &= -MKk^2(k^2 - k_c^2), f'' \equiv (\partial^2 f/\partial c^2)_{c_B T}, k_c^2 = K^{-1}|f''| \text{ for } f'' < 0. \end{aligned} \tag{61}$$

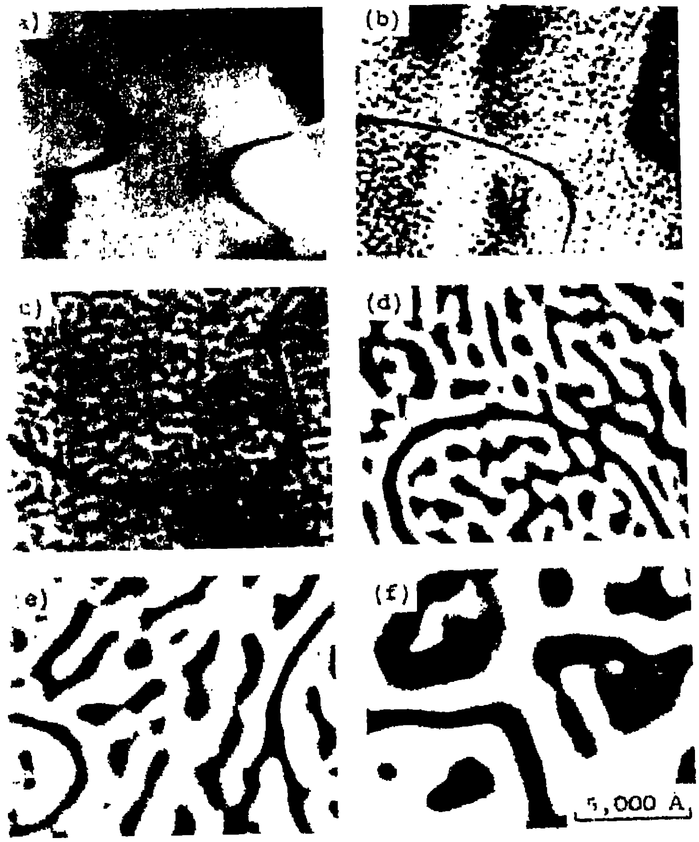

Figure 32. Domain structures of Fe-24·7 at % Al alloy quenched from 630°C and annealed at 570°C. Shown here are the dark field micrographs with 200 reflection. (a). quenched. (b). annealed for 10 min (c). (d). (e). (f). annealed for 100, 1000, 3000 and 10000 min respectively (after Oki *et al* 1974).

This is the gift of Cahn's theory.

At this stage, it is worth emphasizing the contributions made by Cahn. Firstly he noted that instead of writing the diffusion current as

$$j(r) = -M\nabla(\partial f/\partial c) \tag{62}$$

as one usually does, one must allow for the possibility of the chemical potential varying from point to point in the medium and rewrite the current as

$$j(r) = -M\nabla\frac{\delta F\{c(r)\}}{\delta c(r)} \tag{63}$$

with F as in (57) and (58). (It is interesting that Cahn was not aware of the Ginzburg-Landau theory at that time!).

Another question addressed by Cahn is that of coherency strain (figure 33). Sketched in figure 33 are two different scenarios for the coformation of the two phases α and β

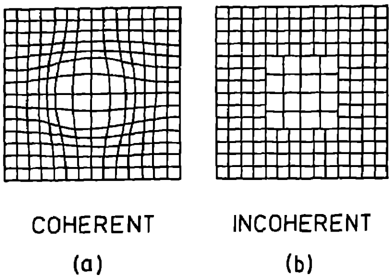

Figure 33. Illustration of the concept of the coherency strain. (**a**). A cluster that is coherent with the matrix. The lattice spacing changes gradually from the grain to the surrounding region through a distortion zone. The strain associated with this distortion is the coherency strain, and makes a contribution to the energy. In the sketch in (**b**) there is atomic mismatch at the boundary, and no coherency strain. The cluster in this case is said to be incoherent.

(say) after the quench*. In figure 33b there is complete atomic mismatch at the boundaries separating the α and β regions. With such a discontinuity, the clusters are said to be *incoherent*. By contrast, in figure 33a there is a gradual accommodation of the lattice parameter change through a distortion zone; the corresponding clusters are called *coherent*. While incoherency is the terminal state, the phases initially formed are coherent whence the free energy has a contribution associated with coherency strain. Assuming the medium to be elastically isotropic, an energy density $\eta^2 Y(c - c_B^{\text{crit}})^2$ must then be added to $f(c)$. Here $\eta = (\mathrm{d}\ln a/\mathrm{d}a)$, a being the lattice constant, and Y is given in terms of the Young's modulus E and Poisson's ratio ν as $Y = E/(1-\nu)$. Consequent to this addition, $\alpha(k)$ gets modified as

$$\alpha(k) = -Mk^2(Kk^2 + f'' + 2\eta^2 Y). \tag{64}$$

It is now seen from (61) and (64) that the sign of α depends on a balance of various factors. If coherency strain is absent and if f'' is negative, then α (in (61)) can assume a positive value in the range $0 \leqslant k \leqslant k_c$ as illustrated in figure 34. Thus compositional fluctuations with wavevectors in this region will grow, the component corresponding to k_m dominating. All other fluctuations will decay. Simple diffusion theory on the other hand predicts $\alpha(k) = -Mk^2 f''$ whence *all* fluctuations will grow, the short wavelength ones preferentially.

Referring now to figure 35 we see that f'' is negative only for a certain range of compositions. One could therefore plot within the two-phase region, the locus of points where $f'' = 0$. This is the spinodal and, as may be seen from figure 35 it divides the two-phase region into two zones (—see also figure 29).† If a quench is made into the region within the spinodal, an *instability* occurs causing the system to evolve to equilibrium through the growth of long wavelength compositional waves. Ordering thus sets in on a macroscopic scale, and increases gradually in amplitude (—hence the reference to

---

* It must be mentioned that spinodal decomposition is also possible in certain binary fluid mixtures. However, there, one does not have coherency strain. For a comprehensive review of both alloys and liquid mixtures, see Gunton (1982).

† The Chamber's dictionary defines spinode as a cusp, the root being the Latin word *spina* meaning thorn. From figure 29 we see the relationship of the cusp to the critical manifold, although one is more used to the projection on the (a, x) plane rather than the projection on the (a, b) plane. See also Kikuchi and de Fontaine (1976).

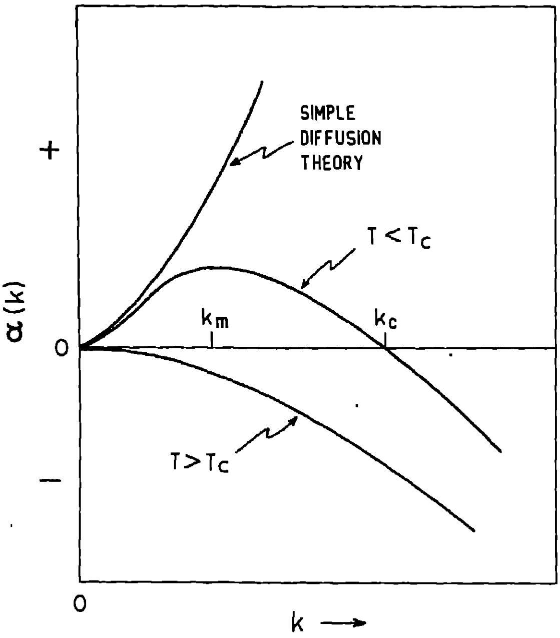

Figure 34. Plots of α *vs* k as given by linear theories.

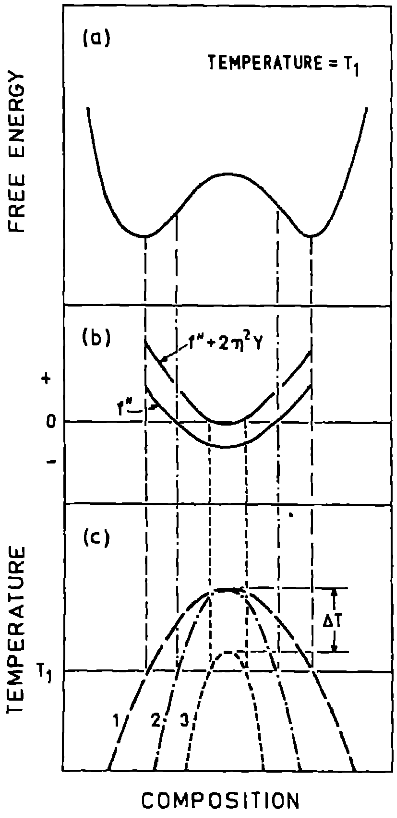

Figure 35. At the top is sketched the usual double well form of the free-energy *vs* composition. (See also figure 5 and (58)). The second derivative f'' is sketched in the middle. Instability is connected with f'' being negative. If coherency strain is included then $(f'' + 2\eta^2 Y)$ must be negative. At the bottom are shown the coexistence curve 1 and the spinodals 2 and 3.

"continuous" ordering). Outside the spinodal but within the coexistence line, there is *metastability* instead of instability. If a quench is made into the metastable region, the system evolves through the nucleation of order in several localized regions. These pockets grow in size and eventually link up so that order percolates everywhere. It appears that after equilibrium is finally reached, it is immaterial what route exactly was taken towards its attainment *i.e.* whether it was quenched into the metastable or the unstable region. However, immediately after nonequilibrium conditions are established, the scenario does depend on whether one is in the region of metastability or of instability. It is in this context one wishes to know where f'' vanishes, and this is precisely where a plot as in figure 25c is useful.

If coherency strain is included, then

$$k_c^2 = K^{-1}|f''+2\eta^2 Y|, \tag{65}$$

and for instability one must have $(f''+2\eta^2 Y)$ negative rather than f''. As a result, the spinodal is depressed with respect to the (incoherent) coexistence curve (see figure 35c). In liquids, such a depression is absent for obvious reasons. In passing, it should also be pointed out that the phase diagrams deduced from theory as in § 3.2 refer to the *coherent* phase diagrams whereas those determined by experiment (Hansen 1958) refer to *incoherent* phase diagrams.

While Cahn's theory gave some clue as to the origin of spinodal decomposition, quantitatively it was inadequate as it assumed linearity. Now one of the stringent tests for a theory is to compare the structure factor $S(k, t)$ predicted by it in the small k region with that observed experimentally. In Cahn's theory

$$S(k,t) \equiv \langle c(k,t)c(-k,t)\rangle = S(k,0)\exp[2\alpha(k)t]. \tag{66}$$

Based on figure 34, one would expect $S(k, t)$ to peak at k_m for all t whereas experiment showed that $k_m \to 0$ as $t \to \infty$. Another failing of Cahn's theory is that it predicts the decay of $S(k, t)$ to zero for $k > k_c$ whereas it must actually approach that appropriate to the fluctuations at temperature T (to which the sample has been quenched). Cook (1970) traced this deficiency to the absence of fluctuations in Cahn's theory (recall remarks circa equation (53)) and therefore modified Cahn's diffusion equation into a Langevin equation, *i.e.* he wrote

$$\frac{\partial c}{\partial t} = -\nabla j + \zeta j = -M\nabla(\delta F/\delta c), \tag{67a}$$

with

$$\langle \zeta(r,t)\zeta(r',t')\rangle = 2M\delta(r-r')\delta(t-t'). \tag{67b}$$

Cook's model produced only marginal improvements to that of Cahn's since it too relied on linearity. The real breakthrough came with the work of Langer and coworkers (Langer 1969, 1980; Langer and Turski 1973; Langer *et al* 1975) who not only included fluctuations (as Cook did), but also the nonlinearities (though only approximately).

To understand Langer's work we start with the formal equation of motion for $S(\mathbf{k}, t)$ which is obtained as described in § 4.2 circa equation (56). Ignoring elastic effects, the equation for $S(\mathbf{k}, t)$ is:

$$\frac{\partial S(k,t)}{\partial t} = -2Mk^2\Big[(Kk^2+f'')S(k,t)+\tfrac{1}{2}(\partial^3 f/\partial c^3)_{c_B}S_3(k,t) + \tfrac{1}{6}(\partial^4 f/\partial c^4)_{c_B}S_4(k,t)+\ldots\Big]+2Mk_BTk^2. \tag{68}$$

Here

$$S_n(r_1 - r_2, t) = \langle \delta c^{n-1}(r_1, t)\delta c(r_2, t) \rangle \tag{69}$$

and $S_n(k, t)$ is the Fourier transform of $S_n(r, t)$. From (68) we see that Cahn had only the first term of the series and that Cook added the noise term.

A major difficulty with (68) is that it involves the higher-order correlation function $S_n(k, t)$ to know which we need additional equations of motion! One thus ends up with a hierarchy of coupled equations, a familiar malaise of many-body theory. Langer and coworkers argued that no matter what n is, S_n always involves only two spatial positions $\mathbf{r}_1$ and $\mathbf{r}_2$. It should therefore be possible to compute S_n for any n (albeit-approximately), given a knowledge of the two-point distribution function $P_2[c(\mathbf{r}_1), c(\mathbf{r}_2)]$. The latter was approximated by

$$P_2[c(\mathbf{r}_1), c(\mathbf{r}_2)] = P_1[c(\mathbf{r}_1)]P_1[c(\mathbf{r}_2)] \times \left\{1 + \frac{\langle \delta c(\mathbf{r}_1)\ \delta c(\mathbf{r}_2) \rangle\, \delta c(\mathbf{r}_1)\ \delta c(\mathbf{r}_2)}{\langle (\delta c)^2 \rangle \quad \langle (\delta c)^2 \rangle}\right\}. \tag{70}$$

If there were no correlations between the concentrations at $\mathbf{r}_1$ and $\mathbf{r}_2$, then P_2 would just be a simple product of the one-point probabilities. In Langer's scheme, the correction is proportional to $\langle \delta c(\mathbf{r}_1)\ \delta c(\mathbf{r}_2) \rangle$. The equation of motion now simplifies to

$$\frac{\mathrm{d}S(k, t)}{\mathrm{d}t} = -2Mk^2[Kk^2 + A(t)] + 2Mk_BTk^2, \tag{71}$$

where $A(t)$ itself depends on $S(k, t)$ and must therefore be calculated by a self-consistent scheme. For comparison, Cahn's theory gives

$$\frac{\mathrm{d}S(k, t)}{\mathrm{d}t} = -2Mk^2[Kk^2 + f''], \tag{72}$$

while Cook's theory gives

$$\frac{\mathrm{d}S(k, t)}{\mathrm{d}t} = -2Mk^2[Kk^2 + f''] + 2Mk_BTk^2. \tag{73}$$

The major success of the Langer theory is the prediction that k_m shifts towards the origin as time increases, in accord with experiment. Another important finding is that the structure factor satisfies dynamic scaling *i.e*

$$S_T(k, t; c_B) = \varepsilon^{-\gamma}\tilde{S}[k\varepsilon^{-\nu}, t\varepsilon^{\gamma}, (c - c_B^{\text{crit}})] \tag{74}$$

where $\varepsilon = (1 - T/T_c)$, and β, ν, γ have their usual meanings (Stanley 1971). Equation (74) is significant because it shows that dynamic scaling can apply to relaxation *far from equilibrium*.

The theory of Langer also is not without blemishes. One shortcoming is that it exhibits metastable states of infinite life-time. A related defect is the inability to describe properly the late stages of the separation. According to Binder (1977) these failings can be cured by explicitly building in features related to nucleation and growth. The late stage behaviour will be briefly touched upon again in a subsequent section.

To counter the impression one might get that it is all theory (!), we now present some representative but important experimental results. Figure 36 shows small-angle

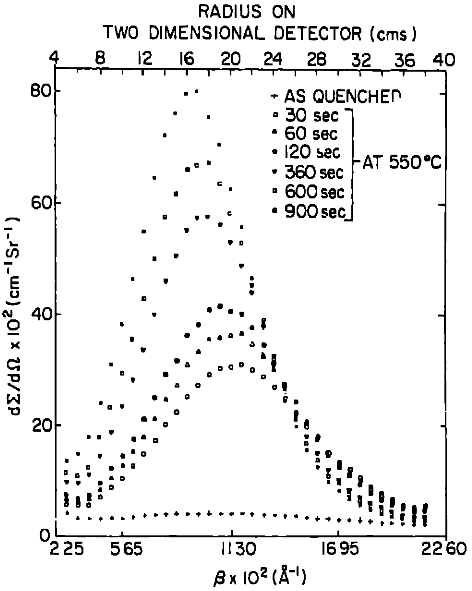

Figure 36. Differential scattering cross-section ($d\Sigma/d\Omega$) *vs* scattering vector β (k in our notation) for Au-60 at % Pt alloy quenched from 1270°C and aged at 550°C. In making the measurements, an "arresting technique" as illustrated in figure 44 was used (after Singhal *et al* 1978).

neutron scattering results for a Au-60 at % Pt alloy obtained by Singhal *et al* (1978). The sample was quenched from 1270 ($\pm$ 5)°C into iced brine and subsequently aged at 550°C. After aging for a certain time, the sample was quenched into water to prepare for measurements (which were done at room temperature). The sample was then successively subjected to additional aging treatment, followed in each case by a measurement to monitor the state of ordering. The data clearly indicates the shift of k_m towards zero with increasing time.

The next result we discuss is that of Schwahn and Schmatz (1978) for Al-40 at % Zn alloy. This was a clever experiment designed to check the fact that due to coherency strain, T_c the critical temperature associated with the spinodal is depressed below the (incoherent) phase boundary (see figure 35). Starting from the one-phase region, the sample was quenched to a temperature T just *above* T_c. Holding the sample at T, small-angle neutron scattering measurements were carried out. In contrast to what one observes in a usual second-order phase transition while approaching T_c from above, it was noticed that $S(k)$ changed with time. The reason is that though $T > T_c$, the sample was actually below the equilibrium (*i.e* incoherent) phase boundary. Thus, with passage of time, ordering occurred slowly *via* nucleation and growth and $S(k)$ probably went over to a form appropriate to that process. Under the circumstances, the spectrum measured just after quench is the one representative of critical scattering *i.e.* the excess scattering arising out of the proximity of T to T_c (coherent). A rapid increase of scattered intensity (so isolated) was indeed observed as $T \rightarrow T_c^+$, and it was firmly established that T_c (coherent) was 28°C below the incoherent critical point of 351·5°C (see figure 37). Further, $S(k)$ immediately after quench had the well-known Ornstein-Zernike (1914) form usually found while approaching a second-order phase transition. Only, in this case the Ornstein-Zernike form was transient, giving way to a fluctuation spectrum appropriate to other processes.

Spinodal decomposition has no doubt been explored by a variety of tools but of these, small-angle neutron scattering is perhaps the most useful for checking out aspects we are interested in presently. The spectrometers currently available at the various high-flux reactors are quite powerful, being placed in cold-neutron beams and equipped with 2-D detectors and online computers. The possibility of rapid, real-time measurements (as in the Schwahn and Schmatz experiment) is a very attractive feature. At the new DHRUVA reactor at Trombay, a cold neutron source is being planned, and a small-angle measurement facility is also being contemplated. Such a spectrometer would give a great impetus to the above type of experiments in the country. While neutron scattering has an edge at the moment, x-rays have a strong possibility of staging a comeback, especially with the advent of synchrotron-radiation sources.

Computer simulation is another important technique employed to test theoretical predictions. Lebowitz *et al* (1982) for example, have used the Monte Carlo method to study quenching under various conditions (see figure 38). In each case $S(k, t)$ was determined, with time measured in units of α^{-1} where α^{-1} is the average time interval

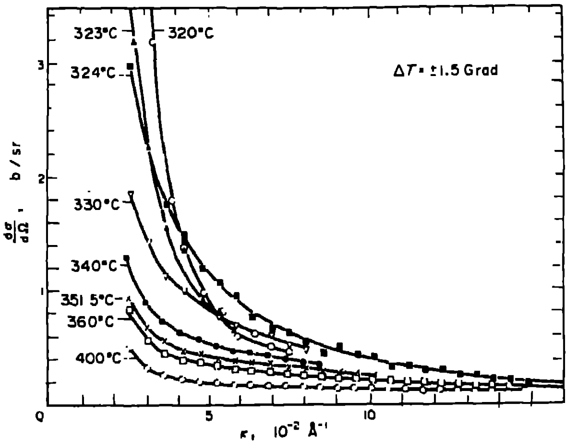

Figure 37. Differential scattering cross-section *vs* wavevector observed at various temperatures in the neighbourhood of the (coherent) critical temperature (~ 324°C). The sharp rise at small k is characteristic of critical behaviour. No critical scattering was found at 351°C the incoherent critical temperature. The k-dependence near 324°C follows the Ornstein-Zernike form (after Schwan and Schmatz 1978).

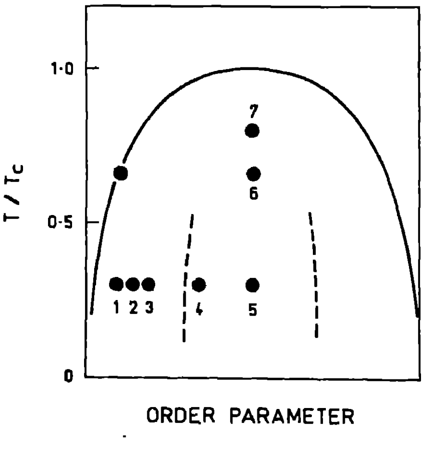

Figure 38. Phase diagram of the Ising model used by Lebowitz *et al* (1982) in their computer simulation studies. The broken lines are spinodals. The dots correspond to the various quenches made. In each case, the system is started from an infinite temperature (after Lebowitz *et al* 1982).

between two attempts at exchanging a specific site. A time range up to $10^4\alpha^{-1}$ was scanned, and, as expected, phase separation occurred with varying speeds depending on the nature of the quench. The relaxation was fastest for quench 5 and slowest for quench 1. A problem arises in making comparisons with experimental data since time in the latter is measured in real physical units *i.e.* seconds. However a link is possible since the unit of time in the simulations appropriate to a temperature T can be taken as $a^2/6D(T)$ where a is the lattice constant and D is the diffusion coefficient of A atoms in a crystal of B atoms. Using such a scaling, Lebowitz *et al* (1982) made comparisons with data obtained by Singhal *et al* (1978). The comparison is reproduced in figure 39 and the notable feature is that one could make the data from the actual and computer experiment lie on the same curve by only rescaling the vertical axis. Further comments on the scaling behaviour will be made when we consider long-term behaviour.

4.4 *Late stages of phase separation kinetics*

Subsequent to quenching, the system will after sometime, segregate locally into regions of A-rich and B-rich phases (referred to as grains or droplets or domains). With further passage of time, two things happen. Firstly, within individual grains itself, the atoms continue to approach an organization characteristic of the equilibrium configuration. In addition, the droplets themselves grow, coarsen or ripen, whichever way one wants to describe it. A proper theory for $S(k, t)$ must reflect both these aspects (see figure 40, Binder 1980b), but such a theory does not exist. Present theories have only one length scale whereas what figure 40 shows is the need for two.

Quantitatively, the above ideas may be expressed as

$$S(k, t) \approx S_{\mathrm{DW}}(k, t) + S_{\mathrm{ID}}(k, t) \tag{75}$$

where DW refers to domain wall and ID to intradomain. As $t \to \infty$, $S_{\mathrm{DW}} \to \text{const} \times \delta(k)$ while $S_{\mathrm{ID}} \to S_{\mathrm{ID}}(k, eq)$. Immediately after quench, DW's are not important and $S \sim S_{\mathrm{ID}}$. However, during late stages, it is S_{DW} that is more interesting as it gives an insight into the coarsening processes.

One interesting discovery concerning late-stage behaviour is the existence of scaling. Since there is a characteristic length ($\sim$ domain size), associated with the process, it has

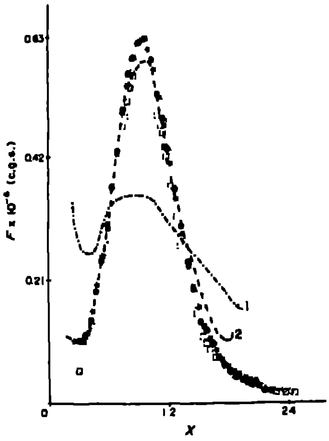

Figure 39. Comparison of the computer simulation results (empty symbols) with experimental data (Singhal *et al* 1978) for Au-60 at % Pt alloy quenched to $T \sim 0{\cdot}6\,T_c$. The broken line is for $t = 0$ (the initial sample was already decomposed to some extent) (after Lebowitz *et al* 1982).

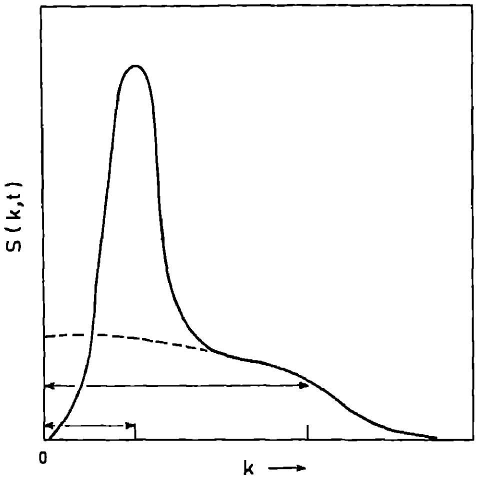

Figure 40. Sketch of $S(k, t)$ vs k at long time. The two arrows show the two wavevectors corresponding to the two length scales (intra domain correlations and domain size). (After Binder 1980b).

been conjectured (Binder 1977; Lebowitz *et al* 1982) that

$$S_{\mathrm{DW}}(k, t) \sim b(t)\mathscr{F}(k/K(t)) \tag{76}$$

where $K(t)$ is the characteristic wavevector associated with the characteristic length, and $b(t)$ is a normalizing function. Lebowitz *et al* (1982) have analyzed the data of Singhal *et al* (1978) for Au-Pt alloy and found good confirmation of this hypothesis (see figure 39).

The question of coarsening has been considered even earlier in the context of nucleation theories. Lifshitz and Slyozov (1961) and independently Wagner (1961) have discussed the growth of droplets of B-rich phase immersed in an A-rich matrix. This theory was really derived for small supersaturation such as one obtains in the late stages of a nucleation and growth process (*e.g.* in clouds). It is however often assumed that the LSW theory can also be applied to the late stage coarsening of a spinodally decomposing system. The basic idea is that larger droplets grow at the expense of smaller droplets *via* the diffusion of B atoms between different droplets. An important conclusion of the theory is that the average droplet size $\bar{R}(t)$ (which is the characteristic length of the system) satisfies a $t^{1/3}$ power law. Lebowitz *et al* (1982) found that $K^{-1}(t)$ derived from simulation studies appeared to show such a behaviour. Attention must here be drawn to the fact that existing studies on grain growth neglect the possible influence of coherency strain, a factor that is pertinent in alloys, though not in liquids (Binder 1977).

There is one aspect of late stage behaviour we now wish to comment on that does not appear to have received attention thus far. It was noticed many years ago by de Fontaine (1967) during a simulation of spinodal decomposition (in one dimension) that whereas a compositional wave of well-defined wavelength develops immediately after instability is established, pretty soon a period doubling occurs. At that time, the possibility of period doubling as a route to chaos was not known (Feigenbaum 1978, 1979, 1980). The question of whether the formation of irregular domains is due to chaos appears worth a fresh examination. It is pertinent here to point out that de Fontaine (1975a) has mapped the problem of concentration evolution into a Hamiltonian problem and examined system evolution in terms of trajectories in a (c, dc/dx) phase space. More recently, Aubry (1981, 1983) has in the study of certain defect structures, carried out a similar trajectory analysis and, what is more interesting, discovered the possibility of chaos under certain conditions. One wonders whether it would not be worthwhile to go back to the de Fontaine problem and reexamine it from this new perspective. In support of such a suggestion, we call attention to figure 41 which shows a computer simulated spinodal structure and that for a real binary glass (Hopper 1982): The simulated structure was obtained by superposing twenty 3-D waves of a *single* wavelength but of random orientation and phases. Notwithstanding this, there appears to be a regularity of sorts in the simulated pattern as compared to the real micrograph. Perhaps features related to stochasticity arising out of period doubling do play a role.

4.5 *Ordering reactions*

The extensive theoretical work on spinodal decomposition reviewed in § 4.3 has been extended to some extent (Binder 1973; Billotet and Binder 1979) to ordering reactions, although there has not been matching experimental work on the kinetic aspects. However, some attention has been paid to critical phenomena one expects near phase boundaries.

We have already called attention to the early work of Johansson and Linde (1928). A more recent example is provided by the work of Hashimoto *et al* (1976) who studied ordering in Cu_3Au. Starting from the one-phase region, the sample was quenched to and held at various temperatures T below the (first-order) transition temperature T_t of 391°C. At each temperature, the electrical resistivity was monitored as a function of time, and the relaxation time τ for approach to equilibrium was deduced. A plot of τ *vs* T showed a sharp increase as $T \rightarrow T_t^-$. Other probes have also been used to study critical phenomena *e.g.* Zener relaxation (Radelaar and Ritzen 1969) and isothermal release of energy (d'Heurle and Gordon 1961).

X-rays have always been popular (see, for example the review by Cohen 1970), a recent example being the study of Hashimoto *et al* (1978). Cu_3Au the work horse, was the material investigated. The specimen was first annealed at a temperature $T > T_t$ and later quenched to a temperature below T_t and annealed at the latter temperature for various spells. After each spell, the sample was quenched into water and the x-ray intensity in the superlattice region (110) was scanned. Initially, only a broad and diffuse

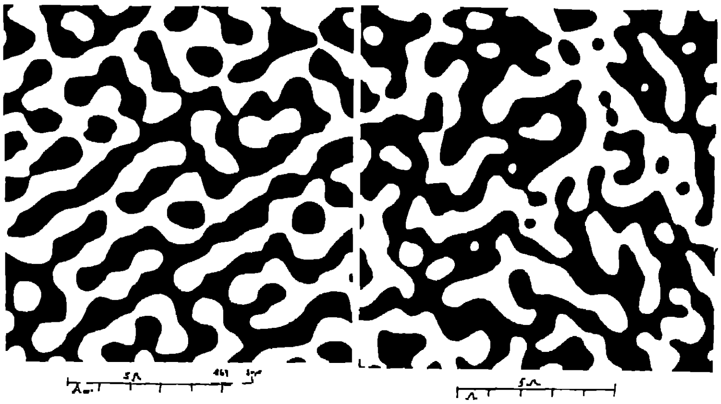

Figure 41. On the right is an electron microscope picture of a real binary glass, showing the phase-separated structure. On the left is the simulated structure obtained using a *single* wavelength (after Hopper 1982).

peak was observed but on increasing annealing time the peak narrowed and intensified, signalling the onset of order. From a plot of linewidth as a function of annealing duration, the relaxation time τ could be extracted. A slowing down of relaxation was markedly evident as $T \to T_t^-$. Another investigation meriting particular mention is that of Chen and Cohen (1977). The unique feature was that by employing single crystals, Chen and Cohen were able to study τ as a function of k. Figure 42 shows their results for $Cu_{81.5}Au_{18.5}$ obtained after a temperature change 355° and 330°C. As expected, τ peaks near the superlattice position.

Earlier (in § 4.3) we noted that under certain conditions, phase separation takes on the character of a continuous transition. Is such a scenario possible in *ordering* systems? Indeed it is, as has been emphasized by de Fontaine (1981). The basic concept is easily understood with a reference to figure 43. In figure 43a is shown a family of free energy curves appropriate to a system undergoing a first-order phase transition. If the temperature is gradually lowered from above, order will set in at $T = T_t$ (figure 43b) *via* a nucleation and growth process. On the other hand, a sudden quench to a temperature below T_t can produce the situation depicted in figure 43c. The system responds to the instability through the generation of an ordering wave of wavevector corresponding to the minimum of $V(k)$. The wave swells in amplitude gradually, spreading order everywhere. Therefore, vis-a-vis nonequilibrium situations, one can think of an instability temperature T_{instab} ($< T_t$) below which *continuous ordering* occurs.

While the concept seems possible, there is as yet no direct evidence for the existence of the instability temperature, although in an experiment due to Bardhan *et al* (1977) on Cu_3Au there is a strong suggestion. The analogue of the Schwahn-Schmatz experiment (§ 4.3) would be desirable. Incidentally, the dashed line in figure 15b is the variation of T_{instab} with composition, as deduced from CVM.

In some situations, continuous ordering is possible with an interesting twist. Following the creation of an instability, the system responds with a compositional wave whose wave vector does *not* coincide with that corresponding to the superlattice reflection.

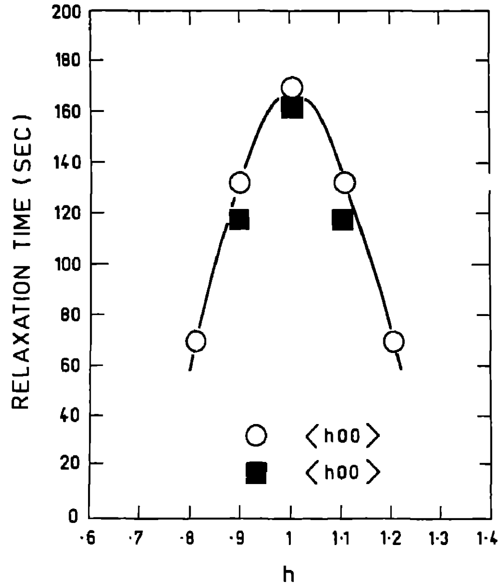

Figure 42. Wavevector-dependent relaxation time τ (k). Shown here are data obtained along ⟨h00⟩ and ⟨hh0⟩ lines. The continuous line is a guide to the eye (after Chen and Cohen 1977).

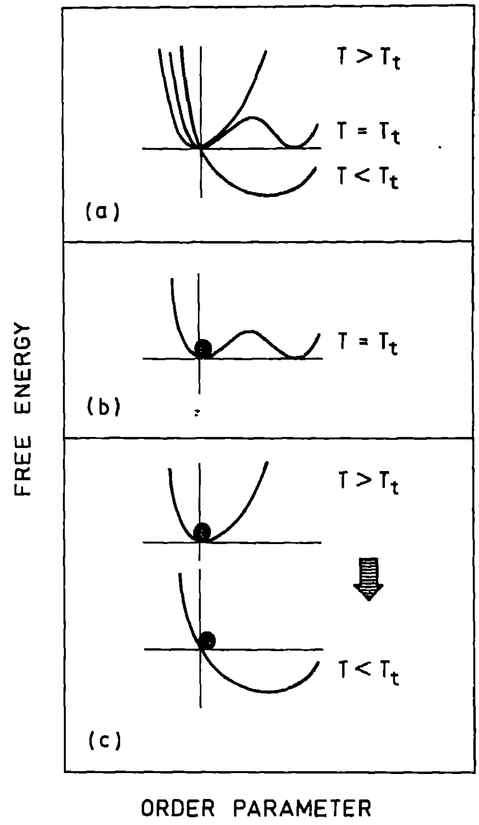

Figure 43. System response to different temperature treatments (a). free energy curves for a first order transition, with transition temperature T_t. When slowly cooled from above, the system experiences metastability on reaching T_t, and orders by a nucleation and growth process. If suddenly cooled to a temperature well below T_t as schematically illustrated in (c), it experiences an instability.

However, the system somehow seems to realize this during its evolution, and comes up with a suitable mid-course correction (rooted in nonlinearities?) so that the correct ordered structure results on attainment of equilibrium. Apparently, the point of maximum instability in reciprocal space need not always coincide with the wavevector corresponding to the ordering wave. de Fontaine (1975b) has suggested that Ni-Mo is a good candidate system for exhibiting such a schizophrenic behaviour! Here the instability is associated with a $\langle 1\ \frac{1}{2}\ 0 \rangle$ wave whereas the ordering is based on a $\langle 100 \rangle$ wave. There is some evidence from x-ray diffraction (Chakravarti *et al* 1974) and electron microscopy (Das *et al* 1973) in support of the idea but a convincing test would be through a suitably designed real-time experiment.

On the theoretical side, Cook *et al* (1969) extended the Cahn-type analysis (which was essentially applied to a continuum) to discrete lattice systems and demonstrated that under suitable conditions, ordering with the formation of a superlattice was possible. In fact, the curves of figure 22 are the products of such a *linear* theory. In an effort to incorporate nonlinearities, Billotet and Binder (1979) have followed the footsteps of Langer with, however, due allowance for the fact that the order parameter is *not* conserved. (Recall remarks made in § 4.2 regarding conserved and nonconserved order parameters). Earlier, Binder (1973) had tried a time-dependent Ginzburg-Landau type approach, with as much success as may be expected of a mean field theory.

Billotet and Binder (1979) report many numerical calculations but unfortunately, barring some simulation results, they do not have much experimental data to compare with. In fact Binder and Stauffer (1976) attempted to stimulate experimenters by explicitly calling attention to various aspects of the behaviour of electrical resistivity of binary alloys at phase transitions but the response of the experimental community does not seem to be adequate.

A few remarks now about late stage behaviour in ordering systems. It has been noted (Binder 1980b) that as in clustering reactions, one has to recognize the existence of two length scales (see figure 40), one of which is related to intradomain ordering and the other to domain size. Since one is dealing with an ordering reaction, the intradomain part can be conveniently explored near superlattice positions in a diffraction experiment. The domain-wall effects on the other hand, are best picked up in a small-angle scattering experiment.

There is another aspect of domain walls that has occasionally been mentioned in the literature (*e.g.* Gunton 1982) but does not appear to have been examined in depth. Now the formation of different domains is usually thought of in terms of nucleation of ordering in different regions and the subsequent growth of the latter, leading to the formation of interfaces. In the symmetry-breaking language on the other hand, each ordered region corresponds to a manifestation of one of the possible ground states. The macroscopic physical system is thus trapped in different ground states in different physical regions. The resulting configuration/defect (*i.e.* DW) is therefore a topological entity. The topological aspects of DWs have barely been investigated and are probably worth a closer scrutiny.

Finally, a brief hark back to long-period oscillations (see § 3.1) (Aubry 1981, 1983). One wonders whether some of the considerations in Aubry's analysis of incommensurate structures do not have relevance to LPO seen in some ordered systems. This also appears worth looking into.

We close this section by calling attention to an authoritative review by Freidel (1974) on the electronic aspects of order-disorder transformations (which we have skipped!). Physicists wishing to study order-disorder transformations, should not miss this paper!

5. What can experimenters do?

The title of this section is not intended to suggest that experimenters have been slack but merely that there is a dearth of certain types of information *e.g.* relaxation data.

Now each probe has its own characteristic sensitivity, and it is necessary to integrate for a certain time τ_M during the experiment to obtain a signal above the background. When exploring nonequilibrium phenomena this poses a problem if the relaxation time τ_R is less than τ_M. One then has to use an "arresting" technique as illustrated in figure 44, wherein the system is periodically "frozen" in its coast down and then monitored. For example, the data of figure 36 was obtained in this fashion. However, if the signal is strong, one may be able to follow temporal changes directly in realtime. Improvements are therefore necessary for many techniques, if realtime measurements are to become feasible. In some cases like electrical resistivity, the required sensitivities are already there but nevertheless, the capabilities do not appear to have been fully exploited. Where neutron and x-ray scattering are concerned, increase in the primary source strength is an important factor. The availability of synchrotron radiation sources is therefore a welcome development in respect of x-ray scattering. Hardly any results pertaining to phase transformations have been reported using synchrotron sources, and there is much room for innovation and ingenuity.

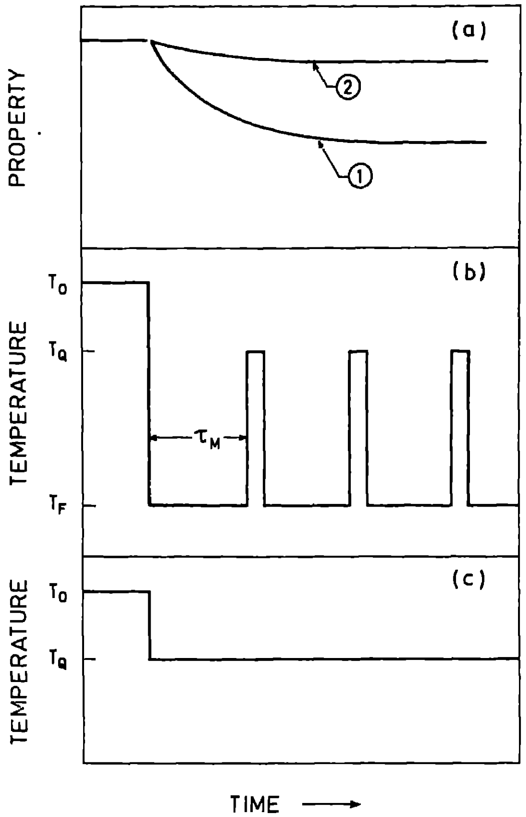

Figure 44. (a) Time variations of some property when a system is quenched as in (c). If the decay is rapid as in case (1), then the system must be periodically arrested in its coast down as illustrated in (b). This gives convenient measurement slots whose width τ_M can be chosen suitably to optimize (signal/noise) ratio. However, if the measurement time is small, then one can follow the decay in realtime i.e. the time-temperature profile will be as in (c). In the examples shown, this could be applied to case (2).

While discussing realtime measurements, it must be remembered that depending on the temperature, composition etc., the relaxation times can vary over several orders of magnitude. Attention is drawn in this context to the various quenches attempted by Lebowitz *et al* (1982) in their simulation experiments (see figure 38) and the wide spread in relaxation times observed by them. Thus, many techniques can in fact be used on an as-available basis without waiting for improvements, provided one chooses the conditions of experiment properly. In passing, it is worth noting that computer simulation is an expensive way of obtaining relaxation times. It is therefore very desirable to back it up with more extensive studies using a convenient probe (like resistivity).

The types of probes one could think of are many. Some, like resistivity, have already been mentioned. Others include internal friction, ultrasonic attenuation etc. Binder and Stauffer (1976) have discussed in detail how resistivity measurements can be linked to order parameter dynamics. They have also called attention to the need for conventional studies of scaling behaviour as one crosses the phase boundaries. For instance, it would

M-→ 5

be very interesting to follow the variation of resistivity with concentration at various temperatures as sketched in figure 45. The sharp rise and fall in the indicated regions are closely related to critical dynamics of the order parameter.

In contrast to "macroscopic" probes like resistivity, the Mössbauer effect provides a probe that is nucleus sensitive. Oki *et al* (1977) have, for example, exploited this method to examine aspects of transformations in Fe-Al alloys. There is clearly more scope for work of this kind. Indeed, one could also consider NMR. With high-power pulsed NMR systems now commercially available, relaxation studies of the type considered here are no longer a mere theoretical possibility. The neutron is yet another nucleus-sensitive probe. In addition, it can also undergo magnetic scattering. Both these factors can be skilfully exploited, particularly where magnetic alloys are concerned. As of now, there appear to be very few examples of ordering kinetics studied using neutrons. One investigation I am aware of is the experiment of Collins and Teh (1973) on Ni_3Mn. These authors upquenched in the ordered state, and for each step change ΔT of temperature, they measured the time required for the order parameter to stabilize to its new value. The kinetics of the order parameter were monitored *via* Bragg intensity of an appropriate reflection. Of course, a sophisticated technique like neutron scattering is not always required. Nowick and Weisenberg (1958) for example, simply followed the time variation of the Young's modulus in their upquench experiments on ordered Cu_3Au. In general, there is a paucity of information about system dynamics following a quench. One needs both upquench and downquench experiments, within a given phase (Binder 1977) as well as across a boundary.

While it is natural to think of relaxation time studies in the time domain, we should not forget traditional spectroscopy which also can give information about relaxation time, though of smaller magnitude. An experiment one could think of would be the analogue of the soft-mode studies made in connection with structural phase transitions (—for a review of this area, see Venkataraman 1979). There one has a lattice dynamical

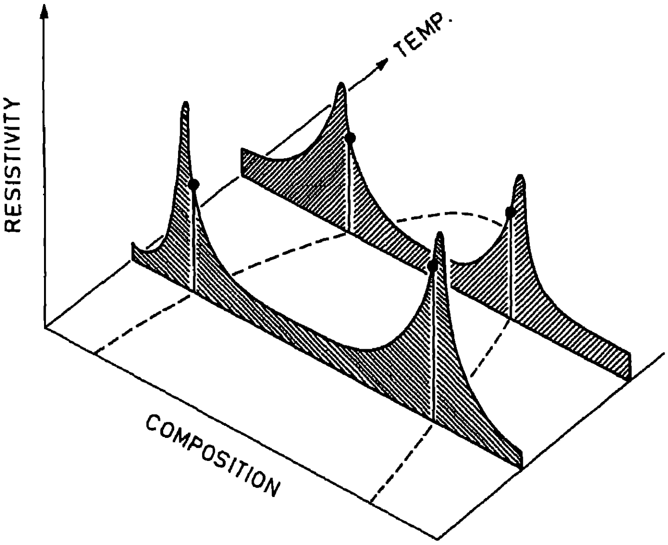

Figure 45. Schematic plot of resistivity *vs* composition at various temperatures. The dots show the regions where there is a sharp rise or fall. (after Binder and Stauffer 1976).

mode whose frequency diminishes as $T \rightarrow T_c^+$. In ordering reactions, we have a compositional wave but of zero frequency. The scattering of radiation from this wave gives rise to intensity in the superlattice region. If an energy scan is made of the scattered intensity (—and this is possible with neutrons), then one will observe a certain frequency spread around $\omega = 0$, the spread being related to the relaxation time of the concerned compositional fluctuation. As $T \rightarrow T_c^+$, the line width must decrease, indicative of critical slowing down of the compositional fluctuations. A systematic, quasi-elastic scattering investigation of the 'softening' of compositional fluctuations does not appear to have been made so far.

Our preoccupation with long-range order should not blind us to short-range order which too is an important quantity! As the name itself indicates, the focus is on ordering on a localized scale. The key quantity is the (Ising) spin correlation $\langle S_l S_m \rangle$. By suitable definitions (de Fontaine 1979), this spin correlation function can be related to the pair correlation function g ($\mathbf{R} = \mathbf{m} - \mathbf{l}$) well-known in theory of liquids, and to experimentally measured quantities like the Warren-Cowley parameters. Clearly, short-range order would be of particular interest in the early stages after a quench, and in the disordered phase close to T_c. With synchrotron sources now available, it may be possible to follow the evolution of short-range order in realtime, at least in select cases. The results can then be linked to models for spin dynamics. Other possible studies concerning short-range order have been mentioned in § 3.3.

At a recent Discussion Meeting on the Physical Basis of Mechanical Behaviour organized under the auspices of the Academy (where, incidentally, Prof. Ramaseshan delivered the keynote address), Dr G Srinivasan raised the interesting question of heat liberated following a quench. In the discussion that followed, Prof. C K Majumdar drew attention to the pioneering work of Bragg and Williams (1935) wherein the approach to order had been discussed in terms of a fictious temperature. Today, with our knowledge of magnetic resonance etc., we would identify this as the Ising spin temperature and the approach to equilibrium as a spin-lattice relaxation problem. This digression in the Discussion Meeting served to focus attention on the paucity of thermal measurements. Subsequently, I have come across one paper (d'Heurle and Gordon 1961) wherein calorimetry experiments on Au_3Cu during ordering are reported. By and large, studies on the energetics of ordering appear to be rare.

While comparing relaxation times obtained *via* different techniques, we should note that the coupling of the various probes to the order parameter is not the same. Moreover, some like resistivity, integrate the fluctuations of the order parameter over the wavevectors. Two such "integral" probes may not weight the different k's in the same manner. In this sense, x-rays and neutrons enjoy the advantage that one can select a specific wavevector for study. All the same, other probes have their own utility in that they are usually faster and also less expensive!

Thus far, we have confined attention to *equal-time* correlation functions of the form $\langle \psi(r, t)\ \psi(r', t) \rangle$. This function continually changes with time till equilibrium is attained at $t = \infty$. Probes like x-rays sample equal-time correlation function because they essentially produce an "instantaneous snapshot" of the system. We now extend consideration to *unequal* time correlation functions *i.e.*, functions of the form $\langle \psi(r, t)\ \psi(r', t') \rangle$. The relevance of such functions to experiment will be discussed shortly.

Billotet and Binder (1980) were the first to consider such functions in the context of phase transformations. The kinetics of such functions were modelled closely after Langer's and their own earlier work on equal-time correlation function. They start with the conditional probability $P^{\text{cond}}(\{\psi^1\}, t_1; \{\psi^2\}, t_2)$ which is the probability that the system is in the state $\{\psi^2\}$ at time t_2, given that it was in state $\{\psi^1\}$ at t_1. The continuity equation for P^{cond} is:

$$\frac{\partial}{\partial t_2} P^{\text{cond}}(\{\psi^1\}, t_1; \{\psi^2\}, t_2) = -\int \mathrm{d}\mathbf{r} \frac{\delta J_r^{\text{cond}}(\{\psi^1\}, t_1; \{\psi^2\}, t_2)}{\delta \psi_r^{(2)}}, \tag{77}$$

the expression for J_r^{cond} being an obvious extension of (48). The sequence of steps thereafter is essentially the same as before, and, as earlier, a decoupling approximation is made for $P(\psi_{r_1}^{(1)}, t_1; \psi_{r_2}^{(2)}, t_2)$ which is the probability that we have a state $\psi_{r_1}^{(1)}$ at $\mathbf{r}_1$ at time t_1 and a state $\psi_{r_2}^{(2)}$at $\mathbf{r}_2$ at time t_2. In this way, they finally arrive at the following expression for $S(\mathbf{k}, t_2, t_1)$:

$$S(\mathbf{k}, t_2 t_1) = S(\mathbf{k}, t_1) \exp\left[-C \int_{t_1}^{t_2} \mathrm{d}t \{Kk^2 + A(t)\}\right], t_2 > t_1. \tag{78}$$

with $C = Mk^2$ if the order parameter is conserved.

The need for unequal-time correlation functions arises from the fact that some techniques probe the system not instantaneously, but over a certain period of time. For example, in an ultrasonic attenuation experiment, a time ~ (1/frequency) is involved. Similarly, in a neutron inelastic scattering experiment, fluctuations on a time scale $t \sim (\hbar/\Delta E)$ are explored where ΔE is the energy transfer (Brockhouse 1958). Now in a system in thermodynamic equilibrium, one can exploit the fact that the system is stationary and express a correlation function of the form

$$\langle \psi(t)\, \psi(t') \rangle \text{ as } \langle \psi(0)\, \psi(t'-t) \rangle.$$

Stationarity however does not obtain in our kind of situations. At best, one can divide the whole time range into suitable slots, and hope for stationarity within each slot (Stratanovich 1963).

Figure 46 offers a schematic comparison of the measurement of equal-time and unequal-time correlation functions. The total time span from $t = 0$ (instant of quench) to $t = \infty$ (when terminal equilibrium is attained) is imagined to be divided into convenient (not necessarily equal!) intervals such that there is local stationarity in each time slot in the Stratanovich sense. An experiment like x-ray diffraction if done in real time, would give the "average" structure for each time slot. Fluctuations *within* each slot will not be explored. For that, it is necessary to either use a "frequency sensitive" probe or directly a correlation technique. Owing to the overall nonstationary nature of the process, the correlation function $C(k, \tau; n)$ will depend on the index n of the time slot.

As just indicated, one method of exploring fluctuations is to employ a frequency-dependent probe like slow neutron inelastic scattering. Billotet and Binder (1980) have used their model for fluctuations to compute $S(k, \omega; n)$. Their spectra show pronounced deviations from the usually expected Lorentzian line shapes; also there are oscillations. However, they obtain negative cross-sections which, as they themselves note, is unphysical. Billotet and Binder attribute this to the inadequacy of their approximations. If earlier experience in the theory of liquids is any guide (de Gennes 1959), then I suspect that the trouble probably lies in the fact that the decoupling approximation for P has failed to respect the relevant sum rules.

While as of now theory is in a somewhat poor shape, there is nothing to prevent experimenters from studying fluctuations under nonequilibrium conditions using the various probes at their disposal. In particular, slow neutron scattering, ultrasonic

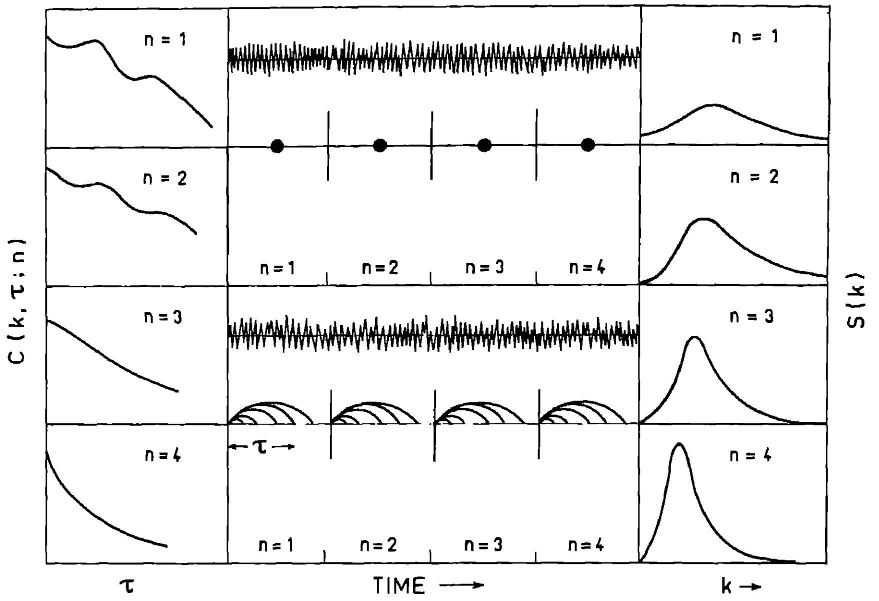

Figure 46. Shown in the middle are signals and their compartmentalization into slots indexed by n. In each slot, there is assumed to be stationarity. A conventional x-ray experiment measures equal-time correlation function for each slot, and the results finally appear as on the right. By performing an intensity correlation experiment in each slot, one can obtain information related to $\langle \psi(k, t)\psi(k, t+\tau) \rangle_n$ for each slot. Sketches of $C(k, \tau; n)$ are given on the left. For each n, one will have different $C(\tau)$ plots for the different k's.

attenuation, internal friction are some of the tools which could be tried. Vigorous experimentation could in fact act as a spur to theory!

An alternative method of exploring unequal-time correlation functions is to resort to the newly emerging technique of fluctuation spectroscopy (Magde 1977; Venkataraman 1982). Here one observes a suitable quantity Q (which couples to the order parameter) over a time span corresponding to one of our slots, and records all its fluctuations. One then processes the data to obtain $\langle Q(t)Q(t') \rangle_n$. One example of fluctuations observed by neutron scattering is given in figure 47 (Pederson and Riste 1980). Of course in this particular example the system was in a stationary state but that is not necessarily a requirement. In fact, Kim *et al* (1978) have carried out a similar experiment but using light, and have actually studied phase separation kinetics in a fluid binary mixture. Intensity fluctuation spectroscopy (Berne and Pecora 1976) is being regularly used for exploring biophysical problems but its use in condensed matter physics is still rare. Where alloys are concerned light scattering is not possible but one could resort to a study of resistivity fluctuations (*e.g.* Venkataraman and Balakrishnan 1979). No such experiment relating to kinetics of phase separation in solids has been reported so far. However, Kim *et al* (1980) have used precisely this technique to study fluctuations in a binary fluid mixture near its critical point. If sufficient intensity is available, even x-ray and neutron experiments to explore fluctuations in the time domain can be attempted. In brief, the entire subject of fluctuations during decay to equilibrium is largely unexplored both theoretically and experimentally.

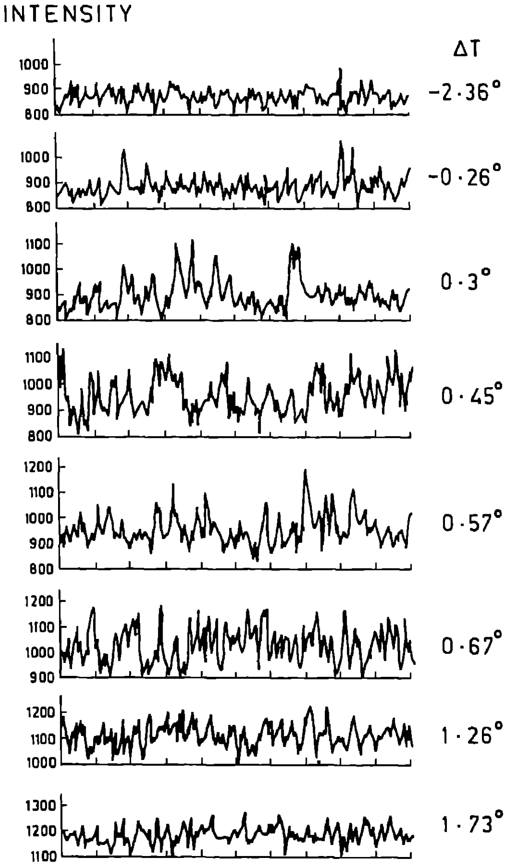

Figure 47. Fluctuations of the scattered neutron intensity from a liquid crystal with a temperature gradient across. The system is in a stationary but nonequilibrium state. Observe that as the temperature gradient is varied, the fluctuation amplitude becomes large at a certain stage. This is associated with the onset of turbulence in the material (after Pedersen and Riste 1980).

6. Lamellar eutectic growth

In addition to the solid-to-solid transformations so far considered, certain liquid-to-solid transformations are also interesting, besides being important technologically. To understand such transformations, we refer to figure 48 which shows a binary phase diagram of the type we are currently interested in. For example, Ag-Cu and Pb-Sn systems exhibit such diagrams. Consider an alloy of composition C_0 and at a temperature such that its state is represented by the point *a* in the figure. On cooling and crossing the liquidus curve, one enters the region marked $(\alpha + L)$ which is a two-phase region where a liquid and a solid both coexist, the solid with composition C and the liquid with composition C_L. The relative proportions of the solid and the liquid vary continuously as one moves down the line *abc* until at the temperature T_E called the eutectic temperature, the liquid (of composition C_e) freezes. Of course one could come down along *df*; then one would have a pure liquid phase until T_E at which point freezing occurs. This phase transformation *i.e.*, the freezing of the eutectic liquid is often called a eutectic reaction.

The solid state microstructure of the material having the composition C_e will be an intimate mixture of two phases α and β which are often present in the form of thin (around a few microns) platelets or rods. The lamellar microstructure of a typical

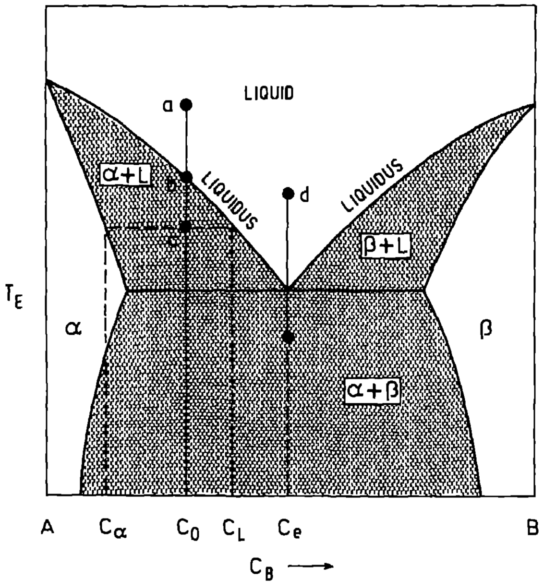

Figure 48. Illustration of the eutectic reaction.

eutectic is shown in figure 49 (Lyman 1972). The pattern is quite striking, undoubtedly reminding physicists of the patterns associated with hydrodynamic instabilities, for example. Indeed Langer has recently noted such similarities and has pointed out that as in the well-known Benard patterns associated with convective instability, the relevant steady state equations are incapable of predicting the unique behaviour observed experimentally. Specifically, the steady state theory of lamellar eutectic permits a wide range of lamellar spacings at any growth velocity whereas experiments seem to indicate a unique spacing. Accordingly, Datye and Langer (1981) have performed (as in hydrodynamics) a stability analysis for a model thinfilm eutectic. A major conclusion to emerge is that for off-eutectic compositions, there occurs a short wavelength instability. Figure 50 taken from the work of these authors shows a sketch of the oscillatory mode at its point of marginal instability. There is apparently some evidence from experiment for the existence of such a mode. As Langer notes, there is scope for much more work in this area both experimental and theoretical (especially in relation to kinetics). It certainly would be interesting to attempt experiments which are the analogue of those discussed in figure 47.

7. Summary

In this article, a broad overview of phase transformations has been attempted, essentially from a physicist's angle. While there are many aspects that might appeal to physicists, three areas have been highlighted since overlap with physics is manifestly evident. They are: The study of ground structures, the study of phase diagrams and the study of kinetics. In each area there are no doubt specifics and important details such as metallurgists are usually interested in, but there are also general features amenable to a basic analysis which physicists are likely to be attracted to.

In the area of ground state structures, the emphasis thus far appears to have been mainly on structures derived from bcc and fcc lattices. There is an obvious need to

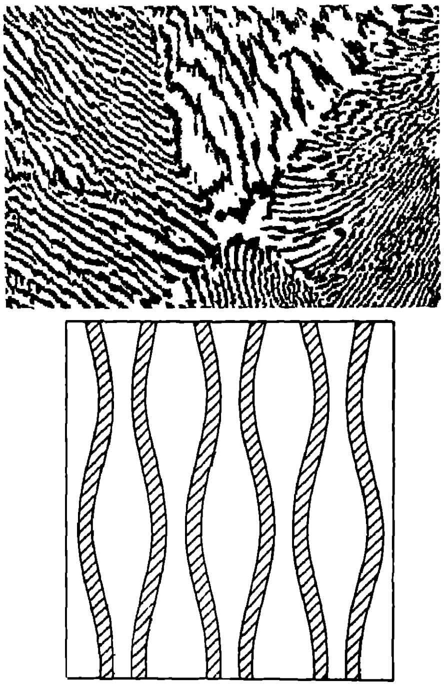

Figure 49–50. **49.** Picture of a 63 Sn-37 Pb eutectic (softsolder). The lead-rich solution appears dark in a matrix of tin lamellae (light) (after Lyman 1972). **50.** Oscillatory mode at its point of marginal instability (after Datye and Langer 1981).

extend this to other systems like hcp etc. We call attention also to formal papers (Progov and Sinai 1975, 1976; Slawny 1979) on the subject lest such activity be dismissed as pedestrian! Inputting potential derived from first principles has thus far been largely avoided but given the vast progress made in pseudopotentials in recent years and the prospects for bigger and faster computers, one could envisage a new thrust. No doubt there is the additional complication of relaxation energy (see equation (19)) but one now knows how to handle this, at least in principle.

Study of phase diagrams *via* simulation has made impressive progress but there is still a vast territory ahead. The viability of the CVM has been well established although there is room for improvement both in terms of going to larger clusters (which, incidentally, will call for fresh computational ingenuity) as well as allowing the exchange integral to vary with composition. The possibility of frustration is a stimulating discovery and so far, theory has not addressed itself to this question. Given the vigorous study made of this concept in spin glass, one could envisage exciting new vistas in the study of ordered systems also. The mappings that phase diagram investigations have achieved vis-a-vis models popular in the study of magnetism should act as an extra stimulant to physicists. Indeed one could probably now hunt around for suitable systems which are proving grounds for various kinds of Potts model etc.

As regards kinetics, there is a pressing need for real-time measurements. This therefore is an area where physicists can make important contributions, given their vast experience with the study of relaxations. Of course the experiments may not be always easy, and ingenuity may be required in many cases! Correlation techniques have a bright future if one is bold enough to apply them (although theoretical support for interpretation is at present not available). Neutron scattering and x-ray scattering (especially using synchrotron radiation sources) are the preferred tools but others like

Mössbauer spectroscopy, ultrasonic attenuation and even resistivity can provide useful complements, being less expensive and also less time-consuming. Thus, while neutron scattering could be reserved for select measurements, back-up wide ranging scans can come from the other probes mentioned. Where theory is concerned, the area of kinetics is a veritable jackpot in as much as one is faced with fascinating questions about phase changes far from equilibrium.

To keep the discussion relatively simple we have confined ourselves to substitutional systems (usually, metals with metals give such systems). If we extend consideration to systems where the B atoms enter interstitially in A (*e.g.* 0 in Ti), then it opens up a new world altogether. And then there are ternaries. No doubt they complicate matters, but who knows what surprises they have in store? In addition, there are the mixed oxides and mixed glasses which too, under certain circumstances, show phase separation. The interesting point about these systems is that they are amenable to study by light scattering (Schroder 1977), a technique we have barely mentioned. In respect of light scattering, the new wave of interest on colloidal crystals (Pieranski 1983) is also noteworthy. It is quite conceivable that various kinetic studies of colloidal crystals can be performed using laser light the way one usually investigates alloys using x-rays.

We have stayed away from defects, for example vacancies. One knows vacancies affect diffusion and therefore the role of vacancies may require examination. Perhaps for the present, these questions are best left to the metallurgists!

We have also not dwelt much on microstructure. Metallurgists relish them! Certainly the patterns are fascinating but one tends to dismiss any underlying universality on the grounds that microstructure is probably controlled by local factors like dislocation density etc. This may be true to some extent but at the same time it is difficult to believe that Nature has no basic rules governing domain formation etc. Now that some links between defects and symmetry have been established (Mermin 1979), it is worth searching for possible universalities governing microstructure formation and evolution. Such deep insight can come only from physics but it requires a really bold venture!

8. Concluding remarks

The story goes that towards the end of the twenties when the Golden Age of quantum mechanics was drawing to a close, Dirac remarked that, 'the rest is all chemistry'. Such an extreme view of physics has continued to prevail, and as late as 1970, van Hove (who has himself made notable contributions to condensed matter physics) observed during an after-dinner address at the Batelle Colloquium on Critical Phenomena that, "We should constantly recall and reassert that the elucidation of the fundamental laws remain the most essential task of physics". Referring to critical phenomena and topics of a similar kind he said, "It seems to me that physics now looks more like chemistry in the sense that in percentage, a much larger portion of the total research activity deals with complex systems, structure and processes, as against a smaller fraction concerned with the fundamental laws of motion and interaction. This Colloquium is a good example. Surely we all believe that the fundamental laws of classical mechanics, of the electromagnetic interaction and of statistical mechanics dominate the multivarious transitions and critical phenomena you discuss this week, and I presume that none of you expects his work on such problems to lead to the modification of these laws. You know the basic equations better than the phenomena. You are after the missing link between them *i.e.* the intermediate concepts ". . . . which should allow a quantitative understanding and prediction of the phenomena . . . ". Domb (1981) from whose essay on Critical Phenomena these quotes have been extracted, strongly disputes such a narrow interpretation of the goals of physics and points out that the goal is not restricted to the discovery of fundamental laws alone but encompasses the understanding of natural phenomena in general. Asserting that the giants of the past followed such an approach Domb observes, "Clerk Maxwell tried to construct a mechanical model to illustrate Faraday's laws of induction. He drew heavily on the theory of vortices in a perfect fluid and classical elasticity and was thereby led to introduce his famous displacement current. It was only later that he removed the 'scaffolding' to reveal the beautifully symmetric pattern of Maxwell's equations".

It is ironic that just around the time van Hove expressed his misgivings, Wilson did his celebrated work on critical phenomena which later earned for him the highest accolade of Science— the Nobel Prize. More significant, this paved the way for important feedback from statistical mechanics to particle physics (— *e.g.* there have been Monte Carlo simulations in connection with lattice gauge theories (Callaway and Rahman 1982), not dissimilar to the simulations discussed in §3.3).

In a different context, Anderson (1972) too has taken exception to the excessive importance attached to the study of fundamental laws. He observes, "The ability to reduce everything to simple fundamental laws does not imply the ability to start from those laws and reconstruct the Universe. In fact, the more the elementary particle physicists tell us about the nature of the fundamental laws, the less relevance they seem to have to the very real problems of the rest of science, . . .". Illustrating his point with examples from many-body physics, he questions whether a cooperative phenomenon like symmetry breaking (which lies at the heart of a phase transition) can be predicted starting purely from a knowledge of the basic interaction between the constituent elementary objects. As he succinctly puts it, more is different! Incidentally, symmetry breaking is another area where there has been a profitable feedback from condensed matter physics to particle physics.

The purpose of the above remarks and quotes is not merely to reinforce the point that condensed matter physics can as much be a frontier area, as, say, particle physics but also to remind condensed matter physicists that they in turn should avoid a snooty attitude towards materials science. As we have tried to argue in this article, there are many fascinating questions in materials science also, buried in the 'complexities' that traditional physicists shun. For those who dare to delve into these complexities and isolate the basic questions, the rewards could be great.

Beauty, it is said, is in the eyes of the beholder. Where physics is concerned, something similar appears to be true. The physics, turned out, often depends more on the investigator than on the phenomenon (at least the usual perception one has of it). We merely have to remind ourselves of the magical touch that Einstein gave to the observations of the botanist Robert Brown on the dancing pollen grain. What if he had dismissed it as 'not physics'?

In this country, Prof. Ramaseshan was perhaps the first person to establish a bridge between physics and materials science in a big way. Reared in the traditions of the Raman School, where the emphasis always was on natural phenomena in their totality, he was not averse to taking on the problems of materials when the challenge came. On the other hand, he invariably put to use his rich experience in physics and demonstrated that by doing so, one could introduce novel approaches to familiar problems. Not surprisingly, he made the plea at Baroda for a larger perspective while defining Thrust Areas. It has been a pleasant task for me to amplify and illustrate that theme through this article. I only hope it does full justice to his remarks.

Acknowledgements

My interest in this area was aroused by the lectures I heard a few years ago at Varenna given by Prof. de Fontaine. I am grateful to him for subsequently sending me several of his reprints and preprints which helped me dig deeper into the subject. I would also like to express my thanks to Dr D Sahoo for several discussions, to Radha Ranganathan for assistance with the preparation of the manuscript, to P Subba Rao for efficient and skilful typing and to P Harikumar and R Kannan for taking care of the graphics. Finally, I would like to acknowledge my indebtedness to the many authors whose work I have freely drawn upon in preparing this review.

References

Allen S M and Cahn J W 1972 *Acta Metall.* **20** 423
Anderson P W 1972 *Science* **177** 393
Aubrey S 1981 in *Physics of defects* (ed) R Balian et al (Amsterdam: North Holland) p 431
Aubrey S 1983 *J. Phys.* **44** 147
Bardhan P, Chen H and Cohen J B 1977 *Philos. Mag.* **35** 653
Barker J A 1953 *Proc. R. Soc.* (*London*) **A216** 45
Berne B J and Pecora R 1976 *Dynamic light scattering* (New York: Wiley)
Bethe H A 1935 *Proc. R. Soc.* (*London*) **A150** 552
Billotet C and Binder K 1979 *Z. Phys.* **B32** 195
Billotet C and Binder K 1980 *Physica* **A103** 99
Binder K 1973 *Phys. Rev.* **B8** 3423
Binder K 1977 *Phys. Rev.* **B15** 4425
Binder K 1980a *Phys. Rev. Lett.* **45** 811
Binder K 1980b in *Systems far from equilibrium*, Lecture Notes in Physics 132 (ed) L. Garrido (Berlin: Springer)
Binder K 1981 *Z. Phys.* **B45** 61
Binder K, Lebowitz J L, Phani M K and Kalos M H 1981 *Acta Metall.* **29** 1655
Binder K and Stauffer D 1976 *Z. Phys.* **B24** 407
Bragg W L and Williams E J 1934 *Proc. R. Soc.* (*London*) **A145** 699
Bragg W L and Williams E J 1935 *Proc. R. Soc.* (*London*) **A151** 540
Brockhouse B N 1958 *Nuovo Cimento* **9** (Suppl.) 45
Cahn J W 1961 *Acta Metall.* **9** 795
Cahn J W 1962 *Acta Metall.* **10** 179
Cahn J W 1968 *Trans. AIME* **242** 166
Cahn J W and Hilliard J E 1958 *J. Chem. Phys.* **28** 258
Callaway D and Rahman A 1982 *Phys. Rev. Lett.* **49** 613
Chakravarti B, Starke E A, Sparks C J and Williams R O 1974 *J. Phys. Chem. Solids* **35** 1317
Chen H and Cohen J B 1977 *J. Phys.* **C7** 314
Chen H, Comstock R J and Cohen J B 1979 *Annu. Rev. Mater. Sci.* **9** 51
Cohen J B 1970 in *Phase transformations* (ed) H I Aaronson (Metals Park Ohio: Am. Soc. Metals) p 561
Collins M F and Teh H C 1973 *Phys. Rev. Lett.* **30** 781
Cook H E 1970 *Acta Metall.* **18** 297
Cook H E, de Fontaine D and Hilliard J E 1969 *Acta Metall.* **17** 765
Clapp P C and Moss S C 1968 *Phys. Rev.* **171** 751

Das S K, Okamoto P R, Fisher P M J and Thomas G 1973 *Acta Metall.* **21** 913

Datye V and Langer J S 1981 *Phys. Rev.* **B24** 4155

de Fontaine D 1967 Ph.D Thesis (Evanston Ill: Northwestern University)

de Fontaine D 1975a in *Treatise on solid state chemistry* (ed) N B Hannay (New York: Plenum) p 129

de Fontaine D 1975b *Acta Metall.* **23** 553

de Fontaine D 1979 in *Solid state physics* (eds) H Ehrenreich, F Seitz and D Turnbull (New York: Academic) Vol. 34 p 73

de Fontaine D 1981 *Met. Trans* **A12** 559

de Fontaine D 1982 in *Mechanical and thermal behaviour of materials* (eds) C Caglioti and A Ferro Milone (Amsterdam: North Holland) p 449

de Gennes P G 1959 *Physica* **25** 825

d'Heurle F M and Gordon P 1961 *Acta Metall.* **9** 304

Dienes G J 1955 *Acta Metall.* **3** 549

Domb C 1981 in *Perspectives in statistical physics* (ed) H J Raveche (Amsterdam: North Holland) p 173

Feigenbaum M J 1978 *J. Stat. Phys.* **19** 25

Feigenbaum M J 1979 *J. Stat. Phys.* **21** 665

Feigenbaum M J 1980 *Commun. Math. Phys.* **77** 65

Freidel J 1974 in *Order-disorder transformations in alloys* (ed) H Warlimont (Berlin: Springer) p 1

Gilmore R 1981 *Catastrophe theory for scientists and engineers* (New York: Wiley)

Gunton J D 1982 *First order transitions, metastability and spinodal decomposition* (Temple: University Report)

Haken H 1978 *Synergetics, An introduction* (Berlin: Springer)

Hansen M 1958 *Constitution of binary alloys* (New York: McGraw Hill)

Hashimoto T, Miyoshi T and Ohtsuka T 1976 *Phys. Rev.* **B13** 1119

Hashimoto T, Nishimura K and Takeuchi Y 1978 *Phys. Lett.* **A65** 250

Holsztynski W and Slawny J 1978 *Commun. Math. Phys.* **61** 177

Hopper R W 1982 *J. Non. Crystall. Solids* **49** 263

Iliopoulos J 1980 *Contemp. Phys.* **21** 159

Johansson C M and Linde J O 1928 *Ann. Phys.* **86** 291

Kanamori J and Kakehashi Y 1977 *J. Phys.* **38** C7 274

Katsura S and Narita A 1973 *Prog. Theor. Phys.* **50** 1426, 1750

Kawasaki K 1972 in *Phase transitions and critical phenomena* (eds) C Domb and M S Green (New York: Academic) Vol 2 p 443

Khachturyan A G 1974 in *Order-disorder transformations in alloys* (ed) H Warlimont (Berlin: Springer)

Kikuchi R 1951 *Phys. Rev.* **81** 988

Kikuchi R and de Fontaine D 1976 *Scr. Metall.* **10** 995

Kikuchi R, Sanchey J M, de Fontaine D and Yamauchi H 1980 *Acta Metall.* **28** 651

Kim M W, Chou Y C, Goldburg W I and Kumar A 1980 *Phys. Rev.* **A22** 2138

Kim M W, Schwartz A J and Goldburg W I 1978 *Phys. Rev. Lett.* **41** 651

Kozlov E V, Demetryev V M, Emelyanov V N, Kormin N M, Taylashev A S and Stern D'M 1974 in *Order-disorder transformations in alloys* (ed) H Warlimont (Berlin: Springer) p 58

Krivoglaz M A and Smirnov A A 1965 *Theory of order-disorder in alloys* (Amsterdam: Elsevier)

Kudo T and Katsura S 1976 *Prog. Theor. Phys.* **56** 435

Langer J S 1969 *Ann. Phys.* **54** 258

Langer J S 1980 in *Systems far from equilibrium* Lecture notes in Physics 132 (ed) L Garrido (Berlin: Springer) p 12

Langer J S, Bar-on and Miller H 1975 *Phys. Rev.* **A11** 1417

Langer J S and Turski L A 1973 *Phys. Rev.* **A8** 3230

Lebowitz J L, Marro J and Kalos M H 1982 *Acta Metall.* **30** 297

Lifshitz I M and Slyozov V V 1961 *J. Phys. Chem. Solids* **19** 35

Lyman T (ed) 1972 *Atlas of microstructures of industrial alloys* (Metals Park, Ohio: Am. Soc. Metals) Vol 6, p 318 (picture no: 2628)

Magde D 1977 in *Molecular biology, biochemistry and biophysics* (eds) J Pecht and R Rigler (Berlin: Springer-Verlag) p 43

Mahan G D and Claro F H 1977 *Phys. Rev.* **B16** 1168

Mermin N 1979 *Rev. Mod. Phys.* **51** 591

Morita T 1972 *J. Math. Phys.* **13** 115

Nowick A S and Weisenberg L R 1958 *Acta Metall.* **6** 260

Ogawa S 1974 in *Order-disorder transformations in alloys* (ed) H Warlimont (Berlin: Springer) p 240

Oki K, Sagane H and Eguchi T 1974 *Jpn J. Appl. Phys.* **13** 753

Oki K, Yamamura A, Masaka M and Eguchi T 1977 *Trans. Jpn Inst. Metals* **18** 520

Onsager L 1944 *Phys. Rev.* **65** 117

Ornstein L S and Zernike F 1914 *Proc. Acad. Sci. (Amsterdam)* **17** 793

Paulson W M and Hilliard J E 1977 *J. Appl. Phys.* **48** 2117

Pedersen A M and Riste T 1980 *Z. Phys.* **B37** 171

Pieranski P 1983 *Contemp. Phys.* **24** 25

Progov S A and Sinai Y 1975 *Theor. Math. Fizika* **25** 358

Progov S A and Sinai Y 1976 *Theor. Math. Fizika* **26** 61

Radelaar S and Ritzen J M J 1969 *Phys. Status Solidi* **B31** 277

Richards M J and Cahn J W 1971 *Acta Metall.* **19** 1263

Sanchez J M and de Fontaine D 1978 *Phys. Rev.* **B17** 2926

Sanchez J M and de Fontaine D 1980 *Phys. Rev.* **B21** 216

Sanchez J M and de Fontaine D 1982 *Phys. Rev.* **B25** 1759

Sato H and Toth R S 1961 *Phys. Rev.* **124** 1833

Schwahn D and Schmatz W 1978 *Acta Metall.* **26** 1571

Shockley W 1938 *J. Chem. Phys.* **6** 130

Shroder J 1977 in *Treatise on materials science and technology* (eds) M Tomozowa and R H Doremus (New York: Academic Press) Vol 12 p 158

Singhal S P, Herman H and Koztorz G 1978 *J. Appl. Crystall.* **11** 572

Slawny J 1979 *J. Stat. Phys.* **20** 711

Stanley H E 1971 *Introduction to phase transitions and critical phenomena* (Oxford: Clarendon)

Stratanovich R L 1963 *Topics in the theory of random noise* Vol 1 (New York: Gordon and Breach)

van Baal C M 1973 *Physica* **64** 571

van Hove L 1953 *Phys. Rev.* **89** 1189

Venkataraman G 1979 *Bull. Mater. Sci.* **1** 129

Venkataraman G 1982 in *Mechanical and thermal behaviour of materials* (eds) C Caglioti and A Ferro Milone (Amsterdam: North Holland) p 278

Venkataraman G and Balakrishnan V 1977 in *Proceedings of the Indo-German Seminar on Radiation Damage* (Kalpakkam: RRC) p 273

Venkataraman G and Balakrishnan V 1979 *Mater. Sci. Bull. (India)* **1** 59

Villain J 1959 *J. Phys. Chem. Solids* **11** 303

Vineyard G H 1956 *Phys. Rev.* **102** 981

Wagner C 1961 *Z. Electrochem.* **65** 243

Wulff J 1971 (ed) Structure and properties of materials (Bombay: Wiley-Eastern) Vol II

Yamauchi H and de Fontaine D 1974 in *Order-disorder transformations in alloys* (ed) H Warlimont (Berlin: Springer) p 148

Bull. Mater. Sci., Vol. 6, No. 5, September 1984, pp. 901–922. © Printed in India.

Growth of research and development in rare metals extraction in India

C V SUNDARAM and C K GUPTA*

Reactor Research Centre, Kalpakkam 603 102, India

* Extractive Metallurgy Section, Bhabha Atomic Research Centre, Trombay, Bombay 400 085, India

Abstract. The ushering in of the era of high technology in our country witnessed the emergence and growth of several new technologies which are either totally unconventional or less common in otherwise well known and established areas of industrial practice. A vivid example of the second category of advances is found in the development of extractive processes for obtaining the less common metals particularly required for service in nuclear, aerospace and electronics industries. In this paper, the growth of research and development in rare metals extraction in India is surveyed from its infancy in the fifties to the present stature of a firm footed technology accredited with several directed achievements and well-developed maturity.

Keywords. Rare metal extraction; physical beneficiation; chemical beneficiation; breakdown process; separation process; halide metallurgy; electrolytic reduction.

1. Introduction

One of the greatest technological upheavals in the history of human civilization was triggered by the second world war. During the post war period a large spectrum of high technology industries flourished. The frontiers of established technologies expanded and new highways opened up in the hitherto unexplored regions. The march of human progress entered into what is variously referred to as the nuclear age, the space age and the electronics age.

If one looks at the mainstream technologies which defined the direction and sustained the momentum of such a total technological advance, achievements in metals and materials development stand out, having played a vital role. The development of appropriate metals and materials has always been crucial to transform scientific ideas into practical realities.

We witness today, in our country, wide-ranging activities in the fields of science and technology. Since independence, we have come a long way in securing such an expansion. It is a matter of pride that we observe in the national scene massive development programmes in a number of advancing technological areas, as for instance, in nuclear energy, aeronautics and aerospace, electronics and oceanography—thanks to the efforts made and the support given to usher in this new era.

Tracing back the sequence of science and technology development, it would seem to have started with the launching of the atomic energy programme in the country. Following the institution of the Atomic Energy Commission (AEC) and the modest beginnings made in the early fifties, many disciplines of science and engineering—of relevance to this programme—have evolved and flourished. The wide variety and scope in these disciplines have enabled the progressive transfer of the experience to other areas of science and technology. Developments in space, aeronautics and electronics have gradually entered the national scene.

Any discussion on technological growth has to lead a discussion on materials development which constitutes the supporting structure like a back bone. As indicated in figure 1, while many of the ferrous and non-ferrous metals that are in every day use, are also required for peripheral structural applications in modern technology, they are not adequate for the critical core component applications in these technologies. Several members of the rare metals group *viz* beryllium, titanium, zirconium, hafnium, vanadium, niobium, tantalum, thorium, uranium, plutonium and the rare earths, possess the unique combination of physicomechanical, nuclear, electronic, and chemical properties. Taken together, these characteristics have qualified many of the above mentioned metals for core component applications.

The extractive processes to obtain this specific family of metals indigenously at sufficient purity levels and in adequate quantities were not initially available. The development programme of AEC, however, proceeded on the basic assumption that as it progresses, an adequate, dependable and continuing supply of appropriate metals and materials will be assured. To relieve the dependence on overseas sources for the strategic materials and to keep scientific and technological progress from being impeded or slowed down by materials shortages, pursuits on metals and materials development received close attention. It is needless to mention here that without a strong and sound materials base, it is difficult to attain, in the long run, technological self-sufficiency, particularly in the frontier areas.

India is fortunately blessed with significant raw material reserves with respect to many of the strategic metals. Complete and proper utilization of our natural rare metal resources presupposes the availability of a comprehensive body of scientific knowledge and engineering experience in the field of metal processing. An organization with multidisciplinary resources and skill to support a large spectrum of research projects in virtually all phases of metallurgy (figure 2) could accomplish this feat. This responsibility was thus taken over by the various laboratory and industrial units of the Department of Atomic Energy and, in particular, by the Bhabha Atomic Research Centre (BARC). "Growth of R & D in rare metal extraction in India" then predominantly

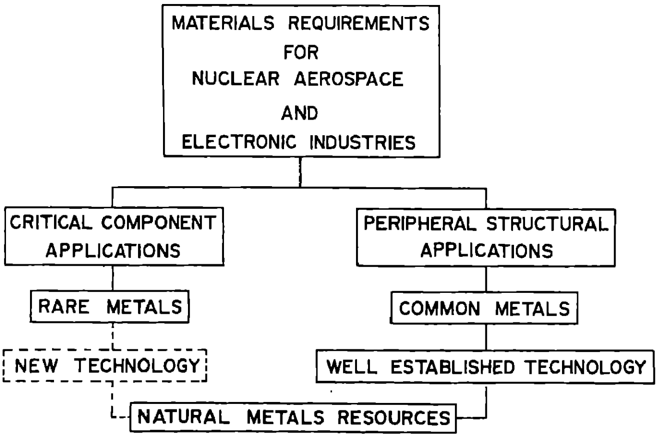
MATERIALS REQUIREMENTS FOR NUCLEAR AEROSPACE AND ELECTRONIC INDUSTRIES
CRITICAL COMPONENT APPLICATIONS
PERIPHERAL STRUCTURAL APPLICATIONS
RARE METALS
COMMON METALS
NEW TECHNOLOGY
WELL ESTABLISHED TECHNOLOGY
NATURAL METALS RESOURCES

Figure 1. Status of materials requirement in high technologies.

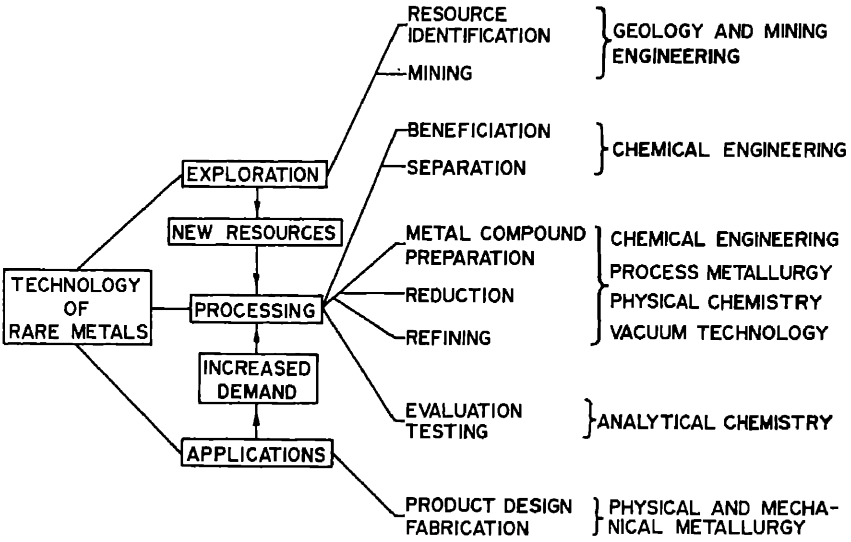

Figure 2. Multidisciplinary content of rare metal extraction.

pertains to tracing the process metallurgy activities of the DAE family during the past three decades.

2. Definition of rare metals extraction

Extractive metallurgy consists of the science and art of winning metals from the mined ore. For most common metals, the extractive metallurgy means the sequence of roasting, smelting and refining operations as indicated in figure 3. This scheme has characteristically failed to work in the extraction of many of the rare metals with which this presentation is concerned. Rare metals occur in nature in very complex forms, often in very low concentration. The procedures involved for recovering metal values are very elaborate, complex and require special equipment, processes and skill. Further, these metals show a high degree of sensitivity to impurities, which influence pronouncedly their physical, chemical and metallurgical properties. This dictates that the rare metals be properly protected at every stage of their production and use.

Broadly, the process sequence for rare metals, as indicated in figure 3 consists of the all important separation step followed by specialised reduction and refining operations. As a further elaboration, figure 4 presents a generalised scheme for rare metal extraction. For an appreciation of such a sequence, a brief reference may be drawn to the extractive metallurgy of niobium, the flow sheet for which appears in figure 5.

The joint occurrence of niobium and tantalum in nature conditioned by their close chemical similarities and the difficulties in separating them from each other halted their industrial development. In the past three decades, with substantial growth in demand and also in technology, complete flowsheets have been developed to get the pure metals in sufficient quantities.

The beneficiated columbite-tantalite ore is fed to the separation step. A pyrovacuum method was first attempted to separate the metals by chlorination but a hydro-

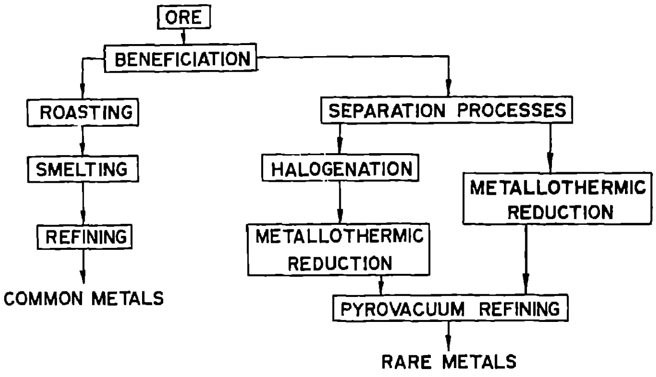

Figure 3. Extraction sequences for common and uncommon metals.

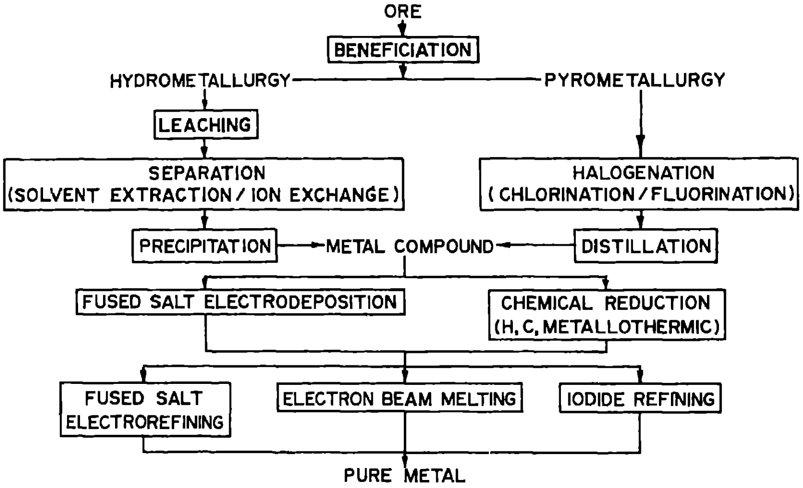
ORE
BENEFICIATION
HYDROMETALLURGY
PYROMETALLURGY
LEACHING
SEPARATION (SOLVENT EXTRACTION / ION EXCHANGE)
HALOGENATION (CHLORINATION / FLUORINATION)
PRECIPITATION
METAL COMPOUND
DISTILLATION
FUSED SALT ELECTRODEPOSITION
CHEMICAL REDUCTION (H, C, METALLOTHERMIC)
FUSED SALT ELECTROREFINING
ELECTRON BEAM MELTING
IODIDE REFINING
PURE METAL

Figure 4. Generalised scheme for rare metal extraction.

metallurgical route involving solvent extraction of the fluoride leach liquor of the beneficiated columbite-tantalite found industrial acceptance sooner. Pure niobium pentoxide obtained after the separation step is converted to the metal by either carbothermic reduction at high temperatures under vacuum or aluminothermic reduction and pyrovacuum refining. Depending on the purity desired, primary niobium is subjected to electron beam melt refining/electron beam floating zone refining to obtain the final product.

Now one can see the path niobium ore travels before it becomes metal. It may be added here that niobium is a well-behaved member of the rare metal family, and in many cases we may have to encounter tougher reactive rare metals.

3. Indian experience in rare metal extraction

The Indian experience in rare metal extraction has been founded on a commitment to provide means by which the current and emerging demands for special metals and

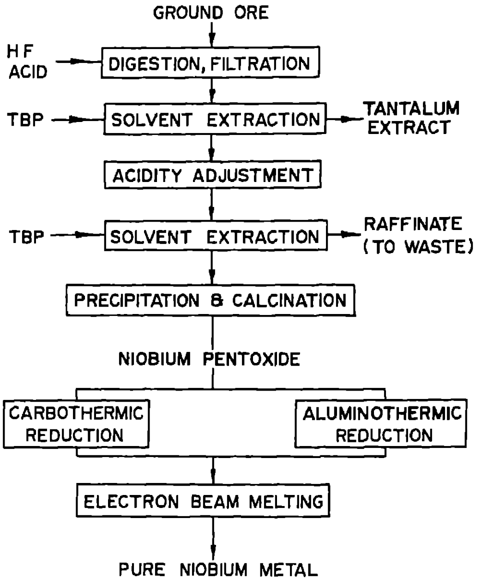

Figure 5. Flow sheet for niobium extraction.

materials in our country could be met. The emphasis has been on developing techniques effective on our indigenous resources. It is needless to say that this development of technology being totally indigenous, we encountered several teething troubles with respect to some processing steps due to scale up which were successfully overcome by persistent efforts. Every effort was made to introduce indigenous equipment which posed considerable problems and cost considerable time. Based on the research and development work at BARC administered mainly under the metallurgy, chemical engineering and chemistry groups, techniques and processes have been successfully evolved and developed to levels conducive to setting up of production plants. By way of some typical examples, mention may be made of:

—uranium oxide and metal production, involving ore leaching, ion exchange, solvent extraction, calcination, hydrofluorination and chemical reduction, induction melting, high temperature sintering and further fabrication;

—zirconium metal production by alkali fusion of zircon, solvent extraction, calcination, chlorination, magnesium reduction and vacuum distillation, vacuum arc melting, extrusion and pilgering;

—tantalum metal production by hydrofluoric acid dissolution of columbite-tantalite, solvent extraction, sodium reduction, powder metallurgy and electron beam melting;

—beryllium metal production by silicofluoride sintering of beryl, leaching, purification, fluoride decomposition, magnesium reduction, vacuum melting and vacuum hot pressing.

The experience has led to the setting up of the Nuclear Fuel Complex (NFC) at Hyderabad which for the past ten years has been engaged in the production of a range of nucler and special materials. Based on the parallel investigation on titanium sponge production and pilot plant demonstration at NFC, a larger production plant for the metal is under establishment at the Defence Metallurgical Research Laboratory (DMRL), Hyderabad. The pilot plant for beryllium, set up at Vashi, New Bombay has commenced operation.

Starting off from this introductory indication of the scope and level of directed R & D efforts that have gone into the emergence and rise of India in the rare metals field in the world, it is now appropriate to proceed a coverage of the Indian experience in more representative detail by looking at each of the unit operations in turn.

4. Physical beneficiation

It is a characteristic of all the rare metal resources that they occur as dilute, multicomponent complex minerals widely dispersed and distributed in various geological formations. Development of beneficiating techniques for these ores has, in fact, grown into a technology of lean ore beneficiation. This technology has also aided in many instances in the beneficiation of lean and complex common metal resources also.

In table 1 are listed the main rare metals minerals occurring in our country. Besides there are at least twice as many secondary minerals for each of these metals. There are then the second line reserves to be prospected. The principal beneficiating methods which are at our disposal are indicated in figure 6. One or more of these methods in combination have been employed for beneficiation. It is instructive to briefly review the processes applied to the important resources of many rare metals, beach sands.

Table 1. Important rare metal resources

Metal	Mineral	Composition	Location
Th	Monazite	(Ce, Y, Ca, Th) PO_4	Beach sands of Kerala, Orissa, Andhra Pradesh, Tamil Nadu
Zr	Zircon	$ZrSiO_4$	Beach sands
Ti	Ilmenite Rutile	$FeTiO_3$ TiO_2	Beach sands
Nb	Columbite	(Fe, Mn) Nb_2O_6	Hazaribagh, Monghyr (Bihar)
	Pyrochlore	$(Na, Ca)_2$ Nb_2O_6 (OH, F)	Dharmapuri Dist (TN), Khammam (AP), Gujarat, Bhilwada Dist (Rajasthan)
	Samarskite	$(Fe, Y, U)_2(Nb, Ti, Ta)_2O_7$	Pegmatites of Hazaribagh, Nellore, Jaipur and Tonk Dist of Rajasthan
Ta	Tantalite	(Fe, Mn) $(Ta, Nb)_2O_6$	Hazaribagh, Monghyr (Bihar)
	Microlite	$(Ca, Na)_2$ Ta_2O_6 (O, OH, F)	Hazaribagh, Monghyr (Bihar)
Be	Beryl (aquamarine, emerald, heliodro, morganite)	Al_2Be_3 (Si_6O_{18})	Bihar, Rajasthan, AP, MP.,
U	Uraninite	$(U^{+4}_{1-x}\ U^{+6}_{x})O_{2+x}$	Jaduguda, Singhbhum (Bihar)
	Pitchblende	Variety of uraninite	South Kanara (Karnataka)

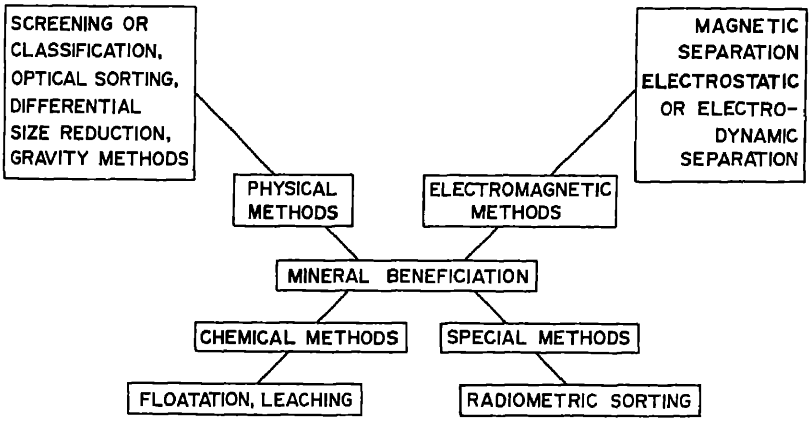
SCREENING OR CLASSIFICATION, OPTICAL SORTING, DIFFERENTIAL SIZE REDUCTION, GRAVITY METHODS
MAGNETIC SEPARATION ELECTROSTATIC OR ELECTRO-DYNAMIC SEPARATION
PHYSICAL METHODS
ELECTROMAGNETIC METHODS
MINERAL BENEFICIATION
CHEMICAL METHODS
SPECIAL METHODS
FLOATATION, LEACHING
RADIOMETRIC SORTING

Figure 6. Beneficiation techniques for rare metals resources.

Table 2. Typical mineral composition of monazite sands

Constituent	Percent
Monazite	0·5–1
Ilmenite	65–80
Rutile	3–6
Zircon	4–6
Sillimanite	2–5
Garnet	1–5

The commonly occurring minerals in beach sand deposits are ilmenite, rutile, zircon, monazite, sillimanite and garnet. Table 2 gives the typical mineral composition of the beach sands. The beach sand minerals occur extensively but in small concentrations in the alluvial deposits. The sand is mined by suction dredging and subjected to preconcentration with a view to obtain a bulk gravity concentrate comprising the heavy minerals. The lean sand deposit containing 2–5% heavy minerals is subjected to concentration using pinched sluices, cone concentrators, spirals and wet tables to obtain a concentrate with more than 80% heavy minerals. The separation of individual minerals is carried out by dry methods. Almost all the principal mineral dressing methods *viz* screening, gravity separation, magnetic separation, electrostatic separation, froth flotation etc are employed in the recovery of economic minerals from beach sand deposits.

Monozite, ilmenite, rutile and zircon are classified as scheduled minerals according to the Atomic Energy Act of 1962. Indian Rare Earths Limited operates three beneficiating plants—two at Manavala Kurichi in Tamil Nadu and one at Chavara, Kerala. Another plant is operated by Kerala Minerals and Metals Limited. At present the country's entire need of beach sand minerals is being met by IRE and KMM. Extensive dense sand deposits along the south Orissa coast over a stretch of 150 km has been located by Atomic Minerals Division and unlike the existing dry mill beneficiating operations, the Chatrapur operation would include a wet plant also for exploiting the Orissa deposit.

5. Chemical beneficiation and breakdown processes

The tenor of the uranium ores—uraninite, pitch blends, brannerite, uranothorite and carnotite—exploited for metal production assays usually around 0·05–0·2% U_3O_8. These low grade ores are directly leached to extract the uranium values since most of the physical beneficiation techniques have not been found economically feasible. There are many methods and techniques in leaching. Ore characteristics, material handling problems, methods employed for metal recovery from the pregnant solution, tailings disposal and many other factors determine the leaching technique.

Except in the case of high grade uranium ores or ores with a high concentration of acid consuming minerals which will necessitate alkali leaching with sodium carbonate, acid leaching with sulphuric acid is particularly suited to the dissolution of uranium values from the ore. As only hexavalent uranium is soluble in aqueous solution, the leaching is performed in the presence of an oxidising agent such as MnO_2, $NaClO_3$ and $Fe_2(SO_4)_3$. Acid concentration and pH are the two important process parameters. In the case of ores containing uraninite and pitchblende, such as the one at Jaduguda, acid concentration is normally controlled by maintaining pH of 1·5 to 2. This type of leaching, under controlled pH conditions helps in preventing the dissolution of acid consuming minerals like spatite. It has been found that high concentration of phosphate in the solution influences the oxidation potentials and complicates the uranium recovery process.

Besides aqueous leaching, chemical breakdown processes involve digestion with acid or alkali solution or more drastic fusion with alkali and alkali fluorides. The major breakdown processes commonly employed in our country to solubilize the metal values are schematically outlined in figure 7. It is understood that, as broadly presented for uranium, several parameters require control for accomplishing successful breakdown operation. The beryl ore is opened up to yield water soluble Na_2BeF_4 by fusing it with sodium silicofluoride and sodium carbonate at 700°C.

Having seen so far the established and commercially operating breakdown processes, we can briefly digress to see the direction for new developments.

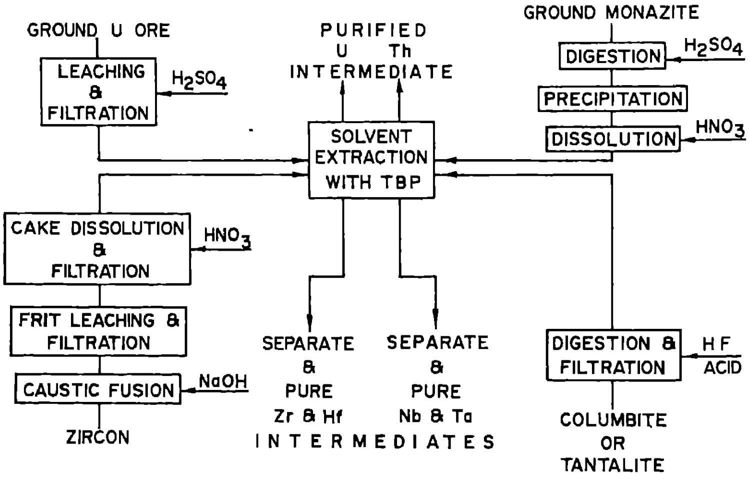

Figure 7. Schematics of ore treatment processes prior to solvent extraction separation.

A powerful new leaching technique is pressure leaching. Complex minerals like ilmenite and pyrochlore can be transformed into relatively pure oxides in a single step by treatment with hydrochloric acid at high temperature and pressure in an autoclave. References abound evidencing application of pressure leaching to many other minerals including those of uranium. A new approach to leaching low grade uranium ores is provided by the so-called bacterial or microbial leaching. Certain types of autotropic bacteria of the thiobacillus-ferrobacillus group act on the sulphate minerals like pyrite and lead to generation of ferric sulphate and sulphuric acid to leach out uranium.

Other breakdown methods developed to various levels of advancement include soda ash sintering of zircon, electrothermal smelting of ilmenite, beneficiation of ilmenite and zircon in plasma furnaces and chlorination breakdown of ores.

6. Separation processes

The leach solution obtained by chemical breakdown of the beneficiated ore is passsd through some unique sequence of "purification" operations peculiar to rare metal extraction. This purification of the pregnant rare metal solution is essentially to separate the co-occurring elements from the desired metal before it is put through subsequent reduction and refining operations. It must be emphasised that the elements co-occurring with the rare metals if allowed to proceed through the reduction step normally cannot be removed from the reduced primary metal by any of the common post reduction refining. This situation may be thought of as arising due to the great reactivity of the rare metals in general. A great deal of effort has gone into the development of separation processes for the purification of uranium and thorium to nuclear grades of purity, separation of rare earth metals from one another, niobium from tantalum and zirconium from hafnium. Of the many alternatives explored and studied at Trombay, two major processes have emerged for effective plant level utilization—solvent extraction and ion exchange.

In solvent extraction, the purification is achieved by selective extraction of compounds of a given element or impurities from aqueous solutions into an organic solvent which is immiscible with water. This is possible when the distribution coefficients of the components in the mixture differ from each other sufficiently. The distribution coefficient which is the crucial parameter in solvent extraction depends on the properties of the solvent, the concentration of the extracted species in the aqueous phase, the presence of other species in the solution, the acidity of the aqueous phase and the temperature. The studies conducted at Trombay were directed not only at optimising these conditions but also obtaining the engineering details such as selection of suitable solvent, collection of equilibrium data, determination of stages, mass transfer rates, choice of contacting equipment and scale-up.

A typical extraction flowsheet is given in figure 8. Starting from its application for recovering uranium from ore leach liquors, solvent extraction has grown in diversity and some of the important systems are presented in table 3. Solvent extraction is practised on a plant scale in our department for the extraction of uranium, thorium, plutonium and for the separation of zirconium from hafnium and niobium from tantalum starting from a variety of aqueous feed solutions using TBP as the organic phase and mixer settlers for contacting equipment.

Ion exchange has been the specialist separation process for use with very dilute feed

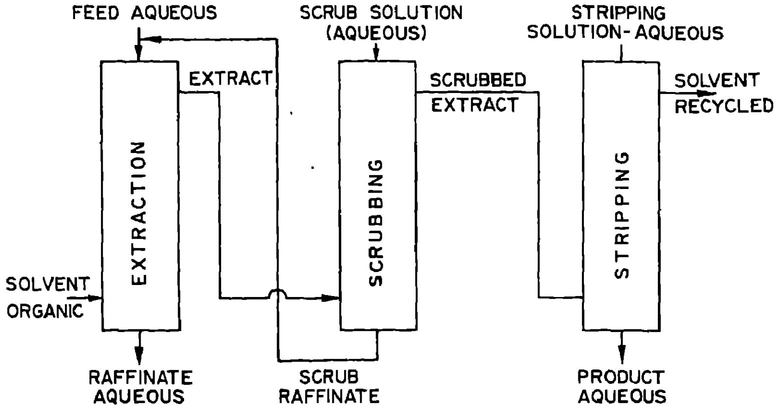

Figure 8. Typical solvent extraction flowsheet.

Table 3. Solvent extraction for separation for purification of rare metals

Metal	Organic phase	Aqueous solution	Remarks
U	TBP	Nitrate	Purification of U to nuclear grade
Th	TBP	Nitrate	Purification of Th to nuclear grade
Zr	TBP	Nitrate	Separation from Hf
Ta	TBP	Fluoride	Separation from Nb
Lanthanides	DEHPA	Chloride	Separation of individual lanthanides

solutions. The most spectacular application of ion exchange has been in the recovery of uranium from low grade ore leach liquors. It is especially better than solvent extraction in such cases.

Ion exchangers are sparingly soluble solids (organic or inorganic) with active functional groups which can be exchanged for ions present in the solution. The schematics of the ion exchange operation is given in figure 9. As the affinity of the ion exchange resin depends on the charge and size of the ionic species involved in the exchange and the distribution coefficient varies with the conditions of the aqueous phase like acidity etc, selective separation and purification can be achieved. Ion exchange separations are generally slow and operate on much less throughputs compared to solvent extraction processes. However as indicated already, for dilute solutions, in cases where separation factors are close and in some cases for processing unclarified solutions ion exchange is particularly sought after. Some important systems processed by ion exchange are given in table 4.

7. Halide metallurgy

The separation steps generally give the pure products in the form of either oxides or halides. These metal compound intermediates are converted to the metal by various reduction processes. Here again, peculiar for rare metals, one encounters a unique

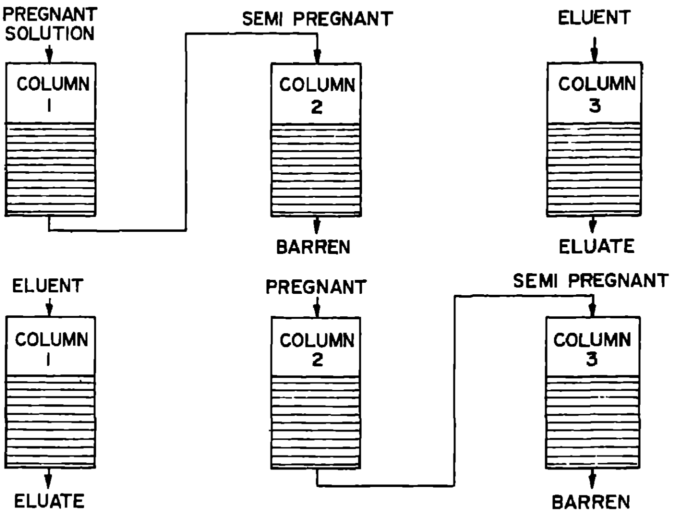

Figure 9. Ion exchange—adsorption, elution flow-sheet.

Table 4. Ion exchange separation for purification of rare metals

Metal	Ion Exchanger	Aqueous feed	Remarks
U	Deacidite FF(530)	Sulphate	Uranium separated from elements co-occurring in the ore
Zr	Cation exchanger ZK-225	Nitrate	Zr is separated from Hf
Ta	Anion exchanger EDE-10P	Fluoride	Ta is separated from Nb
Rare earths	Cation exchanger Dowex 50, ZK 225	Chloride	Rare earth metals are separated from each other

system of metal production. The intermediate which is reduced to obtain the metal is invariably a halide. The involvement of halides in rare metals extraction is certainly not restricted to the reduction step. Its omnipresent close involvement at many other stages of metal extraction also shall be looked into in what follows.

Halogens and halides find application in almost all stages of rare metal extraction from ore beneficiation to metal purification as given in figure 10. The diversity of halide metallurgy can be gauged from the following examples. (i) Ore breakdown: chlorination of zircon, ilmenite, rutile, silicofluoride treatment of beryl, zircon; (ii) Halogenation of crude intermediate: chlorination of zirconium carbide; (iii) Halogenation of pure intermediate: chlorination of zirconium dioxide, titanium dioxide; hydrofluorination of uranium dioxide; (iv) Reduction of metal halides: sodium reduction of K_2TaF_7, calcium reduction of UF_4 magnesium reduction of $TiCl_4$, $ZrCl_4$, BeF_2, electrolysis of RE chlorides; (v) Reclamation of scrap: by chlorination and fused salt electrorefining; (vi) Ultrapurification of commercial grade metal: iodide process for crystal bar titanium, zirconium and hafnium.

Starting with the gas-solid reactions, to carry out the entire range of processes as

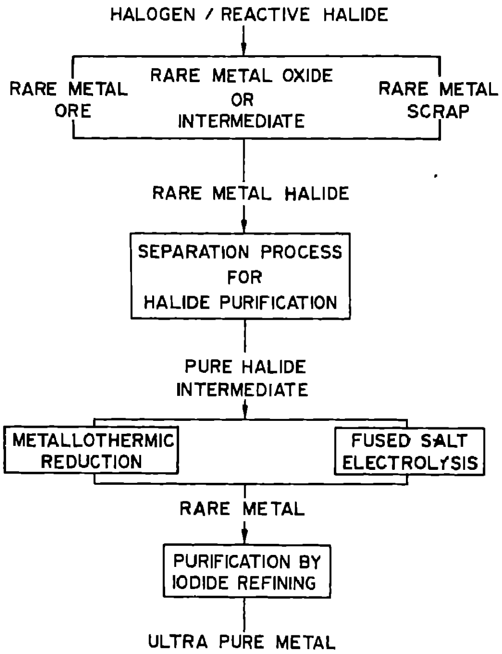

Figure 10. Halogenation in rare metal extraction.

indicated above, a large variety of reactors have been developed and process optimised at Trombay and later transferred to the industrial units of the Department.

The high temperature of these reactions and the corrosive nature of the halogen and the halide vapours, restrict the choice of the material of construction and the type of equipment for large scale operation. While nickel is compatible with fluorine and fluoride vapours upto 800°C, nickel and inconel alloys can withstand chlorine upto 600°C. In the production of $ZrCl_4$ or $TiCl_4$ that involves temperatures of 700–900°C, one has to use quartz or silica in the reaction zone.

Further, a halogenation plant will also include provision for safe metering of the corrosive halogens and the safe disposal of the unreacted halogens by neutralising with alkali or otherwise, due to high toxicity.

At Trombay, a rotating magnesium-tube lined reactor is employed for the production of UF_4 by the hydrofluorination of UO_2 powder. A special constructional feature of the reactor is that it has two concentric tubes with the annular space filled with an inert seal gas. The inside tube is made of magnesium to withstand the corrosive action of hydrofluoric acid, while steel is chosen for the outer tube for ease of fabrication and strength. The leak tightness of the seals between the rotating tube and the stationary end parts of the furnace is obtained by adopting the principle of positive gas pressure seal between teflon inner sealing rings and outer rubber sealing rings. The reactor is held in a slightly inclined position to facilitate smooth flow of UO_2 powder fed through a screw conveyor.

As a further example, one can look at the chlorinator used for the production of zirconium and titanium chloride.

The feed for static bed chlorinators consists of a mixture of oxide and carbon preformed into briquettes. The green briquettes are dried and coked at 800°C in inert nitrogen atmosphere to obtain highly porous briquettes for efficient chlorination. The large scale chlorination is carried out in a high purity silica brick lined furnace. The briquettes are heated by impressing three phase voltage across three graphite electrodes embedded in the charge. The carbonised briquettes possess sufficient electrical conductivity which improves with temperature, and with appropriate voltage and current control, the charge is slowly heated to the reaction temperature of 700–900°C. $ZrCl_4$ vapours evolving from the chlorinator furnace are condensed in a double walled inconel condenser at 150–200°C as dense crystals suitable for metal production. Blocking is a common problem in chlorinators. Hence pressure monitoring gauges, pressure release discs, and clearance ports have to be provided at critical locations.

Most of the chlorination reactions are exothermic in nature and require close control of temperature which is better achieved in fluidised bed reactors. These reactors also offer advantages like excellent gas-solid contact, good heat transfer, relatively inexpensive reactors and easier start-up and shutdown operations. Systems for the multistage fluidised bed hydrofluorination of UO_2 and the fluidised bed chlorination of zircaloy scrap in an inert bed have been developed at this Department.

The volatility of halides, the facility for purifying these by distillation and possibility of reducing these halides with metals like magnesium, sodium, and calcium have provided a powerful means for the production of reactive metals.

8. Metal reduction processes

The reduction of rare metal starts either from a halide or an oxide and follows the route as given in figures 11 and 12.

A majority of the rare metals have been produced by reducing their halides. The reason may either be that it is not possible to reduce the oxide directly at all (*e.g.* Ti, U, Be) or that it is more convenient to reduce the halide (*e.g.* Zr, Hf, Ta, Th).

9. Reduction of halides

The reduction of halides is accomplished by using the metals, sodium, magnesium or calcium as the reducing agent. Depending upon the physical properties of the reactants

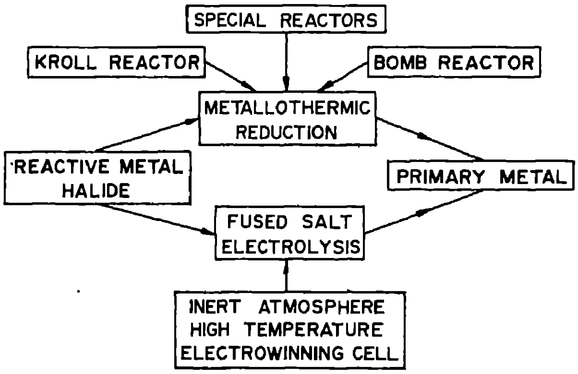

Figure 11. Reduction of rare metals—halide route.

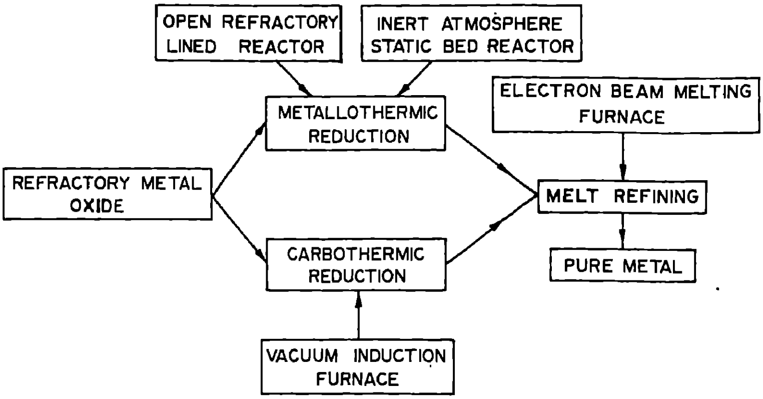

Figure 12. Reduction of rare metals—oxide route.

and products and the heat of reaction, the product metal is recovered as an ingot (U, Th), sponge (Zr, Ti) or powder (Ta). The reduction processes developed for U, Th, Zr, Ti, Ta and Be in fact provide fine examples of process metallurgy of fluorides and chlorides realised on an industrial scale for the production purposes. The exothermic metal reduction processes fall under two major categories—adiabatic (thermit type) and isothermal (Kroll type). Calciothermic reduction of uranium tetrafluoride is a fine example of the thermit type reaction. The uranium metal plant at Trombay has been producing consistently and efficiently uranium metal by the calciothermic reduction route.

In the Trombay practice, high purity UF_4 powder is intimately mixed with calcium granules and the mixture is charged into a leak tight tapered S.S. bomb reactor, which is initially lined with dry CaF_2 powder by vibratory packing. The CaF_2 lining serves for heat insulation and containment of the molten uranium. The calciothermic reduction is triggered—in an argon atmosphere—by electrically igniting a magnesium ribbon embedded at the top of the charge. The reaction is instantaneous, spreads rapidly through the mass, and the resulting liquid uranium droplets coalesce and collect at the bottom, forming a massive solid ingot on cooling.

A reduction route employing indigenous magnesium in place of imported calcium has been developed on a pilot plant scale is due to be adopted in the plant's expansion.

The calciothermic route described for uranium is applicable to the production of thorium and plutonium metals also.

The production of metals by the isothermal Kroll type reduction is exemplified by the magnesium reduction of zirconium tetrachloride. The process that has been tested on pilot plant scale at Trombay and adopted for tonnage production at the Nuclear Fuel Complex, Hyderabad is described below.

The reactor employs a specially designed S.S. retort and a three-zone furnace system for carrying out the reduction reaction. Zirconium tetrachloride and clean magnesium pigs are loaded in separate containers in the retort. After *in situ* purification of the chloride by pumping out the voltalite impurities at 300°C, the magnesium temperature is raised to above its melting point (to 850°C) and the chloride distilled in a controlled manner to react at the surface of molten magnesium. At the end of the reduction the excess magnesium and $MgCl_2$ are separated from the resulting zirconium sponge by pyrovacuum distillation in another heavy-walled retort capable of evacuation down to

< 1 micron at 900°C, the inconel retort is heated to 900°C using an evacuated bell-type furnace.

Similar reduction and pyrovacuum distillation equipment are suitable for production of titanium, thorium and hafnium metals.

For the production of tantalum powder from K_2TaF_7, a liquid-liquid reactor technique was developed at Trombay. Filtered high purity liquid sodium is continuously metered under argon cover on to the stirred mass of molten K_2TaF_7 and NaCl kept at 800–900°C in an inconel alloy 600 reactor. The tantalum metal powder is recovered from the reduced mass after leaching out the by-product fluorides with a series of aqueous reagents. This effort has extended to setting up of a production plant at NFC.

Calcium metal is unsuitable for the reduction of beryllium fluoride due to the formation of highly stable $CaBe_{13}$. Beryllium metal is produced in the form of pebbles by the magnesium reduction of BeF_2 in a graphite crucible in an induction furnace at 1100–1400°C. The metal pebbles owing to their lightness float to the surface of the slag. The beryllium pilot plant at Vashi, New Bombay is designed for the production of the metal and its alloys to meet indigenous requirement.

10. Reduction of oxides

The area of oxide reduction processes has been extensively investigated for producing a number of rare metals. The oxides are characterised by their good stability, they are easily prepared and are often the economically attractive intermediates in metal production processes. As specific examples of the advances at Trombay, reference may be made of fairly large scale production processes operated for preparation of zirconium, hafnium and thorium metal powders through calciothermic reduction of their respective oxides. Another notable advance has been in the aluminothermic reduction technology applied with great ingenuity in the preparation of niobium, tantalum, vanadium and molybdenum.

A metallothermic reduction process that does not generate excess heat and thereby avoids the growth or sintering of reduced metal particles is highly conductive to metal powder preparation. Calcium reduction of zirconium dioxide at 900°C generates only around 43 kcals per g mole of oxide. Further, the reduction is carried out in the presence of a heat sink like $CaCl_2$, very fine metal powder (predominantly 3 micron size) results dispersed in a matrix of CaO and $CaCl_2$. The metal powder is recovered from the reduced mass by careful aqueous leaching and drying. This technique has led to the establishment of a production facility for 1 ton Zr powder per annum at NFC.

Calciothermic reduction has also been investigated in detail for the preparation of hafnium, thorium, niobium and tantalum metal powders from their oxides. The process essentially consists of mixing the charge of calcium metal granules, metal oxide and calcium chloride heat sink in proper proportions and soaking it at the reduction temperature (950–1000°C) in flowing argon atmosphere, for sufficient time; the reduced mass is subsequently leached with dilute acids.

Unlike the static bed reduction described above, in a bomb process, highly exothermic reactions are conducted to prepare high melting metals in their consolidated form. To achieve this objective in reactions releasing inadequate heat, there are various means.

These include: (i) preheating to ignition, (ii) additives acting as thermal boosters, and (iii) combination of both.

The best reductant for the purposes just outlined is aluminium. The aluminothermic reduction may be described as combustion of aluminium to its oxide—the oxygen being released from the metal oxide. The reactions are carried out in an open vessel lined with refractory. The reactants at room temperature are mixed and charged and the charge is primed locally by means of an electric fuse embedded in the charge. In preheating to ignition, the entire charge is set to fire and the reaction is under near adiabatic conditions. The aluminothermic reduction, essentially a non-furnace process, proceeds rapidly to completion, but several hours of cooling is allowed before the contents are taken out. The metal if showing some slag adherence is cleaned by manual chipping.

A flowsheet, based on the aluminothermic reduction, for the production of niobium metal has been chosen for setting up of a plant at NFC.

Carbothermic reduction to produce refractory metals has become a reality only with the advancement in the regime of vacuum technology. The reactions are performed in a high temperature-high vacuum induction furnace where the pelletised oxide-carbon or carbide-oxide charge is reacted in the solid state to yield carbide or metal. A precise control of charge composition and the reaction conditions is very essential for obtaining pure metals having low residual carbon and oxygen contents. Adopting this process, complete flowsheets have been developed at the Metallurgy Division, BARC for the production of reactor grade niobium and capacitor grade tantalum metals.

11. Electrolytic reduction

For electrowinning of the reactive metals, only fused salt systems operating in an inert atmosphere have been found suitable.

Molten salt electrowinning processes for the preparation of refractory metals, particularly tantalum and titanium and rare earths like misch metal and cesium have been extensively investigated at Trombay. The metal compound (chloride, fluoride or oxide) is dissolved in a low melting eutectic salt mixture composed of two or more alkali or alkaline earth chlorides or fluorides. During electrolysis, the high melting rare metals are obtained as adherent dendrite deposits on the cathode (which is kept suspended in the fused salt) or alternatively if the adherence characteristics are poor, the metal is generated in the form of powder, in which case the cell itself is used as the cathode (and the anode is kept suspended).

Tantalum and titanium have been electrodeposited in the dendritic and sponge form by electrolysing KCl-NaCl melt containing respectively potassium tantalum fluoride and titanium chloride as functional salt. While for tantalum a centrally suspended metallic rod has been used as cathode, for titanium a perforated metallic basket served as the cathode. Such electrode arrangement for multivalent titanium has been found essential to separate the catholyte and anolyte.

In the pilot plant work on electrowinning of titanium, a 1000 amp internally heated inert atmosphere electrolytic cell has been used to standardise the parameters. The metals belonging to the rare earth group have been electrodeposited from all-chloride electrolytes.

12. Consolidation and purification of rare metals

The primary sponge metals and metal powders are required to be consolidated by melting or sintering prior to conversion to mill products. In some cases the melting or sintering operation refines the metal to an extent.

The tolerable limits of impurities in rare metals are quite low. All the properties which make these metals unique in comparison with other common metals are drastically impaired even by low levels of metallic and interstitial impurities. Therefore, great care and special techniques are employed in the refining operation as summarised in figure 13.

Most of the purification methods for rare metals involve high temperature and vacuum. The purification methods available for the rare metals include (i) vacuum melting, (ii) iodide refining, (iii) zone melting, and (iv) molten salt electrorefining.

Except the metals uranium and beryllium which are consolidated and to some extent refined by vacuum induction melting and casting, majority of the rare metals are consolidated and refined by arc and electron beam melting procedures. In both these methods, crucible contamination is eliminated by carrying out the meltings in watercooled copper crucibles.

In vacuum arc melting, the heat is generated on the surface of the molten metal by the application of a low voltage high current electric arc from an electrode which may be either consumable or nonconsumable. While nonconsumable method is suitable for consolidation of metals, no appreciable purification is achievable on account of the low vacuum involved. On the other hand, in the consumable arc melting, the material to be melted is preformed into an electrode which is progressively consumed during melting. The process has the advantage of operating under higher vacuum (10^{-2} to 10^{-3} torr) without contamination from electrode material and finds widespread use in the consolidation of rare metals. Facilities available at Trombay allow melting of 4 to 6 in. dia ingots of zirconium and titanium and at NFC metal ingots upto 12 in. dia can be cast.

Electron beam melting furnaces operate in high vacuum and provide high degree of super heat in the melt region and thus enable much greater refining than that possible with arc furnaces. In electron beam melting, the specimen is heated by subjecting it to

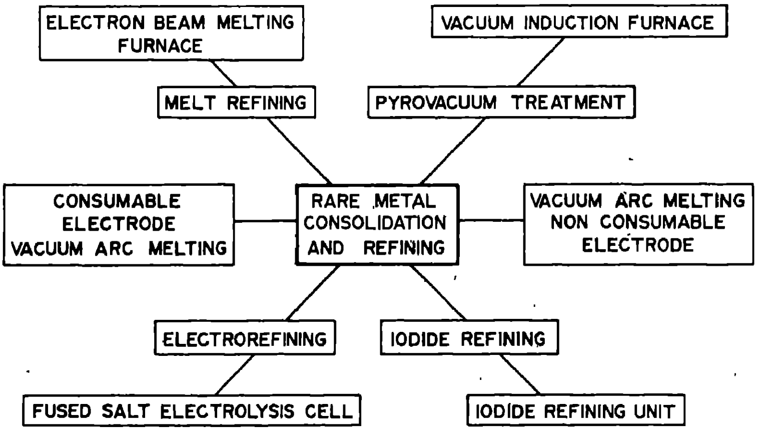
ELECTRON BEAM MELTING FURNACE
VACUUM INDUCTION FURNACE
MELT REFINING
PYROVACUUM TREATMENT
CONSUMABLE ELECTRODE VACUUM ARC MELTING
RARE METAL CONSOLIDATION AND REFINING
VACUUM ARC MELTING NON CONSUMABLE ELECTRODE
ELECTROREFINING
IODIDE REFINING
FUSED SALT ELECTROLYSIS CELL
IODIDE REFINING UNIT

Figure 13. Techniques for consolidation and refining of rare metals.

bombardment by a beam of high energy electrons under a vacuum better than 10^{-4} torr. Electron beam melting has, in fact, played a prominent role in its application to consolidation and purification of primary metals with widely different production history, and to preparation of metals with their finished purities meeting specific application requirements. Electron beam melting is effective and extensively used particularly in the production flowsheets of niobium and tantalum metals.

The reactions and processes that take place during vacuum melting and result in purification include (i) distillation of volatile impurities, (ii) vaporization of suboxides, (iii) carbon deoxidation, and (iv) vacuum degassing.

While vacuum melting is very effective in the purification of refractory metals it is not so with reactive rare metals like titanium, zirconium and hafnium. The so-called iodide refining has been found to be very effective in the refining of these metals.

Iodide refining, also known as the Van Arkel de Boer process, is based on the reversibility of a reaction between a metal and iodine. Purification of zirconium by this process has been studied extensively in the Metallurgy Division, BARC. The process is carried out in an evacuated inconel 600 vessel along the axis of which a high purity zirconium wire is aligned and electrically heated to 1300°C. The crude zirconium sponge is stacked inside the vessel in the annular space between the vessel wall and a concentric screen. Iodine required for the process is sublimed into the evacuated vessel. The vessel is externally heated to 250–400°C to form volatile ZrI_4 by reaction between zirconium sponge and iodine. The iodide vapours decompose on the surface of the high temperature zirconium filament resulting in a deposit of pure metal on it. The iodine vapours simultaneously liberated travel back for further reaction with the crude sponge.

A decomposition assembly developed at Metallurgy Division, BARC has been growing kilogram quantities of high purity crystal bars of zirconium, titanium and hafnium.

Zone melting is essentially a purification process by repeated crystallization from the melt. In practice two liquid-solid interfaces are produced for distribution of impurities by causing a relatively small molten zone to transverse the length of the bar of the charge. Many repetitions of the process lead to considerable purification even in cases where the distribution coefficient is close to unity. The impurities more soluble in the solid concentrate in the starting end.

It has been possible to produce kg quantities of metals such as Bi, Sb, Sn and Cd in their ultra-pure form for use in the semiconductor industry with zone refiners designed and fabricated at Trombay. A larger semi-automatic zone refiner is turning out ultrapure materials at NFC.

Zone refining in vacuum combines the benefits of conventional zone refining in a protective atmosphere, vacuum degassing and selective distribution of impurities. For refining of refractory metals an electron beam floating zone melting unit has been fabricated and used at the Metallurgy Division.

Electrorefining, next to electrowinning of metals is the most important aspect of fused salt electrolysis. While in electrowinning graphite has been found to be the most popular and inexpensive anode material, electrorefining cells essentially employ impure metal as the anode. The metal is crushed to suitable size and spread over the crucible bottom or packed in the annular space between the crucible and a perforated graphite screen to expose a large anode area. Molybdenum is the best reported cathode material in electrorefining. Iron has been used for vanadium electrorefining.

Molten salt electrorefining technique has been perfected for the preparation of high purity metals like niobium, tantalum, vanadium, molybdenum and chromium from their aluminothermically reduced alloy form. More recently electrorefining technique has been proved to be an effective mode for purification of calcium reduced hafnium. It has been possible to apply electrorefining for metal values of zircaloy scrap, and off-grade titanium sponge. Such purification technique has been found suitable not only for clean scrap but also for scraps contaminated with other metals and alloys which cannot be directly re-used in conventional remelting. Thus of all the refining methods applicable to rare metals, electrorefining stands out to be the most powerful technique with a wide range of refining capabilities.

13. Thermodynamics in rare metals extraction

In the development of process metallurgy of rare metals, the role of basic research particularly thermodynamic investigations has been very significant. Thermodynamic data have come to the rescue in many situations either during the choice of process parameters or in explaining many of the system behaviours. Though the involvement of thermodynamic analysis is very extensive and pervades almost all stages of rare metals reduction, refining and service, investigations concerning the vapour pressure and vaporization behaviours at elevated temperatures; solid solubility and phase diagram data have particularly been the main thrust areas for data collection and utilization. Investigations on metal-crucible interaction behaviours and decomposition processes can be cited for some of the direct application areas for thermodynamic data.

At the Extractive Metallurgy Section, several actual processes have been developed based solely on the available thermodynamic data of the system concerned. While it is impossible to carbothermically reduce zirconium and hafnium oxides, the important master alloys zirconium-niobium and hafnium-tantalum have been obtained by a carbothermic reduction process consisting of reduction of niobium pentoxide with zirconium carbide or tantalum pentoxide with hafnium carbide respectively. This scheme of reduction was worked out from the theoretical considerations of the thermodynamic stabilities of carbides and oxides and the stabilities and vaporization behaviours of the suboxides of zirconium, hafnium, niobium and tantalum. Another example of major flow sheet development that was visualised from the thermodynamic properties of the concerned compounds, is found in a recently concluded investigation on the preparation of pure niobium and tantalum through their nitride intermediates. The comparative stability of niobium and tantalum nitrides with respect to the niobium and tantalum carbides at moderate temperatures and the complete instability of these nitrides (in contrast to the persistent stability of the carbides) at higher temperatures and vacuum conditions has made it possible to obtain the pure metals starting from the oxides by a single sequential step consisting of (i) carbothermic reduction of niobium or tantalum pentoxide under a nitrogen atmosphere at 1500–1600°C to obtain the corresponding nitride and (ii) pyrovacuum decomposition of the nitride, at 2000–2100°C under 10^{-4} torr, to pure metal.

In addition to the above mentioned types of applications, thermodynamic analyses have extensively been employed in various pyrovacuum refining operations, leading to successful process operation, improved yield, reduction in number of processing steps and similar improvements.

14. Evaluation of rare metals

The development of flow sheets for the extraction of high pure rare metals has depended to a great extent on the parallel development and availability of powerful analytical techniques which enabled the evaluation of products at various stages. Special efforts are required particularly when the impurity concentrations are vanishingly low. The important analysis techniques applied in the rare metals evaluation are diagramatically presented in figure 14.

15. Concluding remarks

In the evolution and developments of flowsheets for rare metal extraction, the R&D effort has had many facets as summarised in figure 15.

As compared with the historical development of the process metallurgy of common metals, there has been a much more systematic and scientific approach to the chemical metallurgy of rare metals. This has been possible through many advances in analytical chemistry, physical chemistry, instrument and equipment development, physical and chemical engineering which have provided new technologies, and also through entirely

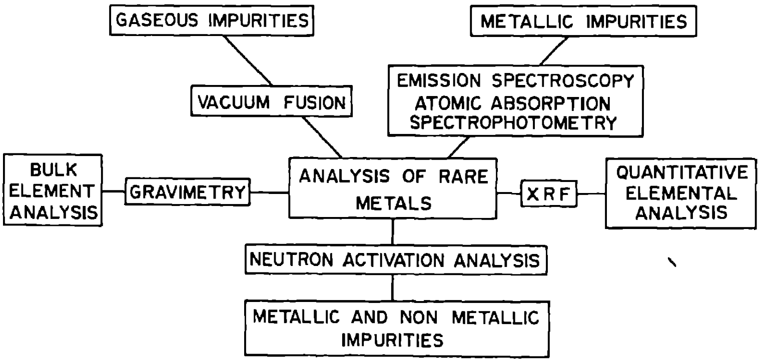
GASEOUS IMPURITIES
METALLIC IMPURITIES
VACUUM FUSION
EMISSION SPECTROSCOPY
ATOMIC ABSORPTION SPECTROPHOTOMETRY
BULK ELEMENT ANALYSIS
GRAVIMETRY
ANALYSIS OF RARE METALS
XRF
QUANTITATIVE ELEMENTAL ANALYSIS
NEUTRON ACTIVATION ANALYSIS
METALLIC AND NON METALLIC IMPURITIES

Figure 14. Evaluation of rare metals.

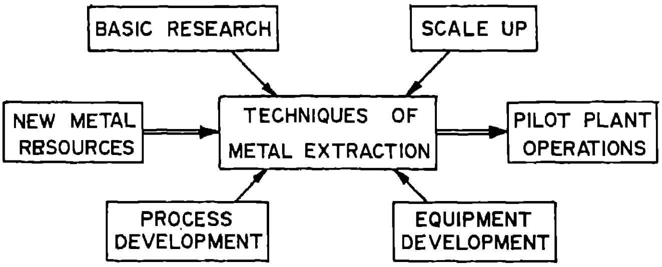

Figure 15. Development of extractive processes for rare metals.

novel metallurgical engineering designs. Our basic understanding of chemical and metallurgical systems, phenomena and reactions has also vastly improved through progress in theory and experiment in rare metals extraction.

Although process metallurgy of rare metals has grown into a powerful, mature and composite discipline, a good deal of scope for further R&D efforts still remains. Specifically one can mention fertile areas like pyrochemical counter current fused salt reactors for achieving separation of zirconium from hafnium, adoption of fluidised bed reactor for gas solid reactions, employment of plasma processing techniques for mineral beneficiation and refractory metal reduction—all of which deserve detailed study.

An interesting aspect of development of processes for rare metals extraction has been that many of these new techniques have important relevance to the common metals processing also. Special mention may be made of the prospects of solvent extraction processes in the copper and nickel industries and ion exchange in certain by-product metal recovery processes from effluent solutions, chlorination processing of complex sulphide ores, and vacuum melt refining.

Growth, development and maturity in operating practice have marked the evolution of various process options taken for investigations at BARC. Whenever possible and desirable, the process development was pursued through the various stages and led to its logical conclusion—setting up of operating production facilities. An important aspect that has marked this style of evolution is that the person or persons who have conceived, tested and developed the idea and the process have also been given the opportunity of setting up the plant and running it. This has made further growth and expansion of the plant feasible and easier. In certain cases, the nature of the project is more suited for effecting a transfer of technology to organizations outside the department. In this context, it is well worth noting that the technology of aluminothermic reduction of ferroalloys viz., ferrovanadium, ferroniobium, ferromolybdenum and ferrotungsten—so well mastered at the Extractive Metallurgy Section has been transferred to industries in Madhya Pradesh. In another instance, based on the flowsheet and technology developed at the Extractive Metallurgy Section, a demonstration plant for the processing of casseterite concentrates is being set up at Raipur by Metallurgy Division jointly with the Madhya Pradesh State Mining Corporation. One would appreciate that such instances are tantamount to bringing the advanced research facilities and expertise within the reach of a wider section of industries and to the greater service for our country's mainstream industrial activity.

The foresight and imagination in the organisation, of the successive stages of the programme, has paid good dividends; strong and comprehensive base that we now have in rare metals processing industry should inspire confidence for further growth and diversification of this technology in our country.

Acknowledgement

The authors appreciate the manysided help rendered by Shri N Krishnamurthy, Metallurgy Division, BARC in the preparation of this paper. Contributions from the various research groups, particularly from the Metallurgy, Chemistry, Chemical Engineering and Ore Extraction Divisions of BARC, Bombay and the Nuclear Fuel Complex, Hyderabad have actually provided the basic theme of this present article.

Representative bibliography

Damodaran A D, Deshpande S G, Majumdar A A, Sastri M S, Jena P K, Bose D K, Chandra S, Gupta C K and Taneja A K 1970 *Proc. Indian Nat. Sci. Acad.* **A36** 306

Gupta C K 1972 in *Recent developments in metallurgical science and technology, Proc. IIM Symp. on Process Metallurgy*, New Delhi p. 515

Gupta C K 1984 Extractive metallurgy of niobium, tantalum and vanadium *Int. Metals Rev.* (Under Publication)

Gupta C K and Sundaram C V 1973 *The Banaras Metall.* **5** 190

Krishnamurthy N, Venkataramani R, Garg S P and Sundaram C V 1981 in *Trends in refractory metals, hard metals, and special materials and their technology, Proc. Tenth Plansee Seminar Metallwerk* Plansee, Reutte, Vol. 1, p 263

Mukherjee T K, Bose D K and Gupta C K 1972 in *DAE Symp. High. Temp. Mat.* Hyderabad, p. 221

Mukherjee T K and Gupta C K 1976 *Trans. SAEST* **11** 127

Mukherjee T K, Garg S P, Gupta C K, Sundaram C V, Taneja A K and Damodaran A D 1978 in *Electron beam melting and welding, Proc. Int. Conf.*, Avignon

Proc. INSA-BARC Winter School on Chemistry and Metallurgy of Rare Metal Extraction, BARC (Jan 1975)

Saratchandran N and Sundaram C V 1970 in *DAE Materials Science Symp.* NAL, Bangalore, p. 251

Subramanyam R B, Saratchandran N and Sundaram C V 1973 *J. Sci. Ind. Res.* **32** 672

Subba Rao K S, Sharma B P, Paul C M and Sundaram C V 1977 *Beryllium development programme in India*, Conf. Preprints: Beryllium, *Fourth Int. Conf.* on Beryllium, The Metals Society, London

Sundaram C V, Garg S P and Sehra J C 1979 in *Metal sciences–The emerging frontiers, Proc. Int. Conf.*, The Indian Institute of Metals

Sundaram C V and Sharma B P 1972 in *Recent developments in metallurgical science and technology, Proc. IIM Symp. on Process Metallurgy*, New Delhi, p. 479

Sundaram C V and Suri A K 1976 in *High temperature reactions and processes Proc. KREC*, Suratkal p. 27

Bull. Mater. Sci., Vol. 6, No. 5, September 1984, pp. 923–958. © Printed in India.

Plutonium metallurgy in India

P R ROY and C GANGULY
Radiometallurgy Division, Bhabha Atomic Research Centre, Bombay 400085, India

Abstract. The embryo of plutonium metallurgy in India, as well as in Asia, was formed nearly 25 years back in Trombay. Thereafter, in the intervening 25 years, significant amount of research and development work have been carried out at BARC on this man-made fissile element and indigenisation has been achieved in the fabrication, characterisation and property evaluation of plutonium metal, delta-stabilised alloys, Al-Pu fuels, Pu-Be neutron sources, $(UPu)O_2$ fuels for thermal and fast reactors and (UPu)C and (UPu)N advanced fuels for liquid metal-cooled fast breeder reactors (LMFBR).

This paper summarises the development of plutonium metallurgy in India highlighting the safety aspects, our achievements and potential of plutonium for generation of nuclear electricity in the coming decades.

Keywords. Plutonium; fissile; delta-stabilised alloys; Al-Pu fuels; Pu-Be neutron sources; Mixed oxide and carbide fuels; fast breeder-test reactor; liquid metal-cooled fast breeder reactors; nuclear electricity.

1. Introduction

The metallurgy of plutonium, the man-made unique and most unusual metal, was introduced in India in 1960 when a team consisting of a chemist, a chemical engineer and a metallurgist successfully isolated mg quantities of plutonium metal beads in the Trombay laboratory by calciothermic reduction of plutonium tetrafluoride. Thereafter, in the intervening 25 years, there has been an enormous scale-up of production and extensive investigation of plutonium metal, its alloys and compounds. A sophisticated plutonium metallurgy laboratory for safe and secured fabrication and characterisation of plutonium fuels has come up in Trombay and today we are on the threshold of intensive utilisation of plutonium for generation of nuclear electricity and breeding of fissile materials simultaneously.

Plutonium does not occur in nature but is synthetically formed by the transmutation of the naturally occurring $^{238}_{92}U$. Soon after its discovery by Seaborg, Wahl and Kennedy in February 1941, in the Berkeley laboratory in USA, plutonium served as a major ingredient of the Manhattan nuclear weapon project during the second world war (Seaborg 1958). However, today it is most significant because of its peaceful potential as a nuclear reactor fuel offering energy thousand times greater than all available fossil fuels.

From the very inception of nuclear energy programme in India in the mid 1950s, the tremendous potential of plutonium for unlocking the huge energy reserves of our limited uranium (Rao 1982) (~ 60000 tons) and abundant thorium (~ 320000 tons) resources was recognised. Accordingly, laboratory separation and analytical procedures for plutonium started in Trombay in 1958 and by 1964 our spent uranium fuel reprocessing plant for recovery of plutonium was commissioned, for the first time in Asia.

The present dissertation summarises the milestones of plutonium metallurgy in India, highlighting our achievements in development and fabrication of plutonium metal and plutonium bearing metallic and ceramic fuels and our future programme for utilisation of plutonium for generation of nuclear electricity.

2. Formation and separation

As is known, uranium occurring in nature contains mainly two isotopes, *viz.* ^{238}U (99·3 %) and ^{235}U (0·7 %). The present generation of nuclear reactors derive energy from the fission of ^{235}U by slow or thermal neutrons and use natural uranium or 2 to 4 % ^{235}U enriched uranium in the form of metal or oxide as fuels. The fission reaction is as follows:

$$^{235}_{92}\mathrm{U} + {}^{1}_{0}\mathrm{n} \rightarrow {}^{236}_{92}\mathrm{U} \rightarrow \text{fission fragments} + 2 \text{ to } 3\ {}^{1}_{0}\mathrm{n} + 200\ \mathrm{MeV}.$$

One of these released fission neutrons is needed for maintaining the chain reaction and out of the remaining neutrons some are captured by the fertile ^{238}U to form ^{239}U which undergoes two successive beta decays, as shown below, leading to the formation of ^{239}Pu, which is an excellent fissile material:

$$^{238}_{92}\mathrm{U} + {}^{1}_{0}\mathrm{n} \rightarrow {}^{239}_{92}\mathrm{U} \xrightarrow[23\cdot5\ \mathrm{m}]{\beta^-} {}^{239}_{93}\mathrm{Np} \xrightarrow[2\cdot3\ \mathrm{d}]{\beta^-} {}^{239}_{94}\mathrm{Pu}$$

Thus, the nuclear reactors, apart from generating power also produce fissile ^{239}Pu as a byproduct, through neutron capture by the fertile ^{238}U. Other prominent isotopes of plutonium namely ^{240}Pu, ^{241}Pu and ^{242}Pu are formed from ^{239}Pu by successive neutron captures. The isotopic content of plutonium in a thermal reactor and the formation of plutonium radionuclides and daughters depend on such factors as discharge burn-up of the fuels, neutron flux and energy spectrum, fuel enrichment, moderator to fuel volume ratio, fuel diameter, cladding materials etc., and are shown in figures 1 and 2 respectively. Typical isotopic composition of plutonium(3) from the spent fuel elements of the 40 MW (th) CIRUS test reactor in Trombay, the 200 MW(e) boiling water reactors (BWR) at the Tarapur Atomic Power Station (TAPS) and the pressurised heavy water reactors (PHWR) at the Rajasthan Atomic Power Station (RAPS) are given in table 1.

The irradiated or the spent uranium fuel elements are a mixture of depleted uranium (^{238}U + < 0·7 % ^{235}U), highly radioactive fission fragments and plutonium. The major

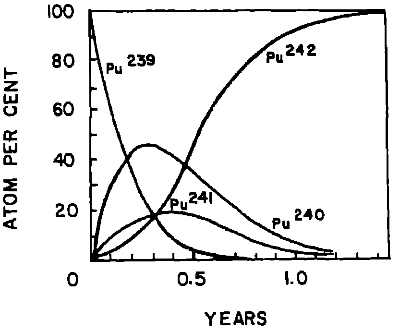

Figure 1. Plutonium isotopic composition as a function of exposure to thermal neutrons.

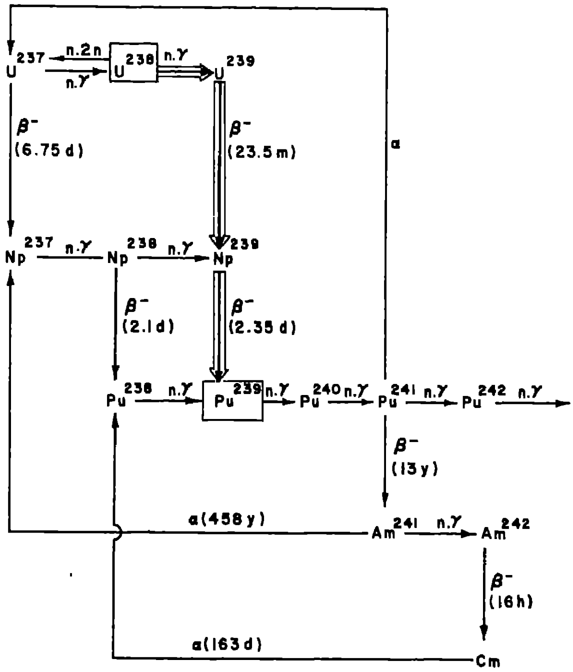

Figure 2. Plutonium radionuclides and daughters.

Table 1. Isotopic composition of plutonium from different reactors.

Reactor	Burn-up (MWD/ton)	^{238}Pu (w/o)	^{239}Pu (w/o)	^{240}Pu (w/o)	^{241}Pu (w/o)	^{242}Pu (w/o)
BWR	6100	0·125	82·7	13·94	2·89	0·339
(TAPS)	9500	0·203	73·54	20·31	4·81	1·080
	13750	0·393	65·77	25.17	6·45	2·21
	29000	0·500	53·40	29·60	10·48	6·01
PHWR	2960	0·02	82.52	15·01	2·2	0·22
(RAPS)	5700	0·05	67·7	26·0	4·8	1·2
	6200	0·06	66·07	26·87	5·52	1·48
CIRUS (Trombay)	1000	0·01	93·32	6·27	0·38	0·02

process steps (Roy 1978) in the separation of plutonium from spent fuels are shown in figure 3. After appropriate cooling for the shortlived radioactivity to die down, the spent fuel elements are transferred to a reprocessing plant where the fuel is first mechanically or chemically dejacketed from the cladding material. Next, the fuel is dissolved in nitric acid and the solution is subjected to solvent extraction for removal of fission products in the first stage and uranium in the second stage. The separated plutonium is further purified by ion-exchange process and obtained as plutonium nitrate.

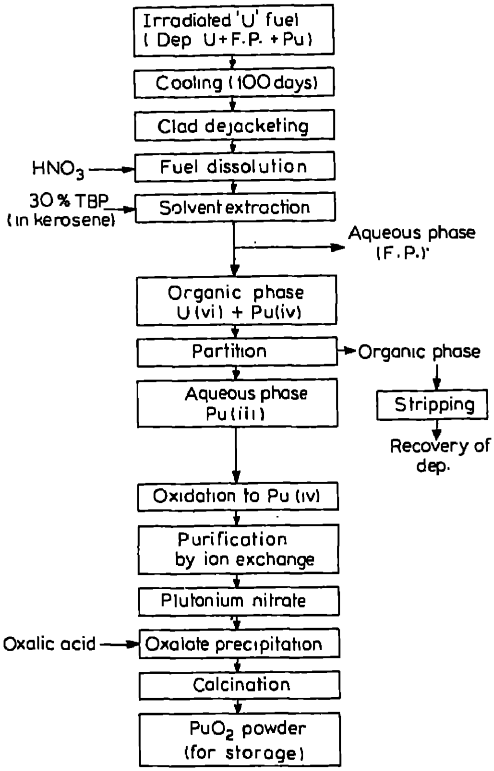

Figure 3. Flowsheet for recovery of plutonium from irradiated fuel.

The nitrate solution is converted to the oxide, mainly by the oxalate precipitation route followed by calcination in air at temperatures ranging from 400–700°C to get PuO_2 powder suitable for subsequent use. The oxalate process has low filtrate losses, good filterability and relatively high decontamination, particularly for iron. Direct calcination of the nitrate to oxide could dispense with the intermediate precipitation process and thus achieve considerable simplification. The process has been performed satisfactorily on laboratory scale, but suffers from the drawback of complete lack of purification and decontamination which is achieved during precipitation step and thus requires a very pure feed solution.

PuO_2 powder is usually the end product of a spent fuel reprocessing plant because it is most convenient to store plutonium in the form of the oxide from the point of chemical stability and ease of subsequent transportation.

3. Safety considerations

The high radiotoxicity, biological behaviour and fissile properties of plutonium present radiological and criticality hazards necessitating special safety considerations in handling of plutonium. In fact, this handling problem makes plutonium metallurgical operations a distinctively different and much more formidable task when compared with that of other conventional metals including uranium. Thus we had to first master the technique of safe handling of plutonium, either as fine powders or as bulk material, before any significant development of its metallurgy.

The decay characteristics of plutonium isotopes and their daughters are given in table 2 (Janardhanan *et al* 1973). ^{239}Pu, the major constituent, and other isotopes of plutonium except ^{241}Pu are predominantly powerful emitters of alpha radiation. Alpha particles emitted by plutonium isotopes do not constitute an external hazard because of its short range in air and body tissue (for ^{239}Pu alphas the range in air and body tissues

Table 2. Radioactive decay characteristics of plutonium isotopes and daughters.

Isotope	Radiation	Yield %	Energy (MeV)	Half-life	Specific activity (Ci/g)
Pu-238	Alpha	100	5·49	86·4 yr	17·4
	Gamma	10^{-3}	0·15		
	Gamma	8×10^{-3}	0·10		
	Gamma	$3{\cdot}8 \times 10^{-2}$	0·044		
	L-X-ray	13	0·017		
Pu-239	Alpha	100	5·14		
	Gamma	2×10^{-3}	0·038		
	Gamma	7×10^{-3}	0·052	$2{\cdot}436 \times 10^{4}$ yr	0·052
	Gamma	2×10^{-3}	0·12–0·20		
	Gamma	3×10^{-3}	0·38		
	L-X-rays	1·4	0·0136		
		2·2	0·0174		
		0·2	0·0205		
Pu-240	Alpha	76	5·162		
	Alpha	24	5·118	$6{\cdot}58 \times 10^{3}$ yr	0·23
	Gamma	10^{-2}	0·044		
	L-X-rays	10	0·017		
	K-X-rays	40	0·102–0·125		
Pu-241	Alpha	3×10^{-3}	4·9	13·0 yr	111·5
	Beta	99·997	0.02		
	Gamma	2×10^{-4}	0·145		
	Gamma	10^{-3}	0·10		
Pu-242	Alpha	76	4·89	$3{\cdot}79 \times 10^{5}$ yr	0·004
	Alpha	24	4·86		
	Gamma	10^{-2}	0·045		
	L-X-rays	10	0·017		
U-237	Beta	100	0·245	6·75 day	$6{\cdot}74 \times 10^{-4}$
	Gamma	61	0·059		
	Gamma	35	0·207		
	Gamma	4	0·334		
Am-241	Alpha	84	5.48		
	Alpha	13·6	5.43	458 yr	3·13
	Gamma	37	0·017		
	Gamma	2·7	0·026		
	Gamma	0·05	0·043		
	Gamma	37	0·059		
	Gamma	0·02	0·099		

Table 3. Maximum permissible concentrations for plutonium radionuclides in body, air and water.

Radionuclide	MPBB		MPC (40 hr exposure/week) (*uc/cc*)	
	uc	*ug*	Air	Water
Pu-238	0·04	$2{\cdot}4 \times 10^{-3}$	2×10^{-12}	10^{-4}
Pu-239	0·04	0·65	2×10^{-12}	10^{-4}
Pu-240	0·04	0·18	2×10^{-12}	10^{-4}
Pu-241	0·9	$8{\cdot}2 \times 10^{-3}$	9×10^{-11}	7×10^{-3}
Pu-242	0·05	12·8	2×10^{-12}	10^{-4}
Am-241	0·05	$1{\cdot}6 \times 10^{-2}$	6×10^{-12}	10^{-4}
U-237	0·06	89	4×10^{-12}	9×10^{-5}

are 3·68 cm and 40 μm respectively). The primary concern in plutonium handling is to prevent particulate matter containing plutonium from entering the body of the operator through inhalation, ingestion or injection because plutonium poses the highest biological hazard when taken into the body. The long biological half-life, the high energy of the emitted alpha particles and the body's selective localisation of plutonium in the bone and lung lead to very low maximum permissible body burdens (MPBB) and maximum permissible concentrations (MPC) in air and water (table 3) (ICRP 1955). Any plutonium-bearing material is, therefore, handled in a well-ventilated laboratory within the confines of hermetically-sealed glove boxes through alpha-tight neoprene gloves. The glove box is maintained under a slightly negative pressure (−0·2 to −2″ WG) under a dynamic flow of air or high purity inert gas (N_2, A or He) in order to have 3–10 box volume changes per hour. Figure 4 gives the view of a glove box train

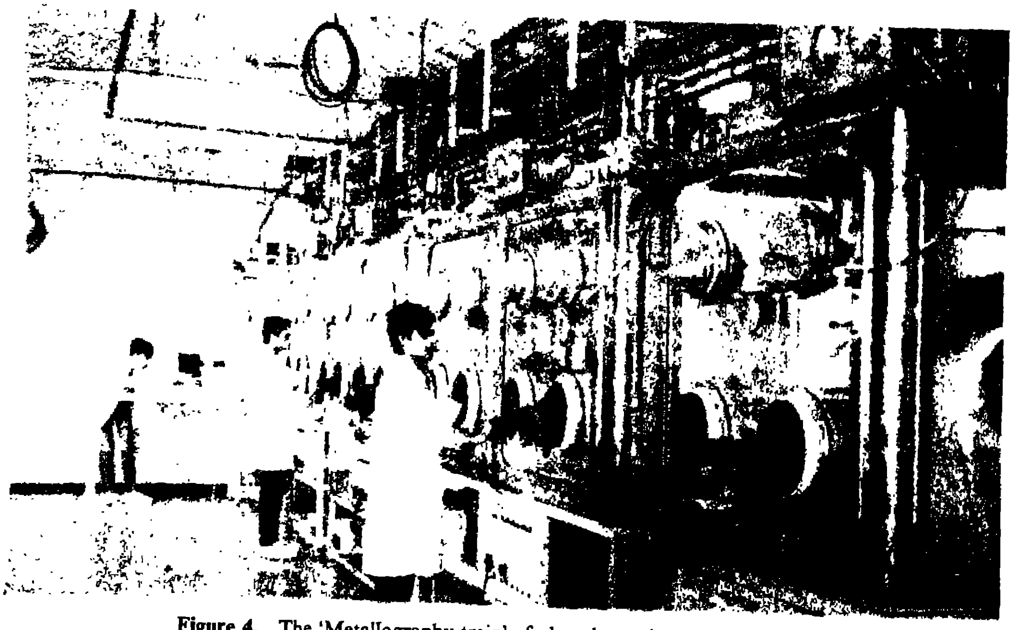

Figure 4. The 'Metallography train' of glove boxes in RMD, BARC.

set up in the Radiometallurgy Division at Trombay for safe handling of plutonium (Ghosh *et al* 1973). Inert atmosphere glove boxes are used for handling plutonium metal, carbide and nitrides which are highly susceptible to oxidation and hydrolysis and are pyrophoric in powder form.

The external hazard of plutonium is mainly from gamma and neutron radiations emitted by higher isotopes of plutonium which are present in significant amounts in high burnup plutonium. The surface dose rate of plutonium since its purification increases with time because of build up of ^{241}Am and ^{237}U, which are the daughter products of the beta emitting ^{241}Pu. Appreciable neutron dose rates are also associated with plutonium mainly from the spontaneous fission neutrons emitted by the even-numbered plutonium isotopes, e.g. ^{238}Pu, ^{240}Pu etc., and to some extent due to (α, n) reactions from plutonium in contact with light elements.

In order to keep the radiation exposure of operators below the permissible limits specified by the International Commission of Radiation Protection (ICRP) the following guidelines are usually followed:

(a) restrictions are imposed on the mass of plutonium that is handled at a time, to minimise mainly the neutron dose;
(b) great emphasis is given towards automation and remotisation during handling of plutonium;
(c) close containment of plutonium bearing powder and dust such that radioactive dust does not build up on equipment and glove box surfaces;
(d) use of external or localised composite lead glass and lucite shield for gamma and neutron radiation and the use of lead-loaded neoprene gauntlets, particularly while handling high burn-up plutonium.

Unlike other metallurgical industries, in a plutonium facility a maximum of a few kg

Table 4. Critical masses of some plutonium compounds.

Compound	Density (g/cc)	Critical mass (kg)	
		Bare	Water reflected
Pu-solution	—	—	0·51
Pu			5·6 α phase 7·6 δ phase
PuO_2	11·46	24·5	12·2
PuN	14·25	18·4	9·23
PuC	13·6	17·93	9·07
PuH_2	10·4	15·64	7·49
PuH_3	9·61	12·69	6·32
Pu_2C_3	12·7	19·72	9·96
Pu_2O_3	11·47	24·95	12·05
$PuCl_3$	5·7	167·05	61·59
PuF_3	9·32	32·59	16·0
PuF_4	7·0	56·29	25·29
$Pu(C_2O_4)_2$	4·5	152·0	66·87
$Pu(NO_3)_4$	6·2	103·96	54·94

of fissile material is handled at a time to avoid spontaneous self-sustaining nuclear chain reaction or what is known as the criticality accident which can be catastrophic to the personnel and its surroundings. The critical mass of plutonium and its compounds depend on the geometry and the environment. Table 4 gives the critical mass of plutonium and some of its important compounds (Hansen and Clayton 1967). The upper safe limit during handling is usually kept at 50% of the critical mass.

In the plutonium metallurgy laboratory at Trombay safety has always been given priority over cost, convenience and even production capacity. As a result, there has not been a single radiation incident till todate.

4. Nuclear parameters

The important nuclear parameters of the three principal fissile nuclides ^{235}U, ^{239}Pu and ^{233}U are listed in table 5 (Hanna *et al* 1969). η, the average number of neutrons produced per neutron absorbed by the fissile nucleus is the most important parameter as it influences the conversion or breeding ratio (CR), *i.e.* the average number of fissile atoms produced in a reactor per fissile atom consumed by fission or capture. The conversion ratio is quantitatively expressed as:

$$\text{CR} = \eta - 1 - L$$

where one neutron is needed to continue the chain reaction and L represents the non-productive absorption and leakage per neutron absorbed by fissile atom.

Since ^{239}Pu and ^{233}U have the highest η values in the fast and thermal neutron range respectively, plutonium breeds best in a fast reactor and ^{233}U is best suited for thermal converter reactors. In fact, in a fast reactor operating on a ^{238}U-^{239}Pu fuel cycle, it is possible to have a breeding ratio in the range of 1·2 to 1·4.

The other advantages of plutonium as a fissile material in fast reactors compared to ^{235}U are the higher fast fission cross-section (Pu : 1·77 barns; U : 1·44 barns), 5% higher

Table 5. Nuclear properties of the principal fissile nuclides.

	Property	^{233}U	^{235}U	^{239}Pu
σ_a =	Neutron absorption cross-section	578 ± 2	578 ± 2	1013 ± 4
σ_f =	Fission cross-section	531 ± 2	580 ± 2	742 ± 3
σ_c =	Neutron capture cross-section	47 ± 1	98 ± 1	271 ± 3
α =	Ratio of captures to fissions	0·089 ± 0·002	0·169 ± 0·002	0·366 ± 0·004
ν =	The number of neutrons produced per fission	2·487 ± 0·007	2·423 ± 0·007	2·880 ± 0·009
η =	The number of neutrons created per neutron absorbed by the nuclide			
	(a) Thermal neutrons	2·284 ± 0·006	2·072 ± 0·006	2·109 ± 0·007
	(b) Fast neutrons	2·31	1·93	2·49

The cross-sections σ_a, σ_f, and σ_c are in barns and α, ν and η are ratios.

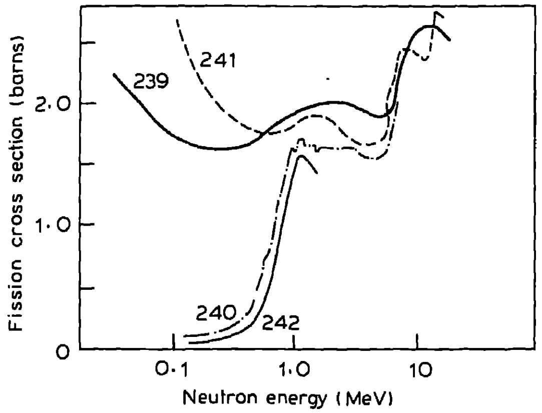

Figure 5. Fast fission cross-section (barns) of Pu isotopes

fission energy release and lower xenon poisoning. Further, ^{241}Pu is fissile in both thermal and fast neuton range and ^{240}Pu and ^{242}Pu, though parasitic, neutron absorber for thermal neutrons, contribute significantly to fast fission. The fission cross-section of important plutonium isotopes in the fast neutron range is shown in figure 5 (Wick 1980).

From reactor physics consideration it may, therefore, be summarised that plutonium is the best fuel for fast reactors but is slightly inferior to ^{233}U and ^{235}U in the thermal neutron range.

5. Plutonium metal

5.1 *Preparation*

While starting plutonium metallurgical work at Trombay, we had already selected uranium metal as the fuel for our CIRUS Research reactor. It was, therefore, logical for us to first direct all the efforts towards manufacture of high purity nuclear grade plutonium metal.

Much of the metallurgical knowledge for preparation of plutonium metal was acquired during the Manhattan Project in the 1940s. The free energy diagrams of oxide and fluoride of plutonium (Coffinberry and Miner 1961) and other metals are shown in figure 6 and table 6 gives the various thermodynamic data of the reduction reaction (Stoller and Richards 1961). Reduction of plutonium halides, in particular, fluoride and chloride remains the only method by which virtually all the metal is produced till today.

The need to obtain plutonium in massive form with a high yield dictates the choice of a reducing reaction. The reduction reaction should be accompanied by evolution of large quantity of heat which should not only melt the reaction products but also keep them molten long enough for good slag-metal separation. The reducing agent should not dissolve in plutonium or form any intermetallic compound with it. Low melting point of the slag and high boiling point of the reducing agent are additional requirements. Considering all these factors it is found that the reduction of plutonium tetrafluoride with calcium is sufficiently exothermic and the slag in this case melts at a

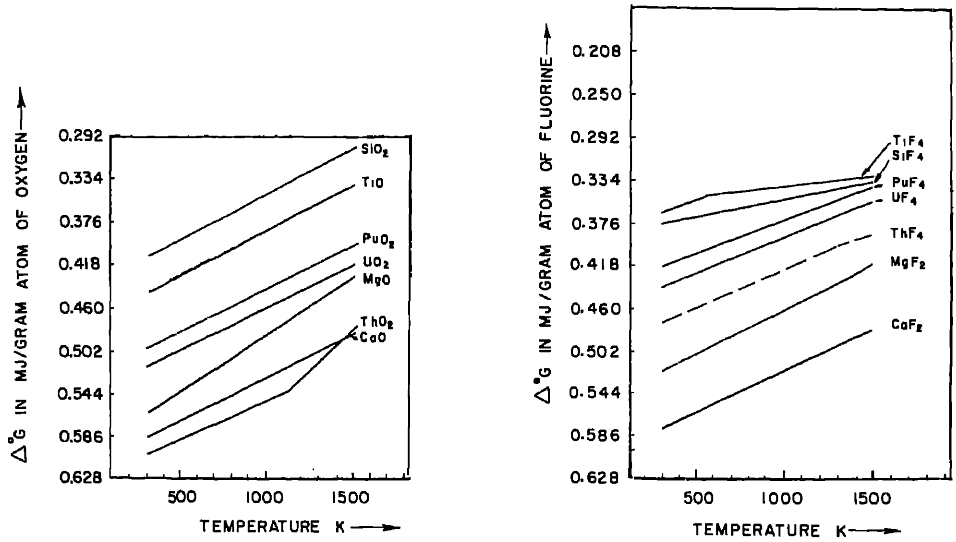

Figure 6. Standard free energy of formation (ΔG°) for important oxides and fluorides of U and Pu.

Table 6. Thermodynamic data of the possible reduction reactions for preparation of plutonium metal

Reaction	ΔH at 291 K, kcal/mol. plutonium	Melting Point of Slag (°C)
$PuO_2 + Ca \rightarrow Pu + 2CaO$	−52·4	2572
$PuO_2 + 2Mg \rightarrow Pu + 2MgO$	−40·5	2500–2800
$PuO_2 + \frac{4}{3}Al \rightarrow Pu + \frac{2}{3}Al_2O_3$	−9	2050
$PuF_4 + 2Ca \rightarrow Pu + 2CaF_2$	−149·5	1414
$PuF_4 + 0{\cdot}3I_2 + 2{\cdot}3Ca \rightarrow$		
$Pu + 0{\cdot}3CaI_2 + 2CaF_2$	−196	1320
$PuF_4 + 2Mg \rightarrow Pu + 2MgF_2$	−104·6	1225
$PuF_4 + \frac{4}{3}Al \rightarrow Pu + \frac{4}{3}AlF_3$	+15	1040
$PuCl_3 + \frac{3}{2}Ca \rightarrow Pu + \frac{3}{2}CaCl_2$	−56·0	772
$PuCl_3 + \frac{3}{2}Mg \rightarrow Pu + \frac{3}{2}MgCl_2$	+0·2	708

reasonably low temperature. It can be further seen that the addition of 0·3 mole of iodine makes the reaction more exothermic and also lowers the melting point of the slag by about 100°C.

Figure 7 shows the flowsheet followed at BARC (Roy and Mahajan 1975) for the reduction of tetrafluoride with calcium. Plutonium tetrafluoride and calcium metal in amount equal to stoichiometric plus 30 to 50% excess are mixed thoroughly and charged into a steel bomb which is capable of withstanding pressures of 0·5–3 MPa and temperature upto 1600°C. The bomb is first purged with argon to exclude any air present. The sealed bomb is subjected to resistance or induction heating to about 600°C when the reduction reaction takes place and the products are melted by the heat

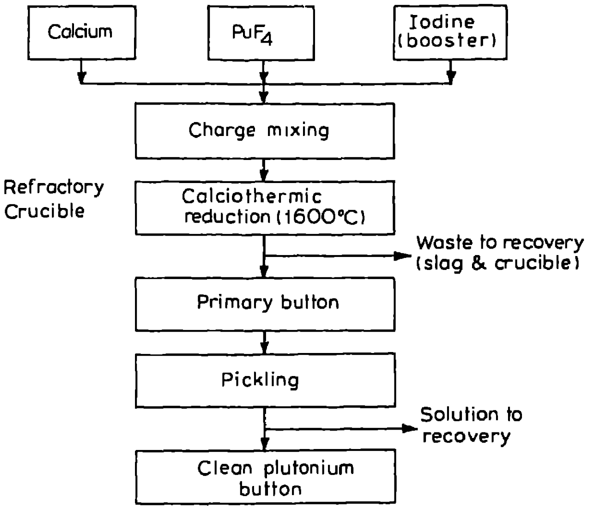

Figure 7. Flowsheet for preparation of plutonium metal.

generated. It is very essential to control the heating rate. If the heating is too rapid, the reaction takes place only at the surface and thus the slag solidifies too rapidly. On the other hand, if preheating period is too long, the calcium particles get coated with CaI_2 retarding the rate of reaction. The start of the reduction reaction is indicated by a sudden rise in the temperature monitored by a thermocouple or by a drop in the neutron emission from the reaction chamber. The yield in this process is generally 97–99 % and the purity normally exceeds 99·8 %. Alternatively PuF_4 and finely divided calcium (50 % excess) are mixed and pressed into pellets. The pellets are loaded into a calcium fluoride crucible and then in a quartz tube. On heating a bright flash shows the initiation of the reaction.

Direct reduction of dioxide would overcome the drawbacks of the fluoride and chloride processes namely high neutron emission and hygroscopicity respectively. It would also simplify the process by the elimination of the costly halogenation step. Recent studies (Wade and Wolf 1969) have shown that by proper modification of the reduction apparatus and by using a suitable flux, it is possible to obtain plutonium in massive form by calciothermic reduction of the oxide. Reduction of dioxide by carbon becomes feasible only at temperatures of the order of 3000°C and requires high vacuum system. It also suffers from the formation of plutonium carbide.

5.2 *Melting and casting*

The fabrication of plutonium involves many of the techniques commonly utilised for working of the common metals. However, all operations are directly affected by the extreme toxicity of plutonium in any form, the tendency of the metal to oxidise rapidly, the pyrophoricity and by the obvious necessity of avoiding conditions of criticality.

The low melting point of plutonium offers a considerable amount of freedom in the selection of melting equipment. Although resistance, arc and electron beam furnace have been used for melting plutonium, inductive heating is most advantageous.

Extremely high reactive nature of molten plutonium poses a big problem in the choice of crucible material. Different types of crucible materials have been used. Of the metallic crucibles, tantalum has been extensively used but its use is limited to a maximum temperature of 1000°C after which it is rapidly dissolved by plutonium. Ceramic materials like CaO, Y_2O_3 and CaF_2 are good but not used because of their fragile nature. Al_2O_3, BeO, ThO_2 lead to contamination of the melt. MgO has been widely used but it also leads to slight contamination of the melt. Graphite has been found to be an excellent crucible material. It is inexpensive, can be easily fabricated and is not subject to thermal shock. However, a suitable coating must be applied to the graphite surface to prevent carbon pick up in the melt. Crucibles may be either tilt-pouring or bottom-pouring type depending upon the type of work to be carried out.

Graphite also serves as the most commonly employed mould material. Metal moulds made of gray cast iron, mild steel, copper and for special purposes tantalum have been used.

Unalloyed plutonium has the general characteristics of a very castable material. The low melting point, high fluidity, high density and extremely small volume change on freezing are all favourable characteristics for casting. Piping and shrinkage porosity observed in most other metals are not encountered when casting plutonium. However, during cooling to room temperature a number of phase transformations take place in pure plutonium metal some of which are accompanied by large volume changes. Accordingly extreme care is exercised in the design of the mould such that the casting does not adhere firmly to the mould and cause cracking. The mould is usually heated to avoid cold shuts in the casting.

6. Aluminium-plutonium alloys

As early as in 1961, side by side with the production of plutonium metal, we had also taken up the preparation of Al-Pu alloys by employing similar metallothermic reduction technique (Roy 1962). This technique is particularly advantageous for plutonium alloy preparation because it eliminates costly steps of plutonium metal production, its handling in inert atmosphere and also avoids the problem of gravity segregation which is a common occurrence when a light metal like aluminium is alloyed with plutonium.

Around 500 mg of Al-6·27% Pu were prepared by aluminothermic reduction of PuO_2 in the presence of excess aluminium and cryolite in a graphite crucible around 1100°C. The reaction involved is as follows:

$$3PuO_2 + 4Al = 3Pu + 2Al_2O_3$$

$$\Delta G_{1500K} = -42 \text{ kcal/mol.}$$

The reduced plutonium immediately alloys with the excess aluminium and the cryolite fluxes the Al_2O_3. The reaction thus proceeds in the forward direction with proper slag metal separation and high yield. The alloy thus made was recovered by breaking the graphite crucible, remelted for proper homogenisation and cast in another graphite crucible. In the very first preparation itself we could get a yield as high as 96%.

No plutonium metallography facility was available in Trombay at that time. A make-shift arrangement was made for sample preparation, *e.g.* cutting, mounting, grinding, polishing and etching of alloy samples inside a glove box. The microscope, however, was kept outside the glove box and the sample was examined through a transparent plastic bag attached to the glove box. The as-cast microstructure of the alloy ingot (figure 8) clearly shows lamellar $PuAl_4$ particles in an Al matrix.

Al-Pu alloys containing 3–20 w/o plutonium have found widespread application in many research reactors. Aluminium because of its low parasitic thermal neutron absorption cross-section (0·22b) and high thermal conductivity is considered as an excellent inert carrier for the fissile plutonium. Since plutonium has negligible solid solubility (Roy 1964; Ellinger *et al* 1962) with aluminium (figure 9) these alloys essentially comprise of a dispersion of the intermetallic $PuAl_4$ in an aluminium matrix.

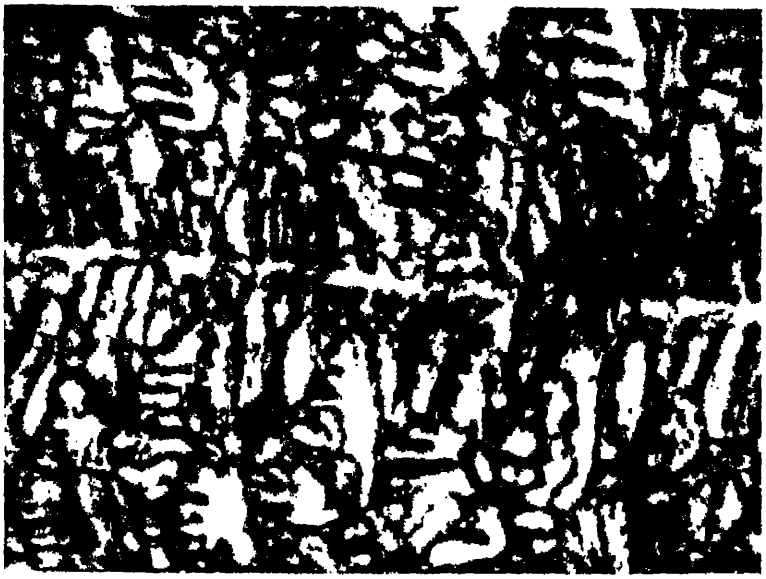

Figure 8. Microstructure of cast aluminium-plutonium alloy (prepared in 1961, × 100).

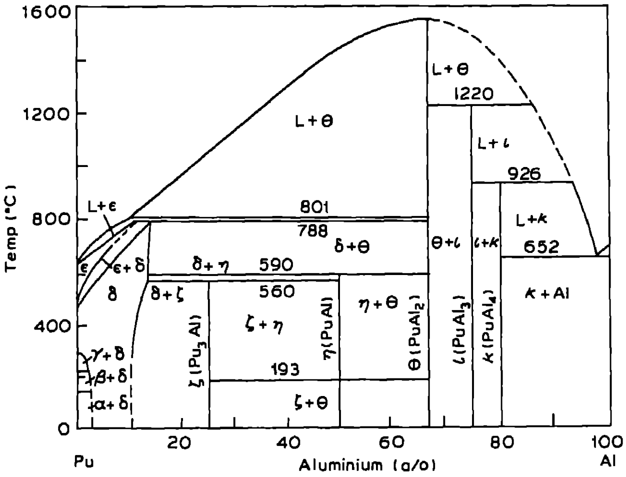

Figure 9. Plutonium aluminium phase diagram.

Such dispersion fuel has the advantage of minimum radiation damage by restricting the fission recoil damage to the area immediately adjacent to the fissile dispersoid particles, namely $PuAl_4$, which are relatively small in size leaving a large area of undamaged non-fissile matrix metal aluminium, which is predominant in volume and in the form of a continuous network surrounding the $PuAl_4$ phase.

Towards the end of 1960s, 60 g of Al-13 w/o Pu in the form of sheets (40 × 40 × 0·5–2 mm) was prepared for nuclear physics experiments (Roy *et al* 1969). Experience in cold rolling of Al-Pu alloys was obtained during this campaign.

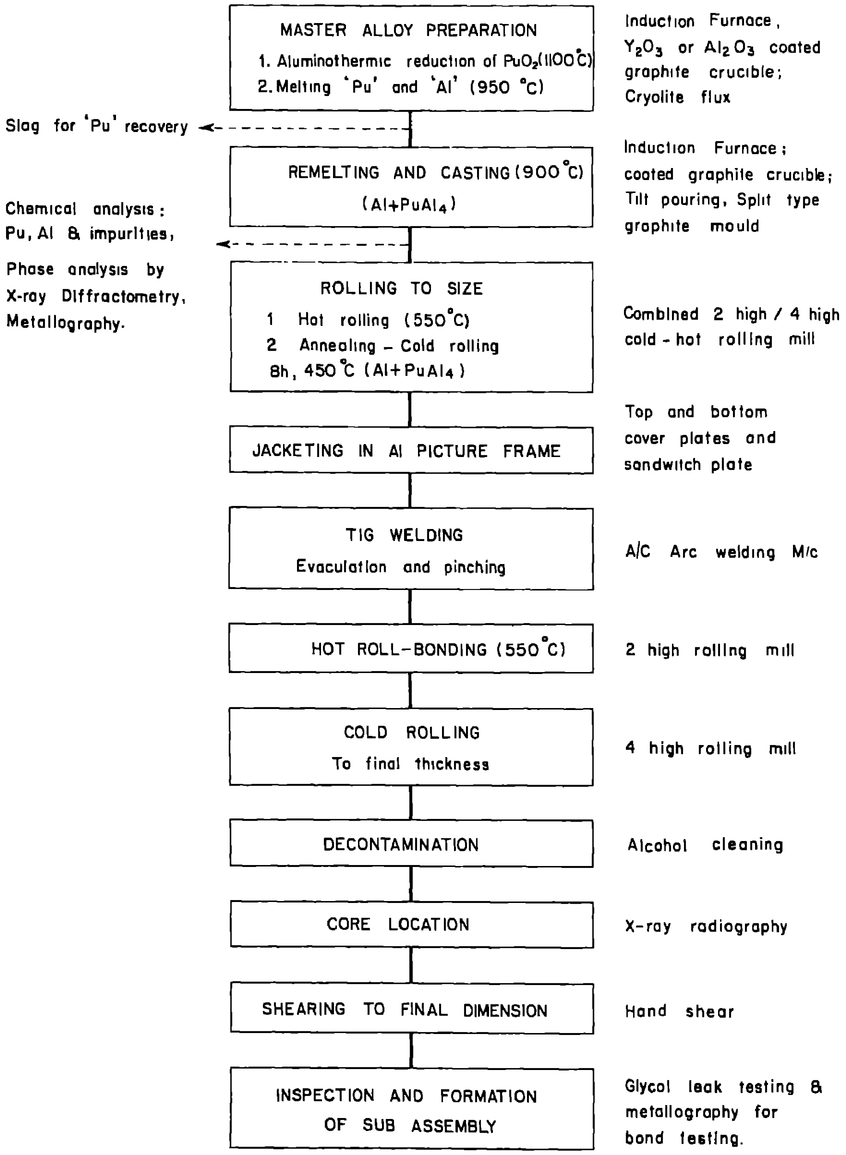
MASTER ALLOY PREPARATION
1. Aluminothermic reduction of PuO₂(1100°C)
2. Melting 'Pu' and 'Al' (950 °C)
Induction Furnace, Y₂O₃ or Al₂O₃ coated graphite crucible; Cryolite flux
Slag for 'Pu' recovery
REMELTING AND CASTING (900°C)
(Al+PuAl₄)
Induction Furnace; coated graphite crucible; Tilt pouring, Split type graphite mould
Chemical analysis: Pu, Al & impurities,
Phase analysis by X-ray Diffractometry, Metallography.
ROLLING TO SIZE
1 Hot rolling (550°C)
2 Annealing – Cold rolling
8h, 450°C (Al+PuAl₄)
Combined 2 high / 4 high cold - hot rolling mill
JACKETING IN Al PICTURE FRAME
Top and bottom cover plates and sandwitch plate
TIG WELDING
Evaculation and pinching
A/C Arc welding M/c
HOT ROLL-BONDING (550°C)
2 high rolling mill
COLD ROLLING
To final thickness
4 high rolling mill
DECONTAMINATION
Alcohol cleaning
CORE LOCATION
X-ray radiography
SHEARING TO FINAL DIMENSION
Hand shear
INSPECTION AND FORMATION OF SUB ASSEMBLY
Glycol leak testing & metallography for bond testing.

Figure 10. Flow sheet followed in BARC for fabrication of Al clad Al-Pu plate fuel element.

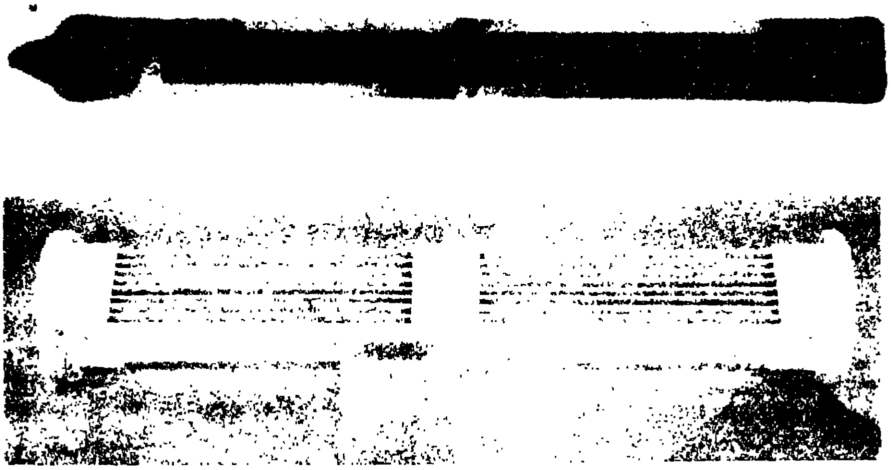

Figures 11, 12. 11. X-ray radiograph of Al clad Al-Pu alloy plate fabricated in radiometallurgy division, BARC. Dark areas show the alloy meat. **12.** 9 plate fuel subassembly of Al clad Al-Pu alloy. After irradiation testing in Zerlina reactor in BARC.

With the commissioning of the new Plutonium Metallurgy Laboratory in 1970, a new pilot scale facility was set up for fabrication of Al-Pu alloy fuel elements at BARC. The main equipment consisted of a high vacuum induction melting-casting unit, a 2 high/4 high cold/hot rolling mill and an annealing furnace.

This facility was utilised in 1973 to fabricate 2 nine plate sub-assemblies of Al-10 w/o Pu and Al-18 w/o Pu plate fuel elements (445 × 51·75 × 1·78 mm) by the "picture-frame technique" according to the flowsheet shown in figure 10 (Prasad *et al* 1976) for nuclear physics experiments in the ZERLINA reactor at BARC. The Al-Pu alloy meat was hot roll-bonded to the aluminium cover plates at 450°C. The radiograph of a roll-bonded Al clad Al-Pu alloy fuel plate and the photograph of a 9-plate sub-assembly fabricated at BARC are shown respectively in figures 11 and 12.

Such Al-Pu plate fuel elements could be utilised as a substitute for the imported aluminium clad Al-13 w/o U(85% enriched ^{235}U) plate fuels used in the Apsara Swimming Pool type test reactor at BARC. It also can be used as boosters in our pressurised heavy water reactors (PHWR) to overcome xenon poisoning following post shut-down start-ups.

7. Plutonium-beryllium alloys

Pu-Be alloys are used as low flux neutron sources utilising the interaction of alpha particles from plutonium with beryllium atoms to generate neutrons according to the reaction $\mathrm{Be}^9\,(\alpha, n)\mathrm{C}^{12}$. The principal advantages of Pu-Be alloys over Ra-Be and Po-Be neutron sources is the stability of the neutron yield with respect to time due to the long half-life of ^{239}Pu (24360 yr) and the relatively small amount of low energy gamma radiation. Moreover, plutonium is relatively non-volatile as compared with radium or polonium and since it readily alloys with beryllium, it is possible to prepare the Pu-Be neutron source as an alloy rather than pressed mechanical mixtures. The alloying further leads to mechanically strong, non-friable body and reproducibility in neutron yield. The neutron yield of Pu-Be alloys, as shown in figure 13 depends on the beryllium to plutonium atom ratio N according to the relation:

$$\frac{n}{n_{\max}} = \frac{N \times S_{\mathrm{Be}}}{(N \times S_{\mathrm{Be}} + S_{\mathrm{Pu}})}$$

where, $n/n_{\max}$ is the fraction of maximum neutron yield, S_{Pu} is the stopping power of Pu = 4·5 and S_{Be} is the stopping power of Be = 0·63. The neutron yield for a beryllium and plutonium ratio of 13, at which the alloy consists of the intermetallic $\mathrm{PuBe_{13}}$ (figure 14) is only 36·7 per 10^6 alphas compared to 54·9 per 10^6 alphas for an atom ratio of 200. An atom ratio of 30 leads to good compromise between the physical size of the source and

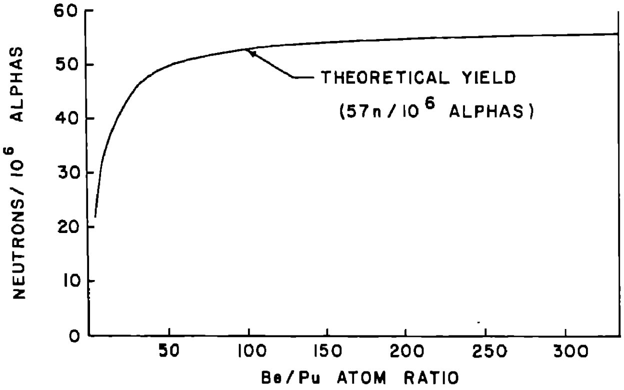

Figure 13. The variation of neutron yield with Be:Pu atom ratio.

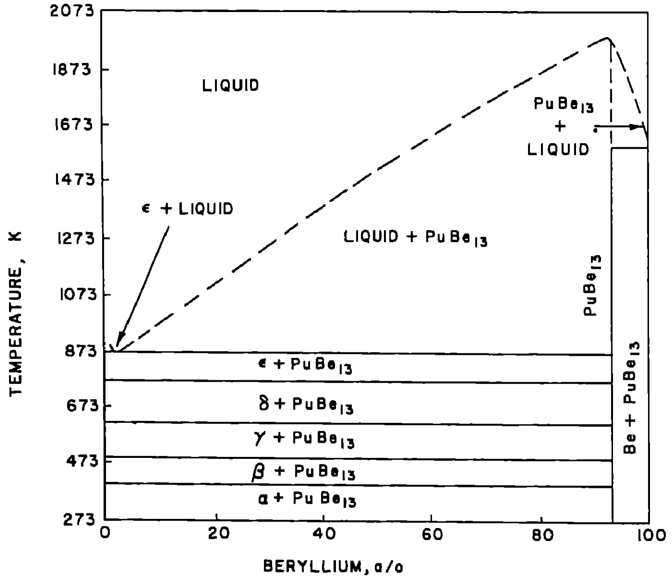

Figure 14. Pu-Be phase diagram.

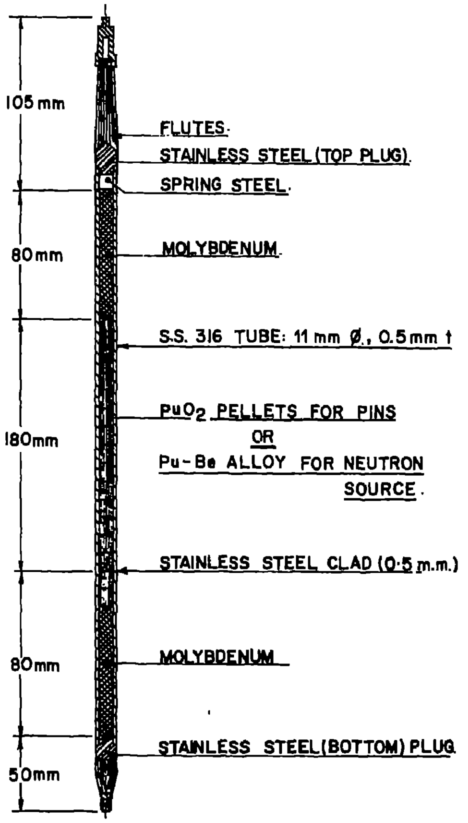
105 mm
FLUTES.
STAINLESS STEEL (TOP PLUG).
SPRING STEEL.
80mm
MOLYBDENUM.
S.S. 316 TUBE: 11 mm Ø, 0.5mm t
PuO2 PELLETS FOR PINS
OR
Pu-Be ALLOY FOR NEUTRON SOURCE.
180mm
STAINLESS STEEL CLAD (0·5 m.m.)
80mm
MOLYBDENUM
STAINLESS STEEL (BOTTOM) PLUG
50mm

Figure 15. Fuel pin and pencil neutron source for Purnima.

its neutron yield of 46 per 10^6 alphas. Further, alloys with $N \geqslant 30$ are easily sintered at a relative low temperature of 1250°C but for N lower than 30 a minimum sintering temperature of 1400°C is required.

The first Pu-Be neutron source of nearly 1 Curie strength was prepared at BARC (Roy *et al* 1967) in 1967. by berylothermic reduction of pellets prepared from a powder mixture of around 18 g each of PuO_2 and Be in vacuum at 1250°C (Be:Pu atom = 30). The reaction is as follows:

$$PuO_2 + 2\,Be = Pu + 2\,BeO \qquad \Delta G_{1000K} = -29{\cdot}4\ \text{kcal/mol.}$$

The presence of BeO in the reaction product does not alter the neutron emission. The alloys thus prepared undergo reaction sintering and consist of a fine dispersion of $PuBe_{13}$ and BeO in a matrix of Be. Subsequently in 1972, the same technique was followed for the preparation of several point and pencil neutron sources of strength between 50 mCi and 5 Ci (Mahajan *et al* 1972).

The Pu-Be neutron sources are encapsulated in metallic cans. For the point source the Pu-Be alloy tablet is first loaded in a one end closed aluminium or stainless steel container with a screwed cap. This sealed inner container is next loaded in an outer container of stainless steel and encapsulated by TIG welding. These point sources have been delivered to several agencies within and outside BARC for calibration of neutron counters, physics experiments and devices for measuring moisture and hydrocarbons in soil. The 900 mCi pencil sources (figure 15) were used for start-up of the PURNIMA reactor at BARC.

8. Delta-stabilised plutonium alloys

Unalloyed plutonium, unlike uranium has never been tried as a nuclear fuel because of its unfavourable metallurgical properties. First, plutonium has a low melting point (640°C). Secondly, there are as many as 6 allotropic transformations of plutonium between 20 and 640°C as shown in table 7 (Zachariasen and Ellinger 1959). No other metal shows as many phase changes within such a narrow temperature range. Particularly undesirable is the large volume change, of the order of 10%, which accompanies the alpha to beta transformation at 122°C. It was, therefore, natural to look for a high temperature phase which could be stabilised down to the room temperature by a proper combination of alloying and heat treatment.

Delta plutonium which is stable between 315 and 456°C has a fcc structure and exhibits the highest ductility and best formability amongst all the plutonium allotropes. The delta phase can be retained at room temperature by small additions of Al, Sn, Zn, Ga, Zr, In, Hf, Tl, Ce, Dy, Er, Tn, La or Th. The delta-stabilised plutonium has many desirable mechanical and metallurgical properties. It is ductile and soft, has a hardness value of 40–45 kg/mm^2 (Vicker's DPH) which is comparable to annealed copper and can be conveniently machined, worked and turned. Further, these alloys have negligible volume change during working, produce good quality casting and are more resistant to oxidation compared to unalloyed plutonium. However, the density of delta-stabilised plutonium is less than unalloyed plutonium.

Delta-stabilised plutonium alloys have been used as fuels in the first fast reactor Clementine of LASL in the late 1940s and subsequently in core IV of EBR I of ANL, ZEPHYR of Harwell and BR-1 and 2 of USSR in the early 1950s.

Delta-stabilised plutonium alloys have been prepared at BARC in the 1970s by vacuum induction melting in coated graphite crucibles and casting in graphite moulds. The principal difficulties faced in melting, and casting these alloys are gravity segregation due to large density difference between plutonium and the alloying elements and adherence of the cast alloy with the mould because of negligible solidification shrinkages of delta plutonium.

Table 7. Allotropes of plutonium and their properties.

Phase	Structure	Stability range (°C)	Density (g/CC)	Coeff. of expansion (micro in./in. °C)	$\Delta V\%$
α	Simple monoclinic	Up to 117	19·84	48·4	10·10
β	Body centred monoclinic	117–213	17·8	38.0	2·58
γ	Face centred orthorhombic	213–315	17·14	34·7	6·75
δ	fcc	315–456	15·92	−8·8	−0·25
δ'	bct	456–475	16·01	−116·0	−3·0
ε	bcc	475–640	16·48	36·5	

9. Plutonium dioxide

In the field of ceramic fuel too the trend developed in the uranium system had set the pattern in the plutonium field. In the 1960s uranium dioxide was universally used in most of the commercial thermal power reactors, including ours, and the technology for the production of zircaloy clad UO_2 fuels by the "pellet-in-tube" process was available in Trombay (Fareeduddin *et al* 1975). This know-how was conveniently extended for the initial development of stainless steel clad PuO_2 fuels in the new plutonium metallurgy laboratory at Trombay in 1970 (Roy 1975).

Subsequently, the first major plutonium fuel fabrication job was executed in 1972 when the complete core for the zero energy fast reactor PURNIMA in BARC consisting of 186 fuel pins containing around 25 kg, of sintered PuO_2 fuel pellets was fabricated. The fuel pin (495 mm long × 11 mm OD) (figure 15) with a cladding thickness of 0·5 mm and consists of a stack of sintered PuO_2 fuel pellets of average density of 90% theoretical, held tight by a spring between a pair of axial molybdenum reflectors in a 316 stainless steel cladding tube which is sealed leak tight by TIG welded end plugs.

PuO_2 pellets were prepared from oxalate derived sinterable PuO_2 powder by the powder metallurgy route of cold compaction at around 25 TSI followed by sintering at 1600°C in $A + 8\%H_2$ atmosphere. The finished fuel pins were subjected to rigorous inspections for dimensional checks, x-ray radiographic examinations, mass spectrometric helium leak detection and surface contamination.

10. Mixed oxide fuels

Pure PuO_2 as such is not suitable for use as fuel in power generating reactors as it fails to satisfy the reactor engineering and safety requirements of bigger reactors. Further, for breeding additional fissile material simultaneously with power generation it is essential to dilute PuO_2 by mixing with fertile materials like UO_2 or ThO_2.

The following mixed oxide fuel compositions have been studied and developed in the last ten years as a part of our fuel development programme for water-cooled thermal and liquid metal cooled fast breeder reactors (LMFBR):

(a) 76% PuO_2–24% natural UO_2 or 70% UO_2–30% PuO_2 (assuming availability of 85% enriched ^{235}U for actual use) fuels for our fast breeder test reactor (FBTR).
(b) UO_2–PuO_2 (up to a maximum of 5 w/o PuO_2), popularly known as the MOX fuel, as substitute for the 2–4% enriched UO_2 fuels for the BWRs at TAPS.

Since UO_2 and PuO_2 are isostructural (fcc, CaF_2 type), mutually solid soluble and have similar physical and chemical properties (table 8), the fabrication flowsheets (figure 16) of the mixed oxides are essentially the same and involves three major steps, namely, (i) simultaneous mixing grinding of the two oxide powders in the desired proportion, (ii) cold compaction of the powder mixture into pellets with or without binder addition, and (iii) sintering the pellets in a controlled atmosphere. The process control steps in pellet fabrication should ensure homogeneous solid solution formation, uniform distribution of plutonium, an oxygen to metal ratio slightly in the hypostoichiometric range and a controlled density.

In addition to the above route, in Trombay we are also working on the "vibrosol" process as an alternative method of preparation of mixed oxide fuel pins (Sood and

Table 8. Selected properties of U, Pu and Th compounds.

Property	Oxide			Carbide		Nitride	
	UO_2	PuO_2	ThO_2	UC	PuC	UN	PuN
Theoretical density (g/cm^3)	10·96	11·46	10·00	13·63	13·60	14·32	14·25
Metal density (g/cm^3)	9·66	10·10	8·79	12·97	12·95	13·52	13·46
Metal fraction (w/o)	88·15	88·19	87·89	95·20	95·20	94·44	94·46
Melting point (K)	3000	2675	3640	2780	1875	3125	2840
Thermal conductivity (W/cm K) for 100% TD material							
1000 K	0·052	0·034	0·062	0·199	0·108	0·185	0·146
1500 K	0·035	0·023	0·024	0·213	0·142	0·248	0·167
2000 K	0·022	0·018	—	0·225	0·159	0·270	0·184

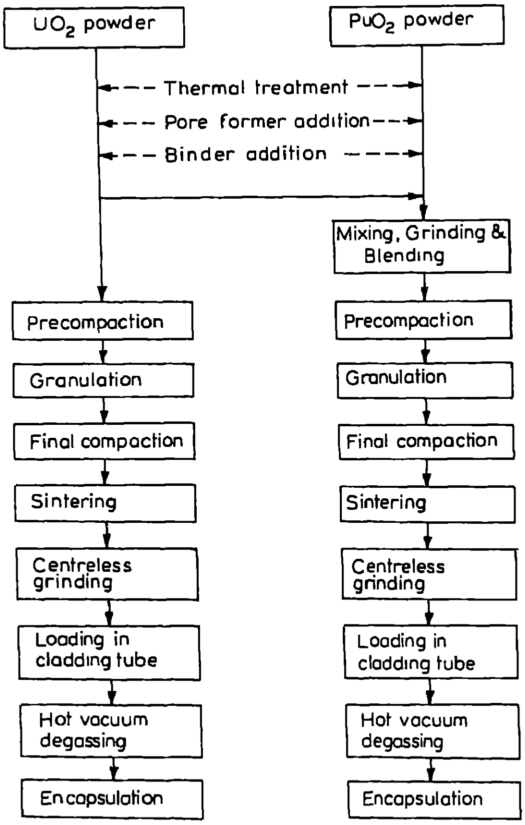

Figure 16. Process flow sheet for UO_2 and UO_2-PuO_2 pellet fuel pin.

Vaidya 1979). This method consists of preparing mixed oxide gels by a "wet chemical route" starting from uranyl and plutonium nitrate solutions followed by calcination of the gels to get mixed oxide microspheres of high density ($\sim$ 98% TD). By blending microspheres of different size fractions in the range of 10–100 μm and packing them in the fuel pin by "vibratory compaction", smear density of the fuel pin can be controlled between 60 and 90% TD. An "internal gelation" (Kanij *et al* 1974) process has been followed for preparing mixed oxide microspheres according to the flowsheet shown in figure 17. The nitrate solutions of the actinides are mixed and cooled. To this, concentrated hexamethylene tetra amine (HMTA) and urea solutions are added which act as internal gelation agents. Droplets of this solution are gelled by contact with hot (~90°C) silicone or paraffin oil.

The vibro-sol method offers the following advantages over the cold pressing sintering process:

(a) There are less number of fabrication steps and maximum flexibility of operation.

(b) A high degree of microhomogeneity is obtained in the microsphere since the blending is effected in the liquid stage and steps like prolonged ball milling of oxide powders for achieving good homogenisation are avoided.

(c) The build-up of radioactive dust on equipment and glove box surfaces which is rather common in the powder metallurgy route is also avoided since no fine powder handling is involved.

(d) The method is more suitable for remote operation and automation.

The main drawback of the vibro-sol route is that in the event of an accidental breach of the cladding tube, there could be more expulsion of fuel particles to the coolant circuit as compared to pellet fuel, thereby causing a gross contamination of the primary coolant.

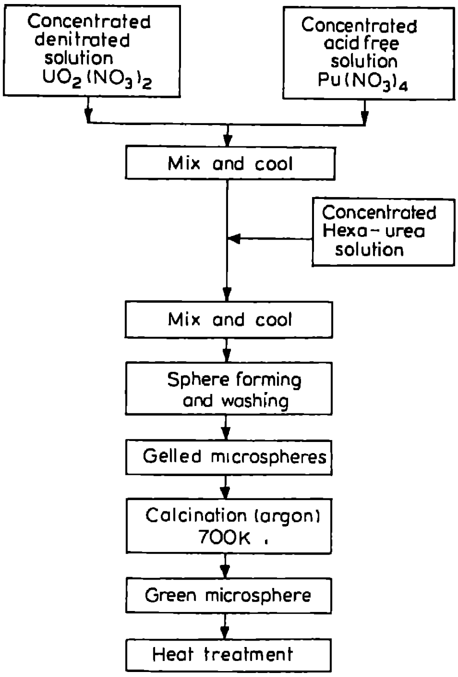
Concentrated denitrated solution $UO_2(NO_3)_2$
Concentrated acid free solution $Pu(NO_3)_4$
Mix and cool
Concentrated Hexa-urea solution
Mix and cool
Sphere forming and washing
Gelled microspheres
Calcination (argon) 700K
Green microsphere
Heat treatment

Figure 17. The kema internal gelation process.

10.1 UO_2–PuO_2 *for* LMFBRS

As a first step of our venture in the LMFBR technology a decision was taken in the 1970s to set up a small 42·5 MW(th) fast breeder test reactor (FBTR), similar to the Rapsodie-Fortissimo reactor of France, at the Reactor Research Centre, Kalpakkam. It was also decided to fabricate the fuel for this reactor in Trombay from our available natural uranium resources and plutonium. Normally, in such small test reactors the fissile requirement of the core, as shown in figure 18, is met by enriched uranium along with plutonium in order to have a high neutron flux level and to compensate for the neutron leakage loss in the small core. However, we preferred to replace the ^{235}U completely by plutonium and consequently looked into the possibility of using 76 % PuO_2–24 % UO_2 in place of already proven 70 % UO_2 (enriched to 85 % ^{235}U)–30 % PuO_2 fuel of Rapsodie.

Unfortunately, preliminary metallurgical investigations revealed that $(U_{0\cdot 24}Pu_{0\cdot 76})O_2$ was not compatible with the sodium coolant and led to the formation of $Na_3(U, Pu)O_4$ with accompanying high swelling as shown in figure 19(a) (Internal Report 1970; Housseau 1974). The sodium-fuel interaction and in turn the swelling could be significantly reduced if the O/M ratio of the fuel was kept around 1·8 (figures 19b, c) but then the already low thermal conductivity of the plutonium rich oxide fuel further reduces by nearly 30 % (figure 20) (Internal report 1974). Moreover, the mixed oxide fuel of this composition with an optimum O/M ratio of 1·98 and pellet density of 92 % TD always had a two-phase microstructure at room temperature as shown in the x-ray diffraction pattern (figure 21) and photomicrograph (figure 22) (Ramachandran *et al* 1981).

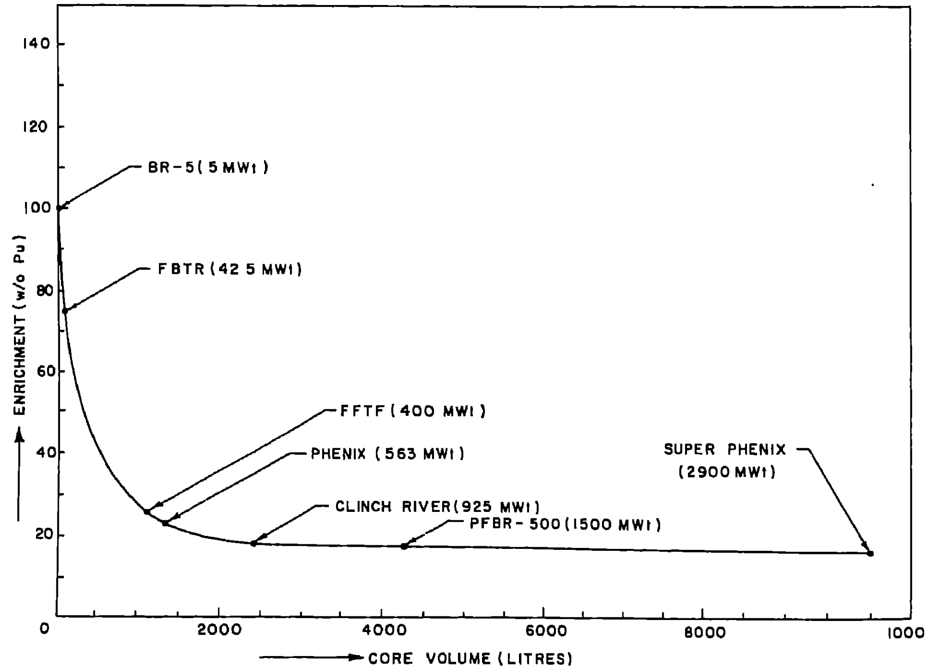

Figure 18. Enrichment—core volume.

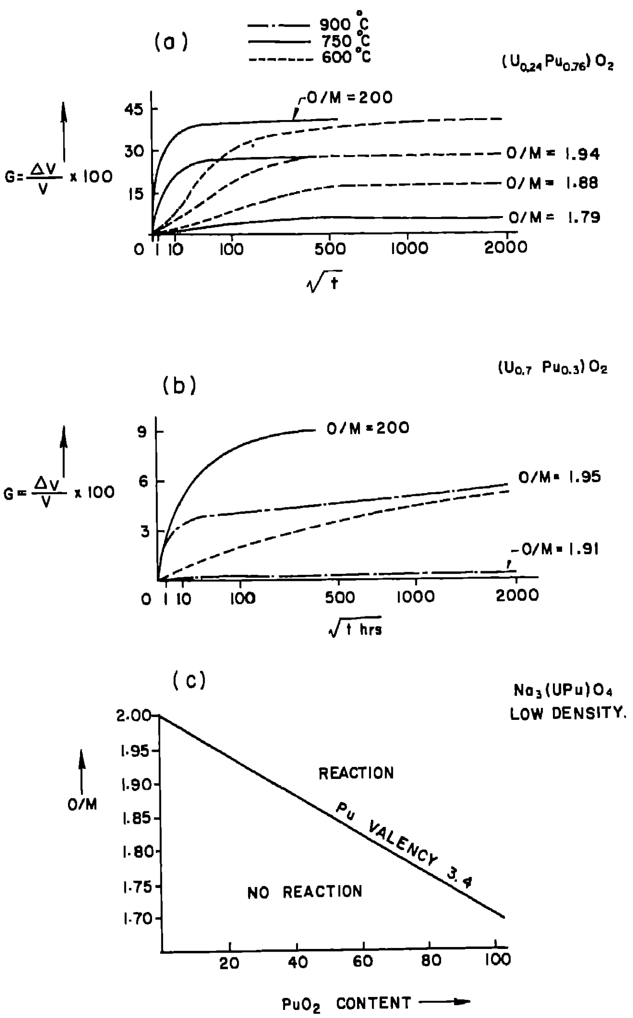

Figure 19. Swelling of uranium and plutonium rich mixed oxide after interaction with sodium.

In view of the above deficiencies, investigation of plutonium rich (U, Pu)O_2 was not pursued further. The next logical step was to revert back to the development of fabrication flowsheet of 70 % UO_2–30 % PuO_2. Single-phase mixed oxide pellets of this composition with density 92 % TD and O/M ratio 1·98 could be reproducibly fabricated in our laboratory (Majumdar *et al* 1984). A typical microstructure of single phase mixed oxide pellet is shown in figure 23.

10.2 MOX *fuel for* TAPS

Zircaloy-2 clad 2–4 % enriched UO_2 is the fuel for the two BWR at TAPS. The enriched uranium for these reactors was imported ever since the reactors were commissioned in 1967. However, with changing political conditions great difficulties were experienced in

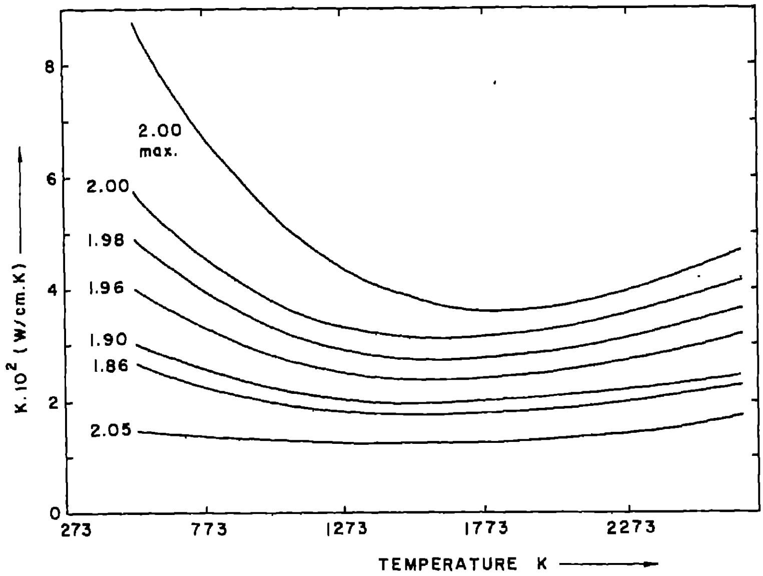

Figure 20. Thermal conductivity *vs.* temperature of 76 % PuO_2-24 %UO_2 pellets of different stoichiometry.

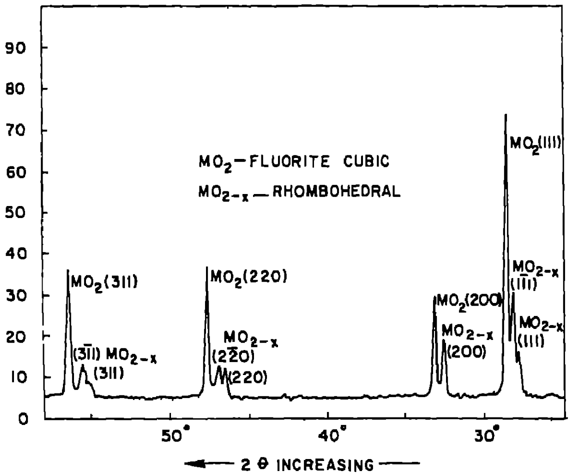

Figure 21. XRD pattern of $(U_{0.24}\ Pu_{0.76})O_{2-x}$ sintered pellet.

importing enriched uranium and a decision was taken in 1978 to explore the possibility of fabricating indigenously MOX fuel containing 2–5 w/o PuO_2 as a substitute for the enriched UO_2 fuel. Accordingly, a crash programme was launched to augment the existing plutonium fuel fabrication laboratory with a capacity of 1 kg fuel per day to 50 kg per day to meet the interim requirement of TAPS.

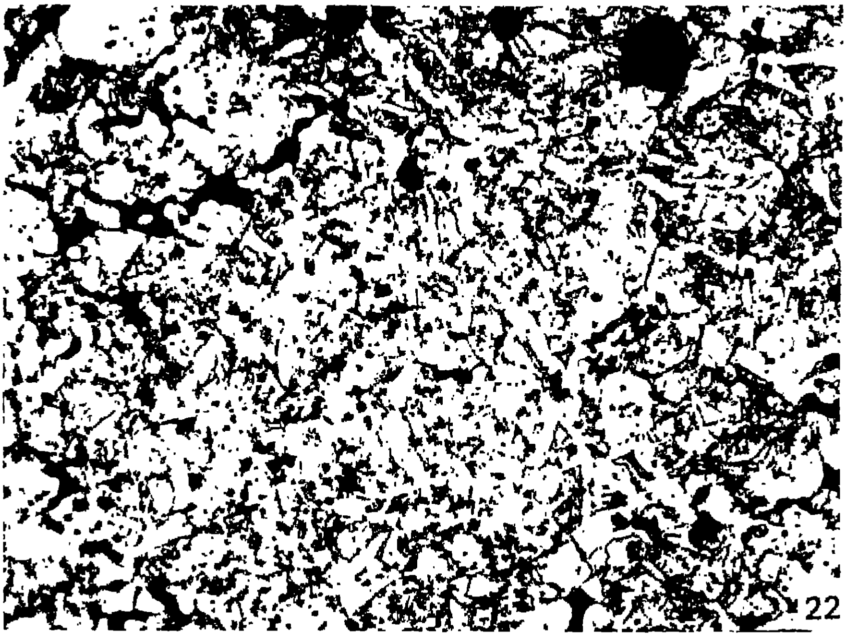

22

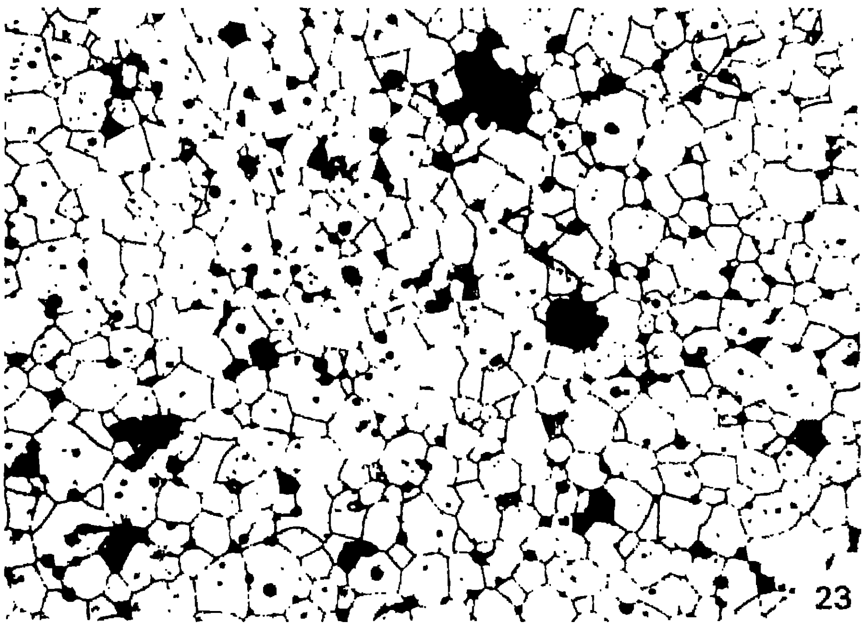

23

Figures 22, 23. **22.** Microstructure of $(U_{0.24}\ Pu_{0.76})O_2$ showing two phases (× 400). **23.** Microstructure of single phase $(U_{0.70}\ Pu_{0.30})O_2$ (× 320).

Though the first MOX fuel experience (Sah *et al* 1977) was acquired in Trombay in 1972 when a test pin of UO_2–1·5 w/o PuO_2 of specifications similar to our PHWR fuel element was fabricated for irradiation testing in the pressurised water loop (PWL) of our CIRUS reactor, the MOX substitute fuel for TAPS was a real challenge to the metallurgists as this was a time bound project involving plant scale handling and fabrication of plutonium fuels in a laboratory originally designed for R and D work only.

After extensive investigation, fabrication flowsheet with optimum process parameters was developed to get MOX fuel pellets according to specification (Roy *et al* 1984). There is a stringent requirement of uniformity of plutonium distribution in the fuel pellets from the view point of in-reactor performance. This has been confirmed from the alpha-autoradiography of the MOX pellets shown in figure 24.

The pilot scale MOX fuel fabrication facility of capacity 50 kg sintered MOX pellets per day has been commissioned in BARC and production trials with a few tons of UO_2 pellets have been successfully completed. The facility essentially consists of:

(a) a train of interconnected glove boxes for preparation of MOX granules starting from UO_2 and PuO_2 powders by milling, blending, precompaction and granulation;
(b) a compaction-sintering train consisting of a 30 ton automatic double action hydraulic press, dewaxing furnaces and a continuous sintering furnace (Sengupta *et al* 1982) (figure 25);
(c) a centreless grinder for grinding pellet to final diameter;
(d) a welding train for vacuum degassing of sintered pellets, followed by loading of pellets in a one end welded preautoclaved 4m long zircaloy-2 tubes and encapsulation by TIG welding under a helium pressure of around 0·3 MPa;
(e) a train of glove boxes for refabrication of sintered MOX pellets from rejected oxide; and
(f) facilities for nondestructive testing (NDT) of zircaloy hardwares and fuel pins by airgauging, ultrasonic testing, radiography, helium leak detection mass spectrometry and other quality control facilities like metallography, x-ray diffractometry and x-ray fluorescence spectrometry.

The mechanical and thermal properties of UO_2 are not significantly affected by addition of up to 5 w/o of PuO_2. With 5 % PuO_2 addition, the thermal conductivity is reduced by around 5 %, the melting point decreases by 26°C, the thermal expansion and density increase marginally by 1 %, the fission gas release and swelling are unaffected and the creep and nuclear self-shielding properties are improved.

Irradiation-testing of a prototype MOX fuel cluster of 6 pins (figure 26) in the PWL, CIRUS was started in December 1979 simulating the operating conditions at TAPS. This MOX fuel cluster has performed very satisfactorily without failure up to the target burn-up of 18000 MWD/ton. A second similar cluster has already been fabricated and is under testing in the reactor.

11. Mixed carbide and nitride fuels

The mixed oxide fuels are not, however, the ultimate in the field of development of plutonium fuels for LMFBR. The oxide fuel has the inherent drawback of relatively low heavy atom density, high light atom fraction and poor thermal conductivity. These factors are responsible for its low breeding ratio and low power ratings. On the other hand the potential of (UPu)C and (UPu)N have all along been recognised as better and advanced LMFBR fuels on the basis of their higher breeding ratio and higher linear and specific power ratings which results in much shorter doubling time. An added advantage is the relatively good compatibility of (UPu)C and (UPu)N with sodium (Sengupta *et al* 1982).

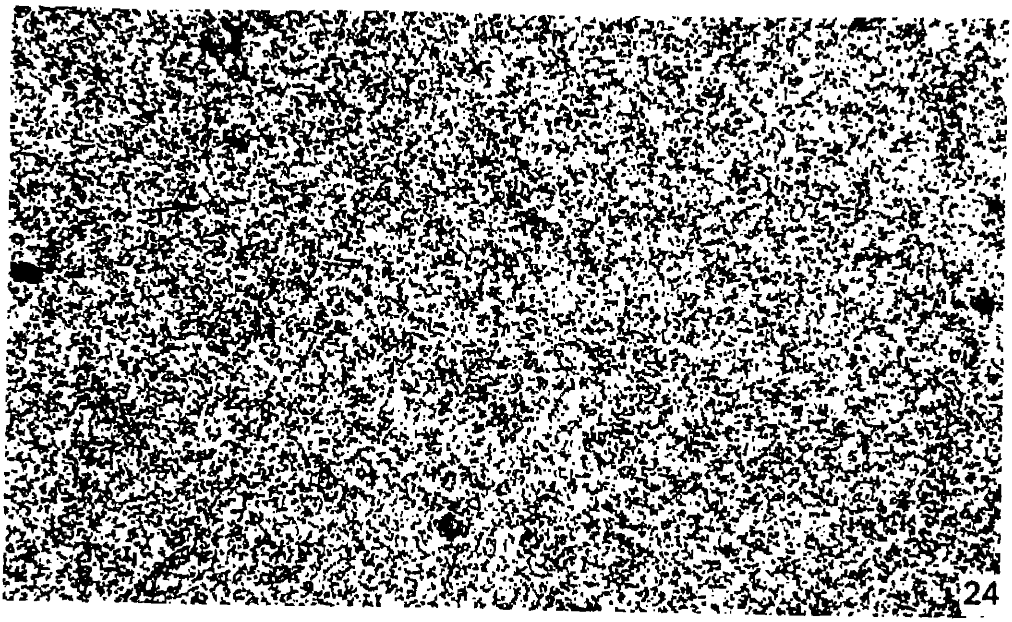

24

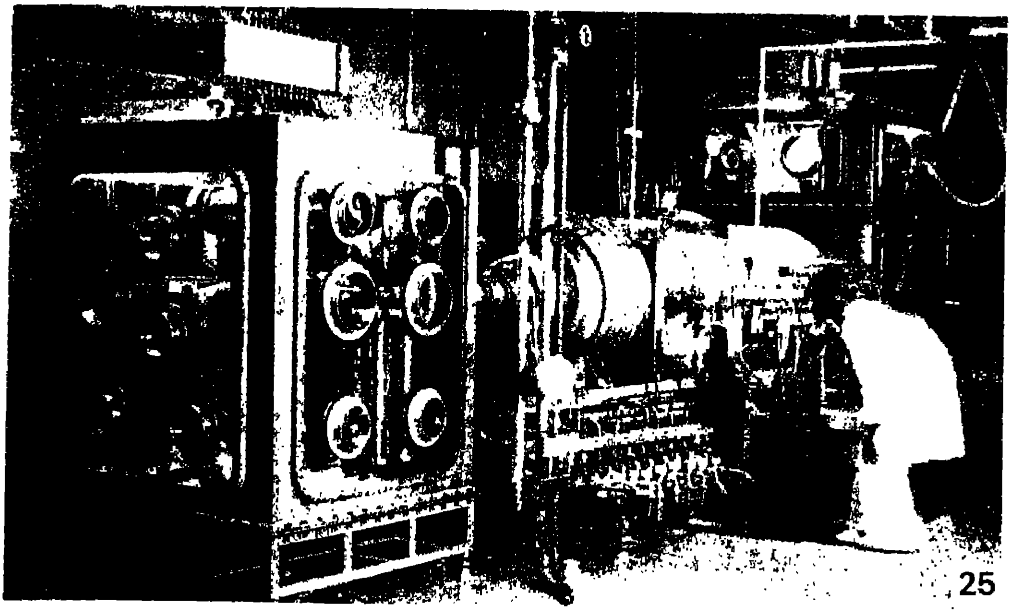

25

Figures 24, 25. **24.** Alpha auto radiograph of MOX pellets (× 80). **25.** Continuous sintering furnace for MOX pellets.

Since plutonium-rich mixed oxide fuels were not suitable for FBTR, efforts were directed to develop the fabrication flowsheet for plutonium rich (UPu)C and (UPu)N fuels. Towards the end of 1970s ($U_{0\cdot3}Pu_{0\cdot7}$)C and ($U_{0\cdot3}Pu_{0\cdot7}$)N pellets of controlled density and phase content were successfully produced in the plutonium metallurgy laboratory at Trombay as per the flowsheet shown in figure 27 (Ganguly 1980).

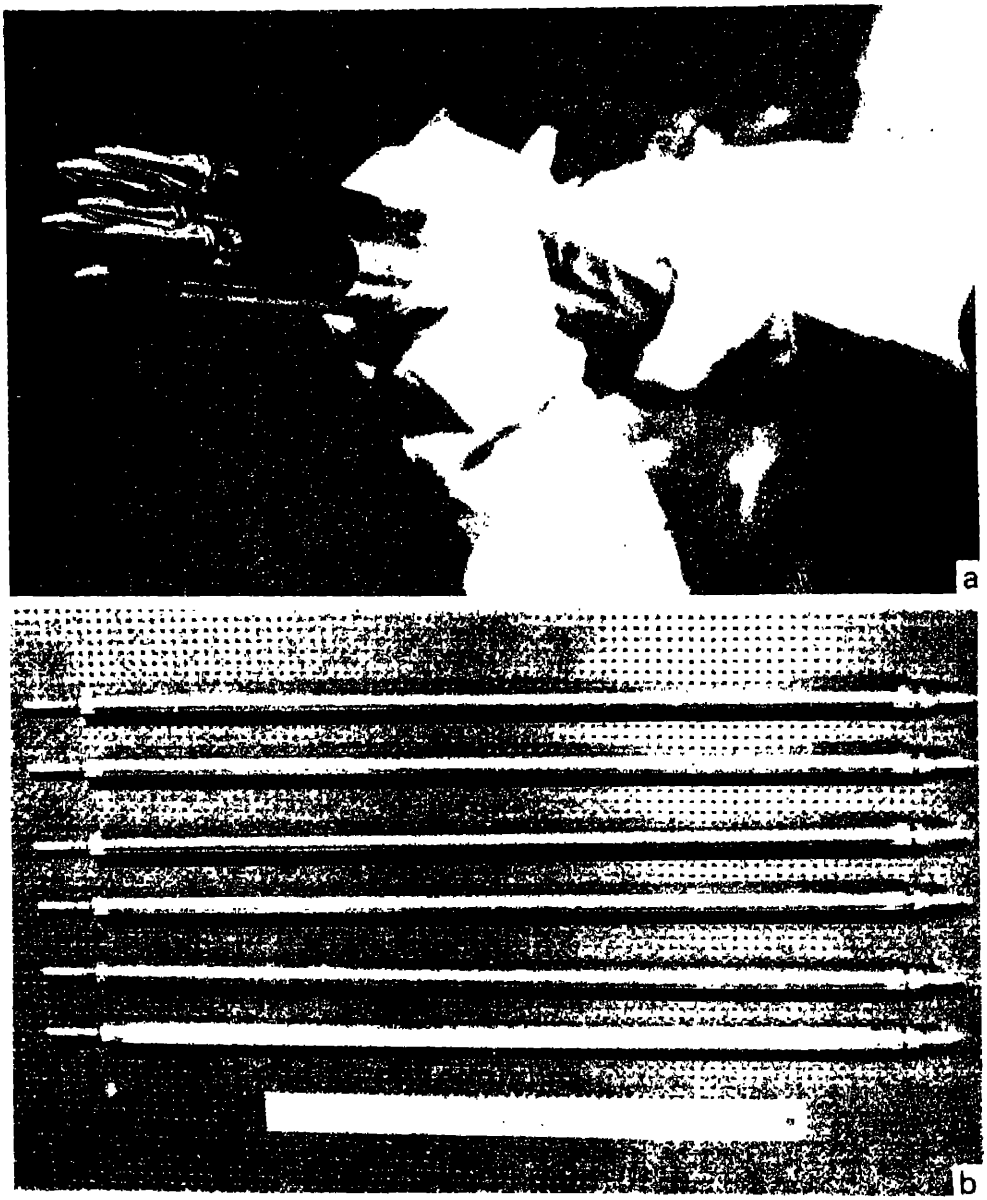

Figure 26. MOX fuel pin cluster for irradiation in PWL, CIRUS (**a**). MOX cluster (**b**). Individual MOX pins.

The two main stages in the fabrication are: (a) synthesis of (UPu)C and (UPu)N by carbothermic reduction of mechanically mixed UO_2, PuO_2 and graphite powders compacted in the form of tablets in vacuum or flowing argon for the carbide and flowing nitrogen or nitrogen + 8 % hydrogen mixture for the nitride; (b) crushing and milling of carbide and nitride clinkers followed by cold pressing and sintering in argon, argon + 8 % hydrogen or vacuum.

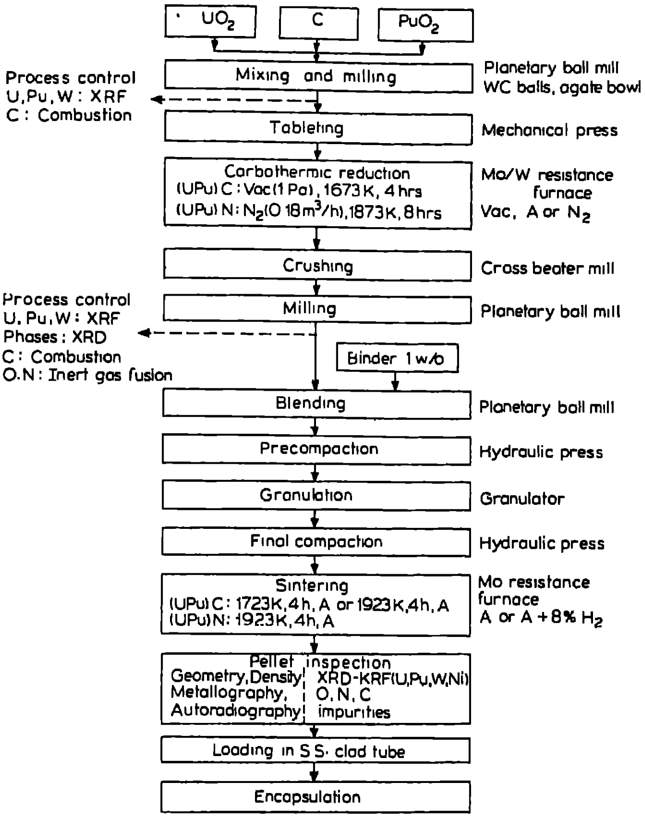

Figure 27. Flow sheet for preparation of $(U_{0.3}\ Pu_{0.7})C$ and $(U_{0.3}\ Pu_{0.7})N$ fuel pellets for LMFBR at BARC.

Equilibrium thermodynamic calculations confirmed by experimental results show that (UPu)C prepared by carbothermic reduction of oxides contain substantial amount of oxygen because of the formation of a mixed uranium plutonium monoxy-carbide solid solution in the final stage of the carbothermic reduction process which above 1625°C remove essentially all the oxygen from the monocarbide but might result in the formation of the undesirable liquid phase PuC_{1-x} by peritectic decomposition and lead to high plutonium volatilisation losses.

In the synthesis of (UPu)N by solid state carbothermic reduction of a powder mixture of UO_2, PuO_2 and graphite, nitrogen plays the dual role of the reactant and the carrier for the removal of CO. The (UPu)N produced by this method has high oxygen and carbon contents.

11.1 *Advantages of plutonium rich (UPu)C and (UPu)N*

Initial theoretical studies on plutonium rich (UPu)C and (UPu)N unfolded the following advantages of this fuel over the uranium rich composition: (a) UC and uranium rich (UPu)C have no carbon solubility range but there is a limited carbon homogeneity range in the PuC and plutonium rich (UPu)C as shown in the U-Pu-C phase diagram (figure 28) (Storms and Ackermann 1974). It is, therefore, relatively simple to prepare $(U_{0.3}Pu_{0.7})C$ as a nearly single phase material.

(b) With nitrogen, plutonium forms only one compound namely PuN whereas uranium has three nitrogen compounds, namely UN, U_2N_3 and UN_2 (Potter 1975). The higher nitrides of uranium, however, are easily decomposed to the mononitride by a high temperature treatment in vacuum or inert gas. Single phase PuN and plutonium rich (UPu)N are therefore relatively easy to prepare.

(c) Pu_2C_3 and $(U_{0.3}Pu_{0.7})C_{1.02}$ have lower carbon potentials compared to U_2C_3 at all temperatures and a lower carbon potential than stainless steel 316 up to 725°C as shown in figure 29 (Gotzmann and Hofmann 1974; Internal report 1980). The chances of carbon transfer from plutonium rich mixed carbide to stainless steel is therefore lower and there will be no clad carburisation if the temperature inside the clad is kept below 725°C.

(d) The melting points of (Sheth and Leibonitz 1974) of PuC and PuN are less than that of UC and UN respectively for which the optimum carbothermic and sintering temperatures of plutonium rich (UPu)C and (UPu)N are 150–200°C lower than their uranium rich counterparts (Ganguly *et al* 1980, 1982). Hence, the plutonium volatilisation losses are relatively less (within 1–2%).

11.2 *Mixed carbide facility for* FBTR

The small scale (60 g) laboratory experiments established the overall feasibility of the fabrication of controlled density (UPu)C and (UPu)N pellets as nearly single phase material as shown in the x-ray diffraction patterns (figure 30) and the microstructures (figure 31). On the basis of this experience a production laboratory was set up during 1981–82 for the fabrication and quality control of 1·5 kg/day of finished mixed carbide fuel pellets from UO_2 and PuO_2 feed materials (Ganguly and Roy 1981). This laboratory has two main facilities, namely (a) pellet production facility, and (b) process control facility.

The pellet production facility consists of a train of 12 interconnected glove boxes housing conventional powder metallurgy equipment. In addition, for rapid process control at different stages in the preparation and sintering of MC and MN

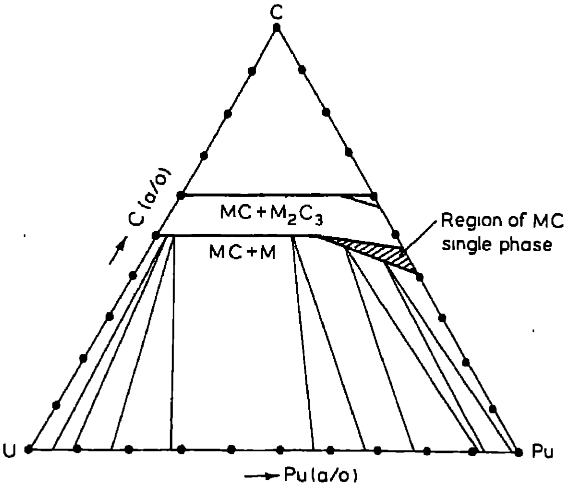

Figure 28. U-Pu-C system at 600°C (M = U, Pu).

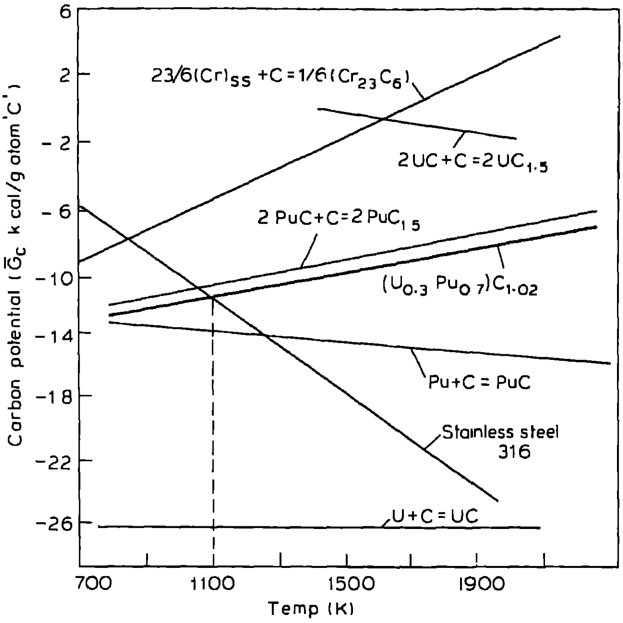

Figure 29. Carbon potentials of carbides.

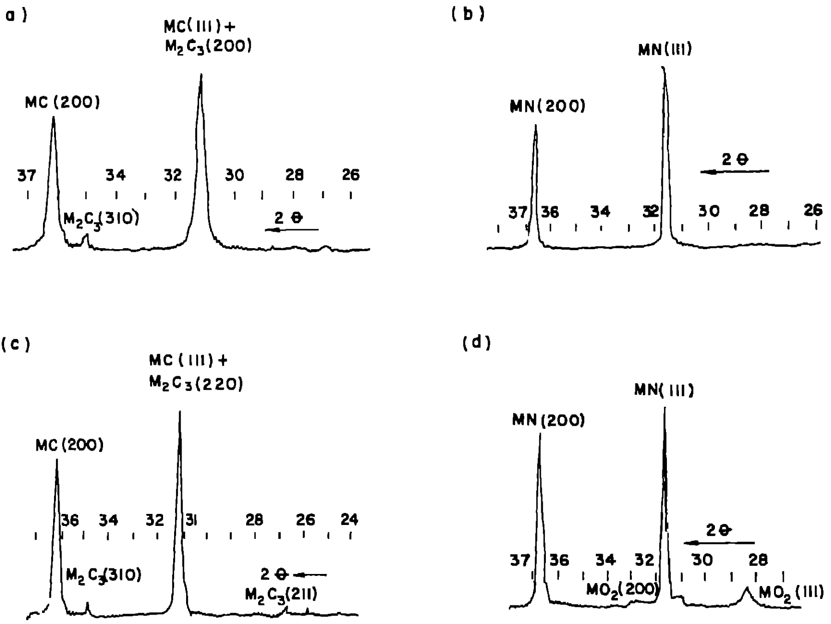

Figure 30. X-ray diffraction pattern of MC and MN; M = ($U_{0.3}$ $Pu_{0.7}$) after carbothermic reduction of UO_2+PuO_2+C for (**a**). carbide (**b**). nitride; after sintering of (**c**). carbide (without -Ni) and (**d**). nitride.

powders the following equipment have also been installed (Ganguly *et al* 1981): (a) a combined and sequential oxygen and nitrogen inert gas fusion analyser for rapid analysis of oxygen and nitrogen in powders and pellets; (b) a rapid carbon analyser for powder and pellet based on the method of combustion and determination by thermal conductivity meter; (c) an automatic, combined and sequential x-ray fluorescence spectrometer and x-ray diffractometer for rapid analysis of U, Pu, tungsten, nickel and different phases present in powder and pellets (figure 32).

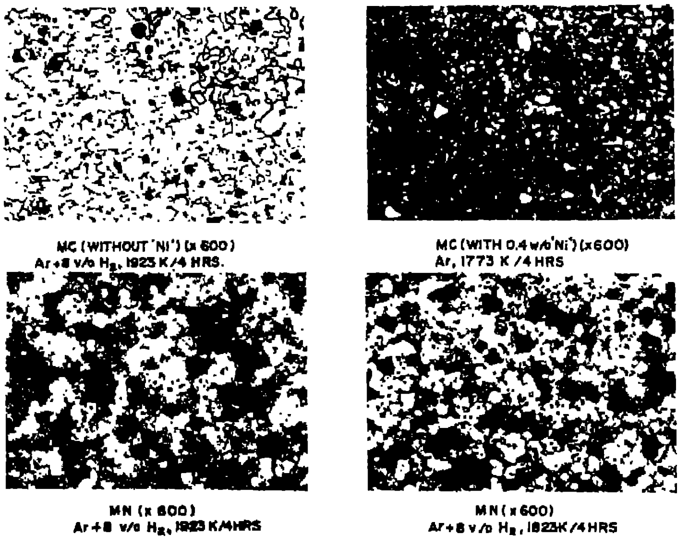
MC (WITHOUT 'NI') (x 600)
Ar+8 v/o H_2, 1923 K/4 HRS.
MC (WITH 0.4 w/o 'Ni') (x600)
Ar, 1773 K /4 HRS
MN (x 600)
Ar+8 v/o H_2, 1923 K/4HRS
MN (x 600)
Ar+8 v/o H_2, 1823K/4HRS

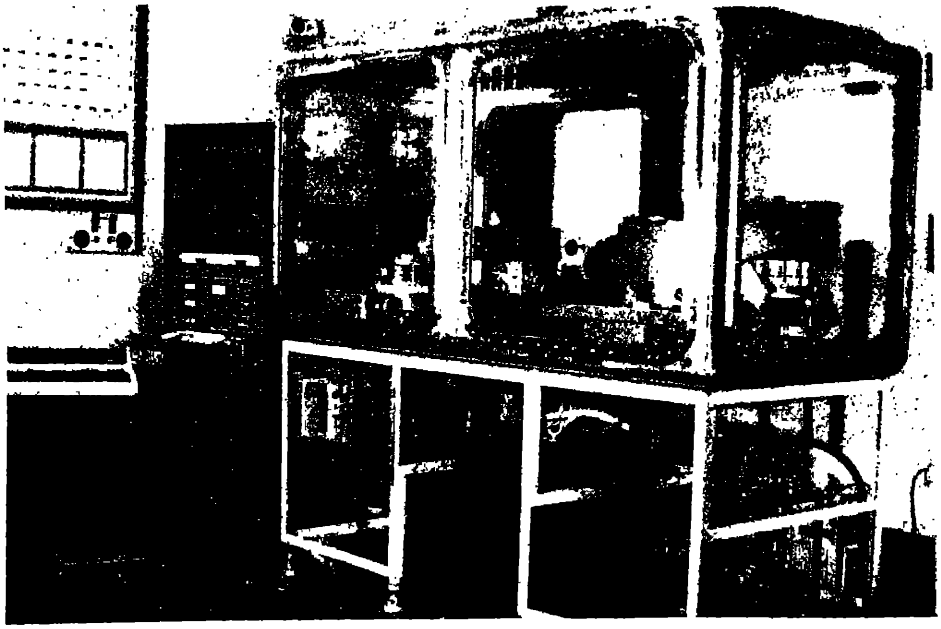

Figures 31, 32. **31.** Microstructure of plutonium rich (U Pu)C and (U Pu)N pellets. **32.** Combined XRD-XRF unit in RMD, BARC under commissioning inside a glove box.

. Looking forward

our travels into the plutonium age over the past quarter of a century, we have passed ny milestones, meeting new challenges, probing new frontiers, indigenising all pects of plutonium metallurgy and fuels and have reached today a stage of mmercial exploitation of plutonium in nuclear power reactors.

Our well-known three stage nuclear power strategy projects the pivotal role of tonium in the coming decades for a viable and rapidly expanding electricity neration programme. The first stage based on our operating and forthcoming natural O_2 fuelled PHWRs will be limited to only 10–15 GW(e) for 30 yr but will produce tween 100–150 tons of fissile plutonium as by-product along with depleted uranium. e second stage, which is likely to start towards the turn of this century, will make st effective utilisation of these large quantities of plutonium by recycling it several nes with depleted uranium in LMFBR. Around 350 GW(e) would be possible for 65 yr th ^{238}U–^{239}Pu fuel cycle and simultaneously ^{232}Th could be converted to ^{233}U. ally, in the third stage, the self sustaining ^{232}Th–^{233}U thermal breeder fuel cycle uld be used in PHWR to unlock 1000 GW(e) for 240 yr, thus establishing that nuclear wer is the only long term answer to our energy crisis.

A plutonium-fuelled prototype fast breeder reactor of 500 MW(e) capacity BR-500) has been already planned for the 1990s (Singh *et al* 1981). This reactor will entially act as a "lead station" to demonstrate the basic safety, reliability and nomics of plutonium fuel reprocessing, refabrication and irradiation on a mmercial scale and will generate data on which "series ordered LMFBR stations" can commissioned with confidence after 2010.

A larger capacity plutonium fuel fabrication plant is coming up at Tarapur to meet r future requirement of plutonium fuels in PFBR-500 and thermal reactors. This plant eing designed and constructed in the philosophy of "secured automated fabrication F)" through a carefully staged development from present glove box operations to ni-remote or remote operations placing emphasis on radiotoxic dust reduction and containment. This development should ultimately result in systems that maximise sonnel radiation protection, restrict and control access to plutonium, provide near l time accountability and improve the uniformity and quality of plutonium fuels.

New fabrication flowsheets for plutonium bearing fuels amenable to automation and notisation are being developed in Trombay. One of the promising process is the 'gel-letisation route' (Gilissen *et al* 1982) which uses gel derived microspheres rather than wder as feed material for pellet pressing. Because of the free flowing and dust-free ure of microspheres, the gel-pelletisation process is ideally suited for remote rication of the fuel pellets. In our preliminary experiments with gelled microspheres (UPu)O_2, high density sintered pellets have been prepared. Figure 33 shows the rostructure of such a pellet and figure 34 shows the alpha autoradiograph.

The ThO_2-PuO_2 (up to maximum of 5% PuO_2) is a promising fuel for our thorium ed PHWR (Ganguly and Roy 1982). If due to technological or political reasons ycling of plutonium is delayed in our LMFBR, such fuels could be conveniently used in r existing PHWR without involving major resource investment and engineering difications.

n conclusion it may be stated that plutonium technology is mostly classified in ure and detailed informations are not available in open literature. In spite of that we e succeeded in the harnessing of plutonium entirely with indigenous resources and

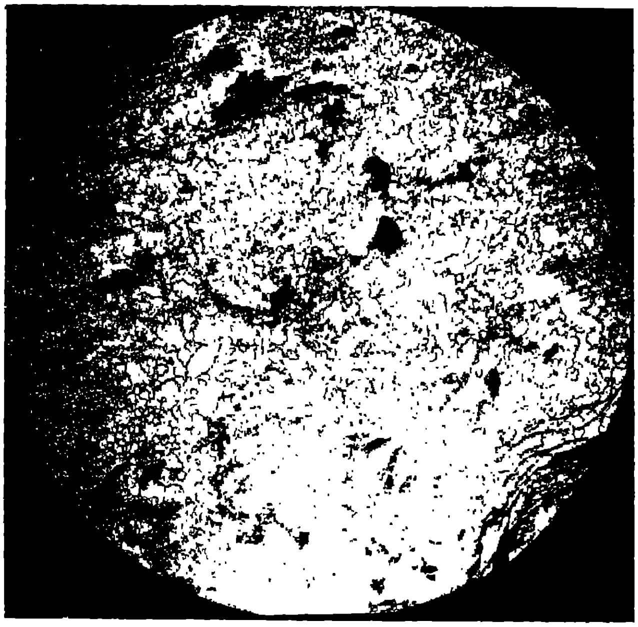

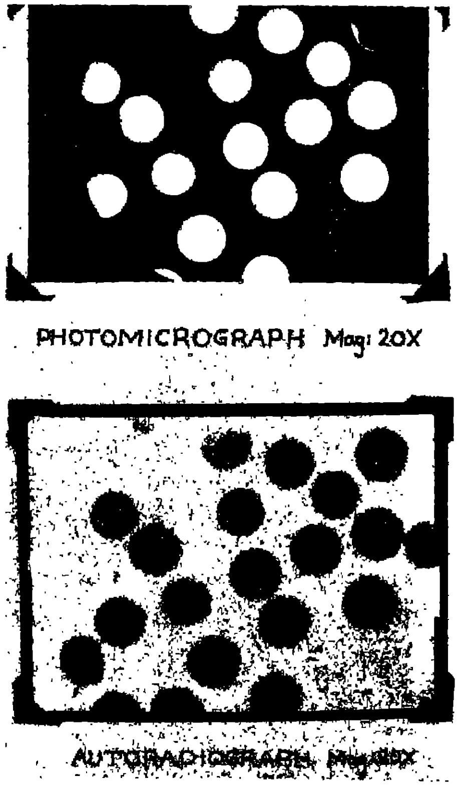

Figures 33, 34. **33.** Microstructure of UO_2 pellet prepared by the gel pelletisation route (× 90). **34.** Microstructure and alpha-autoradiograph of MOX structures.

without any foreign assistance. Only a vertical take off is needed and a few obstacles are to be overcome before this great gift of nature and our control over it bears the fruit of its present promise.

Acknowledgement

Thanks are due to the Radiometallurgy Division as a whole, including the staff members of Post Irradiation Examination, Engineering Services, Oxide Fuels, Advanced Fuels, Quality Control and Inspection and Cladding and Welding Sections. In addition, the support from Fuel Reprocessing Division and Radiochemistry Division is acknowledged. The continuous encouragement received from the higher authorities is also gratefully acknowledged.

References

Coffinberry A S and Miner W N 1961 *The metal plutonium* (Chicago: University Press)

Ellinger F G, Land C C and Miner W N 1962 *J. Nucl. Mater.* 5 165

Fareeduddin S, Garg R K, Gupta U C, Kantan S K, Rajendran R and Rao N K 1964 *3rd Int. Conf. Peaceful use of atomic energy*, IAEA, Vol. II p 345

Ganguly C 1980 *Studies on preparation and sintering of mixed uranium plutonium monocarbide, mononitride and monocarbonitride*; Ph.D. Thesis, University of Calcutta,

Ganguly C, Jain G C and Roy P R 1981 *Proc. of DAE Sym. on Nucl. Chemistry and Radiochemistry*

Ganguly C and Roy P R 1981 *Proc. BNES Conf. on Fast Reactor Fuel Cycles*, London

Ganguly C and Roy P R 1982 *Proc. Int. Sym. in Ceramics*, BHEL Bangalore

Ganguly C, Roy P R and Seal A K 1980 *Trans. PMAI* 7 40

Ganguly C, Roy P R and Seal A K 1982 *Trans. IIM* Vol. 35 No. 2 p 148

Ghosh J K, Roy P R and Moorthy V K 1973 BARC/I-254

Gilissen R, Panwels H, Sleurs J and Smolders A 1982 *Trans. Am. Nucl. Soc.* 40 26

Gotzmann O and Hofmann P 1974 *Proc. of Int. Sym. on Fuel and Fuel Elements for Fast Reactor* IAEA p 233

Hanna G C, Westcott C H, Lemmel H D, Leonard B R Jr., Story J S and Altree P M 1969 *Atomic Energy Rev.* 7 p. 3

Hansen L P and Clayton R D 1967 *Nucl. Appl.* 3 484

Housseau M 1974 *Proc. Sym. on fuel and fuel element for fast reactors*, IAEA p 277

Internal Report prepared on FBTR mixed oxide fuel by DAE, India and CEA, France (Sept. 1970)

Internal Report of DAE working group on mixed uranium plutonium carbide fuels for FBTR (1980)

Janardhanan S, Krishnamurthi T N, Dabhadkar S B and Soman S D 1973 BARC/I-259

Kanij J B W, Noothont A J and Votock I 1974 IAEA-161 p 185, Vienna

Mahajan V K, Ganguly C, Ramakumar M S, Roy P R and Moorthy V K 1972 BARC-629

Majumdar S, Arunkumar, Kamath H S, Ramachandran R, Purushotham D S C and Roy P R 1984 BARC-1182

Majumdar S, Purushotham D S C and Roy P R 1982 BARC/I-730

Potter P E 1975 *Plutonium and other actinides* p 211

Prasad G J, Ganguly C and Roy P R 1976 BARC/I-423

Recommendation of the ICRP-Suppl. 6, 1955 *Br. J. Radiol.*

Ramachandran R, Arunkumar, Purushotham D S C and Roy P R 1981 *Trans. PMAI* 8 277

Rao N K 1982 *Proc. Sym. Int. Conf. on Nucl. Power Experience* IAEA, Vienna

Roy P R 1962 *AEET/Radiochem.* 22

Roy P R 1964 *J. Nucl. Mater.* 11 59

Roy P R 1975 *Proc. IAEA group meeting on facilities and techniques for* ($UPu)O_2$ *fuel fabrication, Mol,* Belgium

Roy P R 1978 *Proc. Seminar on Nucl. Metallurgy*, IIM Bombay

Roy P R, Deshpande R G and Laxminarayanan T S 1967 BARC-294

Roy P R, Laxminarayanan T S, Singh R K and Haraprakash A 1969 BARC/I-37

Roy P R and Mahajan V K 1975 *Proc. IWSA-BARC Winter School*, Bombay

Roy P R, Purushotham D S C, Majumdar S, Ramachandran R, Kamath H S, Ghosh J K and Goswami G L *et al* 1984 BARC-1203

Sah D N, Sahoo K C, Chatterjee S, Majumdar S, Kamath H S, Ramachandran R, Bahl J K, Purushotham D S C, Ramakumar M S, Sivaramakrishnan K S and Roy P R 1977 BARC-918

Seaborg G T 1958 *The transuranium elements* (Massachusetts, USA: Addison-Wesley Publishing Co.)

Sengupta A K, Ganguly C and Roy P R 1982 BARC/I-740

Sheth A and Leibonitz L 1974 ANL-AFP-3

Singh B, Bhoje S B, John T M, Lee S M, Singh R S and Paranjpe S R 1981 *Proc. BNES Conf. on Fast Reactor Fuel Cycles*, London

Sood D D and Vaidya V N 1979 *Proc. Sym. on Sintering and Sintered Products*, BARC, Bombay

Stoller S M and Richards R B 1961 *Reactor Handbook* (New York: Interscience Publishers) 2 454

Storms E K and Ackermann R J 1974 *Proc. of IAEA Panel Meeting on U-Pu-C System*, Grenoble, France

Wade W Z and Wolf T 1969 *J. Nucl. Sci. Technol.* 6 402

Wick O J 1980 *Plutonium handbook* (La-Crange Park, Illinois: American Nuclear Society)

Zachariasen W H and Ellinger F H 1959 *Acta Crystallogr.* 12 175

Bull. Mater. Sci., Vol. 6, No. 5, September 1984, pp. 959–969. © Printed in India.

Internal friction in hexagonal metals

M K ASUNDI and C N RAO

Physical Metallurgy Division, Bhabha Atomic Research Centre, Trombay, Bombay 400 085, India

Abstract. An overview of the studies of internal friction in hexagonal metals and alloys is presented. An outline of the experimental techniques of measurement and the atomistic mechanisms causing internal friction is also given.

Keywords. Anelasticity; internal friction; hexagonal metals.

1. Introduction

All materials possess the intrinsic ability to dissipate mechanical energy by some internal atomistic or microscopic processes. This property is called *internal friction* or damping capacity. Internal friction is mainly observed in systems undergoing periodic vibrations and its magnitude can be determined by the decay of free vibrations or of travelling waves in a test piece. In recent times, internal friction has become an important tool for investigating the atomistic processes in solids. One of the best known examples is the internal relaxation due to the diffusion of interstitial solutes in a bcc solid which can be conveniently studied by low cycle torsion pendulum measurements.

This paper gives a brief account of the various measures of internal friction, the experimental techniques of measurement and the mechanisms for internal friction followed by an overview of the studies on hexagonal materials. The results on zirconium and titanium alloys are given in greater detail due to the extensive studies made on these materials.

2. Relaxation and internal friction

A measure of the damping capacity is the quantity $\Delta W/W$ where ΔW is the energy loss per cycle and W is the total vibrational energy. It is given by the integral $\int \sigma \, d\varepsilon$ over one cycle where σ is the applied stress and ε is the resulting strain. For an ideal elastic body, there will be no dissipation of energy and the integral vanishes. When there is internal dissipation, stress and strain are no longer in phase with each other and the dissipation can be due to static or dynamic hysteresis (figure 1). For static hysteresis (figure 1a) part of the strain is irreversible and the internal friction will generally be independent of the frequency of vibrations, but will be strongly dependent on the amplitude of vibrations.

For dynamic hysteresis (figure 1b) relaxation occurs over a finite time by internal rearrangements in the material and depends on the rate of change of σ and ε. Such a behaviour is called *anelastic*, a term introduced by Zener (1948). For small amplitude of

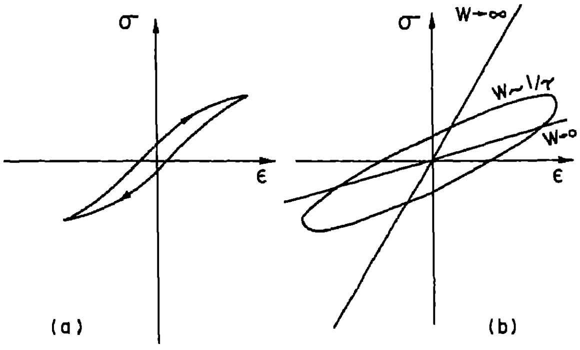

Figure 1. Schematic representation of mechanical hysteresis (**a**) static hysteresis (**b**) dynamic hysteresis.

the vibrations, the relation between σ, ε and their time derivatives is linear and the damping will be independent of amplitude but strongly dependent on the frequency of vibration. At very high frequencies, there is little time for the relaxations to take place and no energy loss will be obtained. At very low frequencies, complete relaxation occurs and the behaviour of the system is purely elastic with a smaller relaxed value of the elastic modulus. At some intermediate frequency ω (of the order of $1/\tau$ where τ is the relaxation time for the internal rearrangement) a maximum in internal friction will occur.

The various parameters used for quantitative specification of damping are dimensionless ratios which are independent of the size of the sample and the nature of the experimental system when the damping is independent of the amplitude of vibration.

2.1 *The logarithmic decrement δ*

The damping of a system freely vibrating in a single mode can be expressed in terms of the rate of decay of the vibration amplitude. The logarithmic decrement is given by

$$\delta = \frac{1}{n}\ln(A_0/A_n), \tag{1}$$

where A_0 and A_n are the amplitudes before and after n cycles of vibration.

2.2 *Q^{-1} value*

For a system undergoing forced vibrations, the amplitude magnification factor Q at resonance and the relative width $\Delta\omega/\omega_r$ of the resonance (where ω_r is the resonance frequency) depend solely on the damping of the system. For the resonance width at half maximum they are related as

$$Q^{-1} = \Delta\omega/\omega_r, \tag{2}$$

and provide a direct measure of the damping.

2.3 *Specific damping capacity, P*

If W is the total energy of the oscillating system at the commencement of a cycle and ΔW the energy dissipated in the cycle, the specific damping capacity is defined as

$$P = \Delta W/W. \tag{3}$$

2.4 *Tangent of the phase angle*

In the case of linear damping, an applied sinusoidal force $f_0 \sin \omega t$ produces a displacement $x_0 \sin(\omega t - \phi)$, where ϕ is the phase lag between the applied force and displacement. The ratio of the components of strain out-of-phase and in-phase with the stress given by $\tan\phi$ can be used as a measure of the damping.

For small damping values, the different quantities defined above are approximately related to each other as

$$\delta/\pi = Q^{-1} = P/2\pi = \tan\phi. \tag{4}$$

3. Experimental methods of measurement

When considering a relaxation effect, four quantities are of interest; (i) the relaxation strength, which determines the peak height; (ii) the relaxation time which determines the peak position on the temperature scale; (iii) the shape of the peak which can be characterized in terms of the width at half maximum; and (iv) the modulus defect which causes a variation of the resonance frequency of the specimen in the temperature range of the damping peak.

Over the years, a variety of equipment have been built in various laboratories to measure internal friction. According to the method by which stresses are generated in the specimen, the techniques can be divided into resonance methods, pulse-echo methods and mechanical after-effect methods. Whereas the pulse-echo technique is restricted to high frequencies (over 1 MHz) and the after-effect method to very long relaxation times (over 10 sec), the resonance methods are useful in the range of low to medium frequencies (0·01 Hz to 100 kHz). In a given type of experimental system one is usually restricted to a limited number of operating frequencies and hence to observe a relaxation process one has to vary the temperature. Thus, practically all the instruments described in the literature provide for measurements over a range of temperature.

A comprehensive description of the experimental methods can be found in the books by Nowick and Berry (1972) and De Batist (1972).

4. Mechanisms of internal friction

A number of atomistic and microscopic mechanisms can contribute to energy dissipation in solids. Some of these are: (a) stress-induced ordering of interstitial and substitutional atoms, commonly known as Snoek and Zener relaxations (Snoek 1941; Zener 1947), (b) grain boundary viscosity (Kê 1949), (c) thermoelastic damping (Waterman 1958), (d) dislocation damping (Read 1940), (e) magnetic damping in ferromagnetic materials (Cochardt 1959) and (f) electronic damping at low temperatures (Bommel 1954).

Covering the various aspects of relaxation processes and experimental results, extensive reviews have been published by Zener (1948), Nowick and Berry (1972), Nowick (1953), Entwistle (1962), De Batist (1972), Berry (1962), Mason (1966), Niblet and Wilks (1960), Wilks (1965), Burdett and Queen (1970), Fantozzi and Ritchie (1981) and Lucke and Granato (1957).

A brief account of the relaxations ascribed to point defects, dislocations and grain boundaries is given below:

4.1 *Internal friction due to point defects*

Point defects produce anelastic behaviour through a process known as stress-induced ordering, in which the equilibrium configuration of a collection of defects in the crystal changes with time to a new state under applied stress. When the stress is removed, the change is reversed and with time the original state of order is restored. The occurrence of stress-induced ordering for point defects depends mainly on the ability of an applied sress to change the free energy associated with the presence of a defect in the crystal. If defects are present in several crystallographically equivalent positions whose free energies can be split by an external stress, a redistribution of the defects among these states will re-establish equilibrium. Only those defects which produce local strains having a lower symmetry than that of the lattice are capable of producing relaxation under shear. Such defects are called *asymmetric defects* or *elastic dipoles*.

An outstanding example of anelasticity produced by an elementary point defect acting as an elastic dipole is provided by the Snoek relaxation, first observed in α-Fe containing small amounts of C or N (Snoek 1941, 1942). The Snoek effect has since been observed in a number of other bcc transition metals containing impurity atoms (like C, N, O, H) in interstitial positions of the lattice. The Snoek peaks due to O, C and N in niobium are shown in figure 2 (Hoffman and Wert 1966).

In α-Fe, the carbon atoms occupy the octahedral sites of the type [1/2, 0, 0] (figure 3). The interstitial atom is an elastic dipole of ⟨100⟩ tetragonal symmetry, which will cause stress induced ordering. The direction of the tetragonal dipole axis may lie along any one of the crystal cube axes X, Y, Z depending on the particular site which the interstitial atom occupies. Sites which produce the tetragonal axis along the X direction have been labelled X in the figure (Similarly Y and Z sites). When an interstitial impurity makes thermally-activated jumps between neighbouring sites, which are $a/2$ apart, the dipole axis re-orients by 90° with each jump. Thus, the relaxation rate is related in a simple way to the mean jump rate of the interstitial atoms.

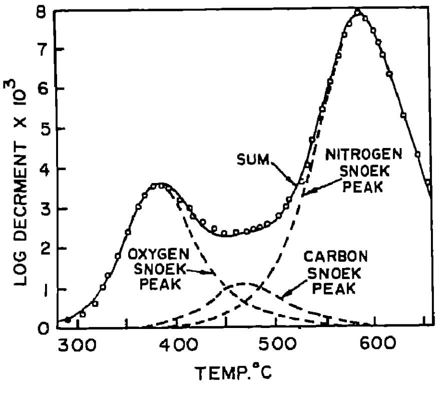

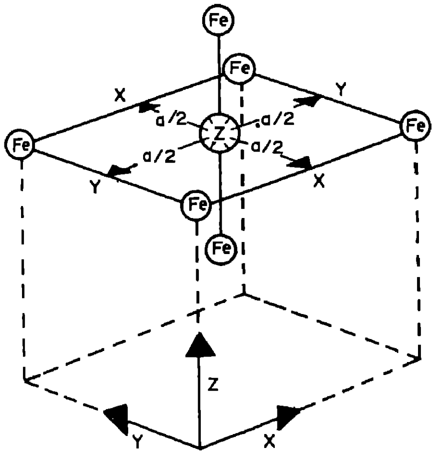

Figure 2. Snoek peaks in a ⟨100⟩ crystal of niobium tested in longitudinal vibration at 80 kHz.

Figure 3. Solute atom (shaded) in an interstitial octahedral site of bcc Fe.

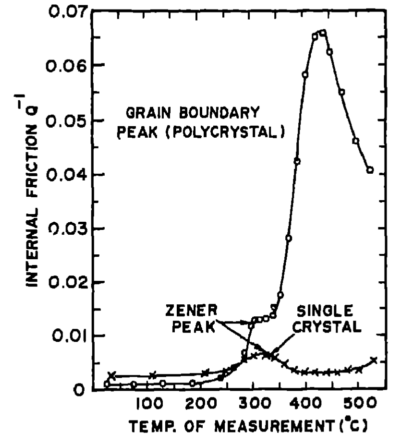

Figure 4. Zener peak in polycrystalline and single crystal specimens of α-brass (torsional vibration at 0·5 Hz).

Another important kind of point defect process, ascribed to stress-induced reorientation of solute pairs, is the Zener relaxation, first observed by Zener (1943) in a single crystal of 70–30 α-brass. Since then, similar relaxation peaks have been found in a number of binary (and other complex) alloys with fcc, bcc and hcp crystal structures. According to the pair reorientation theory of Zener (1947) asymmetric distortions can be expected around two adjacent solute atoms *i.e.* around a nearest neighbour pair. This enables splitting of free energies of differently oriented pairs by an applied stress. Figure 4 gives the Zener peak observed in α-brass.

In addition to the solute-solute (*S*-*S*) defect pair, interaction of substitutional-interstitial (*S*-*I*) pairs, and *I*-*I* pairs may lead to internal friction peaks (see for example Nowick and Berry 1972).

4.2 *Relaxation involving dislocations*

A variety of relaxation peaks occur at temperatures, usually below room temperature, after plastic deformation. They are considered to be caused by the movement and interaction of dislocations with point defects.

In the vibrating-string model (Granato and Lucke 1956) the dislocation line is considered to behave like an elastic string fixed at two points in the lattice, restricted to move in two dimensions in the glide plane. A number of anelastic effects can be deduced from the model. One important result is that the anelastic properties of dislocations should be strongly frequency dependent. Changing the resonance frequency of dislocations by decreasing the free length of the vibrating string (introducing additional pinning centres by irradiation) affords an effective method of checking the results of the dislocation damping theory and to study the production and recovery of defects.

By considering the movement of the dislocation string in a periodic lattice potential—the Peierls potential—additional relaxation effects due to anelastic motion of segments of the dislocation line are predicted.

Dislocation motion described by means of kink diffusion (Brailsford 1961) along dislocation lines can also be used to explain dislocation damping caused by resonance effects as well as relaxation effects.

The trapping of point defects in the stress field of a dislocation will have a profound effect on dislocation damping through variation in free dislocation length. A number of relaxation peaks observed in plastically deformed metals have been attributed to the interaction and motion of point defects and dislocations. The amplitude dependence of dislocation damping can be explained qualitatively in terms of dislocations anchored by point defects.

The Bordoni peak, first observed at low temperatures for deformed copper, has been studied in a number of metals. A second (Niblett–Wilks) peak associated with the Bordoni peak occurs at a lower temperature and is usually much smaller than the main peak (Niblett and Wilks 1956). A series of three peaks has been observed in deformed metals in the range between room temperature and the low temperature Bordoni peaks (Hasiguti *et al* 1962).

4.3 *Boundary relaxation processes*

Grain boundaries, domain boundaries and semi-coherent and incoherent interface boundaries between phases can result in relaxation effects giving an internal friction maximum when the boundary movement corresponds to the frequency of the applied stress field. Such effects will be observed at low frequencies and relatively high temperatures. The grain boundary peak in aluminium is shown in figure 5.

5. Internal friction studies in hexagonal metals

5.1 *Relaxation effects in hcp metals*

In the hexagonal close-packed structure, there are two possible locations for an interstitial (figure 6). The volume associated with the octahedral site is larger than that of the tetrahedral site and hence larger atoms like O, C and N are expected to occupy the octahedral sites. Both the sites have trigonal symmetry, the same as that of the host lattice, and hence single interstitials are not expected to cause anelastic effects, unless there is an interaction between the two kinds of interstitials forming an *I*-*I* pair (Povolo

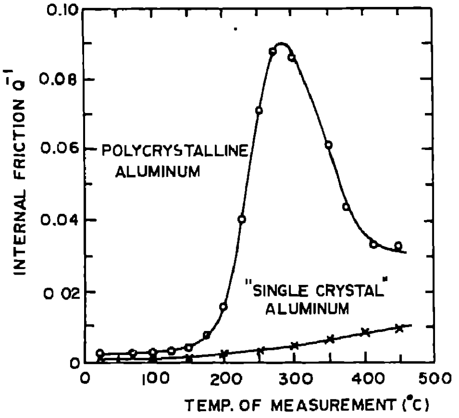

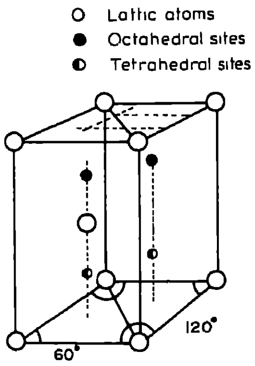

Figure 5. Grain boundary peak in polycrystalline aluminium (Torsional vibration at 0·8 Hz).

Figure 6. Interstitial positions in the hexagonal close packed lattice.

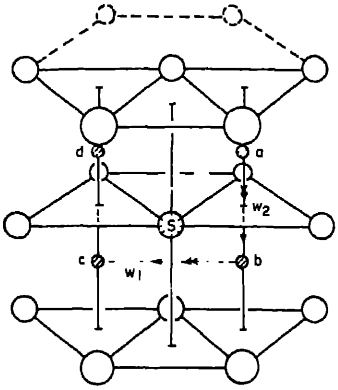

Figure 7. The two types of interstitial jumps producing reorientation of a nearest neighbour *I-S* pair in the hcp structure. W_1 is the jump rate parallel to the basal plane and W_2 is perpendicular to the basal plane.

and Bisogni 1967). This will be possible for small atoms like H which may occupy octahedral as well as tetrahedral sites. In terms of the jump probabilities W_1 for the transition from tetrahedral to octahedral site and W_2 for the reverse jump, the relaxation time τ is given by

$$\tau^{-1} = W_1 + W_2. \tag{5}$$

Relaxation due to interstitial-substitutional (*I-S*) pair in hexagonal crystals has been discussed by Nowick (1967). The nearest neighbour pairs lie in (100) type planes and the (*I-S*) defect is of the $\langle 100 \rangle$ monoclinic type and two kinds of jumps are possible during the relaxation (figure 7). In terms of the probability W_1 for a jump normal to the basal plane and W_2 for a jump within the basal plane, the two relaxation times are given by

$$\begin{aligned} \tau_1^{-1} &= 3W_2 + 2W_1, \\ \tau_2^{-1} &= 3W_2. \end{aligned} \tag{2}$$

In addition to the relaxations due to point defect interactions, relaxation effects can also occur due to dislocations and semi-coherent or incoherent interface boundaries.

5.2 *Relaxations associated with interstitials*

5.2a *I-I interactions*: Relaxation peaks due to hydrogen interstitial pair have been observed by Koster *et al* (1956) in Ti, by Bungardt and Preisendanz (1960) in Zr and by Hasiguti *et al* (1965) in zircaloy-2. Miller and Browne (1970) and Browne (1972) reported a relaxation peak due to oxygen interstitial pair in Ti, Zr and Hf. For *I-I* interaction the relaxation strength should be proportional to the number of such pairs and hence to the square of the interstitial content. Miller and Browne (1970) reported such behaviour for both Ti-O and Ti-C alloys. However, investigations by others (Misra and Asundi 1972a, b; Povolo and Bisogni 1967) failed to identify the *I-I* peak in zirconium and titanium. Interstitials were observed to give rise to relaxation only in conjunction with a substitutional atom.

5.2b *I-S pair relaxations*: Interstitial relaxation in hcp metals involving *I-S* pairs was first reported by Pratt *et al* (1954) for Ti containing oxygen. Similar results were reported by Gupta and Weinig (1962) and Bratina (1962). The height of the *I-S* peak was a linear function of the oxygen content, and was related to the size of the substitutional atom.

Bisogni *et al* (1964) measured the relaxation of oxygen and nitrogen in polycrystalline hafnium containing zirconium as substitutional element. Miller (1962) reported an oxygen peak in 'iodide pure' titanium, but the result could be due to the presence of traces of substitutional atoms. Misra and Asundi (1970, 1972) made extensive study of the internal friction due to oxygen and nitrogen in Ti and Zr with a variety of substitutional atoms having different size factors. In zirconium for all the alloying elements, oxygen gave two peaks, the relaxation strength depending on the concentration of oxygen. At low oxygen concentrations, the high temperature peak was more prominent and was ascribed due to three oxygen atom jumps. At high oxygen concentrations, the low temperature peak was more prominent and was due to a single oxygen jump. In nitrogen, only those substitutional elements with atomic size larger than that of zirconium gave internal friction peaks similar to those for oxygen. In titanium, *S-I* relaxation peaks were studied for various interstitials like C, O and N.

Using the torsion pendulum technique in the frequency range 0·5 to 1·5 Hz and the temperature range −190°C to 800°C, Misra (1976) presented extensive results on a series of Zr and Ti base dilute alloys.

5.2c *I-V pair interactions*: In materials with low temperature irradiation damage interstitial-vacancy pairs may cause relaxation effects. Moser *et al* (1973) have studied *I-V* pair interaction in neutron irradiated bcc, hcp and fcc metals. The influence of oxygen and γ-irradiation on the elastic modulus and internal friction of iodide pure zirconium has been reported by Federov *et al* (1971). It has been shown that stable oxygen-vacancy aggregates of various complexities may exist even after annealing. Three relaxation processes associated with oxygen-vacancy complexes are reported in quenched or irradiated zirconium samples.

5.3 *Boundary relaxations*

There are a number of results in the literature pertaining to twin boundary and grain boundary relaxations. Reed-Hill and Dahlberg (1966) studied the elastic after-effect in iodide pure zirconium prestrained at 77°K. At a prestrain of less than 1%, the microstructure indicated $\{11\bar{2}1\}$ twins. It is very likely that the twin boundaries move easily under load. The activation energy obtained in their study (22·7 kcal/mol) has been interpreted as that for slip ahead of the twin interface.

Studies of internal friction associated with grain boundaries in Ti and Zr were reported by Pratt *et al* (1954), Bratina and Winegard (1956), Bungardt *et al* (1962) and Misra and Asundi (1972a). Bungardt *et al* (1962) observed well-developed peaks around 600°C at 1 Hz, whose magnitude changes with grain size.

Bedford *et al* (1972) in their studies on zirconium having different cell structures found an increase in the damping for finer cell structure similar to that observed for grain boundary relaxations for fine grain structure. The high background damping in deformed zirconium is attributed to relaxation of dislocation cell walls. On recovery, dislocation rearrangement results in polygonized sub boundaries and lowering of the damping at higher temperatures.

5.4 *Dislocation relaxations*

The behaviour of dislocations in hexagonal crystals is highly anisotropic because of the limited number of slip systems that can operate in the structure. Consequently, strong orientation dependence of dislocation damping effects is to be expected in single crystal experiments.

The Bordoni peak in Zr and Ti is generally much smaller than the corresponding peak for fcc metals, probably due to the presence of interstitial impurities. Gruzin and Semenikhin (1963) studied the low temperature damping (Bordoni peak) in high purity zirconium which had been deformed to various amounts using a flextural vibration technique. The effect of alloying as well as fast neutron irradiation on the stability of the peak was studied. Doherty and Gibbons (1971) studied the Bordoni peaks in zirconium using a composite resonator technique in the frequency range of 100 to 150 kHz and found an additional peak towards the low temperature range for a sample cold worked by 38 % reduction in cross-section. Under the application of hydrostatic pressure, both the peaks were observed to increase in height. Fonquet *et al* (1970) studied Zr and Zr base alloys at a frequency of 13 kHz.

Hasiguti (1953) found that there exists an internal friction peak above the temperature of the Bordoni peak in cold worked metals. This type of peak known as the Hasiguti peak has been reported in Ti, Zr, Mg (Hasiguti *et al* 1962) and beryllium (Abrams *et al* 1966). The Hasiguti peak is usually small and has higher activation energy than the Bordoni peak and is caused by dislocation relaxation. Yukiti and Hasiguti (1972) reviewed the basic mechanism of thermally-activated unpinning of dislocations resulting in the Hasiguti peak and deduced that the peak temperature shifts with stress amplitude.

The most extensive study on single crystals was carried out by Tusi and Sack (1967). Internal friction studies and electron microscopic observations were carried out on Mg single crystals. Figure 8 shows the results for magnesium single crystals after 0·5 % compression. (θ is the angle between the crystal axis and the hexagonal axis). A broad peak at around 200°K was observed in 2–40 kHz range. From the orientation dependence, it is inferred that dislocation motion in the basal plane is involved in the relaxation process. The peak height increased with deformation and attained a maximum by 2.5 % deformation by compression. The peak height was quite sensitive to the presence of impurities. About 1 % Li completely suppress it, whereas Fe and Ni prevent the peak from disappearing even in annealed samples. A small peak at about 20°K was noticed in cold worked polycrystals and highly deformed single crystals, presumably due to grain boundary or twin boundary relaxations.

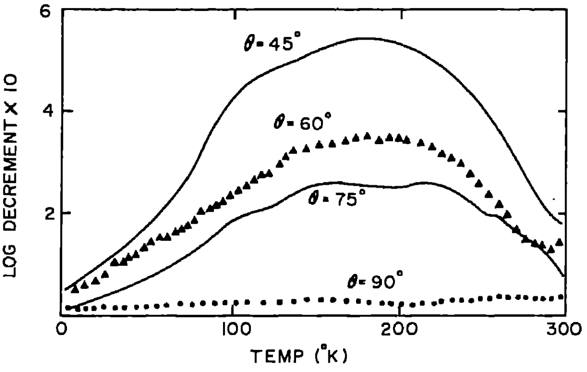

Figure 8. Internal friction of single crystals of magnesium of different orientations after 0·5 % compression.

Amplitude-dependent internal friction in Mg single crystals has been studied by Roberts (1968) in the temperature range of 80–320°K at frequencies 0·015 to 0·75 Hz. Very broad peaks were observed indicating the possibility of a large number of relaxation processes occurring together. The results are interpreted in terms of thermally activated dislocation-dislocation interactions. (Roberts and Hartman 1963; Alefeld 1962).

Esnouf and Fantozzi (1981) observed a strong internal friction peak at about half the melting temperature in high purity polycrystalline Mg. The position of the peak was dependent on strain amplitude. The results are explained in terms of dislocation glide controlled by jog climbing and diffusion of vacancies along dislocations. Atrens (1974) studied the interaction of oxygen as pinning points for dislocations in zirconium. In deformed and annealed zirconium, Ritchie and Sprungmann (1981) observed three internal friction peaks in the temperature range of 480 to 600°C and interpreted them in terms of dislocation core diffusion and unpinning of dislocations.

6. Conclusion

Compared to bcc and fcc metals, the experimental studies on hexagonal metals are fewer and various aspects are to be investigated in detail for a better understanding of the relaxation processes in hexagonal metals. Many of the results were obtained on polycrystalline materials in the form of wires or rods and hence subject to pronounced texture effects. Single crystal studies are desirable for elucidating the orientation effects on dislocation interactions. Such results would be of considerable value in understanding the point defect and dislocation interactions in hcp metals.

References

Abrams E H, Kamber K T and Ang C Y 1966 *Acta. Metall.* **14** 729

Alefeld G 1962 *Z. Phys.* **170** 249

Atrens A 1974 *Scr. Metall.* **8** 401

Bedford A J, Fuller P G and Miller D R 1972 *J. Nucl. Mater.* **43** 164

Berry B S 1962 *Acta Metall.* **10** 271

Bisogni E, Mat G and Wert C 1964 *J. Less Common Metals* **7** 197

Brailsford A D 1961 *Phys. Rev.* **122** 778

Bratina W J 1962 *Acta Metall.* **10** 332

Bratina W J and Winegard W C 1956 *Trans. AIME* **206** 186

Bommel H E 1954 *Phys. Rev.* **96** 220

Browne K M 1972 *Acta Metall.* **20** 507

Bungardt K and Preisendanz H 1960 *Z. Metall.* **51** 280

Bungardt, Preisendanz H and Horn E 1956 *Z. Metall.* **53** 495

Burdett C F and Queen T J 1970 *Metall. Rev.* **143** 47

Cochardt A 1959 in *Magnetic properties of metals and alloys* (ed) R M Bozorth, (Cleveland, Ohio: Am., Soc. Metals) 251

De Batist R 1972 *Internal friction of structural defects in crystalline solids* (Amsterdam: North-Holland Publishing Company)

De Fouquet J, Boch P, Petit J and Hisu G 1970 *J. Phys. Chem. Solids* **31** 1901

Doherty J E and Gibbons D F 1971 *J. Appl. Phys.* **42**

Entwistle K M 1962 *Metall. Rev.* **7** 175

Esnouf C and Fantozzi G 1981 *J. Phys. Colloq (France)* **42** C-5 445

Fantozzi G and Ritchie I G 1981 *J. Phys. Colloq. (France)* **42** C-5 3

Fedorov G B, Kissil A Ye and Festisov G V 1971 *Fiz. Met. Metalloved* **32** 621

Granato A V and Lucke K 1956 *J. Appl. Phys.* **27** 583, 789

Gruzin P L and Semenikhin A N 1963 *Fiz. Met. Metalloved* **15** 791

Gupta D and Weinig S 1962 *Acta Metall.* **10** 292

Hasiguti R R 1953 *Proc. Int. Conf. Theor. Phys.*, Kyoto and Tokyo 577

Hasiguti R R, Igata N and Kamoshita G 1962 *Acta Metall.* **10** 442

Hasiguti R R, Igata N, Tonomae R, Nakumara Y, Saso S and Domato K 1965 *Symp. Nondestructive testing in nuclear technology*, Bucharest

Hoffman R A and Wert C 1966 *J. Appl. Phys.* **37** 237

Ke T S 1949 *J. Appl. Phys.* **20** 274

Koster W, Bangert L and Evers M 1956 *Z. Metall.* **47** 567

Lucke K and Granato A V 1957 in *Dislocations and mechanical properties of metals* (ed) J Fischer, (New York: Wiley)

Mason W P (ed) 1966 *Physical acoustics* (New York: Academic Press) Vol III

Miller D 1962 *Trans. Met. Soc. AIME* **224** 275

Miller D and Browne K M 1970 *The science technology and applications of titanium* (London: Pergamon) 401

Misra S 1976 *Anelastic and internal friction behaviour of zirconium and titanium and their alloys* Ph.D Thesis, The Banaras Hindu University.

Misra S and Asundi M K 1970 *Trans. Indian Inst. Metals* **23** 73 1972a *Can. Met. Q.* **11** 69

Misra S and Asundi M K 1972b *Titanium science and technology* (ed) R I Jaffe and H M Burte (New York: Plenum Press)

Moser P, Verdone J, Chambron W, Nivert V and Pichon R 1973 *5th Int. Conf. Internal Friction and Ultrasonic Attenuation in Crystalline Solids*, Achen

Niblet D H and Wilks J 1956 *Philos Mag* **1** 415

Niblet D H and Wilks J 1960 *Adv. Phys.* **9** 1

Nowick A S 1953 *Prog. Metal Phys.* **4** 1

Nowick A S 1967 *Adv. Phys.* **16** 1

Nowick A S and Berry B S 1972 *Anelastic relaxation in crystalline solids* (New York: Academic Press)

Povolo F and Bisogni E A 1967 *Acta Metall.* **15** 701

Pratt J N, Bratina W J and Chalmers B 1954 *Acta Metall.* **2** 203

Read T A 1940 *Phys. Rev.* **58** 371

Reed-Hill R E and Dahlberg K P 1966 *J. Elec. Chem. Technol* **4** 303

Ritchie I G and Sprungmann K W 1981 *J. Phys. Colloq (France)* **42** C-5 427

Roberts J M 1968 *Trans. Jpn Inst. Metals* **9** 69

Roberts J M and Hartmann D E 1963 *J. Phys. Soc. Jpn* **18** 119

Snoek J L 1941 *Physica* **8** 711

Snoek J L 1942 *Physica* **9** 862

Tusi R T C and Sack H S 1967 *Acta Metall.* **15** 1715

Waterman P C 1958 *J. Appl. Phys.* **29** 1190

Wilks J 1965 *Brit. J. Appl. Phys.* **16** 587

Yukuti R and Hasiguti R R 1972 *J. Less Common Metals* **28** 249

Zener C 1943 *Trans. AIME* **152** 122

Zener C 1947 *Phys. Rev.* **71** 34

Zener C 1948 *Elasticity and anelasticity of metals* (Chicago: University Press)

Bull. Mater. Sci., Vol. 6, No. 6, December 1984, pp. 971–977. © Printed in India.

A novel method of RF powder sputtering

K SOLOMON HARSHAVARDHAN and K N KRISHNA
Materials Research Laboratory, Indian Institute of Science, Bangalore 560012, India

MS received 12 June 1984

Abstract. A new method of RF sputtering by which thin films of metals, semiconductors and insulators can be sputtered from their respective powders, has been successfully demonstrated. The films have been characterized for their surface and crystal structure using conventional methods of SEM and TEM. All the films are amorphous with a relatively smooth surface topography. The relative merits and demerits of the technique have been briefly discussed.

Keywords. RF sputtering; target; shield; Crookes dark space; amorphous films; scanning electron microscopy; transmission electron microscopy.

1. Introduction

Owing to their remarkable performance RF sputtering techniques have evolved as indispensable tools for vapour deposition of materials (Holland 1956; Chopra 1969; Jackson 1970; Maissel and Glang 1970). The technique offers manifold advantages over the other conventional methods such as thermal (resistive heating) and electron beam evaporation when a precise control over the film composition, thickness and adhesion is desired (Chopra 1969).

By definition, sputtering is the physical removal of the surface atoms of a solid target by the energetic particle bombardment and is caused by the momentum transfer of the incoming particles to the atoms near the surface layers of the solid. The ejected atoms can be deposited onto suitably placed substrates. Sputtering can be categorized into DC and RF sputtering. The former method is used effectively for sputtering of metal targets (Maissel and Glang 1970) but fails in insulating (dielectric) and semiconducting targets because of the build-up of a surface charge of positive ions on the insulator (or semiconductor) which prevents any further ion bombardment (Holland 1956; Chopra 1969). Applications of an RF field, in such cases, removes the inherent problems by providing swarms of secondary electrons from the plasma, which neutralize the positive space charge.

Targets used in conventional or commercial systems are fabricated in the form of discs and are secured to the target holders which are often water cooled. The targets are generally supported or suspended horizontally, fastened to the chamber top plate and electrically insulated from it. The substrates are kept below the target on a plate at a distance of ∼ 8 cm and can be maintained either at ground potential or at a negative bias. Fabrication of such targets involves long and cumbersome procedures primarily because of the geometrical constraints of the existing set-up in commercial instruments. Further, the amount of material and the cost involved in making such targets can be enormous, particularly when large area targets are desired. Hence, there is a definite need to improve the geometrical set-up, so that the efficiency of the technique can be considerably enhanced. We have successfully solved this problem by redesigning the apparatus. The present paper reports this simple and versatile technique by which practically all types of materials can be sputtered as thin films, the material being taken in the form of compressed powders.

2. Conventional and redesigned RF sputtering

Block diagrams of a conventional RF sputtering system with its important accessories and the redesigned (modified) apparatus are shown in figures 1a and b respectively. The sputtering system used (Materials Research Corporation, USA, Model SEM-8622) is provided with a 13·56 MHz RF generator capable of producing a maximum output power level of 1·5 kW. A capacitatively coupled tuning network is used for impedance matching between the generator and the load. Before each sputtering run, the system is evacuated ($\sim 10^{-7}$ Torr) using standard high speed oil diffusion pumps (Varian Associates, USA). Sputtering was performed in an argon plasma at a constant pressure of 2×10^{-3} Torr. The pressure was controlled using a micrometer leak valve. High purity argon gas (99·999 %, Indian Oxygen Limited) was used. During sputtering, liquid nitrogen was circulated in the cryo-trap to reduce contamination either from the backstreaming of vapours of diffusion pump oil or from the adsorbed gases inside the chamber.

Unlike in the conventional system (figure 1a), the cathode in the modified set-up (figure 1b) is at the bottom of the chamber and the substrates are kept on the top at a distance of $\sim$ 8 cm. The powdered form of the material to be sputtered is uniformly spread into a circular trough (0·5 mm depth and 50 mm dia.) machined out from a stainless steel plate. The target and the target holder are thus integrated into one single element. The powder is first compressed into the trough using a hydraulic press at loads of $\sim$ 5000–10000 kg and the holder is then secured to the cathode which is watercooled.

The circular area surrounding the target (usually < 6 mm in thickness) which does not glow during the sputtering process is called the Crookes dark space (Maissel and Glang 1970; Chopra 1969). When electrons leave the target and move under the influence of an RF field, they travel some distance before picking up energy from the field and making ionizing collisions with inert gas atoms. This distance is determined by the pressure of the gas. As a result there is no ionization in this region and hence no discharge in the immediate vicinity of the target. This fact has been exploited by us for placing a shield over the cathode (figure 1b). The shield has a central aperture, the area of the aperture being determined by the area from which sputtering from the target is desired. The crucial feature of the design is that, the shield is at the ground potential and the shield to target distance is less than the Crookes dark space. Further, the annulus in the shield must follow all the contours of the cathode-target combination such that at no point the distance between them exceeds the length of the Crookes dark space, at the working pressure of the sputtering gas. The target-to-shield distance should not be made very small so as to avoid loss of power to the target. The typical distance used was 4 mm at a working pressure of $\sim 2 \times 10^{-3}$ Torr and the aperture diameter was $\sim$ 50 mm. It may be worthwhile to note that the plasma is confined in space in the shape of a truncated cone, with its smaller end fitting into the annulus in the shield (figure 1b). Further, for a fixed area of the aperture, the cone diameter at the minimum can be made

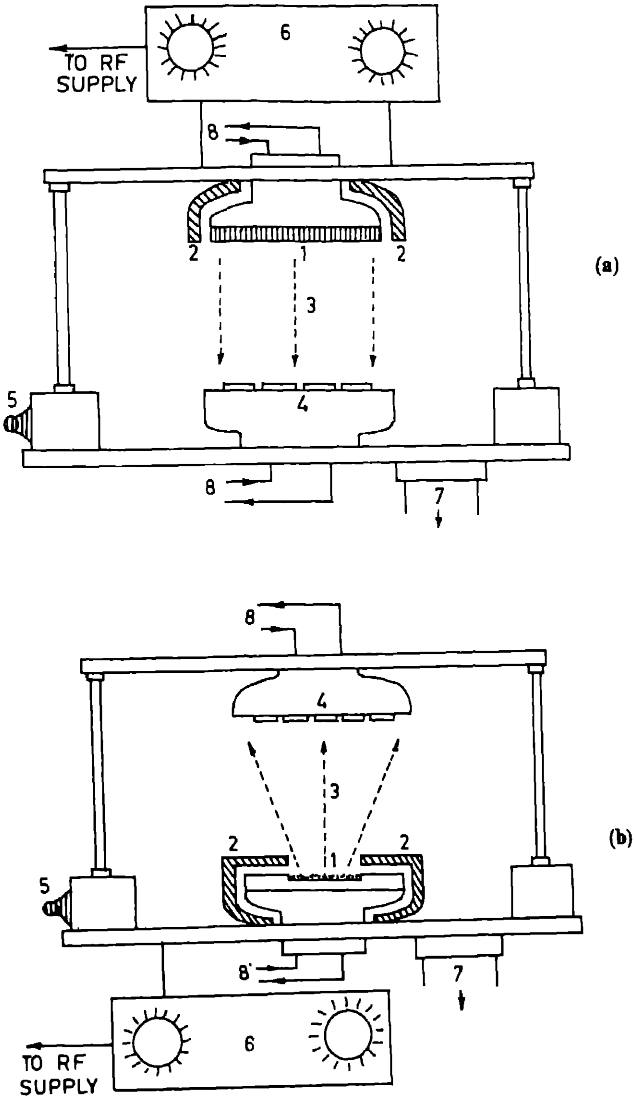

Figure 1. Block diagrams of the RF sputtering system with the important accessories **a**. Conventional and **b**. Modified. (1-target, 2-cathode shield, 3-plasma region, 4-anode (substrate holder), 5-argon gas inlet, 6-RF tuning network, 7-gasoutlet, 8-coolant water).

smaller by reducing the argon gas pressure. However, this flexibility is limited and beams approximately 20 mm less than the aperture diameter can be obtained.

3. Sputtering and characterization of films

This method which is essentially a powder sputtering method has been successfully used by us for depositing thin films of metals such as Cu and Al, semiconductors such as Ge, Se, As_2Se_3 and insulators such as SiC. Typical RF power levels and other sputtering parameters used are listed in table 1.

Table 1. Deposition parameters of various materials.

Material sputtered	RF power (W)	Target potential (V)	Sputtering pressure ($\times 10^{-3}$) (Torr)	Nature of the films: Present work	Nature of the films: Earlier Reports (References)
Cu	200	1000	2	Amorphous	Polycrystalline (Buckel 1959; Patten *et al* 1971; Segmuller 1973)
Al	325	700	2	Amorphous	Polycrystalline (Barna *et al* 1970; Bosnel and Thomas 1972; Tellier and Tosser 1977; Sherman 1977)
Ge	175	1200	2	Amorphous	Amorphous (de Neufville 1972; Kolomiets *et al* 1976; Tauc 1970)
Se	100	1200	2	Amorphous	Amorphous (Grigorovici 1969; Kolomiets *et al* 1976; Lucovsky 1967)
As_2Se_3	75	60	2	Amorphous	Amorphous (de Neufville 1972; Kolomiets *et al* 1976; Tauc 1970)
SiC	325	1800	10	Amorphous	Amorphous (Fritzsche 1973), Polycrystalline (Nishino *et al* 1977)

The powder sputtered films of various materials were characterized for their surface morphology and structures. The surface morphology, surface roughness and the topology of the gross microstructure were investigated (Cambridge Stereoscan-150 SEM). Prior to the analysis, the films were coated with a thin layer of sputtered gold (when non-conducting specimens were studied), to reduce the charging and blurring effects which lead to the loss of definition and resolution of the image particularly at higher magnifications. The surface of most of the films had no distinguishing features. The SEM for a typical case of As_2Se_3 (figure 2) depicts a fairly smooth surface. Since

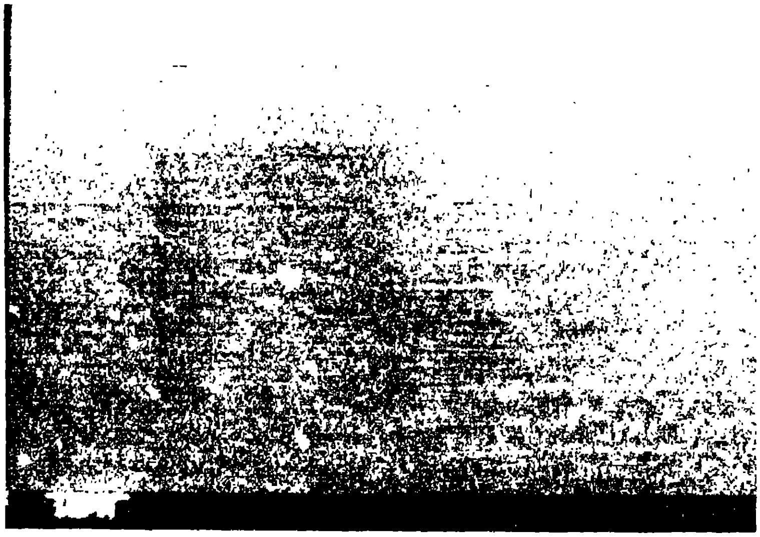

Figure 2. Scanning electron micrograph of As_2Se_3 film ($\times$ 1200).

Figure 3. Laue photographs of amorphous films of **a.** Al **b.** Cu **c.** Ge **d.** Se **e.** As_2Se_3 **f.** SiC.

⟶

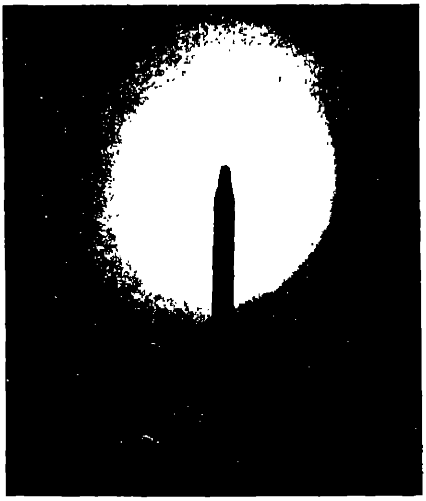

(a)

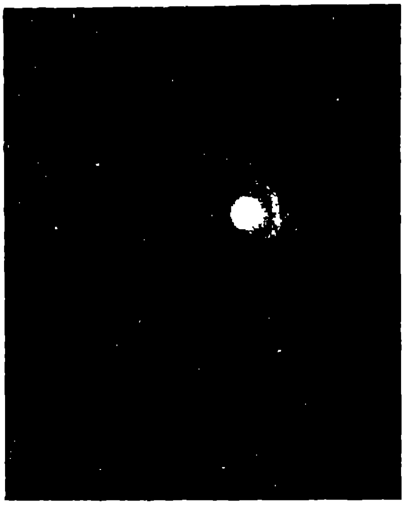

(b)

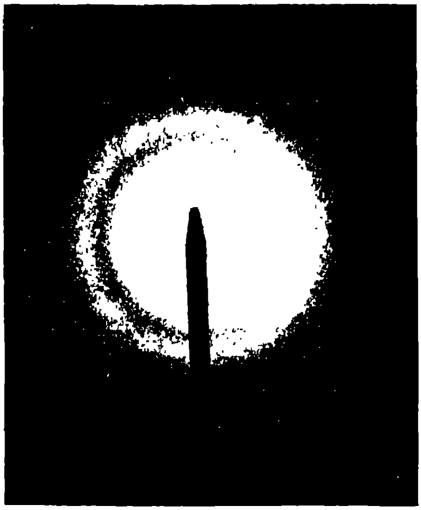

(c)

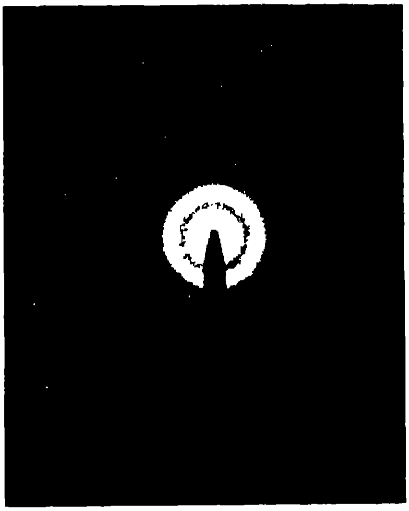

(d)

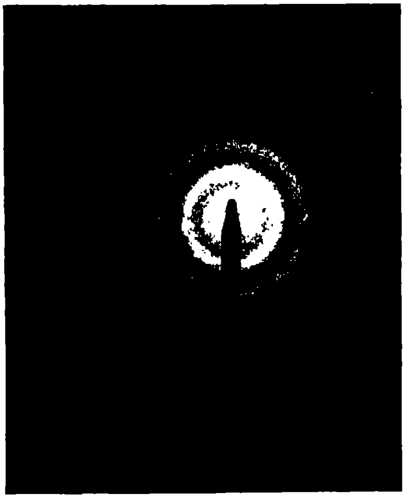

(e)

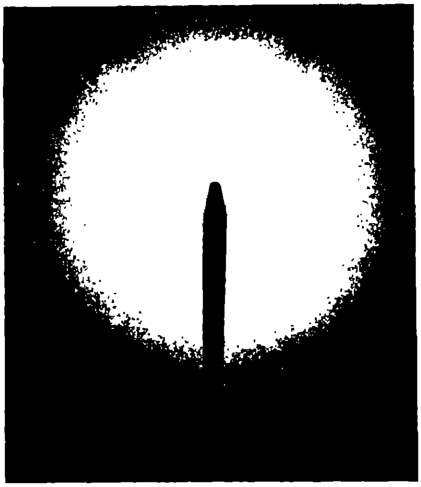

(f)

sputtering is a high temperature deposition process, the smooth surface structure can be attributed to high adatom mobility of the sputtered species, which agrees with earlier reports (Holland 1956; Chopra 1969; Maissel and Glang 1970).

Structures of these films were investigated using electron diffraction technique. Films of thickness 500–1000 Å were deposited onto freshly cleaved NaCl single crystals and floated in distilled water. Films were lifted onto 400 mesh copper grids. The grids were then transferred to the specimen holder of a Philips EM 301 electron microscope and examined. The diffraction patterns as well as the micrographs were recorded for all the films studied. Low beam conditions ($\sim 10^{-6}$ A/cm^2) were used for the semiconducting films to minimize the heating effects as well as the electron beam-induced structural changes. A striking feature of all the films studied has been that their diffraction patterns were featureless halos indicating that the films were all amorphous. Though our results for semiconducting films agree with similar results (Lucovsky *et al* 1967; Grigorovici 1969; Tauc 1970; de Neufville 1972; Kolomiets *et al* 1976), there are surprising differences in the case of sputtered metal films of Al and Cu, which were reported to give polycrystalline sputtered films (Buckel 1959; Patten *et al* 1971; Segmuller 1973; Barna *et al* 1970; Bosnel and Thomas 1972; Tellier and Tosser 1977; Sherman 1977) but were found to be amorphous in our studies. RF sputtered films of SiC have been reported to be both amorphous (Fritzsche 1973) like in the present case, and polycrystalline (Nishino *et al* 1977) depending on the sputtering conditions. Laue photographs of various films are shown in figures 3(a–f).

4. Limitations and possible improvements of the set-up

We have noted that the present set-up offers several advantages over the conventional sputtering methods. However, there are a few disadvantages associated with the present design. (i) By employing the cathode shield with a central aperture, the area of sputtering has been controlled but the thickness uniformity has been adversely affected. This can be minimized by a proper choice of target to substrate distance and redesigning of the substrate holder. (ii) It may be reasonably argued that undesirable gases and impurities are entrapped in the target in the present design. But such effects have not been well understood and some of these aspects are being presently investigated.

5. Conclusions

In the present study a simple and versatile technique for RF sputtering of thin films of metals, semiconductors and dielectrics has been described and its use has been successfully demonstrated. The method offers a cost effective means of sputtering of various materials particularly when commercial targets are not available.

Acknowledgements

The authors would like to thank Prof. C N R Rao for encouragement and Prof. K J Rao for helpful discussions.

References

Barna A, Barna P B, Pocza J F and Pozsgai I 1970 *Thin Solid Films* **5** 201
Bosnell J and Thomas C B 1972 *Solid State Electron.* **15** 1261
Buckel W 1959 *Proc. Int. Conf. on Structure and Properties of thin films* (eds) C A Neugebauer, J B Newkirk and D A Vermilyea (New York: John Wiley) p. 53
Chopra K L 1969 *Thin Film Phenomena* (New York: McGraw Hill)
de Neufville J P 1972 *J. Non-Cryst. Solids* **8–10** 85
Fritzsche H 1973 *Electronic and structural properties of amorphous semiconductors* (eds) P G LeComber and J Mort (New York: Academic Press) p. 106
Grigorovici R 1969 *J. Non-Cryst. Solids* **1** 303
Holland L 1956 *Vacuum deposition of thin films* (Chapman and Hall) Chap. 14
Jackson G N 1970 *Thin Solid Films* **5** 209
Kolomiets B T, Lantrotova S S, Lyubin V M, Pukh V P and Tagirdzhanov M A 1976 *Sov. Phys. Solid State* **18** 866
Lucovsky G, Mooradian A, Taylor W, Wright G B and Keezer R C 1967 *Solid State Commun.* **5** 133
Maissel L I and Glang R 1970 *Handbook of thin film technology* (New York: McGraw Hill) Chap. 4
Nishino S, Matsunami H, Odaka M and Tanaka T 1977 *Thin Solid Films* **40** L27
Patten J W, McClanahan E D and Johnston J W 1971 *J. Appl. Phys.* **42** 4371
Segmuller A 1973 *Thin Solid Films* **18** 287
Sherman D 1977 *Thin Solid Films* **45** 537
Tauc J 1970 *Optical properties of solids* (ed) F Abeles (Amsterdam: North Holland)
Tellier C R and Tosser A J 1977 *Thin Solid Films* **43** 261

Bull. Mater. Sci., Vol. 6, No. 6, December 1984, pp. 979–989. © Printed in India.

Preparation and characterisation of β''-Al_2O_3

H S KALSI, R P TANDON, BALBIR SINGH, R C GOEL and B K DAS
National Physical Laboratory, New Delhi 110012, India

MS received 6 August 1983; revised 6 April 1984

Abstract. Beta alumina solid electrolyte is a potential candidate in the fabrication of Na-S batteries. In the present study, it has been prepared in the form of discs by uniaxially as well as isostatically pressing and sintering in the temperature range 1585–1630°C, the highest sintered density of 3·25 g/cm^3 has been achieved in the samples isostatically pressed and sintered at 1630°C. X-ray analysis of the samples shows formation of β''-phase. Microstructure of the sintered samples reveals some darker regions which are attributed to low soda content. Resistivity at 300°C measured by the two-probe method at a frequency of 1 MHz on samples having vacuum-deposited silver electrodes is 15 ohm-cm, which is slightly higher than the value of 5–13 ohm-cm reported in literature using molten sodium electrodes. The activation energy of conductivity is 0·24 eV which is comparable to the literature value of 0·24–0·35 eV.

Keywords. Conducting ceramic; ionic conductor; sodium beta alumina; solid electrolyte.

1. Introduction

Beta-alumina ceramics have potential application in a variety of devices such as (a) electrolyte in the Na-S battery (Kummer and Weber 1968) for automotive propulsion or electric utility load levelling (b) thermoelectric devices (Weber 1974) and electrochemical devices for measuring sodium and oxygen activities. Amongst these, the sodium sulphur battery system based on beta alumina is the most advanced one.

The general formula for beta alumina is $Na_2O \cdot x\text{-}Al_2O_3$, where x varies from 5–11. Two structural forms of beta type alumina exist (Kummer 1972). At $x = 11$ the composition yields β-alumina which starts converting in β''-alumina as the sodium content increases and at $x = 5$, the β-phase is completely converted into the β''-phase. β''-alumina has higher ionic conductivity than β-alumina but is unstable at a temperature greater than 1500°C. As the sintering temperature of β''-alumina is >1500°C, some stabilizing agent like lithium oxide or magnesium oxide or both are added (Gordon *et al* 1977).

Lithium-stabilised β''-alumina was synthesised from reactive α-alumina which was prepared at NPL, India (Das *et al* 1982). To compare the results, reactive α-alumina of M/s Reynolds, USA was also used to synthesise β''-alumina.

2. Experimental procedure

β''-Al_2O_3 was synthesised using two varieties of reactive α-Al_2O_3 (NPL, India; M/s Reynolds USA (which has particle size $\leq 0{\cdot}7$ μm and purity $>99{\cdot}6$%)). The other two raw materials, sodium carbonate and lithium carbonate were of AR grade. The material was processed by using zeta process (Youngblood *et al* 1977) in which sodium-alumina composition and a lithium alumina composition known as zeta alumina were processed and calcined separately and the two were then mixed in proper proportions to yield the desired composition.

The composition chosen for this experiment was 84·09 % Al_2O_3, 13·54 % Na_2O and 2·37 % Li_2O all taken in mole percent. $Na_2O5{\cdot}25\,Al_2O_3$ and $Li_2O5{\cdot}5Al_2O_3$ prepared for making the above composition were separately calcined at 1340°C for 2 hr and the compositions dry-ball milled to a particle size of $< 1\ \mu m$. The powder was then mixed with polyvinyl butyral and benzene, which acts as a binder for about 2 hr and the slurry dried in air. The material was granulated using a nylon sieve and pressed uniaxially and isostatically into discs (15 mm dia and 2·5 mm thickness). A flow chart of the zeta process is shown in figure 1. To study the effect of particle size on the density, the

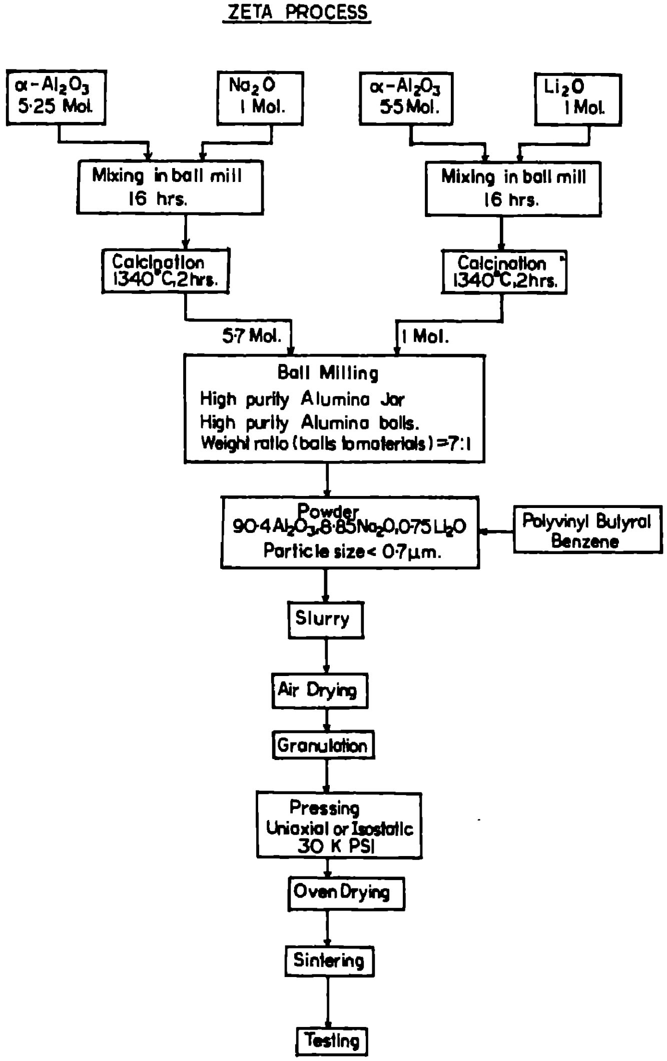

Figure. 1. Flow chart of zeta process for the synthesis of β''-Al_2O_3.

Table 1. Particle size analysis of powders A–E.

Particle size (μm)	Materials (comm %)				
	A	B	C	D	E
+1·8	0·4	0·2	0·1	0	0
+1.15	4·2	3·4	2·3	1·2	1·2
+0·8	14·0	12·1	10·7	9·5	9·2
+0·65	26·3	22·6	21·3	19·9	20·2
+0·57	38·2	33·2	32·5	31·1	31.3
+0·5	49·2	43·2	43·0	42·3	42·3
+0·46	59·0	52·3	52·6	51·3	51·5
+0·43	67·5	60·5	61·0	59·3	59·5
+0·36	86·3	83·2	83·8	77·8	77·4
+0·33	94·0	90·3	89·9	85·6	86·4
+0·30	98·4	95·5	95·9	92·4	92·9
+0·28	100·0	98·8	99·2	97·6	97·5
+0·26	100·0	100·0	100·0	100·0	100·0
Mean Particle size	0·56	0·54	0·52	0·5	0·5

material was ground for various durations of time to yield different particle size distributions. Five such powders (table 1) having different particle size distribution were processed by pressing uniaxially and isostatically at different pressures. The pressed tablets were dried overnight in an oven (160°C) and then covered with coarse beta alumina powder and sintered in super kanthal furnace at a temperature ranging from 1585–1630°C for various time intervals (2–32 min). The temperature schedule of the sintering is shown in figure 2. The material was annealed at 1480°C for 4 hr for complete conversion into the β''-phase. An almost similar two-step sintering schedule was adopted by Kvachkov *et al* (1981, 1982).

Rectangular samples (33 × 32·7 × 2·7 mm) for x-ray analysis were prepared by uniaxially pressing and sintering at a temperature ranging from 1585–1630°C. Tables 2a and 2b give the x-ray analysis and it is evident that mostly the β''-phase is present (Ray and Subbarao 1975; ASTM 1967). The density of the sintered discs was measured by Archemedes principle by immersion in xylene.

For microstructural evaluation the discs were broken into small pieces and the broken faces examined under a scanning electron microscope (JEOL JSM-35 CF). Energy dispersive spectroscopy (EDS) mode was employed for the elemental analysis of aluminium and sodium.

The electrical resistivity was measured by employing evaporated silver full face electrodes and by using Siemen's Bridge at 1 MHz to avoid interface polarisation (Yao and Kummer 1967) in a temperature range of 20–300°C.

3. Results and discussions

3.1 *Effect of compacting pressure on green density*

Figure 3 depicts the effect of uniaxial as well as isostatic pressure on the green density of the materials (Kalsi *et al* 1983). The green density increases with pressure. The highest

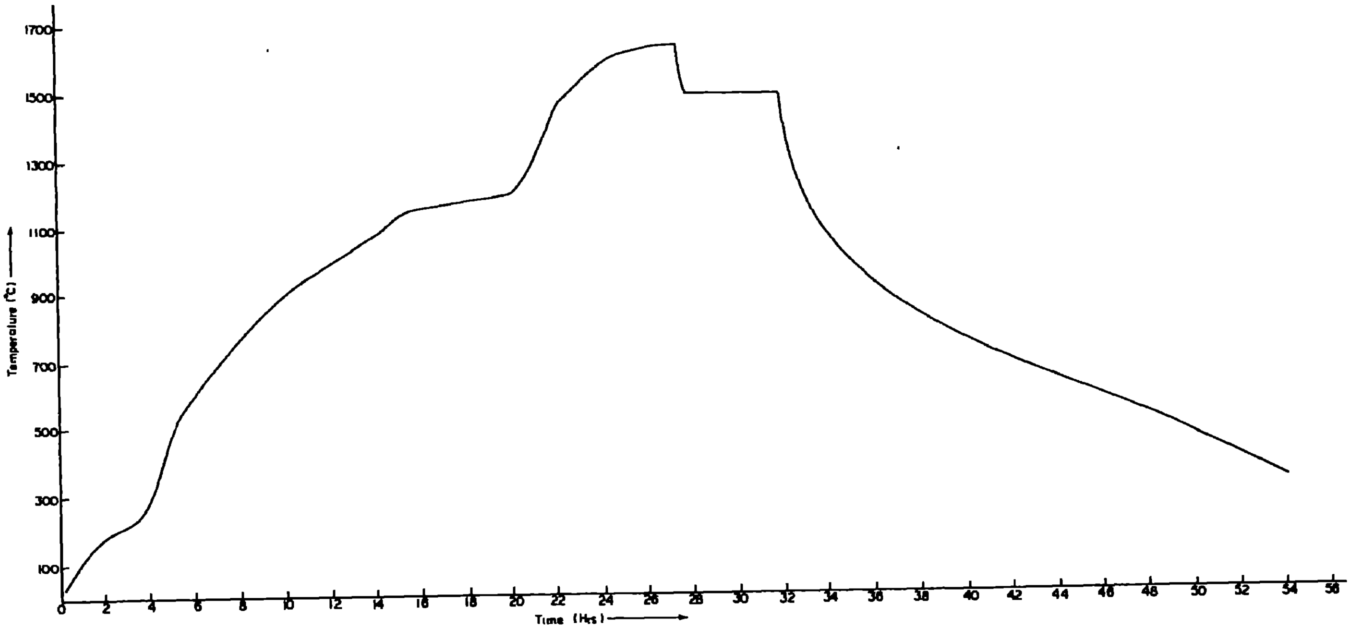

Figure 2. Temperature profile of sintering cycle.

Table 2(a). X-ray diffraction data for β''-Al_2O_3 prepared from powder D.

dA°	I/I_1	*hkl*
11·632	100	003
5·644	47	006
4·495	5	100
4·086	3	001
2·818	12	110
2·683	24	114
2·515	16	116
2·429	9	$00\underline{14}$
		200
2·380	3	204
		118
2·254	13	110
2·132	9	$10\underline{14}$
		207
2·040	9	209
1·973	5	$20\underline{10}$
1·943	7	$10\underline{16}$
1·596	6	2014
1·559	6	306
1·406	17	220

Table 2(b). X-ray diffraction data for β'' Al_2O_3 prepared from powder E.

dA°	I/I_1	*hkl*
11·632	100	003
5·717	56	006
4·484	7	100
4·086	6	001
2·818	16	110
2·691	28	114
2·600	5	101
		$00\underline{13}$
2·515	22	116
2·417	12	$00\underline{14}$
		200
2·383	3	203
2·254	18	110
2·139	12	$10\underline{14}$
		207
2·045	16	200
1·973	5	2010
1·943	8	1016
1·596	8	2010
1·559	8	306
1·486	4	309
1·404	25	220

green density of 2·27 g/cm^3 was obtained in powder A (table 1) at a uniaxial compacting pressure of 3600 kg/cm^2 whereas at an isostatic pressure of 2600 kg/cm^2 a highest green density of 2·3 g/cm^3 was obtained for the same powder.

The variation of green density with particle size presented in figure 3 shows that the density decreases with particle size.

3.2 *Effect of compacting pressure on the sintered density*

Variation of the sintered density with uniaxial and isostatic pressure is shown in figure 4. The highest sintered density of 3·22 g/cm^3 was obtained for powder D (table 1) compacted at uniaxial pressure of 1800 kg/cm^2 and sintered at 1630°C, whereas for the isostatically pressed samples sintered at 1630°C, the sintered density is independent of the isostatic pressure in the range of 700–2600 kg/cm^2. The highest sintered density of 3·25 g/cm^3 for powder D was obtained.

The variation of sintered density with particle size is also shown in figure 4 and it is clear that as the particle size decreases the sintered density increases.

3.3 *Shrinkage studies*

The shrinkage was measured as a function of uniaxial compacting pressure for all the five powders by sintering at 1630°C. The results are shown in figure 5. Shrinkage is higher at lower pressures with no significant change beyond 3000 kg/cm^2. Powder D exhibits the highest shrinkage followed by powder E (table 1).

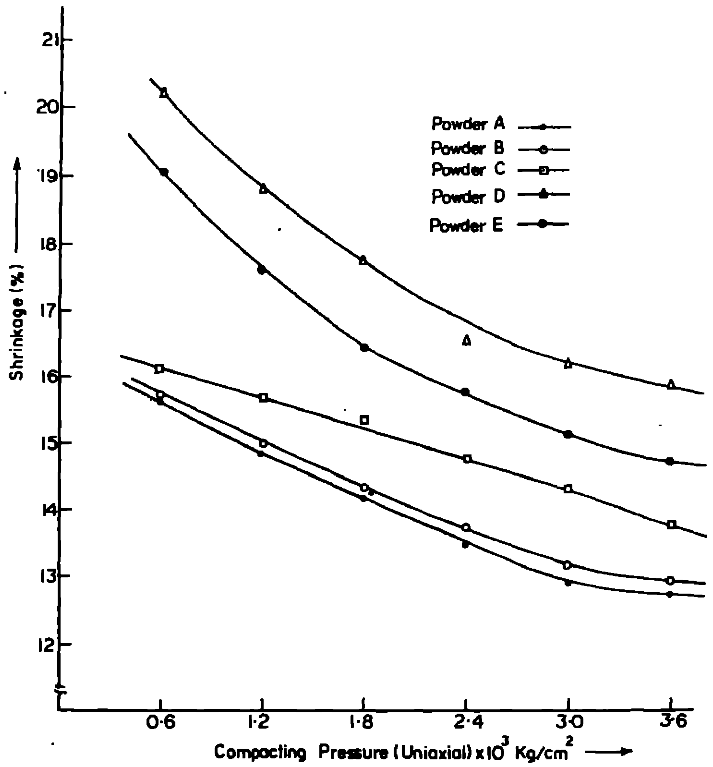

Figure 5. Variation of shrinkage with uniaxial compacting pressure for samples of different initial particle sizes and sintered at 1630° C for 20 min.

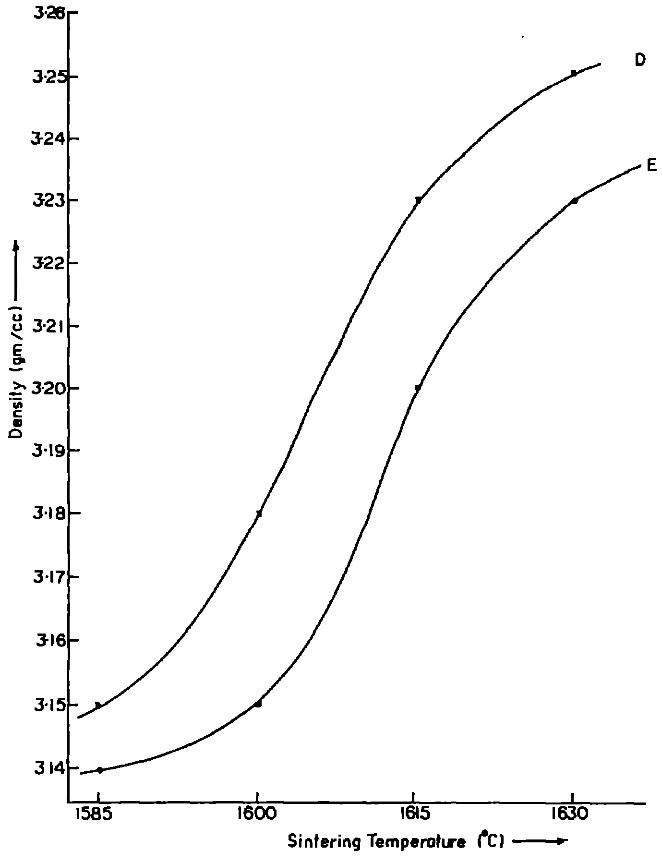

Figure 6. Variation of sintered density of powders D and E as a function of sintering temperature.

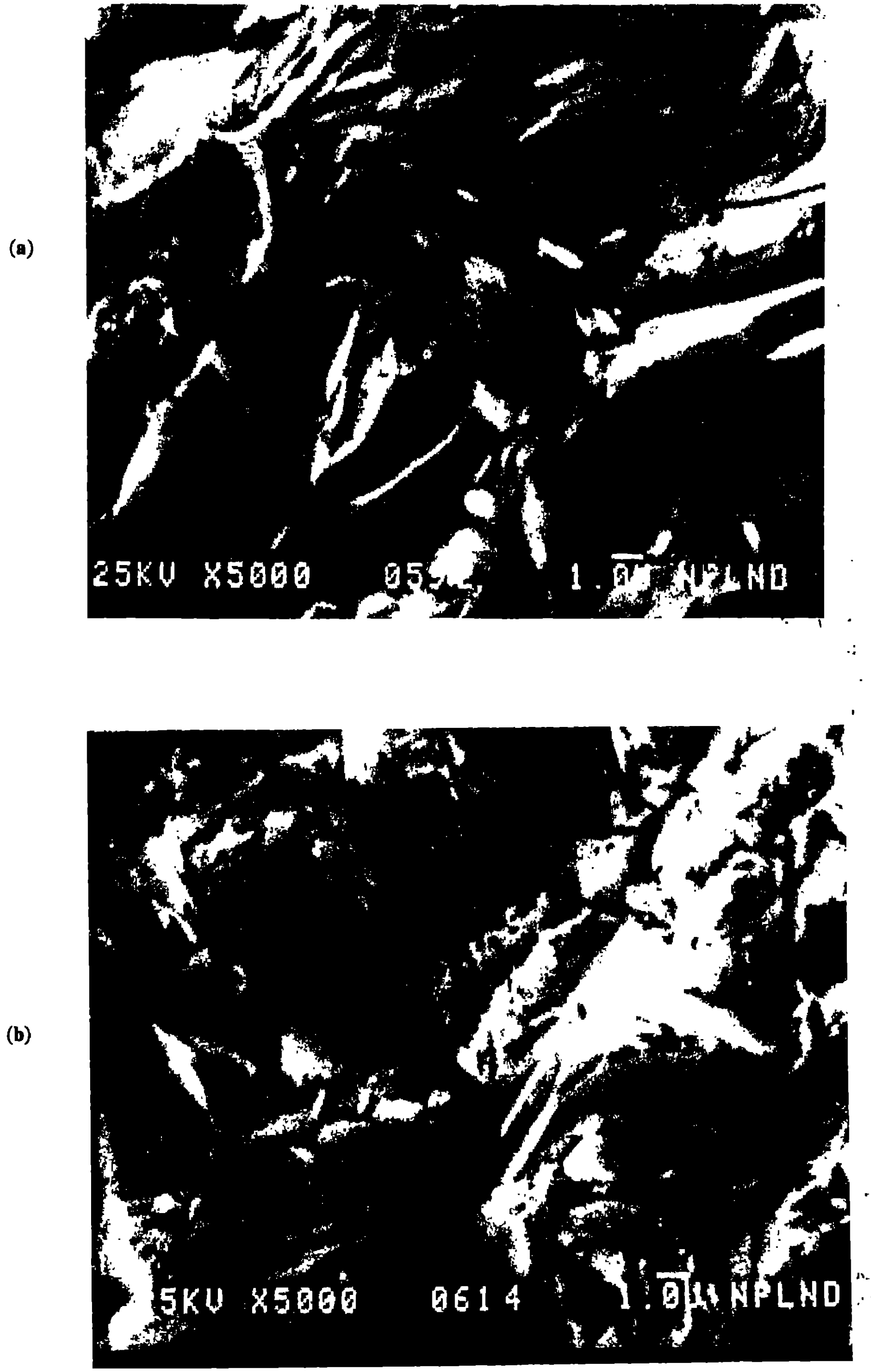

Figure 7. Microstructure of β''-Al_2O_3 prepared from a. powder D and b. the powder E and sintered at 1630°C for 20 min.

4. Conductivity measurements

Ionic conductivity of beta alumina type superionic conducting material has been studied by several investigators (Wynn and Miles 1971; Demontt and Hancock 1971; Kummer 1972; Whittingham and Huggins 1971). Such measurements need either reversible electrodes *i.e.* molten sodium (Demontt and Hancock 1971) or $NaNO_2/NaNO_3$ (Sudworth *et al* 1973) eutectic mixture, in which case conductivity is independent of the frequency. For measurements made using platinum or silver blocking electrodes the conductivity becomes frequency dependent below 1 MHz. At 1 MHz and above, it is independent of the frequency. In this study the measurements were made at 1 MHz using evaporated silver blocking electrodes; and resistivity of the order of 15 ohm-cm at 300°C was obtained.

The activation energy of conductivity was 0·24 eV which is close to the value reported (Kalsi *et al* 1983) for Li_2O doped compositions of β''-Al_2O_3. It may be pointed out here that this is slightly higher (Kalsi *et al* 1983) than those for the corresponding MgO-doped compositions. This difference could be due to the difference in structure or atomic jump mechanism which controls the ionic conductivity.

5. Conclusion

In β''-Al_2O_3 samples isostatically pressed and sintered at 1630°C a density of 3·25 g/cm^3 has been obtained. A maximum shrinkage of 20% was observed in samples uniaxially pressed at 600 kg/cm^2 and sintered at 1630°C. X-ray analysis reveals the formation of β''-phase. The microstructure reveals randomly oriented elongated crystals of β''-Al_2O_3 having some darker portions; which are regions of low soda content. The resistivity of the order of 15 ohm-cm at 300°C has been obtained. An activation energy of 0·24 eV was obtained which is close to the value reported in literature.

Acknowledgement

The authors thank the Director, NPL, New Delhi for facilities. Thanks are due to Mr S U M Rao and Shri D K Suri for scanning electron microscopy and x-ray diffraction analysis work respectively. This work is supported financially by the Department of Nonconventional Energy Sources, New Delhi.

References

ASTM 1967 19–1173

Das B K, Kalsi H S, Khullar S M, Kumar Rahul, Goel R C and Misra S C K *Int. Symp. on Ceramics* 27–30 Nov. 1982 Bangalore (India) Vol. I Part II

Demont D S and Hancock P 1971 *Proc. Br. Ceram. Soc.*

Fielder W L, Kantz H E, Fordyce J S and Singer J 1975 *J. Electrochem. Soc.* **122** 528

Gordon R S, McEntire B J, Miller M L and Virkar A V 1977 *Mater. Sci. Res.* Vol. 11, p. 1405

Hodge J D 1983 *J. Am..Ceram. Soc.* **66** 166

Kalsi H S, Tandon R P and Das B K 1983 *Symp. on Adv. in electrochemical Energy Storage and Conversion* 21-1-1983, CECRI, Karaikudi (India)

Kummer J T 1972 *Prog. Solid State Chem.* **7** 141

Kummer J T 1972 *Prog. Solid State Chem.* (ed.) H Reiss and J O McCaldin (New York: Pergamon Press) Vol. 7

Kummer J T and Weber N 1968 *Soc. Automotive Eng. Trans.* **76** 1003

Kvachkov R, Yanakiev A, Poulieff C N, Bakanor I, Yankulov P D and Budevski E 1981 *J. Mater. Sci.* **16** 2710

Kvachkov R, Yanakiev A, Poulieff C N, Yankulov P D, Rashkov S and Budevski E 1982 *Solid State Ionics* **7** 151

Ray A K and Subbarao E C 1975 *Mater. Res. Bull.* Vol. **10** 583

Sudworth J L, Tilley A R and South K D 1973 *East ion transport in solids* (ed.) W Van Gool (Amsterdam: North Holland) p. 581

Weber N 1974 *Energy Convers.* **14** 1

Whittingham M S and Huggins R A 1971 *J. Electrochem. Soc.* **118** 1

Wynn Jones I and Miles L T 1971 *Proc. Br. Ceram. Soc.* 161

Yao Y F V and Kummer J T 1967 *J. Inorg. Nucl. Chem.* **29** 2453

Youngblood C E, Virkar A V, Canon W R and Gordon R S 1977 *Am. Ceram. Soc. Bull.* **56** 206

Bull. Mater. Sci., Vol. 6, No. 6, December 1984, pp. 991–996. © Printed in India.

Evidence of screw dislocations on (002) cleavages of lithium carbonate single crystals

K S RAJU*, M PALANISWAMY, P RAMASAMY and G S LADDHA

Crystal Growth Centre, AC College of Technology, Anna University, Madras 600 025, India
*Department of Crystallography and Biophysics, University of Madras, Guindy Campus, Madras 600 025, India

MS received 2 April 1983; revised 8 December 1983

Abstract. Well-defined triangular etch pits are produced on etching (002) cleavages of lithium carbonate single crystals with 2 % citric acid. On etching of cleavage face and matched face these pits nucleate at the intersection sites of dislocations with the cleavage face. On successive etching of a cleavage face, shallow irregular arrays of pits do not enlarge in size as compared to other isolated pits on the same face. These irregular arrays of pits have reasonable correspondence on an etched match face, suggesting they form at dislocation sites.

Keywords. Chemical etching; tilt boundaries; twist boundaries; spiral etch pits; lithium carbonate single crystal.

1. Introduction

Etch methods have been applied to understand the history of growth of crystals and their dislocation content (Gilman and Johnston 1956; Patel and Tolansky 1957; Patel and Goswami 1964; Patel and Raju 1966, 1967; Raju 1981). It was established that the geometric shape of the etch pits on a crystal face is strictly related to the symmetry of the crystal face and the nature of the etchant (Patel and Singh 1968; Hari Babu and Bansigir 1968; Buckley 1958; Borle and Bagai 1976; Connick and May 1969; Wehner 1958 etc). Irregular arrays comprising of edge and screw dislocations on (0001) and $(10\bar{1}1)$ faces of hematite (Sunagawa 1968) as well as on (010) faces of gypsum (Raju 1980) have been reported.

In the present paper spiral etch pits observed along the irregular arrays on (002) cleavage faces of Li_2CO_3 single crystals are reported.

2. Experimental

In the present work, transparent single crystals (Palaniswamy *et al* 1982) of lithium carbonate were cleaved parallel to the (002) plane and etched in 2 % citric acid for the required time. The etch patterns were studied by optical methods. Silver coating on the etched cleavages was avoided as it would spoil the surface for further etching. For examining the cleavage surfaces at higher resolution and magnification, scanning electron microscope (Cambridge Stereoscan model S-150 and operating voltage 20 kV) was used after sputtering the crystal surface with gold.

3. Observations

3.1 *Successive etching of an isolated cleavage*

Figures 1 and 2 reveal the etch patterns produced on etching a (002) basal cleavage face of lithium carbonate crystal with 2% citric acid for 2·5 and 4 min respectively. It is clear that on successive etching, some isolated etch pits enlarge in size and shape whereas the array (marked XY in figure 1) remains almost the same (marked X′Y′ in figure 2). The

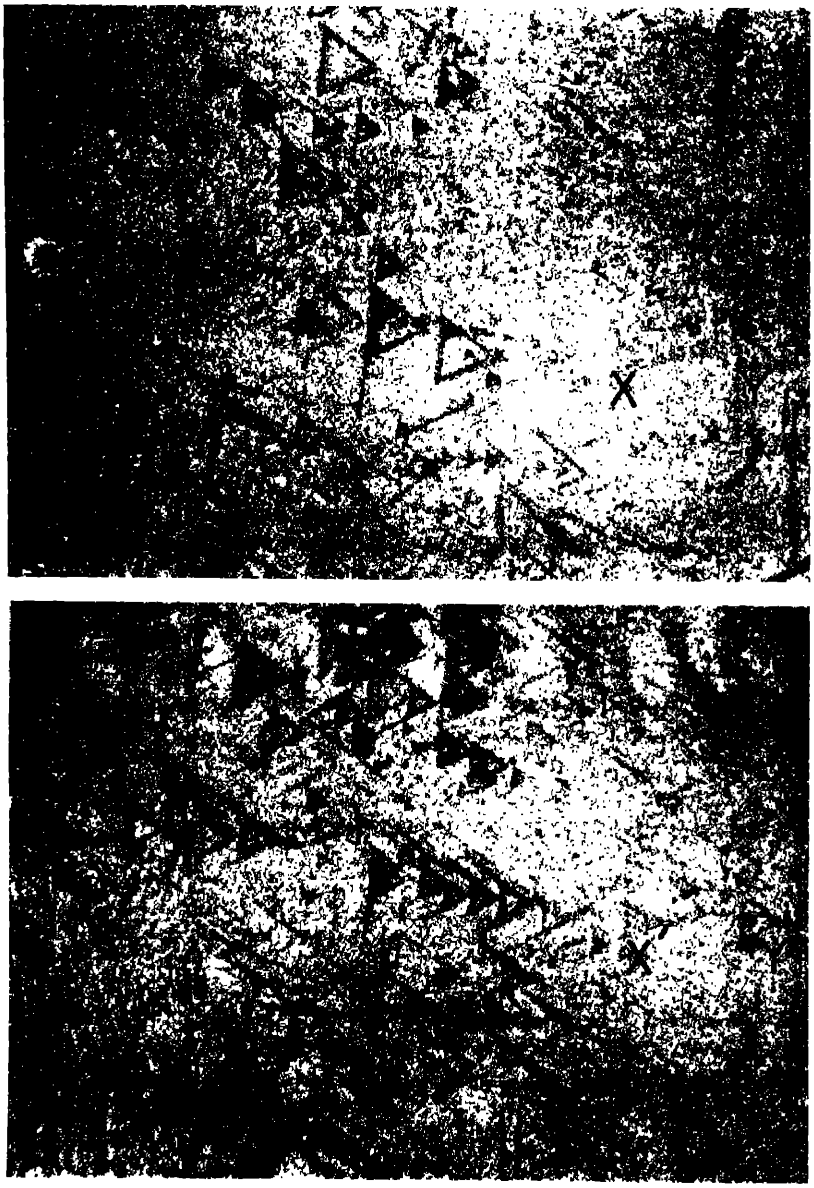

(1)

(2)

Figures 1 and 2. (× 200) Etch pattern **1.** on (002) cleavage etched 2% citric acid for 2½ min. **2.** of the region of figure 1 etched for a total of 4 min pit marked Y in figure 1 on successive etching appears like a clockwise spiral as seen in the pit marked Y′ in figure 2.

3.2 *Etching of a matched pair*

In order to investigate the irregular arrays of etch pits, a matched face is etched identically for 2½ min in 2% citric acid. Figures 3 and 4 clearly show a reasonable

(3)

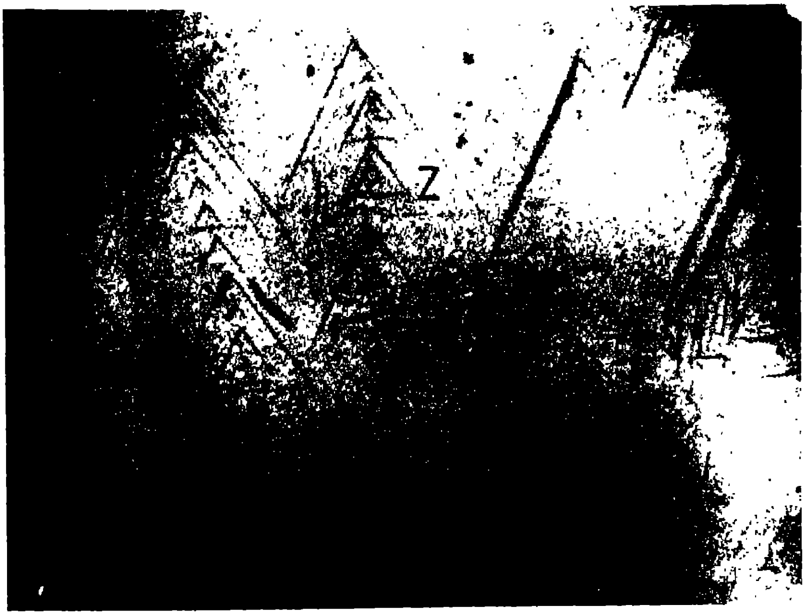

(4)

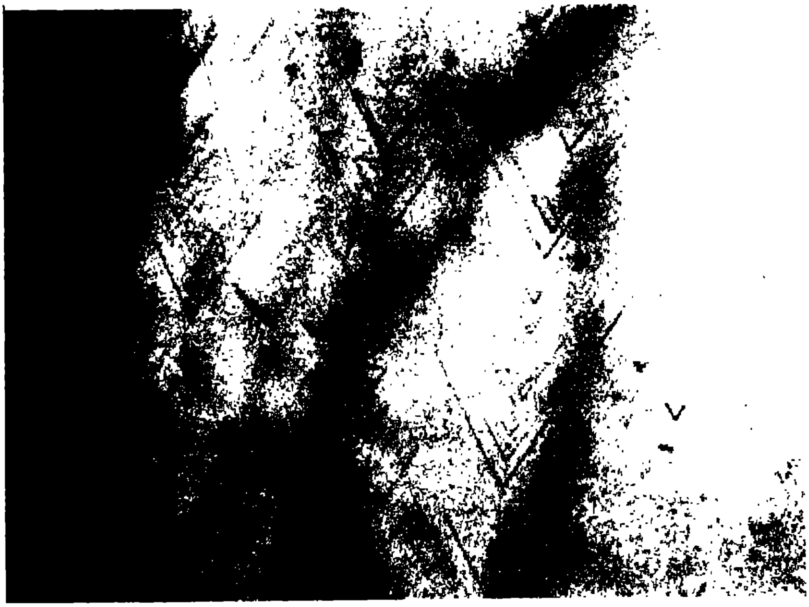

Figures 3 and 4. (× 325) Etch patterns of a matched cleavage etched in 2% citric acid for 2½ min.

amount of correlation in the three dominant irregular arrays of etch pits. The pit marked Z in the central array of figure 3 resembles an anticlockwise spiral.

3.3 SEM *studies*

One of the arrays in figure 3 is scanned in the electron microscope (figure 5). The pit marked M clearly looks like a clockwise spiral of single turn, while the pit marked N is

(5)

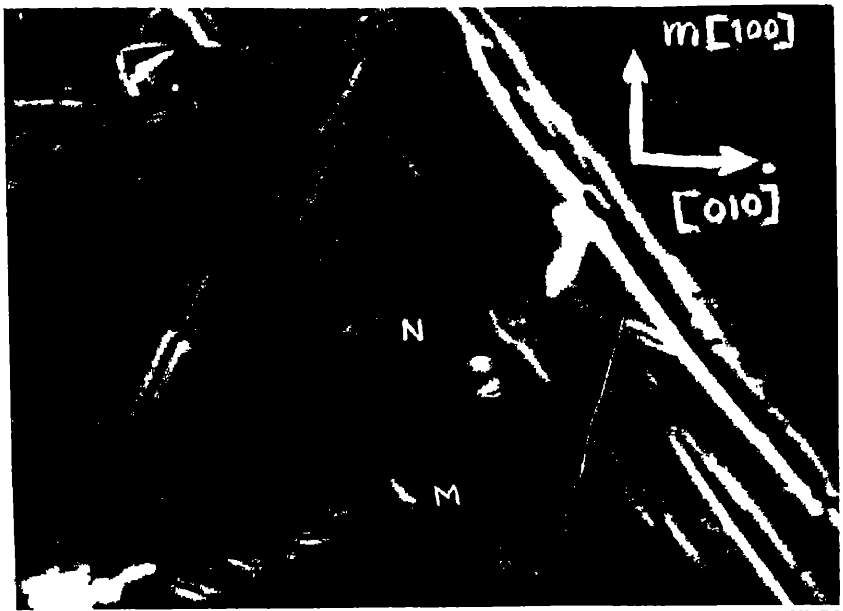

(6)

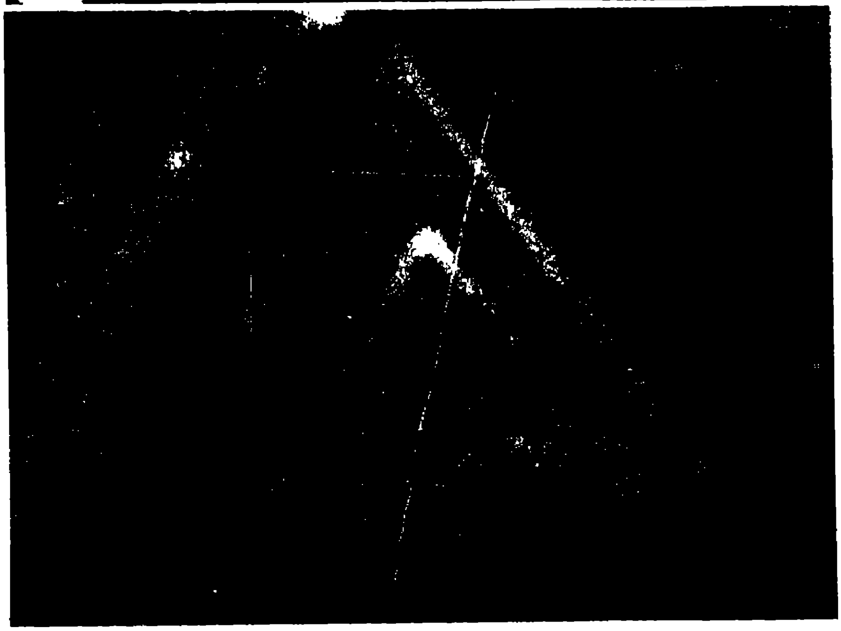

Figures 5 and 6. SEM photograph **5.** revealing an irregular array of etch pits (× 2000) **6.** of the magnified region of figure 5 (× 7500).

not clear. Hence the pit N is observed at higher magnification as shown in figure 6. It is interesting to note that pit N also resembles a clockwise spiral having a white contour.

4. Discussion

The shape of the etch pits on (002) cleavage face of Li_2CO_3 single crystal has been observed to be triangular, irrespective of the etchants used (Palaniswamy *et al* 1982). Li_2CO_3 is monoclinic and has the space group *C*2/*c* which is a part of class 2/*m*. The (002) cleavage in 2/*m* is mono-symmetrical, which means it contains one mirror plane. Etch pits on (002) plane must show mirror symmetry. The mirror symmetry axis *m* [100] is perpendicular to the base of the etch pits, which happens to be the two-fold axis [010] as shown in figure 5.

On successive etching, the isolated pits enlarge in size retaining their shape, suggesting dislocation of etch pits. This has been supported by the exact correspondence of isolated etch pits on matched faces. That the irregular arrays remain shallow without enlarging reasonably in depth on successive etching and reveal correspondence on etched match faces suggest that these are also dislocation arrays of a different nature than those of isolated dislocation pits. One of the pits marked Z in the irregular array in figure 3 indicates that this dislocation may be of screw type, anticlockwise. That the pits forming the irregular array etch differently than those of isolated pits enlarging in size, may be attributed to the association of screw dislocations in the array of pits.

That the pits (marked M and N in figure 5) constituting the irregular array resemble spirals support the conjecture that they reveal screw dislocations in the crystal (Patel and Raju 1966).

These irregular arrays of etch pits may represent general grain boundaries having both edge and screw dislocations, which might have been formed due to the impingement of misoriented guest crystals causing stresses in the growing crystal. This agrees with the findings of Sunagawa (1968) on hematite and Raju (1980) on gypsum.

5. Conclusions

That the spiral etch pits observed are along irregular arrays and these irregular arrays (of etch pits) have correspondence on match faces indicate that they may reveal tilt or twist boundaries consisting of edge and screw dislocations in the crystal. Therefore it is concluded that the spiral etch pits forming the components of irregular arrays represent the sites of screw dislocations on (002) basal cleavages of lithium carbonate single crystal.

Acknowledgements

The authors thank Dr N Ramanathan, Director, Central Leather Research Institute, Adyar, Madras for permission to use the scanning electron microscope and to Dr A Rajaram for the assistance in SEM studies. One of the authors (KSR) thanks Dr E Pippel and Dr W Neumann for valuable discussions. MP thanks Anna University for the award of a fellowship.

References

Buckley H E 1958 *Crystal growth* (New York: John Wiley) 4 edn p. 321

Borle W N and Bagai R K 1976 *J. Cryst. Growth* **36** 259

Connick W and May F G J 1969 *J. Cryst. Growth* **5** 65

Gilman J J and Johnston W G 1956 *J. Appl. Phys.* **27** 1018

Hari Babu V and Bansigir K G 1968 *J. Cryst. Growth* **2** 9

Patel A R and Tolansky S 1957 *Proc. Roy. Soc.* (*London*) **A243** 41

Patel A R and Goswami K N 1964 *Acta Crystallogr.* **17** 569

Patel A R and Raju K S 1966 *Acta Crystallogr.* **21** 190

Patel A R and Raju K S 1967 *Acta Crystallogr.* **23** 217

Patel A R and Singh R P 1968 *J. Cryst. Growth* **2** 373

Palaniswamy M, Gnanam F D, Ramasamy P and Laddha G S 1982 *Cryst. Res. Technol.* **17** 911

Raju K S 1980 *Bull. Mater. Sci.* **2** 139

Raju K S 1981 *J. Mater. Sci.* **16** 2512

Sunagawa I 1968 *Mineral Mag.* **36** 625

Wehner G K 1958 *J. Appl. Phys.* **29** 217

Bull. Mater. Sci., Vol. 6, No. 6, December 1984, pp. 997–1000. © Printed in India.

Etch pit observations on the habit faces of gel grown nickel molybdate crystals

K V KURIEN* and M A ITTYACHEN

Department of Physics, University of Kerala, Kariavattom 695 581, Trivandrum, India
*Department of Physics, Mar Thoma College, Tiruvalla 689 105, India

MS received 30 April 1983; revised 30 April 1984

Abstract. The results obtained from etching experiments on the habit faces of $NiMoO_4 \cdot xH_2O$ are described. Dilute solutions of chemical reagents such as HNO_3, CH_3COOH, NaOH, KOH are found to be the best etchants for revealing dislocation etch pits. The shape and nature of the etch pits are also described.

Keywords. Etch pits; dislocation; habit faces; gel grown; $NiMoO_4 \cdot xH_2O$ crystals

1. Introduction

Etching is a well-known technique for dislocation studies in crystals. It is the result of variation in surface reaction or dissolution rates influenced by crystallographic orientation effects, lattice imperfection and chemical combination. Etch patterns observed on crystal faces play an important role in obtaining information on the history of growth of crystals, as their etch patterns are intimately related to the growth phenomena. The first attempt to provide an explanation for the process of etching is due to Goldschmidt (1904). A satisfactory explanation regarding the origin of etch pits and their development has been given on the concept of lattice defect known as dislocation. A dislocation etch is an attractive means of studying the early stages of deformation in crystalline solids. This has led to the discovery of a number of etchants.

In the present work, an attempt has been made to investigate the nature and shape of etch pits by etching the (001) and (011) surfaces of gel-grown nickel molybdate crystals (Kurien and Ittyachen 1980). Well-shaped square and octagonal platelets (average size $3 \times 2 \times 0{\cdot}3\ mm^3$) have been selected for this purpose.

2. Experimental and results

As there is no previous study of etching behaviour of these crystals, a number of prospective etchants were tried to reveal the dislocation sites and dislocation density. Water and quite a few acids were found to etch the cleavage faces of their flakes of nickel molybdate crystals. Nitric acid, acetic acid, sodium hydroxide, potassium hydroxide and a mixture of nitric acid and hydrochloric acid are suitable etchants for their action on the (001) face. Water has some polishing action on the surface. Sulphuric and hydroflouric acids were unsuitable for etching the faces of gel-grown nickel molybdate

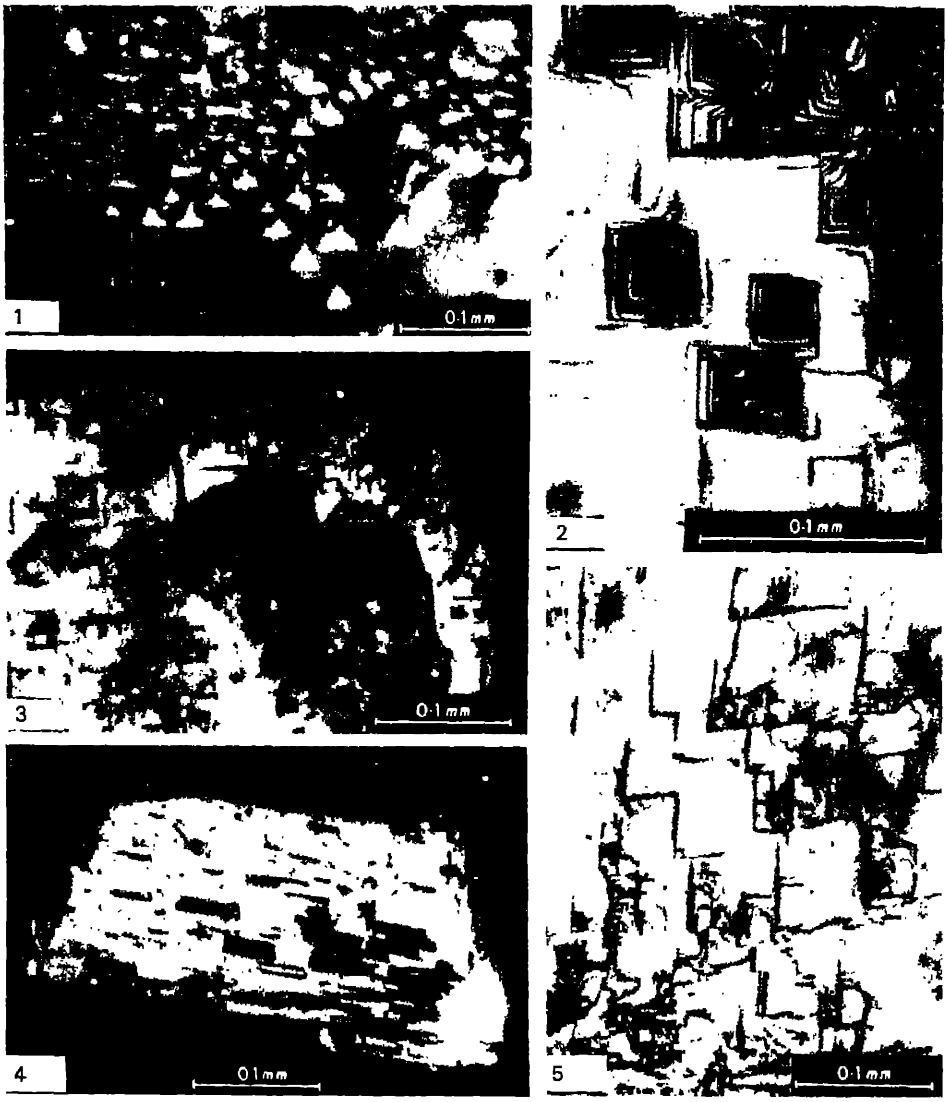

Figures 1–5. **1.** Square type etch pits on the (001) face when etched in nitric acid. **2.** Well-defined square and rectangular etch pits with terrace when etched in acetic acid. **3.** Square-shaped pits with two sides well developed when etched in sodium hydroxide. **4.** Rectangular pits on the (001) face when etched in nitric acid. **5.** Square-shaped pits with two sides well-developed when etched in potassium hydroxide.

crystals. Increase in concentration or temperature resulted in the increase of surface dissolution without forming the visible pits tabulated in table 1. A large number of clusters of pits were formed first on the surfaces of thin flake-like crystals in the initial stages of etching. However, on repeated etching most of the pits became flat-bottomed, enlarged and eventually vanished. But some of the pits remained nearly constant during successive etching. A large number of pits were symmetrical pits, composed of closed rectangular and square terraces. Both nitric and acetic acids could yield identical etch

Table 1. Experimental conditions for etch pit formation on the (001) and (011) faces of gel grown nickel molybdate crystals

Etchant	Concentration	Time (min)	Observation
HCl	1:100 1:150	1	Rapid attack
	1:200	1	Few perfect pits were observed on the (001) and (011) faces
HF	1:150 1:200 1:400	1	Rapid attack
HNO_3	1:200 1:300 1:400	1–2	Well-defined square and rectangular pits were obtained on the (001) (figure 1) and (011) (figure 4) faces
CH_3COOH	1:200	1	Clustered etch pits of smaller size
	1:100 1:150	2	Well-defined square and rectangular pits with terrace (figure 2)
NaOH	0·05–0·1 N	2	Square-shaped pits with two sides well developed (figure 5)
$HF+HNO_3$	1:300	1	Destructive reaction: no etch pit formation

The experiment was conducted at room temperature.

pits. But in the case of sodium and potassium hydroxides only two sides of the square pits were well-developed. The sides of the square pits in all cases were parallel to the $\langle 100 \rangle$ direction. The average etch pit density was of the order of 10^4–10^5 cm^{-2}. In isolated crystals, the dislocation density was between 10^2 and 10^3 cm^{-2}.

3. Discussion

Studies on different types of etch pits and their densities give useful information regarding the nature of the defects, impurity content and the history of growth of crystals. Etch pits may be produced due to several reasons. In the present case, initially a clustering of etch pits is formed. They are well-defined, very small point-bottomed, rectangular square pits. However, on repeated etching most of the pits became flat-bottomed and eventually vanished. The origin of flat-bottomed pits is due to the localised defects such as microprecipitates, vacancies etc. (Michael *et al* 1970). Evidently in this case etch pits are not being formed at the dislocation sites but at the impurity sites. The large flat-bottomed pits were assumed to be due to edge dislocations produced during the later stages of crystal growth (Johnston 1962). The edge and screw dislocations give rise to two distinct types of pits. The etch pits due to edge dislocations were generally small compared to those due to screw dislocation (Amelinckx 1976). The terrace nature of pits is a common phenomenon in the case of calcite, mica, etc. (Patel *et al* 1963). The terrace nature of pits obtained in this study can be explained by postulating the precipitation of some sort of impurities along the dislocation line which inhibits the action of the etchant depending on the nature, density and location of the impurities. The impurities might be evenly spaced along the dislocation line which result into pits having various types of terraces. The number of times the inhibition action is operated can be judged by the number of terraces—obtained when the inhibition action lasts longer, widely terraced pits are produced.

4. Conclusion

The high density etch pits obtained in the initial stages of etching suggests that the crystals have a high density of impurities adsorbed on the surfaces in the later stages of growth.

References

Amelinckx S and Dekeyser N 1952 *Naturwissenschaften* **39** 448
Amelinckx S 1976 *J. Appl. Phys.* **31** 1359
Goldschmidt V 1904 *Z. Kristallogr.* **38** 273
Gilman J J and Johnston W G 1956 *J. Appl. Phys.* **27** 1018
Horn F H and Gevers W 1952 *Philos. Mag.* **43** 1210
Johnston W G 1962 *Progress in ceramic science* (ed.) J E Burke (New York: Pergamon) Vol 2
Kurien K V and Ittyachen M A 1980 *Krist. Tech.* **15** 7, 763
Michael F, Ehman G R, Jindal J W, Faust Jr and William B White 1970 *J. Appl. Phys.* **41** 7
Patel A R and Goswami S 1963 *Physica* **29** 33
Patel A R and Ramanathan S 1963 *Amer. Miner.* **48** 691

Bull. Mater. Sci., Vol. 6, No. 6, December 1984, pp. 1001–1007. © Printed in India.

Elastic properties of As-Sb-Se glasses

A GIRIDHAR, SUDHA MAHADEVAN and A K SINGH
Materials Science Division, National Aeronautical Laboratory, Bangalore 560017, India

MS received 27 June 1983; revised 23 August 1983

Abstract. Results of measurement of elastic modulii on As-Sb-Se glasses are reported and their composition dependence discussed. The Young's and the shear modulii lie in the range of 170–210 and 65–80 kb respectively. These values are typical of chalcogenide glasses. For (As, Sb)$_{40}$Se$_{60}$ glasses, the modulii increase monotonically with increasing Sb_2Se_3 content. The observed composition dependence of the modulii for the As$_x$Sb$_{15}$Se$_{85-x}$ glasses is examined in terms of the chemically ordered structural units in the glasses.

Keywords. As-Sb-Se glasses; elastic properties; CONM model.

1. Introduction

The results of measurement of glass transition temperature (T_g), electrical conductivity and density (d) on glasses of the As-Sb-Se system were reported earlier (Giridhar and Sudha Mahadevan 1982). The study covered two groups of glasses: (i) those whose composition could be represented by (As, Sb)$_{40}$Se$_{60}$ and (ii) those whose composition could be represented by As$_x$Sb$_{15}$Se$_{85-x}$. The (As, Sb)$_{40}$Se$_{60}$ glasses fall along the (As_2Se_3) (Sb_2Se_3) pseudobinary section and represent the so-called 'stoichiometric' compositions of the As-Sb-Se system. The T_g, electrical conductivity and d of these glasses showed a monotonic increase with increasing Sb_2Se_3 content. In the As$_x$Sb$_{15}$Se$_{85-x}$ glasses, with the stoichiometric As$_{25}$Sb$_{15}$Se$_{60}$ composition as reference, glasses with more than 60 at. % of Se were referred to as Se-rich glasses and those with less than 60 at. % of Se as As-rich glasses of this family. The As$_x$Se$_{100-x}$ and Ge$_x$Sb$_{15}$Se$_{85-x}$ glasses show an extremum in T_g and d at the respective stoichiometric compositions (Myers and Felty 1967; Mohan *et al* 1981; Narasimham *et al* 1981; Giridhar *et al* 1981). The composition dependence of T_g and d of the As$_x$ Sb$_{15}$ Se$_{85-x}$ glasses exhibit an interesting feature, namely, that the T_g and d of the As-rich glasses of this family are higher than those of the As$_{25}$Sb$_{15}$Se$_{60}$ composition (Giridhar and Sudha Mahadevan 1982).

The results of measurements of elastic properties on eight glass compositions are reported in this paper. Four of these compositions can be represented by (As, Sb)$_{40}$Se$_{60}$, while the other four belong to the As$_x$Sb$_{15}$Se$_{85-x}$ family.

2. Experimental

The cylindrical samples (about 12 mm in diameter and 6 mm in length) suitable for ultrasonic sound velocity measurements were obtained by the following procedure.

The elemental components (5N purity, from Koch Light Co.) in appropriate proportions were sealed in a quartz ampoule (12 mm in diameter) under a vacuum of 10^{-3} torr. The contents of the ampoule were melted in a rotary furnace at about 950°C for 24 hr. The melt was then cooled to 800°C and quenched in water at 90°C. Care was taken to see that the ampoule stayed in a vertical position during the quenching operation. Quenching in hot water rather than in cold water was found essential to prevent any cracking or shattering of the cylindrical sample during further processing. The ampoule was then introduced into a tubular furnace where the glass was annealed at a temperature of about 5° higher than T_g for 1 hr and then brought to room temperature by slow cooling. Just before breaking open, the ampoule was chilled in an ice bath for 15 min to facilitate retrieval of the specimen from the ampoule. The faces of the cylindrical samples thus obtained were rendered flat and parallel (the wedge angle being better than 0·2 sec) using a lapping-polishing jig specially designed and fabricated for this purpose. Using Salol (phenyl salicilate) as the bonding material the longitudinal and transverse velocities in the samples were measured (at 25°C) by using 10 MHz X-cut and Y-cut transducers, by McSkimin's pulse superposition technique (McSkimin 1961; McSkimin and Andreatch 1962). As already indicated (Sudha Mahadevan *et al* 1983), an ultrasonic pulse echo interferometer (supplied by Systems Dimensions, Bangalore, model SDUI-003) in conjunction with a 50 MHz Philips oscilloscope and frequency/time interval counter (accuracy of one nsec) was used for this purpose. The accuracy of velocity measurements limited mainly by thickness measurements (for which a Mitutoyo height master transfer stand combination was used), was 0·03 %; A spread of about 1·5% was observed in the velocities in different specimens of the same composition. The typical quality of the echo pattern obtained in our set up is shown in figures 1–3. A train of 10–12 echoes could be obtained in most cases (figure 1); this is because of the high parallelism of the faces. The measurement of the delay time was facilitated by the good resolution obtained in the amplitude of the expanded echoes (figures 2 and 3).

3. Results and discussion

3.1 $(As, Sb)_{40}Se_{60}$ glasses

The results for these glasses are summarised in figure 4 and table 1. The shear (*G*), the Young's (*E*), the bulk (*K*) modulii and the Poisson's ratio (σ) of $(As, Sb)_{40}Se_{60}$ glasses increase monotonically with increasing Sb_2Se_3 content (figure 4). Extrapolation of *G*, *E*, *K* and σ values (figure 4) of these glasses to zero Sb_2Se_3 content, which corresponds to As_2Se_3, gives the values of modulii which agree well with one set of reported values for As_2Se_3 (Thompson and Bailey 1978). The other values (Hilton and Hayes 1975; Soga and Kunugi 1973) fall slightly away from the extrapolated data. Also shown in figure 4 is the variation of the mean atomic volume with composition. For isostructural crystalline compounds, the bulk modulus increases with decrease in volume (Anderson and Nafe 1965). However, in our discussion (Sudha Mahadevan *et al* 1983) of the variation of *K* with mean atomic volume of several chalcogenide glass systems, namely Ge-Sb-Se, Ge-As-Se, Ge-Sb-S and Ge-Se, it was seen that the mean atomic volume is not the only factor determining the bulk modulus of these glasses. Besides volume, other factors such as the nature of the type of bonding could also be effective in

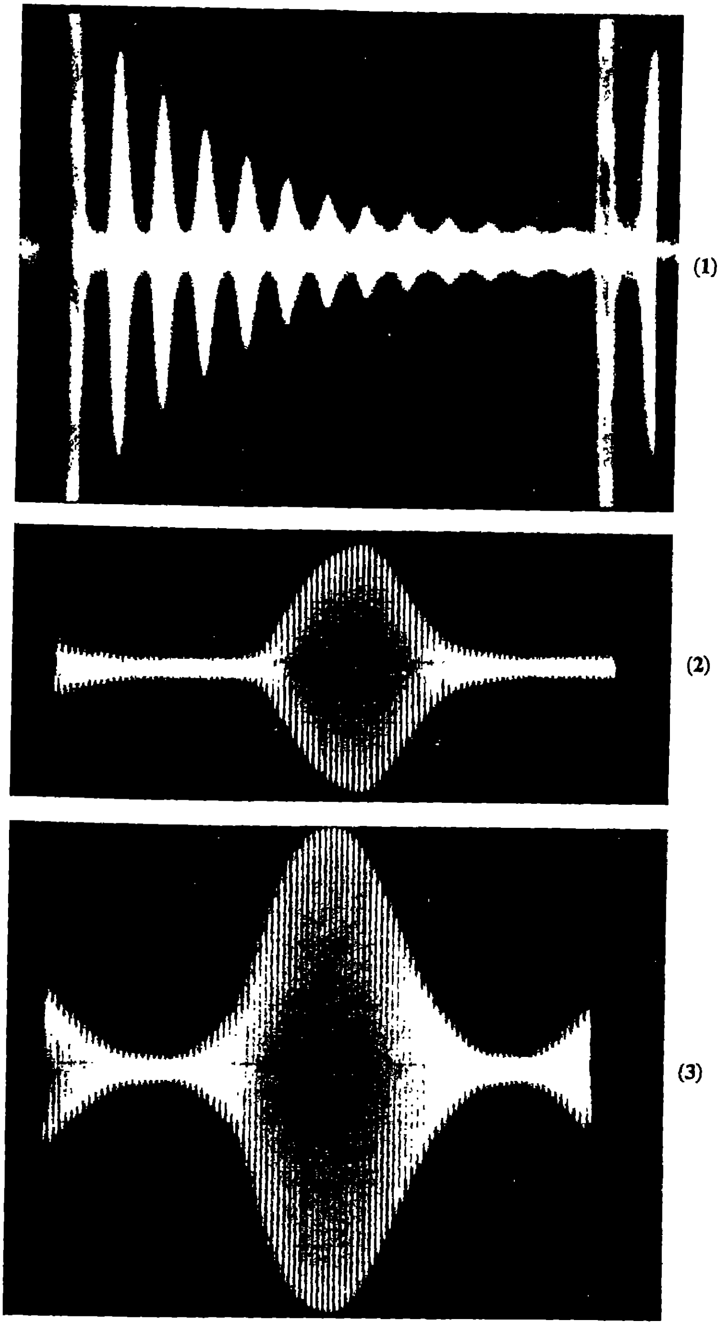

Figures 1–3 1. Typical exponential echo train for a $As_{10}Sb_{15}Se_{75}$ sample for longitudinal waves. 2. Expanded echo wave form for pulse superposition for $p = 2$, minimum amplitude. 3. Expanded echo wave form for pulse superposition for $p = 2$, maximum amplitude.

determining the bulk modulus. In (As, Sb)$_{40}$Se$_{60}$ glasses, (figure 4) the bulk modulus increases with increasing Sb$_2$Se$_3$ content while the corresponding volume has also increased. Therefore, the type of bonding, rather than the volume has greater influence in determining the bulk modulus of these glasses.

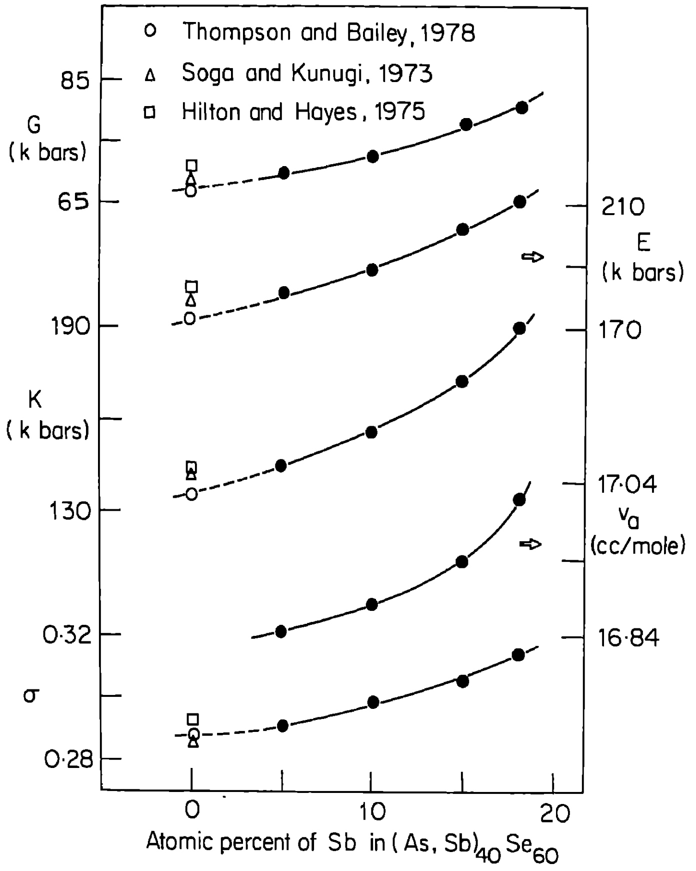

Figure 4. Variation of elastic modulii and mean atomic volume for (As, Sb)$_{40}$Se$_{60}$ glasses shown as a function of Sb content. Data for As$_2$Se$_3$ are from literature.

Table 1. Elastic data for As-Sb-Se glasses

Composition (As:Sb:Se)	d(g/cc)	Long. vel. C_l (m/sec)	Trans. vel. C_t (m/sec.)	Shear mod. G (kbars)	Young's mod. E (kbars)	Bulk mod. K (kbars)	Poisson's ratio σ
35:15:50	4·990	2302	1253	78·34	202·05	159·97	0·2895
30:15:55	4·983	2294	1245	77·24	199·46	159·21	0·2912
25:15:60	4·980	2358	1248	77·56	202·30	173·26	0·3054
20:15:65	4·920	2243	1208	71·80	186·05	151·78	0·2957
10:15:75	4·850	2121	1170	66·39	170·14	129·66	0·2813
35: 5:60	4·730	2245	1218	70·17	181·24	144·80	0·2914
30:10:60	4·860	2281	1222	72·57	188·50	156·07	0·2987
22:18:60	5·040	2429	1263	80·40	211·40	190·14	0·3147

3.2 $As_xSb_{15}Se_{85-x}$ *glasses*

The data for $As_xSb_{15}Se_{85-x}$ glasses are shown in figure 5 and table 1. With the stoichiometric composition $As_{25}Sb_{15}Se_{60}$ as reference, the G and E of As-rich glasses are seen to be essentially constant while those of the Se-rich glasses show a decrease with increasing Se-content. The bulk modulus exhibits a maximum for the stoichiometric composition (figure 5). Also shown in figure 5 is the variation of the mean atomic volume with composition. Based on the decrease of the mean atomic volume with increasing As content in the As-rich glasses, an increase of bulk modulus is expected, while it is seen that the bulk modulii of these glasses have decreased (figure 5).

In Ge-Sb-S and Ge-Sb-Se systems (Hayes *et al* 1974; Hilton and Hayes 1975; Sudha Mahadevan *et al* 1983) the Poisson's ratio (σ) increases with increasing chalcogen content. As σ denotes the ratio of transverse to longitudinal strains which arise from a single tensile stress, its increase with increasing chalcogen content has been attributed to a change in glass structure from an essentially network to a chain-like form (Hilton and Hayes 1975). However, in the $As_xSb_{15}Se_{85-x}$ glasses studied presently, σ exhibits a maximum for the stoichiometric composition and there is a decrease of σ for the Se-rich glasses in contrast to the expected increase.

The chemically-ordered network model (CONM) wherein the maximum number of

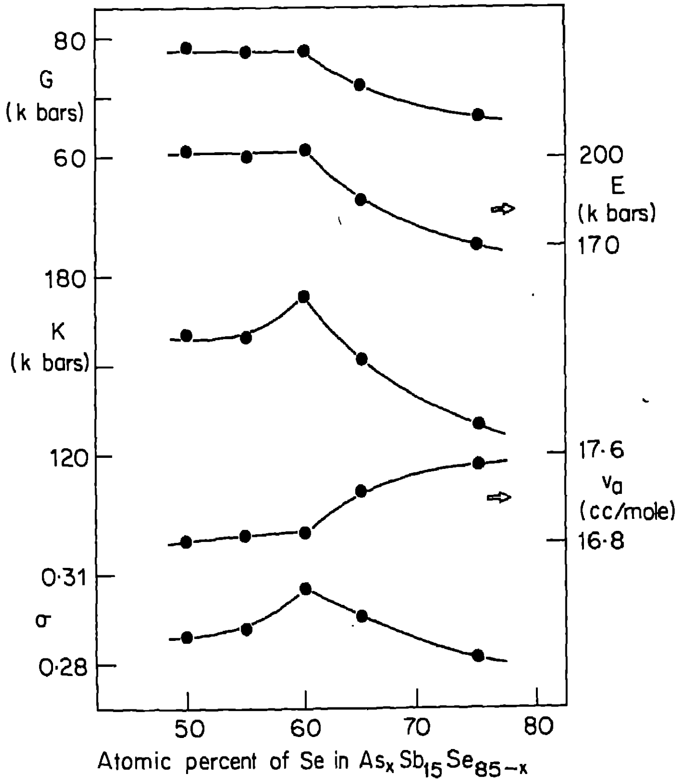

Figure 5. Variation of elastic modulii and mean atomic volume with composition for $As_xSb_{15}Se_{85-x}$ glasses.

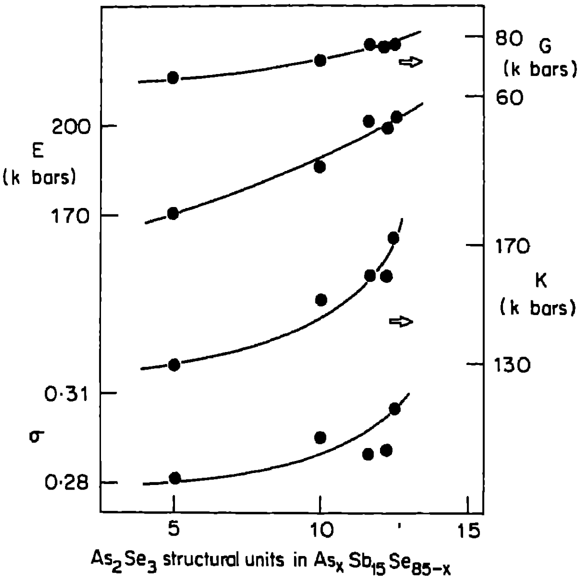

Figure 6. Dependence of elastic modulii on the As_2Se_3 structural units in $As_x Sb_{15}Se_{85-}$ glasses.

heteropolar bonds are formed first and the remaining part of the valence requirement is met with by homopolar bonding at random accounted satisfactorily for the composition dependence of the density of these glasses (Giridhar and Sudha Mahadevan 1982). For a correlation of the elastic properties with composition, the results were examined using the CONM model. A close study of the glass compositions in view of the results of figure 5 indicates the importance of As_2Se_3 content (*i.e.* As-Se bonds) in determining the elastic properties of these glasses, as the observed features in the composition dependence of K and σ can be linked to the As_2Se_3 content in these glasses. It can be seen (figure 6) that the modulii do show in general an increase with increasing As_2Se_3 content in the glasses. Though scatter in the points is seen in the dependence of the modulii on the As_2Se_3 content (figure 6), the increase in these quantities is obvious.

4. Conclusions

Elastic modulii of $(As, Sb)_{40}Se_{60}$ glasses decrease monotonically with decreasing $As_2 Se_3$ content in the glasses.

In the $As_xSb_{15}Se_{85-x}$ glasses, with the $As_{25}Sb_{15}Se_{60}$ glass as reference, the shear and Young's modulus of As-rich glasses do not vary much with the composition, while those of the Se-rich glasses decrease with increasing Se content. The bulk modulus and the Poisson's ratio of these glasses exhibit a maximum at the stoichiometric composition. An examination of the results indicates that the elastic properties of these glasses are sensitive to the As_2Se_3 content in these glasses.

References

Anderson O L and Nafe J E 1965 *J. Geophys. Res.* **70** 3951

Giridhar A, Narasimham P S L and Sudha Mahadevan 1981 *J. Non-Cryst. Solids* **43** 29

Giridhar A and Sudha Mahadevan 1982 *J. Non-Cryst. Solids* **51** 305

Hayes D J, Rechtin M D and Hilton A R 1974 *Ultrasonics Symp. Proc.* p. 502 (ed.) De Klerk, Institution of Electrical and Electronics Engineers, New York

Hilton A R and Hayes D J 1975 *J. Non-Cryst. Solids* **17** 339

McSkimin H J 1961 *J. Acoust. Soc. Am.* **33** 12

McSkimin H J and Andreatch P 1962 *J. Acoust. Soc. Am.* **34** 609

Mohan R, Panchapakesan T S and Rao K J 1981 *Bull. Mater. Sci.* **3** 29

Myers M B and Felty E J 1967 *Mater. Res. Bull.* **2** 535

Narasimham P S L, Giridhar A and Sudha Mahadevan 1981 *J. Non-Cryst. Solids* **43** 365

Soga N and Kunugi M 1973 *J. Phys. Chem. Solids* **34** 2143

Sudha Mahadevan, Giridhar A and Singh A K 1983 *J. Non-Cryst. Solids* **57** 423

Thompson J C and Bailey K E 1978 *J. Non-Cryst. Solids* **27** 161

Bull. Mater. Sci., Vol. 6, No. 6, December 1984, pp. 1009–1012. © Printed in India.

DC electrical conductivity of Na_2O-ZnO-B_2O_3 glass system

R V ANAVEKAR, N DEVARAJ and J RAMAKRISHNA*

Department of Physics, Bangalore University, Bangalore 560001, India
*Department of Physics, Indian Institute of Science, Bangalore 560012, India

MS received 12 December 1983

Abstract. The d.c. electrical conductivity of Na_2O-ZnO-B_2O_3 glass system has been measured as a function of temperature in the range of 350–600°K. The conductivity data show that the activation energy of Na^+ ions is dependent on ZnO concentration. The results have been discussed in the light of the cluster model of glasses.

Keywords. Na_2O-ZnO-B_2O_3 glass; electrical conductivity; density; activation energy.

1. Introduction

It is well known that glasses containing alkali ions are essentially solid cationic electrolytes, the current being carried by relatively mobile alkali ions. The motion of alkali ions in glasses is important, not only because of its relation to electrical conductivity, but also to chemical durability and to ion exchange kinetics. Similar work has been earlier reported on binary silicate and binary borate glasses. Some studies on borate glasses containing two different alkali oxides and alkali-alkaline earth oxides have also been reported (Israd 1969; Erzukyan 1969; Day 1976; Sakka *et al* 1979; Mutusita *et al* 1980). In the present work we report the d.c. electrical conductivity of sodium borate glasses with different concentrations of ZnO. The behaviour of activation energy of Na^+ ions has been discussed on the basis of the cluster model of glasses (Rao and Rao 1982).

2. Experimental

Analytical grade chemicals were used to prepare glasses corresponding to their glass-forming region (Rawson 1967). Appropriate quantities of boric acid (H_3BO_3), sodium carbonate (Na_2CO_3) and zinc oxide (ZnO) were taken and melted in a crucible at 1100°C for about 2 hr. The melt was then poured on a brass-block and it was quickly pressed with a polished copper-block. The glasses formed were annealed at about 400°C for 2 hr. X-ray studies showed that the glasses were amorphous. Samples of dimensions ($\sim 20 \times 20 \times 2$ mm) suitable for the measurement of electrical conductivity were prepared by grinding and polishing (using rough powder) the two flat surfaces. Silver paint was applied to these flat surfaces to serve as electrodes.

Measurements were made with glasses of the compositions listed in table 1. To measure the resistance of the samples, a special sample holder was designed following Mahadevan *et al* (1977). The resistance of the samples was determined by measuring the

Table 1. Glass composition, density and activation energy (E_a).

Mol% composition			Density (gm/cm^3)	Activation energy (eV)	
Na_2O	ZnO	B_2O_5		(600–500)°K	(500–400)°K
10	5	85	2·04	0·77	—
10	10	80	2·49	0·97	0·15
10	15	75	2·60	0·95	0·17

current through the sample for an applied voltage (25 V); the voltage was briefly applied to avoid polarization. The temperature was measured with a chromel-alumel thermocouple placed very close to the sample. The d.c. electrical conductivity was measured as a function of temperature over the range 350–600°K. Density was also measured by the Archimedes method using benzene and the values are given in table 1.

3. Results and discussion

The variation of the d.c. electrical conductivity as a function of $1/T$ for three different compositions is shown in figure 1. The activation energies are calculated from the Arrhenius equation;

$$\sigma = \sigma_0 \exp\left(\frac{-E_a}{kT}\right)$$

where σ_0 is the pre-exponential factor, E_a is the activation energy for conduction and k is the Boltzmann constant. The variation of E_a as a function of ZnO concentration is shown in figure 2. The values of activation energy obtained are shown in table 1. The conductivity behaviour in figure 1 shows that the glass with 5 mol% ZnO has a single activation barrier and also has a higher conductivity, while the glass with 10 and 15 mol% ZnO has two conductivity regions and lower overall conductivity. In order to understand the behaviour of $\ln\sigma$ in figure 1, we note the following features about borate glasses.

In borate glasses the principal structural elements present are boroxol, tetraborate and diborate groups. The diborate groups get converted into triborate and pentaborate units. In the glasses investigated here the extent of any such borate grouping which consist of tetrahedral borons depends upon the total quantity of added oxides ($Na_2O + ZnO$). In order to investigate the role of Zn^{2+} ion in these glasses, we note that the e/r^+ ratio (2·7) is quite high. It is likely that it acts as a network former, particularly in low Zn^{2+} concentration. Such Zn^{2+} positions in the network also help in cross-linking the borate chains. Zn^{2+} ions in such situations can modify the diborate groups into more open rings without affecting the extent of tetrahedral borons (Selvaraj and Rao 1983). However at higher concentrations Zn^{2+} ions act as network modifiers and may ultimately lead to phase separation. In glasses containing 5 mol% ZnO, therefore, $\ln\sigma$ variation as a function of $1/T$ is linear. Addition of 5 mol% ZnO is unlikely to cause any phase separation. The activation energy of Na^+ ions (0·77 eV) may be compared with that of (0·60 eV) 10 mol% Na_2O-90 mol% B_2O_3 glass (Chakravorty and Chakraborti 1980). This may perhaps reflect the fact that incorporation of Zn^{2+}

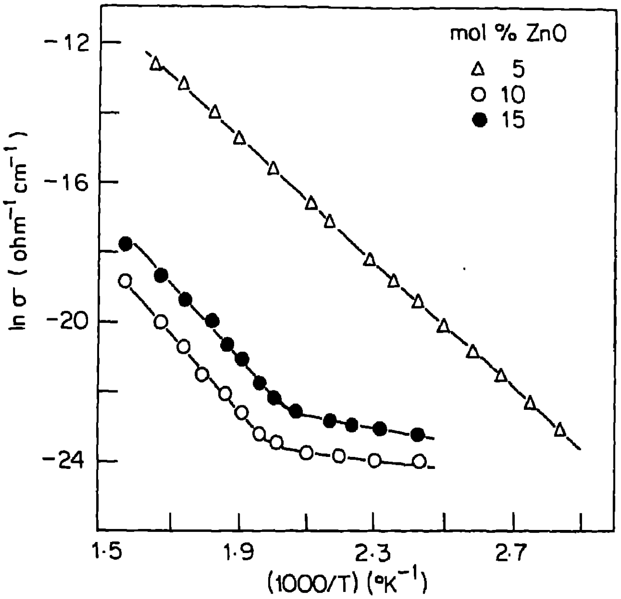

Figure 1. Variation of d.c. conductivity with temperature.

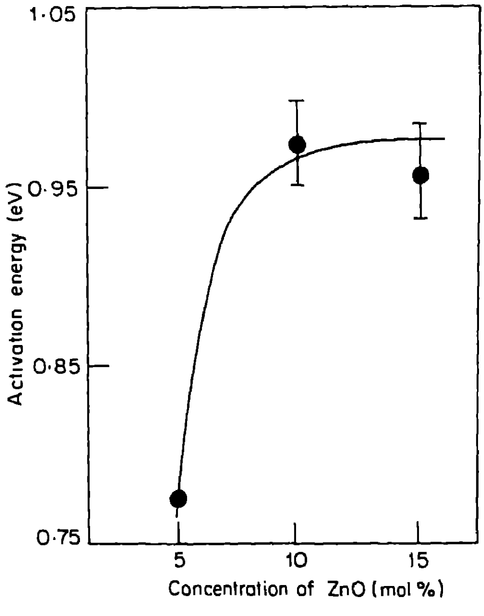

Figure 2. Variation of activation energy with concentration of ZnO.

into cross-linking positions increases the cohesion and density, thereby increasing the activation barrier for migration of Na^+ ions. In samples with 10 mol% ZnO and 15 mol% ZnO there appears to be two regions of conductivity (figure 1) characterized by two values of activation energy (E_a). This possibly indicates the presence of two distinct regions which act as precursors to phase separations. We feel that the two phases correspond to oxide-poor and oxide-rich regions (oxide representing the total quantity of Na_2O and ZnO). The oxide-poor region can be expected to be less dense with lower E_a and lower conductivity (low concentration of charge carriers and perhaps even low mobility). The oxide-rich region corresponds to high E_a and high conductivity. The charge carriers being primarily Na^+ ions, one can see that the conductivity is slightly lower for lower effective concentration of Na^+ ions. The activation barriers for both glasses (10 mol% and 15 mol% ZnO) are virtually constant (figure 2) which should be the case if conduction is mainly by the oxide-rich region and hence we find that the results support a two-region model for these glasses.

The two-region model is essentially a cluster model recently described by Rao and Rao (1982). The more ordered cluster region is likely to be an oxide-rich region while the oxide-poor region corresponds to the tissue (less order) region. Indeed AgI-Ag_2O-MoO_3 glasses (Senapati *et al*, private communication) also exhibit such two-region conductivity behaviour in accordance with the cluster model of glasses. In 5 mol% ZnO glass, the regions are not sufficiently differentiated to exhibit two-region conductivity at high temperatures; it is likely to be seen in low temperature measurements.

Acknowledgements

The authors (RVA and ND) express their thanks to Prof. P Paramasivaiah for his interest and encouragement and to Prof. K J Rao of IISc., Bangalore for many useful discussions.

References

Chakravorty D and Chakraborti S 1980 *J. Non-Cryst. Solids* **38 and 39** 295
Day D E 1976 *J. Non-Cryst. Solids* **21** 343
Erzukyan E 1969 *Arm. Khim. Zh.* **22** 109
Isrspecial J O 1969 *J. Non-Cryst. Solids* **1** 235
Mahadevan S, Giridhar A and Rao K J 1977 *J. Phys.* **C10** 4499
Mutusita K, Takayama S and Sakka S 1980 *J. Non-Cryst. Solids* **40** 149
Rao K J and Rao C N R 1982 *Mater. Res. Bull.* **17** 1337
Rawson H 1967 *Inorganic glass-forming system* (New York: Academic Press) pp. 97
Sakka S, Mutusita K and Kimiya K 1979 *Phys. Chem. Glasses* **20** 25
Selvaraj U and Rao K J 1983 *Spectra. Chim. Acta.* (communicated)
Senapati H, Parthasarathi G and Rao K J (Private communication)

Bull. Mater. Sci., Vol. 6, No. 6, December 1984, pp. 1013–1018. © Printed in India.

Photon, electron and ion beam induced physical and optical densification in chalcogenide films

K L CHOPRA, L K MALHOTRA, K SOLOMON HARSHAVARDHAN and S RAJAGOPALAN
Department of Physics, Indian Institute of Technology, New Delhi 110016, India

MS received 10 October 1983

Abstract. Irradiation of 80° deposited Se-Ge films with band gap photons, 8 keV electrons and 50 keV He^+ ions produces, primarily irreversible red shift of the absorption edge and major changes in doping and electrochemical adsorption processes. These changes have been attributed predominantly to the radiation-induced thickness and hence volume contraction resulting due to the physical collapse of the low density columnar microstructure of the obliquely deposited films. The far IR and Urbach tail studies reveal an enhanced strength of electron-phonon coupling, in obliquely deposited films having a very porous columnar microstructure, compared to normally deposited films. It has been shown that this enhanced electron phonon coupling is conducive to large thickness contraction and associated changes. These changes have been used in reprographic and lithographic applications. A correlation has been established between the thickness contraction and lithographic parameters. The possibility of generating both positive and negative relief patterns on the same film by controlling the etching time has been demonstrated.

Keywords. Chalcogenide films; optical densification.

1. Introduction

Thin films of amorphous Se-Ge have been shown to behave as inorganic resists for visible, UV and deep UV light as well as electron beam and ion beam exposures and possess many advantages over the conventional organic resists currently in use (Yoshikawa *et al* 1976, 1977, 1980; Tai *et al* 1979; Balasubramanyam *et al* 1981; Venkatesan 1981). Using the light, electron beam or ion beam induced doping, or the darkening effects, both negative and positive type resists can be realized. Extensive studies carried out in our laboratory have shown that very large thickness and hence volume contraction (physical densification) takes place in $Se_{75}Ge_{25}$ films deposited at 80° incidence and exposed to photons, electrons or ions (Singh *et al* 1979, 1980a; Chopra *et al* 1981, 1982). The thickness contraction results in a much larger darkening in these films, compared to that obtained on exposure of films deposited at normal incidence. Thickness contraction occurs also when $Se_{75}Ge_{25}$ films overcoated with a very thin (100–200 Å) layer of a metal, such as Ag, are irradiated. This affects the doping of Ag into the chalcogenide film. Both the positive and negative resist behaviour of the obliquely deposited films are expected to be different from that of the normal incidence films and to be correlated with the thickness contraction resulting in these films on irradiation. In the present study, we have examined this correlation and utilized it to (a) yield a better lithographic sensitivity and contrast, both for the negative and positive resist behaviour, and (b) obtain both positive and negative resist characteristics in the same film.

2. Experimental

The experimental details for vacuum deposition of amorphous Se-Ge films are the same as reported earlier (Singh *et al* 1979; Rajagopalan *et al* 1979). The films were masked with a sharp edge and exposed to photons and ions. A 250 W mercury vapour lamp with an intensity of 30 mW/cm^2 was used for band gap photon illumination. Ion (He^+) irradiation was carried out with a 50 keV ion beam, using an ion accelerator (Sames J-15) in a vacuum of 10^{-7} torr, at room temperature. No ion sputtering or deformation of the film occurred during irradiation. The films were irradiated with an 8 keV, 0·2 μm diameter electron beam (PHI 590-A Super SAM instrument) for electron beam exposures. The thickness contraction was determined by measuring the thickness difference between the exposed/irradiated and the unexposed/unirradiated regions with the help of Talystep and then normalized against the original starting thickness of the as-deposited film.

For studying the negative resist behaviour, thin layers of Ag and Cu, (about 200 Å thick), were deposited on the as-prepared Se-Ge films by electrochemical adsorption (dipping in 0·025 M $AgNO_3$ 1 M $CuSO_4$ respectively) as well as by thermal evaporation. The resulting metal-Se-Ge films were then irradiated with photons, electrons and ions in the same way as described above and the thickness contraction was determined. The chemical dissolution rates of the films, with and without the metal overlayer, were determined by developing the films in 0·25 M NH_4OH solution.

3. Results and discussion

A comparison of the thickness contraction brought about by the irradiation of the 80°-deposited $Se_{75}Ge_{25}$ films by photons, electrons and ions is shown in figure 1. A

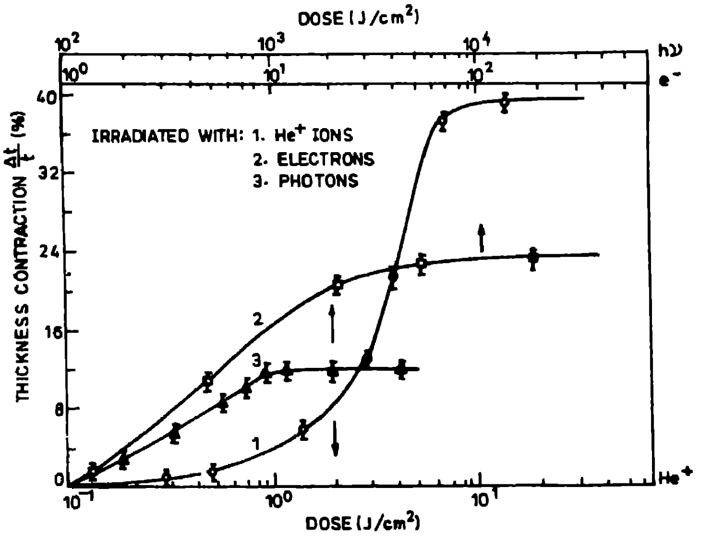

Figure 1. Thickness contraction as a function of incident flux for photon, electron and ion beam-irradiated 80°-$Se_{75}Ge_{25}$ films.

comparison of the incident energy reveals that ions are more effective in bringing about contraction followed by electrons and then photons. It may be pointed out that calculations of projected range and range straggling for He^+ ions in $Se_{75}Ge_{25}$ film show that there is no ion implantation in the film since the film thickness is smaller than the projected range.

The as-deposited Se-Ge films dissolve readily in an alkaline solution. The solubility is increased on irradiation. For $Se_{75}Ge_{25}$ films deposited at normal incidence, the increase in the solubility is rather small and hence not a very useful effect. The large thickness contraction occurring in 80° films leads to large microstructural changes which in turn increases the solubility difference between the irradiated (contracted) and unirradiated regions (Singh *et al* 1980b). The dissolution rates can be obtained from figure 2 which shows the normalized remaining thickness *vs* normalized etching time (*i.e.* the time taken to remove a certain thickness of an irradiated or a virgin film divided by the total time taken for the complete removal of the irradiated or the virgin film) for an as-deposited and irradiated (with ions, electrons and photons) $Se_{75}Ge_{25}$ film. Two kinds of etching selectivity are obtained as a function of the etching time. In the initial stages of etching, the unexposed regions etch faster than the exposed regions, *i.e.*, a negative resist behaviour is obtained even without the use of an overlayer metal. The etching behaviour changes to a positive resist type (exposed portion dissolving faster than the unexposed portion) after a certain etching time which is higher for photons and comparatively much lower for electrons and ions. If the etching is stopped when the exposed or irradiated portion has been completely etched off, the fractional final thickness remaining in the unirradiated or unexposed portion is about 88 % for the ion irradiated, 78 % for electron irradiated and 33 % for photon irradiated films. A comparison of this data with that reported by earlier workers reveals that a much higher remaining thickness is obtained by us (Yoshikawa *et al* 1976, 1977; Tai *et al* 1979;

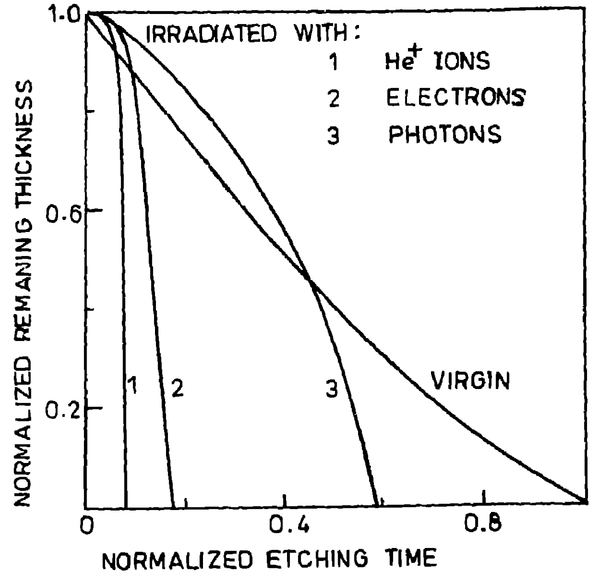

Figure 2. Normalized remaining thickness *vs* normalized etching time for a virgin and irradiated (with ions, electrons and photons) 80°-$Se_{75}Ge_{25}$ films.

Balasubramanyam *et al* 1981; Venkatesan 1981). Thus the value of 33 % obtained in photon-irradiated films in the present case is much higher than 13 % reported by Yoshikawa *et al* (1976), in normal incidence $Se_{75}Ge_{25}$ films obtained by sputtering. The difference can be attributed to the large thickness contraction obtained in the 80° films and absent in normal incidence films. Similarly, the large value of 88 % in the ion-irradiated case obtained in the present study is much higher than 58 % reported by Balasubramanyam *et al* (1981), on obliquely deposited films of the same material possibly due to the larger thickness contraction in our films resulting from the use of heavier He^+ ions. Thus, a control of etching time can permit both positive and negative relief patterns to be generated on the same film.

Figure 3 shows the normalized remaining thickness *vs* ion dosage corresponding to an etching time just sufficient for the complete removal of the exposed portion. As mentioned above; a very large selective etching of 88 % has been obtained. A contrast (γ) of 4·5 and sensitivity (S) $\sim 10^{-4}$ C/cm^2 have been obtained. Though the sensitivity is lower than the conventional organic resists, the large selective etching and a reasonably good value of contrast make the films suitable for positive resist applications. Typical values of the lithographic parameters for positive resist applications for different radiations are listed in table 1.

Negative resist characteristics are obtained when the films with an overlayer of Ag or Cu are irradiated with ions, electrons or photons. Figure 3 shows our results on the negative resist characteristics for He^+ irradiated Se-Ge films with an overlayer of Ag. A sensitivity $\sim 1{\cdot}4 \times 10^{-5}$ C/cm^2 and a contrast of 8·3 have been obtained. The negative resist characteristics for different radiations obtained by this process are also listed in table 1. The high value of contrast should produce a high intrinsic resolution in these films for ion beam lithographic applications. Submicron lithographic patterns have been generated by us and other workers routinely (Balasubramanyam *et al* 1981; Venkatesan 1981; Chopra *et al* 1982).

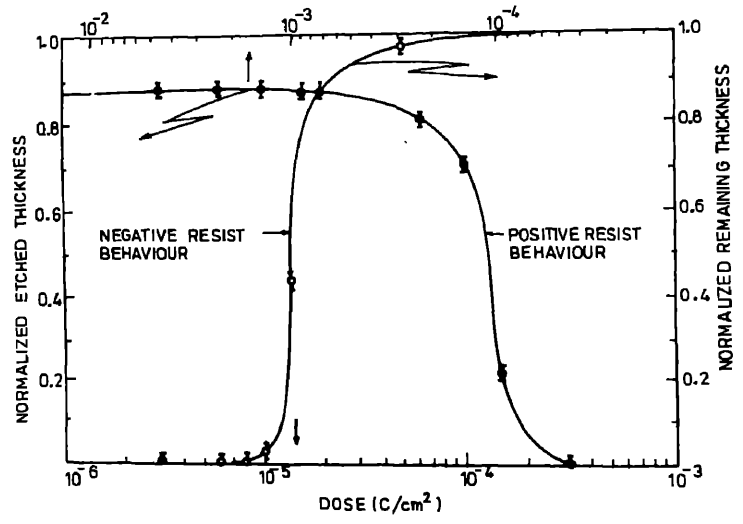

Figure 3. Positive and negative resist characteristics of 80°-$Se_{75}Ge_{25}$ films subjected to He^+ irradiation.

Table 1. Lithographic parameters (sensitivity, S, and contrast, γ) for different radiations for $80°\text{-}Se_{75}Ge_{25}$ films.

Radiation	As-positive resist		As-negative resist	
	S	γ	S	γ
He^+ ions	$\sim 1{\cdot}2 \times 10^{-4}$ C/cm^2	4·5	$\sim 1{\cdot}6 \times 10^{-5}$ C/cm^2	8·3
Electrons	$\sim 8 \times 10^{-4}$ C/cm^2	4	$\sim 1 \times 10^{-4}$ C/cm^2	7·6
Band gap photons	$\sim 10^{20}$ photons/cm^2	1·7	$\sim 10^{19}$ photons/cm^2	3·5

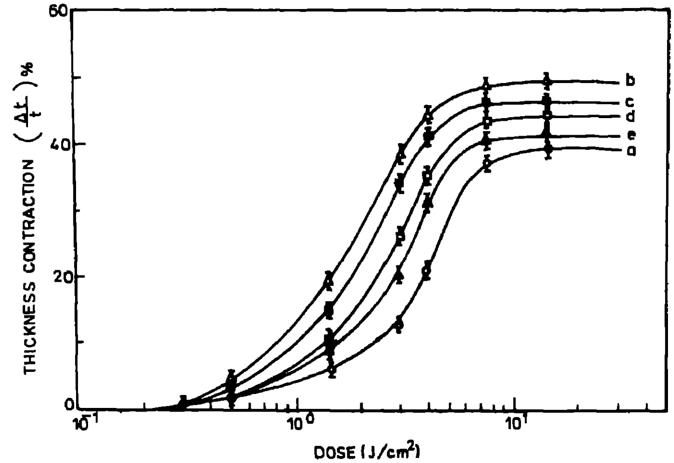

Figure 4. Thickness contraction as a function of ion dosage for: **a.** as-deposited, **b.** as-deposited with an overlayer of electrochemically adsorbed Ag, **c.** as-deposited with an overlayer of evaporated Ag, **d.** as-deposited with an overlayer of electrochemically adsorbed Cu, and **e.** as-deposited with an overlayer of evaporated Cu.

Our studies show that the thickness contraction plays an important rolė in the negative resist action in the obliquely deposited films. Figure 4 shows the thickness contraction as a function of ion dosage for: (a) as-deposited, (b) as-deposited with an overlayer of electrochemically adsorbed Ag, (c) as-deposited with an overlayer of evaporated Ag, (d) as-deposited with an overlayer of electrochemically adsorbed Cu, and (e) as-deposited with an overlayer of evaporated Cu. It is noteworthy that the thickness contraction is larger in a film having an overlayer of a metal than in one without an overlayer. The improved negative resist characteristics in obliquely deposited films is therefore a direct consequence of enhanced thickness contraction.

Acknowledgements

The authors are grateful to Mr A K Tyagi of RRC Kalpakkam, for ion irradiation and Miss M Rajeswari for assistance. The financial aid from the Electronics Commission, Government of India, is gratefully acknowledged.

References

Balasubramanyam K, Karapiperis L K, Lee C A and Ruoff A L 1981 *J. Vac. Sci. Technol.* **19** 1
Chopra K L, Harshavardhan K S, Rajagopalan S and Malhotra L K 1981 *Solid State Commun.* **40** 387
Chopra K L, Harshavardhan K S, Rajagopalan S and Malhotra L K 1982 *Appl. Phys. Lett.* **40** 428
Rajagopalan S, Singh B, Bhat P K, Pandya D K and Chopra K L 1979 *J. Appl. Phys.* **50** 1
Singh B, Rajagopalan S, Bhat P K, Pandya D K and Chopra K L 1979 *Solid State Commun.* **29** 167
Singh B, Rajagopalan S, Bhat P K, Pandya D K and Chopra K L 1980a *J. Non-Cryst. Solids* **35–36** 1053
Singh B, Rajagopalan S and Chopra K L 1980b *J. Appl. Phys.* **51** 1768
Tai K L, Sinclair W R, Vadimsky R G, Moran J M and Rand M J 1979 *J. Vac. Sci. Technol.* **16** 1977
Venkatesan T 1981 *J. Vac. Sci. Technol.* **19** 1368.
Yoshikawa A, Ochi O, Nagai H and Mizushima Y 1976 *Appl. Phys. Lett.* **29** 10
Yoshikawa A, Ochi O, Nagai H and Mizushima Y 1977 *Appl. Phys. Lett.* **31** 3
Yoshikawa A, Ochi O and Mizushima Y 1980 *Appl. Phys. Lett.* **36** 107

Bull. Mater. Sci., Vol. 6, No. 6, December 1984, pp. 1019–1027. © Printed in India.

Oxidation of thin films of tin at room temperature in hydrogen sulphide atmosphere

C I MUNEERA and V UNNIKRISHNAN NAYAR
Department of Physics, University of Kerala, Kariavattom, Trivandrum 695 581, India

Abstract. The oxidation of thin films of tin at room temperature in an atmosphere containing 10 % H_2S and 90 % air has been studied by measuring the changes in resistance of thin films. Morphological studies have also been carried out using optical and scanning electron microscopes. Reaction kinetics change from logarithmic law at ordinary atmospheres to a power law in the presence of H_2S. The basis of formation of sulphide along with the oxide is explained, the former growing on a lower layer and the latter on an upper layer.

Keywords. Oxidation; tin; hydrogen sulphide; thin films; resistance change.

1. Introduction

Hydrogen sulphide is a naturally occurring gas forming part of the sulphur-cycle (Minster 1963). Owing to its highly corrosive nature, H_2S testing on metals and alloys is of industrial importance. Tin is a metal of widespread use in external atmosphere mainly as a sacrificial coating on metals. Extensive studies on the oxidation of tin have been carried out by Boggs and coworkers (Boggs *et al* 1961a, b, 1963, 1964a; Boggs 1961c, 1964b). Chan duc Thiep *et al* 1977a, b employed the selective Mössbauer spectroscopy method to study the oxidation mechanism of thin films of tin deposited on glass. The formation of sulphur containing mixed films on tin was discussed by Gabe (1977). The present paper contains investigations about the effect of H_2S on the oxidation of thin films of tin at constant relative humidities (≈ 85 %) and at room temperature (≈ 303 K).

2. Experimental

The oxidation rate was followed by measuring the rate of increase of resistance of thin films (900 A) of tin (99·999 %) which had been evaporated on to optically plane glass substrates at room temperature. Thick electrode films of tin were previously deposited at the ends of the glass substrates, which were cleaned by chemical and ion-bombardment methods. All evaporations were carried out in a conventional vacuum line at pressures greater than 10^{-5} torr. The films and electrodes were evaporated from a molybdenum boat.

After measuring the resistances, the films coated in the same pump-down were quickly transferred to an enclosed glass chamber (Muneera *et al* 1983) evacuated to a pressure of 10^{-2} Torr. The required amount of air was then admitted into the chamber followed by 10 % by volume of dry H_2S stored in a reservoir. The relative humidity inside the chamber was assessed using a dry and wet thermometer assembly. Resistances of the films were measured at regular intervals for several hours using a vernier potentiometer of accuracy 10^{-6} v. div^{-1}. After about ten days, the films were taken out and photographed. Both optical and scanning electron microscopes were used to study the structure of the oxide films formed. Resistance could not be measured for longer periods due to the failure of metal contacts used for external connections. Studies with higher percentage of H_2S were also not possible because of the vigorous attack by the highly corrosive gas on the metal contacts used.

3. Results and discussion

The change in resistance of the thin film can be related to the oxide thickness (Hunt and Ritchie 1972). If the evaporated thin film is regarded as a thin isotropic metal sheet which oxidises on one surface only and obeys Ohm's law, then it follows that the film resistance R and the oxide thickness X are related by the equation

$$x = \frac{\phi \rho l}{\omega}\left(\frac{1}{R_0} - \frac{1}{R}\right), \tag{1}$$

where ϕ is the thickness of the oxide, derived from unit thickness of metal, ρ is the resistivity of the metal film, l is the length of the film between contacts, ω is the width of the film and R_0 is the resistance of the film prior to oxidation. In deriving this equation it has been assumed that the resistivity of oxide formed is very much larger than that of the metal. This condition is satisfied in the present studies as the oxide and sulphide formed on the thin film of tin at room temperature are amorphous (Bound and Richards 1939; Hart 1952; Britton and Bright 1957; Boggs *et al* 1961b; Raymond and Donald 1955). From (1) it is clear that the oxide thickness x is proportional to $-1/R$.

The oxidation of tin at room temperature obeys a direct logarithmic rate law (Tamman and Köster 1922; Katz 1956; Britton and Bright 1957; Gabe 1977). With the introduction of 10 % H_2S, the oxidation rate changed from a direct logarithmic law to a power law of the form

$$x^n = kt, \tag{2}$$

where x is the oxide thickness and k and n are constants. This is evident from the plot of log $1/R$ vs log t in figure 1.

The surface structures developed on the film after about ten days of exposure to H_2S + air atmosphere are shown in figures 2–8. There are two types of nucleation centres: the slightly large bright centres and the more distributed form of fine grains or powdery nuclei (figure 2). Some of the former grow into larger growth centres near the edges of the films (figures 3–5). They are different from the wheel-shaped or dendritic growth centres (Boggs *et al* 1961b; Muneera *et al* 1983) observed on films exposed to normal atmospheres (figures 9–10). Figure 6 shows the larger growth centre along with the other nucleation centres. Growth centres under different stages of growth are observed on the same specimen.

The various chemical reactions which can take place when the film is kept in an atmosphere containing 10% H_2S and 90% air are as given below (Boggs *et al*

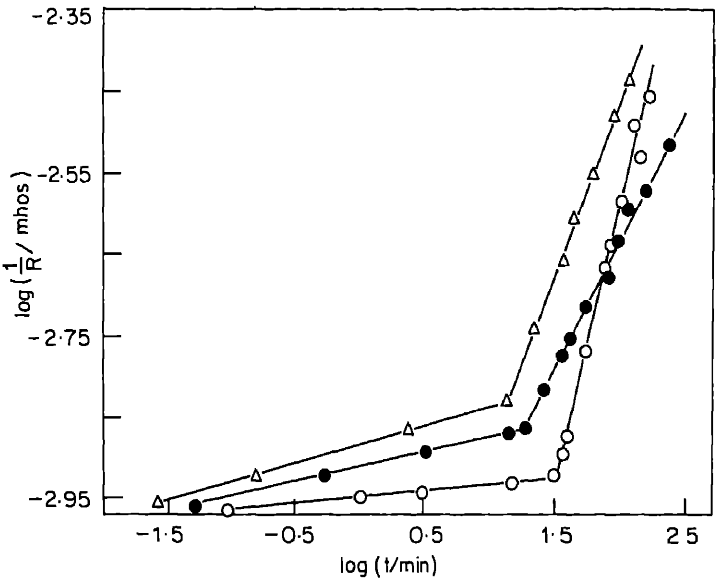

Figure 1. Plot of log $1/R$ vs log t. The oxidation rate for the initial period is different as observed usually.

Figure 2. The two types of nucleation centres observed on a film kept in 10 % H_2S + air atmosphere for about ten days (× 220).

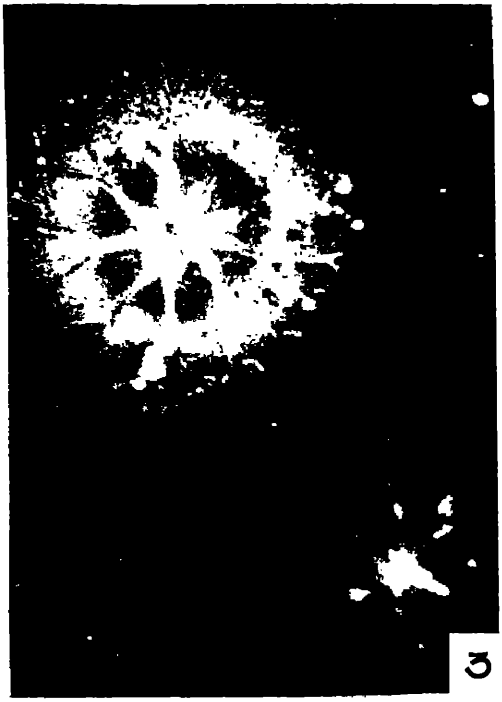

Figure 3. Optical micrograph of the wheel-shaped dendrites seen at the edges of the film (×480).

1961 a, b, c; Gabe 1977). The relevant thermodynamical data are obtained from Kubaschewski *et al* (1967)

$$\mathrm{Sn} + 1/2\ \mathrm{O_2} \rightleftharpoons \mathrm{SnO};\ \Delta G_T = -68400 + 23.3\,T\ \text{cal.} \approx -61{\cdot}46\ \text{kcal}\ (T = 303\ \text{K}), \tag{3}$$

$$\mathrm{Sn} + \mathrm{H_2S} \rightleftharpoons \mathrm{SnS} + \mathrm{H_2};\ \Delta G_T = -22100 + 14{\cdot}96\,T \approx -17{\cdot}64\ \text{kcal.}\ (T = 303\ \text{K}) \tag{4}$$

Thermodynamically the greater possibility of reaction is the one in which there is maximum decrease in free energy change. Thermodynamic equilibrium will not be attained for short periods of oxidation and at room temperature, the conditions under which the present studies are made. In such cases the reaction kinetics determine the possibility of occurrence of a particular chemical reaction. It has been reported that the oxide formed on tin at room temperature is SnO (Boggs *et al* 1961 a, b, 1963; Gabe 1977). Therefore considering the higher partial pressure of O_2 (143·64 mm of Hg) and greater electron affinity of sulphur, both SnO and SnS are expected to form, although the free energy change associated with reaction (4) is less than that with reaction (3).

The oxidation of tin at room temperature takes place by the outward migration of cations (Boggs *et al* 1961). In the presence of 10% H_2S and 90% air, both hydrogen sulphide and oxygen are expected to be adsorbed on the surface. Because of the higher partial pressure of oxygen, it seems reasonable that SnO is formed first and grows by

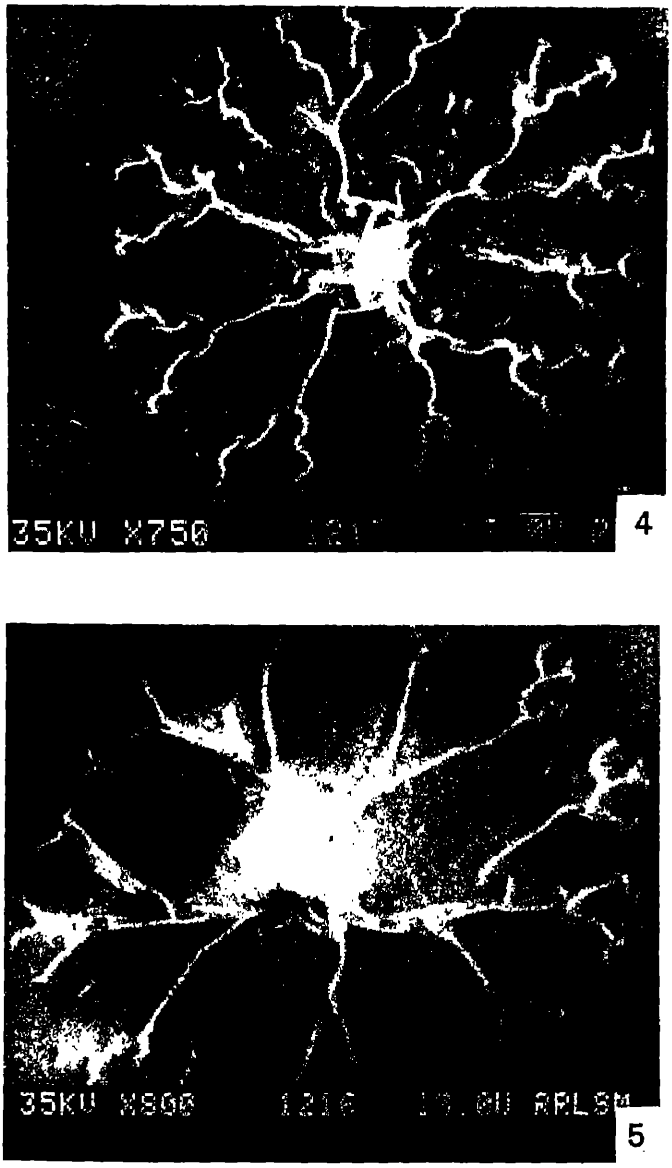

Figures 4–5. SEM of the rosette-shaped dendrite in which the lower sulphide layer 4. also grows into branches following the upper oxide dendrites and 5. forms a circular bed for the radiating oxide dendrites.

outward migration of cations. From SEM and optical microscopic studies, it can be concluded that at sites where SnO grows into 'radially symmetric dendrites', the sulphide forms a layer beneath the oxide layer (figures 3–5). The oxide and sulphide together forms 'wheel-shaped' (figure 3) or 'rosette shaped' (figures 4–5) dendrites at these sites. Even at other sites where SnO forms comparatively smaller growth centres the powdery or fine-grain like SnS is observed on a lower layer (figures 2, 6). Therefore

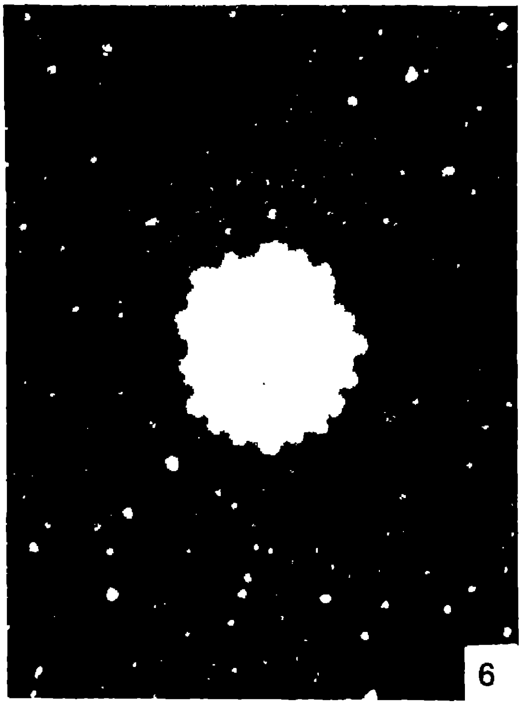

Figure 6. The larger growth centre along with the two types of nucleation centres (× 220).

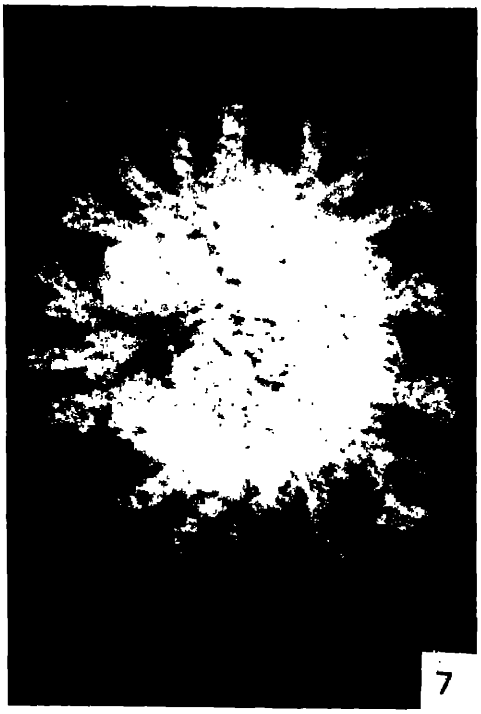

Figure 7. Optical micrograph of figure 4 under transmitted light showing podia-like extensions at the boundary (× 540).

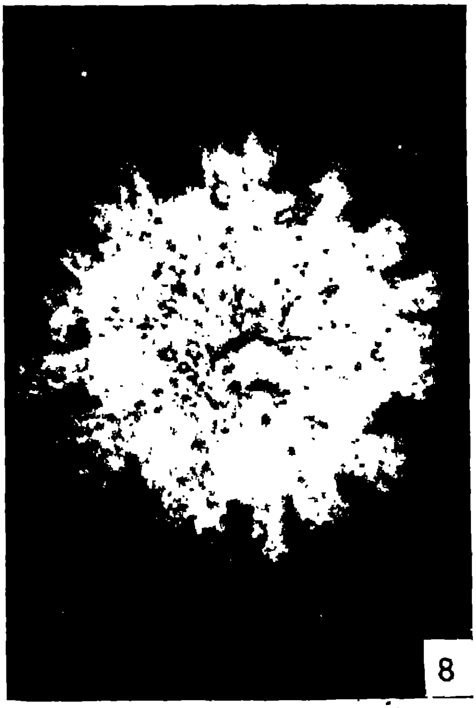

8

Figure 8. Later growth stage of a pattern similar to that shown in figure 7 (× 500).

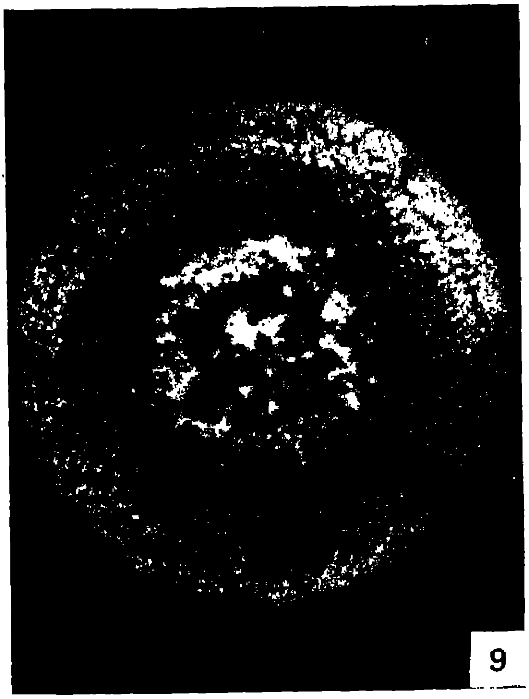

9

Figure 9. Wheel-shaped growth centre observed on a film kept in normal atmosphere (× 1440).

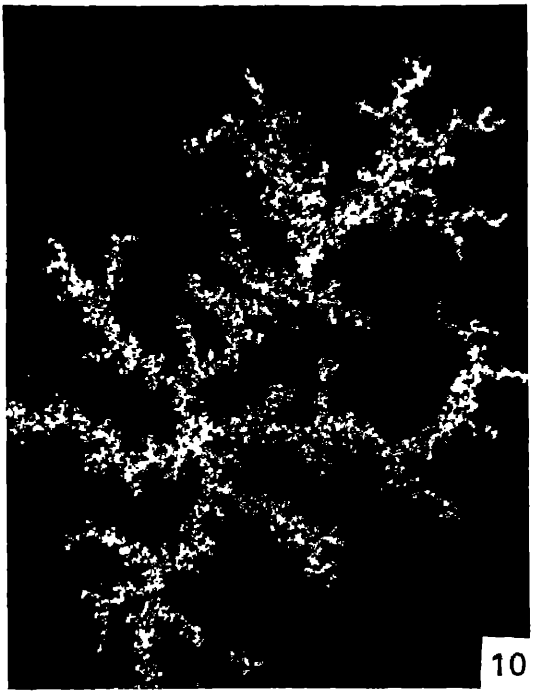

Figure 10. The dendritic growth of oxide observed on the film kept in normal atmosphere (×200).

SnS is presumed to form between the metal and the oxide layer, *i.e.*, at the oxide-metal interface. It must grow by the inward migration of sulphur through the oxide layer reacting with cations and electrons at the sulphide-oxide interface. The presence of sulphur in the oxide remarkably enhances the cation diffusivity (Wooten and Birks 1972; Lawless 1974). The oxidation rate is therefore increased to that of a power law when 10% H_2S is introduced.

The radially symmetric dendrites may be formed in a way similar to that of the dendrites found at low oxygen pressures (Boggs *et al* 1961b). These structures are commonly observed near the edges of the films where the chance of finding high density of grain-boundaries is greater. Although the partial pressure of oxygen is considerably high, the presence of H_2S and the higher electron affinity of sulphur leads to an initial adsorbed layer of variable oxygen concentration. The 'wheel-shaped' or 'rosette shaped' dendrites grow laterally in radial directions (see the small growth centre in figure 3). The areas between adjacent primary branches become depleted in oxygen as oxygen in the adsorbed layer is consumed during the formation of radiating branches. These branches grow outward into areas richer in oxygen uniformly forming secondary and tertiary branches and a well-defined radially symmetric circular pattern is obtained. The sulphide layer also grows laterally forming a circular bed for the radiating dendrites (figure 5). In figure 3 the sulphide layer formed below the radially symmetric dendrite forms a rim at its boundary. In certain cases (figure 4) the sulphide layer also grows into branches following the oxide dendrites. When viewed under transmitted light using an optical microscope, figure 4 appears as shown in figure 7. The distinction between oxide and sulphide layer is less clear in figure 7. At the boundary of the growth centre, the oxide and sulphide together form 'podia'-like extensions (figures 7, 8). The tips of the branches seem to have thickened. With further oxidation, the area between podia-like extensions get filled up gradually (figure 8).

4. Conclusion

With the presence of 10 % H_2S, the rate equation changes from a logarithmic law to a power law, indicating an increase in oxidation rate. This is explained on the basis of formation of sulphide along with the oxide, the former growing on a lower layer and the latter on the upper layer. The oxide and sulphide together forms 'wheel-shaped' or 'rosette-shaped' dendrites at the edges of the film.

References

Boggs W E, Kachik R H and Pellissier G E 1961a *J. Electrochem. Soc.* **108** 6
Boggs W E, Trosso P S and Pellissier G E 1961b *J. Electrochem. Soc.* **108** 13
Boggs W E 1961c *J. Electrochem. Soc.* **108** 124
Boggs W E, Kachik R H and Pellissier G E 1963 *J. Electrochem. Soc.* **110** 4
Boggs W E, Kachik R H and Pellissier G E 1964a *J. Electrochem. Soc.* **111** 636
Boggs W E 1964b *Br. Pat.* **963** 763
Bound M and Richards D A 1939 *Proc. Phys. Soc. London* **51** 256
Britton S C and Bright K 1957 *Metallurgia* **56** 163
Chan duc Thiep, Ts. Bonchev, Mitrikov M, St. Peneva, Topalova K and Zukeva E 1977a *Bulg. J. Phys.* **4** 130
Chan duc Thiep, Ts. Bonchev, Nguyen Chi Toa and St. Peneva 1977b *Bulg. J. Phys.* **4** 399
Gabe D R 1977 *Surf. Technol.* **5** 463
Hart R K 1952 *Proc. R. Soc. (London)* **B65** 955
Hunt G L and Richie I M 1972 *J. Chem. Soc., Faraday Trans. I*, **68** 1413
Katz W 1956 *Stahl Eisen* **76** 1672
Kubaschewski O, LL Evas E and Alock C B (eds) 1967 *Metallurgical thermochemistry* (New York: Pergamon Press)
Lawless K R 1974 *Rep. Prog. Phys.* **37** 231
Minster J T 1963 *Nature (London)* **199** 474
Muneera C I, Varghese S and Unnikrishnan Nayar V 1983 *Oxid. Met.* **19** 187
Raymond E K and Donald F O (eds) 1955 *Kirk-Othmer encyclopedia of chemical technology* (New York: Interscience) vol. 14
Tamman G and Kōster W 1922 *Z. Anorg. U. Allegm. Chem.* **123** 196
Wooten M R and Birks N 1972 *Corrosion Sci.* **12** 829

Bull. Mater. Sci., Vol. 6, No. 6, December 1984, pp. 1029–1033. © Printed in India.

Annealing behaviour of electron-beam deposited tin dioxide films

ARJEESH GUPTA, POONAM GUPTA and V K SRIVASTAVA
Department of Physics, University of Roorkee, Roorkee 247 672, India

MS received 23 November 1983; revised 31 March 1984

Abstract. The sheet resistivity of tin dioxide films deposited by electron-beam evaporation has been studied during annealing, both as a function of time and temperature. The annealing behaviour of SnO_2 films under the above two different conditions is consistent. A qualitative interpretation has been given for the decrease and the minimum observed in the resistivity. The increase in resistivity has been confirmed by scanning-electron micrographs. The films were also characterized by x-ray diffractometry.

Keywords. Tin dioxide films; electron beam evaporation; annealing behaviour; sheet resistivity.

1. Introduction

Thin transparent conducting films of SnO_2, because of their wide application in solar cells, have currently become a subject of intense investigation. The SnO_2 film is a transparent conductor which is sometimes known as Nesa glass (Ishiguro *et al* 1958). The optical and electrical properties of SnO_2 films were studied by Arai (1960) who found them to be polycrystalline *n*-type degenerate semiconductor with a free carrier density of 7×10^{18}–$1{\cdot}7 \times 10^{19}\ \mathrm{cm}^{-3}$ and an energy band gap of about 3·5 eV. The change in the conductivity of the material (SnO_2) in thin films as compared to that in bulk arises due to anion oxygen defects.

It is known (Raccanelli and Madalena 1976; Viscrian and Georgescu 1969; Shanthi *et al* 1980) that post-annealing treatment of SnO_2 films can result in change of electrical properties. It has recently been reported (Ghosh *et al* 1978; Nagatoma *et al* 1979) that the annealing of SnO_2 films plays an important role in the improvement of the performance characteristics of SnO_2/Si solar cells. It has been found that on annealing the resistivity of pure SnO_2 single crystals reduces and that of the SnO_2 films deposited by hydrolysis of an ether-alcohol solution of Sn $(OC_2H_5)_4$ first decreases and then increases drastically on annealing at temperatures higher than 500°K (Jarzebeski 1976). But no satisfactory explanation is available for the phenomenon.

As far as the authors are aware, investigations on the annealing behaviour of electron beam deposited SnO_2 film, which are important in solar cells, have not been reported. The present work was therefore undertaken.

2. Experimental

2.1 *Sample preparation*

SnO_2 films were prepared by electron-beam evaporation at a pressure $\sim 10^{-6}$ torr. Undoped SnO_2 (99·90 %) was evaporated by an electron-beam gun onto chemically cleaned glass substrates at room temperature (300°K). An evaporation rate of 4 Å $\sec^{-1}$ was maintained to produce films of SnO_2 with approximately uniform thickness of about 1300 Å. The thickness of the films was measured during evaporation by a quartz crystal thickness monitor and also by the interferometry method.

2.2 *Resistivity measurement*

The resistivity of the films was measured in a furnace during annealing as a function of time. The temperature of the furnace was maintained constant (± 5°C). The sheet resistivity of SnO_2 films was also measured during annealing as a function of temperature in the range (623–808 K). The temperature of the furnace was regulated at approximately 3°C/min. The temperature was measured with a chromel-alumel thermocouple. X-ray diffraction measurements of the films were made (Philips x-ray diffractometer, model No. PW-1140/90) and scanning electron micrographs taken (SEM-501, Philips make).

3. Results and discussion

The sheet resistivity of the as-deposited SnO_2 films was very high (> 20 MΩ) and decreased with annealing in air. The variation of sheet resistivity as a function of time during isothermal annealing at different temperatures is shown in figure 1. The as-deposited or unannealed SnO_2 films (evaporation temperature above 1800°C) are expected to be amorphous in character as shown by its high resistivity. This amorphous character is confirmed by x-ray diffractometric characterisation (figure 2a). The peaks of the x-ray diffraction pattern show crystallization with time during annealing at 717, 701 and 688 K respectively (figure 2) as also indicated by decrease in resistivity. As expected, the general shape of the isothermal annealing curves (figure 1), at different temperatures is very similar.

It was observed that the time at which the films became conducting increases as the annealing temperature decreases. This is expected because the thermally activated process of transformation from the amorphous to the polycrystalline phase will slow down with decrease of annealing temperature. This also explains the broadening of the minima with decreasing annealing temperature. The decrease in sheet resistivity with time (figure 1) may be attributed to the reduction in defect density as shown by the x-ray diffraction results, and in addition chemisorption of oxygen also takes place which further reduces the resistivity of the films (Shanthi *et al* 1980). The sheet resistivity attains a minimum when the defect distribution may be assumed to be in equilibrium (Chopra 1969). The increase in the observed resistivity after the minimum is dominated by the formation of pores and further increase in size of the pores. The SEM photographs (figures 3a, b) corresponding to 37 and 60 min annealing give only pores with their size increasing.

The variation in sheet resistivity with temperature on annealing the SnO_2 film in air is plotted in figure 4. The film showed irreversible decrease in sheet resistivity, perhaps due to the reduction of defect density with increasing temperature. This mechanism governing the resistivity of films is well known (Maissel and Glang 1970). The minimum nearly corresponds to the Debye temperature of SnO_2 [~ 500° K], so that the largest

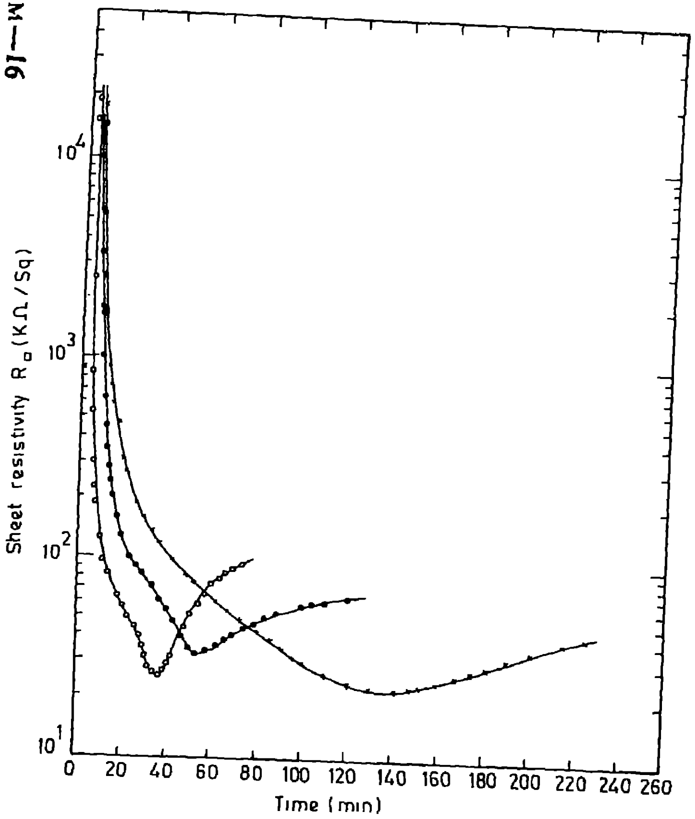

Figure 1. Sheet resistivity *vs* time for SnO_2 films deposited on glass substrate during isothermal annealing (o)-701 K; (●)-688 K; (×)-660 K.

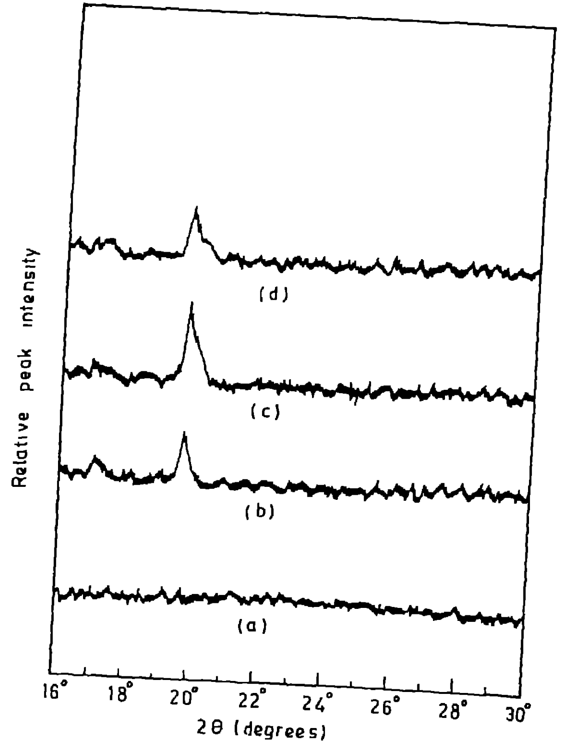

Figure 2. X-ray diffraction pattern for SnO_2 films deposited on glass substrate. **a.** Unannealed films, **b.** $t = 4$ min annealed at 717 K, **c.** $t = 37$ min annealed at 701 K, **d.** $t = 1$ hr annealed at 688 K.

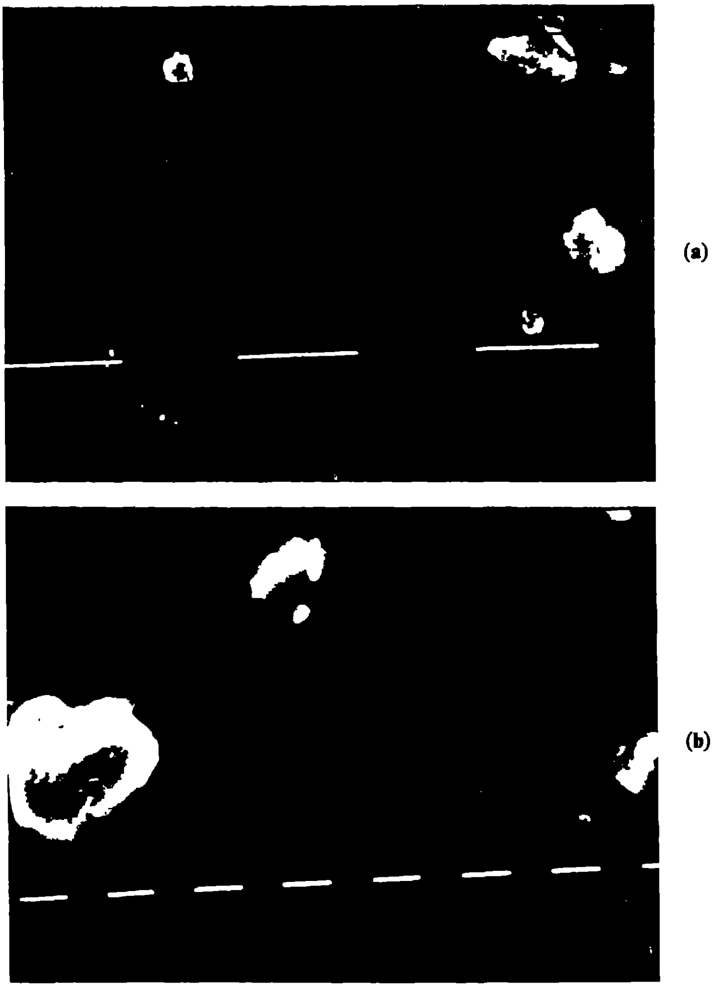

Figure 3. Scanning electron micrograph of SnO_2 films deposited on a glass substrate annealed at 701 K, **a.** annealed for 37 min (magnification: 160 × 1·1). **b.** annealed for 1 hr (magnification 640 × 1).

part of the lattice defects is removed because of the maximum frequency of the lattice vibrations (Chopra 1969). Therefore, beyond this point the resistivity increases.

We have attempted here to give a qualitative interpretation of the results obtained on the annealing behaviour of tin dioxide films. A quantitative study is in progress.

Acknowledgement

AG and PG are thankful to CSIR (India) for financial support. The authors express their sincere thanks to Mr N K Saini for help in carrying out SEM experiments.

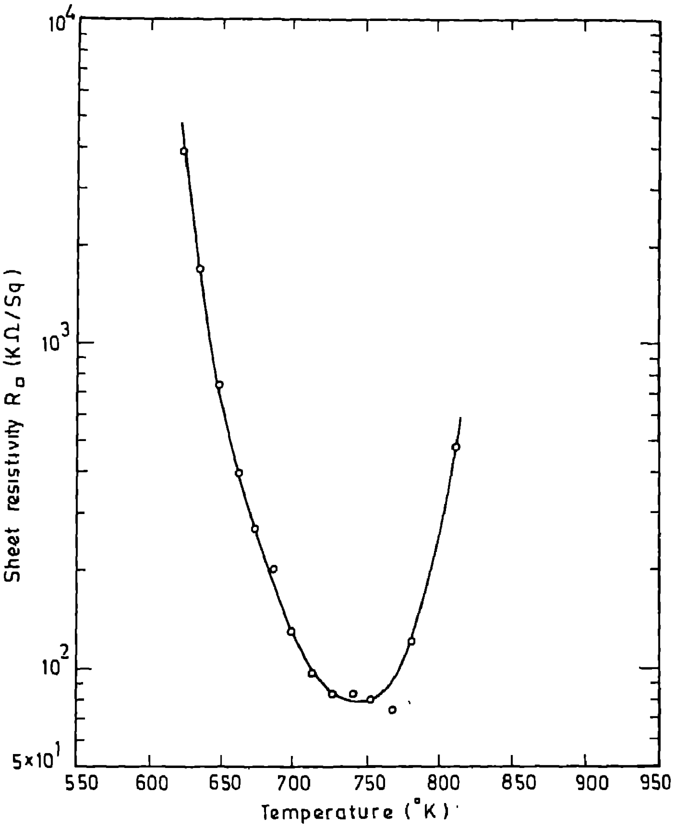

Figure 4. Sheet resistivity *vs* temperature for SnO_2 film deposited on a glass substrate.

References

Arai T 1960 *J. Phys. Soc. Jpn* **15** 916

Chopra K L 1969 *Thin film phenomenon* (New York: McGraw Hill) 381–387

Ghosh A K, Fishman C and Feng T 1978 *J. Appl. Phys.* **49** 3490

Ishiguro K, Sasaki T, Arai T and Imai I 1958 *J. Phys. Soc. Jpn* **13** 296

Jarzebeski Z M 1976 *J. Electrochemical Soc.* **123** 299C

Maissel L I and Glang R 1970 *Handbook of thin films technology* (New York: McGraw Hill) 13–26

Nagatoma T, Endo M and Omoto O 1979 *Jpn J. Appl. Phys.* **18** 1103

Raccanelli A and Madalena A 1976 *J. Am. Ceram. Soc.* **59** 425

Shanthi E, Banerjee A, Dutta V and Chopra K L 1980 *Thin Solid Films* **71** 237

Viscrian I and Georgescu V 1969 *Thin Solid Films* **3** R17

M—17

Bull. Mater. Sci., Vol. 6, No. 6, December 1984, pp. 1035–1039. © Printed in India.

Temperature dependence of microhardness in mixed crystals

SANKAR P SANYAL and R K SINGH

Department of Physics, Rani Durgawati University, Jabalpur 482 001, India

MS received 7 October 1983

Abstract. The temperature dependence of microhardness of mixed KCl-KBr crystals has been studied using the Kataoka and Yamada theory which considers plastic deformation and internal stress field due to elastic interactions in mixed crystals. The microhardness showed systematic variation with temperature in both the components and the mixed crystals and the probable reasons for this variation are indicated.

Keywords. Mixed crystals; microhardness; temperature dependence; Kataoka-Yamada theory.

1. Introduction

In recent years, considerable attention has been paid to the study of mixed crystal properties as they are useful in many technological applications (*e.g.* mixed crystals of alkali halides are used for laser windows). One well-known property is microhardness, which for mixed crystals always exceeds its value for the component crystals (Armington *et al* 1973; Hari Babu *et al* 1975). A number of theories (Gilman 1973; Shukla and Bansigir 1976; Boser 1972; Ridhagani and Asimow 1968) have been proposed to explain this extra hardness of mixed crystals. Earlier theories of Gilman (1973) and Shukla and Bansigir (1976) could not explain the microhardness of mixed crystals as indicated by Bhimshankaran (1974), and Srivastava (1980). Kataoka and Yamada (1977) have given a theory according to which the random distribution of doped ions can produce an internal stress field interaction that increases the microhardness of the mixed crystals. This theory has been applied to mixed alkali halides (Srivastava 1980) and mixed silver halides (Sanyal and Singh 1982).

Motivated by the success of the theory of Kataoka and Yamada theory, we have applied it to study the temperature dependence of microhardness of KCl_xBr_{1-x} system from 300–1000 K. It is known (Subba Rao and Hari Babu 1978) that the excess of microhardness in mixed crystals results from the increased value of dislocation density. However, this dislocation density in mixed crystals decreases with increase in temperature. Thus, it seems worthwhile to investigate the exact nature of change of microhardness with temperature in mixed crystals. Srivastava (1980) used the Kataoka-Yamada theory to explain the microhardness of KCl_xBr_{1-x}, measured by Subba Rao and Hari Babu (1978) at 300 K only. In doing so, he used the measured microhardness values of KCl, KBr and $KCl_{0.48}Br_{0.52}$ as the input data. Thus, the predictions made by Srivastava are more or less borne out. In the present analysis, however, the results of microhardness of $KCl_{0.48}Br_{0.52}$ have only been used at 300 K to determine a parameter. The values of microhardness of component crystals (KCl and KBr) have been obtained in terms of Debye temperatures (Bollmann 1980).

2. Theory

The microhardness (H_v) of binary ionic solids is related to the Schotky defect formation energy (w_s) as (Shukla and Bansigir 1976)

$$H_v = 205{\cdot}8\ W_s/r^3, \tag{1}$$

where r is the interionic separation. According to Sastry and Mulimani (1969), W_s is also related to the Debye temperature (Θ_D), such that

$$W_s = (\Theta_D/32.37)^2\ M V^{2/3}. \tag{2}$$

Here, M and V are the molar mass and volume. Now, H_u can be written in terms of the Debye temperature as:

$$H_v = 6{\cdot}833\ (M V^{2/3}/r^3)\ \Theta_D^2 \times 10^{-5}\ (\mathrm{kg/mm^2}), \tag{3}$$

from (1) and (2). This equation is, however, valid only for the component crystals and not for mixed crystals, as it fails to account for the extra hardness in them. We have therefore considered the extra hardness using the Kataoka-Yamada theory in which the doped ions are assumed to behave as a source of constriction and expansion in the lattice in order to maintain the crystal symmetry. The random distribution of these ions produces a fluctuating stress in the mixed crystals and is responsible for the increase in their hardness. The mean expectation value of the internal stress, τ_0, arising from the random distribution of anions is given by (Kataoka and Yamada 1977)

$$\tau_0 = \frac{4\sqrt{2}}{\pi}\,\alpha\left(\frac{\alpha}{\alpha'}\right)^{1/2} \frac{\sigma^2 r^2}{\lambda}\left(\frac{\Delta V}{r^3}\right)\beta_1\beta_2, \tag{4}$$

where α and α' are the lattice sums. ΔV is the difference in anion volume of the two components and β_1 and β_2 are fractional molar concentrations of the two components in the mixed crystals. The symbols σ and λ are related to the second order elastic constants by

$$\sigma = \tfrac{1}{2}(C_{11} - C_{12}) \tag{5}$$

and

$$\lambda = \tfrac{1}{2}(C_{11} + C_{12})\left[\frac{C_{44}(C_{11} - C_{12})}{C_{11}(C_{11} + C_{12} + C_{44})}\right]^{1/2} r^2. \tag{6}$$

In terms of τ_0 the hardness due to internal stress field can be expressed as

$$H_{\mathrm{isf}} = F\tau_0 \tag{7}$$

with F as a constant. Thus, the microhardness of mixed crystals is ultimately given by

$$H_m = \beta_1 H_1 + \beta_2 H_2 + H_{\mathrm{isf}}, \tag{8}$$

where H_1 and H_2 are the hardness of the component crystals.

3. Results and discussion

The microhardness (H_v) values of the component crystals, KCl and KBr at different temperatures (300–1000 K) were calculated from (3) using the values of Debye temperature (Θ_D) and interionic separation (r_0) reported by Tolpadi (1977) and

Subramaniam (1979). Their values for KCl and KBr at different temperatures are listed in table 1 and are compared with their measured data at 300 K (Bollman 1980; Subba Rao and Hari Babu 1978). The microhardness (H_m) values for the mixed crystals at different temperatures have been calculated from (8) using the required values of elastic constants reported by Subramaniam (1978). The variations of microhardness with temperature for the component crystals and mixed KCl-KBr are presented in figure 1 and those with mole percentage of KBr are presented in figure 2.

Table 1. Microhardness (H_v) of KCl and KBr at different temperatures.

Temperature (K)	H_v (kg/mm^2)	
	KCl	KBr
300	10·306 9·9^a	8·468 7·9^b
400	9·464	8·231
500	8·906	7·785
600	8·317	7·329
700	7·706	6·847
800	7·020	6·331
900	6·236	5·784
1000	5·293	5·133

^{a} Bolmann (1980); ^{b} Subba Rao and Hari Babu (1978).

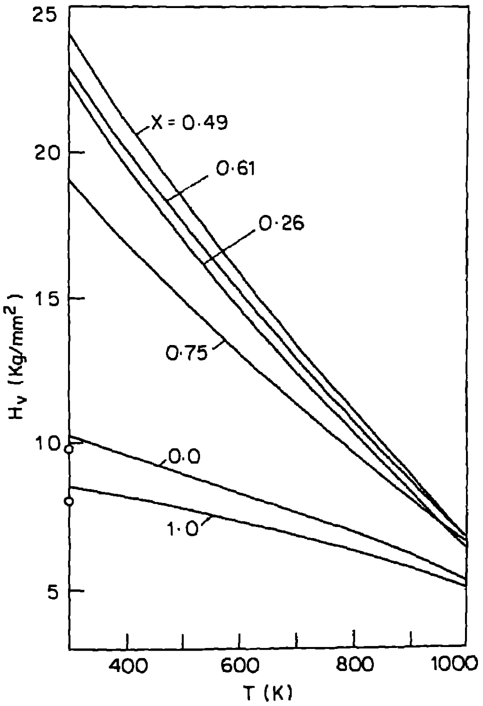

Figure 1. Variation of microhardness of KCl_xBr_{1-x} system with temperature. Experimental points (o) at 300 K have been taken from Subba Rao and Hari Babu (1978).

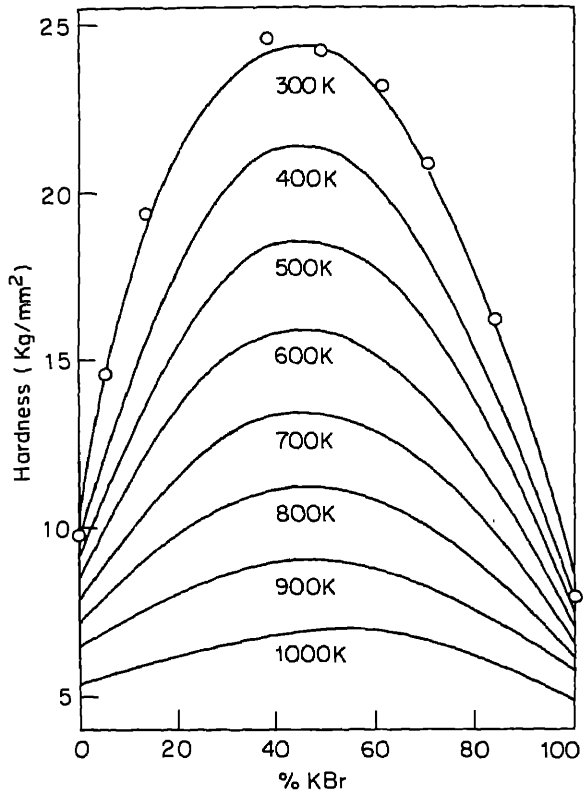

Figure 2. Variation of microhardness of KCl_xBr_{1-x} system with % of KBr in KCl at different temperatures. Experimental points are taken from Subba Rao and Hari Babu (1978).

Table 1 shows that the microhardness of the component crystals can be satisfactorily predicted by using (3). These values decrease almost linearly with temperature as shown in figure 1. This might be so because the microhardness is a measure of the resistance offered by dislocation motion which becomes easier when the temperature is raised. The variation of H_v with temperature in mixed crystals is, however, not linear, perhaps due to the elastic effects arising from the size misfit of cations.

Figure 2 shows that the extra hardness in mixed crystals (Hari Babu and Subba Rao 1978) at 300 K has been adequately explained even without using the H_v values of the component crystals. This prediction is better than that achieved by Subba Rao and Hari Babu (1978) where they neglected the effects due to elastic interactions (Kataoka and Yamada 1977). Our results on H_v at higher temperatures could not be compared due to lack of measured data. Their variation with temperature is, however, systematic and consistent with the measured results in other solids (Bhatt and Desai 1982).

References

Armington A F, Posen H and Lipson H 1973 *J. Electron. Mater.* **2** 127
Bhatt V P and Desai C F 1982 *Bull. Mater. Sci.* **4** 23

Bhimasankaran T 1974 Ph.D. Thesis, Osmania University, AP
Bollman W 1980 *Phys. Status Solidi* **A6** 395
Boser O 1972 *Metall. Trans.* **3** 843
Gilman J J 1973 *J. Appl. Phys.* **44** 983
Hari Babu V, Subba Rao U V and Venkata Ramaiah K 1975 *Phys. Status Solidi* **A28** 269
Kataoka T and Yamada T 1977 *Jpn J. Appl. Phys.* **16** 1119
Riddhagni B R and Asimow R M 1968 *J. Appl. Phys.* **39** 4164
Sanyal S P and Singh R K 1982 *J. Phys.* **D15** 1083
Sastry P V and Mulimani P G 1969 *Philos. Mag.* **20** 859
Shukla M and Bansigir K G 1976 *J. Phys.* **D9** L49
Srivastava U C 1980 *J. Appl. Phys.* **51** 1510
Subba Rao U V and Hari Babu V 1978 *Pramana* **11** 149
Subramaniam B 1979 *Indian J. Phys.* **A54** 109
Tolpadi S 1977 *Indian J. Phys.* **A51** 181

Bull. Mater. Sci., Vol. 6, No. 6, December 1984, pp. 1041–1046. © Printed in India.

Some aspects of dislocation-precipitate interaction in under-aged aluminium-germanium alloy

KISHORE

Department of Metallurgy, Indian Institute of Science, Bangalore 560 012, India

MS received 6 September 1982; revised 13 December 1983

Abstract. The glide dislocation-precipitate interaction in under-aged alloy is investigated by microscopy and low-temperature deformation techniques. Slip-line features of room temperature deformed samples were observed by optical microscopy. From tensile tests at various temperatures the variation of flow stress with $T^{2/3}$ was established. Comparing the present results with those obtained on the peak-hardened condition of the same alloy it is concluded that moving dislocation shear through the small rod-shaped germanium precipitates.

Keywords. Under-aged; dislocation-precipitate interaction; slip lines; flow stress.

1. Introduction

The interaction between glide dislocations and precipitate particles has been studied in detail in many age-hardenable alloy systems (Nicholson and Nutting 1961; Kelly 1963; Lutzering and Weissman 1970; Raynor and Silcock 1970; Nourbakhsh and Nutting 1980). From mechanical property studies coupled with microscopy, it is possible to arrive at the likely interaction between moving dislocations and precipitate particles. While efforts are not wanting in understanding the dislocation precipitate interaction in peak-aged and over-aged states, the partially-aged condition has received hardly any attention. The purpose of the present work is to study the dislocation-precipitate interaction in under-aged aluminium-2% germanium alloy using microscopy and mechanical deformation techniques.

2. Experimental

Weighed quantities of super-pure aluminium and germanium were melted together in an argon atmosphere in a resistance furnace and cast in a graphite-lined metal mould. The Ge content was 1·98% by weight. The cast ingot was lightly worked by hammering before annealing at 400°C for 48 hr. The homogenised rod was reduced to a 1 mm thick strip by cold-rolling coupled with intermediate annealing treatment. Tensile and hardness samples were cut from the rolled strip and electropolished after mechanical polishing. They were solutionised at 450°C for 2 hr and quenched into ice-water mixture maintained close to 0°C. Thermostatically-controlled paraffin oil bath, maintained at 165°C, was used for ageing the samples. Hardness variation with ageing time was determined using a Vicker's unit. From such a data it was possible to establish the peak-hardened condition. In the present experiment as the peak hardness occurred at around 70 hr, the tensile test specimens were aged for 18 hr to have the microstructure corresponding to the under-aged condition.

The partially-aged test specimens with a gauge length of 20 mm were pulled in a modified Hounsfield tensometer (Prasad *et al* 1969) at a strain rate of about 10^{-3} $\sec^{-1}$ at temperatures varying between 77 and 420°K. From the load-elongation plot, the flow stress was determined. The tensile-deformed samples were viewed under a light microscope for slip-line features. Using the window technique and an electrolyte of 90/10 acetic acid/perchloric acid mixture maintained at −15°C, electron transparent thin specimen in aged condition was prepared for viewing under a Philips 301 microscope. Electrolytic thinning was achieved by applying a voltage of 18 V between the electrode and the specimen.

3. Results and discussion

Figure 1 shows the variation in Vickers hardness number as a function of time of ageing at 165°C. The data points follow the typical trend seen in any age-hardenable alloy system, namely, an increase of hardness as ageing occurs, a peak followed by a decrease. The peak corresponding to an optimum dispersion of precipitates (Mott and Nabarro 1940) occurs around 70 hr as mentioned earlier. Figure 2, a TE micrograph, depicts the appearance and distribution of precipitates in the under-aged condition. Small and dense rod-shaped Ge precipitates can be clearly seen in the photomicrograph. The inter-particle spacing and the size of the rods in the under-aged sample are smaller (figure 2) compared to the peak-aged condition (figure 3).

The slip-line pattern of partially-aged and room temperature-deformed sample is shown in figure 4. They are straight running, continuous and thin. Slip-line features resemble the pattern obtained for peak-aged state (Kishore and Vasu 1978). It is known that slip bands give reliable information about the mechanism of plastic deformation of the materials (Seeger 1963). The slip-line appearance could change with a change in the type of obstacle present in the matrix. When small coherent particles are present, the dislocation can easily shear the particle aggregates and the appearances of the line in such cases are only slightly different from those obtained for the pure metal or solid

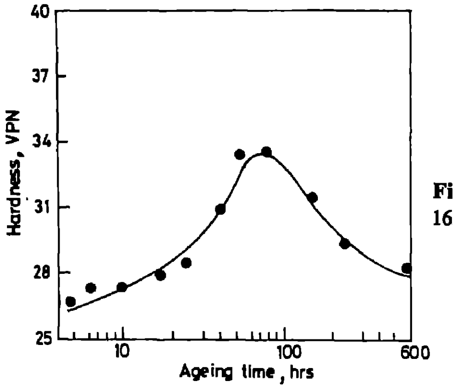

Figure 1. Hardness variation with time during ageing at 165°C (T_q = 450°C).

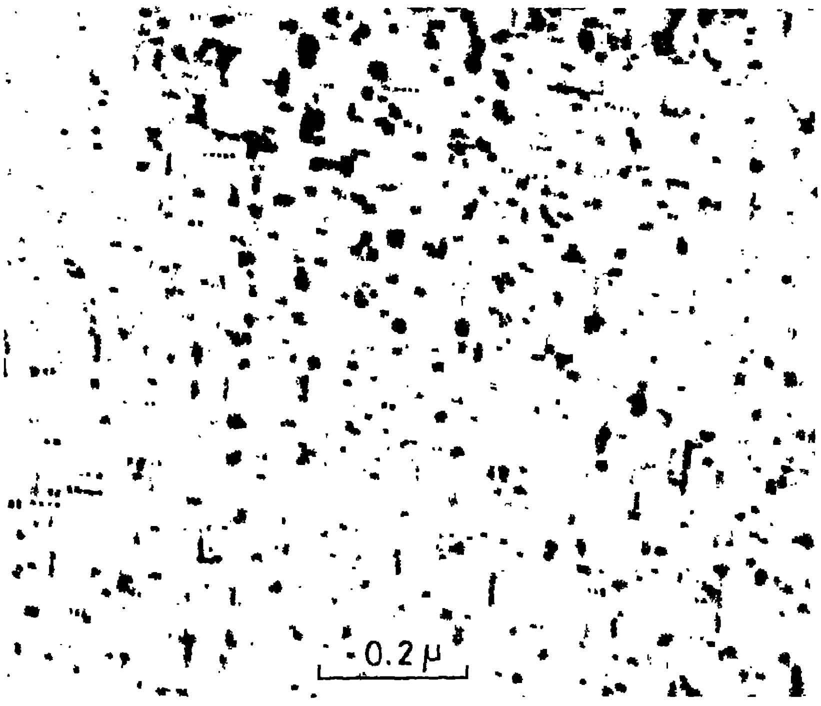

Figure 2. Electron micrograph of partially-aged sample showing small and dense rod-shaped precipitates ($T_q = 450°C$, $T_a = 165°C$, $t_a = 18$ hr).

solution (Greetham and Honeycombe 1960–61; Silcock 1960; Thomas and Nutting 1956–57, 1957–58). Wavy, fragmented slip lines are seen when incoherent, large nondeforming particles are encountered during the movement of glide dislocations (Wilcox and Gilbert 1967; Greetham and Honeycombe 1960–61; Price and Kelly 1962). Starke *et al* (1973) have shown that small germanium clusters can be sheared. As the slip traces in partially-aged condition used in this work are similar to those obtained on peak-hardened condition (Kishore and Vasu 1978) and the longer and somewhat widely spaced rods of peak-aged state have been shown to be sheared by moving dislocation using TEM (Kishore *et al* 1976), it may be inferred that in the present under-aged condition also the precipitate particles are cut through by the glide dislocations. Further evidence to this deduction comes from an examination of $\tau - T^{2/3}$ relation following the report of Chun and Byrne (1969). They examined the strengthening in a Mg-5% Zn alloy by determining the temperature dependence of CRSS for the as quenched, fully-hardened and overaged conditions. The shearing of the precipitates in the peak aged state, and the linear variation of flow stress, τ with $T^{2/3}$ were noticed by them. Lipsitt (1971) also showed that yield strength in the Al-Zn alloy varies linearly with $T^{2/3}$. In figure 5 are plotted the data showing variation of flow stress with $T^{2/3}$ for the under-aged Al-Ge alloy. For the sake of comparison the results obtained in the peak-aged state are also included. It is noteworthy that the points lie on a straight line in both the cases suggesting the existence of similar interaction between the glide dislocations and the precipitate particles. Hence, it may be inferred that as in the peak-hardened

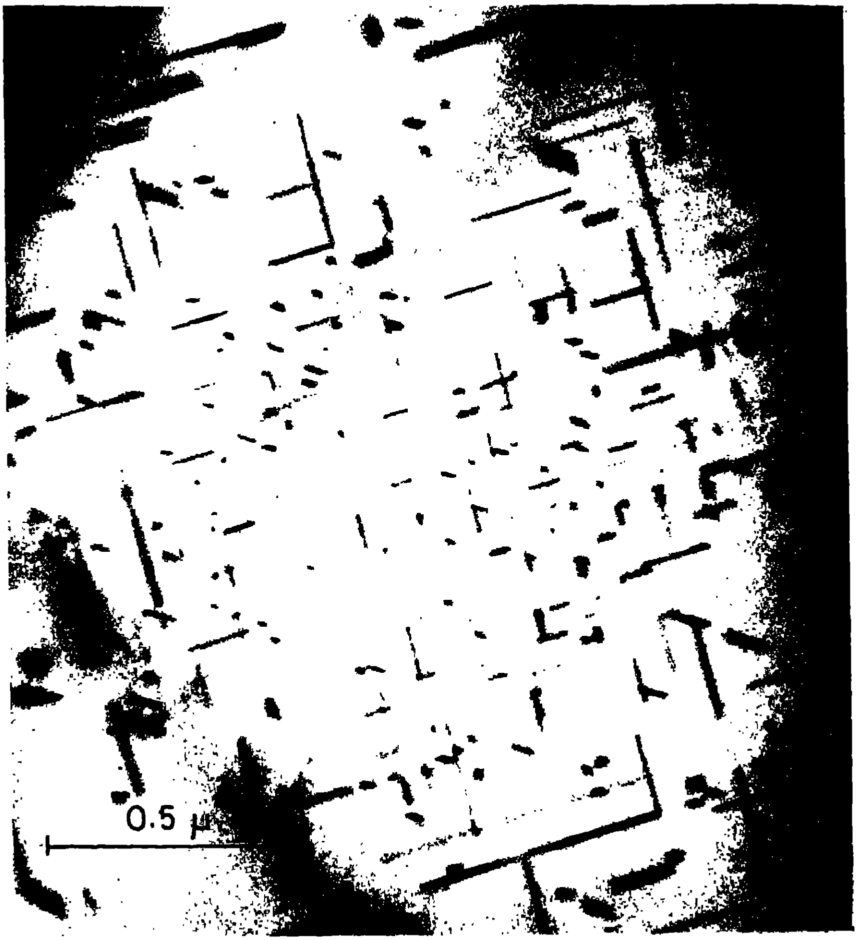

Figure 3. A TEM photograph of the peak-hardened alloy (70 hr at 165°C) showing rod-, triangular-, and rectangular-shaped precipitates.

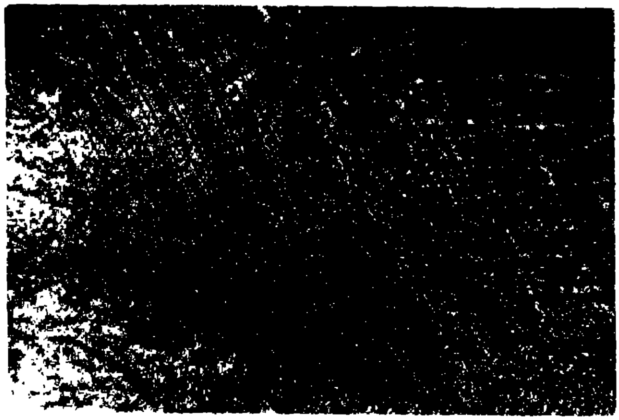

Figure 4. Slip traces in under-aged sample deformed at room temperature ($\varepsilon = 25\%$; 200×).

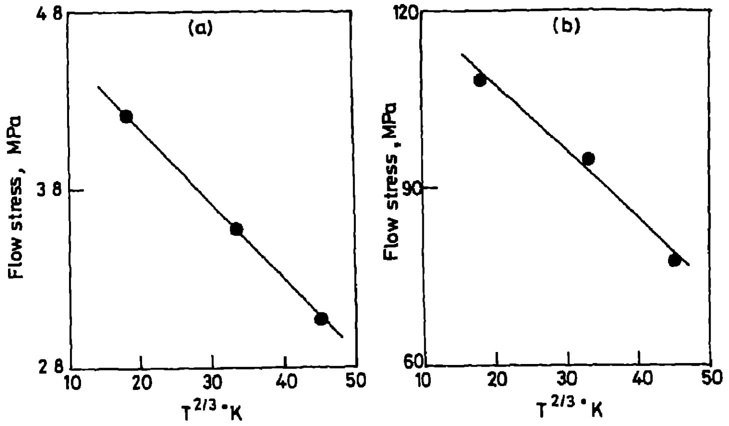

Figure 5. Flow stress-(temperature)$^{2/3}$ relation for (a), under-aged (b), peak-aged conditions ($\dot{\varepsilon} = 9{\cdot}8 \times 10^{-4}$ sec^{-1}).

state, in the under-aged state too, the dislocations penetrate the germanium precipitates.

In view of the similarity of behaviour of flow stress variation with temperature as well as nature of slip traces in the under-aged condition with peak-aged alloy reported earlier (Kishore and Vasu 1978) it can be said that in the partially-aged condition also the Ge precipitates are sheared by the glide dislocations.

4. Conclusions

Partially-aged alloy exhibit straight slip traces. The flow stress of the dilute alloy varies linearly with $T^{2/3}$ and the moving dislocations cut through the germanium precipitates.

Acknowledgements

The author thanks Prof. K I Vasu for his interest in the work. The assistance received from colleagues in the Department is gratefully acknowledged.

References

Chun J C and Byrne J G 1969 *J. Mater. Sci.* **4** 861
Greetham G and Honeycombe R W K 1960–61 *J. Inst. Metals* **89** 13
Kelly A 1963 in *Electron microscopy and strength of crystals* (eds) G Thomas and J Washburn (New York: Interscience) p. 947
Kishore, Sastry D H and Vasu K I 1976 *Proc. Second Int. Conf. on Mechanical Behaviour of Materials*, Boston, USA 1851
Kishore and Vasu K I 1978 *Metallography* **11** 51
Lipsitt H A 1971 *Metall. Trans.* **2** 1739
Lutzering G and Weissman S 1970 *Acta Metall.* **18** 785
Mott N F and Nabarro F R N 1940 *Proc. Phys. Soc.* **52** 86
Nicholson R B and Nutting J 1961 *Acta Metall.* **9** 332
Nourbakhsh S and Nutting J 1980 *Acta Metall.* **28** 357

Prasad Y V R K, Sastry D H and Vasu K I 1969 *J. Indian Inst. Sci.* **51** 377

Price R J and Kelly A 1962 *Acta Metall.* **10** 980

Raynor D and Silcock J M 1970 *Metal Sci.* **J.4** 121

Seeger A 1963a *J. Phys. Soc. Jpn* **18** p. 59

Seeger A 1963b *Proc. at NPL*, Vol I Symp. No. 15 The relation between structure and mechanical properties of metals 4

Silcock J M 1960 *Acta Metall.* **8** 589

Starke E A, Kralik G and Gerold V 1973 *Mater. Sci. Eng.* **11** 319

Thomas G and Nutting J 1956–57 *J. Inst. Metals* **85** 1

Thomas G and Nutting J 1957–58 *J. Inst. Metals* **86** 8

Wilcox B A and Gilbert A 1967 *Acta Metall.* **15** 601

Bull. Mater. Sci., Vol. 6, No. 6, December 1984, pp. 1047–1052. © Printed in India.

Evaluation of magnetic hyperfine field distributions from Mössbauer spectra of disordered alloys and metallic glasses

C BANSAL
School of Physics, University of Hyderabad, Hyderabad 500 134, India

MS received 15 March 1983

Abstract. A simple computer program is described to evaluate magnetic field distributions from complex Mössbauer spectra of magnetic alloys. The use of this program for test cases of Vitrovac 4040 amorphous sample and a simulated spectrum of two gaussian peaks is discussed.

Keywords. Mössbauer spectra; metallic glasses; magnetic hyperfine field distributions.

1. Introduction

The Mössbauer spectra for disordered magnetic alloys and metallic glasses are generally complex because of the overlap of the component lines due to a wide variety of environments in which the Mössbauer atom is situated. In some cases when the overlap is not too large the average hyperfine field can still be evaluated if the field is distributed around an average value (Bansal *et al* 1975). In other cases when the broadening is large this may not be possible. When two or more types of magnetic behaviour are present *i.e.* magnetic splitting due to magnetically ordered regions and a single line due to a paramagnetic contributions it is again very difficult to extract useful information from Mössbauer spectra (Bansal and Chandra 1979).

Several methods have been proposed to obtain the distribution of magnetic fields which generate the complex spectra (Window 1971; Hesse and Rübartsch 1974; Logan and Sun 1976) and improvements on them also given (LaCaer and Dubois 1979; Wivel and Morup 1981).

2. Window's method

Amongst these, the method due to Window is a model-independent field distribution analysis which assumes an arbitrary probability distribution of the magnetic hyperfine fields $P(H)$ and expands it in a Fourier series of trignometric functions.

$$P(H) = \sum_{n=1}^{N} a_n [\cos (n \pi H/H_{\max}) - \cos n \pi]. \tag{1}$$

The field distribution in this form satisfies the boundary conditions: (i) $P(-H) = P(H)$, since in the absence of an external field the lines produced due to a field H are in the same positions as those produced by a field $-H$. The series therefore contains only cosine terms. (ii) There is an upper cut-off point beyond which $P(H)$ goes to zero smoothly *i.e.*

$$\left.\frac{\mathrm{d}P(H)}{\mathrm{d}H}\right]_{H=H_{\max}} = 0.$$

If now the coefficients a_n of the series can be determined so as to fit the experimental spectrum, the required field distribution is known.

The Mössbauer spectrum generated at velocity v due to this distribution is given by

$$S(v) = \int_0^{H_{\max}} P(H)\, L_6(v, H)\, \mathrm{d}H, \tag{2}$$

where

$$L_6(v, H) = \sum_{i=1}^{6} \frac{1}{\pi} \frac{\Gamma_i/2}{(\Gamma_i/2)^2 + (v - \alpha_i H)^2}, \tag{3}$$

is the normalised Lorentzian shape function of the lines of a component spectrum for field H. Γ_i are the linewidths of the six lines of the component spectrum and $\alpha_i H$ are their positions. Equation (2) can be rewritten as

$$S(v) = \sum a_n \int_0^{H_{\max}} f_n(H)\, L_6(v, H)\, \mathrm{d}H,$$

$$= \sum_n a_n S_n(v), \qquad (4$$

where $$S_n(v) = \int_0^{H_{\max}} f_n(H)\, L_6(v, H)\, \mathrm{d}H$$

is the spectrum created by the term $f_n(H)$. If the experimental spectrum at velocity v i denoted by $W(v)$, the coefficients a_n of the field distribution can be found by minimizin the function

$$\phi = \sum_v [S(v) - W(v)], \qquad ($$

with respect to the parameters a_n or other parameters like isomer shift if necessary. A χ nonlinear least square fitting procedure is normally used to obtain the require coefficient a_n. This procedure is iterative and therefore time-consuming. If the isome shift is also required to be obtained from a fit to the spectrum this procedure is justifie However in most systems when one is not concerned with relatively small isomer shi values exactly one can safely assume a constant isomer shift for all the elementary field H. A good guess for this can usually be obtained from the centroid of the spectrum c from a spectrum above the Curie temperature. This then can be given as a fixe parameter.

3. Procedure

We get N simultaneous equations which are linear in a_n if we differentiate ϕ in (4), with respect to a_n's and set them equal to zero.

$$\phi = \sum_v \left[\sum_n a_n S_n(v) - W(v) \right]^2,$$

$$\frac{1}{2}\frac{\partial \phi}{\partial a_n} = \sum_v [S(v) - W(v)]\, S_n(v). \tag{6}$$

Differentiating once again w.r.t a_m

$$\frac{1}{2}\frac{\partial^2 \phi}{\partial a_m \partial a_n} = \sum_v S_m(v)\, S_n(v) = X_{mn} \text{ (say)}. \tag{7}$$

Substituting (7) in (6) and setting $\partial\phi/\partial a_n = 0$

$$\sum_m a_m X_{mn} - \sum_v W(v) = 0.$$

There are n such equations for $n = 1, 2 \ldots . N$.
Defining the matrices

$$\beta_n = \left[\sum_v W(v) S_n(v) \right],$$

$$X_{mn} = \left[\sum_v S_m(v) S_n(v) \right],$$

we get the matrix equation

$$aX = \beta.$$

This can be solved to get the matrix of the coefficients a_n

$$a = X^{-1}\beta.$$

A simple computer program can be written to set up the matrices X and β, finding the inverse of X and then calculating a. These coefficients can then be used to generate the field distribution $P(H)$.

4. Examples of use

A test usage of the program is illustrated in figures 1 and 2. In figure 1, spectrum A is the Mössbauer spectrum simulated for two Gaussian fields of equal intensity as shown in A'. The intensity ratios of the component spectra were constrained in the ratio 3:2:1:1:2:3 and the isomer shift fixed at zero. Using 5 terms in the fourier series expansion of $P(H)$ the field distribution obtained using the program outlined above is shown in B′. The two peaks are unresolved. When 10 terms are included in the Fourier series the distribution marked C′ is obtained and the simulated and fitted spectrum agree very well as shown in C.

Figure 2 shows the experimental Mössbauer spectrum for an amorphous sample (Vitrovac 4040 from Vacuumschmelze GMBH, Hanau, Germany) together with the

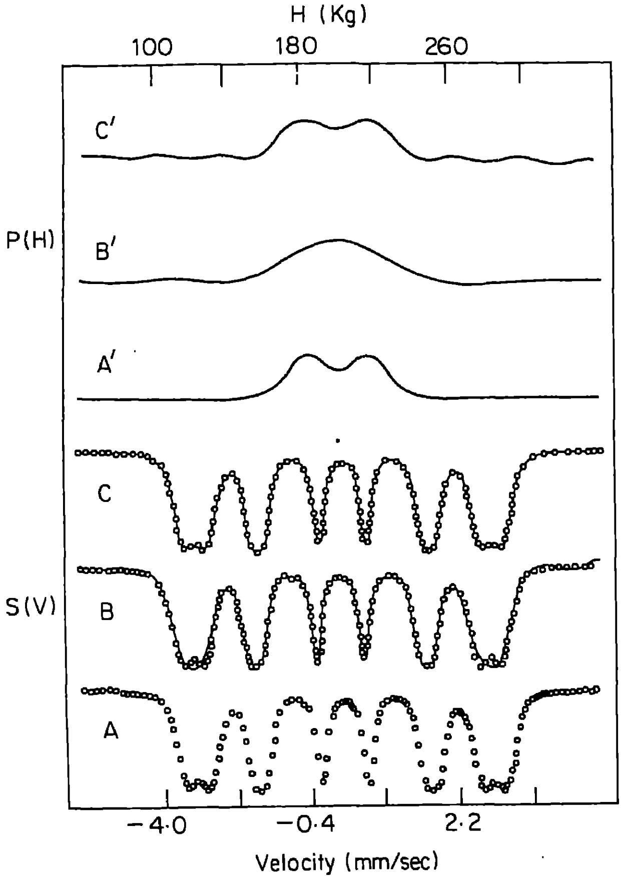

Figure 1. The Mössbauer spectrum A is simulated for two Gaussian peaks shown in A′. The field distribution B′ is obtained using the computer program described here when 5 terms are used in the Fourier series expansion of $P(H)$. The corresponding Mössbauer spectrum is shown in B. For 10 terms in $P(H)$ the distribution C′ is obtained and the corresponding fit is shown in C.

field distributions obtained using this program. In fitting such spectra there is uncertainty in the value of the intensity ratios to be chosen for the elementary spectra. One of the ways generally used is to vary the intensity ratio in the form $3{:}x{:}1{:}1{:}x{:}3$ and use that value of x which gives the best fit to the experimental spectrum. The field distributions for various x values are shown in figure 2. For a value $x = 2{\cdot}5$ one gets a good fit to the spectrum.

The number of terms in the Fourier series that should be retained in the expansion for $P(H)$ also has to be chosen carefully. For a small number of terms the resolution is poor. As seen in figure 1, the two Gaussian peaks are not resolved when only 5 terms are used but are seen separately for 10 terms in the expansion. However if the number of terms is made very large there occurs another difficulty. The distribution tries to fit the statistical fluctuation in data which are unphysical and thereby produces oscillations in the field distribution.

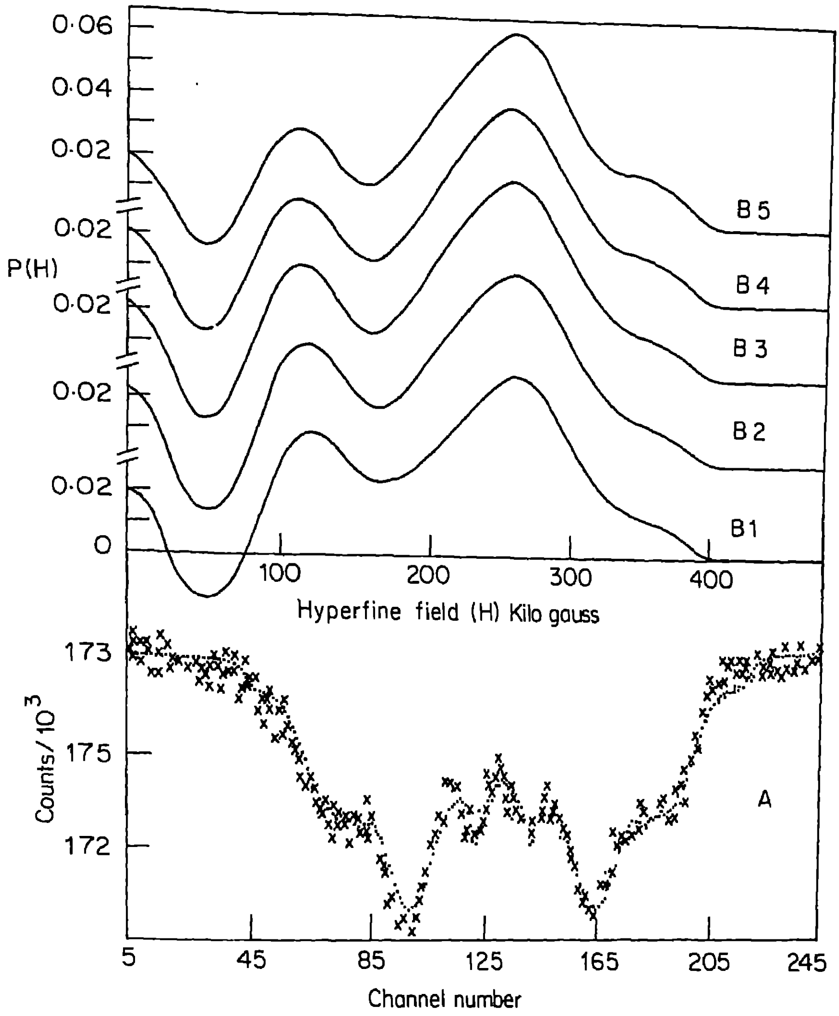

Figure 2. The experimental Mössbauer spectrum for Vitrovac 4040 sample (+) and fitted spectrum (·) for the field distribution in B2. The field distributions for various values of x (intensity ratio of 2nd and 5th lines relative to 3rd and 4th lines) are shown as B1 ($x = 2$), B2 ($x = 2\cdot5$), B3($x = 3$), B4($x = 3\cdot5$), B5($x = 4$).

5. Conclusions

The program described above is simple to write and can be simply modified to analyse spectra which have a paramagnetic single line in addition to distributions at higher velocities or for situations in which the baseline is parabolic. A listing of the program is available with us and has about 175 statements in Fortran IV.

Acknowledgement

The author is grateful to Dr R G Pillay of the TIFR, Bombay, for help in writing the program and testing it.

References

Bansal C, Ray J and Chandra G 1975 *J. Phys.* **F5** 1663
Bansal C and Chandra G 1979 *Phys. Rev.* **B20** 3357
Hesse J and Rübartsch A 1974 *J. Phys.* **E7** 526
LaCaer G and Dubois J M (1979) *J. Phys.* **E12** 1083
Logan J and Sun E 1976 *J. Noncryst. Solids* **20** 285
Window B 1971 *J. Phys.* **E4** 401
Wivel C and Morup S 1981 *J. Phys.* **E14** 605

Bull. Mater. Sci., Vol. 6, No. 6, December 1984, pp. 1053–1057. © Printed in India.

Spin wave relaxation processes in polycrystalline yttrium iron garnets

S N BHATIA, P B JOSHI and C M SRIVASTAVA

Department of Physics, Indian Institute of Technology, Powai, Bombay 400076, India

MS received 7 May 1983

Abstract. The wavevector and temperature dependence of the spinwave linewidth in yttrium iron garnets has been studied for polycrystalline samples of average grain diameter 12·8 μm and has been compared with the calculated relaxation times of basic three-magnon confluence and four-magnon scattering processes.

Keywords. Relaxation; spin-wave line-widths; yttrium iron garnets

1. Introduction

The nature of the intrinsic relaxation processes which determine the dissipative characteristics of magnetically ordered materials is well understood for the crystalline state (Gurevich and Anisimov 1975). The uniform precession mode which is created in the parallel pumping experiment loses its energy into the degenerate magnon modes. The small wavevector (k) magnons thus generated relax by the three-magnon confluence process (3c) while the larger k magnons, $4 \times 10^5 < k < 9 \times 10^5\ \mathrm{cm}^{-1}$, attain equilibrium *via* scattering involving four magnons (4sc). The splitting process requiring magnons of high frequencies is therefore restricted to $k > 10^6\ \mathrm{cm}^{-1}$. The observed temperature and k dependences of these processes have been established to be in accord with the theoretical results (Sparks 1967; Vaks *et al* 1968; Gurevich and Anisimov 1975). Such an understanding is lacking for the polycrystalline materials. Vrehan's (1966) transit time model has been used successfully by Patton (1970) and Scotter (1972) to explain the observed relaxation time for the $k \to 0$ limit in large grains but the model fails for finite k and small grain samples. An empirical relation based on the predictions of transit time model for the wavevector dependence of the spin-wave linewidth, obeyed by samples of grain size 1–12 μm has been arrived at by Prakash and Srivastava (1980). However no attempt appears to have been made to correlate such measurements with the fundamental processes involving the magnons. We have measured the spin-wave linewidths of polycrystalline YIG as functions of the wavevector and temperature for samples of various grain sizes and analysed them in terms of the basic scattering processes of the magnons.

2. Experimental

Polycrystalline YIG samples (densities > 99 % average grain diameter 0·9–12·8 μm) were prepared using the normal sintering and hot pressing techniques.

A high power microwave bench giving pulses of 4 μsec duration, 80 kW peak power with a repetition frequency of 50 pulses/sec and operating at microwave frequency 9·391 GHz was used to study the parallel pumping instability threshold (h_c) in these samples. A reflection-type rectangular cavity operating in TE_{104} mode was used and the sample was mounted at its $3\lambda g/2$ position in a vacuum-jacketed glass tube. Liquid nitrogen vapour was blown through this tube to regulate the sample temperature between 120 and 300 K.

3. Results

The instability threshold field (h_c) has been observed as a function of the applied magnetic field H_0. The spin-wave linewidth (ΔH_k) is calculated from h_c through the relation

$$h_c = (\omega_k/\omega_m)/(\Delta H_k/\sin^2\theta_k),$$

where ω_k is the operating frequency, $\omega_m = 4\pi\gamma M$ and θ_k is the angle between the direction of propagation of the spin-waves and H_0. The h_c *vs* H_0 curve was used to calculate ΔH_k up to $(h_c)_{\text{min}}$, the corresponding k value being obtained from the standard dispersion relations. ΔH_k vs k curves for the grain size 12·8 μm are shown in figure 1. Temperature is displayed as a parameter on these curves.

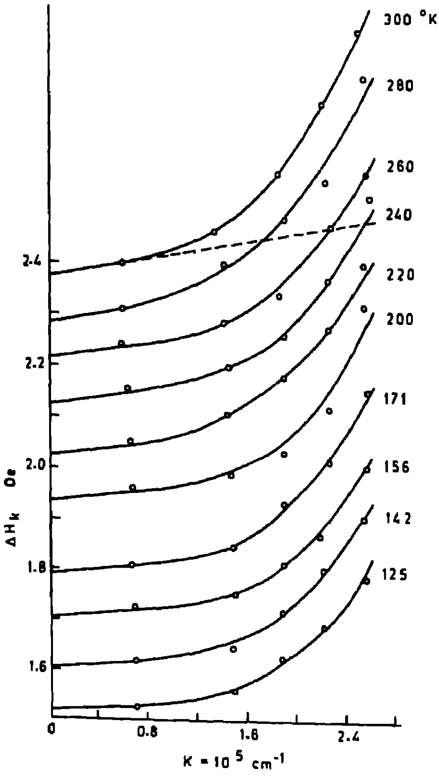

Figure 1. Wavevector dependence of the spin-wave line-width for polycrystalline YIG.

The striking feature of these curves is the nonlinear dependence of ΔH_k on k for all temperatures. This is in contrast to the linear dependence reported earlier (Patton 1970; Prakash and Srivastava 1980) and is attributed to the rather large range of k used in the present graphs. Over the limited range of $1{\cdot}5 \times 10^5 < k < 3 \times 10^5\,\mathrm{cm}^{-1}$ used in earlier studies, the present data also shows an almost linear dependence of ΔH_k on k. A similar linear dependence was also observed by White *et al* (1979) between 88 and 368 K. Their most dense sample appears to have lesser $4\pi M_s$ and therefore more porosity than ours. Pores could be the dominant scattering centres (Scotter 1972).

The initial portion of each curve however appears to be a straight line up to a certain value of the wavevector k_{min}, after which the nonlinearities begin. k_{min} appears to decrease with increasing temperature. This initial portion of each graph was fitted to the equation,

$$\Delta H'_k = \Delta H_{k\to o}(T) + a(T)k. \tag{1}$$

After substracting $\Delta H'_k$ from the observed ΔH_k for $k > k_{\mathrm{min}}$, the difference $\Delta H_k - \Delta H'_k$ was fitted to

$$\Delta H_k - \Delta H'_k = b(T)k^2, \tag{2}$$

for each temperature. The observed variations of $a(T)$ and $b(T)$ with temperature are shown in figure 2. Also shown in this figure is the number of thermal magnons excited $n(T)$ which is linear with T as the energy of these magnons

$$\hbar w_k \simeq \gamma H_0 + Dk^2 \approx \gamma H_0 \approx 1, k_\beta \ll k_\beta T.$$

The increase in $a(T)$ and $b(T)$ with temperature can be attributed to the larger number of magnons present at higher temperatures. Two processes *viz* the three-magnon confluence and the four-magnon scattering brought on by the dipolar forces, show respectively a linear and a quadratic dependence on both k and T. Their respective contributions to ΔH_k for single crystals are

$$(\Delta H_k)_{3c} = \frac{\pi M \gamma k_B}{2D\omega_k} Tk = C_{3c}Tk, \tag{3}$$

$$\begin{aligned}(\Delta H_k)_{4sc} &= \frac{1}{3\pi}\frac{\omega_k}{\gamma}\frac{k_\beta^2 T^2}{(4\pi MD)^2}\left(\ln\frac{\hbar w_k}{k_\beta T}\right)^2 k^2 \\ &= C_{4sc}T^2k^2.\end{aligned} \tag{4}$$

These expressions are valid for magnons with predominant Zeeman energy ($Dk^2 \ll \gamma H_0$) and at high temperatures, ($\hbar\omega_k \ll k_\beta T$). As mentioned above both these conditions are valid here.

We notice from figure 2 that the coefficients $a(T)$ and $b(T)$ are roughly linearly and quadratically proportional to T suggesting that (1) and (2) could be representing the 3c and 4sc processes and consequently the proportionalities.

$$a(T) \propto C_{3c},$$
$$\text{and} \quad b(T) \propto C_{4sc}.$$

However (3) and (4) which are valid for single crystals cannot be used directly here for polycrystalline materials as their contributions to ΔH_k are an order of magnitude smaller than the experimentally observed values at all temperatures. Thus for

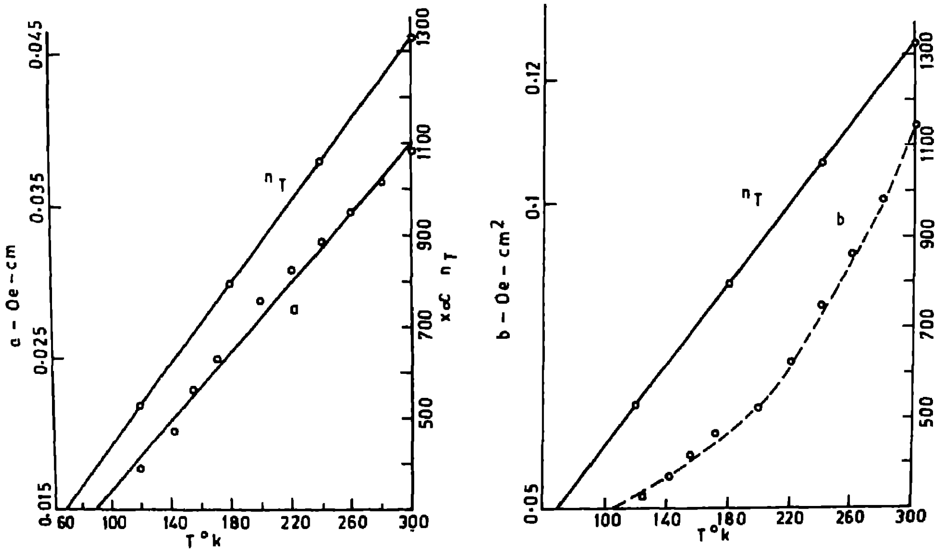

Figure 2. Temperature variation of the coefficients a and b. $n(T)$ is proportional to the number of thermal magnons excited at these temperatures.

$k = 2 \times 10^5\,\mathrm{cm}^{-1}$ experimental ΔH_k values are 0·2 and 0·1 Oe at 300 and 120 K respectively as against 0·02 and 0·004 Oe calculated for the 4*sc* processes. Thus it appears that in changing over from the single crystal to the polycrystalline materials, only the form of these expressions is preserved.

$\Delta H_{k\to 0}$ obtained from figure 1 is plotted against T in figure 3. Again a linear dependence on T is indicated with the data at the lowest temperatures showing some deviations from this line. This is again contrary to the observations of White *et al* (1979) who report an essentially temperature-independent ΔH_k, and is also contradictory to the transit time model. This dissipation parameter contains contributions which may depend upon k but do not vanish as $k \to 0$. In the present case, 3*c* and 4*sc* processes do not contribute to $\Delta H_{k\to 0}$. Major contribution to $\Delta H_{k\to 0}$ is stipulated to come from the Kasuya-LeCraw magnon-phonon processes (Sparks 1964) which show a similar temperature dependence. Here again magnitude-wise the observed $\Delta H_{k\to 0}$ is an order of magnitude larger than that predicted for single crystals (Sparks 1964). However more data at temperatures below 120 K are required to justify this association.

4. Conclusion

For the sample with average grain size 12·8 μm the dissipation processes occurring appear to be identical to those in single crystals with two major differences, (i) the minimum k value at which the 4*sc* processes start contribution is significantly smaller here ($k_{\mathrm{min}} < 1{\cdot}2 \times 10^5\,\mathrm{cm}^{-1}$ at 300 K) than in single crystals (typically $2 \times 10^5\,\mathrm{cm}^{-1}$) and (ii) the magnitudes of the contributions of the respective processes are an order of magnitude greater here than in single crystals. This increased scattering of magnons could be due to the grain boundaries present in the polycrystalline materials. This

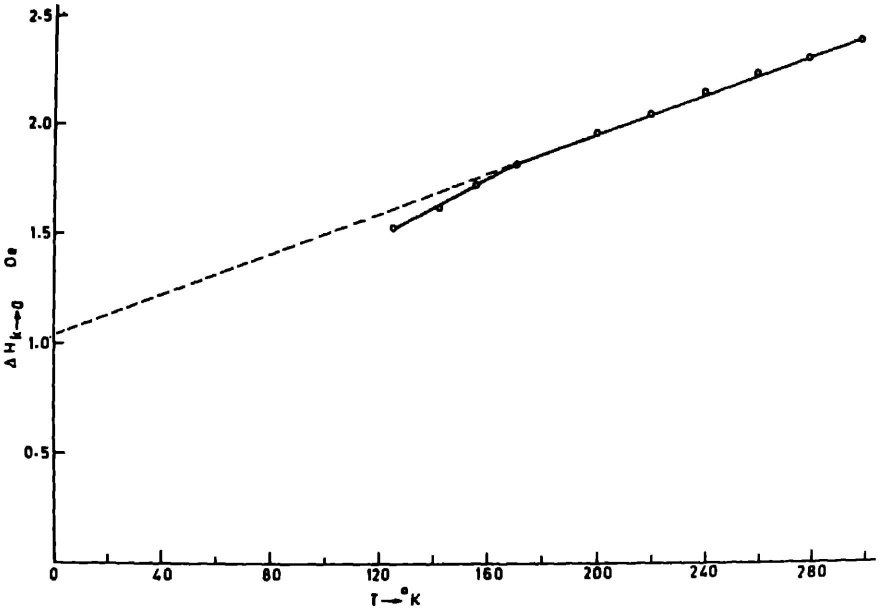

Figure 3. Temperature dependence of the spin-wave linewidth ΔH_k for $k \to 0$. Note the deviations from linearity at the lower temperatures.

scattering should be more intense in smaller grain samples where there are more boundaries which is in qualitative agreement with the previous observations of Prakash and Srivastava (1980). The details of this mechanism are being investigated.

References

Gurevich A G and Anisimov A N 1975 *Sov. Phys.* **41** 336
Patton C E 1970 *J. Appl. Phys.* **41** 1637
Prakash O and Srivastava C M 1980 *Bull. Mater. Sci.* **2** 181
Scotter D G 1972 *J. Phys.* **D5** L93
Sparks M 1967 *Phys. Rev.* **160** 364
Sparks M 1964 *Ferromagnetic relaxation theory* (New York: McGraw-Hill)
Vaks V G, Larkin A I and Pikin S A 1968 *Sov. Phys. JETP* **26** 647
Vrehans Q H F 1966 *J. Appl. Phys.* **40** 1849
White G, Patton C E and Edmondson 1979 *J. Appl. Phys.* **50** 2118

Bull. Mater. Sci., Vol. 6, No. 6, December 1984, pp. 1059–1062. © Printed in India.

Spin-wave excitations in amorphous ferromagnets

ANIL K BHATNAGAR, B BHANU PRASAD, N RAVI and
R JAGANNATHAN*

School of Physics, *School of Chemistry, University of Hyderabad, Hyderabad 500 134, India

MS received 7 May 1983

Abstract. Mössbauer measurements have been performed on a number of metallic glasses. The temperature dependence of average hyperfine or internal magnetic field $H_{\text{eff}}(T)$ arises from long wavelength spin wave excitations in these glasses. Values of $B_{3/2}$ and $C_{5/2}$ are in general much higher than those observed for crystalline ferromagnets indicating higher density of states for spin waves in amorphous ferromagnets.

Keywords. Spin wave excitations; amorphous ferromagnets; Mössbauer measurements; metallic glasses; temperature dependence.

1. Introduction

Amorphous metallic alloys, prepared by rapid quenching of molten alloys, have become an important class of materials from theoretical as well as practical points of view in recent years. There have been extensive studies of magnetic and electrical properties of iron-rich metallic glasses in the past decade. Study of magnetic phenomena in these glasses presents a fascinating field for theorists and experimentalists as magnetism is a structure sensitive property, and therefore, it is expected to be affected in amorphous solids. In this paper we discuss the temperature dependence of hyperfine magnetic field of iron-rich metallic glasses as measured by the ^{57}Fe Mössbauer spectroscopy. Results are interpreted in terms of excitations of long wavelength spin waves.

2. Experimental

Mössbauer spectra of a number of commercially available metallic glasses ($Fe_{81}B_{13.5}Si_{3.5}C_2$, $Fe_{78}B_{13}Si_9$, $Fe_{79}B_{16}Si_5$, $Fe_{40}Ni_{40}B_{20}$ and $Fe_{67}Co_{18}B_{14}Si_1$) were recorded in the temperature range 77–900 K using an Elscint spectrometer coupled with a 256 channel MCA. The spectrometer was used in the constant acceleration mode and the source was ^{57}Co in rhodium matrix. The Curie temperatures of $Fe_{81}B_{13.5}Si_{3.5}C_2$, $Fe_{78}B_{13}Si_9$, $Fe_{40}Ni_{40}B_{20}$ and $Fe_{79}B_{16}Si_5$ were determined by the constant Doppler velocity thermal-scan method (Bhanu Prasad *et al* 1983), while that of $Fe_{67}Co_{18}B_{14}Si_1$ was estimated by plotting hyperfine magnetic field, $H_{\text{eff}}(T)$ *vs* temperature since the Curie temperature, T_c, in this case was larger than the crystallization temperature (Bhanu Prasad *et al* 1980). $H_{\text{eff}}(T)$ values were determined by fitting each spectrum to the Lorentzian line-shape sextet pattern. The spectrometer was calibrated using a thin iron foil.

3. Results and discussion

The decrease in magnetization of a crystalline ferromagnet at low temperatures can be explained if the low lying magnetic excitations are spin waves which obey the following dispersion relation:

$$\hbar w(q) = Dq^2 + Eq^4 + \ldots \tag{1}$$

where $\hbar w(q)$ is the energy of spin wave with propagation wave number q, and D and E are the stiffness constants. Usually E is much smaller than D. This dispersion relation leads to the following temperature dependence of magnetization $M(T)$,

$$M(T) = M(O)\,(1 - BT^{3/2} - CT^{5/2} - \ldots), \tag{2}$$

where B and C are constants and are related to D and E as given below.

$$B = 2{\cdot}612[g\mu_B/M(O)]\,(k_B/4\pi D)^{3/2} \tag{3}$$

$$C = 1{\cdot}341[g\mu_B/M(O)]\,(k_B/4\pi D)^{5/2}(15\pi E/D) \tag{4}$$

where k_B is the Boltzmann constant, μ_B is the Böhr magneton and g is the usual g factor. Equation 2 can be rearranged to give

$$\frac{M(T) - M(O)}{M(O)} = -BT^{3/2} - CT^{5/2} - \ldots \tag{5}$$

or

$$\frac{M(T) - M(O)}{M(O)} = -B_{3/2}(T/T_c)^{3/2} - C_{5/2}(T/T_c)^{5/2} - \ldots \tag{6}$$

Inelastic neutron scattering measurements on some of amorphous ferromagnets have established the existence of long wavelength spin waves obeying the dispersion relation given by (1) (Lynn *et al* 1976; Rhyne *et al* 1979). Similarly magnetization measurements (Tsuei *et al* 1968; Kaul 1981) and ferromagnetic resonance studies (Spano and Bhagat 1981) have shown that the temperature dependence of $M(T)$ follows the behaviour predicted by (2).

From Mössbauer measurements the average internal magnetic field $H_{\text{eff}}(T)$ is determined. It has been found experimentally that for most iron-rich metallic glasses, the average internal magnetic field is directly proportional to the magnetization to a good approximation and the proportionality constant is approximately 135 kOe/μ_B (Chien *et al* 1979). Therefore, (5) and (6) can be expressed in terms of $H_{\text{eff}}(T)$ as follows:

$$\frac{H_{\text{eff}}(T) - H_{\text{eff}}(O)}{H_{\text{eff}}(O)} = -BT^{3/2} - CT^{5/2} - \ldots \tag{7}$$

or

$$\frac{H_{\text{eff}}(T) - H_{\text{eff}}(O)}{H_{\text{eff}}(O)} = -B_{3/2}(T/T_c)^{3/2} - C_{5/2}(T/T_c)^{5/2} - \ldots \tag{8}$$

where B, C, $B_{3/2}$, and $C_{5/2}$ constants remain the same as in (5) and (6). Thus the temperature dependence of $H_{\text{eff}}(T)$ at low temperatures can also be interpreted in terms of excitations of spin waves. At first it may seem surprising that spin waves can be excited in noncrystalline solids. However, the situation is quite akin to the sound wave propagation in glasses. This is so because the long wavelength modes are not sensitive to the local order or disorder. In particular Herring and Kittel (1951) have shown that long wavelength spin waves can exist even in a ferromagnetic continuum medium.

Average hyperfine magnetic fields of various metallic glasses were determined as explained in § 2. A plot of $[H_{\text{eff}}(T) - H_{\text{eff}}(O)]/H_{\text{eff}}(O)$ *vs* $(T/T_c)^{3/2}$ for various metallic glasses is shown in figure 1. A computer least square fit of (7) and (8) to experimental data yields values of B, C, $B_{3/2}$ and $C_{5/2}$ which are given in table 1. For sake of comparison, the values of these constants for crystalline Fe and Ni, and glassy $Fe_{40}Ni_{40}P_{14}B_6$, $Fe_{80}B_{20}$ and $Fe_{82}B_{12}Si_6$ are also listed in the table. It is observed that $B_{3/2}$ values range from 0·2–0·4 and are much larger than the values for crystalline Fe and Ni. Also $T^{3/2}$ dependence of relative change in $H_{\text{eff}}(T)$ extends to much higher temperatures than observed for crystalline ferromagnets. $T^{3/2}$ plus $T^{5/2}$ dependence, as given by (7) and (8), can be fitted to experimental data over a large temperature interval. Values of $B\,(B_{3/2})$ and $C\,(C_{5/2})$ depend upon the temperature interval used to fit the data (Bhatnagar *et al* 1982; Saegusa and Morrish 1982). If data is fitted over a large temperature interval then it has the effect of reducing the $B\,(B_{3/2})$ value and increasing the $C\,(C_{5/2})$ value which is expected. It has also been observed that B and C values

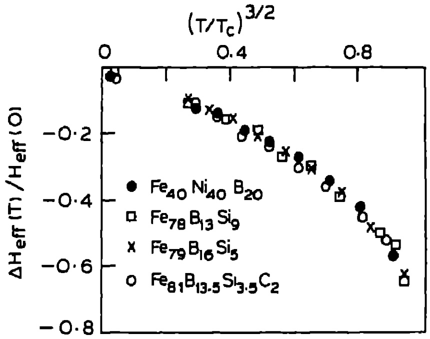

Figure 1. Plot of $[H_{\text{eff}}(T) - H_{\text{eff}}(O)]/H_{\text{eff}}(O)$ vs $(T/T_c)^{3/2}$ for various iron-rich metallic glasses.

Table 1. Sample compositions, Curie temperature T_c, coefficients B, C, $B_{3/2}$ and $C_{5/2}$ for amorphous ferromagnets and crystalline Fe and Ni.

System	T_c(K)	$B(10^{-6}\,K^{-3/2})$	$C(10^{-8}\,K^{-5/2})$	$B_{3/2}$	$C_{5/2}$	Reference
$Fe_{80}B_{20}$	685	22	1·2	0·40	0·17	Chien (1978)
$Fe_{40}Ni_{40}B_{20}$	695	22	0·4	0·40	0·06	Present work
$Fe_{40}Ni_{40}P_{14}B_6$	537	38	1·2	0·47	0·08	Chien and Hasegawa (1977)
$Fe_{78}B_{13}Si_9$	733	10	2·4	0·21	0·35	Present work
$Fe_{79}B_{16}Si_5$	730	11	2·3	0·22	0·33	Present work
$Fe_{82}B_{12}Si_6$	658	—	—	0·34	0·21	Ok and Morrish (1980)
$Fe_{81}B_{13.5}Si_{3.5}C_2$	698	16	2·1	0·30	0·27	Present work
$Fe_{81}B_{13.5}Si_{3.5}C_2$	668	—	—	0.30	0.29	Saegusa and Morrish (1982)
Crystalline Fe	1042	3·4	0·1	0·114	0·04	Chien and Hasegawa (1977)
Crystalline Ni	637	7·5	1·5	0·117	0·15	Chien and Hasegawa (1977)

become much smaller after the amorphous material crystallizes (Hasegawa and Ray 1979). Hence, the high $B(B_{3/2})$ and $C(C_{5/2})$ values seem to be the characteristic of the amorphous state. Higher B values in glassy ferromagnets also mean lower values of D, the stiffness constant, for glassy systems as seen from (3). Lower values of D also mean that the density of states for spin waves are higher in the amorphous state. Theoretical calculations do show higher density of states for spin waves in amorphous materials due to fluctuations in the exchange interaction arising from the random atomic arrangement (Montgomery *et al* 1970; Simpson 1974). Thus the existence of spin wave excitations in amorphous ferromagnets is clearly demonstrated by Mössbauer measurements as well as by magnetization (Kaul 1981) and inelastic neutron scattering measurements (Lynn *et al* 1976; Axe *et al* 1977; Rhyne *et al* 1979).

4. Conclusion

The temperature dependence of the average internal magnetic field of a number of ferromagnetic metallic glasses can be described by the expression $H_{\text{eff}}(T) = H_{\text{eff}}(O)\,(1 - BT^{3/2} - CT^{5/2} - \ldots)$, which is indicative of spin wave excitations in these solids. Values of $B(B_{3/2})$ are much higher than those for crystalline Fe, Ni etc. This observation can be explained if higher density of states for spin waves are assumed in the amorphous ferromagnets. Values of $B(B_{3/2})$ and $C(C_{5/2})$ are found to depend upon the temperature interval used to fit experimental data to the $T^{3/2}$ and $T^{5/2}$ dependence.

Acknowledgements

Authors thank the Science and Engineering Research Council (DST, India) and the Department of Atomic Energy for support.

References

Axe J D, Shirane G, Mizoguchi T and Yamauchi K 1977 *Phys. Rev.* **B15** 2763

Bhanu Prasad B, Bhatnagar A K and Jagannathan R 1980 *Solid State Commun.* **36** 661

Bhanu Prasad B, Bhatnagar A K and Jagannathan R 1983 *J. Appl. Phys.* **54** 2019

Bhatnagar A K, Bhanu Prasad B, Ravi N, Jagannathan R and Anantharaman T R 1982 *Solid State Commun.* **44** 905

Chien C L 1978 *Phys. Rev.* **B18** 1003

Chien C L and Hasegawa R 1977 *Phys. Rev.* **B16** 2115

Chien C L, Musser D, Gyorgy E M, Sherwood R C, Chen H S, Luborsky F E and Walter J L 1979 *Phys. Rev.* **B20** 283

Hasegawa R and Ray R 1979 *Phys. Rev.* **B20** 211

Herring C and Kittel C 1951 *Phys. Rev.* **81** 869

Kaul S N 1981 *Phys. Rev.* **B24** 6550

Lynn J W, Shirane G, Birgeneau R J and Chen H S 1976 *AIP Conf. Proc.* **34** 313

Montgomery C G, Krugler J I and Stubbs R M 1970 *Phys. Rev. Lett.* **25** 669

Ok H N and Morrish A H 1980 *Phys. Rev.* **B22** 4215

Rhyne J J, Lynn J W, Luborsky F E and Walter J L 1979 *J. Appl. Phys.* **50** 1583

Saegusa N and Morrish A H 1982 *Phys. Rev.* **B26** 10

Simpson A W 1974 *Wiss Z. dTH Dresden* **3** 1020

Spano M L and Bhagat S M 1981 *J. Magn. Mag. Mater.* **24** 143

Tsuei C C, Longworth G and Lin S C H 1968 *Phys. Rev.* **170** 603

Bull. Mater. Sci., Vol. 6, No. 6, December 1984, pp. 1063–1067. © Printed in India.

Infrared absorption in spinel ferrites

T T SRINIVASAN, C M SRIVASTAVA, N VENKATARAMANI* and M J PATNI*

Department of Physics, *Materials Science Centre, Indian Institute of Technology, Powai, Bombay 400 076, India

MS received 31 May 1983

Abstract. The IR spectra of a number of ferrites, MFe_2O_4, M(Mn, Fe, Co, Ni, Cu and Zn) have been studied at room temperature in the range 200–1000 cm^{-1}. In all the cases the spectrum consists of four bands, two of which have strong absorption while the other two have weak absorption and often appear as shoulders on the main band. However up to 20 % of the inverse ferrite, the shoulder in the low energy side appears as a band. In this paper we have analysed the origin of the above bands.

Keywords. IR spectrum; ferrites; centre frequency; force constants.

1. Introduction

Infrared spectrum of ferrites has been studied by Waldron (1955). The effect of a Jahn-Teller ion on the lattice vibrational frequencies of nickel ferrite has also been studied by Srivastava and Srinivasan (1982). Waldron has assumed that the 14 atoms in the primitive unit cell of a spinel lattice can be divided into two MO_4 groups and one Fe_4 group of tetrahedral symmetry. This allows the classification of the vibrations into the point group T_d. The conclusions reached by him are not very satisfactory. For example, the force constants K_t for the *t–o* bond for the normal ferrite $ZnFe_2O_4$ and $MnFe_2O_4$ are substantially smaller than that for the inverse spinels like Co, Fe and Ni ferrites. The normal ferrites are formed due to the strong tetrahedral site preference of the divalent ions like Zn^{2+}. As the size of the Zn^{2+} (0·74 Å) ion is larger than the Fe^{3+} (0·64 Å) ion, the overlap and strength of the *t–o* bond is expected to be greater for $ZnFe_2O_4$ than say for Fe_3O_4. We would therefore expect that the increased covalency in the bond would more than compensate for the decrease in the electrostatic energy due to the change for 3+ and 2+ state of the metal ion. Further each of the two broad bands showed asymmetry in the line shape. Waldron (1955) has also reported the presence of low as well as high frequency shoulders in his observations. We have analysed them as additional vibrational modes of the system. The IR frequencies are given in tables 1 and 2.

2. Experimental

The samples were prepared using the normal conventional ceramic technique. All the samples had densities higher than 97 % of their x-ray density. The x-ray analysis showed a single phase and a spinel structure.

Table 1. IR spectral frequencies of ferrites.

MFe_2O_4	Centre frequency (linewidth)cm^{-1}			
M =	T_2^0	$T_2^{\prime}$	E^0	$E^{\prime}$
Mn	330 (88)	400 (100)	545 (78)	640 (90)
Fe*	350 (62)	410 (55)	590 (78)	640 (100)
Co*	340 (67)	390 (50)	570 (75)	650 (78)
Ni	340 (105)	396 (40)	587 (100)	660 (110)
Cu	330 (70)	400 (90)	565 (80)	620 (75)
Zn	338 (105)	415 (120)	550 (85)	660 (160)

*Waldron's (1955) data.

Table 2. IR spectral frequencies of $Zn_{1-x}Ni_xFe_2O_4$ ($0 \leqslant x \leqslant 1$).

x	Centre frequency of (cm^{-1})			
	T_2^0	$T_2^{\prime}$	E^0	$E^{\prime}$
0	338	415	550	660
0·02	338	415	555	670
0·04	338	420	553	670
0·06	340	420	555	670
0·08	338	421	555	670
0·15	340	421	559	670
0·2	340	422	562	670
1	340	396	587	660

The ferrite powders were dispersed in KBr and pressed to get a clear disc. The spectra in the range of 200–1000 cm^{-1} were recorded at room temperature (SP 2000 IR Spectrameter, TYPE UNICHEM make). In order to examine the effect of the transformation from the normal to the inverse ferrite on the lattice modes of vibration we have studied the IR spectra of $Zn_{1-x}Ni_xFe_2O_4$ [$0 \leqslant x \leqslant 0{\cdot}2$ and $x = 1$]. These are shown in figure 1. The spectrum has been analysed in terms of four bands, each having a Lorentzian shape.

3. Analysis and discussion

Our observations show that the spectrum in all the cases consists of four bands, two of which have strong absorption. The remaining two have weaker absorption, and in some

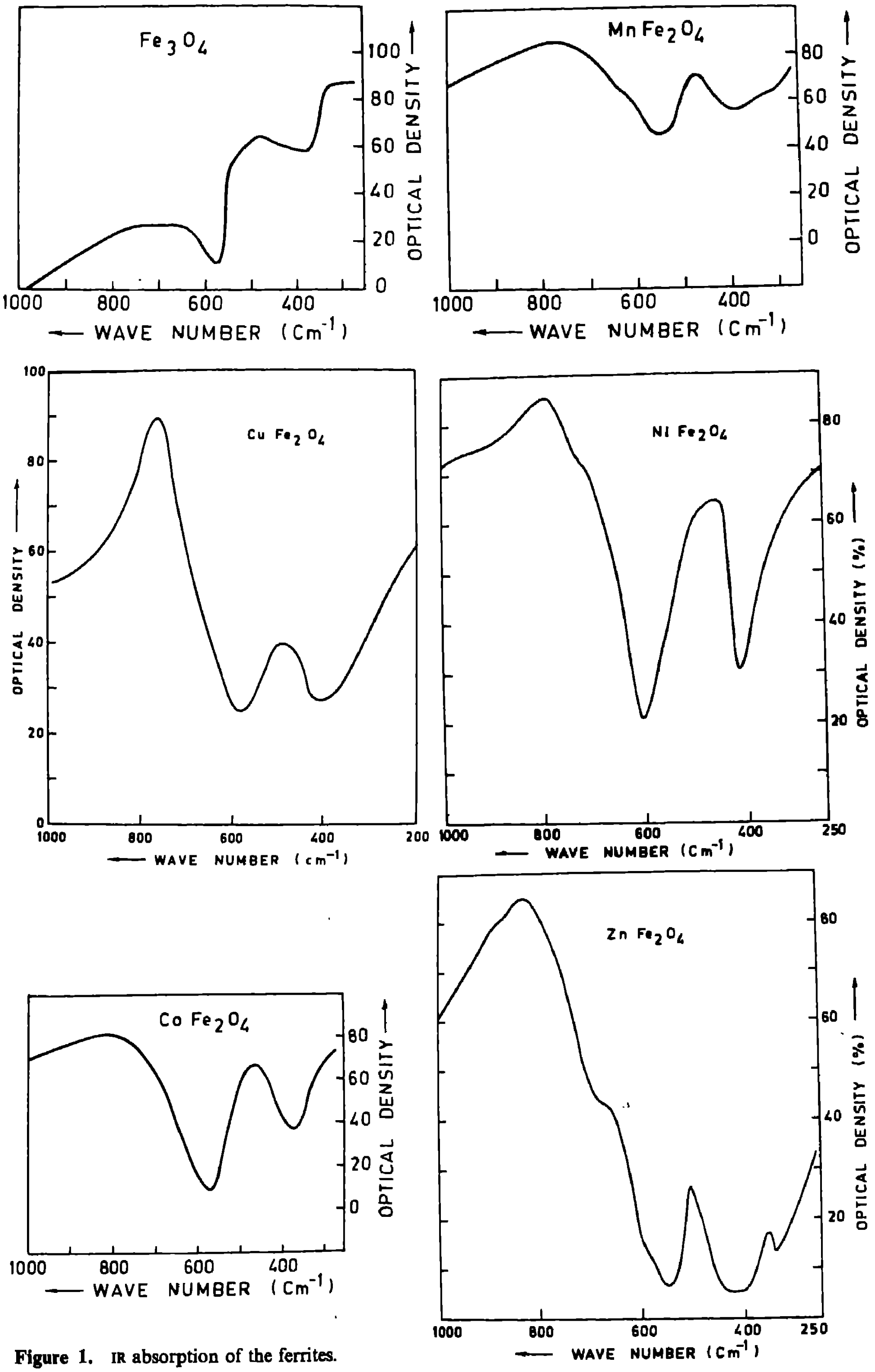

Figure 1. IR absorption of the ferrites.

cases appear as a shoulder to the main bands. We have attributed these to the absorption by lattice vibrations having E and T_2 symmetries. These type of phonon modes have been assumed by Bates and Steggles (1975) for the analysis of EPR data in Fe^{2+} in Al_2O_3. As there are two types of metals in the sites, we have E^o, E^t, T_2^o and T_2^t phonon modes where the superscripts '*o*' and '*t*' indicate the E and T_2 symmetry of the atomic displacements around the octrahedral and tetrahedral metal ions. The bands were identified on the systematics of the observed central frequencies as the metal ion M was changed from d^5 to d^{10} configurations. The frequency increases in the following order

$$\nu(T_2^o) < \nu(T_2^t) < \nu(E^o) < \nu(E^t).$$

It is difficult to assign the precise nature of atomic displacements for these modes of vibrations. We assume that those of the T_2 type would be bond-bending while the E type would be bond-stretching so that in general $\nu(T_2) < \nu(E)$. Again we would assume that the bond stretching for tetrahedral site would lead to a higher force constant than that for the octrahedral site. On this basis we would be able to assign the bands in the order given in tables 1 and 2. The IR frequencies as a function of the number of d electrons in M^{2+} ion are plotted in figure 2. It is seen that with an assignment the stretching mode of the tetrahedral *t–o* bond (E^t) has a larger value for $ZnFe_2O_4$ as compared to others. This mode however has a relatively weak absorption. The stretching modes (E^o) for the normal Mn and Zn ferrites have identical frequencies as these have only Fe^{3+} ions on the B-site. The bond stretching modes (E^o) on the B-site have a strong absorption. For Ni^{2+}, it shows a higher frequency and a narrow band. This seems to be related to the ground singlet state of the ion. Even T_2^t bands in this ferrite ($\Delta\nu \approx 40\,cm^{-1}$) is narrower as compared to others. The bond-bending frequencies T_2^t and T_2^o are nearly the same as expected. In table 2 the variation of centre frequencies as one goes from normal ferrite ($ZnFe_2O_4$) to inverse ferrite ($NiFe_2O_4$) is given for all the four bands.

In an inverse ferrite the octahedral site is occupied by Fe^{3+} and the divalent ion M^{2+}. Due to charge imbalance the oxygen ion is likely to shift towards the Fe^{3+} ion making

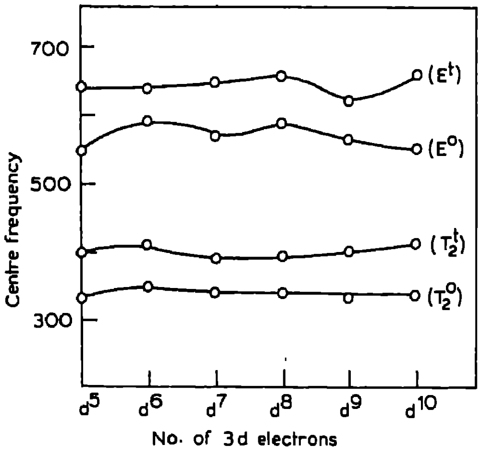

Figure 2. IR frequencies as a function of the number of d electrons in $M^{2+}(MFe_2O_4)$.

the force constant between Fe^{3+} and O^{2-} more. Hence we expect an increase in the bond stretching E^o phonon mode, frequencies as we go from normal to inverse spinels. This is supported by our results on $Zn_{1-x}Ni_xFe_2O_4$ in which we find that $\nu(E^o)$ increase as x is increased and the others T_2^o, T_2^t and E^t do not change with the type of spinel structure, given in table 2.

4. Conclusions

IR spectrum of spinel ferrites in the range of 200–1000 cm^{-1} consists four bands. These bands have been assigned on the basis of E and T_2 phonon symmetries around the crystallographic metal ion sites, A and B. On gradual change from normal to inverse spinel structure only one of the bands is affected as expected.

References

Bates C A and Steggles P 1975 *J. Phys.* **C8** 2283
Srivastava C M and Srinivasan T T 1982 *J. Appl. Phys.* **53** 8148
Waldron R D 1955 *Phys. Rev.* **99** 1727

Bull. Mater. Sci., Vol. 6, No. 6, December 1984, pp. 1069–1074. © Printed in India.

Influence of spin orbit coupling and lanthanide contraction on the exchange interaction in rare earth garnets

C M SRIVASTAVA, C SRINIVASAN and R AIYAR

Department of Physics, Indian Institute of Technology, Bombay 400076, India

MS received 7 May 1983

Abstract. The exchange constants observed in the rare earth iron garnets, obtained from fitting magnetization and paramagnetic susceptibility as a function of temperature have been analysed in terms of Anderson's theory of superexchange. The transfer integrals and covalency parameters have been obtained for various rare earth ions overlapping with oxygen.

Keywords. Exchange constants; superexchange; transfer integrals; covalency parameters; molecular field constants.

1. Introduction

In an earlier paper (Srivastava *et al* 1982) we had reported the simultaneous fitting of saturation magnetisation (M_s) and paramagnetic susceptibility (χ) for the ferrimagnetic garnets $R_3Fe_5O_{12}$ where R is yttrium or a trivalent rare earth ion with configuration $(Xe)\ 4f^n$ ($7 \leqslant n \leqslant 13$). We had used the molecular field constants to determine the exchange constants by means of the equation

$$J_{ij} = \frac{g_i g_j \mu_B^2 n_j \lambda_{ij}}{2Z_{ij}}, \tag{1}$$

where g_i, g_j are the g factors of the sublattices i and j, λ_{ij} are the molecular field constants, n_j is the number of j ions per unit mole and Z_{ij} is the number of $n-nj$ ions to an ion on ith sublattice. But if one of the ions involved is a rare earth ion then (1) is not the correct expression to convert the molecular field constants to J_{ij}. This is because for the rare earths the orbital momentum is not quenched and hence the exchange energy is

$$E_i = -2n_j Z_{ij} J_{ij} (g_i - 1) \bar{J}_i \cdot \bar{S}_j. \tag{2}$$

Here, we have assumed that the ith ion is a rare earth and the factor $(g_i - 1)$ comes because the rare earth spin has to be projected on J_i the angular momentum. In terms of λ_{ij}, E_i is given by

$$\begin{aligned} E_i &= -\mu_i \cdot \mu_j = -g_i \bar{J}_i \mu_B \cdot \lambda_{ij} \bar{M}_j, \\ &= -n_j g_i g_j \mu_B^2 n_j \lambda_{ij}\ \bar{J}_i \cdot \bar{S}_j \end{aligned} \tag{3}$$

From (2) and (3) we get

$$J_{ij} = \frac{g_i g_j \mu_B^2 n_j \lambda_{ij}}{2Z_{ij}(g_i - 1)}. \tag{4}$$

Table 1. Exchange constants (°K) in garnets ($R_3Fe_5O_{12}$).

	Values in °K		
R	$-J_{ac}$	$-J_{dc}$	$-J_{cc}$
Y	0	0	0
Gd	0·60	1·8	0
Tb	1·12	2·0	0
Dy	2·97	2·97	−0·9
Ho	2·64	2·80	0
Er	2·70	3·40	0
Tm	2·64	3·96	0
Yb	21·00	16·1	−0·2

The $-J_{aa}$, $-J_{ad}$ and $-J_{dd}$ values are 6·45, 30·40 and 12·05 respectively in all the cases.

Equation (4) differs from (1) because of the factor $(g_l - 1)$ in the denominator. Hence the exchange constants have to be corrected by dividing the values reported earlier (Srivastava *et al* 1982) by $(g_l - 1)$ where g_l is the g factor of the rare earth site. These are shown in table 1.

2. Exchange constants from Anderson's theory

We give below the calculation of exchange constants from Anderson's theory of superexchange for these garnets. For the exchange between a rare earth and Fe^{3+} ions in garnets Levy (1966) has shown that if the Z axis for the interaction is chosen as the RE-O^{2-} bond direction then the only orbital on the RE ion contributing to the exchange is the one with $m_l = 0$ (*i.e.* f_{z^3} orbital). Following the same convention we find that the only transfer integral in Anderson's expression for 180° superexchange interaction is $b_{\sigma\sigma}$ arising from the overlaps of f_{z^3} orbital on RE ion and $e_g(d_{z^2})$ on Fe^{3+} with a p_z orbital on the O^{2-} ion. Similarly the only transfer integral for the 90° exchange is $b_{\pi\sigma}$ arising from overlaps of t_{2g} and f_{z^3} orbitals with p_z orbital on oxygen. Thus we have (ignoring direct overlap of magnetic orbitals)

$$J_{ij} = -\frac{1}{4(g_i - 1)\,J_i S_j}\,2\frac{b^2_{\sigma\sigma}}{U} \text{ for 180° superexchange} \tag{5a}$$

$$J_{ij} = -\frac{1}{4(g_i - 1)\,J_i S_j}\,2\frac{b^2_{\pi\sigma}}{U} \text{ for 90° superexchange} \tag{5b}$$

In rare earths the spin orbit interaction is very strong compared to the crystal field energy, hence the ground state wavefunction will have admixtures of states with all values of m_l. However, as explained above only the $m_l = 0$ state contributes to the superexchange. Hence if we assume that all the m_l states have equal probability of being occupied then the probability that the state $m_l = 0$ has unpaired electron is $1 - (n-7)/7 = 2 - (n/7)$ where n is the number of electrons in the $4f$ shell ($n \geqslant 7$). Using this in (5) and noting that J_{ac} is a predominantly 90° exchange while J_{dc} is a 180°

exchange we get for a $f^n - d^5$ superexchange interaction

$$J_{dc} = -\frac{1}{4(g_l-1)J_lS_j}2\frac{b^2_{\sigma\sigma}}{U}\left(2-\frac{n}{7}\right), \tag{6a}$$

$$J_{ac} = -\frac{1}{4(g_l-1)J_lS_j}2\frac{b^2_{\pi\sigma}}{U}\left(2-\frac{n}{7}\right). \tag{6b}$$

The values of the coulomb energy can be estimated by a procedure used by Anderson (1959) to evaluate U for the $3d$ series transition metal ions. Taking the free ion ionisation potential (IP) for these ions we find that $I_4 - I_3$ *i.e.* the difference between the 4th and 3rd IP gives the free ion U. This has to be corrected in the solid. Firstly the transfer of electrons take place through a finite distance and not to infinity as is the case for calculating IP. Anderson estimated this correction to be 4 eV for $3d$ electrons. We shall assume the same correction for R^{3+} ions. The next correction is the dielectric polarisation correction because the coulomb repulsion takes place in a dielectric medium and not in vacuum. This gives another correction of 4 eV. Finally because of covalency another 10% correction is required. Using the IP calculated by Sugar and Reader (1973) and using the above method we get $U = 10\,\text{eV} \pm 1\,\text{eV}$ for all the rare earth ions except Gd^{3+} as shown in table 2. Since the ground state of Gd^{2+} is $5d^2f^7$ and not f^8, the U value for Gd will reduce if the correct IP for $4f^7$——f^8 transition is taken Hence we can assume $U = 10$ eV for all the heavy rare earths. Using (4) instead of (1) as was used in our earlier work (Srivastava *et al* 1982) to get the correct values of J_{ij} we have obtained the values of $b_{\sigma\sigma}$ and $b_{\pi\sigma}$ using (7) for all these garnets which are given in table 3. In table 3 we also give the distance of closest approach of the rare earth and oxygen orbitals

$$S^{-1} = \frac{r_{R\text{-}O} - (r(R^{3+}) + r(\text{O}^{2-}))}{r(R^{3+}) + r(\text{O}^{2-})}.$$

The values of $r_{R\text{-}O}$, $r(R^{3+})$, $r(\text{O}^{2-})$ are from Tchéou *et al* (1970), Khattak and Yang (1979) and CRC handbook (1980) respectively. Figure 1 gives a plot of b^2 against S^{-1} for both $b^2_{\sigma\sigma}$ and $b^2_{\pi\sigma}$. This curve resembles the curve obtained by Slater (1953) for metals. However, $b^2_{\sigma\sigma}$ does not show the peak in the observed region of overlap. Yb does not fit in the above scheme because as shown by Copland (1970) the $5p$ shell plays a

Table 2. Coulomb energy U (eV) for rare earth ions.

Ion	Ionisation potential (eV) I_3	Ionisation potential (eV) I_4	Free ion $U = I_4 - I_3$ (eV)	Corrected U (eV)	Covalency correction (10%)	Corrected U in solid (eV)
Gd	20·63	44·01	23·78	15·38	1·54	13·84
Tb	21·91	39·79	12·88	9·88	0·99	8·89
Dy	22·79	41·47	18·68	10·68	1·07	9·61
Ho	22·84	42·48	19·64	11·68	1·17	10·57
Er	22·74	42·65	19·91	11·91	1·19	10·92
Tm	23·68	42·69	19·01	11·01	1·10	9·91
Yb	25·03	43·74	18·71	10·71	1·07	9·64

The correction for $n - n$ and dielectric polarization was 8 in all the cases.

Table 3. Transfer integrals in garnets $R_3Fe_5O_{12}$.

R	J_l	$b^2_{\sigma\sigma}$ (eV)^2	$b^2_{\pi\sigma}$ (eV)^2	S^{-1} $\frac{r(R\text{–O}) - r(R^{3+}) - r(O^{2-})}{r(R^{3+}) + r(O^{2-})}$
Gd	3·5	0·0271	0·0091	0·016
Tb	6·0	0·0295	0·0168	0·022
Dy	7·5	0·0448	0·0448	0·024
Ho	8·0	0·0419	0·0398	0·026
Er	7·5	0·0513	0·0408	0·032
Tm	6·0	0·0596	0·0398	0·035
Yb	3·5	0·0240	1·15	0·037

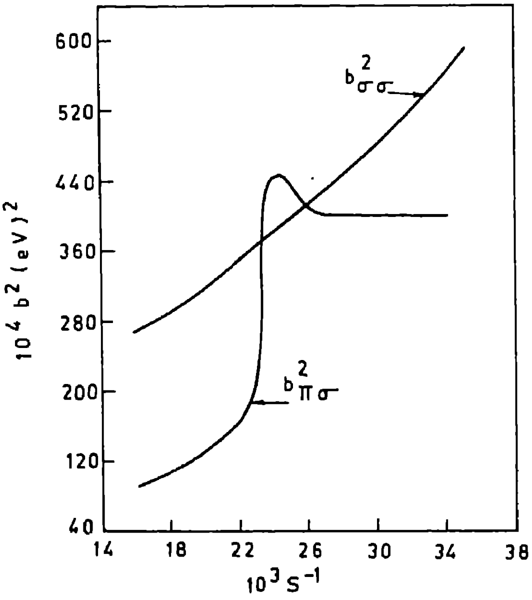

Figure 1. Transfer integrals in garnets.

dominant role in superexchange in YbIG, unlike the other garnets where the 4*f* shell is the dominant orbital contributing to superexchange.

3. Covalency parameters

Zeiger and Pratt (1973) have shown that the transfer integrals b_{ij} are related to the covalency parameters λ_{ic} and λ_{jc}, where c refers to the intervening anion by

$$b_{ij} = \lambda_{ic}\lambda_{jc}\Delta E_c$$

where ΔE_c is the one electron ionization energy of the anion. For the Fe^{3+}-Fe^{3+}

Table 4. Covalency parameters and transfer integrals in garnets.

	Type of exchange	Transfer integral	Value of b_k(eV)	λ_σ (Fe^{3+}-O^{2-})	λ_π (Fe^{3+}-O^{2-})	λ_σ (R^{3+}-O^{2-})
Fe^{3+}	J_{ad}	$b_{\sigma\sigma}$	0·48	0·24		
		$b_{\pi\pi}$	0·18		0·14	
		$b_{\sigma\sigma'}$	0·12	0·12		
	J_{dd}	$b_{\pi\sigma}$	0·30	0·25	0·14	
Gd^{3+}	J_{ac}	$b_{\pi\sigma}$	0·095		0·14	0·078
	J_{dc}	$b_{\sigma\sigma}$	0·16	0·25		0·08
Tb^{3+}	J_{ac}	$b_{\pi\sigma}$	0·13		0·14	0·107
	J_{dc}	$b_{\sigma\sigma}$	0·17	0·25		0·08
Dy^{3+}	J_{ac}	$b_{\pi\sigma}$	0·21		0·14	0·17
	J_{dc}	$b_{\sigma\sigma}$	0·21	0·25		0·098
HO^{3+}	J_{ac}	$b_{\pi\sigma}$	0·20		0·14	0·16
	J_{dc}	$b_{\sigma\sigma}$	0·20	0·25		0.094
Er^{3+}	J_{ac}	$b_{\pi\sigma}$	0·20		0·14	0·17
	J_{dc}	$b_{\sigma\sigma}$	0·22	0·25		0·105
Tm^{3+}	J_{ac}	$b_{\pi\sigma}$	0·20		0·14	0·16
	J_{dc}	$b_{\sigma\sigma}$	0·24	0·25		0·11
Yb^{3+}	J_{ac}	$b_{\pi\sigma}$	1·07		0·14	0·8
	J_{dc}	$b_{\sigma\sigma}$	0·15	0·25		0·07

exchange we have

$$\begin{aligned} b_{\sigma\sigma} &= \lambda_\sigma(Fe^{3+})\lambda_\sigma(Fe^{3+})\Delta E_c \\ b_{\pi\pi} &= \lambda_\pi(Fe^{3+})\lambda_\pi(Fe^{3+})\Delta E_c \\ b_{\pi\sigma} &= \lambda_\pi(Fe^{3+})\lambda_\sigma(Fe^{3+})\Delta E_c \\ b_{\sigma\sigma'} &= \lambda_\sigma(Fe^{3+})\lambda_{\sigma'}(Fe^{3+})\Delta E_c \end{aligned} \tag{7}$$

For $Fe^{3+} - R^{3+}$ exchange we have

$$\begin{aligned} b_{\pi\sigma} &= \lambda_\sigma(R^{3+})\lambda_\pi(Fe^{3+})\Delta E_c \\ b_{\sigma\sigma} &= \lambda_\sigma(R^{3+})\lambda_\sigma(Fe^{3+})\Delta E_c \end{aligned} \tag{8}$$

The electron affinity of oxygen is -1.47 eV and for O^- it is 7·2 eV so that $\Delta E_c = 8{\cdot}67$ eV. Using this in (7) and (8) we obtain the λ values which are listed in table 4.

We observe that $\lambda_\sigma > \lambda_\pi$ for Fe^{3+} exchange as expected from chemical bond theory. Also λ_σ values for the rare earth ions are generally lower than that for the Fe^{3+} bonds. This also agrees with the chemical theory of covalent bonds where it is known that the covalent bonds involving the 3*d* orbitals are stronger than those involving the 4*f* orbitals.

References

Anderson P W 1959 *Phys. Rev.* **115** 2
Copland G M 1970 *Chem. Phys. Lett.* 7 175

CRC Handbook of Chemistry and Physics 1980–81, 61st (CRC Press Florida) p. F.216
Khattak C P and Yang F F Y 1979 *Handbook of physics and chemistry of rare earths* (ed.) Schneider Jr and L Eyrings (Amsterdam: North Holland) Vol. 3 p. 565
Levy P M 1966 *Phys. Rev.* **147** 311
Slater J C 1953 *Rev. Mod. Phys.* **25** 199
Srivastava C M, Srinivasan C and Aiyar R 1982, *J. Appl. Phys.* **53** 781
Sugar J and Reader J 1973 *J. Chem. Phys.* **59** 2083
Tchéou F, Fuess H and Bertaut H 1970 *Solid State Commun.* **8** 1745
Zeiger H J and Pratt G W 1973 *Magnetic interactions in solids* (Oxford: Clarenden) p. 242

Bull. Mater. Sci., Vol. 6, No. 6, December 1984, pp. 1075–1086. © Printed in India.

Electrical properties of films at microwave frequencies

D C DUBE
Physics Department, Indian Institute of Technology, New Delhi 110016, India

MS received 1 June 1983

Abstract. A technique suitable for the measurement of electrical properties of films/sheets at microwave frequencies has been described. Groups of materials are identified for which the absence of any kind of electrodes in these microwave measurements can be utilised with advantage. Results are presented for a variety of materials such as metal films, superionic conductors, semiconductors and insulating polymers.

Keywords. Microwaves; waveguide; dielectric constant; a.c. conductivity.

1. Introduction

Knowledge of the electrical properties of films at microwave frequencies is helpful in material study and characterization for device fabrication. Thin metal and insulating films, for example, are extensively used in microwave integrated circuits. There, it is of interest to know the attenuation and phase produced by a particular film and variation of these quantities with parameters such as film thickness, temperature etc. Thin semimetal and metal films were studied by several workers (Gunn 1967; D'Aiello and Freedman 1969; Duggal and Rup 1969; Ramey *et al* 1970). The microwave applications of thin metallic films have also gained importance as exemplified by the use of films as microwave mirrors and as large size film reflectors (Korolev and Gridnev 1963). Microwave measurements are essential in the above cases. But in many situations advantage can be taken of the fact that at microwave frequencies the measurements basically are electrodeless and therefore these are recommended to study materials which require special type of electrodes. Groups of materials may be identified where contacts do pose problems, such as *e.g.* (i) semi-conductors (ii) fast ion conducting solids (iii) membranes and other biological systems. Such materials can be conveniently studied at microwave frequencies.

Section 2 describes few techniques including the one developed earlier (Dube and Natarajan 1973), for the measurement of dielectric constant, loss and conductivity of films and foils. Finally the results are presented for a variety of films.

2. Measurement techniques

The most widely used method for microwave measurements of dielectric parameters of solids is the short-circuited line technique of Von Hippel (Von Hippel 1961). The technique involves the measurement of VSWR (voltage standing wave ratio $= E_{\max}/E_{\min}$) on the standing waves set-up when the microwaves are totally reflected from a short circuit. A dielectric specimen in the form of a small block which completely

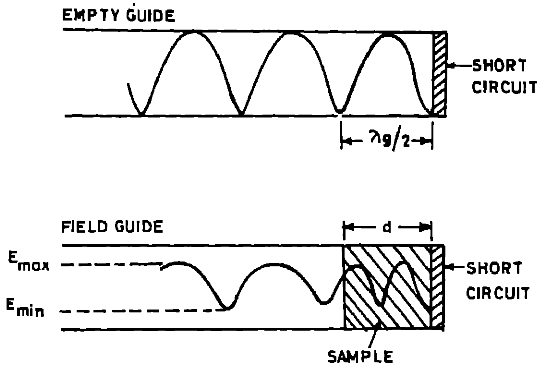

Figure 1. Standing wave pattern in empty and field guide.

fills the section of waveguide is placed next to the short circuit. This alters both the position of standing wave pattern and the size of the voltage ratio by amounts which depend on the dielectric constant and loss of the material and on the length of the 'filled guide' (figure 1).

Von Hippel's method when applied to a very thin specimen does not give accurate results, the reason being the lack of strong interaction between the e.m. wave and the thin specimen. Therefore the presence of the specimen shifts the voltage minima only slightly (often insignificantly) and the change in standing wave ratio is also small (often not measurable accurately).

Recently, Von Hippel's technique has been modified to suit thin samples by measuring impedance not only with short circuit (figure 1) but also using an open circuit and matched terminations (Das Gupta and Pramanic 1982). The method is effective only for high dielectric constant films.

Cavity methods which measure the change in resonance frequency and broadening of resonance response on introduction of the specimen are also not very successful for the same reasons of lack of strong interaction when the specimen is very thin. However, attempts have been made to study thin samples using specific forms of cavities (Conklin 1965; Sobol and Hughes 1967) and other forms of sample holders (Pilipenko *et al* 1970). Cavity perturbation technique has also been used (Rzepecka and Hamid 1972).

3. An accurate and convenient technique

In the above techniques such as that of Von Hippel, the accuracy of measurement is poor due to weak interaction of e.m. wave with the specimen. And the reason for the poor interaction is the fact that in normally used TE_{10} mode of excitation the electric field is maximum at the centre of the waveguide and diminishes to zero at the side walls (figure 2); most of the portion of the specimen lies in the weak field regions. Keeping this in view, a suitable technique was developed (Dube and Natarajan 1973) to study thin film specimens. In this technique the thin specimen is placed longitudinally at the centre of the broad side of a hollow rectangular waveguide excited in the TE_{10} mode so that the whole specimen remains in maximum electric field as shown in figure 3. In this geometry Maxwell's equations can be solved for the TE_{10} mode by taking Z variations of the form $\exp(-i\beta Z)$ (axis of waveguide is along the z-direction). Then by usual

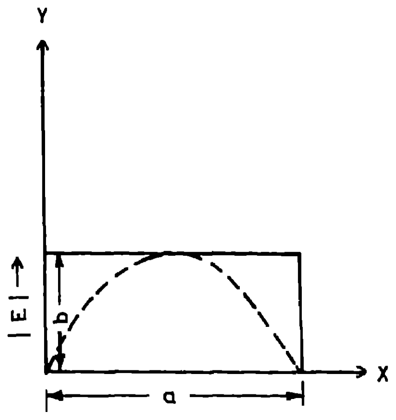

Figure 2. Electric field distribution in a rectangular waveguide in the TE_{10} mode.

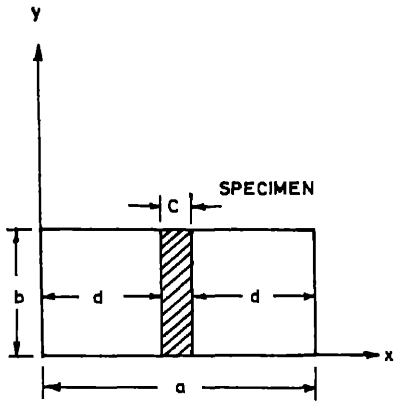

Figure 3. Cross-section of a rectangular waveguide with specimen.

methods (Collin 1960), the following dispersion relation is obtained

$$\tan\left[d(k^2-\beta^2)^{1/2}\right]\tan\left[\tfrac{1}{2}c(\varepsilon k^2-\beta^2)^{1/2}\right]=\frac{(k^2-\beta^2)^{1/2}}{(\varepsilon k^2-\beta^2)^{1/2}} \tag{1}$$

where $k=\omega/C_0$ is the free space propagation vector and ω is the angular frequency. Equation 1 is a transcendental equation, and its solution can be obtained only by graphical methods. For complex dielectric constants, the solution of (1) is very difficult even graphically. Therefore, we simplify (1) under the approximation $\frac{1}{2}c(\varepsilon k^2-\beta^2)^{1/2}<1$, which holds very well in the case of thin films; hence using $\varepsilon=\varepsilon_r-i\varepsilon_i$ and $\beta=\beta_r-i\beta_i$, we get the following expressions for the real and imaginary parts of the complex dielectric constant:

$$\varepsilon_r=\frac{1}{k^2}\left((\beta_r^2-\beta_i^2)+\frac{a_1a_3+a_2a_4}{a_3^2+a_4^2}\cdot\frac{1}{\frac{1}{2}cd}\right), \tag{2}$$

$$\varepsilon_i=\frac{1}{k^2}\left(2\beta_r\beta_i-\frac{a_2a_3-a_1a_4}{a_3^2+a_4^2}\cdot\frac{1}{\frac{1}{2}cd}\right), \tag{3}$$

where

$$a_1 = d\,\mathrm{Re}\,(k^2-\beta^2)^{1/2},$$

$$a_2 = d\,\mathrm{Im}\,(k^2-\beta^2)^{1/2},$$

$$a_3 = \frac{2\sin 2a_1}{\exp(2a_2)+\exp(-2a_2)+2\cos 2a_1},$$

and

$$a_4 = \frac{\exp(2a_2)-\exp(-2a_2)}{\exp(2a_2)+\exp(-2a_2)+2\cos 2a_1},$$

and

β_i = attenuation introduced by unit length of the specimen (measured in nepers m^{-1})

$\beta_r = \beta_p + \beta_0$ (measured in radians m^{-1})

where

β_p = phase shift produced by the unit length of the specimen

and

$\beta_0 = 2\pi/\lambda g$, where λg is the guide wavelength in the empty guide,

c = thickness of specimen, and

$d = \frac{1}{2}(a-c)$, a being the width of the waveguide (figure 3).

Thus, in complex dielectrics, the value of ε_r and ε_i can be obtained from (2) and (3). For loss-free dielectrics the solution of (1) can be obtained without any approximations. The two main quantities required to be measured experimentally are the phase and attenuation introduced by the specimen. Two experimental arrangements have been proposed (Dube and Natarajan 1973, 1974). Either may be used for these measurements. Both make use of rectangular waveguide system excited in the TE_{10} mode. One arrangement has been shown in figure 4.

Microwave power is obtained from a Klystron source. The power is divided into two arms at the 10-dB directional coupler. The lower arm contains the standard impedance, *i.e.*, a standard variable attenuator and a standard variable phase shifter (0° → 360°). The upper arm contains the sample holder which is an approximately 10 cm long waveguide having a sharply cut longitudinal slot at the middle. The sample is introduced through this slot. The powers from the upper and the lower arms are again combined at a 3-dB directional coupler. The power output from the directional coupler is fed to the detecting system.

To start with, a null point is obtained in the detector by properly adjusting the variable attenuator and the phase shifter. The introduction of the specimen disturbs the balance. The null conditions are restored by varying the attenuator and phase shifter. Thus the phase shift and attenuation introduced by the sample can be accurately measured. Large sample lengths should be used for producing large phase shifts and attenuations.

Reflections from the edge of the sample are normally extremely small. But these can be detected by a separate experiment and if required, tuner no. 8 in figure 4 may be used for matching purposes.

The minimum detectable phase shift and attenuation in the measuring system were 0·25° and 0·02 dB, respectively.

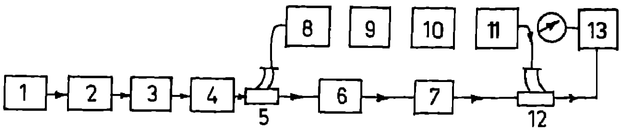

Figure 4. Schematic diagram of the experimental set up: 1. Klystron power source; 2. Frequency meter; 3. Padder attenuator: 4. Ferrite isolator; 5. and 12, Directional couplers; 6. Calibrated variable phase shifter; 8 and 11 tuners; 9. Variable attenuator; 10. sample holder waveguide; 13. Amplifier and meter.

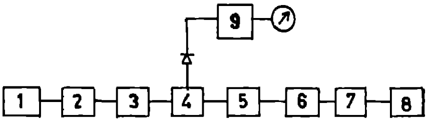

Figure 5. Schematic diagram of the experimental set-up; 1. Klystron power source; 2. Frequency meter; 3. Ferrite isolator; 4. Waveguide travelling detector; 5. variable attenuator; 6. E-H tuner; 7. sample holder waveguide; 8. movable short; 9. Amplifier and meter.

To study dielectric parameters as a function of temperature, the guide section containing the specimen may be cooled by a low temperature bath around the section or may be heated by a cylindrical furnace.

The other experimental set-up (Dube and Natarajan 1974) is shown in figure 5. This is a simpler arrangement and does not require calibrated variable phase shifter and attenuator and is as accurate as the first set-up.

Here the travelling wave detector is used to measure the shift of the voltage minimum when the specimen is introduced. Let the specimen length be L cm and the phase shift produced be X cm, then phase introduced by the specimen per unit length is

$$\beta_s = \beta_0 \frac{X}{L}$$

Thus the total phase constant β_r is given by

$$\beta_r = \beta_0 + \beta_s$$

or

$$\beta_r = \beta_0 \left(1 + \frac{X}{L}\right)$$

For measuring the dielectric loss, the VSWR is taken with and without the specimen. Let these be ρ_1 and ρ_2; then

$$r = \frac{\rho_1 - 1}{\rho_1 + 1} = \exp(-\alpha), \tag{4}$$

and

$$r' = \frac{\rho_2 - 1}{\rho_2 + 1} = \exp - (\alpha + 2\beta_l L), \tag{5}$$

where r and r' are the reflection coefficients of the system with and without the sample and α is the attenuation constant. Hence β_l can be calculated from (4) and (5).

4. Results and discussion

The accuracy of the proposed technique for measuring the dielectric parameters of films was checked by studying two materials namely, myler and teflon whose dielectric properties are well known over a wide frequency range including microwaves. Results are summarised in table 1.

In the recent past the technique has been used to study films/sheets/wafers of varying nature and differing widely in electrical properties. Some of the results are given below.

Complex permittivity and conductivity have been studied for silicon semiconductor (Natarajan *et al* 1978). ε_r and ε_i values for one sample of *p*-silicon for various thicknesses are given in table 2. The thickness of the starting sample was reduced by etching and lapping.

The d.c. conductivities measured by the four-probe technique and the microwave conductivities obtained from the relation $\sigma_{\text{a.c.}} = \omega\varepsilon_0\varepsilon_i$ are compared in table 3 for three samples of *p*-silicon.

The microwave conductivity is slightly less than the d.c. values. This is somewhat

Table 1. Dielectric parameters of teflon and mylar films at 9·375 GHz at room temperature (310°K)

Sample	Sample thickness (μm)	Phase shift per unit length (deg.)	Dielectric constant: Present work	Dielectric constant: Literature
Teflon	90	0·61	2·03	2·08[a]
	130	0·96	2·03	2·07 ± 0·03[b]
	186	1·28	2·02	
Mylar	75	1·15	3·13	
	130	1·91	3·10	3·145[c]
	250	3·74	3·18	

[a] Von Hippel (1961); [b] Pilipenko *et al* (1970); [c] Conklin (1965).

Table 2. Complex permittivity for a *p*-type silicon (5·45 Ω cm) at room temperature (310°K) and at a frequency of 9·410 GHz

Thickness (microns)	Phase shift per unit length (degrees)	Attenuation per unit length (decibles)	ε_r	ε_i
272	15·0	8·6	11·61	30·58
226	13.0	7·5	11·65	32·12
200	12·0	6·9	11·81	33·13
180	10.8	6·1	11·58	32·68
140	8·6	5·1	11·62	34·61
94	5·8	3·4	11·41	34·76
70	4·5	2·4	11·63	32·69

Table 3. Comparison of d.c. and a.c. conductivities for three samples of *p*-silicon

d.c. conductivity by four-probe technique $(\Omega\,\mathrm{m})^{-1}$	Microwave conductivity from $\sigma_{\mathrm{a.c.}} = \omega\varepsilon_0\varepsilon_i$ $(\Omega\,\mathrm{m})^{-1}$
10.26	9.79
15.63	15.17
18.35	17.97

consistant with the usual expressions for a.c. and d.c. conductivities.

$$\sigma_{\mathrm{a.c.}} = \frac{ne^2 v}{m[v^2 + \omega^2]},$$

and

$$\sigma_{\mathrm{d.c.}} = \frac{ne^2}{mv},$$

where m, e, n and v are the mass, charge, concentration and collision frequency of the holes in *p*-silicon.

The microwave data may also be used to determine other transport parameters of silicon. The dielectric constant and conductivity in terms of effective mass m^* and relaxation time τ may be written as

$$\varepsilon_r = \varepsilon_L - \frac{ne^2\tau^2}{\varepsilon_0 m^*[1 + (\omega\tau)^2]},$$

$$\sigma = \frac{ne^2\tau}{m^*[1 + (\omega\tau)^2]} = \omega\varepsilon_0\varepsilon_i,$$

where ε_L is the lattice dielectric constant and ε_0 is the permittivity of free space. From the above two equations, we get

$$\tau = \frac{\varepsilon_L - \varepsilon_r}{\omega\varepsilon_i}.$$

With the present results the relaxation time in silicon comes out to be around 10^{-13} sec, which agrees well with the data ($\simeq 10^{-13}$ sec) produced by Blatt (1968).

The conductivity variations with temperature for *p*-silicon samples (d.c. resistivities 10·5, 40 and 170 ohm cm) in the temperature range 190–525°K are plotted in figure 6. The curves for the three silicon samples exhibit broadly similar characteristics. *viz* the conductivity initially decreases with increase of temperature and later increases very rapidly with temperature. This is, of course, expected, considering the relative predominance of extrinsic and intrinsic conduction mechanisms. The conductivity of the samples (having resistivities 10·5 and 40 ohm-cm) decreases from room temperature to 440°K. In this temperature region lattice scattering by acoustical phonons plays the dominant role (Blackmore 1969). As the temperature is raised further, the concentration of free electrons and holes increases and the intrinsic conduction predominates thereafter. In the case of the third sample (170 ohm cm, the highest resistivity of all the

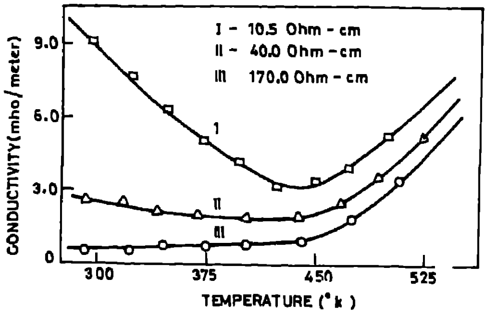

Figure 6. Microwave conductivity variation of silicon wafers in the temperature range 293–523°K.

three) the conductivity rises slowly from room temperature up to 440 K and increases very rapidly subsequently thereby showing its intrinsic behaviour right from room temperature. Bhar (1963) made similar measurements on temperature variations of microwave conductivity for bulk *p*-silicon samples having conductivities 0·7 and 0·1 mho m^{-1} in the temperature range 273–480°K. His results also resemble the curves of figure 6.

Electrical parameters have been measured for metal and semimetal films of thicknesses less than the skin depths deposited on glass substrates by vacuum thermal evaporation technique (Dube *et al* 1978).

Figures 7 and 8 show the phase shift and attenuation constants as a function of film thickness for the semimetal bismuth. Table 4 contains the results for ε_r and ε_i for bismuth films of different thicknesses. The high values of ε_r and ε_i are attributed to the presence of free carriers and are consistent with the results of Rahneberg (1971) for bismuth films measured by a different technique at 14·50 GHz. Gold and aluminium films also show high dielectric parameters of the order of 10^5 (Dube *et al* 1978).

Dielectric behaviour of pure polyvinyl chloride (PVC) and iodine-doped PVC has been studied at microwave frequencies using the proposed technique (Natarajan and Dube 1981). Pure PVC films were obtained by dissolving the polymer powder in tetrahydrofuran and permitting the evaporation of the solvent at room temperature. Iodine-doped PVC samples were prepared from the PVC solution in which a requisite amount of iodine was dissolved. The concentration of iodine in the samples varied from 4–40 % by weight.

Figure 9 depicts the variation of ε_r with temperature for all PVC samples. It is seen that at any fixed temperature, the dielectric constant increases as the iodine content in the sample increases. This effect is more pronounced for iodine concentrations above ~ 5 % (by weight). For temperatures above 90°C the dielectric constant decreases for all samples containing iodine.

The rise in ε_r with iodine concentration may be attributed to the presence of highly polarizable molecular iodine in the specimen. The presence of free iodine was detected in the absorption spectrum in the visible region.

The volume expansion due to transition from glassy to rubbery state seems to account for the decrease of ε_r with temperature in the vicinity of 85°C as the glass transition temperature (T_g) of PVC falls in the region 70–105°C (Brandrup and Immergut 1975). Variation of loss-tangent (tan δ) with temperature for different iodine

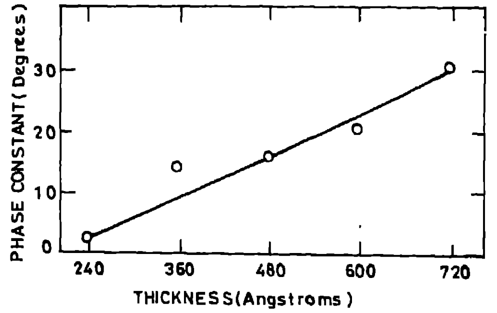

Figure 7. Variation of phase constant as a function of bismuth film thickness.

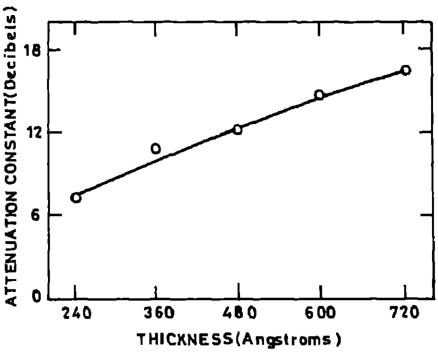

Figure 8. Variation of attenuation constant as a function of bismuth film thickness.

Table 4. Complex permittivity for thin bismuth films for various thicknesses at 310°K and at a frequency of 9·410 GHz.

Thickness (angstroms)	Phase shift/ length (degrees)	Attenuation/ length (decibels)	Dielectric parameters (× 10^5)	
			ε_r	ε_i
240	2·5	7·5	0·36	3·12
360	12·0	10·8	0·91	2·91
480	15·5	12·2	0·89	2·38
600	20·0	13·7	0·83	1·83
720	30·0	16·3	1·05	1·86

dopings has been shown in figure 10. For iodine content of 10% and above, well-defined loss-peak appears at around 90°C in each case. With increasing iodine content, the position of loss peak does not change; however, the peak height changes considerably. The fact that loss tangent maxima does not change in position but only in magnitude with iodine concentration shows that on increasing the doping the number of dipoles participating in the orientation process increases, while the frequency of orientation remains unchanged.

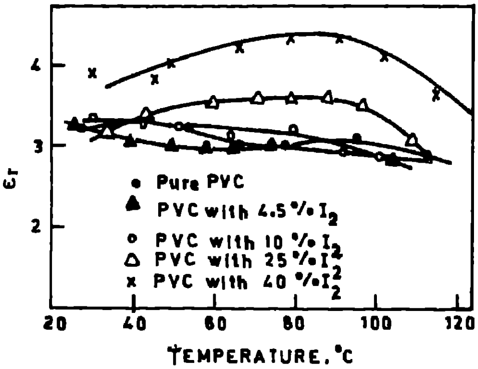

Figure 9. Variation of ε_r with temperature for pure and iodine doped PVC.

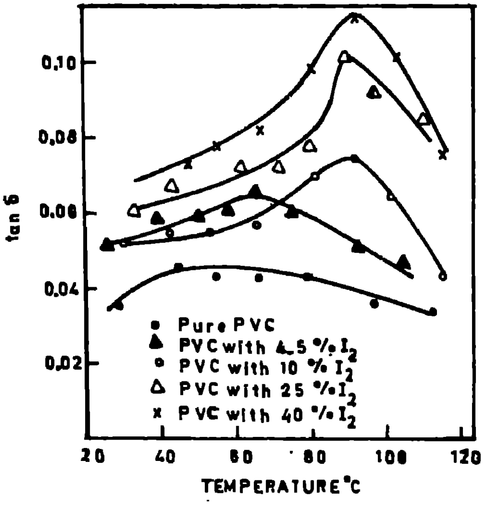

Figure 10. Variation of tan δ with temperature for pure and iodine doped PVC.

Fast ion conducting solids (also called superionic conductors) have become very important in the recent past due to their applications in many electrochemical devices. Electrical measurements on these materials require special attention due to the variety of electrodes (blocking, reversible and their combinations) (Bottelberghs 1978) used making the analysis more complex. The ionic conduction has been studied recently at microwave frequencies (Dube and Saraswat 1982) in silver iodide in the high conductivity α-phase. Thin pellets of AgI of varying packing density were used and dielectric and conductivity data obtained. This data can be transformed to 100 % dense bulk using correlation formulae (Landau and Lifshitz 1960; Leoyenga 1965; Dube 1970).

$$\varepsilon_p'^{1/3} - 1 = \delta(\varepsilon_b'^{1/3} - 1),$$

$$\varepsilon_b'' = \frac{\varepsilon_p''}{\delta}(\varepsilon_b'/\varepsilon_p')^{2/3},$$

Table 5. Conductivity and dielectric constant for α-AgI ($T = 160°C$) at 10 kHz

Packing fraction %	Observed parameters for pellets		Values converted to 100% density by correlation formulae		Values reported in literature in microwave region (Gebhardt *et al* 1980)	
	Dielectric constant	Conductivity $(\Omega \mathrm{cm})^{-1}$	Dielectric constant	Conductivity $(\Omega \mathrm{cm})^{-1}$	Dielectric constant	Conductivity $(\Omega \mathrm{cm})^{-1}$
72	12·0	0·044	21·74	0·092	22·00	1·22
82	15·4	0·076	22·30	0·119		
86	16·9	0·084	22·45	0·110		
92	19·4	0·088	22·75	0·116		

and

$$\sigma_b = \omega\varepsilon_0\varepsilon_b'',$$

where ε_p' and ε_p'' are the dielectric constant and loss factor for the pellet of packing fraction δ and ε_b', ε_b'' are the corresponding parameters for the bulk. σ_b is the conductivity at angular frequency ω. ε_0 is permittivity of free space ($= 8{\cdot}85 \times 10^{-12}\ \mathrm{Fm}^{-1}$). Various results have been summarised in table 5. It is seen that while the deduced dielectric constant data match with experimentally reported value of 22, the conductivity results are found reduced by an order of magnitude. This reduction in conductivity is attributed to the presence of grain boundaries in the unsintered samples used in the above studies.

In conclusion, it may be said that the microwave technique described is very convenient and accurate and can be used to study electrical transport behaviour of materials differing widely in characteristics.

References

Bhar J N 1963 *Proc. IEEE* **51** 1623
Blakemore J S 1969 *Solid State Physics* (Toronto: Saunders Company)
Blatt F J 1968 *Physics of electronic conduction in solids* (New York: McGraw-Hill)
Bottelberghs P H 1978 in *Solid electrolytes: General principles, characterization, materials, applications* (eds) Paul Hagenmuller and W Van Gool (New York: Academic Press)
Brandrup J and Immergut E M (eds) 1975 *Polymer handbook* (New York: John Wiley) 2nd edn p. 44
Collin R E 1960 *Field theory of guided waves* (New York: McGraw-Hill) Chap. 6
Conklin G E 1965 *Rev. Sci. Instrum.* **36** 1347
D'Aiello R V and Freedman S J 1969 *J. Appl. Phys.* **40** 2156
Das Gupta C and Pramanick P 1982 *Microwave* 76
Dube D C 1970 *J. Phys.* **D3** 1648
Dube D C and Natarajan R 1973 *J. Appl. Phys.* **44** 4927
Dube D C and Natarajan R 1974 *J. Phys.* **E7** 256
Dube D C, Natarajan R and Tripathi V K 1978 *Indian J. Phys.* **A52** 405
Dube D C and Saraswat A K 1982 *J. Appl. Phys.* **53** 7095
Duggal V P and Rup R 1969 *J. Appl. Phys.* **40** 492
Gebhardt K F, Soper P D, Merski J, Balle T J and Flygare W H 1980 *J. Chem. Phys.* **72** 272
Gunn M W 1967 *IEEE Proc.* **114** 207
Korolev F A and Gridnev V I 1963 *Radiotekh. Electron.* **8** 1480

Landau L D and Lifshitz F M 1960 *Electrodynamics of continuous media* (London: Pergamon) *p*. 46
Looyenga H 1965 *Physica* **31** 401
Natarajan R, Dube D C and Tripathi V K 1978 *Indian J. Phys.* **52** 567
Natarajan R and Dube D C 1981 *Indian J. Pure Appl. Phys.* **19** 675
Pilipenko V V, Polovnikov G G, Sologub V G and Shestopilov V P 1970 *Sov. Phys. Tech. Phys.* **14** 1662
Rahneberg E W 1971 *Measurement of the Complex Permittivity of Thin Bismuth Films within the Ku-band* Ph.D. Thesis, University of Arizona USA
Ramey R L, Landes H S and Manus E A 1970 *IEEE Trans. Microwave Theory Technol.* **MTT-18** 196
Rzepecka M A and Hamid M A K 1972 *IEEE Trans. Microwave Technol.* **MTT-20** 30
Sobol H and Hughes J J 1967 *IEEE Trans. Microwave Technol.* **MTT-15** 377
Von Hippel A R 1961 Dielectric materials and applications (New York: Wiley)

Bull. Mater. Sci., Vol. 6, No. 6, December 1984, pp. 1087–1091. © Printed in India.

Surface modification of polyvinyl chloride towards blood compatibility

GEETHA KURIAN and CHANDRA P SHARMA

Department of Biomedical Engineering, Sree Chitra Tirunal Institute for Medical Sciences and Technology, Trivandrum 695 012, India

MS received 29 January 1983; revised 6 September 1983

Abstract. The surface modification of medical grade polyvinylchloride (PVC) from various sources with the ionic bonding of polyelectrolyte is investigated by exposing the PVC sheets to 1% zephiran chloride for 10 min and then to 50 mg% solution of polyelectrolyte for 10 min. Surface energy and platelet adhesion studies were carried out to demonstrate the suitability of our improved surface towards blood compatibility. Relative changes due to γ-irradiation are also discussed.

Keywords. Polyvinyl chloride; surface modification; blood compatibility

1. Introduction

Polyvinylchloride (PVC) with a wide choice of additives and ingradients such as plasticizers, fillers, stabilisers etc (Ownes and Read 1979) is being used for various biomedical applications. However the surface of the PVC may change depending upon the additives used. Since the prosthetic blood interaction is dependent on the nature of the surface, various surfaces may behave differently. Therefore, we have attempted in this paper to mention the modification of the medical grade PVC from different sources using polyelectrolyte towards improved blood compatibility.

Polyelectrolytes from synthetic poly (*cis*-1,4 isoprene) possess anticoagulant activity (van der Does *et al* 1979) and have been used for surface modification of polymers (Sederel *et al* 1983). Therefore we have chosen natural rubber, (Source Hevea Brasiliensis "Para Rubber") to obtain the polyelectrolyte for our studies. It seems the effect of surface modification with this method is independent of the PVC type and therefore appears quite promising for future investigations.

2. Experimental work

The PVC sheets of different sources are dipped in 0·1% soap solution. They are thoroughly cleaned with distilled water, finally rinsed with methanol and dried in vacuum oven. Polyelectrolyte (synthesised from natural rubber, van der Does *et al* 1979) is ionically bound on the various PVC sheets by first exposing to 1% Zephiran chloride for 10 min and then to polyelectrolyte (50 mgm% in water) for 10 min. The bare as well as the polyelectrolyte coated PVC sheets were irradiated at room temperature (CO^{60} gamma source) with a constant dose rate of 0·25 M rad (strength 843/Rontgen/hr/m) for 4 hr 30 min.

Inherent viscosity of the various bare PVC sheets was compared and the results are given in table 1. Variation of contact angle with time are also studied with a goniometer at room temperature using double distilled water as shown in figures 1–4.

2.1 *Blood coagulation studies*

Calf blood is used for evaluating the recalcification time under controlled pH and temperature with the PVC coated tubes. Glass tubes of 7·5 cm length and 1 cm diameter are coated with 10% solution of PVC in tetrahydrofuran. The tubes are dried at 60°C in a

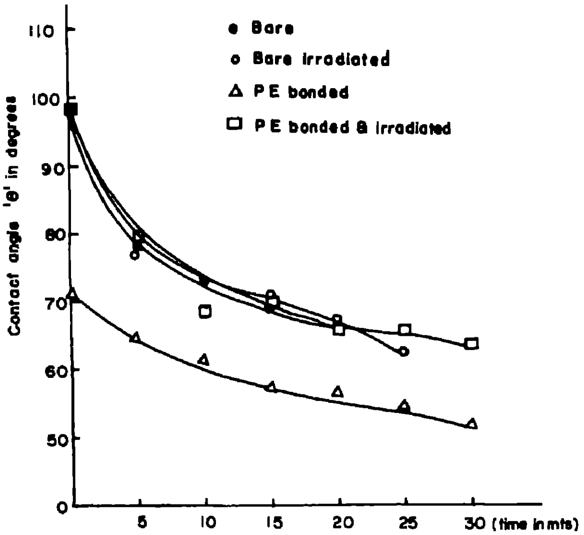

(1)

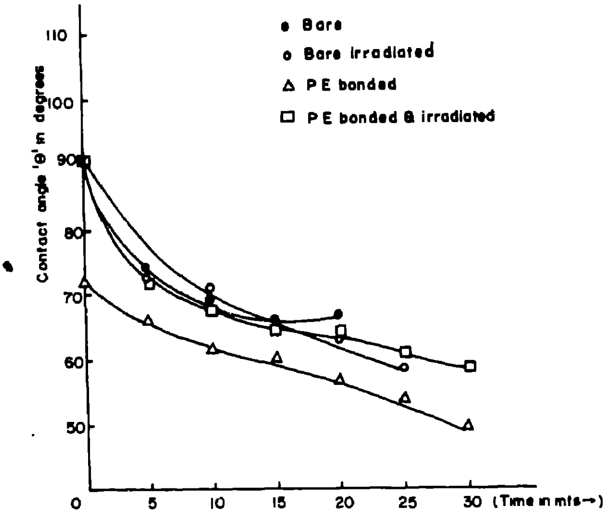

(2)

Figures 1–2. Change in contact angle with time on PVC surfaces **1.** Bhor **2.** SCTIMIST.

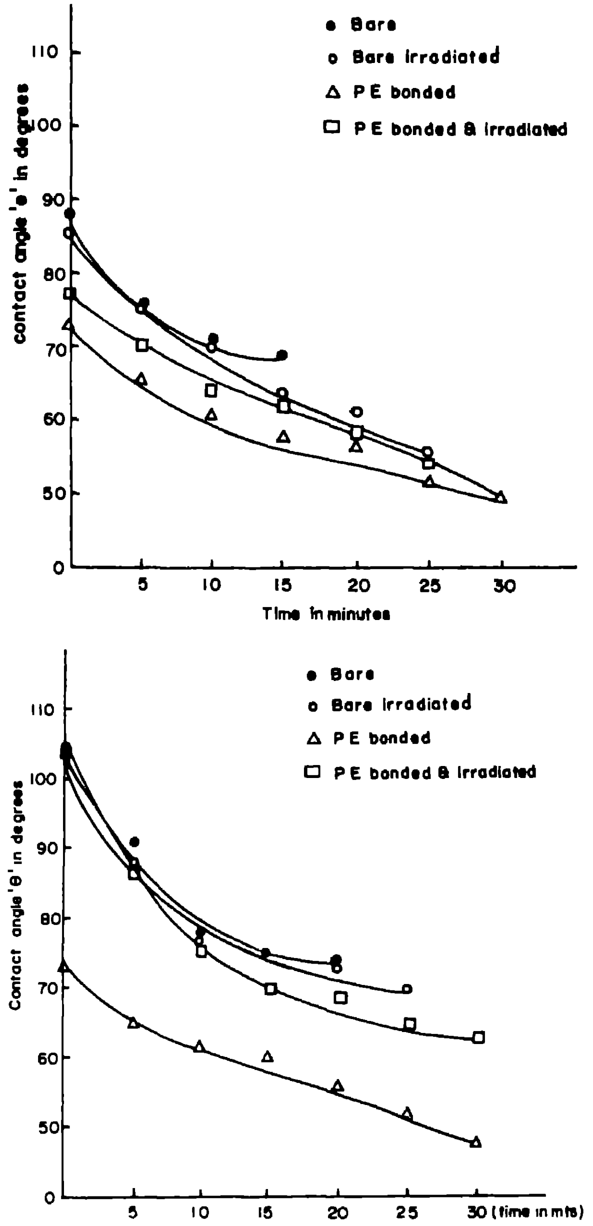

(3)

(4)

Figures 3–4. Change in contact angle with time on PVC surfaces 3. TUTA 4. Fenwal.

vacuum oven. The clotting time for the plasma is determined at 37°C (Austen and Rhymes 1975). The results are tabulated in table 2.

2.2 *Platelet adhesion on PVC surfaces: Preparation of platelet suspension*

Washed calf platelets are prepared and suspended in tyrode solution (Sharma and Chandy 1982) for adhesion studies. The washed PVC sheets are exposed to platelet

Table 1. Inherent viscosity data of various PVC sheets.

PVC sheets	Viscosity (dl/g)
I	1·27
II	1·03
III	1·01
IV	1·08

I—Bhor Industry India Product for SCTIMST. II—Polymer Technology Division Product of our Institute for blood bag applications, submitted by S N Pal, SCTIMST. III—Tuta Industry Australia, blood bag. IV—Fenwal, Travenol Inc. (USA), blood bag.

Table 2. Plasma recalcification time

Surfaces	Plasma recalcification time (sec) SD ($n = 5$)
Plain glass	140 ± 2
I	187 ± 5
II	166 ± 11
III	340 ± 3
IV	198 ± 20

I, II, III and IV are as noted in table 1.

Table 3. Platelet adhesion on various PVC sheets.

	Bare PVC sheets		Polyelectrolyte coated PVC sheets	
PVC sheets	Before γ-irradiation ($n = 10$)	After γ-irradiation ($n = 10$)	Before γ-irradiation ($n = 10$)	After γ-irradiation ($n = 10$)
I	5·8 ± 0·8	4·9 ± 0·7	3·6 ± 0·5	4·2 ± 0·4
II	5 ± 0·8	4·9 ± 0·7	3·6 ± 1·2	4·2 ± 0·5
III	5 ± 1·0	4·9 ± 0·7	3·6 ± 0·53	3·8 ± 1·0
IV	5·8 ± 0·8	5 ± 0·7	3·6 ± 1·2	4·4 ± 0·6

I, II, III and IV are as noted in table 1.

suspension for 1 hr, rinsed with phosphate buffer of pH 7·4 under uniform flow for about 3 min and the platelets are fixed with Coomassie Blue G. The number of platelets adhered to the PVC sheets are accounted using an optical microscope. Different fields are read randomly and averaged in a similar fashion for all samples. The results are given in table 3.

3. Results and discussion

Platelet adhesion and contact angle studies were carried out on bare as well as on polyelectrolyte coated PVC surfaces to investigate the effect of polyelectrolyte coating on PVC towards blood compatibility.

It seems when polyelectrolytes are on the surface the material is improved towards blood compatibility. Platelet adhesion is relatively less as indicated in table 3. Although they are different before modification as indicated by our plasma recalcification time (table 2) and the change in contact angle with time (figures 1–4), the contact angle becomes relatively more stable and the behaviour of the various PVC sheets becomes alike (figures 1–4). After irradiation the effect of polyelectrolyte is no longer obvious as shown in figures 1–4. It becomes a part of the PVC structure such that leaching components do not have any additional resistance as it was before irradiation. Therefore we suggest that PVC surfaces can be improved towards blood compatibility like polyelectrolyte as described above, provided the material is already sterilised by γ-irradiation, since for long term applications ionic bonding of polyelectrolytes with PVC surface may not be stable enough. This modification is suggested for all short term medical applications of PVC coming in contact with blood such as oxygenators and blood bags etc. No adverse change in platelet adherance is observed on modified surfaces if autoclaving sterilization (Sharma and Nirmala 1983) is used instead of CO^{60}, γ-irradiation.

Acknowledgement

The authors appreciate the help received from Dr V N Krishnamurthy of Vikram Sarabhai Space Centre, Trivandrum for ^{60}Co γ-irradiation of our samples, Dr A V Lal for providing calf blood, Mr S N Pal for the PVC samples and Mr Thomas Chandy and Mrs M K Sheela for help.

References

Austen D E G and Rhymes I L 1975 *A laboratory manual of blood coagulation* (Oxford: Blackwell Scientific Publications) p. 35.

Owen B D and Read R L 1979 *J. Polym. Sci., Polym. Chem. Ed.* **17** 2719

Sederel L C, van der Does E, Evverman B J, Bantjes A, Kluft C and Kempen H J M 1983 *Biomaterials* **4** 3

Sharma C P and Chandy T 1982 *J. Colloid Interface Sci.* **89** 479

Sharma C P and Nirmala N V 1983 *Polyvinyl chloride compatibility* at National Seminar on *Recent developments in Polymer Science*, AC College Campus, Madras, December 22 and 23rd, Proceedings to follow in honour of Prof. M Santappa

van der Does L, Bengeling T, Frochling P E and Bantjes A J 1979 *Polym. Sym.* **66** 337

Errata

I. "Lithium solid electrolytes and their application" by D N Bose and D Majumdar, *Bull. Mater.* Sci **6** pp. 223–230 May 1984

The paper falls under the subject "Electrical Properties" and not under "Glasses" as printed in the Contents Page of the Journal.

II. "Electrical properties of polycrystalline silicon and zinc oxide semiconductors" by S N Singh, S Kumari and B K Das, *Bull. Mater. Sci.* **6** pp 243–258 May 1984

(i) On page 247 the lines following the description of eq (3) should read as

For a discrete energy level, on the other hand, ϕ_B is obtained from the solution of equation (Martinez and Piqueras 1980)

$$(8\varepsilon N_D q\phi_B)^{1/2} = qN_{\mathrm{is}}\left[\frac{1}{1+\exp[(E_T - E_{FG} - q\phi_B)/kT]} - \frac{1}{1+\exp[(E_T - E_{FB})/kT]}\right], \tag{4}$$

and (ii) On page 250, the first line of last paragraph of section 2.2c should read as

"A comparison of (11) and (17) shows that the activation energies of μ_{eff} and σ are not identical."

Bulletin of Materials Science

Volume 6, January–December 1984

SUBJECT INDEX

A.C. conductivity
Electrical properties of films at microwave frequencies 1075
Accelerator irradiation
High voltage electron microscope irradiation and observations in metallic glasses 595
Activation energy
Electron transport in non-crystalline garnet films 53
DC electrical conductivity of Na_2O-ZnO-B_2O_3 glass system 1009
Alloy design
Mechanisms and empirical equations for deformation and some principles of alloy design 677
Al-Pu fuels
Plutonium metallurgy in India 923
Al-rare earth system
High resolution electron microscopic studies of $HoAl_3$, $Er_{0.5}$ $Gd_{0.5}$ Al_3 and $Y_{0.91}$ $Er_{0.09}$ Al_3 in thin film form 603
Aluminium alloy
Analytical electron microscopy of aluminium alloys 513
Amorphous character
Effect of compositional modifications on the piezoelectric properties of spray dried lead zirconate titanate ceramics 83
Amorphous ferromagnets
Spin-wave excitations in amorphous ferromagnets 1059
Amorphous films
A novel method of RF powder sputtering 971
Amorphous semiconductors
Electronic conduction in bulk $Se_{1-x}Te_x$ glasses at high pressures and at low temperatures 231
Analytical microscopy
Metallic glasses 579
Anelasticity
Internal friction in hexagonal metals 959
Annealing behaviour
Annealing behaviour of electron-beam deposited tin dioxide films 1029
Anodic dissolution
Electrochemical preparation of potassium gold cyanide 165
Antimony film
Electron diffraction analysis of antimony films 611
Antiphase boundaries
High resolution electron microscopy of long range ordered alloys 417
As-Sb-Se glasses
Elastic properties of As-Sb-Se glasses 1001
Atomistic behaviour
Field ion microscopic observations of LaB_6 on tungsten 573
Austenite
Structure and properties of an investment—cast austenitic stainless steel 119
BCS theory
On the mechanism of pairing in the BCS theory 273
Beam broadening
X-ray microanalysis in the transmission electron microscope 503
Biological molecules
Investigation of hydrogenous materials using neutrons 151
Biquadratic exchange interaction
A Mössbauer study of hyperfine interactions in the boroferrite $Fe_{3-x}Ga_xBO_6$ $(x = 0, 0{\cdot}12)$ 33
Blood compatibility
Surface modification of polyvinyl chloride towards blood compatibility 1087
Boroferrite
A Mössbauer study of hyperfine interactions in the boroferrite $Fe_{3-x}Ga_xBO_6$ $(x = 0, 0{\cdot}12)$ 33
Boron
Structural and magnetic investigations of some new boron containing rare earth intermetallic compounds 263
Breakdown process
Growth of research and development in rare metals extraction in India 901
Burgers vectors
Grain boundary-dislocation interactions 699

Carbon-carbon composites
  Use of coal tar pitch for carbon-carbon composites 91

Carbon matrix
  Use of coal tar pitch for carbon-carbon composites 91

Catalytic oxide
  MnO_2 catalyzed carbon electrodes for dioxygen reduction in concentrated alkali 259

Cavity
  Fracture of particulate composites 799

Centre frequency
  Infrared absorption in spinel ferrites 1063

Ceramic materials
  Effect of compositional modifications on the piezoelectric properties of spray dried lead zirconate titanate ceramics 83

Cermet
  Metal-to-ceramic bonding in (Al_2O_3 + Fe) cermet studied by Mössbauer spectroscopy 13

Chalcogenide films
  Photon, electron and ion beam induced physical and optical densification in chalcogenide films 1013

Chalcogenide glasses
  Electronic conduction in bulk $Se_{1-x}Te_x$ glasses at high pressures and at low temperatures 231

Chaos
  Elementary concepts in chaos and turbulence 807

Chemical beneficiation
  Growth of research and development in rare metals extraction in India 901

Chemical etching
  Evidence of screw dislocations on (002) cleavages of lithium carbonate single crystals 991

Classical statistical mechanics
  Computer simulation of tensile testing 643

Coal-fired MHD generator
  High temperature materials for magnetohydrodynamic channels 71

Cohesive energy
  Strength and electronic structure 717

Composite
  Fracture of particulate composites 799
  Glass-metal particulate composites 193
  Some recent advances in materials technology 405

Computer simulation
  Computer simulation of tensile testing 643

Conducting ceramic
  Preparation and characterisation of β''-Al_2O_3 979

Conducting polymers
  Some recent advances in materials technology 405

CONM model
  Elastic properties of As-Sb-Se glasses 1001

Continual mechanical twinning
  Serrated plastic flow 653

Convergent beam electron diffraction
  Scanning transmission electron microscopy and microdiffraction techniques 477

Cooper pairing
  On the mechanism of pairing in the BCS theory 273

Cooperative behaviour
  Repeated yield drop phenomena as a cooperative effect 665

Corrosion resistance
  Structure and properties of an investment cast austenitic stainless steel 119

Covalency parameters
  Influence of spin orbit coupling and lanthanide contraction on the exchange interaction in rare earth garnets 1069

C-periodicity
  High resolution electron microscopy as a tool for structural investigations 459

Critical exponent
  Magnetic structure of zinc ferrite 27

Critical temperature
  On the mechanism of pairing in the BCS theory 273

Crookes dark space
  A novel method of RF sputtering 971

Crystal puller
  Sophisticated equipment developed for growth and evaluation of perfection of nearly perfect crystals 129

Crystalline solids
  Relevance of liquid state to solid state properties 773

Crystallization behaviour
  Metallic glasses 579

Crystallization temperature
  High voltage electron microscope irradiation and observations in metallic glasses 595

Curie temperature
  Curie temperatures and 0°K magnetic moments of zinc-substituted lithium ferrites 39

Curvature tensor
  Elastic continuum theories of lattice defects: A review 775

Cycle period
  Elevated temperature low cycle fatigue studies on AISI 304 steel 111

Defect characteristics
  High voltage electron microscope irradiation and observations in metallic glasses 595

Defects
  Repeated yield drop phenomena as a cooperative effect 665

Defects
  Effects of mechanical deformation: Exoemission 755

Defect structure
  High resolution electron microscopy of superconductors 453

Deformation mechanisms
  Mechanisms and empirical equations for deformation and some principles of alloy design 677

Delta ferrite
  Structure and properties of an investment cast austenitic stainless steel 119

Delta-stabilised alloys
  Plutonium metallurgy in India 923

Densification mechanism
  Dependence of microstructure on process variables in manganese zinc ferrites 65

Density
  DC electrical conductivity of Na_2O-ZnO-B_2O_3 glass system 1009

Diametral strain
  Elevated temperature low cycle fatigue studies on AISI 304 steel 111

Dielectric constant
  Electrical properties of films at microwave frequencies 1075

Dielectric studies
  Dielectric and pyroelectric studies on triglycine sulphate-polymer composites 105

Diffusional flow
  Superplasticity 689

Dioxygen reduction
  MnO_2 catalyzed carbon electrodes for dioxygen reduction in concentrated alkali 259

Disclinations
  Elastic continuum theories of lattice defects: A review 775

Dislocation
  Etch pit observations on the habit faces of gel grown nickel molybdate crystals 997

Dislocation creep
  Superplasticity 689

Dislocation density correlations
  Elastic continuum theories of lattice defects: A review 775

Dislocation density tensor
  Elastic continuum theories of lattice defects: A review 775

Dislocation dynamics
  Mechanisms and empirical equations for deformation and some principles of alloy design 677

Dislocation interactions
  Grain boundary-dislocation interactions 699

Dislocation-precipitate interaction
  Some aspects of dislocation-precipitate interaction in under-aged aluminium-germanium alloy 1041

Dislocations
  Effects of mechanical deformation: Exoemission 755
  Relevance of liquid state to solid state properties 773
  Elastic continuum theories of lattice defects: A review 775

Disordered materials
  Investigation of hydrogenous materials using neutrons 151

Disordered zones
  Electron microscopy of defect clusters produced by radiation damage 537

Domain structures
  High resolution electron microscopy of long range ordered alloys 417

Dual phase steels
  Applications of scanning transmission electron microscope microanalysis in the study of materials 491

Ductility
  Superplasticity 689

Ductility minimum
  Serrated plastic flow 653

Dynamic strain ageing
  Serrated plastic flow 653

Elastic continuum theory
  Elastic continuum theories of lattice defects: A review 775

Elastic field equations
  Elastic continuum theories of lattice defects: A review 775

Electron emission
  Effects of mechanical deformation: Exoemission 755

Electronic energy
  Strength and electronic structure 717

Electron-mediated interactions
  Strength and electronic structure 717

Electron microscopy
  High resolution electron microscopy of superconductors 453
  Electron microscopy of defect clusters produced by radiation damage 537
  Electron microscopy of layered single crystals grown by direct vapour transport method 549

Electrical conductivity
  Fast ion conducting lithium glasses Review 201
  DC electrical conductivity of Na_2O-ZnO-B_2O_3 glass system 1009

Electrical properties
  Glass-metal particulate composites 193
  Electrical properties of polycrystalline silicon and zinc oxide semiconductors 243

Electrolytic reduction
  Growth of research and development in rare metals extraction in India 901

Electro-optic
  Hydrothermal growth of $A^{II}B^{VI}$ semiconductors 177

Electron beam evaporation
  Annealing behaviour of electron-beam deposited tin dioxide films 1029

Electron diffraction
  Electron diffraction analysis of antimony films 611

Electron exchange
  Influence of the presence of Fe^{2+} ion in nickel-zinc ferrite 7

Electron diffraction
  Formation of lamellar $M_{23}C_6$ on and near twin boundaries in austenitic stainless steels 617

Electron transport
  Electron transport in non-crystalline garnet films 53

Electrochemical preparation
  Electrochemical preparation of potassium gold cyanide 165

Electronic simulation
  Instabilities in yielding 645

Empirical equations
  Mechanisms and empirical equations for deformation and some principles of alloy design 677

Epoxy resin
  Amine-cured epoxy/glass fibre composites 99

Equation of state
  The pressure-volume relation of ytterbium up to 9 GPa 395

Etch pits
  Etch pit observations on the habit faces of gel grown nickel molybdate crystals 997

Exchange constants
  Influence of the presence of Fe^{2+} ion in nickel-zinc ferrite 7
  Influence of spin orbit coupling and lanthanide contraction on the exchange interaction in rare earth garnets 1069

Exchange parameter
  Curie temperatures and 0°K magnetic moments of zinc-substituted lithium ferrites 39

Fast breeder-test reactor
  Plutonium metallurgy in India 923

Ferrimagnetism
  Amorphous state ferroelectricity, magnon scattering and phase stability in microparticle materials 327

Ferrites
  Curie temperatures and 0°K magnetic moments of zinc-substituted lithium ferrites 39
  Infrared absorption in spinel ferrites 1063

Ferroelasticity
  Ferroelasticity 733

Ferroelectric ferroelastics
  Ferroelasticity 733

Ferroelectricity
  Pyroelectric materials 317
  Amorphous state ferroelectricity, magnon scattering and phase stability in microparticle materials 327

Ferroelectrics
  Investigation of hydrogenous materials using neutrons 151

Ferromagnetic resonance
  Ferromagnetic resonance in metallic glasses: study of fracture, stress and thermal stability 1

Field ion microscope
  Details of an imaging atom probe 569

Field ion microscopy
  Field ion microscopic observations of LaB_6 on tungsten 573

First order phase transitions
  Instabilities in first order phase transitions 701

Fissile
  Plutonium metallurgy in India 923

Flow stress
  Serrated plastic flow 653
  Some aspects of dislocation-precipitate interaction in under-aged aluminium-germanium alloy 1041

Fluctuations in materials
  Experimental study of fluctuations in materials 805

Fluorescence and absorption corrections
  X-ray microanalysis in the transmission electron microscope 503

Force constants
  Infrared absorption in spinel ferrites 1063

Fractals
  Fractals 817

Fracture
  Ferromagnetic resonance in metallic glasses: study of fracture, stress and thermal stability 1
  Fracture of particulate composites 799

Frequency-modified life
  Elevated temperature low cycle fatigue studies on AISI 304 steel 111

Gamma Fe_2O_3
  Amorphous state ferroelectricity, magnon scattering and phase stability in microparticle materials 327

Gamma ferric oxide
  Development of pure and doped gamma ferric oxide 59

Garnet
  Mössbauer spectroscopy of titanium-substituted iron garnets 17

Gel grown
  Etch pit observations on the habit faces of gel grown nickel molybdate crystals 997

Glass-forming ability
  Metallic glasses 579

Glass-metal composites
  Glass-metal particulate composites 193

Glass structure
  Fast ion conducting lithium glasses—Review 201

Glassy electrolytes
  Fast ion conducting lithium glasses—Review 201

Gold plating salt
  Electrochemical preparation of potassium gold cyanide 165

Grain boundary
  Superplasticity 689
  Grain boundary—dislocation interactions 699

Grain boundary effects
  Electrical properties of polycrystalline silicon and zinc oxide semiconductors 243

Grains
  Fractals 817

Growth technique
  Electron microscopy of layered single crystals grown by direct vapour transport method 549

Growth temperature
  Preparation of single crystal films of magnetic bubble materials—Rare earth yttrium iron gallium garnets by liquid phase epitaxy and their physical properties 47

Habit faces
  Etch pit observations on the habit faces of gel grown nickel molybdate crystals 997

Hallide metallurgy
  Growth of research and development in rare metals extraction in India 901

Hardness pendulum
  Observations on the physical basis of mechanical behaviour 627

Heat bath
  Experimental study of fluctuations in materials 805

Helium embrittlement
  Radiation effects in nuclear reactor materials—Correlation with structure 339

Hexagonal metals
  Internal friction in hexagonal metals 959

High pressure
  Lithium solid electrolytes and their applications 223
  The pressure-volume relation of ytterbium up to 9 GPa 395

High resolution analysis
  Analytical electron microscopy of aluminium alloys 513

High resolution electron microscopy
  High resolution electron microscopy of long range ordered alloys 417
  High resolution electron microscopy as a tool for structural investigations 459

High resolution electron microscopy
  High resolution electron microscopic studies of $HoAl_3$, $Er_{0.5}Gd_{0.5}Al_3$ and $Y_{0.91}Er_{0.09}Al_3$ in thin film form 603

High resolution microscopy
  Metallic glasses 579

High strength and low alloy steels
  Applications of scanning transmission electron microscope microanalysis in the study of materials 491

High temperature electrode
  High temperature materials for magnetohydrodynamic channels 71

High voltage electron microscopy
  High voltage electron microscope irradiation and observations in metallic glasses 595

High voltage pulser
  Details of an imaging atom probe 569

Hot pressing
  Dependence of microstructure on process variables in manganese zinc ferrites 65

Hydrogen sulphide
  Oxidation of thin films of tin at room temperature in hydrogen sulphide atmosphere 1019

Hydrogenous materials
  Investigation of hydrogenous materials using neutrons 151

Hydrothermal growth
  Hydrothermal growth of $A^{II}B^{VI}$ semiconductors 177

Hyperfine field
  Mössbauer spectroscopy of titanium-substituted iron garnets 17
  Magnetic structure of zinc ferrite 27

Hyperfine interactions
  A Mössbauer study of hyperfine interactions in the boroferrite $Fe_{3-x}Ga_xBo_6$ ($x = 0, 0{\cdot}12$) 33

Imaging atom probe
  Details of an imaging atom probe 569

Imide-amine hardness
  Amine-cured epoxy/glass fibre composites 99

Impact resistance
  Mechanisms and empirical equations for deformation and some principles of alloy design 677

Inhomogeneities
  Elastic continuum theories of lattice defects: A review 775

Instabilities
  Instabilities in yielding 645
  Instabilities in first order phase transitions 701

Insulator materials
  High temperature materials for magnetohydrodynamic channels 71

Intensity ratio
  X-ray microanalysis in the transmission electron microscope 503

Internal friction
  Internal friction in hexagonal metals 959

Investment casting
  Structure and properties of an investment—cast austenitic stainless steel 119

Ionic conductivity studies
  Lithium solid electrolytes and their applications 223

Ionic conductor
  Preparation and characterisation of β''-Al_2O_3 979

Iron garnet
  Mössbauer spectroscopy of titanium-substituted iron garnets 17

Irradiation creep
  Radiation effects in nuclear reactor materials—Correlation with structure 339

Irradiation effects
  Radiation effects in nuclear reactor materials—Correlation with structure 339

Irradiation embrittlement
  Radiation effects in nuclear reactor materials—Correlation with structure 339

Irradiation growth
  Radiation effects in nuclear reactor materials—Correlation with structure 339

Irradiation hardening
  Radiation effects in nuclear reactor materials—Correlation with structure 339

IR spectrum
  Infrared absorption in spinel ferrites 1063

Jahn-Teller ion spinels
  Influence of the presence of Fe^{2+} ion in nickel-zinc ferrite 7

Kataoka-Yamada theory
  Temperature dependence of microhardness in mixed crystals 1035

Lamellar $M_{23}C_6$
  Formation of lamellar $M_{23}C_6$ on and near twin boundaries in austenitic stainless steels 617

Lanthanum hexaboride
  Field ion microscopic observations of LaB_6 on tungsten 573

Laser devices
  Hydrothermal growth of $A^{II}B^{VI}$ semiconductors 177

Lattice defects
  Elastic continuum theories of lattice defects: A review 775

Lattice imaging
  High resolution electron microscopy as a tool for structural investigations 459
  High resolution electron microscopic studies of $HoAl_3$, $Er_{0.5}Gd_{0.5}Al_3$ and $Y_{0.91}Er_{0.09}Al_3$ in thin film form 603

Lead zirconate titanate
  Effect of compositional modifications on the piezoelectric properties of spray dried lead zirconate titanate ceramics 83

Lead zirconate titanate
  Amorphous state ferroelectricity, magnon scattering and phase stability in microparticle materials 327

Limit cycle solutions
  Repeated yield drop phenomena as a cooperative effect 665

Liquid metal-cooled fast breeder reactors
  Plutonium metallurgy in India 923

Liquid phase epitaxy
  Preparation of single crystal films of magnetic bubble materials—Rare earth yttrium iron gallium garnets by liquid phase epitaxy and their physical properties 47

Liquid state properties
  Relevance of liquid state to solid state properties 773

Lithium carbonate single crystals
  Evidence of screw dislocations on (002) cleavages of lithium carbonate single crystals 991

Lithium ion conductors
  Lithium solid electrolytes and their applications 223

Localised spin canting
  Curie temperatures and 0°K magnetic moments of zinc-substituted lithium ferrites 39

Long range order
  High resolution electron microscopy of long range ordered alloys 417

Low cycle fatigue
  Elevated temperature low cycle fatigue studies on AISI 304 steel 111

Macroscopically defect free cement
  Some recent advances in materials technology 405

Magnetisation
  Curie temperatures and 0°K magnetic moments of zinc-substituted lithium ferrites 39

Magnetic bubble materials
  Preparation of single crystal films of magnetic bubble materials—Rare earth yttrium iron gallium garnets by liquid phase epitaxy and their physical properties 47

Magnetic properties
  Magnetic properties of metallic glass $Fe_{39}Ni_{39}Mo_4Si_6B_{12}$ 21
  Glass-metal particulate composites 193

Magnetic recording materials
  Development of pure and doped gamma ferric oxide 59

Magnetic structure
  Magnetic structure of zinc ferrite 27

Magnetic susceptibility
  Structural and magnetic investigations of some new boron containing rare earth intermetallic compounds 263

Magnetic hyperfine field distributions
  Evaluation of magnetic hyperfine field distributions from Mössbauer spectra of disordered alloys and metallic glasses 1047

Magnon scattering
  Amorphous state ferroelectricity, magnon scattering and phase stability in microparticle materials 327

Martensitic transformation
  Deformation and martensitic transformation 703

Manganese zinc ferrites
  Dependence of microstructure on process variables in manganese zinc ferrites 65

Mechanical behaviour
  Observations on the physical basis of mechanical behaviour 627
  Experimental study of fluctuations in materials 805

Mechanical deformation
  Effects of mechanical deformation: Exoemission 755

Mechanical properties
  Structure and properties of an investment—cast austenitic stainless steel 119
  Glass-metal particulate composites 193

Melt-quenching
  Metallic glasses 579

Metglasses
  Some recent advances in materials technology 405

Metal-ceramic joint
  High temperature materials for magnetohydrodynamic channels 71

Metal excess systems
  Structure and superconductivity in ternary systems of compounds 283

Metal-hydrogen systems
  Investigation of hydrogenous materials using neutrons 151

Metastable crystalline states
  Electron diffraction analysis of antimony films 611

Metastable phases
  Analytical electron microscopy of aluminium alloys 513

Metallic glasses
  Ferromagnetic resonance in metallic glasses: study of fracture, stress and thermal stability 1
  Magnetic properties of metallic glass $Fe_{39}Ni_{39}Mo_4Si_6B_{12}$ 21
  Metallic glasses 579
  High voltage electron microscope irradiation and observations in metallic glasses 595
  Spin-wave excitations in amorphous ferromagnets 1059
  Evaluation of magnetic hyperfine field distributions from Mössbauer spectra of disordered alloys and metallic glasses 1047

Microanalysis
  Applications of scanning transmission electron microscope microanalysis in the study of materials 491

Microdiffraction
  Scanning transmission electron microscopy and microdiffraction techniques 477

Microemulsion
  Amorphous state ferroelectricity, magnon scattering and phase stability in microparticle materials 327

Microfocus x-ray generator
  Sophisticated equipment developed for growth and evaluation of perfection of nearly perfect crystals 129

Microhardness
  Temperature dependence of microhardness in mixed crystals 1035

Microparticle
  Amorphous state ferroelectricity, magnon scattering and phase stability in microparticle materials 327

Microstructure
  Structure and properties of an investment—cast austenitic stainless steel 119

Microwaves
  Electrical properties of films at microwave frequencies 1075

Mixed crystals
  Temperature dependence of microhardness in mixed crystals 1035

Mixed oxide and carbide fuels
  Plutonium metallurgy in India 923

MnO_2
  MnO_2 catalyzed carbon electrodes for dioxygen reduction in concentrated alkali 259

Modulated phases
  High resolution electron microscopic studies of $HoAl_3$, $Er_{0.5}Gd_{0.5}Al_3$ and $Y_{0.91}Er_{0.09}Al_3$ in thin film form 603

Modulated structure
  High resolution electron microscopy of long range ordered alloys 417

Molecular field constants
  Influence of spin orbit coupling and lanthanide contraction on the exchange interaction in rare earth garnets 1069

Morphotropic phase boundary
  Effect of compositional modifications on the piezoelectric properties of spray dried lead zirconate titanate ceramics 83

Mössbauer measurements
  Spin-wave excitations in amorphous ferromagnets 1059

Mössbauer spectra
  Mössbauer spectroscopy of titanium-substituted iron garnets 17

Mössbauer spectra
  Evaluation of magnetic hyperfine field distributions from Mössbauer spectra of disordered alloys and metallic glasses 1047

Mössbauer spectroscopy
  Metal-to-ceramic bonding in $(Al_2O_3 + Fe)$ cermet studied by Mössbauer spectroscopy 13
  Magnetic properties of metallic glass $Fe_{39}Ni_{39}Mo_4Si_6B_{12}$ 21
  Amorphous state ferroelectricity, magnon scattering and phase stability in microparticle materials 327

Mössbauer study
  A Mössbauer study of hyperfine interactions in the boroferrite $Fe_{3-x}Ga_xBO_6$ ($x = 0, 0{\cdot}12$) 33

Na_2-ZnO-B_2O_3 glass
  DC electrical conductivity of Na_2O-ZnO-B_2O_3 glass system 1009

Neutrons
  Investigation of hydrogenous materials using neutrons 151

Nickel alloys
  Radiation effects in nuclear reactor materials—Correlation with structure 339

Nickel-zinc ferrite
  Influence of the presence of Fe^{2+} ion in nickel-zinc ferrite 7

$NiMoO_4 \cdot xH_2O$ crystals
  Etch pit observations on the habit faces of gel grown nickel molybdate crystals 997

NMR
  Lithium solid electrolytes and their applications 223

Non-crystalline garnet
  Electron transport in non-crystalline garnet films 53

Non-integral dimensions
  Fractals 817

Nonlinear dynamics
  Elementary concepts in chaos and turbulence 807

Nonlinear Langevin equations
  Repeated yield drop phenomena as a cooperative effect 665

Non-local elasticity
  Elastic continuum theories of lattice defects: A review 775

Nuclear electricity
  Plutonium metallurgy in India 923

Nuclear reactor materials
  Radiation effects in nuclear reactor materials—Correlation with structure 339

Optical densification
  Photon, electron and ion beam induced physical and optical densification in chalcogenide films 1013

Optical properties
  Glass-metal particulate composites 193

Ordering kinetics
  Phase transformations—a physicist's perception 837

Overlap integrals
  Magnetic structure of zinc ferrite 27

Oxidation
  Oxidation of thin films of tin at room temperature in hydrogen sulphide atmosphere 1019

Oxide glasses
  Glass-metal particulate composites 193

Pairing interaction
  On the mechanism of pairing in the BCS theory 273

Phase changes
  Electron diffraction analysis of antimony films 611

Phase diagrams
  Phase transformations—a physicist's perception 837

Phase identification
  Analytical electron microscopy of aluminium alloys 513

Phase transformations
  Electron microscopy of layered single crystals grown by direct vapour transport method 549
  Phase transformations—a physicist's perception 837

Phase transitions
  Ferroelasticity 733

Physical beneficiation
  Growth of research and development in rare metals extraction in India 901

Piezoelectric
  Hydrothermal growth of $A^{II}B^{VI}$ semiconductors 177

Piezoelectricity
  Effect of compositional modifications on the piezoelectric properties of spray dried lead zirconate titanate ceramics 83
  Pyroelectric materials 317

Plastic deformation
  Deformation and martensitic transformation 703

Plastic properties
  Elastic properties of As-Sb-Se glasses 1001

Plating
  Electrochemical preparation of potassium gold cyanide 165

Plutonium
  Plutonium metallurgy in India 923

Point defect clusters
  Electron microscopy of defect clusters produced by radiation damage 537

Polycrystalline semiconductors
  Electrical properties of polycrystalline silicon and zinc oxide semiconductors 243

Polymers
  Investigation of hydrogenous materials using neutrons 151

Polysilicon
  Electrical properties of polycrystalline silicon and zinc oxide semiconductors 243

Polytype in SiC
  High resolution electron microscopy as a tool for structural investigations 459

Polytype structures
  Structural disorder and solid state transformations in single crystals of $Zn_xCd_{1-x}S$ and $Zn_xM_{1-x}S$ 369

Polyvinyl chloride
  Surface modification of polyvinyl chloride towards blood compatibility 1087

Potassium gold cyanide
  Electrochemical preparation of potassium gold cyanide 165

Precipitation morphology
  Formation of lamellar $M_{23}C_6$ on and near twin boundaries in austenitic stainless steels 617

Pressure-induced semiconductor-to-metal transitions
  Electronic conduction in bulk $Se_{1-x}Te_x$ glasses at high pressures and at low temperatures 231

Pseudoelasticity
  Deformation and martensitic transformation 703

Pu-Be neutron sources
  Plutonium metallurgy in India 923

Pyroelectricity
  Pyroelectric materials 317

Pyroelectric studies
  Dielectric and pyroelectric studies on triglycine sulphate-polymer composites 105

Quantitative model
  X-ray microanalysis in the transmission electron microscope 503

Quadrupole splitting
  Mössbauer spectroscopy of titanium-substituted iron garnets 17

Radiation damage
  Radiation effects in nuclear reactor materials—Correlation with structure 339
  High resolution electron microscopy of superconductors 453
  Electron microscopy of defect clusters produced by radiation damage 537

Random distribution model
  A Mössbauer study of hyperfine interactions in the boroferrite $Fe_{3-x}Ga_xBO_6$ ($x = 0, 0{\cdot}12$) 33

Rapid solidification techniques
  Metallic glasses 579

Rare earths
  Structural and magnetic investigations of some new boron containing rare earth intermetallic compounds 263

Rare metal extraction
  Growth of research and development in rare metals extraction in India 901

Relaxation
  Spin wave relaxation processes in polycrystalline yttrium iron garnets 1053

Repeated yield drop
  Repeated yield drop phenomena as a cooperative effect 665

Resistance change
  Oxidation of thin films of tin at room temperature in hydrogen sulphide atmosphere 1019

RF sputtering
  A novel method of RF powder sputtering 971

Saturation temperature
  Preparation of single crystal films of magnetic bubble materials—Rare earth yttrium iron gallium garnets by liquid phase epitaxy and their physical properties 47

Scanning electron microscopy
  A novel method of RF powder sputtering 971

Selective surfaces
  Some recent advances in materials technology 405

Semiconductors
  Hydrothermal growth of $A^{II}B^{VI}$ semiconductors 177

Separation process
  Growth of research and development in rare metals extraction in India 901

Serrated flow
  Serrated plastic flow 653

Shape memory effect
  Deformation and martensitic transformation 703

Sheet resistivity
  Annealing behaviour of electron-beam deposited tin dioxide films 1029

Shield
  A novel method of RF powder sputtering 971

Shock deformation
  Shocks and high velocity deformation 633

Shock front
  Mechanisms and empirical equations for deformation and some principles of alloy design 677

Shock melting
  Shocks and high velocity deformation 633

Shock propagation
  Shocks and high velocity deformation 633

Single crystals
  Structural disorder and solid state transformations in single crystals of $Zn_xCd_{1-x}S$ and $Zn_xMn_{1-x}S$ 369

Silicon carbide
  High resolution electron microscopy as a tool for structural investigations 459

Sintering
  Dependence of microstructure on process variables in manganese zinc ferrites 65
  Effect of compositional modifications on the piezoelectric properties of spray dried lead zirconate titanate ceramics 83

Slag ceramic interaction
  High temperature materials for magnetohydrodynamic channels 71

Slip lines
  Some aspects of dislocation-precipitate interaction in under-aged aluminium-germanium alloy 1041

Sodium beta alumina
  Preparation and characterisation of β''-Al_2O_3 979

Solid electrolyte
  Preparation and characterisation of β''-Al_2O_3 979

Solid state batteries
  Fast ion conducting lithium glasses—Review 201

Solid state properties
  Relevance of liquid state to solid state properties 773

Spinel
  Metal-to-ceramic bonding in (Al_2O_3 + Fe) cermet studied by Mössbauer spectroscopy 13

Spinodal decomposition
  Phase transformations—a physicist's perception 837

Spin-reorientation
  A Mössbauer study of hyperfine interactions in the boroferrite $Fe_{3-x}Ga_xBO_6$ ($x = 0, 0{\cdot}12$) 33

Spin wave excitations
  Spin-wave excitations in amorphous ferromagnets 1059

Spin-wave line-widths
  Spin wave relaxation processes in polycrystalline yttrium iron garnets 1053

Spiral etch pits
  Evidence of screw dislocations on (002) cleavages of lithium carbonate single crystals 991

Spray drying
  Effect of compositional modifications on the piezoelectric properties of spray dried lead zirconate titanate ceramics 83

Stacking fault energy
  Electron microscopy of layered single crystals grown by direct vapour transport method 549

Stacking sequence
  High resolution electron microscopy as a tool for structural investigations 459

Stainless steel
  Structure and properties of an investment—cast austenitic stainless steel 119
  Radiation effects in nuclear reactor materials—Correlation with structure 339

STEM
  Applications of scanning transmission electron microscope microanalysis in the study of materials 491

Strain rates
  Elevated temperature low cycle fatigue studies on AISI 304 steel 111

Strength
  Strength and electronic structure 717

Strengthening mechanisms
  Strength and electronic structure 717

Stress
  Ferromagnetic resonance in metallic glasses: study of fracture, stress and thermal stability 1
  Effects of mechanical deformation: Exoemission 755

Stress and strain rate
  Superplasticity 689

Structural characterization
  High resolution electron microscopic studies of $HoAl_3$, $Er_{0{\cdot}5}Gd_{0{\cdot}5}Al_3$ and $Y_{0{\cdot}91}Er_{0{\cdot}09}Al_3$ in thin film form 603

Structural disorder
  Structural disorder and solid state transformations in single crystals of $Zn_xCd_{1-x}S$ and $Zn_xMn_{1-x}S$ 369

Structural investigation
  High resolution electron microscopy as a tool for structural investigations 459

Sublattices
  Influence of the presence of Fe^{2+} ion in nickel-zinc ferrite 7

Superconducting compounds
  Structure and superconductivity in ternary systems of compounds 283

Super conducting materials
  High resolution electron microscopy of superconductors 453

Superconductivity
  On the mechanism of pairing in the BCS theory 273

Superconductors
  Investigation of hydrogenous materials using neutrons 151

Superexchange
  Influence of spin orbit coupling and lanthanide contraction on the exchange interaction in rare earth garnets 1069

Superplasticity
  Superplasticity 689

Superstructure
  High resolution electron microscopy of long range ordered alloys 417

Surface modification
  Surface modification of polyvinyl chloride towards blood compatibility 1087

Surface states
  Observations on the physical basis of mechanical behaviour 627

Surface studies
  Scanning transmission electron microscopy and microdiffraction techniques 477

Structural investigations
  Structural and magnetic investigations of some new boron containing rare earth intermetallic compounds 263

Surface roughness
  Observations on the physical basis of mechanical behaviour 627

Symmetry
  Ferroelasticity 733

Target
  A novel method of RF powder sputtering 971

Temperature dependence
  Spin-wave excitations in amorphous ferromagnets 1059
  Temperature dependence of microhardness in mixed crystals 1035

Tensile testing
  Computer simulation of tensile testing 643
  Instabilities in yielding 645

Ternary systems
  Structure and superconductivity in ternary systems of compounds 283

Theoretical models
  Structural disorder and solid state transformations in single crystals of $Zn_xCd_{1-x}S$ and $Zn_xMn_{1-x}S$ 369

Thermal decomposition
  Development of pure and doped gamma ferric oxide 59

Thermal hysteresis
  A Mössbauer study of hyperfine interactions in the boroferrite $Fe_{3-x}Ga_xBO_6$ ($x = 0, 0{\cdot}12$) 33

Thermal stability
  Ferromagnetic resonance in metallic glasses: study of fracture, stress and thermal stability 1

Thermo-compression bonds
  Metal-to-ceramic bonding in (Al_2O_3 + Fe) cermet studied by Mössbauer spectroscopy 13

Thermoplastic
  Use of coal tar pitch for carbon-carbon composites 91

Thermopower
  Lithium solid electrolytes and their applications 223

Thin films
  Electron transport in non-crystalline garnet films 53
  Oxidation of thin films of tin at room temperature in hydrogen sulphide atmosphere 1019

Tilt boundaries
  Evidence of screw dislocations on (002) cleavages of lithium carbonate single crystals 991

Tin
  Oxidation of thin films of tin at room temperature in hydrogen sulphide atmosphere 1019

Tin dioxide films
  Annealing behaviour of electron-beam deposited tin dioxide films 1029

Torsion tensor
  Elastic continuum theories of lattice defects: A review 775

Transfer integrals
  Influence of spin orbit coupling and lanthanide contraction on the exchange interaction in rare earth garnets 1069

Transition metal dichalcogenides
  Electron microscopy of layered single crystals grown by direct vapour transport method 549

Transmission electron microscopy
  X-ray microanalysis in the transmission electron microscope 503
  A novel method of RF powder sputtering 971

Transport number
  Fast ion conducting lithium glasses—Review201

Triglycine sulphate polymers
  Dielectric and pyroelectric studies on triglycine sulphate-polymer composites 105

Tungsten field evaporation
  Field ion microscopic observations of LaB_6 on tungsten 573

Turbulence
  Elementary concepts in chaos and turbulenCe 807

Twin boundaries
  Formation of lamellar $M_{23}C_6$ on and near twin boundaries in austenitic stainless steels 617

Twinning
  Ferroelasticity 733

Twist boundaries
  Evidence of screw dislocations on (002) cleavages of lithium carbonate single crystals 991

Under-aged
  Some aspects of dislocation-precipitate interaction in under-aged aluminium-germanium alloy 1041

Uranium
  Radiation effects in nuclear reactor materials—Correlation with structure 339

Vacuum casting
  Structure and properties of an investment—cast austenitic stainless steel 119

Void growth
  Fracture of particulate composites 799

Void nucleation
  Fracture of particulate composites 799

Void swelling
  Radiation effects in nuclear reactor materials—Correlation with structure 339

Waveguide
  Electrical properties of films at microwave frequencies 1075

Work hardening peaks
  Serrated plastic flow 653

X-ray diffraction
  The pressure-volume relation of ytterbium up to 9 GPa 395
  Electron microscopy of layered single crystals grown by direct vapour transport method 549

X-ray diffraction topography camera
  Sophisticated equipment developed for growth and evaulation of perfection of nearly perfect crystals 129

X-ray diffractometer
  Sophisticated equipment developed for growth and evaluation of perfection of nearly perfect crystals 129

X-ray microanalysis
  X-ray microanalysis in the transmission electron microscope 503
  Analytical electron microscopy of aluminium alloys 513

Yielding
  Instabilities in yielding 645

Ytterbium
  The pressure-volume relation of ytterbium up to 9 GPa 395

Yttrium iron garnet
  Amorphous state ferroelectricity, magnon scattering and phase stability in microparticle materials 327
  Spin wave relaxation processes in polycrystalline yttrium iron garnets 1053

Zinc ferrite
  Magnetic structure of zinc ferrite 27

Zirconium alloys
  Radiation effects in nuclear reactor materials—Correlation with structure 339

ZnO varistors
  Electrical properties of polycrystalline silicon and zinc oxide semiconductors 243

AUTHOR INDEX

Agarwal M K
Electron microscopy of layered single crystals grown by direct vapour transport method 549

Aiyar R
see Venkataramani N 65
see Srivastava C M 1069

Amelinckx S
High resolution electron microscopy of long range ordered alloys 417

Ananthakrishna G
Repeated yield drop phenomena as a cooperative effect 665

Anantharaman M R
Development of pure and doped gamma ferric oxide 59

Anavekar R V
DC electrical conductivity of Na_2O-ZnO-B_2O_3 glass system 1009

Asundi M K
Internal friction in hexagonal metals 959

Ayyub P
see Multani M S 327

Bahadur D
see Srivastava C M 17
Electron transport in non-crystalline garnet films 53

Balakrishnan V
Summary and outlook 823

Balasubramanian N
see Ramaseshan S 405

Banerjee S
Electron microscopy of defect clusters produced by radiation damage 537
Instabilities in first order phase transitions 701

Bansal C
Metal-to-ceramic bonding in (Al_2O_3 + Fe) cermet studied by Mössbauer spectroscopy 13
Evaluation of magnetic hyperfine field distributions from Mössbauer spectra of disordered alloys and metallic glasses 1047

Bhatia S N
Spin wave relaxation processes in polycrystalline yttrium iron garnets 1053

Bhatnagar Anil K
see Parashar R S 1
see Prasad B Bhanu 21
Spin-wave excitations in amorphous ferromagnets 1059

Bhat T Balakrishna
Mechanisms and empirical equations for deformation and some principles of alloy design 677

Bose D N
Lithium solid electrolytes and their applications 223

Chakravorty D
Glass-metal particulate composites 193

Chandrasekharaiah M N
see Prasad B Bhanu 21

Chatterjee S N
see Kishan Pran 39

Chidambaram R
Shocks and high velocity deformation 633

Chopra K L
Photon, electron and ion beam induced physical and optical densification in chalcogenide films 1013

Cowley J M
Scanning transmission electron microscopy and microdiffraction techniques 477

Dasannacharya B A
Investigation of hydrogenous materials using neutrons 151

Das B K
see Singh S N 243
see Kalsi H S 979

Datta K K
see Seth R L 91

Devaraj N
see Anavekar R V 1009

Dhar Ajay
see Sreenivas K 105

Dhar D
Fractals 817

Dhar S K
see Malik S K 263

Dube D C
Electrical properties of films at microwave frequencies 1075

Embury J D
see Ramachandran T R 513

Ganguly C
see Roy P R 923

Geetha Balakrishnan
see Rao G V Subba 283

Geetha Kurian
Surface modification of polyvinyl chloride towards blood compatibility 1087

Giridhar A
Elastic properties of As-Sb-Se glasses 1001

Goel R C
see Kalsi H S 979

- Gopal E S R
  - *see* Parthasarathy G 231
- Goyal P S
  - *see* Dasannacharya B A 151
- Gupta Arjeesh
  - Annealing behaviour of electron-beam deposited tin dioxide films 1029
- Gupta C K
  - *see* Sundaram C V 901
- Gupta M S
  - *see* Singh Anand Kumar 603
- Harshavardhan K Solomon
  - *see* Chopra K L 1013
  - A novel method of RF powder sputtering 971
- Houghton D C
  - *see* Ramachandran T R 513
- Indira Rajagopal
  - Electrochemical preparation of potassium gold cyanide 165
- Ittyachen M A
  - *see* Kurien K V 997
- Jagannathan R
  - *see* Vithal M 33
  - *see* Bhatnagar Anil K 1059
- Jebaraj P M
  - Structure and properties of an investment—cast austenitic stainless steel 119
- Joag D B
  - Field ion microscopic observations of LaB_6 on tungsten 573
- Joglekar S M
  - *see* Srivastava C M 7
- Joshi P B
  - *see* Bhatia S N 1053
- Kalsi H S
  - Preparation and characterisation of β''-Al_2O_3 979
- Kanitkar M M
  - *see* Joag D B 573
- Kanitkar P L
  - *see* Joag D B 573
- Keer H V
  - *see* Anantharaman M R 59
- Kishan Pran
  - Curie temperatures and 0°K magnetic moments of zinc-substituted lithium ferrites 39
- Kishore
  - Some aspects of dislocation-precipitate interaction in under-aged aluminium-germanium alloy 1041
- Krishna K N
  - *see* Harshavardhan K Solomon 971
- Krishan Lal
  - Sophisticated equipment developed for growth and evaluation of perfection of nearly perfect crystals 129
- Krishnan R
  - *see* Rodriguez P 339
- Krishna P
  - *see* Sebastian M T 369
- Kshatriya J D
  - *see* Agarwal M K 549
- Kulkarni A R
  - Fast ion conducting lithium glasses—Review 201
- Kumari S
  - *see* Singh S N 243
- Kurien K V
  - Etch pit observations on the habit faces of gel grown nickel molybdate crystals 997
- Kuzmina I P
  - *see* Kuznetsov V A 177
- Kuznetsov V A
  - Hydrothermal growth of $A^{II}B^{VI}$ semiconductors 177
- Laddha G S
  - *see* Raju K S 991
- Lal C
  - *see* Seth R L 91
- Lal Ramji
  - Effect of compositional modifications on the piezoelectric properties of spray dried lead zirconate titanate ceramics 83
- Landuyt J Van
  - *see* Amelinckx S 417
- Laroia K K
  - *see* Kishan Pran 39
- Lorimer G W
  - X-ray microanalysis in the transmission electron microscope 503
- Maiti H S
  - *see* Kulkarni A R 201
- Majumdar D
  - *see* Bose D N 223
- Malhotra L K
  - *see* Chopra K L 1013
- Malik S K
  - Structural and magnetic investigations of some new boron containing rare earth intermetallic compounds 263
- Manoharan R
  - MnO_2 catalyzed carbon electrodes for dioxygen reduction in concentrated alkali 259
- Mansingh Abhai
  - *see* Sreenivas K 105
- Mittal V P
  - *see* Seth R L 91
- Mohandas E
  - *see* Seshadri V R 569
- Mukhopadhyay G
  - Effects of mechanical deformation: Exoemission 755

Multani M S
Amorphous state ferroelectricity, magnon scattering and phase stability in microparticle materials 327

Muneera C I
Oxidation of thin films of tin at room temperature in hydrogen sulphide atmosphere 1019

Murthy H R Krishna
Relevance of liquid state to solid state properties 773

Nagpaul L K
see Kishan Pran 39

Nandedkar R V
High voltage electron microscope irradiation and observations in metallic glasses 595

Nayar V Unnikrishnan
see Muneera C I 1019

Neelakantan K
see Seshadri V R 569

Om Prakash
see Srivastava C M 17

Palaniswamy M
see Raju K S 991

Palkar V R
see Multani M S 327

Pande C S
High resolution electron microscopy of superconductors 453

Parashar R S
Ferromagnetic resonance in metallic glasses: study of fracture, stress and thermal stability 1

Parthasarathy G
Electronic conduction in bulk $Se_{1-x}Te_x$ glasses at high pressures and at low temperatures 231

Patel J V
see Agarwal M K 549

Patel P D
see Agarwal M K 549

Patni M J
see Srivastava C M 7
see Srinivasan T T 1063

Paul A
see Kulkarni A R 201

Poonam Gupta
see Gupta Arjeesh 1029

Prabhawalker P D
Electron diffraction analysis of antimony films 611

Pragati Mukhopadhyay
Preparation of single crystal films of magnetic bubble materials—Rare earth yttrium iron gallium garnets by liquid phase epitaxy and their physical properties 47

Prasad B Bhanu
Magnetic properties of metallic glass $Fe_{39}Ni_{39}Mo_4Si_6B_{12}$ 21
see Bhatnagar Anil K 1059

Purdy Gary R
Applications of scanning transmission electron microscope microanalysis in the study of materials 491

Raghavan K Srinivasa
Superplasticity 689

Raghunathan V S
see Seshadri V R 569

Rai R S
see Singh G 459

Raj R G
see Varma D S 99

Rajagopalan S
see Chopra K L 1013

Rajagopalan S R
see Indira Rajagopal 165

Rajan K Govinda
Strength and electronic structure 717

Raju K S
Evidence of screw dislocations on (002) cleavages of lithium carbonate single crystals 991

Ramachandran T R
Analytical electron microscopy of aluminium alloys 513

Ramakrishna J
see Anavekar R V 1009

Ramakrishnan P
see Lal Ramji 83

Ramakrishnan T V
see Murthy H R Krishna 773

Ramasamy P
see Raju K S 991

Ramaswamy Ramakrishna
Elementary concepts in chaos and turbulence 807

Ramaseshan S
Some recent advances in materials technology 405
Observations on the physical basis of mechanical behaviour 627

Ranganathan S
Grain boundary-dislocation interactions 699

Rao C N
see Asundi M K 959

Rao K R
Experimental study of fluctuations in materials 805

Rao T Sudersena
see Sreenivas K 105

Rao G V Subba
Structure and superconductivity in ternary systems of compounds 283

Rao B Uma Maheshwar
see Srivastava C M 17
see Pragati Mukhopadhyay 47